SF2A 2013
L. Cambrésy, F. Martins, E. Nuss and A. Palacios (eds)

Proceedings of the annual meeting of the French Society of Astronomy & Astrophysics

Montpellier, June 4-7, 2013

Credit: Christophe Mercier

Contents

Foreword

The 2013 annual meeting of the French Society of Astronomy and Astrophysics (Société Française d'Astronomie et d'Astrophysique – SF2A) was hosted by the Laboratoire Univers et Particules de Montpellier from June 4 to 7. These "Journées" gathered about 320 professional astronomers and astrophysicists, who participated to plenary sessions organized by the SF2A and to workshops organized by the scientific committees of the "National Programs" and "Actions Spécifiques" of INSU-CNRS, several of them in collaboration with our special guest, the Nederlandse Astronomenclub (NAC).

During the plenary sessions excellent scientific reviews were presented on outstanding scientific results obtained recently by our community. Also, general interest talks led to topical discussions on scientific projects (e.g. at CFHT as presented by D. Devost) as well as on the organization and the future of french astronomical research in the international environment. In particular, the latest news on the reform of the International Astronomical Union was introduced by the General Secretary T. Montmerle, D. Mourard provided the community with information of the Institut National des Sciences de l'Univers (INSU-CNRS), and G. Chardin presented the activities related to astrophysics at the Institut National de Physique Nucléaire et de Physique des Particules (IN2P3-CNRS).

This year fifteen scientific workshops were organized on topical subjects, and two additional sessions were devoted to outreach and communication in astronomy and in sciences of the universe at large and to the organization of astronomy teaching at the Master level. A special session was organized between post-docs/students and former members of hiring committees in order to help the young researchers to build their applications for local and national jobs.

A large number of SF2A members attended the General Assembly where the annual activity and financial reports of our Society were presented by the president and treasurer of the SF2A Council, C.Reylé and S.Boissier. The 2013 SF2A "Thesis Prize" was presented to A. Strugarek by F. Combes (Paris Observatory) and the 2013 SF2A prize "Jeune Chercheur" was presented to K. Belkacem by J.P. Zahn (Paris Observatory) and G. Richard (HP). We warmly thank the sponsors of these prizes, respectively EdP Sciences and the HP company, for their continuing interest in our science and support to our Society. The first prize for the best French-Spanish collaboration was presented to E. Lellouch and P. Santos-Sanz by C. Reylé (president of the SF2A) and F. Figueras (vice president of the SEA). Following the award ceremony an excellent cocktail was served in the buildings and patio of the old Faculty of medicine (the oldest in France). The guests could enjoy wine tasting organized by local wine producers.

Along the Journées a number of social, outreach, and cultural events were organized. The SF2A Prize "Découvrir l'Univers" sponsored by EdP Sciences and Bayard Jeunesse was a wonderful success, with no more than twenty projects from schools all over Languedoc-Roussillon. The prizes were presented to collège de Lédignan, collège François Mitterrand of Toulouges, and école primaire Le Parterre of Bédarieux. The Montpellier city special prize was presented to école maternelle Cervantes of Montpellier. The award ceremony was held in the planetarium Galilé of Montpellier Agglomération. It was followed by a movie session offered by the planetarium to all the laureates. The official SF2A reception was offered by the city of Montpellier in the new city hall, where A. Crida gave an excellent public conference on the formation of the solar system.

We wish to thank the INSU-CNRS, the IN2P3-CNRS, the University of Montpellier II, the labex OCEVU, the Laboratoire Univers et Particules de Montpellier, as well as the CNES, the CEA, the National Programs and Actions Spécifiques of INSU-CNRS, the Mairie de Montpellier, Montpellier Agglomération and the Région

Languedoc-Roussillon for their financial and organisational support. We are extremely grateful to the University of Montpellier I for hosting the Journées.

We warmly thank the members of the Local Organizing Committee: the chairs, A. Palacios and E. Nuss, and the team E. Martinez., C. Prévot, F. Amat, S. Colaiocco, A. Lèbre, D. Talbi, C. Mercier, Y. Gallant, E. Josselin, A. Marcowith, F. Piron, B. Plez, M. Renaud, F. Martins, D. Puy. Their outstanding work and their generous contributions were absolutely crucial for making the "Journées" such a success. Thanks also to SF2A board and council for its active contribution, and to the editors of these proceedings.

Céline Reylé Présidente de la SF2A

List of participants

ADAMI Christophe (e-mail: christophe.adami@oamp.fr)
ALINA Dana (e-mail: dana.alina@irap.omp.eu)
ALVAN Lucie (e-mail: lucie.alvan@cea.fr)
ALVES Marta (e-mail: marta.alves@ias.u-psud.fr)
AMARD Louis (e-mail: louis.amard@univ-montp2.fr)
AMAT Françoise (e-mail: francoise.amat@univ-montp2.fr)
ARNAUD Monique (e-mail: monique.Arnaud@cea.fr)
ARNOLD Luc (e-mail: luc.arnold@oamp.fr)
ARZOUMANIAN Doris (e-mail: doris.arzoumanian@ias.u-psud.fr)
ASTUDILLO-DEFRU Nicola (e-mail: nicola.astudillo@obs.ujf-grenoble.fr)
AUBERT Dominique (e-mail: dominique.aubert@astro.unistra.fr)
AUSSEL Herve (e-mail: herve.aussel@cea.fr)
BABUSIAUX Carine (e-mail: carine.babusiaux@obspm.fr)
BALLET Jean (e-mail: jballet@cea.fr)
BARRET Didier (e-mail: didier.barret@irap.omp.eu)
BAUDIN Frédéric (e-mail: frederic.baudin@ias.u-psud.fr)
BELKACEM Kevin (e-mail: kevin.belkacem@obspm.fr)
BERIO Philippe (e-mail: philippe.berio@oca.eu)
BERNARD Jean-philippe (e-mail: Jean-Philippe.Bernard@irap.omp.eu)
BERTONE Stefano (e-mail: stefano.bertone@obspm.fr)
BETHERMIN Matthieu (e-mail: matthieu.bethermin@cea.fr)
BEUZIT Jean-Luc (e-mail: jean-luc.beuzit@obs.ujf-grenoble.fr)
BITEAU Jonathan (e-mail: biteau@in2p3.fr)
BLONDIN Stéphane (e-mail: stephane.blondin@oamp.fr)
BOHM Torsten (e-mail: tboehm@irap.omp.eu)
BOISSIER Samuel (e-mail: samuel.boissier@oamp.fr)
BOMMERSBACH Loïc (e-mail: loic.bommersbach@cnrs-dir.fr)
BONFILS Xavier (e-mail: xavier.bonfils@obs.ujf-grenoble.fr)
BONTEMPS Sylvain (e-mail: bontemps@obs.u-bordeaux1.fr)
BOQUIEN Médéric (e-mail: mederic.boquien@oamp.fr)
BOSELLI Alessandro (e-mail: alessandro.boselli@oamp.fr)
BOSMA Albert (e-mail: bosma@oamp.fr)
BOSNJAK Zeljka (e-mail: bosnjak@iap.fr)
BOUCHET François (e-mail: bouchet@iap.fr)
BOUCHY François (e-mail: bouchy@iap.fr
BOUFFET Romuald (e-mail: romuald.bouffet@obs.u-bordeaux1.fr)
BOULANGER Francois (e-mail: francois.boulanger@ias.u-psud.fr)
BOUR Cyril
BOURET Jean-claude (e-mail: jean-claude.bouret@oamp.fr)
BRACCO Andrea (e-mail: andrea.bracco@ias.u-psud.fr)
BRAHIC André (e-mail: brahic@cea.fr)
BRAINE Jonathan (e-mail: braine@obs.u-bordeaux1.fr)
BRIOT Danielle (e-mail: danielle.briot@obspm.fr)
BROWN Anthony (e-mail: brown@strw.leidenuniv.nl)
BRUN Allan (e-mail: sacha.brun@cea.fr)

BRUN Pierre (e-mail: pierre.brun@cea.fr)
BUAT Veronique (e-mail: veronique.buat@oamp.fr)
BURGARELLA Denis (e-mail: denis.burgarella@oamp.fr)
BURGEY Edith (e-mail: edith.burgey@utinam.cnrs.fr)
BUSCA Nicolás (e-mail: ngbusca@in2p3.fr)
CABANE Michel
CABRIT Sylvie (e-mail: sylvie.cabrit@obspm.fr)
CAMBRESY Laurent (e-mail: cambresy@astro.unistra.fr)
CAPUTI Karina (e-mail: karina@astro.rug.nl)
CARMONA Andres (e-mail: andres.carmona@obs.ujf-grenoble.fr)
CATALA Claude (e-mail: claude.catala@obspm.fr)
CAUCHIES Natacha (e-mail: natacha.cauchies@obs.ujf-grenoble.fr)
CELLIER-HOLZEM Flora (e-mail: cellier@lpnhe.in2p3.fr)
CHANTEREAU William (e-mail: chantereau.william@gmail.com)
CHARBONNEL Corinne (e-mail: Corinne.Charbonnel@unige.ch)
CHARDIN Gabriel (e-mail: gabriel.chardin@in2p3.fr)
CHARDIN Jonathan (e-mail: jonathan.chardin@astro.unistra.fr)
CHARIGNON Camille (e-mail: camille.charignon@cea.fr)
CHARLOT Patrick (e-mail: charlot@obs.u-bordeaux1.fr)
CHARLOT Stephane (e-mail: charlot@iap.fr)
CHAULAGAIN Uddhab (e-mail: uddhab.chaulagain@obspm.fr)
CHAUVIN Gael (e-mail: gael.chauvin@obs.ujf-grenoble.fr)
CHAUVINEAU Bertrand (e-mail: chauvineau@oca.eu)
CHAVES Ryan
CHESNEAU Olivier (e-mail: Olivier.Chesneau@oca.eu)
CHIEZE Jean-Pierre (e-mail: jean-pierre.chieze@cea.fr)
CIESLA Laure (e-mail: ciesla@physics.uoc.gr)
CLÉNET Yann LESIA (e-mail: yann.clenet@obspm.fr)
COGNARD Ismaël (e-mail: icognard@cnrs-orleans.fr)
COLAS François (e-mail: colas@imcce.fr)
COLLIN-ZAHN (e-mail: suzy.collin@obspm.fr)
COMBES Francoise (e-mail: francoise.combes@obspm.fr)
COMIS Barbara (e-mail: barbara.comis@lpsc.in2p3.fr)
CORBEL Stéphane (e-mail: stephane.corbel@cea.fr)
CORNET Thomas (e-mail: thomas.cornet@univ-nantes.fr)
COUGRAND Catherine (e-mail: catherine.cougrand@ias.u-psud.fr)
COURTIN Régis (e-mail: regis.courtin@obspm.fr)
CRIDA Aurélien (e-mail: crida@oca.eu)
CRIFO Francoise (e-mail: francoise.crifo@obspm.fr)
CROUZIER Antoine (e-mail: antoine.crouzier@gmail.com)
CUBY Jean-gabriel (e-mail: jean-gabriel.cuby@oamp.fr)
DAIGNE Frédéric (e-mail: daigne@iap.fr)
DAMIANI Cilia (e-mail: cilia.damiani@lam.fr)
DE BARROS (e-mail: stephane.debarros@unige.ch)
DE GEYTER (e-mail: gert.degeyter@ugent.be)
DE LAVERNY (e-mail: laverny@oca.eu)
DE SA Lionel (e-mail: lionel.desa@obspm.fr)
DECRESSIN Thibaut (e-mail: thibaut.decressin@unige.ch)
DELEUIL Magali (e-mail: magali.deleuil@oamp.fr)
DELFOSSE Xavier (e-mail: Xavier.Delfosse@obs.ujf-grenoble.fr)
DENNEFELD Michel (e-mail: dennefel@iap.fr)
DESGARDIN Thibaut (e-mail: thibaut.desgardin@etud.univ-montp2.fr)
DESSART Luc (e-mail: Luc.Dessart@oamp.fr)
DEVOST Daniel (e-mail: devost@cfht.hawaii.edu)
DI FOLCO Emmanuel (e-mail: difolco@obs.u-bordeaux1.fr)

DIAMOND Phil (e-mail: diamond@skatelescope.org)
DINTRANS Boris (e-mail: boris.dintrans@irap.omp.eu)
DISSEAU Karen (e-mail: karen.disseau@obspm.fr)
DONATI Jean-François (e-mail: jean-francois.donati@irap.eu)
DRUARD Clément (e-mail: druard@iram.fr)
DUBOIS Yohan (e-mail: dubois@iap.fr)
DUCOUT Anne (e-mail: ducout@iap.fr)
DURRET Florence (e-mail: durret@iap.fr)
EGGL Siegfried (e-mail: siegfried.eggl@imcce.fr)
EGRET Daniel (e-mail: daniel.egret@obspm.fr)
ETCHEVERRY Sylvie (e-mail: sylvie.etcheverry@obs-mip.fr)
EZZEDDINE Rana (e-mail: Ranaezzeddine@gmail.com)
FALGARONE Edith (e-mail: edith.falgarone@ens.fr)
FANCIULLO Lapo (e-mail: lfanciul@ias.u-psud.fr)
FECHTENBAUM Sarah (e-mail: sara.fechten@orange.fr)
FÉLIX Sophie (e-mail: sophie.felix@cea.fr)
FERRIÈRE Katia (e-mail: Katia.Ferriere@irap.omp.eu)
FLORES Hector (e-mail: hector.flores@obspm.fr)
FOSCHINO Sacha
FOUCHET Thierry (e-mail: Thierry.Fouchet@obspm.fr)
FOUQUET Sylvain (e-mail: sylvain.fouquet@obspm.fr)
FOURTUNE-RAVARD Chloé (e-mail: chloe.fourtune-ravard@obspm.fr)
FRAIX-BURNET Didier (e-mail: fraix@obs.ujf-grenoble.fr)
FREUNDLICH Jonathan (e-mail: jonathan.freundlich@obspm.fr)
FULCONIS Marc (e-mail: marc.fulconis@oca.eu)
FUSCO Thierry (e-mail: thierry.fusco@onera.fr)
GALLAIS Pascal (e-mail: pascal.gallais@cea.fr)
GALLET Florian (e-mail: florian.gallet@obs.ujf-grenoble.fr)
GARCIA-MELENDO Enrique (e-mail: egarcia@foed.org)
GARSDEN Hugh (e-mail: hugh.garsden@cea.fr)
GAURAT Mathieu (e-mail: mathieu.gaurat@etud.univ-montp2.fr)
GAVILAN Lisseth (e-mail: lissethgavilan@gmail.com)
GENOVA Françoise (e-mail: francoise.genova@astro.unistra.fr)
GHESQUIERE Pierre (e-mail: pierre.ghesquiere@univ-montp2.fr)
GILLES Dominique
GIRARD Julien N. (e-mail: julien.girard@obspm.fr)
GISSINGER Christophe (e-mail: christophe.gissinger@lps.ens.fr)
GLICENSTEIN Jean-françois (e-mail: glicens@cea.fr)
GONNEAU Anais (e-mail: anais.gonneau@astro.unistra.fr)
GONZALEZ-PEREZ Violeta (e-mail: gonzalez@cppm.in2p3.fr)
GOOSMANN René (e-mail: rene.goosmann@astro.unistra.fr)
GOUNELLE Mathieu (e-mail: gounelle@mnhn.fr)
GOUPIL Mariejo (e-mail: mariejo.goupil@obspm.fr)
GOURGOULHON Eric (e-mail: eric.gourgoulhon@obspm.fr)
GRIESSMEIER (e-mail: jean-mathias.griessmeier@cnrs-orleans.fr)
GRISÉ Fabien (e-mail: fgrise@iac.es)
GUÉDÉ Céline (e-mail: celine.guede@obspm.fr)
GUERLET Sandrine (e-mail: sandrine.guerlet@obspm.fr)
GUETH Frédéric (e-mail: gueth@iram.fr)
GUIBERT Jean (e-mail: jean.guibert@obspm.fr)
GUILET Jérôme (e-mail: jg613@cam.ac.uk)
GUILLARD Pierre (e-mail: pierre.guillard@ias.u-psud.fr)
GUILLOTEAU Stéphane (e-mail: Stephane.Guilloteau@obs.u-bordeaux1.fr)
GUIRIEC Sylvain (e-mail: sylvain.guiriec@gmail.com)
GUSDORF Antoine (e-mail: antoine.gusdorf@googlemail.com)

HALBWACHS Jean-louis (e-mail: jean-louis.halbwachs@astro.unistra.fr)
HAMMER Francois (e-mail: francois.hammer@obspm.fr)
HARDY Emilie (e-mail: emilie.hardy@onera.fr)
HAYWOOD Misha (e-mail: Misha.Haywood@obspm.fr)
HEALD George (e-mail: heald@astron.nl)
HEBRARD Elodie (e-mail: elodie.hebrard@irap.omp.eu)
HÉBRARD Guillaume (e-mail: hebrard@iap.fr)
HENNEBELLE Patrick (e-mail: patrick.hennebelle@cea.fr)
HERVÉ Anthony (e-mail: anthony.herve@univ-montp2.fr)
HESTROFFER Daniel (e-mail: hestro@imcce.fr)
HEUSSAFF Vincent (e-mail: Vincent.Heussaff@irap.omp.eu)
HIRTZ LEON Sylvie (e-mail: sylvie.leon@cnes.fr)
HURIER Guillaume (e-mail: ghurier@ias.u-psud.fr)
ILBERT Olivier (e-mail: olivier.ilbert@oamp.fr)
ILIC Stéphane (e-mail: stephane.ilic@ias.u-psud.fr)
ITAM Johanna (e-mail: johanna.itam@gmail.com)
JAFFE Tess (e-mail: tess.jaffe@irap.omp.eu)
JOBLIN Christine (e-mail: christine.joblin@irap.omp.eu)
JORDA Laurent (e-mail: laurent.jorda@oamp.fr)
JOSSELIN Eric (e-mail: eric.josselin@univ-montp2.fr)
JOUVE Laurene (e-mail: ljouve@irap.omp.eu)
KERN Pierre (e-mail: pierre.kern@obs.ujf-grenoble.fr)
KERVELLA Pierre (e-mail: pierre.kervella@obspm.fr)
KIEFER Flavien (e-mail: kiefer@iap.fr)
KNöDLSEDER Jürgen (e-mail: jurgen.knodlseder@irap.omp.eu)
KOECHLIN Laurent (e-mail: laurent.koechlin@irap.eu)
KOUACH Driss (e-mail: driss.kouach@obs-mip.fr)
LAEVENS Benjamin (e-mail: benjamin.laevens@astro.unistra.fr)
LAGAGE Pierre-olivier (e-mail: pierre-olivier.lagage@cea.fr)
LAGARDE Nadège (e-mail: lagarde@bison.ph.bham.ac.uk)
LAMBERT Julien (e-mail: julien.lambert@univ-montp2.fr)
LAMY Laurent (e-mail: laurent.lamy@obspm.fr)
LANZ Thierry (e-mail: thierry.lanz@oca.eu)
LAVALLE Julien (e-mail: jlavalle@um2.fr)
LE BOUQUIN Jean-baptiste (e-mail: Jean-baptiste.lebouquin@obs.ujf-grenoble.fr)
LE COROLLER Hervé (e-mail: herve.lecoroller@oamp.fr)
LE FEVRE Olivier (e-mail: olivier.lefevre@oamp.fr)
LEFEVRE Charlène
LE FLOCH Bertrand (e-mail: lefloch@obs.ujf-grenoble.fr)
LELLOUCH Emmanuel (e-mail: emmanuel.lellouch@obspm.fr)
LE PENNEC Maëlle (e-mail: maelle.le-pennec@cea.fr)
LE PONCIN-LAFITTE Christophe (e-mail: christophe.leponcin@obspm.fr)
LEBRE Agnès (e-mail: Agnes.Lebre@univ-montp2.fr)
LEMAIRE Jean-louis (e-mail: jean-louis.lemaire@obspm.fr)
LESTÉ-LASSERRE Nicolas (e-mail: nicolas.leste@obspm.fr)
LEVRIER Francois (e-mail: francois.levrier@ens.fr)
LEYRAT Cedric (e-mail: cedric.leyrat@obspm.fr)
LIGI Roxanne (e-mail: roxanne.ligi@oca.eu)
MACARIO Giulia (e-mail: giulia.macario@oca.eu)
MALBET Fabien (e-mail: Fabien.Malbet@obs.ujf-grenoble.fr)
MALLER Jennifer (e-mail: maller@subatech.in2p3.fr)
MAQUET Lucie (e-mail: lucie.maquet@obspm.fr)
MARCELIN Michel (e-mail: michel.marcelin@oamp.fr)
MARCOWITH Alexandre (e-mail: Alexandre.Marcowith@univ-montp2.fr)
MARIN Frederic (e-mail: frederic.marin@astro.unistra.fr)

MARTIN Jean-michel (e-mail: jean-michel.martin@obspm.fr)
MARTIN Olivier (e-mail: olivier.martin@obspm.fr)
MARTINET Nicolas (e-mail: martinet@iap.fr)
MARTINS Fabrice (e-mail: fabrice.martins@univ-montp2.fr)
MATHIS Stéphane (e-mail: stephane.mathis@cea.fr)
MAURON Nicolas (e-mail: nicolas.mauron@univ-montp2.fr)
MEIJERINK Rowin (e-mail: meijerink@astro.rug.nl)
MELIANI Zakaria (e-mail: zakaria.meliani@gmail.com)
MELIN Jean-baptiste (e-mail: jean-baptiste.melin@cea.fr)
MERLE Thibault (e-mail: tmerle@ulb.ac.be)
METRIS Gilles (e-mail: Gilles.Metris@oca.eu)
MODOLO Ronan (e-mail: ronan.modolo@latmos.ipsl.fr)
MONTARGES Miguel (e-mail: miguel.montarges@obspm.fr)
MONTEUX Julien (e-mail: julien.monteux@univ-nantes.fr)
MONTMERLE Thierry (e-mail: montmerl@iap.fr)
MOSSER Benoît (e-mail: benoit.mosser@obspm.fr)
MOURARD Denis (e-mail: denis.mourard@oca.eu)
MOUTOU Claire (e-mail: claire.moutou@oamp.fr)
NEHLIG François (e-mail: francois.nehlig@astro.unistra.fr)
NEYSKENS Pieter (e-mail: pieter.neyskens@ulb.ac.be)
NUSS Eric (e-mail: eric.nuss@univ-montp2.fr)
ORIGLIA Livia (e-mail: livia.origlia@oabo.inaf.it)
PADOVANI Marco (e-mail: padovani@lra.ens.fr)
PALACIOS Ana (e-mail: ana.palacios@univ-montp2.fr)
PANTIN Eric (e-mail: eric.pantin@cea.fr)
PARMENTIER Vivien (e-mail: vivien.parmentier@yahoo.fr)
PELLO Roser (e-mail: rpello@irap.omp.eu)
PETIT Pascal (e-mail: ppetit@irap.omp.eu)
PETITEAU Antoine (e-mail: petiteau@apc.univ-paris7.fr)
PETROV Romain (e-mail: petrov@unice.fr)
PICHON Bernard (e-mail: Bernard.Pichon@oca.eu)
PIERRET Frédéric (e-mail: frederic.pierret@obspm.fr)
PIRON Frédéric (e-mail: piron@in2p3.fr)
PLEZ Bertrand (e-mail: bertrand.plez@univ-montp2.fr)
POMMIER Mamta (e-mail: mamta.pommier@univ-lyon1.fr)
POUSSE Alexandre (e-mail: apousse@imcce.fr)
PRAT Vincent (e-mail: vincent.prat@irap.omp.eu)
PRATT Gabriel (e-mail: gabriel.pratt@cea.fr)
PREVOT Carole (e-mail: carole.prevot@univ-montp2.fr)
PROUST Dominique (e-mail: dominique.proust@obspm.fr)
PUECH Mathieu (e-mail: mathieu.puech@obspm.fr)
PUY Denis (e-mail: Denis.Puy@univ-montp2.fr)
RAIMBAULT Manuela (e-mail: manuela.raimbault@eleves.ec-nantes.fr)
RAIMOND Séverine (e-mail: severine.raimond@obspm.fr)
RAJPUROHIT Arvind Singh (e-mail: arvind@obs-besancon.fr)
RAMBAUX Nicolas (e-mail: Nicolas.Rambaux@imcce.fr)
REBOUL Henri (e-mail: henri.reboul@univ-montp2.fr)
RECIO-BLANCO Alejandra (e-mail: arecio@oca.eu)
RENAUD Matthieu (e-mail: mrenaud@lupm.univ-montp2.fr)
REYLÉ Céline (e-mail: celine@obs-besancon.fr)
RICHARD Johan (e-mail: johan.richard@univ-lyon1.fr)
RICHARD Olivier (e-mail: olivier.richard@univ-montp2.fr)
RIEUTORD Michel (e-mail: Michel.Rieutord@irap.omp.eu)
RIGBY Emma Leiden (e-mail: rigby@strw.leidenuniv.nl)
RISTORCELLI Isabelle (e-mail: Isabelle.Ristorcelli@irap.omp.eu)

ROBIN Annie (e-mail: annie.robin@obs-besancon.fr)
RODRIGUEZ Sebastien (e-mail: sebastien.rodriguez@cea.fr)
ROUAN Daniel (e-mail: daniel.rouan@obspm.fr)
ROUSSET Gérard (e-mail: Gerard.Rousset@obspm.fr)
SALOMON Jean-baptiste (e-mail: jean-baptiste.salomon@astro.unistra.fr)
SANTERNE Alexandre (e-mail: alexandre.santerne@astro.up.pt)
SARGENT Mark (e-mail: mark.sargent@cea.fr)
SAURY Eléonore (e-mail: eleonore.saury@ias.u-psud.fr)
SAUTTER Violaine
SCHMIDER Francois-xavier (e-mail: schmider@oca.eu)
SCHNEIDER Nicola (e-mail: nicola.schneider@wanadoo.fr)
SEMIKOZ Dmitri (e-mail: semikoz@gmail.com)
STEHLE Chantal (e-mail: chantal.stehle@obspm.fr)
STRUGAREK Antoine (e-mail: antoine.strugarek@cea.fr)
SZOPA Cyril (e-mail: cyril.szopa@latmos.ipsl.fr)
TALBI Dahbia (e-mail: dahbia.talbi@univ-montp2.fr)
TALLON Michel (e-mail: mtallon@obs.univ-lyon1.fr)
TANG Ya-wen (e-mail: ywtang@asiaa.sinica.edu.tw)
THEUREAU Gilles (e-mail: theureau@cnrs-orleans.fr)
THI Wing-fai (e-mail: Wing-Fai.Thi@obs.ujf-grenoble.fr)
TIGE Jérémy (e-mail: jeremy.tige@oamp.fr)
TOPLIS Michael (e-mail: mtoplis@irap.omp.eu)
TORCHINSKY Steve (e-mail: torchinsky@obs-nancay.fr)
TURCK-CHIÈZE Sylvaine (e-mail: cturck@cea.fr)
TURON Catherine (e-mail: catherine.turon@obspm.fr)
VAKILI Farokh (e-mail: Farrokh.Vakili@unice.fr)
VALETTE Elodie (e-mail: valettelodie@gmail.com)
VAN DER HULST Thijs (e-mail: vdhulst@astro.rug.nl)
VAN DRIEL Wim (e-mail: wim.vandriel@obspm.fr)
VANGIONI Elisabeth (e-mail: vangioni@iap.fr)
VAUGLIN Isabelle (e-mail: vauglin@obs.univ-lyon1.fr)
VECCHI Manuela (e-mail: manuela.vecchi@cern.ch)
VERDUGO Celia (e-mail: celia.verdugo@obspm.fr)
VERGANI Susanna (e-mail: susanna.vergani@obspm.fr)
VIAENE Sebastien (e-mail: sebastien.viaene@ugent.be)
VIAL Jean-claude (e-mail: jean-claude.vial@ias.u-psud.fr)
VIALLET Maxime (e-mail: mviallet@mpa-garching.mpg.de)
VIENNE Alain (e-mail: alain.vienne@univ-lille1.fr)
VINATIER Sandrine (e-mail: sandrine.vinatier@obspm.fr)
VINCENT Frederic (e-mail: frederic.vincent@obspm.fr)
VOLONTERI Marta (e-mail: martav@iap.fr)
WIDEMANN Thomas (e-mail: thomas.widemann@obspm.fr)
WILLIGER Gérard
WISE Michael (e-mail: wise@astron.nl)
WOUTERS Denis (e-mail: denis.wouters@cea.fr)
WOZNIAK Hervé (e-mail: herve.wozniak@astro.unistra.fr)
ZAHN Jean-paul (e-mail: jean-paul.zahn@obspm.fr)
ZARKA Philippe (e-mail: philippe.zarka@obspm.fr)

Session SF2A

Session Plénière

SF2A 2013
L. Cambrésy, F. Martins, E. Nuss and A. Palacios (eds)

GAIA, COUNTING DOWN TO LAUNCH

Anthony G.A. Brown[1]

Abstract. In this contribution I provide an overview of the the European Space Agency's Gaia mission just ahead of its launch scheduled for November 2013.

Keywords: Gaia, space astrometry, Milky Way, photometry, spectroscopy, surveys

1 The Gaia mission

ESA's Gaia mission is the next European breakthrough in astrophysics, a cornerstone mission scheduled for launch in November 2013 which is designed to produce the most accurate 3D map of the Milky Way to date (Perryman et al. 2001). The scientific power of Gaia rests on the combination of three desirable qualities in a single mission: (1) the ability to make very accurate (global and absolute) astrometric measurements; (2) the capability to survey large and complete (magnitude limited) samples of objects; and (3) the matching collection of synoptic and multi-epoch spectrophotometric and radial velocity measurements (cf. Lindegren et al. 2008). The range of science questions that can be addressed with such a data set is immense and Gaia will revolutionize studies of the Milky Way. Moreover, such a massive survey is bound to uncover many surprises that the universe still holds in store for us. The numerous science cases for Gaia can be found in, for example, in the proceedings of the conferences 'The Three-Dimensional Universe With Gaia' (Turon et al. 2005) and 'Gaia: At the Frontiers of Astrometry' (Turon et al. 2011). A recent extensive description of the Gaia mission and its expected performances was provided by de Bruijne (2012).

The astrometric measurements are collected employing a wide photometric band (the Gaia G band) which covers the range 330–1000 nm. Multi-colour photometry will be obtained for all objects by means of low-resolution spectrophotometry. The photometric instrument consists of two prisms dispersing all the light entering the field of view. One disperser — called BP for Blue Photometer — operates in the wavelength range 330–680 nm; the other — called RP for Red Photometer — covers the wavelength range 640–1000 nm. In addition radial velocities with a precision of 1–15 km s^{-1} will be measured for all objects to 17$^{\rm th}$ magnitude, thus complementing the astrometry to provide full six-dimensional phase space information for the brighter sources. The radial velocity instrument (RVS) is a near-infrared (847–874 nm, $\lambda/\Delta\lambda \sim 11\,000$) integral-field spectrograph dispersing all the light entering the field of view.

The focal plane of Gaia comprises an array of 106 CCD detectors which serve the three instruments mentioned above. The observing programme is based on the autonomous on-board detection of celestial sources, which is unbiased and complete to $G = 20$ ($V \sim 20$–22). Gaia will be located at L2 and scan the sky with its two telescopes by continuously spinning around the axis perpendicular to the two lines of sight. The spin axis in addition makes a precessing motion around the spacecraft-sun direction, and as a result Gaia will scan the whole sky roughly every 6 months. Each celestial source will on average be observed about 70 times during the 5 year mission lifetime with a quasi-regular time sampling. The number of times a source is observed is not uniform across the sky as illustrated in figure 1. The regions in the annuli located 45° away from the ecliptic poles are observed most often, while the regions around the ecliptic are covered less often. The number of stars in the Gaia catalogue is estimated to be $\sim 7 \times 10^5$ to $G = 10$, 48×10^6 to $G = 15$ and 1.1×10^9 to $G = 20$. About 60 million stars are expected to be seen as binary or multiple systems by Gaia, among which about 10^6–10^7 eclipsing binaries. In addition the catalogue will contain astrometry and photometry for $\sim 3 \times 10^5$ solar systems bodies, $\sim 5 \times 10^5$ quasars, and some 10^6–10^7 galaxies. The sky survey by Gaia will also produce the most accurate optical all-sky map ever, with an angular resolution comparable to that of the Hubble Space Telescope.

[1] Sterrewacht Leiden, Leiden University, P.O. Box 9513, 2300 RA Leiden, The Netherlands

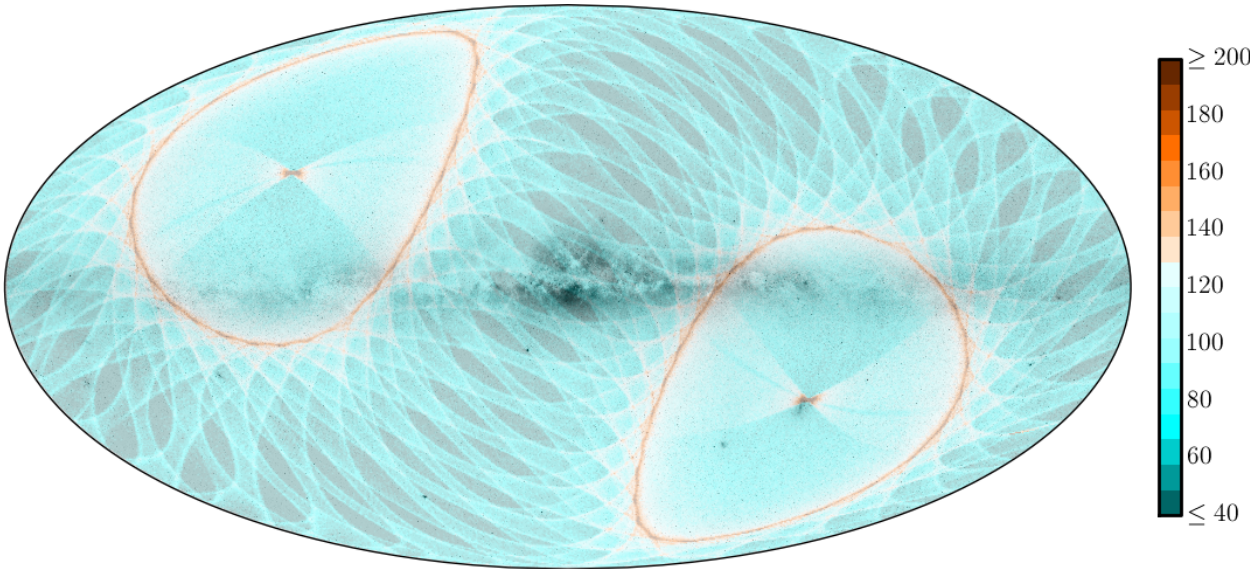

Fig. 1. The predicted sky coverage of Gaia in Galactic coordinates projected on an image of the night sky. The colours indicate the number of times a particular region on the sky is observed. The two annuli where most of the observations are reflect the constant 45° angle between the Gaia spin axis and the direction from the spacecraft to the sun. The extra coverage around the ecliptic poles reflects the early phases of the mission when these areas will be covered repeatedly. The scan law simulation was done with the DPAC AGISLab software (Holl et al. 2010). The background image is the red band of the ESO Milky Way panorama (ESO/S. Brunier).

2 Scientific performances

The expected scientific performance of Gaia in terms of the astrometric, photometric, and radial velocity accuracies achieved is described in de Bruijne (2012) and more details can be found on the Gaia web pages at the following link: `http://www.rssd.esa.int/index.php?project=GAIA&page=Science_Performance`. The performance predictions have been confirmed following extensive tests conducted in December 2012 with the Gaia payload module in cold vacuum. Figure 2 shows the dramatic improvement over the Hipparcos mission, in both astrometric accuracy and survey depth, that will be achieved by Gaia.

The photometric capabilities of Gaia are described in detail in Jordi et al. (2010), while the expected accuracies to which stars can be characterized (in terms of temperature, surface gravity, metallicity, extinction) on the basis of the Gaia photometry can be found in Liu et al. (2012). The RVS instrument of Gaia and its science capabilities were most recently summarized by Cropper & Katz (2011) and Katz et al. (2011). Much more detail on the RVS can be found in Katz et al. (2004) and Wilkinson et al. (2005).

3 Launch and commissioning

Gaia will be launched on November 20 2013 from the European spaceport in French Guiana by a Soyuz-STB/Fregat rocket. After launch the spacecraft will be inserted into a trajectory to L2 where it will arrive in a few weeks. Soon after the commissioning of Gaia's scientific instruments will take place, an activity which is expected to take about 3–4 months. During this phase Gaia will be operated in a special survey mode which ensures that it repeatedly scans over the Ecliptic Pole regions which have been extensively surveyed from the ground in anticipation of the mission. The data so collected will allow a detailed check of the performances of the Gaia instruments in terms of the achieved source detection efficiency, image quality, photometric throughput, spectroscopic resolving power, and attitude noise. These ingredients will allow a detailed assessment of the expected Gaia astrometric, photometric and spectroscopic (radial velocity) performances.

During this phase the Gaia Data Processing and Analysis Consortium (cf. section 4) will process the Gaia telemetry and participate in the detailed performance verification for Gaia. The assessment of the Gaia instruments as they actually behave in flight and updated science performance predictions will be published in the course of 2014 in order to give the scientific community an early insight into what can be expected from Gaia.

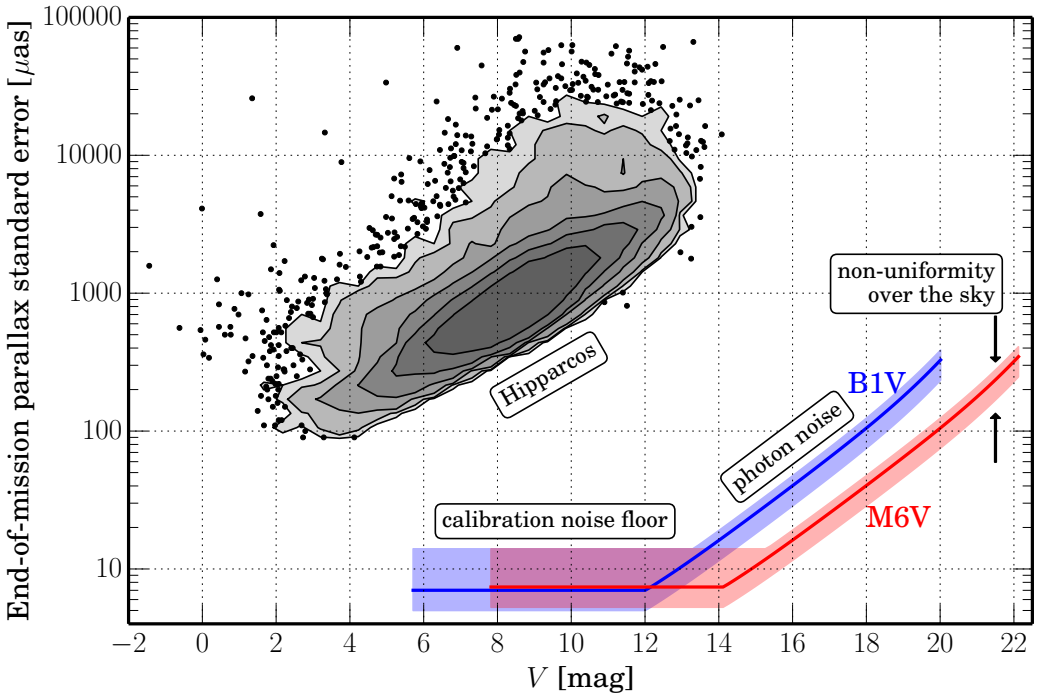

Fig. 2. Parallax accuracies as a function of source brightness in the V-band for Gaia and Hipparcos.The contours and dots show the Hipparcos parallax errors, where the values are taken from van Leeuwen (2007). The lines show the predictions of the Gaia sky averaged parallax standard errors. At the bright end calibration errors will dominate and the parallax accuracies will range from ~ 5 to ~ 14 μas. At the faint end the behaviour of errors as a function of V is dictated by photon noise. The parallax accuracies are shown for an early and a late spectral type star to illustrate that at a given V the astrometric accuracies are better for red stars. As a function of G the differences are negligible. The bands around the average relations reflect the uncertain calibration errors at the bright end and the variation in sky coverage at the faint end. The accuracy predictions (obtained from the Gaia web pages) include a rough estimate of the effects of radiation damage and a 20% margin (factor 1.2) to account for unmodelled effects. The standard errors in position and proper motion can be obtained by applying factors of ~ 0.7 and ~ 0.5, respectively, to the parallax standard errors.

4 Gaia data processing

The on-ground data processing for Gaia is a very large and highly complex task, linking all astrometric, photometric and radial velocity measurements into a large iterative solution. For the astrometric instrument the iterative solution is aimed at transforming the source image location measurements in pixel coordinates to angular field coordinates through a geometrical calibration of the focal plane, and subsequently to coordinates on the sky through calibrations of the instrument attitude and the basic angle between the lines of sight of the two telescopes. Moreover, corrections for systematic chromatic shifts need to be made (using the photometric measurements), as well as aberration corrections, corrections for perspective acceleration (involving the RVS measurements) and corrections for general-relativistic light bending due to the Sun, the major planets, some of their moons, and the most massive asteroids. Image location shifts caused by the radiation damage induced stochastic charge trapping and de-trapping in CCDs also need to be understood and calibrated with high precision. Repeated observations by Gaia of every star permit a complete determination of each star's five basic astrometric parameters — two angular positions, two proper motions and the parallax. More information on the astrometric processing can be found in Lindegren et al. (2012).

The treatment of the spectrophotometry (cf. Busso et al. 2012) starts with the pre-processing of the raw dispersed images (e.g., bias and sky background removal) and the disentangling of overlapping images in crowded fields. This is followed by an iterative process of internal calibration in which all measurements are transformed to the same mean instrumental system by accounting for differences across the focal plane in the prism dispersion curves, point spread function, and geometric calibration, as well as performing flat fielding and correcting for CTI effects. The last step is to perform and absolute calibration of the spectrophotometry using standard stars.

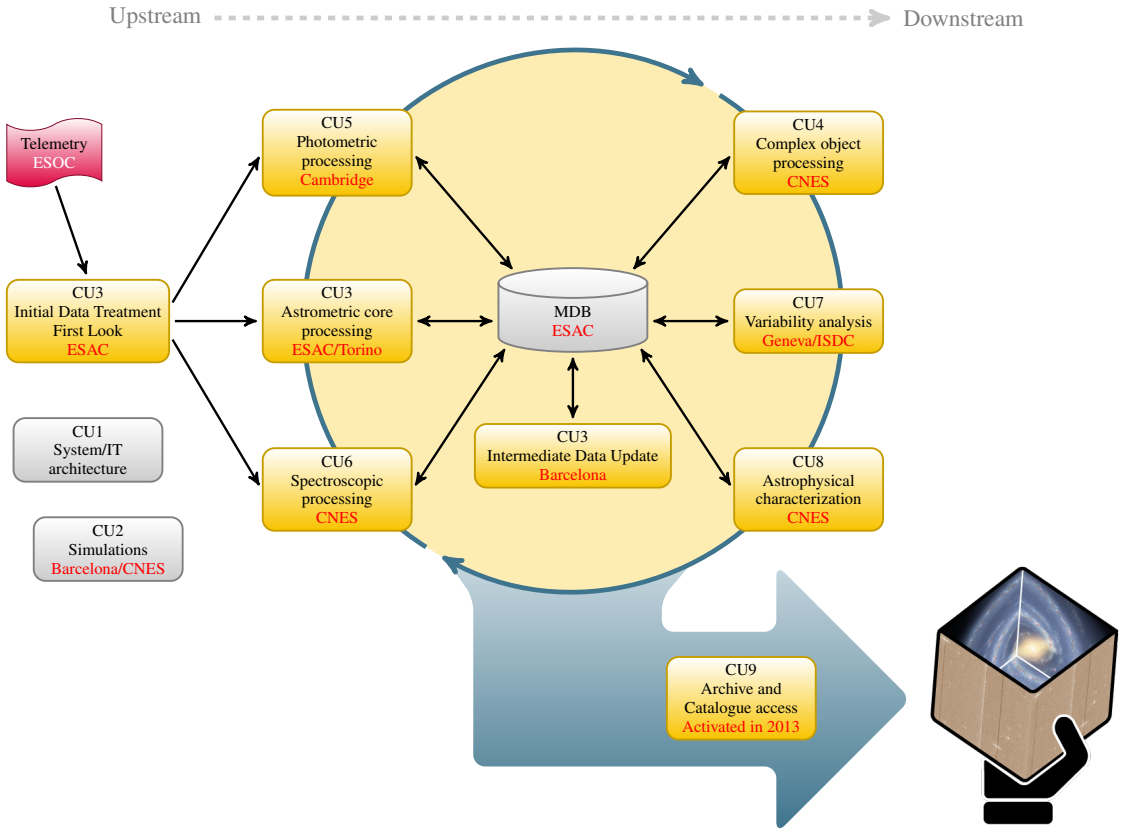

Fig. 3. Schematic overview of the organization of the data flow withing the Gaia Data Processing and Analysis Consortium. For each DPAC coordination unit the processing tasks listed in the boxes are carried out at the data processing centre indicated in red. See text for more explanations.

For the radial velocity spectrograph similar processing steps are taken (Katz et al. 2011). In addition the very low signal levels at the faint end of the RVS magnitude range mandate a careful 'stacking' of multiple spectra collected for each source in order to allow the determination of the radial velocity. At the bright end detailed epoch spectra can be obtained for each source. The RVS instrument is especially sensitive to the effects of CTI and electronic bias non-uniformities which have to be modelled and accounted for in the calibrations. The data processing for both the RVS and photometric instruments relies on the knowledge of source positions on the sky and of the spacecraft attitude, quantities that are derived in the astrometric data processing.

This highly interlinked 'upstream' processing produces raw astrometric, photometric and RVS results which are further processed. A detailed analysis will be made of multiple stars, extended sources, galaxies, exoplanets and solar system objects and the spectra from the photometers and RVS will be used to characterize the astrophysical properties of every source observed by Gaia. Finally the repeated observations of each source can be used to carry out a detailed variability analysis. More details on these 'downstream' processing tasks can be found in Pourbaix (2011) (double and multiple stars), Sozzetti (2013) (exoplanets) Tanga & Mignard (2012) (solar system objects), Tsalmantza et al. (2012); Krone-Martins et al. (2013) (galaxies), Bailer-Jones et al. (2013) (astrophysical parameters of Gaia sources), and Eyer et al. (2012) (variable stars).

The multitude of tasks described above will be undertaken by the scientific community in Europe which has organized itself into the Gaia Data Processing and Analysis Consortium (DPAC). The data processing activities will be structured around nine 'coordination units' (CUs) and six data processing centres. Each CU is responsible for delivering a specific part of the overall data processing system for Gaia. The role of each CU and of the data processing centres is illustrated schematically in figure 3.

In this diagram the flow of data within DPAC and between the data processing centres is shown. The Gaia telemetry is sent from ESOC to the Science Operations Centre at ESAC where it is unpacked and processed by the Initial Data Treatment and First Look pipelines. The latter serves to monitor the instrument health of Gaia in great detail while the former prepares the raw telemetry for further processing by CUs 3 (astrometry),

5 (photometry) and 6 (spectroscopy and radial velocities). The results from these 'upstream' CUs are then stored in the Main Data Base (MDB) housed at ESAC. The 'downstream' CUs 4, 7, and 8 then pick up the processing results from the MDB and carry out the processing of non-single stars and non-stellar sources, the classification and characterization of all sources, and the variability analysis (detection, classification, and derivation of variable source light curves). The results from these CUs also go back into the MDB. The iterative loop is closed by the intermediate data update in which improved instrument calibrations are derived (taking into account the results from all CUs 3/5/6 and 4/7/8) which are then applied to derive improved upstream and downstream data products. Finally, when a particular version of the Main Data Base contents is deemed of sufficient quality to warrant a data release the MDB contents are passed onto CU9 for extensive validation, documentation, and release of the Gaia processing results.

5 Data release scenario

The final Gaia catalogue release is foreseen to take place around 2022. This is of course still some time away and hence in the mean time intermediate data releases are foreseen. The data release scenario for Gaia can be found on the Gaia web pages at `http://www.rssd.esa.int/index.php?project=GAIA&page=Data_Releases`. The release scenario has been designed by carefully considering the complex data processing described above, the available staff effort within DPAC, and assuming smooth operations from the start. Hence, the precise times of data releases cannot be fixed at this moment.

The very first data to be released from the Gaia mission will be the data associated with the so-called Science and Solar System Alerts streams. The Science Alerts concern transient sources that should be followed up promptly from the ground, while the solar system alerts are intended for follow-up observations of newly discovered or very fast moving solar system objects.

The first catalogue release is foreseen to take place 22 months after launch (so roughly end 2015) and will consist of an all sky map (positions and magnitudes) for most of the Gaia sources. In addition, for stars in common with the Hipparcos Catalogue, Gaia and Hipparcos positions will be combined to give very accurate ($\sim$ 30–190 μas/yr) proper motions (see de Bruijne & Eilers 2012).

The list of subsequently planned data releases can be found on the pages above and will include data of increasing accuracy and diversity. It should be stressed here that none of the data releases will be preceded by a proprietary period for the DPAC. The releases are immediately publicly available world wide. This is in fact a unique aspect of the Gaia mission. More information on the expected Gaia catalogue contents and the ideas being developed for making the data available can be found in Brown (2012) and Luri et al. (2013).*

6 Preparing yourself for Gaia

The Gaia mission will result in a large catalogue (over 1 billion sources) containing a very rich diversity of information. Scientifically exploiting such a data set will not be trivial and thus some preparation within the astronomical community is required. The Gaia community will support this process and I give here some examples of activities that astronomers can profit from in their preparations for the use of the Gaia data.

- The Gaia Science Performance web pages† provide, among others, background information on the instruments and the error modelling, interpolation tables and formulae for simulating the errors, the predicted variations of errors over the sky, transformations from the Johnson and Sloan systems to Gaia photometric system, and references to the relevant literature. The information on these pages allows one to realistically simulate the performance of Gaia in order to prepare for the scientific exploitation of the data.

- Simulated Gaia catalogues are being created by DPAC and are made available through, for example, the Centre de Données astronomiques de Strasbourg (CDS). The Gaia Universe Model Snapshot has already been made available (see Robin et al. 2012). It contains a simulated 'universe' (i.e. true properties of sources observed by Gaia) from which the simulated Gaia catalogue is subsequently generated (observable quantities and their errors). The simulated catalogue is currently in production and will be made available later this year. These simulated data sets are representative of the actual Gaia catalogue and can be used to exercise one's data analysis algorithms.

*Available at `http://www.rssd.esa.int/SA/GAIA/docs/library/XL-033.htm`.
†`http://www.rssd.esa.int/index.php?project=GAIA&page=Science_Performance`

- Since 2009 the Gaia Research for European Astronomy Training (GREAT) network[‡], funded through the European Science Foundation, has been stimulating activities in anticipation of the Gaia mission. Numerous workshops and conferences have been organized, focusing on Gaia science topics and how to prepare for exploiting the mission data. The topical working groups within the network are still open to new members, contributions, and ideas. Refer to the GREAT web pages for more information. A notable outcome of the GREAT networking activities is the Gaia-ESO survey (Gilmore et al. 2012).

- The Gaia community is now in the process of defining how the Gaia results will be made accessible to astronomers. This includes developing the data archiving and querying systems, as well as producing detailed documentation and providing sophisticated data analysis and data mining tools (Luri et al. 2013). The astronomical community was consulted, through the GREAT network, to collect requirements on the way the Gaia data should be made available. This was done by inviting the submission of 'use cases' which will drive the requirements specifications for the Gaia catalogue and archive access mechanisms. Your ideas are still welcome and can be submitted through the following wiki pages: `http://great.ast.cam.ac.uk/Greatwiki/GaiaDataAccess`.

References

Bailer-Jones, C. A. L., Andrae, R., Arcay, B., et al. 2013, arXiv:1309.2157

Brown, A. G. A. 2012, Science from Gaia: How to Deal with a Complex Billion-Source Catalogue and Data Archive, ed. L. M. Sarro, L. Eyer, W. O'Mullane, & J. De Ridder, 17

Busso, G., De Angeli, F., & Montegriffo, P. 2012, in Society of Photo-Optical Instrumentation Engineers (SPIE) Conference Series, Vol. 8442, Society of Photo-Optical Instrumentation Engineers (SPIE) Conference Series

Cropper, M. & Katz, D. 2011, in EAS Publications Series, Vol. 45, EAS Publications Series, 181–188

de Bruijne, J. H. J. 2012, Ap&SS, 341, 31

de Bruijne, J. H. J. & Eilers, A.-C. 2012, A&A, 546, A61

Eyer, L., Palaversa, L., Mowlavi, N., et al. 2012, Ap&SS, 341, 207

Gilmore, G., Randich, S., Asplund, M., et al. 2012, The Messenger, 147, 25

Holl, B., Hobbs, D., & Lindegren, L. 2010, in IAU Symposium, Vol. 261, IAU Symposium, ed. S. A. Klioner, P. K. Seidelmann, & M. H. Soffel, 320–324

Jordi, C., Gebran, M., Carrasco, J. M., et al. 2010, A&A, 523, A48

Katz, D., Cropper, M., Meynadier, F., et al. 2011, in EAS Publications Series, Vol. 45, EAS Publications Series, 189–194

Katz, D., Munari, U., Cropper, M., et al. 2004, MNRAS, 354, 1223

Krone-Martins, A., Ducourant, C., Teixeira, R., et al. 2013, A&A, 556, A102

Lindegren, L., Babusiaux, C., Bailer-Jones, C., et al. 2008, in IAU Symposium, Vol. 248, IAU Symposium, ed. W. J. Jin, I. Platais, & M. A. C. Perryman, 217–223

Lindegren, L., Lammers, U., Hobbs, D., et al. 2012, A&A, 538, A78

Liu, C., Bailer-Jones, C. A. L., Sordo, R., et al. 2012, MNRAS, 426, 2463

Luri, X., O'Mullane, W., Alves, J., et al. 2013, Delivering the promise of Gaia. Proposal for the Gaia Archive

Perryman, M. A. C., de Boer, K. S., Gilmore, G., et al. 2001, A&A, 369, 339

Pourbaix, D. 2011, in American Institute of Physics Conference Series, Vol. 1346, American Institute of Physics Conference Series, ed. J. A. Docobo, V. S. Tamazian, & Y. Y. Balega, 122–133

Robin, A. C., Luri, X., Reylé, C., et al. 2012, A&A, 543, A100

Sozzetti, A. 2013, in European Physical Journal Web of Conferences, Vol. 47, European Physical Journal Web of Conferences, 15005

Tanga, P. & Mignard, F. 2012, Planet. Space Sci., 73, 5

Tsalmantza, P., Karampelas, A., Kontizas, M., et al. 2012, A&A, 537, A42

Turon, C., Meynadier, F., & Arenou, F., eds. 2011, EAS Publications Series, Vol. 45, Gaia: at the Frontiers of Astrometry

Turon, C., O'Flaherty, K. S., & Perryman, M. A. C., eds. 2005, ESA Special Publication, Vol. 576, The Three-Dimensional Universe with Gaia

van Leeuwen, F. 2007, Astrophysics and Space Science Library, Vol. 350, Hipparcos, the New Reduction of the Raw Data

Wilkinson, M. I., Vallenari, A., Turon, C., et al. 2005, MNRAS, 359, 1306

[‡] `http://www.ast.cam.ac.uk/GREAT`

SF2A 2013
L. Cambrésy, F. Martins, E. Nuss and A. Palacios (eds)

BIBLIOGRAPHY OF FRENCH ASTROPHYSICS IN 2012

D. Egret[1]

Abstract. This is the second paper of a series analyzing the production of French astronomical research units. We have used the ADS information system to collect a complete database of refereed publications from French Astrophysics (i.e. with at least one of author with affiliation in a French institution). We find 2400 publications for the year 2012 —an increase of about 6% with respect to 2011. We present some statistics to characterize this scientific production.

Keywords: bibliography

1 Introduction

Following the analysis done for year 2011 (Egret 2012, hereafter Paper I) we have collected in the SAO/NASA Astrophysics Data System (ADS ; see e.g. Kurtz et al. 2000)) 2400 refered publications in 2012 for which at least one author is affiliated in a French institution. This constitutes a complete database of the bibliographic production of French astrophysics in 2012. These 2400 papers represent about 10% of the world publication in the domain.

We present also, in a last section, the distribution of papers per thematic categories — this analysis has been performed on the data collection of papers from 2011.

2 Selection criteria

We have used the following selection criteria:

- Refereed articles: We have used the filter for "refereed articles" as available from the SAO/NASA ADS interface.
- Astrophysics domain: We have restricted the data collection to articles from the ADS Astrophysics database, which roughly corresponds to the Astronomy-Astrophysics (hereafter AA) domain of the French *Institut National des Sciences de l'Univers* (INSU).
- Affiliation in a French institution: an article is retained in the list if and only if one of the authors provides an affiliation with a French institution.

3 Query modes

In order to be approximately complete we used two complementary approaches, and merged their results.

One is the *Affiliation search* mode of ADS. In the present context, it proved to be quite efficient, as least for recent years, although the address information is missing from the database for a few journals.

The other query mode is the classical *search by author names*: for that, lists of permanent staff have been extracted from the CNRS directory of laboratories and research units. About thirty research units or "UMR" are relevant to the AA domain. These units are generally located in *observatoires des sciences de l'Univers* (with the notable exception of AIM-SAp —a department of the French nuclear research center CEA) and they actually constitute the core of French professional astrophysics.

By using this double query approach we are rather confident that we are more than 95% complete (see Egret 2012).

[1] LUTH, Observatoire de Paris, CNRS, Univ. Paris Diderot, Place Jules Janssen, 92190 Meudon, France

4 Result: a collection of 2400 refereed articles for the year 2012

We have compiled through the method described above a data collection of 2400 refereed articles constituting the bibliography of French Astrophysics for the year 2012. This database is a managed as a *private library* within the ADS system, and is available from the author on request.

This collection is about 10% of the world production in the domain that we estimate to be about 25,000 papers per year. Of course, because of very frequent wide international co-authorship, this does not mean that French contribution accounts for 10% of the total world production in the Astrophysics domain: a better estimation is 6% (see Paper I).

If we restrict ourselves to the twelve principal astronomy and astrophysics journals, 1610 articles out of a total of 10,250 papers (i.e. 16%) have at least one author affiliated to a French institution.

In which journals do French authors publish ?

Figure 1 provides the distribution of published articles by journals: 28% are published in the European journal *Astronomy & Astrophysics* (A&A) —this is 35% of the articles published in 2012 in this journal— 18% in the *Astrophysical Journal*, and 14% in the *Monthly Notices of the Royal Astronomical Society*.

67% of the articles are published in one of the twelve major journals of the astrophysics domain.

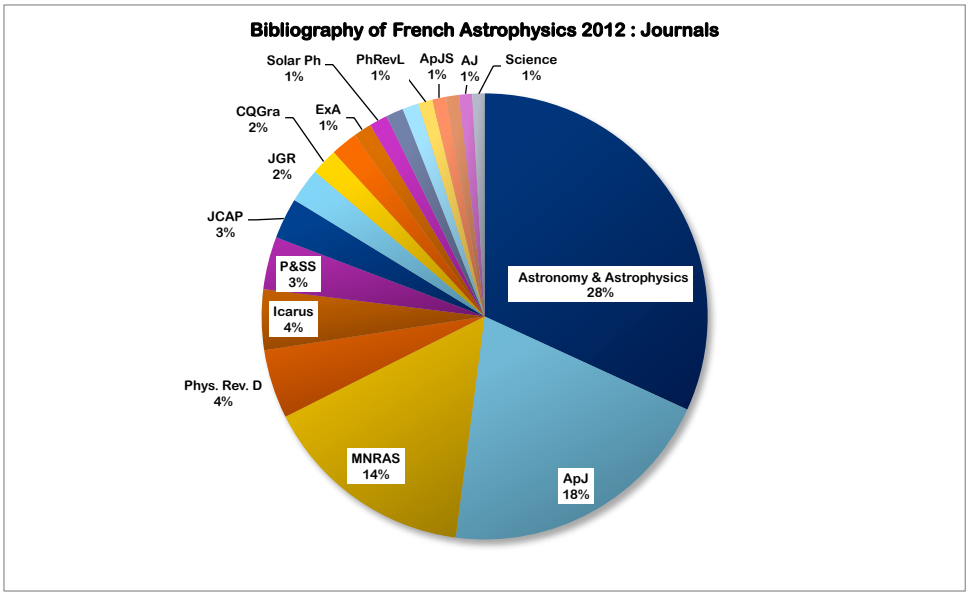

Fig. 1. Left : Bibliography French Astrophysics 2012 : Distribution of Journals and Reviews in which the articles have been published.

5 The production of French astrophysics research units

As a reference, we gave in Fig. 2 of Paper I a histogram of the French research units according to their number of permanent research staff. This list of 2011 can also be used as a reference for 2012.

Figure 2 provides the statistics of the refereed articles issued from the main astrophysics research units for the year 2012. Data for the year 2011 are also displayed for comparison. Note that the total number of entries is larger than the number of articles because of the multiple authorship.

For research units dealing with several domains (e.g. astrophysics and geophysics, or astrophysics and astroparticle physics), this does not reflect the total number of publications of the unit, because only astrophysics publications are counted here.

Comparison between 2011 and 2012 shows a slight global progression of the number of publications including authors with a French affiliation. We estimate the increase to be about 6%, which is larger than the overall increase of the world production of the domain (less than 4%).

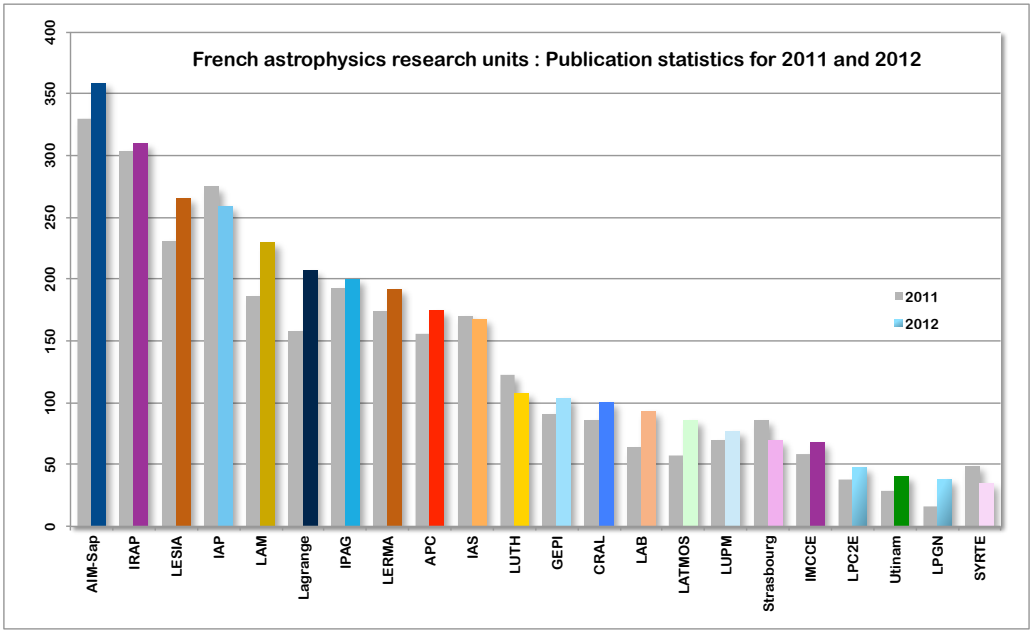

Fig. 2. Astro France 2012: research units sorted by their number of refereed publications

6 The rapid growth of the number of authors appears to stabilize

In 2012, 50% of the papers have more than 6 authors, 11% have more than 30 authors. Average is 30. This is very similar to what has been observed in 2011 after a very rapid growth observed e.g. with respect to year 2006 (see paper I, Egret 2012).

7 Scientific topics

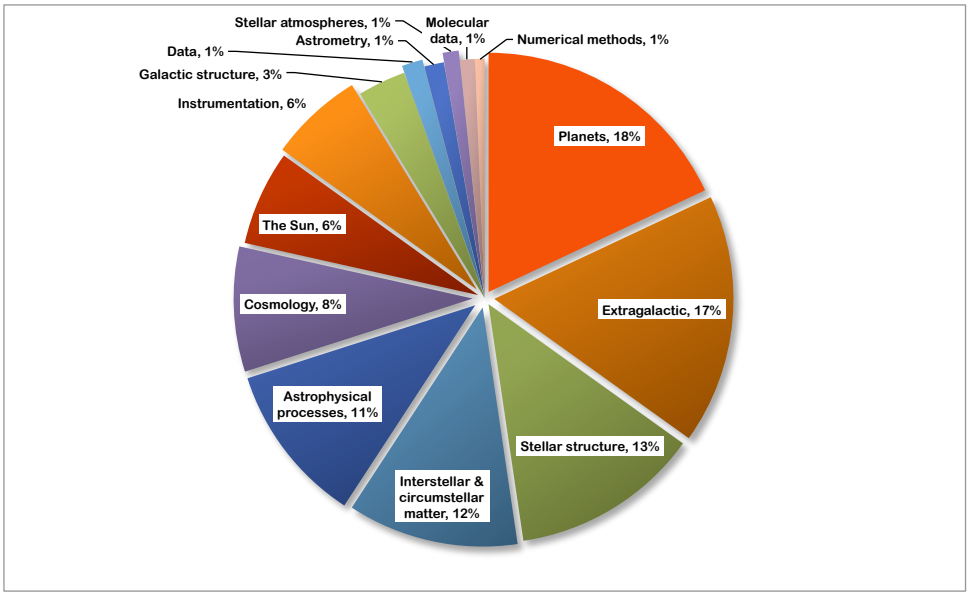

Fig. 3. French Astrophysics 2011: Distribution of the articles according to scientific categories

Figures 3 and 4 are based on an analysis of the scientific production of French astrophysics in 2011 (2150 articles; see Paper I) which has been performed with the help of Claude Bertout by assigning a keyword to each

article, according to the categories used for the European Journal *Astronomy & Astrophysics*.

Figure 3 presents the global distribution of articles per scientific topics.

Figure 4 shows how the growth of number of authors affects in a very inhomogeneous way the different categories, from astrometry (average number of authors : 6) to instrumentation (average number : 58).

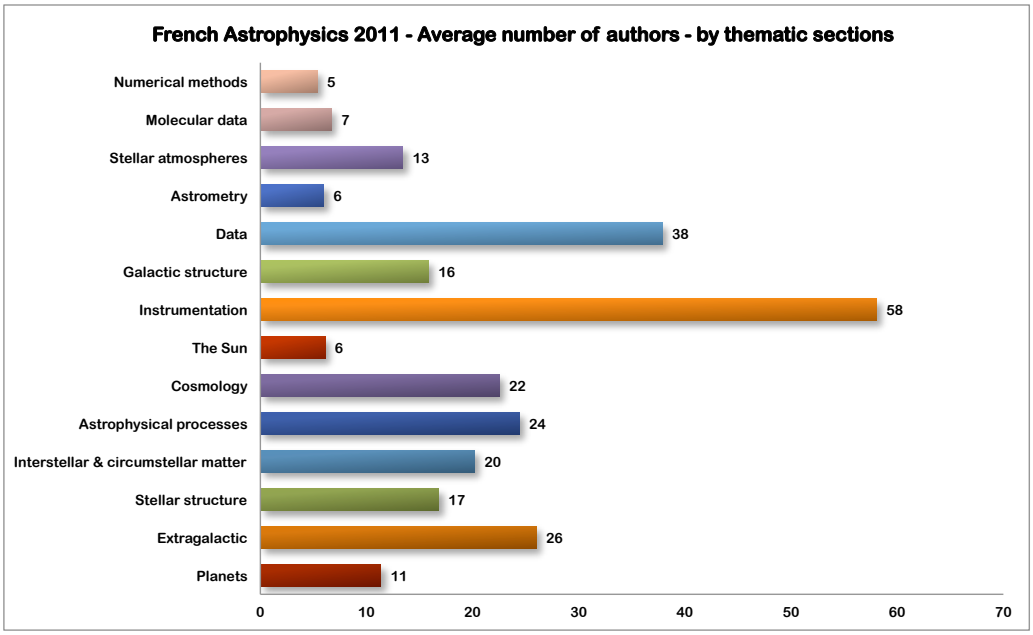

Fig. 4. French Astrophysics 2011: Histogram of the number of authors according to categories

8 Conclusion

This paper is the second of a series to characterize the current production of French Astrophysics, and analyze the trends. It shows a continued increase of the number of publications with respect to 2011 (6%) and a stabilization of the number of authors par paper.

This research has made use of SAO/NASA's *Astrophysics Data System*. I thank Claude Bertout and Piercarlo Bonifacio for useful discussions.

References

Egret, D. 2012, in SF2A-2012: Proceedings of the Annual meeting of the French Society of Astronomy and Astrophysics, ed. S. Boissier, P. de Laverny, N. Nardetto, R. Samadi, D. Valls-Gabaud, & H. Wozniak, 9–13

Kurtz, M. J., Eichhorn, G., Accomazzi, A., et al. 2000, A&AS, 143, 41

SF2A 2013
L. Cambrésy, F. Martins, E. Nuss and A. Palacios (eds)

INTERSTELLAR MAGNETIC FIELDS

Katia Ferrière [1]

Abstract. We review the observational properties of interstellar magnetic fields in the disk and halo of our Galaxy. These properties are inferred from a variety of observational methods, primarily based on polarization of starlight and dust thermal emission, Zeeman splitting, Faraday rotation, and synchrotron emission. We briefly present each of these methods and explain how it has contributed to our present knowledge and understanding of interstellar magnetic fields.

Keywords: ISM: magnetic fields – (ISM:) cosmic rays – ISM: general

1 Introduction

It was Alfvén (1937) who opened the era of interstellar magnetic fields when he correctly pointed out that a magnetic field threading interstellar space could naturally explain the confinement of cosmic rays in our Galaxy. Pushing this notion one step further, Fermi (1949) wrote in a seminal paper on the origin of cosmic radiation that "cosmic rays are originated and accelerated primarily in the interstellar space of the Galaxy by collisions against moving magnetic fields." He went on to add, with surprising accuracy for the time, that "the magnetic field in the dilute matter is of the order of magnitude of 5×10^6 gauss, while its intensity is probably greater in the heavier clouds."

At about the same time, two major advances occurred in observational astronomy. First, Hall (1949) and Hiltner (1949a,b) independently discovered that the optical light from nearby stars is linearly polarized – a phenomenon that Davis & Greenstein (1951) attributed to anisotropic extinction by elongated dust grains which are aligned by a coherent interstellar magnetic field. Second, Kiepenheuer (1950) realized that the general radio continuum emission from our Galaxy is synchrotron emission – a process that implies the presence of relativistic electrons spiraling about the lines of force of an interstellar magnetic field.

Thus, more than 60 years ago, two pioneering theoretical ideas as well as two ground-breaking observational discoveries pointed to the existence of interstellar magnetic fields in our Galaxy. Since then, a multitude of observations have provided convincing evidence that strong interstellar magnetic fields do indeed pervade our Galaxy. It has also become clear, from a theoretical point of view, that these magnetic fields play a crucial role in the interstellar medium (ISM): not only are they responsible for the acceleration and confinement of cosmic rays, but they also have a profound impact on the spatial distribution, dynamics, and energetics of the interstellar matter.

Sixty years down the road, how much have we actually learned about interstellar magnetic fields in our Galaxy? What do we really know about their typical strength and direction, their overall configuration, their spatial distribution . . . ? The purpose of the present article is precisely to address these important questions. In the next four sections, we successively discuss the four main methods employed to detect and observe interstellar magnetic fields, and in the last section, we try to piece together the different observational results into a coherent picture (with admittedly a few remaining gaps).

2 Linear polarization of starlight and dust thermal emission

Interstellar dust grains generally have irregular shapes, which, in a directional stellar radiation field, cause them to feel radiative torques. These torques have two important effects (see Draine & Weingartner 1996; Lazarian & Hoang 2007; Hoang & Lazarian 2008). First, they spin up the grains to suprathermal rotation about their short axes. Second, they gradually bring the grain spin axes into alignment with the local interstellar magnetic field. As a result, dust grains tend to line up with their long axes perpendicular to the local magnetic field.

[1] IRAP, Université de Toulouse, CNRS, 9 avenue du Colonel Roche, BP 44346, F-31028 Toulouse Cedex 4, France

The magnetically aligned dust grains collectively act like a polarizing filter for starlight. More precisely, since they preferentially block the component of starlight with polarization vector parallel to their long axes, the starlight that passes through is linearly polarized in the direction parallel to the interstellar magnetic field. In consequence, measuring the direction of starlight polarization directly reveals the magnetic field orientation in the plane of the sky. This technique applied to nearby stars indicates that the interstellar magnetic field in the Galactic plane within a few kpc of the Sun is horizontal, i.e., parallel to the Galactic plane, and nearly azimuthal (Mathewson & Ford 1970), making a small angle $\simeq -7^\circ$ to the azimuthal direction (Heiles 1996). See Figure 1.

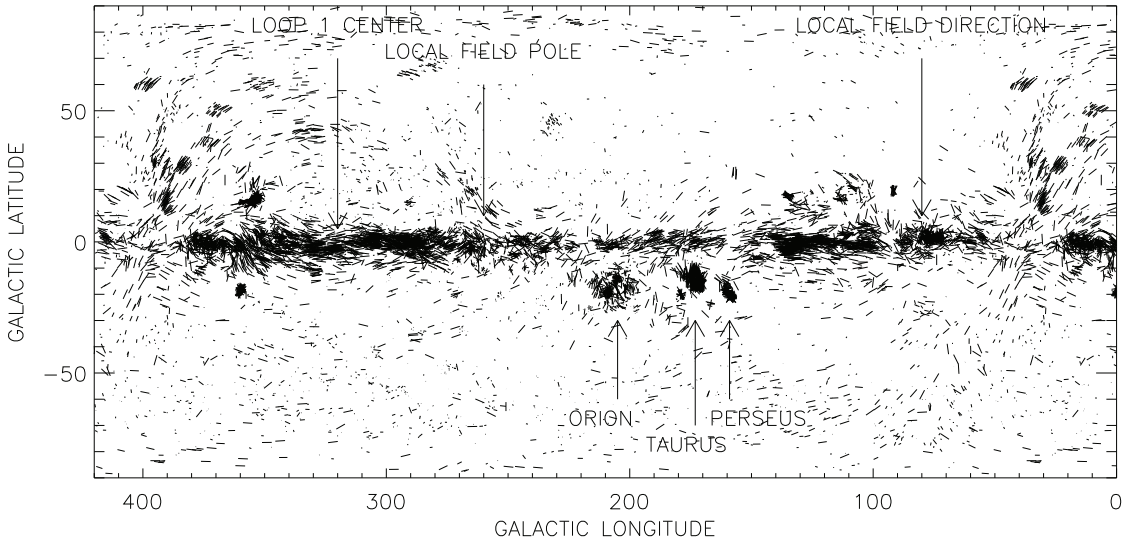

Fig. 1. Sky map in Galactic coordinates of the polarization vectors of 8 662 stars from the compilation by Heiles (2000). Figure credit: Heiles & Crutcher (2005).

In addition to polarizing starlight, the magnetically aligned dust grains also emit infrared thermal radiation in an anisotropic manner. Here, the direction of maximum emission is parallel to the long axes of the grains, i.e., perpendicular to the interstellar magnetic field (Hildebrand 1988). It then follows that dust thermal emission is linearly polarized in the direction orthogonal to starlight. This prediction was nicely borne out by the 850 μm observations of the Archeops balloon experiment (Benoît et al. 2004), which led to the same magnetic field orientation in the Galactic plane as the starlight polarization study of 10^4 stars by Crutcher et al. (2003). Much more detailed information on dust polarized emission will become available in 2014, after the release of the polarization data from the *Planck* satellite.

3 Zeeman splitting

In neutral (atomic or molecular) regions of the ISM that are sufficiently cold and dense, magnetic field strengths can be inferred from Zeeman splitting measurements.

Zeeman splitting of a given atomic or molecular spectral line results from the interaction between the magnetic moment of the valence electrons and an external magnetic field. The frequency-amplitude of Zeeman splitting, $\Delta\nu$, is directly proportional to the magnetic field strength, B, so that, in principle, it suffices to measure $\Delta\nu$ in order to obtain B in the region of interest. In practice, however, $\Delta\nu$ is usually too small compared to the line width to be measurable. Under these conditions, one measures instead the Stokes parameter V, which is directly proportional to the line-of-sight component of the magnetic field, $B_\parallel$.

A vast body of Zeeman splitting measurements has now built up, both for the 21 cm line of HI (in atomic clouds) and for several centimeter lines of OH and other molecules (in molecular clouds). With appropriate statistical corrections for projection effects, it is found that in atomic clouds, the field strength is typically a few μG (median value $\simeq 6\ \mu$G), with a slight tendency to increase with increasing density (Troland & Heiles 1986; Heiles & Troland 2005), while in molecular clouds, the field strength increases approximately as the square root of density, from $\sim 10\ \mu$G to $\sim 3\,000\ \mu$G (Crutcher 1999, 2007).

4 Faraday rotation

In ionized regions of the ISM, the interstellar magnetic field can be probed with Faraday rotation measures of Galactic pulsars and extragalactic sources of linearly polarized radio waves.

Faraday rotation of a linearly polarized radio wave occurs when the wave propagates along the magnetic field of an ionized region, as a result of its interaction with free electrons gyrating about magnetic field lines. The angle by which the direction of polarization rotates is equal to wavelength squared times the so-called rotation measure,

$$\mathrm{RM} \;=\; C \int_0^L n_e \, B_\parallel \, ds \,, \tag{4.1}$$

where C is a numerical constant, n_e the free-electron density, and L the path length from the source to the observer. In practice, the rotation measure of a given radio source can be determined by measuring the direction of polarization of the incoming radiation at at least two different wavelengths.

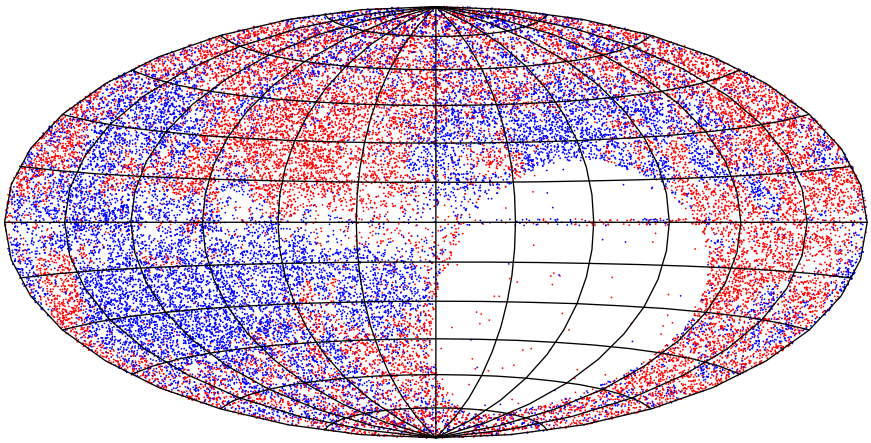

Fig. 2. All-sky map in Galactic coordinates (with the Galactic center in the middle) of the rotation measures of 39 439 extragalactic polarized radio point sources from the large catalog of Taylor et al. (2009) and several smaller catalogs. Positive (negative) rotation measures, wich correspond to a magnetic field pointing on average toward (away from) the observer, are plotted in red (blue). Figure credit: Ferrière & Terral (in preparation).

Rotation measures have now been derived for about 1 200 Galactic pulsars and almost 40 000 extragalactic radio sources (see Figure 2). Used in conjunction either with a model for the spatial distribution of free electrons or, in the case of Galactic pulsars, with their distances and dispersion measures, these numerous rotation measures have made it possible to gather a wealth of information on the strength, direction, and spatial configuration of the interstellar magnetic field, **B**, in ionized regions. Here are the key points that have emerged from Faraday rotation studies.

1) **B** has a regular component, $\mathbf{B}_{\rm reg}$, and a turbulent component, $\mathbf{B}_{\rm turb}$. Near the Sun, $B_{\rm reg} \simeq 1.5\ \mu$G and $B_{\rm turb} \sim 5\ \mu$G (Rand & Kulkarni 1989). Away from the Sun, $B_{\rm reg}$ increases toward the Galactic center, to $\gtrsim 3\ \mu$G at $R = 3$ kpc (Han et al. 2006), i.e., with an exponential scale length $\lesssim 7.2$ kpc. Moreover, $B_{\rm reg}$ decreases away from the Galactic plane, albeit at a very uncertain rate; for reference, the exponential scale height inferred from the rotation measures of extragalactic radio sources is ~ 1.4 kpc (Inoue & Tabara 1981).

2) In the Galactic disk, $\mathbf{B}_{\rm reg}$ is nearly horizontal and generally dominated by its azimuthal component. Near the Sun, $\vec{B}_{\rm reg}$ runs clockwise at an angle $\simeq -8°$ to the azimuthal direction (Han et al. 1999), which is very close to the pitch angle $\simeq -7°$ inferred from starlight polarization. Away from the Sun, $\mathbf{B}_{\rm reg}$ reverses direction at least a couple of times with decreasing Galactic radius, but the exact number and radial locations of the field reversals are still highly controversial (Rand & Lyne 1994; Han et al. 1999; Vallée 2005; Han et al. 2006; Brown et al. 2007; Nota & Katgert 2010). These field reversals have often been interpreted as evidence that $\mathbf{B}_{\rm reg}$ is bisymmetric (azimuthal wavenumber $m = 1$), while an

axisymmetric ($m = 0$) field would be expected from dynamo theory. In reality, Men et al. (2008) showed that neither the axisymmetric nor the bisymmetric picture is consistent with the existing pulsar rotation measures, and they concluded that $\mathbf{B}_{\rm reg}$ must have a more complex pattern.

3) In the Galactic halo, $\mathbf{B}_{\rm reg}$ could have a significant vertical component. At the horizontal position of the Sun, Taylor et al. (2009) obtained $(B_{\rm reg})_z \simeq -0.14\ \mu$G above the Galactic midplane ($z > 0$) and $(B_{\rm reg})_z \simeq +0.30\ \mu$G below the midplane ($z < 0$), whereas Mao et al. (2010) obtained $(B_{\rm reg})_z \simeq 0.00\ \mu$G toward the north Galactic pole and $(B_{\rm reg})_z \simeq +0.31\ \mu$G toward the south Galactic pole. In contrast to the situation prevailing in the Galactic disk, the horizontal component of $\mathbf{B}_{\rm reg}$ shows no sign of reversal with decreasing radius.

4) $\mathbf{B}_{\rm reg}$ displays some symmetry properties with respect to the Galactic midplane. At low latitudes (basically, in the disk), $\mathbf{B}_{\rm reg}$ appears to be roughly symmetric in z (Rand & Lyne 1994; Frick et al. 2001), while at high latitudes (in the halo), the rotation-measure sky exhibits a rather striking antisymmetry/symmetry in z in the inner/outer Galactic quadrants (Oren & Wolfe 1995; Han et al. 1997, 1999), which suggests that $\mathbf{B}_{\rm reg}$ is roughly antisymmetric in z inside the solar circle (Han et al. 1997, 1999, but see also Frick et al., 2001). Finding $\mathbf{B}_{\rm reg}$ to be symmetric in the disk and antisymmetric in the inner halo is consistent with the predictions of dynamo theory and with the results of galactic dynamo calculations (e.g., Ruzmaikin et al. 1988; Moss & Sokoloff 2008; Moss et al. 2010).

5 Synchrotron emission

A global method to map out the interstellar magnetic field in the general ISM, through both neutral and ionized regions, rests on the observed Galactic synchrotron emission.

Synchrotron emission is produced by relativistic electrons spiraling about magnetic field lines. The synchrotron emissivity at frequency ν due to a power-law energy spectrum of relativistic electrons, $f(E) = K_e\, E^{-\gamma}$, is given by

$$\mathcal{E}_\nu \;=\; \mathcal{F}(\gamma)\, K_e\, B_\perp^{\frac{\gamma+1}{2}}\ \nu^{-\frac{\gamma-1}{2}}\ , \tag{5.1}$$

where $\mathcal{F}(\gamma)$ is a known function of the electron spectral index and $\mathbf{B}_\perp$ is the total magnetic field projected onto the plane of the sky.

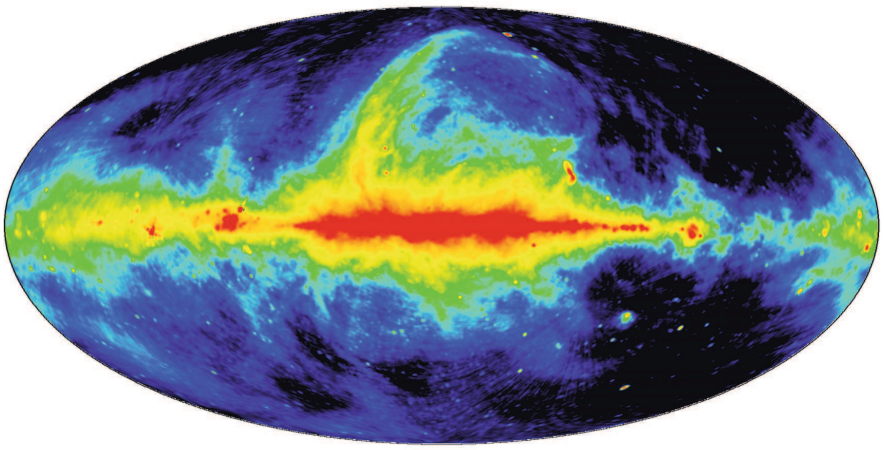

Fig. 3. All-sky 408 MHz radio continuum map in Galactic coordinates (with the Galactic center in the middle) from Haslam et al. (1982). Figure credit: Wielebinski (2009).

The spatial distribution of the Galactic synchrotron emissivity was modeled by Beuermann et al. (1985), based on the all-sky 408 MHz radio continuum map of Haslam et al. (1982) (see Figure 3). Several authors then used this synchrotron distribution model to derive the magnetic field distribution in our Galaxy. To do so, the vast majority of them resorted to the standard double assumption that (1) relativistic electrons represent a fixed fraction of the cosmic-ray population and (2) cosmic rays and magnetic fields are in (energy or pressure) equipartition. Relying on the cosmic-ray ion and electron spectra directly measured by the *Voyager* spacecraft, Ferrière (1998) verified that, locally, cosmic rays and magnetic fields are indeed close to (pressure) equipartition, with a total magnetic field strength $B \simeq 5\ \mu$G. She also found that the total field strength has a radial scale length $\simeq 12$ kpc and a vertical scale height near the Sun $\simeq 4.5$ kpc.

Because synchrotron emission is linearly polarized perpendicular to $\mathbf{B}_\perp$, information can also be gained on the orientation of $\mathbf{B}_\perp$. Evidently, if the observing frequency is too low to avoid Faraday rotation, the received polarized signal must somehow be "de-rotated" in order to recover the true magnetic field orientation. In addition, if the magnetic field has a turbulent component, the contributions from isotropic magnetic fluctuations to the polarized emission cancel out, leaving only the contribution from the ordered (i.e., regular + anisotropic random) magnetic field, $\mathbf{B}_{\rm ord}$.

Thus, while the *total* synchrotron intensity yields the strength of the *total* magnetic field (projected onto the plane of the sky), the *polarized* synchrotron intensity yields the strength and the orientation of the *ordered* magnetic field (again projected onto the plane of the sky).

Near the Sun, the ratio of ordered to total magnetic field strengths turns out to be $\simeq 0.6$ (Beck 2001). Together with $B \simeq 5\ \mu$G, this ratio implies an ordered magnetic field strength $B_{\rm ord} \simeq 3\ \mu$G.

Magnetic field orientations are more difficult to determine. Due to the importance of magnetic fluctuations and to the presence of large discrete structures, they can usually not be directly read off radio polarization maps. Instead, radio maps are often used in combination with magnetic field modeling. In this spirit, Sun et al. (2008) and Sun & Reich (2010) developed comprehensive 3D models of the Galactic magnetic field, constrained by observations of the Galactic total and polarized emission over a wide range of radio frequencies together with an all-sky map of extragalactic-source rotation measures. They achieved a good fit to all the data for axisymmetric models where the disk field is purely horizontal, has a constant pitch angle of 12°, reverses inside the solar circle, and is symmetric in z (clockwise near the Sun), while the halo field is purely azimuthal and antisymmetric in z (counterclockwise/clockwise above/below the midplane at all radii). They also came to the conclusion that bisymmetric models are incompatible with rotation measure data.

6 Conclusions

Our current view of interstellar magnetic fields in our Galaxy is still incomplete. While a growing number of magnetic field properties can now be considered as reasonably firmly established, a few crucial pieces of the puzzle are still missing.

In a nutshell, here is what we believe we know about (1) the strength of the Galactic magnetic field and (2) the direction of its regular component, first near the Sun and second in the Galaxy at large.

1) **Magnetic field strength.** Near the Sun, the regular, ordered (regular + anisotropic random), and total magnetic fields have approximately the following strengths: $B_{\rm reg} \simeq 1.5\ \mu$G, $B_{\rm ord} \simeq 3\ \mu$G, and $B \simeq 5\ \mu$G. Although the values of $B_{\rm reg}$ and $B_{\rm ord}$ were estimated with two completely independent methods (Faraday rotation and polarized synchrotron emission, respectively), their significant difference might be real and, therefore, indicative of the presence of anisotropic random magnetic fields. The latter, in turn, could be generated by compression or shearing of turbulent magnetic fields – for instance, at spiral arms (Beck 2008). Moving away from the Sun, both $B_{\rm reg}$ and B increase toward the Galactic center and decrease toward the halo.

2) **Magnetic field direction.** Near the Sun, the regular magnetic field, $\mathbf{B}_{\rm reg}$, is horizontal and nearly azimuthal, running clockwise with a pitch angle $\simeq -8°$. In the rest of the Galactic disk, $\mathbf{B}_{\rm reg}$ remains approximately horizontal and dominated by its azimuthal component, running clockwise in some regions and counterclockwise in others. In the Galactic halo, $\mathbf{B}_{\rm reg}$ has both horizontal and vertical components; inside the solar circle, the horizontal component is probably counterclockwise at $z > 0$ and clockwise at $z < 0$.

Aside from these presumably well-established facts, a number of open questions remain, concerning, in particular, the azimuthal structure of the magnetic field, the number, radial locations and origin of field reversals in the Galactic disk, the magnetic field parity with respect to the Galactic midplane, the possible connection between the magnetic field in the disk, in the halo, and near the Galactic center ... One may hope that with the abundant observational data recently collected by the *Planck* satellite as well as those expected from the LOFAR low-frequency radio telescope, some of these thorny questions will finally find clear and firm answers.

References

Beck, R. 2001, Space Science Reviews, 99, 243

Beck, R. 2008, in American Institute of Physics Conference Series, Vol. 1085, American Institute of Physics Conference Series, 83–96

Benoît, A., Ade, P., Amblard, A., et al. 2004, A&A, 424, 571

Beuermann, K., Kanbach, G., & Berkhuijsen, E. M. 1985, A&A, 153, 17

Brown, J. C., Haverkorn, M., Gaensler, B. M., et al. 2007, ApJ, 663, 258

Crutcher, R., Heiles, C., & Troland, T. 2003, in Lecture Notes in Physics, Berlin Springer Verlag, Vol. 614, Turbulence and Magnetic Fields in Astrophysics, ed. E. Falgarone & T. Passot, 155–181

Crutcher, R. M. 1999, ApJ, 520, 706

Crutcher, R. M. 2007, EAS Publications Series, Volume 23, 2007, pp.37-54, 23, 37
Davis, Jr., L. & Greenstein, J. L. 1951, ApJ, 114, 206
Draine, B. T. & Weingartner, J. C. 1996, ApJ, 470, 551
Fermi, E. 1949, Physical Review, 75, 1169
Ferrière, K. 1998, ApJ, 497, 759
Frick, P., Stepanov, R., Shukurov, A., & Sokoloff, D. 2001, MNRAS, 325, 649
Hall, J. S. 1949, Science, 109, 166
Han, J. L., Manchester, R. N., Berkhuijsen, E. M., & Beck, R. 1997, A&A, 322, 98
Han, J. L., Manchester, R. N., Lyne, A. G., Qiao, G. J., & van Straten, W. 2006, ApJ, 642, 868
Han, J. L., Manchester, R. N., & Qiao, G. J. 1999, MNRAS, 306, 371
Haslam, C. G. T., Salter, C. J., Stoffel, H., & Wilson, W. E. 1982, A&AS, 47, 1
Heiles, C. 1996, ApJ, 462, 316
Heiles, C. 2000, AJ, 119, 923
Heiles, C. & Crutcher, R. 2005, in Lecture Notes in Physics, Berlin Springer Verlag, Vol. 664, Cosmic Magnetic Fields, ed. R. Wielebinski & R. Beck, 137
Heiles, C. & Troland, T. H. 2005, ApJ, 624, 773
Hildebrand, R. H. 1988, QJRAS, 29, 327
Hiltner, W. A. 1949a, ApJ, 109, 471
Hiltner, W. A. 1949b, Science, 109, 165
Hoang, T. & Lazarian, A. 2008, MNRAS, 388, 117
Inoue, M. & Tabara, H. 1981, PASJ, 33, 603
Kiepenheuer, K. O. 1950, Physical Review, 79, 738
Lazarian, A. & Hoang, T. 2007, MNRAS, 378, 910
Mao, S. A., Gaensler, B. M., Haverkorn, M., et al. 2010, ApJ, 714, 1170
Mathewson, D. S. & Ford, V. L. 1970, MmRAS, 74, 139
Men, H., Ferrière, K., & Han, J. L. 2008, A&A, 486, 819
Moss, D. & Sokoloff, D. 2008, A&A, 487, 197
Moss, D., Sokoloff, D., Beck, R., & Krause, M. 2010, A&A, 512, A61
Nota, T. & Katgert, P. 2010, A&A, 513, A65+
Oren, A. L. & Wolfe, A. M. 1995, ApJ, 445, 624
Rand, R. J. & Kulkarni, S. R. 1989, ApJ, 343, 760
Rand, R. J. & Lyne, A. G. 1994, MNRAS, 268, 497
Ruzmaikin, A. A., Sokolov, D. D., & Shukurov, A. M., eds. 1988, Astrophysics and Space Science Library, Vol. 133, Magnetic fields of galaxies
Sun, X.-H. & Reich, W. 2010, Research in Astronomy and Astrophysics, 10, 1287
Sun, X. H., Reich, W., Waelkens, A., & Enßlin, T. A. 2008, A&A, 477, 573
Taylor, A. R., Stil, J. M., & Sunstrum, C. 2009, ApJ, 702, 1230
Troland, T. H. & Heiles, C. 1986, ApJ, 301, 339
Vallée, J. P. 2005, ApJ, 619, 297
Wielebinski, R. 2009, A&A, 500, 245

SF2A 2013
L. Cambrésy, F. Martins, E. Nuss and A. Palacios (eds)

PROBING THE OUTER SOLAR SYSTEM SMALL BODIES WITH STELLAR OCCULTATIONS

L. Maquet[1], F. Roques[1], A. Doressoundiram[1], C.-Y. Liu[1,2], H.-K. Chang[2], S. I. Chun[1] and Miosotys Team

Abstract. MIOSOTYS (Multi-object Instrument for Occultations in the SOlar system and TransitorY Systems) is a multi-fiber positioner coupled with a fast photometry camera. This is a visitor instrument mounted on the 193 cm telescope at the Observatoire de Haute-Provence, France. Our immediate goal is to characterize the spatial distribution and extension of the Kuiper Belt, and the physical size distribution of TNOs.

We present the observation campaigns during 2010-2012, objectives and observing strategy. We report the detection of potential candidates for occultation events of TNOs. We will discuss more specifically the method used to process the data and the modelling of diffraction patterns.

Keywords: Occultations, TNO, Kuiper belt

1 The instrument

MIOSOTYS (Multi-object Instrument for Occultations in the SOlar system and TransitorY Systems) is a newly refurbished instrument designed at Observatoire de Paris and now mounted as a visitor instrument on the 193-cm telescope at Observatoire de Haute-Provence (France) and 123-cm telescope at Calar Alto in the south of Spain (see fig. 1).

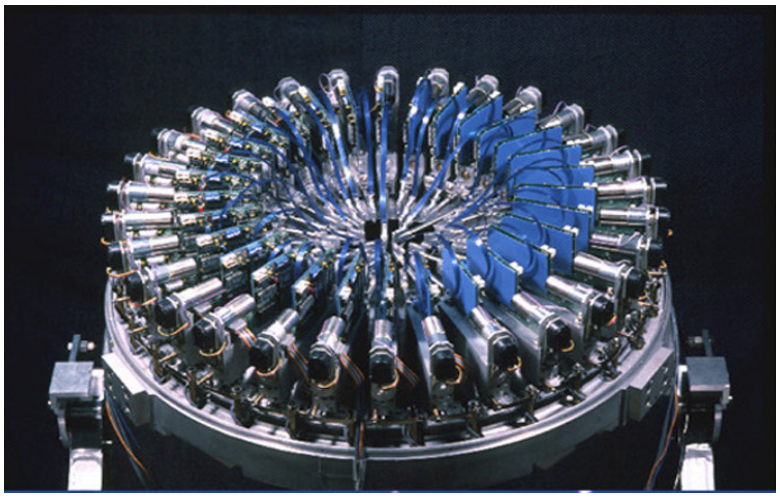

Fig. 1. The system is set in a circle like "fisherman around a pool"

The instrument has been upgraded from a past instrument, MEFOS (Meudon ESO Fibre Optical System, Felenbok et al. (1997)). MIOSOTYS is a multi-fiber positioner coupled with a fast photometry camera. It is an arm positioner using 29 arms in a 26 arcminute field. Each arm is equipped with an individual viewing system for accurate setting and carries one individual fiber that intercept 13 arcsec on the sky. All the 29 fibers are aligned on a CCD for fast photometry acquisition.

[1] Observatoire de Paris, LESIA, 92195 Meudon Cedex, France
[2] Dept. of Physics,Institute of Astronomy, National Tsing Hua University, Hsinchu, 30013, Taiwan

2 Science case and method

The scientific aim of this project is the detection of the diffraction shadow of serendipitous stellar occultations by small (numerous) Trans-Neptunian Objects (TNOs). For that, we are able to simulate this diffraction patterns (Roques & Moncuquet 2000). You can see two examples of diffraction patterns in fig. 2.

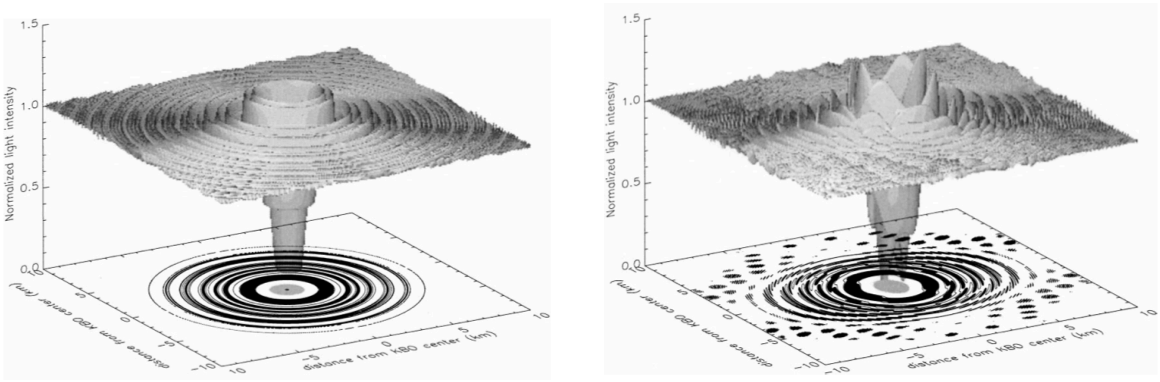

Fig. 2. Examples of diffraction patterns (see Roques & Moncuquet (2000)). **Left:** The TNO is circular. **Right:** The TNO is irregular (the limb is about 6% corrugated) and elliptical (the eccentricity is 0.7 and the semi major axis is $\frac{4}{3}$ km).

We observe small size stars in fast photometry to optimize the detectability of hundreds meters TNOs. The goal is to constraint the radial and azimuthal distribution of the objects size in the Kuiper disk.

3 Observations an data analysis

3.1 Observations

Observations have been obtained during MIOSOTYS campaigns at OHP in 2010-2012 at an acquisition rate of 20 Hz and with median SNR of 20. Photometry has been obtained in a standard manner and lightcurve information has been extracted from the data (see fig. 3).

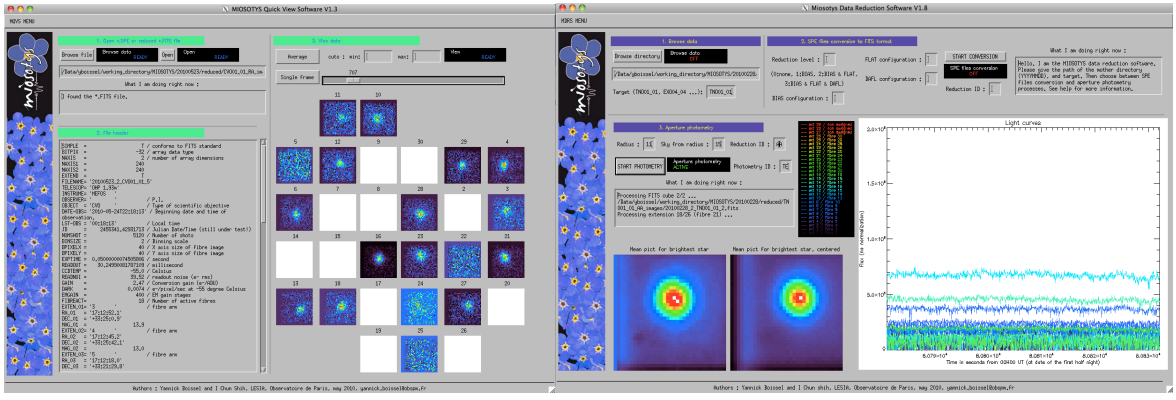

Fig. 3. Left: MIOSOTYS quick view software. **Right:** MIOSOTYS data reduction software.

A total of 38 nights, that is 3782 star-hours has been investigated for occultation events.

3.2 Search method

The search method consists in computing the variance over a running window of 2 seconds:

$$var = \frac{\sum_{j=1}^{n}(x_{ij} - \bar{X}_{we_i})}{n} \tag{3.1}$$

With the current time resolution of 0.05 sec of MIOSOTYS and based on the size of small TNOs and their relative velocity to the observer on the Earth, we estimated *we* to range between 3 and 7 points (0.15 and 0.30 sec).

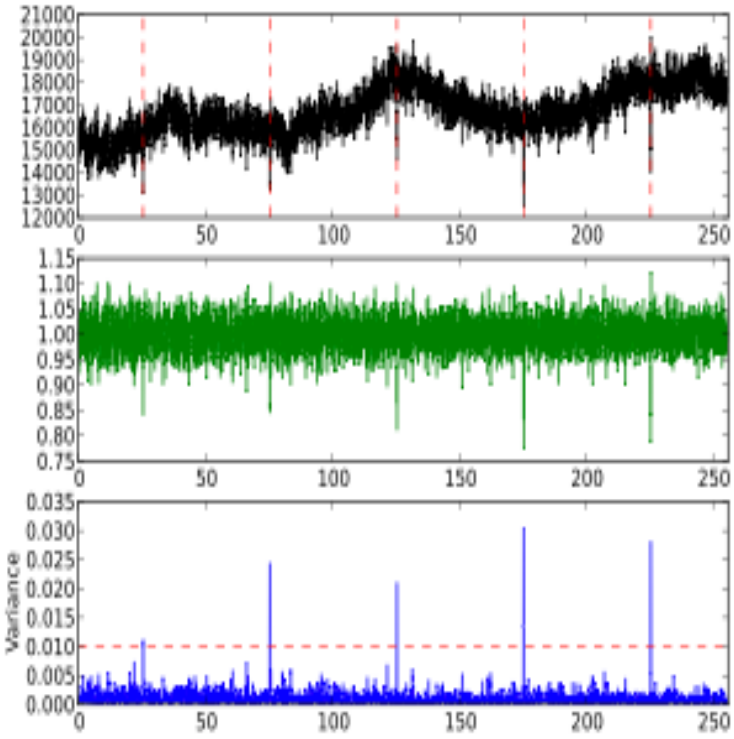

Fig. 4. Search test on synthetic events implanted in real data (red vertical lines)

Then, this first-pass selection of positive events are reviewed against spurious effects that can mimic real events: cosmics, seeing variations, detector artifacts, transparency variations,.

4 Modelling and discussion

4.1 The model

We consider that we are in the Fraunhofer diffraction regime. The stellar flux is diffracted and smoothed on the observed bandwidth, on the stellar disc and on the integration step. The simulated pattern depends on several parameters (size and distance of the TNO, size of the star)

4.2 The fit

We simulate several patterns with different sets of parameter values (the radius of the TNO varies between 0 and 1 km and its distance between 30 and 60 AU). Then, we compare the observation and the simulation by calculating the $\chi^2 \propto \sum(observation - model)^2$. We search the set of values that minimize the χ^2. The figure 5 show an example of the procedure for one event.

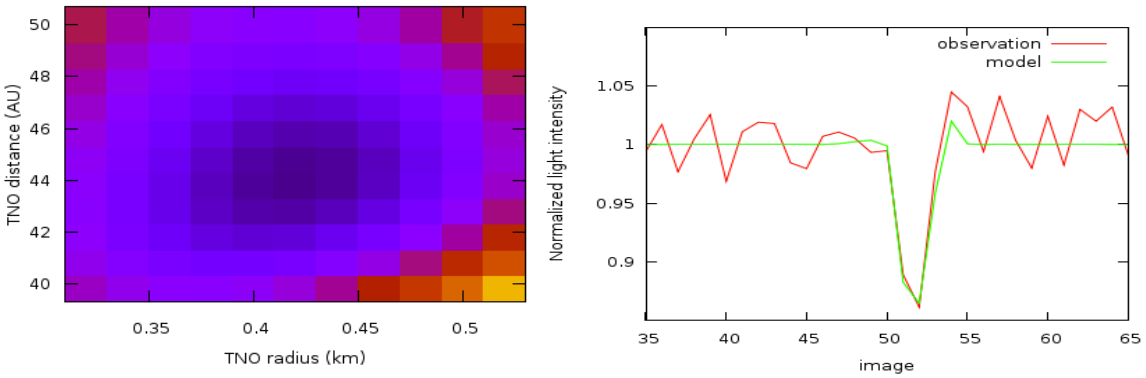

Fig. 5. Left: χ^2 map in relation with the size and the distance of the TNO. Blue colors are low χ^2 (good fit), yellow colors are high χ^2 (bad fit). **Right:** Observation (red line) versus model (green line). The fitted parameters are the TNO radius (0.42 km) and the TNO distance (44 UA)

4.3 Criterion of detection

To consider that an event is compatible with an occultation, the difference between observation and the modeled patterns have to be less than the value of the noise.

5 Conclusions

We have explored the Kuiper disk through stellar occultation and have found a couple of events that could be fitted by hectometer size TNOs. These results, to be further refined, put some constraint on the size distribution of the Kuiper Belt.

References

Felenbok, P., Guerin, J., Fernandez, A., et al. 1997, Experimental Astronomy, 7, 65

Roques, F. & Moncuquet, M. 2000, Icarus, 147, 530

SF2A 2013
L. Cambrésy, F. Martins, E. Nuss and A. Palacios (eds)

LA SECTION 17 DU COMITÉ NATIONAL DE LA RECHERCHE SCIENTIFIQUE

M. Marcelin[1]

Abstract. Cet article présente la Section 17 du Comité National de la Recherche Scientifique.

Keywords:

1 Composition de la Section

La Section 17, dont l'intitulé exact est "Système solaire et Univers lointain", est composée de 18 chercheurs et 3 ingénieurs. Les chercheurs ne sont pas seulement issus du CNRS, mais il y a aussi des astronomes du CNAP, des enseignants-chercheurs ou encore des astrophysiciens du CEA. De ce fait, il s'agit bien d'une représentation de l'ensemble de la recherche scientifique en astrophysique, de même que les autres sections du comité national de la recherche scientifique (41 au total) ne sont pas une simple émanation du CNRS (comme la similarité des sigles CoNRS et CNRS le laisse malheureusement sous-entendre). On retrouve d'ailleurs un peu la même chose au CNAP et au CNU. La composition détaillée est donnée sur le site web de la Section : `https://section17.ias.u-psud.fr/foswiki`.

2 Rôle de la Section

Parmi les principales prérogatives de la Section 17 on trouve le recrutement et l'évaluation des chercheurs CNRS tout au long de leur carrière, avec les promotions. De plus, la Section participe à l'évaluation des unités de recherche dans lesquelles travaillent des chercheurs dont la thématique relève de ses compétences. A ce sujet, la mise en place de l'AERES avait considérablement diminué la participation du comité national à l'évaluation des unités de recherche. On ne connait pas encore les modalités de fonctionnement du haut comité d'évaluation qui va remplacer l'AERES mais on peut espérer que le comité national reprenne de l'importance dans ce processus. La Section 17 s'occupe également de beaucoup de choses moins connues, comme l'attribution des médailles du CNRS (qui ne sont pas attribuées uniquement à des chercheurs CNRS), l'attribution de la PES (Prime d'Excellence Scientifique), l'accueil en délégation d'enseignants-chercheurs (qui peuvent ainsi bénéficier d'une décharge partielle ou totale de leur enseignement, leur permettant de se consacrer pleinement à leurs activités de recherche), l'évaluation (en vue de financement éventuel par le CNRS) de colloques et écoles thématiques. Citons enfin la prospective en astronomie et astrophysique de l'INSU, exercice qui a lieu tous les 4 ou 5 ans et auquel la Section 17 participe activement.

3 Concours

A propos des concours, quelques points méritent d'être soulignés.

3.1 Concours CR1 et règle des 3 cartouches

A ce sujet, on peut lire la chose suivante sur le site web du CNRS : "Les candidats ne peuvent se présenter à plus de 3 sessions pour les concours de CR1 ; s'ils ont été deux fois admissibles, ils peuvent se présenter à une 4e session." Attention ! Être admissible ne veut pas dire être admis à l'audition mais figurer sur la liste d'admissibilité que la Section publie à l'issue des concours. Il y a ensuite le jury d'admission qui donne la liste définitive des candidats reçus au concours (il s'agit là d'une différence notable avec le CNAP qui est jury d'admission).

[1] Aix Marseille Université, CNRS, LAM (Laboratoire d'Astrophysique de Marseille) UMR 7326, 13388, Marseille, France

3.2 Concours DR2

On note une nette baisse du facteur de pression à ce concours. Cela résulte, entre autres, du fait que le nombre de postes ouvert à ce concours a été significativement augmenté au cours des dix dernières années, permettant ainsi de résorber le bouchon qui s'était créé au fil du temps. On notera par ailleurs que la fraction de DR en Section 17 est proche de 50% alors qu'elle est entre 35 et 45% pour la grande majorité des Sections du comité national. Il a été envisagé de réduire le nombre de postes DR2 mis au concours en Section 17 afin d'augmenter le nombre de postes CR1. Mais on se heurte alors à un sérieux problème budgétaire car il faut 5 DR2 pour faire 1 CR1 ! En effet, les chercheurs admis au concours DR2 sont en grande majorité des chercheurs issus du CNRS qui sont donc déjà rémunérés comme CR1 par le CNRS, il s'agit alors d'une simple augmentation et pas d'une création de poste à part entière. **Note importante** : Lors du concours de recrutement DR2 de 2013, le jury d'admission a déclassé 3 candidats qui n'étaient pas titulaires de l'HDR (Habilitation à Diriger des Recherches) et que la Section 17 avait classés en bonne place dans sa liste d'admissibilité. Il est donc fortement recommandé aux candidats de soutenir leur HDR avant de postuler à ce concours (bien que les textes officiels ne l'exigent pas).

3.3 Concours handicap

Chaque année, le CNRS met des postes au concours pour les personnes handicapées. C'est un concours spécifique qui se déroule juste après la session de concours habituelle. Cette année il y avait une dizaine de postes ouverts à ce titre, sur l'ensemble des 41 sections, dont un pour la Section 17. Les directeurs d'unité ayant des doctorants ou post-docs au handicap reconnu peuvent contacter le CNRS afin de faire mettre des postes au concours sur leurs thématiques. Ce dispositif permet à des chercheurs handicapés d'être recrutés sur la base d'un contrat d'une période d'un an renouvelable une fois donnant lieu à titularisation. Des détails de la procédure sont donnés sur le site web du CNRS : `http://www.dgdr.cnrs.fr/drhchercheurs/concoursch/handicap/default-fr.htm`

4 Les médailles du CNRS

La répartition des médailles est la suivante : Médaille de bronze : Une par Section du comité national. Médaille d'argent : Une par Institut (INSU : S17, S18, S19 et S30). Médaille d'or : Une pour tout le CNRS. L'examen des dossiers se fait chaque année en session d'automne (du 18 au 20 novembre pour 2013). Les dossiers sont généralement transmis par les directeurs d'unités et par les programmes nationaux, sollicités à cet effet. Rappelons que tout chercheur ou enseignant-chercheur peut recevoir une médaille du CNRS et que celles-ci ne sont pas attribuées uniquement à des chercheurs CNRS.

5 La Prime d'Excellence Scientifique

La PES est un sujet de discorde parmi les chercheurs, au point que certaines Sections du comité national refusent d'examiner les dossiers de demande de PES. La Section 17 a néanmoins discuté de l'attribution de la PES cette année, même si plusieurs de ses membres n'ont pas souhaité participer à la discussion. Tout comme l'avaient fait ses prédécesseurs, les membres de la nouvelle Section qui ont participé à la discussion ont privilégié l'attribution de la PES aux jeunes. A ce sujet, un message est adressé aux jeunes chercheurs (CR2 plus particulièrement) pour les encourager à déposer un dossier de candidature si la PES existe toujours l'année prochaine.

Rappel des critères d'attribution de la PES (information donnée sur le site web du CNRS) : *"Attribuée pour une période de quatre ans renouvelable, elle bénéficiera aux personnels lauréats d'une distinction scientifique de niveau national ou international ; aux personnels apportant une contribution exceptionnelle à la recherche ; et aux chercheur(e)s dont l'activité est jugée d'un niveau élevé par les instances d'évaluation dont ils relèvent et satisfaisant à la réalisation d'un enseignement ou d'une activité équivalente. Qu'ils ou qu'elles soient, au CNRS, chargé(e)s de recherche, directeurs ou directrices de recherche ou agents détachés dans ces corps. La campagne PES 2012 a bénéficié à 591 chercheur-e-s du CNRS : 137 femmes (23%) et 454 hommes (77%). Depuis sa mise en place, 2412 chercheurs de notre organisme bénéficient de la PES."*

SF2A 2013
L. Cambrésy, F. Martins, E. Nuss and A. Palacios (eds)

RED GIANTS SEISMOLOGY

B. Mosser, R. Samadi, K. Belkacem[1]

Abstract. The space-borne missions CoRoT and *Kepler* are indiscreet. With their asteroseismic programs, they tell us what is hidden deep inside the stars. Waves excited just below the stellar surface travel throughout the stellar interior and unveil many secrets: how old is the star, how big, how massive, how fast (or slow) its core is dancing. This paper intends to *paparazze* the red giants according to the seismic pictures we have from their interiors.

Keywords: Stars: oscillations – Stars: interiors – Stars: evolution – Methods: data analysis

1 Introduction

As denoted by many authors, red giant seismology is an exquisite surprise provided by the space missions CoRoT and *Kepler*. The analysis of a wealth of light curves recorded with unique length, continuity and photometric precision has already revealed many secrets. The most striking results, up to now, are provided by the observation of mixed modes (Fig. 1). Such modes result from the coupling of gravity waves, propagating in the radiative core region, with pressure waves propagating in the stellar envelope. They directly reveal information from the stellar core: the nature of the nuclear reaction (Bedding et al. 2011) and the mean core rotation rate (Beck et al. 2012).

An analysis of red giant seismic observational results has been given in Mosser (2013). Tricky points related to the data analysis are presented in a companion paper (Mosser et al. 2013a), where emphasis is given on red giant interior structure as revealed by asteroseismology. Only ensemble asteroseismology results are presented in this paper, obtained from the monitoring of a cohort of stars. Analysis and modelling of individual stars are not considered. They have started for a handful of targets (di Mauro et al. 2011; Jiang et al. 2011; Baudin et al. 2012). Such individual analysis are crucial for enhancing the understanding of the stellar interior structure and of the physical input to be considered, such as the measurement of the location of the helium second-ionization region (Miglio et al. 2010), or the measurement of differential rotation (Beck et al. 2012; Deheuvels et al. 2012).

In this work, ensemble asteroseismology results are derived from the observations of evolutionary sequences (Section 2). For red giants, asteroseismology benefits from the large homology of their interior structure, which translates into homologous properties of the oscillation spectrum (Section 3). In this Section, we also show how mixed-modes directly probe the stellar cores, and then investigate how stellar evolution is monitored by seismology on the RGB and in the red clump. Scaling relations derived from the homologous properties of red giants are discussed in Section 4, with a special emphasis on the mass and radius scaling relations and on their calibration. Rotation is discussed in Section 5. A recent leap toward oscillations detected in semi-regular variables is presented in Section 6.

2 Evolutionary sequences

The observation of thousands of red giants with CoRoT (e.g., Dupret et al. 2009; Mosser et al. 2010) and *Kepler* (e.g., Huber et al. 2010; Stello et al. 2013) allows us to address ensemble asteroseismology. According to the distance measurements derived from the scaling relations, red giants with magnitudes up to 13 are monitored vast regions of the Galaxy (Section 4.5). They show a large variety of metallicity (Bruntt et al. 2012). Independent of a specific population analysis (e.g., Silva Aguirre et al. 2011, for a one-solar-mass evolutionary sequence), we note

[1] LESIA, CNRS, Université Pierre et Marie Curie, Université Denis Diderot, Observatoire de Paris, 92195 Meudon cedex, France; e-mail: benoit.mosser@obspm.fr

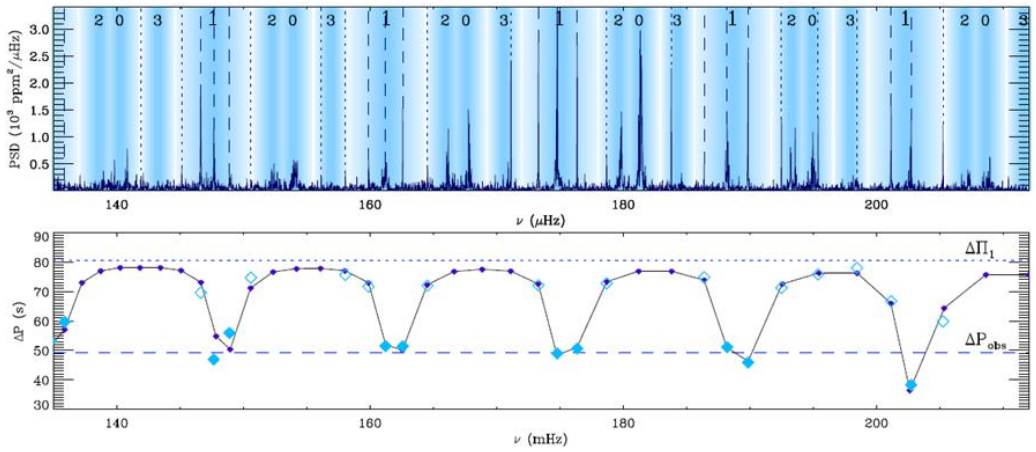

Fig. 1. Top: Typical red giant oscillation pattern. Radial ($\ell = 0$) and quadrupole ($\ell = 2$) follow a regular comb pattern. **Bottom:** Period spacing between dipole modes; they have a mixed character and therefore show an irregular pattern; they can be identified with the asymptotic expansion. Figure from Mosser et al. (2012c).

that, apparently, the cohort of stars provided by both missions provide evolution sequence of low-mass stars. A reason justifying that we address sequences of evolution is provided by the global asteroseismic parameters $\nu_{\rm max}$ and $\Delta\nu_{\rm obs}$: $\nu_{\rm max}$ is the frequency of maximum oscillation signal; $\Delta\nu_{\rm obs}$ is the mean large frequency separation of radial modes observed around $\nu_{\rm max}$ (e.g., Mosser & Appourchaux 2009). The frequency $\nu_{\rm max}$ provides a proxy of the acoustic cutoff frequency, hence of $M\ R^{-2}\,{T_{\rm eff}}^{-1/2}$ (Belkacem et al. 2011). Following Belkacem et al. (2013), we consider that $\Delta\nu_{\rm obs}$ provides an acceptable proxy of the dynamical frequency ν_0 that scales as $\sqrt{\mathcal{G}M/R^3}$. From these scalings, we derive

$$\Delta\nu_{\rm obs} \simeq \nu_0 \propto M^{-1/4}\ {T_{\rm eff}}^{3/8}\ \nu_{\rm max}^{3/4}. \tag{2.1}$$

On the main sequence, the frequency $\Delta\nu_{\rm obs}$ scales as $\nu_{\rm max}^{0.8}$ (Verner et al. 2011b). The discrepancy between this exponent and the 3/4 value in Eq. 2.1 is due to the fact that low-mass and high-mass evolution tracks are in different regions of the main sequence. On the contrary, the observed scaling exponent on the RGB is much closer to 3/4 (Fig. 2) since the RGB regroups the evolution of low-mass stars. The agreement between Eq. 2.1 and global oscillation parameters observed over more than four decades in the red giant regime, completed by measurements on red supergiant stars (Kiss et al. 2006), indicates that the stellar red giant populations observed by CoRoT or *Kepler* constitute a set of stars homogenous enough to mimic stellar evolution, then justifying the relevance of the scaling relations. The difference between the observed exponent and 3/4 is small enough to be interpreted either by the very low variation of $T_{\rm eff}$ with $\nu_{\rm max}$, or by the difference between $\Delta\nu_{\rm obs}$ and ν_0, and by other parameters that need to be calibrated but necessary have a limited influence. Masses in the range 0.9 – 2 $M_\odot$ are present at all stages, hence for all $\nu_{\rm max}$, so that the mass parameter in Eq. 2.1 plays no significant role.

Before addressing the scaling relations, we discuss about stellar homology, seen by both radial and non-radial oscillation modes.

3 Homology

3.1 From interior structure homology to seismic homology

Red giant interior structure is divided in three main regions; the dense helium core, the surrounding thin hydrogen-burning shell, and the thick, mostly convective envelope (Kippenhahn & Weigert 1990). Homology is ensured by the fact that this structure is dominated by generic physics: the thermodynamical conditions of the hydrogen-burning shell being related on the one side with the helium core and on the other side with the convective envelope, the core and envelope properties are closely linked together (Montalbán et al. 2013). Consequently, CoRoT observations have shown evidence of a very simple and useful property of the red giant oscillation pattern: following the interior structure homology, the oscillation pattern can also be defined as homologous. The concept of *universal red giant oscillation pattern* was therefore introduced by Mosser et al.

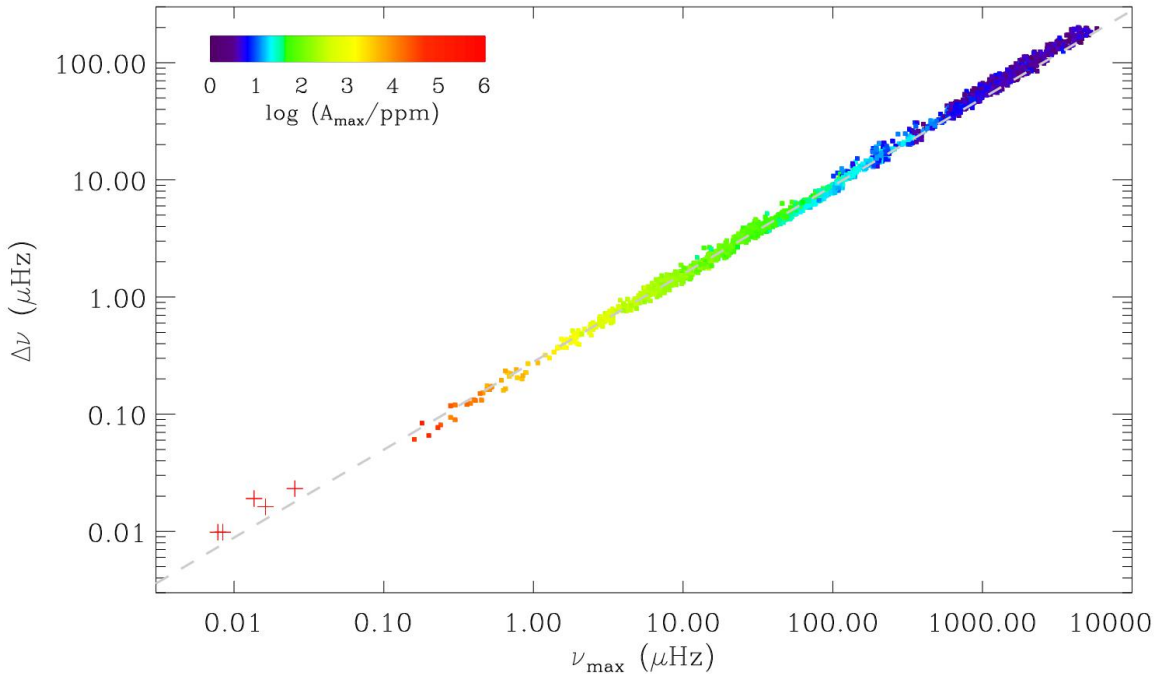

Fig. 2. $\nu_{\rm max}$ – $\Delta\nu_{\rm obs}$ relation, with data from Verner et al. (2011b), Mosser et al. (2012c), and Mosser et al. (2013b). Plusses are red supergiants showing at least two oscillation modes observed by Kiss et al. (2006), with $\Delta\nu_{\rm obs}$ and $\nu_{\rm max}$ derived from a combination of the frequencies. The colors code the mean maximum amplitude $A_{\rm max}$ of the radial oscillations. The grey dashed line has a slope 3/4, in agreement with Eq. 2.1

(2011b), as an alternative form to the usual asymptotic expansion (Tassoul 1980), with the observed large separation as the only free parameter. The second-order asymptotic expansion expresses, for low angular degrees ($\ell \ll n$), as

$$\nu_{n,\ell} = \left(n + \varepsilon_{\rm obs}(\Delta\nu_{\rm obs}) + d_{0\ell}(\Delta\nu_{\rm obs}) + \frac{\alpha}{2}\,(n - n_{\rm max})^2 \right)\ \Delta\nu_{\rm obs}, \tag{3.1}$$

where the dimensionless parameter $n_{\rm max}$ is defined by $\nu_{\rm max}/\Delta\nu_{\rm obs} - \varepsilon_{\rm obs}$. Homology is expressed by the dependence in the observed large separation $\Delta\nu_{\rm obs}$ of the offsets $\varepsilon_{\rm obs}$ and $d_{0\ell}$. The radial offset $\varepsilon_{\rm obs}$ helps locate the radial ridge; the non-radial offsets $d_{0\ell}$ express the shifts of the different degrees ℓ compared to the radial modes (e.g., Corsaro et al. 2012). Homology is illustrated in Fig. 3, where *Kepler* red giant oscillation spectra are plotted on the same graph, with a dimensionless frequency in abscissa, and sorted by increasing large separation values. The alignment of the ridges, each one corresponding to a given radial order n and angular degree ℓ, demonstrates the universality of the oscillation pattern.

The form of Eq. 3.1, which includes a quadratic term, accounts for the measurement of $\Delta\nu_{\rm obs}$ around $\nu_{\rm max}$ in non-asymptotic conditions. The asymptotic form writes

$$\nu_{n,\ell} = \left(n'_\ell + \frac{A_\ell}{n'_\ell} \right)\ \Delta\nu_{\rm as} \quad \text{with} \quad n'_\ell = n + \varepsilon_{\rm as} + \frac{\ell}{2} \tag{3.2}$$

The asymptotic large separation $\Delta\nu_{\rm as}$ is slightly greater than the observed value. The link between the observed and asymptotic parameters is explored in Mosser et al. (2013c). The asymptotic counterpart of $\varepsilon_{\rm obs}$ is, for low-mass stars, $\varepsilon_{\rm as} \equiv 1/4$ (Tassoul 1980). The high accuracy level reached by Eq. 3.1 has been show in previous comparison work (Verner et al. 2011b; Hekker et al. 2011, 2012). A quantitative analysis of the accuracy of the measurement of $\Delta\nu_{\rm obs}$ with Eq. 3.1 is done in Mosser et al. (2013a): the uncertainty is about 0.02 μHz for all evolutionary stages.

3.2 Sounding the core

Asteroseismology aims at probing the whole stellar interior structure. In the Sun, such an analysis performs very efficiently, but less efficiently in the core, since pressure modes do not probe the core as efficiently as they

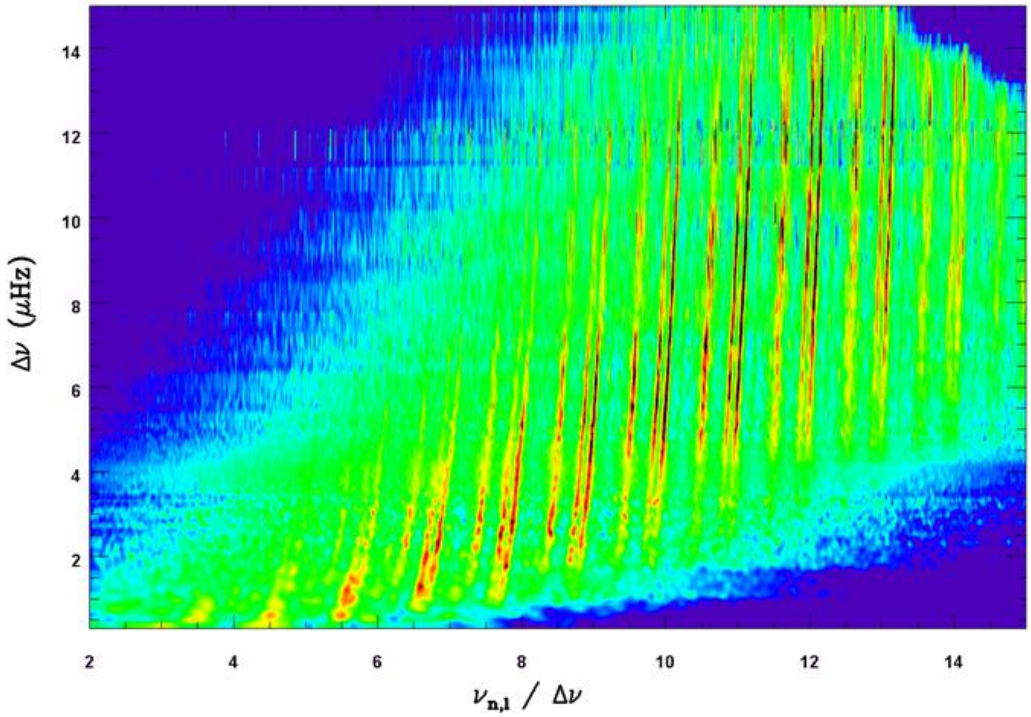

Fig. 3. *Kepler* red giant oscillation spectra, as a function of the dimensionless frequency $\nu_{n,\ell}/\Delta\nu$, sorted by increasing large separation (y-axis). The colors code the oscillation amplitude normalized to the maximum oscillation signal. The close parallel ridges are drawn by quadrupole and radial modes, from the radial orders 3 to 13; the width of the dipole ridges is wider, due to the presence of mixed modes.

probe the other regions, the number of pressure modes sounding the solar core being low. This explains the quest for solar gravity modes that precisely probe the core (Appourchaux et al. 2010).

In red giants, g modes are not present, but appear indirectly through the coupling of gravity waves propagating in the core with pressure waves propagating in the envelope. A toy model for explaining this coupling is given in Mosser et al. (2013a). Since the first observation of mixed modes in red giants (Beck et al. 2011), a wealth of information has been provided by their analysis. Bedding et al. (2011) and Mosser et al. (2011a) have shown that different mixed-mode patterns help distinguish helium-core burning giants in the red clump from hydrogen-shell burning giants on the RGB. Mosser et al. (2012c) have proposed that an asymptotic expansion is able to depict the mixed-mode pattern. This expansion, derived from the formalism developed by Unno et al. (1989), introduces the gravity period spacing $\Delta\Pi_1$ defined by an integral function of the Brunt-Väisälä frequency in the inner radiative region. The measured values of $\Delta\Pi_1$ are accurately reproduced for red giant ascending the RGB, but not in the clump (Montalbán et al. 2013). This discrepancy in the clump is not yet understood and deserves further work.

Homology seen in the radial red giant oscillation pattern is also seen in the $\Delta\nu$ – $\Delta\Pi_1$ diagram (Fig. 4). All low-mass stars on the RGB lie on the same track, independent of their mass and composition. With $\Delta\nu$ representing the stellar mean density and $\Delta\Pi_1$ representing the density of the core, we derive from Fig. 4 that the properties of the core and of the envelope are closely correlated. The inert helium core of an RGB star necessarily contracts when the star ascends the RGB; accordingly, its mass increases, as a result of the hydrogen burning shell which surrounds it. Its contraction and mass increase yield a decreasing $\Delta\Pi_1$ term, as observed and as seen in the modeling (Montalbán et al. 2013). This contraction implies that the density of the hydrogen burning shell increases. This increase boosts the energy production. Hence, the hydrogen envelope expands.

Homology is reinforced in the red clump, since a further similar event has participated to erase the initial differences between low-mass stars. Their helium core being degenerate, the helium flash occurs in very similar conditions (Montalbán et al. 2013), so that they nearly reach the same location in the $\Delta\Pi_1$ – $\Delta\nu_{\rm obs}$ diagram, close to $\Delta\Pi_1 \simeq 300\,$s and $\Delta\nu \simeq 4\,\mu$Hz.

The precision we have on the mixed mode determination is so high that we may expect, from an accurate modelling, a highly precise age determination. During the evolution on the RGB, the gravity period spacing

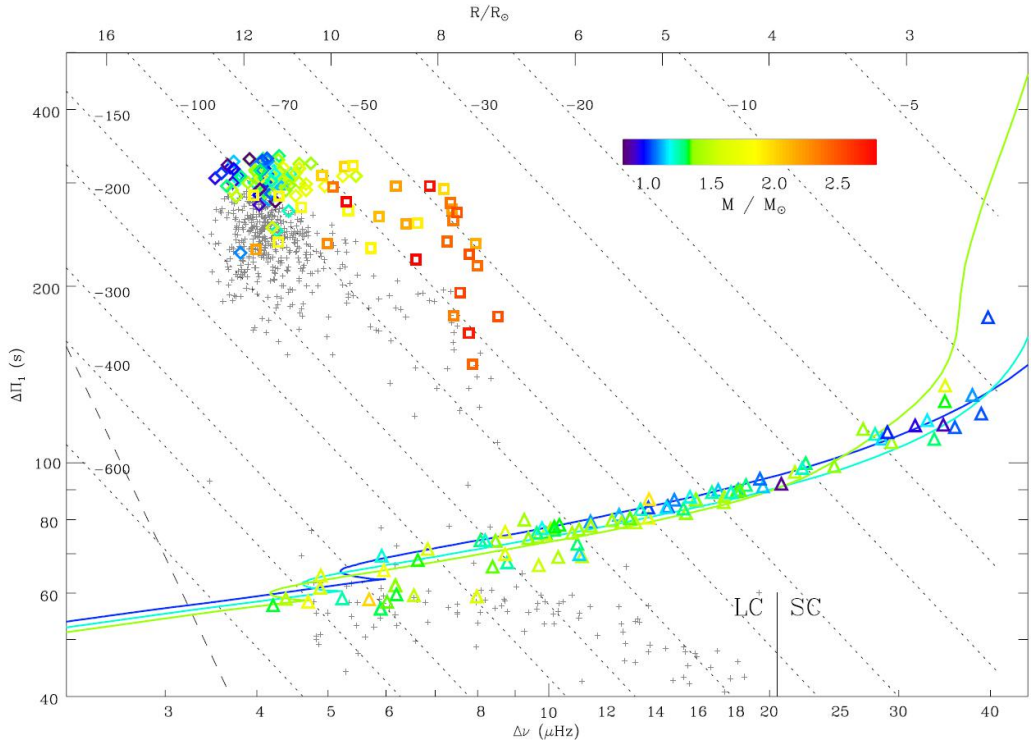

Fig. 4. Gravity-mode period spacing $\Delta\Pi_1$ as a function of the pressure-mode large frequency spacing $\Delta\nu$, for a set of red giants observed with *Kepler*. Long-cadence data (LC) have $\Delta\nu \leq 20.4\,\mu$Hz. RGB stars are indicated by triangles; clump stars by diamonds; secondary clump stars by squares. Uncertainties in both parameters are smaller than the symbol size. The seismic estimate of the mass is given by the color code. Small gray crosses indicate the bumped periods ΔP measured by Mosser et al. (2011a). Dotted lines are n_g isolines. The dashed line in the lower left corner indicates the formal frequency resolution limit. The upper x-axis gives an estimate of the stellar radius for a star whose ν_{max} is related to $\Delta\nu$ according to the mean scaling relation $\nu_{max} = (\Delta\nu/0.28)^{1.33}$ (both frequencies in μHz). The solid colored lines correspond to a grid of stellar models with masses of 1, 1.2 and 1.4 $M_\odot$, from the ZAMS to the tip of the RGB. Figure from Mosser et al. (2012c).

Table 1. Scaling relations

parameter		unit	coefficient α	exponent β
large separation	$\Delta\nu_{obs}$	μHz	0.274 ± 0.004	0.757 ± 0.004
	$n_{max} = \nu_{max}/\Delta\nu - \varepsilon_{obs}$	–	3.26 ± 0.031	0.242 ± 0.005
FWHM	$\delta\nu_{env}$	μHz	0.73 ± 0.03	0.88 ± 0.01
	$n_{env} = \delta\nu_{env}/\Delta\nu$	–	2.49 ± 0.12	0.13 ± 0.01
Height at ν_{max}	H_{max}	ppm^2 μHz^{-1}	$(2.03 \pm 0.05)\ 10^7$	-2.38 ± 0.01
Background at ν_{max}	B_{max}	ppm^2 μHz^{-1}	$(6.37 \pm 0.02)\ 10^6$	-2.41 ± 0.01
HBR	H_{max}/B_{max}	–	3.18 ± 0.09	0.03 ± 0.03
Granulation	P_g	ppm^2 μHz^{-1}		-2.15 ± 0.12
	τ_g	s		-0.90 ± 0.005
	$P_g(\tau_g)$	ppm^2 μHz^{-1}		2.34 ± 0.01
radius	R	$R_\odot$	63.1 ± 1.1	-0.49 ± 0.01
effective temperature	T_{eff}	K	3922 ± 50	0.051 ± 0.05

- All results were obtained with the COR pipeline (Mosser et al. 2012a). Granulation data are from Mathur et al. (2011).
- Each parameter is estimated as a power law of ν_{max}, with α the coefficient and β the exponent, except $P_g(\tau_g)$.

$\Delta\Pi_1$ change is about 100 s (Fig. 4). Since the measurement of $\Delta\Pi_1$ is more precise than 0.1 s, it is formally possible to track the timing of the ascent of a red giant with a precision as high as 0.1 %.

4 Scaling relations

4.1 Seismic parameters

As a result of homology, the red giant global seismic parameters conform to a large numbers of scaling relations. Their variations with $\nu_{\rm max}$ are summarized in Table 1, where we consider:

- The mean observed large separation $\Delta\nu_{\rm obs}$ measured in a broad frequency range around $\nu_{\rm max}$, and $n_{\rm max} = \nu_{\rm max}/\Delta\nu_{\rm obs} - \varepsilon_{\rm obs}$ which provides an estimate of the radial order at $\nu_{\rm max}$; $n_{\rm max}$ significantly decreases when $\Delta\nu_{\rm obs}$ decreases. For the Sun, $n_{\rm max} \simeq 22$; at the red clump, $n_{\rm max} \simeq 8$; and at the tip of the RGB, $n_{\rm max} \simeq 2.5$.

- $\delta\nu_{\rm env}$ is the full-width at half-maximum of the smoothed excess power; $n_{\rm env} = \delta\nu_{\rm env}/\Delta\nu_{\rm obs}$ provides $\delta\nu_{\rm env}$ is large separation unit; as $n_{\rm max}$, $n_{\rm env}$ significantly decreases when $\Delta\nu_{\rm obs}$ decreases since $\delta\nu_{\rm env}$ approximately scales as $\nu_{\rm max}$.

- $H_{\rm max}$ (in ppm$^2\,\mu$Hz^{-1}) is the mean height of the modes at $\nu_{\rm max}$, defined according to the description of smoothed excess power as a Gaussian envelope (e.g., Mosser et al. 2012a).

- $B_{\rm max}$ (in ppm$^2\,\mu$Hz^{-1}) is the value of the stellar background B at $\nu_{\rm max}$. The background is described by Harvey-like components (Michel et al. 2008). Each component is a modified Lorentzian of the form $b(\nu) = a/[1 + (2\pi\,\nu\tau)^\alpha]$, where τ is the characteristic time scale. The exponent α is in the range 2 – 4 (Mathur et al. 2011). $H_{\rm max}/B_{\rm max}$ is representative of the height to background ratio (HBR) at $\nu_{\rm max}$. This ratio shows no significant variation all along the RGB.

- Properties of the granulation signal are also considered (Mathur et al. 2011): $P_{\rm g}$ is the height of the granulation component ; $\tau_{\rm g}$ is the time scale of this background component related to the granulation signal. We note that the exponent of the $P_{\rm g}(\tau_{\rm g})$ scaling relation is, in absolute value, very close to the exponent of the $B_{\rm max}(\nu_{\rm max})$ scaling relation. This means that the energy content in the granulation and in the oscillations are certainly linked.

- Finally, we provide estimates of the fundamental parameters R and $T_{\rm eff}$.

Some of the scaling relations are illustrated in Fig. 5 that shows, compared to the Sun, oscillation spectra of red giants from the bottom to the top of the RGB. Currently, we lack theoretical models for explaining most of these relations. Large efforts have been devoted to explain the scaling relations of the mean amplitude $A_{\rm max}$. This global parameter can be fitted, in limited frequency range, as in Mosser et al. (2012a). However, the fit heavily depends on the method (Stello et al. 2011a; Huber et al. 2011), so that it is not yet possible to provide a physically relevant result (Corsaro et al. 2013). Samadi et al. (2012) have shown that scaling relations of mode amplitudes cannot be extended from main-sequence to red giant stars because non-adiabatic effects for red giant stars cannot be neglected. Samadi et al. (2013a) have recently proposed a theoretical model of the oscillation spectrum associated with the stellar granulation as seen in disk-integrated intensity. With this model, Samadi et al. (2013b) have highlighted the role of the photospheric Mach number for controlling the properties of the stellar granulation.

4.2 Mass and radius scaling relations

As already stated, the seismic global parameters $\nu_{\rm max}$ and $\Delta\nu$ scale, respectively, as the atmospheric cutoff frequency and as the square root of the mean density. Hence, seismic relations with $\Delta\nu_{\rm obs}$ and $\nu_{\rm max}$ can be used to provides proxies of the stellar masses and radii. Following Mosser et al. (2013c), we stress that it is necessary to avoid confusion between the large separation $\Delta\nu_{\rm obs}$ observed around $\nu_{\rm max}$, the asymptotic large separation $\Delta\nu_{\rm as}$, and the dynamical frequency ν_0 that scales with $\sqrt{\mathcal{G}M/R^3}$. The measurement of $\Delta\nu_{\rm obs}$ is perturbed by frequency glitches due to the rapid local variation of the sound speed in the stellar interior, related to the density contrast at the core boundary or to the local depression of the sound speed that occurs in the helium second-ionization region (Miglio et al. 2010). The scaling relations write then:

$$\frac{R}{R_\odot} = \left(\frac{\nu_{\rm max}}{\nu_{\rm ref}}\right)\,\left(\frac{\Delta\nu_{\rm as}}{\Delta\nu_{\rm ref}}\right)^{-2}\left(\frac{T_{\rm eff}}{T_\odot}\right)^{1/2}, \tag{4.1}$$

$$\frac{M}{M_\odot} = \left(\frac{\nu_{\rm max}}{\nu_{\rm ref}}\right)^{3}\left(\frac{\Delta\nu_{\rm as}}{\Delta\nu_{\rm ref}}\right)^{-4}\left(\frac{T_{\rm eff}}{T_\odot}\right)^{3/2}, \tag{4.2}$$

with the calibrated references $\nu_{\rm ref} = 3104\,\mu$Hz and $\Delta\nu_{\rm ref} = 138.8\,\mu$Hz. Such reference values were determined in order to avoid systematic bias between the seismic proxies and modeled values (Mosser et al. 2013c).

Compared to scaling relations heavily used elsewhere (e.g., Mosser et al. 2010; Kallinger et al. 2010; Chaplin et al. 2011; Verner et al. 2011a; Silva Aguirre et al. 2011; Stello et al. 2013; Hekker et al. 2013), Eqs. 4.1 and

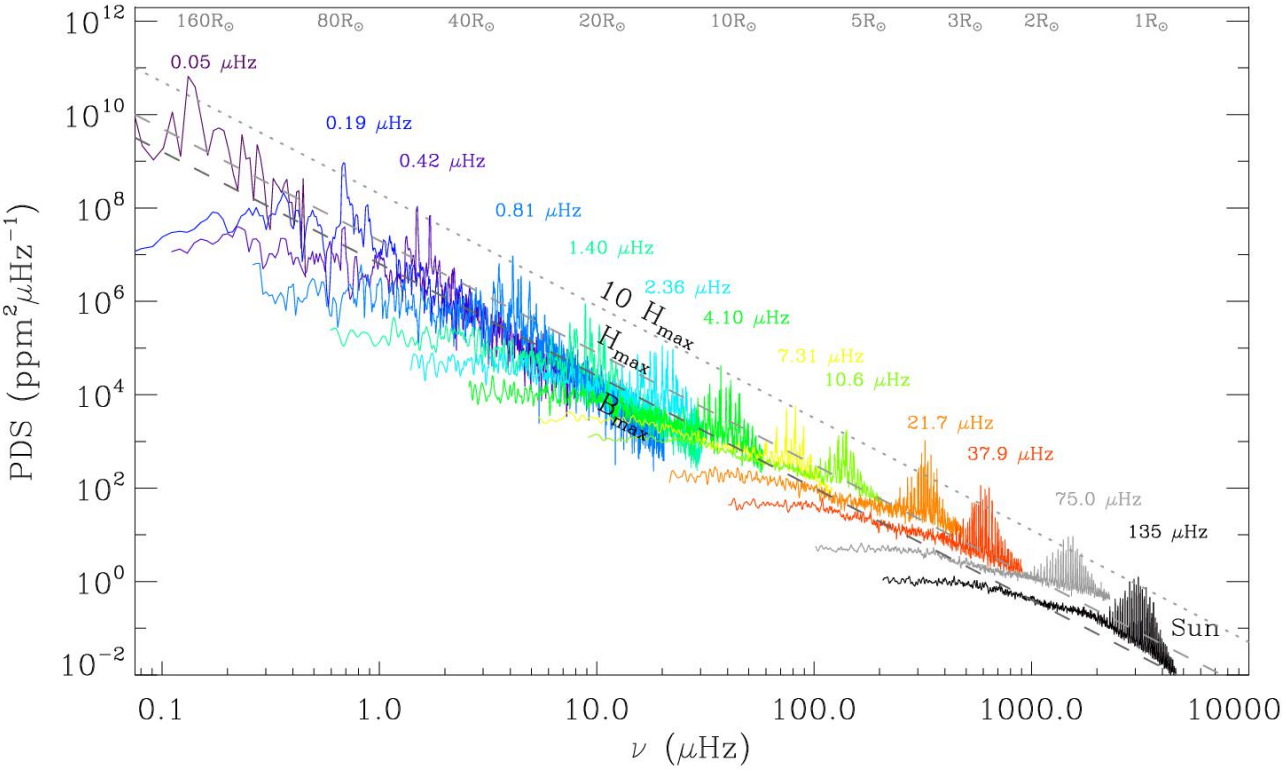

Fig. 5. Superimposition of red giant oscillation spectra from the bottom to the tip of the RGB. Each spectrum is identified by the large separation $\Delta\nu_{\rm obs}$. The Sun spectrum (in black) and another main-sequence spectrum (in grey) are shown for comparison. Except at very low frequency, all spectra were filtered, with a filter width varying with $\nu_{\rm max}$. The fit of the background and mean height at $\nu_{\rm max}$ (Table 1) are indicated with dashed lines. A proxy of the stellar radius is provided along the upper frequency ($\nu_{\rm max}$) axis. Data from Mosser et al. (2012c) and Mosser et al. (2013b)

Table 2. Calibration of the mass and radius scaling relations

	Modeling	Calibration	Observation
$M, R \leftrightarrow$	$\Delta\nu_{\rm as,mod} \leftrightarrow$	?	$\leftrightarrow \Delta\nu_{\rm as,obs} \leftrightarrow \Delta\nu_{\rm obs}$
	$\nu_{\rm max,mod} \leftrightarrow$	?	$\leftrightarrow \nu_{\rm max,obs}$

Calibration process unveiling all formal steps for a proper calibration of the mass and radius scaling relations, with checking of the asymptotic values, determined in the modeling process from $1/(2\int_0^R {\rm d}r/c)$ and in observations from the asymptotically corrected $\Delta\nu_{\rm obs}$.

4.2 make use of the asymptotic large separation instead of the observed large separation. They introduce a correction which can be expressed by

$$R_{\rm as} \simeq \left[1 - 2\,(\zeta - \zeta_\odot)\right] R_{\rm obs} \quad \text{and} \quad M_{\rm as} \simeq \left[1 - 4\,(\zeta - \zeta_\odot)\right] M_{\rm obs}, \tag{4.3}$$

with $\zeta = 0.57/n_{\rm max}$ in the main-sequence regime and $\zeta = 0.038$ in the red giant regime. The amplitude of the correction takes into account the fact that scaling relations are calibrated on the Sun, so that one has to deduce the solar correction $\zeta_\odot \simeq 0.026\,\%$. These asymptotic corrections represent a first step towards the proper calibration of the relation. Contrary to the forms based on the observed large separation, they are not biased, and free of the perturbation of the glitches (Mosser et al. 2013a). This result might contradict Belkacem et al. (2013), who state that $\Delta\nu_{\rm obs}$ provides a better proxy of ν_0 than $\Delta\nu_{\rm as}$. In fact, the contradiction is apparent only: the calibration effort has still to link the asymptotic values derived from the models or derived from the observations (Table 2).

4.3 Calibration of the mass and radius scaling relations

For a proper calibration of the mass and radius scaling relations, we should use the dynamical frequency ν_0 instead of $\Delta\nu_{\rm obs}$ or $\Delta\nu_{\rm as}$, and the acoustic frequency $\nu_{\rm c}$ instead of $\nu_{\rm max}$. As this is not the case, an intensive

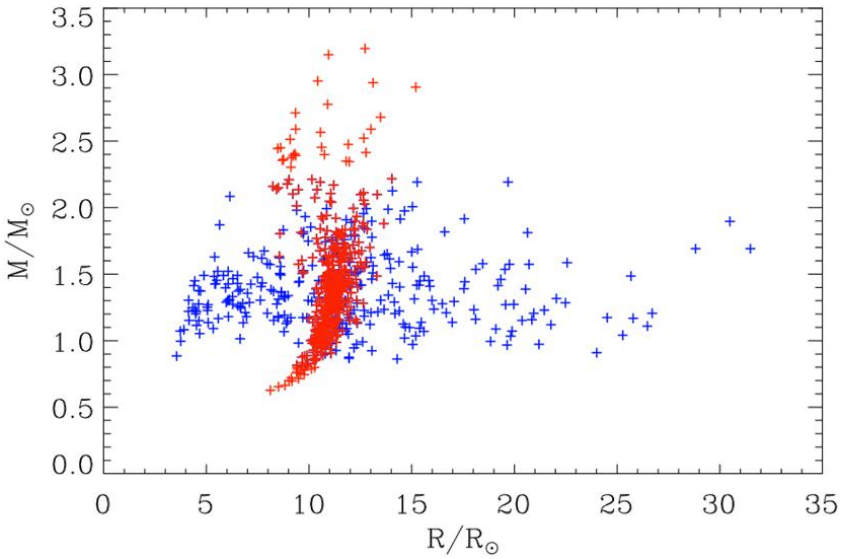

Fig. 6. Mass – radius relation for *Kepler* red giants, with RGB stars in blue and clump stars in red. Adapted from Mosser et al. (2012a).

calibration effort is undertaken:

- An independent verification has been made for stars that have accurate Hipparcos parallaxes, by coupling asteroseismic analysis with the InfraRed Flux Method (Silva Aguirre et al. 2012). The seismic distance determinations agree to better than 5 %: this shows the relevance and the accuracy of the scaling relations in the subgiant and main-sequence regime.

- With long-baseline interferometric measurement of the radius of five main-sequence stars, one subgiant and four red giant stars for which solar-like oscillations have been detected by either Kepler or CoRoT, Huber et al. (2012) have shown that scaling relations are in excellent agreement within the observational uncertainties. They finally derive that asteroseismic radii for main-sequence stars are accurate to better than 4 %.

- Oscillations in cluster stars (Basu et al. 2011) were used to compare scaling relations for red giants in the red clump or on the RGB. Miglio et al. (2012a) have found evidence for systematic differences in the $\Delta\nu_{\rm obs}$ scaling relation between He-burning and H-shell-burning giants. This implies that a relative correction between RGB and clump stars must be considered. As this correction is also related to mass loss, it is currently not possible to measure it precisely. Independent of this, oscillations in cluster stars provide useful constraints on membership (Stello et al. 2011b). They also help constrain the relations depicting the parameters of the pressure mode spectrum (Corsaro et al. 2012).

4.4 Radius, mass and mass loss

The mass and radius scaling relations are illustrated by a mass – radius diagram (Fig. 6). The uncertainties on the inferred mass and radius values discussed above warn us that the absolute values of the data reported here are not yet fully calibrated. However, the trends and the relative variations are relevant, so that it is possible to derive unique information:

- Most of the stellar masses observed on the RGB are in the range [1, 2 $M_\odot$]; less-massive stars spend a longer lifetime on the main sequence, so that they need time to reach the RGB; more massive stars are intrinsically rare and evolve quickly on different evolutionary tracks, especially in the instability strip. So, many of them do not experience solar-like oscillations before having met the RGB; they reach it with a larger radius than lower-mass stars;

- In the red clump, consequently after the tip of the RGB where strong episodes of mass loss occur, the mass distribution is significantly different. Stars with mass down to 0.6 $M_\odot$ are observed: they have necessarily suffered from efficient mass loss near the tip of the RGB. Stars with mass over 2 $M_\odot$ are present, since they spend more time in the helium-burning phase than ascending the RGB in the region where solar-like oscillations are observed.

- The mass-radius relation in the red clump shows a limited spread. All stars in this stage share common

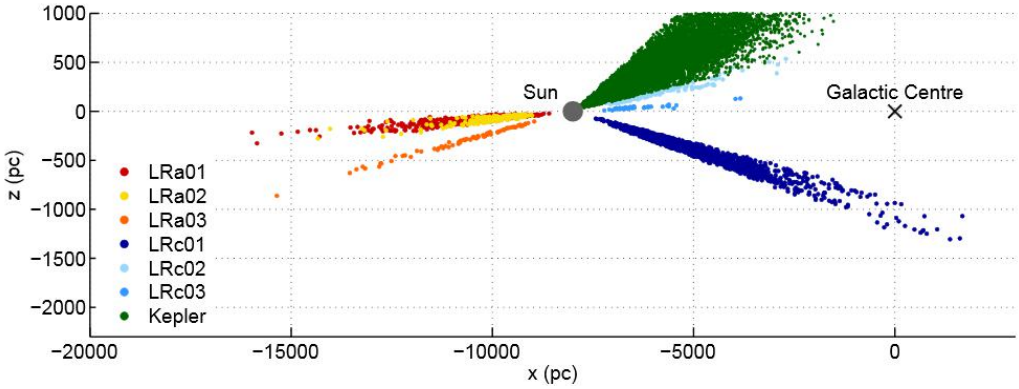

Fig. 7. Solar-like oscillating red giants observed in several CoRoT fields of view and by *Kepler*: projection on the $x - z$ plane. Figure from Miglio et al. (2012b).

properties, as derived from the examination of the $\Delta\Pi_1 - \Delta\nu_{\rm obs}$ relation on the RGB (Fig. 4 and Section 3.2). If we add the information of the effective temperature in Fig. 6, we note that, at fixed mass, the hottest stars have the smallest radius, in agreement with a thinner envelope.

- Secondary-clump stars show a larger spread in the mass-radius diagram compared to clump stars. The difference may arise from the ignition of helium having started in non-degenerate conditions. As already stated above, the mass of transition between the primary and secondary clumps, about $1.8\,M_{\odot}$, is indicative only. Its precise determination requires the careful calibration of the scaling relation (Eq. 4.2).

4.5 Distance measurements and stellar population

An important consequence of the measurement of asteroseismic radii for field stars is the capability of measuring stellar distance. Miglio et al. (2013) have shown that red giants represent a well-populated class of accurate distance indicators, spanning a large age range, which can be used to map and date the Galactic disk in the regions probed by observations made by the CoRoT and *Kepler*. They have determined precise distances for 2000 stars spread across nearly 15 000 pc of the Galactic disk, exploring regions which are a long way from the solar neighbourhood (Fig. 7). Significant differences in the mass distributions of these two samples are interpreted as mainly due to the vertical gradient in the distribution of stellar masses (hence ages) in the disk.

5 Rotation

Rotational splittings have been first observed in a handful of red giants, putting in evidence a significant radial differential rotation (Beck et al. 2012; Deheuvels et al. 2012). Mosser et al. (2012c) have developed a dedicated method for automated measurements of the rotational splittings in a large number of red giants. They have also shown that these splittings, dominated by the core rotation, can be modeled with a Lorentzian function that resembles the mixed-mode pattern organization. Under the assumption that a linear analysis can provide the rotational splitting, they note a small decrease of the mean core rotation rate of stars ascending the RGB. Alternatively, an important slow down is observed for red-clump stars compared to the RGB. They also show that, at fixed stellar radius, the specific angular momentum increases with increasing stellar mass (Fig. 8).

With the same hypothesis of linear splittings, Goupil et al. (2013) have described the morphology of the rotational splittings. They have proven that the mean core rotation dominates the splittings, even for pressure dominated mixed modes. For red giant stars with slowly rotating cores, the variation in the rotational splittings of dipole modes with frequency depends only on the large frequency separation, the g-mode period spacing, and the ratio of the average envelope to core rotation rates. Thus, they have proposed a method to infer directly this ratio from the observations and have validated this method using *Kepler* data. In case of rapid rotation, rotation cannot be considered as a perturbation any more and the linear approach fails (Ouazzani et al. 2013).

For investigating the internal transport and surface loss of the angular momentum of oscillating solar-like stars, Marques et al. (2013) have studied the evolution of rotational splittings from the pre-main sequence to the red-giant branch (RGB) for stochastically excited oscillation modes. They have shown that transport by meridional circulation and shear turbulence cannot explain the observed spin-down of the mean core rotation. They suspect the horizontal turbulent viscosity to be largely underestimated.

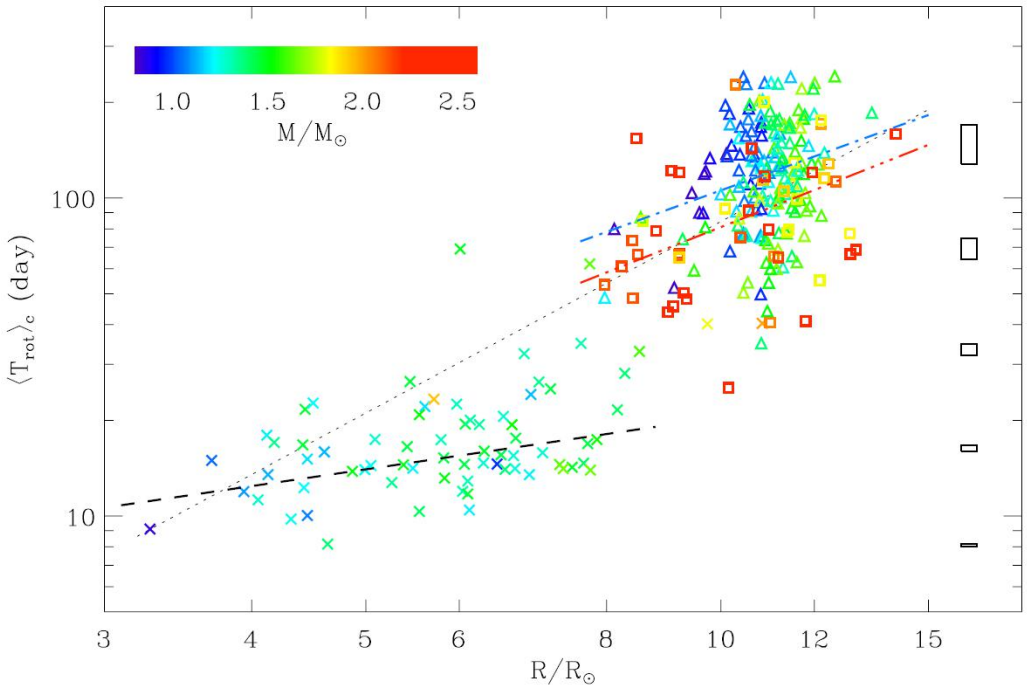

Fig. 8. Mean period of core rotation as a function of the asteroseismic stellar radius, in log-log scale. The dotted line indicates a rotation period varying as R^2. The dashed (dot-dashed, triple-dot-dashed) line indicates the fit of RGB (clump, secondary clump) core rotation period. The rectangles in the right side indicate the typical error boxes, as a function of the rotation period. Figure from Mosser et al. (2012b).

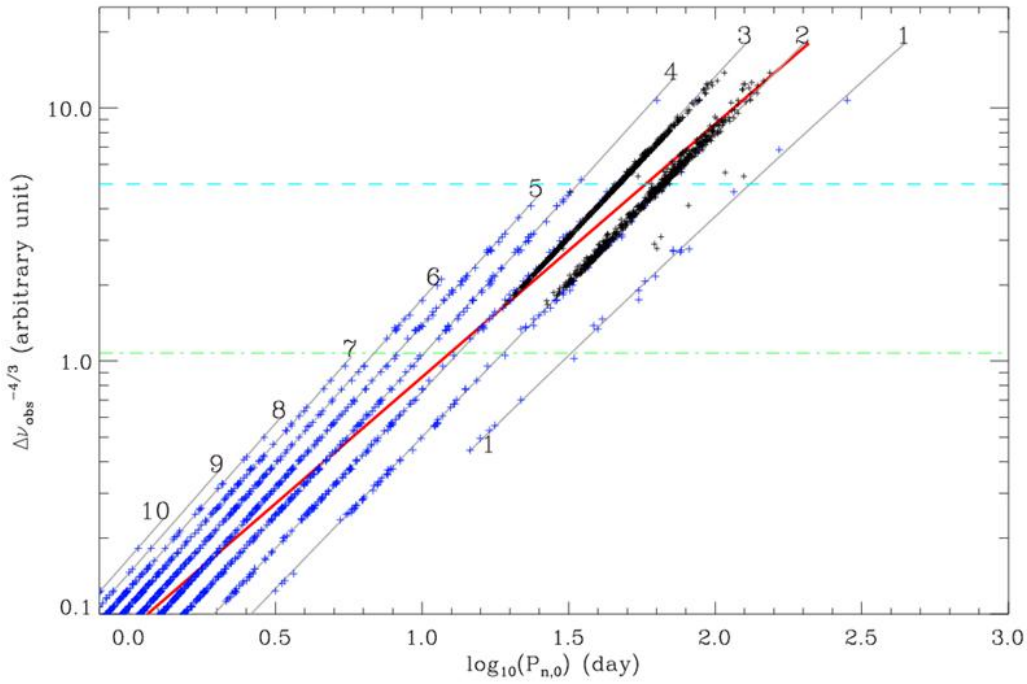

Fig. 9. Period-luminosity relations with *Kepler* (blue) and OGLE data (black), from Mosser et al. (2013b). The blue dashed line indicates the location of the tip of the RGB.

6 Oscillations in evolved M giants

Semi-variability in evolved M giants is suspected to be due to solar-like oscillations. However, until recently, only indirect information was available for sustaining this hypothesis (e.g., Dziembowski & Soszyński 2010). The question concerning the nature of these oscillations is now solved with *Kepler* observations (Mosser et al. 2013b). According to scaling relations, such oscillations occur at very low frequency: at the tip of the RGB, $1/\nu_{\rm max}$ corresponds to periods of 50 days. The monitoring of such oscillations has benefitted from the unique length of *Kepler* observation (more than 3 years) and is unfortunately out of reach with CoRoT observations limited to five months (e.g., Barban et al. 2009).

The solution for unambiguously identifying solar-like oscillations at very low frequency is based on two arguments. First, the relevance of the universal red giant oscillation pattern for less-evolved evolutionary stages implies that, at late stages, oscillation spectra very certainly show homologous properties. Second, the $\varepsilon_{\rm obs}(\Delta\nu_{\rm obs})$ relation observed in the whole red giant oscillation regime is justified by the validity of the second-order asymptotic expansion. Consequently, this relation was extrapolated to very low $\nu_{\rm max}$, and iteratively adapted to provide an acceptable fit of the M-giant oscillation spectra. The success of the fits for all red giants, except in a limited number of cases with a very low signal-to-noise-ratio oscillation spectrum or frequency leakage due to binarity, has proven the relevance of the method.

Period-luminosity relations interpreted as solar-like oscillations are shown in Fig. 9; OGLE data are superimposed. When the large separation decreases, the radial orders of the observed modes decrease too, down to $n_{\rm max} = 2$. The fits show that mostly radial $n = 2$ and 3 modes are observed below the tip of the RGB. Interpreting oscillations in semi-regular variables has many consequences: the parametrization of the oscillation spectrum will help reanalyze the ground-based observations and to define more accurately the different sequences. Interpreting period-luminosity relations in red giants in terms of solar-like oscillations might by used to reinvestigate with a firm physical basis the time series obtained from ground-based microlensing surveys. This will provide improved distance measurements and open the way to extragalactic asteroseismology, with the observations of M giants in the Magellanic Clouds. Mosser et al. (2013b) have also shown that the acceleration of the external layers of red giant with solar-like oscillations is about the same order of magnitude as the surface gravity when the stars reach the tip of the RGB. This shows that oscillations might play a non-negligible role in the mass-loss process.

7 Conclusions?

Ensemble asteroseismology is an active field in current progress. Any conclusion written now will be out of date tomorrow. Plenty of work remains to be done:

- examining the fine structure of the universal red-giant oscillation pattern;
- establishing a thorough calibration of the mass and radius scaling relations;
- modelling a large number of stars, with improved stellar physics;
- deriving precise stellar ages;
- irrigating many connected themes: distance measurement, population study, gyrochronology, late stages evolution...

Following the successful space missions CoRoT and *Kepler*, a next-generation seismic project requires simple but demanding characteristics: long, continuous, and ultra-precise photometric observations. A complete survey of the sky, twin of the ESA Gaia mission, able to derive the seismic global indices $\Delta\nu_{\rm obs}$ and $\nu_{\rm max}$ for millions of stars, is certainly a highly-promising project.

Funding for the Discovery mission *Kepler* is provided by NASA's Science Mission Directorate. The authors acknowledge financial support from the "Programme National de Physique Stellaire" (PNPS, INSU, France) of CNRS/INSU and from the ANR program IDEE "Interaction Des Étoiles et des Exoplanètes" (Agence Nationale de la Recherche, France).

References

Appourchaux, T., Belkacem, K., Broomhall, A.-M., et al. 2010, A&A Rev., 18, 197
Barban, C., Deheuvels, S., Baudin, F., et al. 2009, A&A, 506, 51
Basu, S., Grundahl, F., Stello, D., et al. 2011, ApJ, 729, L10
Baudin, F., Barban, C., Goupil, M. J., et al. 2012, A&A, 538, A73
Beck, P. G., Bedding, T. R., Mosser, B., et al. 2011, Science, 332, 205
Beck, P. G., Montalban, J., Kallinger, T., et al. 2012, Nature, 481, 55

Bedding, T. R., Mosser, B., Huber, D., et al. 2011, Nature, 471, 608
Belkacem, K., Goupil, M. J., Dupret, M. A., et al. 2011, A&A, 530, A142
Belkacem, K., Samadi, R., Mosser, B., Goupil, M. J., & Ludwig, H.-G. 2013, ArXiv e-prints
Bruntt, H., Basu, S., Smalley, B., et al. 2012, MNRAS, 423, 122
Chaplin, W. J., Kjeldsen, H., Bedding, T. R., et al. 2011, ApJ, 732, 54
Corsaro, E., Fröhlich, H.-E., Bonanno, A., et al. 2013, MNRAS, 430, 2313
Corsaro, E., Stello, D., Huber, D., et al. 2012, ApJ, 757, 190
Deheuvels, S., García, R. A., Chaplin, W. J., et al. 2012, ApJ, 756, 19
di Mauro, M. P., Cardini, D., Catanzaro, G., et al. 2011, MNRAS, 415, 3783
Dupret, M., Belkacem, K., Samadi, R., et al. 2009, A&A, 506, 57
Dziembowski, W. A. & Soszyński, I. 2010, A&A, 524, A88
Goupil, M. J., Mosser, B., Marques, J. P., et al. 2013, A&A, 549, A75
Hekker, S., Elsworth, Y., De Ridder, J., et al. 2011, A&A, 525, A131
Hekker, S., Elsworth, Y., Mosser, B., et al. 2013, A&A, 556, A59
Hekker, S., Elsworth, Y., Mosser, B., et al. 2012, A&A, 544, A90
Huber, D., Bedding, T. R., Stello, D., et al. 2011, ApJ, 743, 143
Huber, D., Bedding, T. R., Stello, D., et al. 2010, ApJ, 723, 1607
Huber, D., Ireland, M. J., Bedding, T. R., et al. 2012, ApJ, 760, 32
Jiang, C., Jiang, B. W., Christensen-Dalsgaard, J., et al. 2011, ApJ, 742, 120
Kallinger, T., Mosser, B., Hekker, S., et al. 2010, A&A, 522, A1
Kippenhahn, R. & Weigert, A. 1990, Stellar Structure and Evolution
Kiss, L. L., Szabó, G. M., & Bedding, T. R. 2006, MNRAS, 372, 1721
Marques, J. P., Goupil, M. J., Lebreton, Y., et al. 2013, A&A, 549, A74
Mathur, S., Hekker, S., Trampedach, R., et al. 2011, ApJ, 741, 119
Michel, E., Baglin, A., Auvergne, M., et al. 2008, Science, 322, 558
Miglio, A., Brogaard, K., Stello, D., et al. 2012a, MNRAS, 419, 2077
Miglio, A., Chiappini, C., Morel, T., et al. 2013, MNRAS, 429, 423
Miglio, A., Montalbán, J., Carrier, F., et al. 2010, A&A, 520, L6
Miglio, A., Morel, T., Barbieri, M., et al. 2012b, in European Physical Journal Web of Conferences, Vol. 19, EPJWC, 5012
Montalbán, J., Miglio, A., Noels, A., et al. 2013, ApJ, 766, 118
Mosser, B. 2013, in European Physical Journal Web of Conferences, Vol. 43, EPJWC, 3003
Mosser, B. & Appourchaux, T. 2009, A&A, 508, 877
Mosser, B., Barban, C., Montalbán, J., et al. 2011a, A&A, 532, A86
Mosser, B., Belkacem, K., Goupil, M., et al. 2011b, A&A, 525, L9
Mosser, B., Belkacem, K., Goupil, M., et al. 2010, A&A, 517, A22
Mosser, B., Belkacem, K., & Vrard, M. 2013a, ArXiv e-prints
Mosser, B., Dziembowski, W., Belkacem, K., et al. 2013b, ArXiv e-prints
Mosser, B., Elsworth, Y., Hekker, S., et al. 2012a, A&A, 537, A30
Mosser, B., Goupil, M. J., Belkacem, K., et al. 2012b, A&A, 548, A10
Mosser, B., Goupil, M. J., Belkacem, K., et al. 2012c, A&A, 540, A143
Mosser, B., Michel, E., Belkacem, K., et al. 2013c, A&A, 550, A126
Ouazzani, R.-M., Goupil, M. J., Dupret, M.-A., & Marques, J. P. 2013, A&A, 554, A80
Samadi, R., Belkacem, K., Dupret, M.-A., et al. 2012, A&A, 543, A120
Samadi, R., Belkacem, K., & Ludwig, H.-G. 2013a, ArXiv e-prints
Samadi, R., Belkacem, K., Ludwig, H.-G., et al. 2013b, ArXiv e-prints
Silva Aguirre, V., Casagrande, L., Basu, S., et al. 2012, ApJ, 757, 99
Silva Aguirre, V., Chaplin, W. J., Ballot, J., et al. 2011, ApJ, 740, L2
Stello, D., Huber, D., Bedding, T. R., et al. 2013, ApJ, 765, L41
Stello, D., Huber, D., Kallinger, T., et al. 2011a, ApJ, 737, L10
Stello, D., Meibom, S., Gilliland, R. L., et al. 2011b, ApJ, 739, 13
Tassoul, M. 1980, ApJS, 43, 469
Unno, W., Osaki, Y., Ando, H., Saio, H., & Shibahashi, H. 1989, Nonradial oscillations of stars, ed. Unno, W., Osaki, Y., Ando, H., Saio, H., & Shibahashi, H.
Verner, G. A., Chaplin, W. J., Basu, S., et al. 2011a, ApJ, 738, L28
Verner, G. A., Elsworth, Y., Chaplin, W. J., et al. 2011b, MNRAS, 415, 3539

SF2A 2013
L. Cambrésy, F. Martins, E. Nuss and A. Palacios (eds)

A NEW GENERATION OF INFRARED SKY SURVEY FOR THE E-ELT ERA

I. Vauglin[1], M. Langlois[1], G. Moretto[2], N. Epchtein[3], E. Aristidi[3], M. Carbillet[3] and L. Abe[3]

Abstract. A New Generation Infrared Sky Survey (ANGISS) is proposed for the next decade offering performances matching the requests of the new extremely large telescopes such as the E-ELT in order to prepare and follow-up their programmes. This will require the coverage of thousands of square degrees at K $\sim$ 25 or better, with an angular resolution of $\sim$ 300 mas and time domain exploration. Set up on the Antarctic Plateau, a NGISS using a relatively modest telescope (2.5 to 4 m) looks particularly attractive. Moreover, an off-axis optical combination is preferred to fully benefit from the exceptional atmospheric properties of the site and to explore the 2.3-4 m window in optimal thermal emission conditions.

Keywords: off-axis telescope, infrared astronomy, Antarctic astronomy

1 Introduction

A new era for optical/IR astronomy will begin by the end of this decade with JWST, LSST, EUCLID and 30/40 m class ground based telescopes such as the E-ELT. Such instruments providing gains in sensitivity of several orders of magnitudes will require new large scale surveys (such as LSST) that will accompany their missions and key-programs to single out and follow-up new sources. Renewed canonic documents such as digitized catalogues and maps will be required. In the infrared range, projects are currently proposed to supersede 2MASS by a factor $\sim$ 1000 in sensitivity and $\sim$ 3 in angular resolution, such as SASIR in the Northern Sky. We propose a project of a New Generation Infrared Sky Survey (NGISS) for the Southern sky that could benefit from the Polar atmospheric conditions to optimize the performances and to extend the spectral coverage beyond 2.3μm.

2 Requirements and performances

The 2MASS survey is not deep enough for preparing, accompanying and making the follow-up of ELT IR key-programs. A NGISS should also supersede VISTA in sky coverage, sensitivity, angular resolution and spectral range. Its coverage of the Southern Sky will be 5 to 15 000 square degrees and its high sensitivity bring a of gain $\sim$ 1000 with respect to 2MASS at K. Figure 1 compares NGISS sensitivity to other surveys. Its off-axis telescope design reaches a high contrast and thanks to the site qualities added to a GLAO system, a high angular resolution of 0.3 arcsec or better is obtained. With an extend spectral coverage beyond 2.3μm (in particular the K dark and L windows) ANGISS will bridge ground and space surveys (WISE, Spitzer,).

The PLT would be the most sensitive instrument ever installed on the ground at 2μm pushing the limit at least 2 magnitudes below the VISTA achievement (Dalton 2010). Table 1 summarizes the point source and extended object limiting sensitivities (in AB magnitudes) for a 5σ, 1 hour integration, assuming that the sky background is summed over 4 times the FHWM disc (for point sources), that the telescope temperature is stabilized at 227 K with 5% emissivity, and the overall optical efficiency is 50% (including throughput, detector efficiencies, and secondary mirror obscuration).

[1] Centre de Recherche Astrophysique de Lyon, UMR 5574, F-69230, Saint-Genis Laval, France, Université Lyon1, Université de Lyon, F-69622, Lyon, France
[2] Institute of Nuclear Physics of Lyon, IN2P3-CNRS, Université de Lyon, F-69622, Lyon, France
[3] Laboratory J-L. Lagrange, UNS, OCA, F-06108, Nice, France

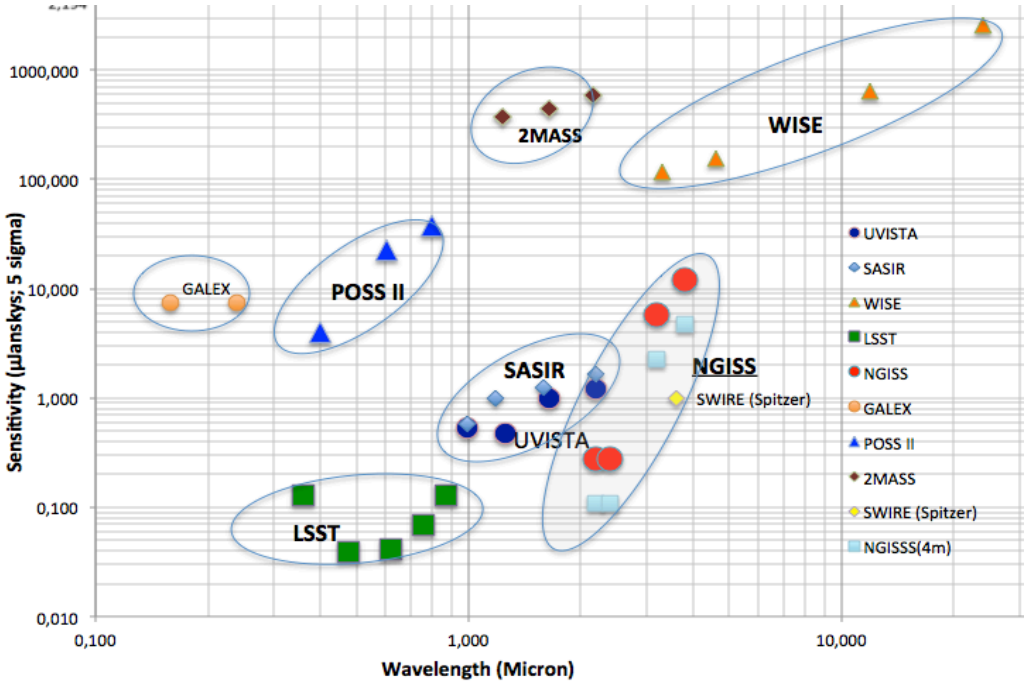

Fig. 1. The expected sensitivity of NGISS compared to other surveys

Band	λ (μm)	**R** ($\lambda/\Delta\lambda$)	**FWHM** ($''$)	$\mathbf{m_{AB}}$ mag.	$\mathbf{m_{AB}}$ /arc^2
Kd	2.40	10	0.32	25.3	24.7
Ls	3.40	6	0.38	20.8	20.1
L′	3.76	5.8	0.40	21.2	20.8
M	4.66	19	0.46	19.6	19.4

Table 1. Expected sensitivity of the PLT adapted from Lawrence 2009

3 Top sciences drivers

The science cases for which observations in polar environment could bring important breakthroughs was debated at the international level, particularly in Europe within the former ARENA network (*see,* Epchtein and Candidi 2007, Zinnecker, Epchtein and Rauer 2008, Spinoglio and Epchtein 2010), Three top science drivers that will take benefit from a NGISS are pinpointed:
(i) the distant universe: high redshift galaxies. The H_2 line is one of the main tracers of star formation. It lies in the K band for $z = 2$ to 3, the peak for star bursts in the evolution of galaxies. In the L band the $z = 4$ to 5 range can be explored. Survey and light curve follow-up of type Ia Sne in dusty galaxies would allow to improve constraints on the cosmological parameters derived from SNIa.
(ii) Extragalactic stellar populations: a synoptic time monitoring of Magellanic Stellar populations (extension of VMC- deeper- $\lambda > 2.3\mu$m) in order to understand star formation processes and extreme populations of AGB stars.
(iii) Low mass stars and exoplanet science: K and M–type stars have their maximum brightness in this spectral domain, allowing a systematic study of planets around these stars. Such a census is necessary for a full appraisal of the planet formation process. The transit and micro-lensing techniques of detection and characterization of exoplanets can benefit from the unique properties of Dome C. Applying these in the near infrared can enable to reach a remarkable depth.

4 Instrumental concept

Such an IR facility installed in an exceptional site should have: (1) the highest possible dynamic range, (2) the best angular resolution and (3) wide-field imaging capabilities in the near- and thermal-infrared range.

At Dome C, the boundary layer contributes to 90% to the total integrated atmospheric turbulence. If this low turbulence is corrected, then Dome C appears to be twice as good as the best temperate siteswith a median free-atmosphere seeing of about 0.3 arcsec at 500 nm. Isoplanatic angles are larger by a factor of two to three at any altitude compared to other ground-based sites and reaches about 6 arcsec. To reach such a goal, ground-layer adaptive optics (GLAO) has been proposed.

A telescope that optimally meets the science and site performance possibilities is an off-axis telescope.
An off-axis telescope can have a superior constrast because it provides an inherently low scattered light design because there are no obstructions in the beam. There are a minimal number of scattered light sources. All mirrors can be robustly supported and articulated because of the easy access allowed by this design. All warm components, sources of the telescope self-thermal emission, will be out of optical beam minimizing its emissivity allowing observations in the K and L-windows. Thus it has a tremendous advantage for detecting faint planets around star. Another advantage is for adaptative optics performances because this configuration has no azimuthal PSF structure, no extrapolated wave front errors. A description of this configuration can be found in Moretto et al.(2012) and Moretto et al. 2012b.

5 Project for an assessment study

We propose a project whose major objectives are:
(1) to define the sciences cases that a new survey could tackle notably in synergy with the coming extremly large telescopes and space missions like E-ELT, EUCLID, JWST. These topics must be precise topics in which observations in polar conditions will bring important breakthroughs;
(2) to design and build a 0.5 - 1 m prototype off-axis telescope to validate the concept;
(3) to design a GLAO device compliant with the specific atmospheric turbulence properties of the site; and
(4) to monitor the sky background emission in K and L-bands at the franco-italian polar station of Concordia, using IRAIT.
Our final goal is the design of 3 - 4 m telescope that would be operational in the beginning of the early 20's, at the E-ELT's arrival.

6 Conclusions

A New Generation Infrared Sky Survey is proposed for the next decade offering performances matching the requests of the new extremely large telescopes such as the E-ELT in order to prepare and follow-up their programmes. This will require the coverage of thousands of square degrees at mag in K better than 25, with an angular resolution of 300 mas and time domain exploration. In the Southern hemisphere, a NGISS using a relatively modest aperture telescope (2.5 to 4 m) set up on the Antarctic Plateau at Dome C looks particularly attractive. Moreover, an off-axis optical combination is preferred to fully benefit from the exceptional atmospheric properties of the site and to explore the $2.3-4\mu$m windows in optimal thermal emission conditions.

References

Moretto G., Epchtein N., Langlois M., Vauglin I., Proc. of SPIE Vol. 8444, 84445E, 2012

Gredel, R., Proc. 3rd ARENA Conf., eds. L. Spinoglio & N. Epchtein, EDP EAS Ser. Vol. 40, 11, 2010

Moretto G.,Vauglin I.,Langlois M., Epchtein N., Proc. SF2A 2012, Eds S. Boissier, P. de Laverny, N. Nardetto, R. Samadi, D. Valls-Gabaud, H. Wozniak, pp. 707, 2012

Epchtein N. (coordinator) and the ARENA consortium, 2010, *A Vision for European Astronomy and Astrophysics at the Antarctic station Concordia, DomeC*, the ARENA roadmap, Novaterra (http://arena.unice.fr)

Session 01

Cassini: révolutions autour de Saturne

SF2A 2013
L. Cambrésy, F. Martins, E. Nuss and A. Palacios (eds)

IMPACT OF TIDAL INERTIAL WAVES DAMPING ON ORBITAL DYNAMICS

P. Auclair-Desrotour[1,2,3], C. Le Poncin-Lafitte[1] and S. Mathis[2,4]

Abstract. Almost all regular satellites of Solar System giant planets exert tidal forcing at frequencies within the range for which inertial waves can be excited in their fluid envelope. Their damping, through their interaction with the turbulent friction of convection, provides an efficient mechanism of tidal dissipation that strongly depends on tidal frequency and leads to the orbital evolution of the satellites. We present in this work a first attempt to understand this evolution with taking hydrodynamics of planetary interiors into account.

Keywords: celestial mechanics, hydrodynamics, planet-star interactions, planet and satellites: dynamical evolution and stability

1 Introduction

Gravitational tides are a key element to understand the dynamical evolution of planets because of exchanges of angular momentum induced between orbits and spins. Since Goldreich & Soter (1966), this interaction has often been modelized by a constant quality factor Q calibrated empirically and bound to the friction inside the body. However, the dependence of Q with respect to the tidal frequency χ is nowadays progressively taken into account (e.g. for rocky planets see Efroimsky & Lainey 2007, refeered as Paper I). Indeed, most of the existing models assume a smooth variation of Q as a function of χ. But, Ogilvie & Lin (2004), refeered as Paper II, showed that dissipation due to inertial waves in convective fluid planets is written as a sum of resonant terms with a strong dependence on χ. Following Paper II, we then consider the impact of this resonant dissipation on the orbital dynamics of the tidal perturber. First, we give the general set-up. Then, dynamical equations are presented together with qualitative results. Finally, we propose a quantitative scaling law establishing the link between the internal physics of the central body and the orbital dynamics of the perturber.

2 Physical set-up

In Paper I, the authors studied the fall of Phobos on Mars using a coplanar, circularized, two body rocky system. Here, we modify their set-up by considering a fully convective fluid central body A with the mass of Mars. Let us quote M_A its mass, R_A its radius, k_2 its Love number, and $\mathbf{\Omega}_A$ its spin that we suppose to be constant in this work. The fluid is newtonian and viscous, with a density ρ and a kinematic viscosity ν. The satellite is assumed to be puctual of mass M_B, and orbiting with a mean motion n_B and a semi-major axis a.

To determine the energy dissipated by viscous friction acting on tidally excited inertial waves in A, we use the local model derived in Paper II where the rotating fluid is contained in a cartesian box of lenght L and submitted to the tidal excitation (see Fig. 1). Paper II showed that such a model already provides the main properties of tidal dissipation in rotating fluid planets.

[1] SYRTE, Observatoire de Paris, UMR 8630 du CNRS, UPMC, 77 Av. Denfert-Rochereau, 75014 Paris, France
[2] Laboratoire AIM Paris-Saclay, CEA/DSM - CNRS - Université Paris Diderot, IRFU/SAp Centre de Saclay, F-91191 Gif-sur-Yvette Cedex, France
[3] IMCCE, Observatoire de Paris, UMR 8028 du CNRS, UPMC, 77 Av. Denfert-Rochereau, 75014 Paris, France
[4] LESIA, Observatoire de Paris, CNRS UMR 8109, UPMC, Univ. Paris-Diderot, 5 place Jules Janssen, 92195 Meudon, France

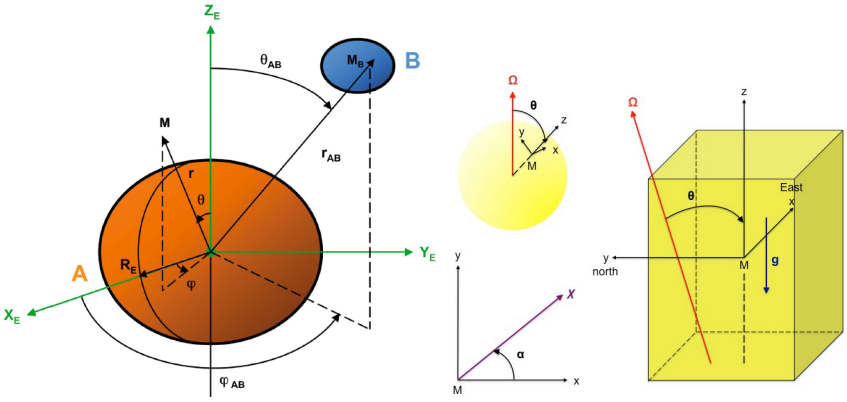

Fig. 1. Left: two-body system; here $\theta_{\rm AB} = \pi/2$ (figure taken from Mathis & Le Poncin-Lafitte 2009, courtesy Astronomy & Astrophysics). **Right:** The rotating cartesian box.

The dynamical equations are the same as in Paper I. First, we have for a:

$$\frac{da}{dt} = -\frac{3k_2 R_A^5 n_B M_B}{M_A a^4} Q^{-1}(\chi)\,\mathrm{sgn}(\chi)\,, \tag{2.1}$$

where χ is here the main tidal frequency $\chi = 2(n_B - \Omega_A)$ and Q is explicitly a function of χ. This dependence links the dynamical evolution to the internal structure, dynamics, and rheology of A.

Our local fluid model provides us the viscous dissipation in fluid, $D(\omega)$, which is proportional to $\omega\, Q^{-1}(\omega)$, $\omega = \chi/2\Omega_A$ being the normalized tidal frequency. Assuming that the box is located at the pole as in Paper II, the dissipation is expressed as a sum of resonant terms:

$$D(\omega) = D_0 \sum_{\{m,n\}\in\mathbb{N}^*\times\mathbb{N}^*} \frac{(m^2+n^2)\,|\tilde{\omega}^2| + n^2}{|(m^2+n^2)\,\tilde{\omega}^2 - n^2|^2}\,(m^2+n^2)\,|n f_{mn} - m h_{mn}|^2\,, \tag{2.2}$$

where the index m and n correspond to the wave-vectors in the azimutal and radial directions, respectively. We introduce in this formula a characteristic complex frequency, $\tilde{\omega} = \omega + iE(m^2+n^2)$, parametrized by the Ekman number of the fluid, $E = \nu/(2\Omega L^2)$. The external volumic excitation intervenes through the Fourier coefficients f_{mn} and h_{mn} describing the tidal forcing. The tidal dissipation strongly depends on tidal frequencies and presents resonances linked to the rheological parameters of the rotating fluid, *i.e.* the Ekman number.

Using the set of parameters of Paper I, we compute the evolution of the semi-major axis a over time with our fluid model and a constant Q. In Fig. 2 (left), we plot the spectrum of viscous dissipation as a function of χ. Next, in Fig. 2 (right), we see the difference between the evolution of a in the case of a Q constant model and the resonant one. The first one causes a regular fall while the fluid model induces an erratic evolution. Indeed, each time the system meets a resonant peak corresponding to a dissipation far higher than the background, the position of the satellite changes abruptly, and so does its mean motion simultaneously. This is the resonance locking identified in the stellar case by Witte & Savonije (1999).

3 Scaling law

As illustrated in Fig. 2 (right), the jumps in the evolution of the semi-major axis do not have the same amplitude. Indeed, it depends on the characteristics of the peak, which are themselves defined by the fluid properties because orbital dynamics and rheology are coupled through the shape of resonances. Equation (2.2) enables us to express the amplitude of a jump in terms of the main characteristics of the associated peak, namely its height H_p and width at mid-height l_p, which are functions of the Eckman number E. Near a resonance, one of the terms of the sum dominates all the others. Considering that the width of a peak is small compared to the distance which separates it from its nearest neighbours and that the numerator varies smoothly compared to the denominator,

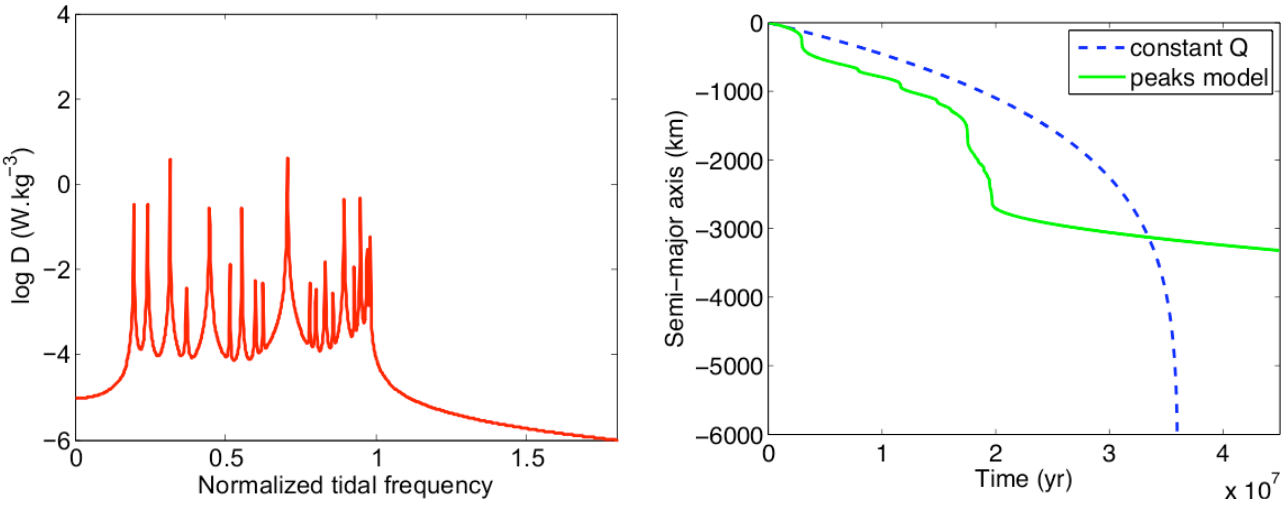

Fig. 2. Left: Resonant tidal dissipation spectrum as a function of the normalized tidal frequency assuming $m \leq 5$ and $n \leq 5$. The vertical axis is in logarithmic scale. **Right:** Evolution of the semi-major axis a of the satellite over time with a Q^{-1} proportionnal to the dissipation of tidal inertial waves (green curve) and with a constant Q factor (blue dashed curve).

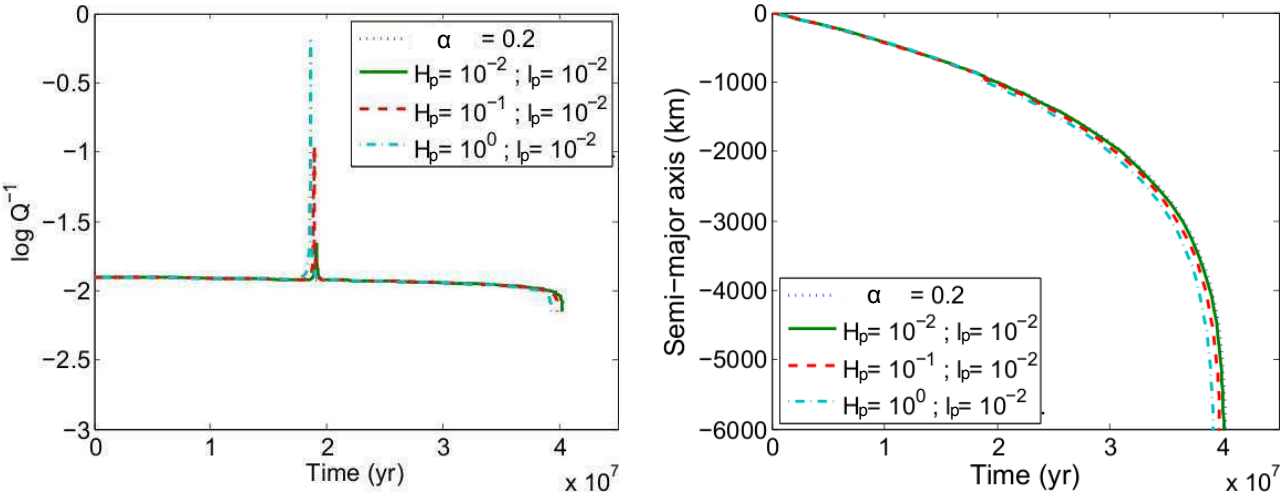

Fig. 3. Left: Evolution of the quality factor over time for various values of H_p. **Right:** Corresponding evolution of the semi-major axis. The grey dotted line corresponding to $\alpha = 0.2$ is superposed to the continuous green one except at the position of the peak for Q^{-1}.

we can isolate the synthetic resonant quality factor $Q_\mathrm{p}^{-1}(\omega)$:

$$Q_\mathrm{p}^{-1}(\omega) = \frac{H_\mathrm{p}}{\left[4\left(\sqrt{2}-1\right)\left(\dfrac{\omega-\omega_\mathrm{p}}{l_\mathrm{p}}\right)^2+1\right]^2}, \tag{3.1}$$

ω_p being the resonant frequency. Then, for a single peak, $Q^{-1}(\omega) = Q_0^{-1}(\omega) + Q_\mathrm{p}^{-1}(\omega)$, Q_0^{-1} being a smooth regular background varying slowlier than Q_p^{-1}. Assuming that the amplitudes of the variations caused by the peak on the semi-major axis Δa and the tidal frequency $\Delta\omega$ are such as $\Delta a \ll a$ and $\Delta\omega \ll \omega$, and considering that the resonance dominates , *i.e.* $Q_\mathrm{p}^{-1} \geq Q_0^{-1}$, we obtain the amplitude of Δa:

$$\frac{\Delta a}{a} \approx \frac{2l_\mathrm{p}}{3\sqrt{\sqrt{2}-1}\,(1+\omega_\mathrm{p})}\left(\sqrt{\frac{H_\mathrm{p}}{Q_0^{-1}(\omega_\mathrm{p})}}-1\right)^{\frac{1}{2}}. \tag{3.2}$$

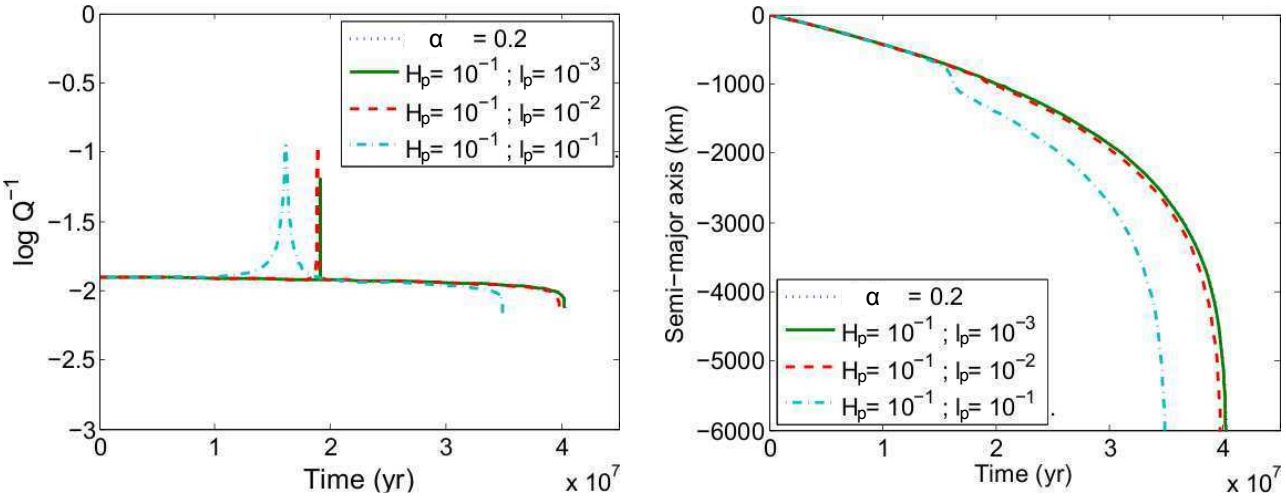

Fig. 4. Left: Evolution of the quality factor over time for various values of $l_{\rm p}$. **Right:** Corresponding evolution of the semi-major axis. The grey dotted line corresponding to $\alpha = 0.2$ is superposed to the continuous green one except at the position of the peak for Q^{-1}.

The impact of rheology is given by $\omega_{\rm p}\,(E)$, $H_{\rm p}\,(E)$, $l_{\rm p}\,(E)$ and $Q_0^{-1}\,(\omega_{\rm p})$. In a forthcoming article, we will explicitly give their expressions.

Following Paper I, where a synthetic smooth background $Q_0^{-1}\,(\omega) \propto |\omega|^{\alpha}$, α being a parameter, we simulate numerically the effect of a resonance on the semi-major axis of the satellite for different values of $H_{\rm p}$ and $l_{\rm p}$ as illustrated in Fig. 3 & 4. As predicted by Eq. 3.2, the simulations clearly demonstrate that the width of the peak $l_{\rm p}$ has a much stronger influence on the amplitude of the jump Δa than its height $H_{\rm p}$.

4 Conclusions

This work constitutes a first attempt to study tidal evolution of planet-moon systems with taking self-consistently hydrodynamical tidal dissipation in the central planet into account. It underlines the role played by inertial waves in convective rotating fluids and shows that dissipation may result from mechanisms narrowly bound to tidal frequency. A resonance between inertial waves and tidal excitation means a damping peak and a jump in the evolution of the satellite semi-major axis. Using the physical expression of viscous dissipation obtained in Paper II, we get a scaling law for jumps amplitude as a function of the height and the width at mid-height of the corresponding resonance. In a forthcoming article, we will detail their analytical expressions with respect to the fluid properties. Note that the obtained results can also be applied to star-planet systems and binary stars.

P. Auclair Desrotour was supported by the Paris Observatory (SYRTE). This work was supported by the Programme National de Planétologie (CNRS/INSU), the GRAM specific action (CNRS/INSU-INP, CNES), the Paris Observatory, the Campus Spatial de l'Université Paris Diderot, and the Emergence-UPMC grant (contract number: EME0911).

References

Efroimsky, M. & Lainey, V. 2007, Journal of Geophysical Research (Planets), 112, 12003

Goldreich, P. & Soter, S. 1966, Icarus, 5, 375

Mathis, S. & Le Poncin-Lafitte, C. 2009, A&A, 497, 889

Ogilvie, G. I. & Lin, D. N. C. 2004, ApJ, 610, 477

Witte, M. G. & Savonije, G. J. 1999, A&A, 350, 129

SF2A 2013
L. Cambrésy, F. Martins, E. Nuss and A. Palacios (eds)

SATURNS RINGS OBSERVED BY THE CASSINI SPACECRAFT (I.S.S.)

André Brahic[1]

Abstract. After 9 years of observations by the Cassini spacecraft Imaging Sub System (ISS), we review the main discoveries on Saturns rings. We have been able to follow the evolution of the rings as a function of time with variations on time scales as short as days. This exploration provided new information on the structure of the rings, on waves, on resonances phenomena, and on ring - satellites interactions. A detailed study of the rings edges, of the spokes and of the F, G, E and D rings has been performed. The discovery of propellers, meteoroid impacts, and of the opposition effect gave new insights on rings evolution. New ideas about the nature of the particles and the age of the rings have been developed.

Keywords: planetary rings, Cassini ISS observations

1 Introduction

The disc around Saturn is a system of colliding particles submitted to the gravitational influence of Saturn and of small nearby satellites. It can be considered as a natural laboratory of dynamics, cosmogony, granular flow and particle and field physics. The structure of the rings is determined by their origin and by dynamical processes which depend upon the sizes and collisional properties of the ring particles, and on the gravitational effects of the satellites. Electromagnetic processes play a role on the motion of charged particles.

Since they were first discovered by Galileo in 1610, the nature of Saturns rings has been a continuing challenge to observation and theory. From the beginning, observational resolution seemed to be just short of revealing the essential nature of the rings. The effort to understand rings has always attracted outstanding scientific minds. Galileos first detection of something strange around Saturn was open to several interpretations. Huygenss revelation of a disc-like structure did not bring any information about rings nature. Cassini suggested that the rings might consist of a myriad of small particles without being able to prove it. Laplace and Maxwell showed that a solid ring would be unstable. Beginning with Poincar, a general picture of collisional flattening and spreading emerged, with structure governed in part by resonances with the satellites. Dynamical theory was adequately consistent with Earth-based observations of seemingly smooth, continuous rings. Optical and radio properties seemed in good agreement with a swarm of small, icy particles of various sizes. Until 1980, theoretical models seemed in harmony with most observed properties.

The space exploration has completely changed our understanding of rings. In spite of 370 years of telescopic observations from the Earth, no one imagined before 1980 the wealth and the diversity of structures inside planetary rings. In a few years, our conception of rings underwent a revolution. In 1980 and 1981, the Voyager spacecrafts revealed countless detailed features and structures that had never been imagined and, in 1984 and 1985, arcs were detected around Neptune by the author as they occulted a star. After the surprises of the Voyager flybys in 1980 and 1981, the Cassini spacecraft, with considerable improvements in resolution and sensitivity, is revealing a system still more complex than foreseen. I have selected a list of 15 observations which completely change our understanding of rings evolution and I briefly quote the list of these important discoveries, without entering into technical details in this short paper.

[1] Université Paris Diderot, C.E.A. Saclay

2 The ring structure

Our understanding of the structure of Saturns rings has improved dramatically over the course of Cassinis initial 9-year mission. This has enabled, for the first time, a detailed observation of non-axisymmetric structures as well as vertical structures in the rings. This continuous observation of the rings during almost a decade and comparison with Voyager observations more than thirty years ago reveal changes in ring structure and variations with time with time scales varying from several years to only a few days.

Saturns rings can be broadly grouped into two categories : dense rings (A, B and C) and tenuous rings (D, E, G and the Cassini Division). The lettered rings contain multiple ringlets within them. Several thousands of structures have been observed. Inside the dense rings, typical optical depths are greater than 0.1 while the dusty rings have optical depths of 10-3 and lower.

Different structures can be observed on all scales inside the rings. The most prominent features of Saturns A ring are the multitude of density waves launched at Lindblad resonances with nearby moons and the two gaps (Encke and Keeler gaps) cleared respectively by Pan and Daphnis. The fine-scale texture of the A ring is dominated by self-gravity wakes. Small moonlets can create in their surroundings small disturbances, which have received the nickname of propellers . The microstructure of the A ring has been observed in unprecedented detail thanks to radio and stellar occultations. The optical depth averages around 0.5 in the A ring.

The B ring contains much of the total mass of the Saturns ring system, but its higher optical makes the detailed observations more difficult. Many density and bending waves as well self-gravity wakes have been detected in this ring. Large-scale irregular structures have been observed in most of the B ring. In its denser part, a nearly bimodal distribution of ring optical depth has been revealed with much of this ring being essentially opaque and with abrupt transitions in optical depth. This may be due to previously unsuspected instabilities in the rings.

The Cassini Division and the C ring are similar in many ways. The most obvious similarity is their optical depth, which averages around 0.1 for both regions and only rarely exceeds 0.5. There are also several narrow gaps, with five of them within the 18 000 kilometres wide C ring while the Cassini Division has eight within its width of only 4 500 kilometres. In comparison, the A ring has only two empty gaps and the B ring has none.

The F ring, located near the Saturns Roche limit and gravitationally perturbed by Prometheus and Pandora, has a variety of unique features. Faint rings (G and E) extend well beyond the Roche zone.

3 Waves

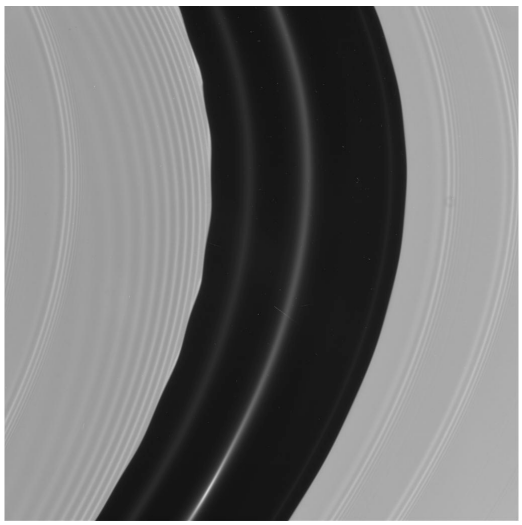

Fig. 1. Waves on the edges of the Encke gap, spiral density waves (on the right) and moonlet wakes (on the left) can be seen in this image. (NASA-JPL / ESA document).

Saturns rings is a waves heaven. Dozens of spiral waves have been observed and five bending waves have been clearly identified. Spiral density waves are densely packed throughout the A ring because a large number of moonlets and satellites are close to this ring and the resulting resonances are closely spaced. These spiral waves

are generated at the locations of resonances with perturbing moons, they propagate away from the resonance location in a single radial direction. Spiral waves are compressional waves while bending waves are transverse waves that arise at locations where a ring particles vertical frequency is in resonance with a perturbing moon. These waves serves as an in situ probe, by which local properties of the rings can be obtained. Spiral density waves transfer angular momentum between the rings and the forcing moons; thus, the orbits of the perturbing moons evolve outward, while those of the ring particles decay inward.

4 Ring-satellite interactions

Moons are intimately involved with much of the structure of the rings. The outer edges of the A and B rings are shepherded and sculpted by resonances respectively with the Janus - Epimetheus co-orbital satellites and Mimas. Density waves at the location of orbital resonances with nearby and embedded moons make up the majority of the large-scale features in the A ring. Pan and Daphnis are massive enough to clear gaps in the A ring. Large ring particles, which are not massive enough to clear a gap, can produce localised propeller-shaped disturbances kilometre long. Clumps and strands are observed in the A, B and F rings. Near the Roche limit, accretion and disruption phenomena are competing in the F ring. Clumps and strands form and are disrupted all the time.

The interactions between satellites and rings are not only gravitational. There also exchanges of material between the satellites and the rings. Enceladus is bringing dust to the E ring while Prometheus is regularly taking away material from the F ring.

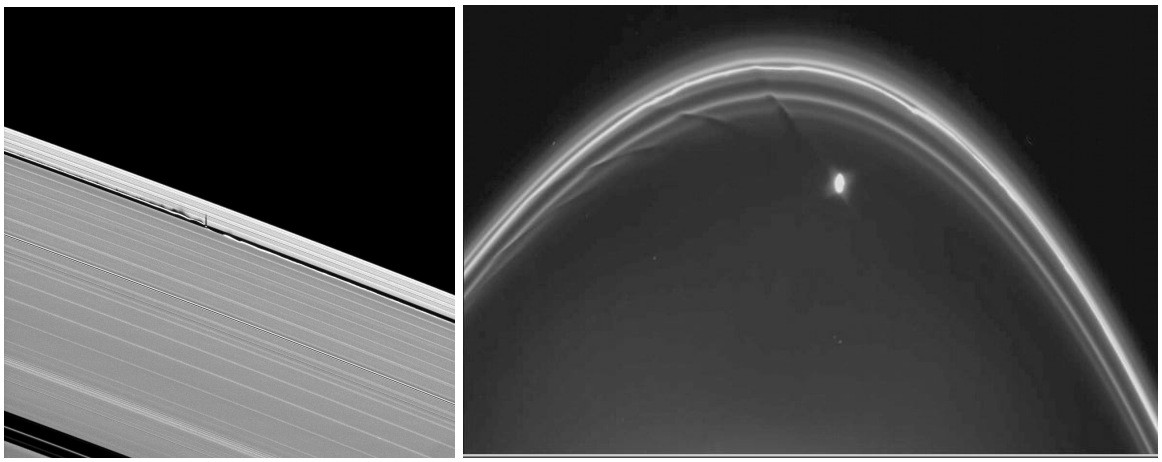

Fig. 2. On the left, the moon Daphnis clear a gap in the A ring and sculpts the edge into waves that have both horizontal and vertical components. On the right, at each close passage, the shepherding moon Prometheus triggers the formation of channels with clumps at the edges. (NASA-JPL / ESA document).

5 Resonances

Resonances in Saturns rings create waves, gaps, wavy edges, vertical structure, material confinement and several other phenomena, making the rings a laboratory of physics and dynamics. Several different types of resonances are at work in Saturns rings, including orbital resonances, mean-motion orbital resonance, secular resonances, Lindblad resonances, vertical resonances, Kozai resonances, etc.

The outer edges of the A and B rings both occur at strong resonances. At the outer edge of the A ring, the ring particle orbital period is equal to 6/7 Janus orbital period while the ring particle orbital period at the outer edge of the B ring is equal to 1/2 Mimas orbital period. The perturbations from the moons cause the edges to move in and out.

Different resonances produce different waves, which can be observed for example at the location of the 5/6 Janus, the 12/13 Pandoras or the 18/19 Prometheus orbital periods. These localised disturbances can even lead to changes in the apparent brightness of the ring, which can be observed for example at the location of the 3/4 Janus, the 4/5 Janus, the 3/5 Mimas orbital periods.

6 Ring edges

Unusual mottled-looking narrow region, with a radial width varying with longitude from 5 to 10 kilometres, have been seen for the first time about 60 kilometres inside the outer edge of Saturns A ring. The mottled regions are probably caused by particle clumping brought about by gravitational disturbances. The outer A ring edge is sculpted into a seven-lobed pattern called a Lindblad resonance by the co-orbital satellites Janus and Epimetheus. The resonant perturbations in this region are complicated by the presence of these two moons whose orbits are within 50 kilometres of each other.

Other kinds of new features like ropy structures have also been found. For example, at the outer edge of the Encke gap, rope-like features can be seen between the first two wakes nearest the gap edge. Theses ropy features appear to be a product of the enhanced gravitational disturbances that occur when the particles pass through the wakes caused by Pan and consequently are squeezed close together. These disturbances obviously persist even outside the wakes, as is evident in the presence of the ropy structures in the bands in between the wakes.

The inner edges of the A and B rings are remarkably similar morphologically. The A ring edge is confined by the 7:6 Lindblad resonance with the co-orbital moons Janus and Epimetheus. Cassini mapping of the edge reveals complex structure, with a time-variable component which may be due to changes in Janus and Epimetheus orbits.

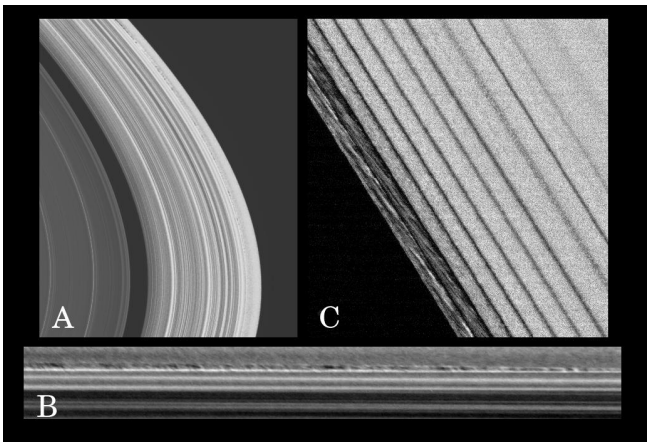

Fig. 3. Image A displays, at the edge of the A ring, a mottled-looking narrow region which have never be seen before. The image B is a close-up of the region. Image C shows the outer edge of the Encke division and the region exterior to it. The wakes of Pan are clearly seen. A different example of mottled structure is seen in the eight Pan wake from the edge, as well as ropy structure within the first two bands exterior to the gap. (NASA-JPL / ESA document).

7 Propellers

Moonlets with sizes much smaller than Daphnis are unable to clear a complete circumferential gap, because their gravitational torques are too feeble to overcome viscous diffusion. However, they do create local disturbances that can be observed. The propellers provide the first direct observation of the dynamical effects of moonlets of about 100 meters in diameter. Such unseen size-class of particles can be detected indirectly. Such disturbances, shaped like propellers due to Keplerian shear, were predicted theoretically and subsequently observed by Cassini.

The radial separation between the two lobes is a few times the moonlet's diameter.Many propellers seem to be confined in the mid-A ring. Variations of propellers' orbits have been observed.

The outer A ring contains swarm of 100-meters size objects, just large enough to disturb nearby ring material into propellers. A handful of extremely large propellers was discovered and tracked. It was found that their orbits were changing with time. This seems to be mainly due to librations in the gravity well of the channel they create.

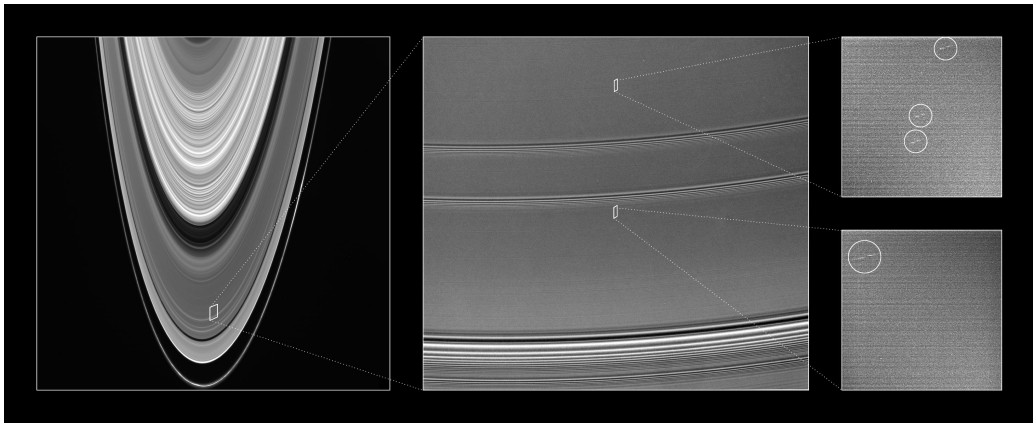

Fig. 4. This zoom shows the first discovered propellers. The centre image is a close view of the A ring, showing the radial locations were where propellers features were spotted. At the right, the propellers appear as double dashes and are circled. The unseen moonlets lie in the centre of each structure. (NASA-JPL / ESA document).

8 Opposition effect

The Cassini cameras captured the opposition effect in Saturns main rings with a fine radial resolution at extremely small phase angles. When Saturns rings are viewed with the Sun directly behind the observer, this opposition effect can be seen. The opposition effect is a sudden nonlinear rise in the reflectance with decreasing phase angle that occurs as the phase angle approaches zero.

Studies of this effect are useful to constrain a number of the properties of ring particles, such as their size and spatial distribution. The observations of this phenomenon are under analysis.

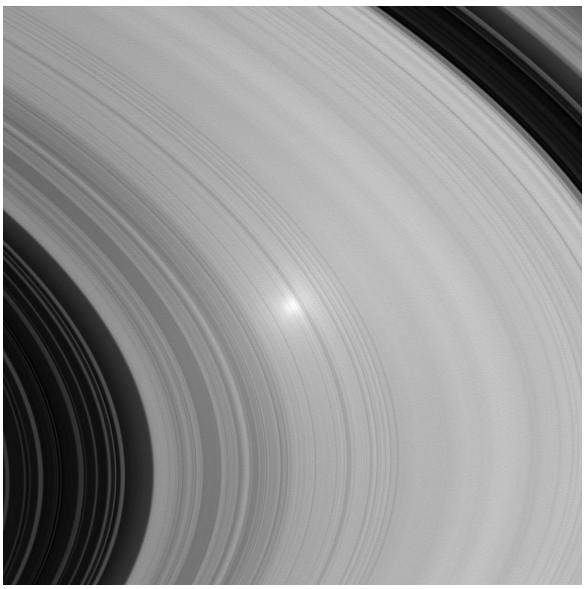

Fig. 5. The opposition effect : The bright spot occurs where the angle between the spacecraft, the Sun and the rings is near zero. (NASA-JPL / ESA document).

9 The Cassini Division

There are many similarities, both in particle properties and structure, between the C ring and the Cassini Division. The location of the Cassini division corresponds to a 1/2 resonance with Mimas. This division, separating the A and B rings by about 4 500 kilometres, is may be the signature of the past orbital evolution

of Mimas. A large diversity of structures can be observed in the Cassini division : gaps, ringlets, plateaux, ramps, etc. The inner edge of 6 gaps are eccentric. Near the A ring, outside 120 400 kilometres, the Cassini Division takes a very different aspect, with no gaps and with a smoothly-varying optical depth with a monotonic increase towards the inner edge of the A ring.

10 The D ring

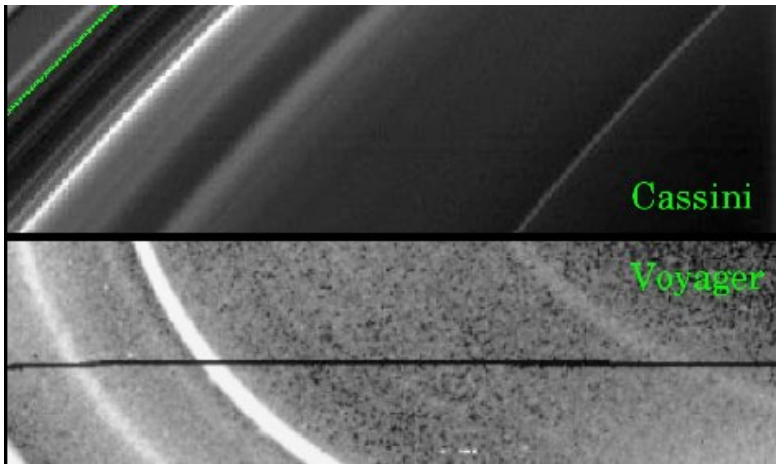

Fig. 6. As seen in the above images, structural evolution has occurred in Saturns D ring during the 25 years separating the Voyager and Cassini missions. The lower image, taken by Voyager 1 in 1980, shows from left to right, the bright inner edge of the C ring and three discrete ringlets: D 73, D 72, and D 68. The upper image, obtained by Cassini, shows the same region from a similar viewing geometry, but there have been some very significant changes in the appearance of the D ring. The green line marks the inner edge of the C ring. The D 72 ringlet has decreased in brightness by more than an order of magnitude relative to the other ringlets. It has also moved inward bout 200 kilometres relative to the others. With a much higher resolution than was possible for Voyager, Cassini revealed surprising fine-scale structures between the C ring and D 73 (inset). (NASA-JPL / ESA document).

The D ring, which is between the inner C ring and the top of Saturns clouds, is among the most complex of the faint rings. It has significantly changed since Voyager. For example, the ringlet located at 72000 kilometres from Saturns centre, called the D72 ringlet, is now much fainter than it used to be, and its centre of light has shifted of about 200 kilometres inwards relative to the other features in the D ring. We see new ringlets exterior to the D73 ringlet. There no longer appears to be any wave-like structure in the diffuse material.

Cassini has observed the D ring at much higher resolution than was possible for Voyager, revealing surprising fine-scale structures with a periodic wave-like structure with a wavelength of 30 kilometres. This complex pattern can be decomposed into multiple series of alternating bright and dark bands tilted relative to the local radial direction.

11 The F ring

Saturns F ring is a narrow, eccentric, inclined ring with unusual, time varying structure. The F ring is located near the Roche limit. Accretion and disruption phenomena are competing. The F ring contains a long-lived core and several narrow peripheral strands, tens of kilometre wide, that vary on time scales of hours to decades. A fainter dust belt spanning about 1 500 kilometres surrounds the strands. Nearby Prometheus causes the primary perturbations, distorting the ring by tens of kilometres at each passage. The phenomenon can be compared to the wakes produced by Pan and Daphnis but is complicated by the large variations in closest approach distance resulting from the orbital eccentricities of the ring and Prometheus.

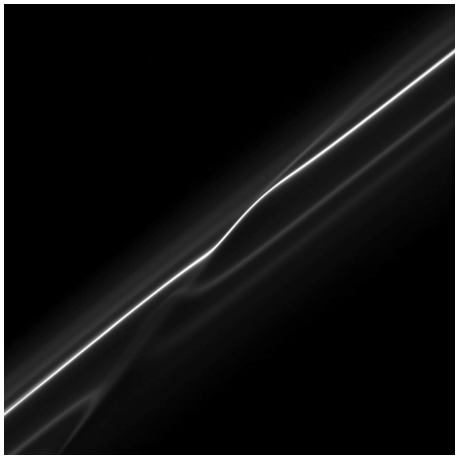

Fig. 7. In this image of the F ring, taken shortly after its ring particles encountered the shepherd moon Prometheus, the disruption to the ring caused by the moon is evident. The bright core of the ring and its neighbouring faint strands show kinks where the moon's gravity has altered the orbits of the ring particles.(NASA-JPL / ESA document).

12 The G and E rings

The E ring is the most extensive planetary ring in the solar system, enveloping many Saturns satellites from Mimas to Titan with Enceladus, Tethys, Dione and Rhea. The maximum edge-on brightness occurs near Enceladuss mean orbital distance, suggesting that this satellite is the source of the E ring. Cassini spacecraft has identified a geologically unique and presently active province at the South pole of Enceladus. This 505-kilometres diameter bright icy moon is active. Cassini imaging, thermal and other data indicate clearly that this satellite is presently heated by some mechanism. Tidal heating associated with the eccentricity of Enceladus orbit, forced by its 2:1 mean motion resonance with Dione, has long been suspected.

The E ring has been extensively imaged by the Cassini spacecraft. In addition, in-situ measurements during passages through the rings, have provided a complementary view of the E ring. We have a better understanding of the E ring thanks to two Cassini discoveries, i.e. the active dust-producing geysers in Enceladus s south polar regions and the fact that the E ring has a large radial span and reaches Titans orbit. Enceladus is filling Saturns entire magnetosphere with dust and particles are transported outwards due to plasma drag and they lose mass via sputtering.

The G ring is a tenuous ring outside the main ring system. It is not clear why the outer part of the G ring is brighter than other parts. Arcs are visible in some images of this ring. However, their existence might hold clues about how this ring was formed and where the material which makes up this ring comes from. Arcs of material confined by corotation resonances with Mimas have been found at the orbits of the small moon Anthe and Methone.

13 Meteoroid impacts

A spectacular collision between the rings and a large asteroid should lead to the escape of many particle, to waves formation and also to a large amount of material out of the Saturn equatorial plane. An inclined ring should appear and collisions between particles should reduce the inclination. Material which has not escaped Saturns system after the asteroid collision should come back to the main rings system in the equatorial plane of Saturn.

ISS has observed several impacts in the rings. They are thought to be the results of bombardment by meter-or-smaller size meteoroids. Observed ripples in the C and D rings are probably due to an asteroid collision. Something tilted the ring plane slightly in spring 1984. Saturns oblateness caused inclined orbits to wobble, inner orbits moving faster than outer ones. Twenty-five years later, ripples are still visible.

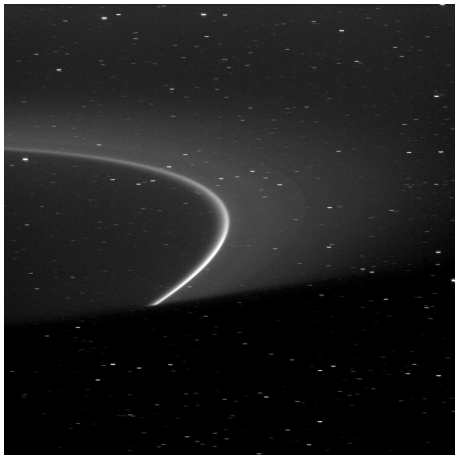

Fig. 8. The G ring has a sharp inner edge and a much smoother outer edge. The bright arc of material is trapped by the 7:6 corotation resonance with Mimas. (NASA-JPL / ESA document).

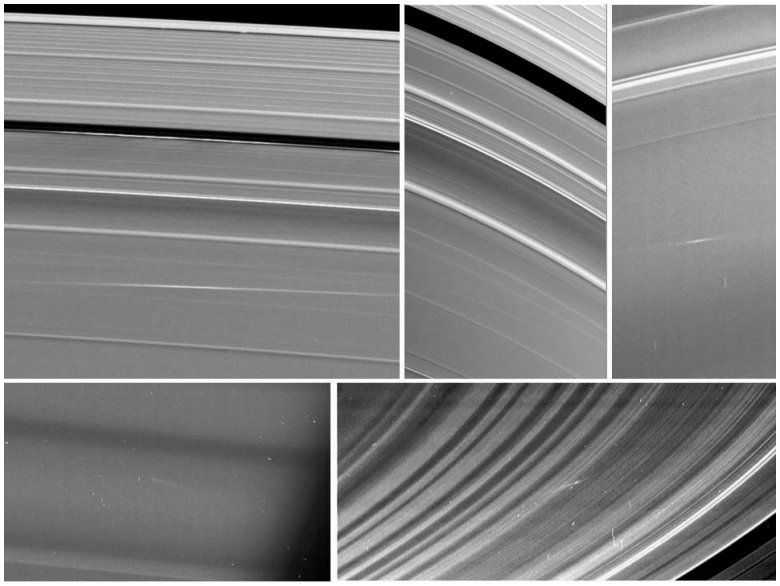

Fig. 9. Meteoroid impacts : The scratches are due to meteoroid bombardment. (NASA-JPL / ESA document).

14 Spokes

Spokes are intermittent, approximately radial markings on Saturns B ring. Cassini ISS saw no spokes until the solar elevation angle dropped below about 10 because of a solar flux related ring charging effect. These ephemeral features are still believed to be caused by sudden releases of micron-size dust particles across a wide radial extent, where the extent and tilt of the spoke change with time until it fades. The typical periodicity of spoke abundance is close, but not equal, to a number of planetary magnetic and ionospheric periods, which themselves are varying with time.

15 Nature of the particles

Saturns rings are composed of myriad individual particles which continually collide. It seems that a number of particles are in fact agglomerates of smaller elements temporarily stuck together. Competing processes lead to both growth and fragmentation. The balance between these processes yields a distribution of particle sizes and velocities. Some particles are temporary rubble piles. The size of Saturns ring particles extends from fine micron-size dust to kilometre size moonlets.

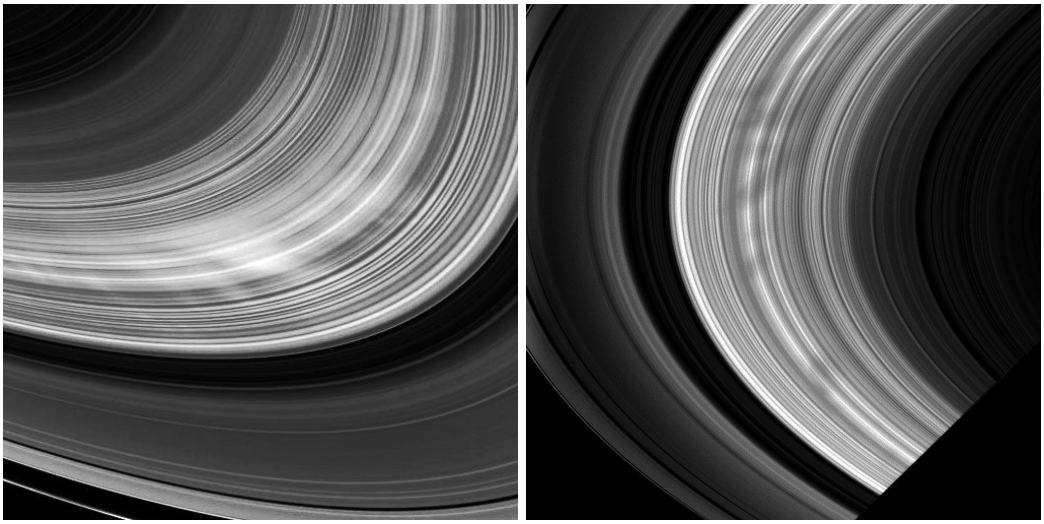

Fig. 10. The spokes are seen in reflected light (left) and diffuse light (right). (NASA-JPL / ESA document).

Reflection spectra and colour give some indication of particle composition. Saturns rings are bright and predominantly water ice. Colour variations, indicating varying composition, may be due to the effect of interplanetary dust that bombards the rings and darkens the particles. Saturns ring particles have rough, irregular surfaces resembling frost rather than solid ice.

The primary composition of the rings is water ice. Ring composition varies from place to place. The A and B rings contain 90 to 95% of water ice. The C ring and the Cassini division contain more dust, they are more contaminated by non-icy material than the A and B rings. The composition of this pollution remains uncertain. Saturns extensive ring system is exposed to the ambient photon radiation field, the magnetospheric plasma and the meteoroid flux. As a consequence, ejection of surface material fill up a gaseous envelope around the rings. In this ring atmosphere, scattered atoms and molecules extend form Saturn s atmosphere to beyond Titan orbit.

16 Rings origin and age

The origin and age of Saturns rings is still an unsolved problem. There are so many destructive mechanisms identified (spreading of the rings due to collisions, meteoroid bombardment, momentum transfer, etc.) that the rings should have been destroyed for a long time if they were formed at the same time than the planet. In addition, rings should be much darker if they are old. But, renewal mechanisms can be at work. We dont know if the rings are old or young and if the rings been formed with the planet Saturn or if they appeared later? Several scenarios have been developed by various researchers. The main rings can be remnants from the Saturns nebula. They can be remnants from a destroyed satellite, for example during the Late Heavy Bombardment. They can also be remnants from a tidally split comet. Cassini observations gave us new constraints and new information for a better understanding of rings origin. More sophisticated models have to be developed and compared to Cassini data. In particular, an estimation of the meteoroid flux at Saturn, a better knowledge of individual particles and a good measurements of the B ring mass should be particularly useful to solve the question of rings origin.

The rings are probably constantly formed and destroyed. Like an old roman building, the monument is old, but several stones have been exchanged.

17 Conclusion

A wealth of new observations need to be explained. The study of Saturns rings which is one of the oldest problem in astronomy should last in the future during several additional centuries. Future observations by new spacecrafts should bring new discoveries. The words of Maxwell in his seminal Adams Prize essay of 1856 are still particularly well adapted to the study of rings: *I am not aware that any practical use has been made*

of Saturns Rings, either in Astronomy or in Navigation . But when we contemplate the Rings from a purely scientific point of view, they become the most remarkable bodies in the heavens .

18 Bibliography

Several thousands of articles have been published about Saturns rings since their discovery. A presentation of the main properties of planetary rings as well as a discussion of dynamical processes can be found in the book Planetary Rings edited by Richard Greenberg and Andr Brahic and published by The University of Arizona Press in 1984 after the Voyager flybys of Jupiter and Saturn.

The first results of the Cassini mission have been presented in the number 5713, volume 307 of Science on February 25, 2005 and in the pages 375 to 575 of the book Saturn from Cassini-Huygens edited by Michele K. Dougherty, Larry W. Esposito and Stamatios M. Krimigis and published by Springer in 2009.

SF2A 2013
L. Cambrésy, F. Martins, E. Nuss and A. Palacios (eds)

SATELLITE FORMATION : SPREADING OF RINGS BEYOND THE ROCHE RADIUS

A. Crida[1] and S. Charnoz[2,3]

Abstract. When a disk of solid particles (like Saturns rings) spreads beyond the Roche radius (inside which planetary tides prevent aggregation), satellites form and migrate away. After a quick derivation of the Roche radius, here we describe analytically this process. When the spreading is fast, only one large satellite forms, as was the case for Pluto and Earth. When the spreading is slow, a retinue of satellites appear with masses increasing with distance to the Roche radius, in excellent agreement with Saturns, Uranus, and Neptunes satellite systems. This suggests that Uranus and Neptune used to have massive rings that disappeared to give birth to their regular satellites. Thus, we argue in Crida & Charnoz (2012) that most regular satellites in the Solar System probably formed in this way.

Keywords: Solar System: satellites, Saturn, accretion disks

1 Introduction

Planets form in proto-planetary discs of gas and dust around young stars. Giant planets open gaps in this disc, and are then surrounded by a circum-planetary disc. It is generally thought that their satellites form inside this disc, like a miniature Solar System, although the delivery and growth of solids are different (e.g. Canup & Ward 2002, 2006; Sasaki et al. 2010; Mosqueira & Estrada 2003a,b). However, these models can not explain the particular mass-distance distribution of the regular satellites of the giant planets, in particular the three following features : (i) no satellite is found at an orbital radius smaller than ~ 2.5 planetary radii ; (ii) the masses of the satellites increase with orbital distance, starting from 0 at this particular radius ; (iii) a pile-up of small bodies is observed just outside this radius, while the number density of satellites decreases outwards.

Recently, Charnoz et al. (2010) have shown that 5 small moons of Saturn, orbiting just outside the rings, were actually born from ring material spreading beyond the outer edge of the rings. This model has been extended using numerical simulations to all the medium size moons of Saturn, explaining their stochastic composition (Charnoz et al. 2011). Here, we study analytically the spreading of a dynamically cold, self-gravitating ring of solid particles. The SF2A conference being held this year in Montpellier, the city of Édouard Roche, we first show in section 2 why the particles constituting the rings aggregate only beyond a given distance to the central planet, called the Roche radius. In section 3, the equations describing the spreading of the rings beyond the Roche radius and the evolution of the subsequent forming moons are derived. This model is compared to the observed satellite systems in section 4, where the agreement is found to be very good for most planets of the solar system.

2 Tides and the Roche radius

Consider two spheres of radius a, mass m and density ρ, orbiting around a planet of mass M at a distance r, the two spheres being in contact, aligned along the radial direction (see Fig. 1). Their orbital angular velocity

[1] Laboratoire Lagrange (UMR 7293) — Université Nice Sophia Antipolis / C.N.R.S. / Observatoire de la Côte d'Azur Boulevard de l'Observatoire, BP 4229, F-06304 NICE cedex 4, France. contact : crida@oca.eu

[2] Laboratoire AIM — Université Paris Diderot, Sorbonne Paris Cité / CEA -Service dAstrophysique 91191 Gif-sur-Yvette cedex, France.

[3] Institut Universitaire de France — 103 bd Saint Michel, 75005 Paris, France.

is given by Kepler's law : $\Omega = \sqrt{GM/r^3}$. In the frame corotating with the spheres, they feel the centrifugal acceleration and the gravity from the central planet. These two forces balance exactly at r, but the spheres are actually at distances $r \pm a$ from the central object. Thus, they feel a gravitational force $F_g = GMm/(r \pm a)^2$ towards the planet, and a centrifugal force $F_c = m\Omega^2(r \pm a)$ in the opposite direction. To first order in a/r, the total force felt by the sphere located at $r \pm a$ is $F_t = \pm 3\Omega^2 am$. This is the tidal force, that tends to separate the spheres.

On the other hand, the spheres gravitationally attract each other, with the force $F_{sg} = \mp Gm^2/(2a)^2$. Consequently, self-gravity wins over tides if and only if $|F_{sg}| > |F_t|$ which, using $m = \frac{4}{3}\pi a^3 \rho$, is equivalent to :

$$r > \left(\frac{9M}{\pi\rho}\right)^{1/3} \equiv r_{\rm R} \qquad (2.1)$$

Self-gravitating aggregates are only possible beyond a particular radius, called the Roche radius.

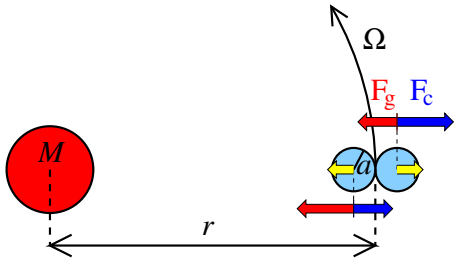

Fig. 1. Sketch of the centrifugal force (F_c, blue) and gravitational force (F_g, red) acting on two spheres in orbit around a central mass.
The resultant total force is the tidal force (yellow).

It should be noted that this simple model is not the original derivation by (Roche 1849). He considered equipotentials of a liquid sphere, and found $r_{\rm R} = 2.456\, R(\rho_p/\rho)^{1/3}$, where R and ρ_p are the radius and density of the central planet, respectively. The two expressions are almost identical. In the case of the rings of Saturn ($M = 5.86 \times 10^{24}$ kg, $\rho = 600$ kg.m^{-3}), Eq. (2.1) gives $r_{\rm R} \approx 140\,000$ km, which is the outer edge of the main rings. This is why the rings do not coalesce into one large moon. They are prevented to do so by the tides. We call such a system a *tidal disc*.

3 Analytical model

Be $T_{\rm R}$ the orbital period at the Roche radius $r_{\rm R}$, F the flow of mass from the rings through $r_{\rm R}$, and $\tau_{\rm disc} = M_{\rm disc}/FT_{\rm R}$ the normalised life time of the tidal disc ($M_{\rm disc}$ being its mass). We also note $q = M_{\rm sat}/M$ and $D = M_{\rm disc}/M$ the normalised masses of the satellite and the disc respectively (M being still the mass of the central object).

3.1 Continuous regime

Assume that 1 satellite forms by self-gravitating aggregation of the material beyond $r_{\rm R}$. Then, its mass is obviously $M_{\rm sat} = Ft$, where t is the time. It is well-known (Lin & Papaloizou 1979) that the satellite will then feel a torque from the tidal disc, given by $\Gamma = \frac{8}{27} q^2 \Sigma r^4 \Omega^2 \Delta^{-3}$, where Σ is the surface density of the disc, and $\Delta = (r - r_{\rm R})/r_{\rm R}$. Thus, the migration rate of the satellite is given by :

$$\frac{d\Delta}{dt} = \frac{2^5}{3^3}\, q\, D\, T_{\rm R}^{-1} \Delta^{-3} \qquad (3.1)$$

Using $q(t) = Ft/M$, this leads to :

$$q(t) = \left(\frac{\sqrt{3}}{2}\right)^3 \tau_{\rm disc}^{-1/2} \Delta(t)^2 \ . \qquad (3.2)$$

We call this the *continuous regime*, in which the mass of the satellite grows linearly with time, while its distance to rings is proportional to the square root of its mass.

This model is valid as long as the Roche radius is within the feeding zone of the satellite. The feeding zone is generally considered to have a width of 2 Hill radii, where the Hill radius is $r_{\rm H} = r(q/3)^{1/3}$. The condition of validity of the continuous regime is thus $\Delta < 2(q/3)^{1/3}$. Using Eq. (3.2), this is equivalent to :

$$\Delta < \sqrt{\frac{3}{\tau_{\rm disc}}} \equiv \Delta_{\rm c} \qquad\qquad q < \frac{3^{5/2}}{2^3}\, \tau_{\rm disc}^{-3/2} \equiv q_{\rm c} \qquad (3.3)$$

As the rings start spreading, $\Delta = q = 0$ and this condition is fulfilled. The continuous regime happens at the beginning of the process. When $\Delta > \Delta_{\rm c}$, the satellite is too far to accrete the material that flows from the rings. It keeps then migrating outwards at constant mass, while a new satellite forms at the Roche radius.

3.2 Pyramidal regime

Say satellites of the critical mass are produced regularly at the critical distance (this is the natural outcome of the continuous regime). They migrate outwards slower and slower as they go away. Thus, they approach each other. If their mutual distance decreases below 2 Hill radii, they merge. This gives birth to satellites twice more massive, who migrate outwards twice faster, but eventually approach each other, and merge further. This gives birth to satellites four times more massive, and so on... We call this the *pyramidal regime*, as a hierarchical history of mergers governs the evolution of the system, like a genealogical tree.

Using Eq. (3.1), we show that in the pyramidal regime, the mass is doubled (a merging event takes place) every time the distance Δ is multiplied by $2^{5/9}$. This means that $q \propto \Delta^{9/5}$. In addition, the number density of satellites is proportional to $1/\Delta$. This explains the pile-up of small satellites just beyond the Roche radius, starting with $q = 0$ at $r = r_{\rm R}$.

Beyond the 2:1 mean motion resonance with the rings (located at $\Delta_{2:1} = 0.58$), Eq. (3.1) doesn't apply anymore, and the migration of the satellites is dominated by the tides from the central planet. Still, the equations can be solved, and lead to $q \propto r^{3.9}$. In the end, satellites formed in the pyramidal regime have their masses such that :

$$q \propto \mathcal{Q}(\Delta) = \begin{cases} (\Delta/\Delta_{2:1})^{9/5} & \Delta < \Delta_{2:1} \\ \left(\frac{\Delta+1}{\Delta_{2:1}+1}\right)^{3.9} & \Delta > \Delta_{2:1} \end{cases} \tag{3.4}$$

4 Application

Amazingly, the critical mass or distance (Eq. (3.3)) corresponding to the end of the continuous regime depends on only one parameter : $\tau_{\rm disc}$. The spreading of the disc can be modelled as a viscous process, with a time scale $t_\nu = r_{\rm R}^2/\nu$. Daisaka et al. (2001) provide a prescription for ν in the case of a tidal disc, that lead to $\tau_{\rm disc} = t_\nu/T_{\rm R} = 0.0425/D^2$.

Then, assuming the mass of the putative tidal disc that gave birth to a satellite system was 150% of the total mass of the present satellites, we can apply our model to all the planets of the Solar System.

Saturn : Today's Saturn's rings would produce tiny moonlets of $q_c = 10^{-18}$. But even if one takes $D \approx 4\times10^{-4}$ (more than the mass of all the regular satellites, including Titan), $\tau_{\rm disc} \approx 2 \times 10^8$, and $\Delta_c < 0.01$; so, this system should be dominated by the pyramidal regime. In fact, the satellite system of Saturn represented in the $q - \Delta$ plane is shown in Fig. 2, and is very well fitted by Eq. (3.4) (dashed line) : considering the pair Janus-Epimetheus as 1 object, no satellite is further than 60% from the expected mass. This could be considered as the smoking gun, the observational proof that Saturn's regular satellite have been formed by the spreading of the rings in the pyramidal regime.

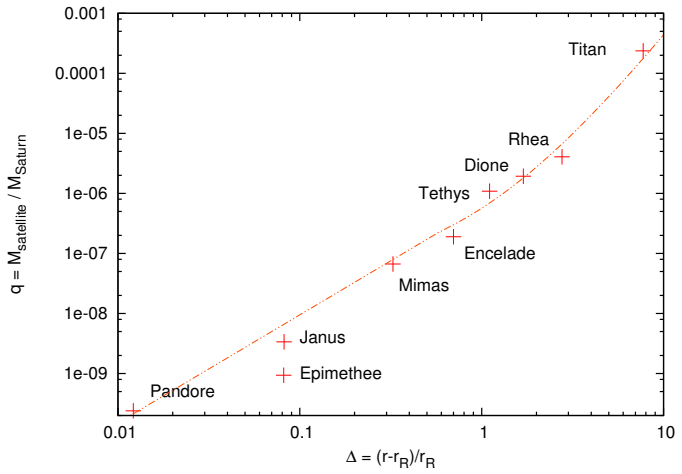

Fig. 2. Mass - Distance distribution of the regular satellites of Saturn. The dashed curve is given by Eq. (3.4)

.

Actually, it has been shown by Salmon et al. (2010) that Saturn's rings could have been much more massive in the past. As a matter of fact, Canup (2010, see also Crida & Charnoz (2010)) propose a scenario for their origin in which they must have been at least as massive as half Titan, so that she suggested that their spreading may have given birth to the satellite inside Tethys. Last, Lainey et al. (2012) have shown that the tidal dissipation inside Saturn is higher than previously thought, which allows the outward migration of all the satellites from the Roche radius to their present orbit within the age of the Solar System (Charnoz et al. 2011). Put together, these works make a consistent scenario for the formation of the rings and satellite system of Saturn, which is well supported by observations and theory.

Uranus and Neptune The satellite systems of the two ice giants follow the same mass-distance distribution. In the case of Neptune, the fit is remarkable, except for Despina, whose mass seems to be three times too high. In the case of Uranus, the distribution is more scattered around the theoretical curve ; however, this system is chaotic, and still evolving : collisions are supposed to occur quite frequently, and ringlets may accrete into new satellites. This can be seen as the pyramidal regime still at play.

Therefore, we claim that Uranus and Neptune used to have massive rings, that have spread, given birth to the regular satellites observed today, and vanished.

Earth-Moon : In the case of the Earth's Moon forming disc, we would have $D \approx 0.02$, $\tau_{\rm disc} \approx 125$, and then $q_c \approx D$. This means that only one satellite forms in the continuous regime, that absorbs all the mass in the tidal disc. Obviously, the Earth has only one large satellite...

The structure of the Moon forming disc is much more complex than a peaceful, cold tidal disc. However, once it has condensed, our calculations show that this disc preferentially forms one single Moon than many.

The case of a possible Charon forming disc around Pluto is similar.

5 Conclusion

The formation of satellites through the spreading of a tidal disc beyond the Roche radius appears to be a generic process in the Solar System, from the terrestrial to the giant planets. Whether only one large satellite forms or a series of small satellites appears, is only controlled by the rapidity of the spreading ($\tau_{\rm disc}$), itself determined by the mass of the disc. But the physical process at play is intrinsically the same.

This work has been published recently, and all the details of the calculations can be found in the supplementary material of Crida & Charnoz (2012, `http://arxiv.org/abs/1301.3808`).

A video presenting this mechanism in a pedagogical way for the general audience is available in English at `http://vimeo.com/55613414` or in French (`http://vimeo.com/64293772`).
Realisation : Frédéric Durillon — animea , under creative commons licence.

References

Canup, R. M. 2010, Nature, 468, 943
Canup, R. M. & Ward, W. R. 2002, AJ, 124, 3404
Canup, R. M. & Ward, W. R. 2006, Nature, 441, 834
Charnoz, S., Crida, A., Castillo-Rogez, J. C., et al. 2011, Icarus, 216, 535
Charnoz, S., Salmon, J., & Crida, A. 2010, Nature, 465, 752
Crida, A. & Charnoz, S. 2010, Nature, 468, 903
Crida, A. & Charnoz, S. 2012, Science, 338, 1196
Daisaka, H., Tanaka, H., & Ida, S. 2001, Icarus, 154, 296
Lainey, V., Karatekin, Ö., Desmars, J., et al. 2012, ApJ, 752, 14
Lin, D. N. C. & Papaloizou, J. 1979, MNRAS, 186, 799
Mosqueira, I. & Estrada, P. R. 2003a, Icarus, 163, 198
Mosqueira, I. & Estrada, P. R. 2003b, Icarus, 163, 232
Roche, E. 1849, Mémoire de la section des sciences, Académie des sciences et des lettres de Montpellier, 1, 243
Salmon, J., Charnoz, S., Crida, A., & Brahic, A. 2010, Icarus, 209, 771
Sasaki, T., Stewart, G. R., & Ida, S. 2010, ApJ, 714, 1052

SF2A 2013
L. Cambrésy, F. Martins, E. Nuss and A. Palacios (eds)

SATURN'S STRATOSPHERIC TEMPERATURE AND COMPOSITION FROM CASSINI/CIRS

S. Guerlet[1], T. Fouchet[2], B. Bézard[2], A. Spiga[1], M. Sylvestre[1,2], J. Moses[3] and F.M. Flasar[4]

Abstract. We present a short review of our current knowledge on Saturn's stratospheric thermal structure and composition (hydrocarbons) based on recent Cassini/CIRS observations. Anomalies in the temperature field and in the meridional distribution of hydrocarbons hint at atmospheric dynamical phenomena at play. The two most notable features are an obseved asymmetry in the hydrocarbons distribution at high altitudes, hinting at inter-hemispheric transport, and the discovery of an equatorial oscillation in temperature and zonal wind, hinting at interactions between vertically-propagating waves and the mean zonal flow. The physical processes behind these observed anomalies need to be better understood, and these results advocate for the development of climate models of Saturn's stratosphere.

Keywords: Saturn, Cassini

1 Introduction

Saturn's stratosphere is host to a rich hydrocarbon photochemistry initiated by the photolysis of methane (CH_4) near the homopause level that produces various hydrocarbons, from the main products ethane (C_2H_6) and acetylene (C_2H_2) to benzene (C_6H_6). Their meridional distribution and their variations with altitude and time (seasons) are governed by coupled photochemical and dynamical processes. Saturn's stratospheric circulation is still poorly known, as direct wind measurements are lacking. However, detailed measurements of hydrocarbons' meridional distribution and their vertical gradients can provide indirect constraints on atmospheric meridional and vertical transport. In addition, anomalies in the temperature field can also reveal atmospheric dynamical phenomenon at play.

Saturn's stratosphere can be probed by mid-infrared spectroscopic measurements. Onboard the Cassini spacecraft, the Composite and Infrared Spectrometer (CIRS) measures spectra of Saturn's thermal emission in the range 10–1400 cm^{-1}, with a spectral resolution tunable between 0.5 and 15.5 cm^{-1}. CIRS comprises three focal planes (FP1, FP3 and FP4), with FP3 and FP4 consisting of two linear arrays of ten detectors. Their individual projected field of view is typically 70km on Saturn, ie. 1 to 1.5 scale height. In limb viewing geometry, each detector probes a different altitude, allowing the retrieval of atmospheric profiles with a good vertical extent and resolution. We use a line-by-line radiative transfer model coupled to a constrained linear inverse method to first retrieve a temperature vertical profile from the analysis of the CH_4 emission band centered at 1305 cm^{-1} and from the H2-He collision-induced emission (590-660 cm^{-1}). Typically, using limb data, the temperature profile is constrained between 20 mbar and a few microbars, while nadir observations probe the stratospheric temperature in the range 5–0.5 mbar (see Fig. 1 for a typical temperature profile of Saturn's atmosphere along with the vertical sensitivity of Cassini/CIRS nadir and limb data). Once the temperature is constrained, we retrieve the volume mixing ratio vertical profiles of five hydrocarbons from their emission bands: C_2H_6 (centered at 822 cm^{-1}), C_2H_2 (730 cm^{-1}), C_3H_8 (748 cm^{-1}), C_4H_2 (628 cm^{-1}) and C_3H_4 (633 cm^{-1}).

Hereafter, we review results obtained from Cassini/CIRS data analysis (between 2005 and 2010, coresponding to mid-summer to autumn in the southern hemisphere) and their implications for Saturn's stratospheric dynamics.

[1] Laboratoire de Meteorologie Dynamique/IPSL/CNRS, Paris, France
[2] LESIA/Observatoire de Paris, Meudon, France
[3] Space Science Institute, TX, USA
[4] NASA/GSFC, Greenbelt, MD, USA

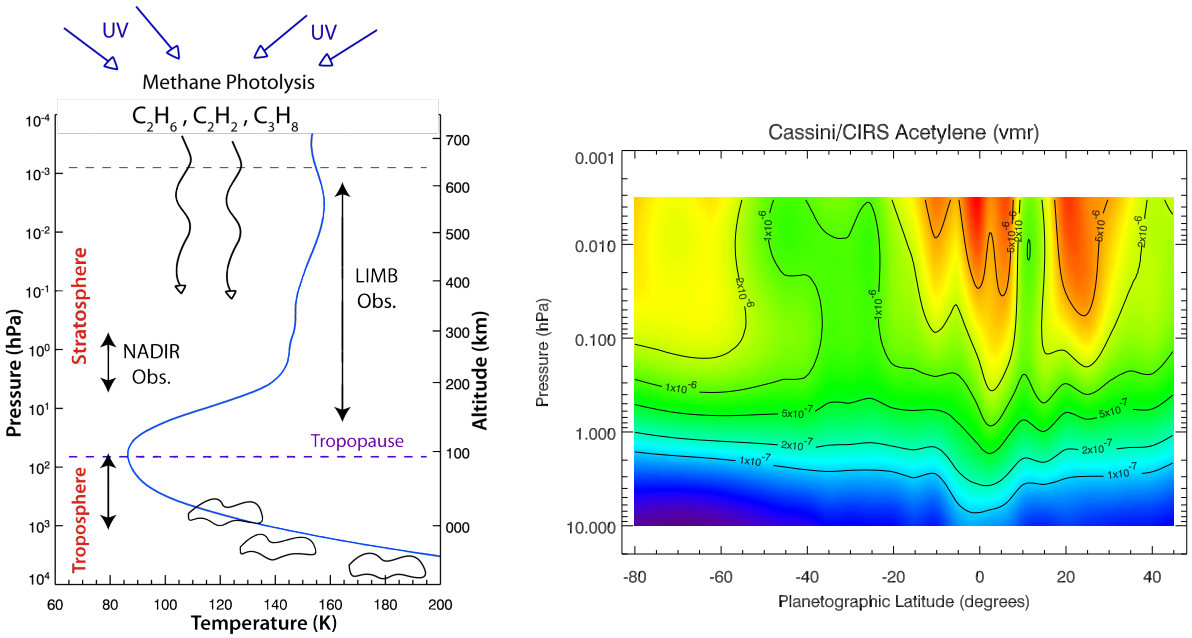

Fig. 1. Left: Example of a Saturn's atmospheric temperature profile with altitude and pressure, along with the vertical sensitivity of limb and nadir spectroscopic observations. **Right:** Map of the volume mixing ratio of acetylene (C_2H_2) with latitude and pressure, from 2005 and 2006 Cassini/CIRS limb data analysis.

2 Results from Cassini/CIRS data analysis

2.1 Anomalies observed in trace species distributions

The distribution of several hydrocarbons based on Cassini/CIRS measurements has been discussed in details in Howett et al. (2007); Hesman et al. (2009); Sinclair et al. (2013) from nadir data analysis and in Guerlet et al. (2009, 2010) from limb data analysis. An example of the distribution of C_2H_2 based on limb observations is presented in Fig. 1 . The most striking feature is that in the lower stratosphere (below the 1 mbar pressure level), acetylene's meridional distribution is symmetric with respect to the equator (C_2H_2 decreases towards both poles), while in the upper stratosphere its meridional distribution is strongly asymmetric, with about 5 times more C_2H_2 at 30N than at 30S (Guerlet et al. 2009). A similar asymmetry at high altitudes is found for C_2H_6. However, in the lower stratosphere, its distribution differs from that of C_2H_2, as we find that C_2H_6 concentration does not vary significantly with latitude (Guerlet et al. 2009). Other studies based on CIRS nadir data and ground-based data, which probe the lower stratosphere, revealed a similar behaviour at the 2-mbar pressure level. We also note that on Jupiter, a similar configuration of the C_2H_6 and C_2H_2 distribution at 2-mbar was determined from Cassini/CIRS data analysis (Nixon et al. 2007), as the spacecraft flew by Jupiter in 2000.

Seasonal photochemical models developed for Satun's atmosphere (Moses & Greathouse 2005) predict that ethane and acetylene should have long photochemical lifetimes in the lower stratosphere (about 700 and 100 years at 2 mbar, respectively), much longer than Saturn's year (30 Earth years). Consequently, their distribution should follow the yearly averaged solar insolation, ie be maximum at the equator and decrease towards both poles. Acetylene was found to follow this trend, whereas ethane was found to either slightly increase towards the south pole, or remain constant with latitude (depending on the studies). This was interpreted as the consequence of a global meridional distribution by dynamics from the equator to the poles, which would efficiently transport the long-lived C_2H_6 but much less efficiently C_2H_2, that is more rapidly destructed by photodissociation than transported. This provided an estimation of the timescale of this global circulation, in between the two photochemical lifetimes of the considered species, i.e. 100 to 700 years.

First attempts to reproduce the observed distribution of hydrocarbons in the lower stratosphere of Saturn and Jupiter using simple dynamical assumptions have failed. Indeed, two models coupling photochemistry and eddy mixing have been tested (Liang et al. (2005) for Jupiter and Moses et al. (2007) for Saturn) but none could simultaneously reproduce the C_2H_2 and C_2H_6 distribution with realistic values of eddy mixing coefficients. One

difficulty lies in the chemical coupling between C_2H_6 and C_2H_2: when ethane is transported towards the poles, its photodissociation should also lead to producing more C_2H_2, in a way such that the two molecules should exhibit rather uniform distributions. A full General Circulation Model is thus needed to investigate transport by circulation cells (and not only by eddy mixing), to try to reproduce the observations and to investigate whether the current difference between the models and the reality arises from a dynamical or chemical origin.

At higher altitudes (at the 0.01 mbar level), hydrocarbons' lifetimes are shorter and these species are now influenced by seasonal variations of solar irradiation. The photochemical model of Moses & Greathouse (2005) predict that at the subsolar point (at about 30S at this time), photochemical production is maximum, thus hydrocarbon abundance should be high. On the other hand, under the shadow of the rings (at 25N at this time) photochemical production is low, thus the abundance should show a dip at these latitudes. Limb observations revealed the exact opposite pattern, with a sharp, local maximum of hydrocarbons centered at 25N and a large minimum in the region 20-40S (Guerlet et al. 2009). This can be interpreted as the signature of a (seasonal) circulation cell similar to the Earth Hadley cells, or to Brewer-Dobson circulation, inducing downwelling under the ring's shadows which brings hydrocarbon-rich air. This is the first evidence of a seasonal circulation pattern on a giant planet.

Finally, limb data acquired by Cassini/CIRS also have the advantage to increase the sensitivity to trace species (as the lightpath is increased). Using this technique, maps of propane, methylacetylene and diacetylene have been obtained for the first time in the lower stratosphere (Guerlet et al. 2010). Having different lifetimes than ethane and acetylene, these minor species can potentially be employed as dynamical tracers and improve the constraints on atmospheric dynamics, although a full dynamical model is needed to exploit this information and yield more quantitative constraints on the circulation.

2.2 Anomalies in the temperature field

Cassini/CIRS data analysis also provided detailed maps of the stratospheric temperature. From the resolution of the thermal wind equation, zonal wind maps could also be derived. Those maps led to the discovery of Saturn's equatorial oscillation (Fouchet et al. 2008), characterized by alternate bands of eastward and westward jets with altitude at the equator, and alternate extrema of temperature. Its period has been estimated to half a kronian year from ground-based observations (Orton et al. 2008) and from the study of the descending pattern with time (Guerlet et al. 2011). A similar oscillation have been discovered in Jupiter's stratosphere (Friedson, 1999, Simon-Miller et al., 2007). Both are qualitatively analogous to the Earth's QBO (Quasi-Biennal Oscillation), a dynamical phenomenon triggered by the interaction between waves and the mean zonal flow. This represents a good example of comparative planetology, and these multiple observations are a unique opportunity to learn more about equatorial oscillations in general. These oscillations have different periods on the three planets and the wave activity is supposedly quite different, although weakly characterized for Jupiter and Saturn.

Modeling of the Quasi-Quadriennal Oscillation on Jupiter (QQO) indicated that most of the previously observed planetary-scale Rossby waves were not a likely cause for the Jupiter QQO, but could not be ruled out as a contributing factor. Other waves, depositing energy in the upper troposphere ($\sim$300 mbar), were able to somewhat reproduce a QQO signal in the stratosphere (Friedson 1999; Li & Read 2000), but predicted a much larger QQO amplitude in actual temperature than was found in earlier brightness temperature analyses. Numerical efforts, coupled to more observations and characterization of waves, are thus still needed to try to reproduce the equatorial oscillations and understand their different periods.

The meridional temperature profiles also exhibit features left unexplained by the predictions of a seasonal radiative transfer model (that of Greathouse et al. (2008) applied by Fletcher et al. (2010)). The model predicts that under the ring's shadow the temperature should significantly decrease, by 10 to 20K with respect to the surrounding latitudes. This effect should be visible in the whole stratosphere (20 mbar to 10^{-2} mbar). However, this low temperature region is not visible in Cassini/CIRS observations. We interpret this as another sign of the seasonal circulation cell that we mentioned earlier. Indeed, downwelling below the ring's shadow will not only enrich the atmosphere in hydrocarbons, it would also likely warm up the stratosphere by adiabatic compression. As the radiative equilibrium model of Greathouse et al. (2008) did not include dynamics, this assumption could not be tested and quantified.

3 Conclusions

Cassini/CIRS nadir and limb data analysis have allowed to map Saturn's stratospheric thermal structure and the distribution of hydrocarbons, by-products of a complex photochemistry. These results have revealed anomalies that cannot be explained by current seasonal radiative or photochemical models. Another example of anomaly not discussed here is the spectacularly warm anticyclone that developed in the stratosphere after the December 2010 Great White Storm (Fletcher et al. 2012). All these features hint at complex atmospheric dynamical phenomena at play and advocate for the development of a General Circulation Model (GCM) of Saturn's upper troposphere and stratosphere. Such a GCM is currently under development at the Laboratoire de Meteorologie Dynamique, where we benefit from the experienced gained through the development of GCMs for the atmospheres of the Earth, Mars, Venus, Titan and even exoplanets (Forget et al. 1999; Wordsworth et al. 2011).

We also emphasize that future observations (by Cassini's extended mission till 2017, as well as ground-based) remain crucial to bring more constraints on our understanding of how giant planets' atmosphere behave and evolve.

We acknowledge funding from the French ANR under grant agreement ANR-12-PDOC-0013.

References

Fletcher, L. N., Achterberg, R. K., Greathouse, T. K., et al. 2010, Icarus, 208, 337
Fletcher, L. N., Hesman, B. E., Achterberg, R. K., et al. 2012, Icarus, 221, 560
Forget, F., Hourdin, F., Fournier, R., et al. 1999, J. Geophys. Res., 104, 24155
Fouchet, T., Guerlet, S., Strobel, D. F., et al. 2008, Nature, 453, 200
Friedson, A. J. 1999, Icarus, 137, 34
Greathouse, T. K., Strong, S., Moses, J., et al. 2008, in AGU Fall Meeting Abstracts, B6+
Guerlet, S., Fouchet, T., Bézard, B., Flasar, F. M., & Simon-Miller, A. A. 2011, Geophys. Res. Lett., 38, 9201
Guerlet, S., Fouchet, T., Bézard, B., et al. 2010, Icarus, 203, 214
Guerlet, S., Fouchet, T., Bézard, B., Simon-Miller, A. A., & Flasar, F. 2009, Icarus, 203, 214
Hesman, B. E., Jennings, D. E., Sada, P. V., et al. 2009, Icarus, 202, 249
Howett, C. J. A., Irwin, P. G. J., Teanby, N. A., et al. 2007, Icarus, 190, 556
Li, X. & Read, P. L. 2000, Planet. Space Sci., 48, 637
Liang, M.-C., Shia, R.-L., Lee, A. Y.-T., et al. 2005, ApJ, 635, L177
Moses, J. I. & Greathouse, T. K. 2005, Journal of Geophysical Research (Planets), 110, 9007
Moses, J. I., Liang, M.-C., Yung, Y. L., & Shia, R.-L. 2007, in Planetary Atmospheres, 85–86
Nixon, C. A., Achterberg, R. K., Conrath, B. J., et al. 2007, Icarus, 188, 47
Orton, G. S., Yanamandra-Fisher, P. A., Fisher, B. M., et al. 2008, Nature, 453, 196
Sinclair, J. A., Irwin, P. G. J., Fletcher, L. N., et al. 2013, Icarus, 225, 257
Wordsworth, R. D., Forget, F., Selsis, F., et al. 2011, ApJ, 733, L48

SF2A 2013
L. Cambrésy, F. Martins, E. Nuss and A. Palacios (eds)

SCIENCE GOALS AND CONCEPTS OF A SATURN PROBE FOR THE FUTURE L2/L3 ESA CALL

F.-X. Schmider[1], O. Mousis[2], L. N. Fletcher[3], K. Altwegg[4], N. André[5], M. Blanc[5], A. Coustenis[6], D. Gautier[6], W. D. Geppert[7], T. Guillot[1], P. Irwin[3], J.-P. Lebreton[6,8], B. Marty[9], A. Sánchez-Lavega[10], J. H. Waite[11] and P. Wurz[4]

Abstract. Comparative studies of the elemental enrichments and isotopic abundances measured on Saturn can provide unique insights into the processes at work within our planetary system and are related to the time and location of giant planet formation. In situ measurements via entry probes remain the only reliable, unambiguous method for determining the atmospheric composition from the thermosphere to the deep cloud-forming regions of their complex weather layers. Furthermore, in situ experiments can reveal the meteorological properties of planetary atmospheres to provide "ground truth" for orbital remote sensing. Following the orbital reconnaissance of the Galileo and Cassini spacecraft, and the single-point in situ measurement of the Galileo probe to Jupiter, we believe that an in situ measurement of Saturn's atmospheric composition should be an essential element of ESA's future cornerstone missions, providing the much-needed comparative planetology to reveal the origins of our outer planets. This quest for understanding the origins of our solar system and the nature of planetary atmospheres is in the heart of ESA's Cosmic Vision, and has vast implications for the origins of planetary systems around other stars.

Keywords: Saturn, formation, atmospheric processes, in situ measurements, spacecraft missions

1 Introduction

Remote-sensing observations have always been the favoured approach of astronomers for studying the giant planets of our Solar System. However, the efficiency of this technique has some limitations when used to study the bulk atmospheric composition crucial to understanding planetary origins. A remarkable example of these restrictions is illustrated by the exploration of Jupiter, where key measurements such as the determination of the noble gases and helium abundances have only been made in situ by the Galileo probe. These measurements revealed unexpected results concerning the Ar, Kr and Xe enrichments with respect to their solar abundances, which suggest that the planet accreted icy planetesimals formed at temperatures possibly as low as 20–30 K to allow the trapping of these noble gases.

Another remarkable result was the determination of the Jovian helium abundance obtained by a dedicated instrument aboard the Galileo probe (von Zahn et al. 1998) with an accuracy of 2%. Such accuracy on the He/H_2 ratio is impossible to derive from remote sensing, irrespective of the giant planet considered, and yet precise

[1] Observatoire de la Côte d'Azur, BP 4229, 06304 Nice, France
[2] Institut UTINAM, 41 bis Avenue de l'Observatoire, BP 1615, 25010 Besançon Cedex France
[3] Atmospheric, Oceanic and Planetary Physics, University of Oxford, Clarendon Lab., Oxford, OX1 3PU, UK
[4] Universität Bern, Physics Institute, Sidlerstrasse 5, 3012 Bern, Switzerland
[5] IRAP, Observatoire Midi-Pyrénées, France
[6] LESIA-Observatoire de Paris, CNRS, UPMC Univ Paris 06, Univ. Paris-Diderot, France
[7] Stockholm University Astrobiology Centre, Sweden
[8] LPC2E, Université d'Orléans, France
[9] CRPG-CNRS, 15 Rue Notre Dame des Pauvres BP 20, 54501 Vandoeuvre Les Nancy, Cedex France
[10] Universidad del País Vasco (UPV/EHU), Alda. Urquijo s/n, 48013, Bilbao, Spain
[11] Southwest Research Institute, San Antonio, TX, USA

knowledge of this ratio is crucial for the modelling of giant planet interiors and their thermal evolution. The Voyager mission has already shown, through remote sensing, that the He/H_2 ratios are far from being identical, which is presumably result of their evolution. An important result also obtained by the mass spectrometer aboard the Galileo probe was the determination of the $^{14}N/^{15}N$ ratio, which suggested that nitrogen present in Jupiter today originated from the solar nebula essentially in the form of N_2 (Owen et al. 2001). The mass spectrometer aboard Galileo unfortunately did not make measurements at levels deeper than 22 bars, precluding us from determining the H_2O abundance at levels representative of the bulk oxygen enrichment of the planet. Furthermore, the probe descended into a region depleted in certain volatiles and gases by unusual "hot spot" meteorology (Orton et al. 1998; Wong et al. 2004), so the Galileo measurements may not be representative of the planet as a whole. Nevertheless, the Galileo probe provided a giant step forward in our understanding of Jupiter, but one can wonder if these measurements are really representative or not of the whole set of giant planets of the solar system. In situ exploration of more than one giant planet is the only way to address this crucial question for planetary science.

In the following, we describe the reasons why in situ exploration is vital to understand giant planet formation and atmospheric processes from the thermosphere to deep below the clouds, and we state the case specifically for a Saturn probe as a vital comparison to the Galileo results. Despite the wealth of remote sensing data returned by the Cassini spacecraft for Saturn, several key questions still require an in situ probe to investigate.

2 Planet formation and the origin of the solar system

Formation and evolution models indicate that the total mass of heavy elements present in Jupiter may be as high as 42 $M_\oplus$whereas the mass of the core is estimated to range between 0 and 13 $M_\oplus$(Saumon and Guillot 2004). In the case of Saturn, the mass of heavy elements can increase up to 35 $M_\oplus$with the mass in the envelope varying between 0 and 10 $M_\oplus$and the core mass ranging between 0 and 20 $M_\oplus$(Helled and Guillot 2013). The masses of heavy elements are found to be in the 10.9–12.8 and 12.9–15.2 $M_\oplus$ranges for Uranus and Neptune, respectively (Helled et al. 2011). Direct access to heavy materials within giant planet cores to constrain these models is impossible, so we must use the composition of the well-mixed troposphere to infer the properties of the deep interiors. These questions must be addressed by in situ exploration. The availability of planetary building blocks (metals, oxides, silicates, ices) is expected to vary with position within the original nebula, from refractories in the warm inner nebula to a variety of different ices like water, CH_4, CO, NH_3, N_2 and other simple molecules in the cold outer nebula. Turbulent radial mixing, and the evolution of the pressure-temperature gradient in the disk could have led to distinct regions where some species dominated over others (e.g., the water-ice snow line or N_2 over NH_3). Furthermore, both inward and outward migration of the giants during their evolution could have provided access to different material reservoirs at different epochs.

A giant planet's bulk composition therefore depends on the timing and location of planet formation, subsequent migration and the delivery mechanisms for the heavier elements. By measuring a giant planet's chemical inventory, and contrasting it with measurements of (i) other giant planets, (ii) primitive materials found in comets and asteroids, and (iii) the abundance of our parent star and the local interstellar medium, can reveal much about the conditions at work during the formation of our planetary system. Furthermore, comparison to the compositions of the larger ensemble of extrasolar giant planets would place our own planetary origins in a broader context.

Galileo at Jupiter: to date, the Galileo probe at Jupiter (1995) remains our only data point for interpreting the bulk composition of the giant planets. Galileo found that Jupiter exhibited an enrichment in carbon, nitrogen, sulfur, argon, krypton and xenon compared to the solar photospheric abundances, with some notable exceptions – water was found depleted, may be due to meteorological processes at the probe entry site; and neon was depleted, possibly due to rain-out to deeper levels (Niemann et al. 1998, Wong et al. 2004). In any case the oxygen abundance in Jupiter remains an enigma. The Juno mission, which will arrive at Jupiter in 2016, may provide an estimate of the tropospheric O/H ratio. Interestingly, the nitrogen isotope composition of Jupiter is similar within uncertainties to the protosolar nebula value (Marty et al. 2011) whereas the N isotope composition of comets is very different (enriched in ^{15}N by a factor of two). Explaining the high abundance of noble gases requires either condensing these elements directly at low temperature in the form of amorphous ices (Owen et al. 1999), trapping them as clathrates in ices (Gautier et al. 2001; Hersant et al. 2008; Mousis et al. 2009, 2012) or photoevaporating the hydrogen and helium in the protoplanetary disk during the planet's formation (Guillot and Hueso 2006). The Galileo measurements at Jupiter also include a precise determination of the planet's helium abundance, crucial for calculations of the structure and evolution of the planet. Figure 1

represents fits of the volatile enrichments measured at Jupiter in the context of two different formation models, both being based on the hypothesis that Jupiter's building blocks formed from a mixture of rocks and crystalline ices but postulating a different oxygen abundance in the formation zone of Jupiter in the primordial nebula. While the quality of matching the volatile abundances is fairly similar, these two scenarios provide different predictions of the oxygen abundance in Jupiter. These calculations illustrate the strong connection between the formation conditions of the planet and its bulk composition, and similar measurements for Saturn or an ice giant would enable comparison of their formation mechanisms with Jupiter.

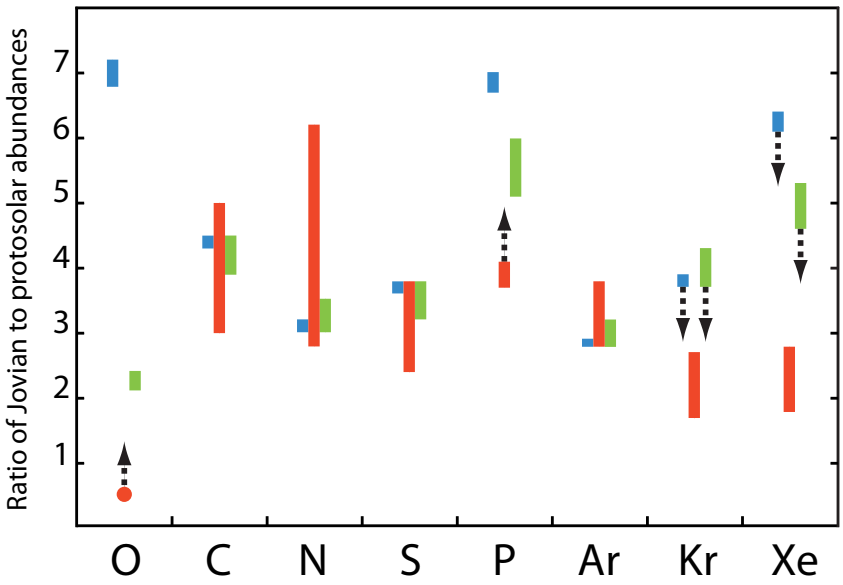

Fig. 1. Ratio of Jovian to protosolar abundances (adapted from Mousis et al. 2012). Red bars and the red dot correspond to observations made by the Galileo probe. Green and blue bars correspond to calculations based on an oxygen abundance that is 0.5 and 1 times the protosolar value in the feeding zone of Jupiter, respectively. The corresponding oxygen abundances are predicted to be about 2 and 7 times protosolar in the Jovian atmosphere. Arrows pointing up correspond to the possibility that the measured oxygen and phosphorus abundances are lower than their bulk abundances, and arrows pointing down to the possibility that planetesimals could be depleted in krypton and xenon (Mousis et al. 2009).

Saturn Probe: because of the absence of in situ measurements, the noble gas abundances are unknown in Saturn. However there is some indication for a non-uniform enrichment in C, N and S. Hersant et al. (2008) suggest that ground-based and space-based (Cassini) observations are well fitted if the atmospheric carbon and nitrogen of the planet were initially mainly in reduced forms at 10 AU in the solar nebula. Alternatively, Mousis et al. (2009) find that it is possible to account for the volatile enrichments in Saturn in a way that is consistent with those measured at Jupiter if the building blocks of the two planets shared a common origin. A determination of the oxygen abundance on Saturn via in situ exploration would distinguish between these scenarios. Furthermore, a determination of noble gases is essential in understanding the formation conditions of Saturn. On one hand, Hersant et al. (2008) predict that Ar and Kr should be solar in Saturn while Xe could be supersolar, whereas Mousis et al. (2009) find that all these species should be significantly supersolar. In addition, a determination of the volatile enrichments in Saturn could also provide a constraint on its rotation period, which will help to better infer its internal structure (Helled and Guillot 2013; Nettelmann et al. 2013). Moreover, as Saturn's atmosphere is believed to be depleted in helium as a result of H_2/He phase separation and subsequent helium rain, a precisely measured He/H_2 value of Saturn's atmosphere is crucial for probing the theoretical H/He demixing phase diagram, which is impossible with current laboratory technology for high-pressure physics. Helium-rain has long been predicted to occur in Saturn as an explanation for its high luminosity. Therefore, an entry probe measurement of the helium abundance is required to resolve this riddle.

3 Planetary atmospheric processes

Planetary atmospheres constitute our only accessible gateway to the processes at work within the deep interiors of the giant planets, and yet we must extrapolate from this thin, dynamic region over many orders of magnitude in pressure, temperature and density to infer the planetary properties far below the clouds. Remote sensing at a wide range of wavelengths provides insights into the complexity of the transitional zone between the external environment and the fluid interior, but there is much that we still do not understand. In situ measurements are the only method providing ground-truth to connect the remote-sensing inferences with the environmental conditions below the clouds. The scientific objectives, which have relevance for Saturn, are summarized in Fig. 2.

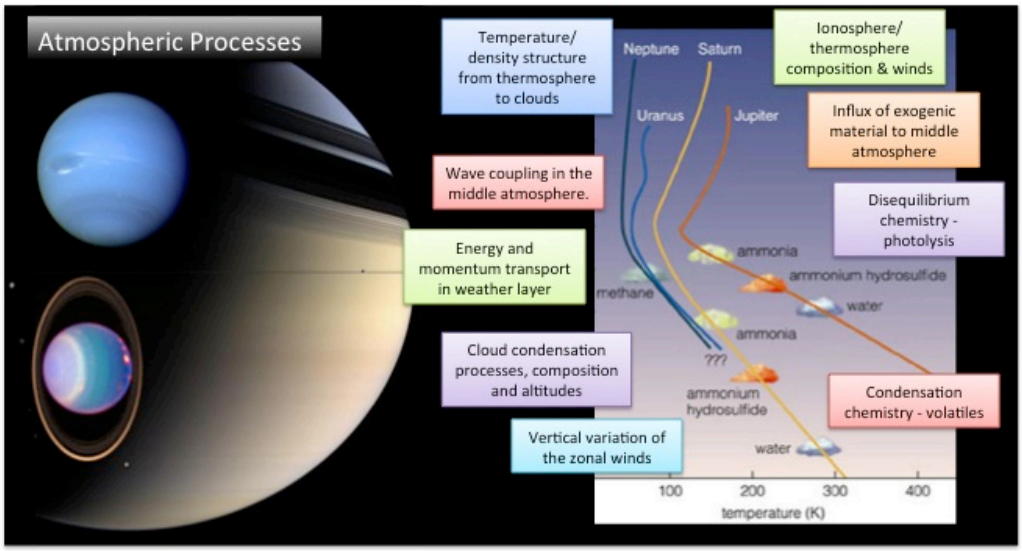

Fig. 2. Examples of the vertical temperature structures of the giant planets, highlighting the scientific themes to be addressed via in situ and remote sensing. Vertical profiles of temperature, density, radiant flux, chemical and aerosol composition will all be acquired during the descent of an entry probe from the upper atmosphere to depths within and below the cloudforming regions.

4 Conclusions

The in situ exploration of Saturn addresses two major science themes: the formation history of our Solar System and the processes at work in the atmospheres of giants. The concept of a Saturn probe can be considered as the next natural step beyond Galileo's in situ exploration of Jupiter, and the Cassini spacecraft's orbital reconnaissance of Saturn. Considered mission designs include the KRONOS concept previously proposed to ESA (Marty et al. 2009) and other studies for future missions are currently in place.

References

Gautier, D., Hersant, F., Mousis, O., & Lunine, J. I. 2001, ApJ, 550, L227
Guillot, T., & Hueso, R. 2006, MNRAS, 367, L47
Helled, R., & Guillot, T. 2013, ApJ, 767, 113
Helled, R., Anderson, J. D., Podolak, M., & Schubert, G. 2011, ApJ, 726, 15
Hersant, F., Gautier, D., Tobie, G., & Lunine, J. I. 2008, Planet. Space Sci., 56, 1103
Marty, B., Chaussidon, M., Wiens, R. C., Jurewicz, A. J. G., & Burnett, D. S. 2011, Science, 332, 1533
Marty, B., Guillot, T., Coustenis, A., et al. 2009, Experimental Astronomy, 23, 947
Mousis, O., Lunine, J. I., Madhusudhan, N., & Johnson, T. V. 2012, ApJ, 751, L7

Mousis, O., Marboeuf, U., Lunine, J. I., et al. 2009, ApJ, 696, 1348
Nettelmann, N., Püstow, R., & Redmer, R. 2013, Icarus, 225, 548
Niemann, H. B., Atreya, S. K., Carignan, G. R., et al. 1998, J. Geophys. Res., 103, 22831
Orton, G. S., Fisher, B. M., Baines, K. H., et al. 1998, J. Geophys. Res., 103, 22791
Owen, T., Mahaffy, P. R., Niemann, H. B., Atreya, S., & Wong, M. 2001, ApJ, 553, L77
Owen, T., Mahaffy, P., Niemann, H. B., et al. 1999, Nature, 402, 269
Saumon, D., & Guillot, T. 2004, ApJ, 609, 1170
von Zahn, U., Hunten, D. M., & Lehmacher, G. 1998, J. Geophys. Res., 103, 22815
Wong, M. H., Mahaffy, P. R., Atreya, S. K., Niemann, H. B., & Owen, T. C. 2004, Icarus, 171, 153

SF2A 2013
L. Cambrésy, F. Martins, E. Nuss and A. Palacios (eds)

SIX YEARS OF CONTINUOUS OBSERVATION OF TITAN CLOUD ACTIVITY WITH CASSINI/VIMS

S. Rodriguez[1], S. Le Mouélic[2,3], P. Rannou[4], C. Sotin[2,5] and R.H. Brown[6]

Abstract. Since Saturn orbital insertion in July 2004, the Cassini orbiter has been observing Titan throughout most of the northern winter season (October 2002August 2009) and the beginning of spring, allowing a detailed monitoring of Titans cloud coverage at high spatial resolution with close flybys on a monthly basis. This study reports on the analysis of all the near-infrared images of Titans clouds acquired by the Visual and Infrared Mapping Spectrometer (VIMS) during 67 targeted flybys of Titan between July 2004 and April 2010. The VIMS observations show numerous sporadic clouds at southern high and mid-latitudes, rare clouds in the equatorial region, and reveal a long-lived cloud cap above the north pole, ubiquitous poleward of 60^{o}N. These observations allow us to follow the evolution of the cloud coverage during almost a 6-year period including the equinox, and greatly help to further constrain global circulation models (GCMs). After 4 years of regular outbursts observed by Cassini between 2004 and 2008, southern polar cloud activity started declining, and completely ceased 1 year before spring equinox. The extensive cloud system over the north pole, stable between 2004 and 2008, progressively fractionated and vanished as Titan entered into northern spring. At southern mid-latitudes, clouds were continuously observed throughout the VIMS observing period, even after equinox, in a latitude band between 30^{o}S and 60^{o}S. During the whole period of observation, only a dozen clouds were observed closer to the equator, though they were slightly more frequent as equinox approached.Although the latitudinal distribution of clouds is now relatively well reproduced and understood by the GCMs, the non-homogeneous longitudinal distributions and the evolution of the cloud coverage with seasons still need investigation. If the observation of a few single clouds at the tropics and at northern mid-latitudes late in winter and at the start of spring cannot be further interpreted for the moment, the obvious shutdown of the cloud activity at Titans poles provides clear signs of the onset of the general circulation turnover that is expected to accompany the beginning of Titans northern spring. According to our GCM, the persistence of clouds at certain latitudes rather suggests a sudden shift in near future of the meteorology into the more illuminated hemisphere. Finally, the observed seasonal change in cloud activity occurred with a significant time lag that is not predicted by our model. This may be due to an overall methane humidity at Titans surface higher than previously expected.

Keywords: Titan, Atmosphere, Clouds, Meteorology

1 Introduction

Methane on Titan plays a role similar to that of water on Earth. Gaseous methane can condense in the form of liquids or solids at specific latitudes and altitudes and can occasionally precipitate onto the surface, feeding surface and sub-surface reservoirs of liquid methane. Because methane humidity remains low near the surface, liquid methane evaporates, thus maintaining this exotic, active meteorological cycle (Flasar, 1998; Tokano, 2001; Rannou et al., 2006). Ethane and other condensable byproducts are also thought to condense and form clouds, mostly in high latitudes regions during the winter season (Rannou et al., 2006; Griffith et al., 2006). Clouds on Titan were detected as early as 1995 through ground-based telescopic observations (Griffith et al.,

[1] Laboratoire AIM, Université Paris 7/CNRS/CEA-Saclay, DSM/IRFU/SAp, France
[2] Université de Nantes, Laboratoire de Planétologie et Géodynamique, Nantes, France
[3] CNRS, UMR-6112, Nantes, France
[4] Groupe de Spectrométrie Moléculaire et Atmosphérique, Université de Reims Champagne-Ardenne, France
[5] Jet Propulsion Laboratory, California Institute of Technology, Pasadena, CA, USA
[6] Lunar and Planetary Lab and Steward Observatory, University of Arizona, Tucson, AZ, USA

1998) and have been regularly observed since. The regular flybys of Titan by the Cassini spacecraft provide a unique opportunity to track the cloud activity. The search for Titan clouds location and the monitoring of their long-term activity contribute to the global understanding of Titan climate and atmospheric dynamics, which are key questions to be addressed by the Cassini-Huygens mission.

Investigations from ground-based telescopes using adaptive optics facilities (allowing direct imaging) gathered the first statistical constraints on the location and lifetime of Titan clouds, revealing in particular the variability and periodicity of outbursts of the large South Polar clouds (Brown et al., 2002; Bouchez and Brown, 2005; Schaller et al., 2006a, 2006b; Hirtzig et al., 2006). Ground-based observations also reported in 2004 the first detection of a temperate-latitude cloud system occurring at 40^oS (Roe et al., 2005a, 2005b). Since its insertion into Saturn orbit in July 2004, the Cassini mission has viewed Titan clouds in unprecedented detail with, on average, a monthly close flyby of Titan. The Cassini view widely complements the ground-based observations and provides new constraints on the seasonal evolution of Titan meteorology. Several southern and other discrete clouds were observed during the first flybys by using the Cassini Imaging Science Subsystem (ISS) camera (Porco et al., 2005) and the Visual and Infrared Mapping Spectrometer (VIMS) (Griffith et al., 2005, 2006; Baines et al., 2005; Rodriguez et al., 2009, 2011; Le Mouélic et al., 2012). This latter instrument acquires hyperspectral images in 352 contiguous spectral channels between 0.3 and 5.2 μm (Brown et al., 2003), allowing the detection of clouds not only from their morphologies in simple imagery but also from their spectral behavior. Here, we present the first comprehensive mapping of Titan clouds detected in the full VIMS dataset between the Cassini insertion in July 2004 and April 2010 (i.e., during 67 Titan flybys). .

2 Semi-automatic detection of Titan clouds within VIMS spectro-images

The atmosphere of Titan is opaque at infrared wavelengths, except for seven narrow spectral windows where methane absorption is the weakest (at λ = 0.93, 1.08, 1.27, 1.59, 2.03, 2.75 and 5 μm). Because clouds are efficient reflectors in the near-infrared and substantially reduce the path-length of solar photons in Titan atmosphere, their spectra present a brightening in all spectral windows with particularly bright windows at 2.75 and 5 μm. Wed found that the most robust automated detection criterion to separate pixels that contain cloudy spectral component from any other components is to use the simultaneous brightening of the 2.75 and 5 μm windows (Rodriguez et al., 2009, 2011). Taking a single window or a combination of two other windows leads systematically to false positive detections. We produce, for each VIMS datacube, histogram distributions for the 2.75 and 5 μm windows areas. Two-sigma conservative thresholds on the two areas distributions are automatically calculated in order to only select these cloudy pixels. The reliability of the thresholds is controlled and finely tuned up using the 2.1 μm VIMS channel image as a reference, which is sensitive to tropospheric clouds.

3 Global view of the 2004−2010 cloud coverage of Titan

Figure 1 presents the integrated fractional cloud coverage we observe with VIMS between July 2004 and April 2010. On a global scale, we found that Titans cloud coverage is very low relative to terrestrial standards, with a very patchy cloud coverage. Averaged over the period interval between July 2004 and April 2010, the cloud coverage only represents 10% of Titans entire globe. In comparison, the instantaneous cloud coverage on Earth is seven times greater (75%) on average. Between northern winter and the beginning of spring (the 2004–2010 period), Titan clouds have mostly occurred in three areas which are well delineated in latitude: (1) the north polar region, (2) the temperate southern latitudes, and (3) the south pole. Other regions are almost completely free of clouds, except for very sporadic tropical outbursts and two small clouds at northern mid-latitudes (40^oN).

The northern polar region of Titan is systematically blanketed by an ever-present thin cloud system from the first Cassini observations in mid-2004 until early 2008. As Titans north pole progressively emerges from the night, this large, stratiform cloud system is found to cover the polar region at all longitudes and from 60^oN latitude up to the pole (Griffith et al., 2006; Rodriguez et al., 2009, 2011; Le Mouélic et al., 2012). Poleward of 60^oN the fraction of cloud coverage, averaged over the 2004–2010 period, is greater than 70%. Its total surface coverage however has slightly diminished with time. Very stable between 2004 and 2006, with an overall fractional coverage greater than 80%, this large cloud started slowly recessing since mid-2006. After mid-2008, the north polar cloud began to fractionate and collapse at some places, leaving a cloud ring centered at 60^oN with only small, but more opaque and convective-type cloud patches in its central region. Later on, as Titan passed the spring equinox in August 2009, all that had remained from the large north cloud cap, including the

thin 60^{o}N cloud ring, finally disappeared, leaving the north pole free of cloud, apart from small and sporadic clouds, likely to be convective in nature.

Large clouds are also clearly visible at the south pole since the early VIMS observations of Titan in 2004. Cloud events at Titans south pole have been previously reported from Earth-based observation campaigns since December 2001. From telescopic observations, these clouds appeared to be tropospheric large scale stormy outbursts with variability timescales (related to their changes in size and/or height) of a few hours . These storms have sustained their activity almost continuously until November 2004, from which time they were also observed by Cassini. Contrary to what was previously thought from Earth-based imaging, south polar clouds have still retained a substantial activity after this date. They were indeed constantly detected by VIMS after November 2004 up to December 2005, during almost all Cassini flybys of Titan. Nevertheless these events were dimmer and less spatially extended than those seen since 2002, possibly preventing Earth-based telescopes from resolving them. After December 2005, the cloud activity at the south pole began to decline. For the first time since 2001, no clouds near the south pole were observed for 8 months, between January and September 2006. Large outbursts were then regularly detected again for almost a year. Except for some rare and small scale events in 2008, the south pole of Titan ceased all stormy activity starting from the last dissipation in mid-2007, 2 years before the northern spring equinox . This decline is illustrated by the gradual decrease of the mean fractional coverage in clouds poleward of 60^{o}S between 2004–2006 (15%) and 2009–2010 (down to 0%) periods.

Southern mid-latitude clouds were observed by Cassini on a regular basis between July 2004 and April 2010. Indeed, recent VIMS observations show that southern midlatitudes (regions of Titan between 30^{o}S and 60^{o}S) showed a relatively stable fractional coverage in clouds of 10% during the entire 20042010 time interval, reaching a peak mean fractional coverage of 15% between July 2009 and April 2010. These clouds were thus still present, and quite active, at the time of the northern spring equinox (August 2009), and do not seem to display any sign of decline after that date thus far. Southern mid-latitude clouds are generally found to be elongated in the eastwest direction, likely stretched by zonal wind shear at the altitude where they form.

After December 2006, we identify some clouds further north in Titans tropics, equatorward of 30^o latitudes. Most of them are found in the southern hemisphere. However, contrary to what we observed in the high- to mid-latitude regions of the southern hemisphere, these near-equatorial clouds were in general much smaller and significantly more scarce, appearing in less than 5% of the 67 Cassini flybys between July 2004 and April 2010. Equatorial clouds appear with a slightly higher frequency after February 2008, during the approach of equinox.

Finally, we also observe the first, consecutive appearances of two small elongated clouds at northern mid-latitudes (flybys T62 and T63). These unique clouds have an elongated morphology similar to the 40^{o}S clouds, and are not connected to the north polar cloud. They first appeared in late 2009, right after the northern spring equinox, and were observed while 40^{o}S clouds were still active.

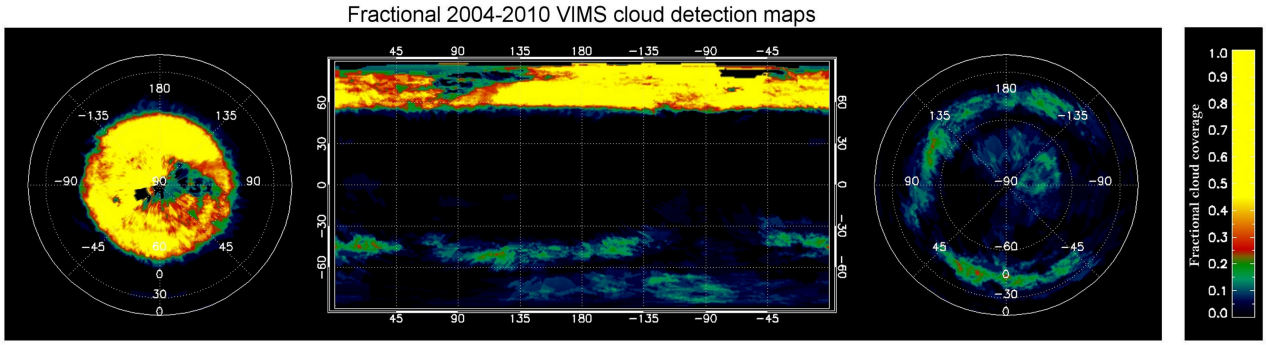

Fig. 1. Fractional cloud coverage in the 2004–2010 period. The mapping projection is rectangular with grid marks every 45^o of longitude and 30^o of latitude (0^o longitude is on the left). Longitude is in degrees east. For the northern (left) and southern (right) polar projections, grid marks are also shown every 45^o of longitude and 30^o of latitude (0^o longitude is down).The resolution of the projection maps are of 0.3^o in longitude and latitude (i.e.14 km per pixel at the equator).The color scale saturates at 0.45 to enhance the southern cloud distribution and equatorial transient events. The fractional coverage in clouds of the north polar region exceeds 0.7 almost everywhere poleward of 60^{o}N. The clouds of Titan mainly cluster at three distinct latitudes during the course of southern summer and at the beginning of southern fall: poleward of 60^{o}N, poleward of 60^{o}S and at 40^{o}S.

4 Discussion and conclusion

The persistence, location, and periodicity of the clouds were compared with the forecast of the global circulation models (GCMs) (Rannou et al., 2006; Mitchell et al., 2006, 2009). These new constraints, along with ground-based observations, can contribute to the refinements of GCMs predictions and to a better understanding of Titans climate. Between 2004 and 2008 (i.e., late northern winter), we show that Titans meteorology was very stable: (1) a widespread and long-lived cloud capped the entire northern polar vortex region, poleward of 60^oN; apart from the polar cloud, the northern hemisphere (winter hemisphere) was entirely cloud-free and (2) sporadic clouds were regularly seen at mid-latitudes and above the pole in the southern hemisphere (summer hemisphere). Our observations support the interpretation that the winter (northern) polar cloud is caused by the sinking and cooling of stratospheric air into the colder troposphere and the preferential condensation of droplets of ethane, and that the summer (southern) stormy clouds are more likely convective in nature and mainly composed of methane droplets. The latitudinal clustering of the clouds and the hemispheric asymmetry of their physical and chemical properties are both satisfactorily predicted by the GCMs.

After mid-2008, we observed the first strong evidence of a global decline of Titans cloud activity. At the end of 2008, the clouds at the south pole disappeared. At the same time, the northern polar cloud began to show clear signs of fragmenting, finally to completely vanish after the equinox as predicted by the IPSL-TGCM (Rannou et al., 2006). We also detected a dozen cloud outbursts at the tropics, which seemed to be more frequent as equinox approaches. All these observations show that we are likely witnessing the onset of the seasonal pole-to-pole circulation turnover on Titan. The meteorology is then expected to completely reverse from one hemisphere to another in the next five or six terrestrial years, as predicted by the models. The persistence of southern mid-latitude clouds at 40^oS through mid-2010, and the occurrence, a few months before and after the equinox, of more frequent equatorial clouds along with first appearance of northern mid-latitude clouds seem to suggest rather an abrupt hemispherical reversal of cloud activity, even if these equatorial and northern mid-latitude events are still too rare to be fully significant. The Cassini Solstice Mission will observe Titan up to the beginning of northern summer, in 2017, and should help to definitively solve the question of the meteorological hemispheric reversal, and the question of the type of atmospheric circulation (symmetric or asymmetric).

References

Baines, K.H. et al., 2005, EM&P 96, 119..
Bouchez, A.H. & Brown, M.E., 2005, ApJ 618, L53.
Brown, M.E., Bouchez, A.H. & Griffith, C.A., 2002, Nature 420, 795.
Brown, R.H. et al., 2003, Icarus 164, 461.
Flasar, F.M., 1998, P&SS 46, 1109.
Griffith, C.A., Owen, T., Miller, G.A. & Geballe, T., 1998, Nature 395, 575.
Griffith, C.A. et al., 2005, Science 310, 474.
Griffith, C.A. et al., 2006, Science 313, 1620.
Hirtzig, M. et al., 2006, A&A 456, 761.
Le Mouélic, S. et al., 2012, P&SS 60, 86.
Mitchell, J.L., Pierrehumbert, R.T., Frierson, D.M..W. & Caballero, R., 2006, PNAS 103, 18421.
Mitchell, J.L., Pierrehumbert, R.T., Frierson, D.M..W. & Caballero, R., 2009,Icarus 203, 250.
Porco, C.C. et al., 2005, Nature 434, 159.
Rannou, P., Montmessin, F., Hourdin, F. & Lebonnois, S., 2006, Science 311, 201.
Rodriguez et al., 2009, Nature 459, 678.
Rodriguez et al., 2011, Icarus 216, 89.
Roe, H.G., Bouchez, A.H., Trujillo, C.A., Schaller, E.L. & Brown, M.E., 2005a, ApJ 618, L49.
Roe, H.G., Brown, M.E., Schaller, E.L., Bouchez, A.H., & Trujillo, C.A., 2005b, Science 310, 477.
Schaller, E.L., Brown, M.E., Roe, H.G. & Bouchez, A.H., 2006a, Icarus 182, 224.
Schaller, E.L., Brown, M.E., Roe, H.G., Bouchez, A.H. & Trujillo, C.A., 2006b, Icarus 184, 517.
Tokano, T., 2001, Icarus 153, 130.

Session 03

Modélisation numérique en physique stellaire

SF2A 2013
L. Cambrésy, F. Martins, E. Nuss and A. Palacios (eds)

3D SIMULATIONS OF INTERNAL GRAVITY WAVES IN SOLAR-LIKE STARS

L. Alvan[1], A.-S. Brun[1] and S. Mathis[1]

Abstract. We perform numerical simulations of the whole Sun using the 3D anelastic ASH code. In such models, the radiative and convective zones are non-linearly coupled and in the radiative interior a wave-like pattern is observed. For the first time, we are thus able to modelize in 3D the excitation and propagation of IGWs in a solar-like star's radiative zone. We compare the properties of our waves to theoretical predictions and results of oscillation calculations. The good agreement obtained allow us to validate the consistency of our approach and to study the characteristics of IGWs. In the 3D domain, we focus on the excitation of IGWs and on the form of their spectrum where we suspect that both g-modes and propagative waves are present.

Keywords: hydrodynamics, waves, stars: oscillations, methods: numerical

1 Introduction

Internal gravity waves (IGWs) can propagate deeply in radiation zones. For this reason, they are essential to probe stellar interiors (Garcia et al. 2007) and to understand angular momentum transport in stars (Charbonnel & Talon 2005; Mathis et al. 2013). The work presented here follows Alvan et al. (2012) and Mathis et al. (2013). We present results of numerical simulations of a solar-like star where convective and radiative zones are coupled, resulting in the excitation of internal gravity waves. We first present two new developments of the Anelastic Spherical Harmonic (ASH) code and then focus on recent results concerning gravity waves.

2 Recent improvements in the ASH code

In order to study the generation of internal gravity waves by convective motions in solar-like stars, we use the anelastic spherical harmonic (ASH) code (Brun et al. 2004). Our model nonlinearly couples a convective envelope to a stable radiative interior (Brun et al. 2011), assuming a realistic solar stratification from r = 0 up to 0.97R (Brun et al. 2002), by solving the full set of anelastic equations in a rotating spherical shell.

$$\vec{\nabla}.\left(\bar{\rho}\vec{\mathrm{v}}\right) = 0 \tag{2.1}$$

$$\bar{\rho}\left(\frac{\partial\vec{\mathrm{v}}}{\partial t}+\left(\vec{\mathrm{v}}.\vec{\nabla}\right)\vec{\mathrm{v}}\right) = -\vec{\nabla}P+\rho\vec{\mathrm{g}}-2\bar{\rho}\vec{\Omega}_0\times\vec{\mathrm{v}}-\vec{\nabla}.\vec{\mathcal{D}}-\left[\vec{\nabla}\bar{P}-\bar{\rho}\vec{\mathrm{g}}\right] \tag{2.2}$$

$$\begin{aligned}\bar{\rho}\bar{T}\frac{\partial S}{\partial t}+\bar{\rho}\bar{T}\vec{\mathrm{v}}.\vec{\nabla}\left(S+\bar{S}\right) &= \bar{\rho}\epsilon+\vec{\nabla}.\left[\kappa_r\bar{\rho}c_p\vec{\nabla}\left(T+\bar{T}\right)+\kappa\bar{\rho}\bar{T}\vec{\nabla}S+\kappa_0\bar{\rho}\bar{T}\vec{\nabla}\bar{S}\right] \\ &+ 2\bar{\rho}\nu\left[e_{ij}e_{ij}-1/3\left(\vec{\nabla}.\vec{\mathrm{v}}\right)^2\right]\end{aligned} \tag{2.3}$$

We note $\bar{\rho}$, $\bar{P}$, $\bar{T}$ and $\bar{S}$ the reference density, pressure, temperature and specific entropy. Fluctuations about this reference state are denoted by ρ, P, T and S. $\mathrm{v}=(\mathrm{v}_r,\mathrm{v}_\theta,\mathrm{v}_\varphi)$ is the local velocity in spherical coordinates in the frame rotating at constant angular velocity $\vec{\Omega}_0$, $\vec{\mathrm{g}}$ is the gravitational acceleration, c_p is the specific heat per unit mass at constant pressure, κ_r is the radiative diffusivity, $\mathcal{D}$ is the viscous stress tensor and ν, κ and κ_0

[1] Laboratoire AIM Paris-Saclay, CEA/DSM-CNRS-Université Paris Diderot, IRFU/SAp, F-91191 Gif-sur-Yvette Cedex, France

are the effective eddy diffusivities. A volume heating term $\bar{\rho}\epsilon$ is also included in these equations, representing the energy generation by nuclear burning.

Two recent improvements in the code have been taken into account in this work. The first one concerns the anelastic treatment. Brown et al. (2012) have performed a detailed study showing that the anelastic equations written above do not conserve energy and instead conserve a stratification weighted pseudo-energy. As a consequence, these equations obtain incorrect frequencies and radial eigenfunctions for gravity waves. To correct this bias in ASH, we have rewritten the set of equations to implement the Lantz-Braginsky-Roberts equations (e.g., Lantz 1992; Braginsky & Roberts 1995; Lantz & Fan 1999; Jones et al. 2009). This is done by introducing a reduced pressure $\bar{\omega} = P/\bar{\rho}$ instead of the fluctuating pressure P and by converting the buoyancy term to a codensity where only entropy fluctuations S contribute to buoyancy. The resulting momentum equation is

$$\frac{\partial \vec{\mathrm{v}}}{\partial t} + \left(\vec{\mathrm{v}}.\vec{\nabla}\right)\vec{\mathrm{v}} = -\vec{\nabla}\bar{\omega} - \frac{S}{c_p}\vec{g} - 2\bar{\rho}\vec{\Omega}_0 \times \vec{\mathrm{v}} - \vec{\nabla}.\vec{\mathcal{D}} \tag{2.4}$$

The effect of this correction is visible when we calculate precisely the frequencies of IGWs as presented in the following part. The second change in the code allows us to treat the singularity at the center of the star. Following Bayliss et al. (2007), we have implemented regularity conditions at $r = 0$. Only $l = 1$ modes can go through the center. The detail of this work will be presented in Alvan et. al (2013) (in prep).

3 Internal gravity waves : excitation

These numerical improvements allow us to study with improved accuracy the spectrum of internal gravity waves excited by the turbulent convection. In fig. 1, we represent the radial velocity v_r/v_{rms} where v_{rms} is the root mean square radial velocity at each radius. It shows two consecutive zoom starting from an equatorial slice ($\theta = 90^o$, all φ).

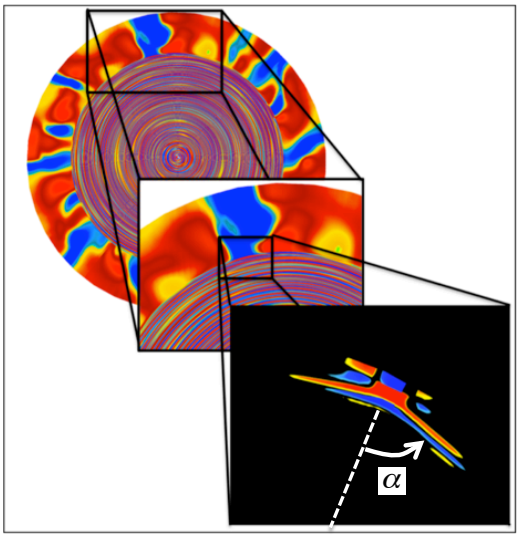

Fig. 1. Gravity waves pattern observed in the radiative (inner) zone and zoom at the base of a downflow (blue) to highlight the St. Andrew's cross. Waves excited by this process have a very low frequency (about 0.01mHz).

In the outer convective zone, we clearly see downward (blue) and upward (red) flows. We observe wavefronts (almost circular spiral) propagating in the radiative zone. To understand the way IGWs are excited we zoom at the base of a downflow. The second zoom shows a classical result of fluid mechanics concerning excitation of IGWs by a localized disturbance in a stably stratified fluid. Waves excited by the pummeling of downward convective flows propagate inside beams, which develop around a St. Andrew's cross in the plane orthogonal to the main direction of the plume. The cross forms an angle α to the vertical given by

$$\alpha = \arccos \frac{\omega}{N}, \tag{3.1}$$

where ω is the frequency of the wave and N the Brunt-Vaisala frequency. In the last zoom, we have distorded the radius in order to highlight the cross. The real value of α is close to 90^o that corresponds to very low frequency waves (about 0.01mHz) and explain the almost circular wavefronts.

4 Internal gravity waves : spectrum

Starting from a temporal sequence of the radial velocity field $V_r(r_0, \theta, \varphi, t)$ at a given depth r_0, we switch from the real space to the spectral space by successively applying a spherical harmonic transform at each time step, which gives $\hat{V}_r(r_0, l, m, t)$, and a temporal Fourier transform on the whole temporal sequence. In Fig. 2, we represent the quantity

$$E(r_0, l, \omega) = \sum_m |\tilde{V}_r(r_0, l, m, \omega)|^2 \tag{4.1}$$

as a function of frequency ω and order l for three given depths. The spectrum obtained is extremely rich and close to the one predicted by the linear theory.

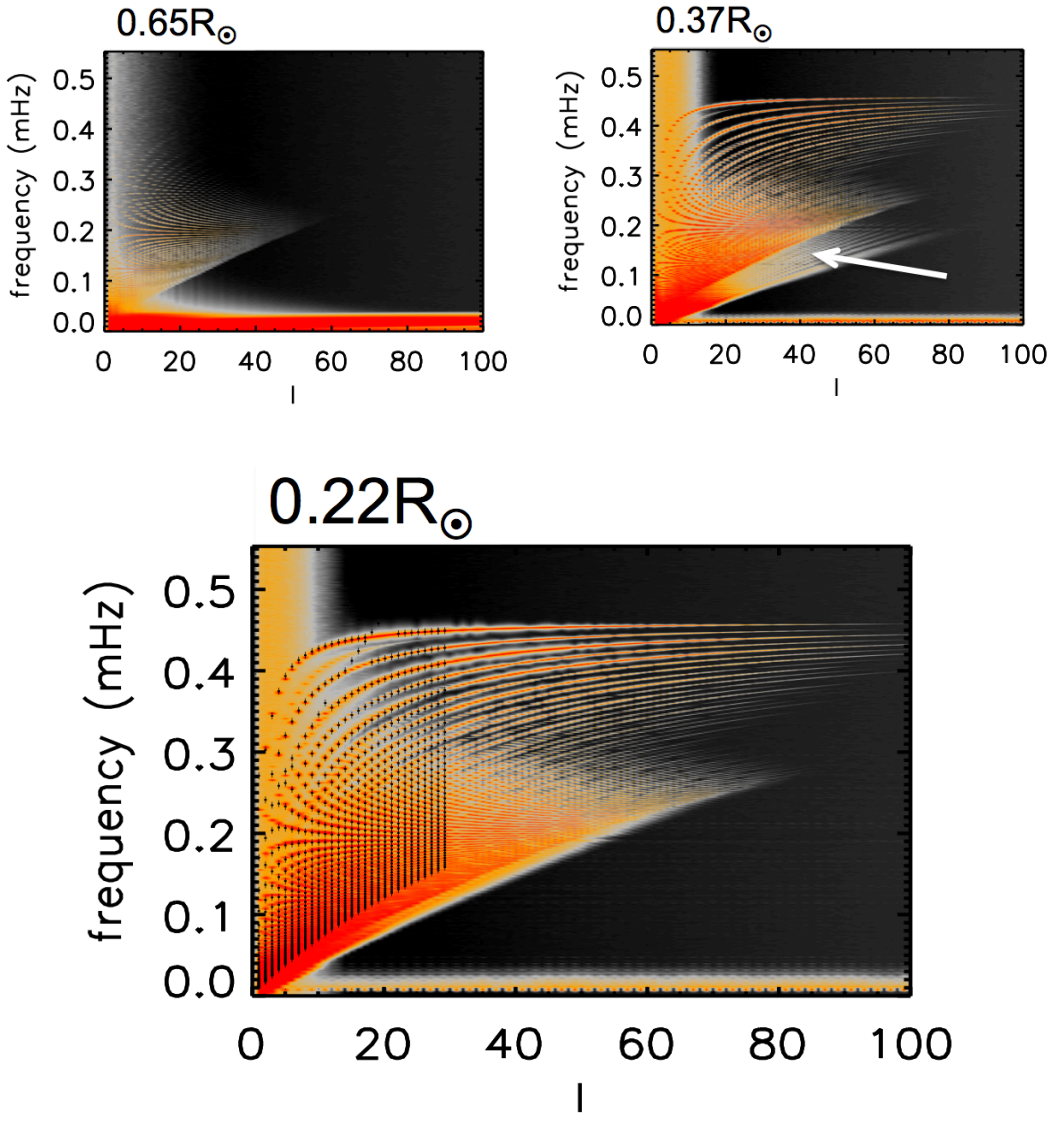

Fig. 2. Spectrum of gravity waves calculated at three different depths in the radiative zone. Black crosses in the panel at r=0.22 $R_\odot$ represent the frequencies obtained by the ADIPLS oscillation code.

In the bigger panel of Fig. 2, we have superimposed the frequencies obtained by the ADIPLS code* to show the good agreement obtained (black crosses). At high frequencies, ridges are formed by modes with the same radial order n (number of zeros in the radial direction in the eigenfunctions). They tend to an asymptote corresponding to the maximum value of the Brunt-Vaisala frequency N. We note that the spectrum's global aspect is different depending on the depth. We do not show the convective zone since no modes are visible. Indeed, IGWs are evanescent in regions where the entropy gradient is negative. At $0.65R_\odot$, where $R_\odot$ is the solar radius, only the low frequency part of the spectrum is observed and a big bump of energy is visible (in red) at very low frequency. We suspect it to correspond to very low frequency waves excited by plumes as explained in the previous section. In the second panel corresponding to $0.37R_\odot$, the spectrum is more complete but we see a region looking different of the rest at low frequency. The energy in this region does not form peaks regularly spaced in period, such as g-modes should do. Consequently, we interpret this region as propagating gravity waves that do not form g-modes. The fact that this zone reduces and disappears when we move down into depth reinforces this hypothesis since it corresponds to the action of the radiative damping on these waves.

5 Conclusions

We have shown that a detailed analysis of IGWs in 3D non-linear dynamical simulations is possible. For the first time, we are able to model the behaviour of both propagative and standing waves in a realistic 3D cavity. The results presented here do not take into account the rotation of the model since we have added up all the asimuthal number m. But the contribution of 3D simulations is also important for studying the effect of the rotation on gravity waves and for measuring rotational splitting. Moreover, excitation rates could be applied as an input for dynamical stellar evolution codes such as STAREVOL.

The authors warmly thanks the SF2A organizing committee and the four editors of the proceedings. We also acknowledge financial support by ERC STARS2 207430 project, by CNES - GOLF and FP7-IRSES, and access to supercomputers through GENCI project 1623.

References

Alvan, L., Brun, A. S., & Mathis, S. 2012, in SF2A-2012: Proceedings of the Annual meeting of the French Society of Astronomy and Astrophysics. Eds.: S. Boissier, 289–293

Bayliss, R. A., Forest, C. B., Nornberg, M. D., Spence, E. J., & Terry, P. W. 2007, Physical Review E, 75, 26303

Brown, B. P., Vasil, G. M., & Zweibel, E. G. 2012, astro-ph

Brun, A. S., Antia, H. M., Chitre, S. M., & Zahn, J.-P. 2002, Astronomy and Astrophysics, 391, 725

Brun, A. S., Miesch, M. S., & Toomre, J. 2004, ApJ, 614, 1073

Brun, A. S., Miesch, M. S., & Toomre, J. 2011, ApJ, 742, 79

Charbonnel, C. & Talon, S. 2005, Science, 309, 2189

Garcia, R. A., Turck-Chièze, S., Jiménez-Reyes, S. J., et al. 2007, Science, 316, 1591

Mathis, S., Decressin, T., Eggenberger, P., & Charbonnel, C. 2013, Astronomy and Astrophysics, 558, 11

*Christensen-Dalsgaard, J. 2011, *ADIPLS: Aarhus Adiabatic Oscillation Package (ADIPACK)*

SF2A 2013
L. Cambrésy, F. Martins, E. Nuss and A. Palacios (eds)

EFFECT OF INTERNAL GRAVITY WAVES ON THE TRANSPORT OF ANGULAR MOMENTUM DURING THE PMS

T. Decressin[1], C. Charbonnel[1,2], L. Amard[3], A. Palacios[3] and S. Talon[4]

Abstract. In stellar interior rotation profile can be changed by stellar contraction, meridional circulation, shear turbulence and internal gravity waves. These waves are generated at the edge of the convective zones and propagate inside the radiative zone where they damped by thermal diffusivity and viscosity in corotation resonance. The differential damping between prograde and retrograde let its imprint on the rotation profile along with other hydrodynamic transport processes. This interplay will be discussed for low-mass stars along the PMS.

Keywords: stars: evolution – stars: interiors – stars: low-mass – stars: rotation

1 Introduction

We present pre-main sequence (hereafter PMS) models for low-mass rotating stars (0.6 to 2.0 $M_{\odot}$) at solar metallicity computed with the stellar evolution code STAREVOL (see Siess et al. 2000; Palacios et al. 2003; Decressin et al. 2009; Lagarde et al. 2012, for more details). Initially we assume a solid-body law for rotation with a surface velocity equals to 5% of the critical velocity when the radiative core appears. Our models reach surface velocity around 50-80 km.s^{-1} on the zero age main sequence (hereafter ZAMS). We follow the formalism developed by Zahn (1992) and Mathis & Zahn (2004) for the transport of angular momentum by meridional circulation, shear turbulence and internal gravity waves (hereafter IGW). In these computation we assume no loss of angular momentum by radiative winds during the PMS (see Charbonnel et al. 2013, for more details). Such models with a self-consistent treatment of rotation evolution can be used to understand the observations of surface velocity in open cluster stars (Irwin & Bouvier 2009; Gallet & Bouvier 2013).

2 IGW excitation

In this work we follow the formalism developed by Talon & Charbonnel (2005) for the excitation and the transport of angular momentum by IGW by the convective envelope and the convective core when present. Both prograde and retrograde waves are taken into account and the excitation is computed at each time-step to account for the structural changes along the PMS. Once emitted a wave travels through the radiative interior and it mainly damps near its critical layer (*i.e.*, the location where the local relative frequency of a given wave to the rotational frequency of the fluid tends to zero, see also Alvan et al. 2013) where they will extract or deposit angular momentum. As prograde and retrograde waves are damped in different region, a net transport of angular momentum happens.

The excitation by Reynolds stress and the buoyancy in the bulk of convective regions is computed following Goldreich et al. (1994) and Kumar & Quataert (1997). We multiply the resulting luminosity by a factor 2 to account the recent results by Lecoanet & Quataert (2012). The obtained spectra for IGW are still uncertain as we include neither the generation by convective overshooting plumes (Garcia Lopez & Spruit 1991) nor the effects of Coriolis force (Mathis 2009).

[1] Observatoire de Genve 51, chemin des Maillettes CH-1290 Sauverny, Switzerland
[2] IRAP, CNRS UMR 5277, Universit de Toulouse, 14 Av. E. Belin, 31400 Toulouse, France
[3] LUPM, Universit Montpellier II, CNRS, UMR 5299, Place E. Bataillon, 34095 Montpellier, France
[4] Calcul Qubec, Universit de Montral (DGTIC), C.P. 6128, succ. Centre-ville, Montral (Qubec) H3C 3J7, Canada

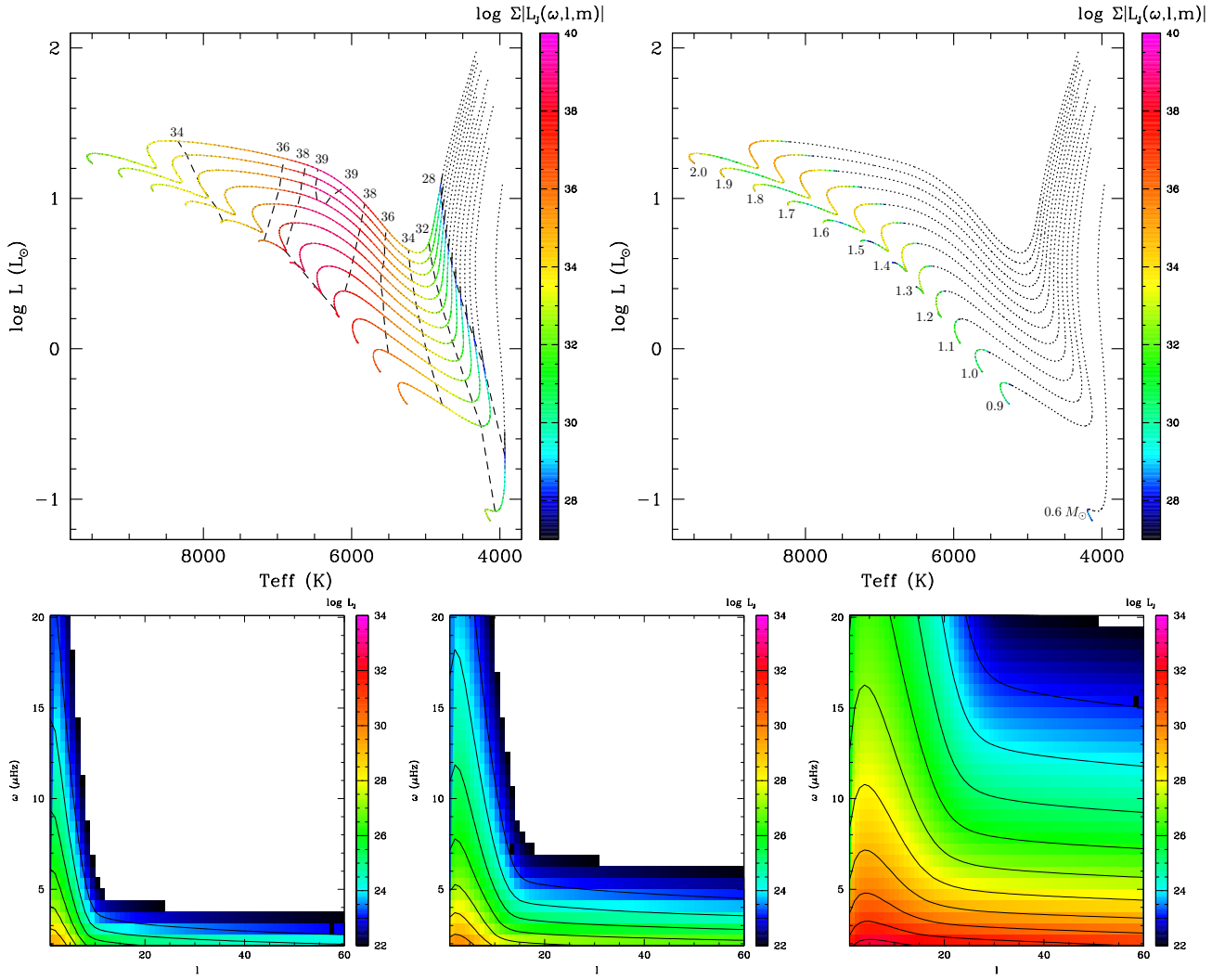

Fig. 1. *Top panels*: tracks along the PMS for 0.6 to 2.0 $M_\odot$ stars at solar metallicity with the colours indicate the total luminosity of IGW excited by the convective envelope (left) and the convective core (right). Dotted lines indicate when the stars are fully convective or have no convective core. *Bottom panels*: spectra of the IGW emitted by the convective envelope of a 1 $M_\odot$ with solar metallicity at 5.8, 14 and 35 Myr.

Figure 1 shows the computed total excitation luminosity of IGW for all our PMS models both from the convective envelope and convective core. The waves luminosity from the convective envelope rises sharply once a radiative core appears at the end of the vertical Hayashi line and present a maximum around $T_{\rm eff} \simeq 6200$ K. For stars heavier than 1.3-1.4 $M_\odot$ the luminosity decreases when the stars approach the ZAMS as a result of the drop in size (both in radius and mass coordinates) of the convective envelope. On the other side the waves emitted by the convective core at the end of the PMS are always negligible for stars below 1.3-1.4 $M_\odot$, and they becomes only dominant when those heavier stars approach the ZAMS.

The bottom panels of Fig. 1 show the development of the IGW luminosity spectra for a 1 $M_\odot$ star along the PMS reflecting the evolving properties of the convective envelope during the PMS. As the star cools, more waves are efficiently generated while these with low internal frequency and low number l remains the dominant ones (see also Talon & Charbonnel 2003).

3 Effects of IGW during pre-main sequence

The IGW has a strong effects on the transport of angular momentum in radiative interior. In the absence of IGW, angular momentum is mainly advected by meridional circulation which shows only one or two main loops

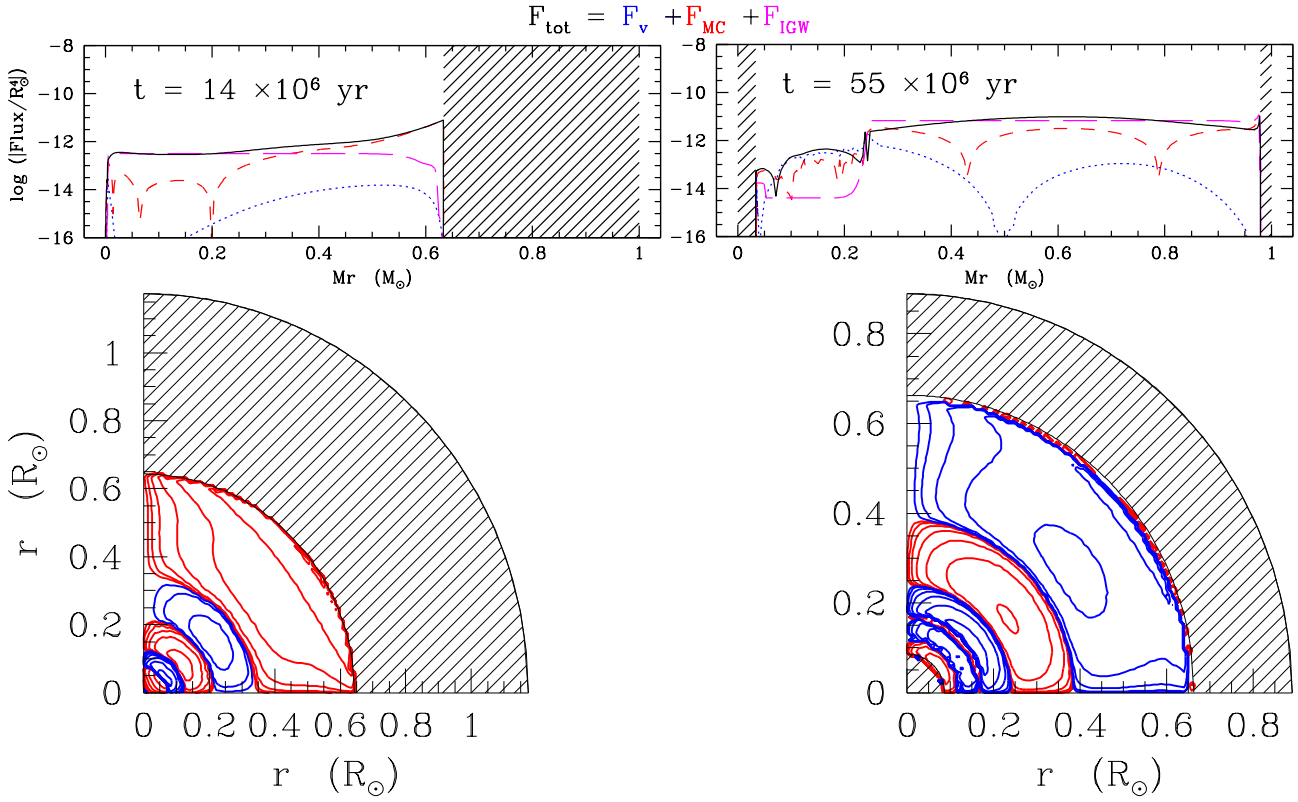

Fig. 2. *Top panels*: Decomposition of the total flux of angular momentum (solid black) into meridional circulation (short-dashed red), shear turbulence (dotted blue), and IGW (long-dashed magenta) in the 1 $M_\odot$, $Z_\odot$, models. The profiles are shown at 14 and 55 Myr. Shaded areas correspond to convective regions. *Bottom panels*: reconstruction of the meridional circulation inside the same star.

(see Decressin et al. 2009; Charbonnel et al. 2013). As shown in Fig. 2 for a 1 $M_\odot$ model, IGW induce a different behaviour as they dominate the angular momentum transport by conveying angular momentum directly from the radiative interior where they damped toward the convective envelope. The meridional circulation and the shear only dominates the transport in the inner radiative interior where IGW are efficiently damped (see top right panel of Fig. 2 below 0.25 $M_\odot$). As a results the angular velocity profile shows a peak in the radiative interior, that in turn will induce numerous loops of meridional circulation as illustrated in the bottom panels of Fig. 2. This multi-loops pattern will persist as long as IGW stay the dominant transport mechanism (see Talon & Charbonnel 2005 and Mathis et al, subm., for a description on the main sequence).

Fig. 3 shows how the rotation profile changes with the addition of IGW at the ZAMS for models with an initial mass from 0.6 to 2.0 $M_\odot$. For stars below 1.4 $M_\odot$, IGW induces a slowly rotating core and a peak in angular velocity, whereas only a monotonous differential rotation is obtained if only meridional circulation and shear turbulence is taken into account. This peculiar shape in peak results (1) from the overall contraction of the star that produces the negative gradient of angular velocity in the outer part of the radiative envelope and (2) from the extraction of angular momentum by IGW in the centre.

For heavier stars than 1.4 $M_\odot$, similarly a peak in the profile angular momentum formed when the waves from the convective envelope are efficiently generated (see Fig. 1). However when reaching the ZAMS, IGW from the core dominates and transport angular momentum inwards. Thus they tends to accelerate the core and the differences with models without IGW becomes smaller (see Charbonnel et al. 2013).

We acknowledge financial support from the Swiss National Science Foundation (FNS), from the French Programme National de Physique Stellaire (PNPS) of CNRS/INSU, and from the Agence Nationale de la Recherche (ANR) for the project TOUPIES (Towards Understanding the sPIn Evolution of Stars).

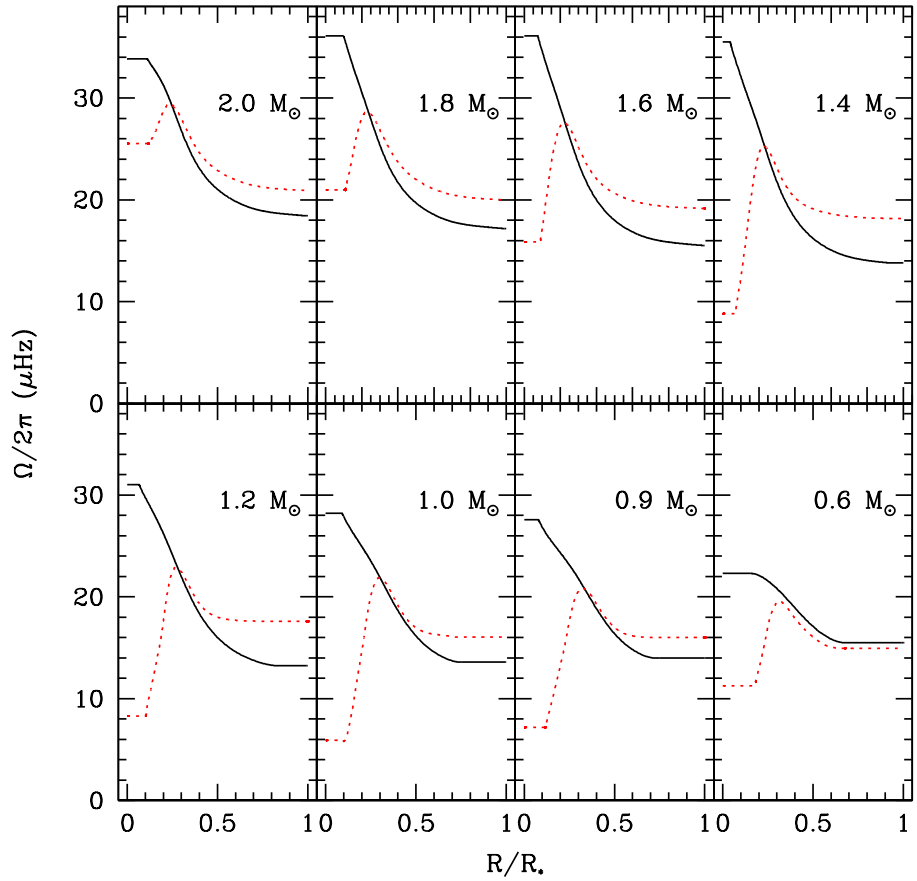

Fig. 3. Internal angular velocity profile for stars from 0.6 to 2.0 $M_{\odot}$, $Z_{\odot}$, at the ZAMS with taking into account the effect of IGW (dashed lines) and without them (full lines).

References

Alvan, L., Mathis, S., & Decressin, T. 2013, A&A, 552, 121

Charbonnel, C., Decressin, T., Amard, L., Palacios, A., & Talon, S. 2013, A&A, 554, 40

Decressin, T., Mathis, S., Palacios, A., et al. 2009, A&A, 495, 271

Gallet, F. & Bouvier, J. 2013, A&A, 556, A36

Garcia Lopez, R. J. & Spruit, H. C. 1991, ApJ, 377, 268

Goldreich, P., Murray, N., & Kumar, P. 1994, ApJ, 424, 466

Irwin, J. & Bouvier, J. 2009, in IAU Symposium, Vol. 258, IAU Symposium, ed. E. E. Mamajek, D. R. Soderblom, & R. F. G. Wyse, 363–374

Kumar, P. & Quataert, E. J. 1997, ApJ, 475, L143

Lagarde, N., Decressin, T., Charbonnel, C., et al. 2012, A&A, 543, A108

Lecoanet, D. & Quataert, E. 2012, ArXiv e-prints

Mathis, S. 2009, A&A, 506, 811

Mathis, S. & Zahn, J.-P. 2004, A&A, 425, 229

Palacios, A., Talon, S., Charbonnel, C., & Forestini, M. 2003, A&A, 399, 603

Siess, L., Dufour, E., & Forestini, M. 2000, A&A, 358, 593

Talon, S. & Charbonnel, C. 2003, A&A, 405, 1025

Talon, S. & Charbonnel, C. 2005, A&A, 440, 981

Zahn, J.-P. 1992, A&A, 265, 115

SF2A 2013
L. Cambrésy, F. Martins, E. Nuss and A. Palacios (eds)

ANGULAR MOMENTUM EVOLUTION MODEL FOR SOLAR-LIKE STARS

Florian Gallet [1]

Abstract. We present new models for the rotational evolution of solar-like stars between 1 Myr and 10 Gyr with the aim to reproduce the rotation period distributions observed for star forming regions and young open clusters within this age range. The models include a new wind braking law based on recent numerical simulations of magnetized stellar winds and specific dynamo and mass-loss prescriptions are adopted to link angular momentum loss to angular velocity. The model additionally assume constant angular velocity during the disk accretion phase and allow for decoupling between the radiative core and the convective envelope as soon as the former develops. The models reproduce reasonably well the rotational behaviour of solar-type stars between 1 Myr and the age of the Sun. We conclude that this class of semi-empirical models successfully grasp the main trends of the rotational behaviour of solar-type stars as they evolve and make specific predictions that may serve as a guide for further development.

Keywords: Stars: solar-type, Stars: evolution, Stars: rotation, Stars: mass-loss, Stars: magnetic field

1 Introduction

Simulations of physical events are now essential if we want to understand what happen in the stellar interior and within the stellar environment. These simulations are the only tools we have to test our knowledge and mathematical prescriptions that we use to describe our favourite objects : the stars. There is lots of different fields of physical modelling such as stellar structure, magnetic field and mass-loss rate evolution models. Obviously, the evolution of all these different physical components are somehow link to each other since the structure of the stellar interior will affect the generation of the magnetic field that will in turn affect the quantity of material launched through the stellar winds.

There is few "global" models in the literature that try to combine several isolated physical models. One of these "global" models is the angular momentum evolution that actually rely mainly on the evolution of the stellar interior, magnetic field, and mass-loss rate (e.g., Irwin et al. 2007; Bouvier 2008; Denissenkov et al. 2010; Spada et al. 2011; Reiners & Mohanty 2012). The origin and evolution of stellar angular momentum still remains partly unknown. Recently, new observational constraints on the rotation period distributions of low-mass stars belonging to numerous star forming regions and open clusters, covering an age range from 1 Myr to about 10 Gyr (see, e.g., Irwin & Bouvier 2009; Hartman et al. 2010; Agüeros et al. 2011; Meibom et al. 2011; Irwin et al. 2011; Affer et al. 2012, 2013), have been gained from large photometric surveys. This provides us with the detailed view of how surface rotational velocity changes as the stars evolve from the pre-main sequence (PMS), through the zero-age main sequence (ZAMS) to the late-main sequence (MS). To satisfy observational constraints, most of these models have to incorporate three major physical processes: star-disk interaction during the accretion phase, stellar winds, and redistribution of angular momentum in the stellar interior.

We present here a new angular momentum evolution models for solar-type stars, from 1 Myr to the age of the Sun, that incorporate some of the most recent advances described above and to compare their predictions to the full set of newly available observational constraints. One of the major differences between this study and previous similar studies lies in the wind braking relationship used in the models presented here that relies on recent stellar wind simulations by Matt et al. (2012) and Cranmer & Saar (2011).

[1] UJF-Grenoble 1/CNRS-INSU, Institut de Planétologie et d'Astrophysique de Grenoble (IPAG) UMR 5274, F-38041 Grenoble, France

2 Phenomenological model

2.1 Internal structure

We adopt the Baraffe et al. (1998) NextGen models computed for solar-mass stars of solar metallicity, with a mixing length parameter $\alpha = 1.5$, and helium abundance $Y = 0.275$. Low mass stars are composed of two regions: an inner radiative core and an outer convective envelope. We follow MacGregor & Brenner (1991) by assuming that both the core and the envelope rotate as solid bodies but with different angular velocity. The amount of angular momentum ΔJ to be transferred from the core to the envelope in order to balance their angular velocities is given by

$$\Delta J = \frac{I_{env} J_{core} - I_{core} J_{env}}{I_{core} + I_{env}}, \tag{2.1}$$

where I and J refer to the moment of inertia and angular momentum, respectively, of the radiative core and the convective envelope. As in Allain (1998), we assume that ΔJ is transferred over a constant time-scale τ_{c-e}, which we refer to as the core-envelope coupling timescale.

2.2 Stellar wind

Solar-type stars lose angular momentum as they evolve because of magnetized stellar winds (Schatzman 1962; Weber & Davis 1967). Assuming a spherical outflow, the angular momentum loss rate due to stellar winds can be expressed as

$$\frac{dJ}{dt} \propto \Omega_* \cdot \dot{M}_{wind} \cdot r_A^2, \tag{2.2}$$

where r_A is the averaged value of the Alfvén radius that accounts for the magnetic lever arm, Ω_* is the angular velocity at the stellar surface, and $\dot{M}_{wind}$ is the mass outflow rate. Matt et al. (2012) derived the expression

$$r_A = K_1 \left[\frac{B_p^2 R_*^2}{\dot{M}_{wind} \sqrt{K_2^2 v_{esc}^2 + \Omega_*^2 R_*^2}} \right]^m R_*, \tag{2.3}$$

where $K_1 = 1.30$, $K_2 = 0.0506$, and $m = 0.2177$ are obtained from numerical simulations of a stellar wind flowing along the opened field lines of a dipolar magnetosphere. In Eq. 2.3, R_* is the stellar radius, B_p is the surface strength of the dipole magnetic field at the stellar equator, and $v_{esc} = \sqrt{2GM_*/R_*}$, where M_* is the stellar mass, is the escape velocity. To implement this angular momentum loss rate into our models, we have to express the Alfvénic radius as a function of stellar angular velocity only. We must therefore adopt a dynamo prescription that relates the stellar magnetic field to stellar rotation, as well as a wind prescription that relates the mass-loss rate to the stellar angular velocity. In Eq. 2.3, B_p is the strength of the dipole magnetic field at the stellar equator. Even though the real stellar magnetic field is certainly not a perfect dipole, we identify B_p to the strength of the mean magnetic field $B_* f_*$.

We assume the stellar magnetic field to be dynamo generated, i.e., that the mean surface magnetic field strength scales to some power of the angular velocity. We thus have

$$f_* B_* \propto \Omega_*^b, \tag{2.4}$$

where b is the dynamo exponent, B_* is the strength of the magnetic field, and f_* is the filling factor, i.e., the fraction of the stellar surface that is magnetized (cf. Reiners & Mohanty 2012). Magnetic field measurements suggest that the magnetic field strength B_* is proportional to the equipartition magnetic field strength B_{eq} (see Cranmer & Saar 2011)

$$B_* \approx 1.13 \sqrt{\frac{8\pi \rho_* k_B T_{eff}}{\mu m_H}}, \tag{2.5}$$

with ρ_* the photospheric density, k_B the Boltzmann's constant, T_{eff} the effective temperature, μ the mean atomic weight, and m_H the mass of a hydrogen atom. For the filling factor we used the expression f_{min} from

Cranmer & Saar (2011), but we slightly modified it in order to reproduce the average filling factor of the present Sun ($f_\odot$ = 0.001-0.01, see Table 1 of Cranmer & Saar 2011)

$$f_* = \frac{0.55}{[1 + (x/0.16)^{2.3}]^{1.22}}. \tag{2.6}$$

We used the BOREAS* subroutine, developed by Cranmer & Saar (2011) to get the mean magnetic field $B_* f_*$ as a function of stellar density, effective temperature, and angular velocity. The photospheric density is calculated by BOREAS at the age steps provided by the Baraffe et al. (1998) stellar structure models, and f_* is derived form Eq. 2.6 above. We used the Rossby prescription from Cranmer & Saar (2011), i.e., for a solar-mass star $\tau_{conv} \approx$ 30d at 10 Myr, decreasing to 15d at an age $\geq$ 30 Myr. Measurements of stellar magnetic fields suggest that saturation is reached at $Ro \approx 0.1 - 0.13$ (see Reiners et al. 2009, Fig. 6). With $\tau_{conv} \approx$ 15 days, this translates into a dynamo saturation occurring at $\Omega_{sat} \sim 13 - 17\ \Omega_\odot$, which is consistent with the value we derive here. A more detailed description of the model can be found in Gallet & Bouvier (2013).

2.3 Star/disk interaction

For a few Myr during the early pre-main sequence, solar-type stars magnetically interact with their accretion disk. This star-disk magnetic coupling involves complex angular momentum exchange between the components of the system, including the accretion disk, the central star, and possibly both stellar and disk winds. Recently, accretion-powered stellar winds have been proposed as a way to remove from the central star the excess of angular momentum gained from disk accretion (Matt & Pudritz 2005, 2008a,b). However, Zanni & Ferreira (2011) showed that mass and energy supplied by accretion may not be sufficient to provide an efficient spin-down torque by accretion-driven winds. Zanni & Ferreira (2013) proposed that magnetospheric reconnection events occurring between the star and the disk lead to ejection episodes that remove the excess angular momentum. Hence, a free parameter of the models is the accretion disk's lifetime, τ_{disk}, i.e., the duration over which the star/disk interaction occur. After a time τ_{disk}, the star is released from its disk, and is only subjected to angular momentum loss due to magnetized stellar winds (see below). Note that during most of the pre-main sequence, once the disk has been dissipated, angular momentum losses due to magnetized stellar winds are however unable to prevent the star from spinning up as its moment of inertia rapidly decreases towards the ZAMS (cf. Bouvier et al. (1997); Matt & Pudritz (2007); Gallet & Bouvier (2013)). In this model we didn't use any physical star/disk interaction process and the surface angular velocity of the stars is simply held constant during all the disk's lifetime.

3 Angular velocity evolution

The free parameters of the model are the initial rotational period at 1 Myr P_{init}, the core-envelope coupling timescale τ_{c-e}, the disk lifetime τ_{disk}, and the scaling constant of the wind braking law K_1. The value of these parameters are to be derived by comparing the models to the observed rotational evolution of solar-type stars. The models for slow, median, and fast rotators are illustrated in Fig. 1.

For the fast rotator model ($P_{init} = 1.4d$), the disk lifetime is taken to be as short as 2.5 Myr, resulting in a strong PMS spin up. This is required to fit the rapid increase of angular velocity between the youngest clusters at a few Myr ($\Omega_* \simeq 10 - 20\ \Omega_\odot$) and the 13 Myr h Per Cluster ($\Omega_* \simeq 60\ \Omega_\odot$). The choice of P_{init} = 1.4 d for this model is dictated by the fast rotators in the two youngest clusters (ONC and NGC 6530). The core-envelope coupling timescale of the fast rotator model is 12 Myr which is comparable to the 10 Myr coupling timescale adopted by Bouvier (2008), but much longer than the 1 Myr value used in Denissenkov et al. (2010).

The parameters for the median and slow rotator models are quite similar to each other. The initial rotational periods are 7d and 10d for the median and slow rotator models, respectively, as indicated by the rotational distributions of the youngest PMS clusters. For both models we chose a disk lifetime of 5 Myr in order to reproduce the late PMS clusters and the slow rotation rates still observed in the 13 Myr h Per cluster ($\Omega_* \leq 7\ \Omega_\odot$). To account for the weak PMS spin up of the envelope, which leads to moderate velocities on the ZAMS ($\Omega_* \leq 6\ \Omega_\odot$), we had to assume a much longer core-envelope coupling timescale than for fast rotators, namely 28 and 30 Myr for median and slow rotator models, respectively. These values are significantly smaller

*https://www.cfa.harvard.edu/~scranmer/Data/Mdot2011/

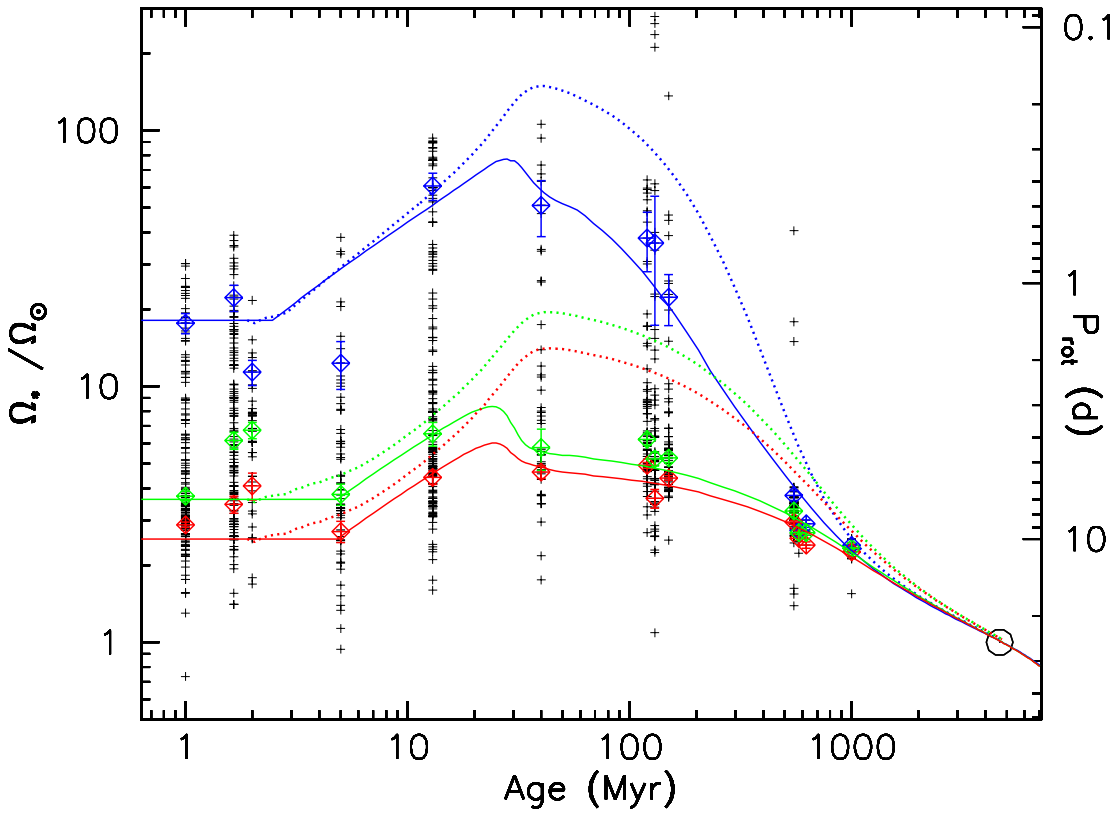

Fig. 1. Angular velocity of the radiative core (dashed lines) and of the convective envelope (solid lines) is shown as a function of time for fast (blue), median (green), and slow (red) rotator models. The angular velocity is scaled to the angular velocity of the present Sun. The blue, red, and green tilted squares and associated error bars represent the 90^{th} percentile, the 25^{th} percentile, and the median, respectively, of the rotational distributions of solar-type stars in star forming regions and young open clusters obtained with a rejection sampling method (see Gallet & Bouvier 2013). The open circle is the angular velocity of the present Sun.

than the 100 Myr coupling timescale derived by Bouvier (2008) and comparable to the value of 55±25 Myr derived by Denissenkov et al. (2010).

By 1 Gyr, the slow, median, and fast rotators models have all converged towards the same surface angular velocity and stars are thereafter braked at a low pace, following Skumanich's relationship (Skumanich 1972), i.e., $\Omega_* \propto t^{-1/2}$. It is quite noticeable, however, that this relationship is not valid earlier on the MS, nor does a unique relationship between age and surface rotation prior to about 1 Gyr for solar-type stars (Epstein & Pinsonneault 2012). All the models presented here yield a complete recoupling between the radiative core and the convective envelope by the age of the Sun, as requested by helioseismology results (Thompson et al. 2003). We emphasize that the evolution of core rotation strongly depends on the core-envelope coupling timescale assumed in the models and currently lacks observational constraints, apart from the solar case.

4 Conclusions

The rotational evolution of solar-type stars can be reasonably well reproduced by the class of phenomenological models presented here. In these models, the physical processes at play are addressed using simplified assumptions that either rely on observational evidence or are based on recent numerical simulations. The fundamental processes such as the generation of surface magnetic fields, stellar mass loss, and angular momentum redistribution, can all be scaled back to the surface angular velocity, which allows us to compute rotational evolution tracks. Pending more physical models still to be developed, these simplified models appear to grasp the main trends of the rotational behavior of solar-type stars between 1 Myr and 4.5 Gyr. The models additionally predict the amount of differential rotation to be expected in stellar interiors. We caution that these predictions are

mostly qualitative, as the two-zone model employed here is a crude approximation of actual internal rotational profiles. Also, we show that the evolution of internal rotation as the star ages is quite sensitive to the adopted braking law. In spite of these limitations, one of the major implications of these models is the need to store angular momentum in the stellar core for up to an age of about 1 Gyr. The build-up of a wide dispersion of rotational velocities at ZAMS and its subsequent evolution on the early MS partly reflect this process.

I thank the SF2A organisational committee for this very nice and fruitful week in Montpelier.

References

Affer, L., Micela, G., Favata, F., & Flaccomio, E. 2012, mnras, 424, 11
Affer, L., Micela, G., Favata, F., Flaccomio, E., & Bouvier, J. 2013, ArXiv e-prints
Agüeros, M. A., Covey, K. R., Lemonias, J. J., et al. 2011, apj, 740, 110
Allain, S. 1998, aap, 333, 629
Baraffe, I., Chabrier, G., Allard, F., & Hauschildt, P. H. 1998, aap, 337, 403
Bouvier, J. 2008, aap, 489, L53
Bouvier, J., Forestini, M., & Allain, S. 1997, aap, 326, 1023
Cranmer, S. R. & Saar, S. H. 2011, apj, 741, 54
Denissenkov, P. A., Pinsonneault, M., Terndrup, D. M., & Newsham, G. 2010, apj, 716, 1269
Epstein, C. R. & Pinsonneault, M. H. 2012, ArXiv e-prints
Gallet, F. & Bouvier, J. 2013, aap, 556, A36
Hartman, J. D., Bakos, G. Á., Kovács, G., & Noyes, R. W. 2010, mnras, 408, 475
Irwin, J., Berta, Z. K., Burke, C. J., et al. 2011, apj, 727, 56
Irwin, J. & Bouvier, J. 2009, in IAU Symposium, Vol. 258, IAU Symposium, ed. E. E. Mamajek, D. R. Soderblom, & R. F. G. Wyse, 363–374
Irwin, J., Hodgkin, S., Aigrain, S., et al. 2007, mnras, 377, 741
MacGregor, K. B. & Brenner, M. 1991, apj, 376, 204
Matt, S. & Pudritz, R. E. 2005, apjl, 632, L135
Matt, S. & Pudritz, R. E. 2007, in IAU Symposium, Vol. 243, IAU Symposium, ed. J. Bouvier & I. Appenzeller, 299–306
Matt, S. & Pudritz, R. E. 2008a, apj, 678, 1109
Matt, S. & Pudritz, R. E. 2008b, apj, 681, 391
Matt, S. P., MacGregor, K. B., Pinsonneault, M. H., & Greene, T. P. 2012, apjl, 754, L26
Meibom, S., Barnes, S. A., Latham, D. W., et al. 2011, apjl, 733, L9
Reiners, A., Basri, G., & Browning, M. 2009, apj, 692, 538
Reiners, A. & Mohanty, S. 2012, apj, 746, 43
Schatzman, E. 1962, Annales d'Astrophysique, 25, 18
Skumanich, A. 1972, apj, 171, 565
Spada, F., Lanzafame, A. C., Lanza, A. F., Messina, S., & Collier Cameron, A. 2011, mnras, 416, 447
Thompson, M. J., Christensen-Dalsgaard, J., Miesch, M. S., & Toomre, J. 2003, ARA&A, 41, 599
Weber, E. J. & Davis, Jr., L. 1967, apj, 148, 217
Zanni, C. & Ferreira, J. 2011, apjl, 727, L22+
Zanni, C. & Ferreira, J. 2013, aap, 550, A99

SF2A 2013
L. Cambrésy, F. Martins, E. Nuss and A. Palacios (eds)

SPECTROSCOPIC AND ASTEROSEISMIC DIAGNOSTICS ON MIXING PROCESSES INSIDE RED GIANT STARS

N. Lagarde[1, 2]

Abstract. The availability of asteroseismic constraints for a large sample of stars from CoRoT and *Kepler* paves the way for various statistical studies of the seismic properties of stellar populations, and becomes a powerful tool to better understand stellar structure and evolution. I will present predictions of stellar models computed with the code STAREVOL including thermohaline mixing together with rotational mixing. I will briefly present a comparison between our theoretical predictions and spectroscopic observations, and discuss why asteroseismic diagnostics are relevant in this context.

Keywords: Stars: evolution, stars: interiror, stars: rotation, instabilities, hydrodynamics

1 Introduction

The standard theory of stellar evolution predicts that during the first dredge-up (Iben 1967) the chemical composition of the stellar surface is modified when the deepening convective envelope mixes the external layers with hydrogen-processed material. Dilution then changes the surface abundances of helium-3, beryllium, boron, carbon, nitrogen, and in some cases sodium (e.g. Charbonnel 1994). Standard models predicts no variation of chemical composition at the surface of red giants between the first dredge-up and the RGB tip. However, numerous spectroscopic observations (e.g. Smiljanic et al. 2009; Tautvaišienė et al. 2013) show a clear signatures of "extra mixing" on the upper red giant branch (RGB) in low-mass stars, which modifies the surface composition. On the other hand, asteroseismology has emerged during the last decade as a powerful tool to investigate the internal structure of stars, and more particularly of red giant stars (Chaplin & Miglio 2013).

2 STAREVOL : Stellar evolution code

2.1 Physical inputs

The models are computed with the lagrangian implicit stellar evolution code STAREVOL (v3.00, see Siess et al. 2000; Palacios et al. 2003, 2006; Decressin et al. 2009; Lagarde et al. 2012). In the lagrangain description, the equations of stellar internal structure are written with two independent variables, a temporal one t, and a spatial one m_r which represents the mass of a fluid element. With this description we can write equations to describe the stellar structure as follow :

- Mass conservation:

$$\frac{dr}{dm_r} = \frac{1}{4\pi r^2 \rho} \tag{2.1}$$

- Energy conservation:

$$\frac{\partial L_r}{\partial m_r} = \epsilon_{nuc} - \epsilon_\nu + \epsilon_{grav} \tag{2.2}$$

where ϵ_{nuc}, ϵ_ν, and ϵ_{grav} are the energies produced by the nuclear reactions, lost by neutrinos, and due to gravitational heating, respectively.

[1] School of Physics and Astronomy, University of Birmingham, Edgbaston, Birmingham, B15 2TT, UK
[2] Stellar Astrophysics Centre (SAC), Department of Physics and Astronomy, Aarhus University, Ny Munkegade 120, DK-8000, Aarhus C, Denmark

- Conservation of motion

$$\frac{\partial u}{\partial t} = -\left(4\pi r^2 \frac{\partial P}{\partial m_r} + \frac{G m_r}{r^2}\right), \tag{2.3}$$

where P is the pressure given by the equation of state, and $u = \frac{\partial r}{\partial t}$.

- Heat transport

$$\frac{dT}{dm_r} = \frac{1}{\pi r^2}\left(g + \frac{du}{dt}\right)\frac{T}{P}\nabla, \tag{2.4}$$

where $\nabla = \frac{\partial ln T}{\partial ln P}$ corresponds to $\nabla_{\rm rad} = \frac{3}{16\pi acG}\frac{\kappa L_r P}{m_r T^4}$ and to $\nabla_{\rm conv}$ in radiative and convective zones respectively.

- Chemical species transport:

$$\left(\frac{dY_i}{dt}\right) = \left(\frac{\partial Y_i}{\partial t}\right)_{nuc} + \frac{\partial}{\partial m_r}\left[(4\pi r^2\rho)^2 \mathcal{D}\frac{\partial Y_i}{\partial m_r}\right] \tag{2.5}$$

where T is the temperature, ρ the density, L_r the luminosity, r the radius of the fluid, Y_i represents the abundance of species i, and $\mathcal{D}$ the diffusion coefficient.

The physical ingredients used to solve this system of equations, such as nuclear reaction rates, opacities, equation of state, the treatment of convection and atmosphere, are presented in details in Lagarde et al. (2012).

2.2 Transport processes in radiative zones

To follow the effects of transport processes on the evolution of chemical species, we have to introduce the corresponding diffusion coefficient $\mathcal{D}$ in equation 2.5. In STAREVOL, different transport processes of chemical species can be considered: e.g. overshooting, semi-convection, atomic diffusion, transport by gravity waves (see Decressin et al. in this volume), thermohaline instability, and rotation-induced mixing ; as well as the transport of angular momentum (Palacios et al. 2006).

2.2.1 Rotation-induced mixing

For the treatment of rotation-induced mixing, we use the complete formalism developed by Zahn (1992) and Maeder & Zahn (1998), that takes into account advection by meridional circulation and diffusion by the shear turbulence (for a decryption of the implementation in STAREVOL, see Palacios et al. (2003, 2006); Decressin et al. (2009)). The transport of chemicals resulting from meridional circulation and both horizontal and vertical turbulence is computed as a diffusive process throughout evolution.

2.2.2 Thermohaline mixing

When the density of a fluid depends on variation of two components, a stably stratified system can undergo instability leading to significant vertical transport corresponding to thermohaline instability. It is a mixing process that corresponds to a double diffusive instability. Indeed, this instability evolves with two components, one of which is the stabilizing one (temperature), that diffuses faster than the other, whose stratification is unstable.

Thermohaline mixing develops along the red giant branch at the bump luminosity in low-mass stars and on the early-AGB in intermediate-mass stars, when the gradient of molecular weight becomes negative ($\nabla_\mu = \frac{d\ln\mu}{d\ln P} < 0$) in the external wing of the thin hydrogen-burning shell surrounding the degenerate stellar core (Charbonnel & Zahn 2007b,a; Siess 2009; Stancliffe et al. 2009; Charbonnel & Lagarde 2010). This inversion of molecular weight is created by the ^{3}He(^{3}He, 2p)^{4}He reaction (Ulrich 1971; Eggleton et al. 2006, 2008).

We use the prescription advocated by Charbonnel & Zahn (2007a); Charbonnel & Lagarde (2010). It is based on Ulrich (1972) with an aspect ratio (length/width) of instability fingers α =5, in agreement with laboratory experiments (Krishnamurti 2003). It includes the correction for non-perfect gas (Kippenhahn et al. 1980) in the diffusion coefficient for thermohaline mixing that is given by:

$$\mathcal{D}_{th} = \mathcal{C}_T K_T \frac{\varphi}{\delta} \frac{-\nabla_\mu}{\nabla_{ad} - \nabla} \tag{2.6}$$

where K is the thermal diffusivity; $\varphi = (\partial ln\rho/\partial ln\mu)_{P,T}$; $\delta = -(\partial ln\rho/\partial ln\mu)_{P,\mu}$; and with the non-dimentional coefficient $\mathcal{C}_t = \frac{8\pi^2}{3}\alpha^2$.

The value of α in actual stellar conditions was recently questionned by the results of two- and three-dimentional hydrodynamical simulations of thermohaline convection for which α is close to unity (Denissenkov 2010; Denissenkov & Merryfield 2011; Rosenblum et al. 2011; Traxler et al. 2011). However, these simulations are still far from the stellar regime, hence we decided to use in the following discussion the prescription described above since it successfully reproduces the abundances data for evolved stars of various masses and metallicities (see Charbonnel & Lagarde 2010; Lagarde et al. 2011, for a more detailed discussion).

3 Theoretical predictions

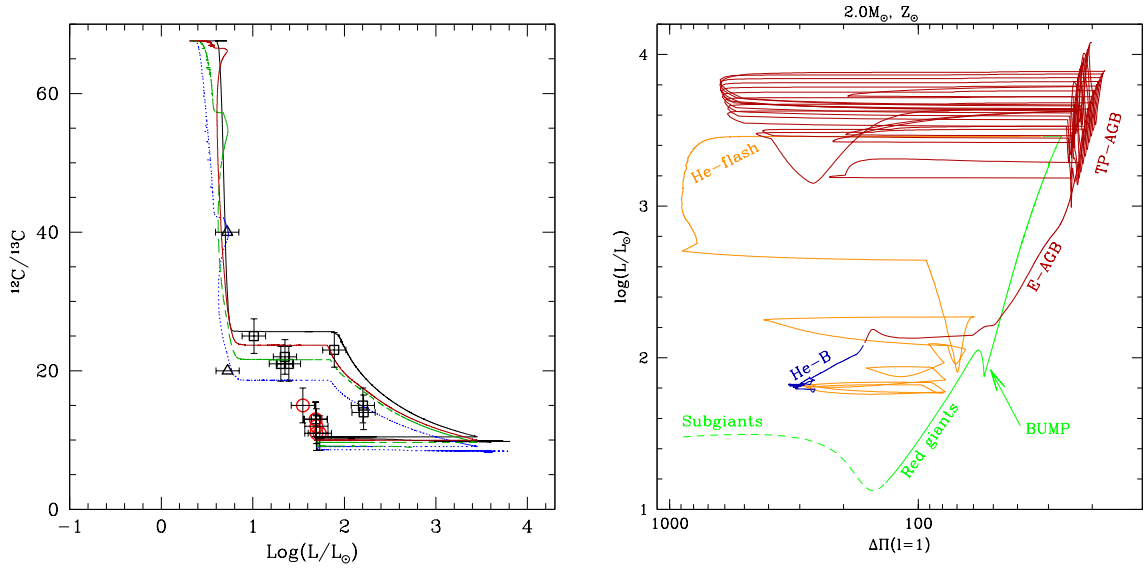

Fig. 1. *left panel: figure from Charbonnel & Lagarde (2010).* Evolution of $^{12}C/^{13}C$ value as a function of stellar luminosity for the 1.25 $M_\odot$ models including thermohaline instability and rotation-induced mixing (for initial rotation velocities of 50, 80, and 110 km.s^{-1} shown as solid red, dashed green, and dotted blue lines respectively). The black solid line represents the non rotating case. Spectroscopic observations along the evolutionary sequence of the open cluster M67 (Gilroy & Brown 1991) are represented by black triangles which only a lower value could be obtained, black squares, and red circles, for sub giants, RGB and clump stars respectively. *Right panel: figure from Lagarde et al. (2012).*The stellar luminosity as a function of the asymptotic period spacing of g-modes for the standard 2.0 $M_\odot$ model at solar metallicity. Evolutionary phases are color-labeled: sub giant (green dashed), helium-flash episodee (orange), helium-burning (blue), and asymptotic giant branch (red).

3.1 Spectroscopic properties

Rotation-induced mixing has an impact on the internal abundance profiles during the main sequence, although its signature are revealed only later in the evolution when the first dredge-up occurs on the sub giant branch (e.g. Palacios et al. 2003; Smiljanic et al. 2010; Charbonnel & Lagarde 2010). Indeed, when rotation-induced mixing is accounted for, the post-dredge-up value$^{12}C/^{13}C$ ratio, for example, is lower than in non-rotating case (see left panel of Fig. 1). Figure 1 displays observations of $^{12}C/^{13}C$ ratio in stars of open cluster M67 (M_{TO} =1.2$M_\odot$) from Gilroy & Brown (1991), compared with theoretical prediction of our 1.25$M_\odot$ models computed with three different initial velocities, and including thermohaline mixing. The dispersion for stars that have not yet reached the bump luminosity (log $(L/L_\odot)_{bump}$ ∼2.2) reflects only the dispersion in initial rotation velocity.

On the other hand, thermohaline instability occurs at the bump luminosity by inversion of gradient molecular weight. Contrary to standard predictions, models including thermohaline mixing leads to decrease the carbon isotopic ratio (see Fig 1) at the BUMP luminosity, and then reproduce very well the low value of $^{12}C/^{13}C$ in evolved stars (i.e., red giants brighter than the BUMP luminosity, and clump stars).

3.2 Asteroseismic diagnostics

Asteroseismic observations with CoRoT and *Kepler* pave the way for various statistical studies of seismic properties of stellar populations. In Lagarde et al. (2012), we have evaluated the impact of thermohaline mixing and rotation-induced mixing using our new stellar evolution models, on global asteroseismic quantities as large separation, acoustic radii, and period spacing of g-modes. We showed a net signature of rotation-induced mixing on the global asteroseismic parameters. Thermohaline instability cannot be characterized by these asteroseismic parameters, although it can be identified by its effects on spectroscopic studies. The right panel of Fig. 1 presents the asymptotic period spacing of gravity modes $\Delta\Pi(l = 1)$ for standard model of 2.0 $M_{\odot}$ at solar metallicity. This quantity allows us to distinguish two stars that have the same luminosity, one being at the RGB bump and the other one being at the clump undergooing He burning (e.g. Bedding et al. 2011). $\Delta\Pi(l = 1)$ is larger in clump stars compared to in RGB stars, because of the differences in the stellar structure, and the presence of convective core affecting the domain where the g-modes are trapped (Montalbán et al. 2013). Asteroseismic parameters help us to establish the evolutionary stages, as well as its radius, and mass (e.g. Kallinger et al. 2010). The large number of evolved stars observed by CoRoT and *Kepler* will allow us to run detailed comparisons between models predictions and observations, which were so far limited to giants in clusters.

Moreover, thanks to asteroseismology, we can now determine the internal rotation profile of giant stars (Deheuvels et al. 2012; Beck et al. 2012; Mosser et al. 2012), and then in the future better test models of transport of angular momentum (Eggenberger et al. 2012; Ceillier et al. 2013).

Asteroseismic studies represent a very useful tool to understand structure and evolution of giant stars, and to better constrain the physics of different transport processes as rotation-induced mixing. Moreover, these observations sampling in different regions of the Galaxy, promises to improve our understanding on the Milky Way's constituents. To exploit all potential of asteroseismic data from CoRoT and *Kepler* missions, it would be crucial to combine them with spectroscopic constraints (APOGEE and GAIA surveys).

I acknowledge financial support from the Swiss National Fund, and funding for the Stellar Astrophysics Centre which is provided by The Danish National Research Foundation (Grant agreement no.: DNRF106).

References

Beck, P. G., Montalban, J., Kallinger, T., et al. 2012, Nature, 481, 55
Bedding, T. R., Mosser, B., Huber, D., et al. 2011, Nature, 471, 608
Ceillier, T., Eggenberger, P., García, R. A., & Mathis, S. 2013, A&A, 555, A54
Chaplin, W. J. & Miglio, A. 2013, ARA&A, 51, 353
Charbonnel, C. 1994, A&A, 282, 811
Charbonnel, C. & Lagarde, N. 2010, A&A, 522, A10+
Charbonnel, C. & Zahn, J. 2007a, A&A, 476, L29
Charbonnel, C. & Zahn, J.-P. 2007b, A&A, 467, L15
Decressin, T., Mathis, S., Palacios, A., et al. 2009, A&A, 495, 271
Deheuvels, S., García, R. A., Chaplin, W. J., et al. 2012, The Astrophysical Journal, 756, 19
Denissenkov, P. A. 2010, ApJ, 723, 563
Denissenkov, P. A. & Merryfield, W. J. 2011, ApJ, 727, L8+
Eggenberger, P., Montalbán, J., & Miglio, A. 2012, A&A, 544, L4
Eggleton, P. P., Dearborn, D. S. P., & Lattanzio, J. C. 2006, Science, 314, 1580
Eggleton, P. P., Dearborn, D. S. P., & Lattanzio, J. C. 2008, ApJ, 677, 581
Gilroy, K. K. & Brown, J. A. 1991, ApJ, 371, 578
Iben, Jr., I. 1967, ApJ, 147, 624
Kallinger, T., Weiss, W. W., Barban, C., et al. 2010, A&A, 509, A77

Kippenhahn, R., Ruschenplatt, G., & Thomas, H.-C. 1980, A&A, 91, 175
Krishnamurti, R. 2003, Journal of Fluid Mechanics, 483, 287
Lagarde, N., Charbonnel, C., Decressin, T., & Hagelberg, J. 2011, A&A, 536, A28
Lagarde, N., Decressin, T., Charbonnel, C., et al. 2012, ArXiv e-prints
Maeder, A. & Zahn, J.-P. 1998, A&A, 334, 1000
Montalbán, J., Miglio, A., Noels, A., et al. 2013, ApJ, 766, 118
Mosser, B., Goupil, M. J., Belkacem, K., et al. 2012, A&A, 548, A10
Palacios, A., Charbonnel, C., Talon, S., & Siess, L. 2006, A&A, 453, 261
Palacios, A., Talon, S., Charbonnel, C., & Forestini, M. 2003, A&A, 399, 603
Rosenblum, E., Garaud, P., Traxler, A., & Stellmach, S. 2011, ApJ, 731, 66
Siess, L. 2009, A&A, 497, 463
Siess, L., Dufour, E., & Forestini, M. 2000, A&A, 358, 593
Smiljanic, R., Gauderon, R., North, P., et al. 2009, A&A, 502, 267
Smiljanic, R., Pasquini, L., Charbonnel, C., & Lagarde, N. 2010, A&A, 510, A50+
Stancliffe, R. J., Church, R. P., Angelou, G. C., & Lattanzio, J. C. 2009, MNRAS, 396, 2313
Tautvaišienė, G., Barisevičius, G., Chorniy, Y., Ilyin, I., & Puzeras, E. 2013, MNRAS, 430, 621
Traxler, A., Garaud, P., & Stellmach, S. 2011, ApJ, 728, L29+
Ulrich, R. K. 1971, ApJ, 168, 57
Ulrich, R. K. 1972, ApJ, 172, 165
Zahn, J.-P. 1992, A&A, 265, 115

SF2A 2013
L. Cambrésy, F. Martins, E. Nuss and A. Palacios (eds)

LOCAL DIRECT NUMERICAL SIMULATIONS OF TURBULENT MIXING IN STELLAR RADIATIVE ZONES

V. Prat [1, 2] and F. Lignières [1, 2]

Abstract. A major issue of stellar evolution theory is the influence of the transport processes related to rotationally driven macroscopic motions on the internal structure and the evolution of stars. Turbulent mixing of chemical elements due to differential rotation in stellar radiative zones is currently taken into account in many stellar evolution codes through transport coefficients firstly derived by Zahn (1992, A&A, 265, 115). Our aim is to constrain one of these coefficients, the radial diffusion coefficient driven by radial differential rotation through local direct numerical simulations of steady homogeneous stably stratified sheared turbulence, and to compare the results with phenomenological models. In particular, we have determined the dependence of the turbulent diffusion coefficient on thermal diffusivity and chemical stratification.

Keywords: DNS, mixing, stellar interiors, turbulence

1 Introduction

The effects of macroscopic, rotationally induced motions on stellar evolution are still poorly understood. There are large-scale axisymmetric motions, such as differential rotation and meridional circulation, which can be either directly computed in 2D stellar evolution codes or modelled in 1D codes (e.g. the shellular model of Zahn 1992), but there are also small-scale turbulent motions generated by various instabilities. As fundamentally 3D motions, the latter need to be modelled in both 1D and 2D stellar evolution codes. In many current stellar evolution codes, transport of chemical elements is taken into account through a set of diffusion coefficients initially proposed by Zahn (1992).

One of these coefficient, the radial transport coefficient due to shear instability forced by radial differential rotation, is likely to be dominant in radiative zones of stars and is given in Zahn's model by

$$D_{\rm t} = \frac{\kappa}{3}\frac{Ri_{\rm c}}{N^2}\left(r\sin\theta\frac{{\rm d}\Omega}{{\rm d}r}\right) = \frac{\kappa}{3}\frac{Ri_{\rm c}}{Ri}, \tag{1.1}$$

where κ denotes thermal diffusivity; $Ri = (N/S)^2$ the Richardson number, comparing stratification (with the Brunt-Väisälä frequency N) and shear (with the shear rate $S = r\sin\theta{\rm d}\Omega/{\rm d}r$); $Ri_{\rm c}$ the critical value of the latter; r, θ the spherical coordinates and Ω the angular velocity of the star. The derivation of this coefficient is based on four arguments: (i) turbulent flows tend to reach a steady state which is marginally stable; (ii) for high thermal diffusivities, the stability of shear flows is determined by $RiPe$ where $Pe = SL^2/\kappa$ is the Péclet number based on the length scale L of the shear; (iii) the relevant Péclet number in a turbulent state is $Pe_\ell = u\ell/\kappa$, based on turbulent velocity and length scales u and ℓ; (iv) the diffusion coefficient is given by $D_{\rm t} \simeq u\ell/3$.

Models of turbulent transport are currently constrained mainly by measurements of surface chemical abundances from absorption lines (Meynet & Maeder 2000). Recently, internal rotation profiles obtained by asteroseismology allow us to put additional constraints on transport processes (Deheuvels et al. 2012). Here we use local direct numerical simulations of steady homogeneous stably stratified sheared turbulence as numerical experiments to test existing prescriptions.

The framework used to solve our problem is presented in Sect. 2. In Sect. 3 we explore the dependence of the diffusion coefficient on thermal diffusion and in Sect. 4 we study the dynamical effect of chemical stratification on the diffusion coefficient. Finally, we conclude on our results and give some prospects in Sect. 5.

[1] Université de Toulouse; UPS-OMP; IRAP; Toulouse, France
[2] CNRS; IRAP; 14, avenue Édouard Belin, F-31400 Toulouse, France

2 Framework

We study a flow configuration with a uniform vertical shear and vertical uniform temperature and concentration gradients thanks to the versatile (magneto-)hydrodynamical code *Balaïtous*, able to solve either incompressible, Boussinesq or fully compressible equations to study various problems such as convection, dynamo or double diffusion. Its main characteristics are cartesian coordinates, a Fourier collocation method in the horizontal directions, compact finite differences in the vertical one, and a 4th-order Runge-Kutta method in time. We solve the non-dimensional form of the Boussinesq equations with the dynamical effect of chemical stratification:

$$\vec{\nabla}\cdot\vec{v} = 0, \tag{2.1}$$

$$\frac{\partial\vec{v}}{\partial t}+(\vec{v}\cdot\vec{\nabla})\vec{v} = -\vec{\nabla}p+(Ri\theta+Ri_\mu c')\vec{e}_z+\frac{1}{Re}\Delta\vec{v}, \tag{2.2}$$

$$\frac{\partial\theta}{\partial t}+\vec{v}\cdot\vec{\nabla}\theta+v_z = \frac{1}{Pe}\Delta\theta, \tag{2.3}$$

$$\frac{\partial c'}{\partial t}+\vec{v}\cdot\vec{\nabla}c'+v_z = \frac{1}{Pe_\mathrm{c}}\Delta c', \tag{2.4}$$

where $\vec{v}$ and p are the velocity and the pressure, θ and c' the temperature and concentration fluctuations around the linear mean profiles, Ri_μ the chemical equivalent of the Richardson number, $Re=UL/\nu$ the Reynolds number and $Pe_\mathrm{c}=UL/D_\mathrm{m}$ the chemical Péclet number characterising respectively the viscosity ν and the molecular diffusivity D_m. The small-Péclet-number approximation (SPNA) is an asymptotic development of the Boussinesq equations for very high thermal diffusivities (Lignières 1999), which allow us, with $\psi=\theta/Pe$, to replace Eqs. (2.2) and (2.3) by

$$\frac{\partial\vec{v}}{\partial t}+(\vec{v}\cdot\vec{\nabla})\vec{v} = -\vec{\nabla}p+(RiPe\psi+Ri_\mu c')\vec{e}_z+\frac{1}{Re}\Delta\vec{v}, \tag{2.5}$$

$$v_z = \Delta\psi. \tag{2.6}$$

The first of Zahn's hypotheses is verified by tuning Ri (respectively $RiPe$ in SPNA simulations) so that we reach a statistical steady state. Then, we determine the turbulent diffusion coefficient thanks to the relation

$$D_\mathrm{t}=-\frac{\langle v_z c'\rangle}{\mathrm{d}C/\mathrm{d}z}, \tag{2.7}$$

where $\langle\rangle$ denotes the spatial average and $C(z)$ the mean concentration profile.

3 Thermal diffusion

We are interested here in the case $Ri_\mu=0$. As described in Prat & Lignières (2013), we have performed a series of Boussinesq simulations at decreasing Péclet numbers down to 0.34 and one simulation in the SPNA, which show that the quantity $D/(\kappa Ri^{-1})$ tends to a constant value as Pe_ℓ decreases, as illustrated in Fig. 1. Thus, D_t is proportional to κRi^{-1}, which is in agreement with Zahn's model (1.1). In addition, we are able to give a quantitative estimate of the proportionality constant, around 5.58×10^{-2} *vs.* 8.33×10^{-2} in Zahn (1992), and of the critical value $Ri_\mathrm{c}=0.427$, what is quite different from the classical value 1/4.

Figure 1 also clearly shows that Zahn's model is not valid out of the domain of small Péclet numbers. We performed other simulations with increasing Péclet numbers up to $Pe_\ell=437$ and found that in this regime, our results are incompatible with the model proposed by Maeder (1995) but in good agreement with that of Lindborg & Brethouwer (2008), proposed in the geophysical literature, where the diffusion coefficient reads

$$D_\mathrm{t}=\frac{\varepsilon_\mathrm{P}}{N^2}, \tag{3.1}$$

ε_P denoting the specific dissipation rate of turbulent potential energy. Figure 2 represents the ratios between each model (Zahn's, Lindborg's and the sum) and the diffusion coefficient estimated in our simulations. We see that the sum of both models is close to the estimated coefficient for the whole range of Péclet numbers.

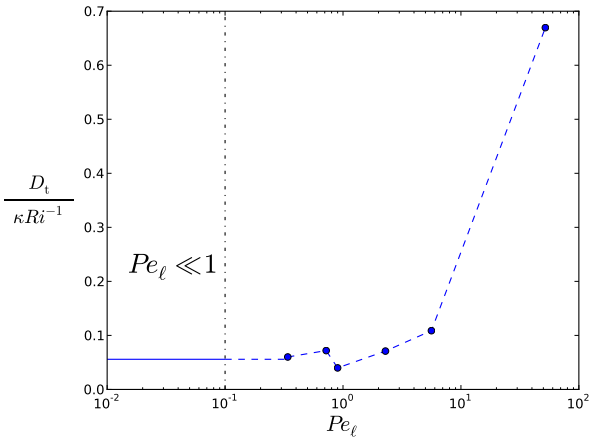

Fig. 1. $D_t/(\kappa Ri^{-1})$ as a function of Pe_ℓ. Dots correspond to Boussinesq simulations, the solid line to the SPNA one.

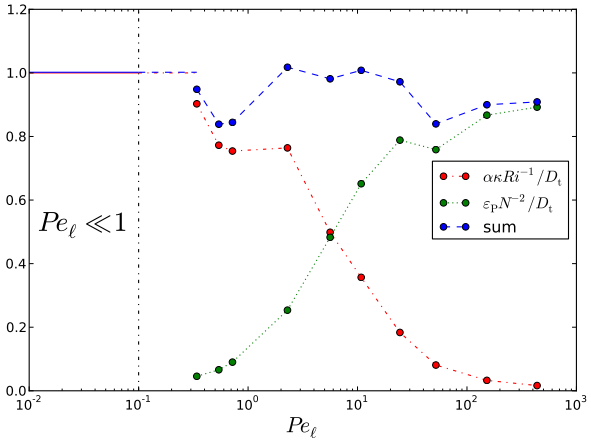

Fig. 2. Ratios between models and effective diffusion coefficient as a function of the turbulent Péclet number

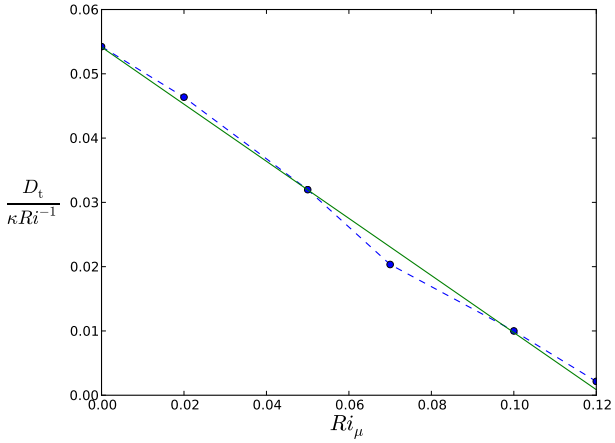

Fig. 3. $D_t/(\kappa Ri^{-1})$ as a function of Ri_μ. Dots correspond to simulations and the solid line to the linear regression.

4 Chemical stratification

We performed simulations in the SPNA with different values of the chemical Richardson number Ri_μ and estimated for each one the value of the turbulent diffusion coefficient. As shown in Fig. 3, the quantity $D_\mathrm{t}/(\kappa Ri^{-1})$ is well represented by an affine function of Ri_μ. We can thus write

$$\frac{D_\mathrm{t}}{\kappa Ri^{-1}} = \beta(Ri_\mathrm{c} - Ri_\mu), \tag{4.1}$$

with $\beta = 0.45$ and $Ri_\mathrm{c} = 0.12$. Then, it yields

$$D_\mathrm{t} = \beta\kappa\frac{Ri_\mathrm{c} - Ri_\mu}{Ri}. \tag{4.2}$$

Equation (4.2) has been derived by Maeder & Meynet (1996) in the domain of small Péclet numbers using the hypothesis that the stabilising effect of chemical stratification is not affected by thermal diffusion and can thus completely inhibit the transport. This is not the case of all other models used in stellar evolution theory.

The model of Maeder (1997), for example, is based on the hypothesis that thermal diffusion affects equally thermal and chemical stratifications. As we can see in Eq. (2.5), this is incompatible with the SPNA, where κ and Ri can be very large while Ri_μ remains finite. In this limit, the diffusion coefficient of Maeder (1997),

$$D_\mathrm{t} = \beta\kappa\frac{Ri_\mathrm{c}}{Ri + Ri_\mu}, \tag{4.3}$$

reduces to a form similar to Eq. (1.1), which does not depend on Ri_μ. This is clearly not what we observe in Fig. 3. This model is thus incompatible with our numerical simulations in the domain of small Péclet numbers.

The case of Talon & Zahn (1997) is more complex, as they assume that a very efficient horizontal diffusion is able to reduce the stabilising effect of chemical stratification. In our simulations, horizontal diffusion is not much larger as the vertical one, so we cannot conclude on the validity of this model.

5 Conclusion

This work demonstrates the potential of numerical simulations applied to the physics of stellar interiors. Indeed, in the domain of small Péclet numbers, we have validated Zahn's model in steady homogeneous stably stratified sheared simulations. In addition, we are able to give a quantitative estimate of the turbulent diffusion coefficient. In the domain of large Péclet numbers, we have shown that the diffusion coefficient is given by the model of Lindborg & Brethouwer (2008), which is incompatible with the model of Maeder (1995). As for the dynamical effect of chemical stratification, our simulations have allowed us to choose between two existing models, Maeder & Meynet (1996) and Maeder (1997). A recent study by Meynet et al. (2013) compares the predictions of a stellar evolution code using various prescriptions for radial mixing and shows that the latter model has the best fit with the observations, thus suggesting that a significant additional source of mixing may exist.

To go further, compare to other models and possibly propose new prescriptions, several features need to be implemented, such as the effect of horizontal diffusion induced by horizontal differential rotation. Another idea is to study the influence of a magnetic field on shear instability, as initiated by Lecoanet et al. (2010).

References

Deheuvels, S., García, R. A., Chaplin, W. J., et al. 2012, ApJ, 756, 19
Lecoanet, D., Zweibel, E. G., Townsend, R. H. D., et al. 2010, ApJ, 712, 1116
Lignières, F. 1999, A&A, 348, 933
Lindborg, E. & Brethouwer, G. 2008, J. Fluid Mech., 614, 303
Maeder, A. 1995, A&A, 299, 84
Maeder, A. 1997, A&A, 321, 134
Maeder, A. & Meynet, G. 1996, A&A, 313, 140
Meynet, G., Ekstrom, S., Maeder, A., et al. 2013, in Lecture Notes in Physics, Vol. 865, 3
Meynet, G. & Maeder, A. 2000, A&A, 361, 101
Prat, V. & Lignières, F. 2013, A&A, 551, L3
Talon, S. & Zahn, J.-P. 1997, A&A, 317, 749
Zahn, J.-P. 1992, A&A, 265, 115

SF2A 2013
L. Cambrésy, F. Martins, E. Nuss and A. Palacios (eds)

PRESENT STATUS OF TWO-DIMENSIONAL ESTER MODELS: APPLICATION TO BE STARS

M. Rieutord[1, 2] and F. Espinosa Lara[1,2]

Abstract. ESTER two-dimensional models solve the steady state structure of fast rotating early-type stars including the large scale flows associated with the baroclinicity of the radiative zones. Models are compared successfully to the fundamental parameters of the two main components of the triple system δ Velorum that have been derived from interferometric and orbit measurements. Testing the models on the Be star Achernar (α Eri), we cannot reproduce the data and conclude that this star has left the main sequence and is likely crossing the Herzsprung gap. Computing main sequence evolution of fast rotating stars at constant angular momentum shows that their criticality increases with time suggesting that the Be phenomenon and the ensuing mass ejections is the result of evolution.

Keywords: Stellar models, Rotation, Be stars

1 Introduction

One of the grand challenges of stellar modelling is the design of realistic models for fast rotating stars. Many observational data either from interferometry, from asteroseismology, from spectroscopy (chemical abundances) require models that are not limited to small rotation rates. These models are necessarily two-dimensional because these stars are no longer spherically symmetric and also because they are pervaded by large-scale fluid flows (differential rotation and meridional circulation) that are key elements to understand their chemical and dynamical evolution.

Here, we wish to give a brief presentation of the first results of the ESTER project, its promises as far as interpretation of data are concerned and its future developments.

2 The physical content of ESTER models

Present ESTER models are describing the internal structure of an isolated fast rotating star in a steady state. No time evolution is included and only early-type stars (mass larger than 1.7 $M_\odot$) can be computed. The modeling of an outer convection zone is still a problem that needs to be solved. The central convective core is assumed to be isentropic. With these prerequisites ESTER models solve the four following partial differential equations:

$$\begin{cases} \Delta\phi = 4\pi G\rho \\ \rho T\vec{v}\cdot\vec{\nabla}S = -Div\vec{F} + \varepsilon_* \\ \rho(2\vec{\Omega}_*\wedge\vec{v} + \vec{v}\cdot\vec{\nabla}\vec{v}) = -\vec{\nabla}P - \rho\vec{\nabla}(\phi - \frac{1}{2}\Omega_*^2 s^2) + \vec{F}_v \\ Div(\rho\vec{v}) = 0. \end{cases} \tag{2.1}$$

where we recognize the Poisson, entropy, momentum and continuity equations respectively. They are completed by the microphysics from OPAL and NACRE (opacities, equation of state and reaction rates). Boundary conditions are stress-free for the velocity field and match black body radiation for temperature (see Rieutord & Espinosa Lara 2013; Espinosa Lara & Rieutord 2013, for details).

The equations are solved using the discretization of spectral elements in the radial direction with Chebyshev polynomial (fluid layers are of spheroidal shape). The horizontal coordinate uses the decomposition in spherical harmonics. Various tests measure the quality of the numerical solution. The ESTER code is under GNU public license and can be downloaded at `http://code.google.com/p/ester-project` .

[1] Université de Toulouse; UPS-OMP; IRAP; Toulouse, France
[2] CNRS; IRAP; 14, avenue Edouard Belin, F-31400 Toulouse, France

Table 1. Comparison between observationally derived parameters of the stars and tentative two-dimensional models. Data from δ Vel are from Mérand et al. (2011), those of Achernar are from Domiciano de Souza et al. (2012). The models compare nicely with observationally constrained data for the two components of δ Vel A (an eclipsing binary) but have difficulties with Achernar. Here ε is the flatness, ω_k the ratio of the equatorial angular velocity to the keplerian one, j is the mean specific angular momentum of the star and $X_{env.}$ is the hydrogen mass fraction in the envelope.

Star	Delta Velorum Aa		Delta Velorum Ab		Achernar (α Eri)	
	Observations	Model	Observations	Model	Observations	Model
Spectral type	A2 IV		A4 V		B4 Ve	
Mass ($M_\odot$)	2.43 ± 0.02	2.43	2.27±0.02	2.27		8.20
R_{eq} ($R_\odot$)	2.97±0.02	2.95	2.52±0.03	2.52	11.6±0.3	11.5
R_{pol} ($R_\odot$)	2.79±0.04	2.77	2.37±0.02	2.36	8.0±0.4	7.9
ε		0.061		0.064		0.310
ω_k		0.36		0.37		0.92
i	90°		90°		101°	
T_{eq} (K)	9450	9440	9560	9477	9955^{+1115}_{-2339}	11250
T_{pol}(K)	10100	10044	10120	10115	18013^{+141}_{-171}	16800
L ($L_\odot$)	67±3	65.2	51±2	48.5	4500±300	3700
V_{eq} (km/s)	143	143	150	153	298±9	339
j (10^{17} cm^2/s)		1.02		0.98		5.33
k [$j/R_{eq}^2\Omega_{eq}$]		0.0348		0.0363		0.0196
P_{eq} (days)		1.045		0.832		1.72
P_{pol} (days)		1.084		0.924		1.68
$X_{env.}$		0.70		0.70		0.74
$X_{core}/X_{env.}$		0.10		0.30		0.05
Z		0.011		0.011		0.04

3 Results

3.1 Modeling stars observed with optical or infra-red interferometers

In Tab. 1 we show a comparison between ESTER models and two main sequence stars Aa and Ab of δ Velorum. The two stars are members of a binary system but their wide separation makes the tides of weak influence. We first note that the model parameters nicely fit those derived from the interferometric (and orbit) data even if for such stars some surface convection should be expected (but it is not efficient enough to alter the radii). These two stars are coevolving. We note that the most massive has less hydrogen in its core as expected and that both require the same metallicity also as expected. We note that their mean specific angular momentum (angular momentum per unit mass) is quite the same putting interesting constraints on the dynamics of the formation of this system.

3.2 Achernar and Be stars

The case of the Be star Achernar (α Eri) is quite interesting. It has been much observed with infra-red interferometry at VLTI (e.g. Domiciano de Souza et al. 2012, and references therein) since it is the nearest Be star. As may be seen, ESTER models are not performing as well as for δ Velorum, especially on the mass determination. Indeed, it is known that Achernar is a binary star where the companion is an A-type star orbiting the actual Be star in 15 yrs (Kervella et al. 2008). Mass inferences of Achernar A is near 6.1 $M_\odot$(Domiciano de Souza, private communication) clearly below our value. This discrepancy may be of various origin: (i) it may well be that Achernar has left the main sequence and is crossing the Herzsprung gap, a configuration that is beyond reach of ESTER models at the moment, or (ii) presently observed values are perturbed somehow by circumstellar material including the companion. We give in Fig. 1 the expected view of this star according to the best estimate of the ESTER models.

ESTER models can also be used to mimic evolution of early-type stars by decreasing the hydrogen content of the convective core. For stars that do not lose angular momentum, we can examine the evolution of the

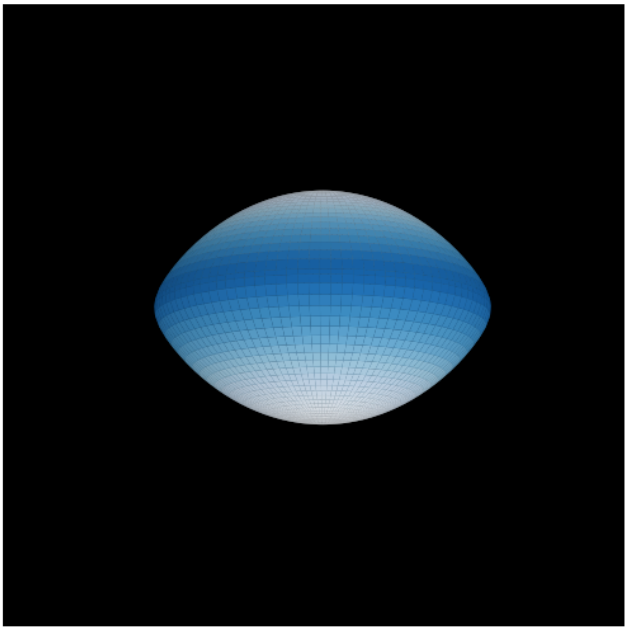

Fig. 1. A view of the surface brightness (the local flux) of Achernar with the model of Tab. 1 (values are derived from Domiciano de Souza et al. 2012).

ratio of angular velocity to critical angular velocity (which we call the Ω-criticality). According to Zorec & Royer (2012) and Alecian et al. (2013), A-type stars lose a negligible amount of angular momentum and this is probably the case for late B-type stars. In the case of zero-angular momentum loss, Fig. 2 shows the evolution of Ω-criticality when the star evolves along the main sequence. We consider a 7 $M_\odot$ model of solar metallicity that initially rotates at $V_{\rm eq}$ = 350 km/s ($R_{\rm eq}/R_{\rm pol}$ = 1.17). This result suggests that Be stars result from the evolution of initially fast rotating B stars. Mass-loss may complicate the view, but our models show that initially fast rotating B-stars will inevitably reach critical rotation if mass loss is weak enough.

4 Conclusions

Present ESTER models can describe rather faithfully rapidly rotating early-type main sequence stars. They therefore can be used to interpret interferometric and asteroseismic data. In this latter case, they need to be completed by a code that can deal with rotation non-perturbatively (presently two codes do this job: TOP of Reese et al. (2009) and ACOR of Ouazzani et al. (2012)).

In the future, developement of ESTER should include time evolution either from chemical evolution or from gravitational contraction so as to be able to describe early-type stars from the birthline to the giant state. In parallel, the other challenge is to include outer convection zone so as to be able to describe low-mass solar type stars.

The authors acknowledge the support of the French Agence Nationale de la Recherche (ANR), under grant ESTER (ANR-09-BLAN-0140). This work was also supported by the Centre National de la Recherche Scientifique (CNRS, UMR 5277), through the Programme National de Physique Stellaire (PNPS). The numerical calculations have been carried out on the CalMip machine of the 'Centre Interuniversitaire de Calcul de Toulouse' (CICT) which is gratefully acknowledged.

References

Alecian, E., Wade, G. A., Catala, C., et al. 2013, MNRAS, 429, 1027

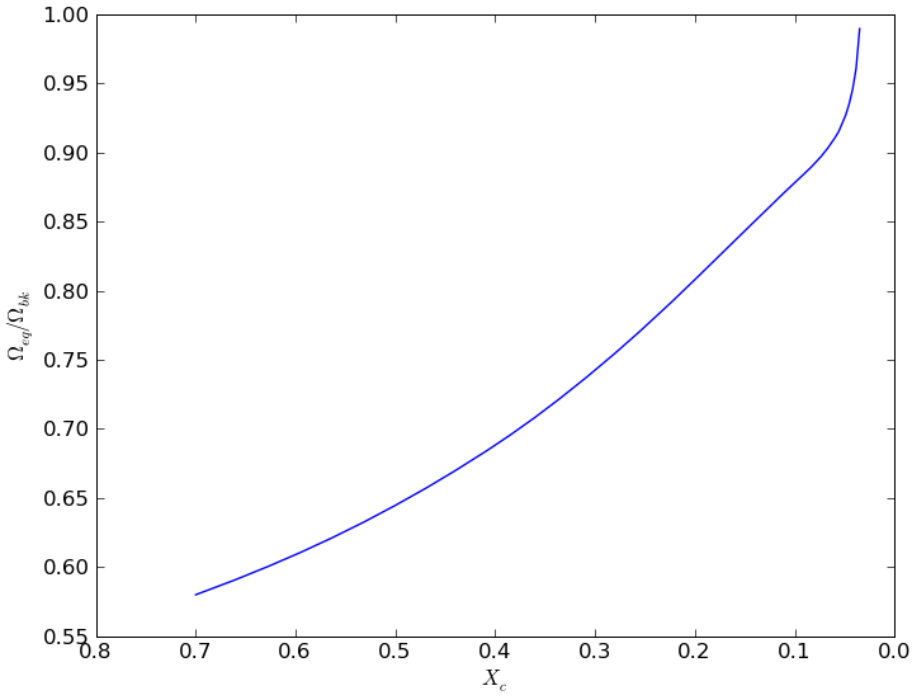

Fig. 2. Equatorial angular velocity divided by the keplerian angular velocity at equator as a function of the hydrogen mass fraction of the star for a constant total angular momentum. Metallicity is solar and M=7 $M_{\odot}$.

Domiciano de Souza, A., Hadjara, M., Vakili, F., et al. 2012, A&A, 545, A130

Espinosa Lara, F. & Rieutord, M. 2013, A&A, 552, A35

Kervella, P., Domiciano de Souza, A., & Bendjoya, P. 2008, A&A, 484, L13

Mérand, A., Kervella, P., Pribulla, T., et al. 2011, A&A, 532, A50

Ouazzani, R.-M., Dupret, M.-A., & Reese, D. R. 2012, A&A, 547, A75

Reese, D. R., MacGregor, K. B., Jackson, S., Skumanich, A., & Metcalfe, T. S. 2009, A&A, 506, 189

Rieutord, M. & Espinosa Lara, F. 2013, in Lecture Notes in Physics, Berlin Springer Verlag, Vol. 865, SeIsmology for studies of stellar Rotation and Convection, ed. M. Goupil, K. Belkacem, C. Neiner, F. Lignières, & J. J. Green, 49–73, astro–ph/1208.4926

Zorec, J. & Royer, F. 2012, A&A, 537, A120

SF2A 2013
L. Cambrésy, F. Martins, E. Nuss and A. Palacios (eds)

THE STELLAR OPACITIES

S. Turck-Chièze[1], D. Gilles[1], F. Gilleron[2], J.C. Pain[2] and the international OPAC consortium

Abstract. Opacities are fundamental ingredients of stellar physics. Helioseismology and asteroseismology have put in evidence anomalies that could be attributed to an insufficient knowledge of the photon-plasma interactions. We work on a revision of this plasma physics in the conditions where the anomalies have been found: the region of the iron opacity peak near log T= 5.2 and the inner radiative region of Sun and solar-like stars. The international OPAC consortium performs new calculations, compares them and looks for the origin of their differences. In parallel, experimental campaigns are realized, others are in preparation to validate some conclusions on the reliability of the new proposed calculations. New tables for astrophysics will be performed in the framework of the ANR OPACITY and their influence on seismic observables will be studied. We explicit here the difficulty of the computations together with some computation resources.

Keywords: helioseismology, atomic processes, diffusion, oscillations, plasma, radiative transfer

1 Introduction

Seismology of stars has the potential to be a driver for introducing dynamical processes in stellar modeling. Rotation profiles begin to be determined in different types of stars and the subsurface magnetism is now followed in time for the Sun. Precise neutrino fluxes will have in parallel the potential to catch deep motions in the solar core. Face to this tremendous progress, it is important to ensure the reliability of the microscopic physics and to begin to consider the interplay of macroscopic physics on microscopic one.

A new investment on the photon-plasma interaction is justified by some evident discrepancies between seismic observations and their predictions. Two of them are well known: the solar sound speed profile and the excitation of modes of SPB and β-Cephei stars. In this invited review, we show first the two astrophysical conditions that we would like to improve. Then we present the general strategy of computation of opacity spectra, the used codes, our different actions and results and finally the future plan and some computer performances.

2 The astrophysical facts

Helioseismology produces an exigent check of the standard solar model (SSM) hypotheses. Today a clear discrepancy exists between their respective sound speed profiles. This fact is confirmed by the marginal agreement between the neutrino flux predictions of SSM and their detections, but one has identified a very good agreement between helioseismology and neutrinos through a seismic model (Turck-Chièze & Couvidat 2011; Turck-Chièze 2013). So the hypotheses of the SSM are questioned and in particular the reliability of the opacity coefficients. Among others, two possibilities are proposed, a direct inaccurate photon plasma calculations or an indirect effect coming from an inaccurate central composition of the Sun. If the second solution is the good one, that means that one can question not only directly the opacity calculations but also the way one treats the slow gravitational settling and the joined radiative accelerations of each element, in particular the heavier ones: C, N, O, Fe. In the two cases, a detailed examination of the whole calculation of the transfer of radiation is required.

On the other side, asteroseismology observes now a large range of stars of different masses. In particular it has put in evidence some excited modes which were not predicted by stellar models, in SPB and β-Cephei. These modes are supposed to be excited by κ mechanism, involving the iron group opacity peak around log T =5.2, the main contributors are iron, nickel and chromium (Pamyatnykh 1999; Zdravkov & A. 2009). This

[1] SAp/IRFU/CEA, CE Saclay, 91191 Gif sur Yvette cedex, France
[2] CEA/DAM/DIF, 91297 Arpajon, France

fact has been observed for different metallicities (Salmon et al. 2012). So opacities have been suspected, more surprisingly in some specific cases, the OP tables were more predictive and in other cases, the OPAL tables have appeared more appropriate, creating a confusion on which tables are the good ones to use for these stars.

3 The strategy for performing new opacity tables

The mentioned difficulties complicate the interpretation of the seismic observations of Sun and intermediate-type stars. Stellar evolution equations use the mean Rosseland values $\kappa(T, \rho, X_i)$ in the radiative transfer equation but radiative accelerations use directly the spectral opacity $\kappa_\nu(T, \rho, X_i)$ (Turck-Chièze et al. 2009) so any progress needs not only to modify the used tables for Astrophysics but also to compute the whole energy spectra for individual elements and then tables for a required mixture. Three years ago, we have decided different actions and the formation of the international OPAC consortium * composed by astrophysicists, plasma physicists and experimentalists (Turck-Chièze et al. 2011a) to gather together all the useful specialities. We define thermodynamical conditions available in laboratory and useful for astrophysics. We compare new opacity calculations done by different groups of different institutes between them and with the existing tables to estimate the validity of the approximations which are generally used to limit the computation time (Turck-Chièze et al. 2011a), we perform experiments when it is possible to guarantee better calculations before delivering them to the astrophysical community (Turck-Chièze et al. 2011b, 2013), the objectives of the ANR OPACITY.

In the envelopes of SPB or β-Cephei, the $10^{-6} - 10^{-7}$g/cm^3 density is too small for a foil of iron or nickel to be manufactured. So when the astrophysical conditions are not accessible to laboratory, we work on equivalent conditions, that means on conditions corresponding to the same distribution of ionic charges, typically slightly higher temperature and 2 or 3 orders of magnitude higher in density. Present laser facilities like LULI2000 in France deliver sufficient power to perform such experiments. For the solar radiative interior and for solar-like stellar conditions T $= 2$ to $15\,10^6$ K, $\rho = 0.2$ to 150 g/cm^3, one needs more energetic facilities like LMJ in France which will be operational in 2016 or the NIF in USA. A first tentative by Bailey et al. (2007) has been realized with the Z pinch at Albuquerque.

Such activities are useful for stellar physics but also for fusion research, inertial fusion in LMJ and magnetic fusion in ITER as in these three disciplines the interaction of photon with the plasma is required in very large thermodynamical conditions. The main difficulties come from the numerous calculations to compute and the related computer times. Ten years ago, the available machines were limited in computation capabilities and approximations were generally made. In addition to that problem, plasma effects play some role that only new experiments could confirm if one can reach high density and high temperature with laser facilities.

4 Rapid description of the used codes

The different codes of the collaboration use different approximations, which when justified, can tremendously reduce the number of transitions to perform, see Figure 1. The exact description of atomic structure relies on the fine structure calculation of electronic configurations, i.e. the determination of the energy levels (characterized by the total angular momentum J) connected by electric-dipole lines (DLA: detailed-line accounting). The numerous levels can be grouped into relativistic configurations, connected by spin-orbit-split arrays (SOSA) represented by Gaussian distributions whose strength, average energy and variance can be calculated analytically using Racah algebra. The relativistic configurations in turn can be grouped into non-relativistic configurations, connected by unresolved transition arrays (UTA) also represented by Gaussian distributions. If the number of configurations remains too large, they can be grouped finally into "superconfigurations" (a superconfiguration is an ensemble of configurations close in energy) connected by super-transition arrays (STA). The total opacity is the sum of photo-ionization, inverse Bremsstrahlung, scattering spectra and a photo-excitation spectrum relying on the following expression for the opacity:

$$\kappa\left(h\nu\right) = \frac{1}{4\pi\epsilon_0}\frac{\mathcal{N}}{A}\frac{\pi e^2 h}{mc}\sum_{X\to X'} f_{X\to X'}\mathcal{P}_X\Psi_{X\to X'}(h\nu)$$

*S. Turck-Chièze, J. E. Ducret, D. Gilles, M. Le Pennec, SAp/ CEA France, C. Blancard, T. Caillaud, P. Cossé, T. Blenski, J. Farriaut, G. Faussurier, F. Gilleron, J. C. Pain, M. Poirier, C. Reverdin, V. Silvert, F. Thais, B. Villette CEA France, F. Delahaye, C. Zeippen Obs. Meudon France, S. Bastiani Ecole Polytechnique France, M. Busquet, ARTEP, USA, J. Bailey, G. Loisel Albuquerque, USA, J. Guzik, J. Colgan, D.P. Kilcrease, N.H. Magee, Los Alamos, USA, and J. W. Harris AWE England.

where h is Planck constant, $\mathcal{N}$ the Avogadro number, ϵ_0 the vacuum polarizability, m the electron mass, A the atomic number and c the speed of light. $\mathcal{P}$ is a probability, f an oscillator strength, $\Psi(h\nu)$ a profile. The sum $X \rightarrow X'$ runs over lines, UTAs or STAs of all ion charge states present in the plasma. Special care is taken to calculate the probability that can be either a level, a relativistic configuration, a non-relativistic configuration or a superconfiguration as it is the starting point for different transitions (DLA, SOSA, UTA, STA).

We rapidly describe some codes of the collaboration, others are also described in Turck-Chièze et al. (2011a).

The SCO-RCG opacity code (Porcherot et al. 2011) combines DLA calculations (when they are tractable and useful) with statistical approaches (UTA, SOSA and STA) when the DLA calculation is impossible from a computational point of view or if the lines coalesce into unresolved structures due to physical broadening mechanisms.

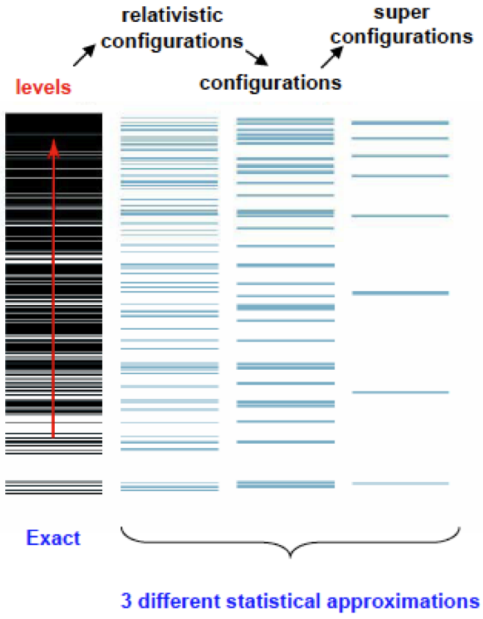

Fig. 1. : The different approximations generally found in opacity calculations.

OP (Opacity Project) is an on-line atomic database used in astrophysics (Badnell et al. 2005; Seaton 2007). TOPbase contains the most complete dataset of LS-coupling term energies, f-values and photoionization cross sections for the most abundant ions (Z = 126) in the universe. They have been computed in the close-coupling approximation by means of the R-matrix method with innovative asymptotic techniques. TOPbase also contains large datasets of f-values for iron ions with configurations 3sx 3px 3dx, referred to as the PLUS-data, computed with the atomic structure code SUPERSTRUCTURE.

The OPAS code (Blancard et al. 2012) calculates radiative opacity in LTE. Based on the average atom model SCAALP, it combines detailed configurations and level accounting treatments. The bound-bound opacity uses detailed line accounting and/or statistical methods. The bound-free opacity neglects the configuration level splitting. In warm dense matter, plasma and many-body effects can be important, the free-free opacity is obtained by interpolating between the Drude-like opacity and the opacity derived from the Kramers formula including a Gaunt factor and an electron degeneracy effect correction. Photon scattering by free electrons includes collective effects and relativistic corrections.

ATOMIC is a multi-purpose code (Colgan et al. 2013), developed in Los Alamos, that generates LTE or non-LTE quantities at various levels of approximation. Just now, they compute new LTE opacity data for elements from H to Zn. The tables up to Ne are complete, and a new Fe opacity table will be available soon. The calculations include fine-structure details and represent a systematic improvement over the LEDCOP legacy code. They incorporate atomic structure data from the CATS code, based on Cowan's atomic structure codes, and photoionization cross section data computed from the Los Alamos ionization code GIPPER. They use a new equation-of-state (EOS) model based on the chemical picture. ATOMIC incorporates some physics packages

from LEDCOP and improved free-free cross sections and additional scattering mechanisms.

HULLAC code has been developed by Bar-Shalom et al. (2001). It is a powerful fine-structure relativistic code able to generate thousands of configurations and billions of lines and to compute LTE and non-LTE spectra. But the number of levels to be treated in full CI mode often give dramatic increase of the computation time. The flexibility of HULLAC-v9 (Busquet et al. 2006) allows to see the role of different terms or CI approximations. In the full CI mode the computation of fine structure levels is chosen for defined groups of levels (GRL), see Busquet & al (2012). Selecting the CIinNRC mode, HULLAC-v9 computes the usual Relativistic CI (RCI) between all levels of one Non Relativistic Configuration (NRC). The diagonalisation of the Hamiltonian matrix for all levels of same J is performed in a GRL. It is also possible to turn off the CI calculation using sub mode NoCI. Other GRL can be selected.This code is used in Saclay (Gilles et al. 2011, 2012).

HULLAC, OP and ATOMIC are the only calculations that introduce full CI, i.e. CI between all levels (Bar-Shalom et al. 1999). So these codes are extremely useful for some specific checks of the different approximations. They are also used to calculate precisely the interaction when the other codes are insufficient. OPAS, SCO-RCG are interesting to qualify the deep interiors.

5 Present results, next s

First comparisons between codes has been done for iron and nickel (T = 15 eV and 27 eV, and ρ = 3-5 mg/cm^3) using OP, LEDCOP, OPAS, STA, SCO-RCG codes. They correspond to conditions similar to the iron opacity bump that excites the intermediate-type stellar oscillations. Detailed comparisons are given in Gilles et al. (2011); Turck-Chièze et al. (2013) including ionic distribution, spectra and mean Rosseland and Planck values. Figure 2 summarizes this study in showing the compared spectra that present very different behaviors, in particular for nickel. The Rosseland values vary by more than 30% for iron and up to a factor 3 for nickel. So a complementary investigation of the differences has been realized with detailed HULLAC and ATOMIC codes.

5.1 First conclusions

The HULLAC and ATOMIC codes help us to understand the discrepancies between OP and OPAL in the iron bump which excites the modes observed in β-Cephei and SPB stars. We note that iron opacities are better estimated by OP calculations than by OPAS, LEDCOP, SCO-RCG ones because the interaction of configuration reduces the spectral opacity between 40-60 eV (so not too far from the maximum of the mean Rosseland values) (Gilles et al. 2012). But OP nickel opacities are not correct in the two conditions shown in Figure 2. Indeed the differences for nickel have a different origin: the OP calculations have been incorrectly extrapolated from iron calculations. ATOMIC full CI and HULLAC predict values between the OP and OPAL results. In that case, the interaction of configuration is located at lower energy and has a smaller impact on the mean Rosseland values. The inappropriate OP nickel spectra have been confirmed by the first experiment performed at LULI2000 (Turck-Chièze et al. 2013), see also Loisel (2010) for the description of the experimental set up. The second campaign shows that all the other calculations are in better agreement than OP. These facts are not in contradiction with the assumptions of Salmon et al. (2012).

The iron group peak varies strongly with stellar age, mass and composition, so the opacities of the different elements of the iron group (chromium, iron, nickel) need to be precisely calculated on a range of T and Ne that we are determining (Le Pennec & Turck-Chièze 2013). News tables are in construction thanks to HULLAC and ATOMIC codes. Then, radiative acceleration and non LTE-conditions will also be investigated.

5.2 Work in progress

In parallel to this activity, another one is dedicated to solar-like stars, both on new spectra from OPAS and the preparation of new tables and on the preparation of experiments on large facilities in order to focus first on the region of transition between radiative and convective zones.

6 Performances of the calculations

It is important to consider the consuming time to perform the astrophysical tables. We give here some estimates of the spectra calculations for individual elements.

Let first consider the Sun and OPAS calculations that are not detailed calculations. These calculations are done in CEA/DAM on 2PC 8CPU, 16 Goctets RAM, the calculations for Z $<$ 10 are done in several seconds as

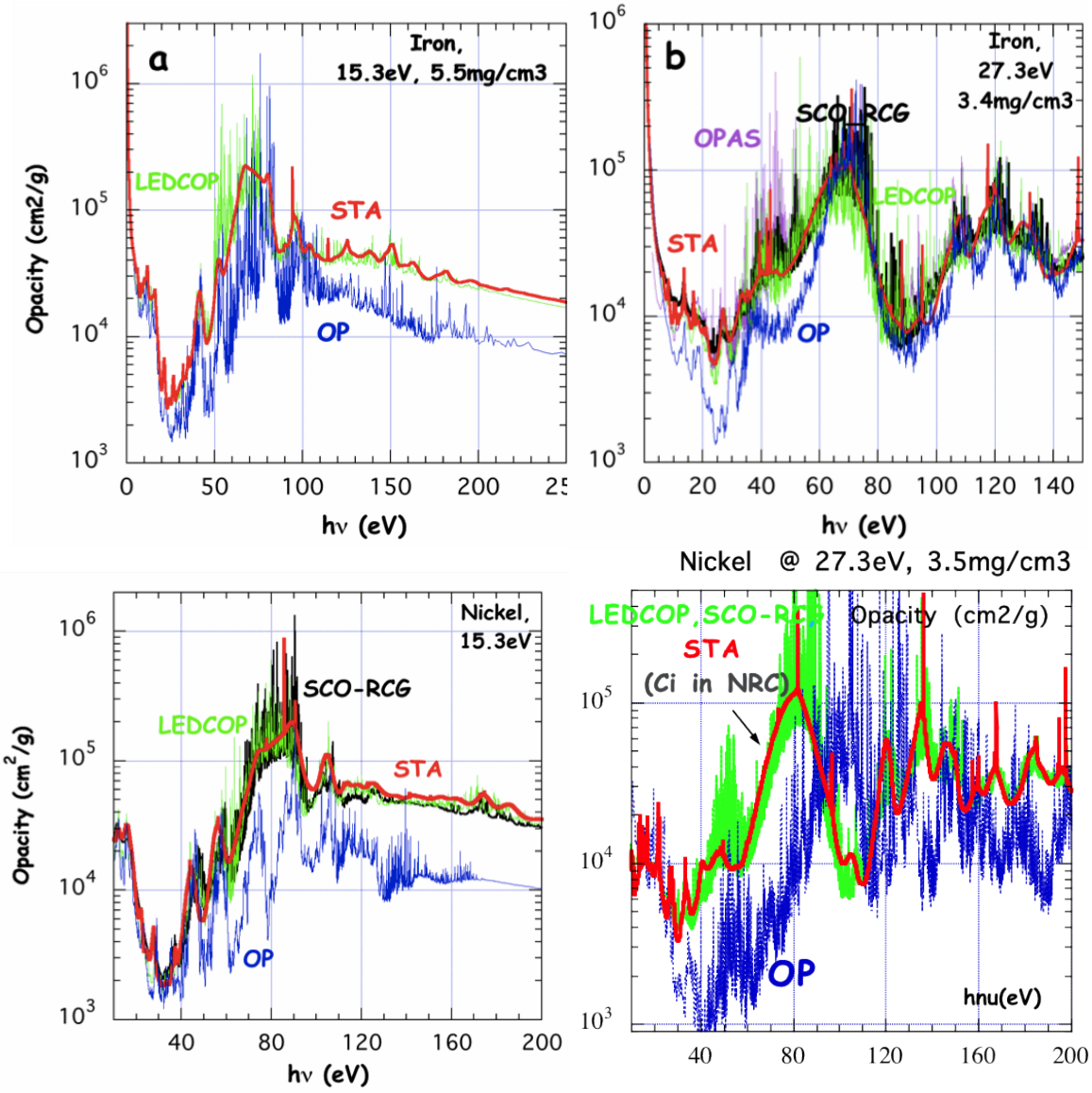

Fig. 2. : Comparison of calculations for iron and nickel in conditions near the realized LULI experiments, equivalent conditions of the opacity iron bump of the envelopes of intermediate-type stars. From Gilles et al. (2011)

these elements are totally ionized, for Z= 20, several seconds at the center (this element is also totally ionized), but 6 mn at the base of the convective zone (BCZ). In the case of iron, 20s at the center and 40h at the BCZ. These performances have been obtained on the basis of 100 Goctets of stored fundamental information to speed up these calculations.

For envelopes of stars, the ionic distribution is extremely unfavorable and the number of levels tremendous (see Figure 3), the OP calculations take several months for one condition. The HULLAC calculations are performed on Intel computer with 20 cores, 64 Goctets RAM and more than 1 Tera of stored memory. For the mentioned conditions discussed previously, the main contributors come from ions Fe IV (Z^*= 3) to Fe XII (Z^*=13) where Z^* is the number of free electrons. The size of the matrixes depends on the number of levels NI included in the atomic description which depends itself on the number of active electrons Ne defined as Ne = Z-Z^*-10 for M shell transitions with closed shells n=1 and n=2. Moreover the full CI treatment involves also a large number of coefficients NCI which can be so large that the calculation can be hardly tractable, so extreme care and strategy must be developed to lead to accurate results. For example, for FeV one counts Nl= 301610, NCI= 3 061 241 715; for FeX Nl= 117427, NCI= 493 527 664, which requires a computer time of 425 h to be

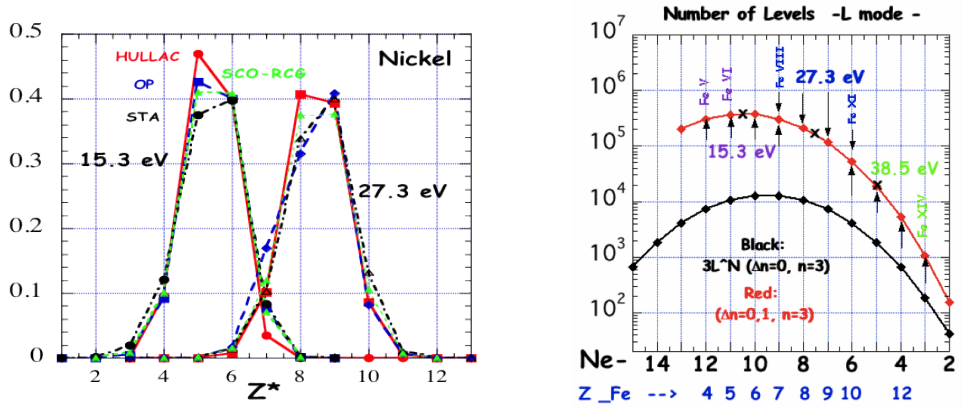

Fig. 3. Left: Ionic distribution of nickel obtained by different calculations for the two thermodynamical conditions, idem for iron. **Right:** Number of levels considered in HULLAC in function of the number of active electrons, the red curve corresponds to the transitions n=3 to n= 4, and the black curve to n=3 n=3.

performed. For Fe IX, Nl= 210 631, NCI = 1 488 790 396, so one needs to properly choose the transitions to calculate to converge in the calculation. In these conditions it is important to compare different codes to take the adopted decision in function of the range of photon energy that one considers and the accuracy we need to get.

In the ANR OPACITY, we hope to distribute new tables which have been largely discussed and for which we have decided when approximations are relevant. In parallel we continue to prepare new experiments to validate some choices.

References

Badnell, N. R., Bautista, M. A., Butler, K., et al. 2005, MNRAS, 360, 458

Bailey, J. E., Rochau, G. A., Iglesias, C. A., et al. 2007, Physical Review Letters, 99, 265002

Bar-Shalom, A., Klapisch, M., & Oreg, J. 2001, J. Quant. Spec. Radiat. Transf., 71, 169

Bar-Shalom, A., Oreg, J., Klapisch, M., & Lehecka, T. 1999, Phys. Rev. E, 59, 3512

Blancard, C., Cossé, P., & Faussurier, G. 2012, ApJ, 745, 10

Busquet, M., Bar-Shalom, A., Klapisch, M., et al. 2006, Journal de Physique IV, 133, 973

Colgan, J., Kilcrease, D. P., Magee, N. H., et al. 2013, High Energy Density Physics, 9, 369

Gilles, D., Turck-Chièze, S., Busquet, M., et al. 2012, in EAS Publications Series, Vol. 58, First European Conference on Laboratory Astrophysics (EDP Sciences), 51–55

Gilles, D., Turck-Chièze, S., Loisel, G., et al. 2011, High Energy Density Physics, 7, 312

Le Pennec, M. & Turck-Chièze, S. 2013, in Precision Asteroseismology, in press

Loisel, G. 2010, PhD thesis, Université Paris XI Orsay, France

Pamyatnykh, A. A. 1999, Acta Astronomica, 49, 119

Porcherot, Q., Pain, J.-C., Gilleron, F., & Blenski, T. 2011, High Energy Density Physics, 7, 234

Salmon, S., Montalbán, J., Morel, T., et al. 2012, MNRAS, 422, 3460

Seaton, M. J. 2007, MNRAS, 382, 245

Turck-Chièze, S. 2013, in Nuclear Physics in Astrophysics VI, Journal of Physics: Conference Series No. in press (IOP)

Turck-Chièze, S. & Couvidat, S. 2011, Reports on Progress in Physics, 74, 086901

Turck-Chièze, S., Delahaye, F., Gilles, D., Loisel, G., & Piau, L. 2009, High Energy Density Physics, 5, 132

Turck-Chièze, S., Gilles, D., Le Pennec, M., et al. 2013, High Energy Density Physics, 9, 473

Turck-Chièze, S., Loisel, G., Gilles, D., et al. 2011a, Ap&SS, 336, 103

Turck-Chièze, S., Loisel, G., Gilles, D., et al. 2011b, Journal of Physics Conference Series, 271, 012035

Zdravkov, T. & A., P. A. 2009, in Stellar Pulsations: Challenges for Theory and Observations, Vol. 1170, American Institute of Physics Conference Series, ed. J. A. Guzik & P. A. Bradley, 388–390

SF2A 2013
L. Cambrésy, F. Martins, E. Nuss and A. Palacios (eds)

FULLY-COMPRESSIBLE HYDRODYNAMICAL SIMULATIONS OF TURBULENT CONVECTION

M. Viallet [1]

Abstract.
Convection is a key process in stellar interiors. It is characterized by large Reynolds numbers, implying a highly turbulent regime. In this talk, I presented 3D Implicit Large Eddy Simulations of turbulent convection in two very different astrophysical contexts: the oxygen-burning shell of a supernova progenitor and the envelope of a red giant stars. I highlighted common properties and discussed important differences, illustrating how a careful analysis of 3D data allow us to gain insight into this complex phenomenon.

Keywords: convection - stars: interiors - turbulence

1 Summary

Currently, most of our physical understanding of stellar interiors and evolution largely relies on one-dimensional calculations. The description of complex physical processes like time-dependent turbulent convection, rotation or MHD processes mostly relies on simplified, phenomenological approaches, with a predictive power hampered by the use of several free parameters. These approaches have now reached their limits in the understanding of stellar structure and evolution. The development of multi-dimensional hydrodynamical simulations becomes crucial to progress in the field of stellar physics and to meet the enormous observational efforts aimed at producing data of unprecedented quality (COROT, Kepler GAIA).

The talk summarized our recently published paper, Viallet et al. (2013b) , which presents a comparison of 3D Implicit Large Eddy Simulations of turbulent convection in two very different astrophysical contexts: the oxygen-burning shell of a supernova progenitor and the envelope of a red giant stars. The oxygen-burning shell data is similar to the one described in Meakin & Arnett (2007); Arnett et al. (2009). The red giant data was produced with the MUSIC code (see Viallet et al. 2011, 2013a). The analysis framework is provided by mean-field equations that result from averaging the hydrodynamical equations, see Viallet et al. (2013b) for details. Such an averaging procedure allows for a quantitative analysis and comparison of complex 3D data sets. The averaged data and scripts are provided online at www.stellarmodels.org (PI: Casey Meakin).

I acknowledge support from the Newton Alumni Program from the Royal Society.

References

Arnett, D., Meakin, C., & Young, P. A. 2009, ApJ, 690, 1715
Meakin, C. A. & Arnett, D. 2007, ApJ, 667, 448
Viallet, M., Baraffe, I., & Walder, R. 2011, A&A, 531, A86
Viallet, M., Baraffe, I., & Walder, R. 2013a, A&A, 555, A81
Viallet, M., Meakin, C., Arnett, D., & Mocák, M. 2013b, ApJ, 769, 1

[1] Max-Planck-Institute für Astrophysik, Karl-Schwarzchild Strasse 1, D-85741 Garching

Session 05

Gaia : Quelles perspectives pour la physique stellaire ?

SF2A 2013
L. Cambrésy, F. Martins, E. Nuss and A. Palacios (eds)

TOWARDS A BETTER UNDERSTANDING OF MULTIPLE POPULATIONS IN GLOBULAR CLUSTERS

W. Chantereau[1], C. Charbonnel[1,2], T. Decressin[1] and G. Meynet[1]

Abstract. Globular clusters (GCs) are self-graviting aggregates of hundreds of thousands of stars and count among the oldest structures of the Universe. Although they have long been considered as perfect laboratories for stellar physics, their dynamical and chemical evolution remain largely unknown. Moreover recent observations show that they are much more complex than originally thought. In individual GCs we observe some chemical features in long-lived low-mass stars on both the main sequence and the red giant branch; however in order to explain this features these stars have to reach very high temperatures in their interior which is not the case, thus they must have inherited their chemical properties when they were born from the intracluster medium. This implies that a first generation (1G) of massive and fast evolving stars has polluted the intracluster gas with H-burning products from their ejecta while a second generation (2G) of stars formed. The Gaia mission will help disentangling between the possible polluter scenario; indeed its high quality data will provide membership probabilities, distances, proper motions for the Milky Way GCs and thus will allow to better understand their formation and evolution.

Keywords: globular cluster, multiple populations, horizontal branch, stars: evolution, stars: low-mass, stars: abundances

1 Introduction

We know for a few years that GCs host at least two stellar generations. Indeed photometric studies (HST) of GC color-magnitude diagrams (CMD) show multiple main sequences (MS), sub and red giant branches (SGB & RGB), and extended horizontal branch (e.g. Bedin et al. 2004 and Milone et al. 2010). In addition spectroscopic surveys revealed large star-to-star abundance variations of the light elements involved in H-burning at high temperature, in particular the well-documented C-N, O-Na and Mg-Al anticorrelations, while the heavier elements and the iron stay constant (see e.g. Gratton et al. 2012 and Carretta et al. 2009a). These chemical abundance variations have to come from the intracluster medium in which the 2G stars were forming, already enriched by H-burning products ejected from a first generation of stars. Nowadays two main "self-polluting scenarios" are privileged depending on the polluters, being either fast rotating massive stars (FRMS, M$\geq$ 25 $M_{\odot}$; e.g. Prantzos & Charbonnel 2006 and Decressin et al. 2007b) or massive asymptotic giant branch stars (M between 6 and 11 $M_{\odot}$; e.g. Ventura et al. 2001 and Ventura & D'Antona 2011).

These two scenarios differ especially in the amount of He released in the polluters' ejecta. Indeed within the AGB model, the He mass fraction (Y) of 2G stars must be of maximum $\sim$ 0.37 (Ventura et al. 2012) while the FRMS model allows to reach extreme values such as Y = 0.8 (Decressin et al. 2007a).

Here we present the consequences of the chemical pollution induced by the FRMS scenario on the evolution of 2G stars and on the morphology of the GCs. In §2 we remind the guidelines of the FRMS scenario. In §3 we study the evolutionary behaviour of 2G star models. Finally in §4 we highlight some consequences on the GCs morphology and just say a few words on why Gaia would be a great step in the near future for the GCs field.

[1] Geneva Observatory, University of Geneva, 51 Chemin des Maillettes, 1290 Versoix, Switzerland
[2] IRAP, UMR 5277 CNRS and Université de Toulouse, 14 Av. E. Belin, 31400 Toulouse, France

2 Fast Rotating Massive Stars scenario

In the FRMS scenario, massive stars (initial masses between 25 and 120 $M_{\odot}$) of the 1G burn hydrogen on the MS at a very high temperature ($\sim$ 75 MK) and are able to eject H-burning products due to internal mixing and rotation at critical velocity (see Decressin et al. 2007b and Krause et al. 2013). This mass loss occurs until the beginning of the He-burning phase through a slow equatorial mechanical wind (slow enough to be retained in the potential well of the GC) and forms a Keplerian equatorial disc around the progenitor star. Our group proposed that 2G stars from in this disc, thus composed of the ejecta enriched by the H-burning products diluted with the intracluster medium. After the birth of this 2G, the remnants activation blows out most of the remaining intracluster gas, inducing the loss of most 1G stars. This loss of most of the 1G stars is consistent with the current observed ratio of 1G and 2G stars within GCs, which is in average respectively 30 and 70 %; (Carretta et al. 2009b and Decressin et al. 2009).

3 Second Generation star behaviour

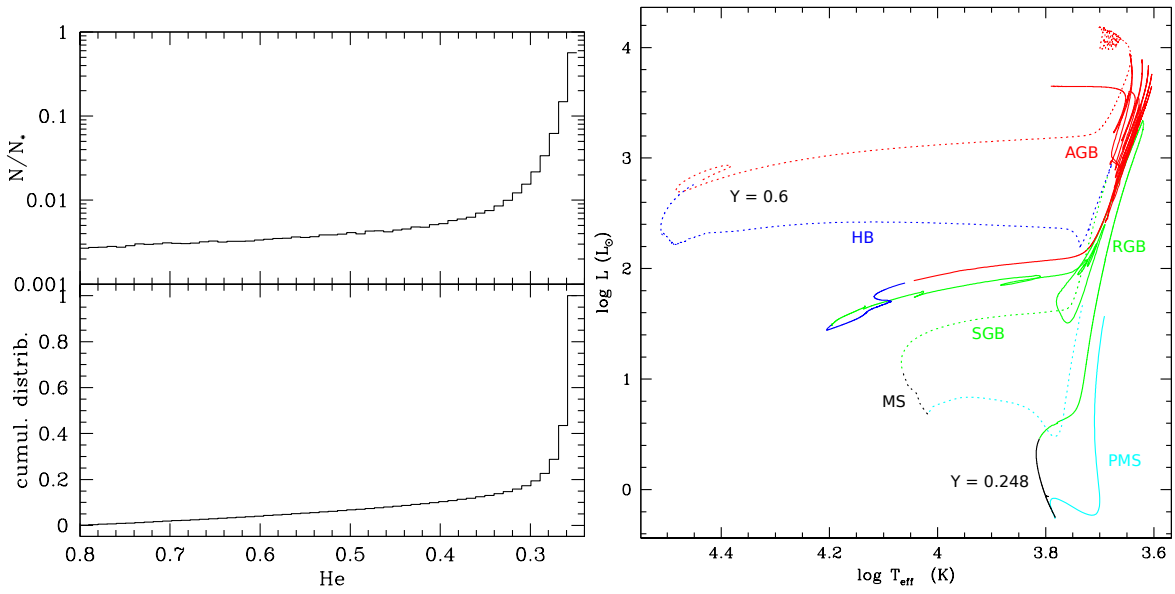

Fig. 1. Left: Initial He distribution for the 2G stars according to the FRMS scenario (Decressin et al. 2007a). **Right:** Evolutionary path in the HRD of the 0.8 $M_{\odot}$ star for two initial He mass fractions of 0.248 and 0.6. The pre-main sequence is in light blue, MS in black, the SGB and RGB in green, the central helium burning in blue and the later phases to the thermally pulsing AGB one -if the star undergoes it- in red).

We computed standard stellar models at Z = 5 x 10^{-4} with initial masses between 0.3 $M_{\odot}$ and 1.0 $M_{\odot}$ with the evolution code STAREVOL (e.g. Lagarde et al. 2012). For the initial chemical abundances we used the data from the FRMS scenario for the case of NGC 6752 ([Fe/H] = -1.56, Carretta et al. 2007); the initial He mass fraction varies between 0.248 and 0.8 (figure 1, left panel) and the abundances of carbon, nitrogen, oxygen, magnesium, sodium and aluminium are scaled accordingly. For the mass-loss process we used the Reimers (1975) prescription (η=0.5).

The impact of the initial chemical abundance on the evolution of a 2G star is shown in figure 1 (right panel) for a star of 0.8 $M_{\odot}$, which is the typical turnoff mass in old GCs ($\sim$ 13 Gyr). The higher the initial He, the higher the mean molecular weight and the lower the opacity, thus the higher the stellar luminosity (L) and the internal temperature (also the effective one, T_{eff}). As a consequence, the lifetime is significantly shortened, thus we do not expect to see today a big fraction of He-rich and super He-rich stars (He > 0.4) in very old GCs.

Moreover low-mass and super He-rich stars behave like more massive ones (intermediate mass), indeed they do not undergoe the He flash, for instance on the left panel of the figure 2, we do not have the bend (typical of the He flash) during the RGB tip for the star with Y = 0.6.

Since the internal temperature is higher for the He-rich stars, their He core after the MS is much more massive. In the most extreme cases, this can prevent the helium to ignite as usual, in fact the central He-

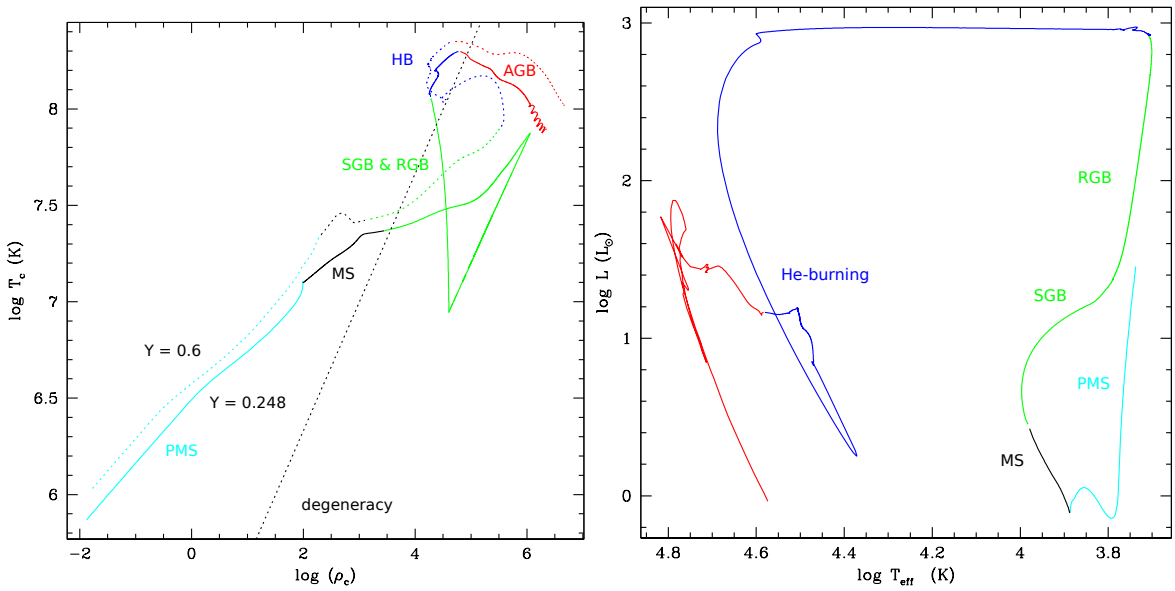

Fig. 2. Left: Central temperature as a function of the central density of the 0.8 $M_\odot$ star for an initial He content of 0.248 and 0.6. **Right:** Evolutionary path in the HRD of the 0.45 $M_\odot$ star for an initial He content of 0.7.

burning, if it starts, will take place very lately on the HB or even on the WD cooling curve. Thus the He-richest stars present on the RGB will not come back on the AGB (e.g. for a star with another M_{ini} of 0.45 $M_\odot$, figure 2, right panel), and this could explain why Campbell et al. (2013) do not observe Na-rich stars on the AGB (see Charbonnel et al. 2013 for more details).

4 Implications on GCs

According to the FRMS scenario the fraction of 2G stars initially formed with a He greater than 0.4 is not higher than ~ 7 % (figure 1, left panel). Thus we can foresee that it is difficult to find these super He-rich stars on the MS and on the RGB in GCs today. Moreover given that the HB and AGB are shorter, this fraction is negligible for these advanced phases. Therefore it is very difficult to disentangle the two main polluting scenarios through the He content on the HB.

As discussed in §3, due to this initial He content distribution, stars with different initial masses have very different evolutionary paths and fates. As we can see on figure 3, there is a domain where stars end as He white dwarfs (He WD) without igniting the He, and some of them have a lifetime shorter than the Hubble time; and therefore could greatly contribute to the current WD number. There is also a domain where stars end as carbon and oxygen white dwarfs (CO WD) with or without undergoing the helium flash. Moreover as showed previously stars with a very high initial He content which experience a late He ignition (thus no He flash at the RGB tip), do not climb the AGB.

We can add that Gaia will be very hepful, the proportion of halo stars that come from the stellar clusters (e.g. Martell & Grebel 2010 and Schaerer & Charbonnel 2011) and thus help to understand what was the mechanism of self pollution.

5 Conclusions

We showed that the He content is a suitable explanation to the recent observations of NGC 6752 about the lack of Na-rich stars on the AGB. However a further study is necessary and the next step is to build synthetic GCs from this grid of models in order to foresee the effects of this wide variety of behaviours on the morphology of GCs. Finally Gaia could shed a light on the process which contributed to blow out of the GCs most of the 1G stars, helping to better understand and constrain the self-polluting mechanisms.

We acknowledge support from the Swiss National Science Foundation (FNS).

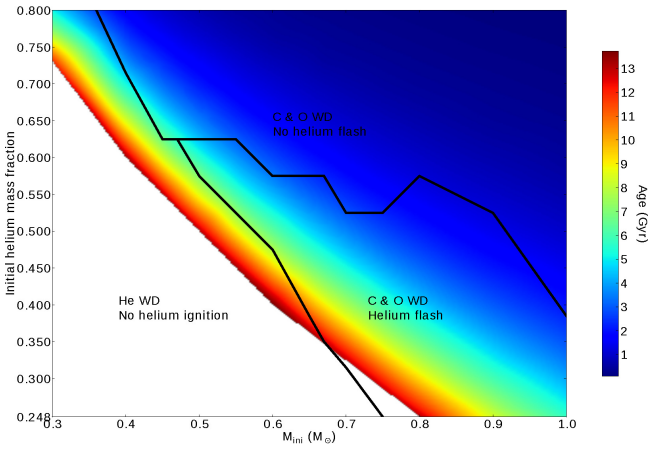

Fig. 3. Diagram representing the fate and the age of stars for different initial masses and He content.

References

Bedin, L. R., Piotto, G., Anderson, J., et al. 2004, ApJ, 605, L125

Campbell, S. W., D'Orazi, V., Yong, D., et al. 2013, Nature, 498, 198

Carretta, E., Bragaglia, A., Gratton, R. G., et al. 2009a, A&A, 505, 117

Carretta, E., Bragaglia, A., Gratton, R. G., et al. 2009b, A&A, 505, 117

Carretta, E., Bragaglia, A., Gratton, R. G., Lucatello, S., & Momany, Y. 2007, A&A, 464, 927

Charbonnel, C., Chantereau, W., Decressin, T., Meynet, G., & Schaerer, D. 2013, A&A, 557, L17

Decressin, T., Baumgardt, H., Kroupa, P., Meynet, G., & Charbonnel, C. 2009, in IAU Symposium, Vol. 258, IAU Symposium, ed. E. E. Mamajek, D. R. Soderblom, & R. F. G. Wyse, 265–274

Decressin, T., Charbonnel, C., & Meynet, G. 2007a, A&A, 475, 859

Decressin, T., Meynet, G., Charbonnel, C., Prantzos, N., & Ekström, S. 2007b, A&A, 464, 1029

Gratton, R. G., Carretta, E., & Bragaglia, A. 2012, A&A Rev., 20, 50

Krause, M., Charbonnel, C., Decressin, T., Meynet, G., & Prantzos, N. 2013, A&A, 552, A121

Lagarde, N., Decressin, T., Charbonnel, C., et al. 2012, A&A, 543, A108

Martell, S. L. & Grebel, E. K. 2010, A&A, 519, A14

Milone, A. P., Piotto, G., King, I. R., et al. 2010, ApJ, 709, 1183

Prantzos, N. & Charbonnel, C. 2006, A&A, 458, 135

Reimers, D. 1975, Memoires of the Societe Royale des Sciences de Liege, 8, 369

Schaerer, D. & Charbonnel, C. 2011, MNRAS, 413, 2297

Ventura, P. & D'Antona, F. 2011, MNRAS, 410, 2760

Ventura, P., D'Antona, F., Di Criscienzo, M., et al. 2012, ApJ, 761, L30

Ventura, P., D'Antona, F., Mazzitelli, I., & Gratton, R. 2001, ApJ, 550, L65

SF2A 2013
L. Cambrésy, F. Martins, E. Nuss and A. Palacios (eds)

NON-LTE IRON ABUNDANCE DETERMINATION OF A SAMPLE OF KEPLER RED GIANTS

Rana Ezzeddine[1], Thibault Merle[2] and Bertrand Plez[1]

Abstract. In the aim of calibrating non-LTE effects in atoms, particularly iron, for which quantum mechanical calculations for collisions with neutral hydrogen do not exist, we re-analyzed a sample of *Kepler* K red giant stars and determined both LTE and non-LTE FeI and FeII abundances, using asteroseismic fundamental atmospheric parameters. 1D, spherical MARCS model atmospheres were used for the abundance determinations. FeI and FeII lines with reliable oscillator strength values were selected. Results show better mutual agreement in abundances between neutral and singly ionized Fe lines as a function of equivalent width and excitation potential in NLTE as compared to that in LTE.

Keywords: Iron abundances, NLTE, Red Giants

1 Introduction

The study of iron abundances in cool stars plays an important role in understanding the Galactic chemical evolution, since there exists a wealth of Fe spectral lines even in metal-poor stars, which makes it a proxy for the total metal content in the star. Iron is also an important opacity contributor in the stellar atmosphere of late-type stars. Moreover, iron lines are used to derive fundamental atmospheric parameters (Effective temperature $T_{\rm eff}$, surface gravity log$g$ and microturbulent velocity ξ) of the star.

In stellar atmospheres, the statistical equilibrium of neutral iron can deviate from thermodynamic equilibrium due to the deviation of the mean intensity of ionizing radiation J_ν from the Planck function B_ν (Mashonkina et al. 2011), and thus it is important to perform non-local thermodynamic equilibrium (NLTE) line formation calculations in order to accurately determine abundances.

In his review, Asplund (2005) described NLTE as the case where "Everything depends on everything, everywhere". And thus in order to correctly synthesize and model stellar spectra to determine NLTE abundances, one has to take into account accurate atomic data including all possible radiative and collisional transitions between the corresponding levels of a model atom of the element under study, especially the collisions with neutral hydrogen which become important in metal poor stars where $\rm n_H/n_e \sim 10^5$. However, collisional rates with hydrogen are usually treated using the semi-classical Drawin approximation (Drawin 1969) which is based on classical rather than quantum mechanics, and has been shown to overestimate the collisional rates up to 5 orders of magnitude (Belyaev & Barklem 2003). And since quantum mechanical data are not yet available for iron, we attempt to calibrate these collisional rates by accurately modelling and determining NLTE FeI/FeII abundances.

2 Method

For this study, we selected a sample of bright *Kepler* red giants which have reliable asteroseismic fundamental atmospheric parameters, $T_{\rm eff}$ and log g. We used high resolution (R=67000) spectra (Thygesen et al. 2012) from the FIES (FIber-fed Echelle Spectrograph) spectrograph of the NOT (Nordic Optical Telescope) at La Palma,

[1] Laboratoire Univers et Particules de Montpellier (LUPM), Université de Montpellier 2-CNRS, France.
[2] Institut d'Astronomie et Astrophysique, Université Libre de Bruxelles, Belgique.

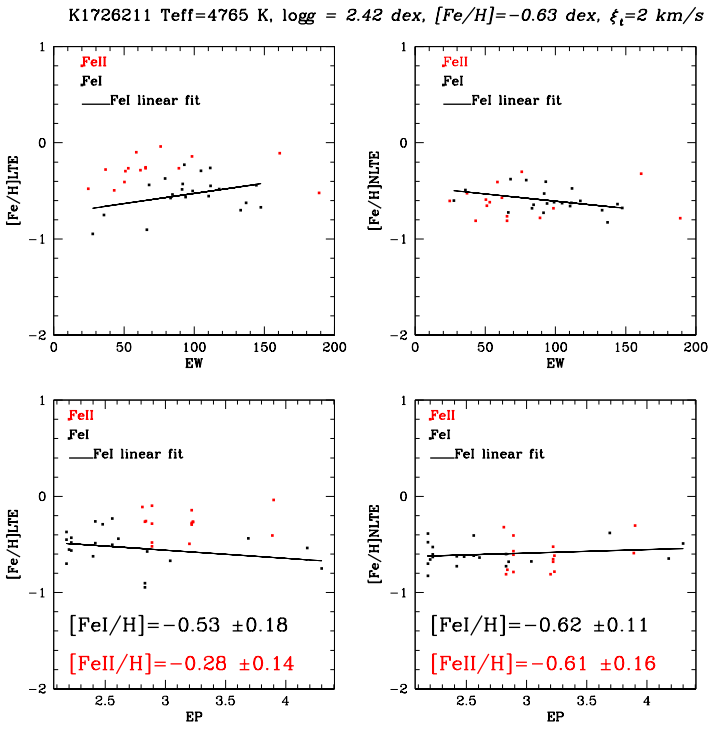

Fig. 1. Diagnostic plots of the results for FeI and FeII in LTE (left column) and NLTE (right column): abundances versus excitation potential and equivalent width for one of the sample stars of KIC ID 1726211.

to measure equivalent widths of a well selected list of non-blended lines from the INSPECT database* (Bergemann et al. 2012). The chosen lines have up-to-date averaged experimental oscillator strengths values from Gehren et al. (2001). Spherical 1D model atmospheres were interpolated† from the MARCS database (Gustafsson et al. 2008) and used with an FeI/FeII model atom (Thévenin & Idiart 1999) to determine NLTE abundances using the spectral synthesis code MULTI2.2 (Carlsson 1986) and a curve-of-growth technique, while LTE abundances were calculated using the TURBOSPECTRUM code (Alvarez & Plez 1998), (Plez 2012).

3 Results and Conclusions

Our LTE results show less deviations with respect to the mean in FeI abundances as a function of excitation potential and equivalent width ($\sim$ 0.25 dex) as compared to that of previous work on these stars. Bruntt et al. (2011) calculated LTE abundances and imposed ionization equilibrium between FeI and FeII lines to derive atmospheric parameters ($T_{\rm eff}$, log g and ξ). The deviations from the mean in their plots are up to 0.5 dex. It is important to note that there is also a difference of up to 400 K in $T_{\rm eff}$, 0.23 dex in log g and 0.2 dex in metallicity, between our asteroseismic and their spectroscopic values of atmospheric parameters. This can have serious consequences on the further abundance determination using these parameters, and thus they have to be carefully chosen.

Our results also show better mutual agreement between FeI and FeII lines in NLTE as compared to LTE (see Fig.1) as a function of equivalent width and excitation potential, without imposing ionization equilibrium between the singly and ionized iron lines.

Future work aims at improving our results by calculating more accurate NLTE abundances, using a better and more complete iron model atom with up-to-date atomic data, and using the updated version of MULTI

*www.inspect-stars.net
†Masseron code: http://marcs.astro.uu.se/software.php

(MULTI2.3). This will allow us to quantify the effects of collision with neutral hydrogen and electrons, leading to more accurate iron abundance determinations in giant stars.

References

Alvarez, R. & Plez, B. 1998, A&A, 330, 1109
Belyaev, A. K. & Barklem, P. S. 2003, Phys. Rev. A, 68, 062703
Bergemann, M., Lind, K., Collet, R., Magic, Z., & Asplund, M. 2012, MNRAS, 427, 27
Bruntt, H., Frandsen, S., & Thygesen, A. O. 2011, A&A, 528, A121
Carlsson, M. 1986, Uppsala Astronomical Observatory Reports, 33
Drawin, H. W. 1969, Zeitschrift fur Physik, 228, 99
Gehren, T., Butler, K., Mashonkina, L., Reetz, J., & Shi, J. 2001, A&A, 366, 981
Gustafsson, B., Edvardsson, B., Eriksson, K., et al. 2008, A&A, 486, 951
Mashonkina, L., Gehren, T., Shi, J.-R., Korn, A. J., & Grupp, F. 2011, A&A, 528, A87
Plez, B. 2012, Turbospectrum: Code for spectral synthesis, astrophysics Source Code Library
Thévenin, F. & Idiart, T. P. 1999, ApJ, 521, 753
Thygesen, A. O., Frandsen, S., Bruntt, H., et al. 2012, A&A, 543, A160

SF2A 2013
L. Cambrésy, F. Martins, E. Nuss and A. Palacios (eds)

MAPPING THE INTERSTELLAR GALACTIC EXTINCTION: A MODEL-INDEPENDENT WAY.

C. Fourtune-Ravard[1], C. Babusiaux[1] and A. Gómez[1]

Abstract. All last attempts to establish a 3D map of the Galactic extinction like Marshall et al. (2006) were based on models/data comparisons. In my poster, I presented a new model-independent method to map the Galactic interstellar extinction. We developed an algorithm which detect the Red Clump stars tail on CMDs and convert its position into a distance-extinction sample. We used 2MASS and UKIDSS data which give us a detailed 3D-map in the galactic plane.

Keywords: Techniques: photmetric, surveys, (Stars:) Hertzsprung-Russell and C-M diagrams, Stars: horizontal-branch, (ISM:) dust, extinction, Galaxy: structure

1 Introduction

To perform detailed studies on the Milky Way and its components, we must accurately measure the distance to big structures shaping the Galaxy. Unfortunately, this measurement is difficult because of the pilling up of features in a same line of sight and the high extinction in the disc. Without astrometry, photometric distances needs an accurate extinction value. Establishing a correct extinction map is therefore a crucial step in a stars density mapping process.

All past attempts to establish a 3D map of the Galactic extinction, e.g. Marshall et al. (2006), were based on model/data comparison. In this work, we present a new model-independent method to map the Galactic interstellar extinction. We use the 2MASS and UKIDSS near-infrared (NIR) photometry surveys in the Galactic planez and the Red Clump (RC) stars as a distance indicators.

2 From the detection of the Red Clump tail ...

As one can see in Fig. 1, RC stars extend in a tail due to extinction. We detect the location of this RC tail on our CMDs. Our detection stops at the completeness limit of the studied field. Using the solar neighbourhood properties of the RC, we convert color-magnitude coordinates into a distance-extinction (D, Av) sample. An example of the detection is presented in Fig. 1.

In order to establish a non-cumulative continuous map we need to smooth our detection sample. We take into account the studied field with a 1.0 weight and the two contiguous fields with a 0.05 weight. We force the spline to monotonically increase and use it to construct our 3D-interstellar extinction map.

3 ... To a 3D-interstellar extinction map

One can see on Fig. 2 a clear hole at l $\in$ [4,10]°and D $\in$ [0,3.5] kpc from the Galactic Center (GC) which is inside of the bar radius. At 4 kpc from the GC, we see the molecular ring. On this map, three high extinction areas can be seen at l $\simeq$ 18-19°, l $\simeq$ 23-24°and l $\simeq$ 27-28°. Those features can be associated to the end of the near side of the Galactic bar and the region where is the origin of the Crux-Scutum arm (Hammersley et al. 2000; Green et al. 2011). This map come along with Vallée (2008) spiral arms.

[1] GEPI, UMR 8111, Observatoire de Paris-Meudon, 5 Place Jules Janssen 92190 Meudon, France

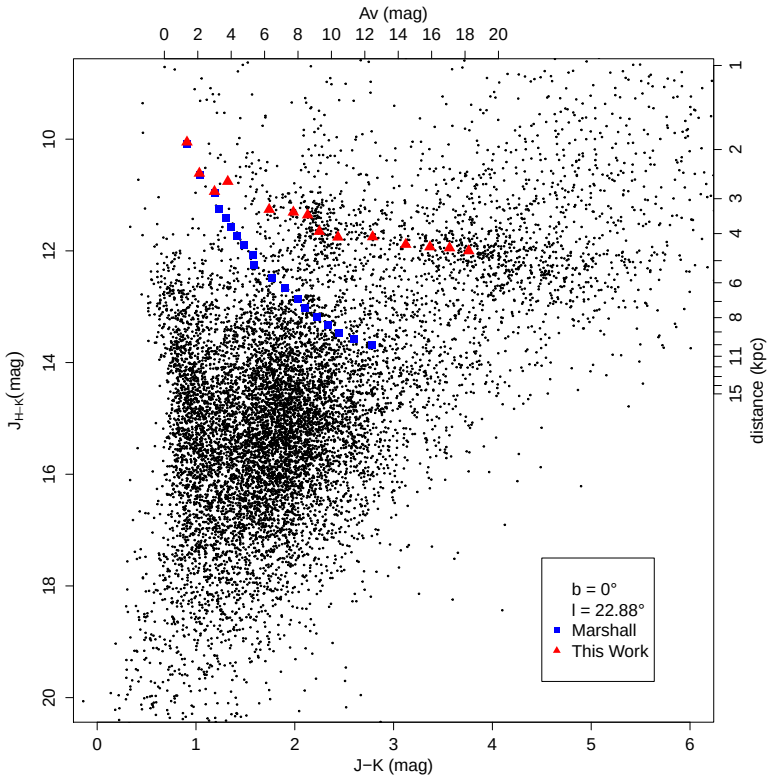

Fig. 1. UKIDSS CMD of the l=22.88°, b=0°field. Distance (D) and cumulative extinction (Av) axis are added to the CMD and calculated for a medium RC star (from solar neighbourhood properties). Following Babusiaux & Gilmore (2005), we used the reddening-independent magnitude as Y-axis. Black dots represent the observed data. Blue squares represent Marshall et al. (2006) model. Red triangles represent the result of the detection algorithm for this field.

4 Perspectives

The method presented here allows us to map the Galactic interstellar extinction but does not give any clue on stellar density. We have begun to work on a new method to deduce both 3D-extinction and stars density map from NIR photometry, including VVV survey to obtain detailed data in both 1st and 4th quarters. To achieve this, we are using a Bayesian method with only isochrones, an initial mass function and a star formation rate as priors.

5 Conclusion

In conclusion, using the Red Clump stars as distance indicators, we have produced a 3D extinction map in the Galactic plane. The 2MASS data gives us an all-sky overview while the UKIDSS data provides a detailed map in the 1st quarter, which will be completed with VVV data in the 4th.

References

Babusiaux, C. & Gilmore, G. 2005, MNRAS, 358, 1309

Green, J. A., Caswell, J. L., McClure-Griffiths, N. M., et al. 2011, ApJ, 733, 27

Hammersley, P. L., Garzón, F., Mahoney, T. J., López-Corredoira, M., & Torres, M. A. P. 2000, MNRAS, 317, L45

Marshall, D. J., Robin, A. C., Reylé, C., Schultheis, M., & Picaud, S. 2006, A&A, 453, 635

Vallée, J. P. 2008, AJ, 135, 1301

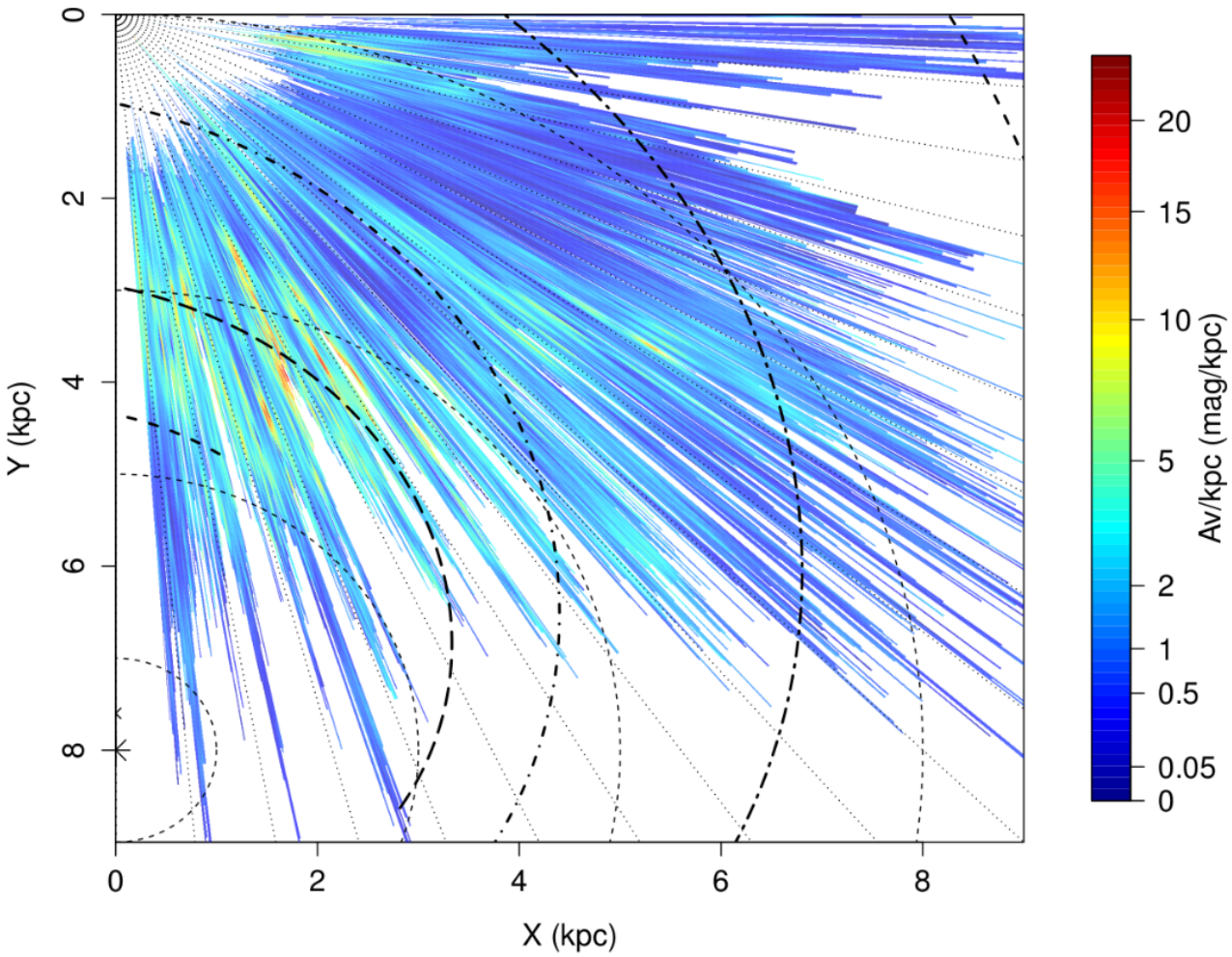

Fig. 2. Map produced using UKIDSS data through the detection-regression process described hereabove. Vallée (2008) arms (bold dashed lines) and circles with R=1,3,5,8 kpc radii (thin dashed lines) are over-plotted.

SF2A 2013
L. Cambrésy, F. Martins, E. Nuss and A. Palacios (eds)

IMPROVED SB2 ORBITS FOR HIP 12081 AND HIP 87895*

J.-L. Halbwachs[1], F. Arenou[2], P. Guillout[1], D. Pourbaix[3], L. Tal-Or[4], B. Famaey[1], Y. Lebreton[2] and T. Mazeh[4]

Abstract. We are observing a selection of about 70 double-lined binaries (SB2s) with the T193/SOPHIE in order to improve their orbital elements. Our goal is to obtain the masses of the components with a 1 % accuracy when the astrometric observations of Gaia are available.

After 6 semesters of observations, the two best observed stars are HIP 12081 and HIP 87895. These stars are used to verify that the 1 % accuracy could really be obtained at the end of the programme. The radial velocities of their components were derived using the TODMOR algorithm, and their orbital elements were calculated. It appears that the minimum masses of the components of HIP 12081 are already both obtained with an accuracy around 0.5 %. For HIP 87895, the relative precisions of the minimum masses of the primary and of the secondary component are 2.7 and 1.5 %, respectively, but they were obtained from only 9 spectra and they should be improved once more observations have been obtained.

Ancient interferometric observations of HIP 87895 are also taken into account and the actual masses of the components are derived. Although these measurements are far from being as accurate as those expected from Gaia, the relative errors of the masses are only 2.6 and 1.5 % respectively. We thus conclude that our programme would lead to masses with the announced accuracy if the observations are continued.

Keywords: binaries: spectroscopic, Stars: fundamental parameters, stars: individual: HIP 12081, HIP 87895

1 Introduction

The double-lined spectroscopic binaries (SB2s) are at the root of the less model–dependent methods used to derive the stellar masses. Their orbital elements are used to derive the products $\mathcal{M}_* \sin^3 i$, where $\mathcal{M}_*$ is the mass of a component and i is the inclination of the orbital plane. Therefore, when the inclination may be obtained from another technique, such as eclipse observations or astrometric measurements, the accuracy of the masses amply depends on that of the SB2 orbital elements.

Gaia will provide an opportunity to derive stellar masses with errors around 1 %, by combining Gaia astrometry with accurate SB2 orbital elements. For that purpose, a large observation program is going on at the Observatoire de Haute-Provence (OHP) with the T193/SOPHIE, in order to improve the orbital elements of a selection of known SBs (Halbwachs & Arenou 2009). The observed sample contains 207 SBs: 50 known SB2s, but also 157 stars which are known as SB1s, since the components of some of them may be separated for the first time thanks to the SOPHIE spectrograph.

In Sect. 2, we present the number of spectra and the classification of the programme stars after 6 semesters of observations. Two stars (HIP 12081 and HIP 87895) are selected on the basis of the number and of the distribution of the measurements they received, and their radial velocities (RV) were obtained as explained in Sect. 3. The spectroscopic orbital elements of these stars, including the minimum masses of their components, are derived in Sect. 4 and 5. The actual masses of the components of HIP 87895 are derived from interferometric measurements in Sect. 6. Sect. 7 is the conclusion.

* BASED ON OBSERVATIONS PERFORMED AT THE HAUTE-PROVENCE OBSERVATORY

[1] Observatoire Astronomique de Strasbourg, UMR 7550, 11, rue de l'université, F-67000 Strasbourg, France

[2] GEPI, Observatoire de Paris, F-92195 Meudon, France

[3] FNRS, Institut d'Astronomie et d'Astrophysique, Université libre de Bruxelles, boulevard du Triomphe, 1050 Bruxelles, Belgium

[4] School of Physics and Astronomy, Tel Aviv University, Tel Aviv 69978, Israel

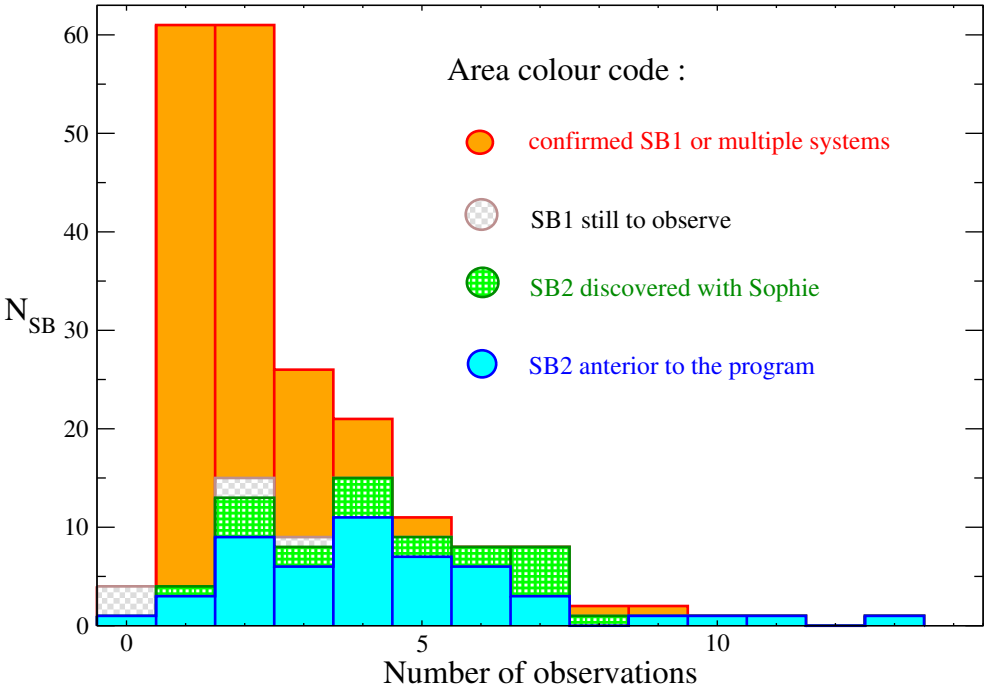

Fig. 1. Histogramme of the programme stars according to the numbers of spectra they received.

2 Status of the programme

The observing programme began in April 2010, and, after 6 complete semesters, we have collected 572 spectra. Each component was detected for 21 SB1s. Some of them were announced in Halbwachs et al. (2011). One hundred and thirty SB1s were discarded from the observations, since they were confirmed as SB1s, or appeared to be multiple systems. The status of 6 SB1s is still uncertain. These stars have eccentric orbits, low RV semi-amplitudes, and long periods; therefore, we are still waiting for the moment when the difference between the velocities of the components could be sufficient to separate the components on the spectrum.

The distribution of the stars according to their status and to their numbers of spectra is presented in Fig. 1. It thus appears that the majority of the SB2 stars received only 4 spectra or even less. It is worth noticing that the minimum number of spectra to derive an SB2 orbit is theoretically 4, when the RV of both components are obtained from each of them. However, if we want to check the reliability of the RV uncertainties for each component, it is necessary to derive the individual orbit of each component, and a minimum of 7 RV measurements is required. In practice, it is also necessary to have observations nearly equally distributed on at least a complete period. The following criteria are finally retained for selecting SB2s usable to derive an assessment: a minimum of 8 RV measurements for each components, and a minimum of one period covered by the observations. Two stars were thus selected, which are HIP 12081 and HIP 87895.

3 Derivation of the Radial Velocities with TODMOR

The RVs of each one of the binary components, as well as their atmospheric parameters and the flux ratio between them, were determined from the SOPHIE spectra using TODMOR (Zucker & Mazeh 1994; Zucker et al. 2004) — a two-dimensional correlation algorithm. In TODMOR, the cross-correlation functions are calculated separately for each echelle order, and then combined to a single cross-correlation function according to the scheme proposed by Zucker et al. (2003).

To construct the templates we used the Phoenix library of synthetic spectra (Hauschildt et al. 1999), with varying values of effective temperature $T_{\rm eff}$, surface gravity $\log g$, metallicity $[m/H]$ and rotational velocity $v \sin i$. The library spans the following intervals in atmospheric parameters: 3000K $< T_{\rm eff} <$ 10000K, $-0.5 < \log g < 5.5$ (cgs), and $-1.5 < [m/H] < +0.5$. The spacing in $T_{\rm eff}$ is 100K for $T_{\rm eff} <$ 7000K, and 200K elsewhere. The spacing in $\log g$ and $[m/H]$ is 0.5 dex. The interval and spacing of $v \sin i$ values in our algorithm are free

Table 1. Best set of template parameters used in TODMOR, and orbital elements of the SB2 orbits. The numbers of measurements separated by "+" refer to the primary and to the secondary components. The two values of σ_{o-c} refer to the RVs of the primary and of the secondary components.

Parameter	HIP 12081	HIP 87895
$T_{\rm eff,A}$ [K]	6600	6000
$\log g_{\rm A}$ [dex]	4.5	4.5
$v \sin i_{\rm A}$ [km s^{-1}]	10	$\lesssim 1$
$T_{\rm eff,B}$ [K]	6000	4500
$\log g_{\rm B}$ [dex]^a	4.5	4.5
$v \sin i_{\rm B}$ [km s^{-1}]	4	$\lesssim 1$
[m/H] [dex]	-0.5	0.0
α [flux ratio]	0.53	0.03
N_{meas} SOPHIE	10 + 10	9 + 8
ΔT (days)	883	1008
Period (days)	443.402 ± 0.114	877.97 ± 1.56
T_0 (BJD−2 400 000)	55906.166 ± 0.979	55651.712 ± 15.0
e	0.58596 ± 0.00130	0.42093 ± 0.00220
ω (deg)	284.240 ± 0.179	135.209 ± 0.362
V_γ (km/s)	-6.4297 ± 0.0175	-30.8650 ± 0.0269
K_1 (km/s)	16.7484 ± 0.0455	11.4134 ± 0.0166
K_2 (km/s)	18.1598 ± 0.0399	17.242 ± 0.212
$a_1 \sin i$ (Gm)	82.747 ± 0.203	124.996 ± 0.353
$a_2 \sin i$ (Gm)	89.719 ± 0.165	188.82 ± 2.33
$\mathcal{M}_1 \sin^3 i$ ($\mathcal{M}_\odot$)	0.54092 ± 0.00259	0.9612 ± 0.0260
$\mathcal{M}_2 \sin^3 i$ ($\mathcal{M}_\odot$)	0.49888 ± 0.00275	0.63629 ± 0.00964
σ_{o-c} (km/s)	0.0428/0.0711	0.0301/0.224

^{a}: Parameter values assumed without optimization.

parameters set by the user, since each synthetic spectrum chosen from the library is convolved with a rotational profile G(v) (e.g., Gray (2005), p. 465; Santerne et al. (2012)) and a Gaussian representing the instrumental broadening of the lines, just before calculating cross-correlation function.

First, we applied TODMOR only to the spectra taken close to quadratures, varying the values of the primary and secondary atmospheric parameters and the flux ratio between them, to derive the best set of template parameters — the one that yielded the highest two-dimensional correlation peak. Then, we fixed all template parameters and applied TODMOR to all of the observed spectra to derive the primary and secondary RVs in each exposure.

The best set of template parameters are listed in Table 1. Fig. 2 shows the TODMOR results for the third SOPHIE exposure of HIP 87895. The upper and lower panels of the figure show primary and secondary *cuts* through the two-dimensional correlation function that run through the correlation peak. The primary cut (upper panel) is parallel to the primary RV axis, freezing the secondary velocity at its derived velocity, while the secondary cut (lower panel) runs parallel to the secondary RV axis, freezing the primary velocity at its derived velocity.

We note that in the upper panel the correlation drops by ~ 0.5 when moving away from the peak, because we change the velocity of the *primary* template in the model. On the other hand, the correlation in the lower panel drops only by ~ 0.003, because we change the velocity of the *secondary* template, which contributes only $\sim 3\%$ of the light. The additional peak in the lower panel at the primary RV is probably caused by imperfect modeling of the primary line profiles, which prevents correct derivation of the secondary RV from exposures made close to alignment.

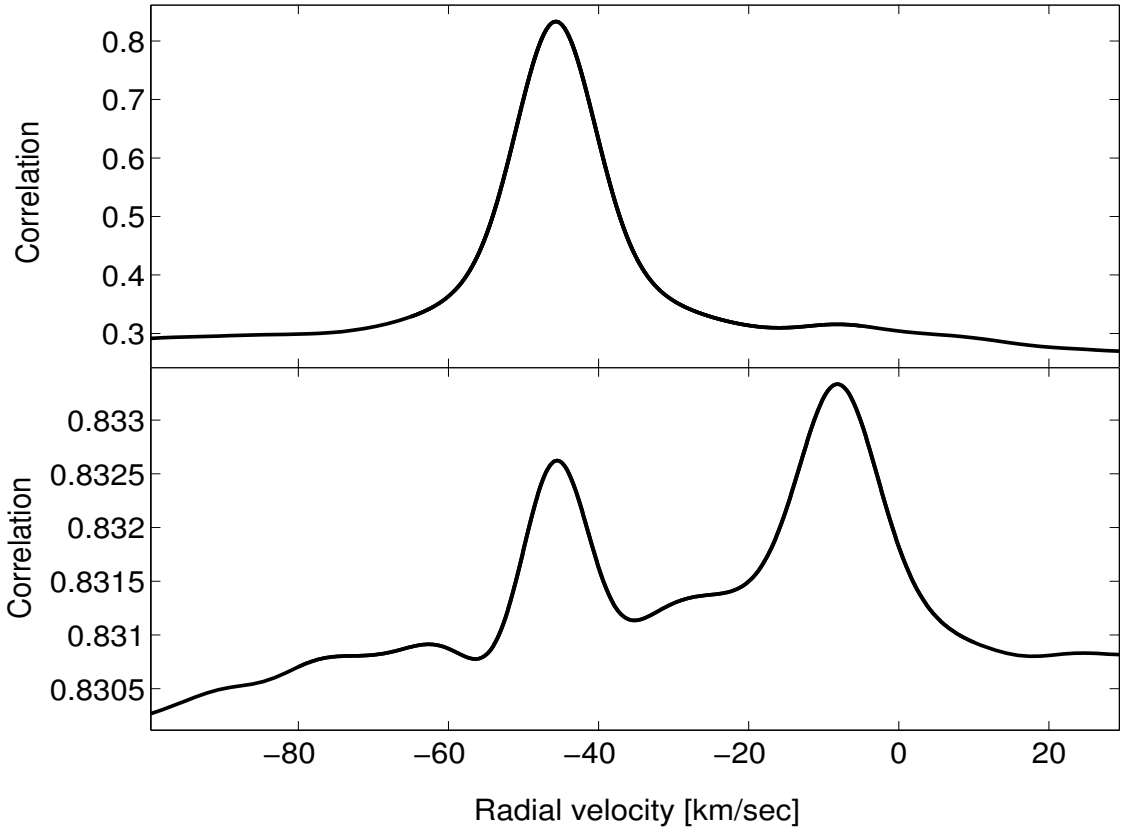

Fig. 2. TODMOR plot for the third SOPHIE exposure of HIP 87895. The upper and lower panels show the primary and secondary *cuts* through the two-dimensional correlation function. Note the different scale.

4 Spectroscopic orbit of HIP 12081

Ten spectra of HIP 12081 were obtained, and the radial velocities of both components were derived for each of the 10. The flux ratio of this system is rather large (0.53), and the accuracy of the RVs is altered by the contamination of the spectrum of each component by that of the other. The uncertainties thus are around 70 m/s for the RV of the primary component, and around 90 m/s for that of the secondary. The elements of the SB1 orbit were derived for the primary and for the secondary component, and the F_2 estimator of the goodness-of-fit (Stuart & Ord 1994) was -1.16 and +1.39, respectively. Since F_2 is a random variable obeying the standard normal distribution, we infer that the uncertainties of the RVs obtained from TODMOR are quite reliable, and they are assumed hereafter.

Another point to be verified is the coincidence of the zero of the RVs of the primary and of the secondary components. Using inadequate templates would introduce a shift of the RVs of one component with respect to the other. This shift is added to the unknowns of the model, and it is thus found that the secondary RVs could be smaller than the primary ones, with the difference: (-95.1 ± 56.8) m/s. This value is not significant, however, since it may be obtained at random with a 9.3 % probability. It is probably much smaller than -95.1 m/s in reality, and it was decided to ignore it.

The solution derived from the SOPHIE measurements is presented in Table 1. It thus appears that the minimum masses of the components, $\mathcal{M}_{1,2} \sin^3 i$, are obtained with errors as small as 0.48 and 0.55 %. It is quite possible that the masses will be evaluated with errors smaller than 1 % once the Gaia astrometric measurements are available, although this is not certain: the final errors will depend on the actual inclination of the system (Halbwachs & Arenou 2009).

A previous orbit was obtained by Griffin (2005), based on 47 RV observations. Since these RV received all

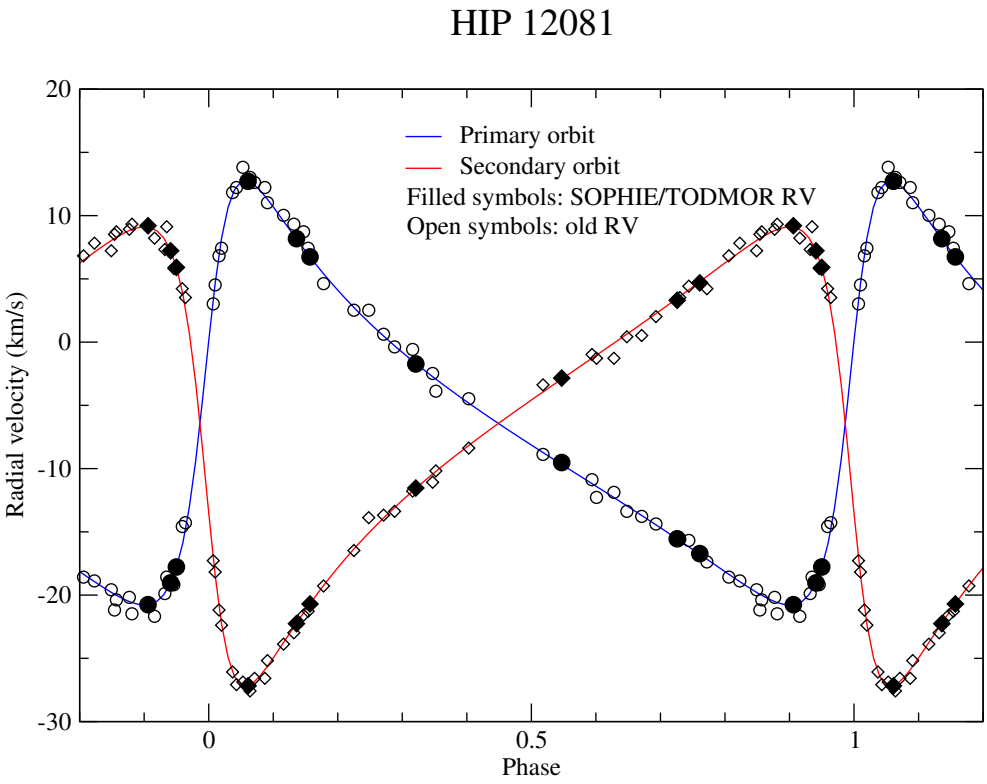

Fig. 3. SB2 orbit of HIP 12081, assuming the elements in Table 2. The circles are the RV measurements of the primary component, and the diamond that of the secondary component. The old measurements are from Griffin (2005).

the same weight, we fix their uncertainties to 0.57 km/s, in order to recover the Griffin's orbit with $F_2 = 0$. The uncertainties of the relative errors of the minimum masses are as large as 2.0 and 1.9 %, respectively. However, when these measurements are added to the SOPHIE RVs to derive again the orbital elements, the uncertainty of the period is significantly improved (see the new elements in Table 2, and the plot of the orbit in Fig. 3). As a consequence, the relative errors of the minimum masses are finally 0.46 and 0.52 %, respectively. It is worth noticing that the improvement with respect to the results obtained from our RVs alone is nearly negligible.

5 Spectroscopic orbit of HIP 87895

Eight spectra of HIP 87895 were obtained during the first six semesters of the programme, but a ninth spectrum has been obtained in May 2013. The secondary component is much fainter than the primary one (the flux ratio is only 3 %, see Table 1), and it was not possible to derive the RV of the secondary from one of the spectra. The RV uncertainties are about 30 m/s for the primary component, but 450 m/s for the secondary. It is possible, however, that the uncertainties of the RV of the secondary component were overestimated: when a SB1 orbit is derived from these measurements, the goodness-of-fit is $F_2 = -1.99$, and the probability to be so far from 0 by random is only 4.7 %. Alternatively, $F_2 = 0$ when the uncertainties are divided by 7.9, leading to actual errors around 60 m/s. This will be clarified in the future, once more measurements are available; for the moment, the uncertainties estimated by TODMOR are assumed. It is worth noticing that the SB1 orbit of the primary component is obtained with $F_2 = 1.42$, which is quite acceptable, but which could also suggest that the primary RVs have uncertainties that could be around 68 % larger than that assumed. Anyway, the SB2 orbit in Table 1 was obtained with $F_2 = -0.03$, indicating that the overestimation of the errors of one component, if it really exists, is perfectly compensated by the possible underestimation of the errors of the other. At the end, in view of the mean residuals of the SB2 orbit, Table 1 confirms the idea that the uncertainties of the secondary RVs are smaller than assumed, but by a factor of about 2 rather than 7.9. On the other side, the uncertainties of the primary RVs seem a bit larger than the assumed 30 m/s.

Another point to be verified is the possible shift between the RVs of both components. A calculation indicated that this shift could be (152 ± 183) m/s. Its large uncertainty makes the shift not significant at all,

Table 2. The orbital elements of the SB2 orbits when the ancient measurements are added to the SOPHIE RVs.Data about the SOPHIE observations alone are in Table 1

Parameter	HIP 12081	HIP 87895
N_{meas} Ancient	47 + 47	106 + 16
$RV_{SOPHIE} - RV_{Ancient}$	0.4195 ± 0.0634	1.9108 ± 0.0483
ΔT (days)	4486	13041
Period (days)	443.3377 ± 0.0335	881.6355 ± 0.0785
T_0 (BJD−2 400 000)	55906.160 ± 0.979	55650.250 ± 0.789
e	0.58560 ± 0.00121	0.41776 ± 0.00123
ω (deg)	284.241 ± 0.172	135.328 ± 0.327
V_γ (km/s)	-6.4285 ± 0.0609	-30.8955 ± 0.0446
K_1 (km/s)	16.7659 ± 0.0421	11.4010 ± 0.0161
K_2 (km/s)	18.1578 ± 0.0372	17.190 ± 0.201
$a_1 \sin i$ (Gm)	82.848 ± 0.191	125.585 ± 0.170
$a_2 \sin i$ (Gm)	89.726 ± 0.157	189.35 ± 2.21
$\mathcal{M}_1 \sin^3 i$ ($\mathcal{M}_\odot$)	0.54178 ± 0.00247	0.9627 ± 0.0248
$\mathcal{M}_2 \sin^3 i$ ($\mathcal{M}_\odot$)	0.50025 ± 0.00260	0.63850 ± 0.00910
σ_{o-c} SOPHIE (km/s)	0.0490/0.0722	0.0394/0.202
σ_{o-c} Ancient (km/s)	0.634/0.541	0.84/1.24

and leads to assume that it is probably negligible.

The orbital elements of HIP 87895 were derived from the SOPHIE RVs, and they are summarized in Table 1. The relative uncertainties of the minimum masses of the two components are 2.7 and 1.5 %, respectively.

This star was observed in the past, and McAlister et al. (1995) collected RVs from 5 different sources. They obtained 106 measurements of the primary component, but the secondary was observed only 16 times. Again, the uncertainties were derived from the weights, and all the secondary RVs receive $\sigma_{RV} = 2.43$ km/s. With so large errors, it is not surprising that, despite the number of measurements, the relative errors of the masses of the orbit of McAlister et al. were as large as 7.7 and 4.3 %, respectively.

The calculation of the elements was done again, adding the ancient RVs to the SOPHIE RVs. The results are in Table 2, and the orbit is plotted on Fig. 4. Again, the extension of the timespan of the observation leads to significantly improve the accuracy of the period. Nevertheless, the final relative uncertainties of the minimum masses of the two components are 2.6 and 1.4 %, respectively, instead of 2.7 and 1.5 %. The improvements due to the ancient measurements are very small when the minimum masses are considered.

6 Masses of the components of HIP 87895

HIP 87895 is not only known as a SB, but it is also a "visual" binary, with 24 observations of the position of the secondary with respect to the primary recorded in the on-line catalogue described in Hartkopf, Mason & McAlister (2001). Twenty-one observations were performed with telescopes with diameters between 1 and 6 m, and have very large errors. Fortunately, 3 were obtained from an interferometer with a 110 m long base and have separations with errors around 0.3 or 0.4 mas. So it is possible to derive the inclination of the orbit, and the masses of the components.

The common solution obtained from all these data is not satisfactory, since we obtained $F_2 = 4.81$. This comes obviously from the censoring of the measurements when the actual separation is too close for the telescope: only measurements with large overestimation of the angular separation are then possible. This appears clearly on Fig. 5, where the 3 measurements in the South have all very large errors when the components were very close in reality. In order to avoid this problem, we decided to keep only the 3 observations obtained with a long-base interferometer. It is worth noticing that the astrometric measurements are two-dimensional, and that the contribution of the astrometric data results in adding to the orbit only three more elements (the inclination,

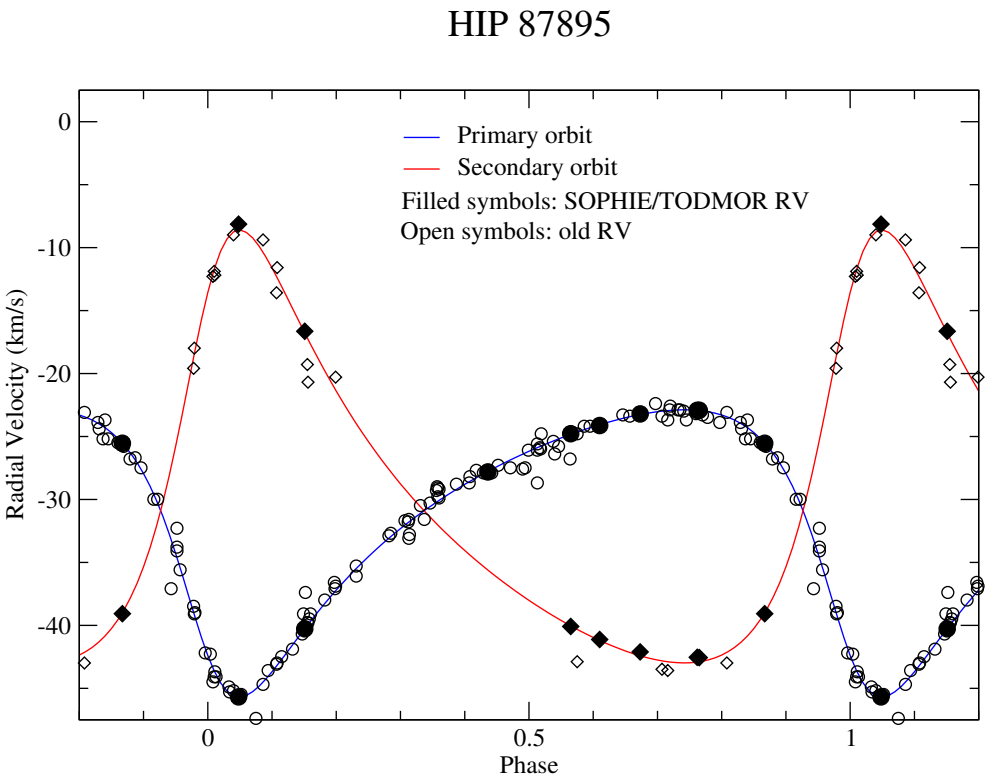

Fig. 4. SB2 orbit of HIP 87895. The circles are the RV measurements of the primary component, and the diamond that of the secondary component. The old measurements are from McAlister et al. (1995).

the position angle of the ascending node, and the parallax of the system). Therefore, only two astrometric measurements would even have been sufficient.

A combined solution was thus obtained from all the RVs and from the 3 accurate astrometric measurements. The inclination is (72.852 ± 0.367) deg, and the masses are $\mathcal{M}_1 = (1.1033 \pm 0.0292)\mathcal{M}_\odot$ and $\mathcal{M}_2 = (0.7317 \pm 0.0113)\mathcal{M}_\odot$. The relative uncertainties are 2.6 and 1.5 %, ie almost the same as for the minimum masses obtained from the spectroscopic data alone. For comparison, McAlister et al. (1995) found $\mathcal{M}_1 = (1.16 \pm 0.12)\mathcal{M}_\odot$ and $\mathcal{M}_2 = (0.77 \pm 0.05)\mathcal{M}_\odot$.

The combined solution includes also the parallax of the binary, which is $\varpi = (36.629 \pm 0.220)$ mas. Again, this result is much better than that of Pourbaix (2000), who found $\varpi = (37. \pm 1.8)$ mas. The improvement is due to the quality of the long-base interferometric measurements, but also to that of the RVs obtained from SOPHIE and TODMOR.

7 Conclusion

After 3 years of observations, two stars of our program received enough SOPHIE observations for a first verification of the quality of data. It was found that, when the two components have similar brightnesses, the minimum masses of the components may be obtained with uncertainties quite smaller than 1%, even when the number of spectra is only 10. When the secondary component is faint, the uncertainties of the RVs obtained from TODMOR are a bit large, and the errors of the minimum masses may be around 2 or 3 %. However this was obtained from only 9 spectra, and the accuracy should be much better when more observations will be available.

Errors around 2.7 and 1.5 % were obtained for the masses of the components of HIP 87895, using only 3 interferometric relative positions with errors around 0.3 mas. Since Gaia will provide astrometric measurements in a large quantity and with a much better accuracy, and taking into account the fact that the orbit of the Gaia photocenter will be only 9 times smaller than the relative orbit, we still expect an improvement with the astrometric data by a factor around 2 or 3. In conclusion the announced accuracy of 1 % should be reached for a large part of the 140 components of our programme, if the observations are continued.

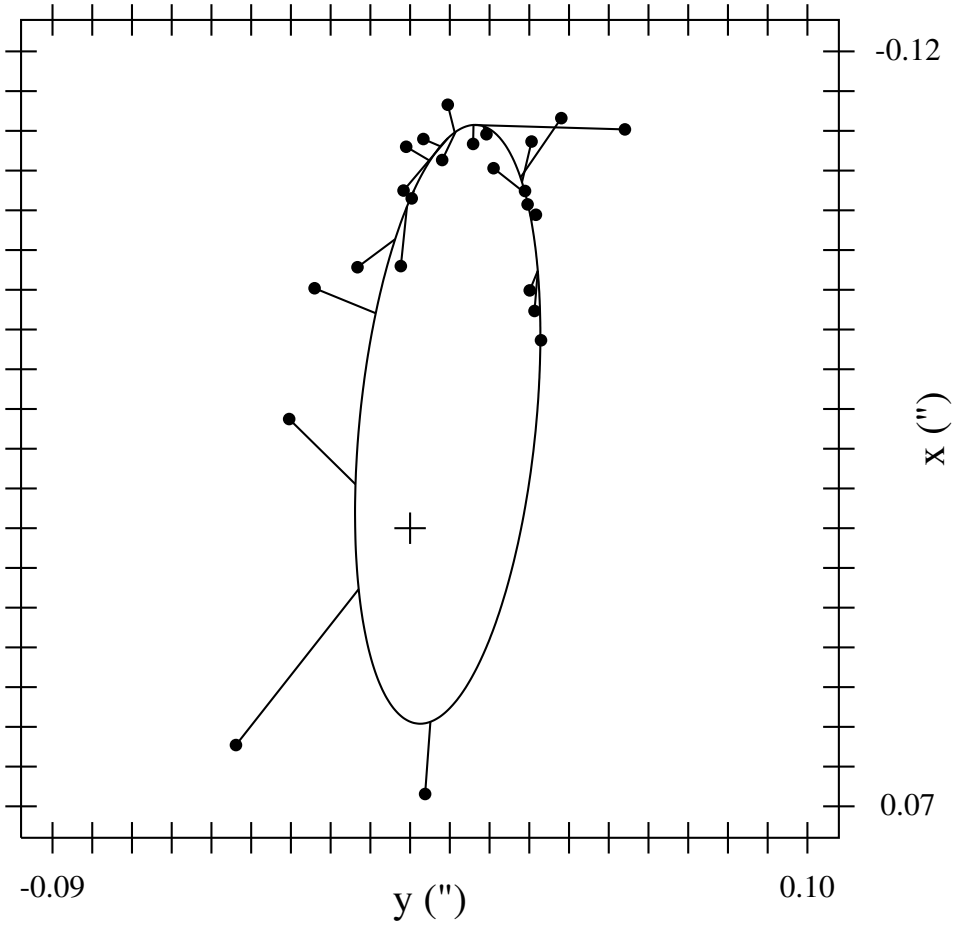

Fig. 5. A preliminary solution of "visual" orbit of HIP 87895, obtained combining the RVs and the apparent positions. It is easy to recognize the three long-base interferometric measurements, since they fit perfectly the orbit.

This programme is supported by the PNPS and by the Action Spécifique Gaia. We are grateful to the staff of the OHP for their kind assistance. Jean-Baptiste Salomon participated to the observations. The SB9 database, `http://sb9.astro.ulb.ac.be/`, (Pourbaix et al. 2004) was used to recover the ancient measurements.

References

Gray, D. F. 2005, "The Observations and Analysis of Stellar Photospheres, 3rd Edition, by D. F. Gray. ISBN 0521851866. Cambridge, UK: Cambridge University Press, 2005."

Griffin, R.F. 2005, the Observatory, 185, 367

Halbwachs, J.-L., Arenou, F. 2009, Proceedings SF2A 2009, M. Heydary–Malayeri, C. Reylé et R. Samadi édr., p. 53

Halbwachs, J.-L., Arenou, F., Famaey, B., Guillout, P., Lebreton, Y., & Pourbaix, D. 2011, Proceedings SF2A 2011 – G. Alecian, K. Belkacem, S. Collin, R. Samadi & D. Valls-Gabaud edr., 303

Hartkopf, W.I., Mason, B.D., McAlister, H.A. 2001 AJ, 122,3480, Fourth Catalogue of Interferometric Measurements of Binary Stars, http://ad.usno.navy.mil/wds/int4.html

Hauschildt, P. H., Allard, F., & Baron, E. 1999, ApJ, 512, 377

McAlister, H.A., Hartkopf, W.I., Mason, B.D., Fekel, F.C., Tokovinin, A.A., Griffin, R.F., & Culver, R.B. 1995, AJ, 110, 366

Pourbaix, D. 2000, A&AS, 145, 215

Pourbaix, D., Tokovinin, A.A., Batten, A.H. et al. 2004, A&A 424, 727

Santerne, A., Moutou, C., Barros, S. C. C., et al. 2012, A&A, 544, L12

Stuart, A., & Ord, K. 1994, Kendall's Advanced Theory of Statistics, vol. 1 (Edward Arnold, London)

Zucker, S., & Mazeh, T. 1994, ApJ, 420, 806

Zucker, S., Mazeh, T., Santos, N. C., Udry, S., & Mayor, M. 2003, A&A, 404, 775
Zucker, S., Mazeh, T., Santos, N. C., Udry, S., & Mayor, M. 2004, A&A, 426, 695

SF2A 2013
L. Cambrésy, F. Martins, E. Nuss and A. Palacios (eds)

KINEMATIC VERSUS SPECTROSCOPIC RADIAL VELOCITIES FOR THE GAIA RVS

G. Jasniewicz[1], F. Thévenin[2], A. Chiavassa[2], L. Bigot[2], L. Chemin[3], F. Crifo[4], D. Hestroffer[5], D. Katz[4], P. Sartoretti[4], C. Soubiran[3], S. Udry[6] and C. Zurbach[1]

Abstract. The Gaia spectrometer (RVS) has no built-in calibration device and the RVS will rely on its own observations to carry out the wavelength calibration. A small sample ($\sim$ 1420) of bright RVS F-G-K standard stars will be used for the Radial Velocity Zero Point (RVZP) of the RVS. These standard stars have been observed on the ground with the Sophie, Coralie and Narval spectrometers, and their Spectroscopic Radial Velocities (SRVs) have been published by Soubiran et al. (2013). These SRVs are not Kinematic Radial Velocities (KRVs) which are what we need for studies of galatic dynamics. However in this paper we show that these SRVs are well suited to establish the Radial Velocity Zero Point of the Gaia RVS, provided that CU6 pipelines of the DPAC such as Calibration of the RVS (DU630) and Determination of RVs by cross-correlation with templates (DU650 STA) really use wavelength lines and spectra computed with 3D hydrodynamical model atmospheres, which conveniently treat the convective shifts. Final SRVs given by the Gaia CU6 pipelines and later published in the Gaia final catalogue would then only be corrected from the gravitational shift by the DPAC CU8 in order to become true KRVs.

Keywords: Gaia, RVS, Radial velocities

1 Introduction

Reference stars have been observed on the ground and their RVs will be used to determine the RVZP of the Gaia RVS. This RVZP will also be checked by asteroids, even if bright asteroids ($V < 10$) will not be often observed by the RVS (see Jasniewicz et al. 2011). A lot of ground-based observations of reference stars selected by Crifo et al. (2010) and asteroids have been performed during 5 years at Observatoire de Haute Provence, Pic du Midi and La Silla (Chile). Radial Velocities of these objects have been determined thanks to standard pipelines by Cross-Correlation techniques using stellar masks. The main point of this paper is to give some preliminary results concerning the comparison between observed and computed RVs of asteroids, as they are the only sources for which both RVs are available, and to investigate the best strategy to determine the RVZP for the Gaia RVS.

In the following, the Kinematic Radial Velocity of an object (star or asteroid) is defined as the line-of-sight component of space velocity whereas the Spectroscopic Radial Velocity is deduced from observed spectral-line displacements interpreted as Doppler shifts. Intrinsic stellar spectroscopic effects such as convective motions in the stellar atmosphere and gravitational redshift imply that the measured wavelengths do not correspond to the precise centre-of-mass motion of the star. According to the general theory of relativity, the gravitational redshift is GM/cR. This shift is 636 m.s^{-1} for the Sun, and for a typical white dwarf of 0.6M$_{\rm sun}$ it is between 5 to 13 km.s^{-1}.

If we reduce the solar wavelengths to a system at rest with respect to the solar center of mass, and if we correct the solar wavelengths from the gravitational redshift, then the solar absorption lines generally (not all) appear blueshifted with regard to laboratory wavelengths ; these shifts are connected to convective motions in the

[1] LUPM UMR 5299 CNRS/UM2, Université Montpellier II, CC 72, 34095, Montpellier Cedex 05, France
[2] Laboratoire Lagrange, CNRS, Université de Nice Sophia-Antipolis, Nice, 06300, France
[3] LAB UMR 5804, Univ. Bordeaux - CNRS, 33270, Floirac, France
[4] GEPI, Observatoire de Paris, CNRS, Université Paris Diderot, 5 place Jules Janssen, 92190, Meudon, France
[5] IMCCE, Observatoire de Paris, UPMC, CNRS UMR 8028, 77 Av. Denfert-Rochereau, 75014, Paris, France
[6] Observatoire de Genève, Université de Genève, 51 Ch. des Maillettes, 1290, Sauverny, Switzerland

Table 1. Observed Radial Velocities versus Computed Radial Velocities of asteroids

Spectrometer + Telescope	Number of measurements	$< O-C >$ m.s^{-1}	σ m.s^{-1}
Coralie + La Silla, Euler swiss telescope	42	19.4	58.6
Sophie + OHP, 193cm	184	37.7	31.1
Narval + OPM, TBL	78	44.5	19.8

atmosphere. Dravins (1982) has shown that typical solar photospheric lines are blueshifted by about 400 m.s^{-1}. 1D atmospheric models do not take into account convective shifts. If the estimated errors on RV given by the Gaia RVS are really smaller than 1km.s^{-1} for G-stars, it will be possible to test the accuracy of convective shifts included in 3D model atmospheres because the KRV of the nearest stars will also be derived from astrometry. In this paper, we firstly give some results concerning the comparison between Observed and Computed RVs of asteroids by the IMCCE (Institut de Mécanique Céleste et de Calcul des Ephémérides) herefater called $O-C$; secondly we recall some recent results concerning the convective shift in stars ; and finally we discuss the way to transform the RVS SRVs into KRVs.

2 Observed versus Computed Radial velocities of asteroids

Computed Kinematic Barycentric Radial Velocities of asteroids are given by :
KBRV = KGRV + KRV$_{\rm sun}$−BERV
where:
KGRV is the Geocentric Radial Velocity of the asteroid
KRV$_{\rm sun}$ is the component due to the asteroid's radial motion toward the Sun
BERV is the Barycentric Earth´s Radial Velocity

In the following, we write O − C = SRV$_{\rm (observed)}$− KBRV$_{\rm (computed)}$

Asteroids reflect the solar light, thus their spectra include the gravitational and convective solar shifts. At first we assume that the G2 masks built for Sophie/Coralie/Harps are wavelength-calibrated with 1D synthetic spectra of the Sun ; since the observed solar spectrum is blueshifted by 0.4 km.s^{-1} with regard to these masks (see Sect. 1), the RV of an asteroid determined by cross-correlation with such a mask should be corrected from the convective and gravitational shifts of the Sun (see Sect. 1): -0.4 + 0.6 km.s^{-1}, that is about 0.2 km.s^{-1}. But the average $< O-C >$ of asteroids given in Table 1 are much smaller for each ground-based instrument. Residuals O-C are also plotted for each asteroid in Fig. 1 as a function of phase. Here we have chosen the phase on the abcissa, only because there is no obvious correlation between phase and O-C. The very small values for O-C mean that there is somewhere in the software pipelines and/or the building of the masks a compensation of the solar gravitational redshift and convective shifts. This point is still under investigation for details.

3 Observed Radial velocities versus Kinematic Radial velocities of stars

Realistic modelling of stellar atmospheres is crucial for a better interpretation of future Gaia data and, in this context, three-dimensional (3D) Radiative-HydroDynamical (RHD) models such as these developed by Magic et al. (2013) are needed for a quantitative correction of the radial velocities (few hundreds m.s^{-1}) for all the stars observed and, in evolved stars, for the determination of the photocenter positions. According to Chiavassa et al. (2011) the convective lineshift is stronger for high excitation lines and it ranges, in average, from -0.22 km.s^{-1} (K giant with [Fe/H]=-3.0) to -0.75 km.s^{-1} (F star).The amplitude of the shift increases when going from K giants to the F star, as a consequence of the more vigorous convective motions. Moreover, the Ca II triplet lines are *redshifted* because these lines are formed in the upper part of the photosphere where the granulation pattern is reversed. Red supergiant stars (RSGs) show a completely different behavior with strong redshifted Fe I up to 2.80km.s^{-1} and blueshifted Ca II up to 8km.s^{-1} In conclusion, velocity shifts of F and K giant stars are of the order of RVS accuracy (1km.s^{-1}), and they are even larger for RSG stars.
If the stellar masks used for ground-based observations of stars are wavelength-calibrated from observed spectra (see also Sect.2), then RVs determined by Cross-Correlation are true KRVs for all stars whose spectra are very

close to these masks. We can expect some residuals between SRVs and KRVs for all other stars in the CU6 catalogue of standard stars by Soubiran et al. (2013).

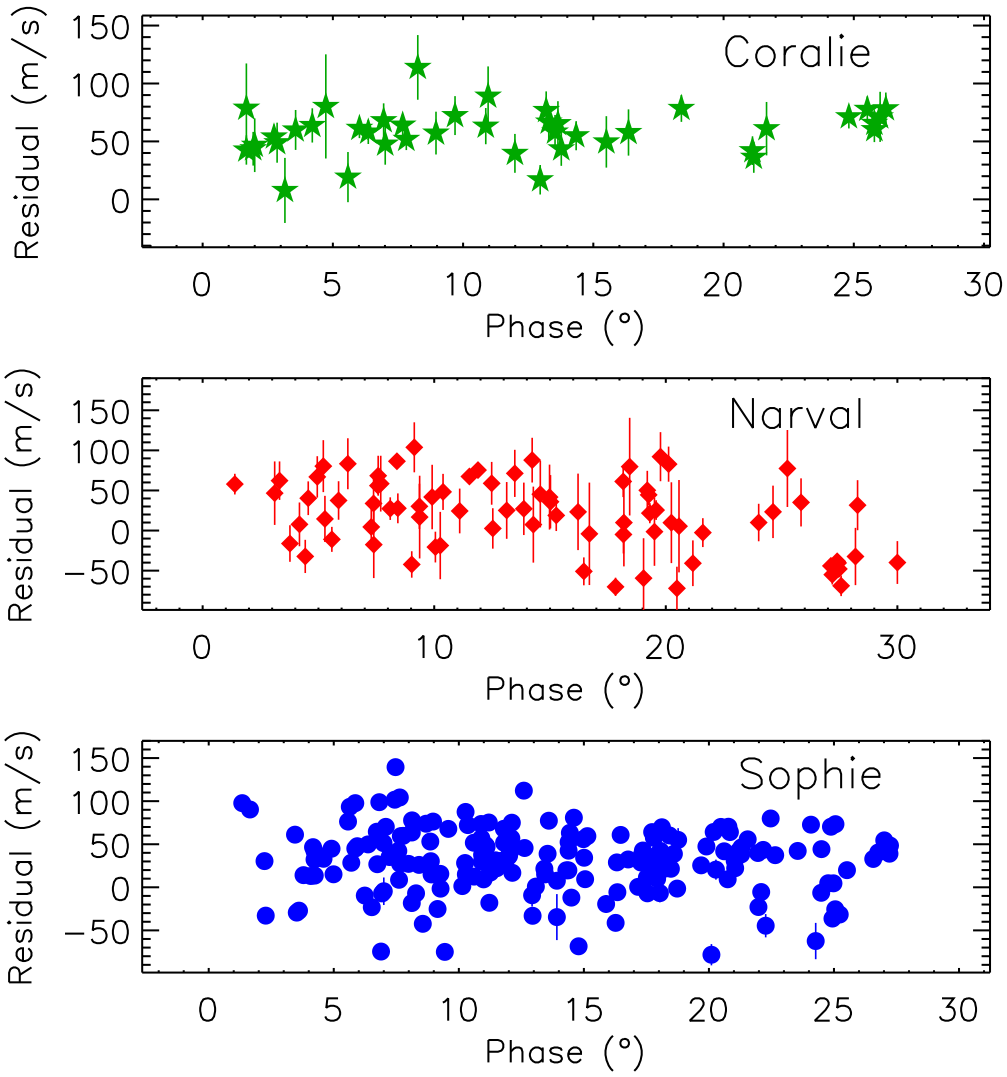

Fig. 1. Residual O(bserved) - C(omputed) Radial Velocities of asteroids versus the phase. Observed Coralie, Narval and Sophie RVs have been determined by Cross-Correlation with G2 masks. Computed RVs come from the IMCCE.

4 Conclusions

In the CU6 Gaia context, we have called Astrophysical Zero Point (AZP) the corrections to be made on the RVS Spectroscopic Radial Velocities (SRVs) in order to get Kinematic Radial Velocities. According to this poster and the Technical Note (TN) GAIA-C6-TN-FT-001-1 by Thévenin et al. (2011)at the ESA livelink, we strongly recommend the use of 3D RHD atmosphere models for both CU6 and CU8. The critical points are the following :

- SRVs of the RVS STD stars published by the DU640 team (Soubiran et al. 2013), seem to be rather well corrected from the convective shift (see Sect. 3), and rigorously corrected from the convective and gravitational shifts for stars the spectrum of which is very near of a mask used in the ground-based pipelines (Sophie, Coralie, Harps, etc). Thus these published RVs which will be used for the RV Zero Point (RVZP) of the RVS, are KRVs.
- The 3D RHD models take into account the convective shift. As a consequence, the RVS CU6 pipelines such as Calibration (DU630) and STA (DU650) should use them, and would be consequently compatible with the DU640 Catalogue of RVs.

- AZP software will only correct the RVS RVs from the gravitational redshift thanks to the APs determined by CU6 and CU8.

Abbreviations used in the text
AP : Astrophysical Parameter
AZP : Astrophysical Zero Point
CC : Cross- Correlation
DU : Development Unit
KBRV : Kinematic Barycentric Radial Velocity
KRV : Kinematic radial velocity
O-C : O(bserved)-C(omputed) radial velocities
RHD : Radiative HydroDynamical
RV : Radial Velocity
RVZP : Radial Velocity Zero Point
SRV : Spectroscopic Radial Velocity
RVS : Gaia Radial Velocity Spectrometer
TN : Technical Note
WP: Work Package

Many thanks to the CNRS national programs (PNPS, PNG) and AS Gaia for their support in funding the ground-based observing runs at Observatoire de haute Provence, TBL Pic du Midi, and swiss telescope at ESO, La Silla. A follow up of these observations during the next 5 years is mandatory in order to check the high RV stability of our RVS standard stars during the Gaia project. Discussions with scientists on the making of the masks used in the Sophie, Coralie and Harps pipelines are in progress, and we especially thank very much D. Queloz, F. Bouchy, C. Lovis and M. Mayor for their help.

References

Chiavassa, A., Bigot, L., Thévenin, F., et al. 2011, Journal of Physics Conference Series, 328, 012012

Crifo, F., Jasniewicz, G., Soubiran, C., et al. 2010, A&A, 524, A10

Dravins, D. 1982, ARA&A, 20, 61

Jasniewicz, G., Crifo, F., Soubiran, C., et al. 2011, in EAS Publications Series, Vol. 45, EAS Publications Series, 195–200

Magic, Z., Collet, R., Asplund, M., et al. 2013, A&A, 557, A26

Soubiran, C., Jasniewicz, G., Chemin, L., et al. 2013, A&A, 552, A64

SF2A 2013
L. Cambrésy, F. Martins, E. Nuss and A. Palacios (eds)

MODEL ATMOSPHERES AND FUNDAMENTAL STELLAR PARAMETERS

B. Plez[1]

Abstract. I start by illustrating the need for precise and accurate fundamental stellar parameters through there examples: lithium abundances in metal-poor stars, the derivation of stellar ages from isochrones, and the chemical composition of planet-hosting stars. I present widely used methods (infrared flux method, spectroscopy) in the determination of $T_{\rm eff}$, and $\log g$. I comment upon difficulties encountered with the determination of stellar parameters of red supergiant stars, and I discuss the impact of non-LTE and 3D hydrodynamical effects.

Keywords: lithium, red supergiant stars, Betelgeuse, metal-poor stars, NLTE, atomic diffusion, stellar atmospheres, stellar parameters

1 Why do we need accurate and precise stellar parameters

Stellar parameters are the tags with which we identify key properties of the stars we study. Most often stellar parameters we refer to are limited to two: the effective temperature, $T_{\rm eff}$, and the surface gravity, or its logarithm, $\log g$, to which we add the metallicity, or its proxy [Fe/H]. Other parameters include the radius R, and the luminosity L, and of course the detailed element abundance distribution. I will here mostly discuss the primary parameters, linked by the well known relations : $L = 4\pi R^2 \sigma T_{\rm eff}^4$, and $g = GM/R^2$. Before recalling a few commonly used methods to derive stellar parameters, I illustrate the need for accurate and precise stellar parameters through three examples: Li abundances and element diffusion in stellar interiors, stellar ages derived from isochrones, and the possible correlation of the abundance of some elements with the presence of planets.

1.1 Lithium abundances and atomic diffusion

Element diffusion is known to take place in the radiative zones inside stars. Elaborate models have been developed including very detailed physical processes and data, but also an unknown amount of turbulent mixing. This turbulent mixing appears necessary to diminish the predicted effects of combined radiative acceleration and gravitational settling (Richard et al. 2005). The impact of element diffusion is to hide the real stellar chemical composition from our view. The atmospheric abundances we determine differ from the interior and mean abundance of the star. This of course is true only for stars that are not deeply convective. Korn et al. (2007) used the deviation from the internal composition that is largest at the turn-off (TO), diminishes on the lower red giant branch (RGB), and vanishes during the ascension of the RGB to calibrate the amount of turbulent mixing in the models. They observed stars at various evolutionary stages in a cluster (NGC 6397), determining their atmospheric Fe, Ti, Ca, and Mg abundances. A comparison to models allowed them to chose the right turbulent mixing. This model was then applied to correct the abundance of Li measured in the same stars. It turns out that the correction reconciles the Li plateau abundance with the cosmological WMAP calculation (Spergel et al. 2007). This work relies on abundance uncertainties of the order of ± 0.05 dex, in order to secure a detection of the effect at the $3-\sigma$ level. Such a precision in abundances requires a very careful calibration of the $T_{\rm eff}$-scale of TO and RGB stars, as discussed in detail by Korn et al. (2007).

[1] LUPM, Laboratoire Univers et Particules de Montpellier, Université Montpellier 2, CNRS, Montpellier, France

1.2 Stellar ages from isochrones

Individual stellar ages can be derived from isochrones: knowing the $T_{\rm eff}$, L, and the metallicity of a star, it can be placed on the right set of isochrones computed at the proper metallicity. The isochrone on which it falls will provide a mass, an age and the initial metallicity, as it is affected by diffusion (Korn et al. 2007). This seemingly straightforward method is, however, not always easy to apply, nor giving an unambiguous answer. Isochrones do overlap. Methods can be used that allow a better estimate of stellar age than just by reading out a single isochrone (Jørgensen & Lindegren 2005), but it remains crucial to input precise and accurate stellar parameters.

1.3 Planet-hosting stars

The question whether the chemical composition of stars with and without planets differ is still a matter of debate. One recent development lies in the claim that some planetary systems may have C/O>1 (Delgado Mena et al. 2010; Petigura & Marcy 2011), which would have interesting consequences on the planetary chemistry, including the possibility of "carbon planets". In a follow-up paper, Nissen (2013) notes that the abundances derived in these papers rely on high-excitation carbon lines, and on the zero-excitation forbidden oxygen line. This makes the conclusions very sensitive to the adopted $T_{\rm eff}$, and atmospheric temperature structure. In his detailed study Nissen (2013) shows that systematic effects on the C/O ratio can be important. Using a spectroscopically derived gravity and the forbidden oxygen line leads to C/O ratios higher by about 0.2 compared to using a photometric gravity and the oxygen IR triplet. The different gravities also induce a trend with metallicity. This careful work demonstrates that the discussion of small abundance effects is hampered by uncertainties in fundamental parameters. In this context, better parameters are needed, in particular constrained by distance determinations. Only then can small abundance effects be discussed, with smaller scatter and less systematics.

2 Determination of stellar parameters

Stellar parameters can be derived using various methods, that are more or less dependent on stellar models. Here I only recall two of them used for the determination of $T_{\rm eff}$, and $\log g$.

2.1 The infrared flux method, temperatures, and angular diameters

For the determination of effective temperatures, a direct method was devised by Blackwell & Shallis (1977), who were initially most interested by the measurement of angular diameters of stars. This method, dubbed the Infrared Flux Method (IRFM) has been improved through the years. Casagrande et al. (2010) discuss in detail the various developments and present a comparison of various temperature scales.

The IRFM relies on the comparison of the ratio $\mathcal{R}_{\rm obs} = f_{\rm bol}(earth)/f_\lambda(earth)$, of the bolometric and monochromatic observed fluxes, with the ratio of stellar surface fluxes $F_{\rm bol}(star)/F_\lambda(star) = \sigma T_{\rm eff}^4/F_\lambda(mod) = \mathcal{R}_{\rm calc}$, which can be readily computed using a model atmosphere. The key idea is to choose λ in the IR where the stellar flux is not very temperature sensitive. Starting from a guess temperature, a few iterations until $\mathcal{R}_{\rm calc} = \mathcal{R}_{\rm obs}$ will lead to a value of $T_{\rm eff}$. It will also provide the angular diameter θ of the star given by, e.g., $\theta^2/4 = f_{\rm bol}(earth)/(\sigma T_{\rm eff}^4)$. This implies, however, that the stellar radius can be well defined and that the relation can be written for both the bolometric and the monochromatic flux, i.e., one has also $\theta^2/4 = f_\lambda(earth)/F_\lambda(star)$. Casagrande et al. (2010) compare IRFM derived angular diameters with diameters from interferometry. They find a good agreement, but this comparison is only made for a few stars, and differences amount up to 10 or 20%. This question of the radius is worth discussing further. In stellar atmosphere models the radius can be readily defined at the layer where the Rosseland optical depth $\tau_{\rm Ross} = 1, {\rm or}\ 2/3$. This is a definition that is commonly adopted in 1D hydrostatic models. The effective temperature is thus a measure of the average energy flux at this radius. This can obviously not be done for observations. Interferometric measurements of the radius depend on the center-to-limb intensity variation, and on the wavelength. A discussion of the difficulties faced to properly define the radius and the effective temperature both in models and observations can be found in, e.g., Baschek et al. (1991). I also discuss below a problem recently uncovered with the $T_{\rm eff}$- (and the radius-) scale, of red supergiant (RSG) stars.

2.2 spectroscopic temperatures and gravities

Spectroscopy offers a powerful way of simultaneously deriving $T_{\rm eff}$ and $\log g$ from a set of neutral and ionized lines of the same element, most often iron. The method is based on the idea that if local thermodynamical equilibrium (LTE) prevails, then the fraction Fe II/Fe I is given by the ionization equilibrium (Saha equation), and the Fe I and Fe II energy level populations are given by the Boltzmann equation. Consequently, the abundances derived from a set of lines, by comparing computed line profiles or equivalent widths to observations should not depend on the ionization stage, or the excitation energy. Therefore the $T_{\rm eff}$ of the model is varied until there is no trend in abundance with excitation, and the gravity is adjusted until there is no difference in abundance between the two ionization stages. In hydrostatic 1D models, there is also the need to adjust the micro-turbulent velocity to ensure that the abundance does not depend on the line equivalent width. This is a very widely used method, which is however sensitive to non-LTE effects, and to inhomogeneities due to 3D hydrodynamical effects.

Modern studies, based on very competitive instruments, require a high precision and accuracy of the analysis, as shown above on a few examples. One should therefore not use the assumption of LTE to derive parameters, including the chemical abundances, without circumspection. The paper by Nissen (2013) discussed above offers a good example of how to check the spectroscopic method output. Nissen first combines photometric data, with a bolometric correction, an extinction correction, and a distance to derive the luminosity of each star of his sample. The $T_{\rm eff}$ is computed from photometry or spectroscopy, and finally isochrone fits provide a mass. From these the surface gravity can be calculated for each object. The gravities are also derived using the ionization equilibrium method underlined above. It turns out that there is a trend in $\log g_{\rm phot} - \log g_{\rm spec}$ with $T_{\rm eff}$, from about +0.1 at 5300 K, to about -0.2 at 6400 K. This trend is not understood so far. A similar trend with [Fe/H] exists. We must remain cautious!

3 A number of open problems

3.1 NLTE effects

LTE is an approximation that in principle only holds when collisions are sufficiently numerous to counteract radiative transitions that lead to non-equilibrium populations. It is of course a very convenient approximation allowing quick calculations. We can not, however, be lazy, and we must dare to leave this approximation behind us. We must at least check that NLTE effects are not too strong, and can be safely ignored, or that they can be corrected a posteriori.

Examples of the impact of NLTE effects can be found in numerous papers. Fuhrmann et al. (1997) discuss the case of Procyon, for which they derive an LTE spectroscopic gravity ($\log g = 3.6$), which they compare to an astrometric gravity based on the distance, and the binarity of the star ($\log g = 4.05$). This difference in gravity of a factor of almost 3, stems from a very high sensitivity of Fe II lines to surface gravity, and of Fe I lines to temperature. NLTE effects at work impact severely the ionization balance, leading to this large difference in gravity. Adopting LTE, and setting the gravity to its astrometric value would require an increase of $T_{\rm eff}$ by 300 K, which is unrealistic.

Recently, Ruchti et al. (2013) determined stellar parameters of a large sample of metal-poor stars. The $T_{\rm eff}$ were determined using Balmer line fitting, after checking against interferometric measurements that this method performed better than the IRFM. The analysis was done both in LTE, and including NLTE corrections for Fe. Their conclusion is that large errors are made when using LTE in metal-poor stars. The differences between NLTE and LTE determinations, that are small at near-solar metallicity, increase to more than 400 K at [Fe/H]=-3.0 for $T_{\rm eff}$, while errors in $\log g$ amount to 1.5 dex, and are more than 0.4 dex in [Fe/H]. Differences in the micro-turbulence parameter can be up to -0.6 km/s.

The main difficulty in carrying proper NLTE calculations is the scarcity of physical data for collisions between atoms and electrons, or hydrogen atoms. Quantum computations are difficult, and have only be made for a handful of atoms, e.g. magnesium (Barklem et al. 2012). Therefore, one has relied on the classical Drawin approximation (Drawin 1969; Steenbock & Holweger 1984) to treat inelastic collisions with hydrogen. A empirical factor, $S_{\rm H}$, was introduced to scale this formula. Korn et al. (2003) attempted to calibrate this factor with standard stars with well known parallaxes. This small sample of four nearby stars with well determined luminosities, $T_{\rm eff}$, radii, masses, and gravities was analyzed using NLTE and various values of $S_{\rm H}$. Only a value of $S_{\rm H}$=3 gave a set of spectroscopic parameters consistent with the Hipparcos data. The small size of the sample does not, however, allow any firm conclusion. This kind of work is also sensitive to inadequacies of the model atmospheres, or to the incompleteness of the model atom used in the calculations, as well as to

observational errors. Such studies must be expanded to large samples of stars with fundamental parameters well-known from sources independent of spectroscopy, like parallaxes and analyses of astero-seismic data. Such data is becoming available for a large number of stars from Kepler and CoRoT, and parallaxes will soon come from Gaia. Ezzeddine et al. (this volume) are conducting a analysis similar to that of Korn et al. (2003) on a larger sample of red giants of various metallicities. This should at least provide guidelines to future quantum mechanical calculations of hydrogen iron collisions. It seems indeed useless to try to calibrate the $S_{\rm H}$ factor, as was shown by Barklem et al. (2011). They checked the Drawin formula against quantum mechanical calculations for Mg, and concluded that the Drawin formula does not contain the essential physics behind direct excitation by H atom collisions. The Drawin formula compares poorly with the quantum mechanical results, and usually overestimates the collision rates by amounts that depend on the transition.

3.2 Red supergiant stars parameters

3.2.1 The example of Betelgeuse

Red supergiant stars parameters are difficult to determine. The example of Betelgeuse illustrates this. Its initial Hipparcos distance of 130 pc was revised to 197 ± 45 pc by Harper et al. (2008), combining Hipparcos and VLA measurements. The angular diameter of Betelgeuse, of about 45 mas (Perrin et al. 2004), is much larger than its parallax (≈ 5 mas). This reflects the fact that RSGs radii are of the order of a few astronomical units (AU). The parallax of these stars is thus determined from the position of the stellar disk photo center, which may wander significantly, and affect the parallax measurement, due to granulation. 3D hydrodynamical simulations of red giant and supergiant atmospheres are now able to make quantitative predictions on the size of granules, their intensity contrast, the shifts and asymmetries affecting spectral line, and their time scales. Chiavassa et al. (2011b) have showed that the fluctuations in the position of the photo center of RSGs are of the order of a fraction of an AU (up to 0.3 AU in the particular simulation shown in their paper). This will result in systematic errors in Gaia's parallax determinations of the order of 5%. In return Gaia measurements will help verify these predictions on a large number of stars, which can not be done with, e.g., interferometers from the ground, as it necessitates repeated observations of a number of stars during a few years.

Due to its proximity, the interstellar extinction towards Betelgeuse is low. The circumstellar extinction is estimated by Harper et al. (2008) to be at most 0.2 mag in V. The dereddened bolometric flux determinations are in reasonable agreement, i.e., $F_{\rm Bol} = 1.0 \pm 0.1 \times 10^{-4}\,{\rm erg\,cm^{-2}\,s^{-1}}$ (Harper et al. 2001), and $F_{\rm Bol} = 1.1 \pm 0.1 \times 10^{-4}\,{\rm erg\,cm^{-2}\,s^{-1}}$ (Perrin et al. 2004). The bolometric luminosity can then be estimated to $\log L/L_{\odot} = 5.10 \pm 0.22$. Using Meynet & Maeder (2003) evolutionary tracks with rotation and mass-loss gives an initial mass of $20\,{\rm M_{\odot}}$ ($18\,{\rm M_{\odot}}$ now). The initial mass estimated by Harper et al. (2008) varies from 17 to $24\,{\rm M_{\odot}}$, with an age from 13 to 8 Myr, depending on the adopted distance (from 150 to 250 pc).

From the distance and the angular diameter above, the radius of Betelgeuse can be estimated to be $950 \pm 200\,{\rm R_{\odot}}$, with the large uncertainty mostly due to the distance error. Levesque et al. (2005) used a fit of the optical spectrum of Betelgeuse to simultaneously derive its $T_{\rm eff} = 3650$ K, and an extinction $A_{\rm V} = 0.62$, which combined give in turn $R = 890\,{\rm R_{\odot}}$, consistent with the interferometric value. The extinction is however larger than the estimate of Harper et al. (2008). In conclusion, it is interesting to note that the fundamental parameters of such a bright and nearby star are still a matter of debate.

3.2.2 The RSG $T_{\rm eff}$-scale

Recent work indicates that there still is an inconsistency in the temperature scale of RSGs. This was found by Davies et al. (2013) using properly calibrated VLT/XSHOOTER (D'Odorico et al. 2006) spectra covering from the B to the K band. When fitting the full spectral energy distribution (SED) with MARCS (Gustafsson et al. 2008) model spectra, they found much hotter effective temperatures than when solely considering the optical part of the spectrum, as done by Levesque et al. (2005). The derived reddening are also larger. The observed SED cannot be reproduced by a single hydrostatic 1D model from the blue to the K band. Davies et al. (2013) suggest that 3D radiative-hydrodynamical model spectra will allow a better fit of the data, based on a single CO5BOLD simulation (Freytag et al. 2012; Chiavassa et al. 2011a). The hint from this simulation is that the fit of observed spectra with 1D hydrostatic model spectra leads to an inconsistent set of parameters (L, Teff, R), i.e. all three must be derived independently. Relying on two of them to compute the third will introduce a systematic error. 3D simulations indeed show that the stellar flux is emitted by only a fraction of the stellar surface, because of the granulation pattern, at least in some spectral region. This might be solved by

introducing an effective radius. This stresses the need for the determination of stellar parameters in a redundant way, using independent methods (spectroscopy, interferometry, parallaxes). Further work is in progress, but eventually accurate distances will be needed for a sizable number of RSGs.

4 Conclusions

As observations become more and more precise and detailed, and as models become more and more sophisticated, we find that stellar parameters might not be what we thought they were, and may be tricky to determine. As an illustration, the picture of $T_{\rm eff}$ representing the photospheric temperature at the depth at which the photons we detect are emitted, is much too simple, and should be abandoned. 3D simulations have demonstrated that there are large temperature fluctuations in stellar atmospheres (Ramírez et al. 2009), and that the stellar flux we observe is the addition of contributions from different depths, depending also on the position on the stellar disk, and on time. NLTE is also a factor of complication, that affects spectroscopic methods, and for which we still do not have all the necessary data at hand. Work is in progress on, e.g., inelastic collisions with hydrogen that should lead soon to improved NLTE calculations. These 3D and NLTE effects tend to become stronger in low gravity, and in low metallicity stars.

We must keep on carefully checking stellar parameter determination methods, as new important data become available such as distances from Gaia, and gravities or $T_{\rm eff}$ from Kepler and CoRoT astero-seismic data. Redundancy in the data is useful to cross-check the determinations. It is even necessary in the case of stars like RSGs, where the stellar surface is very affected by granulation, and the stellar diameter is not easily observationally defined.

Finally, beyond the refinements underlined above, that are indispensable for the validation of our stellar evolution and stellar atmosphere models, and further progress in the field, there are parameters which we know very little about. Accurate Gaia distances will allow us to derive, at last, the most commonly missing parameter in Galactic star studies, the luminosity, greatly impacting Galactic and stellar physics studies.

I thank the Action Spécifique Gaia of the CNRS for inviting me to give this talk at the SF2A astronomy week, and for finacial support. My research is supported in part by the CNRS Programme National de Physique Stellaire.

References

Barklem, P. S., Belyaev, A. K., Guitou, M., et al. 2011, A&A, 530, A94+

Barklem, P. S., Belyaev, A. K., Spielfiedel, A., Guitou, M., & Feautrier, N. 2012, A&A, 541, A80

Baschek, B., Scholz, M., & Wehrse, R. 1991, A&A, 246, 374

Blackwell, D. E. & Shallis, M. J. 1977, MNRAS, 180, 177

Casagrande, L., Ramírez, I., Meléndez, J., Bessell, M., & Asplund, M. 2010, A&A, 512, A54

Chiavassa, A., Freytag, B., Masseron, T., & Plez, B. 2011a, A&A, 535, A22

Chiavassa, A., Pasquato, E., Jorissen, A., et al. 2011b, A&A, 528, A120+

Davies, B., Kudritzki, R.-P., Plez, B., et al. 2013, ApJ, 767, 3

Delgado Mena, E., Israelian, G., González Hernández, J. I., et al. 2010, ApJ, 725, 2349

D'Odorico, S., Dekker, H., Mazzoleni, R., et al. 2006, in Society of Photo-Optical Instrumentation Engineers (SPIE) Conference Series, Vol. 6269, Society of Photo-Optical Instrumentation Engineers (SPIE) Conference Series

Drawin, H. W. 1969, Zeitschrift fur Physik, 225, 483

Freytag, B., Steffen, M., Ludwig, H.-G., et al. 2012, Journal of Computational Physics, 231, 919

Fuhrmann, K., Pfeiffer, M., Frank, C., Reetz, J., & Gehren, T. 1997, A&A, 323, 909

Gustafsson, B., Edvardsson, B., Eriksson, K., et al. 2008, A&A, 486, 951

Harper, G. M., Brown, A., & Guinan, E. F. 2008, AJ, 135, 1430

Harper, G. M., Brown, A., & Lim, J. 2001, ApJ, 551, 1073

Jørgensen, B. R. & Lindegren, L. 2005, A&A, 436, 127

Korn, A. J., Grundahl, F., Richard, O., et al. 2007, ApJ, 671, 402

Korn, A. J., Shi, J., & Gehren, T. 2003, A&A, 407, 691

Levesque, E. M., Massey, P., Olsen, K. A. G., et al. 2005, ApJ, 628, 973

Meynet, G. & Maeder, A. 2003, A&A, 404, 975

Nissen, P. E. 2013, A&A, 552, A73

Perrin, G., Ridgway, S. T., Coudé du Foresto, V., et al. 2004, A&A, 418, 675
Petigura, E. A. & Marcy, G. W. 2011, ApJ, 735, 41
Ramírez, I., Allende Prieto, C., Koesterke, L., Lambert, D. L., & Asplund, M. 2009, A&A, 501, 1087
Richard, O., Michaud, G., & Richer, J. 2005, ApJ, 619, 538
Ruchti, G. R., Bergemann, M., Serenelli, A., Casagrande, L., & Lind, K. 2013, MNRAS, 429, 126
Spergel, D. N., Bean, R., Doré, O., et al. 2007, ApJS, 170, 377
Steenbock, W. & Holweger, H. 1984, A&A, 130, 319

SF2A 2013
L. Cambrésy, F. Martins, E. Nuss and A. Palacios (eds)

STELLAR PARAMETERS AND STELLAR PHYSICS FROM GAIA AND RELATED SPECTROSCOPIC SURVEYS

Alejandra Recio-Blanco[1]

Abstract. Automated stellar parameters are the bedrock of Galactic spectroscopic surveys science. They allow a rapid and homogeneous processing of extensive data sets, necessary for an efficient scientific return. Present Galactic Surveys, including the Gaia mission, have developped a wealth of mathematical approaches that are currently used today. These fundamental stellar parameters will provide important constraints for many stellar physics research fields.

Keywords: methods: data analysis, surveys, stars: abundances, stars: fundamental parameters, Galaxy: abundances

1 Introduction

A suite of ground-based vast stellar surveys mapping the Milky Way and culminating in the ESA Gaia mission, is revolutionizing the empirical information about Galactic stellar populations. In particular, in the recent years, the number of stars analysed with high enough spectroscopic resolution to provide detailed chemical diagnostics has increased from a few hundreds to several tens of thousands. Until the end of 2003, most of the information about the Milky Way was confined to small local samples, for which high-resolution spectroscopic data was obtained. In 2004, the Geneva Copenhagen Survey (Nordström et al. 2004) collected the first large spectro-photometric sample of around 16 000 stars, as part of a Hipparcos follow-up campaign (hence, also confined to 100 pc from the Sun). More recently, optical spectroscopic low-resolution surveys, such as SEGUE (Yanny et al. 2009) and RAVE (Steinmetz et al. 2006), have extended the studied volume to distances of a few kpc from the Sun (mainly in the range 0.5-3 kpc), and increased the numbers of stars with chemo-kinematical information by more than an order of magnitude ($>$ 200 000 spectra for SEGUE and $>$ 500 000 spectra for RAVE).

This effort is now complemented by new vast high-resolution spectroscopic surveys: the Gaia-ESO Survey (GES, 300 nights with the ESO/VLT), the Gaia/Radial Velocity Spectrograph (RVS) survey (part of the Gaia cornerstone mission), the Australian HERMES/GALAH survey, the LAMOST/LEGUE survey and APOGEE (part of the Sloan Digital Sky Survey III and After-SDSSIII).

All the above mentioned Galactic stellar population projects rely on the success of automated techniques of spectral analysis and parameterisation, capable to perform a rapid and homogeneous processing of the data and to allow an efficient scientific return. Figure 1 shows the increase of stars with available spectra in the next five years, as expected from the announced data releases of the different Milky Way surveys. One of the main challenges of Galactic Archaeology will be the correct and rigorous treatment of all those data sets, including the stars' fundamental parameters and the chemical characterization.

Therefore, those projects, including Gaia, the billion stars surveyor, are not only crucial for Galactic physics, but also for stellar physics. They will revolutionize many stellar physics research topics because they will provide, among other things: i) absolute magnitudes with unprecedented precision, crucial for stellar ages estimation, ii) atmospheric parameters and individual element abundances for an extraordinary high number of stars, including rare objects, and iii) precise proper motions and radial velocities.

[1] Laboratoire Lagrange (UMR7293), Université de Nice Sophia Antipolis, CNRS, Observatoire de la Côte d'Azur, BP 4229,F-06304 Nice cedex 4, France

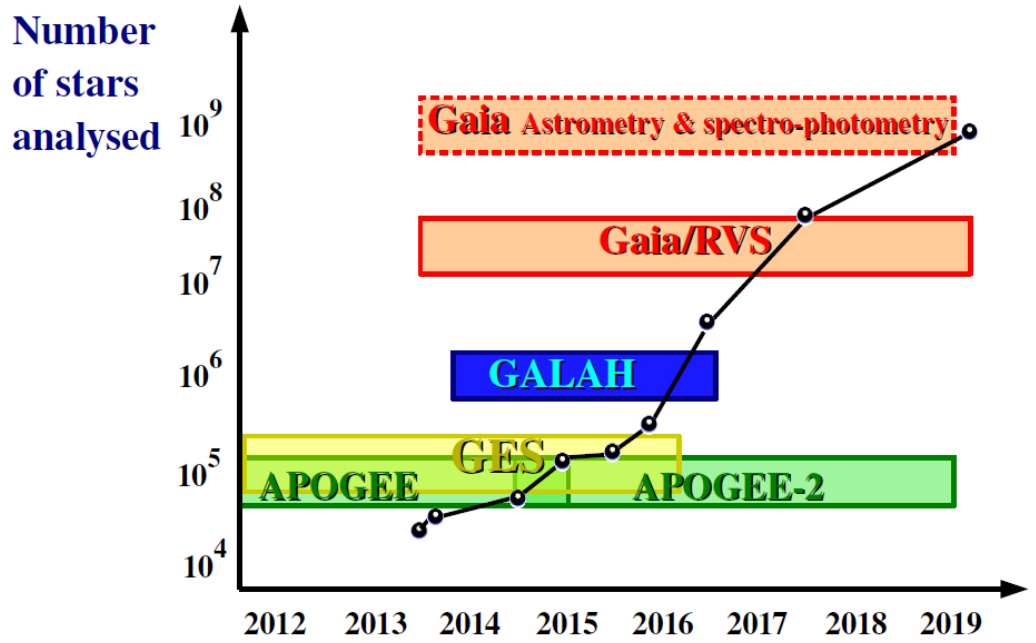

Fig. 1. Number of stars with available spectra in the next years, as expected from the announced data releases of the different Milky Way surveys.

2 Automated parameterization methods

The physical parameterization can be applied when the physics of the studied objects is enough well known, and modeled through continuous variables. For instance, the stellar effective temperature, the surface gravity, the global metallicity and the individual element abundances are more appropriate to describe a stellar spectra than spectral types and luminosity classes. parameterization algorithms use reference data to define the mapping between the observed targets and the models. Those models, usually synthetic spectra, constitute a N-dimensional grid, where N is the number of parameters to determine. There are three main mathematical parameterization approaches: optimization methods, projection methods and classification. All of them try to find the absolute minimum of the distance function, with different techniques (Recio-Blanco 2014).

Figure 2 shows the different types of automated parameterisation methods found in the literature, currently used by Milky Way spectroscopic surveys and Galactic archaeology projects. The algorithms can be divided depending on the way in which the reference models are computed and used: on the fly computations, pre-computed grid of reference models used without and with training. This has an important influence on the computation time and, ultimately, it depends on the implemented mathematical approach. In addition, Figure 2 shows what approaches are used by the main spectroscopic surveys and projects, including the European Space Agency Gaia mission.

2.1 Methods using a pre-computed grid of reference synthetic spectra

The use of a pre-computed grid of synthetic spectra reduces the computing time of the algorithms application. The methods using this kind of approach are divided into those without and with a phase of algorithm training.

- *Without training*:

  This category of methods is based on optimization approaches. It includes the Nelder-Mead method (Nelder & Mead 1965) implemented by Allende Prieto et al. (2006). This non-linear downhill simplex method was already used for the SDSS-SEGUE SSPP pipeline for the derivation of both the atmospheric

Reference spectra		Main applications	Mathematical approach
Computation time ↑	**- On the fly computations:**		
	Spectral Synthesis	**GES, GALAH**	Optimization
	Equivalent widths	**GES**	Optimization
	- Pre-computed grid:		
	Without training	**GES, RAVE, SEGUE, LEGUE**	Optimization
	With training	**GES, RAVE, AMBRE, SEGUE, Gaia**	Projection & Classification

Fig. 2. Different types of automated abundance analysis methods currently used by Milky Way spectroscopic surveys and galactic archaeology projects.

parameters and the [α/Fe] (Lee et al. (2011)) from low resolution stellar spectra. It is also part of the methods used by the Gaia-ESO Survey and it is the core of the APOGEE ASPCAP pipeline.

The penalized χ^2 method of Zwitter et al. (2008) is also in this category of algorithms. It has been used for the RAVE survey first and second data releases for the derivation of the iron abundance. The RAVE survey also developed the Boeche et al. (2011) method for the individual abundance analysis of the high signal-to-noise data (third data release). It is a minimum of distances method using of a grid of pre-computed equivalent widths.

The UlySS method of Koleva et al. (2009) implements a full spectrum fitting and a parametric minimization using χ^2 maps. It was part of the SEGUE SSPP pipeline and it is actually integrated in the LASP LAMOS pipeline for the analysis of the LEGUE survey data.

The GAUGUIN method (Bijaoui et al. 2012) uses the Gauss-Newton algorithm for the determination of the global metallicity simultaneously with stellar atmospheric parameters. It can also be used for the derivation of individual abundances in a second step of the spectrum analysis. The GAUGUIN algorithm is already applied to GES data and it is been prepared for its integration in the Apsis pipeline for the individual abundance analysis of the Radial Velocity Spectrograph (RVS) data, collected by the Gaia mission of the European Space Agency.

- *With training*:

The methods with a faster application are those relying on a training phase. They are based on projection and classification approaches. The neural network algorithms of Re Fiorentin et al. (2007) is an example of this kind of methods. It is part of the SEGUE SSPP pipeline for the derivation of the iron abundance, simultaneously with the effective temperature and the surface gravity. It implements a global and non-linear regression mapping.

The MATISSE and DEGAS methods are part of the algorithms developped by the Nice group. The MATISSE algorithm is a local multi-linear regression method (see Recio-Blanco et al. 2006). The stellar parameters are determined through the projection of the input spectra on a set of vectors, calculated during a training phase. The DEGAS method is based on an oblique k-d decision tree and uses the pattern recognition approach for stellar parameterization. The MATISSE and DEGAS methods have been used in Kordopatis et al. (2011) for a study of the Thick Disc outside the solar neighbourhood (700 stars analysed) and for the last data release (DR4) of the RAVE Galactic Survey (Kordopatis et al. 2013, submitted, 228 060 spectra). These two applications share the same wavelength domain and resolution of the RVS one. In addition, MATISSE is the core method of the AMBRE project. AMBRE (de Laverny et al. 2012, see), under agreement between the European Southern Observatory (ESO) and the Observatoire de la Côte d'Azur, aims at determining the parameters ($T_{\rm eff}$, $\log g$, [M/H] and [α/Fe]) of the high resolution

Acronym	name
DSC	Discrete Source Classifier
ESP	Extended Stellar Parametrizer:
-CS	ESP Cool Stars
-ELS	ESP Emission Line Stars
-HS	ESP Hot Stars
-UCD	ESP Ultra Cool Dwarfs
FLAME	Final Luminosity Age and Mass Estimator
GSP-Phot	Generalized Stellar Parametrizer Photometry
GSP-Spec	Generalized Stellar Parametrizer Spectroscopy
MSC	Multiple Star Classifier
OA	Outlier Analysis
OCA	Object Clustering Algorithm
QSOC	Quasar Classifier
TGE	Total Galactic Extinction
UGC	Unresolved Galaxy Classifier

Table 1. Modules of the Gaia Astrophysical Parameters Inference System (Apsis Bailer-Jones et al. 2013).

stellar spectra contained in the ESO archive. This concerns the FEROS, HARPS, UVES and FLAMES spectrographs. The results of the AMBRE project are presented in Worley et al. (2012) (FEROS data analysis), De Pascale et al. (2013, in preparation; HARPS data analysis) and Worley et al. (2013, in preparation, UVES data analysis). MATISSE has also been used for the characterization of several disc fields observed by the CoRoT mission (Gazzano et al. 2010, 2013). In addition, the MATISSE algorithm is part of the methods used for the stellar parameterization of FGK type targets of the Gaia-ESO Large Public Survey. In particular, the first data release of GES parameters for the FGK-type stars observed with the GIRAFFE spectrograph includes the MATISSE results for those data.

Finally, the spectrum analysis of the Gaia mission is based on this type of algorithms with a training phase. The computational time is a crucial constraint for the Gaia pipeline, as several tenths of millions of RVS spectra will be analysed in cycles of 6 months.

3 The Gaia astrophysical parameters inference system

In addition to its astrometry, Gaia will obtain optical BP/RP low-resolution spectro-photometry for all one billion of its target sources, as well as higher resolution RVS spectra (for the targets brighter than G$\sim$17). These spectra are used to calculate a chromatic calibration of the astrometry, and to estimate the stellar radial velocities, respectively. But they also provide valuable information on the physical properties of the sources.

Figure 3 outlines the architecture of the data processing system developed by DPAC/CU8 for this purpose. Known as Apsis, the Astrophysical Parameters Inference System, it comprises multiple software modules (boxes in the diagram), each charged with a specific task (see Table 1). GSP-Phot, for example, estimates the astrophysical parameters effective temperature, line-of-sight interstellar extinction, metallicity, and surface gravity, for all stars. Other modules examine other types of objects, possibly using the outputs from previous modules (e.g. the GSP-Phot outputs are used by GSP-SPEC, FLAME, ESP, and TGE). The coloured bars show which Gaia data are used for the various modules.

Multiple methods are used for many types of stars (Bailer-Jones et al. 2013), producing multiple results for the end user according to different models and assumptions. Prior to its application to real Gaia data the accuracy of these methods cannot be assessed definitively. But as an example of the current performance, GSP-phot can attain internal accuracies (RMS residuals) on F,G,K,M dwarfs and giants at G = 15 (V = 1517) for a wide range of metallicites and interstellar extinctions of around 100 K in effective temperature (Teff), 0.1 mag in extinction (A0), 0.2 dex in metallicity ([Fe/H]), and 0.25 dex in surface gravity (log g). GSP-spec estimates Teff , log g, global metallicity [M/H], al- pha element abundance [α/Fe], and some individual chemical abundances for single stars using continuum-normalized RVS spectra. GSPspec internal accuracies can attain, at G = 13, 70 K for effective temperature, 0.12 dex for log g and 0.09 dex for metallicity. The individual abundances of several elements (Fe,Ca, Ti, Si) will be measured for brighter stars with an expected internal precision of 0.1

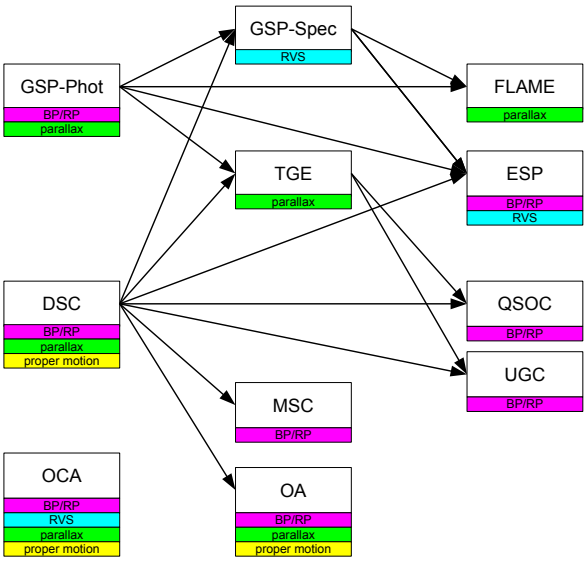

Fig. 3. Architecture of the Gaia Apsis data processing. The coloured bars show which Gaia data are used for the various modules.

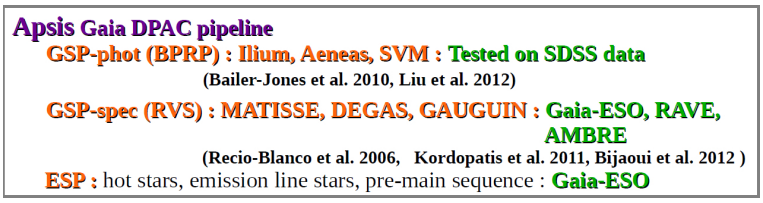

Fig. 4. Algorithms integrated in the stellar parameterisation modules of the Apsis pipeline. In green, the ground-based Galactic projects that allowed the testing of the methods, or that include the same algorithms in their data analysis pipelines.

dex for G < 13. The accuracy is a strong function of the parameters themselves, varying by a factor of more than two up or down over this parameter range.

Finally, the algorithms integrated in the Apsis pipeline for the stellar parameterisation are already being used for the analysis of ground based Galactic projects as the Sloan Digital Sky Survey, the RAVE survey, the Gaia-ESO Survey and the AMBRE project. This is shown in Fig. 4, together with the names of the integrated methods for each stellar parameterisation module.

4 Conclusions

The study of the stellar fundamental parameters is rapidly evolving, and will definitly be revolutionized by the Gaia data. In particular, unprecedented constraints to stellar structure and evolution models from very precise distances and homogeneous parameters will be possible, including stars in rapid evolutionary phases and rare objects. In addition, many other stellar science cases are at the core of the Gaia project and other Galactic spectroscopic surveys as the Gaia-ESO Survey: stellar activity, the interplay between stellar dynamics and evolution in dense environements as globular clusters, brown dwarfs and white dwarfs evolution, stellar variability across the HR diagramme, binary system, binary systems studies, open clusters evolution,... The Gaia era will reveal the synergy between the stellar populations community and the stellar physics research.

References

Allende Prieto, C., Beers, T. C., Wilhelm, R., et al. 2006, ApJ, 636, 804
Bailer-Jones, C. A. L., Andrae, R., Arcay, B., et al. 2013, ArXiv e-prints
Bijaoui, A., Recio-Blanco, A., de Laverny, P., & Ordenovic, C. 2012, Statistical Methodology
Boeche, C., Siebert, A., Williams, M., et al. 2011, AJ, 142, 193
de Laverny, P., Recio-Blanco, A., Worley, C. C., & Plez, B. 2012, A&A, 544, A126
De Pascale, M., Recio-Blanco, A., de Laverny, P., & Worley, C. 2013, in preparation
Gazzano, J.-C., de Laverny, P., Deleuil, M., et al. 2010, A&A, 523, A91
Gazzano, J.-C., Kordopatis, G., Deleuil, M., et al. 2013, A&A, 550, A125
Koleva, M., Prugniel, P., Bouchard, A., & Wu, Y. 2009, A&A, 501, 1269
Kordopatis, G., Recio-Blanco, A., & de Laverny, P. 2013, submitted
Kordopatis, G., Recio-Blanco, A., de Laverny, P., et al. 2011, A&A, 535, A107
Lee, Y. S., Beers, T. C., An, D., et al. 2011, ApJ, 738, 187
Nelder, J. & Mead, R. 1965, Comp. Journal, 7, 308
Nordström, B., Mayor, M., Andersen, J., et al. 2004, A&A, 418, 989
Re Fiorentin, P., Bailer-Jones, C. A. L., Lee, Y. S., et al. 2007, A&A, 467, 1373
Recio-Blanco, A. 2014, in IAU Symposium, Vol. 298, Setting the Scene for Gaia and LAMOST, ed. S. Feltzing, G. Zhao, N. Walton, & P. Whitelock
Recio-Blanco, A., Bijaoui, A., & de Laverny, P. 2006, MNRAS, 370, 141
Steinmetz, M., Zwitter, T., Siebert, A., et al. 2006, AJ, 132, 1645
Worley, C., Recio-Blanco, A., de Laverny, P., & De Pascale, M. 2013, in preparation
Worley, C. C., de Laverny, P., Recio-Blanco, A., et al. 2012, A&A, 542, A48
Yanny, B., Rockosi, C., Newberg, H. J., et al. 2009, AJ, 137, 4377
Zwitter, T., Siebert, A., Munari, U., et al. 2008, AJ, 136, 421

Session 06

Astrométrie de haute précision et applications

SF2A 2013
L. Cambrésy, F. Martins, E. Nuss and A. Palacios (eds)

RELATIVISTIC MODELS FOR GAIA AT THE (CROSS)CHECK-POINT

S. Bertone [2,1], C. Le Poncin-Lafitte[1], M. Crosta[2], A. Vecchiato[3], O. Minazzoli[3] and M.-C. Angonin[1]

Abstract. Given the extreme accuracy of modern space astrometry, a precise relativistic modeling of observations is required. Concerning light propagation, most approaches rely on the solution of the null-geodesic equations. However, another approach based on the Time Transfer Functions (TTF) can be used to define an astrometric observation using an integral-based method derived from the Synge World Function. The availability of several models, formulated in different and independent ways, is indeed a security against the presence of systematic errors in the analysis of future experimental results. It is the case of the forthcoming Gaia mission. In this work, we review the modeling of a Gaia-like astrometric observation using the TTF and two other approaches, namely the Gaia RElativistic Model (GREM) and the Relativistic Astrometric MODel (RAMOD), and we provide explicit relations between their characteristic quantities.

Keywords: astrometry, General Relativity, Gaia, Time Transfer Functions, light propagation

1 Introduction

The space astrometry mission Gaia (Bienayme & Turon 2002), planned to be launched by the European Space Agency (ESA) at the end of this year, will observe about one billion objects in the magnitude range from 6 to 20. In particular, the astrometric core solution will determine the astrometric parameters (position, parallax, and proper motion) for a subset of these sources with an accuracy of several μas. It is an extremely difficult task but also a crucial one for the outcome of the mission. This solution will be performed by the Astrometric Global Iterative Solution (AGIS) software (Lindegren et al. 2012). At the same time, an independent verification unit for AGIS called Global Sphere Reconstruction (GSR) (Vecchiato et al. 2012) has been set within the Gaia Data Processing and Analysis Consortium (DPAC). Both pipelines are intended to operate on the same real data and the comparison of their results will validate the final astrometric catalog. In order to keep the two software as separate as possible, two different relativistic modelings of light propagation have been implemented: AGIS relies on GREM (Klioner 2003), while GSR implements RAMOD (de Felice et al. 2006). Moreover, an independent approach to the modeling of the astrometric observables based on the TTF (Teyssandier & Le Poncin-Lafitte 2008) has been recently put in place. We review these three approaches by translating them into the same notation and providing explicit relations between their characteristic quantities used to describe light propagation in a curved space-time.

2 Notations

In this paper c is the speed of light in a vacuum and G is the Newtonian gravitational constant. The Lorentzian metric of space-time V_4 is denoted by g. The signature adopted for g is $(-+++)$. We suppose that space-time is covered by a global quasi-Galilean coordinate system $(x^\mu) = (x^0, \boldsymbol{x})$, where $x^0 = ct$, t being a time coordinate, and $\boldsymbol{x} = (x^i)$. We assume that $g_{00} < 0$ anywhere. We employ the vector notation $\boldsymbol{a}$ in order to denote $(a^1, a^2, a^3) = (a^i)$. Considering two such quantities $\boldsymbol{a}$ and $\boldsymbol{b}$ we use $\boldsymbol{a} \cdot \boldsymbol{b}$ to denote $a^i b^i$ (Einstein convention on repeated indices is used). The quantity $a = |\boldsymbol{a}|$ stands for the ordinary Euclidean norm of $\boldsymbol{a}$. For any quantity $f(x^\lambda)$, $f_{,\alpha}$ and $\partial_\alpha f$ denote the partial derivative of f with respect to x^α. The indices in

[1] Observatoire de Paris, SYRTE, CNRS/UMR 8630, UPMC - 61 avenue de l'Observatoire, F-75014 Paris, France
[2] INAF, Astrophysical Observatory of Torino, University of Torino - Via Osservatorio 20, 10025 Pino Torinese (Torino), Italy
[3] UMR ARTEMIS, CNRS, University of Nice Sophia-Antipolis, Observatoire de la Côte d'Azur, Nice Cedex 4, France

parentheses characterize the order of perturbation. They are set up or down, depending on the convenience. In the following, we will consider that space-time is perturbed by a system of gravitational mass monopoles represented by a weak-field metric tensor $g_{\mu\nu} = \eta_{\mu\nu} + h_{\mu\nu}$. It has been showed in (Klioner 2003) that in order to get the μas angular accuracy required by modern space astrometry, the gravitational perturbation shall be expanded in the parametrized post-Newtonian (PPN) approximation of GR as

$$h_{00} = \frac{2G}{c^2} \sum_P \frac{\mathcal{M}_P}{R_P(t, \boldsymbol{x})} \quad , \quad h_{0i} = 0 \quad , \quad h_{ij} = \delta_{ij} \gamma h_{00} \ , \tag{2.1}$$

with $\mathcal{M}_P$ the mass of the perturbing body P and $\boldsymbol{R_P}(t, \boldsymbol{x}) = \boldsymbol{x} - \boldsymbol{x}_P(t_C)$, where $\boldsymbol{x}_P(t_C)$ is the position of P at the time of maximum approach with the photon and γ is a PPN parameter (Will 1993).

3 Astrometric observables in the Time Transfer Functions formalism

The goal of astrometry is to determine the position of celestial bodies from angular measurements. One way to get a covariant definition of the astrometric observable is to use the tetrad formalism (Weinberg 1972; Misner et al. 1973; Brumberg 1991), thus giving the direction of observation of an incoming light ray in a particular frame comoving with the observer.

Let us note $\lambda^{\mu}_{(\alpha)}$ the components of this tetrad, where (α) corresponds to the tetrad index and μ is a normal tensor index which can be lowered and raised by using the metric. It has been shown in (Bertone & Le Poncin-Lafitte 2012) that we can express the direction of the light ray in the tetrad frame as

$$n^{(i)} = -\frac{\lambda^0_{(i)} + \lambda^j_{(i)} \hat{k}_j}{\lambda^0_{(0)} + \lambda^j_{(0)} \hat{k}_j} = -\frac{\lambda^0_{(i)} + \hat{k}_j \lambda^j_{(i)}}{u^0 \left(1 + \hat{k}_j \beta^j\right)} \ , \tag{3.1}$$

where $\widehat{k}_i = k_i / k_0$ is the so called light direction triple with $k_\mu = g_{\mu\nu} k^\nu$ the covariant components of the tangent vectors to the light ray $k^\mu \equiv dx^\mu / d\lambda$, u^α represents the unit four-velocity of the satellite and $\beta^i \equiv v^i / c$, v^i being the coordinate velocity of the observer.

Let us suppose the existence of a unique light ray connecting the emission event of the signal $x_A = (ct_A, \boldsymbol{x}_A)$ and its reception event $x_B = (ct_B, \boldsymbol{x}_B)$. In addition, we put $R^i_{AB} \equiv x^i_B - x^i_A$. Under these hypothesis, in the TTF formalism one defines the light direction triple within the post-Minkowskian (PM) approximation of General Relativity (GR) as closed form integrals of the metric tensor and its derivatives along the Minkowskian straight line $z^\alpha_-(\lambda) = (ct_B - R_{AB}, \boldsymbol{x}_B - \boldsymbol{R_{AB}})$ as (Bertone et al. 2013; Hees et al. 2013)

$$\left(\widehat{k}_i\right)_B \equiv \left(\frac{k_i}{k_0}\right)_B = N^i_{AB} - \frac{1}{2} \int_0^1 \left[R^i_{AB} \lambda m_{,0} - R_{AB}(1-\lambda) m_{,i} - \tilde{h}_i \right]_{z_-(\lambda)} d\lambda + \mathcal{O}(h^2), \tag{3.2}$$

where we define $N^i_{AB} = R^i_{AB} / R_{AB}$ and

$$m_{,\alpha} \equiv h_{00,\alpha} + 2 N^k_{AB} h_{0k,\alpha} + N^j_{AB} N^k_{AB} h_{jk,\alpha} \ , \tag{3.3a}$$

$$\tilde{h}_i \equiv N^i_{AB} h_{00} - N^i_{AB} N^j_{AB} N^k_{AB} h_{jk} + 2 h_{0i} + 2 N^j_{AB} h_{ij} \ . \tag{3.3b}$$

Taking the metric (2.1), Eq. (3.2) can be written as

$$(\widehat{k}^B_i)(\boldsymbol{x}_A, \boldsymbol{x}_B) = N^i_{AB} - (\gamma + 1) \sum_P \frac{G \mathcal{M}_P}{c^2 R_{PB}} \frac{1}{1 + \boldsymbol{N}_{PA} \cdot \boldsymbol{N}_{PB}} \times \left[\frac{R_{AB}}{R_{PA}} \boldsymbol{N}_{PB} - \left(1 + \frac{R_{PB}}{R_{PA}}\right) \boldsymbol{N}_{AB} \right] \ , \tag{3.4}$$

where we use $\boldsymbol{R}_{PX} = \boldsymbol{x}_X - \boldsymbol{x}_P(t_C)$. Then, a generic tetrad comoving with the chosen observer and computed at the same accuracy can be used in Eq. (3.1) along with Eq. (3.4) to compute the direction of light in the observer reference frame.

4 The Gaia astrometric models

In the context of the Gaia mission two independent relativistic models have been developed to analyze and interpret the observations: GREM (Klioner 2003) and RAMOD (de Felice et al. 2004). In this section, we shall detail the definition of an astrometric observable in these two models.

4.1 GREM

GREM is actually the most complete relativistic model for astrometry and the basis for the reduction of Gaia observations. it sets several steps for the conversion of the observed quantities into the coordinate ones, from the observed direction of light to the spatial position of the emitter in the BCRS (Klioner 2003).

Adopting the IAU resolution B1.3 (Soffel et al. 2003) for the BCRS and the Comoving Reference System (ComRS), (Klioner 2003) gives the explicit coordinate transformation between the aberration-free direction n^i and the observed direction s^i at μas accuracy as

$$\begin{aligned} s^i &= -n^i + c^{-1}\Big[\boldsymbol{n}\times(\boldsymbol{v_s}\times\boldsymbol{n})\Big]^i \\ &\quad +c^{-2}\left\{(\boldsymbol{n}\cdot\boldsymbol{v_s})\Big[\boldsymbol{n}\times(\boldsymbol{n}\times\boldsymbol{v_s})\Big]^i+\frac{1}{2}\Big[\boldsymbol{v_s}\times(\boldsymbol{n}\times\boldsymbol{v_s})\Big]^i\right\} \\ &\quad +c^{-3}\left\{\Big[(\boldsymbol{v_s}\cdot\boldsymbol{n})^2+(1+\gamma)w(\boldsymbol{x})\Big]\Big[\boldsymbol{n}\times(\boldsymbol{v_s}\times\boldsymbol{n})\Big]^i+\frac{1}{2}(\boldsymbol{v_s}\cdot\boldsymbol{n})\Big[\boldsymbol{v_s}\times(\boldsymbol{n}\times\boldsymbol{v_s})\Big]^i\right\}+\mathcal{O}(c^{-4})\ , \end{aligned} \tag{4.1}$$

where $\boldsymbol{v}_s$ is the coordinate velocity of the observing satellite and $w(\boldsymbol{x})$ is the PPN gravitational potential. Eq. (4.1) contains the aberrational effects up to $1/c^{-3}$. The "aberration free direction" is given by the unit vector $\boldsymbol{n}\equiv\boldsymbol{p}/|\boldsymbol{p}|$, with

$$p^i \equiv c^{-1}\dot{x}^i = \sigma^i + c^{-1}\Delta\dot{x}^i(t)\ , \tag{4.2}$$

with $\dot{x}^i$ the coordinate direction of the photon. To compute Eq. (4.2) at reception coordinates, we need then the unperturbed direction of the light ray at past null infinity

$$\sigma^i = N^i_{AB} - \frac{2G}{c^2}\sum_P \frac{\mathcal{M}_P}{R_{AB}}\left[\frac{(\boldsymbol{N}_{AB}\times\boldsymbol{R}_{PB}\times\boldsymbol{N}_{\boldsymbol{AB}})^i}{R^2_{PB}-(\boldsymbol{N}_{\boldsymbol{AB}}\cdot\boldsymbol{R}_{PB})^2}\big(R_{PA}-R_{PB}-R_{AB}\big)\right]+\mathcal{O}(c^{-4}) \tag{4.3}$$

and the gravitational deflection of the light ray $\Delta\dot{x}^i(t_B)$ given by

$$\frac{\Delta\dot{x}^i_B}{c} = -\frac{2G}{c^2}\sum_P \mathcal{M}_P\frac{1}{R_{PB}}\left\{N^i_{AB}+\frac{(\boldsymbol{N}_{\boldsymbol{AB}}\times\boldsymbol{R}_{\boldsymbol{PA}}\times\boldsymbol{N}_{\boldsymbol{AB}})^i}{R_{PB}-\boldsymbol{N}_{\boldsymbol{AB}}\cdot\boldsymbol{R}_{\boldsymbol{PB}}}\right\}\ . \tag{4.4}$$

Finally, some classical transformations to subtract the parallax and proper motion effects allow to get the barycentric direction of the source.

4.2 RAMOD

Developed by an italian group of relativists and astronomers, RAMOD (de Felice et al. 2004) is based on a complete PM background and it always relies on measurable quantities with respect to a local barycentric observer along the light ray. The unknown is then the local line-of-sight, representing the direction of the light ray in the rest space of the observer $\boldsymbol{u}$, and defined as

$$\bar{\ell}^\alpha = -\frac{k^\alpha}{u_\beta k^\beta} - u^\alpha\ . \tag{4.5}$$

In this formalism, the null-geodesic equation transforms, according to the measurement protocol procedure, into a set of coupled nonlinear differential equations, called "master equations" (de Felice et al. 2004) whose solution at reception coordinates x_B in the case of metric (2.1) gives (Crosta 2013; Bertone et al. 2013)

$$\bar{\ell}^k_B = \frac{x^k_B-x^k_A}{R_{AB}}+\frac{2G}{c^2}\sum_P\mathcal{M}_P\left\{-\frac{N^k_{AB}}{2R_{PB}}+\frac{d^k_B}{d^2_B}\left[-\frac{\boldsymbol{N}_{\boldsymbol{AB}}\cdot\boldsymbol{R}_{\boldsymbol{PB}}}{R_{PB}}+\frac{R_{PB}-R_{PA}}{R_{AB}}\right]\right\}+O\left(c^{-4}\right)\ , \tag{4.6}$$

where $d^i_B\equiv R^i_{PB}-N^i_{AB}(\boldsymbol{R}_{\boldsymbol{PB}}\cdot\boldsymbol{N}_{\boldsymbol{AB}})$. Once solved for $\bar{\ell}^k$, the astrometric observable is defined by its projection on a tetrad $E^\beta_{\hat{a}}$ comoving with the observer (Bini et al. 2003) as

$$n_{(i)} = \frac{(\bar{\ell}_B-\nu)_\beta E^\beta_{(i)}}{\bar{\gamma}(1-\nu_\alpha\bar{\ell}^\alpha_B)}\ , \tag{4.7}$$

where ν_α is the four-velocity of the satellite u_s relatively to the local barycentric observer u and $\bar{\gamma}=-u^\alpha_s u_\alpha$.

An explicit expression of the tetrad $E^\beta_{\hat{a}}$ adapted to Gaia has been obtained in (Crosta & Vecchiato 2010) by successive transformations of the local BCRS tetrad (Bini et al. 2003). Using this approach, RAMOD provides a complete modeling of the astrometric observable.

5 Setting explicit relations among the astrometric models

The comparison of GREM and RAMOD is considered as a priority for the Gaia mission (Crosta & Vecchiato 2010; Crosta 2011) since they will both concur to the creation of the mission catalog. Any inconsistency in the relativistic models would then invalidate the quality and reliability of the estimates, hence all related scientific output. Both models are internally consistent at the μas level required by Gaia but their different conception makes an analytical cross-check a complex task.

In a recent work by (Crosta & Vecchiato 2010), the authors show that the PN expansion of Eq. (4.7) up to the order needed at Gaia accuracy yields the equivalence with the observable defined in Eq. (4.1) for GREM. However, a complete analytical cross-check of the modeling for gravitational light deflection has not been done yet. Moreover, despite their differences, both models aim for the reconstruction of light trajectory from the star to the observer in order to build the astrometric observable. This makes the TTF model presented in section 3 a completely new and independent approach to the problem, particularly adapted to contribute to the verification process of the relativistic solutions to be used for the Gaia mission.

In this section, we present the relations allowing to cross-check the relativistic description of light propagation in GREM, RAMOD and our TTF model by computing the light direction triple $\widehat{k}_i$ in the three models, then by comparing the resulting formulae in the gravitational field of point bodies.

5.1 GREM

The relation between the light direction triple and the photon velocity $\dot{x}^i$ used in GREM is given by

$$\hat{k}_i \;=\; \frac{g_{ij}k^j + g_{0i}k^0}{g_{00}k^0 + g_{0i}k^i} = -\frac{\dot{x}^i}{c} - 2h_{00}\sigma^i + \mathcal{O}(c^{-4})\,, \tag{5.1}$$

noting that $\dfrac{\dot{x}^i}{c} = \dfrac{dx^i/d\lambda}{dx^0/d\lambda} = \dfrac{k^i}{k^0}$. Using Eq. (4.3), Eq. (4.4) and the metric tensor (2.1) into Eq. (5.1) taken at the reception event, it is then straightforward to check the equivalence with Eq. (3.4).

5.2 RAMOD

The relation between the light direction triple $\widehat{k}_i$ and the local line-of-sight $\bar{\ell}^i$ of RAMOD at reception point x_B is obtained by expanding Eq. (4.5) at the order c^{-3} required for Gaia. Considering that $u^0 = 1 + \dfrac{h_{00}}{2} + O(c^{-4})$, we get

$$\left(\widehat{k}_i\right)_B = -\bar{\ell}^i_B \left[1 + \frac{3}{2}h_{00}\Big|_B\right] + \mathcal{O}(c^{-3})\,. \tag{5.2}$$

Substituting for $\bar{\ell}^i_B$ from Eq. (4.6) and using the metric given in Eq. (2.1) into Eq. (5.2), the reader can easily retrieve Eq. (3.4). Combining this result with Eq. (4.7), one also gets the equivalence with the TTF astrometric observable (3.1).

6 Conclusions

In this communication we review three relativistic approaches to the modeling of an astrometric observation, namely GREM, RAMOD and the one based on the TTF. We describe the steps allowing to get the unperturbed direction of the source of a light signal from the direction measured by an observer in motion within a gravitational field. To apply our analysis in the context of the Gaia mission, we work in the weak-field approximation of GR, considering a metric tensor adapted to the μas accuracy. Finally, we give explicit relations between the quantities defined in each approach to describe the direction of a light ray at its reception coordinates. Using these relations (5.1)-(5.2) it is straightforward to show the equivalence of the three approaches at the μas level of accuracy. We shall note that such a cross-checking procedure enters the same thread of model comparison started in (Crosta & Vecchiato 2010), which is essential to fully understand the observational data coming from Gaia in a common experimental context.

S. Bertone thanks UIF/UFI (French-Italian University) for the financial support of this work. S. Bertone, C. Le Poncin-Lafitte and M.-C. Angonin are grateful to the financial support of CNRS/GRAM and CNES/Gaia. The work of M. Crosta and A. Vecchiato has been partially funded by ASI under contract to INAF I/058/10/0 (Gaia Mission - The Italian Participation to DPAC).

References

Bertone, S. & Le Poncin-Lafitte, C. 2012, Memorie della Società Astronomica Italiana, 83, 1020

Bertone, S., Minazzoli, O., Crosta, M., et al. 2013, ArXiv e-prints, accepted by Classical and Quantum Gravity

Bienayme, O. & Turon, C. 2002, EAS Publications Series, 2

Bini, D., Crosta, M. T., & de Felice, F. 2003, Classical and Quantum Gravity, 20, 4695

Brumberg, V. A. 1991, Essential relativistic celestial mechanics

Crosta, M. 2011, Classical and Quantum Gravity, 28, 235013

Crosta, M. 2013, ArXiv e-prints

Crosta, M. & Vecchiato, A. 2010, Astronomy and Astrophysics, 509, A37

de Felice, F., Crosta, M., Vecchiato, A., Lattanzi, M., & Bucciarelli, B. 2004, Astrophysical Journal, 607, 580

de Felice, F., Vecchiato, A., Crosta, M. T., Bucciarelli, B., & Lattanzi, M. G. 2006, Astrophysical Journal, 653, 1552

Hees, A., Bertone, S., & Le Poncin-Lafitte, C. 2013, submitted to Physical Review D

Klioner, S. A. 2003, Astronomical Journal, 125, 1580

Lindegren, L., Lammers, U., Hobbs, D., et al. 2012, Astronomy & Astrophysics, 538, A78

Misner, C., Thorne, K., & Wheeler, J. 1973, Gravitation (San Francisco: W. H. Freeman)

Soffel, M., Klioner, S. A., Petit, G., et al. 2003, Astronomical Journal, 126, 2687

Teyssandier, P. & Le Poncin-Lafitte, C. 2008, Classical and Quantum Gravity, 25, 145020

Vecchiato, A., Abbas, U., Bandieramonte, M., et al. 2012, in Society of Photo-Optical Instrumentation Engineers (SPIE) Conference Series, Vol. 8451

Weinberg, S. 1972, Gravitation and Cosmology: Principles and Applications of the General Theory of Relativity

Will, C. M. 1993, Theory and Experiment in Gravitational Physics

SF2A 2013
L. Cambrésy, F. Martins, E. Nuss and A. Palacios (eds)

RADIO SOURCE STRUCTURE AND VLBI POSITION INSTABILITIES

R. Bouffet[1,2], P. Charlot[1,2] and S. Lambert[3]

Abstract. Astrometric positions of extragalactic radio sources derived from VLBI data are used to build highly-accurate reference frames such as the International Celestial Reference Frame. Despite their distant locations, instabilities in the position of these sources are often seen on time scales of months to years, which is generally thought to be caused by source structure evolution. In this paper, we compare position instabilities and structural evolution for a sample of 68 sources observed over a 10-year period (1994–2003). Our results indicate that the two phenomena are linked at some level although the correlation is not perfect.

Keywords: Reference systems, astrometry, active galactic nuclei, quasars, VLBI

1 Introduction

The current IAU fundamental celestial reference frame, namely the ICRF2 (second realization of the International Celestial Reference Frame), which has been in use since January 1, 2010, includes positions for a total of 3414 extragalactic radio sources distributed over the entire sky. Such positions were determined from VLBI data acquired at 8.4 and 2.3 GHz over 30 years (1979–2009). The ICRF2 has a floor of 40 microarcseconds (μas) in the individual source coordinate accuracies and an axis stability of 10 μas (IERS 2009). Joint observational efforts of the VLBI community aiming at a denser and even more accurate celestial frame continue in order to further improve the quality of the frame.

One limitation in improving the accuracy of the individual VLBI source positions originates in actual astrometric instabilities which are found in these positions. Due to their location at cosmological distances, no proper motions are expected for these sources and their astrometric positions should thus be stable with time. While this is indeed the case on the long term, it is not true for shorter time scales (months to years) where instabilities at the level of several hundreds of microarcseconds are commonly detected (IERS 2009). Such instabilities are usually attributed to varying source structure which is often spatially-extended at the level of the VLBI resolution (Fey & Charlot 2000). Structural variations are generally due to ejection of material from the central VLBI core in a recurrent although unpredictable manner causing shifts in the brightness centroid of the radio emission and hence potential VLBI astrometric instabilities.

In this paper we compare source position instabilities and structural variations based on astrometric and imaging VLBI data covering a period of 10 years (1994–2003). The datasets are presented in Sect. 2 while Sect. 3 describes the analysis scheme. Section 4 reports our findings and discusses correlations between the two phenomena. In the last section, we draw prospects for further work in this area.

2 Observations

The data used to derive astrometric positions were acquired during numerous VLBI sessions conducted by the International VLBI Service for geodesy and astrometry (IVS) over the past 30 years (Behrend 2013). A large number of observations is available for many sources which permits monitoring of their astrometric positions on time scales of days to weeks. Analysis was carried out in a similar way as that described in Gontier et al.

[1] Univ. Bordeaux, LAB, UMR 5804, F-33270, Floirac, France
[2] CNRS, LAB, UMR 5804, F-33270, Floirac, France
[3] Observatoire de Paris - SYRTE, CNRS/UMR 8630 & Université Pierre et Marie Curie, 75005 Paris, France

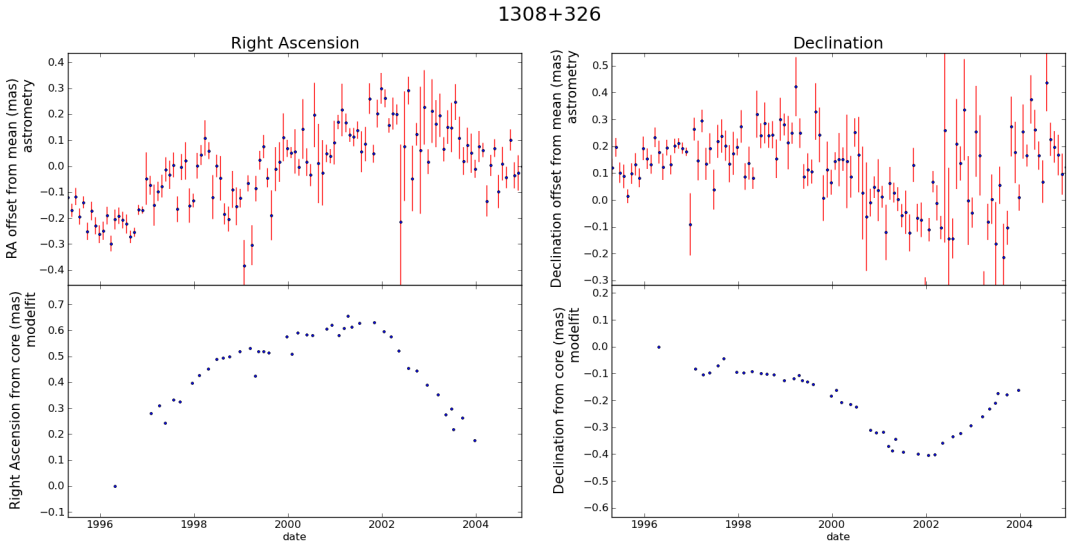

Fig. 1. Comparison of the astrometric position instabilities (upper panels) and brightness centroid motions (lower panels) for the source 1308+326 between 1996 and 2003. The left panels are for right ascension while the right panels are for declination. The vertical scale is in milliarcseconds (mas).

(2006). For our study we averaged the individual session-based positions over monthly intervals in order to have a sampling similar to that of the imaging data.

Structural variations were taken from the analysis of VLBI jet kinematics reported in Piner et al. (2012). This analysis has made use of 2753 images at 8.4 GHz obtained from 50 Research & Development VLBI sessions organized by the IVS and the Very Long Baseline Array between 1994 and 2003. Six such sessions are carried out every year with a sampling of approximately two months. The network includes 15–20 stations, yielding high-quality VLBI images. 68 sources observed at 20 epochs or more (with a median of 43 epochs per source) are included in the present study.

3 Analysis

For our study, we used a simplified representation of the source structures in the form of a limited number of Gaussian components obtained through model-fitting (as available in Piner et al. (2012)). Such a representation was preferred because it identifies the VLBI core of each source from epoch to epoch and aligns automatically the brightness distributions over time, assuming that the core position is stable. This alignment is crucial since the absolute map position is lost during the imaging process due to self-calibration.

Processing further the source structural information, we calculated the centroid of the brightness distribution (i.e. the centroid of the Gaussian components) at every epoch, allowing us to assess the relative motion of the brightness centroid with time. This calculation was carried out for 68 sources observed at 20 epochs or more for which model-fits are available in Piner et al. (2012). The result is a time series of centroid positions which may be compared with the monthly-averaged VLBI astrometric positions. This comparison assumes that the source motion as seen from the astrometric data is well matched with the motion of the centroid of the brightness distribution detected from VLBI imaging.

4 Results and discussion

An example of the comparisons that we carried out using the scheme explained in the previous section is presented in Fig. 1. The upper panels show the evolution in right ascension and declination of the astrometric position of the source 1308+326 over 1996–2003, while the lower panels show the motion of its brightness centroid over the same period of time. Uncertainties in the astrometric positions were derived as weighted averages (over monthly intervals) of the individual session-based uncertainties. Declination has higher uncertainties due

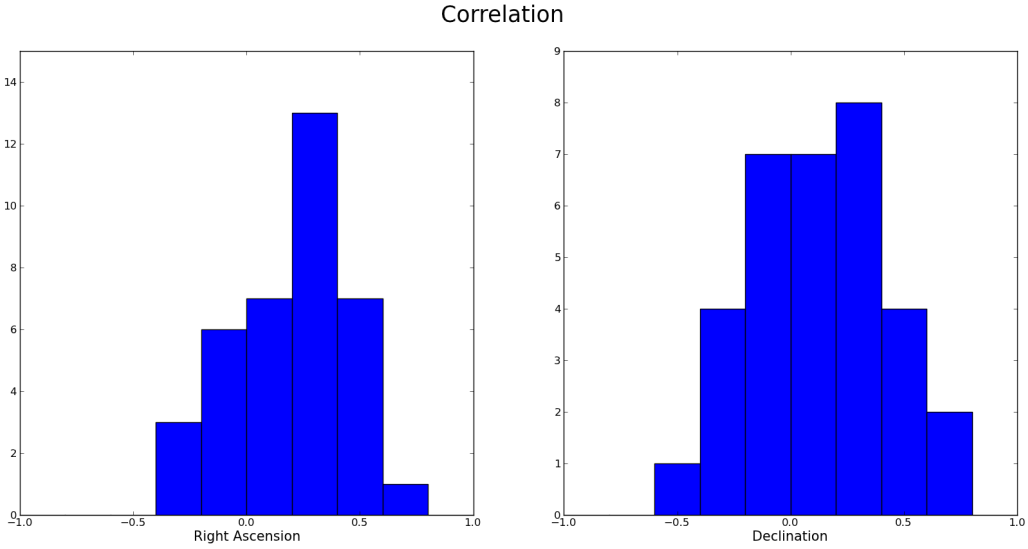

Fig. 2. Distribution of correlation coefficients between astrometric position instabilities and structural variations for all sources with significant astrometric instabilities (reduced $\chi^2 > 4$). Note that the source 0923+392 which shows atypical evolution has been removed from the sample for the purpose of this histogram.

to the predominantly East-West baselines of current VLBI networks. No error bars are given for the centroid positions because model-fitting does not provide a direct mean to estimate reliable uncertainties for the Gaussian components representing the structures.

Examination of the plots in Fig. 1 indicates similar trends in the evolution of the astrometric and brightness centroid positions. This is also confirmed when calculating correlation coefficients between the two series, which are 0.30 in right ascension and 0.63 in declination. Applying the same calculation to all sources, an overall positive correlation is found (median value of 0.22 in right ascension and 0.19 in declination) as shown in Fig. 2. This indicates that structural variations and astrometric instabilities are linked at some level.

Looking at Fig. 2, one also notes that a fraction of the sources show a negative correlation. At this stage, it is not understood however whether this negative trend is real or whether it results from the lack of significance of some of the correlation coefficients. For example, the correlation coefficients may be questionable when there is no notable evolution in both the astrometric and brightness centroid positions. Further studies are thus necessary to assess the significance of the correlation coefficients. Ultimately, every source may have to be examined separately to understand any discrepancy that may happen between the two series of positions.

Different trends in the astrometrically-derived and structurally-derived positions (possibly leading to negative correlation) may result from misidentification of the core component over the successive epochs (thereby affecting the alignment of images and the brightness centroid relative locations) or from effects coming from the S band (2.3 GHz) data. For a full analysis, the S band structures should indeed be considered as well since the astrometric positions are derived from a combination of the data at the two frequencies whereas only the X band (8.4 GHz) structures have been considered in the above comparisons. The S band data have a lower weight though and are thus a priori less likely to affect strongly the positions, hence the reason for neglecting them on first stage.

5 Conclusions

A comparison between the evolution of astrometric positions and the variations of source structure (characterized as the motion of the centroid of the brightness distribution) has been carried out for a sample of 68 sources observed over a period of 10 years between 1994 and 2003. This comparison reveals similar trends in the astrometric and structural time series of positions for some sources showing significant motions like 1308+326. On the other hand, the correlation for sources with smaller motions is more difficult to assess. Overall, a positive correlation is found between the two time series, which favors an explanation of VLBI positions instabilities in terms of structural variations.

In the future, we plan to refine this comparison by examining carefully each individual source in the sample. In some cases, the comparison may not be reliable because position errors are too large and the motions are not significant while in others different trends are seen, which needs to be understood. Possible explanations for such discrepancies include misidentification of the core components over the epochs and effects of the S band data. In the longer term, enlarging the source sample and expanding the time span covered by the astrometric and imaging data up to recent years would be desirable.

The authors gratefully acknowledge support from the CNRS through the "Action Spécifique GRAM" for this project.

References

Behrend, D. 2013, Data Science Journal, 12, WDS81

Fey, A. L. & Charlot, P. 2000, ApJS, 128, 17

Gontier, A.-M., Lambert, S. B., & Barache, C. 2006, in SF2A-2006: Semaine de l'Astrophysique Francaise, ed. D. Barret, F. Casoli, T. Contini, G. Lagache, A. Lecavelier, & L. Pagani, 23

IERS, & IVS Working Group. 2009, IERS Technical Note, 35

Piner, B. G., Pushkarev, A. B., Kovalev, Y. Y., et al. 2012, ApJ, 758, 84

SF2A 2013
L. Cambrésy, F. Martins, E. Nuss and A. Palacios (eds)

ORBIT DETERMINATION METHODS IN VIEW OF THE PODET PROJECT

F. Deleflie[1], D. Coulot[2], R. Decosta[1], A. Vienne[1] and P. Richard[3]

Abstract. We present an orbit determination method based on genetic algorithms. Contrary to usual estimation methods mainly based on least-squares methods, these algorithms do not require any *a priori* knowledge of the initial state vector to be estimated. These algorithms can be applied when a new satellite is launched or for uncatalogued objects

We show in this paper preliminary results obtained from an SLR satellite, for which tracking data acquired by the ILRS network enable to build accurate orbital arcs at a few centimeter level, which can be used as a reference orbit. The method is carried out in several steps: *(i)* an analytical propagation of the equations of motion, *(ii)* an estimation kernel based on genetic algorithms, which follows the usual steps of such approaches: initialization and evolution of a selected population, so as to determine the best parameters. Each parameter to be estimated, namely each initial keplerian element, has to be searched among an interval that is preliminary chosen.

Keywords: orbit determination, analytical propagation, genetic algorithms, space debris

1 Introduction

The main goal of this study consists in finding a way, to compute an orbit from tracking data, when no *a priori* information on the trajectory is available at all. In that case, classical methods such as least-squares can not be used any more (since in that case the function to be minimized can not be linearized in the neighborhood of the *a priori* values of the parameters). Moreover, the usual methods may suffer from many drawbacks which can frequently make them be unappropriated; they are often merely based on keplerian modelings, and can hence not be applied over time scales longer than a couple of hours.

On the contrary, even if other kinds of difficulties have to be managed, methods based on genetic algorithms are supposed to be valid for all dynamical configurations, since the algorithm itself is independent from the orbit propagator used to compute the cost function. With an efficient dynamical modeling, they can be used over different periods of time, from a couple of minutes (for Too-Short Arcs, TSA) up to a couple of days or weeks.

We provide here the preliminary results we obtain with measurement on the Lageos-1 satellite, tracked by the International Laser Ranging Service, the ILRS (Pearlman, 2002) network.

2 Orbital modeling

To keep a reasonable computation time for the propagation step, we use an analytical approach to get orbital element time series. The modeling is supposed to be valid whatever the values of the eccentricity or the inclination, small (even equal to zero), or large: the model is written in a set of equinoctial elements (Deleflie, 2013), namely: a, $\xi = \Omega + \omega + M$, $e\cos(\Omega+\omega)$, $e\sin(\Omega+\omega)$, $i_x = \sin\frac{i}{2}\cos\Omega$, $i_y = \sin\frac{i}{2}\sin\Omega$, where a, e, i, Ω, ω, M stand for the classical keplerian elements.

The whole analytical modeling is governed by the set of mean initial conditions, whereas it is the corresponding osculating initial conditions $E(t_0)$ that are adjusted by the genetic algorithm, and that can be directly compared to the reference orbits, if they are expressed in the same reference frame.

[1] IMCCE, Observatoire de Paris, UPMC, univ. Lille1, CNRS. F-75014 Paris, France
[2] IGN/LAREG, Université Paris Diderot, Sorbonne Paris Cité, Paris, France
[3] Centre National d'Etudes Spatiales, Toulouse, France

3 Multi-Objective Genetic Algorithm (MOGA) used

3.1 Description

The Multi-Objective Genetic Algorithm (MOGA) used here is the ϵ-MOEA (Deb et al., 2003). Between two successive iterations, some vectors of initial conditions are replaced by other ones and the best ones are archived. The evolution through the iterations of the set of initial conditions is governed by mutations (random small changes in vectors of possible initial conditions) and by crossover (mix two vectors of possible initial conditions) ; the probabilities of changes are usual parameters of the approach. At the end of the iteration procedure, a set of solutions is supplied (Coello Coello et al., 2007).

As in many orbit determination algorithms, an evaluation is made up of several steps:

- ϵ-MOEA provides a vector of initial conditions, randomly chosen among a large set of possible (osculating) initial values ;
- These initial conditions are used to propagate an analytical orbit over the period when tracking or astrometric data are available ;
- The analytical orbit, as time series of orbital elements, is used to compute predicted measurements, that can be compared to the available data sets, at the same epochs of the observations ;
- These predicted measurements are compared to the true data ;
- The values of the cost functions are computed.

3.2 Parameterization

The chromosomes represent the initial state of the solution: each one is then made up of six initial orbital keplerian elements, and each chromosome determines a unique orbit. Let us note that the MOGA runs on a population of constant size, but also with an archive of variable size, to keep knowledge of the best solutions found so far. At each iteration, two children may be generated (depending upon the probability of crossover) from two parents randomly taken from both the population and the archive, and mutations may also occur (depending on the probability of mutation).

For this first attempt, we chose a population of 400 chromosomes, with fixed intervals for each keplerian initial element:

- semi–major axis $a \in [12200; 15600]$ km
- eccentricity $e \in [0; 0.1]$
- inclination $i \in [0; 180°[$
- angles Ω, ω $M \in [0; 360°[$

Let us note that to reduce computation time, the search for the initial eccentricity has been reduced to an interval with a wideness of 0.1, and the search of the initial semi major axis to intervals large of a few thousands of kilometers.

The crossover probability has been set up to $p_C = 0.9$, and the mutation probability to $p_m = 1/6 \simeq 0.16667$. The stop condition is the total number of iterations which is here set up to 500 000 (this corresponds to a total CPU time of the order of 30 hours).

3.3 Genetic algorithm handled with range data: the SLR satellite Lageos-1

We use a set of Satellite Laser Ranging (SLR) data acquired on Lageos-1 by 29 stations of the tracking network of the ILRS, and including 2034 measurements, over eight days in April 2012 (from MJD 56 024 to 56 031 included). We consider here two objectives to be optimized: we search not only for the best vector of initial conditions (the RMS of differences between predicted measurements and the real data has to be minimized); but also, we search for an optimal sub-network of SLR stations so that the number of SLR stations involved in the computation has to be maximized.

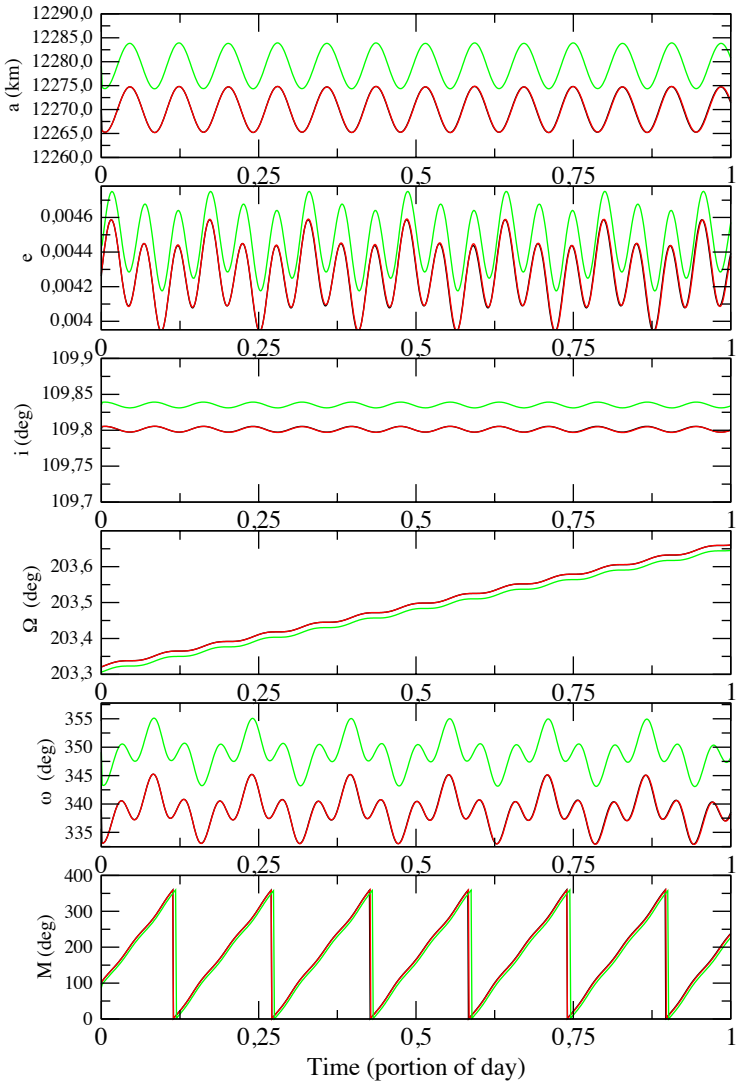

Fig. 1. Time series of each keplerian orbital elements $(a, e, i, \Omega, \omega, M)$, computed for the Lageos-1 satellite, in the inertial frame, where the equations of motion are propagated. X-axis: time (portion of day of 7th April 2012). Black curves correspond to the reference orbit (computed with the Gins CNES s/w) ; the red ones correspond to the trajectories obtained with our analytical modeling and with the reference initial conditions provided by Gins ; the green ones correspond to the trajectories obtained with our approach (with initial conditions estimated with the genetic algorithm).

The RMS of differences between the tracking data and their theoretical equivalent computed with the reference orbit (obtained from post-fit adjustment of a numerical integration with the CNES Gins software) is at the level of 2.15 cm. The adjusted initial conditions, seen as reference ones, are the following:

- $a_0^{\text{ref}} = 12270.009$ km

- $e_0^{\rm ref} = 0.004261$
- $I_0^{\rm ref} = 109.801°$
- $\Omega_0^{\rm ref} = 203.323°$
- $(\omega_0 + M_0)^{\rm ref} = 76.616°$

The best results found by the MOGA are the following:

- $a_0 = 12274.840$ km: $\Delta a = 4.831$km
- $e_0 = 0.004408$: $\Delta e = 0.000147$
- $I_0 = 109.839°$: $\Delta I = 0.038°$
- $\Omega_0 = 203.306°$:$\Delta\Omega = 0.017°$
- $\omega_0 + M_0 = 76.538°$: $\Delta(\omega + M) = 0.078°$

Figure 1 shows the time series of each orbital element, over the given period of time: semi–major axis, eccentricity, inclination, longitude of the node, perigee, mean anomaly. The black curves correspond to the reference orbit obtained with the Gins s/w. The red curves correspond to the analytical propagation of the model presented above, but with the reference initial conditions. It appears that at this scale, the analytical simplified model that we use is suitable to handle the dynamics of the trajectory (at the level of the results). Finally, the green curves show the best trajectory that is found by the MOGA. The differences between the two sets of initial conditions (Δa, Δe, Δi, $\Delta\Omega$, $\Delta\omega$, ΔM above) are quite small with respect to each value to be determined (3 10^{-4} on a, 3% on e, 3 10^{-4} on i, relatively), but induce as well a difference that is not compensated during the propagation. We should keep in mind that *(i)* this level of precision is good enough to use these initial values as *a priori* values in a least-squares adjustment ; *(ii)* genetic algorithms have anyway a good capability over the global scale, but locally they can be less accurate than other approaches ; *(iii)* better results are likely to be obtained when changing the parameterization of the MOGA (in a forthcoming paper); *(iv)* we compare sets of elements expressed in two different reference frames (inertial frame and true of date).

4 Conclusions

In this paper, we combined a MOGA and an analytical satellite motion theory to roughly adjust an orbit on tracking data, without any *a priori* knowledge of the values of the initial conditions to be retrieved. We tested the method on two kinds of data. Some further developments will be enhanced in the future *(i)* the analytical modeling will be improved by adding some significant terms in the model *(ii)* the parameterization of the MOGA will be refined, with a reduced set of chromosomes, and by empirically decreasing the mutation probability throughout the iterations; we will implement as well a better stopping condition to reduce the CPU required time. We will then test the capabilities of the algorithm in downgraded conditions (data sparse in time, very few number of data).

References

Coello Coello, C.A., G.B. Lomont, D.A. Von Veldhuizen, Evolutionary Algorithms for Solving Multi-Objective Problems, Second Edition, Springer, 2007.

Deb, K., M. Mohan, S. Mishra, A Fast Multi-objective Evolutionary Algorithm for Finding Well-Spread Pareto-Optimal Solutions, KanGAL Report Number 2003002, 2003.

Pearlman, M.R., Degnan, J.J.,, and Bosworth, J.M., The International Laser Ranging Service, Adv. In Sp. R., Vol 30, No 2, pp 135-143, 2002.

Deleflie, F., Finalized Analytical Satellite Theory, CNES Internal Report, 2013.

SF2A 2013
L. Cambrésy, F. Martins, E. Nuss and A. Palacios (eds)

HIGH PRECISION ASTROMETRY IN ASTEROID MITIGATION - THE NEOSHIELD PERSPECITVE

S. Eggl[1], A. Ivantsov[1], D. Hestroffer[1], D. Perna[2], D. Bancelin[1,3] and W. Thuillot[1]

Abstract. Among the currently known Near Earth Objects (NEOs), roughly 1400 are classified as being potentially hazardous asteroids. The recent Chelyabinsk event has shown that these objects can pose a real threat to mankind. We illustrate that high precision asteroid astrometry plays a vital role in determining potential impact risks, selecting targets for deflection demonstration missions and evaluating mitigation mission success. After a brief introduction to the NEO-Shield project, an international effort initiated by the European Commission to investigate aspects of NEO mitigation in a comprehensive fashion, we discuss current astrometric performances, requirements and possible issues with NEO risk assessment and deflection demonstration missions.

Keywords: asteroid deflection, NEOShield, astrometry, Near Earth Object

1 Introduction

Catastrophic collisions of our Earth with asteroids larger than 10km are fortunately rare, yet impact frequencies for objects sized between 15m and 500m are non negligible, as the recent event in Chelyabinsk has shown (Harris 2010). Given the fact that roughly 1400 among the currently known Near Earth Objects (NEOs) are potentially hazardous asteroids (PHA), a comprehensive understanding of the orbital and physical properties of these celestial bodies is desirable in order to allow for a reliable threat assessment. The NEOShield project (Harris et al. 2013) constitutes an international effort under European leadership to enhance our understanding of threat mitigation options regarding potential asteroid impacts. In the framework of this project different mitigation strategies, such as blast deflection, kinetic impactors or gravity tractors are not only studied individually, but they are put in context of realistic threat scenarios. Past missions to Comets and asteroids such as Rosetta (ESA), Hayabusa (JAXA) and NASA's DAWN and Deep Impact missions have shown that we are capable of performing rendez-vous as well as high velocity collisions with a minor planet. Many open questions remain, however, regarding the details of asteroid deflection, such as the momentum enhancement due to ejecta, optimum targeting and impacting strategies. The development of a mitigation test mission will, thus, be a focus of the NEOShield project.

Asteroid deflection might seem to be centered on engineering issues. Yet, the importance of high precision astrometry should not be underestimated in this context. In the following sections we will discuss multiple topics that require high quality astrometric data in order to provide vital input to asteroid threat assessment and mitigation evaluation.

2 NEO Threat Assessment

Given the fact that our knowledge of the exact orbit of a NEO at any given time is limited by observational as well as modeling uncertainties, threat assessment has to be conducted on a probabilistic basis. Hereby, the standard approch is to perform an initial orbit determination using a small subset of the available NEO observations. A differential correction method is applied to improve the NEO's orbit using weighted residuals

[1] IMCCE - Observatoire de Paris, 77 Avenue Denfert-Rochereau, 75014 Paris, France
[2] LESIA - Observatoire de Paris, 5, place Jules Janssen 92195 MEUDON Cedex, France
[3] Institute for Astrophysics, University of Vienna, T́urkenschanzstr. 17., 1180 Vienna, Austria

of all available observation data (e.g. Milani & Gronchi 2010). This yields a covariance matrix that contains the observation uncertainties of the nominal trajectory. The covariance matrix of an asteroid's orbital elements at a given epoch is then used to generate initial state vectors of virtual asteroids (VA) or clones following a line of variation (LOV) sampling approach (Milani et al. 2005, 2002). The equations of motion of the nominal asteroid and its clones are solved numerically and their trajectories are monitored for close encounters with the Earth. Should a close encounter occur, then the minimum encounter distance is calculated, and the target plane (b-plane) coordinates of the respective clone are stored together with the minimum encounter distance. Potential virtual impactors (VI) are flagged and the impact probability can be calculated following e.g. (Milani et al. 2005; Valsecchi et al. 2003).

The fact that the uncertainty in an NEO's orbit plays an essential role in the impact prediction machinery makes it necessary to have observational data of sufficient quantity and quality to perform a reliable threat assessment. In other words, the better constrained the initial orbit uncertainties, the more accurate the impact probability estimates. This, of course, provokes the following questions: How well constrained should NEO orbits be to allow for a reliable impact analysis? How many observations are necessary to achieve such constraints?

Global answers to these questions are difficult to obtain, since the achievable improvement depends on many parameters, such as the quantity and quality of previous observations, weighting of residuals the length of the achieved data arc, and so on (Carpino et al. 2003; Baer et al. 2011). Radar observations usually are very valuable in this respect, since range and range-rate measurements are not readily accessible via optical astrometry, unless triangulation can be applied (Eggl 2011). Due to the relatively short range and high cost of radar observations, orbit determination and improvement of asteroids is still performed primarily via optical astrometry. The quality of the latter, thus, plays an essential role in determining whether or not an asteroid poses a potential threat to our planet.

While precise numbers are hard to come by, a rough correlation between the expected orbit quality and the available quantity of observation data can be inferred from plotting the Current Ephemeris Uncertainty (CEU), which is basically the positioning uncertainty in an observer's sky plane (Bowell 2009), against the number and arc-length of observations (Desmars et al. 2013), see Fig. 1.*.

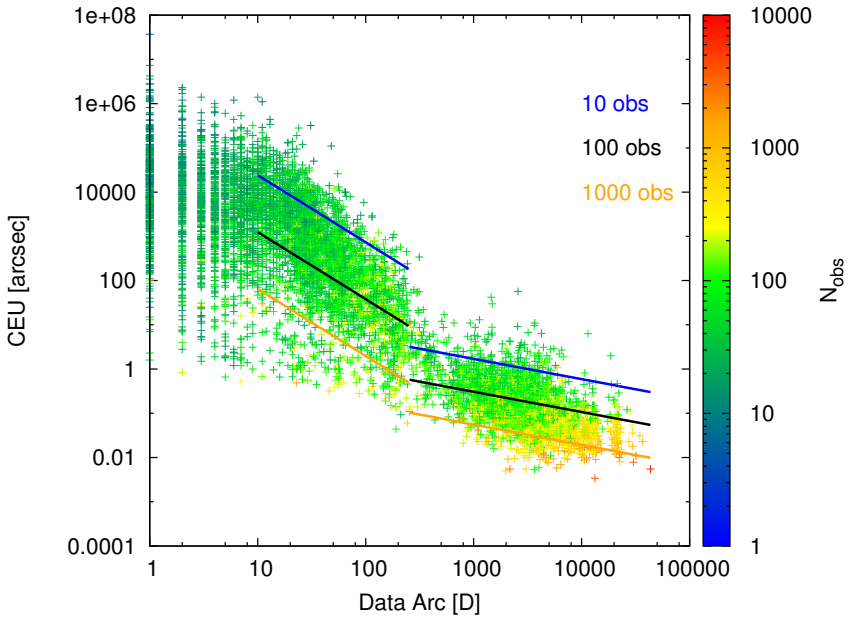

Fig. 1. Current Ephemeris Uncertainty (CEU) of NEOs as a function of the observed arc-length and the number of observations. While the quality of initial orbit determination for very short arcs (< 10 days) can only be evaluated on a case to case basis, trends in single opposition NEOs ($10 < arc < 200$ days) and multi-opposition NEOs ($arc > 360$ days) can be crudely estimated by log-linear least squares fits.

One can see that estimating the accuracy of initial orbit determination is difficult, especially, when only short

*The values shown in Fig. 1 have been generated using the currently discontinued astorb database as of 10/2012.

single opposition:	$a_1 = 7.08 \pm 0.09$	$a_2 = -1.83 \pm 0.04$	$a_3 = -0.93 \pm 0.05$
multi opposition:	$a_1 = 2.34 \pm 0.07$	$a_2 = -0.46 \pm 0.02$	$a_3 = -0.74 \pm 0.02.$

Table 1. Coefficients for the log-linear least squares fits (2.1) shown in Fig. 1.

observational arcs (< 10 days) are available. The transition region from single to multi opposition appears as a gap around 200 days. In order to get a rough idea on the CEU improvement with arc-length and number of observations, we can construct two log-linear least squares fits for single and multi opposition domains

$$\log_{10} CEU = a_1 + a_2 \ \log_{10} \ arc + a_3 \ \log_{10} \ N_{obs}. \tag{2.1}$$

The corresponding coefficients are given in Tab. 1. It is also evident from Fig. 1 that CEU values $\ll 1''$ are hard to achieve unless the NEO has been observed on a regular basis as well as over time spans that cover multiple oppositions. The reason for this apparent limit becomes clear when we consider the average quality of astrometric observations over the past years (Fig. 2).

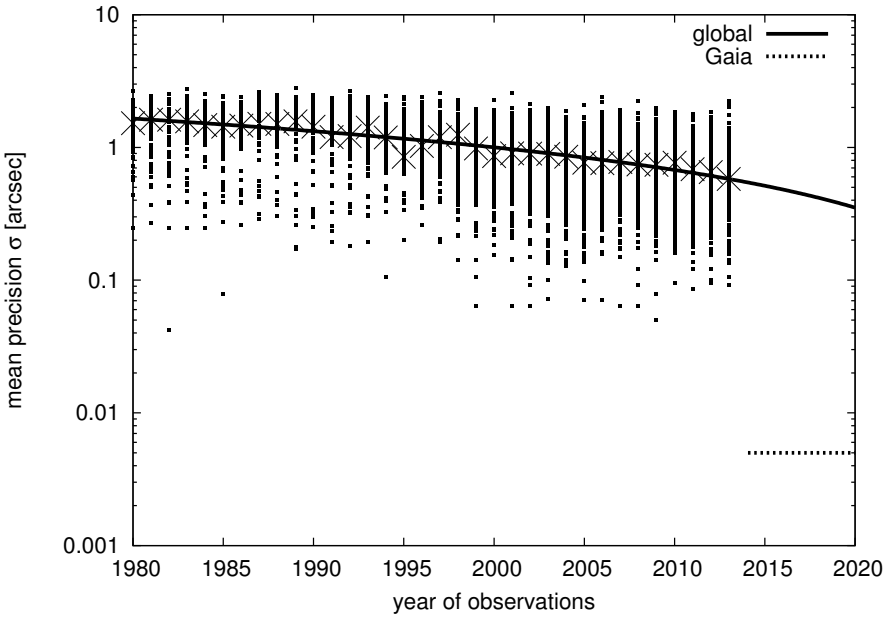

Fig. 2. The yearly astrometric mean precision ($\sigma = \sqrt{(\sigma_\alpha \cos\delta)^2 + (\sigma_\delta)^2}$) of each observatory with a Minor Planet Center designation and at least 10 submitted observations per year is plotted against time (dots). The crosses indicate global yearly averages, i.e. the weighted precision of all observations considered. The full line indicates the least squares trend of the global yearly averages, i.e. the mean quality of astrometric measurements. The dashed line represents pessimistic estimates for the performance of ESA's Gaia mission (Tanga & Mignard 2012).

Here, the yearly astrometric mean precision of each observatory with a Minor Planet Center designation is plotted as a function of time. However, observatories with less than 10 submitted observations per year have been omitted in order to guarantee the validity of the residual statistics. The astrometric mean precision (σ) is defined as $\sigma = \sqrt{(\sigma_\alpha \cos\delta)^2 + (\sigma_\delta)^2}$, where $\sigma_{\alpha,\delta}$ are the yearly mean precisions of all astrometric measurements of asteroids performed by the respective observatory.[†]. A weighted average using the respective number of considered residuals per observatory yields the global astrometric means denoted by the crosses in Fig.1. The linear least squares fit of the latter data can then be used as a crude indicator of the average astrometric performance to be expected given a specific year: $\bar{\sigma} = b_1 + b_2\ t$ with $b_1 = 65.932 \pm 3.619$, $b_2 = -0.032 \pm 0.002$ and $[t] = [yrs]$. It is evident from Fig. 2 that the average astrometric accuracy during the period where most of the NEOs have been discovered ranges between $0.1 - 3''$ with a sightly improving trend. This mirrors the

[†] `http://www.minorplanetcenter.net/iau/special/residuals.txt`

fact that the newly discovered NEOs tend to have CEU values of a similar magnitude (see Fig.1). While high precision astrometry measurements ($\sigma_{\alpha,\delta} < 0.1''$) have been available on a regular basis for about 10 years, their impact on the global NEO astrometric performance is still small. In fact, 98% of the observations in 2013 have a precision in the range of $0.13 - 2.01''$. We also find that current astrometric accuracy is within the same order of magnitude. ESA's Gaia mission is bound to change that. By generating a new celestial reference frame Gaia will solve many of the current problems related to biases in astrometric catalogs (Chesley et al. 2010; Mignard & Klioner 2012), thus impoving the accuracy of ground-based observations. It will also pave the way for unprecedented astrometrical measurement precision with many possible applications to Solar System and asteroid science (Bancelin et al. 2010; Beauvalet et al. 2012; Delbo' et al. 2012; Hestroffer et al. 2010; Ivantsov et al. 2013; Tsiganis et al. 2012). Pessimistic estimates on Gaia's astrometric precision are represented by the dashed lines in Fig. 2.[‡] It is easily seen that even under worst case assumptions Gaia will produce high precision astrometry that is two orders of magnitude beyond the global trend. Even-though this sounds promising, the actual performance of the astrometric orbit improvement has to be studied on a case-by-case basis. Bancelin et al. (2012) have investigated the likely impact of direct observations by Gaia on the orbit of 99942 Apophis. Their findings suggest a possible decrease of the asteroid's orbit uncertainty by two orders of magnitude, not accounting for the additional benefits of the updated catalog. Assuming such a drastic improvement of orbit uncertainties is indeed possible, Gaia will contribute significantly to NEO threat assessment.

3 Follow Up

It is well known that NEOs populate a very active dynamical region in the Solar System. Close encounters with the terrestrial planets, non gravitational forces and interaction with resonances cause their orbits to become chaotic on rather short time-scales with Lyapunov times of no more than a hundred years (Michel 1997; Michel et al. 2005; Wiegert et al. 1998). A continuous update of the orbits of already discovered asteroids becomes, thus, necessary, if one seeks to avoid sudden 'disappearances'. Fortunately, current computational facilities allow asteroids with well constrained orbits to be propagated accurately and thus remain retrievable over decades. The dynamical model that is used to predict future positions, however, has to be complete in the sense that all non-negligible forces are considered. This is especially tricky with respect to unexpected non-gravitational forces (Jewitt 2012) or close encounters with main-belt asteroids. The latter ones are often neglected in ephemeris calculations either for computational reasons, or because the masses involved are not well known. Yet, a preliminary investigation by the authors shows that the Mars-crossing NEO 184266, for instance, will have a close encounter with the main-belt asteroid 52 Europa in 2019. This close approach causes an observable deflection of roughly $0.06''$. If such a deflection is not accounted for, discrepancies between the predicted and the actual position of the NEO can grow very quickly. Thus, frequent observational updates using high precision astrometry can serve not only as a guarantee that known asteroids remain retrievable. Frequent measurements can also serve as a test for the quality of the applied dynamical model. Since Gaia will scan the whole sky several times during its 5 year mission, high precision astrometric follow up of once observed objects is basically guaranteed. Given the relatively short life-time of the Gaia mission, however, one should start to consider a long term follow up program to continue high precision astrometry after the era of Gaia has come to an end.

4 Deflection Validation

So-far we have discussed initial orbit determination and orbit correction as they constitute the main contributions of astrometry to NEO threat assessment. Yet, high precision astrometry can play another important role, namely in validating an asteroid's deflection. Sending a deflection mission to a potentially impacting asteroid could one day become a necessity to avert local or even global disaster. Therefore, the NEOShield consortium aims not only to produce a global response to such threat scenarios. The development of a deflection demonstration mission also constitutes a substantial pillar of the project. Given the political issues involved in launching nuclear missiles as well as the long duration of continuous slow push methods such as the gravity tractor, kinetic impactors seem to be the most economic choice for a deflection demonstration. A straight forward approach has been suggested in the Don-Quijote study (Harris et al. 2006). A space-craft (S/C) is launched and set on a collision course with a NEO. During the impact, the momentum of the S/C is transferred to the

[‡]The astrometric performance was estimated for $V \simeq 20$ objects with an additional penalty factor of 5 due to more rapid proper motion of NEOs (Tanga & Mignard 2012).

asteroid following the slightly adapted momentum conservation equation (4.1)

$$\Delta V = \beta \frac{m}{M} \Delta v, \tag{4.1}$$

where ΔV and Δv are the changes in the heliocentric velocities of the asteroid and the S/C, M and m are the asteroid's and the S/C's masses, respectively, and β denotes the momentum enhancement factor that is due to ejecta of surface material (Holsapple & Housen 2012). Since it is rather expensive to launch a massive S/C with a substantial amount of fuel, test deflections in the order of $\Delta V \simeq cm/s$ are being discussed. In order to being able to see the effect of such a minute push, the asteroid's orbit has to be very well characterized before and after the deflection event. In order to give a rough quantitative estimate on the necessary precision, we will assume that all of the momentum was used to change the NEO's semimajor axis (a). Then we have (Vasile & Colombo 2008):

$$\Delta a = \frac{2a^2}{\kappa} V \Delta V. \tag{4.2}$$

Here, Δa corresponds to the change in semimajor axis and $\kappa = G(M_\odot + m)$ is the gravitational parameter, with gravity constant G. Using the vis-viva equation $V^2 = \kappa(2/r - 1/a)$ and assuming an elliptic orbit for the NEO, i.e. $r = a(1-e^2)/(1 + e\cos\phi)$ we find

$$(\Delta a)^2 = \frac{4a^3}{\kappa} \frac{1 + 2e\cos\phi + e^2}{1 - e^2} (\Delta V)^2. \tag{4.3}$$

It is easily seen from equation (4.3) that a given deflection (ΔV) has the most effect on the semimajor axis when it is applied at the NEO's pericenter ($\phi = 0$). This is not necessarily always the case, as other trade-offs can be involved (Belton et al. 2011). In order to assess the chances of validating a given deflection, we can compare the effective change in semimajor axis with its current uncertainty (σ_a) and define a so-called 'deflection signal-to-noise ratio' (DSNR):

$$DSNR = \sqrt{\frac{(\Delta a)^2}{(\sigma_a)^2}} \tag{4.4}$$

Inserting equation (4.4) into (4.3) we arrive at

$$(\sigma a)^2 = \frac{4a^3}{\kappa} \frac{1 + 2e\cos\phi + e^2}{1 - e^2} \frac{(\Delta V)^2}{DSNR^2} \tag{4.5}$$

Equation (4.5) yields the necessary constraints on the NEO's semimajor axis to allow for a detection of a deflection ΔV with a signal-to-noise ratio $DSNR$. In order to be able to detect the previously assumed $\Delta V = 1\ cm/s$ for an asteroid with $a = 1.05\ au$, $e = 0$ at a signal-to-noise ratio of $DSNR = 10$, its orbital uncertainty in semimajor axis should be no larger than $7 \cdot 10^{-8}\ au$. This translates into permissible observational errors $\ll 1''$. Hence, either high precision astrometry is available before and after the mitigation process, or a radio science experiment much like NEAR is required to guarantee deflection validation (Yeomans et al. 2000).

5 Binary Asteroids

Discovering shortly before a deflection event that a possible target of a mitigation campaign consists in reality of two separate bodies can be considered a rather nasty surprise. Yet, binary asteroids might be favorable targets for a mitigation demonstration mission (e.g. AIDA/DART Cheng et al. 2012). Hence, determining whether a mission target belongs to the roughly 15% of NEOs that are binary should be a priority (Pravec et al. 2006). If the pair is not resolved, astrometry can be very helpful in this respect. The variations in the position of the photocenter due to the asteroids' motion around their common center of gravity can be used to identify multiplicity and generate binary orbital elements (Pourbaix 2002). Such systems are known as 'astrometric binaries'. In order to assess which binary NEO configurations are detectable with standard and high precision astrometry, we estimate the maximum astrometric amplitude (ρ) generated by the mutual orbital motion of binary asteroids following Eggl et al. (2013). Assuming a circular mutual orbit we have

$$\rho = \arctan(\mu a / r), \tag{5.1}$$

where a is the binary's separation and r the distance to the observer. Maximum astrometric amplitudes for NEOs with different separations and mass ratios are presented in Fig. 3. If both asteroids have similar masses,

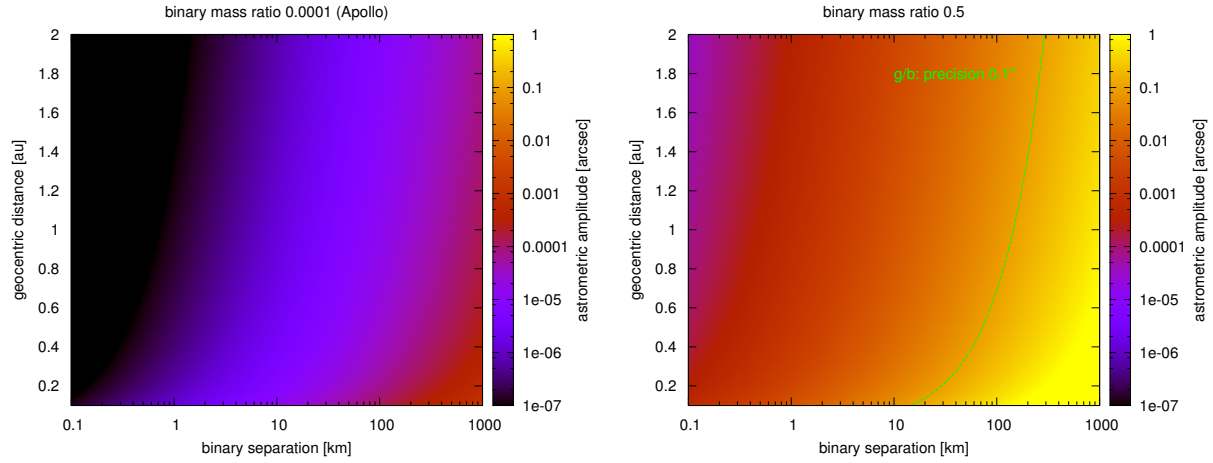

Fig. 3. Left: Expected astrometric amplitudes of the center of brightness of the larger asteroid in a binary configuration where one mass is dominant. The mass ratio is comparable to that of 1862 Apollo. Contemporary ground-based astrometry is not potent enough to resolve the motion of the center of brightness for such mass ratios. **Right:** If both asteroids have comparable masses, however, high precision ground-based astrometry would suffice to cover binary separations $> 10 - 100km$ depending on the asteroid's geocentric distance.

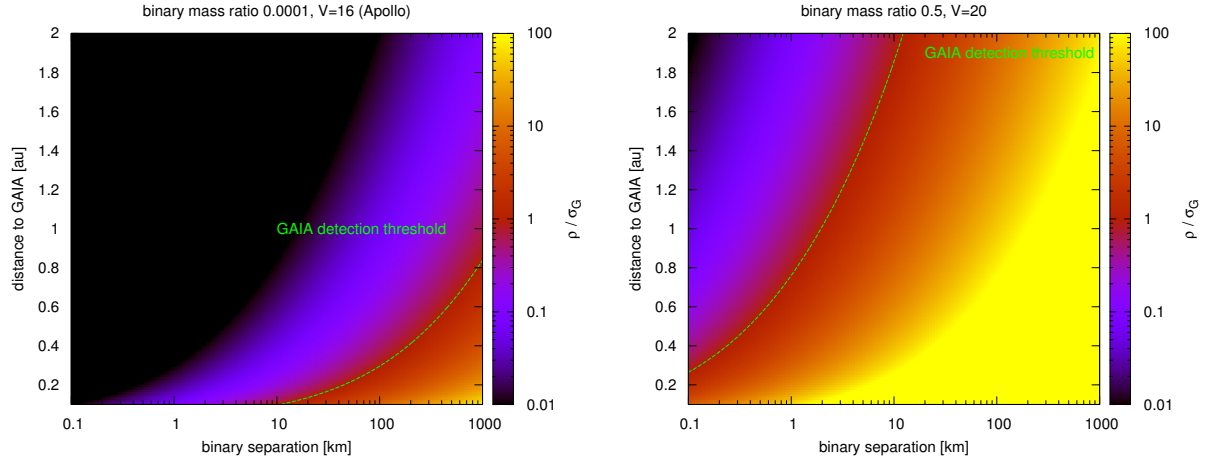

Fig. 4. Following Pravec & Scheirich (2012) the ratio of the astrometric amplitude of the center of brightness divided by Gaia's astrometric precision is shown as a function of binary separation and the geocentric distance of the binary. Here, we assume an angle of $\pi/2$ between the heliocentric position vectors of the asteroid and Gaia. **Left:** A configuration similar to Fig.3 is shown for the case of Gaia observations. Even Gaia will be hard pressed to detect the astrometric 'wobble' of the main component, if the companion is very light. The mass ratio and visual magnitude have been adopted from 1862 Apollo. **Right:** Equally massive binary components have a much better chance of being astrometrically detectable. Even for faint objects with V=20, most of the relevant binary separations are accessible to Gaia.

i.e. a mass ratio (μ) near 0.5, ground-based high precision astrometry can access a range of binary separations $> 10-100km$ depending on the geocentric distance of the NEO. Improving ground-based detection of astrometric binaries requries not only better hardware. As mentioned in section 2, a unified astrometric catalog such as

provided by Gaia will allow for more precise reduction of astrometric data. In any case, Gaia itself should be able to cover almost all relevant NEO binary separations for equally massive binaries, even if they are faint. This is shown in Fig. 4. Here, we follow Pravec & Scheirich (2012) and consider the astrometric amplitude of the wobble of the binary's center of brightness divided by the expected precision of Gaia, with a detection threshold of $\rho/\sigma_G > 1$. Gaia's expected precision is a function of the apparent brightness (V), i.e.

$$\sigma_G = 0.15 \cdot 10^{0.2(V-16)}, \tag{5.2}$$

where σ_G [mas] is the standard uncertainty of a single-epoch measurement of Gaia (Pravec & Scheirich 2012). Furthermore, a constant angle of $\pi/2$ between the object and Gaia is assumed. For asteroids with very small companions, such as 1862 Apollo, however, one can see in the left panel of Fig. 4 that even Gaia might be hard pressed to detect the astrometric oscillations of the center of brightness of the main component, especially if the binary is close. Also, it can be rather difficult to disentangle astrometric signals from other photocenter offsets due to irregular shapes and rotation of the observed object (e.g. Ortiz et al. 2011), and besides to desantagle from other photocenter offsets due to rotation, shape and phase. Hence, 'asteroid moons' might remain undetected in a preliminary threat assessment study, especially if the warning time is short. This fact should be considered in the design of a mitigation mission. A small explorer S/C sent prior to an impactor, for instance, could help to avoid an accidental collision of the impact vehicle with the smaller satellite (Cheng et al. 2012).

6 Conclusions

Acquiring high precision astrometry of NEOs is essential for asteroid threat assessment and mitigation. High quality data can be used to reduce orbit uncertainties, which will allow for quick and precise estimates of impact probabilities. We could show that high precision astrometry is necessary, if the success of an asteroid deflection demonstration mission is to be evaluated via ground-based observations. Furthermore, knowing whether and asteroid is multiple is an essential part of a NEO threat assessment, as it permits an adaption of mitigation strategies and, thus safeguards us against the consequences of deflection failures. A determination of asteroid multiplicity via high precision astrometry seems also feasible with Gaia, at least for binaries with components of similar mass. Even current ground-based facilities might be able to contribute, if the binary has separations larger than 10km and multiple close encounters with the Earth.

Based on observational residuals of NEOs published by the IAU MPC we estimated the current average astrometric performance of ground-based observations to lie between $0.13''$ and $2''$. High precision measurements constituted less than 2% of the total number of observations in 2013. Even considering pessimistic scenarios, ESA's Gaia mission should produce astrometric results for asteroids with a visual magnitude $V < 20$ that are orders of magnitude beyond the current average. However, Gaia's mission lifetime is restricted to 5 years. While the astrometric catalog provided by the Gaia mission will allow for a permanent improvement of ground-based observation accuracy, an astrometric precision comparable to the in-mission performance will be hard to sustain. A long term follow up strategy should be developed that can continue Gaia's astrometric legacy.

The authors would like to acknowledge the support of the NEOShield project funded by the European Union Seventh Framework Program (FP7/2007-2013) under grant agreement no. 282703. A. Ivantsov would like to appreciate the financial support at IMCCE-Observatoire de Paris through the program 'Research in Paris 2012'. D. Bancelin expresses his gratitude towards Austrian FWF projects AS11608-N16 and P22603-N16. This research has made use of data provided by the IAU Minor Planet Center.

References

Baer, J., Chesley, S. R., & Milani, A. 2011, Icarus, 212, 438

Bancelin, D., Hestroffer, D., & Thuillot, W. 2010, in SF2A-2010: Proceedings of the Annual meeting of the French Society of Astronomy and Astrophysics, ed. S. Boissier, M. Heydari-Malayeri, R. Samadi, & D. Valls-Gabaud, 107

Bancelin, D., Hestroffer, D., & Thuillot, W. 2012, Planetary and Space Science, 73, 21

Beauvalet, L., Lainey, V., Arlot, J.-E., et al. 2012, Planet. Space Sci., 73, 62

Belton, M. J. S., Morgan, T. H., Samarasinha, N. H., & Yeomans, D. K. 2011, Mitigation of Hazardous Comets and Asteroids

Bowell, E. 2009, VizieR Online Data Catalog, 1, 2001

Carpino, M., Milani, A., & Chesley, S. R. 2003, Icarus, 166, 248

Cheng, A. F., Michel, P., Reed, C., Galvez, A., & Carnelli, I. 2012, in European Planetary Science Congress 2012, 935

Chesley, S. R., Baer, J., & Monet, D. G. 2010, Icarus, 210, 158

Delbo', M., Gayon-Markt, J., Busso, G., et al. 2012, Planet. Space Sci., 73, 86

Desmars, J., Bancelin, D., Hestroffer, D., & Thuillot, W. 2013, A&A, 554, A32

Eggl, S. 2011, Celestial Mechanics and Dynamical Astronomy, 109, 211

Eggl, S., Haghighipour, N., & Pilat-Lohinger, E. 2013, ApJ, 764, 130

Harris, A., Barucci, M., Cano, J., et al. 2013, Acta Astronautica, 90, 80

Harris, A. W. 2010, in Protecting the Earth against Collisions with Asteroids and Comet Nuclei, ed. A. M. Finkelstein, W. F. Huebner, & V. A. Short, 312

Harris, A. W., Galvez, A., Benz, W., et al. 2006, in COSPAR Meeting, Vol. 36, 36th COSPAR Scientific Assembly, 2002

Hestroffer, D., Mouret, S., Mignard, F., Tanga, P., & Berthier, J. 2010, in IAU Symposium, Vol. 261, IAU Symposium, ed. S. A. Klioner, P. K. Seidelmann, & M. H. Soffel, 325–330

Holsapple, K. A. & Housen, K. R. 2012, Icarus, 221, 875

Ivantsov, A., Hestroffer, D., Thuillot, W., & Bancelin, D. 2013, in EGU General Assembly Conference Abstracts, Vol. 15, EGU General Assembly Conference Abstracts, 11747

Jewitt, D. 2012, AJ, 143, 66

Michel, P. 1997, Icarus, 129, 348

Michel, P., Morbidelli, A., & Bottke, W. F. 2005, Comptes Rendus de Physique, 6, 291

Mignard, F. & Klioner, S. 2012, A&A, 547, A59

Milani, A., Chesley, S. R., Chodas, P. W., & Valsecchi, G. B. 2002, Asteroids III, 55

Milani, A., Chesley, S. R., Sansaturio, M. E., Tommei, G., & Valsecchi, G. B. 2005, Icarus, 173, 362

Milani, A. & Gronchi, G. F. 2010, Theory of Orbital Determination (Cambridge University Press)

Ortiz, J. L., Cikota, A., Cikota, S., et al. 2011, A&A, 525, A31

Pourbaix, D. 2002, A&A, 385, 686

Pravec, P. & Scheirich, P. 2012, Planetary and Space Science, 73, 56

Pravec, P., Scheirich, P., Kunirk, P., et al. 2006, Icarus, 181, 63

Tanga, P. & Mignard, F. 2012, Planetary and Space Science, 73, 5

Tsiganis, K., Varvoglis, H., Tsirvoulis, G., & Voyatzis, G. 2012, Planetary and Space Science, 73, 47

Valsecchi, G. B., Milani, A., Gronchi, G. F., & Chesley, S. R. 2003, A&A, 408, 1179

Vasile, M. & Colombo, C. 2008, Journal of Guidance Control Dynamics, 31, 858

Wiegert, P. A., Innanen, K. A., & Mikkola, S. 1998, AJ, 115, 2604

Yeomans, D. K., Antreasian, P. G., Barriot, J.-P., et al. 2000, Science, 289, 2085

SF2A 2013
L. Cambrésy, F. Martins, E. Nuss and A. Palacios (eds)

SOFTWARE TOOLS FOR THE VALIDATION OF THE IN-FLIGHT CALIBRATION PERFORMANCE OF THE MICROSCOPE SPACE MISSION

E. Hardy[1], A. Levy[1], M. Rodrigues[1], P. Touboul[1] and G. Métris[2]

Abstract. The MICROSCOPE space mission aims at testing the Equivalence Principle (EP) with an accuracy of 10^{-15}. The instrument will be embarked on board a drag-free microsatellite orbiting the Earth, and consists in a differential electrostatic accelerometer composed of two cylindrical test masses submitted to the same gravitational field but made of different materials. The electrostatic accelerations applied to the masses to maintain them relatively motionless are measured; inequality would demonstrate a violation of the universality of free fall.

The accuracy of the measurement exploited for the EP test is limited by our *a priori* knowledge of the instrument physical parameters. An in-orbit calibration is needed to finely characterize them in order to correct the measurement. The calibration procedures have been determined and their analytical performances evaluated. The two stages of the measurement processing are numerically simulated: first the calibration sessions, then the measurement correction using the estimated parameters in order to validate the mission performance on the EP parameter determination.

Keywords: MICROSCOPE, test of the Equivalence Principle, in-orbit calibration, measurement processing

1 Introduction

The MICROSCOPE space mission aims at testing the Equivalence Principle (EP). This principle is at the basis of General Relativity and has for main consequence the Universality of Free Fall: the acceleration of an object in a gravitational field is independent of its mass and its internal composition. It leads to the equivalence between the inertial mass (which measures the resistance of an object to a modification of its motion) and the gravitational mass (coupled to the gravitational field). The Universality of Free Fall has been tested throughout the centuries with an improving accuracy. Recently, sophisticated torsion-balances or Lunar laser ranging experiments have been conducted, leading to a record accuracy of a few 10^{-13} (Gundlach et al. 2009). However, the accuracy of these on-ground experiments is limited by the terrestrial environment's numerous perturbations. Some unification theories, representing alternatives to General Relativity and aiming at merging gravitation with the three other fundamental interactions, expect a violation of the EP at a level never tested before (Damour et al. 2002). Being performed in space, the MICROSCOPE mission will be able to overcome the terrestrial perturbations in order to test the Equivalence Principle with an accuracy of 10^{-15} (Touboul et al. 2001).

MICROSCOPE is a microsatellite developed by CNES with a contribution of ESA. It will orbit around the Earth at low altitude for a two years' mission. The launch of the satellite is scheduled for 2016. The on-board payload is composed of two differential electrostatic accelerometers developed by ONERA, each one consisting in two concentric cylindrical test masses in electrostatic levitation. The position of the masses is detected using a capacitive measurement, and a control loop keeps them at the center of the accelerometer cage. Both masses are submitted to the same gravitational field. For one of the differential accelerometer, the two masses are made of different materials. A difference between the measured forces applied to maintain them on the same trajectory would therefore indicate a violation of the Universality of Free Fall, and thus of the Equivalence

[1] ONERA, FR-92322 Châtillon, France
[2] Universit de Nice Sophia-Antipolis, Centre National de la Recherche Scientifique (UMR 6526), Observatoire de la Cte d'Azur, Goazur, 06130 Grasse, France

Principle. The second accelerometer includes two test masses of the same composition and enables us to test the measurement accuracy.

The accuracy of the measurement exploited for the EP test is limited by our *a priori* knowledge of the instrument physical parameters. It is necessary to finely characterize them in order to correct the measurement. An in-orbit calibration of the instrument is therefore needed. Appropriate calibration procedures have been determined and their analytical performances evaluated. These procedures have been implemented in a numerical simulator in order to validate them numerically (section 2). The estimation of the instrumental parameters is used to correct the scientific measurement and therefore to evaluate the EP violation parameter with the best accuracy. A mission simulator has been developed in order to simulate the measurement processing and thus to validate the mission performances (section 3).

2 In-orbit calibration of the instrument

2.1 Necessity and principle of the in-orbit calibration

The ideal measurement of the MICROSCOPE instrument corresponds to the electrostatic acceleration applied to the internal or the external test mass to keep it relatively motionless at the center of the accelerometer. The real measurement provided by the instrument differs from the ideal measurement because of instrumental parameters: scale factors, couplings, misalignments and quadratic parameters.

The measurements provided for the internal and the external test masses are combined in a common mode (the half sum of both measurements) and a differential mode (the half difference of both measurements). The common mode acceleration is used as a command for the satellite Attitude and Orbit Control System (AOCS). This system compensates for the external non-gravitationnal perturbations, such as the residual drag or the Earth and Sun radiation pressure. The differential mode is used for the EP test.

This differential acceleration includes the potential violation signal due to a non-null EP violation parameter $\delta_{EP} = \frac{m_{g2}}{m_{I2}} - \frac{m_{g1}}{m_{I1}}$, where m_g is the gravitational mass and m_I is the inertial mass respectively of the internal test mass (index 1) and external test mass (index 2). A second order model of the differential measurement has been defined (Hardy et al. 2011). The form of the acceleration measurement along the $\vec{X}$ axis (which is the axis of the test masses cylinders as well as the most sensible axis) is:

$$\Gamma_{mes,dx} = \frac{1}{2}(\Gamma_{mes,1x} - \Gamma_{mes,2x}) = \frac{1}{2} \cdot g_x \cdot \delta_{EP} + \Gamma_{inst,x} \tag{2.1}$$

with:

- g_x the component of the gravitational acceleration along the $\vec{X}$ axis of the instrument;
- Γ_{inst} the perturbative acceleration reducing the accuracy of the EP parameter determination. This acceleration is composed of a stochastic part (noise of the instrument and of the drag-free system) that can be reduced by integrating the measurement over a large duration, and an harmonic part that is due to instrumental parameters (scale factors, off-centering between the two test masses that introduces effect of the Earth gravity gradient and the inertia gradient, misalignements and couplings between the axes of the two sensors or between the axes of the differential accelerometer and the axes of the instrument, quadratical parameters that introduces non linear terms).

The instrumental parameters reduce the accuracy of the estimation of δ_{EP}. The best performances possible for the instrument construction and integration in the satellite lead to a contribution of these terms incompatible with the mission's accuracy objective. It is therefore necessary to correct the measurement. An accurate estimation of the instrumental parameters is not possible on-ground, where the instrument is saturated. That is why in-orbit calibration sessions are needed.

The in-orbit calibration of the MICROSCOPE instrument consists in amplifying the effect of the parameter to be estimated so that the corresponding term is predominant in the measurement, and thus easily measurable. For this purpose, a strong signal at a known frequency is used: either a naturally strong signal is used (the Earth gravity gradient), or a strong signal is created by oscillating the satellite (through the AOCS system) or the test masses (through their control loop) at a chosen frequency and along or around a chosen axis.

A specific calibration procedure has been determined for each instrumental parameter. Each calibration session will last 10 orbits in order to reduce the noise to an acceptable level, and the complete calibration will

be run at least twice during the mission, so as to take into account a potential drift of the parameters value with time.

The performances of the calibration procedures have been evaluated analytically (Levy et al. 2010). The results are compatible with the specification. However, this analysis cannot take into account all the effects that impact the calibration result, in particular the dynamics of the systems. In order to validate their performances numerically, the calibration procedures have been implemented in a simulator.

2.2 The calibration simulator

The calibration simulator has been developed in Simulink (figure 1). It simulates the instrument, the satellite AOCS loop and the external environment.

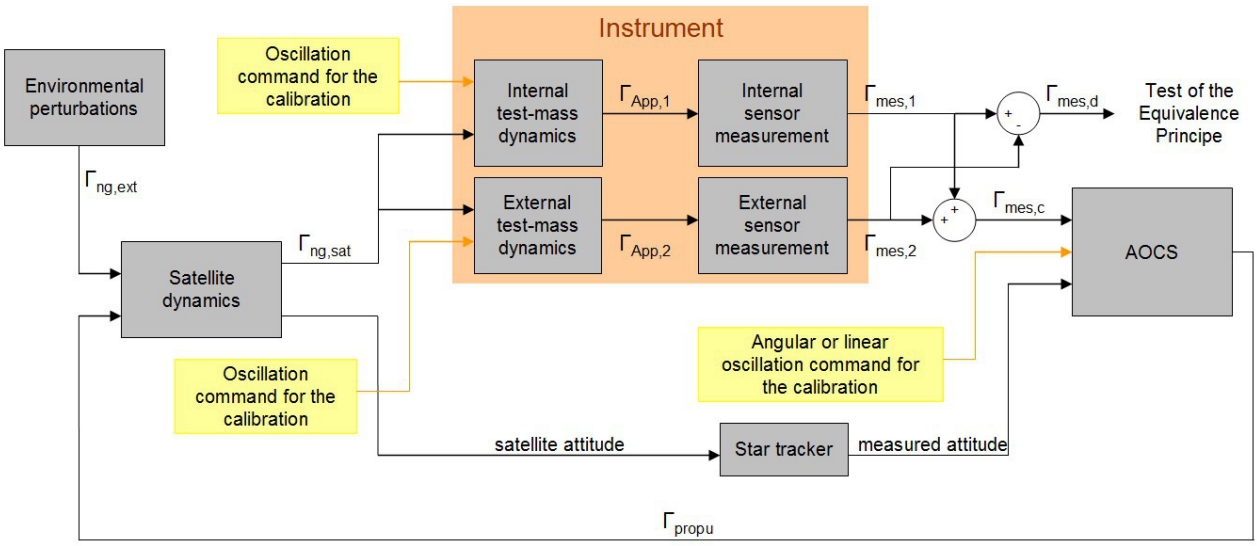

Fig. 1. The calibration simulator: the yellow blocks correspond to secondary inputs designed to oscillate the satellite or the test masses for the calibration.

The simulated differential measurement is processed to estimate the parameter to be calibrated: a pass-band filter is applied around the calibration frequency and a least squares inversion is used. A statistical study based on 100 simulations with a random initialization of the parameters to be calibrated has been conducted. The resulting accuracy on the instrumental parameters estimations is compatible with the specifications (Hardy et al. 2013). The performances of the foreseen calibration procedures are thus numerically validated.

3 Measurement correction

The in-orbit calibration provides an estimation of the instrumental parameters. These estimated values are used to correct the EP test measurement. In order to validate the complete mission scenario, including the in-orbit calibration, the EP test session, the correction and the processing of the scientific measurement, a mission simulator has been developed in FORTRAN starting from a simulator of the OCA initially dedicated to the EP test sessions. The mission simulator enables us to simulate calibration sessions as well as EP test sessions, and the data processing for the estimation of the parameters (including the estimation of the instrumental parameters for the calibration, the correction of the scientific measurement using the estimated values of the instrumental parameters and the estimation of the EP violation parameter).

In contrary to the calibration simulator, the mission simulator takes into account the orbital motion of the satellite. Therefore, an input of the simulator is an ephemerid file. This file provides the speed and acceleration of the satellite along its orbit. For each point of the orbit, the gravity acceleration and the Earth gravity gradient are computed from a model of the Earth gravity potential. Concurrently, the attitude of the satellite is computed. Three attitude laws are possible: inertial pointing of the satellite, spinning pointing, or oscillation of the satellite around one axis chosen for the calibration. These data are used to simulate the measurement

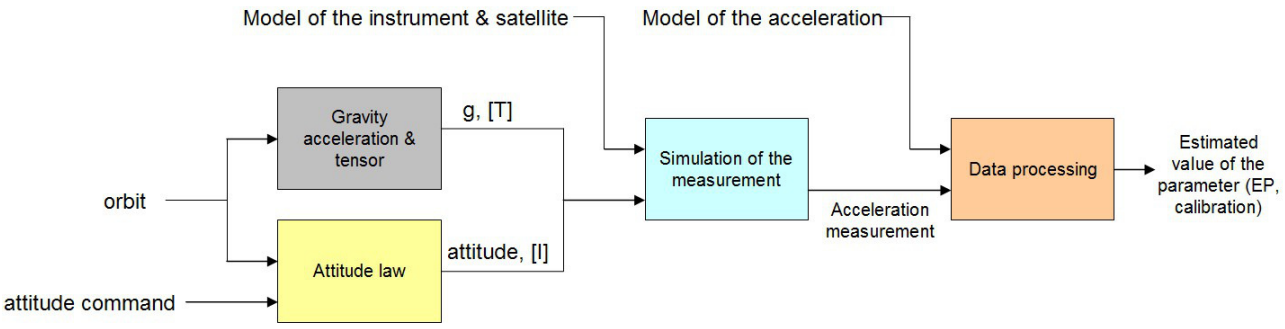

Fig. 2. The mission simulator.

of the electrostatic acceleration provided by the instrument. The simulated measurement is then processed by confronting it with a model of the measurement. The form of the model is:

$$\Gamma_{mes,dx} = \sum_k a_k \cdot p_k \tag{3.1}$$

with:

- p_k one of the parameters (instrumental parameters or EP violation parameter);
- a_k its partial derivate.

The measurement is corrected using the best estimation $\hat{p_k}$ of the parameter p_k available for the analysis:

$$\Gamma_{mes,dx,corr} = \sum_k a_k \cdot (p_k - \hat{p_k}) \tag{3.2}$$

In practice, the estimated value of the instrumental parameters, known from a previous calibration, will be used. After correction, the measurement is processed with a least squares method. The form of the measurement model is:

$$Y = A \cdot X \tag{3.3}$$

with:

- Y the observation vector (the measurement);
- X the vector of the parameter(s) to be estimated;
- A the partial derivates matrix.

The least squares solution is:

$$\hat{X} = (A^T \cdot W \cdot A)^{-1} \cdot A^T \cdot W \cdot Y \tag{3.4}$$

with W a symmetrical weight matrix. The variance of the estimator $\hat{X}$ is minimal if W is chosen so that $W^T \cdot W$ is the inverse of the measurement noise's variance-covariance matrix. This solution is optimal, but induces some difficulties. The variance-covariance matrix is not known: a model of the noise is therefore necessary. Moreover, this matrix has a high dimension (equal to the number of observations), therefore the inversion is difficult. The solution chosen for this study consists in applying a Fourier transform on both sides of the equation before the inversion. In the spectral domain, only the frequencies around the calibration frequency or the EP test frequency are selected. Thus, the number of observations is significantly reduced. Moreover, the noise spectral density can be considered flat on these narrow frequency bands.

The mission simulator has been used to simulate the in-orbit calibration sessions followed by an EP test session, with a simulated EP violation parameter equal to 10^{-15}. The EP test measurement has been corrected using the estimated values of the instrumental parameters, and the EP violation parameter has been estimated. The results of this estimation are gathered in table 1. Thanks to the calibration, the estimation accuracy after the measurement correction is better than 10^{-15}, and thus compatible with the MICROSCOPE accuracy objective.

	Estimation of δ_{EP}	Estimation error
Before calibration	$15.8 \cdot 10^{-15}$	$14.8 \cdot 10^{-15}$
After calibration	$1.25 \cdot 10^{-15}$	$0.25 \cdot 10^{-15}$

Table 1. Results of the mission simulator for an inertial session of 120 orbits, with $\delta_{EP} = 10^{-15}$.

4 Conclusions

The budget of the measurement equation before calibration does not comply with the objective of the EP test accuracy. Several in-flight calibration sessions are therefore necessary during the space experiment in order to estimate the instrumental parameters that limit the measurement accuracy, so as to correct the measurement. Parameters to be calibrated have been identified and appropriate methods of calibration have been proposed. In order to validate the calibration process, a simulation software including models of the instrument and of the satellite drag-free system has been developed and the calibration methods have been implemented in the simulator. The results are compatible with the specifications.

For the data processing validation, a second software has been developed, enabling us to test the entire mission scenario, including the correction of the measurement with the parameters estimated during the calibration process. The simulated estimation of the EP parameter is compatible with the mission accuracy objective and validates the mission performances.

The simulators can also be used to study other effects that have not been taken into account in this paper. For example, missing data can occur because of teletransmission errors. The missing data can be simulated with the mission simulator in order to define its impact on the EP parameter estimation and to test appropriate measurement processing for the reduction of this impact.

This study prepares for the Scientific Mission Center (CMS) which is currently under development at ONERA and whose mission will be to validate the operational data and process the scientific data of the MICROSCOPE mission.

The authors wish to thank the MICROSCOPE teams at CNES and ZARM for the technical exchanges. This activity has received the financial support of ONERA and CNES.

References

Damour, T., Piazza, F., & Veneziano, G. 2002, Phys. Rev. D, 66, 046007

Gundlach, J. H., Schlamminger, S., & Wagner, T. A. 2009, Space Science Reviews, 148, 201

Hardy, E., Levy, A., Métris, G., et al. 2011, in SF2A-2011: Proceedings of the Annual meeting of the French Society of Astronomy and Astrophysics, ed. G. Alecian, K. Belkacem, R. Samadi, & D. Valls-Gabaud, 647–651

Hardy, E., Levy, E., Rodrigues, M., Touboul, P., & Métris, G. 2013, Advances in Space Research

Levy, A., Touboul, P., Rodrigues, M., Métris, G., & Robert, A. 2010, in SF2A-2010: Proceedings of the annual Meeting of the French Society of Astronomy and Astrophsics, ed. R. S. S. Boissier, M. Heydari-Malayeri & D. Valls-Gabaud, 123

Touboul, P., Rodrigues, M., Métris, G., & Tatry, B. 2001, Comptes Rendus de l'Académie des Sciences - Series IV - Physics, 2, 1271

SF2A 2013
L. Cambrésy, F. Martins, E. Nuss and A. Palacios (eds)

PÔDET: A CENTRE FOR EARTH DYNAMICAL ENVIRONMENT

D. Hestroffer[1] and F. Deleflie[1], F. Colas[1], W. Thuillot[1], J. Vaubaillon[1], A. Vienne[1]

Abstract. The monitoring of the Earth space environment has gained some importance these last decades, in particular at the European level, partly because the phenomenon which origin come from space can have socio-economic consequences; and also because our understanding of those phenomenon – their associated prediction and risks – is still limited. For instance, the Space Situational Awareness programme (SSA) at ESA has set up in 2013 a centre and network for aspects connected to space debris (SST), to space weather (SW), and to near-Earth objects (NEO). At IMCCE, the *Pôle sur la dynamique de l'environnement terrestre* (PODET, `podet.imcce.fr`) for the Earth dynamical environment is studying effects and prediction for natural and artificial objects gravitating in the Earth vicinity. These studies englobe near-Earth objects, asteroids, comets, meteoroids, meteorite streams, and space debris. For all object types that are concerned, a general scheme of a functional analysis has been developed. It encompasses data acquisition with dedicated observations—essentially astrometric—or database queries, orbit determination or adjustment, prediction and ephemerides, and eventually impact probability computation and data dissemination. We develop here the general context of this action, the PôDET project, its scientific objectives, interaction with other disciplines, and the development in progress for dedicated tools.

Keywords: NEA near-Earth asteroid, meteoroid, space debris, ephemerides, impact probability, Space Situational Awareness - SSA

1 Introduction & Context

Our planet Earth is not a unique or completely isolated body in space; it is the place of direct interactions with its space environment. Its magnetic field and atmosphere are protecting the Earth against radiation sources and external impacts, and hence ensuring some of the fundamental conditions that allowed life to develop. However, this protection is only partial; several events can still affect the Earth locally with frequencies events that can be of the order of a human generation or a year. Thus we remain dependent of solar activity bursts, reentry of space vehicle or ground impact of natural celestial bodies (meteoroids, asteroids), as well as of artificial body (space debris) and meteoritic streams that affect all space activities. These astronomical phenomena present human and socio-economic risks that have to be addressed carefully.

The PôDET hub* at IMCCE, Paris observatory, France, is carrying out studies and proposing services for topics connected to the Earth space environment. The bodies covered by the activities are the space debris (PôDET-DEB), the meteoroids and meteorite streams (PôDET-MET) and the near-Earth objects (PôDET-NEO), see Fig 1. PôDET has been retained at the 2009 CNES prospective exercise as a data centre. Its activities enter, at the European level, in the general domain of ESA Space Situational Awareness (ESA-SSA), as well as the EC FP7 or Horizon2020 programmes. At the international level, UNO, IAU working group WG/NEO are concerned, as well as the IADC (Inter-Agency Space Debris Coordination Committee). The recommendations and rules on space utilization have been declined as the French Space Operation Act at the French level. The activities developed in the hub are part of other projects, especially *NEOShield* - mitigation of threatening asteroid, *AsteRisk* - decision chain for atmospheric (re)entrance, *FRIPON*, *Cabernet* - surveyance and research of meteorites, *NEOPROP* - orbit propagation of NEO, *MEO parking* - Disposal strategies analysis for MEO orbits.

[1] IMCCE, Observatoire de Paris, UPMC, Univ. Lille1, CNRS, F-75014 Paris, France
*`http://podet.imcce.fr`

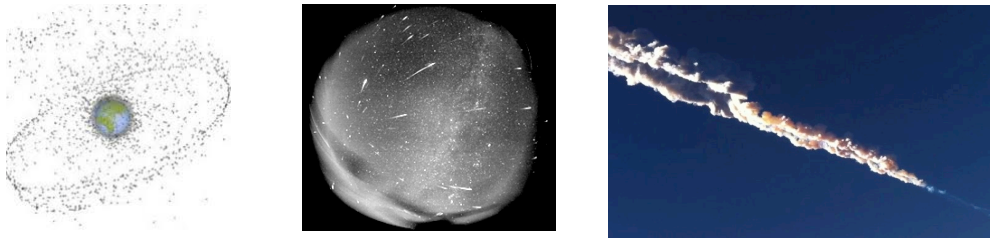

Fig. 1. *PODET covers research activities on three different celestial bodies type: space debris, meteoroids and streams, and near-Earth asteroids. Left: portrait of catalogued debris with different orbital classes (GEO, MEO, HEO,). Middle: image of a meteorite stream monitored with a fish-eye camera. Right: The Chelyabinsk (Tcheliabinsk) event of 2013, Feb. 15 from resulting from an asteroid blast in the atmosphere. (Credits, ESA, IMCCE, N. Plekhanov)*

Research activities encompass different topics including observation analysis, models for propagation and predictions, uncertainties and probabilities for associated risk estimation. The PôDET data center is hence able to provide necessary information to space operators and stakeholders - on different time scales - on the risks inherent in the Earth's space environment. All this in an independent manner, providing also higher robustness to similar predictions obtained by other centers (NEO at JPL/NASA, NEODys at Pisa univ.). Economic or societal benefits expected are far from being negligible.

This paper presents the structure of the data and analysis center PôDET—hosted at IMCCE—which strengthen research capability and development of new services in France dedicated to the dynamic evolution of near-Earth objects, meteoroid streams and space debris.

2 General objectives

Detecting potentially hazardous near-Earth asteroids (PHAs) such as (99942) Apophis in 2004, or more recently 2011 AG_5, for the most known; experimenting the extremely close approach to the Earth of 2012 DA_{14} (in February 2013, less than 28000 km from the surface of the Earth); observing the atmospheric penetration followed by disintegrating airburst of asteroid 2008 TC_3, or even their fall to the ground as that of the object Carancas in 2007, and last the Chelyabinsk event in February 2013; all highlight the interest of research activities for a maximum orbit-determination precision on short notice. The same is true for the identification and tracking of space debris: the importance of this type of orbit determination has increased further after the collision that occurred in 2009 between an Iridium and a Cosmos artificial satellites, or the unpredicted reentry of a piece of Ariane IV tank in Brazil in February 2012 near the village of Anapurus. The knowledge of asteroidal and cometary grains population in the solar system is of importance for the identification of their origin (asteroid or comet and association with a specific body) and of the physical processes that generate them. It is also of importance for the daily management of space missions, since meteor showers may pose a risk to any operational satellite or to habited space vehicles.

The scientific objectives of PôDET aims at a better knowledge of our space environment, and more specifically to develop new methods for the dynamical modeling of the objects under study. Our approach is hence to develop, in an original way, common areas of research and services related to orbital characterization and dissemination of data for the three types of objects that are: near-Earth asteroids and comets, meteoroids and meteor streams, and space debris. The scientific objectives, which are applied for operational services can be summarized as follows.

2.1 Space debris - DEB

Waste of launchers components, fragments from artificial satellites or subsequent collisions; they pose risks to space operations and spaceflight — broad size range is [cm - m].

On the very short term (order of one or two days), the collision-risk assessment with an operating satellite must be done quickly and with sufficient accuracy to plan avoidance maneuvers. In the longer term, it is necessary to have orbital models including a full error budget and precise enough to estimate the lifetime of a satellite before its entry into the atmosphere, or otherwise guarantee its long-term orbital stability. In all cases, a new methodology is required to insure greater precision and stability compared to the models currently in

use in operational centers. This concerns *(i)* the model itself (accuracy, timeliness for simultaneous application to several tens or even hundreds of objects) *(ii)* and the data assimilation (real time or delayed time, with maximum or reduced accuracy, models reset, etc.), and *(iii)* the error budget itself, accounting for parameters that can not be modeled in advance (solar activity for instance). Let's recall that according to the current models, the minimum distance required between the Iridium and Cosmos satellites was supposed to be about 400 meters, before their actual collision.

The challenges faced here are essentially the implementation of high-precision orbit computation methods in terms of orbit determination and propagation, preparing for the arrival of a substantial flow of new data, and the contribution to the estimation of risks for space systems and civil society. These efforts involve the acquisition of high-precision data and the relevant dynamic modeling. Each object in the Earth's space environment is linked to a number of scientific questions, origin and evolution of objects, physical and orbital properties, evaluation of interactions and driving forces that motivate especially research in astrometry, celestial mechanics and space mechanics. Given this context, the objectives (which are partly common with near-Earth asteroids) set in this area are:

- Development and optimization of methods for orbit determination in the short term and with few observations,very useful for newly discovered objects. These include various types of algorithms and methods, e.g. by genetic, Bayesian, or MCMC algorithms (that do not require any *a priori* knowledge of the trajectory (Deleflie et al. 2013), in opposition to classical least square-based LLS methods);
- Development of methods and tools for orbits propagation as well as error propagation (rapid methods and / or accurate) (Deleflie et al. 2013b);
- Systematic exploitation of all series of images acquired by different telescopes for non-trailing satellites (geostationary) and for streaking ones (Laas-Bourez et al. 2008), this step can be largely automated, but not completely, and 'manual' astrometric validation are sometimes required;
- Establishment of a catalog of dynamical parameters (orbital elements, orbital precision estimators) based on a new analytical and fast extrapolation model, alternative to existing ones;
- Constraints, from the observation of the model parameters, on the long-term evolution of the debris population. Estimation of 'dynamical areas' (i.e. not described in terms of spatial positions) of debris concentrations or less densely populated areas;
- Collision probability between satellites and space debris, prediction of minimum approach distances;
- Implementation of the access and dissemination of data, ephemeris, and observations' alert, all following Virtual Observatory (VO) standards (Le Petit et al. 2012; Deleflie et al. 2013c);
- Development of astronomical-observation strategies needed for critical objects, using in particular robotic or dedicated network telescopes, in close cooperation with CNES, and other partners.

2.2 Meteoritic streams & meteoroids - MET

Dust, fragments of comets (or asteroids) yielding meteor showers; they are responsible for damage to artificial satellites, reduced solar panels lifetime and major power outage — broad size range is [μm - m]

Earth in its orbit around the Sun is regularly crossing meteor streams whose origin is generally associated with passages of comets. If the parent-body association is now relatively well established for the biggest well known events, it is not the same for the quantitative characterization of these streams (ZHR, etc.). Neither is it for the association of other smaller individual stream population. These however are sources of damage to artificial satellites and it is essential to quantify and predict their activity over time and space. Moreover, it becomes increasingly likely that some of these streams are associated with near-Earth asteroids. The analysis of this relationship will help a better understanding of both the dynamic characteristics and physical properties of NEOs. In addition, this type of association provides useful information to the scientific study of the conditions of formation of the solar system and its dynamic evolution. The role of a data center on the dynamics of the Earth's environment in this area is also to collect and disseminate relevant physical and dynamical data, streams prediction, and to provide tools for predicting risk associated to collisions with artificial satellites and manned missions. The service should also provide validated data and online data including interoperability through the 'Virtual Observatory' protocol. Given this context, the goals set in this area are:

- Development and optimization of methods for the orbit determination, especially by triangulation of data from Carbernet and FRIPON networks of cameras (Atreya et al. 2012);

- Physical and dynamical modeling of meteor streams - search and identification of the parent body (Rudawska et al. 2012);

- Treatment of observations from international campaigns (IMO, REFORM, FRIPON networks);

- Predictions of meteor streams crossings, and streams activities (dates, and ZHR rate);

- Implementation of data access and dissemination following OV standards.

2.3 Near-Earth objects - NEO

Asteroids and comets whose orbit crosses or approaches the Earth; impact with the planet can produce, according to the object's size and the energy released, a simple yet surprising light and sonic phenomenon, or a crater and other more catastrophic events — broad size range is [m - km]

The technology used to provide astrometric data necessary to the orbital modeling is in constant progress. The next decade—with ongoing or future survey programs—will see a considerable change in the volume of data available. The present detection rate of newly discovered NEOs is already very high, about 900 new bodies per year (see `http://neo.jpl.nasa.gov/stats/`). The advent of new generation telescopes (PanSTARRS, LSST) equipped with performant cameras and adapted observing strategies, moreover supplemented by space missions (Gaia, NEOSSAT), will result in a huge quantitative leap of data to analyse; and sometimes in a considerable need of follow-up activities to avoid any rapid loss of a discovered object.

A major challenge for analysing these objects is obviously the amount of data to handle in an automated way. Another problem arrises from the fact that periods of visibility of these bodies are often reduced (for orbits close to the Earth, the body spends long periods of time behind the Sun). Thus PôDET activities have to tackle orbital and dynamical models precision, associated evaluation and assessment of impact probabilities, and risks. These can be computed at two levels, in the short term (immediately after the discovery) or in the longer term (accurate risk estimation, and computation of uncertainties' evolution over decades). Given this context, the goals set in this area are:

- Development and optimization of methods of orbit determination, especially in the short term and with few observations, including various types of algorithms and methods (parametric as well as non parametric algorithms, genetic, Bayesian, or MCMC algorithms, LLS least-squares, etc.);

- Development of methods and tools for orbits propagation and errors propagation (rapid methods and / or accurate) (Bancelin et al. 2012a,b; Desmars et al. 2012);

- Exploitation of astrometric data, including those obtained directly with associated networks (radar, robotic telescopes, ...) (Thuillot 2011);

- Implement datamining tools for identifying objects in selected archives ('precoveries') and orbits linking methods;

- Establishment of a catalog of dynamical parameters (orbital elements, orbital precision estimators);

- Establishment of a sub-catalog of physical parameters necessary to the dynamical modeling, on the basis of available data centers (PDS, PSA, Gaia,), and dedicated ground-based programs;

- Computation of close encounters with the Earth and other planets, estimation of impact probabilities (Harris et al. 2012);

- Implementation of access and dissemination, following OV standards and protocols, for the data and ephemerides; VO-alerts for observing or following critical objects (Erard et al. 2010; Le Petit et al. 2012).

3 Services

The PôDET centre for the Earth's space dynamical environment benefits from research conducted upstream of the operational services. This research focuses on the modeling of non-gravitational forces and studies of their effects on the orbits, on processing observational data, on real-time orbit determination and adjustment, on statistical inversion methods, on orbit propagation, on error propagation, on impact probabilities, etc. Operational services are intended then to provide useful, adapted, and accessible data. One originality of our approach is to consider a common treatment for all objects treated, and compliant with Virtual Observatory standards and protocols. The functional analysis scheme includes the following topics (see Fig.2):

- data: operating astrometric and photometric data as input, including treatment of Gaia stellar catalog and / or ground-based data;
- orbits: refined dynamical modeling, adapted propagators, adapted data inversion and parameter estimation procedures;
- predictions: ephemeris, uncertainty, and impact probabilities, database and visualization tool as output.

The operational part of the centre will—during its nominal phase—use as inputs three main sources of information (see Fig.2):

- The international databases that deliver orbital and physical information about the objects concerned (IAU/MPC, Lowell Observatory, NEODyS, as examples for the NEOs) as well as surveys that perform new detections (Catalina, PanStarrs, etc.). For what concerns space debris, catalogues maintained by services in the USA, and especially by the French CNES teams will be an essential source of information;
- Observatories archive or accessible space missions catalogues, enabling data mining, in order to detect a serendipitous observation in the past. Such pre-discovery observations can yield fundamental astrometric positions to constrain the orbital models based on too few observations (or equivalently on short arcs). This concerns—to varying degrees—the three categories of objects that are near-Earth asteroids, space debris and meteor streams;
- Dedicated observation sites, including some of the telescopes from the Gaia-FUN-SSO network for NEOs (`https://www.imcce.fr/gaia-fun-sso/`), the CABERNET cameras network (`http://www.imcce.fr/langues/en/ephemerides/phenomenes/meteor/CABERNET/index.php`), and the FRIPON network for meteorites (`http://www.imcce.fr/fripon/`), and possible network of robotic telescopes. In all cases, the aim is to densify new observations, and also to put in place a dedicated follow-up strategy for specific newly discovered or critical objects.

All astrometric data acquired help to improve any preliminary orbits, they also allow orbital models refinement—in particular if they are of high accuracy—by allowing to incorporate all gravitational effects (perturbations by asteroids, relativistic effects, etc.) and non-gravitational forces (Yarkovsky effect, Poynting Robertson, etc.). From the orbital elements one can compute ephemerides and propagate the orbit over the long term; and hence, depending on the object analysed, caracterise close encounters of NEOs with the Earth or other planets, predict meteor streams events strength direction, derive the dynamical stability of artificial satellites when reaching their operational lifetime's end (GNSS or geostationary type). These results are then made available through an interoperable interface to the users concerned. Finally the functional analysis scheme encompass all sequences of data reduction, data analysis, orbit and ephemerides computation, estimation of dedicated parameters and dissemination.

4 Prospective

The centre PôDET at IMCCE/Observatoire de Paris, develops research activities and provides services connected to the near Earth space environment. It aims to encompass – in a common structure – three different kind of celestial objects (natural and artificial): space debris, meteoroids and meteorite streams, near Earth objects (asteroids and comets). In all cases research activities are connected to dedicated observations acquisition and reduction, and orbit computation. A web-site has been made publicly accessible at `http://podet.imcce.fr` since 2013. In the future, operational services will disseminate, as output, dedicated data for a better estimation of the uncertainties, awareness and risks associated to these bodies evolving in the Earth space environment. It

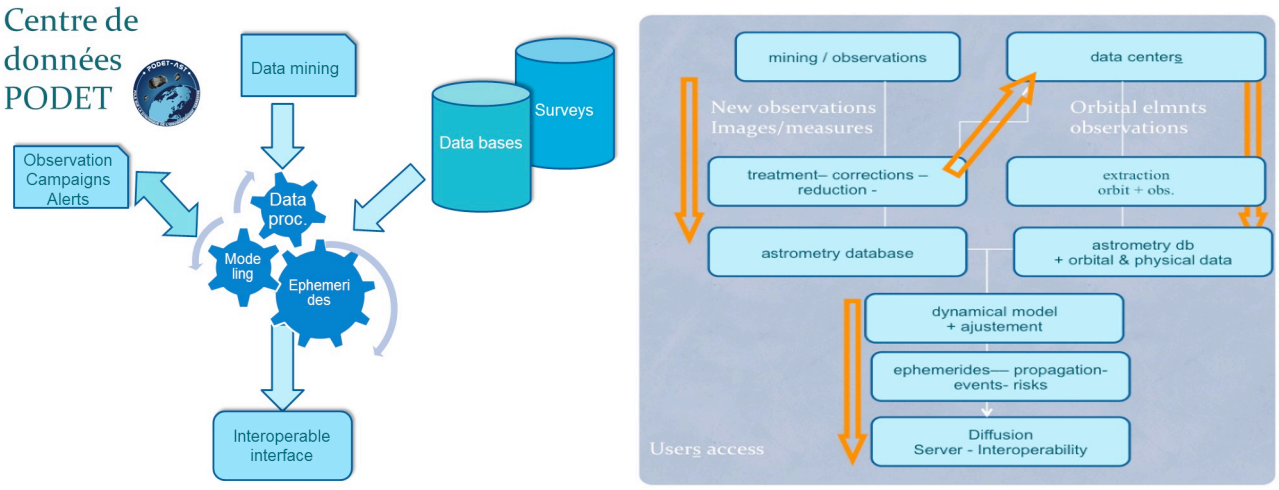

Fig. 2. *General structural scheme for PôDET and functional analysis graph. Observations and data bases are used for orbits adjustments and ephemerides computation, followed by risks estimation, and other adapted data dissemination.*

provides general information and three main sections (Ephemerides, Database, Monitoring) for all three categories of objects (DEB, MET, NEO). Update for the databases, and further developments for orbit propagation will be regularly integrated.

References

Atreya, P.; Vaubaillon, J.; Colas, F.; Bouley, S.; Gaillard, B. 2012. CCD modification to obtain high-precision orbits of meteoroids. MNRAS 423, 2840.

Bancelin, D.; Colas, F.; Thuillot, W.; Hestroffer, D.; Assafin, M. 2012. Asteroid (99942) Apophis: new predictions of Earth encounters for this potentially hazardous asteroid A&A 544, A15

Bancelin, D.; Hestroffer, D.; Thuillot, W. 2012. Numerical integration of dynamical systems with Lie series. Relativistic acceleration and non-gravitational forces. CeMDA 112, 221.

Deleflie, F., D. Coulot, R. Decosta,A. Fernier, P. Richard 2013. *First attempt of orbit determination of SLR satellites and space debris using Genetic Algorithms*, Space Debris Conference, ESA, 2013

Deleflie, F., *Finalized Analytical Satellite Theory*, CNES Internal Report, 2013.

Deleflie, F.; Berthier, J.; Barache, C.; et al. 2013. Time series visualization tools through a Virtual Observatory in geodesy. EGU GA 2013, p.13105.

Desmars, J.; Bancelin, D.; Hestroffer, D.; Thuillot, W. 2012. Statistical and numerical study of asteroid orbital uncertainty. A&A 554, A32.

Erard, S.; Le Sidaner, P.; Aboudarham, J.; Berthier, J.; Henry, F.; Thuillot, W.; Vinatier, S. 2010. Europlanet-IDIS activities in VO-Paris: towards a planetary VO. 38th COSPAR Scientific Assembly, B09-0012-10.

Harris, A.W. et al. 2012. NEOShield: Working towards an international near-Earth object mitigation demonstration mission. EPSC 2012-126.

Algorithms improvement in image processing for optical observations of artificial objects in geostationary orbit with the TAROT telescopes, Bourez-Laas, M.; Klotz, A.; Blanchet, G.; Bor M.; Ducrott, E.; Proceeding of the SPIE Vol. 7000, 700020, 2008.

Le Petit, F.; Aboudarham, J.; Thuillot, W.; Le Sidaner, P.; et al. 2012. VO-Paris Data Centre (VO-PDC). In: Astronomical Data Analysis Software and Systems XXI. ASP Conference Series, Vol. 461, p.399

Rudawska, R.; Vaubaillon, J.; Atreya, P. 2012. Association of individual meteors with their parent bodies. A&A 541, A2.

Thuillot, W. 2011. Objectives and Management of the Gaia-FUN-SSO Network. In: Gaia FUN-SSO workshop proceedings, ISBN 2-910015-63-7, p. 55.

SF2A 2013
L. Cambrésy, F. Martins, E. Nuss and A. Palacios (eds)

MARKOV CHAIN MONTE-CARLO ORBIT COMPUTATION FOR BINARY ASTEROIDS

Dagmara Oszkiewicz[2,1], Daniel Hestroffer[2] and Pedro David[2]

Abstract. We present a novel method of orbit computation for resolved binary asteroids. The method combines the Thiele, Innes, van den Bos method with a Markov chain Monte Carlo technique (MCMC). The classical Thiele-van den Bos method has been commonly used in multiple applications before, including orbits of binary stars and asteroids; conversely this novel method can be used for the analysis of binary stars, and of other gravitationally bound binaries. The method requires a minimum of three observations (observing times and relative positions - Cartesian or polar) made at the same tangent plane - or close enough for enabling a first approximation. Further, the use of the MCMC technique for statistical inversion yields the whole bundle of possible orbits, including the one that is most probable.

In this new method, we make use of the Metropolis-Hastings algorithm to sample the parameters of the Thiele-van den Bos method, that is the orbital period (or equivalently the double areal constant) together with three randomly selected observations from the same tangent plane. The observations are sampled within their observational errors (with an assumed distribution) and the orbital period is the only parameter that has to be tuned during the sampling procedure. We run multiple chains to ensure that the parameter phase space is well sampled and that the solutions have converged. After the sampling is completed we perform convergence diagnostics. The main advantage of the novel approach is that the orbital period does not need to be known in advance and the entire region of possible orbital solutions is sampled resulting in a maximum likelihood solution and the confidence regions. We have tested the new method on several known binary asteroids and conclude a good agreement with the results obtained with other methods. The new method has been implemented into the Gaia DPAC data reduction pipeline and can be used to confirm the binary nature of a suspected system, and for deriving the mass of the binary system.

Keywords: binary, asteroid, MCMC

1 Introduction

The study of the motion of the objects in our Solar system has had one of the most profond impacts on our understanding of the physical world. Indeed it was Kepler's discovery in the 17^{th} century that the planets moved on ellipses with the Sun at one of the focii that produced a major philosophical revolution. Newton's formulation of the "universal" laws of gravitation were very general, in particular all masses were subject to the same acceleration regardless of their composition. This implies that the motions of multiple stellar systems could be viewed in the same manner as multiple asteroids systems.

For the simplest sytem consisting of just two gravitatioanlly bound masses celestial mechanics gives an exact analytical solution, namely a conic section depending on the initial conditions of the involved bodies. For two gravitationaly bound astronomical objects, whatever their nature, there are 2 distinct parts to the recovery of their orbits. First the determination of the apparent orbit, second the determination of the projected true orbit onto the plane perpendicular to the line of sight.

Many methods have been developed for the task of binary orbit determination especially for visual binary stars. We will not dwell on any except for the application of the Thielie–Ines–van der Bos method (TIvB) which has been applied very succesfully in the determination of the orbits of binary stars. This method requires a

[1] Institute Astronomical Observatory, Faculty of Physics, Adam Mickiewicz University, Poznan, Poland
[2] IMCCE, Observatoire de Paris, CNRS, UPMC, Univ. Lille 1

three observations only. When applying the method to binary asteroids, care must be taken in choosing the three points because the proximity of the object to earth introduces a parallax that can not be neglected.

T. N. Thiele observed that the usual orbital elements used to describe the objects in the solar system were not very appropriate for binary stars. In fact, the true orbit can be described with the help of the following four elements, the period, P, the time of passage through the periastron, T, the eccentricity, e, and the semimajor axis, a. The three custumary supplementary elements needed to define the projected orbit; inclination, i, longitude of the ascending node, Ω, and the argument of the perihelion, ω have no intrinsic meaning. T. N. Thiele (1883) proposed a more appropriate set of apparent elements. He considered the points P and R for which the eccentric anomaly is 0° and 90° and their projections on the apparent orbit P' and R'. The set of elements retained by Thiele is T, the mean motion, e, a the length to the point P', A, the position angle of P', b the length to the point R' and the position angle of R'. Then Starting from Kepler's equation, he proceeded to describe a method for obtaining the true orbit of the companion star in a binary system relying on three observational points and the constant of areal velocity (Thiele 1883). In 1926 I.T. A. Innes reformulated Thiele's method in rectangular coordinates instead of polar coordinates, or $A_1 = a\cos A$, $A_2 = a\sin A$, $B_1 = b\cos B$, $B_2 = b\sin B$, which simplified the equations. W.H. van den Bos modified the method for use with the Innes constants. The resulting equations can be found in their 1926 paper (van de Bos 1926). Orbits are usually described by the Innes constants A, B, F, and G. The TIvB method uses only three point out of a possibly larger set. Once a first orbit is determined, it can be differentially corrected to fit the remaining points. Or, another three points can be drawn from the set of observations and a new orbit solution obtained. Again corrections to the orbit can be sought and the initial orbit improved. This procedutre can be continued until a satisfactory orbit is found.

Now, the method will provide one orbit only for any three points chosen. The determined orbit may or possibly may not pass through the other observed data points. Besides, preliminary orbit determination is highly nonlinear and regardless of the success of the inversion method an estimation of the errors on the determined elements is not obtained. Furthermore, for asteroids, as pointed out above, the inherent parallax in the data does not allow the choice of the three points required by the method to be arbitrary. The three points must lie close to or in the same tangent plane, ie the plane perpendicular to the line of sight. So from the determined orbit it still must be established how to pass from one tanget plane to another. The simple procedure applicable to distant binary stars needs a little modification, this is done in e.g. Hestroffer (2005). We propose here to use a Markov Chain Monte Carlo approach which has the power of determing a bundle of orbits, not just one, which will contain the most likely orbit of the binaries and has the added benifit of providing the errors on the determined elements. To do so the parameter phase space is sampled according to the measurement errors as described in (Virtanen 2001).

Knowledge of the asteroid pair's orbit has fundamental implications for our knowledge of these bodies and their evolution. Indeed it is the best method to derive the mass of asteroids with good precision (excluding results from space probes that are limited to only a handfull of bodies), and moreover knowledge of the true orbit in addition to the apparent one can bring insights on formation scenarii.

2 Gaia's contribution

A number of binary asteroids will be observed in the course of the Gaia mission. Particularly the resolved binaries (when the two components are well separated and can be detected as two different bodies) or astrometric binaries (that is when the system appears as a single object but the binarity can be detected by a wobble of the photocenter around the center of mass) are of high interest (Hestroffer 2010, 2002; Tanga 2012). For those objects improved orbits, masses and possibly densities can be computed. It has been shown by Tanga (2012) that asteroid binaries both with large ($\approx$ 100 km) and small ($\leq$ 10 km) primary bodies will be detectable by Gaia, given favourable geometric conditions. For example, binary asteroids with 0.3 arc second seperation or larger and small magnitude difference ($<$ 2 mag) between the two components will be detected by Gaia's sky mapper (see Fig. 1); in other cases both components will still be resolved but on a single window transmitted to ground.

3 Thiele-Innes-van den Bos

The Thiele-Innes-van den Bos method directly provides, if it exists, a Keperian orbit expressed for example in terms of the 7 elements $\mathbf{q} = (a, e, i, \Omega, \omega, P, M = (m_1 + m_2))$, repectively the semimajor axis, the eccentricity, the inclination, the arguement of the ascending node, the argument of perihelion, the orbital period, and the

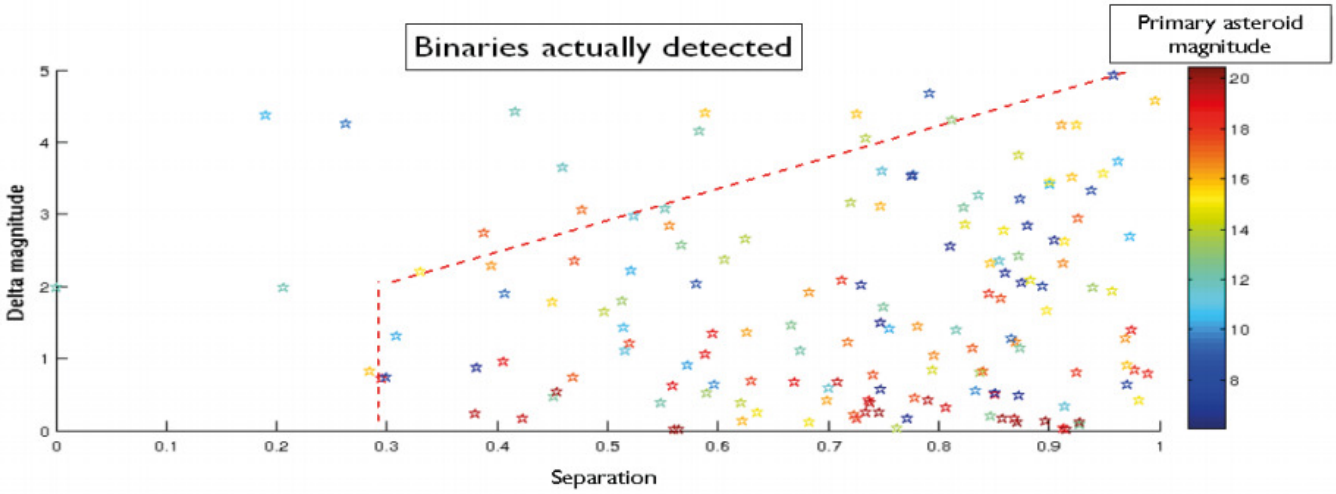

Fig. 1. Binary asteroids detectable by Gaia directly through the sky mapper with a 2 by 2 pixel binning. Angular separation vs. magnitude difference (Tanga 2012).

total mass of the system which is the sum of the mass of the primary m_1 and the mass of the companion m_2. As afore mentioned three observational points are necessary at a minimum in the same tangent plane, (x_i, y_i), where x and y are cartesian positions of the companion relative to the primary at times t_i for $i = 1, 2, 3$ and the orbital period or the areal constant. The compution procedes from the fundamaental equation relating the eccentric anomaly E anf the double areal constant c to the orbital period P see e.g Hestroffer (2010):

$$\begin{aligned} t_k - t_l - \Delta_{lk}/c &= [E_k - E_l - \sin(E_k - E_l)]/n \\ \Delta_{pk} &= x_l y_k - X_k y_l \\ n &= \pi/P \end{aligned}$$

This trascendental set of equations can be solved iteratively, given P, for the areal constant c from which the orbital elements can be computed.

4 MCMC with Thiele-Innes-van den Bos

The inverse problem of computing orbits of binary asteroids simialrly to the one of individual objects (Muinonen 1993; Virtanen 2001) can be taken to be probablistic in nature and therefore treated using the Bayesian approach and appropriate statistical methods. In particular we have developed a novel method combining the well known Thiele–Innes method (Aitken 1918; Argyle 2004) and numerical methods. Principally we use the Metropolis-Hastings (Chib 1995) algorithm to sample the parameters of the Thiele-Innes method. From the whole set of N observations $i = (x_i, y_i)$ made at observation times t_i (where $i = 1 \ldots N$) we randomly select three observations from the same tangent plane and a staring orbital period P. We refer to those seven parameters as the sampling parameters denote by $S = (x_1, x_2, x_3, y_1, y_2, y_3, P)$. From the three selected observations and the period we compute a starting orbital elements $\mathbf{q} = (a, e, i, \Omega, \omega, P, M = (m1{+}m2))$ using the Thiele- Innes method. Once a starting orbit has been computed we start Markov chain Monte–Carlo (MCMC) sampling of the parameters S by adding random deviates to the selected three observations and the orbital period. In practice at each iteration t in a chain a new candidate sampling parameters are proposed using so-called proposal densities. In particular we make use of Gaussian proposal densities for all the seven sampling parameters. For the cartesian coordinates we use proposal densities that are centered around the last accepted sampling parameters in the chain and the size of the proposal density is proportional to the observational noise: $x_i^{(c)} \propto N(x_i^{(t-1)}, \sigma x_i)$, $y_i^{(c)} \propto N(y_i^{(t-1)}, \sigma y_i)$ (where i = 1; 2; 3) for x and y coordinates respectively. For the orbital period we use a normal distribution that is centered around the last accepted period $P^{(c)} \propto N(P^{(t1)}, \sigma_P)$. The size of the proposal density for the orbital period σ_P is the only parameter to be tuned in the method (one could also consider other distributions),

but in general in most of the cases, an educated guess of the size of that parameter can be made. Once a new candidate sampling parameters have been generated $S^{(c)} = (x_1^{(c)}, x_2^{(c)}, x_3^{(c)}, y_1^{(c)}, y_2^{(c)}, x_3^{(c)}, P^{(c)})$ the M-H acceptance coefficient a_r is used to accept or reject the sample parameters. The acceptance coefficient a_r is expressed as:

$$a_r = \frac{p_p(\mathbf{q}^c)}{p_p(\mathbf{q}^{t-1})} \frac{|J^{t-1}|}{|J^c|}$$

where J^c and J^{t-1} are the Jacobians from the sampling parameters for the candidate and the last accepted orbit respectively. $\mathbf{q}^c$ and $\mathbf{q}^{t-1}$ are the p.d.f.s. for the candidate and the last accepted orbit respectively. Next the candidate parameters are accepted or rejected based on the Metropolis-Hastings criteria:

$$\begin{aligned} &\text{if } a_r \geq 1, \quad \text{then} \quad \mathbf{q}_t = \mathbf{q}^c \\ &\text{if } a_r < 1, \quad \text{then} \quad \mathbf{q}_t = \begin{cases} \mathbf{q}^c \text{ with probability } a_r \\ \mathbf{q}_t = \mathbf{q}_{t-1} \text{ with probability } 1 - a_r \end{cases} \end{aligned}$$

In practice, if the new orbit produces a better fit to the full observational data set, it is always accepted. If it produces a worse fit, it is accepted with the probability equal to a_r. The sampling is repeated until a large enough number of orbits have been obtained. After the sampling is completed convergence diagnostics has to be performed to insure that the stationary distribution was reached and to test for the length of burn-in period (the time required for the chain to reach the stationary). The obtained distributions of the orbital parameters reflect the properties of orbital element uncertainties.

5 Preliminary results

To validate the method proposed here, we have computed orbital distributions for some well-constrained systems. In particular we selected the binary asteroids 1998 WW_{31} and 2000 QL_{251} as test cases since for these, the orbital elements have been determined by other methods already reported in the litterature.

In November 1998 WW_{31} was discovered by R. Millis and collaborators at Kitt Peak National Observatory but was reported as a single object in the Kuiper belt. The observations provided a short arc only. The asteroid was subsequently included in follow up studies with the Canada France Hawaii Telescope. Further observations along with reprocessed previous observations finally showed 1998 WW_{31} to be a binary system. Based on observations from the Hubble Space Telescope and the available ground based data, the secondary's orbital parameters relative to the primary were found to be the following, $P = 574 \pm 10$ days, $a = 22300 \pm 800$ km, $e = 0.817 \pm 0.05$ (Veillet 2002).

The primary of 2000 QL_{251} was discovered by M. W. Buie from Cerro Tololo Observatory, La Serena. Hubble Space Telescope observations allowed Noll, Stephens, Grundy, and Levison to detect its companion (Noll 2006). Grundy (2009) give the following elements $a = 5002 \pm 27$ km, $P = 56.451 \pm 0.025$ days, $e = 0.4871 \pm 0.0065$.

The two figures below present preliminary results for those two objects from the MCMC runs. These orbital elements agree with results obtained by others. We expect to improve on these when the implementation of the method is complete and more robust for various cases.

6 Conclusions

We have proposed a novel method for obtaining the orbits of resolved binary asteroids. This method is based on the work of Thiele–Innes–van Bos and Monte Carlo Markov Chain statistics. The method is still being implemented but has already been succesfully applied to a few selected binaries. The preliminary results are very promising and show strong convergence.

This work was supported, by the European Science Foundation under the GREAT ESF RNP programme and Polish National Science Center grant NCN nr 2012/04/S/ST9/00022.

References

Aitken, R., 1918. The binary stars. Semicentennial publications of the University of California, 1868-1918. D.C. McMurtrie.

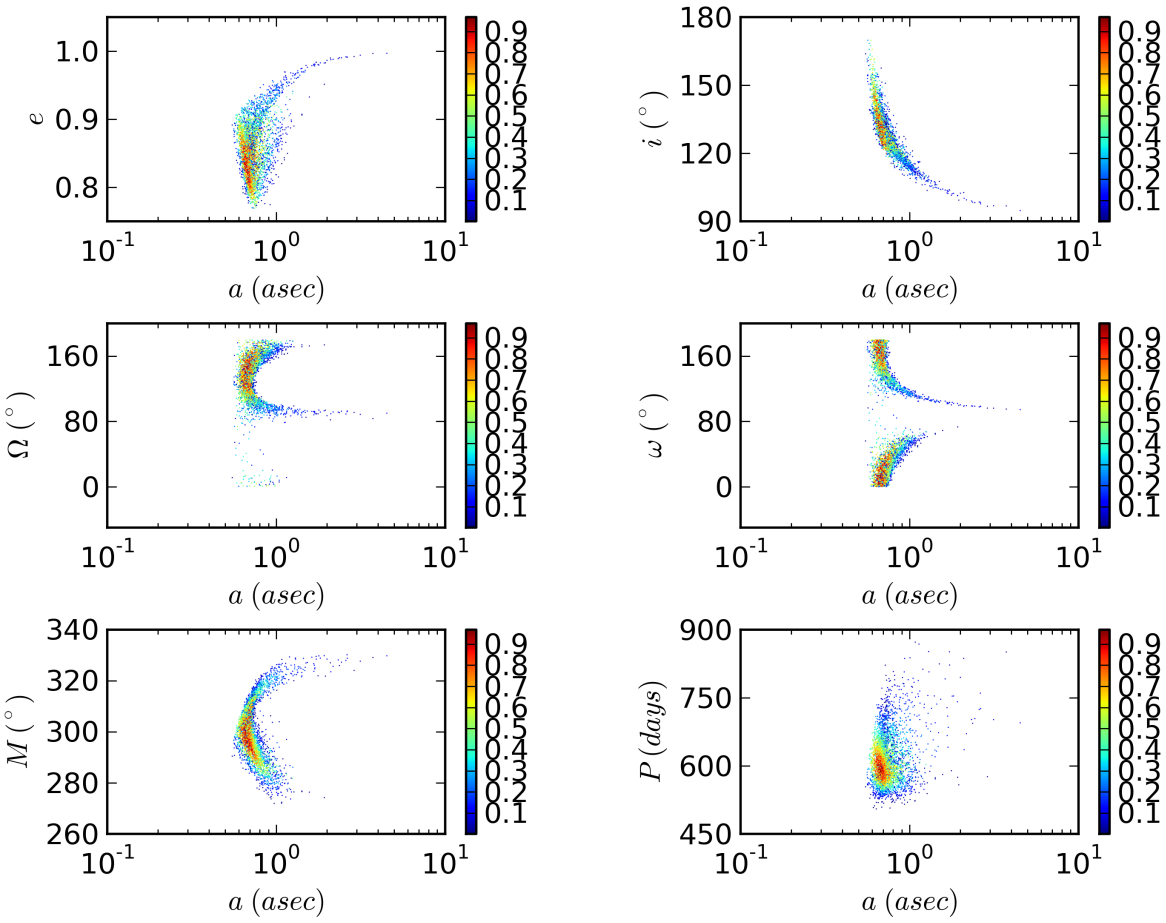

Fig. 2. Distribution of orbital elements for asteroid 1998 WW_{31}. Color corresponds to normalized probability density value.

Argyl, B., 2004. Observing and Measuring Visual Double Stars. No. vol. 1 in Patrick Moores Practical Astronomy Series. Springer.

Chib, S., and Greenberg E., Understanding the Metropolis-Hastings algorithm. The American Statistician 49.4 (1995): 327-335.

Grundy W. M., Stansberry J. A., Noll K. S., Stephens D. C., Trilling D. E., Kern S. D., Spencer J. R., Cruikshank D. P., Levison H. F., 2010. Icarus 191, Issue 1, 286-297

Grundy, W. M., Noll, K. S., Buie, M. W., Benecchi, S. D., Stephens, D. C., Levison, H. F., 2009, Mutual orbits and masses of six transneptunian binaries, Icarus, 200, 627-635

Hestroffer D. et al., 2010. The Gaia mission and the asteroids. Dynamics of Small Solar System Bodies and Exoplanets. Springer Berlin Heidelberg, LNP 790, 251-340

Hestroffer D., Vachier F., Balat B., 2005. EM&P 97, 3-4, pp. 245-260

Hestroffer D., 2002. Preparing GAIA for the Solar System. EAS Publications Series, 359-364.

Muinonen, K., Bowell, E., 1993. Asteroid orbit determination using bayesian probabilities. Icarus 104 (2), 255279.

Noll K. S., Stephens D. C., Grundy W. M., Levison H. F., September 2006. IAU Circ., 8746, 1 (2006). Edited by Green, D. W. E.

Tanga P. and Hestroffer D., Gaia as a Solar System observatory: Perspectives for binary asteroids. Proceedings of the workshop. Vol. 1. 2012.

Thiele T. N., 1883, Astron. Nachr., 1044, 245

van den Bos W. H., 1926, Union Obs. Circ., 2, 356

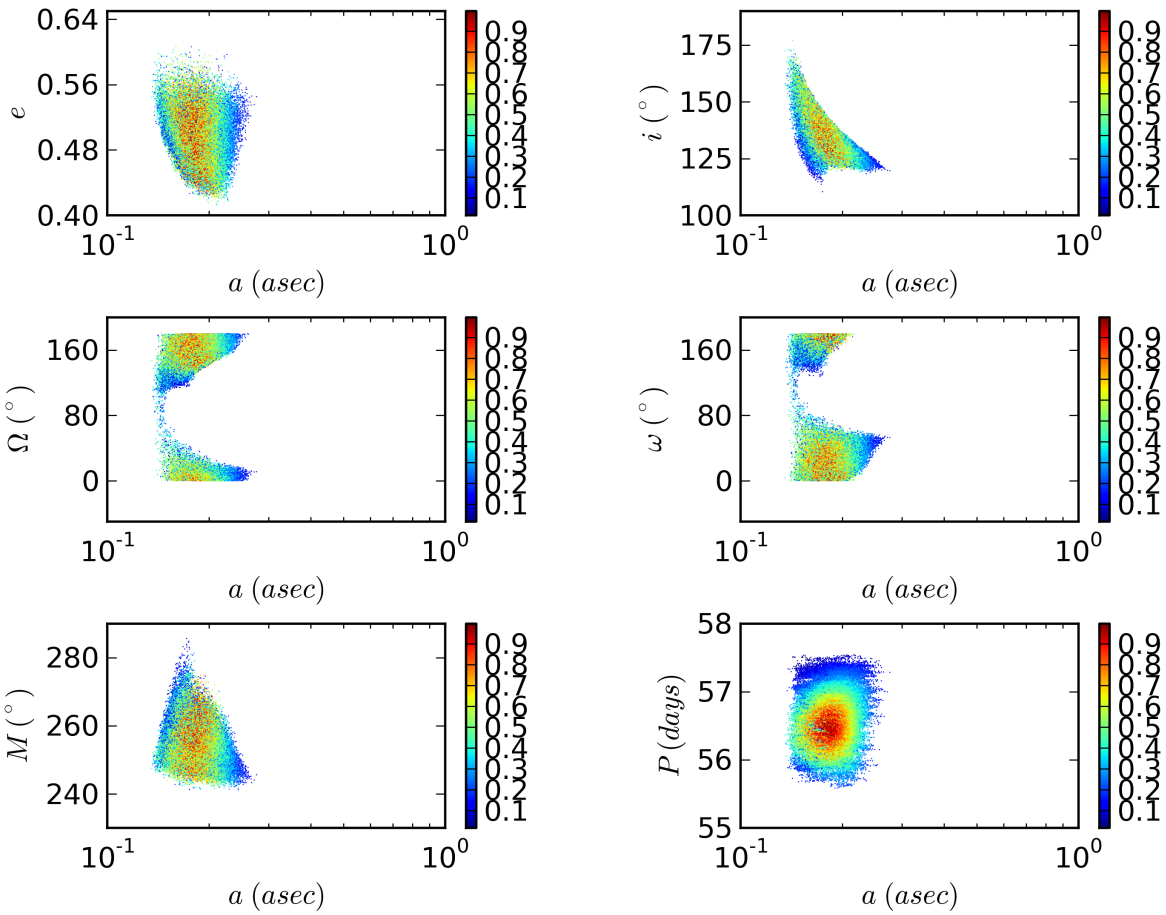

Fig. 3. Distribution of orbital elements for asteroid 2000 QL_{251}. Color corresponds to normalized probability density value.

Veillet C., Parker J. W., Griffin I., Marsden B., Doressoundiramk A., Buie M., Tholen D. J., Connelley M., Holman M. J., 2002, Nature, 416, 711-713

Virtanen, J., Muinonen, K., Bowell, E., 2001. Statistical ranging of asteroid orbits. Icarus 154 (2), 412431.

SF2A 2013
L. Cambrésy, F. Martins, E. Nuss and A. Palacios (eds)

STOCHASTIC PERTURBATION OF THE TWO-BODY PROBLEM

J. Cresson[2,1], F. Pierret[2] and B. Puig[3]

Abstract. We study the impact of a stochastic perturbation on the classical two-body problem in particular concerning the preservation of first integrals and the Hamiltonian structure. Numerical simulations are performed which illustrate the dynamical behavior of the osculating elements as the semi-major axis, the eccentricity and the pericenter. We also derive a stochastic version of Gauss's equations in the planar case.

Keywords: Two-body problem, stochastic perturbation, numerical simulations, stochastic Gauss's equations

1 Introduction

The stability of the solar system is a famous open problem in celestial mechanics (see J. Moser (1978),S. Marmi (1999),J. Laskar (2010),J. Féjoz (2013a)). Since the discovery by Newton of the gravitation law, a mathematical approach to this problem is to study the stability of the n-body problem as an ideal model for the behavior of planetary systems. Numerous advances have been made in this direction. From the analytical point of view, recent contributions deal with application of the Kolmogorov-Arnold-Moser (KAM) theorem and Nekhoroschev theory to the n-body problem (see J. Féjoz (2004),M. Herman (1998),L. Niederman (1996)) for stability and Arnold's diffusion (J. Xia (1993),J. Xia (1994),J. Féjoz (2013b)) for instability. On the numerical side, simulations over very large time scales of the n-body problem in particular by S. Tremaine and Wisdom and J. Laskar give insight that the "solar system" is unstable (chaotic) over very large time.

A common feature of all these works is to deal with a deterministic model for the planetary motion. However, as pointed out by D. Mumford (1999), the meaning of such an assumption with respect to the real behavior of planetary systems is far from being satisfying. D. Mumford remarks that "a major step in making the equation more relevant is to add a small stochastic term".

However, adding a stochastic term is far from being trivial because the nature and origin of such a contribution is more or less unknown. A significant step has been done in Sharma & Parthasarathy (2007) (see also J. Cresson (2011)). Using observations made by I. Mann et al. (2004) about the stochastic fluctuations of the density of the zodiacal dust around the sun, Sharma & Parthasarathy (2007) propose a stochastic perturbation induced by a cloud whose density fluctuates stochastically.
in the whole text In this paper, we continue the study initiated by S.N. Sharma and H. Parthasarathy in several directions : first, we make a new derivation of the stochastic perturbation induced by a cloud having a stochastically fluctuating density. We then study how the classical properties of the two-body problem are affected by this stochastic perturbation. In particular, we discuss the persistence of first integrals like energy and angular momentum and the behavior of the Hamiltonian structure in the context of stochastic Hamiltonian systems introduced by Bismut (1981). Third, we perform numerical simulations in order to observe the dynamical behavior of the osculating elements. The accuracy of the numerical integrator is also discussed. Finally, we derive the stochastic version of Gauss's equations for the variations of the osculating elements which allows us to determine the contribution of the stochastic terms in the observed dynamical behavior.

[1] LMAP/Université de Pau, 64013 Pau, France,
[2] SYRTE/Observatoire de Paris, 75014 Paris, France,
[3] IPRA/Université de Pau, 64013 Pau.

2 The two-body problem

We follow the book (Goldstein (2002),Chap.3) to which we refer for more details. In the whole text the symbol $^{\mathsf{T}}$ denotes the transpose of a vector.

2.1 Description

Let S and P be two bodies and M_S and M_P their masses. The body S is supposed to be the central body typically a star and P is the orbiting body typically a planet or a satellite. The motion is supposed to be in an elliptic configuration. The reduced mass is $m = \frac{M_S M_P}{M_S+M_P}$ and the potential coefficient is $k = GM_S M_P$ where G is the gravitational constant. We define $(S, \vec{x}, \vec{y})$ to be a fixed frame attached to S and $\vec{r}$ the position vector of P in this reference frame with ϕ his position angle. The elliptical motion is described with the semi-major axis a, the eccentricity e and the pericenter angle ω. We associate the polar reference frame $(S, \vec{e_R}, \vec{e_T})$ where $\vec{e_R}^{\mathsf{T}} = (\cos\phi, \sin\phi)$ and $\vec{e_T}^{\mathsf{T}} = (-\sin\phi, \cos\phi)$. In this reference frame we have $\vec{r} = r\vec{e_R}$ where r is the norm of the position vector. The motion is illustrated in Fig. 1

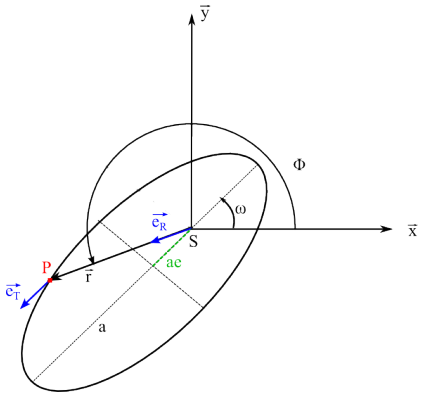

Fig. 1. The classical two body problem.

2.2 Equations of motion

The equations of motion for the two-body problem are given by

$$\left\{ \begin{array}{rcl} \frac{dr}{dt} & = & v, \\ \frac{d\phi}{dt} & = & w, \\ \frac{dv}{dt} & = & rw^2 - \frac{k}{mr^2}, \\ \frac{dw}{dt} & = & -\frac{2vw}{r}. \end{array} \right. \tag{2.1}$$

Classical conserved quantities of motion are the *angular momentum* and *energy* of the system defined by

$$M = mr^2 w, \tag{2.2}$$

$$H = \frac{1}{2}m(v^2 + r^2 w^2) - \frac{k}{r}. \tag{2.3}$$

We will use also the *Laplace-Runge-Lenz vector* defined by $\vec{A} = m\vec{v} \wedge \vec{L} - km\vec{e}_R$ where $\vec{v}$ is the velocity vector and $\vec{L} = m\vec{r} \wedge \vec{v}$ is the angular momentum vector.

3 Perturbation induced by a dust-cloud

In Sharma & Parthasarathy (2007) the authors consider a stochastic perturbation induced by a cloud with a density which fluctuates stochastically. This assumption is supported by observations made by I. Mann et al. (2004) about the zodiacal dust around the Sun. These fluctuations comes from comets and asteroids which produce dust when they come near the Sun due to collisional fragmentation and sublimation, radiation pressure

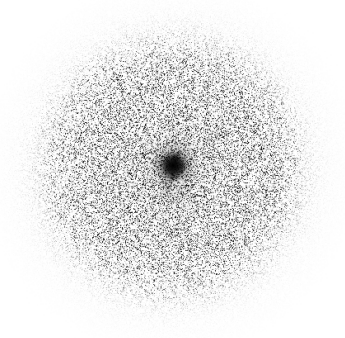

Fig. 2. The dust sphere.

acceleration and rotational bursting. In order to simplify the computations, we assume in the following that the dust cloud is a sphere.

The force $\vec{F}$ induced by a dust sphere of constant density ρ is only a radial force $\vec{F}^{\mathsf{T}} = (\frac{4}{3}\pi G\rho r, 0)$ (see Goldstein (2002) p.122). Our main assumption is that the mean density of this dust cloud is fluctuating randomly that is to say the density is a function of time define as

$$\rho(t) = \sigma_r W_t^r \tag{3.1}$$

where σ_r is a constant and W_t^r is a "white noise". The random force takes then the form

$$\vec{F}^{\mathsf{T}} = (mr\sigma_r W_t^r, 0) \tag{3.2}$$

Now if we add an isotropic tangential component induced by other physical process we obtain

$$\vec{F}^{\mathsf{T}} = \left(mr\sigma_r W_t^r, m\sigma_\phi W_t^\phi\right) \tag{3.3}$$

where σ_ϕ is a constant and W_t^ϕ is also a "white noise" independent of W_t^r.

4 Stochastic perturbation of the two-body problem

4.1 Reminder about stochastic differential equations

We remind basic properties and definition of stochastic differential equations in the sense of Itô. We refer to the book Øksendal (2003) for more details.

A *stochastic differential equation* is formally written (see Øksendal (2003),Chap.V) in differential form as

$$dX_t = \mu(t, X_t)dt + \sigma(t, X_t)dB_t, \tag{4.1}$$

which corresponds to the stochastic integral equation

$$X_t = X_0 + \int_0^t \mu(s, X_s)\, ds + \int_0^t \sigma(s, X_s)\, dB_s, \tag{4.2}$$

where the second integral is an Itô integral (see Øksendal (2003),Chap.III) and B_t is the classical Brownian motion (see Øksendal (2003),Chap.II,p.7-8).

An important tool to study solutions to stochastic differential equations is the *multi-dimensional Itô formula* (see Øksendal (2003),Chap.III,Theorem 4.6) which is stated as follows :

We denote a vector of Itô processes by $\mathbf{X}_t^\mathsf{T} = (X_{t,1}, X_{t,2}, \ldots, X_{t,n})$ and we put $\mathbf{B}_t^\mathsf{T} = (B_{t,1}, B_{t,2}, \ldots, B_{t,n})$, $d\mathbf{B}_t^\mathsf{T} = (dB_{t,1}, dB_{t,2}, \ldots, dB_{t,n})$. We consider the multi-dimensional stochastic differential equation defined by (4.1). Let f be a $\mathcal{C}^2(\mathbb{R}_+ \times \mathbb{R}, \mathbb{R})$-function and X_t a solution of the stochastic differential equation (4.1). We have

$$df(t, \mathbf{X}_t) = \frac{\partial f}{\partial t} dt + (\nabla_{\mathbf{X}}^\mathsf{T} f) d\mathbf{X}_t + \frac{1}{2}(d\mathbf{X}_t^\mathsf{T})(\nabla_{\mathbf{X}}^2 f) d\mathbf{X}_t, \tag{4.3}$$

where $\nabla_{\mathbf{X}} f = \partial f / \partial \mathbf{X}$ is the gradient of f w.r.t. X, $\nabla_{\mathbf{X}}^2 f = \nabla_{\mathbf{X}} \nabla_{\mathbf{X}}^\mathsf{T} f$ is the Hessian matrix of f w.r.t. $\mathbf{X}$, δ is the Kronecker symbol and the following rules of computation are used : $dtdt = 0$, $dtdB_{t,i} = 0$, $dB_{t,i}dB_{t,j} = \delta_{ij}dt$.

4.2 The stochastic two-body problem

The general form of the equations of the perturbed two-body problem by a planar force $\vec{F} = (F_r, F_\phi)$ is easily compute and reads

$$\left\{ \begin{array}{rcl} \frac{dr}{dt} & = & v, \\ \frac{d\phi}{dt} & = & w, \\ \frac{dv}{dt} & = & rw^2 - \frac{k}{mr^2} + \frac{F_r}{m}, \\ \frac{dw}{dt} & = & -\frac{2vw}{r} + \frac{F_\phi}{mr}, \end{array} \right. \tag{4.4}$$

which gives, replacing F by the random force (3.3) :

$$\left\{ \begin{array}{rcl} \frac{dr}{dt} & = & v, \\ \frac{d\phi}{dt} & = & w, \\ \frac{dv}{dt} & = & rw^2 - \frac{k}{mr^2} + r\sigma_r W_t^r, \\ \frac{dw}{dt} & = & -\frac{2vw}{r} + \frac{\sigma_\phi W_t^\phi}{r}. \end{array} \right. \tag{4.5}$$

The classical way to give a sense to this set of equations is to replace W_t by a suitable stochastic process called the *white noise process* which is heuristically obtained as increment of the *Brownian motion* B_t (see Øksendal (2003),p.7-8). We then obtain a stochastic differential equation in Itô sense given by

$$\left\{ \begin{array}{rcl} dr & = & vdt, \\ d\phi & = & wdt, \\ dv & = & \left(rw^2 - \frac{k}{mr^2}\right) dt + r\sigma_r dB_t^r, \\ dw & = & -\frac{2vw}{r} dt + \frac{\sigma_\phi}{r} dB_t^\phi, \end{array} \right. \tag{4.6}$$

where B_t^r and B_t^ϕ are independent. This set of equations describes what we called the *stochastic two-body problem* in the following.

5 Symmetries and First integrals

First integrals and symmetries play a fundamental role in classical mechanics and in particular for the study of the deterministic n-body problem (see V.I. Arnold (1989)). A natural question is to know if symmetries and first integrals of a given deterministic system persist in an appropriate sense. In this Section, we remind the definition of weak and strong first integrals. We prove that the angular momentum is preserved under stochastic perturbation and give rise to a weak first integral of the stochastic two-body problem.

5.1 Definitions

Let $dx/dt = f(x,t)$, $x \in \mathbb{R}^n$ $(\star)$ be an ordinary differential equation. A function $I : \mathbb{R}^n \mapsto \mathbb{R}$ is called a *first integral* of $(\star)$ if for all solutions x_t of $(\star)$ we have $I(x_t) = I(x_0)$ for all t. If I is sufficiently smooth we deduce $\frac{dI(x_t)}{dt} = 0$.

A natural generalisation of this definition in the setting of stochastic differential equations is given for example in Misawa (1999) (see also Bismut (1981),Cresson-Darses (2007a),Cresson-Darses (2007b) and J.A. Lázaro Camí (2008),p.52):

Strong first integral A function $I : \mathbb{R}^n \to \mathbb{R}$ is a *strong first integral* of (4.1) if for all solutions X_t of (4.1), the stochastic process $I(X_t)$ is a constant process, i.e. $I(X_t) = I(X_0)$ or $d(I(X_t)) = 0$.

Such a property is very strong and classical first integral are usually not preserved in the strong sense. However, a weaker property can be looked for:

Weak stochastic first integral A function $I : \mathbb{R}^n \to \mathbb{R}$ is a weak stochastic first integral of (4.1) if for all solutions X_t of (4.1), the stochastic process $I(X_t)$ satisfies $\mathrm{E}(I(X_t)) = \mathrm{E}(I(X_0))$ where E denotes the expectation.

This condition implies that $I(X_t) = I(X_0)$ almost surely.

5.2 Variation of the angular momentum and the energy

Using formulas (2.2) and (2.3) for the angular momentum and energy, the multi-dimensional Itô formula with $X_t^{\mathsf{T}} = (r, \phi, v, w)$ and $B_t^{\mathsf{T}} = \left(B_t^r, B_t^\phi\right)$ leads to

$$dM(X_t) = mr\sigma_\phi dB_t^\phi, \quad dH(X_t) = mrv\sigma_r dB_t^r + mrw\sigma_\phi dB_t^\phi + \frac{m}{2}\left[\sigma_r^2 r^2 + \sigma_\phi^2\right] dt.$$

for the behavior of these first integrals over solutions of the stochastic two-body problem. As expected, there is no persistence of the angular momentum or energy integral in the strong sense.

Remark The strong conservation of the angular momentum is broken by our assumption that an isotropic tangential force exists, i.e. $\sigma_\phi \neq 0$ (see §.3, equation (3.3)).

However, we have the following weak conservation property :

Lemma 5.1 *The angular momentum is a weak first integral of the stochastic two-body problem.*

The proof is simple and relies on classical properties of the Brownian motion.

Proof Let X_t be a solution of the stochastic two-body problem. We have $M(X_t) = M(X_0) + \int_0^t mr\sigma_\phi dB_t^\phi$ where M is the angular momentum function. Using the property that $\mathrm{E}\left(\int_a^b f dB\right) = 0$ for all f sufficiently smooth (see Øksendal (2003),Definition 3.4,p.18 and Theorem 3.7 (iii),p.22), we deduce that $\mathrm{E}(M(X_t)) = \mathrm{E}(M(X_0))$ which concludes the proof.

This result does not extend to the energy first integral. This is due to the existence of a non-trivial deterministic term emerging in the Itô formula. Precisely, we have $H(X_t) = H(X_0) + \int_0^t mrv\sigma_r dB_t^r + \int_0^t mrw\sigma_\phi dB_t^\phi + \frac{m}{2}\int_0^t \left[\sigma_r^2 r^2 + \sigma_\phi^2\right] ds$. Taking expectation, we obtain

$$\mathrm{E}(H(X_t)) = \mathrm{E}(H(X_0)) + \frac{m}{2}\mathrm{E}\left(\int_0^t \left[\sigma_r^2 r^2 + \sigma_\phi^2\right] ds\right).$$

The second term is non zero so that the energy first integral is not preserved even in a weak sense.

The conservation of the angular momentum in the weak sense will be an important information in order to perform simulations because it will be the only quantity that we could check his conservation during the simulations.

6 Simulations

The simulation of stochastic differential equations is more difficult than in the deterministic case (see Kloeden et al. (1999) and Higham (2001)). In the sequel, we use a stochastic Runge-Kutta of weak order 2 due to N.J. Kasdin and L.J. Stankievech in Kasdin et al. (2009). The term of *weak order* refers to the error of the stochastic numerical scheme with respect to the expectation of the solution computed.

Our simulations are made with the same initial conditions and integration time used by Sharma & Parthasarathy (2007), which are :

$$r(0) = 1\ AU, \tag{6.1}$$
$$\phi(0) = 1\ rad, \tag{6.2}$$
$$v(0) = 0.01\ AU/TU, \tag{6.3}$$
$$\omega(0) = 1.1\ rad/TU, \tag{6.4}$$
$$\sigma_r = 0.0121\ TU^{-3/2}, \tag{6.5}$$
$$\sigma_\phi = 2.2 \times 10^{-4}\ AU.TU^{-3/2}, \tag{6.6}$$

where AU is the Astronomical Unit which is the Earth-Sun distance and TU is the Time Unit which is approximately 58 days. These units are called canonical units (see Bate et al. (1971)).

The initials conditions are chosen such that the unperturbed motion is an ellipse and the diffusion constants σ_r and σ_ϕ are chosen such that the stochastic perturbing force is proportional to 1/10 of the gravitational force at the initial time. Numerical integration are performed over 15TU like in Sharma & Parthasarathy (2007). The unperturbed trajectory as well as the perturbed one are plotted in Fig. 3 with color green and red respectively and we still use the same colors on figures to refer to the unperturbed and perturbed case. The accuracy

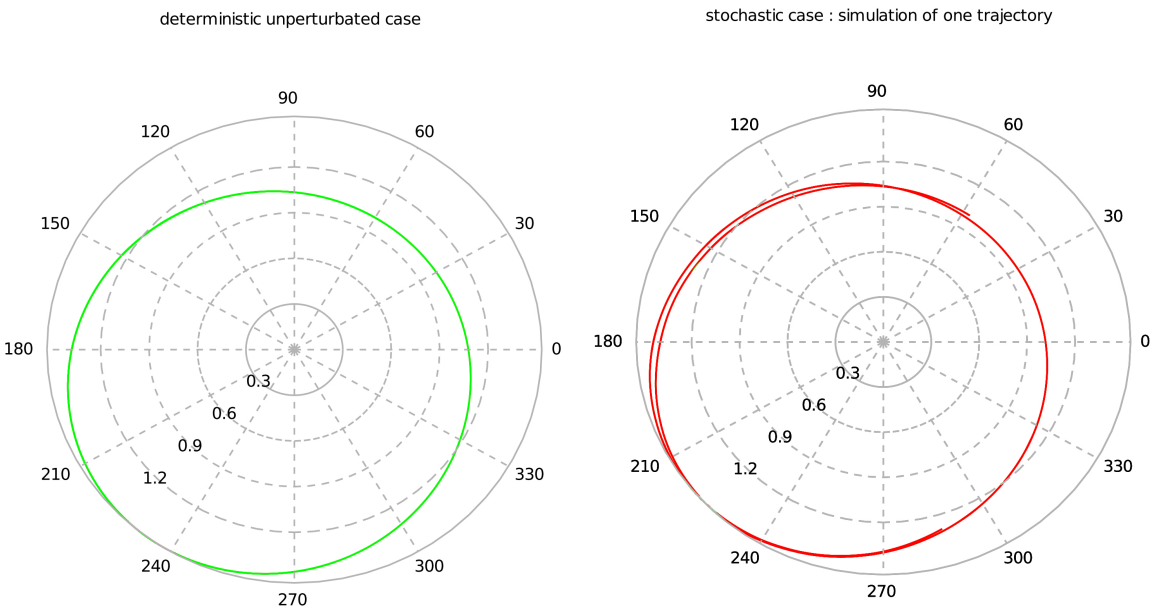

Fig. 3. Left: Unperturbed case. **Right:** Perturbed case.

of the integrator can be tested by looking for the preservation of the weak first integral given by the angular momentum. Expectations are computed using a Monte Carlo method. Our result indicates a very good behavior of the integrator with respect to weak first integrals (see Fig. 4). The dynamical behavior of the semi-major axis, the eccentricity and the pericenter angle for the trajectory of the perturbed motion corresponding to Fig. 3 is given in Fig. 5 as well as the expectation of these elements in Fig. 6.

7 Stochastic planar Gauss equations

To study the variations of orbital elements we derive a stochastic version of the classical Gauss equations (see Goldstein (2002),p.96-103). The strategy to obtain these equations in the planar case is as follows. We consider a stochastic perturbation per unit of mass in polar coordinates

$$d\vec{v}_P = \begin{pmatrix} \bar{R} \\ \bar{T} \end{pmatrix} dt + (\tilde{R}, \tilde{T}) \cdot d\mathbf{B} \tag{7.1}$$

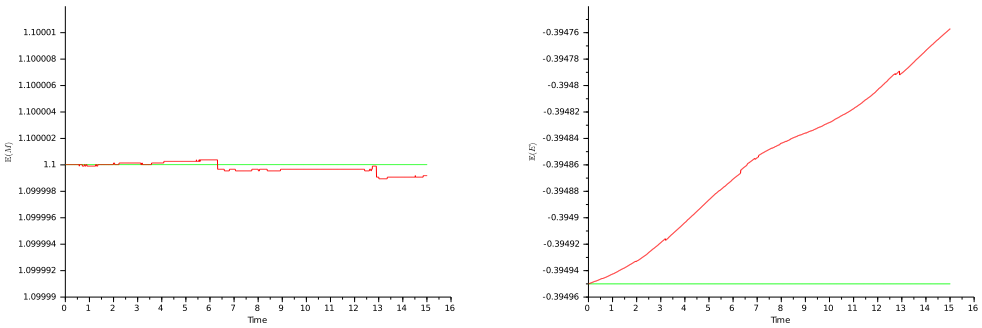

Fig. 4. Left: $\mathrm{E}(M(X_t))$. **Right:** $\mathrm{E}(H(X_t))$.

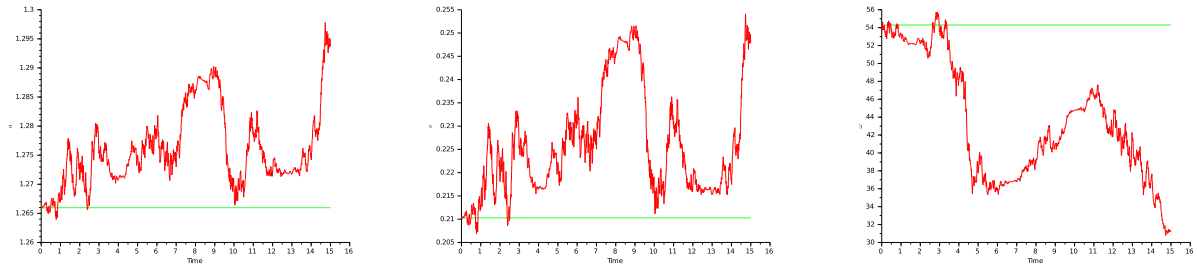

Fig. 5. Left: a the semi-major axis. **Center:** e the eccentricity. **Right:** ω the pericenter angle.

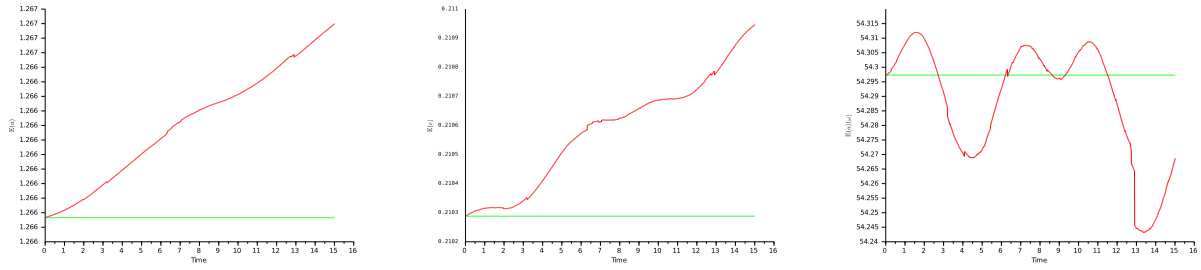

Fig. 6. Left: $\mathrm{E}(a)$. **Center:** $\mathrm{E}(e)$. **Right:** $\mathrm{E}(\omega)$.

where $\tilde{R} = \begin{pmatrix} \tilde{R}_1 \\ 0 \end{pmatrix}$,$\tilde{T} = \begin{pmatrix} 0 \\ \tilde{T}_2 \end{pmatrix}$ and $d\mathbf{B}_t = \begin{pmatrix} dB_t^R \\ dB_t^T \end{pmatrix}$, with B_t^R and B_t^T being independent. In our example we have $\bar{R}$ and $\bar{T}$ equal to zero, $\tilde{R}_1 = r\sigma_r$ and $\tilde{T}_2 = \sigma_\phi$.

The variation of orbital elements is derived from the well known relations (see Goldstein (2002) (3-57) p.96, (3-58) p.97 and (3-84 p.103))

$$H = \frac{-k}{2a}, \quad \frac{M^2}{mk} = a(1-e^2), \quad \tan\omega = \frac{A_x}{A_y}, \tag{7.2}$$

where A_x and A_y are the component of the Laplace-Runge-Lenz vector in $(S, \vec{x}, \vec{y})$. Using Itô formula, we obtain the following stochastic Gauss equations in the planar case

$$da = \left[\frac{2a^{3/2}}{\sqrt{\mu(1-e^2)}} \left(e \sin f \bar{R} + (1 + e\cos f)\bar{T} \right) + \frac{a^2}{\mu} \left(\tilde{R}^2 \left(1 + \frac{4e^2 \sin^2 f}{1-e^2} \right) + \tilde{T}^2 \left(1 + \frac{4(1+e\cos f)^2}{1-e^2} \right) \right) \right] dt$$

$$+ \quad \frac{2a^{3/2}}{\sqrt{\mu(1-e^2)}}\left(e\sin f\tilde{R} + (1+e\cos f)\tilde{T}\right)\cdot dB \tag{7.3}$$

$$\begin{aligned} de &= \left[\sqrt{\frac{a(1-e^2)}{\mu}}\left(\sin f\bar{R} + \left(\cos f + \frac{e+\cos f}{1+e\cos f}\right)\bar{T}\right) + \frac{a(1-e^2)\cos^2 f}{2\mu e}\tilde{R}^2\right. \\ &+ \left.\frac{a(1-e^2)}{\mu e}\left(2 - \frac{\cos f}{2}\left(\frac{2+e\cos f}{1+e\cos f}\right)\left(\cos f + \frac{e+\cos f}{1+e\cos f}\right)\right)\tilde{T}^2\right]dt \\ &+ \sqrt{\frac{a(1-e^2)}{\mu}}\left(\sin f\tilde{R} + \left(\cos f + \frac{e+\cos f}{1+e\cos f}\right)\tilde{T}\right)\cdot dB \end{aligned} \tag{7.4}$$

$$\begin{aligned} d\omega &= \left[\sqrt{\frac{a(1-e^2)}{\mu}}\frac{1}{e}\left(-\cos f\bar{R} + \sin f\left(\frac{2+e\cos f}{1+e\cos f}\right)\bar{T}\right)\right. \\ &+ \left.\frac{a\left(1-e^2\right)}{\mu e}\left[\frac{\sin 2f}{2e}\tilde{R}^2 - \frac{\sin f}{(1+e\cos f)^2}\left(1 + \frac{\cos f}{e}(2+e\cos f)^2\right)\right)\tilde{T}^2\right]\right]dt \\ &+ \sqrt{\frac{a(1-e^2)}{\mu}}\frac{1}{e}\left(-\cos f\tilde{R} + \sin f\left(\frac{2+e\cos f}{1+e\cos f}\right)\tilde{T}\right)\cdot dB \end{aligned} \tag{7.5}$$

where $\mu = \frac{k}{m}$ and the contribution due to the stochastic perturbation is written in red. We refer to F. Pierret (2013) for the general case.

8 Conclusions

The stochastic two-body problem displays a fast change of the dynamics with respect to the classical one despite the smallness of the stochastic perturbation. This result reinforces the necessity to take into account usually ignored stochastic phenomenon in order to obtain relevant predictions on the long term dynamical behavior of dynamical systems. This conclusion is fundamental for the study of the long term evolution of the solar system.

As a consequence, the following list of open problems can be studied :

- Stochastic perturbations induced by the deformation of bodies. As a first step, we would like to study a J_2-problem (see Brouwer, D. and Clemence, G. M. (1961)) with a random or stochastic J_2 constant and its influence on the rotation of the earth.
- In order to perform simulations over a very long time, we need to construct high order stochastic Runge-Kutta type integrators.

References

V.I. Arnold, *Mathematical methods of classical mechanics*, Second edition, Vol. 60 Graduate Texts in Mathematics, Springer-Verlag (1989).

Bate, R., Mueller, D., & White, J. 1971, *Fundamentals of Astrodynamics*, Dover Books on Aeronautical Engineering Series, Dover Publications.

Bismut, J. 1981, *Mécanique aléatoire*, Lecture notes in mathematics (Springer-Verlag).

Brouwer, D. and Clemence, G. M.: 1961, *Methods of Celestial Mechanics*, Academic Press, New York.

Cresson J., The stochastisation hypothesis and the spacing of Planetary systems, Journal of Mathematical Physics, 29.p, 2011.

Cresson J., Darses S., Stochastic embedding of dynamical systems, J. Math. Phys. 48, 072703 (2007) (54 pages).

Cresson J., Darses S., Théorème de Noether Stochastique, C.R. Acad. Sci. Paris, Ser. I 344 (2007) 259-264.

Féjoz J., Démonstration du "théorème d'Arnold" sur la stabilité du système planétaire (d'après M.Herman), Ergod. Th. and Dynam. Sys. (2004), 24, 1-62.

Féjoz J., Le problème de la stabilité du Système solaire, de Lagrange à nos jours, 31 pp. Exposé pour la Journée annuelle de la Société Mathématique de France : Deux cents ans après Lagrange (IHP, 28 juin 2013).

Féjoz J., M. Guardià, V. Kaloshin and P. Roldán, Diffusion along mean motion resonance in the restricted planar three-body problem, 76 pp. Preprint (2013).

Goldstein, H. 2002, *Classical Mechanics*, Pearson Education.

M.R. Herman. Démonstration d'un théorème de V.I. Arnold, Séminaire de Systèmes Dynamiques et manuscript, 1998.

Higham D.J., An algorithmic introduction to numerical simulation of stochastic differential equations, SIAM Review Vol. 43, No.3, pp.525-546.

N.J. Kasdin, L.J. Stankievech, On simulating randomly driven dynamic systems, The journal of Astronautical Sciences, Vol. 57,nos.1 and 2 (2009), pp. 289-311.

Kloeden P.E. and Platen E. *Numerical solutions of differential equations*, Springer-Verlag, Berlin, 1999.

Jacques Laskar, Le Système solaire est-il stable ?, Séminaire Poincaré XIV (2010) 221-246.

J.A. Lázaro Camí, Stochastic geometric mechanics, Ph.D. Universidad de Zaragoza.

Mann, I., Kimura, H., Biesecker, D., et al. 2004, Dust near the Sun, Space Science Reviews, 110, 269.

Marmi, S., Chaotic behavior in the solar system following J. Laskar, Séminaire Bourbaki, 51ème année, 1998-1999, Paper No. 854.

Misawa, T. Conserved quantities and symmetries related to stochastic dynamical systems, Annals of the Institute of Statistical Mathematics, Vol. 51, no.4, 779-802 (1999).

Moser, J., Is the solar system stable ?, Math. Intell. 1, 65-71, 1978.

Mumford D., The dawning of the age of stochasticity, in *Mathematics: Frontiers and perspectives*, V. Arnold, M. Atiyah, P. Lax, B. Mazur editors, AMS, 2000, 197-218.

L. Niederman, Stability over exponentially long times in the planetary problems, Nonlinearity 9 (1996), 1703-1751.

Øksendal, B. 2003, *Stochastic Differential Equations: An Introduction with Applications*, Hochschultext / Universitext (Springer).

F. Pierret, Stochastic Gauss equations, in preparation, (2013).

N. Sharma and H. Parthasarathy, Dynamics of a stochastically perturbed two-body problem, Proc. R. Soc. A 2007 463, 979-1003.

Xia J., Arnold diffusion in the elliptic restricted three-body problem, J. Dynamics Differential Equations 5 (2)(1993).

Xia J., Arnold diffusion and oscillatory solutions in the planar three-body problem, J. Differential Equations 110 (1994) 289-321.

SF2A 2013
L. Cambrésy, F. Martins, E. Nuss and A. Palacios (eds)

RESONANCES DUE TO THIRD BODY PERTURBATIONS IN THE DYNAMICS OF MEOS

L. Stefanelli[1] and G. Metris[1]

Abstract. The dynamics of Medium Earth Orbits (MEO) sees nowadays a renewed interest because of the development of satellites constellations (GNSS), that raises the problem of parking orbits for satellites at end of life. Numerical evidence shows that the resonances related to the presence of a third body can affect the stability of MEO orbits. The goal of our work is to study the effects of resonances on the stability of MEO orbits, over long or very long term (hundreds of years). For orbits above 20,000 km altitude, the perturbation due to a third body (the Moon or the Sun) is not fully negligible, so we take into account the third body perturbation on the secular evolution of the angular variable of the satellite orbits, and thus of the resonant angle. We estimate numerically the evolution of the resonant inclination. We study the stability of some resonances analytically and numerically, and in particular the resonance associated to the operational inclination of the Galileo satellites.

Keywords: Medium Earth Orbits, resonances, stability.

1 Introduction

The region of space hosting the Medium Earth Orbits (MEO) is becoming more and more crowded, especially because of the increasing presence of the satellites constellation, like the GPS and GALILEO families. The lifetime of these satellites is limited, and they have to be replaced regularly. This rises the problem of positioning the inactive satellites on "safe" parking orbits, in order to avoid the classical problems with spatial debris: they can become a danger for the active satellites and can cause the multiplication of the debris by collision. For this reason, understanding the stability properties of MEO orbits for long times can guide the choice of suitable parking orbits. Among the various factors, the study of this stability includes an analysis of the behaviour of the orbits in presence of resonances, which can be a possible source of instability or, on the contrary, can help to keep the orbit stable.

The long term effects of the resonances on the stability of MEO orbits is not yet well understood. Moreover, in the litterature there are only few articles about the case of MEO orbits. In Rossi (2008) several numerical experiments concerning the interactions between resonances and MEO orbits are presented. For the theory of the resonances, the main references are the two papers Hughes (1980) and Hughes (1981), mainly dedicated to list the resonant angular combinations. Some analytical studies about the resonances dependent only on the eccentricity can be found in Breiter (1999) and Breiter (2001), but only for the case of low earth orbits.

In this paper, we deal with resonances due to the presence of a third body, that can be either the Sun or the Moon. These resonances involve linear combinations of the angles of the satellites and of the third body which appear in the development of the potential due to this third body. Such combinations write

$$\psi = (n-2p)\omega + m\Omega + (n-2p+q)M + (n-2k)\omega_{3\mathrm{b}} + m\Omega_{3\mathrm{b}} + (n-2k+j)M_{3\mathrm{b}} \tag{1.1}$$

where ω, Ω, l are the argument of the perigee, the longitude of the ascending node and the mean anomaly of the satellite and $\omega_{3\mathrm{b}}$, $\Omega_{3\mathrm{b}}$, $M_{3\mathrm{b}}$ are the same angles associated to the third body. A resonance occurs when

$$\dot{\psi} \approx 0\,.$$

[1] Geoazur, Université de Nice Sophia-Antipolis, Observatoire de la Côte d'Azur, 250 rue Albert Einstein, 06150 Valbonne (France)

While the frequencies associated to the third bodies (Sun and Moon) are well fixed, the frequencies associated to the satellite strongly depend of its orbit. Hughes (Hughes (1980) and Hughes (1981)) has carefully studied the relation between the possible resonances and the characteristics of the orbit. He has in particular evidenced a class of resonances related to combinations of the form $\alpha g + \beta h$ which involve only secular variations of the satellite angles. These variations are mainly due to the Earth's oblateness (related to the J_2 coefficient of the geopotential) and in this case, the resonance condition is only function of the inclination. One of these resonances occurs for an inclination of about 56° which is very close of the inclination of the Galileo orbits. The study of this particular resonance is thus of practical interest. This paper is a first attempt in this direction.

The article is organized as follows. In section 2, we set up the model for the hamiltonian, including the Earth's gravity potential reduced to its monopolar and quadrupolar terms and the third body gravity potential; moreover we average the hamiltonian with respect to every non resonant angles in order to keep only the driven terms for the very long term evolution (over tens of years). Section 3 contains the results of the study of this averaged system for the case of one selected resonance.

2 The model of resonance

Our fundamental variables will be the Delaunay canonical variables l, g, h, L, G, H but we will also use for convenience the classical orbital elements $a, e, i, \Omega, \omega, M$. The two sets of variables are related by the relations

$$\begin{aligned} &l = M, \quad g = \omega, \quad h = \Omega, \\ &L = \sqrt{\mu a}, \quad G = L\sqrt{1-e^2}, \quad H = G\cos i\,. \end{aligned}$$

Our model takes into account the main part of the Earth's gravity potential as well as the perturbation of a third body, i.e. the Sun or the Moon, which is the source of the resonances, the main subject of this paper. The Hamiltonian of the system is decomposed as

$$\mathcal{J} = \mathcal{J}_{\rm Kep} + \mathcal{J}_{J_2} + \mathcal{J}_{\rm 3b}\,; \tag{2.1}$$

$\mathcal{J}_{\rm Kep}$ is the Hamiltonian corresponding to the keplerian motion, $\mathcal{J}_{J_2}$ is the perturbation due the Earth's oblateness and $\mathcal{J}_{\rm 3b}$ is the perturbation due to the third body. The full expression of these well known perturbations can be found, for example, in Stefanelli et al. (2012). In particular, in this paper, we will focus on the Sun perturbation (so $3\mathrm{b} = \odot$).

Since we want to study the orbital evolution over very long time spans (typically several tens of years), we will discard the short periodic terms related to the fast variables l and $M_\odot$. This is achieved by means of a classical canonical (time dependent) change of variables not detailed here, so that the new hamiltonian no longer depends on l and $M_\odot$.

It is well known that in the J_2 problem, the elimination of the mean anomaly is accompanied, at the first order of the transformation, by the elimination of the perigee argument g (Brouwer (1959)). Thus, we obtain the new Hamiltonian (in principle, we should use new (primed) variables but we will keep the same notations for the sake of simplicity)

$$\overline{\mathcal{J}}_{J_2} = \frac{1}{4} J_2 \frac{\mu}{a} \left(\frac{R_{\rm e}}{a}\right)^2 \frac{1}{\eta^3} \left(1 - 3\cos^2 i\right)\,, \tag{2.2}$$

where $\mu = Gm_e$, and R_e are the Earth's gravitational constant and equatorial radius, respectively, J_2 is the coefficient of the second order zonal armoniccs of the Earth's gravitational potential and $\eta = \sqrt{1-e^2}$.

Concerning the Sun perturbation involving linear combinations of the angles, removing l and $M_\odot$ is equivalent to select the appropriate angular combinations (Stefanelli et al. (2012)):

$$\overline{\mathcal{J}}_\odot = -\mu_\odot \frac{a^2}{a_\odot^3} \mathcal{H}_{2,1,0}(e_\odot) \sum_{m=0}^{2} (2-\delta_{0m}) \frac{(2-m)!}{(2+m)!} \sum_{p=0}^{2} \bar{\mathcal{F}}_{2,m,p}(i) \bar{\mathcal{F}}_{2,m,1}(\epsilon) \mathcal{G}_{2,p,2p-2}(e) \cos\left((2-2p)g + mh\right)\,, \tag{2.3}$$

where ϵ is the obliquity, $\bar{\mathcal{F}}_{n,m,p}$ denotes the modified Allan inclination functions (Allan (1965)) and $\mathcal{G}_{n,p,q}$, $\mathcal{H}_{n,p,q}$ are the eccentricity special functions related to the classical Hansen coefficients (Kaula (1966)).

Note that $\overline{\mathcal{J}}_\odot$ does no longer depend on $\Omega_\odot, \omega_\odot, M_\odot$ and thus on time.

Now the averaged Hamiltonian takes the form

$$\overline{\mathcal{J}} = \quad \overline{\mathcal{J}}_{\rm Kep}(-,-,-,L,-,-) + \overline{\mathcal{J}}_{J_2}(-,-,-,L,G,H) + \overline{\mathcal{J}}_\odot(-,g,h,L,G,H)\,. \tag{2.4}$$

In this paper we will deal with the resonances due to the presence of the Sun. Potentially, a large class of resonances of the form $\alpha\dot{g} + \beta\dot{h} \approx 0$ exists (Stefanelli et al. (2012), Hughes (1980)) but we focus on the resonance, that we will call 2:1,

$$2\dot{g} + \dot{h} \approx 0\,. \tag{2.5}$$

Indeed, this resonance has one of the largest amplitude and it affects orbits with inclination close to 56° or 110°, concerning in particular the Galileo orbits.

To this end, we perform a suitable canonical change of variable $(g, h, G, H) \to (\sigma, \xi, \Sigma, \Xi)$ so that the resonant angle $\sigma = 2g + h$ becomes one of the new angles; one possible choice is the following:

$$\begin{aligned} &\sigma = 2g + h\,, \quad \Sigma = H\,,\\ &\xi = g\,, \quad \Xi = G - 2H\,. \end{aligned} \tag{2.6}$$

In terms of these new variables, the phase entering in $\overline{\mathcal{J}}_\odot$ becomes:

$$(2-2p)g + mh = m\sigma + 2(1-p-m)\xi\,.$$

The next step consists in eliminating the non resonant angles from the Hamiltonian. In other words, we select in the sum (2.3) only terms either free of angular variables or containing only the resonant angle σ:

$$\overline{\overline{\mathcal{J}}}_\odot = -\mu_\odot \frac{a^2}{a_\odot^3} \mathcal{H}_{2,1,0}(e_\odot) \left[\bar{\mathcal{F}}_{2,0,1}(i) \bar{\mathcal{F}}_{2,0,1}(\epsilon) \mathcal{G}_{2,1,0}(e) + \bar{\mathcal{F}}_{2,1,0}(i) \bar{\mathcal{F}}_{2,1,1}(\epsilon) \mathcal{G}_{2,0,-2}(e) \cos(\sigma) \right]. \tag{2.7}$$

In the general case, the new Hamiltonian can be decomposed as

$$\overline{\overline{\mathcal{J}}} = \overline{\overline{\mathcal{J}}}(\sigma, \Sigma, \Xi; L) = \overline{\overline{\mathcal{J}}}_{\rm Kep} + \overline{\overline{\mathcal{J}}}_{J_2,\rm sec} + \overline{\overline{\mathcal{J}}}_{\odot,\rm sec} + \overline{\overline{\mathcal{J}}}_{\odot,\rm res}\,; \tag{2.8}$$

where $\overline{\overline{\mathcal{J}}}_{\rm Kep}(L) = \overline{\mathcal{J}}_{\rm Kep} = \mathcal{J}_{\rm Kep}$ and $\overline{\overline{\mathcal{J}}}_{J_2,\rm sec}(\Sigma, \Xi; L) = \overline{\mathcal{J}}_{J_2}$; we have split the perturbation due to the Sun into a secular part $\overline{\overline{\mathcal{J}}}_{\odot,\rm res}(\Sigma, \Xi; L)$, free of angular variables, and a resonant part $\overline{\overline{\mathcal{J}}}_{\odot,\rm res}(\sigma, \Sigma, \Xi; L)$.

3 Study of the resonance 2:1

The main idea of this section is to study the properties of a resonance by means of the study of the equilibrium points of the Hamiltonian system in the new canonical variables $(\sigma, \xi, \Sigma, \Xi)$.

After performing the averaging and the change of coordinates described in the previous section, we will now study the new Hamiltonian, labelled $\mathcal{K}$, function of the new canonical variables $(\sigma, \xi, \Sigma, \Xi)$, given by

$$\mathcal{K} = \mathcal{K}(\sigma, \xi, \Sigma, \Xi) = \mathcal{K}_{\rm Kep} + \mathcal{K}_{J_2,\rm sec} + \mathcal{K}_{\odot,\rm sec} + \mathcal{K}_{\odot,\rm res}\,. \tag{3.1}$$

The equations of motion associated to this Hamiltonian system are:

$$\dot{\sigma} = \frac{\partial \mathcal{K}}{\partial \Sigma}\,, \quad \dot{\Sigma} = -\frac{\partial \mathcal{K}}{\partial \sigma}\,, \tag{3.2}$$

$$\dot{\xi} = \frac{\partial \mathcal{K}}{\partial \Xi}\,, \quad \dot{\Xi} = -\frac{\partial \mathcal{K}}{\partial \xi}\,. \tag{3.3}$$

Since the Hamiltonian does not depend on ξ, the action Ξ is constant and the value and time evolution of ξ are irrelevant, we take into account only the equations (3.2) that, in view of (3.1), are now:

$$\dot{\sigma} = \frac{\partial \mathcal{K}_{J_2}}{\partial \Sigma} + \frac{\partial \mathcal{K}_{\odot,\rm sec}}{\partial \Sigma} + \frac{\partial \mathcal{K}_{\odot,\rm res}}{\partial \Sigma}\,, \qquad \dot{\Sigma} = -\frac{\partial \mathcal{K}_{\odot,\rm res}}{\partial \sigma}\,, \tag{3.4}$$

with Ξ becoming a parameter set by the initial conditions.

It can be shown that the system (3.4) takes the form

$$\dot{\sigma} = A(a, e, i) + B(a, e, i)\cos\sigma\,, \qquad \dot{\Sigma} = e^2 C(a, e, i)\sin\sigma\,. \tag{3.5}$$

In particular, A is such that $A(a, e, i) = f(a, e)P(\cos i; a, e)$, where $P(\cos i; a, e)$ is a polynomial of degree 2 in $\cos i$ (with coefficients dependent on eccentricity and semimajor axis) admitting two roots $i_1^* \approx 56$ and $i_2^* \approx 110$ for each fixed couple of parameters a, e.

Looking for the equilibrium points means to solve

$$\dot{\sigma} = 0, \qquad \dot{\Sigma} = 0\,; \tag{3.6}$$

note that in oder to have $\dot{\Sigma} = 0$ we have three possibilities.

- $e = 0$: since $B \sim O(e)$, the equation $\dot{\sigma} = 0$ reduces to

  $$A(a, 0, i) = 0$$

  that admits the two aforementioned solutions (or resonant inclinations) i_1^* and i_2^*. Note that these are equilibrium points regardeless to the value of σ.

- If $\sin\sigma = 0$, or equivalently $\sigma = 0$ or π, the first equation reduces to

  $$A(a, e, i) \pm B(a, e, i) = 0\,; \tag{3.7}$$

  for fixed a and e, this gives resonant inclinations i_1^{**} and i_2^{**}. Since the amplitude of the resonant Sun perturbation (related to the function B) is small, i_1^{**} and i_2^{**} are just slightly displaced w.r.t. the resonant inclinations i_1^* and i_2^* of the previus case. To resume, we have four equilibrium points,

  $$\sigma = 0 \text{ or } \pi \qquad \text{and} \qquad i = i_1^{**} \text{ or } 1_2^{**}$$

  and we can show numerically, plotting the phase portraits (figures 1 and 2), that the points such that $\sigma^* = 0$ are two stable points (centers) and $\sigma^* = \pi$ are two unstable points (seddles).

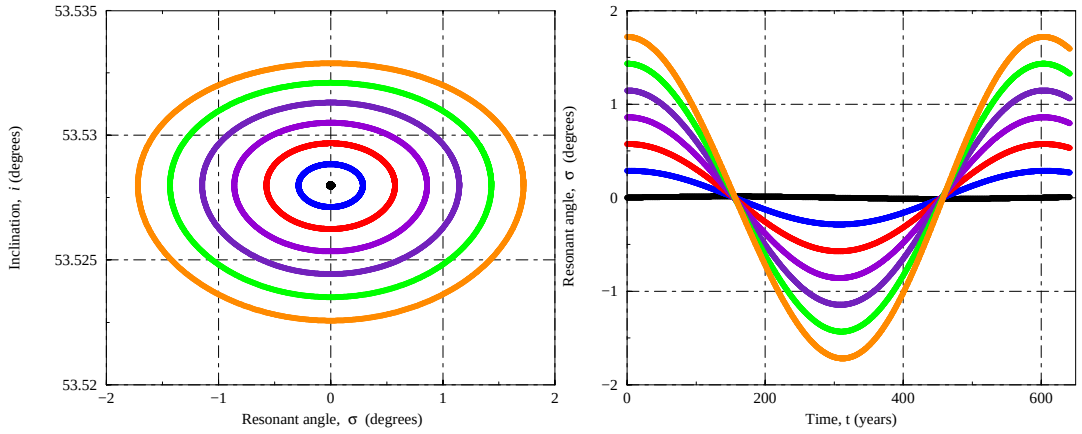

Fig. 1. Initial eccentricicty $e_0 = 0.1$. **Left:** Phase portrait in a neighborhood of one of the centres, $(\sigma, i) = (0, i_1^{**})$. **Right:** Time evolution of the resonant angle for seven orbits with initial conditions in a right neighbourhood of the centre point.

- Finally, if $i = 0$ or π we have $C(a, e, i) = 0$ and the first equation is satisfied if

  $$\sigma = \pm \arccos \frac{A(a, e, i = 0)}{B(a, e, i = 0)}$$

  and the same for $i = \pi$. The stability of this class of equilibrium point will be investigated in a future work.

4 Conclusions

The aim of this work is to understand the effects of lunisolar resonances on the stability of Medium Earth Orbits over long periods (of the order of more centuries). The source of resonance is the presence of a third massive body, which can be the Sun or the Moon; this kind of resonance is due to combinations of frequencies of the satellite and of the third body.

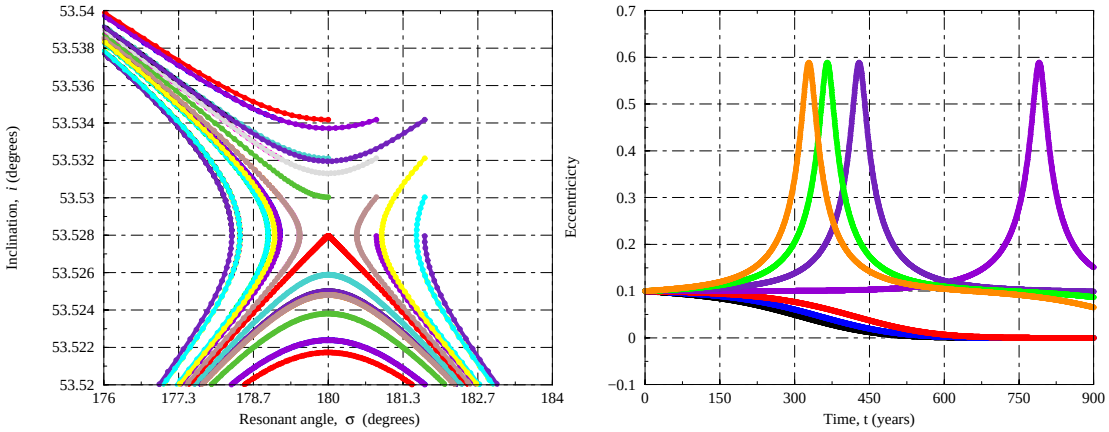

Fig. 2. Initial eccentricicty $e_0 = 0.1$. **Left:** Phase portrait in a neighborhood of the seddle point $(\sigma, i) = (\pi, i_1^{**})$. **Right:** Time evolution of the eccentricity for seven orbits with initial conditions in a neighbourhood of the seddle point.

On the other hand, the orbit of the satellite, and thus its frequencies, is affected by many perturbations: mainly from the Earth's gravity potential, but also, at intermediate altitudes, by the potential of the third body itself; in this work we considered the Sun. Thus, beside the Earth oblateness, our model includes the secular terms of the third body potential and a resonant perturbation related to a selected resonance, $2\omega + \Omega$. This seems to be among the most important lunisolar resonances and the associated resonant inclination is very close to the operational inclinations of the Galileo orbits.

We combined an analytical approach (especially in the case taking into account only the J_2 secular effect and the case of circular orbits) with direct numerical integrations.

The analytical approach, making use of an Hamiltonian model, allowed to study in detail this resonance, looking at the (linearized) equilibrium points of the averaged systems. This method is quite general and could be also extended to other resonances in the future. This allowed to charachterize the stabilty of equilibrium points for the simplest case (only J_2 secular effect) and ensure that, when adding the Sun perturbation, the equilibrium points are just slightly displaced. The numerical integration of the model states that the equilibrium points preserve their stability character and allows to study the time evolution of the other orbital elements of resonant orbits; in particular, the perspective is to focus on the behaviour of the eccentricity, which is of fundamental importance to ensure that orbital crossings do not occur.

LS is grateful to the French space agency (CNES) for her postdoctoral fellowship.

References

Allan, R.R., 1965, Proc. R. Soc. Lond. A., **288**, 60.
Breiter, S., 1999, Celestial Mechanics and Dynamical Astronomy, **74**, 253.
Breiter, S., 2001, Celestial Mechanics and Dynamical Astronomy, **81**, 81.
Brouwer, D., 1959 Astron. J., **64**, 378.
Hughes, S. 1980 Proc. R. Soc. Lond. A., 243.
Hughes, S. 1981, Proc. R. Soc. Lond. A., **375**, 379.
Kaula, W. 1966, Blaisdell Publishing Company.
Rossi, A. 2008, Celestial Mechanics and Dynamical Astronomy, **100**, 267.
Stefanelli, L., 2012, Proceedings of the 64^{th} IAC.

Session 08

Atelier général du PNPS

SF2A 2013
L. Cambrésy, F. Martins, E. Nuss and A. Palacios (eds)

LASER EXPERIMENT TO STUDY RADIATIVE SHOCKS RELEVANT TO ASTROPHYSICS.

U. Chaulagain[1], C. Stehlé[1], J. Larour[2], M. Kozlová[3], P. Barroso[4], L. de Sá [1,5], F. Suzuki-Vidal[6], O. Acef[7], P. Auvray[2], M. Krůs[3,8], J. Dostal[3], J. Prokůpek[3,8], F. Reix[4] and A. Ciardi [1]

Abstract. We present results of recent laboratory experiments on radiative shocks in xenon at low pressure. The shocks are generated with the high energy, sub-nanosecond laser at PALS, European facility. The main diagnostic consists of instantaneous imaging of the whole shock structure using an X-ray laser at 21.2 nm. The shock timing is also analyzed with time-and-space resolved plasma self-emission using high speed diodes. The achieved shock velocities near 50 kms^{-1} are sufficient to generate a radiative shock characterized by the development of a radiative precursor.

Keywords: Radiative shocks, plasma physics, XUV laser, stellar formation, accretion processes.

1 Introduction

Radiative accretion shocks occur in different stages of stellar evolution, for instance, during stellar infancy where the stellar core accretes matter from its surroundings (Commerçon et al. 2011) or in already formed young stars (Bouvier et al. 2007). In the case of accretion shocks in young classical T Tauri stars, the gas is funneled from the circumstellar disk onto the photosphere along the magnetic field lines falling onto the star at the free fall velocity, i.e. at about 400 kms^{-1}. This generates a strong shock which has specific spectral signatures, for instance, emission in the X-ray region (Argiroffi et al. 2007).

These hypersonic accretion shocks are strongly structured by radiation. However, the regime for radiation transport depends on the location of the shock in the stellar atmosphere and may vary between optically thin and optically thick regimes. The first case occurs if the shock is formed in the low density upper chromosphere, and it is characterized by strong post shock radiative cooling. The second case occurs when the shock is formed in the deeper and denser layers of the atmosphere. In this case, the intense radiation emerging from the shock front, which is heated to very high temperature, ionizes and heats the cold upstream gas and will form an ionization wave called 'radiative precursor' (Zeldovich & Zel'dovich 2002). The complicated coupling between hydrodynamics and radiation makes these shocks precious test bench for radiative-hydrodynamic codes (González et al. 2009) and strongly motivates their experimental study.

Radiative shock experiments can be performed at high energy laser facilities (Bouquet et al. 2004; Reighard et al. 2006; Stehlé et al. 2010). A typical laser irradiance of 10^{14} Wcm^{-2} or more allows in few ns to launch radiative shocks in gas cells (Doss et al. 2009; Stehlé et al. 2010) with xenon. Optimal pressure for this purpose is a fraction of 1 bar. Hence, the achieved temperature of the shock is higher for heavier gases at a given shock

[1] LERMA, Observatoire de Paris - Université Pierre et Marie Curie - ENS - Université de Cergy Pontoise - CNRS, 5 Place J. Janssen, 92195 Meudon, FR
[2] LPP, Ecole polytechnique, UPMC, CNRS, Palaiseau, FR
[3] Institute of Physics, Prague, Czech Republic, CZ
[4] GEPI, Observatoire de Paris, University Paris Diderot, CNRS, Paris, FR
[5] Laboratoire AIM, CEA/DSM/IRFU/SAp - CNRS - UniversitÃl' Paris Diderot, Orme des Merisiers, 91191 Gif-sur-Yvette, FR
[6] Imperial College, London, UK
[7] SYRTE, Observatoire de Paris, UPMC, CNRS, LNE, Paris, FR
[8] Czech Technical University in Prague, FNSPE, Czech Republic, CZ

velocity determined by the laser intensity. Nevertheless, many aspects of these experiments are still not fully understood, and thus, there is a need for new diagnostics to measure and constrain some physical parameters of these shocks. Here the results of two complementary diagnostics are presented, namely, instantaneous imaging at a wavelength of 21.2 nm (hereafter called 'XUV' imaging) of the whole shock structure and a measurement of the shock velocity using fast diodes. The present results confirm and strongly improve the quality of the results obtained from the previous proof of principle experimental campaigns (Stehlé et al. (2012a,b)).

2 Experimental Setup and Diagnostics

The experiments were performed at the Prague Asterix Laser System (PALS). This facility can deliver up to 1 kJ of energy at a wavelength of 1.315 µm, a pulse duration of 0.35 ns and a repetition rate of 2 shots/hr (Jungwirth et al. 2001). The PALS laser beam was split into two beams during the experiments: AUX & MAIN .

The AUX beam (with an energy of 60 J and pulse duration of 0.35 ns) was used to drive a shock by focusing the beam to a diameter of 300 µm on a piston attached to a miniaturized shock 'tube', positioned inside a vacuum chamber. The AUX beam achieved nominal irradiance of 2 $\times 10^{14}$ Wcm^{-2} on the target. The MAIN beam (energy of 500 J and pulse duration of 0.35 ns) was focused on a zinc planar target located in a separate vacuum chamber. An X-ray laser (XRL, 3 mJ, 0.2 ns) with a wavelength of 21.2 nm is created by the sequence of strong MAIN and weak pre-pulse beams, typical energy ratio between them is 10^3 (Rus et al. 2002). This X-ray laser was used as an instantaneous side-on back-lighter of the shock wave with a fixed delay of 20 ns respect to the AUX beam. A schematic diagram of the experimental setup showing these three lasers is presented on the left in Fig. (1).

The targets consisted of squared channel with typical length of 6 mm and cross-section of (0.4×0.4 mm^2). The targets were filled *in situ* with xenon at a pressure of 0.3 bar corresponding to a density of 1.5 $\times$ 10^{-3} gcm^{-3} at room temperature. The tube is closed on the one end by the piston, a double layer consisting of a polystyrene foil (10 µm thick) with a gold (0.5 µm) coating. The ablation of the polystyrene layer by the AUX laser generates a shock in the gas by rocket effect. The gold layer aims at blocking the X-rays generated by the interaction between the driving laser and the polystyrene. The shock tube is closed laterally by two membranes made of silicon nitride (Si_3N_4) each having a thickness of 100 nm and placed inside a silicon frame. These membranes have a transmission of 13 % at 21.2 nm, i.e. sufficient to allow probing with the XRL beam (Henke et al. 1993).

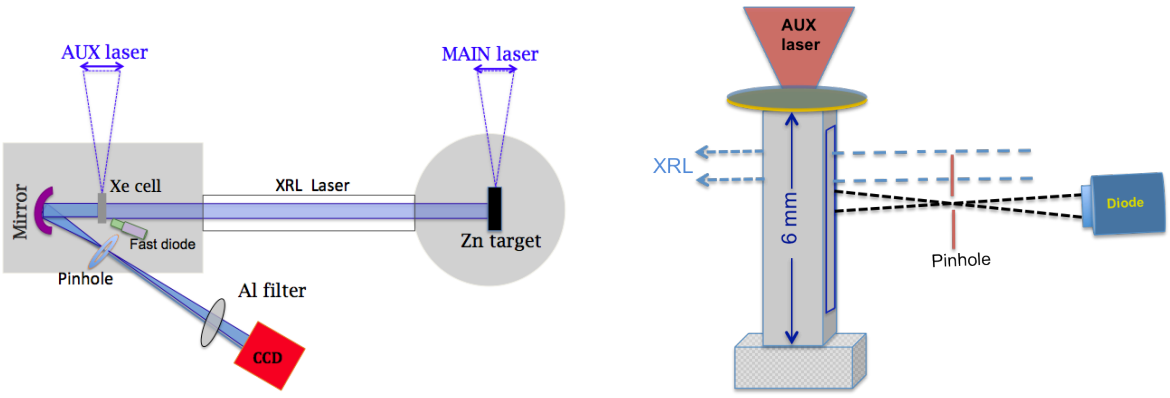

Fig. 1: *Schematic experimental setup with three lasers and XRL imaging (**left**), and side view of high-speed diode diagnostics (**right**). The diode provides 1 mm^2 Silicon detector. The distance between pinhole to Si_3N_4 window of shock tube is 7.7 mm and pinhole to detector is 6.8 mm. The axis between diode diagnostics is in plane perpendicular to the axis of the target and makes an angle of 30 degrees with XRL beam. The diode looks through the small section of the window, located at about 1.8 mm from the piston.*

The XRL beam passes through the shock tube reaching afterwards a spherical XUV mirror (focal length of 300 mm and diameter of 25.4 mm) which focuses the beam into an iron pinhole (diameter = 500 µm). This pinhole blocks the plasma self-emission by reducing the numerical aperture of the imaging system. This also

efficiently reduces the aberrations of the spherical mirror with non-normal incidence. Finally, the XRL beam reaches the cooled CCD filtered with a 10 µm thick aluminium foil which blocks the parasitic visible light (see Fig. 1 on the left). The target is projected with a magnification of 4.8 (Stehlé et al. 2012c; Chaulagain et al. 2012). Since the wavelength of the XRL beam is small compared to the aperture of the optics and the object, any diffraction effects due to the illumination of the object by the XRL beam have a negligible impact on spatial resolution.

The size and alignment of laser focal spot which drives the shock is an important parameter, as it can directly affect the dynamics and symmetry of the shock inside the tube during the experiments. In order to characterise the position and size of the laser spot, the AUX laser, attenuated by 10% gray filter, was also shot onto solid aluminium targets mimicking the experimental targets. The X-ray radiation emitted from the interaction was monitored by a keV pinhole camera. The crater size generated from the laser-target interaction insured a good level of alignment on target (Chaulagain et al. 2012). From these measurements, the laser spot size during the experiments is expected to be about 300 µm.

Silicon diodes were used to record the time-dependent self-emission from the plasma at a fixed position along the shock tube, and thus, estimate the shock velocity (see on the right in Fig. 1). The diodes were located side-on from the shock tube and tilted at an angle of 30 degrees, in order to not block the line of sight of the XRL beam. The diodes had a detection area of 1 mm^2 and a response time of 1 ns, and were positioned at about 14.5 mm from the axis of the shock channel. A tungsten pinhole with a diameter of 200 µm provided spatial resolution and was located at a distance of 6.8 mm from the shock channel. Lastly the diode had an integrated aluminium filter coating in order to record the self emission from the shock in XUV region.

3 Results

3.1 XUV imaging of the shock with XRL laser

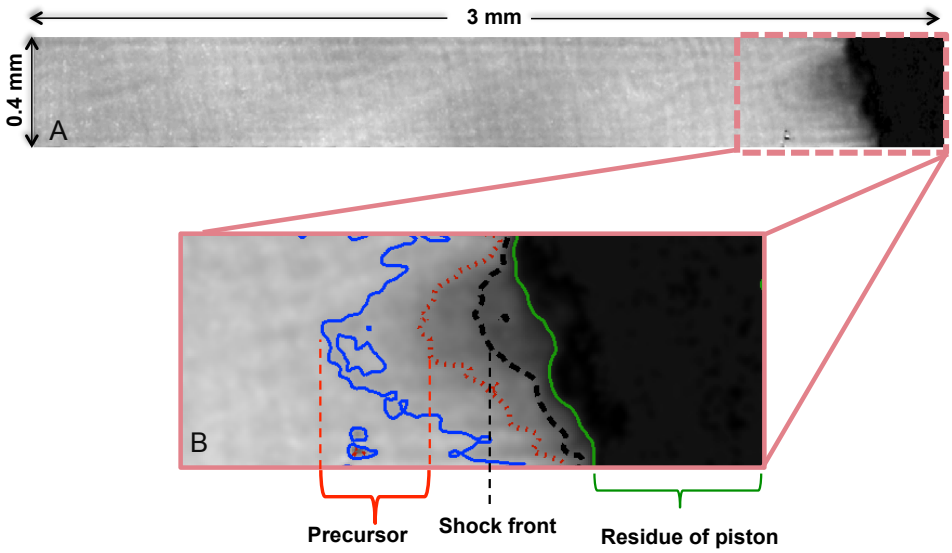

Fig. 2: *A) Snapshot of the shock probed by the XRL laser at 21.2 nm. The imaging laser arrives 20 ns after the shock driving laser. The shock is moving from right to left. B) The enlarged radiograph through Si_3N_4 windows where different parts of shocks are identified.*

In previous experiments (for instance (Bouquet et al. 2004; Stehlé et al. 2010)) visible interferometry demonstrated the presence of a radiative precursor with electron densities of 10^{18} - 10^{19} cm^{-3}. However, due to high electron density, the plasma in the shock front is opaque to visible light as well as the post shock is opaque to visible probing. At the probing wavelength of the XRL beam of 21.2 nm, the critical electron density of the plasma n_c (2.5×10^{24} cm^{-3}) is few hundreds times higher than the visible one, and thus, by using the XRL beam it is possible to probe these shock conditions. Another advantage of using the XRL beam is the instantaneous

imaging of the whole shock structure and the reduction of blurring effects due to refraction. However, residual blurring ($\sim$ 10 - 12 µm) may still be present due to the plasma motion at a velocity of 50-60 kms^{-1} during the short time ($\sim$0.2 ns) of the XRL beam.

Results from XRL probing the shock at 20 ns after its launching are reported in Fig. 2. The driving laser is coming from the right of the Fig. 2. The different parts of the shock are highlighted, with the help of color iso-contours, in Fig. 2B. The contours are normalized to maximum value of the signal after image processing. The darkest zone of the right side of the Fig. 2B corresponds to the residue of piston which is represented by green contour with normalized signal value of 0.2. The post shock and precursor regions are separated by black and blue color contour with normalized value of 0.4, and 0.8, respectively.

The shock front can be seen at a distance of about 400 µm from the right edge of the window. The edge of the Si_3N_4 window is located at a distance $\sim$0.55 mm from the initial position of the piston. Thus, the shock front is located at a distance of $\sim$0.95 mm from the initial position of the piston, which gives the mean shock velocity about $\sim$48 kms^{-1}. The thickness of the shock front at this time is about 10 - 20 µm which is comparable with the crossing time of the front in the field of view during XRL back-lighting.

3.2 Shock velocity from plasma self-emission

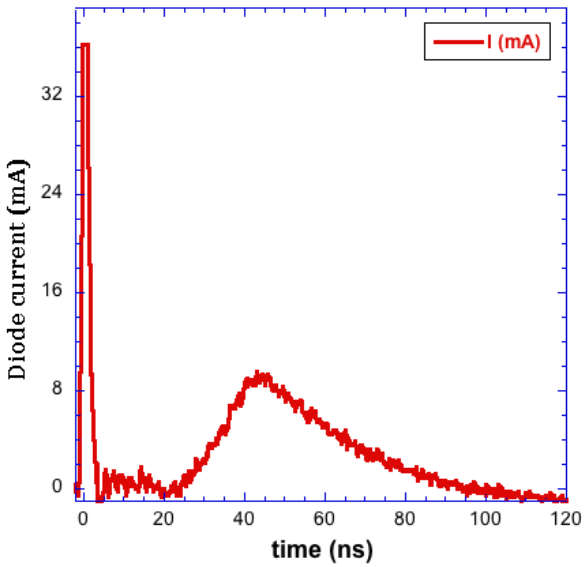

Fig. 3: *XUV signal recorded by a diode placed side on which observes the plasma emission at a distance of $\sim$ 1.8 mm from the initial position of the piston.*

Results of the plasma self-emission in the XUV recorded with high-speed diodes are shown in Fig. 3. The results show a strong peak at t = 0 ns, corresponding to the stray light emitted during the interaction of the AUX laser beam with the piston. Thus, this time can be chosen as zero, corresponding to the laser arrival on the target. The signal rises again sharply after $\sim$ 25 ns and starts peak at 40 ns and then decreases slowly. This is consistent with the dynamics of shock front and post shock in the field of view of the diode. Thus the mean shock velocity at this position can be deduced from peak timing to $\sim$ 45 kms^{-1}, which is comparable with the measurement from XUV imaging at earlier time with the XRL beam.

4 Conclusions

We presented the results of a new experimental study of laser-generated radiative shocks focusing on two diagnostics: XUV instantaneous imaging at 21.2 nm and time and space resolved plasma self-emission using fast diodes. The results obtained from both diagnostics are consistent with each other indicating the shock velocity about 45 kms^{-1} which means upstream Mach number of about 250 (for the initial gas conditions at room temperature)(Drake 2006). The experiments show that the XRL probing is a promising tool to probe shock waves in general. The improvement in the quality of the imaging setup compared to the previous experiment (Stehlé et al. 2012b) enhanced the quality of image and allows to identify shock front without any ambiguity. A more detailed description of the shock parameters will be a subject of future experiments and publications.

The project has been funded by Observatoire de Paris, PNPS, UPMC, ANR-08-BLAN-0263-07 and LASERLAB access program. The authors acknowledge the contribution of the PALS technical staff, the target fabrication group of Observatoire de Paris, V. Petitbon (IPN) for the polystyrene manufacturing, F. Delmotte and E. Meltchakov for the XUV mirror fabrication. J. Prokůpek and M. Krůs acknowledge ELI: Extreme Light Infrastructure - project no. CZ.1.05/1.1.00/02.0061 and OPVK - project no. CZ.1.07/2.3.00/30.0057.

References

Argiroffi, C., Maggio, A., & Peres, G. 2007, arXiv preprint astro-ph/0701765

Bouquet, S., Stehlé, C., Koenig, M., et al. 2004, Physical review letters, 92, 225001

Bouvier, J., Alencar, S. H. P., Boutelier, T., et al. 2007, A&A, 463, 1017

Chaulagain, U., Stehlé, C., de Sá, L., et al. 2012, in SF2A-2012: Proceedings of the Annual meeting of the French Society of Astronomy and Astrophysics, Vol. 1, 305–307

Commerçon, B., Audit, E., Chabrier, G., & Chièze, J.-P. 2011, Astronomy & Astrophysics, 530

Doss, F., Robey, H., Drake, R., & Kuranz, C. 2009, Physics of Plasmas, 16, 112705

Drake, R. P. 2006, High-energy-density physics: fundamentals, inertial fusion, and experimental astrophysics (Springer), pg.113

González, M., Audit, E., & Stehlé, C. 2009, arXiv preprint arXiv:0902.1645

Henke, B., Gullikson, E., & Davis, J. 1993, Atomic Data and Nuclear Data Tables, 54, 181

Jungwirth, K., Cejnarova, A., Juha, L., et al. 2001, Physics of Plasmas, 8, 2495

Reighard, A., Drake, R., Dannenberg, K., et al. 2006, Physics of Plasmas, 13, 082901

Rus, B., Mocek, T., Präg, A., et al. 2002, in AIP Conference Proceedings, Vol. 641, 182

Stehlé, C., Champion, N., Delattre, P., et al. 2012a, EAS Publications Series, 58, 155

Stehlé, C., González, M., Kozlova, M., et al. 2010, Laser and particle beams, 28, 253

Stehlé, C., Kozlová, M., Larour, J., et al. 2012b, Optics Communications, 285, 64

Stehlé, C., Lefevre, R., Chaulagain, U., et al. 2012c, in ICXRL conf. Proc., Vol. 130

Zeldovich, I. B. & Zel'dovich, Y. B. 2002, Physics of shock waves and high-temperature hydrodynamic phenomena (Courier Dover Publications)

SF2A 2013
L. Cambrésy, F. Martins, E. Nuss and A. Palacios (eds)

FIRST UNBIASED SPECTRAL SURVEY OF A YOUNG AND SINGLE MASSIVE PROTOSTAR: CYGX-N63

S. Fechtenbaum[2,1] and S. Bontemps[1,2]

Abstract. We present an unbiased spectral survey of a unique massive protostar in the Cygnus-X region: CygX-N63, performed with the 30m IRAM telescope. We identified 48 molecules over 106 GHz of bandwidth. Two prebiotic molecules were found: CH_2NH (methanimine) and NH_2CHO (formamide) and several rare molecules, such as CF^+ (fluoromethylidynium) or PN (phosphorous nitride). The spectral profiles and the population diagrams of the molecules allowed us to identify three emission regions in the protostar: the envelope, the outflow and a hot core-like region.

Keywords: star formation, chemistry, spectral survey, Cygnus-X

1 Introduction

The early phases of the massive star formation are poorly known. There are two main scenarios to explain the formation of massive stars (more than 8 solar masses). In the first one, a strong microturbulence allows the existence of large Jeans masses but T.Csengeri et al. (2010) found no clear evidence for such a microturbulence. They showed instead that small scale converging flows could initiate the formation of massive stars. This alternative scenario is supported by MHD simulations (B.Commerçon et al. 2011).

In this highly dynamical scenario, filaments play a key role. They are generated by large-scale magneto-hydrodynamic turbulence. Above a critical value of the mass per unit length, they fragment and form low-mass and intermediate mass stars (P.Palmeirim et al. 2013). In this view, high-mass stars could form where the filaments merge into ridges (M.Hennemann et al. 2012), leading to shocks. Therefore, the gas and possibly the grains undergo short temperature and density peaks. The chemical composition of the pre-collapse gas can be significantly modified by these variations. It is therefore crucial to explore precisely the chemical composition of young protostars, looking for signs of this early warm-up phase.

CygX-N63 was first discovered by F.Motte et al. (2007). This close object (1.4 kpc) is ideal to study the early phases of massive star formation. First, it is isolated enough to be observed alone in the beam of the IRAM 30m telescope. Secondly, it is very massive (M_{env}=$\sim$44 M$\odot$ within 2500 AU) (Duarte-Cabral et al. 2013) and not sub-fragmented, as showed by the dust emission, the molecular emission of ^{13}CS, OCS, D_2CO and CH_3CHO (seen with the PdBI in 2012, unpublished) and the presence of a powerful outflow, pointing to one single object. Thirdly, this protostar is still young, with a total luminosity of only 350 L$\odot$(Duarte-Cabral et al. 2013), which indicates that the accretion is not very strong yet. Besides, N63 is chemically very rich, suggesting that this object could be in a pre-hot core phase. We performed an unbiased spectral survey of this object to fully investigate its chemical composition. In a second part, we determined the spatial origin of the molecular emission, based on spectral profiles and population diagrams. Our main goal was to identify the molecules tracing the envelope, which contains the pristine gas at the origin of the massive stars.

2 Observations and data reduction

The unbiased spectral survey was made over 71 GHz at 1 mm and over 35 GHz at 3 mm with the IRAM-30m telescope in september 2012 and january 2013 toward CygX-N63, located at (δRA, δDec) = (20 40 05.2, 41 32 12.0) with respect to the phase center J2000. We used the wobbler switching mode.

[1] Univ. Bordeaux, LAB, UMR 5804, F-33270, Floirac, France
[2] CNRS, LAB, UMR 5804, F-33270, Floirac, France

The spectra were assembled and baseline-corrected with the GILDAS* softwares. We converted the data into main-beam temperature (T_{mb}) using the interpolated forward and main-beam efficiencies (F_{eff} and B_{eff}) given by the IRAM. The spectral resolution is 195 kHz. The analysis was performed with the help of the CASSIS† software using the CDMS, JPL and VASTEL catalogues.

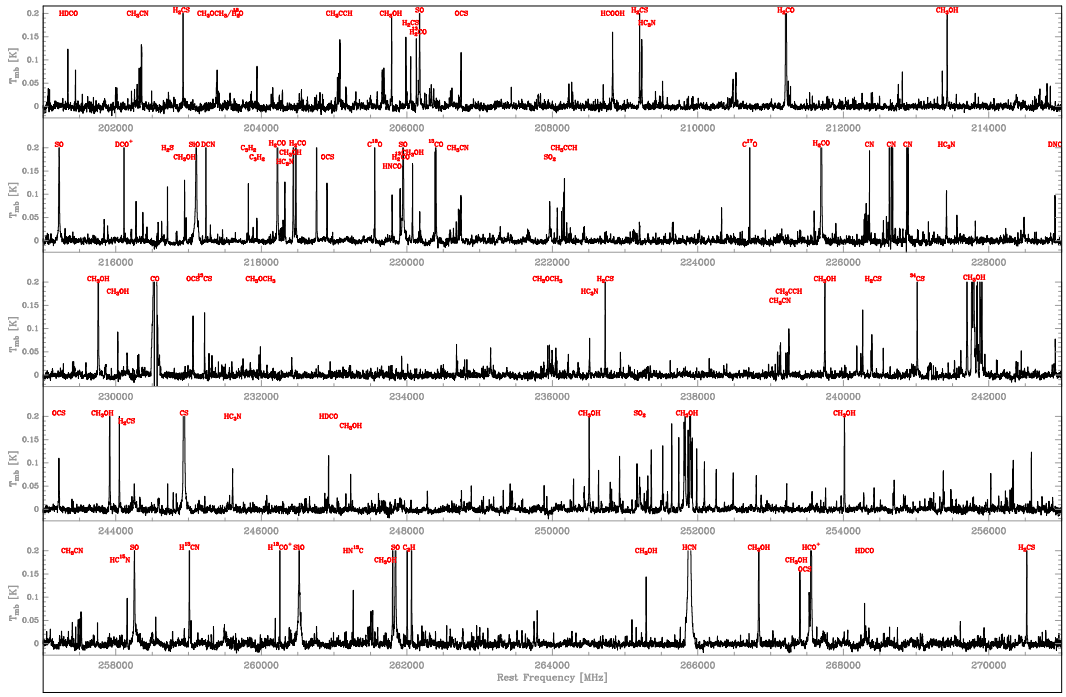

Fig. 1. Spectrum of CygX-N63 at 1mm, with some of the strongest identified lines.

3 Results

3.1 Line identification

We were able to identify $\sim$ 95% of the lines, namely 1702 identified lines. The figure 1 displays the spectrum at 1 mm. 48 molecules were found in CygX-N63, plus 35 isotopologues and 14 deuterated molecules, shown in the table 1. All families of molecules are represented: organic molecules, complex organic molecules (COMs: more than 6 atoms), N-bearing, S-bearing, carbon chains. Some rare molecules were also identified, such as the ion fluoromethyliumylidene CF^+ (see details in S.Fechtenbaum *in prep.*) or the phosphorous nitride PN. Two prebiotic molecules were also observed: the methanimine CH_2NH and the formamide NH_2CHO.

3.2 Chemical composition

We used the software CASSIS to derive the column densities and the excitation temperatures using population diagrams for the molecules for which we had at least two lines. We assumed that the local thermodynamical equilibrium (LTE) was established and that the cosmological background was negligible. For a part of the molecules, such as SO, SO_2, OCS, o-H_2CO, CS, HCO^+ or HCN, we had several isotopologues and could therefore correct the opacity effect. For the other molecules, we know that the column densities may be underestimated.

The beam dilution was taken into account. Based on previous observations of the source with the Plateau de Bure Interferometer (PdBI) at 1 mm, we chose different source size: 10" of diameter for the outflow, 1.4" for the envelope and 0.1" for the hot core-like region. The corresponding size for the hot core-like region is $\sim$ 140 AU, larger than a hot corino. Population diagrams were made by plotting $ln(N_u/g_u)$ as a function of E_u/kT_{ex}, following the relation:

*See `http:/www.iram.fr/IRAMFR/GILDAS/` for more information.
†See `http://cassis.irap.omp.eu/` for more information.

Organic molecules	CO	HCO	CH_3OH	H_2CO	H_2CCO
Complex organic molecules	CH_3OCH_3	$HCOOCH_3$	CH_3CHO	C_2H_5OH	HCOOH
CH_3COCH_3 ?	Ethylene oxide ?	Propanal ?			
Carbon chains	CCH	C_3H	C_4H	o-c-C_3H_2	p-c-C_3H_2
CH_3CCH					
N-bearing molecules	CN	HCN	HNC	HC_3N	HC_5N
C_3N	CH_3CN	C_2H_5CN	HNCO	NO	HCCNC ?
S, P and Si-bearing molecules	CS	CCS	C_3S	H_2S	H_2CS
OCS	SO	SO_2	NS	SiO	PN
Deuterated molecules	CH_2DOH	HDCS	HDCO	NH_2D	o-D_2CO
CCD	DCN	DC_3N	HDO	CH_2DCCH	C_3HD
Ions	HCO^+	$HOCO^+$	N_2H^+	DCO^+	$DOCO^+$?
N_2D^+	HCS^+	CF^+			

Table 1. Molecules detected toward CygX-N63

$$ln\frac{N_u}{g_u} = lnN_{tot} - lnQ(T_{ex}) - \frac{E_u}{kT_{ex}} \qquad with \qquad N_u = W \times \frac{8\pi k\nu^2}{hc^3 A_{ul}} \times C_{tau} \tag{3.1}$$

where N_u is the column density of the energy level u, g_u the statistical weight of this level, W the integrated area of the line and Q is the partition function[‡]. A_{ul} is the Einstein coefficient and C_{tau} the optical depth correction factor. The total column density and the excitation temperature, which is equal to the kinetic temperature if the LTE is established, are then given by CASSIS. The excitation temperatures are presented in figure 2.

To derive the column density of H_2, we used the envelope mass determined by Duarte-Cabral et al. (2013): 44 M$\odot$ within a full width at half maximum (FWHM) of 2500 AU. We took the mass contained in 1.95 σ and derived $n_{H_2} = 7.81 \times 10^{24} cm^{-2}$. We could then obtain the abundances by dividing the column densities by n_{H_2}.

3.3 Spatial origin of the molecular emission

Analyzing the spectral profiles and the rotational diagrams allowed us to find the origin of the emission for a part of the observed molecules. The spectral profiles can be divided into two groups. In the first group, the spectral profiles are well fitted by a single gaussian. The lines have a low average FWHM of (2.3 ± 0.3) km.s^{-1} and the population diagrams give an average excitation temperature of T_{ex} = (18 ± 3) K. This group contains C_4H, DC_3N, HC_5N, HDCS, $HOCO^+$, o-c-C_3H_2 and o-D_2CO. These molecules are probably tracing the envelope, where we expect such low temperature and velocity dispersion.

In the second group, the spectral profiles are better fitted with two gaussians, a narrow and a large. We plotted population diagrams for the two components separately. The features of the first component are a FWHM of (2.8 ± 0.2) km.s^{-1} and T_{ex} = (19 ± 3) K, which is very similar to the first group and therefore indicates that this narrow component may also correspond to the envelope. The large component features T_{ex} = (26 ± 3) K and a FWHM of (9.6 ± 0.5) km.s^{-1}. This group contains SiO, ^{29}SiO, SO, ^{34}SO, SO_2, HC_3N, $H^{13}CCCN$, HNCO, CCS, CH_3CN, a-CH_3CCH, e-CH_3CCH, H_2CCO, CS, CCS, OCS, o-H_2CO, HDCO, HCO^+ and HCN. CygX-N63 is known to have a powerful outflow (T.Csengeri et al. 2010) and some of these molecules, such as SiO, are recognized tracers of the outflow. We can thus infer that all molecules in this group are tracing the outflow, which is consistent with this large velocity dispersion.

On the other hand, we noticed that some molecules display population diagrams with two different slopes, which means two different excitation temperatures. It was the case for several COMs: CH_3OH, $HCOOCH_3$ and CH_3OCH_3, but also for $^{13}CH_3OH$ and CH_2DOH, which suggest that these two different temperatures are not only an effect of the opacity. The two averaged excitation temperatures are (23^{+28}_{-7}) K and (124^{+199}_{-43}) K. Note that these two components were not distinguishable in the spectral profiles, which means that they have approximately the same velocity dispersion. The two emission regions may therefore be spatially related. In addition, the COMs are known to be features of the hot core. Therefore we conclude that the cold component could correspond to the envelope or to the inner edge of the envelope and that the hot component could arise

[‡]See *Formalism for the CASSIS software on* `http://cassis.irap.omp.eu/?page=documentation`

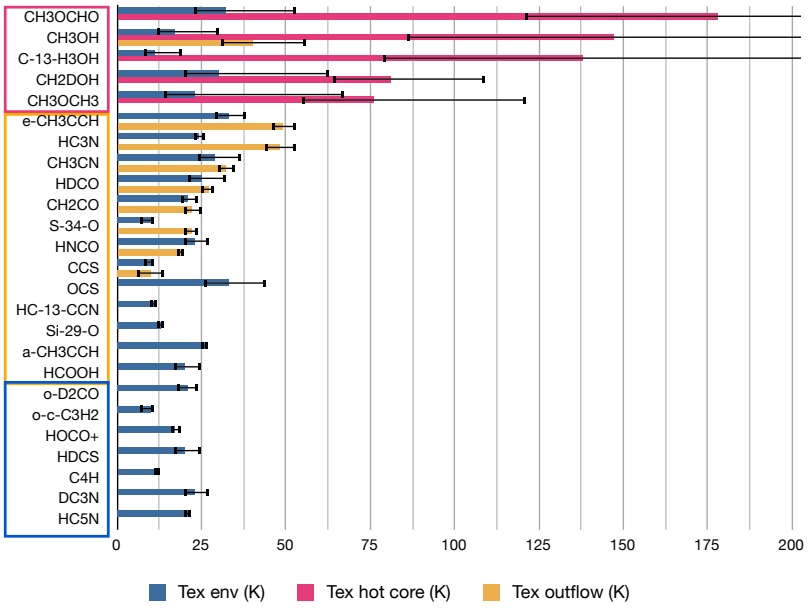

Fig. 2. Excitation temperatures derived from population diagrams. Molecules tracing the envelope are represented in blue, those tracing the outflow in yellow and those tracing the hot core-like region in pink.

from a hot core-like region. The abundances in this heated hot core-like region give a first-order idea of the composition of the grains, because a part of the ice mantle of the grains is sublimated, releasing the molecules.

The excited methanol $^*CH_3OH$ is a particular case because it displays at the same time two components in its spectral profile and two components in its rotational diagram. It traces the envelope, the hot core-like region and the outflow.

4 Conclusions

We performed a large unbiased spectral survey toward a young and massive protostellar object, revealing a very rich chemistry. Population diagrams and spectral profiles allowed us to separate the possible sources of the emission: outflow, envelope and hot core-like region. We were able to identify molecules tracing the cold envelope, which contains the pristine gas at the origin of the massive stars. The next step of our work is to compare the observed abundances, in particular in the envelope and on the grains, to the predictions given by a chemical gas-grain code called Nautilus developed in Bordeaux (U.Hincelin et al. 2013). The aim is to follow the evolution of the physical conditions in the gas which will eventually form the massive star.

References

B.Commerçon, P.Hennebelle, & T.Henning. 2011, The Astrophysical Journal Letters
Duarte-Cabral, A., S.Bontemps, F.Motte, et al. 2013, Astronomy and Astrophysics
F.Motte, S.Bontemps, P.Schilke, et al. 2007, Astronomy and Astrophysics
M.Hennemann, F.Motte, N.Schneider, et al. 2012, Astronomy and Astrophysics
P.Palmeirim, P.André, J.Kirk, et al. 2013, Astronomy and Astrophysics
T.Csengeri, S.Bontemps, N.Schneider, F.Motte, & S.Dib. 2010, Astronomy and Astrophysics
U.Hincelin, Wakelam, V., B.Commerçon, Hersant, F., & S.Guilloteau. 2013, The Astrophysical Journal

SF2A 2013
L. Cambrésy, F. Martins, E. Nuss and A. Palacios (eds)

TOWARDS 3D SIMULATIONS OF CEPHEIDS STARS

S. Félix[1], E. Audit[1] and B. Dintrans[2]

Abstract. We are using the HERACLES hydrodynamic simulation code, to construct simplified 1D and 2D simulations of the kappa-mechanism following Gastine's results obtained with the PENCIL CODE. In this proceeding, we focus on the conduction step for stable and unstable setups, in 1D and 2D with convection. We thus show that we are reproducing PENCIL CODE's results quite well.

Keywords: Cepheid, kappa-mechanism, convection, pulsations, nonlinear simulations, HERACLES

1 Introduction

Cepheids are giant stars displaying periodic variations of luminosity and radius. This phenomenon was explained by Eddington (1917) through the κ-mechanism, an excitation mechanism of stellar oscillations that is related to sharp changes of opacity in ionisation regions.

A simplified κ-mechanism model (the propagation of radial acoustic waves in a partially ionised shell in 1D and 2D cartesian boxes) has been previously investigated with the PENCIL CODE by Gastine & Dintrans (in particular, refer to Gastine & Dintrans (2008), hereafter GD2008). We intend to extend this work to 3D simulations with the hydrodynamic code HERACLES from CEA, France. First step is getting hydrodynamic equilibria and was presented in SF2A 2012 proceedings (Félix et al. (2012)).

Hydrodynamics and gravity equations are solved with an explicit scheme (second order in time & space) on a cartesian-fixed grid of physical size $l \times L$, with constant spacing Δx. In this proceeding, we will focus on the implicit conduction step of HERACLES.

2 Conduction step

In the conduction step, we are solving $c_v\,\rho\,\frac{\partial T}{\partial t} - \vec{\nabla}\cdot(\kappa\vec{\nabla}T) = 0$ where κ denotes the conductivity, T the temperature, ρ the density and c_v the heat capacity at constant volume. Temperatures are normalized to the surface temperature.

The κ-mechanism implies that opacity sharply increases in a definite region of the star envelope. In our code, this opacity bump is shaped by a radiative conductivity hollow, since opacity and conductivity are inversely proportional. The hollow is parametrized as follows:

- $T_{\rm bump}$ is its position in the temperature profile and 3 cases are investigated: $T_{\rm bump} = [1.7,\ 2.1,\ 2.8]$;
- σ is its slope, with $\sigma = 7$ as a standard value;
- $2 * e$ is its FWHM and we usually take $e = 0.4$.

Following GD2008, conductivities κ only depend on temperature and are calculated using the following formula:

$$\kappa(T) = \kappa_{\rm max}\left[1 + \mathcal{A}\frac{-\Pi/2 + \arctan(\sigma T^{+}T^{-})}{\Pi/2 + \arctan(\sigma e^2)}\right],$$

[1] Maison de la Simulation, CEA/CNRS/INRA/U-PSUD/UVSQ (USR 3441), 91191 Gif-sur-Yvette, France
[2] IRAP, CNRS/Université de Toulouse (UMR5277), 14 av. Edouard Belin, F-31400 Toulouse, France

where

$T^{\pm} = T - T_{\rm bump} \pm e$;

$\mathcal{A} = \dfrac{\kappa_{\rm max} - \kappa_{\rm min}}{\kappa_{\rm max}}$, the relative amplitude of the conductivity extrema $\kappa_{\rm max}$ and $\kappa_{\rm min}$;

and $T_{\rm bump}$, σ and e are the already-defined hollow parameters.

2.1 Numerical scheme

HERACLES uses a finite-volume Godunov method. The timestep dt is therefore limited by stability conditions imposing that $\mathrm{dt} \leqslant \min(\mathrm{dt}_{\rm hydro}, \mathrm{dt}_{\rm gravity}, \mathrm{dt}_{\rm radiative\ diffusion}) \leqslant \mathrm{dt}_{\rm radiative\ diffusion}$. Typical dt in that case are $\mathrm{dt} \simeq 10^{-6}$. It leads to lengthy wall times and an implicit scheme has been implemented for the conduction step. As a consequence, the dynamics of the simulation becomes only constrained by the speed of sound and typical dt are now $\mathrm{dt} \simeq 10^{-3}$. This implicit scheme can be used at the first or second order and a simple input parameter allows to switch between both accuracies. Finally, in our simulations, opacities may be given either in an explicit or implicit form.

2.2 Growth rates

The hydrodynamic equilibrium with conduction is perturbed on velocity by the eigenfunctions of the unstable fundamental mode. These eigenfunctions were calculated by GD2008 for our three cases $T_{\rm bump} = [1.7,\ 2.1,\ 2.8]$ and are shown in Figure 1.

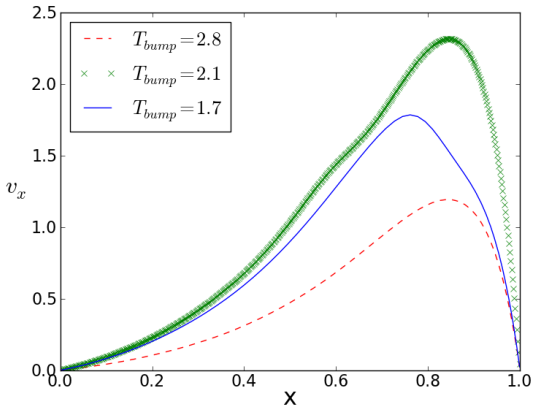

Fig. 1: Eigenfunctions of the unstable fundamental mode (real part of velocity) for $T_{\rm bump} = 1.7$ (solid line), $T_{\rm bump} = 2.1$ (crossed line) and $T_{\rm bump} = 2.8$ (dashed line). Calculations were made by GD2008.

$T_{\rm bump}$	n_x	τ
1.7	512	-2.63×10^{-2}
2.1	512	$+1.97 \times 10^{-2}$
2.8	512	-2.14×10^{-2}

Table 1: Growth rates τ of the mean vertical momentum $< \rho u_x >$ for different setups: $T_{\rm bump}$ is the position of the hollow in the temperature profile and n_x is the number of points along the gravity-directed x-axis of our simulation box.

We then studied the temporal evolution of the mean vertical momentum $< \rho u_x >$ (averaged over the box) and calculated its growth rate τ during the linear phase ($t \lesssim 50$). Results are summarized in Table 1, while Figure 2 shows the corresponding evolutions with time.

Only one setup (hollow with $T_{bump} = 2.1$, green line on Figure 2) is unstable with a positive growth rate. This corresponds to the instability conditions in which the κ-mechanism is efficient, given by GD2008:

1. the hollow has a sufficient slope: $\dfrac{d\kappa_{\rm T}}{dx} < 0$ where $\kappa_{\rm T} = \dfrac{\partial \ln \kappa}{\partial \ln T}$.
2. the instability zone is well located: $\psi = \dfrac{< c_v T_{\rm transition} > \Delta m}{PL} \approx 1$, with P the acoustic mode period and L the luminosity.

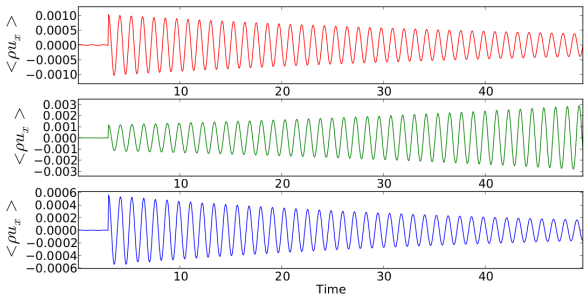

Fig. 2: Temporal evolution of the mean vertical momentum $< \rho u_x >$ for $T_{\rm bump} = 2.8$ (**Upper panel**), $T_{\rm bump} = 2.1$ (**Middle panel**) and $T_{\rm bump} = 1.7$ (**Lower panel**). The perturbation in velocity is added at $t = 3$.

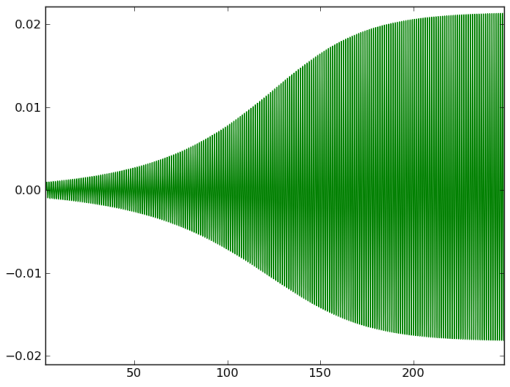

Fig. 3: Temporal evolution of the mean vertical momentum $< \rho u_x >$ for $T_{\rm bump} = 2.1$.

With these criteria, the other two setups ($T_{\rm bump} = 1.7$ and $T_{\rm bump} = 2.8$) are stable because the instability zone is respectively too close or too far from the surface to maintain instability. This shows on Table 1 since $\tau < 0$ for both cases.

One oscillation takes approximatively 1.15 units of time (43 oscillations in a bit less than 50 units of time), which corresponds quite well to what GD2008 got with the PENCIL CODE.

2.3 Nonlinear saturation

Unstable simulations with the initial setup $T_{\rm bump} = 2.1$ keep a positive growth rate until they reach their nonlinear limit-cycle stability, where the mean vertical momentum oscillates between two definite values (see the final plateau at late times in Figure 3). It occurs around $t \approx 200$, which agrees well with the characteristic timescale of instability given by $1/\tau \approx 100$. The dynamics and values of this saturation are also compatible with GD2008's results.

3 Cepheids in 2D

Now that hydrodynamic, gravity and conduction steps are available and accurate, we can go further on to 2D simulations. We choose new setups known to trigger convection (Gastine & Dintrans (2011), hereafter GD2011). As we aim at studying convection-pulsation coupling, conductivity profiles are now shaped such that the temperature gradient becomes superadiabatic around the conductivity hollow and convection may develop there (the so-called Schwarzschild's criterion).

We focused on profiles named G6 and G8 in GD2011 that proved to be the more relevant ones. Figure 4 is similar to Figure 3 in GD2008 but for both G6 and G8 simulations. It shows the conductivity (with the hollow), temperature, density and $d\kappa_{\rm T}/dx$ profiles for these two setups. On the latest, we see that these simulations are set in order to fulfill the first instability condition around the hollow. Convection is indeed triggered as we do observe convection plumes in Figure 6.

Temporal evolution of the mean vertical momentum $< \rho u_x >$ for these two setups (Figure 5) shows that the G6 one is stable while the G8 one is unstable, as GD2011 predicted.

Please note that high resolution simulations are mandatory to properly represent the instability. Numerically speaking, to save computational time and cost, we are doing this conduction step once every ten steps without altering the behaviours or results.

4 Conclusions

With HERACLES, we managed to reproduce GD2008's results (obtained with PENCIL CODE) quite well concerning 1D hydrodynamical simulations with conduction. These simulations show oscillations of the mean vertical

momentum $< \rho u_x >$, leading to a nonlinear saturation for the unstable setup. 2D simulations trigger convection and show a stable or unstable behaviour depending on the initial setup, accordingly to GD2008's and GD2011's results. Finally, we started long-awaited 3D simulations of this convection-pulsations interaction and will present our results in a forthcoming paper.

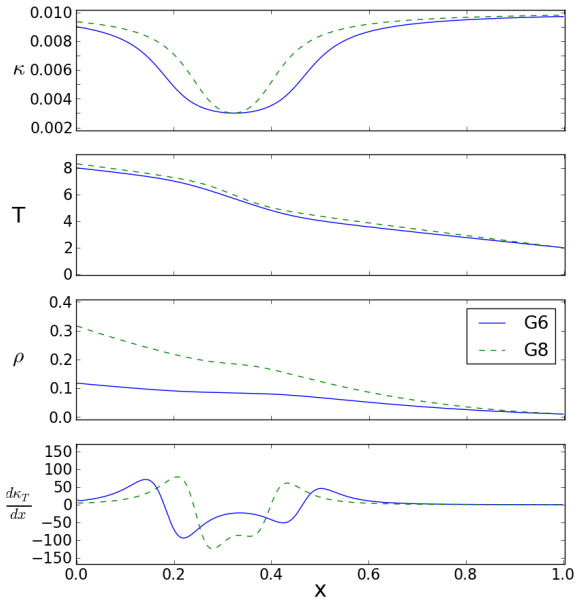

Fig. 4: Conductivity (**Upper panel**), temperature (**Second panel**), density (**Third panel**) and $\frac{d\kappa_T}{dx}$ (**Lower panel**) profiles for G6 and G8 simulations.

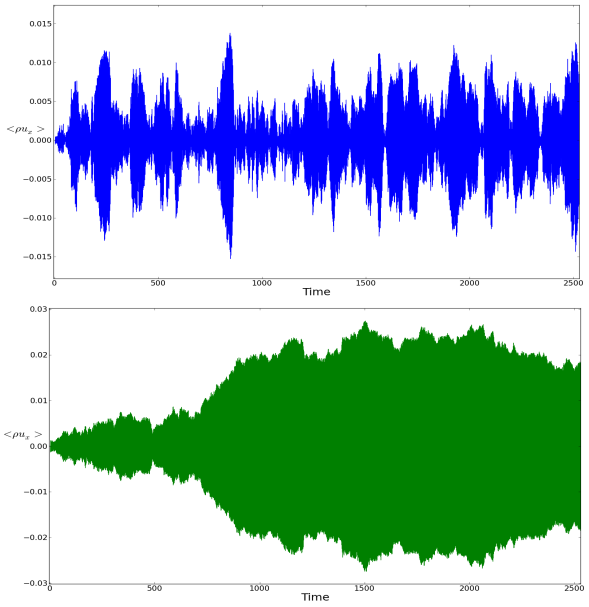

Fig. 5: Temporal evolution of the mean vertical momentum $< \rho u_x >$ for setups G6 (**Upper panel**) and G8 (**Lower panel**).

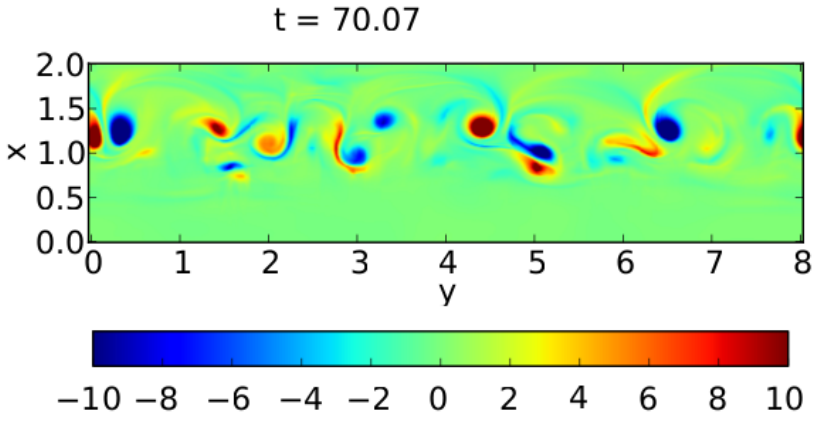

Fig. 6: Snapshot of the vorticity field $\vec{\nabla} \times \vec{u}$ in the 2D model G6 with convection and κ-mechanism.

References

Eddington, A. S. 1917, The Observatory, 40, 290

Félix, S., Audit, E., & Dintrans, B. 2012, in SF2A-2012: Proceedings of the Annual meeting of the French Society of Astronomy and Astrophysics, ed. S. Boissier, P. de Laverny, N. Nardetto, R. Samadi, D. Valls-Gabaud, & H. Wozniak, 329–332

Gastine, T. & Dintrans, B. 2008, A&A, 484, 29

Gastine, T. & Dintrans, B. 2011, A&A, 528, A6

SF2A 2013
L. Cambrésy, F. Martins, E. Nuss and A. Palacios (eds)

IMPACT OF A MAJOR MERGER IN THE LOCAL GROUP

S. Fouquet [1], F. Hammer [1,], Y. Yang [1,2], M. Puech[1] and H. Flores[1]

Abstract. The Local Group (LG) presents three exceptional features: a thick plane made by the Milky Way (MW) dwarf galaxies called the Vast Polar Structure (VPOS), another thick plane made by most of the M31 dwarf galaxies called the Vast Thin Disk of Satellite (VTDS), and two massive irregular dwarf galaxies, the Magellanic Clouds (MCs), that are anormally close to a luminous L* galaxy, the MW. Investigating from our modelling of M31 as a result of a former gas-rich major merger, we find out that these three features can be explained by this event.

Indeed, in our scenario, the major merger, which would have formed M31, would have also generated two tidal tails where tidal dwarf galaxies (TDG) could have formed. These tidal tails formed a thick plane where is included the MW. The part of the tidal tail bound to M31 matches the VTDS inclination and its dwarf galaxy positions. The part of the first tidal tail which is ejected far away M31 can interact with the MW. The simulation of this interaction can lead to a fair reproduction of the VPOS as well as to explain the MCs proximity to the MW.

However this scenario predicts that the LG dwarf spheroidals are free of dark-matter because they are remnants of TDGs. This is in apparent contradiction with their intrinsically large velocity dispersions. To be established or discarded, this scenario requires to further investigate the detailed interactions between TDGs and the MW potential.

Keywords: Local Group, major merger, tidal dwarf galaxies, VTDS, LMC, VPOS

1 Introduction

The anisotropy of the MW satellites spatial distribution had led Lynden-Bell (1976) to suggest that the MCs, Draco, Sculptor and Ursa Minor may form a stream. More recently, Kroupa et al. (2005); Metz et al. (2007, 2009) and Fouquet et al. (2012) found that the classical dwarf galaxies have their positions and orbital motions inscribed into a thick plane, named the VPOS (Pawlowski et al. 2012), which provide an important challenge for the ΛCDM cosmological simulations (Kroupa et al. 2005). Realisations of recent simulations show that the VPOS is too much thin to be reproduced (Wang et al. 2012), and this leads to a general consensus that progenitors of MW dwarves should have reached the MW in a coherent motion, either from a very compact group or from a tidal tail (Pawlowski et al. 2011). Both issues have their pros and cons, because such a compact group seems unlikely (Metz et al. 2009) or because tidal dwarf galaxie (TDGs) are dark-free in contradiction with measurements of their velocity dispersion (Walker et al. 2009).

Perhaps the above problem is related to the MCs proximity to the MW (50 kpc), which is also an enigma given the fact that no similar configuration is found in the nearby Universe. Indeed, the probability to find two massive ($> 10^8$ $M_\odot$) dwarf irregular galaxies close (< 60 kpc) to their host L* galaxies is very small (< 0.4 %, Robotham et al. 2012), and the only examples found are in groups made by two L* galaxy, such as in the LG with M31 and the MW.

More recently, a new feature arises in the Local Group. Ibata et al. (2013) have discovered that 15 dwarf galaxies in the M31 outskirts form a thick plane with a thickness of 12 kpc and a size of more than 200 kpc: the VTDS. This result is based on a statistical analysis of the 3D positions of the M31 dwarf galaxies (Conn et al. 2013). In addition to form a plane, the 15 dwarf galaxies seems to rotate within this plane (Ibata et al. 2013).

[1] Laboratoire GEPI, Observatoire de Paris, CNRS-UMR8111, Univ Paris Diderot, Sorbonne Paris Cité, 5 place Jules Janssen, 92195 Meudon France
[2] National Astronomical Observatoires, Chinese Academy of Sciences, 20A Datun Road, Chaoyang District, Beijing 100012, China

The present work investigates a new scenario linking together the formations of the VPOS, of the VTDS and the position of the MCs. Following Pawlowski et al. (2011), we suggest that the 11 classical dwarf galaxies and the 15 M31 dwarf spheroidals could be ancient TDGs. The difference with the Pawlowski et al. (2011)' scenario comes from our assumption that the TDGs are linked to the last major merger in the M31 tumultuous past history, instead of that of the MW. Our scenario investigates whether the VTDS could be the remant of the part of the tidal tails fallen back on M31, whether the VPOS could be the result of the interaction between the tidal tail linking M31 to the MW, while the exceptional MCs proximity to the MW would simply reflect the tiny probability for a tidal tail send by M31 to interact with the MW.

2 The VTDS - a remnant of tidal tail

According to Hammer et al. (2010), M31 could be the result of a gas-rich major merger (mass ratio $\sim 3 \pm 0.5 : 1$, $r_{pericenter} \sim 25 \pm 5$), with a first passage 8-9 Gyrs ago and a fusion time 5-6 Gyr ago, providing the formation of several tidal tails. The simulations show that the main tidal tail, the first one, and the second one form a thick plane due to the orbital angular momentum of the major merger. A part of these tidal tails falls back towards the remnant of the merger, M31. Therefore, they would create loops rotating around M31. Within these loops some TDGs can form overdensities which can draw the tidal tail shape. Comparison between the simulations and the observatins show that the simulated loops can match the spatial and the kinematical properties of the dwarf galaxies which form the VTDS (see Fig. 1).

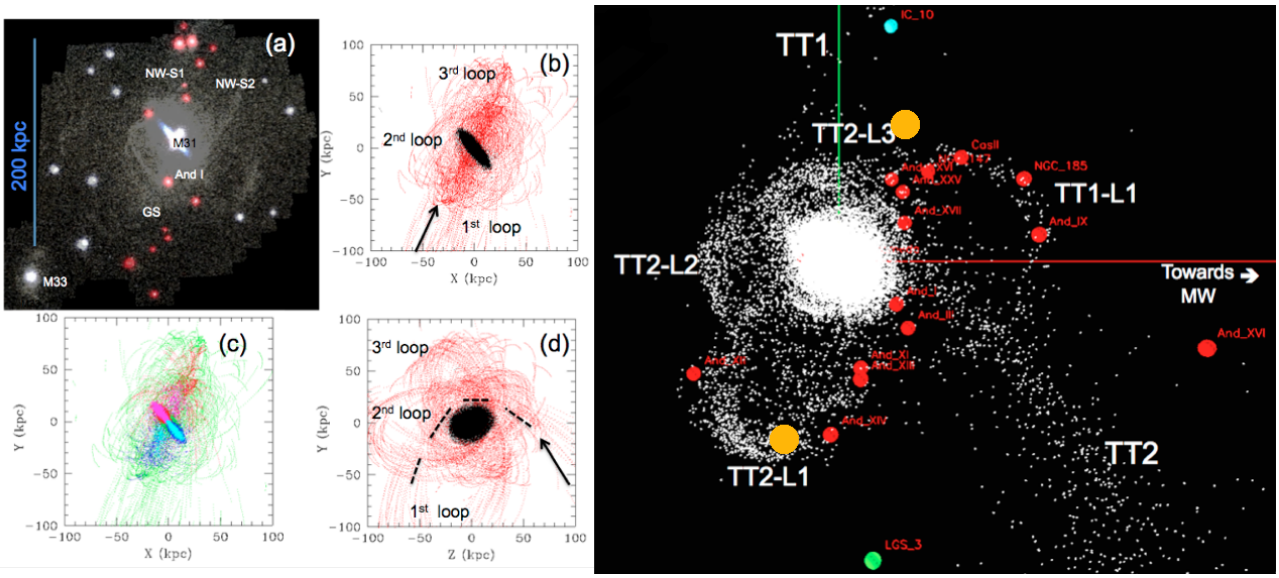

Fig. 1. *Left panels:* the four left panels compare the VTDS position (red points in the panel (a)) with the loops derived from the tidal tails (panel (b), edge-on view, panel (d), face-on view with an example of a particle trajectory represented by the dashed line). The panel (c) shows a clear bimodality in the radial velocity of the loop particles in the M31 rest-frame due to the rotation motion (upper part is redshifted, bottom part is blueshifted). This bimodality is also found in the M31 dwarf galaxies forming the VTDS (Ibata et al. (2013)). *Right panel:* a superimposition of the simulated tidal tail (white dots), which have fallen towards the M31 forming loops, and of the dwarf galaxy positions forming the VTDS (red points) Hammer et al. (2013). Note that the two orange points are new discovered dwarf galaxies which seems to belong to the VTDS. The red line represents the direction towards the MW.

3 TDGs within a tidal tail ejected by M31 towards the MW

At the present-time in the simulations of the major merger, the tidal tail generated during the first passage is presently long enough (> 1.5 Mpc) to reach the Milky Way (785 kpc from M31). However, it could have been ejected towards different directions. In fact, the angular momentum of a tidal tail in a major merger follows the orbital angular momentum which is within $\pm$ 25° to that of the remnant disk. As the M31 disk is nearly edge-on (77°) for a MW observer, the tidal tail should be in a thick plane aligned to the M31 disk and that

includes the MW. An additional constrain is provided by the Giant Stream (with an angular uncertainty of 20°) that is also reproduced by the Hammer et al. (2010) simulations. Consequently, the tidal tail should lie in a quite small solid angle representing only 5% of the 4π steradian sphere (see Fig. 2). It is quite an exceptional coincidence (Fouquet et al. 2012) that the MW also lies in this small solid angle (see Fig. 2, right panel), that strengthens the possibility of an encounter between the MW and a tidal tail originated from M31. Perhaps this is a reminiscence of the investigations of Robotham et al. (2012) in the local volume.

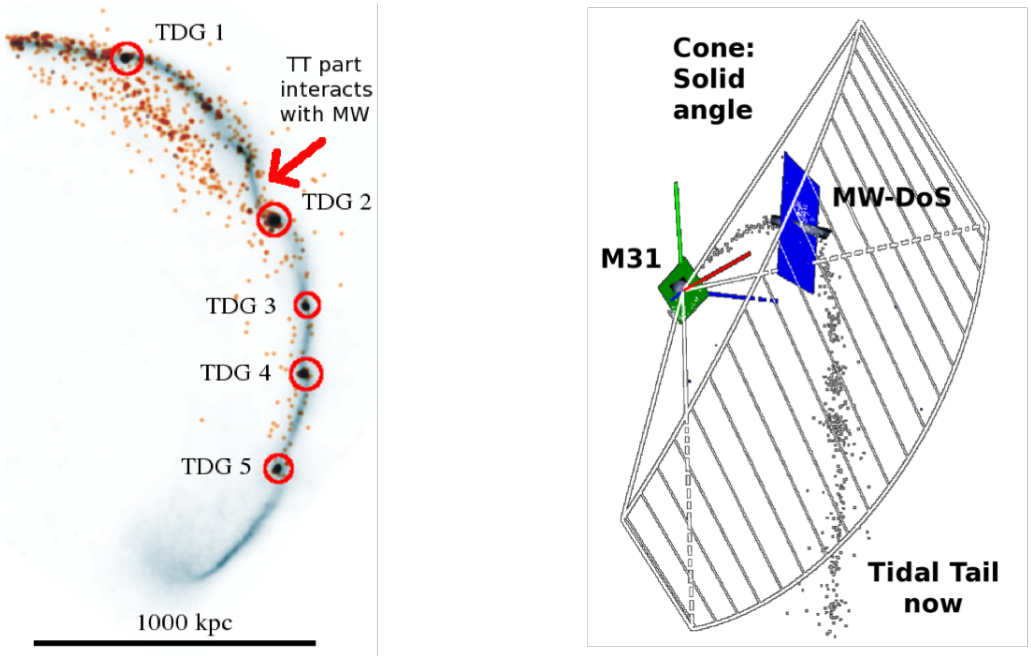

Fig. 2. *Left panel:* An example of a first tidal tail at the present-time with five formed TDGs. The blue color codes for the gas density, and the orange one for the stars. *Right panel:* The tidal tail interacting with the MW. The solid angle represents the space where the tidal tail is constrained to move (Fouquet et al. (2012)).

The left panel of Fig. 2 shows the tidal tail which could interact with the MW at the present time. It is extracted from a GADGET2 simulation for which the number of particles exceeds 2 millions. The five overdensities are TDGs resulting of gas and baryonic matter collapse due to gravitational instability and gas cooling (Wetzstein et al. 2007). Their baryonic masses are larger than 10^8 $M_\odot$ and for the most massive one (TDG 2), its mass is close to 10^9 $M_\odot$, one third of the baryonic LMC mass. The high mass of the TDG2 and its position at the center of the tidal tail and not at the top of it is apparently discrepant from the Bournaud & Duc (2006) results. This could be caused by the high fraction of gas of the progenitors galaxies ($> 60\%$) that is assumed in our study, which make easier the formation of high mass TDG formation (Wetzstein et al. 2007).

4 Reproduction of the VPOS by the MW-tidal tail encounter

From the work made by Hammer et al. (2010), we have confirmed that a tidal tail including several TDGs, could interact with the MW. Then, we have developed a simple formalism to simulate the interaction between the simulated tidal tail with a MW analytic mass profile model to verify whether or not it could reproduce the VPOS (Fouquet et al. 2012).

We have first tried to match the LMC trajectory to that of the tidal tail. We have treated the LMC case alone because its position and 3D velocity are the best known among the MW dwarf galaxies. Tracing back the LMC depends on the current position and velocity of the LMC, the MW and M31, and on their total masses (Yang & Hammer 2010). Observations let significant freedom in establishing the total mass of massive galaxies and even more for the M31 transversal motion. Here we adopt $M_{baryonic}/M_{DM} = 20\%$, instead of half this value from Yang & Hammer (2010). We derive proper motions for which the LMC trajectory and velocity match well the trajectory of the tidal tail for M31, assuming a M31 motion close to that derived by van der Marel et al. (2012).

Then, we have performed N-body simulations to investigate the encountering between the tidal tail and the MW, leading to a reasonable fit of both spatial and orbital motion distributions of the dwarf galaxies that lie in the VPOS, within the measurement uncertainties (see Fig. 3 and Fouquet et al. (2012) for the orbital motions).

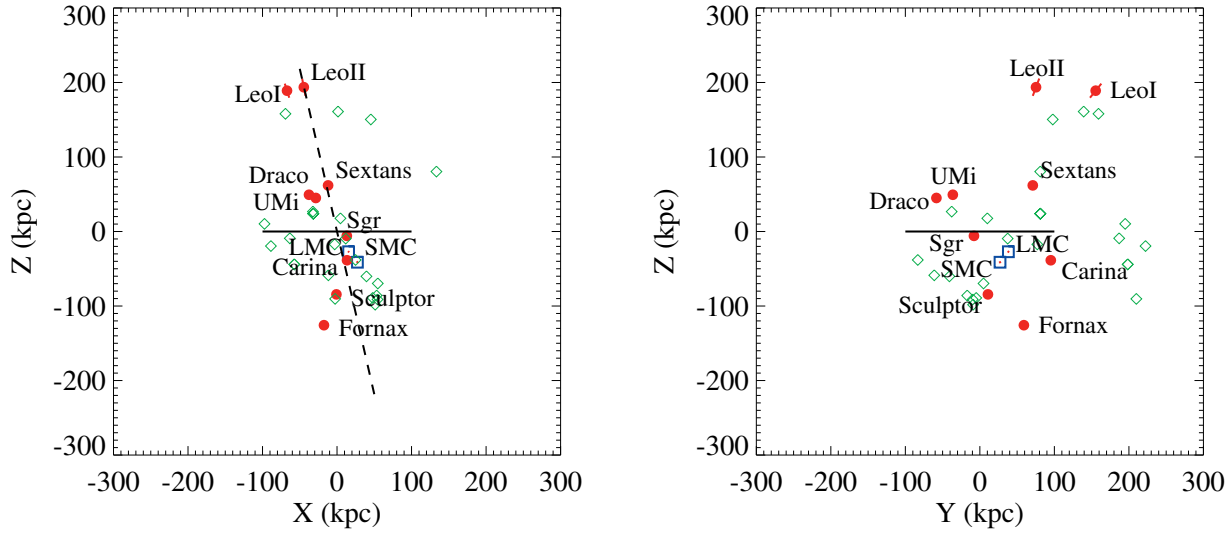

Fig. 3. Spatial distribution of the dwarf galaxies and of the simulated particles (the green diamonds). The blue squares represent the Magellanic Clouds, the red dots the dwarf spheroidals and the red lines their spatial uncertainties. On the two panels, the MW (the solide line) is viewed edge-on. *Left:* the VPOS (the dashed line) is viewed edge-on. *Right:* the VPOS is rotated from the position of the left panel by 90° along the MW disk axis.

5 Conclusion and prospectives

The suggested scenario of LG dwarf formation has the advantage to be consistent with the hierarchical model, for which a significant part of gas-rich major mergers forming disks have occured at z $\sim$ 0.4-0.8 (Hammer et al. 2009), as it could be also the case for M31. Moreover it naturally explains within a single scheme the three exceptional features in the LG, i.e., the VTDS, the VPOS and the proximity of the MCs to the MW.

However, it remains speculative with respect to the large velocity dispersions of the MW dwarf galaxies. Indeed, if they were formed in a tidal tail, they must contain a very small fraction of dark matter providing small M/L ratio, while their M/L ratio deduced from their velocity dispersions reach very large values (Walker et al. 2009). Perhaps the MW dwarf galaxies are not virialised. Indeed, former numerical studies have shown that a dwarf galaxy in interaction with its host galaxy could show apparently large M/L values if it is assumed stable whereas it is not (Kroupa 1997). In this topic, the work made by Yang et al. (2013, submit.) give some hints. Indeed, several simulations of galaxy interaction between TDGs and a MW-like galaxy are studied. It shows that the ram-pressure stripping and the tidal forces could transform in one passage a TDG, full of gas and stable, into a dwarf spheroidal, empty of gas and unstable. The residue of the TDG is in inflation with a surface brightness value which decreases providing a high mass-to-light ratio, mimicking an object full of dark matter.

References

Bournaud, F. & Duc, P.-A. 2006, A&A, 456, 481

Conn, A. R., Lewis, G. F., Ibata, R. A., et al. 2013, ApJ, 766, 120

Fouquet, S., hammer, H., Yang, Y., Puech, M., & Flores, H. 2012, MNRAS

Hammer, F., Flores, H., Puech, M., et al. 2009, A&A, 507, 1313

Hammer, F., Yang, Y., Fouquet, S., et al. 2013, MNRAS, 431, 3543
Hammer, F., Yang, Y. B., Wang, J. L., et al. 2010, ApJ, 725, 542
Ibata, R. A., Lewis, G. F., Conn, A. R., et al. 2013, Nature, 493, 62
Kroupa, P. 1997, New A, 2, 139
Kroupa, P., Theis, C., & Boily, C. M. 2005, A&A, 431, 517
Lynden-Bell, D. 1976, MNRAS, 174, 695
Metz, M., Kroupa, P., & Jerjen, H. 2007, MNRAS, 374, 1125
Metz, M., Kroupa, P., & Jerjen, H. 2009, MNRAS, 394, 2223
Pawlowski, M. S., Kroupa, P., & de Boer, K. S. 2011, A&A, 532, A118
Pawlowski, M. S., Pflamm-Altenburg, J., & Kroupa, P. 2012, MNRAS, 423, 1109
Robotham, A. S. G., Baldry, I. K., Bland-Hawthorn, J., et al. 2012, MNRAS, 424, 1448
van der Marel, R. P., Fardal, M., Besla, G., et al. 2012, ApJ, 753, 8
Walker, M. G., Mateo, M., Olszewski, E. W., et al. 2009, ApJ, 704, 1274
Wang, J., Frenk, C. S., & Cooper, A. P. 2012, ArXiv e-prints
Wetzstein, M., Naab, T., & Burkert, A. 2007, MNRAS, 375, 805
Yang, Y. & Hammer, F. 2010, ApJ, 725, L24

SF2A 2013
L. Cambrésy, F. Martins, E. Nuss and A. Palacios (eds)

THE X-SHOOTER SPECTRAL LIBRARY AND CARBON STARS

A. Gonneau[1,2], A. Lançon[1], S. C. Trager[2], Y. Chen[2], R. Peletier[2], B. Aringer[3,4] and W. Nowotny[4]

Abstract. Until recently, most empirical stellar spectral libraries were limited to a certain wavelength range or combined data from different stars, taken by different instruments of which some have low spectral resolution, limiting for instance our ability to analyze galaxies jointly in the ultraviolet, the optical and the near-infrared. The X-shooter Spectral Library, XSL, obtained using the X-shooter three-arm spectrograph on ESO's VLT, will help solving the current limitations. Here, we focus on spectra of carbon stars, which are part of this library. Carbon stars contribute significantly to the integrated spectra of galaxies containing young and intermediate-age populations, especially in the near-infrared, and therefore should be properly taken into account in stellar population synthesis models. A comparison with theoretical spectra is necessary to estimate the fundamental parameters of the observed stars, as well as to validate the spectral models across the broad ultraviolet to near-infrared wavelength range of X-shooter. We present preliminary results of such comparisons.

Keywords: spectroscopy, x-shooter, near-infrared, carbon stars

1 Carbon stars from the X-shooter Spectral Library

Stellar population models are powerful tools, widely used to determine galaxy ages, metallicities and abundances. The key ingredients for population synthesis are libraries of stellar spectra. However, up to now, no single empirical spectral library provides both a very broad wavelength range and a good spectral resolution. The X-shooter Spectral Library (XSL, Chen et al. 2011) is intended to meet this need.

XSL is being obtained using the X-shooter three-arm spectrograph on ESO's VLT (Vernet et al. 2011). What makes it unique is that it collects spectra over a broad wavelength range – ultraviolet (UVB), visible (VIS) and near–infrared (NIR) – simultaneously, as shown in the right panel of Fig. 1. This characteristic is particularly useful for observing variable stars, such as the cool asymptotic giant branch stars that contribute significantly to the light of galaxies.

Thanks to an ESO Large Programme, this stellar library will consist of about 600 stars, observed at moderate resolution (R $\sim$ 10 000), with complete coverage from 320 to 2480 nm, covering a large range of stellar parameters (L, Teff, [Fe/H]), as shown in the left panel of Fig. 1. The purpose is to sample the full range of relevant spectral types, in order to feed population synthesis models adequately.

Among the diversity of stars in XSL, we focus here on one spectral type: C-star. Carbon stars are among the brightest stellar objects in resolved galaxies containing young and intermediate age populations, mainly radiating in the near-infrared. In addition, they contribute significantly to the integrated spectra of such systems. Thus, it is important to take C stars into account properly in population synthesis.

[1] Observatoire Astronomique de Strasbourg, Université de Strasbourg, CNRS, UMR 7550, 11 rue de l'Université, F-67000 Strasbourg, France
[2] Kapteyn Astronomical Institute, University of Groningen, Postbus 800, 9700 AV, Groningen, Netherlands
[3] Dipartimiento di Astronomica, Università di Padova, Vicolo dell'Osservatorio 2, 35122 Padova, Italy
[4] University of Vienna, Department of Astrophysics, Türkenschanzstraße 17, A-1180 Wien, Austria

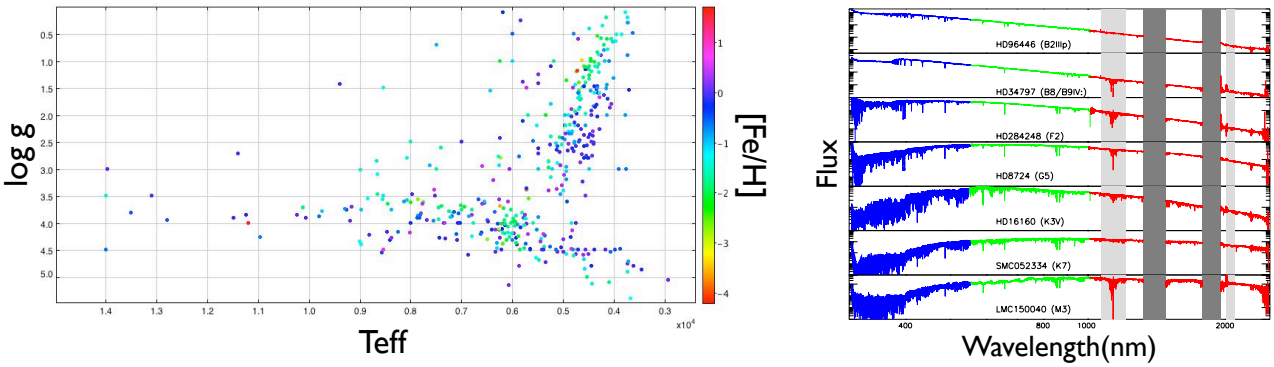

Fig. 1. Left: XSL sample (only 436 stars are represented here). **Right:** A sample of XSL stellar spectra sorted by temperature, taken from Chen et al. (2011). Grey bars cover areas of telluric absorption in the near-infrared.

Forty C-star spectra are currently found in XSL. We focus on a sub-sample of them for this preliminary study. Our goal is to answer this question: can the observed spectra across the whole wavelength range (visible to near-infrared) be reproduced with synthetic spectra based on a specific hydrostatic model atmosphere and artificially reddened according to a standard reddening law? In section 2, we will introduce the models used for this study. Then, in sections 3 and 4, we will present the results of our comparisons.

In this paper, we will not expand on the data reduction. We refer the readers to Chen et al. (2013) for the reduction of the two first semesters of data for the UVB and VIS arms. Details about the procedure adopted for the NIR arm of X-shooter will be provided in a forthcoming paper.

2 Hydrostatic model atmospheres for C-rich giants

The set of models used for this study are the model atmospheres of C-rich giants calculated by Aringer et al. (2009). These authors computed a grid of 746 spherically symmetric COMARCS atmospheres covering effective temperatures between 2400 and 4000 K, surface gravities from $\log(g[\mathrm{cm/s^2}])= 0.0$ to -1.0, metallicities ranging from the solar value down to one-tenth solar and C/O ratios in the interval between 1.05 and 5.0. Figure 2 shows examples of such models.

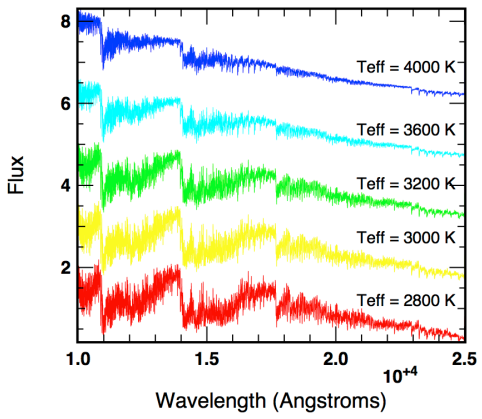

Fig. 2. Synthetic NIR spectra for C-rich giants of a fixed C/O=1.1, adapted from Aringer et al. (2009)

In their analysis, Aringer et al. show that the models reproduce the colours of the warmer carbon stars with weak pulsation. But to deal with cooler objects with intense variations, a proper treatment of the reddening caused by dusty envelope is needed. Thus, more sophisticated model atmospheres are needed to deal with more

evolved red giants for which dynamic phenomena (pulsations of the stellar interiors and developments of dusty stellar winds) become significant, as demonstrated by Nowotny et al. (2011).

In our study, we use a subset of models with solar abundances and a variety of C/O ratios (1.05, 1.1, 1.4 and 2.0) and effective temperatures(2800, 3000, 3200, 3600, 4000 K). All the models are computed with log(g) = 0.0 and 1 $M_{\odot}$, at a constant spectral resolution R = 200 000.

These models focus on objects that can be described by hydrostatic models neglecting dynamical phenomena such as pulsation and mass loss. As a consequence, the reddening due to circumstellar dust is not included.

3 Best fit to NIR observations

In order to see if a single reddened hydrostatic model can reproduce the observed X-shooter C-star spectra, we perform a χ^2 minimization on a three-dimensional parameter space: Teff, C/O and A_V. We redden the dust-free models using a standard extinction law, following the prescription of Cardelli et al. (1989). We focus first on the near-infrared wavelength range, as carbon stars emit mostly in that spectral range.

Figure 3 provides an example of such a comparison. The black curve represents our XSL-NIR spectrum of a C-star with $(J - K) = 1.38$. The red curve is the best fit found. The grey bands mask the regions of strongest telluric absorption. We show the comparisons at two resolutions : a lower one with R $\sim$ 2 300 and a higher one with R $\sim$ 8 000. The models provide a good first order representation of the spectra in the near-infrared arm.

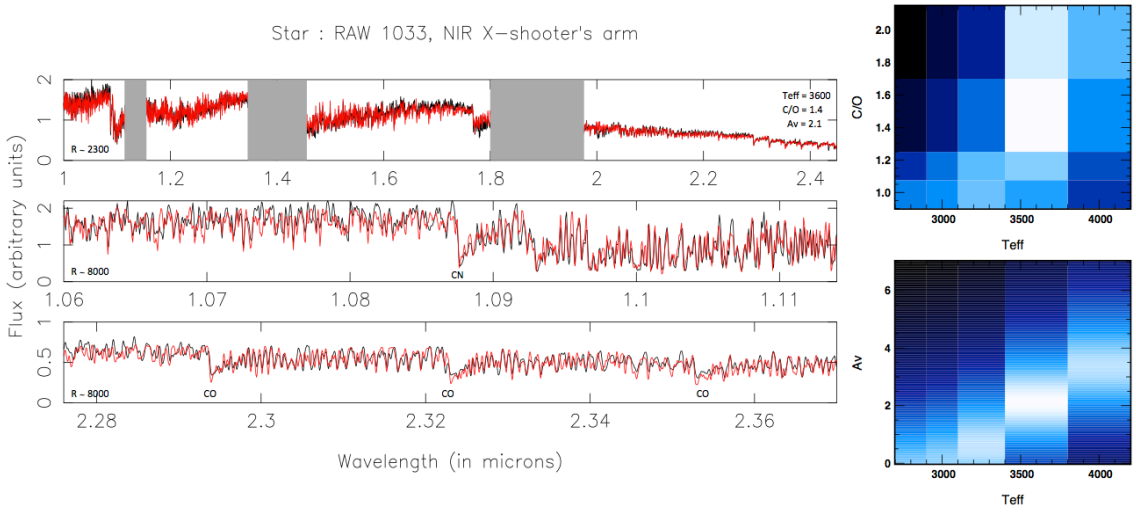

Fig. 3. Best fit (red) to the XSL-NIR spectrum (black) of a C-star (J-K = 1.38). The grey bands mask the regions of deepest telluric absorption. The upper plot shows the spectra smoothed to R $\sim$ 2 300, while the two other ones are for R $\sim$ 8 000. Right hand panels : χ^2 maps. Each map shows the χ^2 values for two dimensions of the grid, and the third is always minimized. White colors indicate the best fit.

4 Extension to the visible

Rare studies that attempt to analyze optical and near-infrared spectra jointly show that results obtained from different wavelength ranges do not agree very well (see Lançon et al. 2008, for an example based on star clusters in the starbust galaxy M82). Here, we make full use of X-shooter's ability to cover these two ranges simultaneously.

As shown in section 3, a good agreement seems to be found in the near-infrared. To see if an agreement is found over the whole visible /near-infrared wavelength range, we extend our best fit to the visible range.

As shown in Fig. 4, this preliminary study indicates that in the visible some deviations of the model spectrum from the observed one can be recognized. Tests performed with other C-stars indicate that bluer stars (for which the circumstellar reddening is less pronounced) are more easily reproduced. The full XSL sample needs to be used to confirm this trend.

To understand and resolve such discrepancies, C-star specific extinction laws and dynamical models now need to be considered. In the meantime, as mentioned by Nowotny et al. (2011), parameters for observed C-star derived from studies based on hydrostatic models should be regarded with caution.

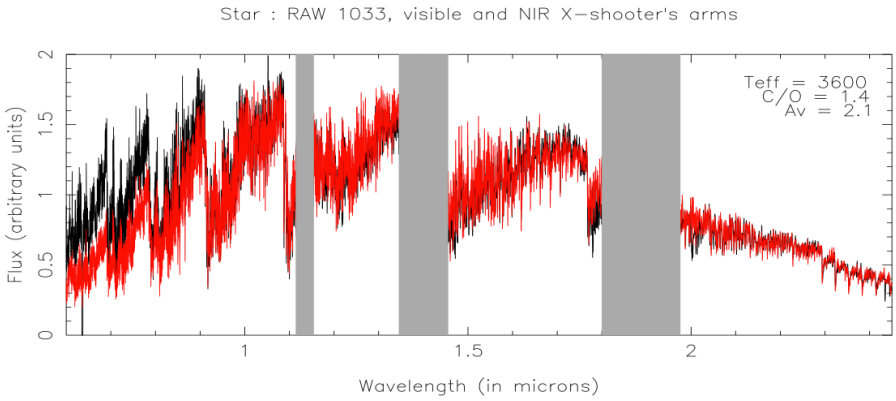

Fig. 4. Best fit (red) to the XSL-NIR spectrum, extended to the visible, and the merged empirical spectrum (black curve). Synthetic and observed spectra are rebinned to R $\sim$ 2300. The grey bands mask the regions of deepest telluric absorption.

5 Conclusions

XSL provides a large collection of stellar spectra, with moderate resolution, broad wavelength coverage and large range of stellar atmospheric parameters. The carbon stars from this collection are key elements for the stellar population synthesis applications. Thus, a proper determination of their fundamental parameters is crucial. Over a single X-shooter arm, good overall agreement is found between the data and theoretical models of static C-star, reddened with a standard extinction law. This is not longer the case over the full range of X-shooter. We are quantifying systematic discrepancies and exploring more complex models, aiming at improving the robustness of fundamental parameter estimates. Making use of X-shooter's spectral resolution, we will also assess detailed spectral features, which will reveal the chemistry and atmospheric structure of individual stars. For population synthesis applications, it is important to identify which ones are precisely understood.

A. Gonneau would like to thank the organizers for this conference, and her colleagues for helpful discussions.
XSL is based on ESO Large Programme 189.B-0925.
This research was funded in part by the Austrian Science Fund (FWF): P21988-N16.

References

Aringer, B., Girardi, L., & Nowotny, W. 2009, A&A, 503, 913
Cardelli, J., Clayton, G., & Mathis, J. 1989, ApJ, 345, 245
Chen, Y., Trager, S., & Peletier, R. 2011, JPhSC, 328, 2023
Chen, Y., Trager, S., Peletier, R., & al. 2013, MNRAS, submitted
Lançon, A., Gallagher, J. S. I., & Mouhcine, M. 2008, å, 486, 165
Nowotny, W., Aringer, B., & Höfner, S. 2011, A&A, 529, 129
Vernet, J., Dekker, H., D'Odorico, S., & al. 2011, A&A, 536, 105

SF2A 2013
L. Cambrésy, F. Martins, E. Nuss and A. Palacios (eds)

ANALYSIS OF STELLAR WIND STRUCTURE OF MASSIVE STAR THROUGH THEIR X-RAY SPECTRA

A. Hervé[1]

Abstract. Massive stars play a key role in the chemical enrichment of the universe. At the end of 90's, the evidence of fragmented wind have been highlighted thanks to observations as well as spectra simulation. During the same time, two X-ray space observatories were launched, opening a new window for the massive star stellar wind analyses.

In this context, we are currently developing a modelling tool to analyse the stellar wind structure as well as a determination of fundamental properties of massive star like mass loss rate and surface abundances thanks to their X-ray spectra.

Our results, with our code, have revealed the absence of porosity of the stellar wind (i.e even through stellar winds are fragmented the space between clumps is thin.) of ζ Pup and ζ Ori. For the first time, we have determined the temperature distribution of the X-ray emitting plasma. The highest temperatures are localized in very thin shells ($\sim$ 1. R_*) at few stellar radius. The lowest temperatures are discovered in very extended shells and the X-ray emission can arise very close to the stellar surface (1.3-1.5 R_*). Finally, we determined CNO abundances and mass loss rate in agreement with previous UV/visible studies.

Keywords: Stars: early-type, Stars: mass-loss, X-rays: stars, Stars: massive, Stars: individual: ζ Pup ζ Ori

1 Introduction

Massive stars are the main agents of the chemical enrichment of galaxies. Due to their high temperature they can synthesize the heaviest elements during their different evolution phases. They release these elements in their local environment during all their life through their powerful stellar winds and at lager scale at the end of their life during supernovae explosion.

At the end of the 90's, some observational studies revealed that some time variability of the spectrum of star is due to the presence of fragmentation (Eversberg et al. 1998). Our traditional point of view of homogeneous stellar winds has evolved to fragmented structures. The implementation of the clumping in modelling code (Bouret et al. 2005) has improved the fitting. But, in consequence the mass loss rate has been divided by a factor between 3 and 10. This huge reduction has consequence on the evolution scheme of the massive star.

In 1999, two X-ray spectrographes were launched, $XMM-Newton$ and $Chandra$. These two instruments have opened a new window to analyse the stellar wind properties of the massive stars. The scientific community can now access to high resolution spectra of massive star in the X-ray band. In these context, we are currently developing and improving a modelling tool which allow us to understand the line formation in the X-ray band and to extract fundamental parameters of massive stars.

We present, in the section 2, our modelling code and the basics of physics included. Then, in the section 3, we present the results obtained by the analyses of X-ray spectra of ζ Pup and ζ Ori. Finally, in the last section, we discuss these results and their impacts in our knowledge of the massive stars.

[1] LUPM, Université Montpellier II, Place Eugène Bataillon, F-34095 MONTPELLIER Cedex 05, France

2 Modelling tool

We are currently developing our own modelling tool in order to analyse high resolution spectra of O-type stars and to determine their stellar wind properties (Hervé et al. (2012); Hervé et al. (2013), Hervé et al, in prep). The code is decomposed in two different parts. First, the code computes synthetic X-ray spectra as a function of different input parameters like the mass loss rate, the surface chemical abundances, and the temperature, the position and the size of the X-ray emitting shell. Then, a second routine combines different X-ray synthetic spectra in order to reproduce observations.

In our code, the X-ray photons production is based on the wind embedded shock scenario. The strong instabilities in the wind drive to collisions, heating plasma to very high temperatures (1-10 10^6 K). Then, this heated matter is embedded by the 'cool' material. In our approach, we consider that the X-ray emitting plasma is optically thin to X-ray. Consequently, we can compute the emission and the absorption separately. So, in a first part, we calculate the X-ray theoretical emission of a shell as a function of its density and of the theoretical emissivity of the plasma. For the latter, we use the AtomDB database (Foster et al. 2012). Then we have modified the Owocki formalism (Owocki & Cohen 2006) to determine the absorption of X-ray photon by the cool material. Now, we include the wavelength and the radial dependence of the mass absorption coefficients, κ, as keeping an analytic solution of the optical depth equation to compute synthetic models fast:

$$\begin{aligned}\tau_\lambda(p,z) &= \int_z^{\sqrt{(R_{lim})^2-p^2}} \frac{\alpha(\kappa_0-\gamma R_*)R_*}{r'\,(r'-R_*)+\alpha\,(\kappa_0+\gamma(r'-R_*))\,h'\,r'}\,dz' \\ &+ \int_z^{\sqrt{(R_{lim})^2-p^2}} \frac{\alpha\gamma R_*}{(r'-R_*)+\alpha(\kappa_0+\gamma(r'-R_*))h'}\,dz' + \int_{\sqrt{(R_{lim})^2-p^2}}^{\infty} \frac{\alpha\kappa_{max}R_*}{r'\,(r'-R_*)+\alpha\kappa_{max}h'\,r'}\,dz'\end{aligned}$$

with $\alpha = \frac{\dot{M}}{4\pi R_* v_\infty}$, κ_0 and κ_{max} are, respectively, the mass absorption coefficient in the innermost part and in the outer part of the wind and γ is the slope. R_{lim} is the position in the wind where κ reaches its plateau value κ_{max}. h' is the porosity length. To determine $\kappa(\lambda, r)$, we use the radiative code CMFGEN (Hillier & Miller 1998). This code solves the radiative transfer equation and statistical equilibrium equations for each ions in Non Local Thermodynamical Equilibrium (NLTE) conditions as a function of stellar and wind parameters. Finally, we combine the emission and the absorption components to obtain a synthetic spectrum.

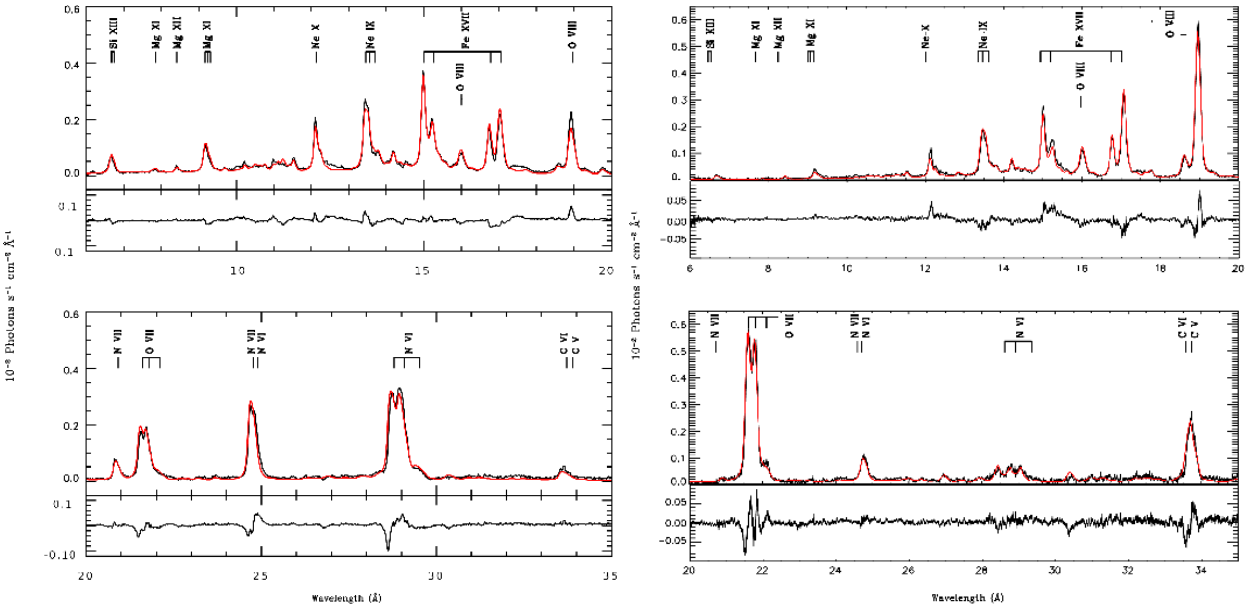

Fig. 1. Left: Comparison of our best fit model (in red) to the RGS spectrum of ζ Pup (in black). Right: Comparison of our best fit model (in red) to the RGS spectrum of ζ Ori. The residuals (in the sense observation minus model) are shown in the panel under the spectra.

In the second part of the code, a fitting routine explores a database of synthetic models, and combines different plasma components with the same chemical composition, h' and $\dot{M}$ in order to fit the observation.

kT in keV	R_{in} in R_*	R_{out} in R_*	hot gas filling factor f_X
0.100	7.5	85	0.012
0.200	1.5	38	0.012
0.400	2.7	4.0	0.020
0.690	3.1	4.1	0.007

Table 1. X-ray temperature distribution in the wind of ζ Pup

The synthetic multi-temperature spectrum is built as follows:

$$S_i = \sum_{j=1}^{n} \sum_{r=R_{in}}^{R_{out}} f_{hotgas,j,r} M_{j,i,r} + \epsilon, \tag{2.1}$$

where S_i is the observed flux at the wavelength i, $f_{hotgas,j,r}$ is the classical volume filling factor of the hot gas component j at the position r, $M_{j,i,r}$ is the synthetic flux of each X-ray emitting plasma component at the wavelength i at the position r, and ϵ is the error of regression. Note that the analysis of ζ Pup was made with a previous version of our code and the radial dependence of f was not included yet.

For each combination of synthetic models, the best-fit values of $f_{hotgas,j}$ are determined with a non negative least-squares algorithm. Then, we calculate the χ^2 by comparing the model to the data. Finally, a minimisation of the χ^2 is performed to obtain the best fit. After several tests, it appears that at least four components are needed to achieve a good fit of the whole fluxed RGS spectra of ζ Pup and ζ Ori.

3 Results

We applied our code to ζ Pup (Nazé et al. 2012; Hervé et al. 2013) and ζ Ori (Hervé et al in prep) which are the two XMM most observed O-type stars. For the first time, we have fitted X-ray spectra as a whole and not like the traditional line-by-line analysis. The results are very good as show in Fig.1. A discrete decomposition of the X-ray emitting plasma in four temperature components from 0.1 keV to 0.690 keV allow us a better understanding of the distribution of the shocks in these stars (Tab.1). In the both case, we found that the hottest temperatures are localized in small shells ($R_{shell} = 1 - 2R_*$) at very few stellar radii ($R_0 \sim 2.5 - 3.5R_*$). The intermediate temperature shell is a little bit larger than the hottest one ($R_{shell} = 1.5 - 2.5R_*$) and localized a little bit closer to the stellar surface ($R_0 \sim 2. - 3R_*$). The two lowest temperature components are different. In the case of ζ Pup, we considered only one shell at a give temperature. Large emitting shells ($R_{shell} = 77.5R_*, 36.5R_*$, for the 0.1 keV and 0.2 keV respectively) are detected. The coolest component starting to emits at large radii ($R_0 = 7.5R_*$) while the component at 0.2 keV starts to emit very close to the stellar surface ($R_0 = 1.5R_*$). In the case of ζ Ori, with the first version of the code, we obtained too much flux in the blue part of the lines produced by the shell with the coolest temperature plasma. The utilization of the porosity to increase the flux in the red part (Owocki & Cohen 2006; Hervé et al. 2012) did not improved the quality of the fit. Consequently, we have modified our code which now takes into account a possible non-continuous emission of X-ray photons of a given shell at a given temperature as well as a possible radial dependence of f. With this new method, we have improved the quality of the fit. We discovered the presence of a small shell very close to the stellar surface ($R_0 = 1.2 - 1.3R_*$). The same shell is may be present in the wind of ζ Pup but as the wind is denser than the wind of ζ Ori, all the photons emit by this shell are totally absorbed by the 'cool' matter component. Unfortunately, this new method leads to a degeneracy of the results. We obtained the same quality of fit with numerous small emitting shells with a huge value of f, or with large shells with a small value of f. We need theoretical constraints of f and/or the size of the emitting shells to break the degeneracy.

Concerning the stellar wind parameters (Tab.3), our code can allow us a determination of mass loss rate, wind structure (porous or homogeneous) and CNO abundances. Taking into account the different approximation in CMFGEN (used in visible and UV analyses) and in our code as well as the accuracy of the atomic data, our determination of the CNO abundances for ζ Pup and ζ Ori is very close to the result obtained in analyses in other wavelength band (Tab.3). For ζ Ori, we obtain solar abundances for the CNO elements as Martins et al. (2012) in their study in yhe visible band. Concerning ζ Pup, we obtain a depletion of carbon and oxygen and a over abundance of nitrogen as the result of Bouret et al. (2012) in their analyses in visible band. Nevertheless, the over abundance of Nitrogen found in our work is less important than in visible band work.

Table 2. Our best stellar wind parameters obtained for ζ Pup and ζ Ori in the X-ray band compared to UV/visible studies.

Object	study	$\dot{M}$ ($M_\odot$ yr^{-1})	X(C) (mass fraction)	X(N) (mass fraction)	X(O) (mass fraction)	h
ζ Ori	Hervé et al in prep in X-ray	1.0 10^{-6}	2.08×10^{-3}	4.45×10^{-4}	3.84×10^{-3}	0
	Martins et al. (2012)	1.7 10^{-6}	2.07×10^{-3}	2.96×10^{-4}	5.27×10^{-3}	*
ζ Pup	Hervé et al. (2013) in X-ray	3.5 10^{-6}	6.00×10^{-4}	7.70×10^{-3}	3.05×10^{-3}	0
	Bouret et al. (2012)	2. 10^{-6}	2.86×10^{-4}	1.02×10^{-2}	1.30×10^{-3}	*

A very important result from our analyses is that the wind of massive stars is not porous. Even though the UV and visible studies of ζ Pup and ζ Ori revealed a fragmented wind, our work reveals that the space between clumps is very thin. Moreover, the determination of the mass loss rate for the both stars in the different wavelength bands are in good agreement. The results obtained in the case of ζ Ori are very close and the small difference is certainly due to the error bar in the both works. In the case of ζ Pup, the difference of the mass loss rate is greater than in the case of ζ Ori, but Bouret et al. (2012) indicate in their paper that the mass loss rate is not enough powerful to support the line driving acceleration in the inner part. They supposed that the mass loss rate is certainly greater than the one they found for their best fit. This remark confirm our result obtained from the X-ray spectrum analysis.

4 Conclusions and Discussions

In conclusion, we have fitted for the first time the whole X-ray spectra of O-type stars. We found that the hottest temperature plasma shells are relatively thin and localized at few stellar radii. Concerning the shell with the lowest temperature plasma, the situation is more complicated. In the case of ζ Pup, we found a continuous emission of X-ray photon from extended shells, one close to the photosphere the other one at large radii. In the case of ζ Ori, our model predicts, with the first version, too much flux in the blue wing of the emission lines ($\lambda \geq 20$Å) produced by the cool temperature (kT=0.1 ,0.2 keV) plasma components. The solution to explain this phenomenon is not the porosity but the presence of a small low temperature X-ray emitting shell very close to the surface of the star ($R_0 \sim 1.2 R_*$). But this result has also revealed a degeneracy of the solution. We have, now, a non continuous X-ray emission for each shell at a given temperature plasma and a radial dependence of the hot gas filling factor. We can fit with the same degree of satisfaction the data with numerous small shells associated to a huge f or few large shells with a small f. We need to better understand the cooling function of X-ray emitting plasma to constrain the size of the emitting shells and to break the degeneracy.

Finally, as expected, the stellar wind parameters determined in our X-ray analyses are in good agreement with the results obtained by other studies in different wavelength bands. The non solar abundances of the CNO elements of ζ Pup indicate that this object is a more evolved star than ζ Ori. The visible/UV works show a fragmentation of the stellar wind and our work indicate that the space between fragments is very thin.

References

Bouret, J.-C., Lanz, T., & Hillier, D.J. 2005, A&A 438, 301
Bouret, J.-C., Hillier, D. J., Lanz, T., & Fullerton, A. W. 2012, A&A, 544, A67
Eversberg, T., Lépine, S., & Moffat, A.F.J. 1998, ApJ 494, 799
Foster, A. R., Ji, L., Smith, R. K., & Brickhouse, N. S. 2012, arXiv:1207.0576
Hervé, A., Rauw, G., Nazé, Y., & Foster, A. 2012, ApJ, 748, 89
Hervé, A., Rauw, G., & Nazé, Y. 2013, A&A, 551, A83
Hillier, J., & Miller, E. 1998, *ApJ*, 496, 416
Martins, F., Escolano, C., Wade, G. A., et al. 2012, A&A, 538, A29
Najarro, F., Hanson, M.M., & Puls, J. 2011, A&A, 535, A32
Nazé, Y., Flores, C. A., & Rauw, G. 2012, A&A, 538, A22
Owocki, S.P., & Cohen, D.H. 2006, ApJ 648, 565

SF2A 2013
L. Cambrésy, F. Martins, E. Nuss and A. Palacios (eds)

STOCHASTIC EXCITATION OF GRAVITO-INERTIAL WAVES IN ROTATING STARS

S. Mathis[1,2] and C. Neiner[2]

Abstract. Stochastic gravity waves have been recently detected and characterised in stars thanks to asteroseismology and they may play an important role in the evolution of stellar angular momentum. Moreover, the observational study of the CoRoT hot Be star HD 51452 suggests a potential strong impact of rotation on stochastic excitation of gravito-inertial waves in rapidly rotating stars. In this work, we present our exploration of the action of rotation on stochastic wave excitation by turbulent convection in stellar interiors. Using a local model, we study stochastic excitation as a function of the waves' Rossby number and we demonstrate that the excitation presents two different regimes for super-inertial and sub-inertial frequencies. Consequences for rapidly rotating stars and the transport of angular momentum in their interiors are discussed.

Keywords: hydrodynamics – waves – turbulence – stars: rotation – stars: evolution

1 Introduction

Gravity waves propagate in the stably stratified radiative core of low-mass stars and the external radiative envelope of intermediate-mass and massive stars (e.g. Aerts et al. 2010). When they (or their signatures) are detected thanks to helioseismology and asteroseismology, they allow us to probe the stellar internal structure and differential rotation (e.g. Garcia et al. 2007; Bedding et al. 2011; Beck et al. 2012; Deheuvels et al. 2012; Mosser et al. 2012; Neiner et al. 2012b). Furthermore, these waves are able to transport and deposit a net amount of angular momentum because of their damping and corotation resonances (e.g. Talon & Charbonnel 2005; Alvan et al. 2013; Mathis et al. 2013a). If frequencies of excited gravity waves are around the inertial frequency 2Ω, where Ω is the angular velocity of the star, which is assumed to be uniform here, their propagation is strongly affected by the Coriolis acceleration and they become gravito-inertial waves (hereafter GIWs; e.g. Dintrans & Rieutord 2000; Mathis 2009; Ballot et al. 2010).

GIWs have been discovered thanks to the CoRoT satellite in the hot Be star HD 51452 (Neiner et al. 2012a). In this star, which rotates close to its critical angular velocity, GIWs are probably excited stochastically by turbulent convection in the core or/and in the subsurface convection zone, since the star is too hot to excite them with the κ-mechanism. Moreover, the detected GIWs with the largest amplitudes have frequencies in the sub-inertial domain (*i.e.* $\sigma < 2\Omega$), which are the most influenced by the Coriolis acceleration. Therefore, this discovery points out how necessary it is to understand the action of rotation on stochatic excitation of GIWs in stellar interiors, which has been poorly explored until now (Belkacem et al. 2009).

To reach this objective, in Mathis et al. (2013b) we chose to generalise the work by Goldreich & Kumar (1990) and Lecoanet & Quataert (2013) taking the action of the Coriolis acceleration into account. This work is summarized here. First, in Sect. 2, we present the local rotating set-up in which we describe the different regimes of the dynamics of GIWs. Next, in Sect. 3. their stochastic excitation by turbulent convective flows is studied and we identify and discuss the impact of rotation.

[1] Laboratoire AIM Paris-Saclay, CEA/DSM - CNRS - Université Paris Diderot, IRFU/SAp Centre de Saclay, F-91191 Gif-sur-Yvette, France

[2] LESIA, UMR 8109 du CNRS, Observatoire de Paris, UPMC, Univ. Paris Diderot, 5 place Jules Janssen, 92195 Meudon Cedex, France

2 Gravito-inertial waves in stellar interiors

2.1 The studied set-up and the Poincaré wave equation

In Mathis et al. (2013b), we chose to study a cartesian region, centered on a point M of a radiation-convection interface. We introduce Θ the angle between the local effective gravity $\vec{g}_{\rm eff}$, which is the sum of the self-gravity $\vec{g}$ and of the centrifugal acceleration $1/2\,\Omega^2\vec{\nabla}s^2$ (s being the distance from the rotation axis), and the rotation vector $\vec{\Omega}$ (see left panel of Fig. 1). Mx, My and Mz are the axes along the local azimuthal, latitudinal and vertical (*i.e.* along $\vec{g}_{\rm eff}$) directions respectively. This "f-plane" (Pedlosky 1982) is co-rotating with the stellar angular velocity $\vec{\Omega}$ and we introduce the two components of this vector along the vertical and latitudinal directions

$$f = 2\Omega\cos\Theta \quad \text{and} \quad \widetilde{f} = 2\Omega\sin\Theta. \tag{2.1}$$

Following Gerkema & Shrira (2005), we go beyond the so-called *traditional approximation* and both components are taken into account to ensure a complete and correct treatment of GIWs' dynamics, both in the radiative and in the convective regions, and of their coupling with inertial waves (see also Gerkema et al. 2008).

To study GIWs' dynamics, we write the linearised equations of motion of the stellar stratified fluid on the non-traditional f-plane assuming the Boussinesq and the Cowling approximations (Gerkema & Shrira 2005; Cowling 1941). We introduce the GIWs' velocity field $\vec{u} = (u, v, w)$, where u, v and w are the components in the local azimuthal, latitudinal and vertical directions respectively. Eliminating the horizontal components of the velocity, the pressure and the buoyancy, the equation for the vertical velocity is obtained

$$\partial_{t,t}\left[\nabla^2 w\right] + 4\left(\vec{\Omega}\cdot\vec{\nabla}\right)^2 w + N^2\nabla_H^2 w = 0, \tag{2.2}$$

where ∇_H^2 is the horizontal Laplacian and $N^2(z) = -\dfrac{\overline{g}_{\rm eff}}{\overline{\rho}}\dfrac{{\rm d}\overline{\rho}}{{\rm d}z}$ is the Brunt-Väisälä frequency, $\overline{\rho}$ being the hydrostatic density profile. We then consider a monochromatic GIW with a frequency σ that propagates in the direction $(\cos\alpha, \sin\alpha)$ in the (Mxy) plane (see left panel of Fig. 1). Introducing the reduced horizontal coordinate $\chi = x\cos\alpha + y\sin\alpha$ (with $\partial_x = \cos\alpha\,\partial_\chi$ and $\partial_y = \sin\alpha\,\partial_\chi$) and substituting $w(\vec{r}, t) = W(\vec{r})\exp[i\sigma t]$, we get the Poincaré equation for GIWs:

$$\left[N^2(z) - \sigma^2 + f_s^2\right]\partial_{\chi,\chi}W + 2ff_s\,\partial_{\chi,z}W + \left[f^2 - \sigma^2\right]\partial_{z,z}W = 0, \tag{2.3}$$

where $f_s = \widetilde{f}\sin\alpha$. We note that GIWs' dynamics is a non-separable bidimensionnal problem because of the mixed derivative $\partial_{\chi,z}$ (see also Dintrans & Rieutord 2000). However, it is possible in our set-up to introduce the transformation

$$W = \Psi(z)\exp\left[ik_\perp\left(\chi + \tilde{\delta}z\right)\right] \quad \text{where} \quad \tilde{\delta} = -\frac{ff_s}{f^2 - \sigma^2}, \tag{2.4}$$

that leads to

$$\frac{{\rm d}^2}{{\rm d}z^2}\Psi + k_V^2(z)\,\Psi = 0, \quad \text{where} \quad k_V^2(z) = k_\perp^2\left[\frac{N^2(z) - \sigma^2}{\sigma^2 - f^2} + \left(\frac{\sigma\, f_s}{\sigma^2 - f^2}\right)^2\right], \tag{2.5}$$

$k_\perp$ being the wave number in the χ direction. This enables us to use the method of vertical modes as in the non-rotating case and the modal functions W_j that verify boundary conditions constitute an orthogonal and complete basis (Gerkema & Shrira 2005). This leads to the allowed frequency spectrum $\sigma_- < \sigma < \sigma_+$ (*i.e.* $k_V^2 > 0$), where

$$\sigma_\pm = \frac{1}{\sqrt{2}}\sqrt{\left[N^2 + f^2 + f_s^2\right] \pm \sqrt{\left[N^2 + f^2 + f_s^2\right]^2 - (2fN)^2}}. \tag{2.6}$$

Moreover, in convective regions, which excite GIWs, the local vertical number (Eq. (2.5)) becomes

$$k_{\rm CZ}^2 \equiv k_\perp^2\frac{\sigma^2}{\left(\sigma^2 - f^2\right)^2}\left[\left(f^2 + f_s^2\right) - \sigma^2\right] = k_\perp^2\frac{\left[\left[\widetilde{R}_{\rm o}(\Theta, \alpha)\right]^{-2} - 1\right]}{\left(1 - R_{\rm o}^{-2}\cos^2\Theta\right)^2}, \tag{2.7}$$

where we defined a local wave Rossby number $\widetilde{R}_{\rm o} = R_{\rm o}\left[\cos^2\Theta + \sin^2\alpha\sin^2\Theta\right]^{-1/2}$ expressed as a function of the wave's Rossby number $R_{\rm o} = \sigma/2\Omega$. We identify for $\alpha = \pi/2$ the allowed frequency domain for inertial waves

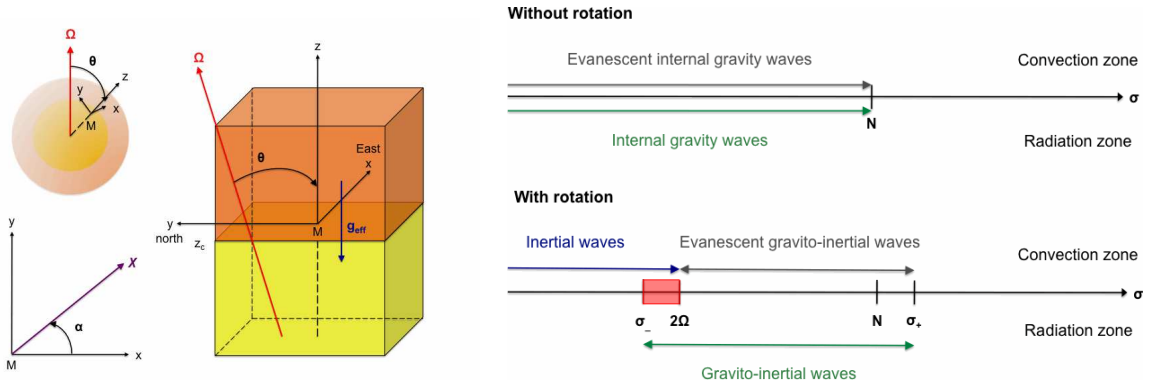

Fig. 1. Left: local studied "f-plane" reference frame. The radiative and convective regions are respectively in yellow and orange. This case corresponds to a low-mass star. The vertical structure of this set-up can be inverted to treat the case of intermediate-mass and massive stars. Right: low frequency spectrum of waves in a non-rotating ($\Omega = 0$, top) and in a rotating star (bottom). For each case, waves in the convective and radiative zones are indicated at the top and bottom, respectively. (Taken from Mathis et al. (2013b).)

$0 < \sigma < 2\Omega$ (i.e. $R_o < 1$). On one hand, in the local super-inertial regime ($\widetilde{R}_o > 1$), there are turning points ($z_{t;i}$) in the radiative zones for which $k_V^2(z_{t;i}) = 0$, *i.e.:*

$$N^2 = \sigma^2 \frac{\left[\sigma^2 - \left(f^2 + f_s^2\right)\right]}{\left(\sigma^2 - f^2\right)} \tag{2.8}$$

and GIWs are evanescent in convective zones. On the other hand, in the local sub-inertial domain ($\widetilde{R}_o < 1$), GIWs propagate in the whole radiative zone and become propagative inertial waves in convective zones. These two behaviours (see right panel of Fig. 1) have been put forward by Dintrans & Rieutord (2000).

2.2 Propagation in rotating stellar convective zones

2.2.1 Super-inertial regime $\left(\widetilde{R}_o > 1\right)$

In the case of the super-inertial regime, there are two turning points ($z_{t;1}$, $z_{t;2}$ with $z_{t;1} < z_{t;2}$) in the radiative zone for which $k_V^2 = 0$ (see Eq. 2.8). In the convective region, GIWs are evanescent and we obtain the complete bidimensionnal expression for the vertical velocity using asymptotic methods, Eq.(2.7) and Eq. (2.4):

$$W(z > z_c, \chi) = \frac{A}{\sqrt{k_\perp p}} \exp\left[-k_\perp p(R_o)(z - z_c) - \Delta(z_{t;2}, z_c)\right] \cos\left[k_\perp\left(\chi + \tilde{\delta}(R_o)\, z\right)\right], \tag{2.9}$$

where we define

$$p = \frac{\sqrt{|1 - \widetilde{R}_o^{-2}|}}{|1 - R_o^{-2}\cos^2\Theta|}, \ \Delta(z_1, z_2) = \int_{z_1}^{z_2} |k_V| \mathrm{d}z' \ \text{ and } \ \tilde{\delta} = -\frac{R_o^{-2}\cos\Theta\sin\Theta\sin\alpha}{R_o^{-2}\cos^2\Theta - 1} \tag{2.10}$$

and we introduce A the amplitude of the wave. In this regime, p is the decay rate of the velocity in the convective zone. The evolution of p and $\tilde{\delta}$ as a function of R_o and Θ is plotted in Fig. 2. In the super-inertial regime, p increases with R_o (with $p \to 1$ for $R_o \to \infty$, *i.e.* the non-rotating case). This means that the decay rate of the wave function in the convective zone decreases when the rotation rate increases until $R_o = 1$. Moreover, $\tilde{\delta}$ tends to vanish at large R_o, while it increases with the rotation rate until $R_o = 1$. Indeed, as soon as rotation becomes important, the problem is non-separable in z and χ (see Eq. 2.3), while it is completely separable in the non-rotating case (i.e. $R_o \to \infty$). Accordingly, modifications of GIW velocity fields occur. This shows the important impact of the Coriolis acceleration, which will modify the couplings of GIWs with convective flows.

2.2.2 Sub-inertial regime $\left(\widetilde{R}_o < 1\right)$

In the case of the sub-inertial regime, waves are propagative in the whole domain without any turning point (*i.e.* $k_V^2 > 0$). In the convective region, we get the complete bidimensionnal expression for the vertical velocity

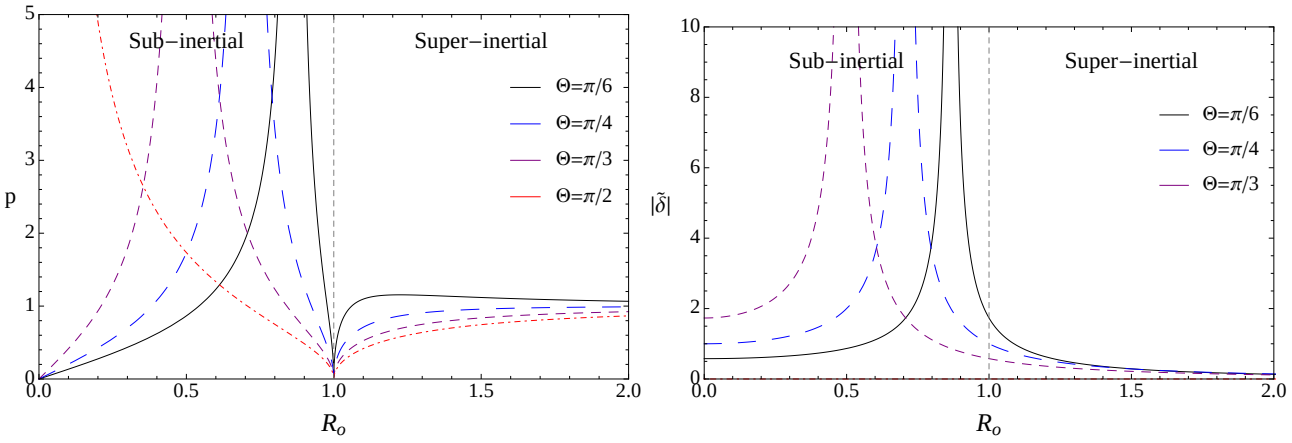

Fig. 2. Evolution of p (left) and $\tilde{\delta}$ (right) as a function of R_o for $\alpha = \pi/2$ and different inclination angle: $\Theta = \pi/6$ (black solid line), $\pi/4$ (blue long-dashed line), $\pi/3$ (purple dashed line) and $\pi/2$ (red dot-dashed line). $\tilde{\delta}$ vanishes for $\Theta = \pi/2$ (see Eq. (2.10)). The border between the sub-inertial and the super-inertial regimes is given by the grey dashed line. (Taken from Mathis et al. (2013b).)

for inertial waves using Eq. (2.7) and Eq. (2.4):

$$W\left(z > z_\mathrm{c}, \chi\right) = \frac{A}{\sqrt{k_\perp p}} \sin\left[k_\perp p\left(R_\mathrm{o}\right)\left(z - z_\mathrm{c}\right) + \Delta\left(z_b, z_c\right)\right] \cos\left[k_\perp\left(\chi + \tilde{\delta}\left(R_\mathrm{o}\right) z\right)\right], \tag{2.11}$$

where p, Δ and δ have been defined in Eq. (2.10). In this regime, p is the vertical wave number of the propagative inertial wave in the convective zone. The variations of p and $\tilde{\delta}$ as a function of R_o in the sub-inertial regime, shown in Fig. 2, imply that the velocity field becomes more and more oscillatory as the rotation rate increases until $R_\mathrm{o} = \cos(\Theta)$ where the denominators of p and $\tilde{\delta}$ vanish. $\Theta_\mathrm{c} = \cos^{-1}\left(R_\mathrm{o}\right)$ corresponds to the critical colatitude above which GIWs are trapped in the radiation zone in the sub-inertial regime (e.g. Mathis & de Brye 2012). This behaviour is very different from the one obtained in the super-inertial regime and will modify GIWs stochastic excitation by convective flows.

3 Stochastic excitation of gravito-inertial wave by turbulent convection

To obtain the amplitude (A) of GIWs excited by turbulent convective zones, we follow Goldreich & Kumar (1990) and Lecoanet & Quataert (2013). The equation for the vertical component of the wave velocity (w) is given for the radiative zone in Eq. (2.2) and for the convective region by

$$\partial_{t,t}\left[\nabla^2 w\right] + 4\left(\vec{\Omega}\cdot\vec{\nabla}\right)^2 w = \partial_t\left[\partial_z\vec{\nabla}\cdot\vec{F} - \nabla^2 F_z\right] = \partial_t \mathcal{S}, \tag{3.1}$$

where we have introduced the convective Reynolds stresses $\vec{F} = \vec{\nabla}\cdot(\vec{u}_\mathrm{c}\vec{u}_\mathrm{c})$ and defined the corresponding source function $\mathcal{S}$ (Belkacem et al. 2009, see also Samadi & Goupil 2001), which vary as a function of the rotation rate. Using the orthogonality of GIW functions in our cartesian set-up, which has been demonstrated by Gerkema & Shrira (2005), we can derive a formal expression for the amplitude of GIWs depending on their super- or sub-inertial behaviour. Following Goldreich & Kumar (1990) and Lecoanet & Quataert (2013), we obtain

$$\begin{aligned} A_\mathrm{sup} = \frac{1}{\mathcal{N}}\frac{1}{2i\sigma\sqrt{\mathcal{A}}}\frac{1}{\sqrt{k_\perp p}}\int_{-\infty}^{t}\mathrm{d}\tau\int_{\mathcal{V}}\mathrm{d}x\,\mathrm{d}y\,\mathrm{d}\zeta\,\Big\{\mathcal{S}\left(x,y,\zeta,\tau;\Omega\right)\exp\Big[-i\,k_\perp\Big[\left(x\cos\alpha + y\sin\alpha\right) + \tilde{\delta}\left(R_\mathrm{o}\right)\zeta\Big] - i\sigma\tau\Big] \\ \times\exp\left[-k_\perp p\left(R_\mathrm{o}\right)\left(\zeta - z_\mathrm{c}\right) - \Delta\left(z_{t;2}, z_c\right)\right]\Big\} \end{aligned} \tag{3.2}$$

and

$$\begin{aligned} A_\mathrm{sub} = \frac{1}{\mathcal{N}}\frac{1}{2i\sigma\sqrt{\mathcal{A}}}\frac{1}{\sqrt{k_\perp p}}\int_{-\infty}^{t}\mathrm{d}\tau\int_{\mathcal{V}}\mathrm{d}x\,\mathrm{d}y\,\mathrm{d}\zeta\,\Big\{\mathcal{S}\left(x,y,\zeta,\tau;\Omega\right)\exp\Big[-i\,k_\perp\Big[\left(x\cos\alpha + y\sin\alpha\right) + \tilde{\delta}\left(R_\mathrm{o}\right)\zeta\Big] - i\sigma\tau\Big] \\ \times\sin\left[k_\perp p\left(R_\mathrm{o}\right)\left(\zeta - z_\mathrm{c}\right) + \Delta\left(z_b, z_c\right)\right]\Big\}, \end{aligned} \tag{3.3}$$

where $\mathcal{V}$ and $\mathcal{A}$ are the volume and the horizontal cross-section of the box respectively and $\mathcal{N}$ is the orthogonality constant. This formal expressions demonstrate that rotation, through the Coriolis acceleration, modifies the stochastic excitation of GIWs, the control parameter being the wave's Rossby number $R_o = \sigma/2\Omega$ (via p and δ, see Eq. (2.10)). On one hand, in the super-inertial regime ($\sigma > 2\Omega$, *i.e.* $R_o > 1$), the evanescent behaviour of GIWs above (below) the external (internal) turning point becomes increasingly weaker as the rotation speed grows until $R_o = 1$. The coupling between super-inertial GIWs and given turbulent convective flows is then amplified as described in Eq. (3.2). On the other hand, in the sub-inertial regime ($\sigma < 2\Omega$, *i.e.* $R_o < 1$), GIWs become propagative inertial waves in the convection zone and the coupling between GIWs and the given turbulent source continue to be sustained (Eq. 3.3).

This result obtained in Mathis et al. (2013b) is of great interest for asteroseismic studies of rotating stars since GIW amplitudes are thus expected to be stronger in rapidly rotating stars. Moreover, the related transport of angular momentum, which until now was believed to become less efficient because of GIWs equatorial trapping in the sub-inertial regime (Mathis et al. 2008; Mathis 2009; Mathis & de Brye 2012), may be sustained thanks to the stronger stochastic excitation by turbulent convective flows. Finally, our prediction is coherent with results obtained in recent realistic numerical simulations of stochastic excitation of GIWs in stellar interiors (Rogers et al. 2012, and L. Alvan, private communication).

This work was supported by the French Programme National de Physique Stellaire (PNPS) of CNRS/INSU, the CNES-SOHO/GOLF grant and asteroseismology support at CEA-Saclay, the CNES-CoRoT grant at LESIA, and the Programme Physique Théorique et ses interfaces of CNRS/INP.

References

Aerts, C., Christensen-Dalsgaard, J., & Kurtz, D. W. 2010, Asteroseismology
Alvan, L., Mathis, S., & Decressin, T. 2013, A&A, 553, A86
Ballot, J., Lignières, F., Reese, D. R., & Rieutord, M. 2010, A&A, 518, A30
Beck, P. G., Montalban, J., Kallinger, T., et al. 2012, Nature, 481, 55
Bedding, T. R., Mosser, B., Huber, D., et al. 2011, Nature, 471, 608
Belkacem, K., Mathis, S., Goupil, M. J., & Samadi, R. 2009, A&A, 508, 345
Cowling, T. G. 1941, MNRAS, 101, 367
Deheuvels, S., Garcia, R., Chaplin, W. J., et al. 2012, The astrophysical journal, 756, 19
Dintrans, B. & Rieutord, M. 2000, A&A, 354, 86
Garcia, R. A., Turck-Chièze, S., Jiménez-Reyes, S. J., et al. 2007, Science, 316, 1591
Gerkema, T. & Shrira, V. I. 2005, Journal of Fluid Mechanics, 529, 195
Gerkema, T., Zimmerman, J. T. F., Maas, L. R. M., & van Haren, H. 2008, Reviews of Geophysics, 46, 2004
Goldreich, P. & Kumar, P. 1990, ApJ, 363, 694
Lecoanet, D. & Quataert, E. 2013, MNRAS, 773
Mathis, S. 2009, A&A, 506, 811
Mathis, S. & de Brye, N. 2012, A&A, 540, A37
Mathis, S., Decressin, T., Eggenberger, P., & Charbonnel, C. 2013a, A&A, 558, A11
Mathis, S., Neiner, C., & Tran Minh, N. 2013b, A&A, submitted
Mathis, S., Talon, S., Pantillon, F.-P., & Zahn, J.-P. 2008, Sol. Phys., 251, 101
Mosser, B., Goupil, M. J., Belkacem, K., et al. 2012, A&A, 548, A10
Neiner, C., Floquet, M., Samadi, R., et al. 2012a, A&A, 546, A47
Neiner, C., Mathis, S., Saio, H., et al. 2012b, A&A, 539, A90
Pedlosky, J. 1982, Geophysical fluid dynamics
Rogers, T. M., Lin, D. N. C., & Lau, H. H. B. 2012, ApJ, 758, L6
Samadi, R. & Goupil, M.-J. 2001, A&A, 370, 136
Talon, S. & Charbonnel, C. 2005, A&A, 440, 981

SF2A 2013
L. Cambrésy, F. Martins, E. Nuss and A. Palacios (eds)

IMPACT OF NEW ATOMIC DATA FOR THE FORMATION OF THE MG I 4571 Å LINE IN BENCHMARK STARS

T. Merle[1], F. Thévenin[2], M. Guitou[3], N. Feautrier[4], A. Spielfiedel[4] and O. Zatsarinny[5]

Abstract.
The Non-Local Thermodynamic Equilibrium (NLTE) formation of magnesium lines in cool stars can be improved by the inclusion of very recent quantum mechanical treatment of inelastic collisions with electrons and hydrogen atoms. We present the study of the intercombination line at 4571 Å in the atmosphere of four benchmark late-type stars: the Sun, Arcturus, HD 84937 (metal-poor dwarf) and HD 122563 (metal-poor giant). This preliminary study relies on a simplified model atom of Mg I with a consistent set atomic data rather than a complete model atom. In this context, results show that even if the 4571 Å line is formed close to LTE in the Sun, its line source function can be larger than the Planck function, especially in metal-poor giant for which we expect to have positive abundance corrections.

Keywords: Non-LTE, line formation, benchmark stars, magnesium, intercombination line

1 Introduction

The magnesium is one of the best α-element to understand the history of the chemical enrichment of our Galaxy and dwarf galaxies in the Local Group (Gehren et al. 2006; Andrievsky et al. 2010). But the departures from LTE suffer the lack of reliable data for the inelastic collisions with neutral hydrogen which could be non-negligible in atmosphere of cool stars (Mashonkina 1996; Barklem et al. 2011). Until recently, the inelastic collisions with H atoms in late-type stars have been neglected or treated with the Drawin's formula (Drawin 1969). This recipe, based on the corresponding oscillator strength of the radiative transition, is scaled by a fudge factor $S_{\rm H}$ to vary the intensity of the H collision rates (see e.g., for magnesium, Shimanskaya et al. 2000; Gehren et al. 2004; Mashonkina 2013).

With the computations of the accurate potentials for the MgH system (Guitou et al. 2010, 2011), the quantum cross-sections in Mg + H collisions (Belyaev et al. 2012) and their collisions rates (Barklem et al. 2012), it is now possible to explore the role of such inelastic collisions with hydrogen for Mg I in late-type stars. In this proceeding, we focus on the formation of the spin-forbidden intercombination line at 4571 Å which rises from the ground stage of Mg I. We performed calculations for benchmark stars for which high resolution and high signal-to-noise ratio are available for comparison. However, no NLTE abundance corrections are attempted here, since a more complete model atom is required to reach good accuracy on population densities.

2 A simplified model atom of Mg I

To assess the impact of the new atomic data on the NLTE abundance corrections, we decided to build a simplified model atom including only energy levels for which we have quantum mechanical data for collision with hydrogen. The model includes the first seven low-lying plus the continuum levels. The oscillator strengths are from the VALD database excepted for the Mg I triplet for which we used data from Aldenius et al. (2007),

[1] Institut d'Astronomie et d'Astrophysique, Université Libre de Bruxelles, CP 226, Bvd du Triomphe, 1050 Brussels, Belgium
[2] Laboratoire Lagrange, UMR7293, Université de Nice Sophia-Antipolis, CNRS, OCA, 06300 Nice, France
[3] Université Paris-Est Marne-la-Vallée, MSME, UMR 8208 CNRS, 77454 Marne-la-Vallée, France
[4] LERMA, Observatoire de Paris, 92195 Meudon Cedex, France
[5] Department of Physics and Astronomy, Drake University, Des Moines, IA 50311, USA

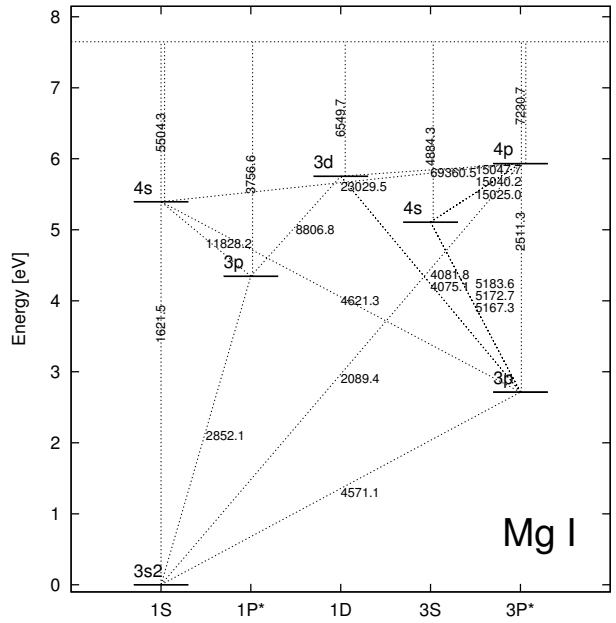

Fig. 1. Grotrian diagram of the Mg I model atom used in this work. Radiative bound-bound and bound-free at the threshold transitions are labeled in Å.

the 8806 and 11828 Å lines for which we use NIST data with an excellent accuracy. The oscillator strength of the 4571 Å is $\log gf = -5.69$. Photoionizations are from the TOPBASE with a treatment following Merle et al. (2011). The Grotrian diagram of the simplified model atom of Mg I is shown in Fig. 1.

For the treatment of inelastic collisions we compute from published rates or cross-sections the effective collision strength Υ as a function of the local temperature T for bound-bound transitions (i lower level $\rightarrow$ j upper level) with electrons (e) and with hydrogen atoms (H). The collisions rates can be then computed as follows:

$$C_{ij}^{\rm e}(T) = 8.629 \times 10^{-6}\ n_{\rm e}\ \frac{\Upsilon_{ij}^{\rm e}(T)}{g_i\sqrt{T}} {\rm e}^{-E_{ij}/kT} \quad [{\rm s}^{-1}] \tag{2.1}$$

$$C_{ij}^{\rm H}(T) = 2.014 \times 10^{-7}\ n_{\rm H}\ \frac{\Upsilon_{ij}^{\rm H}(T)}{g_i\sqrt{T}}\ {\rm e}^{-E_{ij}/kT} \quad [{\rm s}^{-1}] \tag{2.2}$$

where $n_{\rm e}$ and $n_{\rm H}$ are the number density of electrons and hydrogen atoms respectively, g_i the statistical weight of the lower level, k the Boltzmann constant and E_{ij} the energy of the transition. $\Upsilon_{ij}^{\rm e}$ and $\Upsilon_{ij}^{\rm H}$ are dimensionless quantities symmetric with respect to the transition $i \iff j$ ($\Upsilon_{ij} = \Upsilon_{ji}$).

The effective collision strengths with electrons $\Upsilon_{ij}^{\rm e}$ we used are based on quantum mechanical (QM) cross-sections of Zatsarinny et al. (2009) for resonance transitions and on unpublished data of the same author for the remaining transitions. The QM approach is based on the R-matrix close coupling method. From the collision cross-sections $\sigma_{ij}^{\rm e}$ (expressed in units of πa_0^2, with a_0 the Bohr radius) we calculate:

$$\Upsilon_{ij}^{\rm e}(T) = g_i \frac{kT}{E_{\rm H}^{\infty}} \int_0^{\infty} \sigma_{ij}^{\rm e}(x)(x + x_{ij}){\rm e}^{-x}{\rm d}x \tag{2.3}$$

where g_i is the statistical weight of the lower level implied in the collision, $E_{\rm H}^{\infty}$ the Rydberg energy and $x_{ij} = E_{ij}/kT$. Bound-free collisions with electrons are treated using the traditional semi-classical (SC) approach of Seaton (1962b).

The effective collision strengths with hydrogen atoms we used are based on either the SC approach of Drawin (1969), using the formulation of Lambert (1993) to deduce:

$$\Upsilon_{ij}^{\rm H}(T) = 4\sqrt{2}\ \frac{m_{\rm e}(m_{\rm H} + m_{\rm Mg})}{m_{\rm H}^2}\ g_i f_{ij}\ \frac{E_{\rm H}^{\infty}}{E_{ij}}\ \frac{1 + 2/x_{ij}}{x_{ij}} \tag{2.4}$$

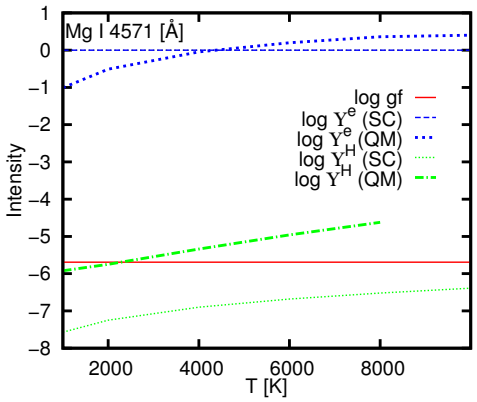

Fig. 2. Comparison of oscillator/collision strengths for the 4571 Å line. Semi-classical (SC) formulae are used for effective collision strengths with electrons $\Upsilon^{\rm e}_{ij}$ from Seaton (1962a) and with neutral hydrogen $\Upsilon^{\rm H}_{ij}$ from Drawin (1969). Quantum mechanical (QM) cross-sections are used for effective collision strengths with electrons $\Upsilon^{\rm e}_{ij}$ from Zatsarinny et al. (2009) (and private communication) and with neutral hydrogen $\Upsilon^{\rm H}_{ij}$ from Barklem et al. (2012).

or on the QM approach of Guitou et al. (2011); Belyaev et al. (2012); Barklem et al. (2012) to deduce:

$$\Upsilon^{\rm H}_{ij}(T) = 4.965 \times 10^6 g_j \sqrt{T}\ \langle \sigma_{ji} v \rangle \tag{2.5}$$

where $\langle \sigma_{ji} v \rangle$ is the downward rate coefficient, in units of cm^3 s^{-1}, computed for the transitions between the seven lowest states of Mg I by Barklem et al. (2012).

An important mechanism to account for is the charge exchange process Mg I+ H $\Longleftrightarrow$ Mg II+ H$^-$ for which we can also define an effective collision strength $\Upsilon^{\rm H}_{\rm ce}$:

$$\Upsilon^{\rm H}_{\rm ce}(T) = 2.483 \times 10^6 g_c \sqrt{T} \langle \sigma_{ci} v \rangle \tag{2.6}$$

where g_c is the statistical weight of the ionic state and $\langle \sigma_{ci} v \rangle$ is tabulated in Barklem et al. (2012).

We compare the SC and QM effective collision strengths with electrons and hydrogen atoms for the 4571 Å line in Fig. 2. The oscillator strength (red line) does not depend on the temperature and its value is very small compared with values for allowed transitions. Effective collision strength with electrons (in blue) using SC approach (here default value set to one for an intercombination line) is of the same order of magnitude as in the QM approach excepted at very low temperature for which the difference can reach one order of magnitude. The difference in effective collision strength with hydrogen (in green) between SC and QM approaches reaches two orders of magnitude at high temperature.

3 Theoretical results for the 4571 Å line

We used the 1D NLTE radiative transfer code MULTI (Carlsson 1986) version 2.2, modified to read and compute properly collision rates from effective collision strengths with electrons and hydrogen atoms. Line blanketing effect is taken into account through the inclusion of background atomic lines of other main species. Statistical equilibrium are computed using model atmospheres from MARCS database (Gustafsson et al. 2008) for the Sun, a metal-poor dwarf HD 84937 (model: $6250/4.0/-2.00/+0.40$), Arcturus (model: $4250/1.5/-0.50/+0.20$) and a metal-poor giant HD 122563 (model: $4500/1.5/-2.50/+0.40$). Excepted for the Sun, the atmospheric parameters are rough estimates that have to be refined for detailed comparisons with observations which is under the scope of this study.

Computations of statistical equilibrium are done with QM approach for collisions with electrons and with (i) no H collisions, (ii) SC H collisions (Drawin's formula with a scaling factor $S_{\rm H} = 1$) or (iii) QM H collisions (including charge exchange process). The departure coefficients are defined by: $b_i = n_i/n_i^*$ where n_i^* is the number density of level i at LTE. The computed statistical equilibrium for the 4 benchmark stars show a general depopulation of the levels due to the overionization of Mg I by UV radiation of non-local origin (trend well known for neutral minority species in atmosphere of late-type stars). Computations including H collisions reduce departures from LTE. The departures from LTE are more reduced if the QM H collisions are used.

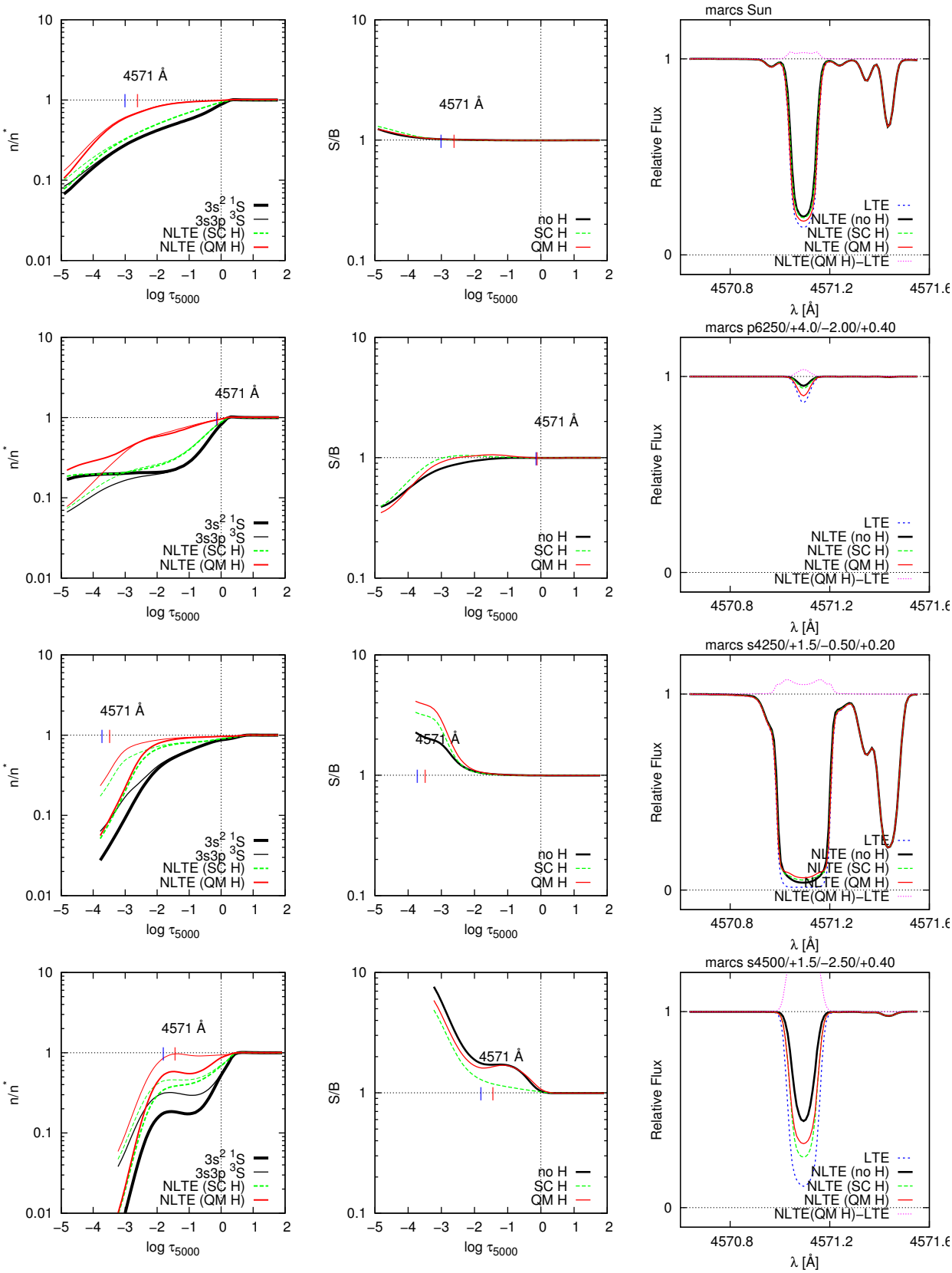

Fig. 3. Formation of the Mg I 4571 Å line in model atmospheres of benchmark stars (atmospheric parameters given at the top of right panels with $T_{\rm eff}/\log g/$[Fe/H]/[α/Fe]). Black profiles are NLTE results with no H collisions; green profiles with Semi-Classic (SC) H collisions and red profiles with quantum mechanical (QM) H collisions. Blue profiles are LTE results. Vertical dashes show the optical depths where the line cores are formed in LTE (blue) and in NLTE (red). **Left:** departure coefficients of the implied levels. **Middle:** line source functions. **Right:** line profiles.

This is contrary to what is expected since it was claimed that Drawin formula gives an upper limit toward the thermalization of the departure coefficients. At solar and subsolar metallicities (in the Sun and Arcturus) the line forms in the upper part of the atmosphere whereas in metal-poor stars the line forms deeper due to a lower abundance value.

In the dwarf stars (two upper series of panels in Fig. 3), upper and lower departure coefficients follow the same trend leading to a source function equals to the Planck function at the line core formation depth. Thus the divergence of the NLTE and LTE profiles is entirely due to the NLTE effect on the line opacity. The reduction of the line opacity induced a weaker line in NLTE. As the depopulation is the lower when using QM H collisions, then the corresponding profile is the closest to the LTE profile.

In the giants (two lower series of panels in Fig. 3), the line formation follow a different process since the upper and lower departure coefficients diverge at the line core formation depth. This will influence the line source functions as shown in middle panels of Fig. 3, normalized to the Planck function. In the Wien regime, $S_{ij}/B_{ij} = b_j/b_i$. The line source function is larger than the Planck function at the line core formation depth leading to weaken the line. NLTE effects on line opacity and source function act in the same way to reduce the line profile. For this line in giants, SC H collisions will give lower abundance correction than QM H ones. And specifically for Arcturus, taking no H collisions into account will provide the lower abundance correction since the divergence between upper and lower departure coefficient is the smallest in this case. In the metal-poor giant, the source function is lower when using SC H collisions leading to a profile closer to the LTE one. Whatever SC or QM H collision, we expect to have strong positive NLTE abundance correction (> 0.1 dex) in metal-poor giants for this line.

4 Conclusion

We have studied the NLTE line formation of the intercombination line at 4571 Å of neutral magnesium in four benchmark stars with the use of semi-classic or quantum mechanical treatment of inelastic collisions with hydrogen atoms. The formation of this spin-forbidden line is known to be controlled by collisions (at least in the Sun) giving a line source function very close to LTE. This is no longer the case in giants stars where departures from LTE also affect the line source function especially in metal-poor giants for which we expect to have strong positive abundance correction (probably larger than +0.1 dex).

References

Aldenius, M., Tanner, J. D., Johansson, S., Lundberg, H., & Ryan, S. G. 2007, A&A, 461, 767

Andrievsky, S. M., Spite, M., Korotin, S. A., et al. 2010, A&A, 509, A88

Barklem, P. S., Belyaev, A. K., Guitou, M., et al. 2011, A&A, 530, A94

Barklem, P. S., Belyaev, A. K., Spielfiedel, A., Guitou, M., & Feautrier, N. 2012, A&A, 541, A80

Belyaev, A. K., Barklem, P. S., Spielfiedel, A., et al. 2012, Phys. Rev. A, 85, 032704

Carlsson, M. 1986, Uppsala Astronomical Observatory Reports, 33

Drawin, H. W. 1969, Zeitschrift fur Physik, 225, 483

Gehren, T., Liang, Y. C., Shi, J. R., Zhang, H. W., & Zhao, G. 2004, A&A, 413, 1045

Gehren, T., Shi, J. R., Zhang, H. W., Zhao, G., & Korn, A. J. 2006, A&A, 451, 1065

Guitou, M., Belyaev, A. K., Barklem, P. S., Spielfiedel, A., & Feautrier, N. 2011, Journal of Physics B Atomic Molecular Physics, 44, 035202

Guitou, M., Spielfiedel, A., & Feautrier, N. 2010, Chemical Physics Letters, 488, 145

Gustafsson, B., Edvardsson, B., Eriksson, K., et al. 2008, A&A, 486, 951

Lambert, D. L. 1993, Physica Scripta Volume T, 47, 186

Mashonkina, L. 2013, A&A, 550, A28

Mashonkina, L. J. 1996, in Astronomical Society of the Pacific Conference Series, Vol. 108, M.A.S.S., Model Atmospheres and Spectrum Synthesis, ed. S. J. Adelman, F. Kupka, & W. W. Weiss, 140

Merle, T., Thévenin, F., Pichon, B., & Bigot, L. 2011, MNRAS, 418, 863

Seaton, M. J. 1962a, Proceedings of the Physical Society, 79, 1105

Seaton, M. J. 1962b, in Atomic and Molecular Processes, ed. D. R. Bates, 375–+

Shimanskaya, N. N., Mashonkina, L. I., & Sakhibullin, N. A. 2000, Astronomy Reports, 44, 530

Zatsarinny, O., Bartschat, K., Gedeon, S., et al. 2009, Phys. Rev. A, 79, 052709

SF2A 2013
L. Cambrésy, F. Martins, E. Nuss and A. Palacios (eds)

A STUDY OF THE RED SUPERGIANT BETELGEUSE AT HIGH ANGULAR RESOLUTION

M. Montargès[1], P. Kervella[1], G. Perrin[1] and K. Ohnaka[2]

Abstract. Betelgeuse (α Ori) is a M2Iab star, prototype for the red supergiant class. These stars contributes to the chemical enrichment of the interstellar medium (ISM) through their heavy mass loss and thanks to the IIP type supernova of whom they are the progenitors. With its proximity ($\sim$ 130 pc) and thus of its large apparent diameter ($\sim$ 42 mas), Betelgeuse is a good candidate for a detailed study of the atmosphere of a red supergiant

Our analysis of VLTI/AMBER data allowed to characterize the close environment of the star: its molecular envelope (MOLsphere). Using a thin layer model at le Local Thermodynamical Equilibrium (LTE), we obtained its angular diameter, temperature as well as the column densities for water vapor and carbon monoxide (CO). For the K band continuum, we reconstructed a one dimension image (profile) and we quantified the inhomogeneities of the photosphere.

Keywords: infrared: stars – techniques: interferometric – stars: supergiants – stars: late-type – stars: atmospheres – stars: individual: Betelgeuse

1 Introduction

Massive stars as Betelgeuse are the chemical laboratories of the Galaxy: when they become supernovae, they synthesize heavy elements. Even during their supergiant phase, they participate to the chemical evolution of the ISM with their heavy mass loss. Material is ejected from the star and is becoming more and more complex as it is cooling, forming molecules and dust.

Betelgeuse has been regularly observed for a century. Many significant results were obtained in the last decade. The circumstellar environment (CSE) of the star was heavily explored: Tsuji (2000) proposed a molecular envelope to fit their observations (the MOLsphere), its characteristics and its composition were computed by Perrin et al. (2004, 2007) using IOTA and VLTI/MIDI. Using VLT/NACO and VLT/VISIR Kervella et al. (2009, 2011) observed the dusty envelope of the star up to several tens of stellar radii. Meanwhile, Ohnaka et al. (2011) observed with VLTI/AMBER for the first time the dynamics of the MOLsphere and particularly motion of CO. The photosphere was also investigated: Haubois et al. (2009) observed two bright spots with the IOTA interferometer in the H band.

Yet, the process which triggers the mass loss has not yet been unveiled. The inhomogeneous shape of the circumstellar envelope and the link between each layer is also unknown and still requires further studies. We focus here on the close ($\sim 1.2R_\star$) molecular layer composed of CO and water vapor: we investigate its size and composition (Sect. 3) we also analyze the shape of the photosphere (Sect. 4).

2 Observations and data reduction

2.1 Observations

Betelgeuse was observed with the ESO Very Large Telescope Interferometer (VLTI, Haguenauer et al. 2010) using the Astronomical Multi-BEam combineR, AMBER (Petrov et al. 2007) on January and February 2011. We used the medium spectral resolution of the instrument ($R = \frac{\lambda}{\Delta\lambda} \sim 1500$) in the H band from 1.45 to 1.80 μm

[1] LESIA, Observatoire de Paris, CNRS, UPMC, Université Paris-Diderot, 5 place Jules Janssen, 92195 Meudon, France
[2] Max-Planck-Institut für Radioastronomie, Auf dem Hügel 69, 53121 Bonn, Germany

and in the K band from 2.1 to 2.45 μm. AMBER recombines the light from two or three telescopes, either Auxiliary Telescopes (ATs) of 1.8 m of diameter or Unit Telescopes (UTs) of 8.2 m. Our observations were performed with the ATs in the E0-G0-H0, E0-G0-I1 and G0-H0-I1 configurations of the VLTI.

Data from January 1st were obtained to get a suitable configuration of the instrument and thus are not relevant for our work here.

2.2 Data Reduction

We reduced the data using the AMBER data reduction software also know as *amdlib* in its version 3.0.3 (Tatulli et al. 2007). This package produces the interferometric observables which give us information about the object's Fourier transform: the visibilities are directly its amplitude and the differential phases (DP) indicate the photocenter shift in a spectral line compared to the continuum and the closure phase (CP) is defined as the sum of the three phases along the close triangle formed by the three baselines: $\phi_{\rm CP} = \phi_{12} + \phi_{23} + \phi_{31}$. This last observable is independent from the atmospheric perturbations and indicates asymmetries in the object.

As Betelgeuse is one of the brightest source of the infrared sky and has one of the bigger angular diameter for a star, we had to use a particular reduction method to estimate the error bars and discriminate among standard and corrupted files. This procedure is described in Montargès et al. (2013). The AMBER pipeline does not include the spectral calibration : we used the telluric lines in our hotter calibrator (HR-1543, spectra type F6V) to perform it.

3 Model fitting

3.1 K band

The K band spectrum is clearly divided in two parts: the continuum domain ($\lambda < 2.245$ μm) where we are mostly sensitive to the star photosphere and the absorption band domain ($\lambda > 2.245$ μm) where are located CO and water vapor absorption band revealing the MOLsphere.

3.1.1 Continuum analysis ($\lambda < 2.245$ μm)

The continuum data allow us to estimate the angular diameter of the star. We use two different models: the uniform disk (UD) and the power-law limb-darkened disk (LDD) described in Hestroffer (1997). As we are only interested in the shape of the star at large scale (the diameter) we only use the low spatial frequency data (first lobe of the visibility function: $f < 50$ arcsec^{-1}). The results of the fits are summarized in Table 1 and the corresponding visibility functions are plotted on the left pannel of Fig. 1 together with the data.

Table 1. Best fit values for the uniform disk ($I = I_0$) and limb-darkened disk ($I = I_0\mu^\alpha$) models.

Model	θ (mas)	α	χ^2
UD	41.01 ± 0.02	-	5.27
LDD	42.28 ± 0.07	0.155 ± 0.009	4.89

Townes et al. (2009) reported a significant decrease of the apparent diameter of Betelgeuse from their 11 μm observations, Ohnaka et al. (2011) analyzed the evolution of the K band diameter of the star along the same period using results from Dyck et al. (1992), Perrin et al. (2004) and Ohnaka et al. (2009, 2011). They saw no evidence for a strong variation. On the right pannel of Fig. 1 , we added our result at the end of this evolution of the K band diameter and distinguished between the data including only the continuum and the whole K band. Clearly, the star appears bigger when considering all the K band: this comes from the contribution of the MOLsphere in the CO and water vapor absorption bands at the highest wavelengths of this domain. Our measurement indicates again that the size of Betelgeuse remains constant over time.

3.1.2 Absorption bands ($\lambda > 2.245$ μm)

As we previously said, wavelengths longer than 2.245 μm contains CO and water vapor absorption lines which allow us to probe the MOLsphere. We model this structure by a single thin layer containing the two molecules at the local thermodynamical equilibrium (LTE) whom lines are computed with the linelist from Goorvitch

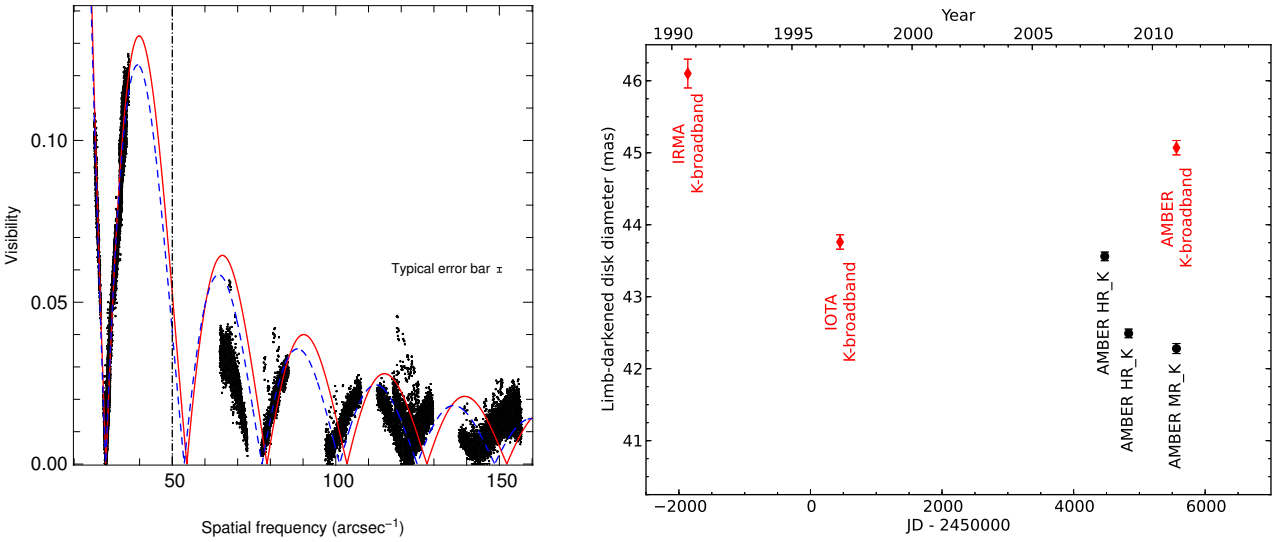

Fig. 1. Left: Best fit model of the continuum data. AMBER continuum data in black. The red continuous curve represent the best fit uniform disk model and the blue dashed curve represent the best fit power-law type limb-darkened model. The dashed-doted black vertical line represents the upper limit of the spatial frequencies considered for our UD/LDD fits. **Right:** Overview of limb-darkened disk measurements of Betelgeuse. The values considering only the continuum of the K band are displayed in black dots, and the K broadband measurements are in red diamonds.

(1994) and Partridge & Schwenke (1997). To model the star we used a stellar atmosphere from the Kurucz grid* (Castelli & Kurucz 2003; Kurucz 2005). The resulting analytical expression is given by :

$$I_{N_{\rm CO},N_{\rm H_2O}}(\lambda,\beta) = I_{\rm Kurucz}(\lambda)\ exp\left(\frac{-\tau(N_{\rm CO},N_{\rm H_2O};\lambda)}{\cos(\beta)}\right) + B(\lambda,T_{\rm MOL})\left[1-exp\left(\frac{-\tau(N_{\rm CO},N_{\rm H_2O};\lambda)}{\cos(\beta)}\right)\right] \quad (3.1)$$

if $\sin(\beta) \leq \frac{\theta_*}{\theta_{\rm MOL}}$ and otherwise:

$$I_{N_{\rm CO},N_{\rm H_2O}}(\lambda,\beta) = B(\lambda,T_{\rm MOL})\left[1-exp\left(\frac{-2\tau(N_{\rm CO},N_{\rm H_2O};\lambda)}{\cos(\beta)}\right)\right] \quad (3.2)$$

Where the five parameters of the model are the photospheric diameter θ_*, the MOLsphere diameter $\theta_{\rm MOL}$, the MOLsphere temperature $T_{\rm MOL}$, the CO and H_2O column densities $N_{\rm CO}$ and $N_{\rm H_2O}$. $B(\lambda,T)$ is the Planck function, β is the angle between the line of sight and the center of the star at the layer surface and $\tau(N_{\rm CO},N_{\rm H_2O};\lambda)$ is the MOLsphere opacity. The complete model is illustrated on Fig. 2.

Then we computed the Hankel transform to get the visibility:

$$V_\lambda(x) = \frac{\int_0^1 I(\lambda,r)J_0(rx)rdr}{\int_0^1 I(\lambda,r)rdr} \quad (3.3)$$

We did not used the data from the core of the CO band heads because amdlib was not able to fit the corresponding fringe pattern, certainly because the signal to noise ratio (SNR) was too low. Consequently, to get data points in this important wavelength domain, we included the AMBER photometry to complete our dataset. We also had to restrain ourselves to wavelengths shorter than 2.348 μm: for longer wavelengths it seems that this single model layer is not complex enough and not correctly reproducing the data (for example the spectrum on pannel right of Fig. 2). We would have had to introduce a second layer, adding 4 parameters to the fit which was already highly degenerated.

To get the best fit parameters of our data, we minimized the χ^2:

$$\chi^2(T_{\rm MOL},\theta_{\rm MOL}) = \sum_{i=1}^{N}\left(\frac{Y_i - M(T_{\rm MOL},\theta_{\rm MOL},N_{\rm CO},N_{\rm H_2O};S_i)}{\sigma_i}\right)^2 \quad (3.4)$$

*http://kurucz.harvard.edu/

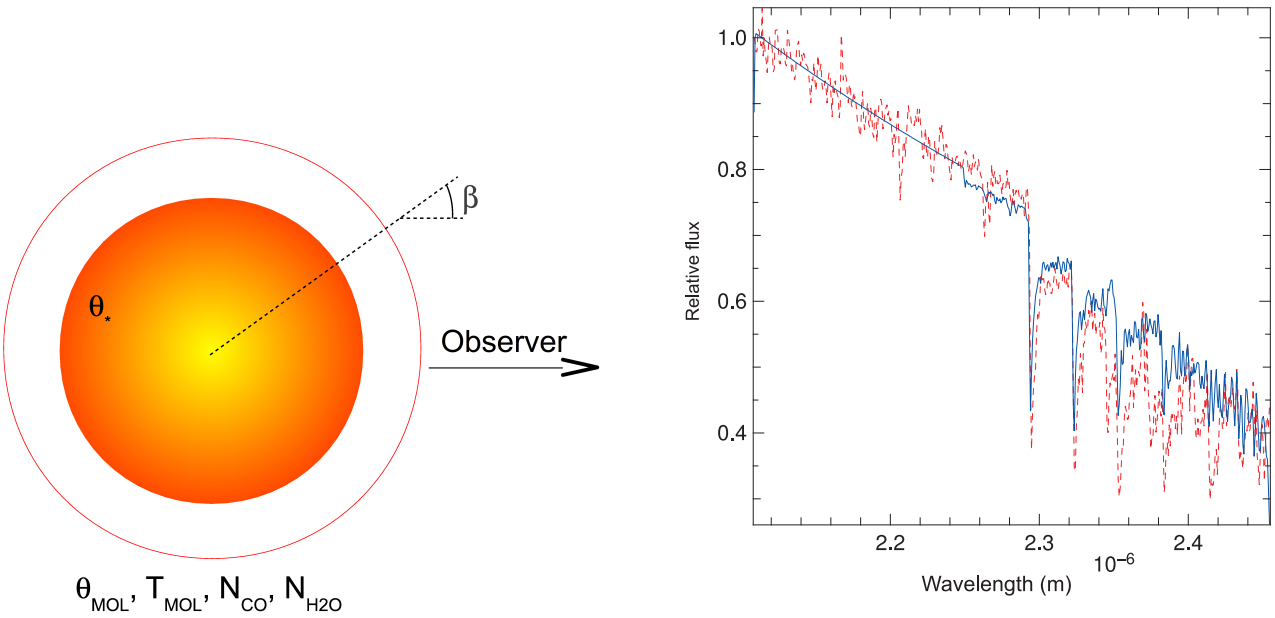

Fig. 2. Left: Illustration of the single layer model of the MOLsphere. β is the angle between the radius vector and the line of sight at the layer surface. **Right:** The red dashed line is the spectrum obtained from the Betelgeuse AMBER data and the blue continuous line is the spectrum obtained from the single layer model. We used the best fit values from Table 2.

Where $S_i = B_p/\lambda$ are the sampled spatial frequencies, Y_i the AMBER data (spectrum and visibilities) and M the corresponding value of the model.

The five parameters of the model are not independent : the size and the temperature of the MOLsphere are of course correlated but the temperature and the two column densities and the column densities themselves are also related. Therefore we use χ^2 map to find the absolute minimum of this function. First we fix the angular diameter of the star to the value of the uniform disk found in Sect. 3.1.1. Then, we fit the $N_{\rm CO}$ on a grid of ($\theta_{\rm MOL}$, $T_{\rm MOL}$) for a constant $N_{\rm H_2O}$. This gives us a χ^2 map associated to a $N_{\rm CO}$ map. To get the equivalent maps for $N_{\rm H_2O}$ we switch round the two column densities and perform the fits again using the best fit $N_{\rm CO}$ value previously found. We iterate this process again and again until the column densities stay in their error bars. This procedure allows us to derive the best fit values for the MOLsphere parameters listed in Table 2.

Table 2. Best fit values with our single thin layer model of the MOLsphere

Parameter	Value
θ_*	41.01 mas (fixed)
$\rm T_{MOL}$	2300 ± 120 K
$\theta_{\rm MOL}$	51.38 ± 1.71 mas
$\rm N_{CO}$	$3.01^{+2.00}_{-0.498} \times 10^{21}$ cm^{-2}
$\rm N_{H_2O}$	$3.28^{+1.73}_{-0.462} \times 10^{20}$ cm^{-2}
χ^2	~ 6

Remarkably, the two χ^2 map for the CO and the water vapor give the same couple of parameters for the size and temperature of the MOLsphere, confirming our hypothesis of a single layer for the two molecules.

3.2 H band

We successfully reduced and calibrated the data in the H band but were unable to clearly distinguish continuum and absorption bands consequently it was not possible to fit the photosphere diameter. Moreover, we did not managed to reproduce all the observed absorption lines using our single layer model : more layers and/or more molecules are needed to reproduce our observations and probably a better spectral resolution.

4 1D profile reconstruction

Our AMBER data on Betelgeuse contain non-zero and non-π closure phases, signatures of inhomogeneities at the star surface. Classical model fitting have proven inefficient to analyze evolving structures observed on star surfaces: one cannot guess the number and localisation of spots. Thus we use the image reconstruction algorithm MIRA (Thiébaut 2008; Renard et al. 2011) which produce an image given a prior to constrain the general shape of the star but also by fitting the data (visibilities and closure phases). Instead of simply minimizing a χ^2, the algorithm minimize a cost function taking into account the classical χ^2 and the prior weighted by the hyper-parameter μ:

$$F_{\rm Cost} = F_{\rm Data} + \mu F_{\rm Prior} \tag{4.1}$$

The best fit limb-darkened disk model found in Sect. 3.1.1 was used as prior. We use a quadaratic regularization which discriminates the strong differences between the prior image and the reconstructed one. Other regularization methods and different values of the hyper-parameter give similar result: this strengthen the reliability of our reconstruction which represent the intensity of the star as it was observed by VLTI/AMBER.

The accuracy of the reconstructed image is partially determined by the coverage of the (u,v) plane. Our VLTI/AMBER data have a very linear (u,v) coverage which makes them more suited to a profile reconstruction along this best covered direction (azimuth 71.39°). As illustrated on Fig. 3 pannel left, we took a 8 mas wide slice along this direction on which we averaged the reconstructed intensity to obtain a profile: the result is a "smooth" convolution of the reconstructed intensity by our rectangular window. We divided this profile by the corresponding profile of the prior to obtain only the contribution of the inhomogeneities (Fig. 3, pannel right).

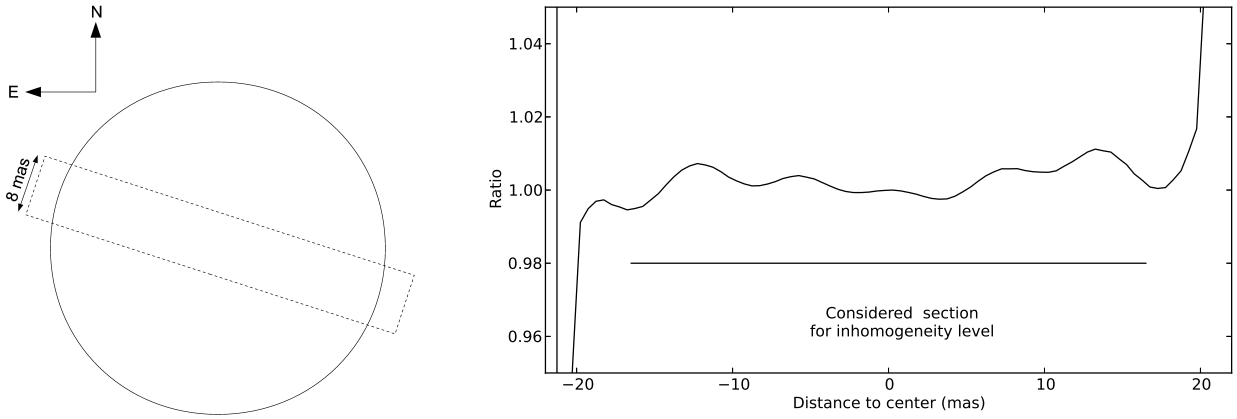

Fig. 3. Left: Considered fraction of the star for the averaged profile. **Right:** Ratio of the final reconstructed profile by the prior (limb-darkened disk). North-East is on the left side and South-West on the right side

To avoid edge fluctuations caused by this ratio we only consider the profile ±16.5 mas from the star center. There we computed an inhomogeneity level (defined in Eq. 4.2) of 0.809 %. It appears that we did not observe strong inhomogeneities at the star surface but we averaged the reconstructed intensity on a 8 mas wide slice meaning that we are not considering the whole star surface.

$$\tau_{\rm inhom} = \frac{I_{\rm max} - I_{\rm min}}{I_{\rm min} + I_{\rm max}} \tag{4.2}$$

5 Conclusions

From VLTI/AMBER data in the K band, we obtained new values for the angular diameter of α Ori which are consistent with the previous ones at the same wavelength. We derived characteristics of the MOLsphere, particularly we got values for the column densities of CO and water vapor. However, our analysis only covers the first two CO band heads of the K band : to get consistent results including the other absorption bands of CO, a more complex model is needed including several molecular thin layers or more probaby thick layers with parameters highly correlated. From a profile reconstruction in the continuum, by deriving an inhomogeneity

level we concluded that there were no signature of strong structures on the photosphere, along our best sampled azimuthal direction.

These observations are part of a wider program aimed at understanding the shape and composition of the CSE of Betelgeuse and involving measurements in several wavelength domains and angular scales but also a monitoring at several epochs.

We are grateful to ESOs Director General Prof. Tim de Zeeuw for the allocation of observing time to our program, as well as to the Paranal Observatory team for the successful execution of the observations. The research leading to these results has received funding from the European Community's Seventh Framework Programme under Grant Agreement 226604. We acknowledge financial support from the Programme National de Physique Stellaire (PNPS) of CNRS/INSU, France. We used the SIMBAD and VIZIER databases at the CDS, Strasbourg (France), and NASAs Astrophysics Data System Bibliographic Services. This research has made use of the `AMBER data reduction package` of the Jean-Marie Mariotti Center[†]

References

Castelli, F. & Kurucz, R. L. 2003, in IAU Symposium, Vol. 210, Modelling of Stellar Atmospheres, ed. N. Piskunov, W. W. Weiss, & D. F. Gray, 20P

Dyck, H. M., Benson, J. A., Ridgway, S. T., & Dixon, D. J. 1992, AJ, 104, 1982

Goorvitch, D. 1994, ApJS, 95, 535

Haguenauer, P., Alonso, J., Bourget, P., et al. 2010, in Society of Photo-Optical Instrumentation Engineers (SPIE) Conference Series, Vol. 7734, Society of Photo-Optical Instrumentation Engineers (SPIE) Conference Series

Haubois, X., Perrin, G., Lacour, S., et al. 2009, A&A, 508, 923

Hestroffer, D. 1997, A&A, 327, 199

Kervella, P., Perrin, G., Chiavassa, A., et al. 2011, A&A, 531, A117

Kervella, P., Verhoelst, T., Ridgway, S. T., et al. 2009, A&A, 504, 115

Kurucz, R. L. 2005, Memorie della Societa Astronomica Italiana Supplementi, 8, 14

Montargès, M., Kervella, P., Perrin, G., & Ohnaka, K. 2013, in EAS Publications Series, Vol. 60, EAS Publications Series, ed. P. Kervella, T. Le Bertre, & G. Perrin, 167–172

Ohnaka, K., Hofmann, K.-H., Benisty, M., et al. 2009, A&A, 503, 183

Ohnaka, K., Weigelt, G., Millour, F., et al. 2011, A&A, 529, A163

Partridge, H. & Schwenke, D. W. 1997, J. Chem. Phys., 106, 4618

Perrin, G., Ridgway, S. T., Coudé du Foresto, V., et al. 2004, A&A, 418, 675

Perrin, G., Verhoelst, T., Ridgway, S. T., et al. 2007, A&A, 474, 599

Petrov, R. G., Malbet, F., Weigelt, G., et al. 2007, A&A, 464, 1

Renard, S., Thiébaut, E., & Malbet, F. 2011, A&A, 533, A64

Tatulli, E., Millour, F., Chelli, A., et al. 2007, A&A, 464, 29

Thiébaut, E. 2008, in Society of Photo-Optical Instrumentation Engineers (SPIE) Conference Series, Vol. 7013, Society of Photo-Optical Instrumentation Engineers (SPIE) Conference Series

Townes, C. H., Wishnow, E. H., Hale, D. D. S., & Walp, B. 2009, ApJ, 697, L127

Tsuji, T. 2000, ApJ, 538, 801

[†]Available at http://www.jmmc.fr/amberdrs

SF2A 2013
L. Cambrésy, F. Martins, E. Nuss and A. Palacios (eds)

HIGH RESOLUTION SPECTROSCOPY OF M SUBDWARFS

A. S. Rajpurohit[1], C. Reylé[1], M. Schultheis[2] and F. Allard[3]

Abstract. M subdwarfs are metal poor and cool stars. They are important probes of the old galactic populations. However, they remain elusive due to their low luminosity. Observational and modeling efforts are required to fully understand the physics and to investigate the effect of metallicity in their cool atmospheres. We perform a detail study of a sample of subdwarfs to determine their stellar parameters and constrain the atmosphere models. We present UVES/VLT high resolution spectra of 21 M subdwarfs. Our atlas covers the optical region from 6400$\AA$ up to the near infrared at 10000$\AA$. We show spectral details of cool atmospheres at very high resolution (R$\sim$ 40 000) and compare with synthetic spectra computed from the recent BT-Settl atmosphere models. Our comparison shows that molecular features (TiO, VO, CaH), and atomic features (Fe, Ti, Na, K) are well fitted by current models. We produce an effective temperature versus spectral type relation all over the subdwarf spectral sequence.

Keywords: subdwarfs, atmosphere

1 Introduction

Due to their lower metallicity and intrinsic faintness, M subdwarfs lie below their solar-metallicity counterpart in the Hertzsprung-Russel diagram. Subdwarfs are typically very old (10 Gyr or more) and belonging to the old Galactic populations: old disc, thick disc and spheroid, as shown by their spectroscopic features, kinematics properties and ages (Digby et al. 2003; Lépine et al. 2003; Burgasser et al. 2003). Detailed studies of their complex spectral energy distributions give new insights on the role of metallicity in the opacity structure, chemistry and evolution of cool atmospheres, and fundamental issues on spectral classification and temperature versus luminosity scales. Gizis (1997) proposed a first classification of M subdwarfs (sdM) and extreme subdwarfs (esdM) based on TiO and CaH band strenghts in low resolution optical spectra. Lépine et al. (2007) has recently revised the adopted classification, and proposed a new classification for the most metal poor, the ultra subdwarfs (usdM). Jao et al. (2008) compared model grids with the optical spectra to characterize the spectral energy distribution of subdwarfs by three parameters: temperature, gravity, and metallicity, and thus gave an alternative classification scheme of subdwarfs. Metallicities have been recently obtained using high resolution spectra by measuring equivalent width of atomic lines in regions not dominated by molecular bands (Bean et al. 2006; Woolf & Wallerstein 2005; Woolf et al. 2009)

Rapid progresses in the investigation of cool atmospheres are expected thanks to the advent of 8 m class telescopes that allow high resolution spectroscopy of these faint targets. In high resolution spectra, access to weak lines allows us to determinate the metallicity disentangled from the other main parameters, gravity and temperature. The pressure changes affect equally all atmospheric parameters and therefore the various absorption bands. The determination of gravity from the pressure broadened wings can be expected to be much more accurate than comparing colour ratios from photometry and/or low resolution spectra. Thus it is necessary to achieve a very good fit in all important absorbers in order to determine atmospheric properties, because the chemical complexity of these atmospheres reacts sensibly to the major opacities. Descriptions of these stars

[1] Institut UTINAM CNRS 6213, Observatoire des Sciences de l'Univers THETA Franche-Comté-Bourgogne, Université de Franche Comté, Observatoire de Besançon, BP 1615, 25010 Besançon Cedex, France
[2] Université de Nice Sophia-Antipolis, CNRS, Observatoire de Côte d'Azur, Laboratoire Cassiopée, 06304 Nice Cedex 4, France
[3] Centre de Recherche Astrophysique de Lyon, UMR 5574: CNRS, Université de Lyon, École Normale Supérieure de Lyon, 46 allée d'Italie, 69364 Lyon Cedex 07, France

therefore need validations by comparing with high resolution spectroscopic observations.

In this paper we present the first high resolution optical atlas of stars covering the whole subdwarf sequence. It consists of 21 sdM, esdM, and usdM observed with UVES at VLT. Using the most recent PHOENIX BT-Settl stellar model atmosphere we have performed a detailed comparison with our observed spectra using a χ^2 minimization technique. In this study we confront the models to the high resolution spectra of subdwarfs and we assign effective temperatures to the M dwarfs. We derive metallicities based on the best fit of synthetic spectra to the observed spectra and perform a detailed comparison of lines profile of individual elements such as Fe I, Ca II, Ti I, Na.

2 Observation and data reduction

The observation were carried out in visitor mode during April and September 2011 with the optical spectrometer UVES (Dekker et al. 2000) on the Very Large Telescope (VLT) at the European Southern Observatory (ESO) in Paranal, Chile. In total 21 targets were observed during period 87. UVES was operated in dichroic mode using red arm with non-standard setting centered at 830 nm. This setting covers the wavelength range 6400 $\AA$-9000 $\AA$, which contains various atomic lines like Fe I, Ti I, K II, Na I and Ca II and is very useful for the spectral synthesis analysis. The spectra were taken with a slit width of 1.0" yielding a nominal resolving power of R = $\lambda/\Delta\lambda$ = 40 000. The signal to noise ratio varies over the wavelength region according to the object's spectral energy distribution and detector efficiency. It reaches 30 in most of the spectral region (6400 $\AA$-9000 $\AA$) so that the dense molecular and atomic absorption features are well discernible from noise. Data were reduced using the ESO based software called REFLEX for UVES data which uses standard ESO pipeline modules.

3 Model Atmosphere

In this study, we use the most recent BT-Settl models partially published in a review by Allard et al. (2012). These model atmospheres are computed with the PHOENIX multi-purpose atmosphere code version 15.5 (Hauschildt et al. 1997; Allard et al. 2001) solving the radiative transfer in 1D spherical symmetry, with the classical assumptions: hydrostatic equilibrium, convection using the mixing length theory, chemical equilibrium, and a sampling treatment of the opacities. The models use a mixing length as derived by the radiation hydrodynamic) simulations of Ludwig et al. (2002, 2006) and Freytag et al. (2012) and a radius as determined by the Baraffe et al. (1998) interior models as a function of the atmospheric parameters ($T_{\rm eff}$, $\log g$, [Fe/H]).

The BT-Settl grid extends from $T_{\rm eff}$ = 300 to 7000 K at a step of 100 K, $\log g$ = 2.5 to 5.5 at a step of 0.5 dex and [Fe/H]= -2.5 to 0.0 at a step of 0.5 dex accounting for alpha element enrichment. We interpolated the grid at every 0.1 dex in $\log g$ and metallicity. For more detail of BT-Sett model atmosphere see Allard et al. (2012); Rajpurohit et al. (2012). The synthetic colours and spectra are distributed with a spectral resolution of around R=100000 via the PHOENIX web simulator*.

4 Comparison with model atmospheres

We perform a comparison between observed and synthetic spectra computed from the BT Settl model to derive the physical parameters of our sample. Furthermore, the comparison with observed spectra is very crucial to reveal the inaccuracy or incompleteness of the opacities used in the model. Fig. 1 shows the comparison of the best fit model for a sdM1 star.

The analysis using synthetic spectra requires the specification of several inputs parameters: effective temperature, surface gravity and the metallicity compared to Sun. As opposed to previous studies in which the best fit was found by trial and error, in this paper we derive the effective temperature by performing a χ^2 minimization technique. Our procedure is a two-step process. We first convolve the synthetic spectrum with a Gaussian kernel at the observed resolution and then rebin the outcome with the observation. For each of the observed spectra we compare these spectra with the grid of synthetic spectra in the wavelength range 6400$\AA$ to 9000$\AA$ using χ^2 minimization technique. We have excluded the spectral region between 6860 to 6960 $\AA$, 7550

*http://phoenix.ens-lyon.fr/simulator

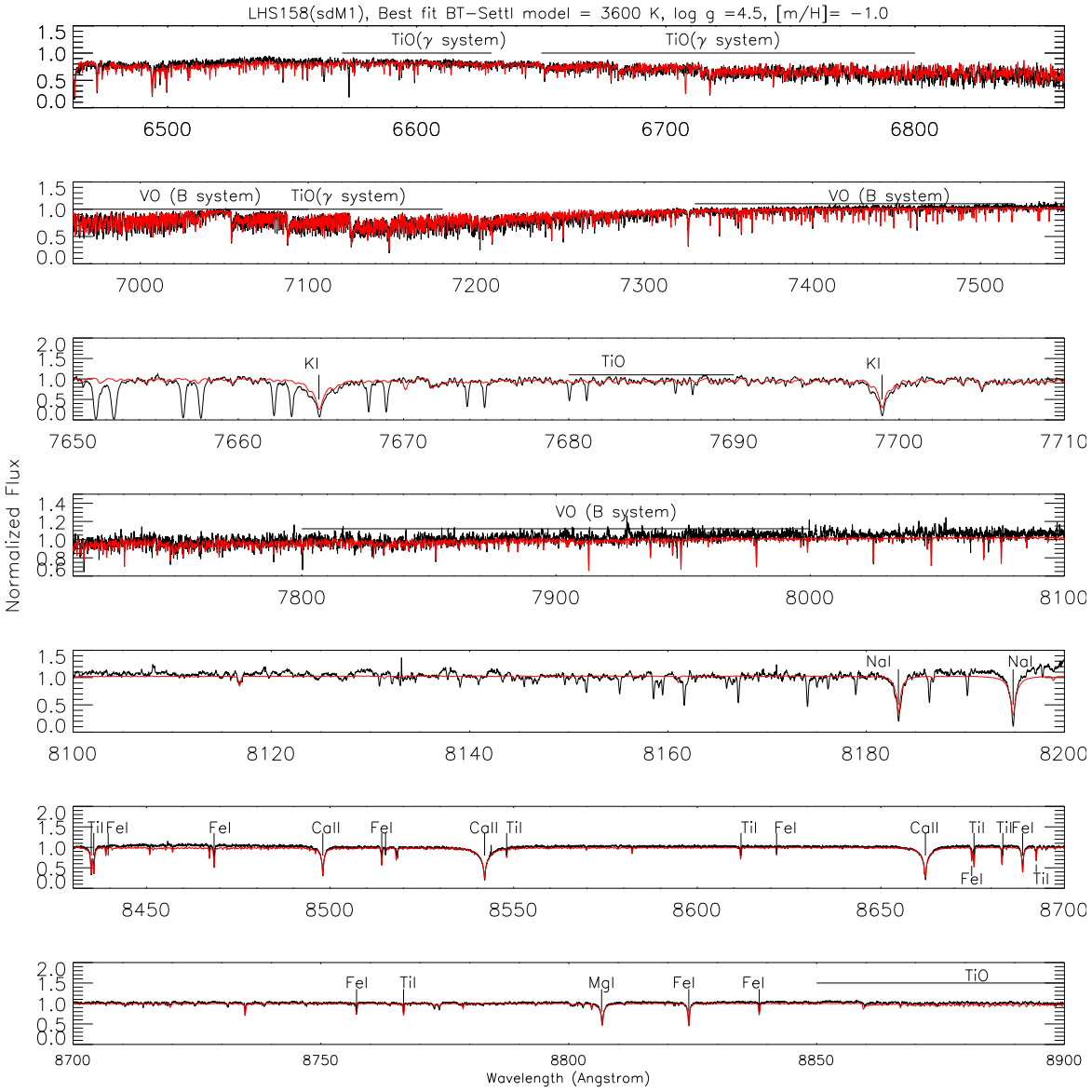

Fig. 1. UVES spectra of the sdM1 star LHS 158 (black) compared to the best fit BT-Settl synthetic spectra (red).

to 7650 $\AA$, and 8200 to 8430 $\AA$, due to presence of atmospheric absorption. In the first step, we keep all the stellar parameter ($T_{\rm eff}$, [Fe/H], $\log g$) free.

In a second step, a χ^2 map is obtained for each of the observed spectra as function of temperature and metallicity. The error bar are derived from standard deviation by taking 5 % from the minimum χ^2 value. The acceptable parameters were finally inspected by comparing it with the observed spectra. We found generally good agreement with BT-settl model and conclude that model fitting procedure can be used to estimate the $T_{\rm eff}$ with an accuracy better than ∼100 K.

We tested the sensitivity of the TiO lines to surface gravity and did not find any significant effect in the parameter space and wavelength range relevant to this study. The surface gravity can be determined by analyzing the width of gravity sensitive atomic lines such as K I and Na I doublets (see Fig. 2) as well as relative strength of metal hydride bands such as CaH. The overall line strength (central depth and equivalent width) increases with gravity as the decreasing ionization ratio due to higher electron pressure leaves more neutral alkali lines in the deeper atmosphere. The width of the damping wings in addition increases due to the stronger pressure broadening, mainly by H_2, He and H I collision.

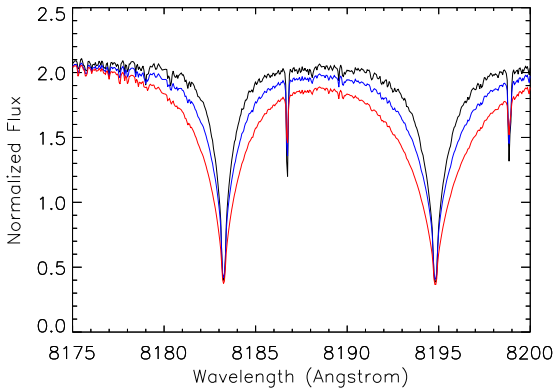

Fig. 2. BT-Settl synthetic spectra with $T_{\rm eff}$ of 3500 K and varying $\log g$ =4.5 (black), 5.0 (blue), 5.5 (red). The effect of gravity and pressure broadening on the sodium doublet is clearly visible.

Table 1. Stellar Parameters of the observed targets.

Target	Spectral Type	$T_{\rm eff}$ (K)	$\log g$	[Fe/H]
LHS 72	sdK4	3900 ±23	4.5±0.13	-1.4± 0.27
LHS 73	sdK7	3800 ±39	4.5±0.13	-1.4±0.19
G 18-37	esdK7	3800 ±78	4.5±0.15	-1.3±0.44
APMPM J2126-4454	sdM0	3700 ±49	4.5 ±0.19	-1.3±0.23
LHS 300	sdM0	3800 ±39	4.5±0.17	-1.4±0.24
LHS 401	sdM0.5	3800 ±26	4.5±0.17	-1.4±0.28
LHS 158	sdM1	3600 ±48	4.5±0.17	-1.0±0.3
LHS 320	sdM2	3600 ±59	4.6±0.23	-0.6±0.31
LHS 406	sdM2	3600 ±40	4.7±0.24	-0.6±0.24
LHS 161	esdM2	3700 ±77	4.8±0.30	-1.2±0.36
LP 771-87	usdM2	3600 ±95	4.8±0.31	-1.4±0.52
LHS 541	sdM3	3500 ±76	5.1±0.31	-1.0±0.39
LHS 272	sdM3	3500 ±66	5.2±0.30	-0.7±0.37
LP 707-15	esdM3	3500 ±68	5.5±0.29	-0.5±0.36
LSR J1755+1648	sdM3.5	3400 ±52	5.1±0.31	-0.5±0.33
LHS 375	sdM3.5	3500 ±79	5.5±0.32	-1.1±0.31
LHS 1032	esdM4	3300 ±63	4.5±0.32	-1.7±0.25
SSSPM J0500-5406	esdM6.5	3200±51	5.4±0.31	-1.6±0.16
LHS 377	sdM7	3100 ±32	5.3±0.25	-1.0±0.16
APMPM 0559-2903	esdM7	3200 ±68	5.4±0.34	-1.7±0.25
SSPM J1013-1356	sdM9.5	3000 ±0	5.5±0.05	-1.1±0.16

For the metallicity determination we fit the synthetic spectra using the same procedure explained above but on restricted regions where molecular absorptions are less strong and atomic lines appear clearly. Our first criterion is that the lines must have fractionally small amount of TiO line blending. This necessitate the use of fairly strong lines. Most of the lines we select occupy a short spectral interval from 8440 $\AA$ to 8900 $\AA$ (see fig. 3). In our analysis we also include the new lines of elemental species such as Ca II triplet, Ti lines, and TiO bandhead around 7088 $\AA$. The best fit parameters ($T_{\rm eff}$, $\log g$, [Fe/H]) are given in Table 3.

5 Discussion

We use the most recent BT-Settl model atmospheres, with revised solar abundances, to determine the scaled solar abundances of the subdwarfs. We compare the synthetic spectra produced the model atmospheres and derive their fundamental stellar parameters. The accuracy of the atmospheric models involved in the metallicity

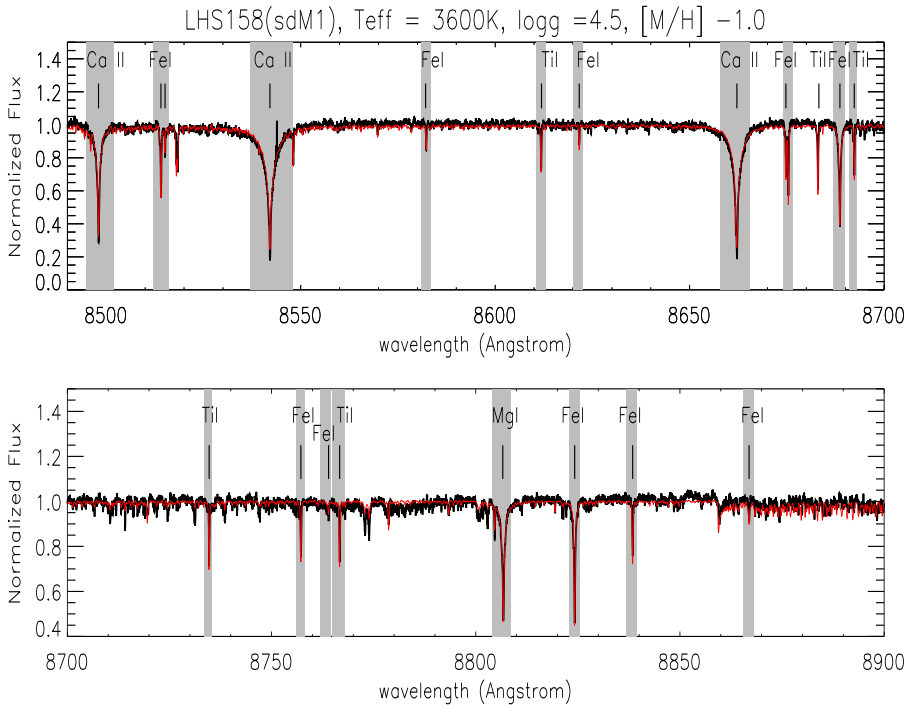

Fig. 3. UVES spectrum of the sdM1 star LHS 158 (black) and the best fit BT Settl synthetic spectrum (red). The spectral region used to determine metallicity is shown only. The atomic features used are highlighted.

determination can be inferred by looking the fit to the individual atomic and molecular lines. Working with these high resolution spectra allowed us to disentangle the atmospheric parameters (effective temperature, gravity, metallicity), which is not possible when using braodband photometry. With this study we were able to constrain for the first time the BT-Settl models at sub solar metallicities.

The effective temperature versus spectral type relation is shown in Fig. 4. The relation determined using UVES sample is compared to the $T_{\rm eff}$ scale of M dwarfs determined by Rajpurohit et al. (2013). $T_{\rm eff}$ of subdwarfs dwarfs is 200-300 K higher than $T_{\rm eff}$ of M dwarfs for the same spectra type except for hot temperature. This is expected since the TiO bands are depleted with decreasing metallicity, and as a result the pseudo-continuum is brighter and the flux is emitted from the hot deeper layer. A comparison to the earlier work from Gizis (1997) is also shown. Gizis (1997) determined the temperature by comparing the low resolution optical spectra of a sample of sdM and esdM with the NextGen model atmosphere grid by Allard et al. (1997). The $T_{\rm eff}$ scales are in agreement within 100 K. This difference is due to the incompleteness of the TiO and water vapor line lists used in the NextGen model atmospheres compared to the new BT-Settl models. Furthermore this work allows us to extend the relation to the coolest M subdwarfs.

References

Allard, F., Hauschildt, P. H., Alexander, D. R., & Starrfield, S. 1997, ARA&A, 35, 137

Allard, F., Hauschildt, P. H., Alexander, D. R., Tamanai, A., & Schweitzer, A. 2001, ApJ, 556, 357

Allard, F., Homeier, D., & Freytag, B. 2012, Royal Society of London Philosophical Transactions Series A, 370, 2765

Baraffe, I., Chabrier, G., Allard, F., & Hauschildt, P. H. 1998, A&A, 337, 403

Bean, J. L., Benedict, G. F., & Endl, M. 2006, ApJ, 653, L65

Burgasser, A. J., Kirkpatrick, J. D., Burrows, A., et al. 2003, ApJ, 592, 1186

Dekker, H., D'Odorico, S., Kaufer, A., Delabre, B., & Kotzlowski, H. 2000, in Society of Photo-Optical Instrumentation Engineers (SPIE) Conference Series, Vol. 4008, Society of Photo-Optical Instrumentation Engineers (SPIE) Conference Series, ed. M. Iye & A. F. Moorwood, 534–545

Digby, A. P., Hambly, N. C., Cooke, J. A., Reid, I. N., & Cannon, R. D. 2003, MNRAS, 344, 583

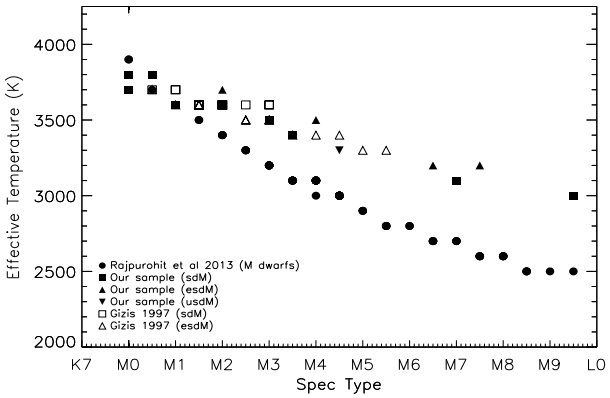

Fig. 4. Effective temperature of subdwarfs versus spectral type relation from our sample (filled symbols) compared to the one from Gizis (1997) (open symbols) and to the M dwarfs $T_{\rm eff}$ scale from Rajpurohit et al. (2013) (filled circles).

Freytag, B., Steffen, M., Ludwig, H.-G., et al. 2012, J. Comp. Phys., 231, 919
Gizis, J. E. 1997, AJ, 113, 806
Hauschildt, P. H., Baron, E., & Allard, F. 1997, ApJ, 483, 390
Jao, W.-C., Henry, T. J., Beaulieu, T. D., & Subasavage, J. P. 2008, AJ, 136, 840
Lépine, S., Rich, R. M., & Shara, M. M. 2003, AJ, 125, 1598
Lépine, S., Rich, R. M., & Shara, M. M. 2007, ApJ, 669, 1235
Ludwig, H.-G., Allard, F., & Hauschildt, P. H. 2002, A&A, 395, 99
Ludwig, H.-G., Allard, F., & Hauschildt, P. H. 2006, A&A, 459, 599
Rajpurohit, A. S., Reylé, C., Allard, F., et al. 2013, A&A, 556, A15
Rajpurohit, A. S., Reylé, C., Schultheis, M., et al. 2012, A&A, 545, A85
Woolf, V. M., Lépine, S., & Wallerstein, G. 2009, PASP, 121, 117
Woolf, V. M. & Wallerstein, G. 2005, MNRAS, 356, 963

Session 09

L'E-ELT : instrumentation et programmes scientifiques

SF2A 2013
L. Cambrésy, F. Martins, E. Nuss and A. Palacios (eds)

ELT-CAM, THE E-ELT FIRST LIGHT IMAGER

Y. Clénet [1]

Abstract.
ELT-CAM is one of the two first-light instruments of the E-ELT, the european ELT. It is a near-infrared (IR) camera working at the telescope diffraction limit either with a single-conjugated (SCAO) or multi-conjugated (MCAO) adaptive optics correction. With a field of view of ∼1 arcmin, this instrument will come with long-slit spectroscopic capabilities, with a spectral resolution of several thousands. The instrumental specifications are targeting a high sensitivity and spatial resolution, a very accurate astrometry and spectroscopy with a large covered bandpass.

This SF2A workshop being the first occasion to make a broad presentation to the French astronomical community of the E-ELT, its instrumentation and its scientific programs, I present here the different characteristics of ELT-CAM as well as few scientific cases, mainly based on the work of the MICADO and MAORY teams during the phase A of these instruments.

Keywords: ELT, instrument, ELT-CAM, MICADO, MAORY, adaptive optics, SCAO, MCAO

1 Overview of ELT-CAM

1.1 ELT-CAM in a nutshell

ELT-CAM is the coupling of two instrumental concepts studied during their phase A between 2008 and 2009: MICADO (Davies et al. 2010), the IR camera, and MAORY (Diolaiti et al. 2010), the MCAO module. This instrument is then a near-IR camera (0.8-2.5 microns) working at the diffraction limit over about a 1 arcmin field of view. It will come with a long slit spectroscopic mode, at a moderate spectral resolution (5000 to 10000). The diffraction-limited observations will be provided either by a MICADO-internal SCAO module or by the MCAO module MAORY. The latter will provide a moderately high Strehl ratio over the entire 1 arcmin field of view while the former will provide better on-axis Strehl ratio.

1.2 Performance drivers

The performance drivers for the design of MICADO were the following:

- sensitivity and resolution: the instrument will correctly sample the E-ELT diffraction limit from the J- to the K-band (6 mas to 10 mas approximatively) and thanks to advanced filters, the gain in sensitivity compared to the JWST is expected to be up to 0.5 mag, and even up to 3 mag in crowded fields.
- precision astrometry: the instrument is expected to measure proper motions down to 40 μas over the 1 arcmin field of view in a single epoch of observations, leading to measurements down to 10 μas/yr after 3 or 4 years of observations (which is equivalent to ∼5 km/s at 100 kpc).
- wide coverage spectroscopy: the design foresees the ability to deliver spectra covering simultaneously the 0.8-2.5 μm bandpass at a spectral resolution of 5000-10000.

[1] LESIA, Observatoire de Paris/CNRS/UPMC/Université Paris-Diderot

1.3 Sensitivity in imaging and spectroscopy

Detailed sensitivity estimations have been made during the instrument phase A, both in imaging and in spectroscopy. These estimations have been made using the PSF provided by the MAORY consortium, considering 6 laser guide stars, a seeing of 0.6".

The 5σ AB magnitude limits in imaging after 5 hours of integration time are 30.8, 30.8 and 29.8 in J, H and K respectively. Using advanced filters with improved efficiency, these numbers become 31.3, 31.3 and 30.1 respectively. This is to be compared to the 30.3 and 30.1 magnitude limit for JWST in J and K respectively.

In spectroscopy, the 5σ AB magnitude limits for point sources after 5 hours of integration time are 26.7, 26.7 and 25.6 in average in J, H and K respectively. Between the OH lines, these numbers become 27.2, 27.2 and 25.7 respectively.

1.4 Main science objectives

The main MICADO science objectives, arranged following the aforementioned performance drivers, are:

- Sensitivity and resolution
  - Star formation history (resolved stellar populations to Virgo cluster)
  - Galaxy formation and evolution (structure of high-z galaxies on 100 pc scales, environment and host galaxies of QSO at high-z)
  - Nuclei of nearby galaxies (stellar cusps, star formation, black holes)
  - Exoplanets "à la NACO"
  - Stellar physics
  - Physical and surface properties of solar system small bodies
- Precision astrometry
  - Stellar motions within light hours of the Galaxy's black hole
  - Intermediate mass black hole in stellar clusters
  - Formation and evolution of the Galaxy (globular cluster proper motions)
  - Dwarf spheroidal motions test dark matter and structure formation
- Wide coverage spectroscopy
  - Galactic centre (stellar types and 3D orbits)
  - Stellar velocities in nearby galaxies: M_{BH}, extended mass distributions
  - Absorption lines: ages, metallicities, central dispersions of first elliptical galaxies at z=2-3
  - Spectra of first supernovae at z=1-6
  - Emission lines: redshifts, velocities, metallicities of starburst galaxies at z=4-6

1.5 MICADO organization and schedule

The MICADO consortium has presented to ESO in october 2012 an updated (compared to phase A) management plan of the project. The PI of MICADO is R. Davies from MPE. The level 1 of the project is made of the MICADO instrument, the MICADO calibration assembly, the SCAO instrument, the MICADO support structure, the common instrument software and the data processing software lead by MPE, MPIA, LESIA, IAG, USM and NOVA respectively.

The current schedule for MICADO is the following:

- mid 2014: MICADO official kick-off, start of phase B, made of 1 year of science and technical trade-off studies and 2 years of preliminary design studies
- mid 2017: preliminary design review, start of phase C, made of 2 year of final design studies
- mid 2019: final design review, start of the 3-year manufacturing, assembly, integration and test phase

- end of 2022: test readiness review and European acceptance test
- 2023 and after: MICADO commissioning with SCAO, E-ELT first light with MICADO in its SCAO mode and MICADO commissioning with MAORY later on.

2 ELT-CAM design

2.1 MICADO design

In its phase A, MICADO's design comprised two arms (Fig. 1). The primary arm was a high throughput ($> 60\%$) imaging camera with a single 3 mas pixel scale, many (> 20) filter slots. This arm was designed with fixed mirrors for superior stability, thus optimizing astrometric precision. An auxiliary arm was designed to provide an increased degree of flexibility with (i) a finer 1.5 mas pixel scale over a smaller field and (ii) a 4 mas pixel scale for a long-slit spectroscopic capability. The auxiliary arm also opened the door to many other options, including a 'dual imager' based on a Fabry-Perot etalon to image separate emission line and continuum wavelengths simultaneously, or a high time resolution detector.

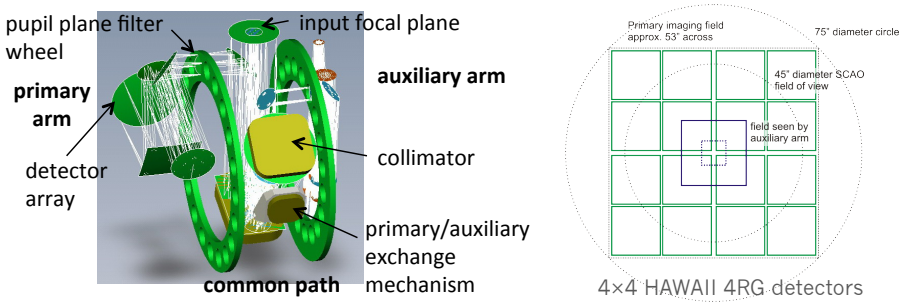

Fig. 1. Left: Overview of MICADO phase A optics, which comprised the common path (ADC (not shown) and collimator) in the centre, the primary arm, and the auxiliary arm. **Right:** Illustration of the phase A focal plane division. The main imaging field was approximately 53"×53" and imaged at a scale of 3 mas/pixel by an array of 4×4 HAWAII-4RG detectors. A selection mechanism enabled one to pick off a smaller field for the auxiliary arm.

Since phase A, after the new E-ELT design and new specifications (both from ESO and internal), the design was updated, merging the two arms, increasing the number of filter slots (∼40), allowing the simultaneous coverage of the 0.8-2.5 μm bandpass in spectroscopy, including the finer 1.5 mas pixel scale over a small field in the now single arm and finally adding high contrast imaging capabilities through the inclusion of coronograph masks in the design.

2.2 ELT-CAM AO: MAORY

To get diffraction-limited images, MICADO will be ultimately coupled to the MCAO instrument MAORY. This instrument is developed within a dedicated project and separately to MICADO, the interfaces being dealt jointly with ESO. To perform the AO correction over the MICADO field of view, MAORY will make use of:

- 6 laser guide stars (LGS), and their 6 Shack-Hartmann wavefront sensors
- 3 natural guide stars, and their 3 near-infrared (H-band) wavefront sensors (two for tip-tilt, one for tip-tilt and focus, each of the 3 being associated to a reference wavefront sensor to monitor the LGS non common path aberrations)
- in addition to the two AO mirrors in the telescope (M4 and M5), two post-focal deformable mirrors, conjugated at two different altitudes for the tomographic reconstruction of the atmospheric turbulence

In its phase A study, MAORY occupied a volume of 7.4 m × 7.2 m × 8 m (length, width and height), MICADO being attached below the MAORY optical bench in a gravity-invariant position (see Fig. 2).

Since its phase A, MAORY optical design has evolved to correct for the output field curvature, to correct for the wedge of the LGS objective lenses, to reduce the dichroic size and finally to decrease the total MAORY volume (7.2 m × 4.3 m × 6.4 m in length, width and height respectively).

The AO performance of MAORY, estimated in phase A, is summarized in the Table 1.

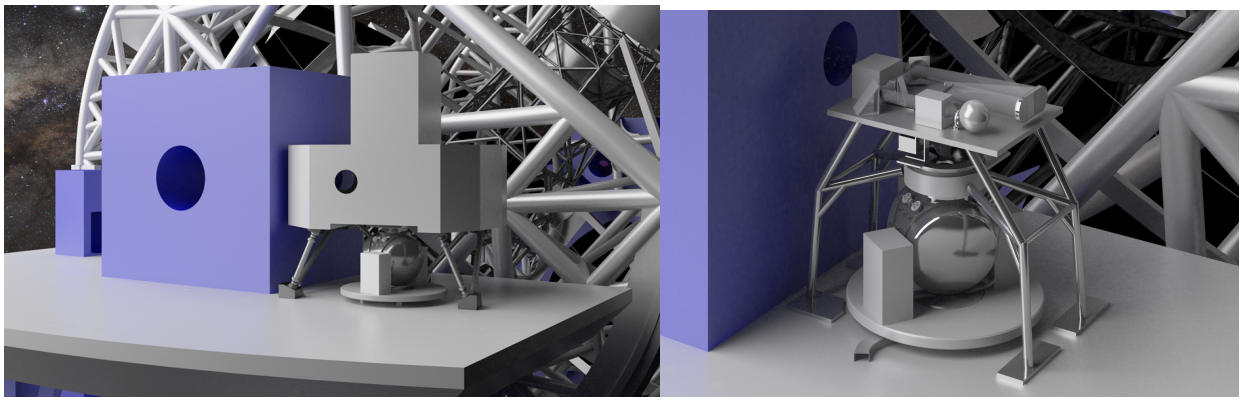

Fig. 2. Left: MICADO mounted under MAORY at the E-ELT Nasmyth platform (as from the MICADO and MAORY phases A). **Right:** MICADO in its SCAO mode configuration, at the E-ELT Nasmyth platform (as from the MICADO phase A).

Table 1. MAORY sky coverage and minimum AO correction for a science field of 53"×53" (the FoV of MICADO) and a seeing of 0.8".

Minimum field-averaged Strehl ratio over 53×53 arcsec^2 FoV				Sky coverage
2.16 μm	1.65 μm	1.215 μm	0.9 μm	
0.53	0.34	0.14	0.03	39%
0.51	0.32	0.13	0.03	50%
0.49	0.30	0.11	0.02	60%
0.47	0.27	0.09	0.01	70%
0.41	0.22	0.06	0.01	80%

2.3 ELT-CAM AO: SCAO

Even if ultimately coupled to MAORY, MICADO includes an internal SCAO module (Clénet et al. 2010). The motivations for this SCAO module are the following:

- Scientific complementarity: SCAO provides the best AO performance for mono target science (exoplanets, solar system, stellar physics, AGNs, Galactic Centre)
- Complementarity for operations: during the MAORY commissioning, which could be long based on the experience of the only similar system (but on an 8m class telescope), GeMS, MICADO will be able deliver diffraction-limited observations
- Risk management: even in case of a delay in the MAORY planning, MICADO will be ready to deliver diffraction-limited observations at the E-ELT scientific first light.

The SCAO module is specified to provide the same mechanical and operational interface as MAORY (Fig. 2). Hence, in its SCAO mode, MICADO is attached to a field derotator mounted under an optical bench supporting an optical relay. The SCAO wavefront sensor is mounted also on the derotator, rotating then jointly to MICADO. To ensure the proper matching of the WFS pupil on M4, the WFS path includes a K-mirror. In phase A, this WFS was using a Schack-Hartmann. This choice will be reconsidered and compared to the performance of a pyramid WFS during the project phase B. Furthermore, the design of the optical relay is under revision after the new E-ELT design and new specifications (both from ESO and internal).

During the MICADO phase A, the AO performance of this SCAO module has been estimated considering a 84×84 Shack-Hartmann WFS operating in the visible (0.45-0.8 μm), a seeing of 0.71", a wind speed of 16.4 m/s, an outer scale of 25 m, a 3e- readout noise and 80% quantum efficiency detector, the windshake residuals on the tip-tilt as provided by ESO (corresponding to 0.28 arcsec rms residuals), a correction by the telescope M4 and M5 mirrors. As shown in Fig. 3, the Strehl ratio can reach more than 75% for the brightest reference sources, which points at the interest of the exoplanet and solar system science for MICADO.

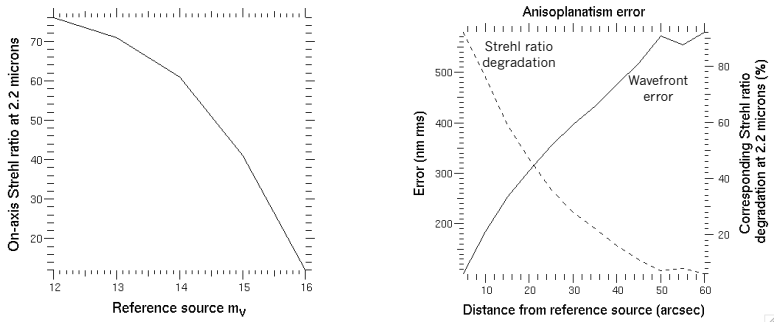

Fig. 3. Left: On-axis Strehl at 2.2 microns for different reference star magnitudes and a seeing of 0.71". **Right:** Anisoplanatism error for a seeing of 0.71" and L_0=25 m, measured by the Strehl ratio degradation compared to the on-axis Strehl ratio at 2.2 microns (dash line) and by the corresponding wavefront error in nm rms (solid line).

3 Focus on two science cases

We make in this section a short presentation of two science cases among those listed in Sect. 1.4: resolved stellar populations in nearby galaxies and exoplanets. The former will take advantage of the MCAO correction of MAORY while the latter needs the SCAO correction to be competitive.

3.1 Star formation history: resolved stellar populations

The science case of resolved stellar populations is a perfect illustration of the gain in sensitivity provided by an improved spatial resolution in crowded field. The ESO MCAO demonstrator MAD (Marchetti et al. 2003) already demonstrated with Omega Cen observations (Fig. 4, Marchetti et al. 2007) that a factor 6 improvement in resolution leads to 3 mag deeper observations in crowded fields.

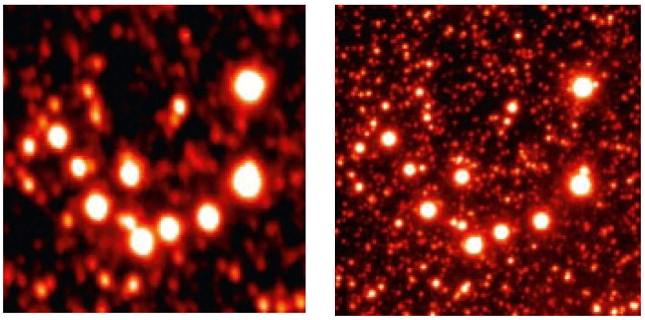

Fig. 4. Comparison between ISAAC (left) and MAD (right) observations of Omega Cen from Marchetti et al. (2007).

From simulations, a similar gain for MICADO is expected in comparison to the JWST: Deep et al. (2011), in the framework of the MICADO phase A, showed that both NIRCam/JWST and MICADO will be able to study stellar populations out to the Virgo Cluster but NIRCam will be limited to probing the fringes of the galaxies at radii of 3-4 R_{eff} while MICADO will be able to work in the central regions at 1-2 R_{eff} (Fig. 5). Interestingly, this study has also shown that the I-band filter could be more efficient to probe the central parts of galaxies because of the lowest sky background at these wavelengths (see again Fig. 5).

3.2 Exoplanets

Exoplanets is a top science of the E-ELT and MICADO in its SCAO mode will be able to start addressing this major prominent goal as soon as the E-ELT first light. The niche for MICADO with respect to near-term instruments (SPHERE, GPI, JWST) is definitely the improvement of the angular resolution with moderate contrasts. For the exoplanet science case, MICADO and its SCAO mode will be for the E-ELT what NACO was for the VLT, a general-purpose imager with adaptive optics offering the highest possible Strehl ratio and contrast on-axis.

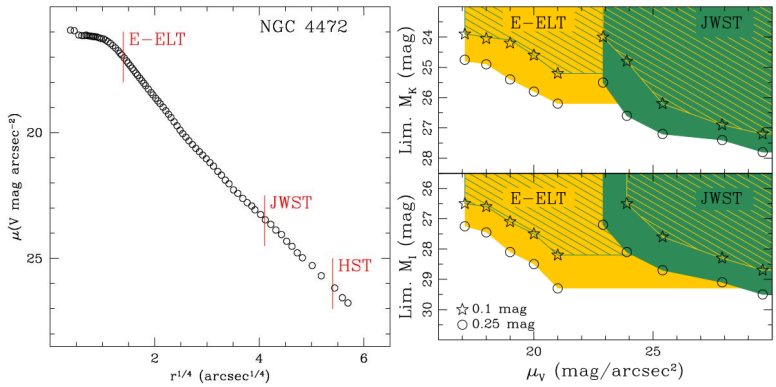

Fig. 5. Left: NGC 4472 surface brightness profile with the best sensitivity reachable by MICADO/E-ELT, NIRCAM/JWST and ACS/HST (figure from Deep et al. 2011). **Right:** I- and K-bands surface brightness and limiting magnitude limits for MICADO/E-ELT and NIRCAM/JWST in the case of an old galaxy at the distance of Virgo (17 Mpc). Open star and open circle symbols correspond to photometric errors of ±0.1 mag and ±0.25 mag respectively.

Assuming the same level of contrasts as NACO will be achieved, a beta Pic b-like object will be detectable at ∼2 AU instead of 8-10 AU. MICADO will have the capability to reach closer physical separations than NACO and even SPHERE on nearby targets (<50 pc). This range is overlapping the one probed with radial velocity technics, which now starts to be applicable on young early type stars although active. Therefore, it will be possible to infer the true mass of a planet from the minimal mass measured by radial velocity technics and from the inclination measured from imaging (several epochs being needed). A more precise calibration of evolutionary models will become feasible hence with the advantage to perform better spectral characterization. In addition, MICADO will be able to search for young giant and massive planets (10 M_J) on wide orbits (>20-30 AU) around young star associations that are more distant than those to be observed with SPHERE (100-150 pc rather than 30-90 pc). Therefore, the number of potential targets is larger. Moreover, these observations performed in several bands (JHK) will allow one to derive near IR colors and to put constraints on some atmospheric properties like temperature and surface gravity.

As for spectral characterization, again the improvement of angular resolution will benefit to long-slit spectroscopy for some planets that are sufficiently separated with the capability to achieve spectral resolution of a few thousands while SPHERE will provide only a few hundreds. In addition to better detect some broad spectral lines (CH_4, NH_3, H_20, CO_2, ...), this higher spectral resolution is of particular interest to bring more constraints on the atmospheric properties (metallicity, clouds and dust). This high level of characterization will be devoted to bright exoplanets.

4 Conclusions

Thanks to the SCAO and the MCAO corrections provided by its internal module and later on by MAORY, MICADO/ELT-CAM will be able to make major contributions to a large range of science cases. The kick-off of the project is expected to be in mid 2014.

I would like to thank the MICADO and MAORY consortia, which provided the material for this presentation and article.

References

Clénet, Y., Bernardi, P., Chapron, F et al. 2010, SPIE, 7736, 77363Q
Deep, A., Fiorentino, G., Tolstoy, E. et al., A&A, 531, id. A151
Davies, R., Ageorges, N., Barl, L. et al. 2010, SPIE, 7735, 77352A
Diolaiti, E., Conan, J.-M., Foppiani, I. et al. 2010, SPIE, 7736, 77360R
Marchetti, E., Hubin, N., Fedrigo, E., et al. 2003, SPIE, 4839, 317
Marchetti, E., Brast, R., Delabre, B. et al. 2007, The ESO Messenger, 129, 8

SF2A 2013
L. Cambrésy, F. Martins, E. Nuss and A. Palacios (eds)

WEB-BASED SCIENTIFIC SIMULATION TOOLS FOR E-ELT INSTRUMENTS

K. Disseau[1], M. Puech [1], Y.B. Yang[1], H. Flores[1], F. Hammer[1] and L. Pentericci[2]

Abstract. In the frame of the EAGLE & OPTIMOS-EVE phase A studies, we have developped a scientific simulator which has been used to constrain the instrument high level specifications. The simulator is coupled to a web interface to allow an easier access by the science teams and run specific simulations covering the scientific objectives. This simulator is now used to constrain the design of MOSAIC, a new MOS concept for the E-ELT. We give a functional description of the simulator and illustrate how it is used in practice to constrain the pixel size of the IFU of MOSAIC.

Keywords: 3D spectroscopy, Integral field spectroscopy, Simulations, Imagery, ELTs

1 Introduction

In the frame of the ESO E-ELT instrument phase A studies (Puech et al. (2008), Evans et al. (2011), Navarro et al. (2010), Puech et al. (2010)), we have developped a scientific simulator coupled to a web interface. It is now used to constrain the MOSAIC design (Hammer et al., these proceedings). We also developped other telescope/instrument simulators, including a general image/datacube simulator which is acessible at `https://websim.obspm.fr`. After a functional description of the simulator we illustrate its use to constrain the IFU pixel size of MOSAIC in the detection of UV interstellar absorption lines and the Ly-α emission line in high redshift galaxies.

2 Methodology

This end-to-end simulator produces datacubes in FITS format, mimicking the result of real observations. An AO system can be modeled through its PSF, which is simulated using a dedicated pipeline not included in this simulator. Iterative simulations allow to converge toward a science versus technique trade-off.
The simulator is coupled to a web interface hosted on a secured server called WEBSIM, and the simulations are run on a science server. When completed, an email is sent to the user who can then download the products consisting in FITS files. The user can choose through this interface the instrument characteristics, such as the IFU size, the spectral resolution, the CCD performances etc, and also the scientific target among several available templates. AO correction of atmospheric turbulence is set through the choice of the PSF (see Fig. 1). Details can be found in Puech et al. (2010)

3 Developments

Updates of this simulator are planned over the next two years, including the implementation of temporal and spatial sky background variations, thanks to the work that has been done in our team to better understand the sky background variations and to develop techniques to properly substract it (Yang et al. (2013)). It is also planned to include telluric features and to implement a batch mode to run several simulations in a row. Moreover, a complete AO PSF library will be offered (LTAO, MCAO, MOAO, XAO) as well as morpho-kinematic templates for simulating a large range of astrophysical objects of interest. This will be done in the frame of the COMPASS project (PI : D. Gratadour), founded by the French ANR.

[1] GEPI, Observatoire de Paris, CNRS, Université Paris-Diderot; 5 place Jules Janssen, 92190 Meudon, France
[2] INAF, Osservatori Astronomico di Roma, via Frascati 33, 00040 Monte Porzio Catone, Italy

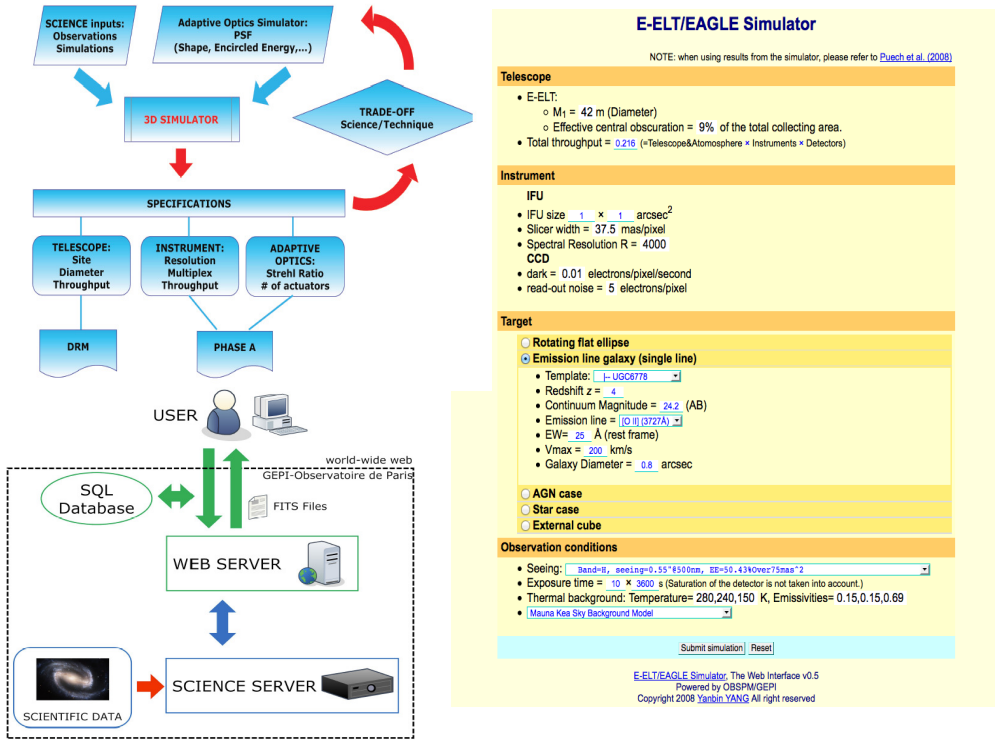

Fig. 1. Left upper pannel: Schematic illustration of the use of simulations to constrain telescope or instrument specifications. **Left bottom pannel :** Overall structure of WEBSIM. **Right pannel:** Web interface of the simulator.

4 Simulations

We considered in these simulations a 39-m diameter telescope with a 11-m secondary mirror. We used an MOAO PSF from EAGLE phase A study which provides 30% of ensquared energy in 80×80 mas^2, and we assumed a spectral resolution $R = 4000$, which is the minimum required to target emission lines between the OH sky lines and to resolve Ly-α profiles with typical FWHM$\sim$150-500 km/s. These simulations aimed at constraining the optimal pixel scale ; we thus simulated different sizes of pixels, from 20 mas to 900 mas. Once the resulting datacubes simulated, we analysed them by constructing integrated spectra following Rosales-Ortega et al. (2012) (see their Fig.2) : spectra are added by order of decreasing S/N until the S/N of the integrated spectrum stops increasing.

4.1 Simulated IFU observations of UV interstellar lines at $z \sim 7$

The spatial distribution of the light is based on hydrodynamical simulations of clumpy disks by Bournaud et al. (2007), which have been rescaled in flux and sizes to observations at $z = 7$. We simulated a range of object apparent magnitudes from $J_{AB} = 25$ to $J_{AB} = 28$. Following the distribution of half light radii of LBG galaxies observed with HST (Grazian et al. (2012)), we assumed three typical sizes for the simulated galaxies : a compact size (R_{half}=100 mas), an average size (R_{half}=150 mas) and a large size (R_{half}=210 mas). Behind each spaxel of the cube is attached a template LBG spectrum from Shapley et al. (2003) resampled at $R = 4000$. The analysis of integrated spectra (illustrated in Fig. 2 and Fig. 3) shows that J_{AB}=26-27 should be detected with t_{intg}=40 hrs and a 80 mas pixel scale, for which the S/N is maximum. Below 80 mas it is limited by the readout noise and above 120 mas by the sky background.

4.2 Simulated IFU observations of Ly-α emission line at $z \sim 9$

The spatial distrubution of light is the same as for UV lines case. The simulated grid was extended to fainter magnitudes (up to $J_{AB} = 30$). Following current observations of LAEs at $z \sim 6$, we modeled the Ly-α line

with a gaussian line truncated in the blue side and with a width of 270 km/s ; we considered also a constant velocity field of 200 km/s (Swinbank et al. (2007)) mimicking a constant outflow. We increased the equivalent width with magnitude, according to data from Jiang et al. (2013) (see their Fig. 6). The results are shown in Fig. 2. The maximal S/N is obtained for pixel sizes ranging between 40 and 120 mas. There is no prefered value in this range since variations of S/N can be easily compensated by variations in integration time in this case. Simulations show that J_{AB}=30 should be easily detected with such pixel scales and with t_{intg}=10hrs (see Fig. 3).

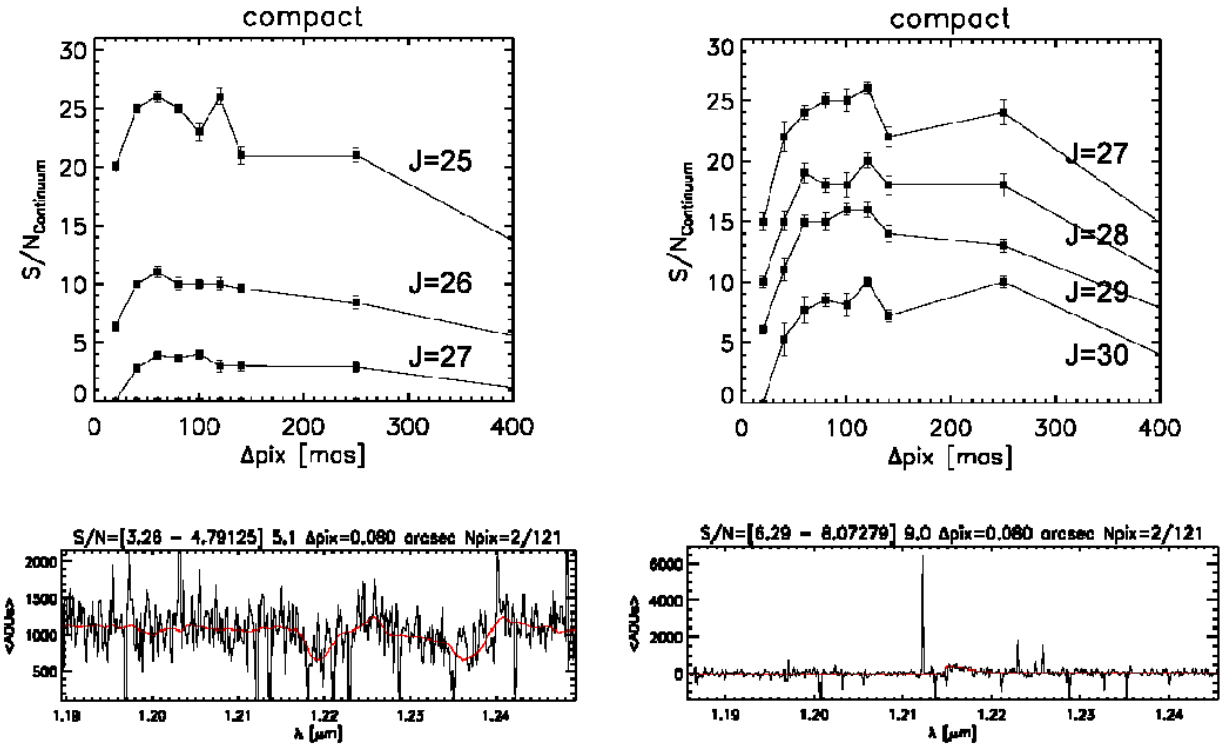

Fig. 2. Left : Simulated IFU observations of UV interstellar absorption lines at $z \sim 7$ with t_{intg}=40hrs on source. The top pannel shows the S/N in the SiII(λ=1527A) absorption line from integrated spectra of compact sources as a function of the IFU pixel size for different object apparent magnitudes. An exemple of such an integrated spectrum is given for J_{AB}=27 and 80 mas/pixel. The range of S/N in the line for the spectra used to construct the combined spectrum are shown in parentheses at the upper left of the spectrum, followed by the S/N of the integrated spectrum itself. **Right :** Simulated IFU observations of Lyman-α emitters redshifted to $z \sim 9$ with t_{intg}=10hrs on source. The S/N plotted in the top pannel is calculated in the Ly-α line. The bottom pannel shows an example of integrated spectrum for a compact source with J_{AB}=29 and 80 mas/pixel.

5 Conclusion

We used WEBSIM to constrain the high level specifications of MOSAIC, especially the IFU pixel scale. We found in the case of observing high redshift galaxies that the more dimensioning case is the study of interstellar UV lines, with a 80 mas pixel scale favored to reach $J_{AB} \sim 27$, assuming 40 hr integration time and a MOAO system delivering an Ensquared Energy of 30% within 80×80 mas^2. Deep LAEs spectra should be obtained with 40-120 mas IFUs and 10 hr integration time, up to $J_{AB} \sim 30$. The next step will consist in simulating the detection of LBGs and LAEs with GLAO-fed fibers in order to compare the performance with IFU integrated spectra.

These simulations will also be repeated with new AO PSFs that will be provided in the frame of COMPASS project, to determine whether the AO system can be simplified without degrading the instrument performances.

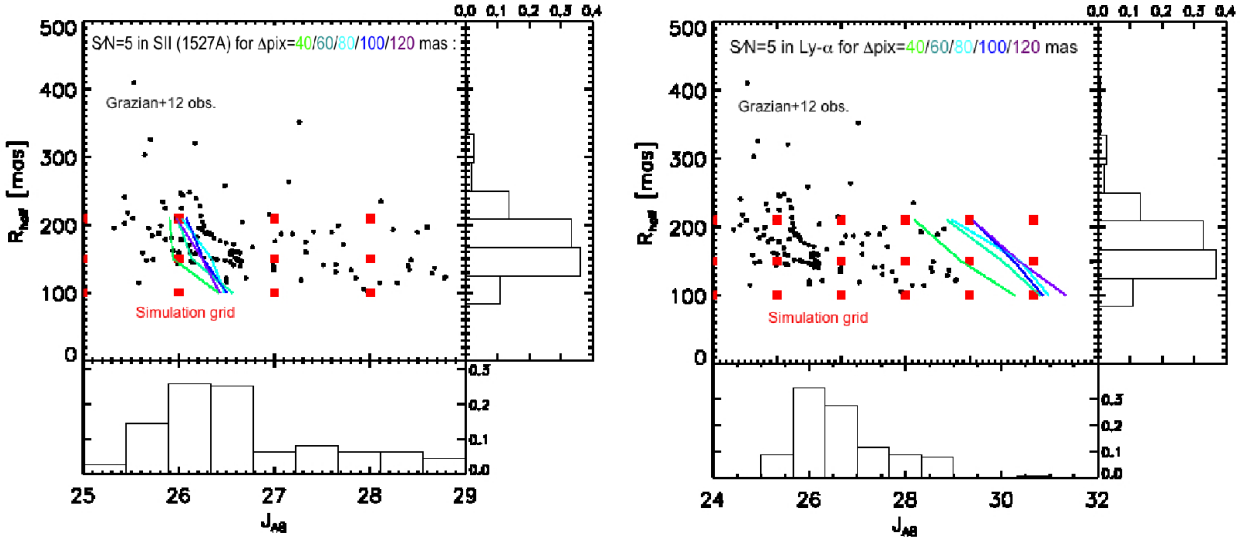

Fig. 3. Observed J_{AB} vs R_{half} distribution of $z \sim 7$ galaxy candidates. Simulated observations are indicated as red squares. The color lines show the limit at which S/N=5 is reached for each simulated pixel size. **Left:** Results for UV absorption lines simulations with t_{intg} =40 hrs. **Right:** Results for LAE simulations with t_{intg} =10 hrs.

References

Bournaud, F., Elmegreen, B.G., Elmegreen, D.M. 2007, ApJ, 670, 237
Evans, C. et al. 2011, A&A, 527, 50
Grazian, A. et al. 2012, A&A, 547,51
Jiang, L. et al. 2013, ApJ, 772, 99
Navarro, R. et al. 2010, SPIE 7735, 88
Puech, M. et al. 2008, MNRAS, 390, 1089
Puech, M. et al. 2010, MNRAS 402, 903
Puech, M., Yang, Y.B., Flores, H. SPIE 7735, 183
Rosales-Ortega, F.F, Arribas, S., Colina, L. 2012, A&A 539, 73
Shapley, A., Steidel, C., Pettini, M. and Adelberger, K. 2003, ApJ, 588, 65
Swinbank, A.M. et al. 2007, MNRAS, 376, 479
Yang, Y.B. et al. 2013, The ESO Messenger, 151, 10

SF2A 2013
L. Cambrésy, F. Martins, E. Nuss and A. Palacios (eds)

MOSAIC AT E-ELT: A MOS FOR ASTROPHYSICS, IGM AND COSMOLOGY

F. Hammer[1] and (on behalf) the MOSAIC team

Abstract. The Universe includes hundreds of billions of galaxies, each of them being populated by hundreds of billions of stars. Astrophysics aims to understand the complexity of an almost incommensurable number of stars, stellar clusters and galaxies, including their spatial distribution, their formation and their current interactions with the interstellar and intergalactic media. A considerable fraction of discoveries in astrophysics require statistics, which can only be addressed by a MOS. A visible/near-IR MOS with capacities adapted from stellar physics to cosmology is technically feasible as recent studies have demonstrated that key issues like sky background subtraction and multi-object AO can be solved.

The E-ELT, which will be the world's largest optical/IR telescope in the 2020s, has to be equipped as soon as possible with a MOS that allows the largest discovery space. The MOS at the E-ELT will be unique to probe the sources of reionisation, to investigate their physics, to study the galaxy mass-assembly history including high-z dwarves, to describe the distribution of the IGM, as well as probing resolved stars at unprecedented distances, from the outskirts of the Local Group for main sequence stars, to a significant volume including nearby galaxy clusters for luminous red supergiants.

Keywords: instrumentation, astrophysics, galaxies, stars

1 Introduction

During the 1990s, the first multiple object spectrographs implemented at the Anglo-Australian and Canada-France-Hawaii Telescopes have produced major breakthroughs simply by multiplying by huge factors the size of the observed Universe. For example, the Canada France Redshift Survey (Hammer et al. 1995; Le Fevre et al. 1995; Lilly et al. 1995) was the first to gather a complete sample at z$\sim$ 1 corresponding to a volume of 150 Gpc^3, instead of 1 Gpc^3 at z$\sim$ 0.15 previously investigated. All the 8 meter-class telescopes are currently equipped with multiple object spectrographs, which gather most of the observing time, and lead to a considerable fraction of the discoveries. LRIS has given to the Keck the glory to be the first in identifying the population of Lyman break galaxies at z$\sim$ 3 (Steidel et al. 1996). At VLT, FORS has revealed the pre-existence of early type galaxies at z >1, and FLAMES has provided the first metal abundances in the dwarf spheroids in the vicinity of the Milky Way by measuring numerous stars at once. There is also a massive investment at VLT with a large community support for wide field, MOS instruments (e.g., KMOS and MUSE).

The crucial need for a MOS, obvious for 4 and 8 meter-class telescopes, still stands for $\geq$ 30 meter-class telescopes. The advent of the ELTs will allow the detection of primordial sources in the Universe as well as to providing detailed diagnostics of sources that are merely detected by present-day telescopes (e.g., galaxy population up to the re-ionization epoch, low-mass & dwarf galaxies at all epochs, individual stars and stellar clusters in galaxies well outside the Local Group etc). The best solution for a MOS is to sample the largest discovery space in terms of wavelength range, spectral and spatial resolutions, and multiplex. Modern astrophysics also requires multiple integral field units (IFUs) at ELTs. Only such devices can measure the kinematics of the gas in very distant galaxies, and are superior to any other system in removing the sky signal, as it can be estimated from pixels surrounding the source of interest.

The MOSAIC white paper (see Evans et al. 2013) highlights six key science cases, from resolving individual stars outside the Local Group to cosmology. We must add, however, that we have been very impressed by the far

[1] GEPI, Observatoire de Paris, UMR 8111, CNRS

larger number of science cases that have been presented during the ELT-MOS meeting in Amsterdam (October 2012) and several national ELT-MOS meetings in different European countries and in Brazil. To account for most of them, we have defined two preferential modes, one with high multiplex (HMM, multiplex=100 to 250, GLAO or seeing resolution), and one with high spatial definition (HDM, MOAO IFUs, multiplex=10 to 20, pixel size from 40 to 80 max). During the writing of the white paper, we have realized that almost all sciences cases will highly benefit from the combination of these two modes, leading to an up-date of the document before 2014.

2 MOSAIC is unique for understanding physics of galaxy & star formation

The scientific objectives of MOSAIC essentially gather those of EAGLE (Cuby et al. 2010) and of OPTIMOS-EVE (Hammer et al. 2010). Combination of high multiplex with different spectral resolutions (R=3000-5000 and R=20000) allows to study individual stars in various environments as well as to study abundances and star formation histories of dwarf galaxies up to z=4. The high multiplex mode with fibers could be slightly less efficient than slits in recovering spectra of ultra-faint objects, though current efforts in optimizing sky-subtraction are very encouraging for reaching accuracy down to 0.4-0.6% of the sky continuum (Yang et al. 2013). Nevertheless, multi-slit spectroscopy is mostly adapted to low resolution spectroscopy that is focused to redshift survey and gross estimates of few quantities. Spectral resolutions from 3000 to 10000 are mandatory for resolving even the smallest galaxies seen in the early epoch of the Universe, in order to properly measure extinctions, star formation rates (see, e.g., Liang et al. 2004), O/H abundances, and especially, kinematics. Such resolutions are generic for fiber spectrographs, and are also mandatory for a proper removal of sky emission lines above 0.72μm.

MOSAIC is potentially the instrument at an ELT that will provide the deepest and most complete insights into the physics of the first galaxies (see contribution by J. G. Cuby, same volume). In fact armed with multiple IFUs, MOSAIC would be able to identify the main physical processes of galaxy formation, since the earliest light in the Universe. The potential of MOSAIC combined with deep imagery at exquisite spatial resolution such as that provided by JWST and E-ELT-CAM, will be without any competitors within the next decades.

To illustrate this, let us compare what has been learnt about galaxy formation from the combination of the VLT and of the HST. With this combination, the deepest and most complete observations of intermediate distant galaxies (z$<$ 1) are rather comparable to what can be done in the nearby Universe, allowing to study the ancestors of present-day galaxies, 6 to 8 billion years ago. Observations included spatially-resolved kinematics from VLT, detailed morphologies from HST and photometry from UV to mid-IR (Spitzer). Six billions years ago, half of the present-day spirals were starbursts experiencing major mergers, evidence for this is provided by their anomalous kinematics and morphologies (Yang et al. 2008; Neichel et al. 2008; Delgado-Serrano et al. 2010). They have been consequently modeled using hydrodynamics models of mergers (Hammer et al. 2009) and it perfectly matches with merger rate predictions by state-of-the-art-ΛCDM semi-empirical models (Hopkins et al. 2010; Puech et al. 2012). Furthermore imprints in the halo of local galaxies such as NGC5907 are likely caused by major merger relics (Wang et al. 2012). This suggests that the hierarchical scenario has played a major role in shaping the massive galaxies of the Hubble sequence (Hammer et al. 2005, 2009). Nowadays, most cosmological simulations (see e.g., Aumer et al. 2013 and references therein) -if not all- are predicting the rebuilding of spiral disks after major mergers, which orbital imprints have settled the disk angular momentum.

A similar, complete investigation of the physical properties of z$>>$ 1 galaxies is presently out of reach, mostly because of their faintness (up to 26-27 AB magnitudes) and compactness (stellar half light radius down to 0.1-0.2 arc sec). Thanks to their considerably large diameters and to the development of adaptive optics, including multiple object adaptive optics (see, e.g., Assemat et al. 2007), E-ELT/MOSAIC and JWST together could be the successful combination to investigate the physics of the first instants of galaxy formation, near or at the time the Universe was still not re-ionized. Such a combination will not be challenged at other 30m-class telescopes, because those will not be equipped with multi-IFUs but with multi-slit spectrographs. In a similar way, MOSAIC will estimate abundances of individual stars in galaxies far outside the Local Group, including Red Supergiants up to 35 Mpc, i.e., in any kind of galactic type or of environment. Here again, MOSAIC will be without competitors because of its relatively large multiplex mode at R= 5000 to 20000 (Davies et al. 2010; Evans et al. 2010).

3 Present status of MOSAIC

The MOSAIC team is led by a France-UK-Netherlands-Brazil consortium, with a strong support from other ESO members, such as Austria, Germany, Italy & Sweden. The core-team includes scientists and engineers who were leading or taking important responsabilities into the realization of FLAMES/GIRAFFE, X-SHOOTER, ISAAC, NACO and KMOS at VLT.

The first activity has been to re-evaluate scientific objectives of both EAGLE and EVE, in the context for which the two first-light instruments have been decided by ESO. This work has been and is currently done by the Science Team that includes 66 scientists from the overall Europe and Brazil, and most of the key Science Cases have been tested using an end-to-end, open-access simulator, realized and maintained at the Paris Observatory (Puech et al. 2010). High level science requirements are now at a stage for which a compromise should be done between, e.g., the HDM pixel size, the possible extent to the K-band, and the HMM multiplex value. Adaptive optics of MOSAIC is also under study, for optimizing the correction, while keeping the complexity/cost reasonable. Other important requirements are also under study requiring simulations of characteristic science cases, such as the wavelength range accessible in one exposure or the aperture size of the HMM fibers. Operating modes and the possible advantage of combining them during the same exposure is also under study. The team is pursuing its effort on improving the best method to subtract the sky with fibers and IFUs. The latter activity has been also useful for MOONS, which is a near-IR fiber fed spectrograph recently selected as a third generation instrument for the VLT, and which is also led by a part of the MOSAIC team.

The technical team has now defined two possible, generic solutions for MOSAIC. The first one allows the two modes (HMM and HDM) to share the same plateau, the second one is envisioning one plateau per mode ("a la FLAMES"), implying that visible and NIR spectrographs are linked to the focal plates by fibers. Both solutions have their advantages and disadvantages, and a final trade-off is expected, probably next year, at the time ESO is expected to launch a Call for an ELT-MOS. As described above, the overall goal of the MOSAIC team is to prepare a relatively versatile instrument for the E-ELT, which has also to be simple and operable enough. Though such a goal could appear unrealistic for the considerable versatility of MOSAIC, we have learned from FLAMES that fibers are quite powerful to limit the complexity and operability risks for multi-mode instruments.

4 Conclusions

A significant part of the European and Brazilian scientific community is supporting the rapid implementation of a MOS at the E-ELT. The combination of ELT-MOSAIC with JWST and other imagers such as ELT-CAM, will be without competitors to investigate physical properties of galaxies since the earliest time of their formation. Their morphologies will be compared to their internal motions from spatially resolved spectroscopy, and together with important physical quantities (masses, SFR, O/H), one will resolve the way galaxies are forming from the primitive gas-rich Universe. Similarly, a relatively large multiplex at R= 5000 to 20000 would make MOSAIC unique for investigating individual stars in a large volume, up to 35 Mpc, allowing to investigate them in every kind of galactic type and of environment.

References

Aumer, M., White, S. D. M., Naab, T., Scannapieco, C., 2013, MNRAS 434, 3142
Assemat, F., Gendron, E. & Hammer, F., 2007, MNRAS, 376, 287
Cuby, J. G., Morris, S., Fusco, T. et al., 2010, SPIE, 7735, 80
Davies, B., Kudritzki, R.-P.; Figer, D. F. 2010, MNRAS, 407, 1203
Delgado-Serrano, R.; Hammer, F.; Yang, Y. B.; Puech, M.; Flores, H.; Rodrigues, M. 2010, A&A, 509, 78
Evans, C. J.; Davies, B.; Kudritzki, R.-P.et al., 2010, A&A, 527, 50
Evans, C., Puech, M., Barbuy, B. et al., 2013, (arXiv1303.0029E)
Hammer, F., Crampton, D., Le Fevre, O. & Lilly, S. 1995, ApJ, 455, 88
Hammer, F., Flores, H., Elbaz, D., Zheng, X. Z., Liang, Y. C., & Cesarsky, C. 2005, A&A, 430, 115
Hammer, F., Flores, H., Puech, M., Yang, Y. B., Athanassoula, E., et al. 2009, A&A, 507, 1313

Hammer, F., Kaper, L., & Dalton, G. 2010, Messenger 140, 36
Hopkins, P. F., Croton, D., Bundy, K. et al., 2010, ApJ., 724, 915
Le Fevre, O., Crampton, D., Lilly, S., Hammer, F., & Tresse, L. 1995, ApJ, 455, 60
Liang, Y. C., Hammer, F., Flores, H., Gruel, N. & Assemat, F., 2004 A&A, 417, 905
Lilly, S., Hammer, F., Le Fevre, O. , & Crampton, D., 1995, ApJ, 455, 75
Neichel, B., et al. 2008, A&A, 484, 159
Puech, M., Rosati, P. & Toft, S. 2010, ASPC, 421, 281
Puech, M., Hammer, F., Hopkins, P. F., Athanassoula, E., Flores, H., Rodrigues, M., Wang, J. L. 2012, ApJ, 753, 128
Steidel, C. C., Giavalisco, M., Pettini, M., Dickinson, M. & Adelberger, K. L. 1996, ApJ 462, 17
Wang, J., Hammer, F., Athanassoula, E., Puech, M., Yang, Y., et al. 2012, A&A, 538, A121
Yang, Y., Flores, H., Hammer, F., et al. 2008, A&A, 477, 789
Yang, Y. B., Rodrigues, M., Puech, M. et al., 2013, Messenger, 151, 10

SF2A 2013
L. Cambrésy, F. Martins, E. Nuss and A. Palacios (eds)

CANARY: A PATHFINDER OF MOAO FOR ELT

O. Martin[1], E. Gendron[1] and G. Rousset[1]

Abstract. MOAO is a wide field adaptive optics system which has been firstly developed to reach the requirements involved for the analysis of the formation and evolution of the high-redshift galaxies. The Canary project was birth from the Eagle project - the first multi-object spectrograph in the near infra-red proposed for the European-Extremely Large Telescope (E-ELT) - as a technical demonstrator of the MOAO. The role of Canary is to demonstrate on-sky the feasibility and reliability of the MOAO and to quantify the nominal performance of MOAO. On-sky results , obtained in 2012 and 2013, are presented in this paper.

Keywords: Adaptive Optics - MOAO - Tomography - Laser Guide Stars - ELT - Canary

1 Introduction

One of the future great challenge in Infra-red astronomy concerns the study of the formation and evolution of the first galaxies of the Universe. Thanks to the collecting power of the Extremely Large Telescopes (Cuby, J.-G. 2010), it will be feasible to deeply analyze by spectroscopy high redshift galaxies ($z \sim 7$). Nevertheless, such an analysis requires an on-sky multiplex observation of more than ten very faint galaxies distributed on a very large field of view of the ELT. Some scientific projects, as EAGLE and EVE (Evans,C.-J. et al. 2012), could involve a few ten of milliarcsec resolution that can be only reached with an large field of view Adaptive Optics system based on Laser Guide Stars to compensate the lack of natural guide stars in such cosmological fields.

Multi-object Adaptive Optics has been revealed as the most adapted adaptive optics system to reach these requirements. However,the feasibility and performance of MOAO has to be demonstrated on-sky, especially the open-loop configuration, the tomographic reconstruction and the instrumental calibrations must be validated on-sky. That is the role of Canary (Myers, R. M. et al. 2008) - the technical demonstrator of MOAO - which is set at the William Hershel Telescope. A first on-sky demonstration of the MOAO using only NGS has already been lead in 2010 (Gendron,E. et al. 2011). We gives in this proceedings an overview of the on-sky results of Canary using both Rayleigh LGS and NGS obtained more recently.

2 The Canary experiment

The Canary project has been started from 2007 and the observation runs take place at the William Hershel Telescope at La Palma. The demonstration of the feasibility of the MOAO using LGS in an EAGLE configuration on a E-ELT has been split into three phases. The first one (phase A) has concerned the on-sky validation of the MOAO using only three NGS and has been successfully passed in 2010 (Gendron,E. et al. 2011). We will present the results of the phase B successfully passed in 2012, using one LGS, and in 2013 using four LGS. Finally, during the phase C, Canary will be design as a single scientific channel MOAO system to simulate EAGLE on a ELT, with a first closed-loop stage to compensate the ground layer and a second stage of pure MOAO.

In order to quantify the on-sky performance of Canary, we are using both a diagnostic Shack-Hartmann sensor - the Truth Sensor (TS) - which is looking at the DM, and an IR camera which delivers PSFs on J (1,28 μm), H (1,67 μm) and K (2,2 μm) band. Thanks to the TS, we are able to close the loop in SCAO and

[1] LESIA, Observatoire de Paris, CNRS, UPMC, University Paris-Diderot, 5 place Jules Janssen, 92195 Meudon, France

compare with the performance of MOAO. We compare with GLAO as well in order to quantify the impact of the tomographic reconstruction in the global performance.

This tomographic reconstruction is performed thanks to the Learn&Apply algorithm (Vidal,F. et al. 2010) based on a Minimum Mean Square Error (MMSE) reconstruction of the TS slopes. This algorithm is split into two steps: the first one is an identification step of the turbulent profile and some calibration parameters. Then, thanks to this identification and a model of the spatial covariance of the turbulence, we are able to compute the MMSE reconstructor to be applied on the off-axis measurements (Martin,O. et al. 2012).

3 On-sky results with LGS

3.1 Phase B1 results

In 2012, We have demonstrated the validity of the MOAO using three NGS and one LGS focused at 13.5 km. We were particularly dominated by a slow ground layer - with an average seeing of 0.7" and an average wind speed of 4 m/s to be compared to respectively 0.25" and 8 m/s for the altitude turbulence. From all the measurements we have got during the phase B1 observation runs, we have computed the histograms of the seeing and wind speeds which have been reported in Fig. 1. From such results, we can conclude that MOAO and GLAO will give close tomographic results since the altitude layers are very weak compared to the ground layer.

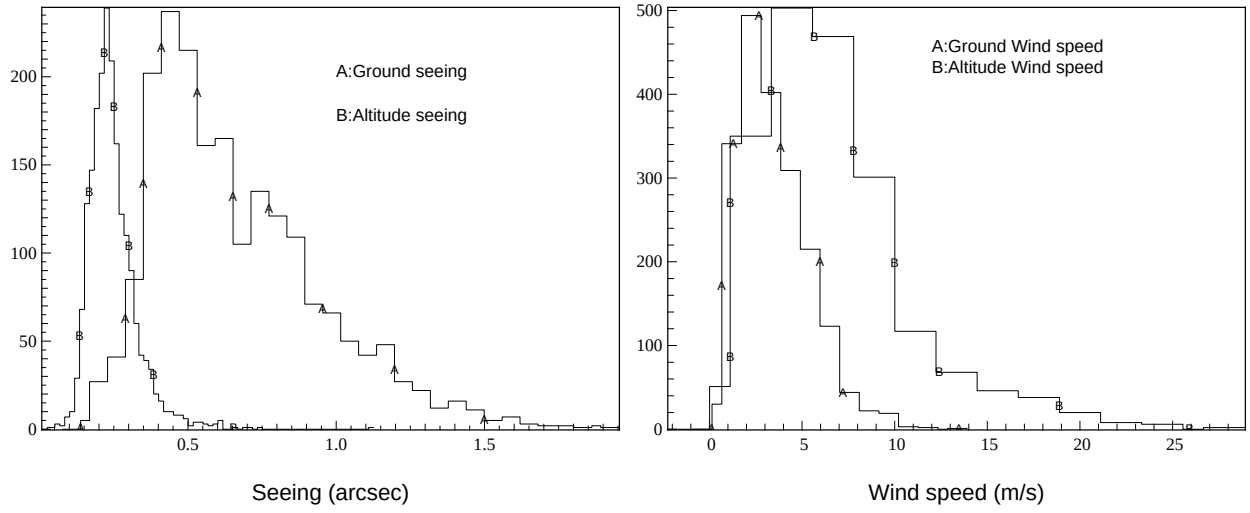

Fig. 1. Left: Histograms of the ground seeing and altitude seeings computed from all the data sets of Canary acquired in 2012.**Right:** Histograms of the ground and altitude wind speed computed from all the data sets of Canary acquired in 2012.

Nevertheless, in Fig. 2, we illustrate that the tomographic reconstruction brings a significant improvements to the global performance measured by the Strehl ratio. In this figure, we note three trends of behaviour on the Strehl ratio as function of the r_0. Despite the scattering of the curves (especially for MOAO and GLAO) due to the variation of the observation conditions - in particular the distribution of the turbulent energy in altitude and the wind speed profile - MOAO looks pretty close to SCAO performance and better than GLAO performance although we were dominated by the ground seeing.

We have also reported in Fig. 2 the tomographic error computed from the difference between the TS slopes in open-loop and the tomographic reconstruction (Martin,O. et al. 2012) that gives a first indication on the tomographic performance of our reconstruction. Finally, we can note that MOAO and GLAO gives very similar results when the r_0 is particularly low, in others words, when the ground layer is strongly turbulent. The constancy of the altitude seeing could be an input for simulation in AO and the ground seeing should be rescaled with respect to the global seeing.

3.2 Phase B2 results

We describe here the results we have got in 2013 on the feasibility of MOAO using 3 NGS and 4 LGS focused at 21 km. In Fig. 3, we have reported the Strehl ratios and the tomographic errors as function of the r_0. Not

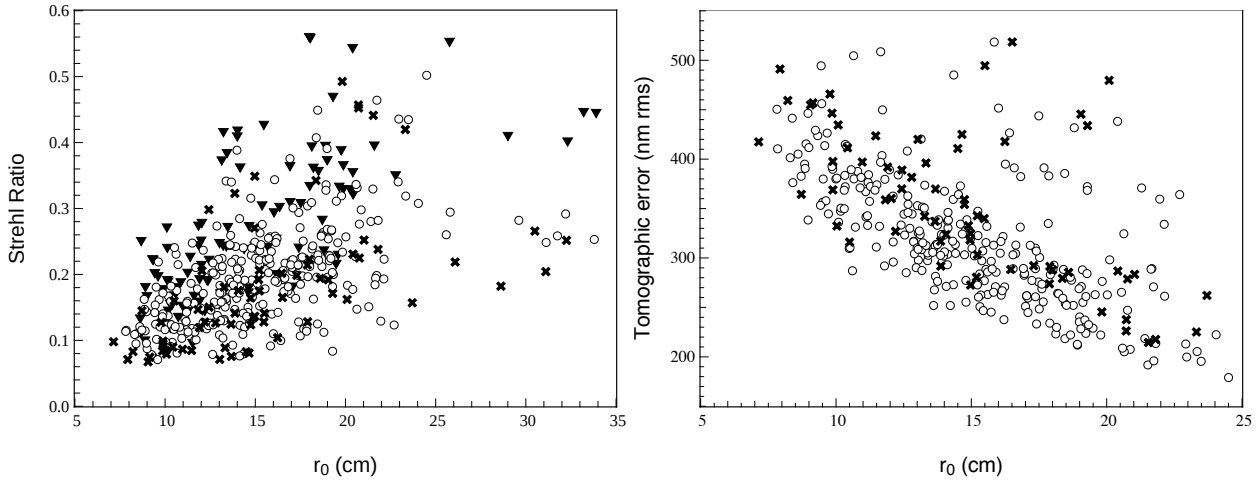

Fig. 2. Left: Strehl ratios measured on-sky in SCAO (triangles), MOAO (circles) and GLAO (crosses) as function of the r_0. **Right:** Tomographic error in MOAO (circles) and GLAO (crosses) as function of the r_0. These results have been acquired by Canary in 2012 using three NGS and one LGS.

surprisingly, we get back the same trends as in 2012, nevertheless MOAO is closer to the SCAO compared to 2012 - especially thanks a greater number of LGS but also thanks to a higher focusing altitude of the LGS with a comparable SNR. We have reported in Fig. 4 IR images of the same target acquired by Canary in 2013 in

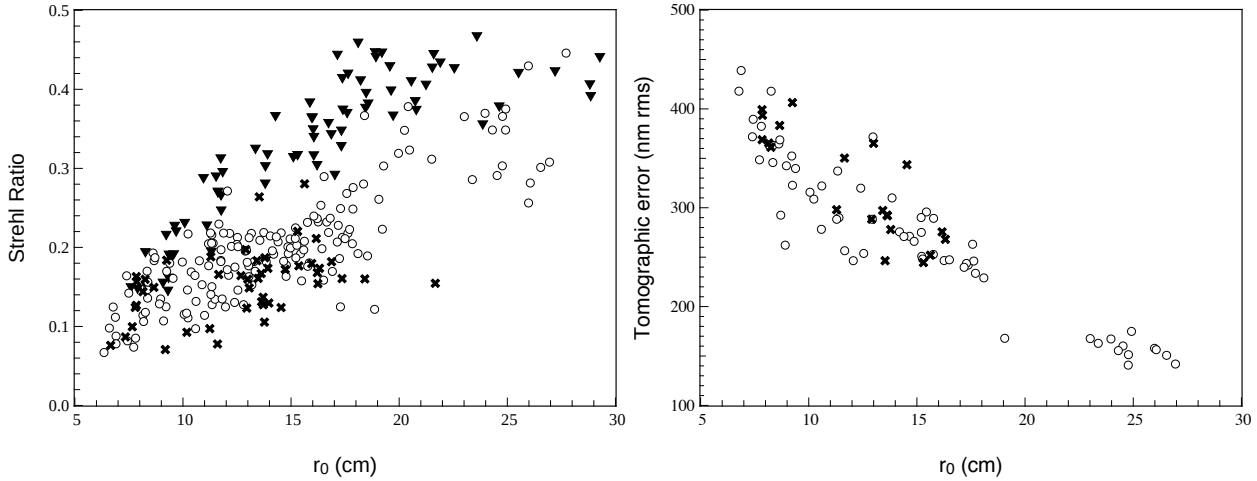

Fig. 3. Left: Strehl ratios measured on-sky in SCAO (triangles), MOAO (circles) and GLAO (crosses) as function of the r_0. **Right:** Tomographic error in MOAO (circles) and GLAO (crosses) as function of the r_0. These results have been acquired by Canary in 2013 using three NGS and four LGS.

open-loop, SCAO, MOAO and GLAO using two NGS and four LGS. These images are an average of thirty one second exposure image and all of them was acquired with very comparable observation condition. When we are running the AO system, we are able to resolve the companion of the binary and the most important is to notice that the MOAO allows to reach a very comparable resolution power than the SCAO and much better than the GLAO.

4 Conclusions

MOAO is a wide field adaptive optics technique which has been developed in order to reach the requirements of a multi-object integral field spectrograph on ELTs. In order to demonstrate the feasibility of MOAO on-sky, the technical demonstrator Canary has been set at the William Hershel Telescope at La Palma. Since 2010,

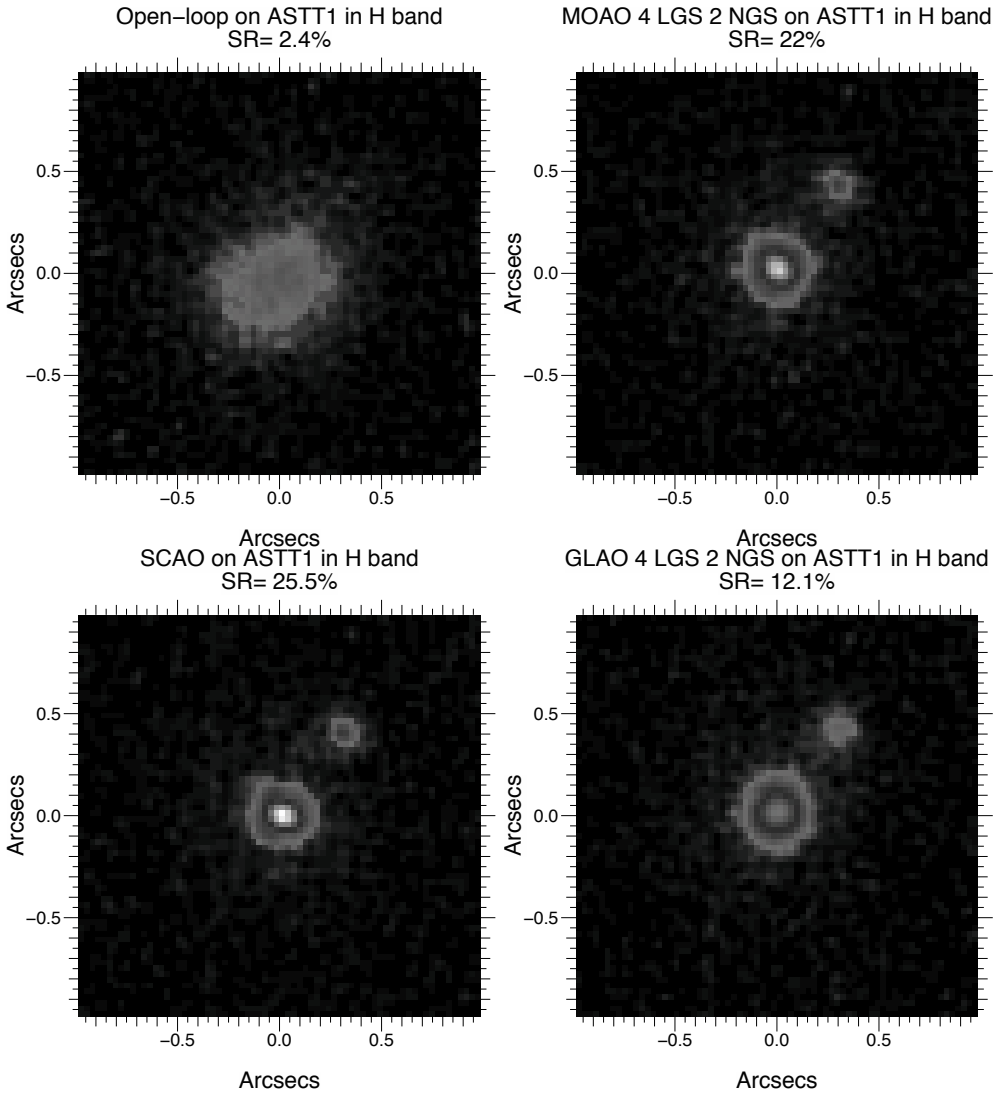

Fig. 4. Psfs in Open-loop - MOAO - SCAO and GLAO on the same object (a binary) and with similar observation conditions acquired in 2013.

we have demonstrated the capability of MOAO using both NGS and Rayleigh LGS and the performance of the mixed NGS/LGS tomographic reconstruction using the Learn&Apply algorithm. MOAO is mandatory for multi-objects spectroscopy on faint galaxies on ELTs and the future results of Canary will give a determinant information for the implementation of MOAO on a ELT.

This work is supported by CNRS, INSU, Observatoire de Paris, University Paris Diderot-Paris 7, Ecole Normale Superieure de Cachan and European Commission Framework Programme (OPTICON JRA1 Grant 226604, 2009).

References

Cuby , J.-G.,"The European ELT: status report", proc SF2A 2010, 2010.

Evans,C.-J., Barbuy,B., Bonifacio,P. et al., "Multi-object Spectroscopy with the European ELT: Scientific synergies between EAGLE & EVE" in *Ground-based and Airborne Telescopes IV*, proc SPIE 2012, 2012

Myers, R. M., Hubert, Z., Morris, T. J. et al., "CANARY: the On-sky NGS/LGS MOAO demonstrator for EAGLE" in *Adaptive Optics System* , proc SPIE 7015, 2008

Gendron,E., Vidal,F., Brangier,M. et al., "MOAO first on-sky demonstration with CANARY" in Astron.Astrphys 529, pp. L2+, 2011

Morris,T.J., Basden,A.-G.,Vidal,F. et al, "Tests of open-loop LGS Tomography with Canary" in *Adaptive Optics System III*,proc SPIE 8447, 2012

Vidal,F.,Gendron,E.,Rousset,G., JOSA A 27, pp. A253-A264, November 2010

Martin,O.,Gendron,E.,Rousset,G.,"Temporal convergence of phase covariance matrix measurements in tomographic adaptive optics" in *Adaptive Optics System III*,proc SPIE 8447, 2012

SF2A 2013
L. Cambrésy, F. Martins, E. Nuss and A. Palacios (eds)

HIRES: A HIGH-RESOLUTION ECHELLE SPECTROGRAPH FOR THE E-ELT

L. Origlia[1] on behalf of the HIRES Consortium[2]

Abstract. HIRES is the study of a High Resolution Spectrograph for the E-ELT. Flagship science cases include the characterization of exoplanet atmospheres with the prospect of the detection of signatures of life on rocky planets, the chemical composition of planetary debris on the surface of white dwarfs, protoplanetary and proto-stellar disks, detailed stellar physics and evolution over the full space of stellar parameters, Galactic archaeology out to the Local Group and beyond, the chemical fingerprints imprinted by population III stars on the Inter-Galactic Medium (IGM) during the epoch of reionization, evolution of galaxies no longer restricted to strongly star-forming and/or very massive galaxies, primordial black holes, and the exciting possibility of paradigm-changing contributions to fundamental physics. Flagship science drivers demands for a stable instrument with a spectral resolution of R≈100,000 and broad, simultaneous spectral coverage extending from 0.37μm to 2.5μm. Most science cases to not require spatially resolved information, and can be pursued in seeing-limited mode, although some of them would benefit of the E-ELT diffraction limited resolution. Some multiplexing as well as some polarimetric capabilities would also be beneficial for a number of the science cases. These various requirements can be met with a highly modular instrument concept that foresees independent and optimized fiber-fed spectrographs, enabling different observing modes and giving access to different wavelength ranges.

Keywords: spectroscopy, high-resolution, science case, instrument concept

1 Introduction

High-resolution spectroscopy is a general definition that applies to R=20,000 domain as well as to the R=100,000 and higher, and in a specific instrument it is tailored to the specific science cases and specialised to different wavelength domains. High resolution spectroscopy has been, during the past twenty years, a rapidly expanding area enabling major, fundamental progresses in most fields of astrophysics, but also in more general areas of fundamental physics.

European astronomers have been leading several of these fields as well as many of the major discoveries thanks to the four high-resolution spectrographs at the VLT (UVES, CRIRES, FLAMES, X-Shooter, covering the full wavelength range from the near-UV at the atmospheric cut-off to 2.5 μm) and HARPS at the 3.6m telescope. This suite of instruments is soon to be joined by the Laser Frequency Comb-calibrated high-fidelity spectrograph ESPRESSO.

This impressive high-resolution capability of the ESO telescopes has delivered excellent science in a wide range of fields from the discovery of exoplanets and the characterization of their atmospheres, stellar chemical abundances, star and planet formation, Galactic Archaeology in our own Galaxy and in the Local Group, the study of supernovae and GRBs, galaxy evolution and the physical state of the IGM, and to interesting constraints on the nature of dark matter and the variation of fundamental constants.

It is clear that in the area of high-resolution spectroscopy, where "photon starving" is the main limiting factor, the discovery space enabled by larger telescopes will be huge. Indeed, ESO had commissioned nine phase A studies for E-ELT instrument concepts that included one optical (CODEX, Pasquini et al. (2010)) and one near-IR (SIMPLE, Origlia et al. (2010)) high-resolution spectrographs.

Based on the result of these phase A studies, the currently applicable E-ELT instrumentation plan will offer a High Resolution Spectrograph as part of its suite of instruments soon after the first-light set of Adaptive

[1] INAF - Bologna Observatory, Via Ranzani 1, 40127 Bologna, Italy
[2] http://www.hires-eelt.org

Optics (AO) modules and Scientific Instruments. This responds to the need to exploit the unprecedented photon-collection power of the E-ELT in the spectral resolution domain.

In this context, HIRES is currently a joint initiative by nine interested partners from Chile, France, Germany, Italy, Portugal, Spain, Sweden, Switzerland and United Kingdom, with the goal of contributing to the definition of a sounded and disruptive science case and of an instrument concept of proven feasibility to implement it.

2 Science Case

The Science Case of HIRES is described in a *white book* (available on the HIRES website) in continuous evolution and constantly updated by the HIRES Science Team. It is built on the experience of the high-resolution community with the suite of VLT high-resolution spectrographs, which has been tremendously successful, and on the Phase A studies of CODEX and SIMPLE. This section summarizes the main science topics detailed in the *white book*.

- Exoplanets are one of the outstanding key science cases for HIRES. Since the discovery almost 20 years ago of the first giant planet outside of the solar system (Mayor & Queloz 1995), the study of exoplanets has become reality and spawned a real revolution in astronomy. Since first discoveries we know more than 800 exoplanets and 2300 additional transiting candidates provided by the Kepler satellite (Batalha et al. 2013). A large fraction of solar-type stars host hot Neptune or super-Earth mass planets, the frequency of multiple planetary systems seems to be very large, and most of smaller planets are observed in multi-planetary systems. With the goal of advancing our understanding of planet formation, evolution, and habitability, the focus of exoplanet science in the E-ELT era will be on the characterization of their atmospheres in terms of chemical composition, stratification and weather. A wide range of planetary masses, from Neptune-like down to Earth-like including those in the habitable zones, need to be explored. The ultimate goal is of course the detection of signatures of life. Such a science goal can be performed by means of transmission spectroscopy during planetary transits. The main instrument requirements of this science case are 1) spectral resolution R=100,000 or higher to separate telluric and exoplanet line systems, to maximize the contrast of narrow molecular lines (hence probing different atmospheric layers), as well as to be sensitive to planet rotation and atmospheric circulation; 2) Simultaneous 0.38-2.40 μm spectral coverage to measure all the interesting features almost everywhere in the visible/near-IR range. The blue limit is set by the inclusion of the Ca II H&K lines for monitoring of stellar activity, while the K-band is desirable for the presence of strong CO bands at $\approx$2.3 μm.; 3) high Point Spread Function stability ($\approx$1/100 of a pixel), pointing towards a fiber-fed instrument in a stable, gravity-invariant environment, with a fixed spectral format and no moving parts inside the spectrograph; 4) good detector stability during planetary transits and high-precision flat-fielding (better than 0.1%). A polarimetric mode would further enhance the exoplanet diagnostic capabilities of HIRES, especially for the detection of bio-signatures.

- In the context of exoplanet science, another hot topic is the chemical characterization of planetary debris (i.e. the building blocks of planetary systems), by the observations of metal-enriched white dwarfs. An E-ELT aperture is critical to observe statistical significant samples of these faint stars and high spectral resolution, high signal to noise in the blue are mandatory to measure the chemistry of the debris.

- The spectroscopic study of protoplanetary and proto-stellar disks in young stellar objects, will provide fundamental information on the dynamics, chemistry and physical conditions in their innermost regions, on the physics of star formation, jet launching mechanisms and planet formation. Such a study requires a near-IR high-resolution (R$\approx$100,000) spectrograph exploited with spatially resolved information (possibly with an IFU mode) at nearly the diffraction limit of the E-ELT. This science case would also benefit from a polarimetric mode, which would provide information on the magnetic field in the inner regions of the accretion disk.

- Our current knowledge of dynamical phenomena and phases of stellar evolution is still very limited and mostly based on studies in the solar neighbourhood. Although new theoretical simulations of stellar convection, differential rotation, stellar activity, mass loss, and interior mixing, as well as star formation and the interaction of stars with protoplanetary disks and planets, are being developed, these efforts are to a considerable degree depending on simplifications and unknown initial conditions, and on free parameters. This primitive state of our knowledge leads to severe limitations of using stars as probes in the empirical study of the evolution of planetary systems and galaxies, and well in cosmology. New,

high-quality observations of stars with different stellar parameters, in different evolutionary stages and located in different environments are urgently needed. When compared to the current generation of ground-based 8-10m class telescopes, the considerably larger aperture of the E-ELT leads to a substantial gain in sensitivity. With an E-ELT and an efficient high-resolution spectrometer covering the full optical and near-IR range, it will be possible to obtain spectra at R≈100,000 and very high signal to noise, thus enabling a detailed determination of the stellar atmosphere structure, physics and chemistry for solar-type and cooler dwarf stars out to distances of several kpc, thus sampling most of the Galactic disk and bulge, or sub-giants and red giants in the outer Galactic Halo and in the neighbouring dwarf galaxies. However, in order to reach the goal, it is fundamentally important that the spectra are not only nominally of high-resolution and have high signal to noise but also very well calibrated (in terms of wavelength, flux, flat-fields, etc.). Some spectro-polarimetric capabilities to probe magnetic fields in a number of stellar conditions, evolutionary stages and environments are also highly desirable.

- An instrument like HIRES on the E-ELT will provide truly revolutionary results in Galactic archaeology out to the Local Group and beyond. At a spectral resolution R≈100,000 and with a broad spectral coverage (0.37-2.5 μm), it will enable the detailed chemical mapping of multiple elements and isotopes, thus revealing the origin and the formation history of ancient stars belonging to different Galactic components. This will be especially crucial for the extremely low metallicity stars, whose photospheres may trace the chemical abundances resulting from the enrichment of the first population of stars (PopIII). HIRES will also be an extremely efficient machine to trace the metal enrichment pattern and dynamics of extragalactic star clusters and resolved stellar populations in other galaxies, if enabled with some multiplexing capability ($\geq$10 objects over a FoV of a few arcmin) with intermediate spectral resolution (R≈20,000) sampling the full spectral range from 0.37-2.5 μm.

- In the context of galaxy formation and cosmology, one of the most exciting prospects for HIRES is the detection of elements synthesized by the first stars in the Universe. HIRES will probably be the first facility that will detect the fingerprint of PopIII stars by measuring the chemical enrichment typical of this population in the IGM and Inter-Stellar Medium in the foreground of Quasars, GRBs and Ultraluminous Supernovae at high redshift, probing in this way the epoch of reionization. The high spectral resolution of HIRES will also allow astronomers to trace in detail the history of the reionization process of the Universe and the subsequent thermal history of the IGM. To reach these outstanding science goals requires a spectral resolution R>50,000 and a spectral coverage extending from about 0.6 to 2.5 μm. If enabled with some multiplexing capability (5-10 objects), HIRES will also be able to obtain a three-dimensional map of the cosmic web of the IGM at high redshift, by probing absorption systems towards multiple lines of sight on scales of a few arcminutes. Most importantly, if the simultaneous wavelength coverage extends from 0.4 to 2.5 μm HIRES will have the unique and exceptional capability of obtaining a three-dimensional map of the distribution of metals in the IGM, which would be a unique probe of the enrichment process of the Universe. For this science case a spectral resolution in the range 10,000-15,000 is optimal.

- The same intermediate spectral resolution, wide simultaneous spectral coverage and multiplexing of 5-10 over a field of view of a few arcminutes are also required to investigate the processes driving the evolution of massive early type galaxies, during the epochs of their formation and assembly (z=1-3), which is still a major unsolved puzzle beyond reach of current facilities.

- If equipped with an IFU sampling the E-ELT diffraction limit, HIRES, with its high spectral resolution (R≈100,000) will be the only tool to measure the low mass end of supermassive black holes in galactic nuclei, which bears signature of primordial black hole seeds.

- Most excitingly perhaps, HIRES will be an instrument capable of addressing issues that go beyond the limited field of Astronomy, breaking into the domain of "fundamental physics". In particular, HIRES will provide the most accurate constraints on a possible variation of the fundamental constants of nature, and in particular of the fine structure constant and of the proton-to-electron mass ratio μ. This measurement will be enabled by a spectral resolution R≈100,000, and high efficiency in the blue part of the spectrum. HIRES will also deliver the most accurate measurement of the deuterium abundance that, compared with the value obtained from the CMB measurements (from Planck), will provide stringent constraints on models of non-standard physics. By measuring the redshift drift-rate dz/dt of absorption features in distant QSOs, HIRES will be the only instrument capable of obtaining a direct, non-geometric, completely

model-independent measurement of the Universes expansion history (the "Sandage test"). This should be regarded as (the beginning of) a legacy experiment, lasting several decades, giving substantial additional value to projects primarily targeting the physics of the IGM with QSO absorption spectra. However, in addition to high-spectral resolution (R≈100,000), this measurement requires a very accurate absolute wavelength calibration of a few cm/s (which can be achieved with laser comb technology and high fiber scrambling efficiency) as well as excellent stability, of the order of a few cm/s, over the duration of an observing night.

3 Instrument Concept

The various science requirements can be met through a highly modular instrument concept, where optimized independent modules enable different observing modes and give access to different wavebands. A modular concept has several advantages.

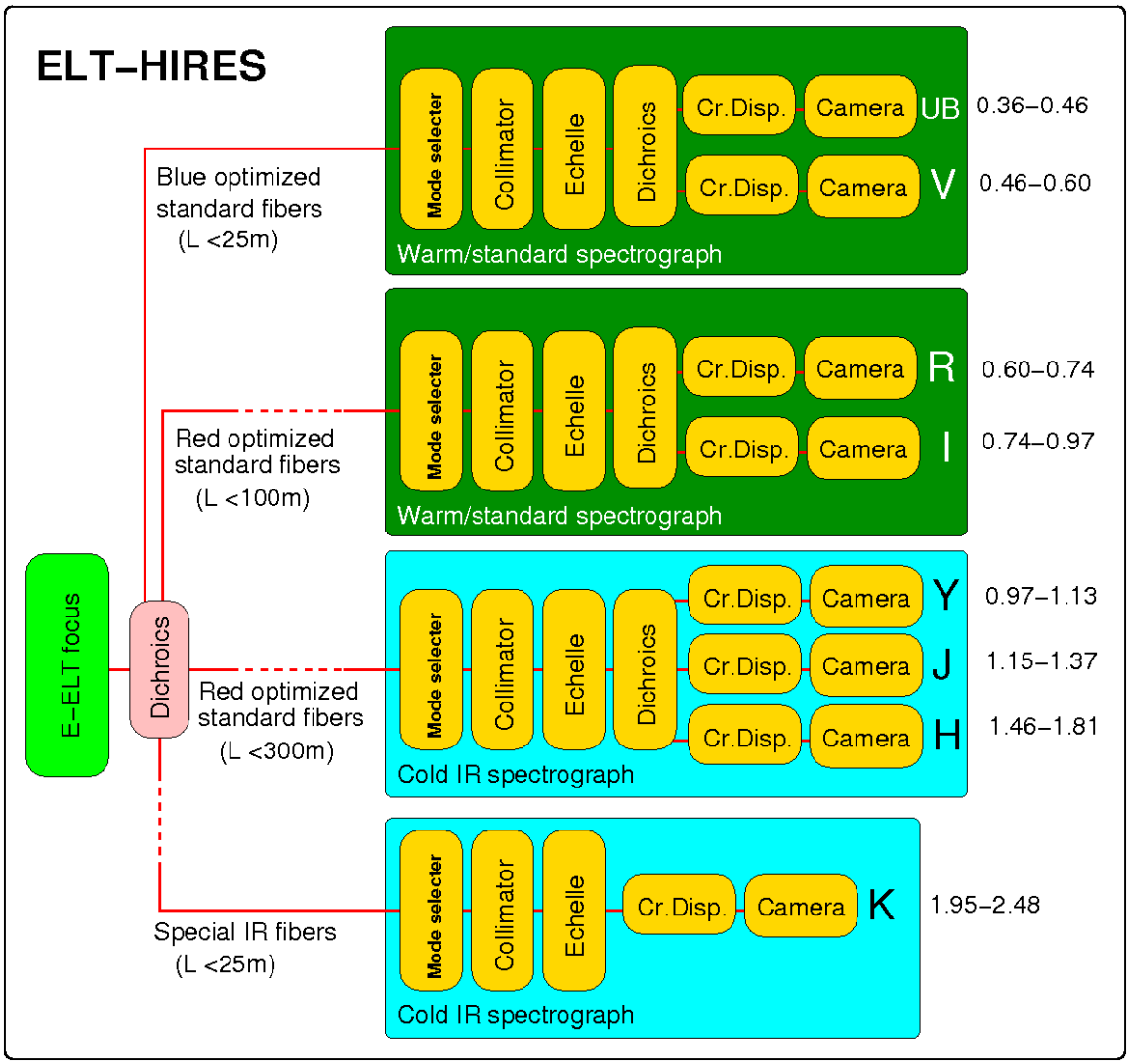

Fig. 1. Possible scheme showing the distribution of the spectroscopic modules for HIRES.

It can be developed in sequential stages, starting with the essential and highest-priority modules, and later upgrading of the instrument with additional less time-critical modules, depending on budget and resources. It reduces the overall risks associated with the project. Technical problems associated with an individual module do not delay the delivery of the other independent modules and their implementation as well as their manteinance at the telescope. Similarly, shortfalls of funding or resources experienced by one of the consortium partners will

only affect the respective module this partner is involved in, and does not prevent the other partners to keep to the delivery schedule of the other modules.

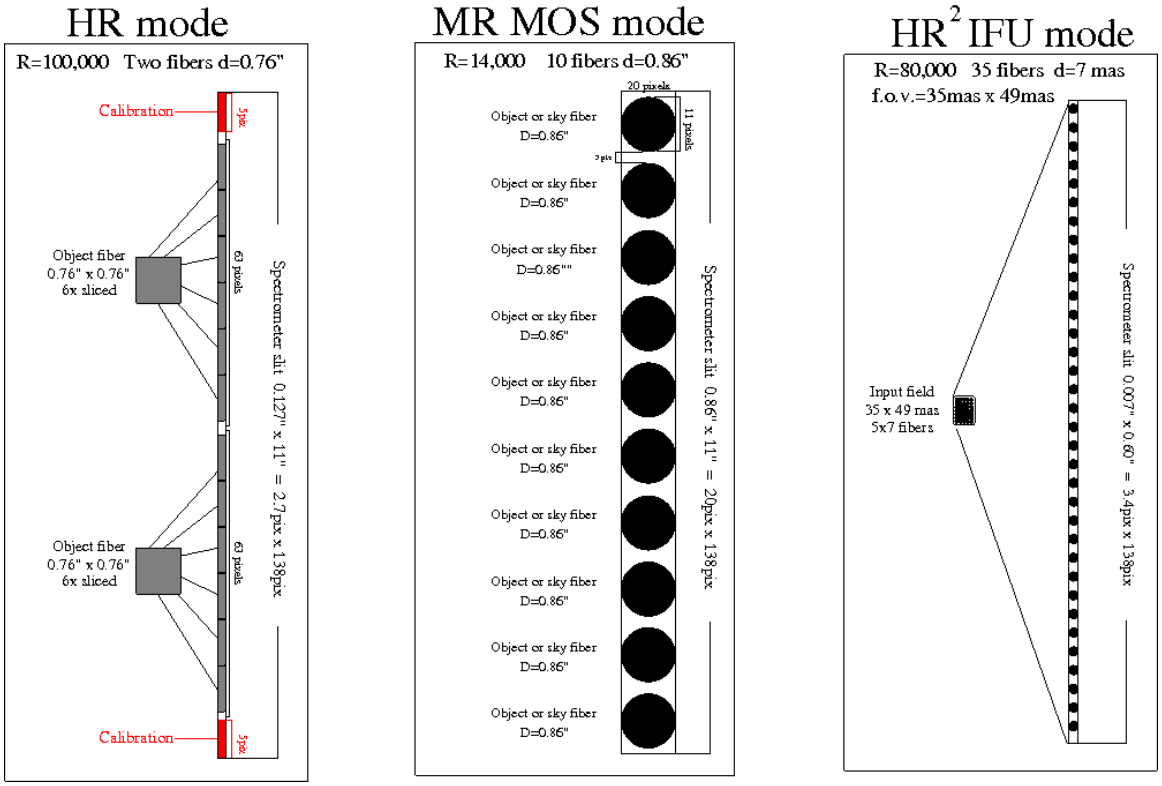

Fig. 2. Illustration of the different possible illuminations of the spectrometer pseudo-slit through different set of fibers.

We propose here that such a modular and versatile system can be realized by a system of fibers that feed simultaneously (through dichroics) different, independent spectrometers optimized for different wavebands. Each spectrometer is fed by fibers optimized for the respective wavelength range.

Such a fiber-fed design provides a natural solution for the implementation of the different observing modes discussed in the science case (high-resolution, moderate multiplexing at intermediate resolution and high spectral and spatial resolution with an IFU assisted by AO. The different modes are obtained by feeding the pseudo-slit in the focal plane of the spectrometers with systems of fibers deployed in different spatial configurations.

Fig. 1 shows a possible scheme of the modular concept: up to four, totally independent spectrometers, optimized in the UB+V and R+I bands and (cryogenic) in the Y+J+H and K bands, fed by a set of optimized fibers. We note that the standard telecommunication (low-OH) fibers in the YJH bands (0.9-1.8 μm) are so transparent that they can be up to 300m long, without affecting the performance of the system. Hence this spectrometer can be accommodated nearly anywhere in the telescope enclosure. The fibers for the blue and K bands, instead, need to be shorter than about 25m to have good throughput, implying that these spectrometers would probably have to sit on one of the Nasmyth platforms.

Fig. 2 shows how the different observing modes can be realized leaving the optics and gratings within the spectrometers fixed, by simply changing the pseudo-slit illumination through a different deployment and feeding of the fibers.

In the basic "high-resolution mode", the light is collected from the telescope by two ≈0.8 arcsec fibers, one for the object and the other for the sky or calibration (a three fibers system can be envisaged, with two fibers allocated for the sky, so to reduce the sky photon noise). A calibration spectrum is always simultaneously recorded at the top and bottom of the pseudo-slit. The light from the fibers is sliced into 2x6 rectangular images aligned along the spectrometer pseudo-slit. Only with the slicing technique is it possible to achieve the required spectral resolution (R≈100,000) with a relatively "small" grating (≈1.2m in size) because the observations are seeing-limited.

In the medium-resolution mode with moderate multiplex the light is collected from the focal plane of the

telescope by 10 fibers (≈0.9 arcsec in diameter), without any slicing. The fibers images are directly arranged onto the pseudo-slit of the spectrometer. Without changing anything within the spectrometer, this setup automatically delivers a spectral resolution of about 15,000. The ten fibers can be all allocated to targets or, for faint objects, half of them can be allocated to the sky. This mode, because of its simultaneous full spectral coverage from U to K, is eventually complementary to the observing modes foreseen by the E-ELT MOS instrument.

A high spectral and spatial resolution IFU mode can be realized with a bundle of fibers fed at the focal plane of a dedicated Single Coniugate AO module, or at the focus of an already existing AO module (e.g. MAORI). The size of the individual fibers would match the diffraction limit in the preferred near-IR band. Inside the spectrograph, the images of the individual IFU fibers would be deployed along the pseudo-slit of the spectrograph. This mode, because of its high spectra resolution (R≈80,000) is eventually complementary to the observing modes foreseen by the E-ELT IFU instrument.

The different observing modes can be selected by a system of two mirrors that relay the light from the different set of fibers to the pseudo-slit of the spectrometer. The system can be realized in such a way that the basic high-resolution mode is the one feeding directly the spectrometer without any relay-mirror. This guarantees that the stability of this basic mode is not affected by the presence of the other observing modes. The other two modes (medium-resolution with moderate multiplexing and IFU+AO), which do not have stringent stability constraints, are enabled by swapping relay mirrors into the beam.

References

Batalha, N. M. et al. 2013, ApJS 204, 24

Mayor, M., & Queloz, D. 1995, Nature, 378, 355

Origlia, L., et al. 2010, SPIE 77352B

Pasquini, L., et al 2010, Msngr. 140, 20, 21

SF2A 2013
L. Cambrésy, F. Martins, E. Nuss and A. Palacios (eds)

THE ELT-MOS WHITE PAPER.

M. Puech[1] and the MOSAIC consortium

Abstract. Several prominent E-ELT science cases will require at least one Multi-Object Spectrograph (MOS). The science cases for an ELT-MOS were revisited and summarized into an ELT-MOS White Paper, which is available on astro-ph. We briefly present its content and discuss two specific requirements on the sky subtraction accuracy with fibers and the optimal IFU pixel scale for galaxy evolution and formation studies.

Keywords: Extremely Large telescopes, multi-object spectroscopy, distant galaxies, sky subtraction, integral field spectroscopy.

1 Introduction: MOSAIC, a new MOS concept for the E-ELT

Multi-object spectrographs are currently the workhorse instruments of the 8-10 meter class observatories. These facilities are indeed very efficient in providing extensive spectroscopic follow-up observations to both ground-based and space-borne imaging surveys. During the E-ELT instrument phase A studies in 2008-2010, several instrument concepts were studied including three MOS concepts, namely EAGLE (Cuby et al. 2010) an near infrared multi-integral field spectrograph fed by multi-object adaptive optics (MOAO), OPTIMOS-EVE, an optical-near infrared MOS (with IFUs or mono-aperture fibers; Navarro et al. 2010), and OPTIMOS-DIORAMAS, an multi-fiber optical-near infrared MOS (Le Fèvre et al. 2010). ESO subsequently announced that the two first light instruments will be a near-infrared camera (ELT-CAM) and a near-infrared mono-object integral field spectrograph (ELT-IFU). The MOS remains in competition for the third slot of the E-ELT instrument road-map.

Since then, as series of meeting were organized to re-examine the scientific needs for a MOS on the E-ELT and find synergies between the different MOS concepts studied in phase A. Two of the three phase A MOS consortia decided to join their efforts into the new MOSAIC international consortium (see Hammer et al., these proceedings). The goal of MOSAIC is to provide the best of the two EAGLE and OPTIMOS-EVE concepts at lower cost and complexity.

2 The ELT-MOS White Paper

As a first step, it was decided the revisit the science cases for an ELT-MOS. This process was stimulated by several international and national meetings held in Amsterdam (in Oct. 2012) and in several European countries (i.e., UK, Italy, Brazil and Netherlands). The conclusions of these meetings were summarized in a White Paper, which is now available on astro-ph (Evans et al. 2012).

We identified the six following prominent science cases for the ELT-MOS:

- SC1: First light and spectroscopy of the most distant galaxies;
- SC2: Spatially-resolved spectroscopy of high-z galaxies;
- SC3: Role of high-z dwarf galaxies in galaxy evolution;
- SC4: Tomography of the IGM;

[1] GEPI, Observatoire de Paris, CNRS-UMR8111, Univ. Paris-Diderot, 5 place Janssen, 92190 Meudon, France

- SC5: Resolved stellar populations beyond the Local Group;
- SC6: Galaxy archaeology with metal-poor stars.

Some of these science cases were detailed using end-to-end simulated observations. Our goal is to update the White Paper regularly with additional inputs from the community and to progressively fill each key science case with such simulations. During the E-ELT instrument phase A studies, we developed a very versatile simulation tool called WEBSIM*. This tool was extensively used to validate the science top level requirements of EAGLE (Evans et al. 2010) and OPTIMOS-EVE (Navarro et al. 2010), as well as during the E-ELT Design Reference Mission (Puech et al. 2010b). It consists in a web interface coupled to an IDL code, which allows the user to conduct full simulations in several observing modes (i.e., mono-aperture fibers, seeing or AO-assisted IFUs) with realistic PSFs. Details about WEBSIM can be found in Puech et al. (2010c).

Investigating these science cases led us to define a Top Level Requirement (TLR) matrix, which list the required spectral and spatial resolution, multiplex, FoV, and spectral bandwidth for each of them. The next step is to prioritize the TLRs and iterate with technical and operational feasibility. The end-to-end simulations are decisive tools to assist in the required trade-offs between these requirements (e.g., spectral bandwidth vs. multiplex vs. spatial resolution; see Disseau et al., these proceedings). The MOSAIC TLRs, as derived from the ELT-MOS White Paper, led us to define two main observing modes, i.e., the High Multiplex Mode (HMM) *à la* OPTIMOS-EVE, with ∼100-250 mono-aperture fibers with GLAO/seeing resolutions, and a High Definition Mode *à la* EAGLE, with ∼10 MOAO-fed IFUs with 40-80 mas sampling. The HMM mode is dedicated to the study of the integrated light emitted by the most compact sources of interest (e.g., very first galaxies, dwarf satellite galaxies), while the HDM is necessary to spatially-resolve the properties of, e.g., distant galaxies, with large enough signal-to-noise ratios. These two modes have been implemented into two preliminary concepts, which are now under evaluation by the consortium against the MOSAIC scientific TLRs (see Hammer et al., these proceedings).

3 SC1: first galaxies and reionisation

This science case is one of the prominent science cases of the E-ELT. The goal is to investigate the sources responsible for the reionisation of the Universe at very high redshift, i.e., between z∼7-20. This is intimately linked to the search of the very first galaxies, which are expected to be very small (i.e., R_{half} ∼100-200 mas) and faint (i.e., J_{AB}=27-30) objects (see, e.g., Grazian et al. 2012). One of the key requirement (see Evans et al. 2012) is to detect galaxies down to J/H_{AB}=27-28 in absorption (using the UV interstellar lines or the Lyman break), and J/H_{AB} ∼30 in emission (using the Ly-α line).

Detecting sources in absorption down to J/H_{AB}=27-28 is very challenging because of the relatively high sky continuum background in the near-infrared, which is typically as bright as J/H_{AB}=19.5-20 between OH lines (e.g., Sullivan & Simcoe 2012). This translates into the requirement that the sky continuum subtraction must be as accurate as 0.1%, otherwise systematic residuals will prevent detecting J/H_{AB}=27-28 sources. It has long been argued that optical fibers cannot reach such a level of accuracy. To address this issue, we tested a cross beam switching observing mode using technical time on sky with FLAMES-GIRAFFE in MEDUSA mode (i.e., the multi-fiber mode of GIRAFFE). This observing mode consists in using the fibers in pairs with constant distance (here 12 arcsec), one pointing at the target, while the second one samples the sky background. Both fibers are sampling the object and sky alternatively using an ABBA sequence (see Fig. 1). This was found to be very efficient in removing the differential fiber response. The residual systematic effect is found to be only 0.6±0.2% of the sky continuum background (Yang et al. 2013), which corresponds to the physical limit associated to the spatial variations of the sky continuum (Puech et al. 2012; Yang et al. 2012). In other words, provided that cross beam switching observations are used, fiber can reach the same accuracy that slits. The remaining limiting effect is found to be scattered light in the instrument. Specific algorithms and purposely-designed instruments should be able to reach an even better accuracy, probably as small as ∼0.1% (Sharp & Parkinson 2010). Even better performances should be reached with the IFUs, since the sky continuum is sampled continuously around the target. Such an observing mode has been adopted as a baseline for MOONS, a third generation MOS for the VLT (Cirasuolo et al. 2012).

*visit https://websim.obspm.fr

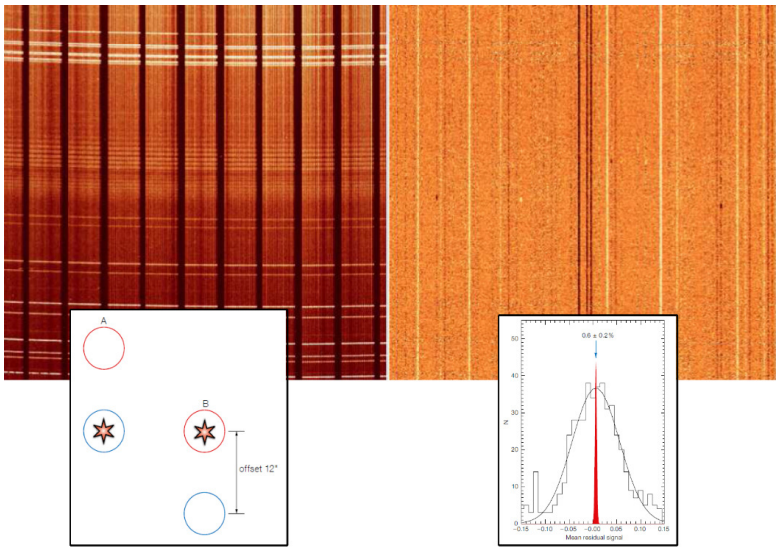

Fig. 1. On-sky demonstration of the cross beam switching observing mode with FLAMES-GIRAFFE fibers. The bottom left panel illustrates the observing operations: the target in observed in a given fiber while the nearby sky signal is measured by another fiber (seq. A); then the telescope is offset by the distance between the two fibers to switch the object and sky w.r.t. the two fibers (seq. B). The upper left panel shows the raw spectra obtained in the GIRAFFE fibers after observing blank regions (i.e., the sky background signal). Wavelength increases along the vertical axis, while columns are different fibers spread over the field of view. The left panel shows the result of the ABBA sequence after subtraction on the raw data. The bottom right panels show the distribution of the residual on the sky continuum background signal after subtraction on the fully reduced data after a detailed analysis (Yang et al. 2013).

4 SC2: spatially-resolved spectroscopy of galaxies

The goal of this science cases is to better understand how galaxies formed and evolved. When observing distant galaxies (i.e., at z≥1), a significant fraction of them reveal relatively thick disks with a clumpy light distribution (e.g., Elmegreen et al. 2007; Puech 2010). Such clumps are thought to be potentially important in galaxy evolution (e.g., Bournaud et al. 2013). Better understanding the relation between these clumps and the underlying disk requires to spatially-resolve the clumps internal kinematics.

Specifying the spatial sampling of an IFU requires determining the optimal trade-off between spatial resolution and sensitivity (Puech et al. 2008). This generally translates into choosing the largest spatial scale which allows one to spatially-resolve the structure of interest, hence providing the best signal-to-noise ratio for resolving it. During the EAGLE Phase A study, this led us to adopt an IFU pixel scale of 37.5 mas to resolve distant clumps. However, it is now known that ELT-IFU will provide from first light exquisite diffraction-limited spatially-resolved observations of distant galaxies. In addition, a lot of efforts are currently underway at the VLT with SINFONI+AO (assisted by the Laser Guide Star, see Newman et al. 2013). It is therefore very likely that samples of tens or perhaps hundreds of clumpy galaxies with high enough spatial resolution will be assembled by the time ELT-MOS will become available. Instead of optimizing the MOSAIC IFU spatial resolution for resolving clumps (as was the EAGLE IFU during Phase A, see Puech et al. 2010a), an alternative would be to optimize the IFU pixel scale for resolving the overall size of distant galaxies, on which the dynamical state is imprinted. This allows distinguishing an ongoing merger from a relaxed rotating disk (Puech et al. 2008, 2010b). Simulations then reveal that this should be possible up to z∼4 and down to sub-M* (or up to z∼5.6 and down to only M* galaxies) with a spatial sampling of only 50-75 mas (see Fig. 2)). Optimizing the ELT-MOS IFU that way in survey speed would be an interesting niche for MOSAIC, which would then be able to observe hundreds of distant galaxies in a limited amount of nights.

5 Conclusions

A MOS on the E-ELT will be essential to achieve a number of prominent science cases. We revisited the ELT-MOS science cases in a White Paper, which is available on astro-ph. New versions with additional inputs

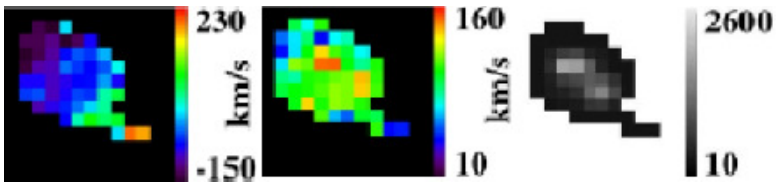

Fig. 2. Kinematics of a major merger as derived from simulations of IFU observations at z4, with 75mas/pixel, integratino time of 24h and MOAO correction with EE=34%. The velocity fields (first column), the velocity dispersion maps (second column), and the emission line flux maps (last column, units are in median counts per dit) are shown. The object size is 0.8 arcsec in diameter, which represents 0.12 kpc at z=4. The two progenitors can be cleary seen in the emission line map. See Puech et al. (2008) for details.

from the community and further observation simulations will be issued regularly. These scientific inputs led us to define MOSAIC, a new conceptual study for an ELT-MOS that builds on the previous EAGLE and OPTIMOS-EVE phase A studies. Simulations of the different ELT-MOS science cases are on-going. If one wants to optimize the MOSAIC IFU pixel scale for survey speed (i.e., in terms of signal-to-noise ratio), the simulations conducted so far suggest an optimal pixel scale close to 80 mas.

We warmly thank all people who have provided inputs for the White Paper and simulations.

References

Bournaud, F., Perret, V., Renaud, F., et al. 2013, ArXiv e-prints

Cirasuolo, M., Afonso, J., Bender, R., et al. 2012, in Society of Photo-Optical Instrumentation Engineers (SPIE) Conference Series, Vol. 8446, Society of Photo-Optical Instrumentation Engineers (SPIE) Conference Series

Cuby, J.-G., Morris, S., Fusco, T., et al. 2010, in Society of Photo-Optical Instrumentation Engineers (SPIE) Conference Series, Vol. 7735, Society of Photo-Optical Instrumentation Engineers (SPIE) Conference Series

Elmegreen, D. M., Elmegreen, B. G., Ravindranath, S., & Coe, D. A. 2007, ApJ, 658, 763

Evans, C. J., Barbuy, B., Bonifacio, P., et al. 2012, in Society of Photo-Optical Instrumentation Engineers (SPIE) Conference Series, Vol. 8446, Society of Photo-Optical Instrumentation Engineers (SPIE) Conference Series

Evans, C. J., Lehnert, M. D., Cuby, J.-G., et al. 2010, in Society of Photo-Optical Instrumentation Engineers (SPIE) Conference Series, Vol. 7735, Society of Photo-Optical Instrumentation Engineers (SPIE) Conference Series

Grazian, A., Castellano, M., Fontana, A., et al. 2012, A&A, 547, A51

Le Fèvre, O., Hill, L., Le Mignant, D., et al. 2010, The Messenger, 140, 34

Navarro, R., Chemla, F., Bonifacio, P., et al. 2010, in Society of Photo-Optical Instrumentation Engineers (SPIE) Conference Series, Vol. 7735, Society of Photo-Optical Instrumentation Engineers (SPIE) Conference Series

Newman, S. F., Genzel, R., Förster Schreiber, N. M., et al. 2013, ApJ, 767, 104

Puech, M. 2010, MNRAS, 406, 535

Puech, M., Flores, H., Lehnert, M., et al. 2008, MNRAS, 390, 1089

Puech, M., Flores, H., Yang, Y. B., et al. 2012, in Society of Photo-Optical Instrumentation Engineers (SPIE) Conference Series, Vol. 8446, Society of Photo-Optical Instrumentation Engineers (SPIE) Conference Series

Puech, M., Lehnert, M., Yang, Y., et al. 2010a, in Adaptative Optics for Extremely Large Telescopes

Puech, M., Rosati, P., Toft, S., et al. 2010b, MNRAS, 402, 903

Puech, M., Yang, Y. B., & Flores, H. 2010c, in Society of Photo-Optical Instrumentation Engineers (SPIE) Conference Series, Vol. 7735, Society of Photo-Optical Instrumentation Engineers (SPIE) Conference Series

Sharp, R. & Parkinson, H. 2010, MNRAS, 408, 2495

Sullivan, P. W. & Simcoe, R. A. 2012, PASP, 124, 1336

Yang, Y., Rodrigues, M., Puech, M., et al. 2013, The Messenger, 151, 10

Yang, Y. B., Puech, M., Flores, H., et al. 2012, in Society of Photo-Optical Instrumentation Engineers (SPIE) Conference Series, Vol. 8446, Society of Photo-Optical Instrumentation Engineers (SPIE) Conference Series

SF2A 2013
L. Cambrésy, F. Martins, E. Nuss and A. Palacios (eds)

THE ROLE OF SUPER STELLAR CLUSTER IN EXTREME STELLAR FORMATION: WHICH PROGRAMME FOR THE E-ELT ?

D. Rouan[1], D. Gratadour[1] and C. Perrot[1,]

Abstract.

In ULIRGs, the intense star formation (up to 1000 Msol / year) induced by the direct interaction of two galaxies is concretized as extremely compact and bright star clusters with no equivalent in the Galaxy. These super star cluster (SSC) which play a major role in the structural and chemical Evolution of galaxies are rare and distant (d ≈ 150 Mpc) with a diameter lower than the resolution achieved with adaptive optics on a 8 -10m telescope. The resolution offered by MICADO on the EELT (10 mas , 8 pc at 150 Mpc) will allow a major leap in three types of programs:

- characterizing the starburst on five times more distant objects
- spatial resolution of the close SSC to address many questions: Schmidt law, filiation with globular clusters, proper spatial structure (IMF, HII region clustering, dust clustering, etc.)
- finding direct links between a starburst and the presence of a central super-massive black hole. Instrumental choices are analyzed against these objectives.

Dans les ULIRGs, l'intense formation d'étoiles (jusqu'à 1000 Msol / an) induite par l'interaction directe de deux galaxies se concrétise sous forme d'amas stellaires extrêmement compacts et lumineux sans équivalent dans la Galaxie. Ces super amas stellaire (SSC) qui jouent un rôle majeur dans l'évolution structurelle et chimique des galaxies, sont rares et lointains (d ≈ 150 Mpc) avec un diamètre inférieur à la résolution atteinte avec l'optique adaptative sur un télescope de 8-10m. La résolution que proposera MICADO sur l'EELT (10 mas, soit 8 pc 150 Mpc) permettra d'effectuer un saut qualitatif important sur trois types de programme :

- caractériser la formation par flambées sur des objets 5 fois plus distants
- résoudre les SSC proches pour aborder de nombreuses questions: loi de Schmidt, filiation avec les amas globulaires, structuration spatiale propre(IMF, région HII, clustering de la poussière) etc.
- trouver des liens directs entre la flambée et la présence d'un trou noir ultra-massif central. Les choix instrumentaux sont analysés en regard de ces objectifs.

Keywords: ULIRGs, Super Star Cluster, star formation, HRA, infrared, imaging, ELT

1 Introduction

Star formation triggered by the encounter of two galaxies is especially intense and may lead to star formation rate as high as 1000 times the one measured in the Milky Way (1 Msol /yr). Those extreme galaxies most generally correspond to the class of ultra-luminous galaxies (ULIRGs) which radiate the essential of their energy in the infrared. This is consistent with the fact that the dust cocoon associated to the interaction-driven concentration of gas responsible for the starburst, absorbs most of the stellar power and re-radiates it at longer wavelength. The dust concentration remains opaque during the first phase, so the near to mid infrared domain is the most appropriate to study those objects. Stellar formation occurs essentially under the form of extremely compact and luminous star clusters, some of them can harboring up to the equivalent 10^4 O7 stars !

One archetypical nearby and medium SSC is R136 in the Large Magellanic Cloud. It features the following characteristics: L = $10^8 L_\odot$, 3500 stars, age: 2-5 Myr, size of the core: 4 pc, density: 200 times the one of an OB association, 42 stars O3 (thus the majority of all known O3 star), an IMF which seems to be Salpeter-like.

Those Super Stellar Cluster (SSC) play a major role in the structural and chemical evolution of the galaxies, as illustrated in the scheme below, because of the large conversion of gas in stellar mass, the production of

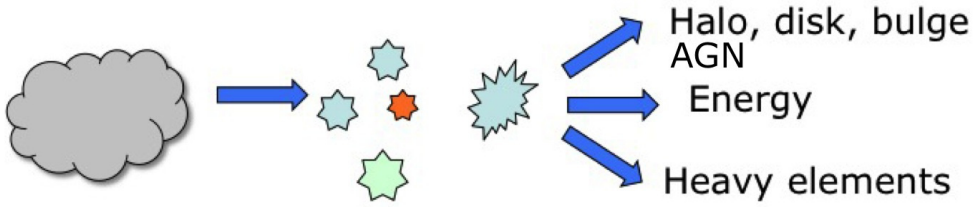

Fig. 1. SSC play a major role in the structural and chemical evolution of the galaxies

heavy elements and their dissemination through SNe, the injection of energy in the whole galactic medium and also because of their presumable role in feeding the super massive black holes at the center of galaxies.

If extensive and more and more complete surveys of ULIRGs do exist (e.g. the recent GOALS sample project: Stierwalt et al. (2013)), the population of SSC themselves remains however badly known because of the large distance of ULIRGs. Especially, their true distribution in mass, size, luminosity, stellar content, dust content, gas content, super-novae rate, etc. remain to be established on a significant sample in order to understand why SSC are so extreme compared to star forming regions in normal galaxies, and how those quantities relate with the intensity of the burst and their location in the system of interacting galaxies.

2 The questions E-ELT should help to anwer

SSC present a clear interest for the study stellar evolution because they show places of ideally synchronous stellar evolution and they allow to study different ages in the same galaxy with a fine temporal evolution. They also present a large coverage in mass and luminosity. General laws, such as the mass function or the related Kennicutt-Schmidt law can be studied in those extreme cases. Finally the question if wether SSC are progenitors of globular cluster and what is their stability (do 10 % of them survive after 40 Myr ?) are important questions.

The typical burst duration being of the order of 10 Myr, ULIRGs are rather rare so that any sample is far enough on the average (typically d = 150 Mpc) for high angular resolution (HAR) to be mandatory. For instance if we consider an ULIRG at 140 Mpc (the median distance in the catalog of Haan et al., 2011) and a typical diameter of a SSC of 20 pc the angular size would be 30 mas. This figure corresponds to half the actual resolution one can achieve in the near-IR on 8m class telescopes equipped with adaptive optics or on the HST in the visible: today, we can barely separate SSC but we cannot make a detailed study of their strucure. On the other hand, HAR will allow to separate SSC in regions where they are concentrated, thus avoiding confusion that would lead to bias the properties of individual SSC towards high values (see Randriamanakoto, 2013). Several programs to study active star formation in ULIRGs have already been conducted using the HST. The survey by Haan et al (2011) is especially noteworthy because it corresponds to a large sample (88 galaxies) and is made in the visible and H bands. There are also several works based on near-IR observations with 8m class telescopes, using spectroscopy or imaging and which are extremely valuable: for instance the recent study of Piqueras-Lopez et al. (2012) presenting an atlas of Integral Field Spectroscopy of 10 LIRGs and 7 ULIRGs and the spectroscopic survey by Davies et al. (2003) of 7 ULIRGs, however both surveys were done under good seeing conditions but not using AO.

The goal that E-ELt should allow to reach is a significant step in angular resolution to study individuals in the population of SSC in several of those distant objects. The study will allow to look for indications on burst propagation and history, as well as relations to a possible AGN, to carry out a statistical analysis of a large set of SSC in various ULIRGs to derive individually, i.e. without confusion, some fundamental properties: extinction-corrected luminosity, precise stellar content (CO bands and H lines), age of the burst or even sequence of ages between SSC (e.g. see Garca-Marin et al. 2006), dust content (IR excess), molecular content (H2 lines); we then will be able to establish overall distributions, especially luminosity and mass function. Correlations and trends between those quantities will also be possible in order to look if they still follow or deviate from known relations found in the nearby Universe, such as the one between the luminosity of the brightest cluster vs the SFR (Bastian, 2008).

[1] LESIA - CNRS, Observatoire de Paris, UPMC, Université Paris-Diderot, Observatoire, F-92195 Meudon

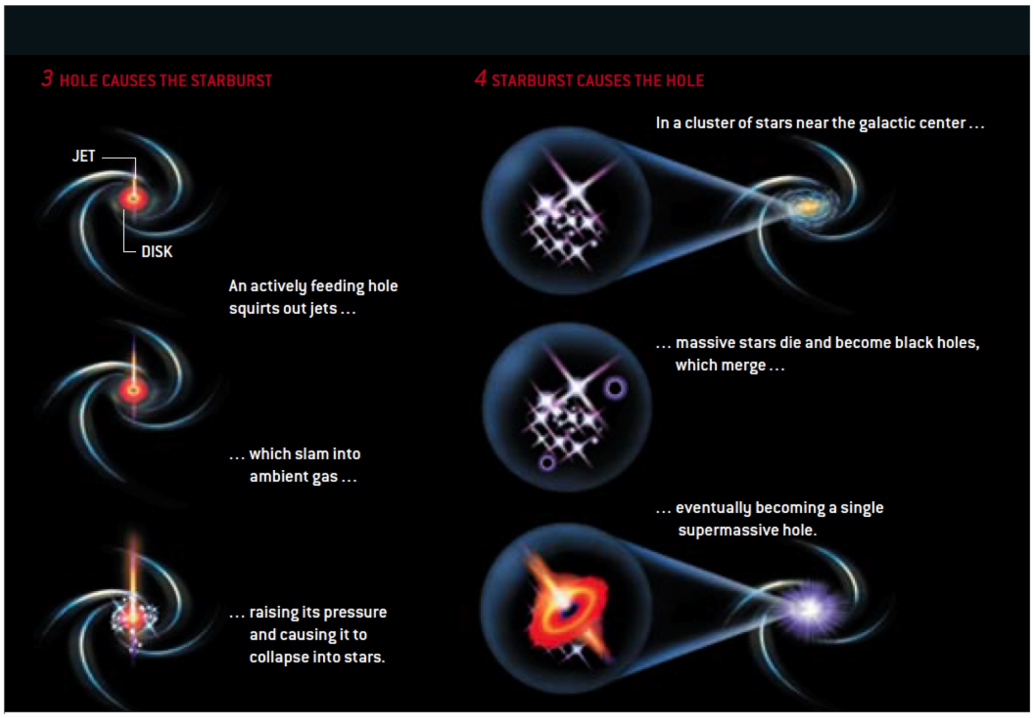

Fig. 2. Does the starburst causes the AGN or the inverse ?

One of the most important point will be the capability to resolve a large number of the SSC in diameter: this will immediately set the star density within the cluster, a fundamental parameter as regards its disruption and its age and allow to tackle some basic questions such as : *i)* the law of radial distribution of stars and its link to the initial collapse; *ii)* the structuration of the SSC as a set of separate HII regions or a unique giant one; *iii)* the propagation of the starburst within the cluster; *iv)* the IMF (Salpeter, top-heavy ?); *v)* the possible formation of a super-wind; *vi)* the link with the fine molecular gas distribution (Alma); *vii)* the clustering of the dust which impacts directly on the UV escape fraction; *vii)* the intra- and inter-cluster dynamics.

The question of the likely link between the starburst and an AGN will be more directly approached when reaching the pc scale, so that the old question of the egg and the chicken (which started first ?), summarized by Fig. 3 will receive new and hopefully conclusive elements.

Finally, another exciting question which is the history of star formation in the Universe will be approached in a more acute way since the distance at which a detailed mapping of SSC in starburst galaxies is still possible would be 5 times larger. This means in particular that studying the characteristics of resolved SSC in galaxies with z=2 will become possible.

3 Which instruments ?

Fig. 3 illustrates the huge gain in resolution brought by the E-ELT in the case of MICADO, the very likely first light imager of the future telescope: a star-forming galaxy at z=2 will be clearly resolved in its main SSC.

For the early science programme, MICADO will likely be the first choice since it will offer most of the features one wishes : broad-band filters to study continuum emission from stars, dust and the ionized gas, hopefully a set of narrow-filter sampling a range of redshift to study the stellar content (CO lines), the ionized gas (H+ lines), the molecular gas (H2 lines) and SNe (FeII lines). Single slit spectroscopy will also be available for detailed line profiles and kinematics studies.

In a second time, METIS the thermal infrared imager will give access to the thermal infrared range and thus to dust contents and heating, as well as to the most extinct regions, likely the youngest ones.

The sensitivity offered should allow to reach the 19-22 magnitudes of a SSC at 400 pc within a rather short time. For more distant objects such as the case illustrated on Fig 3 (z=2) four hours will typically be required to reach a sufficient S/N ratio.

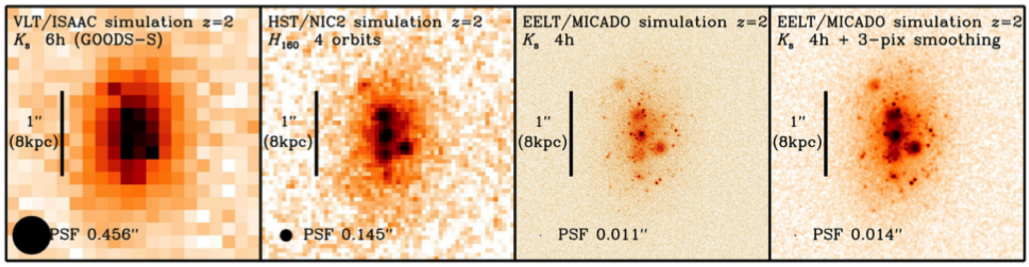

Fig. 3. Simulation of imaging in Ks-band of a distant galaxy at z=2 with MICADO

Finally when multi-objects spectrographs fed by MOAO will become available, another step will be possible, especially to study kinematics and providing a fine spectroscopic diagnostics.

4 Conclusion

The E-ELT with its infrared imagers MICADO and METIS will have an essential asset in the study of extreme star formation in remote galaxies, since it will allow not only to separate SSC and thus study distribution functions, especially mass and luminosity functions, but more fundamentally, it will allow to resolve the SSC themselves opening a completely new field. We will obtain keys elements on the starburst propagation, a possible IMF segregation, dust clustering and UV escape, HII region structure, intra-cluster dynamics, direct link of the nuclear starburst with the AGN etc.

References

Piqueras-Lopez et al. 2012, A&A, 546, 64.
Haan et al. 2011 AJ, 141, 100.
Davies et al. 2003 ApJ, 597, 907.
Garcia-Marin et al. 2006 ApJ, 650, 850.
Bastian 2008 MNRAS, 390, 769.
Stierwalt et al., 2013, AjPS, 206, 1.

Session 10

Atelier PNHE/PNCG

SF2A 2013
L. Cambrésy, F. Martins, E. Nuss and A. Palacios (eds)

CONSTRAINING GAMMA-RAY PROPAGATION ON COSMIC DISTANCES

J. Biteau[1,2]

Abstract. Studying the propagation of gamma rays on cosmological distances encompasses a variety of scientific fields, focusing on diffuse radiation fields such as the extragalactic background light, on the probe of the magnetism of the Universe on large scales, and on physics beyond the standard models of cosmology and particle physics. The measurements, constraints and hints from observations of gamma-ray blazars by airborne and ground-based instruments are briefly reviewed. These observations point to gamma-ray cosmology as a one of the major science cases of the Cherenkov Telescope Array, CTA.

Keywords: Cosmology: miscellaneous, Cosmic background radiation, Intergalactic medium, Gamma rays: galaxies, BL Lacertae objects: general

Gamma-ray astronomy at very high energies (VHE, $30\,\mathrm{GeV} < E < 30\,\mathrm{TeV}$) is driven by ground-based imaging atmospheric Cherenkov telescopes, whose current major representatives are H.E.S.S. (Namibia), MAGIC (Canaries islands) and VERITAS (Arizona). Together with airborne instruments observing the gamma-ray sky at high energies (HE, $300\,\mathrm{MeV} < E < 300\,\mathrm{GeV}$), such as *Fermi*-LAT, they can now probe and constrain the propagation on billion-lightyear distances of the highest-energy photons produced and detected in the Universe. The observational field called gamma-ray cosmology encompasses the study of the extragalactic background light (EBL), an optical-infrared radiative component born with the first stars and that kept on growing since then, of the intergalactic magnetic field, which fills the voids between large scale structures and whose origin remains unidentified, and of physics beyond the standard models of cosmology and particle physics, possibly revealing hints on dark matter candidates and on the laws of nature at the Planck scale.

The science case of gamma-ray cosmology is discussed in Sec. 1. A wide-spectrum but non-exhaustive list of current constraints, hints and measurements in the field is exposed in Sec. 2. Possible refinements in the analyses are discussed in Sec. 3, together with the great expectations from the next generation instrument, the Cherenkov Telescope Array (CTA).

1 Science case of gamma-ray cosmology

Gamma-ray cosmology could be considered as an established domain, with seminal theoretical studies that can be traced back to the '60s (Nikishov 1962; Jelley 1966; Gould & Schréder 1967), but the first powerful enough extragalactic accelerators to be used as probes were detected in the beginning of the '90s. These strong sources are discussed in the following subsection together with the science case addressed.

1.1 Extragalactic sources as gamma-ray beacons

Since the groundbreaking detection of Mrk 421 (Punch et al. 1992) by the first generation ground-based instruments Whipple, the number of detected VHE extragalactic sources has exponentially grown, up to almost 60 sources in mid 2013. CAT and HEGRA, the major second generation instruments, contributed to the effort, yielding a handful of sources in the beginning of the 2000s. As shown in Fig. 1, left, the third generation instruments H.E.S.S., MAGIC and VERITAS have revolutionized the field with the discovery of almost 50 sources in less than ten years, up to redshifts $z > 0.6$, as shown in Fig. 1, right.

[1] Santa Cruz Institute for Particle Physics, Department of Physics, University of California at Santa Cruz, Santa Cruz, CA 95064, USA

[2] Laboratoire Leprince-Ringuet, Ecole polytechnique, CNRS/IN2P3, F-91128 Palaiseau, France

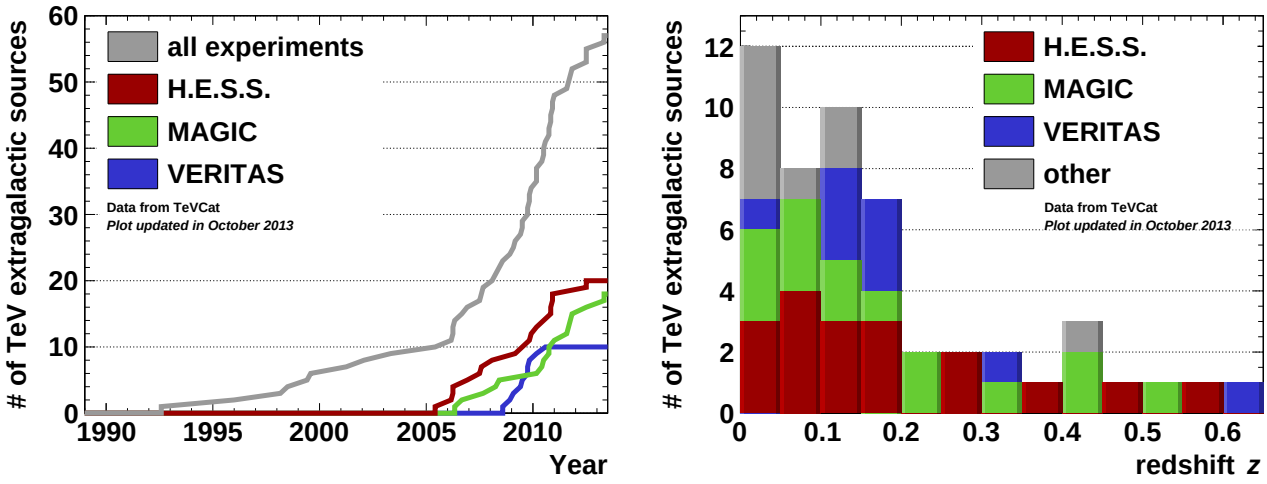

Fig. 1. Left: Number of detected extragalactic emitter of VHE gamma rays as a function of the year of discovery. **Right:** Distribution of the redshifts of the current population of extragalactic VHE emitters with a constrained distance. *Data from TeVCat* `http://tevcat.in2p3.fr`.

Besides the nearby starburst galaxies NGC 253 and M 82, the VHE extragalactic population is exclusively composed of active galactic nuclei (AGN). These objects are thought to host a supermassive black hole, possibly as heavy as a billion solar masses, fed by an accretion disk, with the emission of relativistic jets on each side of the disk for the brightest radio-emitters (see Antonucci 1993; Urry & Padovani 1995, for a unified picture of AGN). With a typical opening angle of few degrees, these jets, which are composed of magnetic fields, accelerated particles and beamed radiation, can either be seen edge on, as for the nearby radio galaxies M 87, Centaurus A and NGC 1275, or they can be closely aligned with the line of sight. In the latter case, the AGN is called a blazar and it appears particularly bright and energetic due to the relativistic beaming and the Doppler shift of the energy of the photons (see e.g. Ghisellini 2013, for a recent discussion on gamma-ray blazars).

Blazars constitute the vast majority of detected AGN at VHE and can be divided in flat-spectrum radio quasars (3 detected at VHE), which exhibit strong emission lines, and BL Lac objects (49 detected at VHE), with weak or absent lines. The broad band emission of blazars is composed of a radio to UV/X-ray component, generally attributed to the synchrotron emission of relativistic electrons in the jet, and of a gamma-ray component, whose origin remains debated. The simplest radiative models attribute it to the Comptonization of the synchrotron field by the very electrons that generated it. This synchrotron self-Compton model (Band & Grindlay 1985) works fairly well for the largest subclass of BL Lac objects, the high-synchrotron-frequency-peaked objects (HSP, sometimes HBL in the literature), whose low-energy components peak in X rays. For objects with a lower-energy synchrotron peak, including flat-spectrum radio quasars, external photon fields coming from the accretion disk (among other regions) could be scattered by the electrons resulting in additional radiative components. The potential correlation of these fields with the black-hole and accretion-rate evolution reduces the value of low-frequency-peaked objects as reliable cosmological gamma-ray beacons (Reimer 2007). Instead, the apparent simplicity of the emission of HSP blazars (with the caveat of their flux variability) makes them the best reference emitters so far to constrain gamma-ray propagation.

1.2 Pair creation on the extragalactic background light

The leading effect on gamma-ray propagation is pair creation on diffuse radiation fields in the Universe. For an isotropic target field of fixed energy ϵ, the cross section is maximum in the comoving frame for a gamma-ray energy $E \sim (2m_e c^2)^2/\epsilon \sim 1\,\mathrm{TeV} \times (\epsilon/1\,\mathrm{eV})^{-1}$ (Jauch & Rohrlich 1976). TeV gamma rays thus strongly interact with eV, i.e. micron-wavelength photons. This is precisely the wavelength where the cosmic optical background is most intense. The cosmic optical background extends from UV to near infrared wavelengths and is composed of the total emission of stars and galaxies since the end of the cosmic dark ages. Its counterpart at lower energy is the cosmic infrared background, with a peak intensity around $\sim 100\,\mu$m, which comes from the reprocessing of UV-optical light by dust. The cosmic optical and infrared backgrounds are usually referred to as the extragalactic background light (EBL) and constitute the second most intense cosmological background

after the CMB, which peaks at even lower energy.

Measuring the EBL directly proves to be difficult because of the foregrounds from the Galaxy and the solar system (zodiacal light) but stringent constraints can be derived accumulating the brightness of known galaxies (e.g., Dole et al. 2006; Madau & Pozzetti 2000; Fazio et al. 2004). Lower limits from galaxy counts typically lie one order of magnitude below upper limits derived from direct measurements. The lower limits are reproduced by EBL models based, e.g., on the local population of galaxies (Franceschini et al. 2008), on the evolution of large samples (Domínguez et al. 2011), or on semi-analytical models (Gilmore et al. 2012). Comprehensive summaries of the observational techniques at these wavelengths as well as of the modeling approaches can be found in Hauser & Dwek (2001), or in Dwek & Krennrich (2013) for a more recent review.

To date, the best way to make local foregrounds negligible consists in integrating the optical/near-infrared emission over cosmological distances, as made possible by gamma-ray observations. Indeed, for a density of photons $n(\epsilon, z')$ in the energy band $[\epsilon; \epsilon + \mathrm{d}\epsilon]$ and at a redshift z' (i.e. $\int \mathrm{d}\epsilon\, n(\epsilon, z')$ is a number of photons per unit volume), gamma rays with observed energy E, emitted by a source at a redshift z, are absorbed (through pair creation) with an optical depth:

$$\tau\,(E, z) = \int_0^z \mathrm{d}z' \frac{\mathrm{d}l}{\mathrm{d}z}(z') \int_0^{+\infty} \mathrm{d}\epsilon\; n(\epsilon, z') \int_{-1}^{1} \mathrm{d}\mu \frac{1-\mu}{2} \sigma_{ee}(\epsilon, E \times (1+z'), \mu) \tag{1.1}$$

The first integral represents the distance, with $\mathrm{d}l/\mathrm{d}z = c/H_0(1+z)\sqrt{\Omega_\Lambda + \Omega_m(1+z)^3}$ in a flat universe. The second is the target density and the third is the cross section with an integration in the center-of-mass frame over the angle θ ($\mu = \cos\theta$) between the directions of the target photon and of the gamma ray. The pair-creation cross section is given by the Bethe-Heitler formula:

$$\sigma_{ee}(\epsilon_1, \epsilon_2, \mu) = \frac{3}{16}\sigma_{\mathrm{T}}(1-\beta^2) \left[2\beta(\beta^2-2) + (3-\beta^4)\ln\left(\frac{1+\beta}{1-\beta}\right)\right] \Theta(\epsilon - \epsilon_{\mathrm{th}}) \tag{1.2}$$

where Θ is the Heaviside function, $\epsilon_{\mathrm{th}} = 2m_e^2c^4/(1-\mu)\epsilon_2$ is the threshold energy and $\beta^2 = 1 - \epsilon_{\mathrm{th}}/\epsilon_1$. The pair creation on the EBL thus results in an energy and redshift dependent absorption shown in Fig. 2 that can be used to probe the EBL itself (see Sec. 2.2).

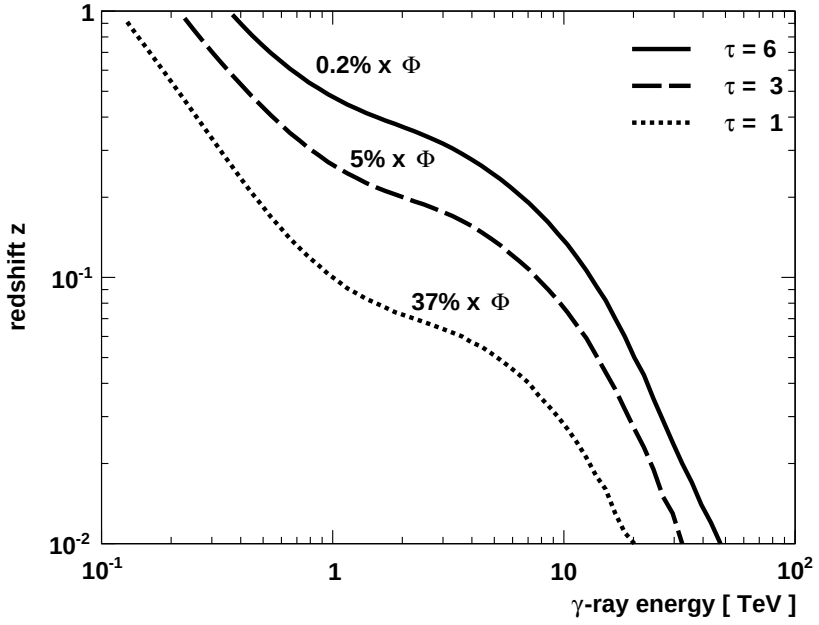

Fig. 2. Optical depth $\tau = 1, 3, 6$ as a function of redshift and observed gamma-ray energy, within the modeling of Franceschini et al. (2008). The frontiers correspond to an observed flux equal to 37%, 5% and 0.2% of the emitted flux.

1.3 Intergalactic magnetic field and the reprocessing of the pairs

A second order effect on gamma-ray propagation is related to the fate of the pairs created by EBL absorption. For a gamma ray of energy $E \sim 1\,\mathrm{TeV}$, each created lepton carries an energy of half a TeV, corresponding to a Lorentz factor $\gamma \sim 10^6$, and can upscatter the most intense photon field in its environment, that is the CMB with photons of energy $\epsilon_{\mathrm{CMB}} \sim 1\,\mathrm{meV}$. In the Thompson regime, the resulting photons carry an energy $E' \sim \gamma^2 \epsilon_{\mathrm{CMB}} \sim 1\,\mathrm{GeV}$. Thus there should be a broad band reprocessing of the signal detected by ground-based VHE instruments into the HE band observed by airborne instruments*, an effect often referred to as pair echo. If the intergalactic magnetic field (IGMF) filling the voids is strong enough (typically between $10^{-15} - 10^{-12}\,\mathrm{G}$), the pairs should be significantly deflected resulting in an extended emission around the point-like blazar, an emission sometimes referred to as pair halo or beam broadened cascade.

The intensity and coherence scale of the IGMF remain largely unknown, though these quantities could be of cosmological importance (see Durrer & Neronov 2013, for a recent review of the observational and theoretical progress). To be amplified through dynamo and compression effects up to their current level, the magnetic fields found in galaxies and galaxy clusters would indeed need seeds. These magnetic seeds could arise either during collapses forming the first structures or during the early Universe, be it inflation or electroweak/QCD transition phases. Current constraints from gamma-ray astronomy are discussed in Sec 2.3.

1.4 Alternatives beyond the Standard Models

Exotic physics beyond the standard models of particle physics and cosmology can also be probed within gamma-ray cosmology. Lorentz invariance violation, studied e.g. within quantum gravity frameworks, would result in an alteration of the dispersion relation for VHE gamma rays. The threshold of the pair creation, derived with simple special relativity arguments, would thus be altered, reducing the EBL opacity to gamma rays (Kifune 1999; Jacob & Piran 2008). The absence of such a feature in the spectrum of Mrk 501, as detected by second generation instruments, already set interesting limits (Stecker & Glashow 2001) but the way remains wide open for refinements with current data.

Another crucial test concerns axion-like particles (ALPs). These belong to the class of weakly interacting slim particles (WISPs) that remain a viable alternative to their massive counterparts (WIMPs) as elementary constituents of cold dark matter (see e.g. Bähre et al. 2013, in the context of the future instrument ALPS-II). Photons and ALPs would indeed mix in the presence of a magnetic field (such as the IGMF or intracluster magnetic fields), which could modify the apparent absorption of gamma rays (e.g., Sánchez-Conde et al. 2009). A gamma ray converted in an ALP would be unaffected by the EBL absorption and could propagate on large distances before converting back into a gamma ray and being detected. The universe would then appear more transparent than expected. Alternatively, for low enough reconversion probabilities, the ALPs would go undetected, potentially increasing the opacity to gamma rays. Recent hints of deviations from a standard EBL absorption (so-called pair production anomaly) are currently debated in the community, as discussed in Sec. 2.4.

2 First measurements, hints and constraints

2.1 A short history of gamma-ray cosmology

The methodology to constrain EBL with VHE gamma-ray blazars was developed with the flat spectrum radio quasar 3C 279, which would eventually be detected with the sensitivity of third generation instruments. Stecker et al. (1992) performed a straight extrapolation of the HE spectrum of 3C 279 as measured by EGRET up to VHE, arguing that the object should be detectable by the Whipple observatory under the assumption of no curvature and no EBL absorption. The non detection proved either an intrinsic curvature in the spectrum or/and that EBL absorption, which increases with energy (cf Fig. 2), is strong enough to suppress the flux. A characterization of the flux suppression could then provide constraints on the EBL.

The detection of Mrk 421 by Whipple enabled the first derivations of upper limits on the EBL (Stecker et al. 1993; Dwek & Slavin 1994; Biller et al. 1998). Further studies followed the detection of Mrk 501 by Whipple and HEGRA (Funk et al. 1998; Aharonian et al. 1999), and later on by CAT (Guy et al. 2000; Renault et al. 2001), then complemented by data from the more distant ($z \sim 0.13$) HSP blazar H 1426+428 (Dwek & Krennrich

*Plasma instabilities resulting in a heating of the medium have nonetheless been invoked as an alternative for the leptons to lose their energy (Broderick et al. 2012). The theoretical debate remains open to date.

2005). More stringent constraints came from third generation instruments, in particular with the detection of 1ES 1101-232 by H.E.S.S. (Aharonian et al. 2006b) and the combination of spectra from 13 blazars by Mazin & Raue (2007). Absorption at the low energy end of the VHE band has also been constrained by *Fermi*-LAT using high redshift blazars and GRBs (Abdo et al. 2010).

The combination of HE and VHE measurements led to the most constraining upper limits to date. For $z < 0.5$, the HE band is indeed virtually unaffected by EBL absorption, and *Fermi*-LAT data can be used to constrain the intrinsic emission, while VHE data probe the absorption (as, e.g., in Georganopoulos et al. 2010; Orr et al. 2011; Meyer et al. 2012).

2.2 Measurements of the EBL

One of the limitations of the studies mentioned above lies in the method originally developed for 3C 279. Since broad band EBL absorption and the intrinsic curvature expected in standard emission scenarios both result in downward going observed flux as a function of energy, a characterization of the fall can only result in an upper limit on the EBL absorption, derived on the basis of a null intrinsic curvature.

This limitation has been tackled by the *Fermi*-LAT and H.E.S.S. collaborations with two slightly different approaches. In Ackermann et al. (2012), the curvature in the spectra of BL Lac objects was measured in an energy range where the EBL is ineffective (typically $1-50$ GeV for $0.5 < z < 1.6$), modeling it with the simplest functional form: a log parabola, i.e. a parabola in log-log scale. Extrapolating the curvature up to 500 GeV enables the derivation of the remaining absorption. To do so, a maximum likelihood approach is adopted, each spectrum being fitted with a model:

$$\phi(E, z) = \phi_{\rm int}(E) \times \exp(-\alpha\tau(E, z, n)) \tag{2.1}$$

where ϕ is the measured flux, $\phi_{\rm int}$ is the extrapolated curved spectrum, the so-called intrinsic spectrum, $\tau(E, z, n)$ is the EBL optical depth for a template EBL model of density n and where α is a normalization factor left free in the fitting procedure.

A log-likelihood profile as a function of α is derived for each source, the sum of these profiles resulting in the combined constraint. Using the model of Franceschini et al. (2008) as a template for the EBL density, a detection (i.e. a normalization factor α differing from zero) at the 5σ level is performed with 50 sources in the redshift range $0.5 < z < 1.6$. Because of the limited gamma-ray energy, the EBL effect remains weak for $z < 0.2$ and $0.2 < z < 0.5$ (2σ measurements shown in gray in Fig. 3, left). One of the strengths of the *Fermi*-LAT study lies in the investigation of a dozen models, showing that the models of Franceschini et al. (2008), Domínguez et al. (2011) or Gilmore et al. (2012) fit rather well the data, despite of their completely different theoretical grounds. One of the weaknesses could lie in the extrapolation of the low-energy flux, with a fixed intrinsic emission that could result in an overestimation of the significance of the effect[†].

The H.E.S.S. collaboration measured the EBL absorption with observations of the seven brightest blazars ($z < 0.2$) detected at VHE in the southern hemisphere (H.E.S.S. Collaboration et al. 2013). The analysis is also based on likelihood profiles as a function of a normalization factor α. One of the weaknesses of the approach lies in the test of a single EBL model (Franceschini et al. 2008), though retrospectively validated by the study of *Fermi*-LAT. Its strength lies in the treatment of the intrinsic spectrum, with the test of five different models with free parameters (even allowing for upward going intrinsic emission). The particular behavior of the EBL absorption between 1 and 10 TeV, due to the depletion of the target EBL photon field between 1 and 10 μm, constitutes a prominent signature that is detected by a combined likelihood analysis at the 9σ level. The normalization factor of the EBL model as measured by H.E.S.S. and *Fermi*-LAT are compared in Fig. 3, left, the top graphic showing the epochs probed for the optical depth. The redshift range $0.2 < z < 0.5$ remains poorly constrained.

Scaling up the template EBL density and accounting for the energy range probed, as in H.E.S.S. Collaboration et al. (2013), results in 1σ confidence contours shown in Fig. 3, right, where statistical and systematic uncertainties are included. The measurements lie in between lower limits from galaxy counts and upper limits from direct measurements as well as below the region excluded by the gamma-ray analyses discussed in Sec. 2.1. The measurements are dominated by systematic uncertainties below 5 μm, with an uncertainty of the order of 20-30%. At higher wavelengths where statistical uncertainties remain dominant, there is room for improvement using larger samples of gamma rays at the highest energies.

[†]The limited energy range in which the extrapolation is performed counterweights a bit this caveat.

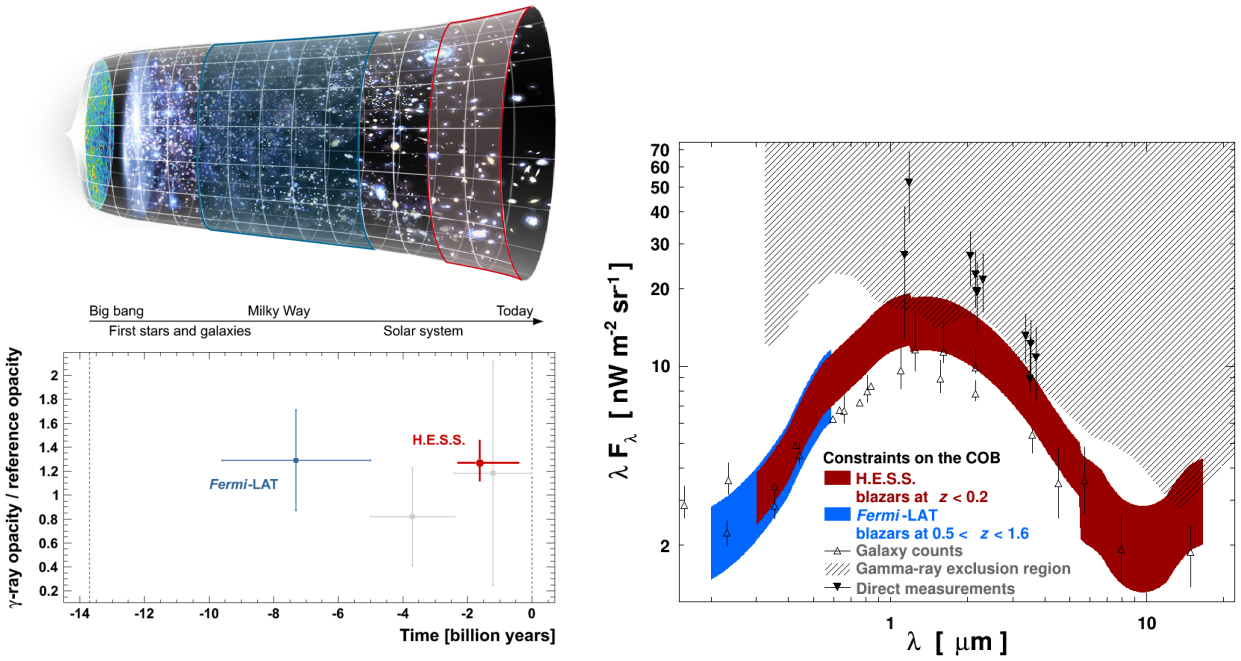

Fig. 3. Left: EBL normalization factor as a function of the distance of the gamma-ray blazars used as beacons. The blue and gray points represent the *Fermi*-LAT measurement and constraints. The red point represents the H.E.S.S. measurement. *Top graphic adapted from an original from NASA/WMAP Science team.* **Right:** Spectral energy distribution of the EBL as measured by H.E.S.S. (red) and *Fermi*-LAT (blue) from UV to near infrared wavelengths (1σ confidence contours). *Adapted from* H.E.S.S. Collaboration et al. (2013).

2.3 Constraints on the IGMF

The IGMF is usually characterized by its intensity, B, and its coherence length, λ_B. As discussed in Durrer & Neronov (2013), the parameter space remains poorly constrained. A strong IGMF coherent on supra-Mpc scales would result in CMB anisotropies extending on large angular scales, resulting in an upper limit of the order $B < 10^{-9}$ G. Large coherence lengths being untestable above the Hubble scale, the parameter space above $\lambda_B > 10^4$ Mpc is left out of the search. On theoretical grounds, MHD turbulence tends to dissipate strong magnetic fields on small scales, heating up the medium, which yields the exclusion region shown in Fig. 4, left.

As discussed in Sec. 1.3, joint observations of gamma-ray sources at HE and VHE can probe the intensity of the IGMF. For low enough B, the EBL-absorption induced pairs should barely be deflected, resulting in a reprocessing of the signal to HE. The non-observation of this signal, mostly in the spectral energy distribution of the HSP blazar 1ES 0229+200, results in a lower limit of the order of $B > 10^{-16}$ G (Neronov & Vovk 2010, shown as a dashed red region in Fig. 4, left), under the assumption of a fixed EBL model and of a longterm steady-state emission of the source. Releasing the latter assumption, Dermer et al. (2011) and Taylor et al. (2011) derived weaker limits of the order 10^{-18} G and 10^{-17} G, the latter being shown as a filled region in Fig. 4, left. Investigating the underlying hypotheses on the source intrinsic emission, Arlen et al. (2012) concluded than present data on 1ES 0229+200 rule the null IGMF hypothesis out at the 3σ confidence level. The strong dependence of these constraints on the EBL level is discussed in Vovk et al. (2012), with an increase in the lower limit of almost a factor of 10 for an increase in the EBL level by 30%, which is representative of the current uncertainties derived by H.E.S.S. Collaboration et al. (2013) and Ackermann et al. (2012).

2.4 Hints of / limits on physics beyond the standard models

Some puzzles remain to be solved at VHE. For example, the spectrum of the blazar PKS 1424+240 measured by the VERITAS collaboration does not seem as absorbed as it should be, given the redshift of the source $z \geq 0.6035$ (inferred from Lyβ and Lyγ absorption in Furniss et al. 2013). Other hints for deviations from nominal EBL opacities have recently been studied in Horns & Meyer (2012) using VHE spectral points. Archival points are

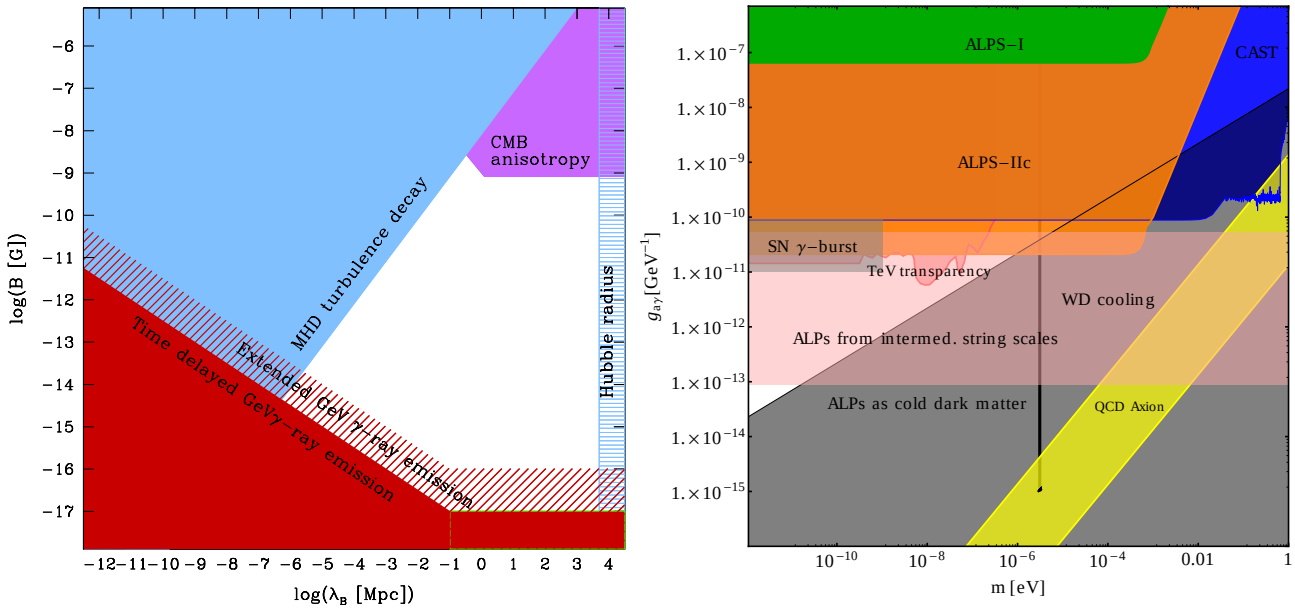

Fig. 4. Left: Excluded regions in parameter space intensity vs coherence length of the IGMF. *Adapted from* Durrer & Neronov (2013). **Right:** Constraints in the parameter space coupling of ALPs with photons vs mass. *Extracted from* Bähre et al. (2013).

fitted with the model described in Eq. 2.1, assuming a power-law or a log-parabolic intrinsic spectrum and using a template EBL model with a normalization factor of one. An estimator of the residual to the fit is defined for each point as:

$$R(E_i) = \frac{F_i - \phi(E_i)}{F_i + \phi(E_i)} \tag{2.2}$$

where F_i is the flux measured at the energy E_i. The authors discard an estimator taking into account the measured uncertainties on the flux, such as $(F_i - \phi(E_i))/\sigma_i$, because of deviations from the expected normal distribution of unity width. At high optical depth, or equivalently at high energies for a given redshift, a 4σ deviation from null residuals is found, indicating an opacity smaller than expected. Systematic uncertainties in the energy scale decrease the effect to the 3.5σ level, and discarding the last points from each spectrum in the study reduces the deviation to the 2.5σ level. In Horns & Meyer (2013), a similar approach is followed using three *Fermi*-LAT events from a gamma-ray burst and two blazars, yielding a 3.5σ effect (preliminary value).

The VHE hint has been used by the same group in Meyer et al. (2013) to constrain the parameter space of ALPs, i.e their coupling to photons as a function of the ALP mass, and claim the first lower-limit on the coupling (complex-shaped dark pink region in Fig. 4, right). The region of interest, denoted as "TeV transparency", lies below the regions excluded by the CAST and ALPS-I experiments and is partially excluded by the signal from SN 1987A. It intersects the light pink band possibly explaining anomalous cooling rates from white dwarves, but remains above theoretical expectations from string theory, cold dark matter scenarios, or standard axions invoked as a solution to the absence of CP-violation in QCD, which are in turn probed by the ADMX experiment between 2 and 3 μeV. Not included in this graphic is the recent result from Brun et al. (2013) that excludes a large fraction of the "TeV transparency" region using VHE data from the HSP blazar PKS 2155-304.

As exciting as these hints could be, some systematic uncertainties could affect the estimated significance level of the effect. The EBL model is subject to large uncertainties in the energy range concerned (typically above 5 μm). For the *Fermi*-LAT event analysis, the method does not seem to account for the energy resolution of the instruments. For the analysis of VHE spectra, the estimator described in Eq. 2.2 does not account for the uncertainties on the flux measurements, which drastically increase with energy. Fitting models to published spectral points, though common practice, does not properly account for measurement uncertainties

and correlations between points[‡]. The last caveat, briefly addressed in the study of systematic uncertainties by Horns & Meyer (2012), concerns the highest energy points in each spectrum. The last point above some minimum significance is indeed usually selected when publishing a VHE spectrum, thus biasing the selection toward upward fluctuations with respect to the actual flux. Suppressing these points largely reduces the significance of the effect (down to 2.5σ), potentially suggesting an accumulation of upward going fluctuations. It could also be argued that these high-energy points are precisely the ones from which the ALP signal is expected. Along with laboratory experiments such as ALPS-II, large improvements in the energy coverage, discussed in Sec. 3, are needed from future generation VHE instruments to decide this issue.

2.5 EBL absorption as a ruler?

From Eq. 1.1, the EBL optical depth first appears as a probe for deviations from the pair-creation cross section (third integral in the equation), as discussed in Sec. 1.4 with Lorentz invariance violation, then as a proxy for the EBL density (second integral), as discussed in Sec. 2.2 with the measurements of H.E.S.S. and *Fermi*-LAT. Alternatively, it also could in principle be used to constrain distances (first integral).

Upper limits on the redshifts of HSP blazars, such as PG 1553+113 (see, e.g., Aharonian et al. 2006a), have been set on a regular basis, going hand in hand with growingly stringent limits on the EBL. Attempts to standardize the multiwavelength emission of blazars at HE and VHE have been led by Prandini et al. (2010), correlating the HE-VHE spectral differences, which trace EBL absorption, with distance. The authors infer a redshift of $z = 0.24 \pm 0.05$ for PKS 1424+240 based on the VERITAS and *Fermi*-LAT spectral measurements, emphasizing the puzzle around this object (cf. Sec. 2.4).

Constraints on the Hubble parameter H_0 have also been derived using the absorption of gamma-rays from blazars (Barrau et al. 2008; Domínguez & Prada 2013). Note however that even for an EBL optical depth virtually perfectly measured, the remaining uncertainties on the EBL density (20-30%) would be directly propagated into the inferred distances and Hubble parameter.

3 Perspectives in gamma-ray cosmology

3.1 Using the multi-wavelength synergy

The constraints derived from gamma-ray cosmology are based on a joint modeling of the source emission, EBL absorption and second order processes, such as the effect of the IGMF or of physics beyond the standard models. Using the spectra derived during multi-wavelength campaigns in the X-ray, HE and VHE gamma-ray bands has proved particularly constraining for the modeling of blazars' emission. Using this multi-wavelength synergy, in particular the evolution of HE-VHE spectra with redshift, Sanchez et al. (2013) have recently confirmed the H.E.S.S. and *Fermi*-LAT measurements.

Using in addition X-ray observations, Mankuzhiyil et al. (2010) and Domínguez et al. (2013) modeled the broad band spectra of blazars within synchrotron self-Compton scenarios and jointly constrained the EBL optical depth, though the same caveat as in Sec. 2.4 (uncertainties and correlations between the points) could be raised. The multi-wavelength approach is crucial for probes of the IGMF based on pair-echo, with the reprocessing of the VHE signal to HE. The IGMF intensity could nonetheless potentially be constrained up to 10^{-12} G solely with CTA data, using pair-haloes / beam-broadened-cascades approaches (Durrer & Neronov 2013; Sol et al. 2013b).

3.2 Scope of current generation instruments

The lowering of the energy threshold of ground-based gamma-ray instruments below 100 GeV is a crucial step in widening the sample of probes of the Universe opacity to gamma rays. To increase the sensitivity to Cherenkov light from low-energy gamma-ray induced atmospheric showers, the VERITAS collaboration opted for high quantum efficiency photomultipliers, while the MAGIC and H.E.S.S. collaborations opted for large size telescopes (28 m diameter for the recently built CT5 telescope of the H.E.S.S. II array). A low energy threshold implies a larger gamma-ray horizon, as shown e.g. in Fig. 2. VHE instruments could then probe the EBL

[‡]VHE points are generally highly correlated due to the steepness of the spectra and the limited energy resolution that imply leakage of events from low to higher energies. Spectral points derived with a maximum likelihood analysis should be considered as residuals to the fit. Therefore, fitting a model to these residuals may not be the most statistically sound approach.

optical depth using blazars at $0.2 < z < 0.5$, which remains uncharted territory (cf. Fig. 3, left). Measuring gamma-ray opacity in various redshift bands would result in a tomography of the EBL density, enabling the comparison of the EBL evolution with e.g. the star formation history (Raue & Meyer 2012).

3.3 Gamma-ray cosmology with CTA

Based on the *Fermi*-LAT population of extragalactic sources, the population detected by ground-based instruments should become less and less dominated by HSP objects, allowing tests of unification schemes of blazars. These investigations, which also constitute a fundamental science case for CTA (see Reimer & Böttcher 2013; Sol et al. 2013a, and references therein), will deepen our knowledge on potential beacons and thus directly benefit gamma-ray cosmology. The knowledge of the Universe opacity at VHE will also directly impact the physics of gamma-ray bursts (see Inoue et al. 2013; Mészáros 2013, in the context of CTA), which should be detected at a rate of a few per year by CTA (Gilmore et al. 2013).

CTA, with its large-size telescopes enabling an energy threshold of 30 GeV or less, its medium-size telescopes boosting the sensitivity by a factor of 10 in the core energy range, and small size telescopes paving a few kilometer-square area that will probe energies above 10 TeV, will take gamma-ray cosmology to its full maturity (see Mazin et al. 2013; Ellis & Mavromatos 2013, for discussions on EBL and Lorentz invariance in the CTA era). CTA will in particular probe the EBL density above 5 μm, where diffuse emission from polycyclic aromatic hydrocarbons could be detected and where physics beyond the standard models could be unveiled, yielding observables for quantum gravity theories or clues on the elusive question of the nature of dark matter.

JB would like to thank D. Williams for his useful suggestions, which improved this text.

References

Abdo, A. A., Ackermann, M., Ajello, M., et al. 2010, ApJ, 723, 1082
Ackermann, M., Ajello, M., Allafort, A., et al. 2012, Science, 338, 1190
Aharonian, F., Akhperjanian, A. G., Bazer-Bachi, A. R., et al. 2006a, A&A, 448, L19
Aharonian, F., Akhperjanian, A. G., Bazer-Bachi, A. R., et al. 2006b, Nature, 440, 1018
Aharonian, F. A., Akhperjanian, A. G., Barrio, J. A., et al. 1999, A&A, 349, 11
Antonucci, R. 1993, ARA&A, 31, 473
Arlen, T. C., Vassiliev, V. V., Weisgarber, T., Wakely, S. P., & Yusef Shafi, S. 2012, arXiv:1210.2802
Bähre, R., Döbrich, B., Dreyling-Eschweiler, J., et al. 2013, Journal of Instrumentation, 8, 9001
Band, D. L. & Grindlay, J. E. 1985, ApJ, 298, 128
Barrau, A., Gorecki, A., & Grain, J. 2008, MNRAS, 389, 919
Biller, S. D., Buckley, J., Burdett, A., et al. 1998, Physical Review Letters, 80, 2992
Broderick, A. E., Chang, P., & Pfrommer, C. 2012, ApJ, 752, 22
Brun, P., Wouters, D., & for the H. E. S. S. collaboration. 2013, arXiv:1307.6068
Dermer, C. D., Cavadini, M., Razzaque, S., et al. 2011, ApJ, 733, L21
Dole, H., Lagache, G., Puget, J.-L., et al. 2006, A&A, 451, 417
Domínguez, A., Finke, J. D., Prada, F., et al. 2013, ApJ, 770, 77
Domínguez, A. & Prada, F. 2013, ApJ, 771, L34
Domínguez, A., Primack, J. R., Rosario, D. J., et al. 2011, MNRAS, 410, 2556
Durrer, R. & Neronov, A. 2013, A&A Rev., 21, 62
Dwek, E. & Krennrich, F. 2005, ApJ, 618, 657
Dwek, E. & Krennrich, F. 2013, Astroparticle Physics, 43, 112
Dwek, E. & Slavin, J. 1994, ApJ, 436, 696
Ellis, J. & Mavromatos, N. E. 2013, Astroparticle Physics, 43, 50
Fazio, G. G., Ashby, M. L. N., Barmby, P., et al. 2004, ApJS, 154, 39
Franceschini, A., Rodighiero, G., & Vaccari, M. 2008, A&A, 487, 837
Funk, B., Magnussen, N., Meyer, H., et al. 1998, Astroparticle Physics, 9, 97
Furniss, A., Williams, D. A., Danforth, C., et al. 2013, ApJ, 768, L31
Georganopoulos, M., Finke, J. D., & Reyes, L. C. 2010, ApJ, 714, L157
Ghisellini, G. 2013, arXiv:1309.4772

Gilmore, R. C., Bouvier, A., Connaughton, V., et al. 2013, Experimental Astronomy, 35, 413
Gilmore, R. C., Somerville, R. S., Primack, J. R., & Domínguez, A. 2012, MNRAS, 422, 3189
Gould, R. J. & Schréder, G. P. 1967, Physical Review, 155, 1408
Guy, J., Renault, C., Aharonian, F. A., Rivoal, M., & Tavernet, J.-P. 2000, A&A, 359, 419
Hauser, M. G. & Dwek, E. 2001, ARA&A, 39, 249
H.E.S.S. Collaboration, Abramowski, A., Acero, F., et al. 2013, A&A, 550, A4
Horns, D. & Meyer, M. 2012, J. Cosmology Astropart. Phys., 2, 33
Horns, D. & Meyer, M. 2013, arXiv:1309.3846
Inoue, S., Granot, J., O'Brien, P. T., et al. 2013, Astroparticle Physics, 43, 252
Jacob, U. & Piran, T. 2008, Phys. Rev. D, 78, 124010
Jauch, J. M. & Rohrlich, F. 1976, The theory of photons and electrons. The relativistic quantum field theory of charged particles with spin one-half
Jelley, J. V. 1966, Physical Review Letters, 16, 479
Kifune, T. 1999, ApJ, 518, L21
Madau, P. & Pozzetti, L. 2000, MNRAS, 312, L9
Mankuzhiyil, N., Persic, M., & Tavecchio, F. 2010, ApJ, 715, L16
Mazin, D. & Raue, M. 2007, A&A, 471, 439
Mazin, D., Raue, M., Behera, B., et al. 2013, Astroparticle Physics, 43, 241
Mészáros, P. 2013, Astroparticle Physics, 43, 134
Meyer, M., Horns, D., & Raue, M. 2013, Phys. Rev. D, 87, 035027
Meyer, M., Raue, M., Mazin, D., & Horns, D. 2012, arXiv:1202.2867
Neronov, A. & Vovk, I. 2010, Science, 328, 73
Nikishov, A. I. 1962, Soviet Physics JETP, 14, 393
Orr, M. R., Krennrich, F., & Dwek, E. 2011, ApJ, 733, 77
Prandini, E., Bonnoli, G., Maraschi, L., Mariotti, M., & Tavecchio, F. 2010, MNRAS, 405, L76
Punch, M., Akerlof, C. W., Cawley, M. F., et al. 1992, Nature, 358, 477
Raue, M. & Meyer, M. 2012, in American Institute of Physics Conference Series, Vol. 1505, American Institute of Physics Conference Series, ed. F. A. Aharonian, W. Hofmann, & F. M. Rieger, 610–613
Reimer, A. 2007, ApJ, 665, 1023
Reimer, A. & Böttcher, M. 2013, Astroparticle Physics, 43, 103
Renault, C., Barrau, A., Lagache, G., & Puget, J.-L. 2001, A&A, 371, 771
Sanchez, D. A., Fegan, S., & Giebels, B. 2013, A&A, 554, A75
Sánchez-Conde, M. A., Paneque, D., Bloom, E., Prada, F., & Domínguez, A. 2009, Phys. Rev. D, 79, 123511
Sol, H., Zech, A., Boisson, C., et al. 2013a, Astroparticle Physics, 43, 215
Sol, H., Zech, A., Boisson, C., et al. 2013b, in IAU Symposium, Vol. 294, IAU Symposium, ed. A. G. Kosovichev, E. de Gouveia Dal Pino, & Y. Yan, 459–470
Stecker, F. W., de Jager, O. C., & Salamon, M. H. 1992, ApJ, 390, L49
Stecker, F. W., de Jager, O. C., & Salamon, M. H. 1993, in Bulletin of the American Astronomical Society, Vol. 25, American Astronomical Society Meeting Abstracts, 1336
Stecker, F. W. & Glashow, S. L. 2001, Astroparticle Physics, 16, 97
Taylor, A. M., Vovk, I., & Neronov, A. 2011, A&A, 529, A144
Urry, C. M. & Padovani, P. 1995, PASP, 107, 803
Vovk, I., Taylor, A. M., Semikoz, D., & Neronov, A. 2012, ApJ, 747, L14

SF2A 2013
L. Cambrésy, F. Martins, E. Nuss and A. Palacios (eds)

SEARCH AND ANALYSIS OF GALAXY-SCALE STRONG GRAVITATIONAL LENSES IN COSMOLOGICAL SURVEYS

F. Brault[1]

Abstract. This article focuses on the development of a novel detector of strong galaxy-galaxy lenses based on the massive modelling of candidates in wide-field ground-based imaging data. Indeed, not only are these events rare in the Universe, but they are at the same time very valuable to understand galaxy formation and evolution in a cosmological context. We use parametric models, which are optimized by MCMC in a bayesian framework, so that we know the distribution of errors. We first generate several training samples : a hundred lenses simulated in HST and CFHT conditions, along with 325 observed lens candidates resulting from a series of preselections on the CFHTLS-Wide galaxies, and that we classify according to their credibility. The whole challenge in designing this detector lies in a subtle balance between the quality of models and the execution time. We massively run the modelling on our samples, beginning with ideal application conditions that we make more complex by stages so as to get closer to the observation conditions and save time. We show that a 7-parameter model assuming a spherical source can recover the Einstein radius from the CFHT simulations with a precision of 7%. We apply a mask to the input data that noticeably enhances the robustness of the models facing environment problems, with a median convergence time of 4 minutes that could be easily reduced by a factor of 10 with more direct optimization techniques. From our results, we define selection contours in the parameter space, resulting in a completeness of 38% and a purity of 55% for the sample of 51 candidates accepted by our robot among the 325 preselected systems.

Keywords: gravitational lenses - galaxies : elliptical - dark matter - observational cosmology - large surveys - methods : statistics.

1 Introduction

Large surveys enable us to tackle the question of galaxy evolution in a cosmological context. In the current state of research, the merger scenario is still unclear but tends to show a dichotomy : cuspy inner profils, as seen in simulations, would result from dissipational mergers (wet mergers), whereas observed cores would result from dissipationless merger (dry mergers). The actual scenario is most probably a mix of those two kinds of mergers, but we need more probes to reveal the density profile of galaxies we observed, and more especially their dark matter (DM) density profile.
Strong lensing modelling gives an accurate mesaure of the total mass (baryons and DM) projected in a characteristic radius called the Einstein radius R_{Ein}. Under the assumption that the lens potential is close to a SIS (Singular Isothermal Sphere), this relation is given by the following formula :

$$R_{Ein} = 4\pi(\frac{\sigma_c}{c})^2\frac{D_{ds}}{D_s} \tag{1.1}$$

where σ_c is the central velocity dispersion of the lens galaxy, D_{ds} the distance between the deflector and the source, and D_s the distance to the source. Nevertheless, there are some drawbacks in contraining the density profile of a galaxy via the strong lensing tool : the mass-sheet degeneracy specific to lensing, the need to know the lens and the source redshifts, along with the fact that strong lenses at galaxy scale are very rare objects.

[1] Institut d'Astrophysique de Paris

Stellar dynamics break the mass-sheet degeneracy by delivering the total mass of the lens galaxy in another radius close to its effective radius. This mass results from the inversion of the Jeans equation. Knowing the mass from the lens modelling and the mass from the stellar dynamics, we get the mass gradient in the inner profile of the lens galaxy.
Ruff et al. 2011 Ruff et al. (2011) and Sonnenfeld and al. 2013 b) Sonnenfeld et al. (2013a) have carried out a joint strong lensing and stellar dynamics analysis that works on the following principles : strong lens modelling gives the Einstein radius, the position angle and the ellipticity of the deflector (see Gavazzi et al. 2012 Gavazzi et al. (2012) and Sonnenfeld et al. 2013 a) Sonnenfeld et al. (2013b)) ; spectroscopic measurements from Keck give the velocity dispersion as well as the deflector and source redshifts z_d and z_s; and the photometry, with the assumption of a Salpeter IMF (Initial Mass Function), gives the fraction of DM in half the effective radius of the deflector. Applying this methodology to a deep survey or to several surveys complementary in redshifts, one gets the cosmic evolution of the density profile inner slope in the lens galaxies and of their dark matter fraction. Figure1 from Ruff et al. 2011 Ruff et al. (2011) shows such evolution trends for a pilot analysis of 11 lenses from the SLACS (Sloan Lens ACS Survey, median $z_d \sim 0.2$), the SL2S (Strong Lensing Legacy Survey, median $z_d \sim 0.5$), and the LSD survey (Lenses Structure and Dynamics survey, median $z_d \sim 0.8$). We will talk in more detail about the SL2S later.

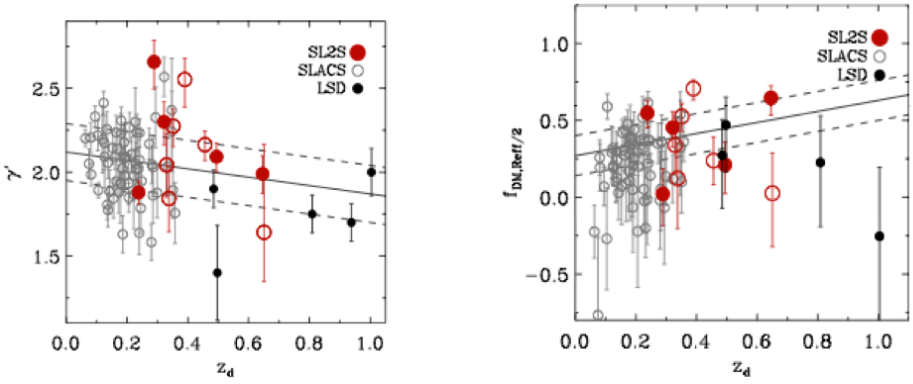

Fig. 1. *Cosmic evolution of the density profile inner slope (on the left) and of the dark matter fraction (on the right) for a pilot analysis of 11 lenses (Ruff et al. 2011 Ruff et al. (2011))*

As one can observe on figure 1, the results obtained so far are quite marginal and not convincing enough. Nevertheless, galaxy surveys are getting larger and larger : although we have only detected few hundreds of galaxy-scale lenses so far with spectroscopic and photometric methods, about 300 000 such lenses are expected in Euclid's 15 000 deg^2. In this context, we need a lens finder that gives a final sample as pure as possible, in other words, a lens finder that knows the lens equation, able to model each input candidate and to assign it a realistic lensing status ("yes it is a lens", "no it is not a lens", or even "there is some probability that it is a lens"). This automated modelling tool could also slighly increase the completeness of actual samples by finding original lenses like, for example, red gravitational arcs.

2 Lens modelling

The lens modelling is carried out by a program called SL-Fit (Gavazzi et al, 2012 Gavazzi et al. (2012)) that fits gravitational arcs from galaxy-galaxy lensing after subtraction of the deflector. It relies on parametric models optimized by MCMC (Monte Carlo Markov Chain) in a bayesian context, which might take more time than other optimization techniques but enables us to know the distribution of errors. A strong assumption is made concerning the potential of the lenses, that we model by a SIE (Singular Isothermal Ellipsoid). Furthermore, to mimic the kind of lenses which have most commonly been observed to date, made of blue arcs around a red galaxy, we assume a De Vaucouleurs luminosity profile for the deflector and an exponential luminosity profile for the source. In the finest application of SL-Fit, the lens models are then described by a set of 9 parameters, 3 for the lens potential and 6 for the source (the lens position is fixed at the center of the lens plane), which are : the Einstein radius R_{Ein}, the potential ellipticity, the potential orientation, the 2 coordinates of the source in the source plane, the intrinsic ellipticity of the source, the intrinsic orientation of the source, the intrinsic

flux of the source F_S, the effective radius of the source R_{effS}. Note that I chose to include the external shear ellipticity and orientation in the lens potential ellipticity and orientation respectively since those parameters are degenerated : it helps minimizing the number of parameters to fit.
Moreover, the MCMC is boosted by a process of simulated annealing (SA) : I have spent time optimizing the influence of the SA on the chain by determining the successive SA steps along with the typical number of iterations that secures the convergence of the chain at each step. This operation provides a Markov chain which is mainly driven by the priors in the early stages of its walk, and that will therefore move faster towards the distribution we are interested in; in parallel to this evolution, more and more weight is regiven to the likelihood as the latter is better known. Because of this modulation of the likelihood, the chain constituents in the SA phase are not considered for the final estimation of the parameters : only are retained the N' last MCMC elements which we think compose the convergence phase. The estimator we take for each parameter is then the median of its marginal distribution on these elements. I have found that we needed $N_{tot} \sim 2700$ iterations to ensure the convergence, along with $N' \sim 90$.
At this point, it appears that the whole challenge in designing this lens finder lies in a subtle balance between speed and robustness.

3 Training samples

3.1 Simulations

I have made ∼100 simulated lenses in HST filters (ACS F814W and F555W) and CFHT filters (Megacam i and g), using the GRAVLENS software (Keeton et al. 2001 Keeton (2001)) with the same assumptions than in section 5. for the MCMC modelling. The main interest of the simulated lenses sample is that, by construction, one knows the input values of each system parameters, to which one will be able to compare its output MCMC model values. This comparison allows to determine the maximum modelling accuracy of the lens finder.

3.2 CFHT data

The real data sample is made of 325 lens candidates found in the CFHTLS Wide (4 independant fields, a total of 155 deg^2, $i < 24.5$) in the framework of the SL2S, a survey that aims at providing a homogeneous sample of strong lenses at several scales from the CFHTLS. Those 325 galaxy-scale lenses result from a set of preselections involving :

- from photometric redshift catalogs containing 2.10^5 objects/deg^2 for T06 (Ilbert et al. 2006 Ilbert et al. (2006), we selected about 3000 ETG candidates/deg^2, that is 413000 Early-Type Galaxies (ETG) candidates in all.

- we run Raphael Gavazzi's Ringfinder Cabanac et al. (2007) (Gavazzi et al., in prep.) : a photometric lens finder for which the selection consists in looking for faint blue background galaxies embedded in bright red foreground galaxies, by substracting images observed in a redder band from their counterpart in a bluer band. We end up with about 14000 candidates in all.

- the remaining objects are then visually inspected and classified to yield a final sample of 325 candidates to be modelled by our new lens finder).

This sample firstly allows to improve the modelling by several methods trying to make it efficient in realistic observing conditions. Moreover, once these candidates are classified with the naked eye and with extra information (space-based images, spectra etc), one is able to encode the finder selection process in the modelling parameter space and derive from it the completeness and purity of the final sample (see the subsection about the selection step).
One can notice that in the first place, this lens finder is designed to work on ground-based data. Indeed, to date, ground-based images have been far more accessible than space-based data; furthermore, the seeing makes ground-based data much more difficult to model, so if the lens finder is able to work on this kind of data, it should be all the more efficient when adapted to a space-based survey like, for example, Euclid (see the part about further research).

4 Development of the lens finder

4.1 Optimizing the modelling step

I massively run SL-Fit modelling on my samples, beginning with ideal application conditions that I made more complex by stages so as to get closer to the observing conditions while saving time. Five progressive stages can be distinguished as follows :

- **(i) the fine modelling of lenses simulated in HST filters** :
  this is the zero complexity level for SL-Fit that fitted all the 9 MCMC parameters described above from clear space-based images;
- **(ii) the fine modelling of lenses simulated in CFHT filters** :
  I fitted all the 9 model parameters again but this time on grouned-based images blurred by seeing, which made a first complication;
- **(iii) the reduced modelling of lenses simulated in CFHT/g** :
  Focussing on the bluer band (g) of the ground-based simulations, where most of the gravitational arcs should more clearly appear, I tried to save time by reducing the number of parameters fitted in the MCMC process : this was made possible through additional simplifying assumptions on the source;
- **(iv) the reduced modelling of SL2S lens candidates observed in CFHT/g**:
  as might be expected, new difficulties arose while modelling the 325 preselected lens candidates, which are mostly due to :
  - the modelling assumptions being oversimple compared to the kinds of lenses that can be observed in the sky and the ones to discover;
  - the fact that, by construction, a perfect subtraction of the deflector can be performed on simulated lenses, whereas concerning the observed candidates, the subtraction is carried out by Galfit (Peng et al. 2002 Peng et al. (2002)) which will necessarily leave a smaller or larger residual at the center of the image : this residual may then be fitted instead of the counter image in the frequent case of double lenses, or will be added to the MCMC modelling residual;
  - the natural environment of observed candidates, which has not been mimicked in the simulations : this environment is made of galaxies that might again be wrongly fitted as a gravitational arc, misleading the Markov chain by making the parameter space exploration chaotic.
- **(v) the masked modelling of SL2S lens candidates observed in CFHT/g**:
  the first difficulty mentionned above while dealing with real data cannot be solved easily since it is not profitable to make the model assumptions more complex in the framework of an automated lens finder dedicated to massive modelling; concerning the environment and the central residual left by the deflector subtraction, I tried to tackle both problems by applying on the input image a uniform mask bounded by a small radius of 0.3" hiding the possible residual inside, and a large radius of 2.5" covering the galaxies beyond; the MCMC fit is still done on all the pixels in the image so that models predicting arcs in the corners are excluded : this disfavours the detection of lenses with large R_{Ein}, which is not a real problem since the latters are the easiest to find by other means.

Figure 2 shows a successful case of modelling by the lens finder on a candidate for which the lensing status has been confirmed by HST imaging.

4.2 Optimizing the selection step

Once a candidate has been modelled by the lens finder, the latter has to decide wether or not it deserves a lensing status. In order to train the finder to make a decision, R. gavazzi and I first classified the real data candidates in five categories, from "excellent candidates" to "bad candidates" and "undetermined candidates". This classification has been carried out with the naked eye but also with extra information from HST and Keck high resolution images and from Keck and VLT spectra. Afterwards I cut through the space of MCMC parameters and other related quantities following these kinds of justifications :

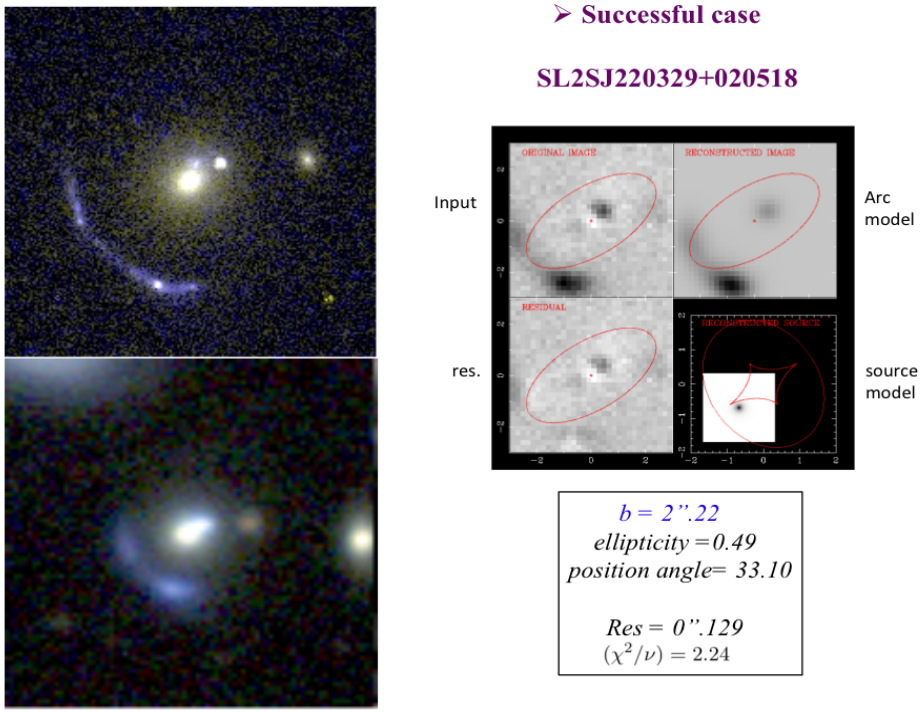

Fig. 2. *Modelling of the confirmed lens SL2SJ220329+020518, showing the HST image (top left), the CFHT image (bottom left), and SL-Fit output (top right) with (in the direction of reading) the input image, the arc model, the residual resulting from the subtraction of the arc model from the input image, and the source model (Brault et al, in prep).*

- physical justifications, like a reasonable range of values for the Einstein radius and the effective radius of the source : $0.''75 < R_{Ein} < 1.''19$ and $0.''015 < R_{effS} < 0.''13$, a lower limit on the amplification : $\mu > 1.5$ (I believe this limit could be easily set higher with a larger training sample), or an upper limit on the distance of the source from the projected center of the lens potential in the source place : $ds < 1.''02$;
- statistical justifications like constraints on the reduced chi-squared to keep a good fit to the data : $1. < (\chi^2/\nu) < 2.5$;
- practical justifications like an upper limit on the time of convergence of the Markov chain in the context of automated massive modelling : $t_{conv} < 7$ min;
- empirical justifications from the repartition of the classified candidates in the parameter space : figure 3 is an example of this repartition in the 2-D space showing the amplification as a function of the Einstein radius plus the error on the Einstein radius; of course the precise contraints given on some parameters above are tuned to converge with those empirical findings.

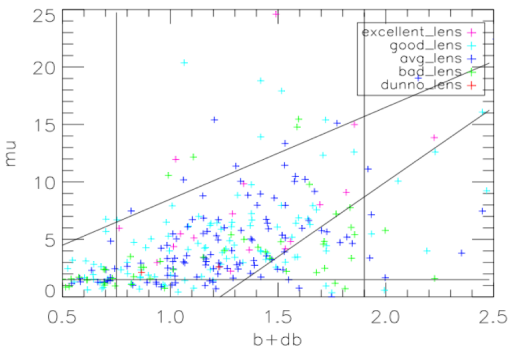

Fig. 3. *Distribution of the 325 SL2S lens candidates in the amplification–{Enstein radius+error} plane with scientifically and empirically justified cuts*

5 Conclusions

As things stand, the main results concerning my lens finder can be summed up as follows :

- I showed that a 7-parameter model assuming a spherical source (which amounts to fixing the the ellipticity and orientation of the source) can recover the Einstein radius from the CFHT simulations with a precision of $\sim 7\%$.
- The median MCMC convergence time is ~ 4 minutes on real data, and could be easily reduced by a factor of 10 using more direct optimization techniques.
- With the selection contours I defined in the parameter space, the final sample selected by the lens finder is $\sim 55\%$ pure and $\sim 37\%$ complete (if one considers the "good" and "excellent" candidates) with the time constrain $t_{conv} < 7$ min. Relaxing that latter contraint, one now gets a purity of $\sim 50\%$ along with a completeness of $\sim 64\%$: there will always be a trade-off to deal with between completeness and purity, but this shows that a high completeness should be reachable by saving even more time in the modelling process.Those are quite encouraging results even though one should keep in mind that this selection is made downstream from the set of preselections detailed above (see section 6, about the training samples) : in particular, the purity should be lower for the new lens finder running alone.

  The automated lens finder described above is being improved in several aspects like its model quality, its execution time, its lens selection, its autonomy and its portability in order to be adaptable and appliable to current and future, ground-based and space-based, wide-field imaging surveys.

References

Cabanac, R. A., Alard, C., Dantel-Fort, M., et al. 2007, A&A, 461, 813
Gavazzi, R., Treu, T., Marshall, P. J., Brault, F., & Ruff, A. 2012, ApJ, 761, 170
Ilbert, O., Arnouts, S., McCracken, H. J., et al. 2006, A&A, 457, 841
Keeton, C. R. 2001, ArXiv 0102340
Peng, C. Y., Ho, L. C., Impey, C. D., & Rix, H. 2002, AJ, 124, 266
Ruff, A. J., Gavazzi, R., Marshall, P. J., et al. 2011, ApJ, 727, 96
Sonnenfeld, A., Gavazzi, R., Suyu, S. H., Treu, T., & Marshall, P. J. 2013a, ArXiv 1307.4764
Sonnenfeld, A., Treu, T., Gavazzi, R., et al. 2013b, ArXiv 1307.4759

SF2A 2013
L. Cambrésy, F. Martins, E. Nuss and A. Palacios (eds)

SUPERNOVA LEGACY SURVEY 5 YEARS : FINAL TYPE IA SUPERNOVA SPECTROSCOPIC SAMPLE

F. Cellier-Holzem[1] and the SNLS collaboration

Abstract. The SuperNova Legacy Survey (SNLS) is a five-year project aiming at constraining the equation of state of the dark energy using a type Ia supernova (SNIa) Hubble diagram. To construct this diagram, a spectroscopic program is essential to secure the type and redshift of the SNIa candidates. SNLS benefited from large time allocated on 8-m class telescopes with 1500 hours of observations. In this talk, I will describe the steps of the data processing and spectral analysis what have allowed to build the full spectroscopic sample with 427 SNeIa. In addition to be used for the final SNLS cosmology analysis, this spectroscopic sample is a rich source of physical information about the SNeIa to test the evolution of their population with redshift.

Keywords: Type Ia supernova, SuperNova Legacy Survey, spectroscopy, dark energy

1 Introduction

Using type Ia supernovae (SNe Ia) as standardisable candles has lead to the discovery of the acceleration of the universal expansion (Perlmutter et al. 1999; Riess et al. 1998). This acceleration is nowadays attributed to a dark energy component that contributes to more than 70% to the energy budget of the Universe. To characterize the nature of this component, a combination of various probes has been used. Among those, the measurement of luminosity distances to SNe Ia provides perhaps the simplest and most direct way of probing dark energy. For this purpose, low and high redshift SNe Ia are compared in a Hubble diagram. Combining the SuperNova Legacy Survey (SNLS) 3 year SNe Ia with low-redshift SNe Ia from the literature, intermediate redshift SNe Ia from the SDSS-II Supernova Survey and high-redshift from the Hubble Space Telescope, Conley et al. (2011) have produced the most advanced supernova Hubble diagram to date with 472 SNe Ia in total. With its 235 SNe Ia in the range $0.15 < z < 1.1$, SNLS is the most comprehensive supernova survey at high redshift to date.

After the publication of the SNLS 3 year cosmological analysis, the effort are now focusing on the SNLS 5 year analysis. Spectroscopy is essential for this analysis to secure the nature of the SN Ia candidates and measure their redshift to build the Hubble diagram. The present article focuses on the spectroscopic analysis of the SNLS 5 year data set to build of the full SNe Ia spectroscopic sample. This new sample will allow us to investigate a key question for cosmology : as SNe Ia are used over a large redshift range, we will test if the SN Ia populations evolve with the redshift. This study is fundamental to validate the used of SNe Ia in cosmology.

2 The SuperNova Legacy Survey experiment

The SNLS is a 5 year experiment conducted from 2003 to 2008. It is a spectro-photometric progam aiming at detecting and following a large number of SNe Ia at intermediate to high redshift in order to measure their luminosity distance and constrain cosmological parameters. The experiment was split in two surveys : an imaginig survey and three spectroscopic programs.

[1] Laboratoire de Physique Nucléaire et des Hautes Énergie, Université Paris 6, 4 place Jussieu, 75252 Paris Cedex 05, FRANCE

2.1 The imaging survey

A photometric program at the Canada-France-Hawaii Telescope implemented a rolling search technics that allowed for the detection of new SN Ia candidates as well as the follow-up of their light curves in several photometric bands. The objects are detected in four 1 square degree field observed every 3-5 nights during 5-6 lunations per years. During the survey, more than 1000 SNe Ia candidates with well sampled multi-bands light curves have been optained (Guy et al. 2010).

2.2 The spectroscopic programs

To assess the type of the candidates and estimates their redshift, spectroscopic follow-up programs have been performed on three 8-10m class telescopes : the Very Large Telescope (VLT), Gemini-North & South and Keck I & II. SNLS benefited from 1500h of observation on these telescopes and spectra have been measured for around half of photometric SN Ia candidates :

- 35% of the SNe Ia have been measured by the Gemini telescopes (Howell et al. 2005; Bronder et al. 2008; Walker et al. 2011) where SNLS benefited from 60 hours of observation per semester during 5 years. Gemini observed preferentially high redshift candidates ($z > 0.6$) in the four SNLS fields,

- the VLT measured 45% of the SNe Ia (Balland et al. 2009; Cellier-Holzem & the SNLS collaboration in prep) during two ESO large programs, corresponding to 60 hours per semester from June 2003 to September 2007. The VLT is a southern telescope and thus observed preferentially the equatorial SNLS fields.

- the remainder of the candidates were sent to the Keck telescopes, in particular the objects of the high latitude fields and candidates with a redshift around 0.5 for dedicated studies. These telescopes measured around 20% of the SNe I (Ellis et al. 2008; Fakhouri & SNLS collaboration in prep).

3 Building the final spectroscopic sample of SNLS

3.1 Redshift estimates

The first step to build the full spectroscopic sample is the redshift estimates of the SN Ia candidates. Redshifts are estimated from strong host features if present (e.g. [O II] at 3727Å or H_β at 4861Å emmission lines or Ca II H&K at 3934Å and 3968Å absorption lines). To estimates the redshift, we perform a gaussian fit of each identified host feature. We assign an error of 0.001 on the redshift, typical of the uncertainty obtained on redshift derived from host lines.

If no apparent host line is present, the redshift is estimated from the supernova features themselves. First a rough estimate is inferred from one of the large absorption line of the supernova (e.g. Ca II around 3700Å or Si II at 4000Å). To refine the redshift, we performed a combined fit of the observed light curves and spectrum with the spectro-photometric model of SN Ia, SALT2 (Guy et al. 2007). A galaxy template representing the host contribution is added to the model to take into account the host contamination and recover the SN Ia signal. As the supernova feature are larger than the host lines, we assign a higher error of 0.01 on the supernova redshift.

3.2 SNe Ia identification

The second aim of the spectroscopy is the SN Ia identification to include only SNe Ia to the Hubble diagram. To assess the nature of the candidates, we inspect the SALT2 fit of the spectrum after the host subtraction. If at least one typical features of SN Ia is seen (e.g. Si II at 4000Å or 6150Å), or if the spectral fit is good over the entire spectral range, the object is certainly a **SN Ia**. For some cases, the candidate is likely a SN Ia but other types can not be excluded given the signal-to-noize and the quality of the SALT2 fit : we classify these objects as **SN Ia⋆**. To not contaminate the SN Ia sample with other types, only SNe Ia and SNe Ia⋆ (which represent 70% of candidates) are considered for inclusion in the Hubble diagram. The objects where a supernova signal is not clearly visible, or with a not SN Ia spectrum are excluded.

3.3 Results : full spectroscopic sample

The final spectroscopic sample of SNLS contains 427 objects, with 76% of SNe Ia and 24% of SNe Ia⋆. These SNe Ia and SNe Ia⋆ subsamples have very similar photometric properties (color, stretch and absolute magnitude at maximum in B-band) on average, which suggest that the SNe Ia⋆ sample is not contaminated by non-Ia-objects with respect to the SN Ia sample.

This pure data set is the largest sample of SNe Ia at intermediate and high redshift to date. Among this sample, two independant sub-samples (two different extractions and without common SNe Ia) of spectra measured by the VLT existe : the VLT 3 year (Balland et al. 2009) and the VLT 5 year (Cellier-Holzem & the SNLS collaboration in prep) samples. These two sub-samples can allow us to test the calibration and the identification in SNLS. For this purpose, we compare the raw data building the mean spectrum for each VLT sub-sample. To build the mean spectra, spectra are first de-redshifted and rebinned to 5Å. We normalize the spectra fixing the flux integral over a wavelength range 4000-4500Å. The average weighted flux and its corresponding uncertainty (1σ error) are then computed in each wavelength bin. The two mean spectra are overlapped in Fig. 1 and are remarkably similar. We conclude the SNe Ia of the two subsamples are identical in average and the spectra are calibrated at 5%.

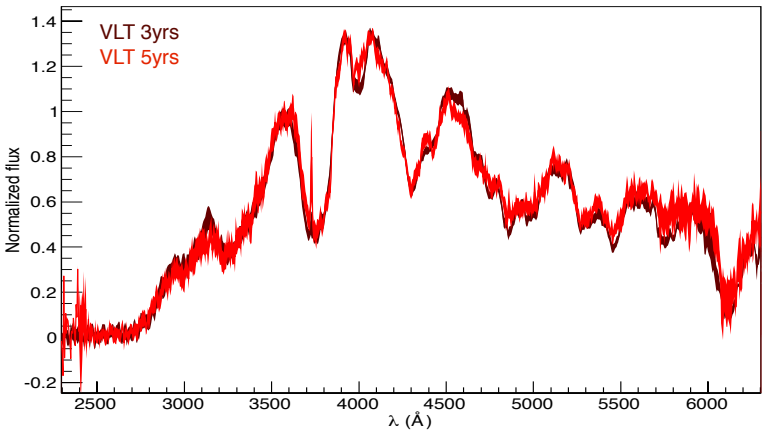

Fig. 1. Mean spectra from VLT 3 year (in dark red) and VLT 5 year (in light red) samples

4 Testing the evolution of SNe Ia properties with the redshift

With this exeptional sample, we can investigate some key questions for cosmology. In particular, as SNe Ia are used over a large redshift range, we have to determine if the SN Ia population properties evolve with redshift to validate the used of SNe Ia in cosmology. Several studies (e.g. Sullivan et al. 2009 or Maguire et al. 2012) investigated this question, comparing low and high redshift spectra and they remarked spectral differences localized in UV : low redshift spectra have depressed flux compared to higher redshift. Several interpretation existe in literature : it could be explained by a demographic evolution of the SN Ia population (Sullivan et al. 2009) or a consequence of the galactic evolution (Maguire et al. 2012) for example. In this controversial context, the SNLS spectra can shed a new light on this key question.

For this purpose, we build mean spectra at low and high redshift from VLT spectra using SNe Ia (not SNe Ia⋆ to limit the bad signal-to-noise spectra) around light maximum ($-4 <$ phase < 4 days) with a cut in color ($-0.2 <$ color < 0.2) to exclude peculiar SNe Ia. Spectra are split into two redshift bins : 15 with $z < 0.5$ and 56 with $z > 0.5$. Mean spectra are built using the previous methode, with a color correction of the spectra to take into account the diversity of SN Ia colors, and are overlapped on the left panel of Fig. 2. Spectra are similar but absorption depth differences are visible : low redshift spectra have deeper absorption lines due to intermediate mass elements (Ca II at 3700Å and Si II at 4000Å). This is consistent with higher SNe Ia beeing bluer (flux excess in UV), brighter and hotter and thus ionasing more intermediate mass elements. Indeed, when

we select two sub-samples with similar photometric properties (on the right panel of Fig. 2), the differences are significantly reduced. We conclude that the differences bewteen low and high redshift SNe Ia are consistent with a selection effect : we select preferentially brighter (bluer and hotter) SNe Ia at high redshift and we do not highlight a demographc evolution of SNe Ia.

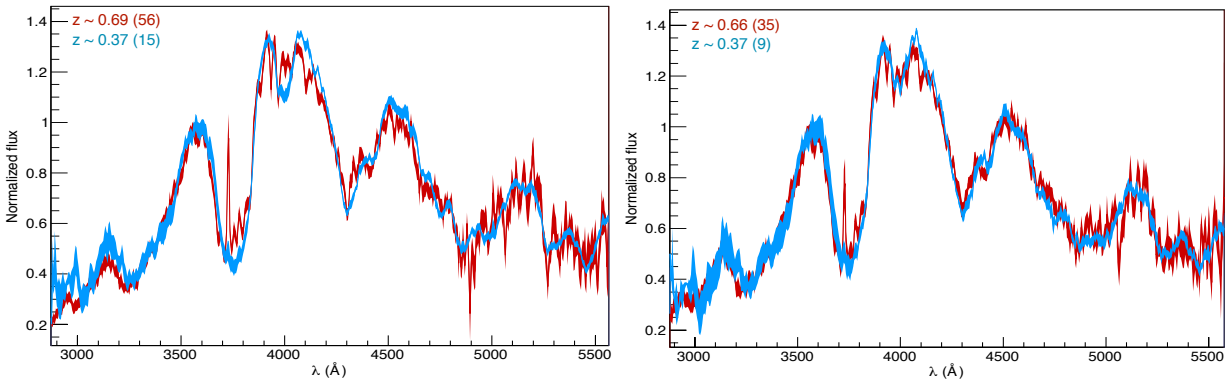

Fig. 2. Mean spectra at low (in blue) and high (in red) redshift built from **Left:** the VLT sample (15 low z and 56 high z spectra), **Right:** from two VLT sub-samples with similar photometric properties in average (9 low z and 35 high z spectra).

5 Conclusions

Spectroscopy is essential in cosmology to estimate the redshift and assess the nature of the SN Ia candidates. For this purpose, SNLS benefited from exceptional spectroscopic surveys with 1500h of observation on 8-10m class telescopes. During the survey, the SNLS collaboration has identified 427 SNe Ia and SNe Ia⋆. This is the largest intermediate to high redshift SN Ia sample to date. The final SNLS cosmology analysis will rely on this spectroscopic sample, after photometric cuts are made.

This exceptional sample can be used to investigate the key question of the evolution of SNe Ia with redshift. Using the VLT spectra, we find evidence for differences in the intermediate mass element absorptions between low and high redshift SN Ia. These differences are consistent with a selection effect and we do not need to invoke a demographic evolution of SNe Ia, which legitimates the use of SNe Ia as "calibrated candels" in cosmology.

References

Balland, C., Baumont, S., Basa, S., et al. 2009, A&A, 507, 85
Bronder, T. J., Hook, I. M., Astier, P., et al. 2008, A&A, 477, 717
Cellier-Holzem, F. & the SNLS collaboration. in prep
Conley, A., Guy, J., Sullivan, M., et al. 2011, ApJS, 192, 1
Ellis, R. S., Sullivan, M., Nugent, P. E., et al. 2008, ApJ, 674, 51
Fakhouri, H. K. & SNLS collaboration. in prep
Guy, J., Astier, P., Baumont, S., et al. 2007, A&A, 466, 11
Guy, J., Sullivan, M., Conley, A., et al. 2010, A&A, 523, A7
Howell, D. A., Sullivan, M., Perrett, K., et al. 2005, ApJ, 634, 1190
Maguire, K., Sullivan, M., Ellis, R. S., et al. 2012, MNRAS, 426, 2359
Perlmutter, S., Aldering, G., Goldhaber, G., et al. 1999, ApJ, 517, 565
Riess, A. G., Filippenko, A. V., Challis, P., et al. 1998, AJ, 116, 1009
Sullivan, M., Ellis, R. S., Howell, D. A., et al. 2009, ApJ, 693, L76
Walker, E. S., Hook, I. M., Sullivan, M., et al. 2011, MNRAS, 410, 1262

SF2A 2013
L. Cambrésy, F. Martins, E. Nuss and A. Palacios (eds)

HOW DID Z=0 GALAXIES IONIZE THEIR ENVIRONMENT DURING THE REIONIZATION EPOCH ?

Jonathan Chardin[1], Dominique Aubert[1] and Pierre Ocvirk[1]

Abstract.
Cosmological simulations of reionization are analyzed in order to assess the reionization history of individual galaxies. A catalog of the evolution of the HII region properties is calculated with a merger tree of HII regions. It is assumed that a galaxy experiences a reionization in isolation until its related HII region merge with another one equal or greater in volume. The lifetime of HII regions related to galaxies and their volume before their fusion with the UV background are calculated. We find that the later a galaxy appears, the smallest is its lifetime and its volume before being incorporated into the UV background. We then use an average mass accretion history of dark matter halo model (AMAH model) to calculate the mass of the galaxies today at $z = 0$. We can thus link the past reionization properties of their related HII regions with the mass of the galaxy observed today. We find that the more a galaxy is massive today, the earliest it appears and the largest its lifetime and volume are before it sees another I-front coming from another galaxy.

Keywords: Reionization, HII regions , first stars - Methods: numerical

1 Introduction

The reionization period is the moment in the history of the Universe that sees the first galaxies ionizing their environment until $z \sim 11 - 6$ (see respectively Komatsu et al. 2009 and Fan et al. 2006) when the whole IGM is transformed into a plasma. One key challenge is to understand how the reionization proceeds locally around individual galaxies instead of focusing on the global transition. It could be a starting point in order to understand how did occur the reionization of our own galaxy or the reionization of the Local Group (see Ocvirk & Aubert 2011 and Iliev et al. 2011 for example). In that spirit, we propose in that work to assess the "local reionization history" of individual galaxies in cosmological simulation of reionization. The basic idea is to evaluate how long can be a galaxy reionized by itself without any contribution from another I-front and what volume a galaxy is able to ionize alone depending on the cosmic time of apparition of the galaxy.

2 Methodology

2.1 merger tree of HII regions

In order to follow the HII regions properties with redshift we built the merger tree of the ionized regions appeared during simulations. The methodology is fully described in Chardin et al. (2012) and is basically performed in two steps: Firstly, the identification of the HII region in all snapshots of a given simulation with a friends-of-friends algorithm (FOF) is performed and secondly the link between the identification number of the regions is done between all the snapshots and for all HII regions. We adopt the criterion that says that a cell is ionized if its ionization fraction $x \geq 0.5$.

[1] Observatoire Astronomique de Strasbourg, Université de Strasbourg, CNRS UMR 7550, 11 rue de l'Université, F-67000 Strasbourg, France

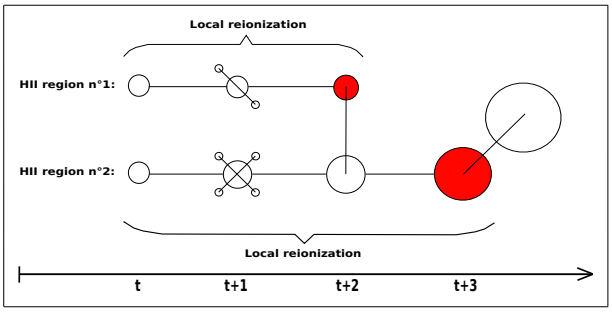

Fig. 1. Illustration of the follow up of the 'local reionization history' fro two distinct HII regions. Red items symbolize that the HII region undergoes a major merger after what the local reionisation history is finished.

2.2 follow up of local reionization histories

Thanks to the merger tree, we built a catalog of HII regions extracted from simulations. For each HII region, the catalog allows to follow its volume at any instant of the simulation, the number of merger with the region and the total volume of the regions that merge with it. We also have access to the mass of the most massive dark matter halo progenitor inside the region at each instant. In that work we want to investigate how long can be a galaxy been reionized in isolation without any influence of neighboring galaxies depending on their cosmic apparition time. To address this question we adopt the definition which says that a galaxy ends its local reionization history when its related HII region merges with regions with a total volume equal or greater than the current volume of the region (see figure 1 for a schematic view of that definition).

2.3 Local reionization seen at $z = 0$

In order to make predictions about the past reionization history of galaxies observed today, we propose to calculate the mass M_0 that would have the dark matter halo progenitors inside the HII regions at $z = 0$. For this purpose, we use the average mass accretion history (AMAH) of dark matter halos model of McBride et al. (2009) to extrapolate the mass of a halo at redshift z to $z = 0$.

2.4 simulations

We propose in this work to apply the merger tree methodology on two simulations of cosmic reionization. We performed a simulation where the stellar particles generated with the RAMSES code (Teyssier 2002) act as ionizing sources with a constant emissivity. Alternately, we performed a model where the dark matter halos extracted from the density fields are assumed as ionizing sources with an emissivity proportional to the halo masses. In all cases the radiative transfer is done with the ATON code (Aubert & Teyssier 2008) and the emissivities are tuned to obtain a reionization redshift at $z \sim 6$. One box size of 200 Mph/h is considered with a coarse resolution of 1024^3 with 3 additional levels of refinements for the hydrodynamic step. Radiative transfer is treated as a post-processing step and has been performed at the same resolution as the hydrodynamic coarse grid (i.e. 1024^3). The full details of the simulations can be found in section 3 of Chardin et al. (2012) (models S200 and H200).

3 Results

3.1 Global evolution

The figure 2 shows the evolution of the mean lifetime t_{life} and the mean volume (at the 3σ uncertainty) of the HII regions before seeing the UV background as a function of their cosmic time of apparition t_{app}. The curves are calculated for both ionizing source models according to the caption of the figure. We observe in both model that t_{life} and the corresponding volume decreases with t_{app}. This tendency is not surprising considering that the later an ionizing source appears during the reionization, the less neutral is the IGM. It then leads to a more accentuated proximity effect between the HII regions and a higher merging rate of the regions. On the contrary,

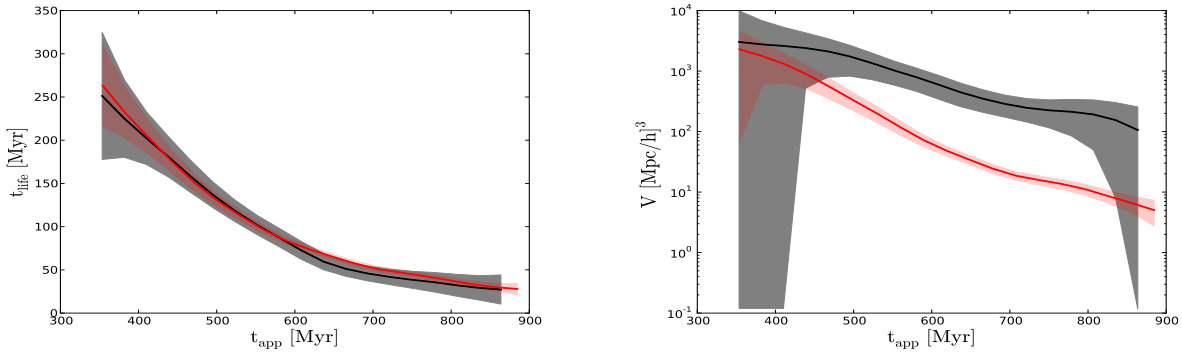

(a) (b)

Fig. 2. (a) Mean evolution of the lifetime of the HII regions before their fusion with the UV background as a function of the apparition time of the regions. (b) Mean evolution of the volume of the HII regions before their fusion with the UV background as a function of the apparition time of the regions. The black and red curve stand respectively for the mean value of the Star and Halo model at the 3σ uncertainty.

early regions can expand during $\sim$ 250 Myr with a volume that can reach until a few 10^3 [Mpc/h]^3 because they appear in a mostly neutral environment.

Otherwise, it is surprising to note that whatever the ionizing source model considered, the mean curves are relatively similar. We expected to find smaller t_{life} in the halo-based model compared to the star model. Indeed, the greater number of halos compared to stars particles leads to a higher number of HII regions that could merge more quickly than in the star prescription. In regards to our results it alternately seems that the I-fronts velocities of the regions is slower in the halo model in order to match the global ionization history of the star-based model. This is although confirmed with the volume of the regions that are smaller in the halo model than in the star-based one.

3.2 Reionization seen at $z = 0$

Figure 3 shows the the evolution of the mean lifetime t_{life} and the mean volume (at the 3σ uncertainty) of the HII regions before seeing the UV background as a function of the mass M_0 at $z = 0$ of the dark matter halo progenitor of the region. The curves are calculated for both ionizing source models according to the caption of the figure.

It is reassuring to note the same trends in both models : the more a halo is massive today, the larger is the lifetime and the volume that the related HII regions can reach before merging with another ionized region. This tendency is natural since the more massive halos at $z = 0$ are the ones appeared the most early and thus in the most neutral environment. In other words the smallest galaxies observed today are the ones appeared late in the reionization epoch and are rapidly swallowed by large HII regions associated to massive galaxies observed today.

We can note that the faster I-fronts in the star-based model lead to a same volume reached by the HII region than in the halo prescription but with a shorter lifetime before seeing the UV background.

In order to make predictions on the past reionization of MW and M31, our results suggests that an object of $\sim 3 \times 10^{11} M_\odot$ should have reionized its close environment in isolation for $\sim 90 \pm 30$ Myrs within a sphere of a typical radius of $\sim$ 2.7 Mpc/h. These results are in agreement with the study of Ocvirk et al. (2013) where constrained simulations of the Local Group show that the reionization of a Milky Way halo ($\sim 3 \times 10^{11} M_\odot$) is done in isolation for 130 Myrs in their photon-rich H43 model (the closest to our emissivity model). However, Ocvirk et al. (2013) found a maximal extent of $\sim$ 1 Mpc/h for the related HII region which is under our estimations. For the exceptional case of the Local Group, with the proximity of MW and M31, it is thus difficult to bring closer our statistical results and those obtained from constrained simulation of the reionization of the Local Group.

However, thinking of the whole Local group as a massive object of a few $\sim \times 10^{12} M_\odot$, our results suggests an HII region extension of a few Mpc before encountering another front. This is a volume large enough to

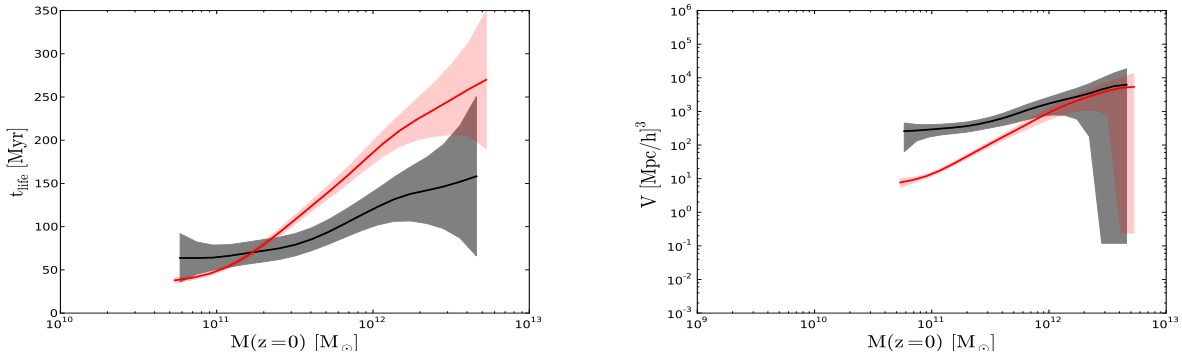

(a) (b)

Fig. 3. (a) Mean evolution of the lifetime of the HII regions before their fusion with the UV background as a function of the mass of their dark matter halo progenitor at z=0. (b) Mean evolution of the volume of the HII regions before their fusion with the UV background as a function of the mass of their dark matter halo progenitor at z=0. The black and red curve stand respectively for the mean value of the Star and Halo model at the 3σ uncertainty.

encompass the whole Local Group. In other words, statistically the Local Group could have been reionized by only its own source content whithout any influence from another front coming from a Virgo-like cluster for example.

4 Conclusions

We have addressed questions related to the reionization history of individual galaxies in numerical simulations of reionization. We used a merger tree of the HII regions in order to follow the duration of the local reionization and the volume that can be reionized by a or a couple of halos. We found that the later an ionizing source appears, the smaller are the lifetime and the volume of its associated HII region before encountering an other I-front. We then tried to link these local reionization histories with the local Universe. We found that a more massive is a galaxy today, the earlier it appears during the reionization and the larger is its local reionization duration and volume. Statistically, we found that MW and M31 reionized in isolation during about 100 Myrs which is consitent with constrained simulation of the reionization of the Local Group. We also found that the whole Local Group would have been reionized by its inner source content without any influence coming from a Virgo-like cluster. These results have to be compared to more constrained simulation at the scale of galaxies in the future. It could be done by using the merger tree approach in a systematic manner.

We want to thank B.Semelin, R. Teyssier and H. Wozniak for comments and discussion.

References

Aubert, D. & Teyssier, R. 2008, MNRAS, 387, 295
Chardin, J., Aubert, D., & Ocvirk, P. 2012, A&A, 548, A9
Fan, X., Strauss, M. A., Becker, R. H., et al. 2006, AJ, 132, 117
Iliev, I. T., Moore, B., Gottlöber, S., et al. 2011, MNRAS, 413, 2093
Komatsu, E., Dunkley, J., Nolta, M. R., et al. 2009, ApJS, 180, 330
McBride, J., Fakhouri, O., & Ma, C.-P. 2009, MNRAS, 398, 1858
Ocvirk, P. & Aubert, D. 2011, MNRAS, 417, L93
Ocvirk, P., Aubert, D., Chardin, J., et al. 2013, ArXiv e-prints
Teyssier, R. 2002, A&A, 385, 337

SF2A 2013
L. Cambrésy, F. Martins, E. Nuss and A. Palacios (eds)

NANÇAY CONTRIBUTION TO THE WORLDWIDE PULSAR PROGRAMS

I. Cognard[1,2], G. Theureau[2,1], L.Guillemot[1], K.Liu[2,1], A.Lassus[1] and G.Desvignes[3]

Abstract. The Nançay radio telescope is involved in two main scientific pulsar programs. Monitoring observations of various types of pulsars provide high quality rotational parameters, full radio polarization profiles and ephemerides to support observations taking place at high energy (*Fermi* LAT). Dense and precise timing measurements of a set of ultra-precise millisecond pulsars is carried out within a European collaboration (EPTA) to search for the subtle effect of gravitational waves, such as emitted by super-massive binary black holes at the center of galaxies.

Keywords: pulsar, Nançay, high energies, gravitational waves

1 Introduction

Radio pulsars are magnetized neutrons stars detected as periodic pulses produced by the intersection of collimated radio beams with radio telescopes on Earth. Detectable from the ionospheric cutoff around 10 MHz to more than 100 GHz, radio pulsars are essentially studied between 100 MHz and 3 GHz while the optimal frequency range for precise timing being 1.4-2 GHz. It is high enough to minimize interstellar scattering effects proportional to ν^{-4}, and not too high to keep signal strong enough despite a mean pulsar spectra following ν^{-2}.

The meridian Nançay radio telescope, equivalent to a ∼100m dish, is still among the 5 most sensitive decimetric telescopes. Having been built on a Kraus design in the 1960s (Lequeux et al. 2010), a given source can be observed for ∼1 hour using receivers moving along a 80m track. Two receivers covering 1.1 to 1.8GHz and 1.7 to 3.5GHz respectively can transmit ∼500MHz of bandwidth to the instrumentation. At 1.4GHz, the telescope is characterized by a system temperature of about 35K and an antenna gain of 1.4K/Jy.

Pulsar observations using the Nançay decimetric radio telescope started in the late 1980s. A swept local oscillator system was designed and built to observe the two millisecond pulsars (MSPs) B1937+21 and B1821-24. Very dense high precision timing measurements were conducted, leading to the detection of an Extreme Scattering Event interpreted as a ionized 'cloud' crossing the line of sight (Cognard et al. 1993), and to the discovery of the first micro-glitch in a millisecond recycled pulsar (Cognard & Backer 2004). Since the mid-2000s, the launch of the *Fermi* LAT and the growing Pulsar Timing Array for gravitational waves detection, the Nançay pulsar programs expanded to 50% of the telescope time with a state of the art instrumentation developped in parallel.

2 Instrumentations

Pulsar observations are hampered by dispersion produced by the free electrons of the interstellar medium. The narrow radio pulses are delayed inversely proportional to the square of the observing frequency and dedicated instrumentations are built to be able to integrate the signal both in frequency and time. Modern instrumentations are using the coherent dedispersion approach where the dispersion is removed directly on the phases of the digitized voltages received by the radio telescope (which are proportional to the electric field of the electromagnetic wave). The dedispersion process is done in the complex Fourier domain of the signal applying an adequate filter. Powerful GPUs (Graphic Processing Units) are used to calculate direct and inverse FFTs in real time over a bandwidth of 512 MHz. Currently at Nançay, the NUPPI 4 nodes - 8 GPUs system is able to process a 16Gbs data stream and provide radio pulse profiles for 128 4 MHz channels every 30 sec (Fig. 1).

[1] LPC2E / CNRS et Université d'Orléans, 45071 Orléans, France
[2] Station de radioastronomie de Nançay, Observatoire de Paris, Paris, France
[3] Max-Planck-Institut für Radioastronomie, Auf dem Hügel 69, 53121 Bonn, Germany

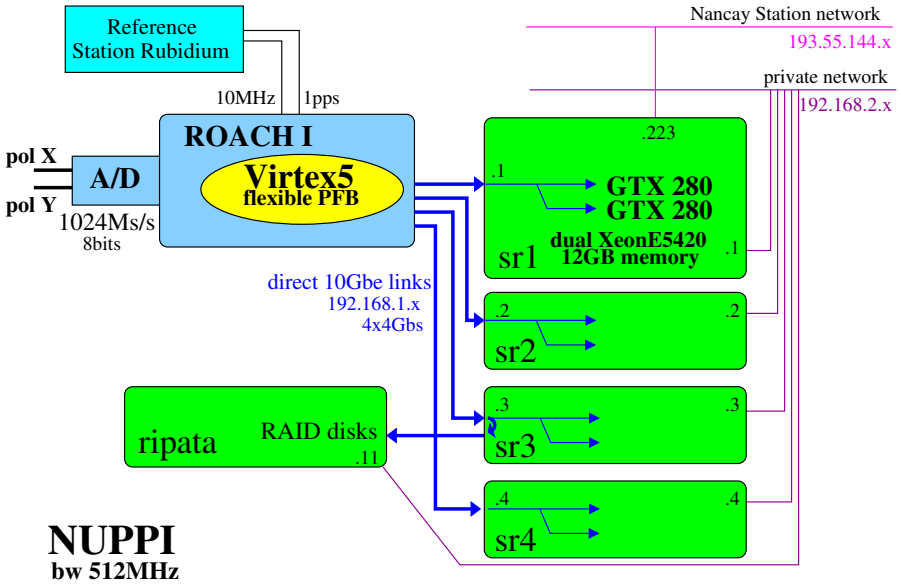

Fig. 1. Schematic of the Nançay NUPPI coherent dedispersion pulsar instrumentation. The two polarizations coming from the receiver of the telescope are 8-bit digitized at 1024Ms/s, pre-processed in a ROACH board to split the whole 512 MHz bandwidth into 128 more manageable 4MHz channels. Four 10Gbs links send data to the four nodes where 8 GPUs GTX 280 are used to dedisperse and fold the pulsar signal. A Rubidium clock provides reference frequency and 1pps signal to accurately time stamp the data stream.

3 Decimetric observations with the Nançay radio telescope

Pulsars can be used for a wide variety of physics and astrophysics problems (Ransom 2013). Connection to High Energy physics (related to the French PNHE Programme National Hautes Energies) mainly comes from the young and energetic pulsars (but also recycled millisecond pulsars since the recent *Fermi* LAT detections) showing complex gamma-ray emission, while connection to Cosmology (related to the French PNCG Programme National de Cosmologie et Galaxies) is through the potential direct detection of gravitational waves from Super-Massive Black Holes Binaries (SMBHB) using very precise timing measurements of a set of ultra-stable millisecond pulsars spread in the Galaxy.

3.1 Multi-wavelength study of pulsars from radio to TeV photons

The main idea of this program is to acquire the radio data necessary to support and complement pulsar observations with the *Fermi* Large Area Telescope (*Fermi* LAT) to improve the Galactic neutron star census. A first aspect is about constrains put on pulsar emission models through detailed studies of individual objects. In the second part, we try to obtain the least-biased population sample possible through varied pulsar searches across different parts of parameter space. All this implies long-term radio pulsar monitoring of gamma-ray pulsar candidates throughout the *Fermi* mission and long search in *Fermi* unidentified sources likely to be hiding yet unknown pulsars. This program is part of an international joint effort between several large radio telescopes as well as X-ray telescopes. For a subset of pulsars being monitored for *Fermi*, the data are also used for accompanying XMM-Newton, AGILE, INTEGRAL, and HESS observations.

A large number of pulsars was detected at high energy with the *Fermi* LAT using radio ephemerides, e.g. Abdo et al. (2009) and Abdo et al. (2013) including a major contribution from Nançay data. Targeted searches for pulsars were conducted in *Fermi* unidentified sources having all the characteristics of a high energy pulsar (no variations and cutoff around a few GeV). More than 50 new MSPs were discovered including 3 from Nançay observations (Cognard et al. 2011; Guillemot et al. 2012), which is already ∼1/4th of all the Galactic Plane MSPs (excluding the MSPs in globular clusters).

3.2 Timing of an array of millisecond pulsars to detect GWs

This program involved a long term high-precision timing campaign on a set of ultra-stable pulsars to search for the signature of gravitational waves. The main target is the Gravitational Wave Background (GWB) coming from the super-massive binary black holes nested in nearby merging galaxies. The up-to-date coherent dedispersion pulsar instrumentation (Fig.1) installed at Nançay is used to time a few dozens of ultra-stable recycled millisecond pulsars. The almost 10 years of Times Of Arrival measurements (ToAs) made on pulsar J1909-3744 at Nançay gives a overview of the stability of the pulsar and of the quality of the instrumentation. ToA uncertainties as low as 10-20ns can be reached as well as an overall rms of ToAs residuals of only ∼90ns rms (Fig.2).

A multi-national european collaboration gathers pulsar astronomers from the five large decimetric European radio telescopes (Jodrell Bank, UK ; Westerbork, NL ; Effelsberg, G ; Cagliari, IT and Nançay, F). This collaboration, called the European Pulsar Timing Array (EPTA, `http://www.epta.eu.org/`), is mainly about coordinating observations, sharing data, common analyses. Two meetings are organized every year since 2006. An even larger organisation exists at the world wide level, the International Pulsar Timing Array (IPTA), gathering the different continental efforts (EPTA for Europe, NanoGrav for North-America and PPTA for Parkes Pulsar Timing Array in Australia).

Characterized by high precision uncertainties (on J1909-3744 for example) together with a high cadence of observations, the Nançay ToAs are dominant in the Gravitational Wave Background limit published two years ago (van Haasteren et al. 2011). Based on 7 datasets for 5 MSPs, among which 4 datasets coming from Nançay, this limit with an amplitude for the characteristic strain of A=6×10^{-15} is still the best published ever. A recent work (see Fig.3 to be put in perspective with Fig.2) confirmed the existence of a non negligible chance of detection in the next few years (Sesana 2013). Finishing his PhD at the LPC2E, Orléans, A.Lassus made an strong contribution for the detection of individuals sources using a bayesian approach.

The Large European Array for Pulsars (LEAP) project is a joint development within the European Pulsar Timing Array (EPTA) collaboration to tie together the five 100 m class telescopes in Europe to make a phased array telescope for high precision pulsar timing. Using specialized software, the simultaneous observations are combined into a telescope with a diameter equivalent to that of a 194 m dish. The increased sensitivity of the phased array telescope allows us to improve pulsar timing accuracy and observe more and fainter pulsars than was presently possible with the telescopes in Europe. A recent observation conducted on pulsar J1713+0747 simultaneously at Effelsberg and Nançay, each characterized by SNR of 1375 et 1450 respectively, ended up with a combined SNR of 2635, almost exactly the sum of the SNRs from individual observations, as expected. Similarly, ToAs uncertainties of 101 and 90ns became 56ns after the combination of the data from the two instruments.

4 Conclusions

Nançay pulsar studies cover a large variety of aspects, from the modelling of radio and gamma-ray emission properties of pulsars to the search for gravitational wave signatures imprinted in the times of arrival of the most stable millisecond pulsars.

The Nançay Radio Observatory is operated by the Paris Observatory, associated with the French Centre National de la Recherche Scientifique (CNRS).

References

Abdo, A. A., Ackermann, M., Ajello, M., et al. 2009, Science, 325, 848
Abdo, A. A., Ajello, M., Allafort, A., et al. 2013, ApJS, 208, 17
Cognard, I. & Backer, D. C. 2004, ApJ, 612, L125
Cognard, I., Bourgois, G., Lestrade, J.-F., et al. 1993, Nature, 366, 320
Cognard, I., Guillemot, L., Johnson, T. J., et al. 2011, ApJ, 732, 47
Guillemot, L., Freire, P. C. C., Cognard, I., et al. 2012, MNRAS, 422, 1294
Lequeux, J., Steinberg, J.-L., & Orchiston, W. 2010, Journal of Astronomical History and Heritage, 13, 29
Ransom, S. M. 2013, in IAU Symposium, Vol. 291, IAU Symposium, 3–10
Sesana, A. 2013, MNRAS, 433, L1
van Haasteren, R., Levin, Y., Janssen, G. H., et al. 2011, MNRAS, 414, 3117

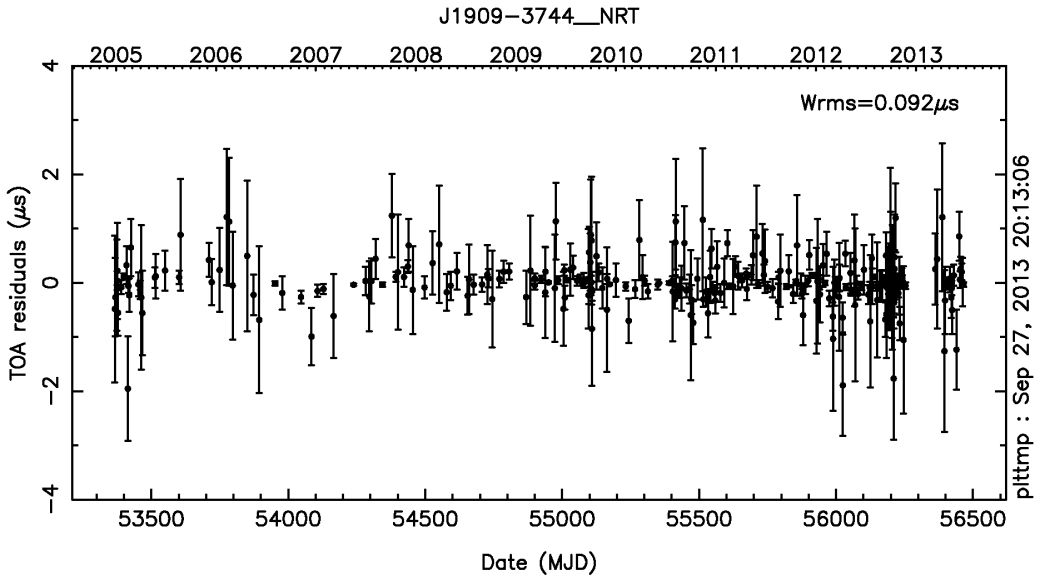

Fig. 2. Times of Arrival residuals obtained for the ultra-stable pulsar J1909-3744 with the Nançay radio telscope. The residuals obtained after substration of all the known propagation and rotational effects are characterized by a weighted rms of only ∼90ns over almost 10 years.

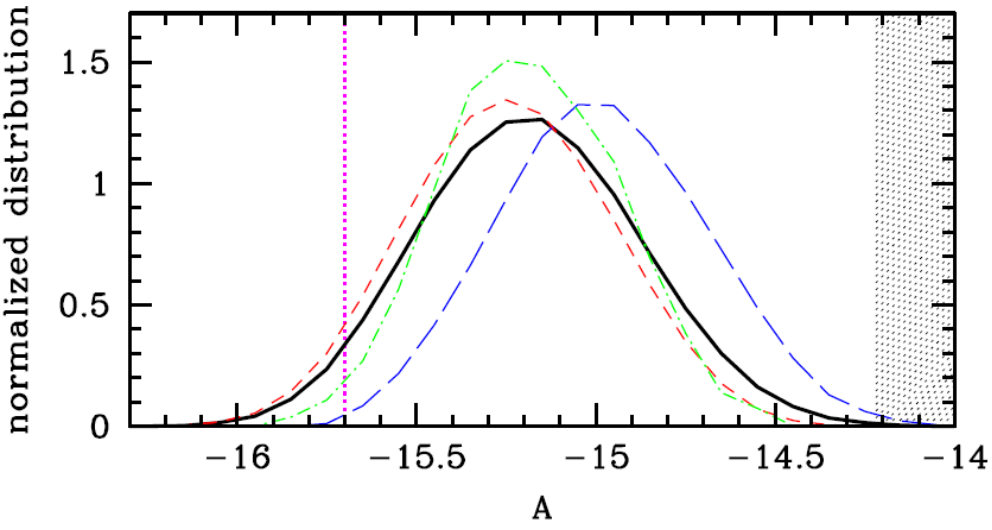

Fig. 3. Normalized distributions of the expected GW amplitude A at a frequency f=1yr^{-1} proposed by Sesana (2013) where the different lines represent different models. The shaded area marks the region excluded by current PTA limits, whereas the vertical solid dotted line represent what can be achieved by timing 20 pulsars at 100ns rms precision for 10 years

SF2A 2013
L. Cambrésy, F. Martins, E. Nuss and A. Palacios (eds)

DETECTION OF THE TSZ EFFECT WITH THE NIKA CAMERA

B. Comis[1], R. Adam[1], A. Adane[2], P. Ade[3], P. André[4], A. Beelen[5], B. Belier[6], A. Benoît[7], A. Bideaud[3], N. Billot[8], O. Bourrion[1], M. Calvo[7], A. Catalano[1], G. Coiffard[2], A. D'Addabbo[7], F.-X. Désert[9], S. Doyle[3], J. Goupy[7], C. Kramer[8], S. Leclercq[2], J.F. Macías-Pérez[1], J. Martino[5], P. Mauskopf[3], F. Mayet[1], A. Monfardini[7], F. Pajot[5], E. Pascale[3], E. Pointecouteau[10,11], N. Ponthieu[9], V. Revéret[4], L. Rodriguez[4], G. Savini [4,12], K. Schuster[2], A. Sievers[8], C. Tucker[3] and R. Zylka[2]

Abstract. We present the first detection of the thermal Sunyaev-Zeldovich (tSZ) effect from a cluster of galaxies performed with a KIDs (Kinetic Inductance Detectors) based instrument. The tSZ effect is a distortion of the black body CMB (Cosmic Microwave Background) spectrum produced by the inverse Compton interaction of CMB photons with the hot electrons of the ionized intra-cluster medium.

The massive, intermediate redshift cluster RX J1347.5-1145 has been observed using *NIKA* (New IRAM KIDs arrays), a dual-band (140 and 240 GHz) mm-wave imaging camera, which exploits two arrays of hundreds of KIDs: the resonant frequencies of the superconducting resonators are shifted by mm-wave photons absorption.

This tSZ cluster observation demonstrates the potential of the next generation *NIKA2* instrument*, being developed for the 30m telescope of IRAM, at Pico Veleta (Spain). *NIKA2* will have 1000 detectors at 140GHz and 2x2000 detectors at 240GHz, providing in that band also a measurement of the linear polarization. *NIKA2* will be commissioned in 2015.

Keywords: Superconducting Detectors, thermal Sunyaev-Zeldovich effect, high resolution observations

1 Introduction

The important role of millimeter wave astronomy for both cosmology and astrophysics is today well established. However, the standard technology for these wavelengths, low-temperature bolometers, requires complex cryogenic readout electronics, which limits the reachable multiplexing ratios well below a hundred. In order to increase the focal plane area and pixel number, an alternative technology intrinsically suited for frequency domain multiplexing, able to provide multiplexing ratios greater than a thousand, looks extremely interesting. It is therefore worth studying and employing Kinetic Inductance Detectors (KIDs) as a promising alternative to bolometers.

[1] Laboratoire de Physique Subatomique et de Cosmologie, Université Joseph Fourier Grenoble 1, CNRS/IN2P3, Institut Polytechnique de Grenoble, 53, rue des Martyrs, Grenoble, France

[2] Institut de RadioAstronomie Millimétrique (IRAM), Grenoble, France

[3] Astronomy Instrumentation Group, University of Cardiff, UK

[4] Laboratoire AIM, CEA/IRFU, CNRS/INSU, Université Paris Diderot, CEA-Saclay, 91191 Gif-Sur-Yvette, France

[5] Institut d'Astrophysique Spatiale (IAS), CNRS and Université Paris Sud, Orsay, France

[6] Institut d'Electronique Fondamentale (IEF), Université Paris Sud, Orsay, France

[7] Institut Néel, CNRS and Université de Grenoble, France

[8] Institut de RadioAstronomie Millimetrique (IRAM), Granada, Spain

[9] Institut de Planétologie et d'Astrophysique de Grenoble (IPAG), CNRS and Université de Grenoble, France

[10] Université de Toulouse; UPS-OMP; IRAP; Toulouse, France

[11] CNRS; IRAP; 9 Av. colonel Roche, BP 44346, F-31028 Toulouse cedex 4, France

[12] University College London, Department of Physics and Astronomy, Gower Street, London WC1E 6BT, UK

*http://ipag.osug.fr/nika2

The New IRAM KIDs Array (*NIKA*) is a dual-band (140 and 240 GHz) KIDs camera developed in Grenoble to work at the IRAM 30m telescope. The first four *NIKA* commissioning campaigns at the IRAM 30 m telescope (Monfardini et al. 2010, 2011; Calvo et al. 2013) have allowed us to demonstrate performances comparable to state-of-the-art bolometer arrays, working at the same wavelengths (e.g. GISMO, Staguhn et al. 2008, observing only at 2 mm).

We report here the first KID-based observation of a galaxy cluster via the thermal Sunyaev-Zeldovich (tSZ) effect, RX J1347.5-1145 has been imaged using the NIKA prototype (Adam & NIKA Collaboration 2013) during the fifth observing run (November 2012, NIKA Collaboration 2013). When observed through the tSZ effect, clusters of galaxies show up as weak extended sources. In fact, this effect is a small spectral distortion (of the order of one-thousandth) of the cosmic microwave background (CMB) intensity, and its detection and mapping have been hard challenges. However, recently, tSZ-selected cluster catalogues containing hundreds of candidates with arcmin resolution have finally been produced (SPT – Reichardt et al. 2013, ACT – Hasselfield & ACT Collaboration 2013 and the Planck Satellite – Planck Collaboration et al. 2013). Consequently, high-resolution tSZ observations and follow-ups are now necessary to deeply explore the cluster internal structure. The NIKA camera at the IRAM 30 m telescope is a well-suited instrument for such observations and follow-ups, given its resolution, its sensitivity and the two observing frequencies.

2 The NIKA camera

Located on Pico Veleta, in a dry and high (2850 m a.s.l.) area, the IRAM 30-m telescope is one of today's largest and most sensitive for mm wavelenghts. In order to completely exploit its angular resolution and the entire field of view, large arrays of (thousands) detectors are needed. For this reason it is worth to develop a camera based on an alternative technology with respect to bolometers, the Kinetic Inductance Detectors. KIDs are superconducting resonators whose resonance frequency changes with the absorbed optical power. The resonant frequencies of the individual resonators can be easily controlled geometrically during array design (Monfardini et al. 2010) and a very large number of pixels, of the order of thousands, can be multiplexed on a single transmission line. Compared to bolometers, KIDs also offer further advantages. They are significantly less sensitive to temperature fluctuations, microphonic noise and magnetic field fluctuations (with respect to Transition Edge Sensor Bolometers).

The New IRAM KIDs Array (*NIKA*) is a dual-band KIDs camera custom designed for the IRAM 30-m Nasmyth-focus telescope, whose detectors are cooled down to $\sim$ 100 mK with a ^{4}He – ^{3}He dilution cryostat. *NIKA*, a prototype of the final camera *NIKA2*, consists of two arrays of Kinetic Inductance Detectors (KIDs) with maximum transmission at about 140 and 240 GHz and respective angular resolutions (FWHM) of 18.5 and 12.5 arcsec and fields of view of 2.0 and 1.2 arcmin. During the test run of November 2012, the 140 GHz band was used with 126 detectors with mean effective sensitivity of 31 mJy.s$^{1/2}$ per beam. Concerning the 240 GHz channel, despite the disfunction of a cold amplifier during this campaign, 91 detectors with mean effective sensitivity of 81 mJy.s$^{1/2}$ per beam where used, recovering the expected mean effective sensitivity of 32 mJy.s$^{1/2}$ per beam by using only eight detectors. More details on the NIKA prototype setup (Run5) can be found in NIKA Collaboration (2013).

3 First tSZ results: mapping of RX J1347.5-1145

Clusters of galaxies are the largest gravitationally bound structures observable in our Universe. They are mainly ($\sim$ 80%) constituted of dark matter, while most of the baryons are in the form of a hot ionized gas, the so-called intra-cluster medium (ICM). The ICM is responsible for the Bremsstrahlung X-ray emission but also for the tSZ effect, a distortion of the black body CMB spectrum produced by the inverse Compton interaction of CMB photons with the hot electrons of the ICM (Sunyaev & Zel'dovich 1972, 1980). This interaction produces a unique spectral signature, a decreased CMB intensity at frequencies lower than $\sim$217 GHz, and an increase at higher frequencies, making the NIKA channels particularly interesting for SZ studies. While the frequency behavior is specific of the effect, the amplitude of the signal is defined by the Comptonization parameter

$$y = \frac{\sigma_{\rm T}}{m_{\rm e}c^2} \int P_{\rm e} dl \tag{3.1}$$

(with m_e the electron rest mass, c the light speed, σ_T the electron Thomson scattering cross-section), which is then a measure of the integrated electronic pressure $P_{\rm e}$ along the line-of-sight, $\vec{l}$.

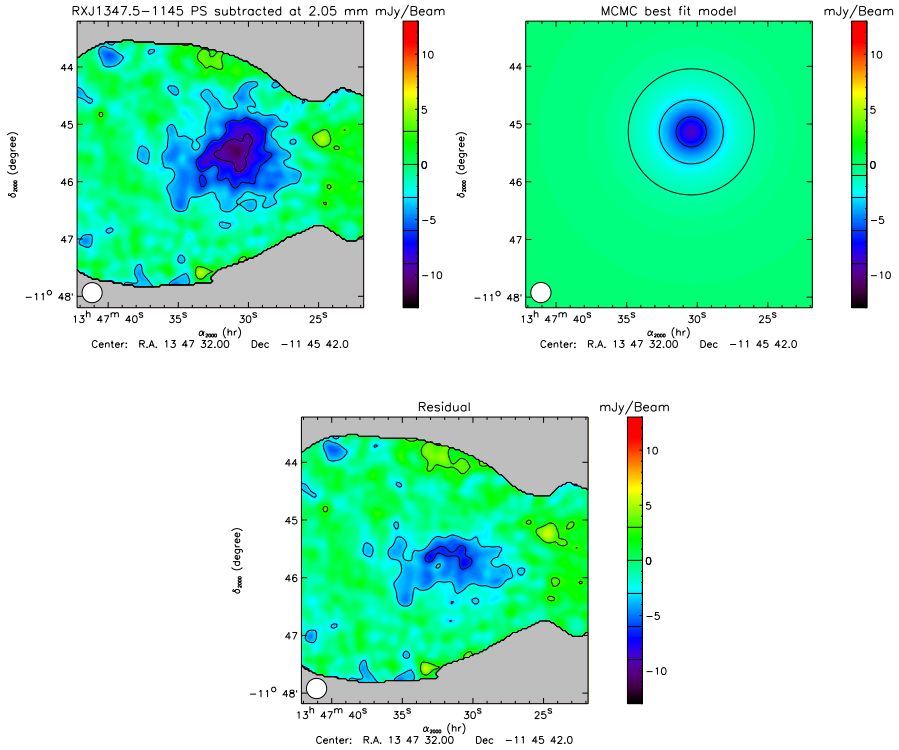

Fig. 1. Upper left: RX J1347.5-1145 reconstructed tSZ map (at 140 GHz), the central radio point source (4.4 mJy) has been subtracted. **Upper right:** Map of the best fitting model for the relaxed cool-core like region, obtained by masking the shock area. **Bottom:** Residuals obtained by subtracting the fitted model to the original map. As expected, the model accounts well for the cluster profile except in the southern shocked area.

RX J1347.5-1145 is one of the most extensively studied clusters. Located at intermediate redshift ($z = 0.451$), it represents a particularly well-suited candidate for the *NIKA* 5^{th} run, being both compact and strong enough for the prototype f.o.v. and sensitivity, as estimated by exploiting the best fitting $P_e(r)$ obtained for the work of Comis et al. (2011) from the X-ray derived pressure profiles of the *ACCEPT* catalogue (Cavagnolo et al. 2009). Furthermore, this cluster is a perfect illustration of the complementarity of tSZ effect and X-ray signals: initially thought to be a well-relaxed (cool-core) object according to its first X-ray data (Schindler et al. 1997), later tSZ observations showed a substructure located at ~ 20" from the center towards the SE region (Komatsu et al. 1999; Pointecouteau et al. 1999). This has been interpreted as a hotter, over-pressured component resulting from a merging event. The non-trivial morphology makes this cluster an ideal target to test *NIKA* capabilities of probing the details of ICM physics.

In Fig. 1 (upper left panel) we report the 140 GHz tSZ map obtained during the *NIKA* 5^{th} run, with a total (unflagged) observing time of 5h 47min (scans of 6min 20s). The analysis used 81 detectors at 140 GHz and 45 at 240 GHz (for the dual-band decorrelation of the atmospheric noise, further details in Adam & NIKA Collaboration 2013).

In order to extract the signal from the shock, produced by the ongoing merger, we have modeled the relaxed region by considering a generalized Navarro, Frenk and White (gNFW, Nagai et al. 2007) pressure profile

$$P(r) = \frac{P_0}{\left(\frac{r}{r_s}\right)^{\gamma}\left[1+\left(\frac{r}{r_s}\right)^{\alpha}\right]^{\frac{\beta-\gamma}{\alpha}}}, \tag{3.2}$$

centered at the X-ray position of the system. P_0 is a scalar normalization of the pressure profile, while the parameters α, β, γ are respectively the slopes for intermediate radii ($r \sim r_s$, a scale radius), the outer region ($r >> r_s$) and the core region ($r << r_s$). The intermediate, outer and inner slopes have been set equal to the cool-core best fitting values of Arnaud et al. (2010), ($\gamma = 0.7736$, $\beta = 5.4905$, $\alpha = 1.2223$). The free parameters

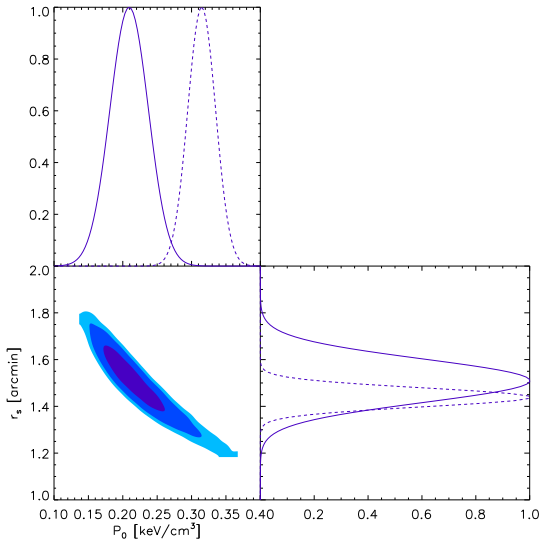

Fig. 2. Posterior likelihood of the MCMC pressure profile fit in the plane $P_0 - r_s$. From dark to light blue, the colors correspond to 68.2%, 95.4% and 99.7% confidence levels. The top and right curves show the marginalized normalized likelihood of P_0 and r_s respectively. The dashed lines allow comparison with the marginalized distribution obtained when no mask is applied to the map.

P_0 and r_s have been constrained through a Markov Chain Monte Carlo (MCMC) approach, masking the South East extension with a half ring, centered on the X-ray peak, with inner and outer radii set to 10 and 80 arcsec. The values obtained are $P_0 = 0.208 \pm 0.028 \pm^{0.052}_{0.032}$ keV/cm^3 and $r_s = 1.510 \pm 0.093 \pm^{0.30}_{0.00}$ arcmin. The systematic uncertainties have been computed using the calibration uncertainty and taking into account bias filtering effects of the analysis estimated from the difference in the input and output simulated profiles (Adam & NIKA Collaboration 2013). Fig. 1 allows comparison between the *NIKA* prototype tSZ map (upper left panel), the best fitting model obtained for the relaxed component (upper right panel), and the residual (bottom panel). The model represents well the northern part of the tSZ map but the southern side cannot be explained without including an overpressure component, that is known to be due to the merging of a sub-cluster (Cohen & Kneib 2002; Allen et al. 2002; Miranda et al. 2008). In Fig. 2 the posterior likelihood of the model parameters is given. Note that in the case of no mask being applied to the map, r_s is still compatible with the value given above (Fig. 2, dashed line).

4 Conclusions

Past NIKA runs have demonstrated the potential for KIDs to provide large pixel arrays for ground-based millimeter astronomy. Now we have also shown the tSZ capabilities of a KIDs-based camera.

The agreement with DIABOLO observations of RX J1347.51145 (Pointecouteau et al. 1999, 2001), performed at the same telescope and with similar resolution and frequency coverage, has been used to validate the *NIKA* tSZ map (Adam & NIKA Collaboration 2013). In addition, the *NIKA* prototype map agrees also with state-of-the-art sub-arcminute resolution tSZ observations, MUSTANG (Korngut et al. 2011, 90 GHz and 8 arcsec resolution) and *CARMA* (Plagge et al. 2012, 30 90 GHz and ∼15 arcsec resolution).

NIKA 5^{th} run has proven that KID arrays are competitive detectors for millimeter wave astronomy and in particular for the observation of galaxy clusters via the tSZ effect. The prototype *NIKA* is now fully operational and will be open to the science community strating from the next Winter (2013/14). The second generation instrument, *NIKA2* (`http://ipag.osug.fr/nika2`), will be made of about 1000 detectors at 140 GHz and 4000 at 240 GHz with a field of view of $\sim$ 6.5 arcmin. With these characteristics, *NIKA2* will be able to provide larger f.o.v., high resolution mapping of clusters. Therefore a perfect instrument for high resolution observations and follow-ups of medium and high redshift cluster. *NIKA2* will be installed for commissioning in 2015.

Acknowledgements: This work has been partially funded by the Foundation Nanoscience Grenoble, the ANR under the contracts MKIDS and NIKA. This work has been partially supported by the LabEx FOCUS ANR-11-LABX- 0013. This work has benefited from the support of the European Research Council Advanced Grant ORISTARS under the European Unions Seventh Framework Programme (Grant Agreement no. 291294). The NIKA dilution cryostat has been designed and built by the Institut Néel Cryogenics Group. In particular, we acknowledge the crucial contributions of Gregory Garde, Henri Rodenas, Jean-Paul Leggeri, Philippe Camus. EP acknowledges the support of grant ANR-11-BS56-015. R. A. would like to thank the ENIGMASS French LabEx for funding this work, B. C. acknowledges support from the CNES post-doctoral fellowship program.

References

Adam, R. & NIKA Collaboration. 2013, in prep.

Allen, S. W., Schmidt, R. W., & Fabian, A. C. 2002, MNRAS, 335, 256

Arnaud, M., Pratt, G. W., Piffaretti, R., et al. 2010, A&A, 517, A92

Calvo, M., Roesch, M., Désert, F.-X., et al. 2013, A&A, 551, L12

Cavagnolo, K. W., Donahue, M., Voit, G. M., & Sun, M. 2009, ApJS, 182, 12

Cohen, J. G. & Kneib, J.-P. 2002, ApJ, 573, 524

Comis, B., de Petris, M., Conte, A., Lamagna, L., & de Gregori, S. 2011, MNRAS, 418, 1089

Hasselfield, M. & ACT Collaboration. 2013, in American Astronomical Society Meeting Abstracts, Vol. 221, American Astronomical Society Meeting Abstracts, 124.05

Komatsu, E., Kitayama, T., Suto, Y., et al. 1999, ApJ, 516, L1

Korngut, P. M., Dicker, S. R., Reese, E. D., et al. 2011, ApJ, 734, 10

Miranda, M., Sereno, M., de Filippis, E., & Paolillo, M. 2008, MNRAS, 385, 511

Monfardini, A., Benoit, A., Bideaud, A., et al. 2011, ApJS, 194, 24

Monfardini, A., Swenson, L. J., Bideaud, A., et al. 2010, A&A, 521, A29

Nagai, D., Vikhlinin, A., & Kravtsov, A. V. 2007, ApJ, 655, 98

NIKA Collaboration. 2013, in prep.

Plagge, T. J., Marrone, D. P., Abdulla, Z., et al. 2012, ArXiv e-prints

Planck Collaboration, Ade, P. A. R., Aghanim, N., et al. 2013, ArXiv e-prints

Pointecouteau, E., Giard, M., Benoit, A., et al. 1999, ApJ, 519, L115

Pointecouteau, E., Giard, M., Benoit, A., et al. 2001, ApJ, 552, 42

Reichardt, C. L., Stalder, B., Bleem, L. E., et al. 2013, ApJ, 763, 127

Schindler, S., Hattori, M., Neumann, D. M., & Boehringer, H. 1997, A&A, 317, 646

Staguhn, J., Allen, C., Benford, D., et al. 2008, Journal of Low Temperature Physics, 151, 709

Sunyaev, R. A. & Zel'dovich, Y. B. 1972, Astrophys. Space Phys. Res., 4, 173

Sunyaev, R. A. & Zel'dovich, Y. B. 1980, ARA&A, 18, 537

SF2A 2013
L. Cambrésy, F. Martins, E. Nuss and A. Palacios (eds)

PLANCK RESULTS - NON GAUSSIANITY CONSTRAINED WITH MINKOWSKI FUNCTIONALS

Anne Ducout[1] and Planck Collaboration

Abstract. We use a morphological tool, the Minkowski Functionals, to constrain non Gaussianity in the Cosmic Microwave Background (CMB) temperature anisotropies measured by the *Planck* satellite. Two types of non Gaussianities are studied, primordial non Gaussianity with the estimate of the 'local' bispectrum parameter $f_{\rm NL}^{\rm local}$, and non Gaussianity induced by cosmic strings, related to the string tension $G\mu/c^2$. We use a Bayesian method to constrain these specific models, on Wiener filtered maps and we account for secondaries and foregrounds using the linear properties of the functionals. We find $f_{\rm NL}^{\rm local} = 4.2 \pm 20.5$ (1σ) consistent with primordial Gaussianity and with bi-spectrum based estimator results. We show no evidence for cosmic strings, with $G\mu/c^2 < 6.0 \times 10^{-7}$ (95% C.L.). Minkowski Functionals prove to be a nice complementary tool to bispectrum estimators in the case of primordial non Gaussianity and an efficient estimator for cosmic strings induced non Gaussianity.

Keywords: Cosmology: Observations, Cosmic Microwave Background, Gaussianity, Methods: Statistical, Numerical

1 Introduction

Non Gaussianity (NG), i.e. any deviation of the CMB anisotropies from the purely Gaussian distribution, is a much powerful probe to constrain fundamental theories and the origin of structure in the universe as it gives access to extreme high energy physics. In particular it could bring new information on the inflation paradigm, and discriminate among simple or more complex mechanisms for the generation of the cosmological perturbations in the early universe (see review in Bartolo et al. 2004). NG could also probe topological defects like cosmic strings, the results of symmetry-breaking phase transitions in the early universe, forming at the end of inflation. They are predicted in supersymmetric and grand unified theories and in higher-dimensional theories for the origin of our universe, such as brane inflation.

Primordial non Gaussianity is easily parametrised when considering the non-linear 'local' coupling parameters $f_{\rm NL}^{\rm local}$, $g_{\rm NL}$, ... which appear in the perturbative development of the *primordial* curvature perturbation around the Gaussian prediction (Okamoto & Hu 2002),

$$\Phi(x) = \phi_{\rm L}(x) + f_{\rm NL}^{\rm local}(\phi_{\rm L}^2(x) - \langle\phi_{\rm L}^2(x)\rangle) + g_{\rm NL}\,\phi_{\rm L}^3(x) + \dots, \tag{1.1}$$

where $\phi_{\rm L}(x)$ is the linear Gaussian part of the Bardeen curvature. We will focus in this paper on constraining the first parameter, $f_{\rm NL}^{\rm local}$. We do not study here the other numerous models to characterize primordial NG, which can be based on theoretical predictions, or which define different triangle shapes for the harmonic transform of the 3-point correlation function – the bi-spectrum.

Estimators of $f_{\rm NL}^{\rm local}$ have been developed using the measure of the bi-spectrum (in particular Komatsu et al. 2005), they have been shown to be optimal estimators as they saturate the Cramér-Rao inequality for a weak non Gaussianity (Babich 2005). On *Planck* data, bi-spectrum based estimators obtained the constraint $f_{\rm NL}^{\rm local} = 2.7 \pm 5.8$ (68 % C.L.) (Planck Collaboration XXIV 2013).

However, alternative statistics to the bi-spectrum exist, that can serve as checks and diagnoses of the results obtained from the bi-spectrum. Indeed, various and numerous systematics and contaminants can bias the results such as inhomogeneous noise, beam asymmetries and foreground residuals, as well as secondary

[1] Institut d'Astrophysique de Paris, CNRS (UMR7095), 98 bis Boulevard Arago, 75014 Paris, France

anisotropies. Most important foreground residuals are induced by our galaxy, but point sources (mostly unresolved radio galaxies), or Cosmic Infrared Background (CIB – mostly unresolved starburst galaxies forming a diffuse background) could as well bias results. Eventually, secondary anisotropies such as integrated Sachs-Wolfe effect (ISW), Sunyaev-Zeldovich effect (SZ) and weak gravitational lensing are all contributing to non Gaussianity. Hence, using different probes is a necessary consistency test, as they will be differently affected by those systematics.

Here we focus on a complete set of morphological tools, the Minkowski Functionals (hereafter MFs) introduced in cosmology by Mecke et al. (1994) and widely used since then as probes of primordial non-Gaussianities (Schmalzing & Buchert 1997; Schmalzing & Gorski 1998; Hikage et al. 2006). For CMB studies, MFs provide a nice complement to the bi-spectrum: they are defined in real space, which makes a robust implementation for MFs in practice much easier than for the bi-spectrum, defined in harmonic space, especially for the mask treatment; MFs are sensitive to the full hierarchy of higher-order correlations, instead of third order only, and can provide additional information on all the non-linear coupling parameters beyond $f_{\rm NL}^{\rm local}$, and on other NG models. However, MFs only probe angular averages of higher order statistics, leaving out the angular dependences, at variance with the bi-spectrum, and can only poorly disentangle between various models of NG.

In this paper, we also studied another source of NG, the cosmic strings. They are defined by an enormous energy per unit length μ and generate a number of observable effects, including gravitational lensing and a background of gravitational waves. Here we shall focus on their non-Gaussian signature, dominantly a second order NG (at the level of the 4-point correlation function, or its equivalent in the harmonic domain, the tri-spectrum). We usually constrain the existence of cosmic strings with the magnitude of the gravitational perturbations they produce on sub-horizon scales: $\frac{G\mu}{c^2} = \left(\frac{\eta}{m_{\rm Pl}}\right)^2$, where η is the energy scale of the string-forming phase transition and $m_{\rm Pl} \equiv \sqrt{\hbar c/G}$ is the Planck mass. Previous NG constraints on this parameter were obtained on *WMAP* data, for example with an analytic trispectrum estimator $G\mu/c^2 < 1.1 \times 10^{-6}$ (95% C.L.) (Fergusson et al. 2010).

This paper is organised as follows. In section 2, we define MFs and the Bayesian method we use to constrain NG models. In section 3, we describe the *Planck* data and its characteristics, while our results are detailed in section 4. Section 5 summarises and discusses the results and future improvements.

2 Minkowski functionals: definitions and method

2.1 Minkowski Functionals on the sphere

Minkowski Functionals of a random field are defined using specific partitions, the excursion sets. For a field $f(x)$ of zero average and variance σ_0^2 on the two-dimensional sphere $\mathbb{S}^2$, an overdense excursion set is defined as

$$\Sigma \equiv \{x \in \mathbb{S}^2 |\, f(x) > \nu\sigma_0\}. \tag{2.1}$$

Its boundary is

$$\partial\Sigma \equiv \{x \in \mathbb{S}^2 |\, f(x) = \nu\sigma_0\}. \tag{2.2}$$

The three MFs on the sphere are then

$$\text{Area} : V_0(\nu) = \frac{1}{4\pi}\int_\Sigma \mathrm{d}\Omega, \qquad \text{Perimeter} : V_1(\nu) = \frac{1}{4\pi}\frac{1}{4}\int_{\partial\Sigma} \mathrm{d}l, \qquad \text{Genus} : V_2(\nu) = \frac{1}{4\pi}\frac{1}{2\pi}\int_{\partial\Sigma} \kappa\,\mathrm{d}l, \tag{2.3}$$

where $\mathrm{d}\Omega$ and $\mathrm{d}l$ are respectively elements of solid angles (surface) and of angle (distance), κ is the geodesic curvature. Note that the Genus can also be expressed as the number of components* in the excursion minus the number of holes in the excursion. We construct a fourth functional – $N_{\rm cluster}$, $V_3(\nu)$, being for $\nu > 0$, the number of components in the excursion. Symmetrically, for $\nu < 0$, it is the number of underdense components (or the number of components in the excursion $\{x \in \mathbb{S}^2 |\, f(x) < \nu\sigma_0\}$).

Analytical expressions for a Gaussian or weakly non Gaussian random field can be derived in terms of ν (see e.g. Vanmarcke 1983; Matsubara 2010). These analytical expressions represent useful descriptions of the MFs as they can be factorized as $V_k(\nu) = A_k v_k(\nu)$, $v_k(\nu)$ being a function of the threshold and A_k a function of only the shape and amplitude of the C_ℓ (see Ducout et al. (2012) for precise definitions). We will use here the normalized – with respect to the C_ℓ – MFs (v_k) to focus on the non Gaussian deviations.

*A component is a connected subset of the excursion.

2.2 Bayesian estimation of specific non Gaussian models

While MFs are sensitive to any departure from the Gaussian statistics, and are used as a generic test for non Gaussianity in *Planck* (Planck Collaboration XXIII 2013), they can also be used to constrain specific models of NG, using a Bayesian approach. The method is described in Ducout et al. (2012) for the estimate of $f_{\rm NL}^{\rm local}$, but it can quite similarly be applied for the string tension measure $G\mu/c^2$. The aim is to compare the normalised functionals v_k measurements on the data to "theoretical" predictions of these functionals for different models and amplitudes of non Gaussianity in order to obtain their posterior distribution.

We measure v_k over an ensemble of $n_{\rm th} = 26$ threshold values ν_i between $\pm\nu_{\rm max} = \pm 3.5$, defining a vector $\hat{v}_k \equiv \{\hat{v}_k(\nu_1), \cdots, \hat{v}_k(\nu_{n_{\rm th}})\}$ for each functional. We combine the 4 functionals into one vector of $4 \times n_{\rm th}$ elements, $\hat{y} = \{\hat{v}_i, \hat{v}_j, \cdots\}$.

For a given NG model parametrised by an amplitude f (hence here, $f_{\rm NL}^{\rm local}$ or $G\mu/c^2$) the Bayes formula is

$$P(f|\,\hat{y}) = \frac{P(\hat{y}\,|f)P(f)}{\int P(\hat{y}\,|f)P(f)\mathrm{d}f}. \tag{2.4}$$

We shall take a flat prior for the parameter f, with $P(f)$ being a constant over a reasonable range of values for f, mostly determined from previous experiments ($f_{\rm NL}^{\rm local}$ between -100 and +100 and $G\mu/c^2$ between 0 and 1e-6). The evidence $\int P(\hat{y}\,|f)P(f)\mathrm{d}f$ is being considered as a normalisation factor.

The likelihood $P(\hat{y}\,|f)$ is a multivariate Gaussian, this allows us to define a simple χ^2 test for f and the posterior becomes

$$P(f|\,\hat{y}) \propto \exp\left[-\frac{\chi^2(\hat{y},f)}{2}\right] \qquad \text{with} \qquad \chi^2(\hat{y},f) \equiv [\hat{y} - \bar{y}(f)]^T\, C^{-1}\, [\hat{y} - \bar{y}(f)] \tag{2.5}$$

where $\bar{y}(f)$ is the model under test.

This model is constructed with direct measurements on realistic simulations of the data, integrating beam effects, inhomogeneous noise, component separation weighting and masks. For $f_{\rm NL}^{\rm local}$, the NG simulations are described in Elsner & Wandelt (2009), 1000 simulations were available for the Gaussian and non Gaussian parts of the CMB, based on *WMAP7*[†] best-fit power spectrum (Komatsu et al. 2011). For the string tension, only 2 string maps were available (Ringeval & Bouchet 2012), the simulations hence consisted mostly in the variation of the *Gaussian*[‡] part of the CMB. So $\bar{y}(f) \equiv \langle\hat{y}(f)\rangle$ is the mean of y measured over $m_{_f}$ simulated maps with a given level of non-Gaussianity f.

Since the considered level of non-Gaussianity is weak, one can compute the covariance matrix C in a Monte-Carlo fashion relying on 10^4 *Gaussian* simulated maps of the CMB (to which we add, when relevant, beam effects, noise, masks).

With those properties, the posterior probability distribution function $P(f_{\rm NL}^{\rm local}|\,\hat{y})$ is expected to be very close to a Gaussian. Indeed, in the weakly non Gaussian regime, $\bar{y}_i(f_{\rm NL}^{\rm local})$ is, at first order, a linear function of $f_{\rm NL}^{\rm local}$. For the string tension posterior however, this is not the case, the posterior has a far more complex shape, as $\bar{y}_i(G\mu/c^2)$ is a more complicated function of $G\mu/c^2$.

3 Planck data, systematics, foregrounds, secondaries and simulations

The *Planck*[§] mission (Planck Collaboration I 2013), has been designed to measure the Cosmic Microwave Background temperature anisotropies with unprecedented sensitivity and resolution over the whole sky. Sensitivity is not limited by noise but by the capacity to remove foregrounds, in particular the Galactic signal from the CMB one. In this paper, we report results obtained on *Planck* nominal data, acquired between 12 August 2009 and 27 November 2010 (Planck Collaboration XXIV 2013; Planck Collaboration XXV 2013).

The pixelisation scheme adopted for *Planck* processed maps is HEALPix[¶] (Górski et al. 2005). Maps were used at $N_{\rm side} = 1024$ for primordial NG constraints and at $N_{\rm side} = 2048$ for cosmic strings, restraining $\ell_{\rm max}$ to 2000 in both cases. We applied a Wiener filter to the map ($W_{\rm M}$).

[†]The bias due to the difference between *Planck* and *WMAP* power spectra is accounted for, at a level of $\Delta f_{\rm NL}^{\rm local} \sim 3$.
[‡]The lensed – hence non Gaussian – CMB was varied in fact.
[§]`http://www.esa.int/Planck`
[¶]Available at http://healpix.jpl.nasa.gov

Table 1. $f_{\rm NL}^{\rm local}$ estimates obtained with MFs on *Planck* `SMICA` map. Foreground and secondaries effects are evaluated in terms of $f_{\rm NL}^{\rm local}$.

	$f_{\rm NL}^{\rm local}$	Source	Corresponding $\Delta f_{\rm NL}^{\rm local}$
Lensed raw map	19.1 ± 19.3		–
Lensing subtracted	8.5 ± 20.5	Lensing	+10.6
Lensing+**PS subtracted**	7.7 ± 20.3	Point sources	+0.8
Lensing+**CIB subtracted**	7.5 ± 20.5	CIB	+1.0
Lensing+**SZ subtracted**	6.0 ± 20.4	SZ	+2.5
All subtracted	4.2 ± 20.5	All	+14.9

Several component separation methods (Leach et al. 2008) have been used to remove the Galaxy from cosmological data, we report here the results obtained with `SMICA`, the results obtained on different methods being globally consistent. Galactic residuals and radio point sources were taken into account by the use of the U73 mask ($f_{\rm sky} = 73\%$ of the sky is unmasked). The smallest point sources holes were inpainted.

Additionally, we estimated the average impact of some residual foregrounds and secondaries (FG) using the linear properties of MFs (Ducout et al. 2012) and foregrounds models processed through the *Planck* simulation pipeline (FFP6 simulations, see Planck Collaboration ES (2013)). Point sources (PS), CIB and SZ clusters[‖] signals can be introduced as a simple additive bias $\Delta\bar{y}^{\rm PS,\cdots}$ on MF curves, measured on simulations, following:

$$\hat{y} = \hat{y}^{\rm FGsubtracted} + \Delta\bar{y}^{\rm PS} + \Delta\bar{y}^{\rm CIB} + \Delta\bar{y}^{\rm SZ}. \tag{3.1}$$

Finally, the lensing by the large scale structures of the Universe was accounted for, as it has an important NG contribution. This lensing contribution was based on *Planck* measurement of the lensing, using simulations (FFP6 simulations). In the case of $f_{\rm NL}^{\rm local}$, we just evaluated it as another additive bias in our data $\hat{y}$, verifying that MFs are linear with the lensing at first order and that primordial non-Gaussianity and lensing contributions are additive. In the case of the string constraints, it was easier to directly include the lensing contribution in the model $\bar{y}(G\mu/c^2)$.

4 Results

4.1 *Primordial NG* - $f_{\rm NL}^{\rm local}$

Results are summarized in Table 4.1 and Minkowski functionals curves are showed on Fig. 1, without including the lensing subtraction ("Lensed curves"). The constraints obtained are consistent with bispectrum-based estimators results, even if we do not include FG contributions, taking into account a larger error bar. Moreover, results are quite robust against Galactic residuals: constraints obtained on other component separation methods (`NILC` and `SEVEM`), with different sky coverages, fairly agreed within a maximum $\Delta f_{\rm NL}^{\rm local} = 1$.

This consistency between different estimators, different component separation methods, masks, assess for the robustness of these results.

4.2 *Cosmic strings tension* - $G\mu/c^2$

Due to the non linearity of MFs with $G\mu/c^2$ and the small number of string simulations, the posterior distribution is quite complex and noisy (see Fig. 2), we then evaluated the posterior at $n_{\rm NL} = 51$ values of $G\mu/c^2$, between 0 and 10×10^{-7}, to obtain the estimate $\hat{G\mu/c^2}$. This estimation is stable and have been validated in realistic conditions with the *Planck* String Challenges described in Planck Collaboration XXV (2013). We eventually integrated the posterior to report credible intervals. Results are summarized in Table 2, for raw data (lensing subtracted) and foreground subtracted data (PS, CIB and SZ subtracted).

[‖]The SZ signal does not include the SZ×lensing NG contribution.

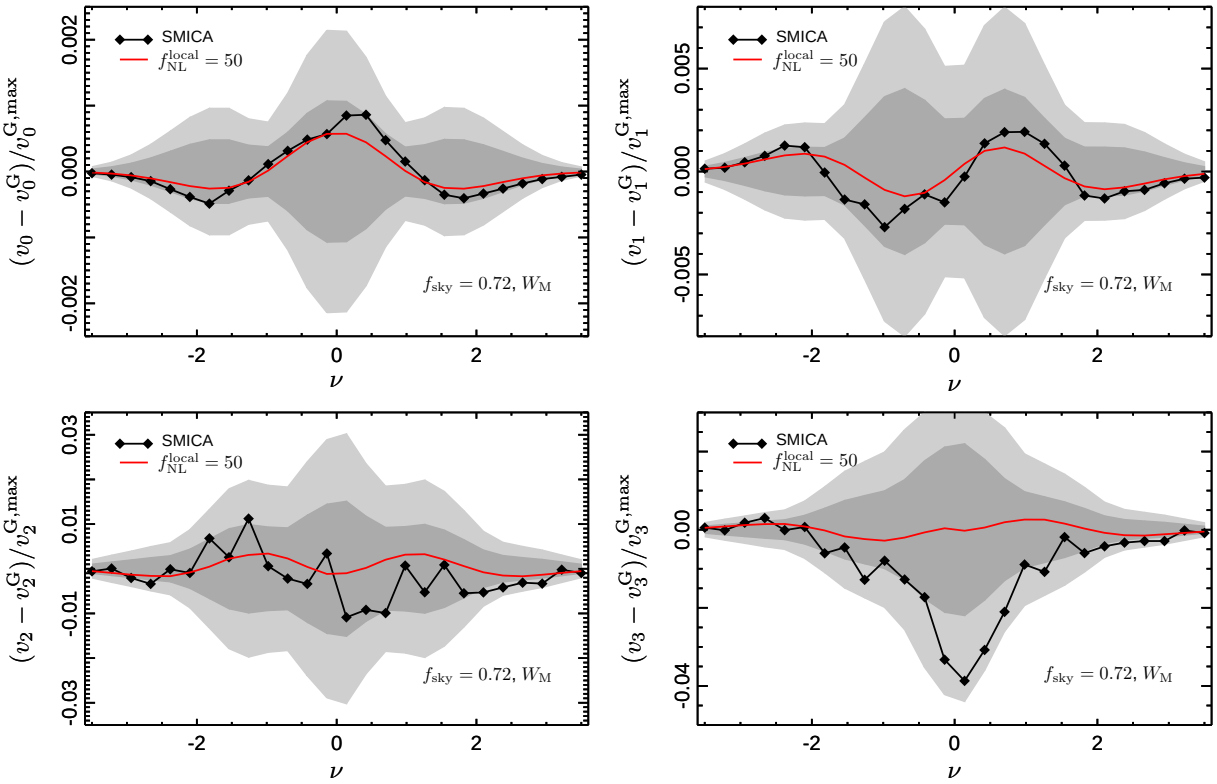

Fig. 1. The 4 Minkowski functionals curves measured on `SMICA` map. The curves are the difference of each normalized MF measured on the data to the averaged measure made on Gaussian *Planck* realistic simulations (not lensed). The difference curves are normalized by the maximum of the Gaussian curve. To compare the curves to the presence of primordial NG, the average difference curves for non Gaussian simulations with $f_{\rm NL}^{\rm local} = 50$ is also represented.

Table 2. MFs constraints obtained on $G\mu/c^2$, at the 95% C.I. The "Raw map" result includes only the lensing contribution to the data, while the "Foreground subtracted map" includes the lensing, Poissonian point sources, CIB and SZ clusters contributions.

	Raw map (lensing accounted for)	With FG correction
$G\mu/c^2$	$< 6.8 \times 10^{-7}$	$< 6.0 \times 10^{-7}$

5 Conclusions and perspectives

In this paper we have reported constraints on primordial NG $f_{\rm NL}^{\rm local}$ parameter and cosmic strings tension $G\mu/c^2$, obtained with Minkowski Functionals on *Planck* nominal data. Many biases have been considered, in particular foreground residuals and secondaries, as they can be easily handled with MFs.

For local primordial NG, MFs find $f_{\rm NL}^{\rm local} = 4.2 \pm 20.5$ (1σ), this confirms the results obtained with the optimal estimators (bispectrum) and assess for its robustness. Moreover using optimal filtering (enhancing information from the gradient of the map) and full mission data, the error bar should decrease by a factor of two.

For the string tension, MFs find $G\mu/c^2 < 6.0 \times 10^{-7}$, the most stringent constraint from NG estimators applied on *Planck* data at this moment. However, one important caveat is the small number of string simulations used to calibrate the estimator. The estimator being mostly sensitive to low-redshift strings (infinite strings, with redshifts between 0 and 30), it is here limited by cosmic variance. As low-redshift strings simulations are faster to produce than complete simulations, the robustness of this result should be assessed very soon.

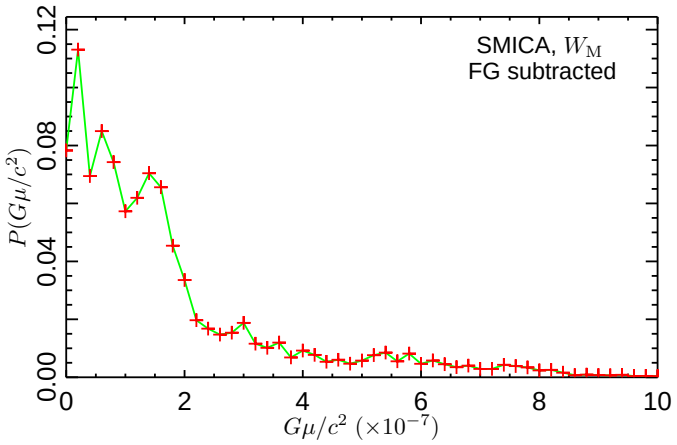

Fig. 2. Posterior distribution of the parameter $G\mu/c^2$ obtained with Minkowski functionals, on `SMICA` map, with a correction for foregrounds.

References

Babich, D. 2005, Phys. Rev. D, 72, 043003
Bartolo, N., Komatsu, E., Matarrese, S., & Riotto, A. 2004, Phys. Rep., 402, 103
Ducout, A., Bouchet, F. R., Colombi, S., Pogosyan, D., & Prunet, S. 2012, MNRAS, 423
Elsner, F. & Wandelt, B. D. 2009, ApJS, 184, 264
Fergusson, J., Regan, D., & Shellard, E. 2010, ArXiv e-prints
Górski, K. M., Hivon, E., Banday, A. J., et al. 2005, ApJ, 622, 759
Hikage, C., Komatsu, E., & Matsubara, T. 2006, ApJ, 653, 11
Komatsu, E., Smith, K. M., Dunkley, J., et al. 2011, ApJS, 192, 18
Komatsu, E., Spergel, D. N., & Wandelt, B. D. 2005, ApJ, 634, 14
Leach, S. M., Cardoso, J.-F., Baccigalupi, C., et al. 2008, A&A, 491, 597
Matsubara, T. 2010, Phys. Rev. D, 81, 083505
Mecke, K. R., Buchert, T., & Wagner, H. 1994, A&A, 288, 697
Okamoto, T. & Hu, W. 2002, Phys. Rev. D, 66, 063008
Planck Collaboration ES. 2013, The Explanatory Supplement to the Planck 2013 results (ESA)
Planck Collaboration I. 2013, Submitted to A&A
Planck Collaboration XXIII. 2013, Submitted to A&A
Planck Collaboration XXIV. 2013, Submitted to A&A
Planck Collaboration XXV. 2013, Submitted to A&A
Ringeval, C. & Bouchet, F. R. 2012, Phys.Rev., D86, 023513
Schmalzing, J. & Buchert, T. 1997, ApJ, 482, L1
Schmalzing, J. & Gorski, K. M. 1998, MNRAS, 297, 355
Vanmarcke, E. 1983, Random Fields (Vanmarcke, E.)

SF2A 2013
L. Cambrésy, F. Martins, E. Nuss and A. Palacios (eds)

STAR FORMATION EFFICIENCY AT HIGH Z AND SUBGALACTIC SCALES

J. Freundlich[1], F. Combes[1], L. J. Tacconi[2], M. C. Cooper[3], R. Genzel[2,4,5], R. Neri[6] and the PHIBSS consortium

Abstract. Massive galaxies in the distant Universe form stars at much higher rates than their local counterparts. Although direct resolution of the star forming regions of these galaxies is still a challenge, recent molecular gas observations at the IRAM Plateau de Bure interferometer enable us to study the star formation efficiency at sub-galactic scales around z = 1.2. We present a method to obtain the gas and star formation rate (SFR) surface densities of ensembles of clumps within galaxies at this redshift, and derive a spatially resolved Kennicutt-Schmidt (KS) relation at a scale of about 8.5 kpc. This method is based on the identification of these structures in position-velocity diagrams corresponding to slices within the galaxies, even though the corresponding scales are not resolved. The data globally indicates an average depletion time of 1.9 Gyr, but with significant variations from point to point within the galaxies.

Keywords: galaxies: evolution, galaxies: high redshift, galaxies: ISM, galaxies: starburst

1 Introduction

Our Milky Way only forms a few stars per year, similar to most nearby spiral galaxies. But ten billion years ago, between redshifts 1 and 3, observed galaxies formed their stars at rates up to ten times higher (Noeske et al. 2007, Daddi et al. 2007). Stars are formed from cold gas clouds which collapse due to their self gravity. A high star formation rate (SFR) thus means a significant gas supply, either brought by major mergers or by continuous processes, for example through filaments of the cosmic web (Kereš et al. 2005, Dekel et al. 2009). Observations show that high redshift galaxies are indeed more gas-rich than their low redshift counterparts, their gas fraction being as high as 30-40% (Tacconi et al. 2010, 2013). This could explain on its own the high SFR, but the star formation processes could also be more efficient, and we would like to characterize them at their relevant sub-galactic scales. High redshift galaxies do not resemble our Galaxy or the galaxies in our neighborhood, as their disk is fragmented to a number of giant molecular clouds, or clumps, where most of the star formation occurs. These structures have sizes of about 1 kpc, masses up to 10^9 $M_\odot$, and contribute 10-25% of the galaxy luminosity (Förster Schreiber et al. 2011). Are the star formation processes qualitatively different in high redshifts clumps than in their low redshift counterparts ?

As stars are formed from cold molecular gas, the SFR density should significantly depend on the gas density. The relationship between the two quantities describes the star formation efficiency, and has often been written as a simple power law (Schmidt 1959, Kennicutt 1998a). We would like to obtain a corresponding Kennicutt-Schmidt (KS) relation for clumps or ensembles of clumps of high redshift galaxies, and compare it to similar observations at low redshift (e.g. Bigiel et al. 2011). Genzel et al. (2010) and Tacconi et al. (2010) study the global properties of galaxies at z=1.2, and we select four galaxies out of their PHIBSS sample (Tacconi et al. 2010). These galaxies are not experiencing major mergers and are typical z=1.2 massive star-forming galaxies,

[1] LERMA, Observatoire de Paris, CNRS, 61 av. de l'Observatoire, 75014 Paris, France
[2] Max-Planck-Institute für extraterrestrische Physik (MPE), Giessenbachstrasse 1, 85748 Garching, Germany
[3] Dept. of Physics & Astronomy, Frederick Reines Hall, University of California, Irvine, CA 92697, USA
[4] Dept. of Physics, Le Conte Hall, University of California, CA 94720 Berkeley, USA
[5] Dept. of Astronomy, Campbell Hall, University of California, CA 94720 Berkeley, USA
[6] IRAM, 300 rue de la Piscine, 38406 St. Martin d'Heres, Grenoble, France

with stellar masses above 3×10^{10} $M_\odot$. High resolution CO observations with the IRAM Plateau de Bure interferometer and Keck DEEP2 spectra enable us to fathom star formation processes at scales lower than the galaxy size. We first determine the total mass of gas and the global SFR of the selected galaxies, then isolate sub-structures through position-velocity diagrams, and finally plot a KS diagram at their sub-galactic scale. More details can be found in Freundlich et al. (2013).

2 Determining global properties of galaxies at z=1.2

2.1 Determination of the total mass of gas

The IRAM Plateau de Bure interferometer is able to observe the CO molecular gas of high redshift galaxies, from which we can determine their total mass of gas. We assume that the CO(3-2) rotational line luminosity is directly proportional to the total mass of gas, and we use a Milky Way like conversion factor $\alpha = 8.7$ between the two (Tacconi et al. 2010):

$$\left(\frac{M_{gas}}{M_\odot}\right) = \alpha \left(\frac{L_{CO(3-2)}}{\mathrm{K\ km\ s^{-1} pc^2}}\right)$$

More precisely, we use a conversion factor of 3.2 between the H_2 mass and the CO(1-0) luminosity, assume a factor 2 for the CO(3-2)/CO(1-0) luminosity ratio, and further correct by a factor 1.36 to account for interstellar helium. The spatial resolution attained by the IRAM Plateau de Bure interferometer is around $1''$; about 8.5 kpc at z=1.2.

2.2 Determination of the global SFR

The Hα recombination line is the most direct and reliable tracer of young massive stars, and thus of the SFR (Kennicutt 1998b). But for z=1.2 galaxies, this line lies in the middle of a low atmospheric transmission band, so ground based spectroscopy is impossible for our set of galaxies, and we have to use different methods to determine the SFR.

We notably estimate the SFR from the collisionally excited [OII] line, using DEEP2 spectra. Even though the [OII] line luminosity is not directly coupled to the ionizing luminosity, it is possible to establish it empirically as a quantitative SFR tracer (Kennicutt 1998b, Kewley et al. 2004):

$$\left(\frac{\mathrm{SFR}}{M_\odot\ \mathrm{yr}^{-1}}\right) \simeq 3.5\ 10^{-8}\ \left(\frac{L_{[OII]}}{L_\odot}\right)$$

The Keck DEEP2 spectra are calibrated with CFHT photometric data and have a spatial resolution comprised between 0.6 and $1.0''$. Dust extinction is determined from spectral energy distributions (SED) obtained by `kcorrect` from CFHT photometric data (Blanton & Roweiss 2007).

Other methods to determine the SFR include an empirical [OII] calibration in terms of B-band luminosity (Moustakas et al. 2006) and a combined UV and IR calibration (Wuyts et al. 2011, Tacconi et al. 2013). The former method is assumed to remove on average the systematic effects of reddening and metallicity and to reduce the scatter in the resulting SFR values, whereas the latter method is expected to be the most reliable in the absence of Hα measurements. Indeed, UV light directly traces unobscured star formation and IR 24 μm emission originates in small dust grains heated by the UV photons, the combination of the two thus tracing unobscured and obscured star formation at the same time. The SFR values obtained with the three methods differ up to 3σ, which shows how the SFR calibration is an important source of uncertainties.

3 Star formation at sub-galactic scales

The kpc-sized clumps of high redshift galaxies are smoothed out at DEEP2 and IRAM resolutions, but spectroscopy helps separate different components, thanks to their kinematics. DEEP2 spectra indeed correspond to position-velocity diagrams (PV diagrams) along the galaxy major axis (Davis et al. 2007), and we are able to separate smoothed ensembles of clumps along the velocity axis. The size of these substructures corresponds to the angular resolution available in both CO and [OII] spectroscopy; i.e., 1-1.5$''$, or about 8.5 kpc at z=1.2. Figure 1 compares the [OII] PV diagram with the corresponding slice in IRAM CO(3-2) data for one of the four galaxies (named EGS13004291 in the AEGIS terminology). The white horizontal lines show the boundaries

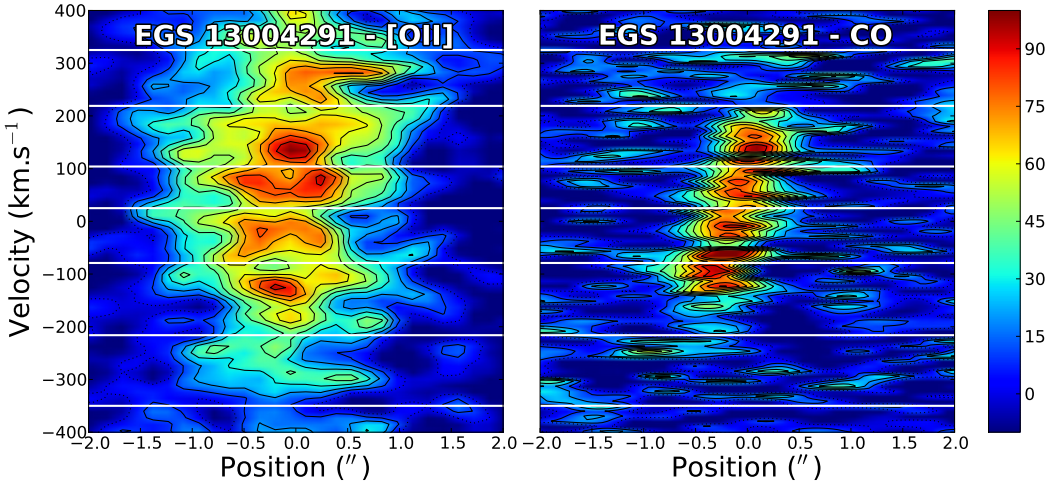

Fig. 1. [OII] and CO line luminosities of one galaxy of our sample (EGS13004291) in position-velocity planes corresponding to the DEEP2 slit. Smoothed ensembles of clumps are separated by eye along the vertical axis, as shown with the white horizontal lines. One arc second corresponds approximately to 8.5 kpc.

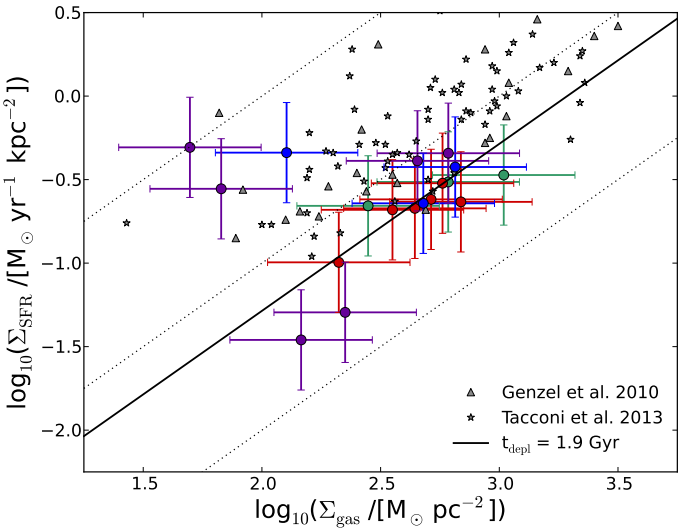

Fig. 2. Kennicutt-Schmidt diagram for 1″ ensembles of clumps of four galaxies at z=1.2, using the Kewley et al. (2004) [OII] SFR calibration. The dotted diagonal lines correspond to constant gas depletion times of 0.1, 1, and 10 Gyr from top to bottom, and the solid black line to a constant depletion time equal to the mean depletion time of the ensembles of clumps, t_{depl} = 1.9 Gyr. The gray data points from Genzel et al. (2010) and Tacconi et al. (2013) are indicated for comparison with whole galaxies.

between the different substructures, determined by eye. We assume that the mass of gas and the SFR of each ensemble of clumps are respectively proportional to the integrated luminosity in the CO and [OII] PV diagrams, so we can deduce the mass and SFR surface densities averaged over areas of about 1″ in diameter.

The mean depletion time ($t_{depl} = M_{gas}/SFR$) for these ensembles of clumps is equal to 1.9±0.3 Gyr, which is comparable to low redshift observational results (Kennicutt 1998b, Genzel et al. 2010, Saintonge et al. 2011, Tacconi et al. 2013, Bigiel et al. 2008, 2011). Figure 2 displays the corresponding resolved KS diagram. The data points scatter around the line of constant depletion time equal to 1.9 Gyr, but there are significant variations from point to point within the galaxies. This suggests that the star formation scaling laws could be different from one ensemble of clumps to the next within a galaxy, even if the scatter is comparable to the ∼0.3 dex observed for resolved local galaxies (Bigiel et al. 2008, 2011).

The main uncertainties come from the SFR calibration, the determination of the extinction and from the conversion factors used to convert the CO luminosity in a mass of gas. These latter quantities are also expected to vary within a single galaxy, and thus influence the slope of the KS relation (Koda et al. 2012, Genzel et al. 2013). Although the three methods to determine the SFR give very different values, it does not affect much the final shape of the KS relation.

4 Conclusion

We have shown that various ensembles of clumps could be separated by their kinematics in PV diagrams, even though the corresponding scales were not resolved. We are able to draw a KS relation for these ensembles of clumps in four galaxies, and our sample is compatible with a constant depletion time of 1.9 Gyr. This adds to the growing evidence that the star formation scaling laws, and thus the star formation processes, are not significantly different at high redshift than in the local Universe. Nevertheless, this method should be applied to a more significant sample of high redshift galaxies to obtain more statistically robust results, notably within the upcoming IRAM PHIBSS2 Legacy Program.

References

Bigiel, F., Leroy, A., Walter, F., et al. 2008, ApJ, 136, 2846
Bigiel, F., Leroy, A., Walter, F., et al. 2011, ApJ, 730, L13
Blanton, M. R., & Roweis, S. 2007, ApJ, 133, 734
Daddi, E., Dickinson, M., Morrison, G., et al. 2007, ApJ, 670, 156
Davis, M., Guhathakurta, P., Konidaris, N. P., et al. 2007, ApJ, 660, L1
Dekel, A., Birnboim, Y., Engel, G., et al. 2009, Nature, 457, 451D
Förster Schreiber, N. M., Shapley, A. E., Genzel, R., et al. 2011, ApJ, 739, 45F
Freundlich, J., Combes, F., Tacconi, L. J., et al. 2013, A&A, 553, A130
Genzel, R., Tacconi, L. J., Gracia-Carpio, J., et al. 2010, MNRAS, 407, 2091
Genzel, R., Tacconi, L. J., Kurk, J., et al. 2013, ApJ, 773, 68G
Kennicutt, R. C. Jr. 1998a, ApJ, 498, 541
Kennicutt, R. C. Jr., 1998b ARA&A, 36, 189
Kereš, D., Katz, N., Weinberg, D. H., & Davé, R. 2005, MNRAS, 363, 2K
Kewley, L. J., Geller, M. J., & Jansen, R. A. 2004, ApJ, 127, 2002
Koda, J., Scoville, N., Hasegawa, T., et al. 2012, ApJ, 761, 41K
Moustakas, J., Kennicutt, R. C., & Tremonti, C. 2006, ApJ, 642, 775M
Noeske, K. G., Weiner, B. J., Faber, S., et al. 2007, ApJ, 660, L43
Saintonge, A., Kauffmann, G., Wang, J., et al. 2011, MNRAS, 415, 61S
Schmidt, M. 1959, ApJ, 129, 243S
Tacconi, L. J., Genzel, R., Neri, R., et al. 2010, Nature, 463, 781T
Tacconi, L. J., Neri, R., Genzel, R., et al. 2013, ApJ, 768, 74T
Wuyts, S., Förster Schreiber, N. M., van der Wel, A., et al. 2011, ApJ, 742, 96W

SF2A 2013
L. Cambrésy, F. Martins, E. Nuss and A. Palacios (eds)

MODELLING THE RELATIVE VELOCITIES OF ISOLATED PAIRS OF GALAXIES

V. Gonzalez-Perez[1], E. Jennings[2], M.-C. Cousinou[1], S. Escoffier[1], A. Tilquin[1] and A. Ealet[1]

Abstract. We study the comoving relative velocities, v_{12}, of model isolated galaxy pairs at $z = 0.5$. For this purpose, we use the predictions from the GALFORM semi-analytical model of galaxy formation and evolution based on a Λ cold dark matter cosmology consistent with the results from WMAP7. In real space, we find that isolated pairs of galaxies are predicted to form an angle t with the line-of-sight that is uniformly distributed as expected if the Universe is homogeneous and isotropic. We also find that isolated pairs of galaxies separated by a comoving distance between 1 and 3 h^{-1}Mpc are predicted to have $\langle v_{12} \rangle \sim 0$. For galaxies in this regime, the distribution of the angle t is predicted to change minimally from real to redshift space, with a change smaller than 5% in $\langle \sin^2 t \rangle$. However, the distances defining the *comoving regime* strongly depend on the applied isolation criteria.

Keywords: galaxies, semi-analytical models, cosmology

1 Introduction

The observed expansion of the Universe is attributed to a dark energy component of which little is known (e.g. Blake et al. 2011; Anderson et al. 2012). Marinoni & Buzzi (2010) (MB) derived a geometrical test on isolated pairs of galaxies that can provide an independent investigation of the abundance and nature of the dark energy. The idea of this test is to measure the relative angle, t, that isolated pairs of galaxies form with the line-of-sight (LOS). The pairs of galaxies can be thought off as dumbbells. In a homogeneous and isotropic universe, the orientation of these dumbbells in the sky will be uniformly distributed and thus, will have a probability distribution of the form $\sin t/2$. Thus, measuring the probability distribution of the angle t can put constraints on the cosmological parameters, in particular, on the characteristics of the dark energy (Alcock & Paczynski 1979; Phillipps 1994). However, galaxies are affected by local gravitational pulls which are separate to the effect of dark energy and MB developed a test taking these into account. Here, we study the average relative comoving velocities, $\langle v_{12} \rangle$, of pairs of galaxies at $z = 0.5$ drawn from a semi-analytical model of the formation and evolution of galaxies. We use the predicted average $\langle v_{12} \rangle$ to split the model galaxies into different velocity regimes in order to check the principles upon which the MB test is based.

2 The galaxy formation model

Galaxies are thought to form within haloes of dark matter, whose gravity allows the galaxies to exist. The formation and evolution of galaxies is affected by a multitude of other processes besides gravity and computational modelling is the only way we can attempt to understand all these processes. For this study we use the GALFORM semi-analytical model (Cole et al. 2000). Semi-analytical models use simple, physically motivated equations to follow the fate of baryons in a universe in which structure grows hierarchically through gravitational instability (see Baugh 2006). In particular, we use the Gonzalez-Perez et al. (2013) model, which exploits a Millennium Simulation class N-body run performed with the WMAP7 cosmology (Komatsu et al. 2011): matter density, $\Omega_{\rm m0} = 0.272$, cosmological constant, $\Omega_{\Lambda 0} = 0.728$, baryon density, $\Omega_{\rm b0} = 0.045$, a normalisation of density fluctuations given by $\sigma_8 = 0.807$ and a Hubble constant today of $H_0 = 100\,h$ km s^{-1}Mpc^{-1}, with $h = 0.704$.

[1] Centre de Physique des Particules de Marseille, Aix-Marseille Université, CNRS/IN2P3, Marseille, France.
[2] The Kavli Institute for Cosmological Physics, University of Chicago, 5640 South Ellis Avenue, Chicago, IL 60637, USA; The Enrico Fermi Institute, University of Chicago, 5640 South Ellis Avenue, Chicago, IL 60637, USA

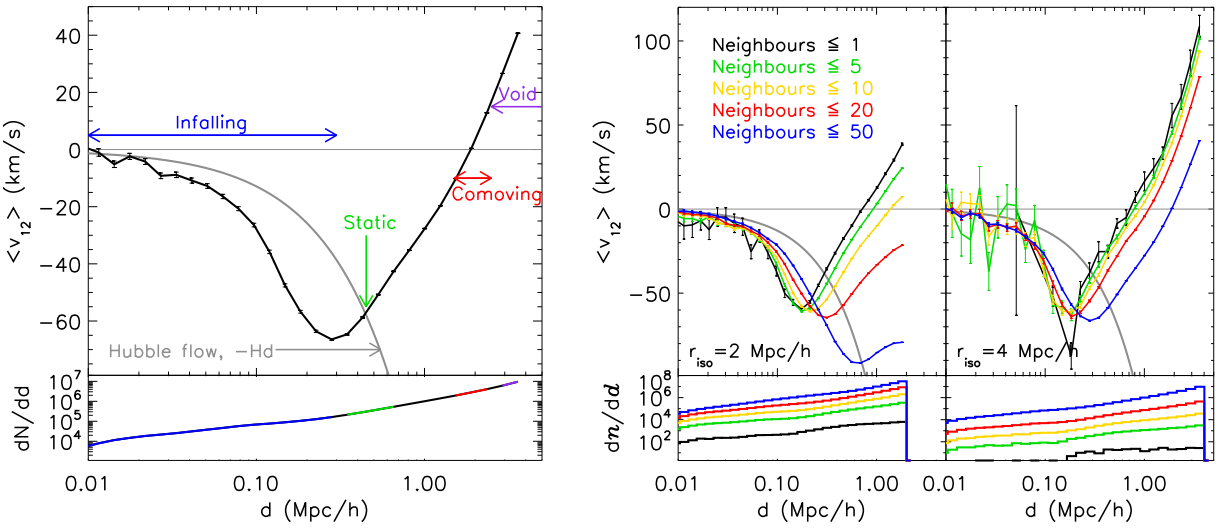

Fig. 1. *Left panel:* In the main panel, the black solid line shows the mean comoving relative velocity, $\langle v_{12} \rangle$, of pairs of galaxies at $z = 0.5$ as a function of their comoving real-space separation, d, as measured from simulations. The pairs of galaxies were selected among those with a maximum of 50 neighbours within a sphere of comoving radius $r_{iso} = 4h^{-1}$Mpc. The different regimes are indicated by arrows. *Right panel:* $\langle v_{12} \rangle$ as a function of d for pairs of galaxies selected by assuming $r_{iso} = 2h^{-1}$Mpc (left) and $r_{iso} = 4h^{-1}$Mpc (right), and different N_{max}, as indicated in the legend. In both panels, the thick grey solid line shows the Hubble flow, $-H(z)d$, and the lower panels show the number of isolated pairs of galaxies per bin in comoving distance.

The Gonzalez-Perez et al. model accounts for the physical processes shaping the formation and evolution of galaxies, including: (i) the collapse and merging of dark matter haloes; (ii) the shock-heating and radiative cooling of gas inside dark matter haloes, leading to the formation of galactic discs; (iii) the quiescent star formation in galactic discs, for which the mass of molecular and atomic gas content is followed explicitly (Lagos et al. 2011); (iv) feedback from supernovae, from active galactic nuclei and from photoionization of the inter galactic medium; (v) chemical enrichment of the stars and gas; (vi) galaxy mergers driven by dynamical friction within common dark matter haloes, leading to the formation of stellar spheroids, which also may trigger bursts of star formation. The end product of the calculation is a prediction of the number and properties of galaxies that reside within dark matter haloes of different masses. The free parameters in the Gonzalez-Perez et al. model were chosen in order to reproduce the rest-frame luminosity functions in b_J and K-bands at $z = 0$ and to give a reasonable match to the observed evolution of the rest-frame ultra violet and K-band luminosity functions.

3 Results

We use model galaxies at $z = 0.5^*$ to study the comoving relative velocities of isolated pairs of galaxies, v_{12}. The isolation criteria is defined by counting the number of neighbours a galaxy has within a sphere of a given comoving radius, $r_{iso}\,h^{-1}$Mpc. If that number is below a certain threshold, N_{max}, we consider the galaxy to be isolated and, thus, it can become part of an isolated pair of galaxies (note that in this way a galaxy can be part of more than one pair). The LOS radial comoving distance to a galaxy with redshift z_A can be defined as (c is the speed of light):

$$\chi(z_A) = \frac{c}{H_0} \int_0^{z_A} \frac{\mathrm{d}z}{E(z)}\,, \quad \text{with} \quad E(z) = \sqrt{\Omega_m(1+z)^3 + \Omega_k(1+z)^2 + \Omega_\Lambda} \quad \text{and} \quad H(z) = H_0 E(z). \qquad (3.1)$$

The Hubble expansion rate, $H(z)$, can also be defined in terms of the expansion parameter, $a = 1/(1+z)$, as $H = \dot{a}/a$. The physical distance to a galaxy, r, is proportional to its comoving distance, χ: $r = a\chi$. Thus, if we

*In the future, we would like to apply the MB test to galaxies from BOSS, which have $\langle z \rangle \sim 0.5$ (Dawson et al. 2013).

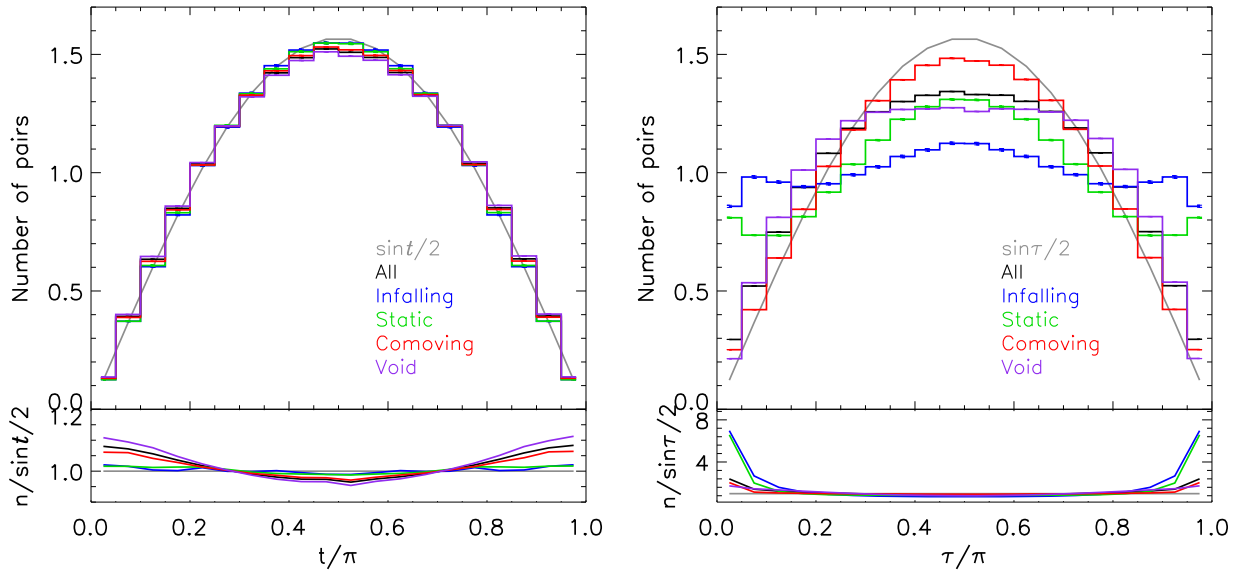

Fig. 2. The main panels show the predicted distribution of the angles that isolated pairs of galaxies form with the LOS in real space (t, left) and redshift space (τ, right). All curves are normalized to have unit area. The grey lines show the theoretical expectation of sin $t/2$. The black histograms show the prediction of all modelled isolated pairs of galaxies ($r_{iso} = 4\,h^{-1}$Mpc, $N_{max} = 50$), the other histograms show the behaviour of the subsample of pairs of galaxies selected by their comoving separation to account for the different regimes of $\langle v_{12} \rangle$, as indicated in the legend. Poisson error bars are shown for each predicted histogram, though they are too small to be seen. The lower panels show the ratio between the predicted distributions and the theoretical expectation.

neglect higher order terms of the total velocity of a galaxy, v, we can express v as the sum of the Hubble flow and the peculiar velocity, v_p: $v = \dot{r} = \dot{a}\chi + a\dot{\chi} = H(z)r + v_p$, or in comoving coordinates, $(1+z)v = H(z)\chi + (1+z)v_p$. For a pair of galaxies, we can define v_{12} as the rate of change in their comoving real-space separation $\dot{d}$ (Bueno Belloso et al. 2012):

$$v_{12} = (1+z)\Delta\overrightarrow{v_p}\hat{d}\,, \quad \text{with} \quad \Delta\overrightarrow{v_p} = \overrightarrow{v_{p2}} - \overrightarrow{v_{p1}} \quad \text{(difference in peculiar velocities)} \quad \text{and} \quad \hat{d} \text{ unitary vector} \quad (3.2)$$

Thus, when $v_{12} = 0$, the pair of galaxies will follow the Hubble flow, $(1+z)(v_2 - v_1) = H(z)d$. If $v_{12} = -H(z)d$ the peculiar velocities of the galaxies will be compensating the Hubble flow, i.e. they will be static with respect to each other in physical space. When $v_{12} < -H(z)d$, the galaxies will be infalling and when $v_{12} > -H(z)d$, they will be moving apart. These different regimes are indicated in the left panel in Fig. 1, which shows the predicted average $\langle v_{12} \rangle$ for isolated model galaxy pairs. The right panel in Fig. 1 shows the average $\langle v_{12} \rangle$ for model galaxy pairs at $z = 0.5$ when different isolation criteria are applied. Increasing N_{max} implies that larger separations between the two galaxies are needed in order for their $\langle v_{12} \rangle$ to approach zero (as shown by Bueno Belloso et al. 2012). In fact, if no isolation criteria is applied, on average, no galaxy pairs are found with $\langle v_{12} \rangle = 0$ (see also Bueno Belloso et al. 2012). Reducing r_{iso} can have a similar effect as increasing N_{max}. Applying observational limits to the model galaxies, such as a range in magnitude or stellar mass, has a similar effect to changing the N_{max}. As an example, pairs of galaxies with $N_{max} = 5$, $r_{iso} = 4h^{-1}$Mpc and $m_{AB}(i) < 20$ have $\langle v_{12} \rangle \sim 0$ only for separations close to $2h^{-1}$Mpc, instead of the $1h^{-1}$Mpc. This happens because when we only take into account either bright or massive galaxies, we are missing galaxy neighbours that interact with those galaxies passing the selection criteria and are thus affecting their peculiar velocities. We have also studied the predicted $\langle v_{12} \rangle$ in simulations with a dynamical dark energy (Jennings et al. 2010, 2012). We find that $\langle v_{12} \rangle$ is less sensitive to changes in the cosmology from an evolving dark energy, than to changes in N_{max}.

3.1 The distribution of the angle that isolated galaxy pairs form with the line-of-sight

MB derived a test based on the idea that, in real space, the probability distribution of the angle t between the pair and the LOS follows sin $t/2$ with $\langle \sin^2 t \rangle = 0.667$. We have measured the distribution of the angles t in

real space (for a flat universe: $\sin t = \sin\theta \cdot \chi_{z_B}/d$) and τ in redshift space for the model galaxies. Fig. 2 shows the distribution of these angles for all isolated pairs. In real space, the distribution for isolated model pairs of galaxies is very close to the theoretical expectation of $\sin t/2$, with a difference smaller than a factor 1.1. In redshift space, when peculiar velocities are included to estimate the observed positions of galaxies, there is an increase in pairs which are aligned along the LOS and we find deviations from the uniform distribution which are largest for angles $\tau/\pi < 0.2$ and $\tau/\pi > 0.8$.

We have split the isolated pairs of galaxies according to their comoving real-space separations, d, which defines the different $\langle v_{12}\rangle$ regimes described above. In real space, the distribution of angles are rather insensitive to the cut in d. The distributions are at most a factor of 1.2 different with respect to the expected $\sin t/2$. However, in redshift space, the distortion of the distribution of τ does depend on the value of $\langle v_{12}\rangle$, since this is a measure of the relative peculiar velocities of the pair. Pairs of galaxies with $\langle v_{12}\rangle \sim 0$ show a very small change between the distributions of t in real space and τ in redshift space. Isolated pairs of galaxies with $N_{max} = 50$, $r_{iso} = 4h^{-1}$Mpc and in the *comoving regime* are predicted to have $\langle \sin^2 t\rangle = 0.658$ in real space, and $\langle \sin^2\tau\rangle = 0.645$ in redshift space, while galaxies in the other regimes are predicted to have a stronger variation of these quantities. Therefore, pairs of galaxies in this regime can be used to constrain cosmology, as we can accurately predict their distribution in redshift space.

4 Conclusions

We have used the Gonzalez-Perez et al. (2013) semi-analytical model of galaxy formation and evolution to study the average comoving relative velocities of isolated pairs of galaxies, $\langle v_{12}\rangle$. This model uses a Millennium Simulation class N-body run performed with the WMAP7 cosmology. We have found that, on average, two isolated galaxies with comoving separations below $\sim 0.5\,h^{-1}$Mpc are infalling towards each other, while two galaxies with separations above $\sim 2\,h^{-1}$Mpc are moving apart. For separations somewhere in between, a regime is found for which $\langle v_{12}\rangle \sim 0$. The exact range in comoving real-space distances that define this *comoving regime* strongly depends on the definition of the isolation criteria used to select pairs of galaxies. For isolated pairs of model galaxies at $z = 0.5$ we have measured in real space the angle that they form with the LOS, finding an excellent agreement with the theoretical expectation for uniformly distributed pairs of galaxies. This finding is practically independent of the average $\langle v_{12}\rangle$ and, thus, validates the assumption made by MB for their cosmological test. In redshift space, due to the effect of peculiar velocities, we find more pairs of galaxies which appear closely aligned with the LOS, though the deviations do depend on $\langle v_{12}\rangle$. We find that isolated pairs of galaxies selected with $\langle v_{12}\rangle \sim 0$ form an angle with the LOS which is practically independent of the effect of peculiar velocities and so are uniformly distributed in both real and redshift space, with $\langle \sin^2 t\rangle \,/\, \langle \sin^2\tau\rangle \sim 1$. Pairs of galaxies in this regime are therefore a potentially promising probe of cosmology.

GALFORM was run on the ICC Cosmology Machine, which is part of the DiRAC Facility jointly funded by STFC, the Large Facilities Capital Fund of BIS, and Durham University. VGP acknowledges financial support from the grant OMEGA ANR-11-JS56-003-01.

References

Alcock, C. & Paczynski, B. 1979, Nature, 281, 358
Anderson, L., Aubourg, E., Bailey, S., et al. 2012, MNRAS, 427, 3435
Baugh, C. M. 2006, Reports of Progress in Physics, 69, 3101
Blake, C., Davis, T., Poole, G. B., et al. 2011, MNRAS, 415, 2892
Bueno Belloso, A., Pettinari, G. W., Meures, N., & Percival, W. J. 2012, Phys. Rev. D, 86, 023530
Cole, S., Lacey, C. G., Baugh, C. M., & Frenk, C. S. 2000, MNRAS, 319, 168
Dawson, K. S., Schlegel, D. J., Ahn, C. P., et al. 2013, AJ, 145, 10
Gonzalez-Perez, V., Lacey, C. G., Baugh, C. M., et al. 2013, arXiv 1309.7057
Jennings, E., Baugh, C. M., Angulo, R. E., & Pascoli, S. 2010, MNRAS, 401, 2181
Jennings, E., Baugh, C. M., & Pascoli, S. 2012, MNRAS, 420, 1079
Komatsu, E., Smith, K. M., Dunkley, J., et al. 2011, ApJS, 192, 18
Lagos, C. D. P., Lacey, C. G., Baugh, C. M., Bower, R. G., & Benson, A. J. 2011, MNRAS, 416, 1566
Marinoni, C. & Buzzi, A. 2010, Nature, 468, 539
Phillipps, S. 1994, MNRAS, 269, 1077

SF2A 2013
L. Cambrésy, F. Martins, E. Nuss and A. Palacios (eds)

MEASUREMENT OF THE THERMAL SUNYAEV-ZEL'DOVICH ANGULAR POWER SPECTRUM WITH PLANCK.

G. Hurier[1] and The Planck Collaboration

Abstract. The Planck experiment allows us to construct the first all-sky map of the thermal Sunyaev-Zeldovich (tSZ) effect by applying dedicated component separation algorithms to the 100 to 857 GHz frequency channel maps. These maps show a clear galaxy cluster tSZ signal that is well matched with blindly detected clusters in the Planck SZ catalogue. To characterize the signal in the tSZ map we have computed its angular power spectrum. We have carefully modeled and subtracted the foreground contaminant, mainly the diffuse thermal dust emission and Cosmic Infrared Background (CIB). Finally, we use the tSZ power spectrum to obtain constraints on cosmological parameters.

Keywords: cosmological parameters, large-scale structure of Universe, Galaxies: clusters: general

1 Introduction

The thermal Sunyaev-Zeldovich (tSZ) effect (Sunyaev & Zeldovich 1972), produced by the inverse Compton scattering of CMB photons by hot electrons along the line of sight, has proved to be a major tool to the study of the physics of clusters of galaxies as well as structure formation in the Universe. In particular, tSZ-selected catalogues of clusters of galaxies have been provided by various experiments including the *Planck* satellite (Planck Collaboration VIII 2011; Planck Collaboration XXIX 2013), the Atacama Cosmology Telescope (ACT, Hasselfield et al. 2013) and the South Pole Telescope (SPT, Reichardt et al. 2013). From these catalogues, and their associated sky surveys, a wealth of studies have been performed both on the physics of clusters of galaxies (Planck Collaboration XII 2011; Planck Collaboration XI 2011; Planck Collaboration X 2011) and on their cosmological interpretation (Planck Collaboration XX 2013; Benson et al. 2013; Das et al. 2013; Wilson et al. 2012; Mak & Pierpaoli 2012).

To date, indirect measurements of the tSZ power spectrum are only available from high resolution CMB oriented experiments like ACT (Sievers et al. 2013) and SPT (Reichardt et al. 2012). In these studies, constraints on the amplitude of tSZ power spectrum at $\ell = 3000$ are obtained by fitting a tSZ template in addition to other components (i.e., CMB, radio and infrared point-source and clustered Cosmic Infrared Background (CIB)) to the measured total power spectrum.

Thanks to its all sky coverage and unprecedented wide frequency range, *Planck* has the unique capability to produce an all-sky Compton parameter (y) map and an accurate measurement of the tSZ power spectrum at intermediate and large angular scales, for which the tSZ fluctuations are almost insensitive to the cluster core physics.

2 Planck Data

This paper is based on the first 15.5 month survey mission corresponding to two full-sky surveys. We refer to Planck Collaboration II (2013) and Planck Collaboration VI (2013) for the generic scheme of Time Ordered Information (TOI) processing and map-making, as well as for the technical characteristics of the *Planck* frequency maps. The *Planck* channel maps are provided in `HEALPix` (Górski et al. 2005) $N_{\rm side} = 2048$ at full resolution. An error map is associated with each channel map and is obtained from the difference of the first half and second half of the survey rings for a given pointing position of the satellite spin axis. The resulting maps, called null maps, are mainly free from astrophysical emission and they are a good representation of the statistical instrumental noise. Null maps have also been used to estimate the noise in the final Compton parameter maps. Here we approximate the *Planck* beams by effective circular Gaussians (Planck Collaboration IV 2013; Planck Collaboration VII 2013). Although tests have been performed using both LFI and HFI channel maps, the work presented here will refer mainly to results using the HFI data only.

[1] Institut d'Astrophysique Spatiale, CNRS (UMR8617) Universit Paris-Sud 11, Btiment 121, Orsay, France

3 The tSZ effect

The thermal SZ Compton parameter in a given direction, $\vec{n}$, is

$$y(\vec{n}) = \int n_e \frac{K_B T_e}{m_e c^2} \sigma_T \, \mathrm{d}s \tag{3.1}$$

where ds is the distance along the line-of-sight, $\vec{n}$, and n_e and T_e are the electron number density and temperature, respectively.

In units of CMB temperature the contribution of the tSZ effect to the *Planck* maps for a given observation frequency ν is

$$\frac{\Delta T}{T_{\rm CMB}} = g(\nu)\, y. \tag{3.2}$$

Neglecting relativistic corrections we have $g(\nu) = \left(x \coth(\frac{x}{2}) - 4\right)$, with $x = h\nu/(k_B T_{\rm CMB})$.

4 tSZ power spectrum

Decomposing the map in spherical harmonics we obtain

$$y(\vec{n}) = \sum_{\ell m} y_{\ell m}\, Y_{\ell m}\,(\vec{n}), \tag{4.1}$$

Thus, the angular power spectrum of the Compton parameter map is

$$C_\ell^{\rm tSZ} = \frac{1}{2\,\ell + 1} \sum_m y_{\ell m} y^*_{\ell m}. \tag{4.2}$$

Note that $C_\ell^{\rm tSZ}$ is an a-dimensional quantity as y.

To model the tSZ power spectrum we consider a two halo model to account for intra-halo and inter-halo correlations

$$C_\ell^{\rm SZ} = C_\ell^{\rm 1halo} + C_\ell^{\rm 2halos}. \tag{4.3}$$

In the case of the tSZ emission the inter-halo term can neglected with respect to the 1-halo term. The 1 halo term, also known as the Poissonian contribution, can be computed by summing the square of the Fourier transform of the projected SZ profile, weighted by the number density of clusters of a given mass and redshift (Komatsu & Seljak 2002):

$$C_\ell^{\rm 1halo} = \int_0^{z_{\rm max}} dz \frac{dV_c}{dz d\Omega} \int_{M_{\rm min}}^{M_{\rm max}} dM \frac{dn(M,z)}{dM} \left|\tilde{y}_\ell(M,z)\right|^2, \tag{4.4}$$

where $dV_c/(dz d\Omega)$ is the comoving volume per unit redshift and solid angle and $n(M,z)dM\, dV_c/(dz d\Omega)$ is the probability of having a galaxy cluster of mass M at a redshift z in the direction $d\Omega$. The quantity $\tilde{y}_\ell = \tilde{y}_\ell(M,z)$ is the 2D Fourier transform on the sphere of the 3D radial profile of the Compton y-parameter of individual clusters,

$$\tilde{y}_\ell(M,z) = \frac{4\pi r_s}{l_s^2} \left(\frac{\sigma_T}{m_e c^2}\right) \int_0^\infty dx\, x^2 P_e(M,z,x) \frac{\sin(\ell x/\ell_s)}{\ell x/\ell_s} \tag{4.5}$$

where $x = r/r_s$, $\ell_s = D_A(z)/r_s$, r_s is the scale radius of the 3D pressure profile, $D_A(z)$ is the angular diameter distance to redshift z and P_e is the electron pressure profile.

5 Reconstruction of an all-sky tSZ map

The contribution of the tSZ effect in the *Planck* frequency maps is subdominant with respect to the CMB and other foreground emissions. Furthermore, the tSZ effect from galaxy clusters is spatially localized and leads to a highly non-Gaussian signal with respect to that from the CMB. CMB-oriented component-separation methods (Planck Collaboration XII 2013) are not optimized to recover the tSZ signal. We therefore need to use specifically tailored component separation algorithms that are able to reconstruct the tSZ signal from the *Planck* frequency channel maps. These optimized all-sky component separation techniques rely on the spatial localization of the different astrophysical components and on their

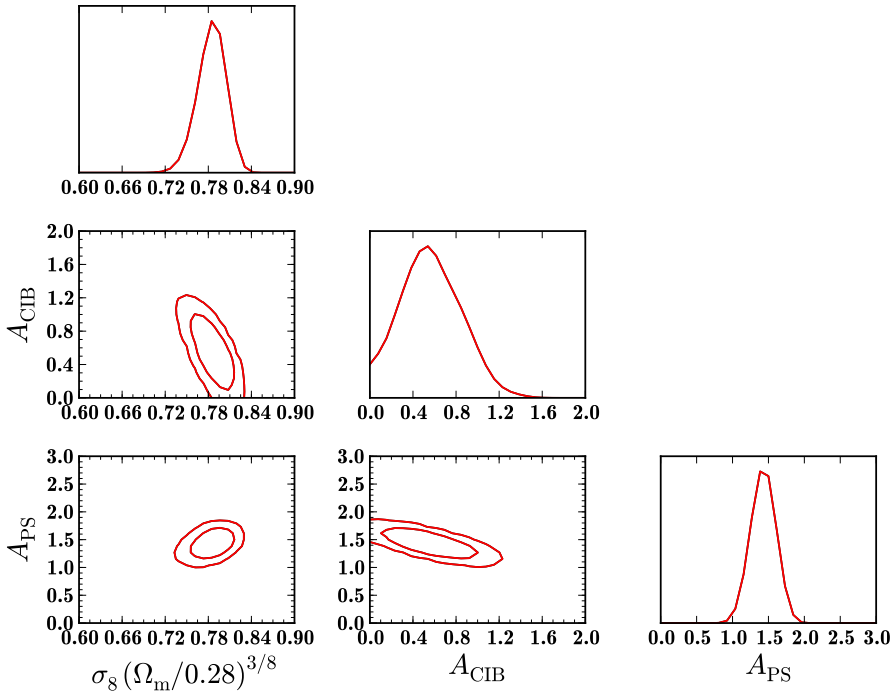

Fig. 1. 2D and 1D likelihood distributions for the combination of cosmological parameters $\sigma_8(\Omega_{\rm m}/0.28)^{3.2/8.1}$, and for the foreground parameters $A_{\rm CIB}$ and $A_{\rm PS}$. We show the 68% and 95.4% C.L. contours here.

spectral diversity to separate them. We present,in the following, the results of two algorithms, MILCA (Modified Internal Linear Combination Algorithm, Hurier et al. 2010) and NILC (Needlet Iindependent Linear Combination, Remazeilles et al. 2011). Both are based on the well known Internal Linear Combination (ILC) approach that searches for the linear combination of the input maps that minimizes the variance of the final reconstructed map under the constraint of offering unit gain to the component of interest (here the tSZ effect, whose frequency dependence is known). Both have been extensively tested on simulated *Planck* data.

6 Power spectrum analysis

As a measure of structure growth, the tSZ power spectrum can provide independent constraints on cosmological parameters and potentially improve their precision. As shown by Komatsu & Seljak (2002), the power spectrum of the tSZ effect is highly sensitive to the normalization of the matter power spectrum, commonly parameterized by the rms of the $z = 0$ mass distribution on $8\,h^{-1}$ Mpc scales, σ_8 (Komatsu & Seljak 2002), and to the total amount of matter $\Omega_{\rm m}$.

Cosmological constraints are obtained from a fit of the NILC F/L cross-power spectrum, for the 50% mask, assuming a three-component model: tSZ; clustered CIB; and radio and infrared point sources. For $\ell > 60$, we can reasonably neglect the Galactic dust contamination. For $\ell > 1411$ the total signal in the tSZ map is dominated by noise. We thus restrict our analysis to the multipole range $60 < \ell < 1411$. The measured power spectrum, $C_\ell^{\rm m}$, is modelled as follows:

$$C_\ell^{\rm m} = C_\ell^{\rm tSZ}(\Omega_{\rm m}, \sigma_8) + A_{\rm CIB}\, C_\ell^{\rm CIB} + A_{\rm PS}\, (C_\ell^{\rm IR} + C_\ell^{\rm Rad}). \tag{6.1}$$

Here $C_\ell^{\rm tSZ}(\Omega_{\rm m}, \sigma_8)$ is the tSZ power spectrum, $C_\ell^{\rm CIB}$ is the clustered CIB power spectrum and $C_\ell^{\rm IR}$ and $C_\ell^{\rm Rad}$ are the infrared and radio source power spectra, respectively.

The tSZ spectrum is computed using the halo model, the Tinker et al. (2008) mass function and the Arnaud et al. (2010) universal pressure profile. In particular, we use the numerical implementation presented in Taburet et al. (2009, 2010, 2011) and integrate in redshift from 0 to 3 and in mass from 10^{13} to $5 \times 10^{15}\,{\rm M}_\odot$. Our model allows us to compute the tSZ power spectrum at the largest angular scales.

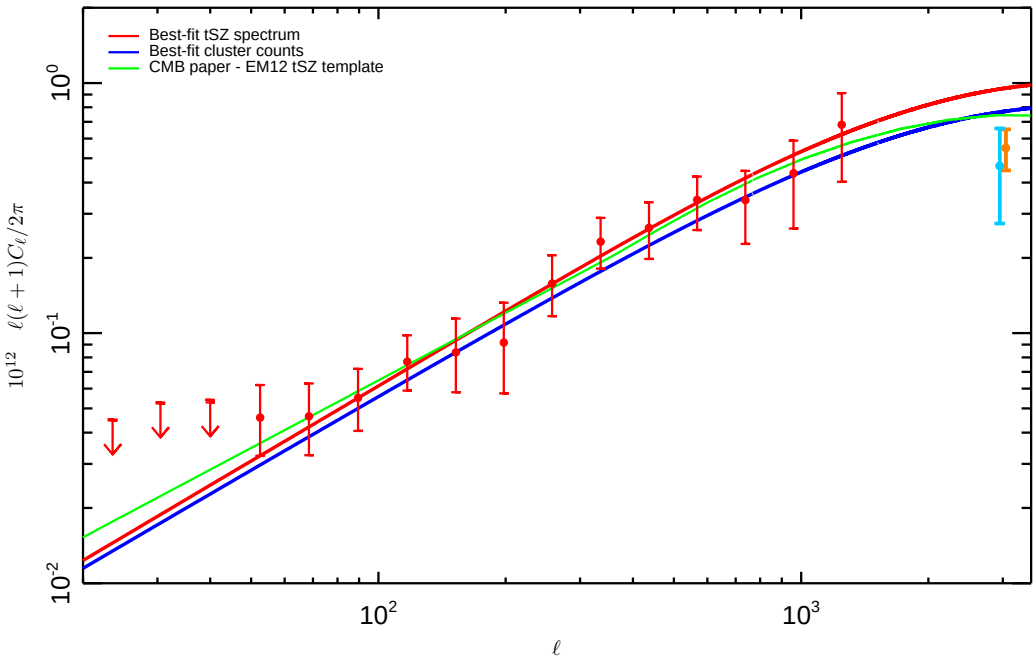

Fig. 2. Marginalized bandpowers of the *Planck* tSZ power spectrum with total (statistical plus foreground) uncertainties (red points). The red solid line represents the best-fit tSZ power spectrum model. We also show as a blue solid line the best-ft tSZ power-spectrum obtained from the analysis of cluster number counts (Planck Collaboration XX 2013). The tSZ power spectrum template used in the CMB cosmological analysis (Planck Collaboration XV 2013; Planck Collaboration XVI 2013) is presented as a green solid line.

We allow for a variation of the normalization amplitudes for the clustered CIB, $A_{\rm CIB}$ and for the point sources, $A_{\rm PS}$, with Gaussian priors centred on one with standard deviation 0.5.

We assume a Gaussian approximation for the likelihood function. Best-fit values and uncertainties are obtained using an adapted version of the `Cosmo-MC` algorithm (Lewis & Bridle 2002). Only σ_8 and $\Omega_{\rm m}$ are allowed to vary here. All other cosmological parameters are fixed to their best-fit values as obtained in Table 2 of Planck Collaboration XVI (2013). The normalization amplitudes $A_{\rm CIB}$ and $A_{\rm PS}$, considered as nuisance parameters, are allowed to vary between 0 and 3. For the range of multipoles considered here, the tSZ angular power spectrum varies like $C_\ell \propto \sigma_8^{8.1}\Omega_{\rm m}^{3.2}$. The results are thus presented in terms of this parameter combination.

Figure 1 presents the 2D and 1D likelihood distributions for the cosmological parameter combination $\sigma_8\Omega_{\rm m}^{3.2/8.1}$, and for the foreground nuisance parameters. The best-fit values and error bars for each parameter are given by $\sigma_8(\Omega_{\rm m}/0.28)^{3.2/8.1} = 0.784 \pm 0.016$, $\sigma_8 = 0.74 \pm 0.06$, $\Omega_{\rm m} = 0.33 \pm 0.06$, $A_{\rm CIB} = 0.55 \pm 0.26$ and $A_{\rm PS} = 0.14 \pm 0.13$. It is worth noting that these values are obtained in a specific framework: all other cosmological parameters fixed and a fiducial fixed model for the signals. Opening up the possibility for relaxing this framework is likely to weaken the constraints.

The red points in Fig. 2 correspond to the marginalized *Planck* tSZ power spectrum (from the `NILC` F/L cross-power spectrum), compared to the best-fit theoretical model presented above (solid red line). Foreground uncertainties are derived from the likelihood curves of the nuisance parameters and added in quadrature to the statistical uncertainties, providing the total errors plotted here. In the range ℓ=60–1411, the *Planck* tSZ power spectrum can be approximated by a power law of the form

$$\ell(\ell+1)C_\ell/2\pi = (1.0 \pm 0.2)\ \ell^{(0.912\pm0.031)}\ 10^{-15}.$$

The measured tSZ power-spectrum is in remarkable agreement with the tSZ power-spectrum (blue solid line) computed using cluster count best-fit parameters (Planck Collaboration XX 2013).

7 Conclusion

Because of its wide frequency coverage from 30 to 857 GHz, the *Planck* satellite mission is particularly well suited for the measurement of the thermal Sunyaev-Zeldovich effect.

We have produced the first measurement of the SZ power spectrum on large angular scales ranging from $0.17^\circ \lesssim \theta \lesssim 3.0^\circ$. In this range, the tSZ power spectrum is almost insensitive to the physics of cluster cores. The detected tSZ signal likely arises from the contribution of warm and hot diffuse gas distributed within groups and clusters, sampling the whole halo mass function, as well as within the larger scale filamentary structures.

We have modelled the tSZ power spectrum via a halo-model analytical approach, in order investigate its dependence in terms of σ_8 and Ω_m and to test it against the measured *Planck* tSZ power spectrum.

The observed consistency between constraints derived from the cluster number counts in Planck Collaboration XX (2013) and from the present work seems to provide a coherent view of the gas content in halos and in larger scale structures. As such, this *Planck* tSZ measurement constitutes the first step towards building a coherent understanding of the integrated tSZ effect due to cosmic structure on all scales and density contrasts.

The development of *Planck* has been supported by: ESA; CNES and CNRS/INSU-IN2P3-INP (France); ASI, CNR, and INAF (Italy); NASA and DoE (USA); STFC and UKSA (UK); CSIC, MICINN, JA and RES (Spain); Tekes, AoF and CSC (Finland); DLR and MPG (Germany); CSA (Canada); DTU Space (Denmark); SER/SSO (Switzerland); RCN (Norway); SFI (Ireland); FCT/MCTES (Portugal); and PRACE (EU). A description of the *Planck* Collaboration and a list of its members, including the technical or scientific activities in which they have been involved, can be found at http://www.sciops.esa.int/index.php?project=Planck&page=Planck_Collaboration. We acknowledge the use of the HEALPix software.

References

Arnaud, M., Pratt, G. W., Piffaretti, R., et al. 2010, A&A, 517, A92

Benson, B. A., de Haan, T., Dudley, J. P., et al. 2013, The Astrophysical Journal, 763, 147

Das, S., Louis, T., Nolta, M. R., et al. 2013, eprint arXiv, 1301, 1037

Górski, K. M., Hivon, E., Banday, A. J., et al. 2005, ApJ, 622, 759

Hasselfield, M., Hilton, M., Marriage, T. A., et al. 2013, eprint arXiv, 1301, 816, 32 pages, 21 figures

Hurier, G., Hildebrandt, S. R., & Macias-Perez, J. F. 2010, ArXiv e-prints

Komatsu, E. & Seljak, U. 2002, Monthly Notice of the Royal Astronomical Society, 336, 1256

Komatsu, E. & Seljak, U. 2002, MNRAS, 336, 1256

Lewis, A. & Bridle, S. 2002, Phys. Rev. D, 66, 103511

Mak, D. S. Y. & Pierpaoli, E. 2012, Physical Review D, 86, 123520

Planck Collaboration II. 2013, Submitted to A&A

Planck Collaboration IV. 2013, Submitted to A&A

Planck Collaboration VI. 2013, Submitted to A&A

Planck Collaboration VII. 2013, Submitted to A&A

Planck Collaboration VIII. 2011, A&A, 536, A8

Planck Collaboration X. 2011, A&A, 536, A10

Planck Collaboration XI. 2011, A&A, 536, A11

Planck Collaboration XII. 2011, A&A, 536, A12

Planck Collaboration XII. 2013, Submitted to A&A

Planck Collaboration XV. 2013, Submitted to A&A

Planck Collaboration XVI. 2013, Submitted to A&A

Planck Collaboration XX. 2013, Submitted to A&A

Planck Collaboration XXIX. 2013, Submitted to A&A

Reichardt, C. L., Shaw, L., Zahn, O., et al. 2012, ApJ, 755, 70

Reichardt, C. L., Stalder, B., Bleem, L. E., et al. 2013, The Astrophysical Journal, 763, 127

Remazeilles, M., Delabrouille, J., & Cardoso, J.-F. 2011, MNRAS, 410, 2481

Sievers, J. L., Hlozek, R. A., Nolta, M. R., et al. 2013, eprint arXiv, 1301, 824

Sunyaev, R. A. & Zeldovich, Y. B. 1972, Comments on Astrophysics and Space Physics, 4, 173

Taburet, N., Aghanim, N., Douspis, M., & Langer, M. 2009, mnras, 392, 1153

Taburet, N., Douspis, M., & Aghanim, N. 2010, mnras, 404, 1197

Taburet, N., Hernández-Monteagudo, C., Aghanim, N., Douspis, M., & Sunyaev, R. A. 2011, MNRAS, 418, 2207

Tinker, J., Kravtsov, A. V., Klypin, A., et al. 2008, The Astrophysical Journal, 688, 709

Wilson, M. J., Sherwin, B. D., Hill, J. C., et al. 2012, Physical Review D, 86, 122005

SF2A 2013
L. Cambrésy, F. Martins, E. Nuss and A. Palacios (eds)

PROBING THE DARK ENERGY THROUGH THE INTEGRATED SACHS-WOLFE EFFECT

S. Ilić[1]

Abstract.
We investigate the detection of the integrated Sachs-Wolfe (iSW) effect through the impact of single superstructures on the cosmic microwave background (CMB) temperature, and its measurement using the stacking of CMB patches. We revisit the analysis of Granett et al. (2008a, Gr08) using our own robust protocol, and extend the study to the two most recent and largest catalogues of voids publicly available. We obtain the radial temperature and photometry profiles from the stacked images. Using a Monte Carlo approach, we computed their statistical significance and identified the angular scale at which the signal-to-noise ratio (S/N) is maximum. We essentially confirm the signal detection reported by Gr08, but for the other two catalogues, a rescaling of the voids to the same size on the stacked image is needed to find any significant signal (with a maximum at $\sim 2.4\,\sigma$). This procedure reveals that the photometry peaks at unexpectedly large angles in the case of the Gr08 voids, in contrast to voids from other catalogues. We also stress the importance of a posteriori selection effects that might arise when intending to increase the S/N, and we discuss the possible impact of void overlap and alignment effects. We argue that the interpretation in terms of an iSW effect of any detected signal via the stacking method is far from obvious.

Keywords: cosmology, cosmic microwave background, dark energy, large scale structures

1 Introduction

The discovery of the acceleration of the expansion of the Universe, made through supernovæ observations at the end of the last century, led us to hypothesize the existence of an unknown "Dark Energy", contributing $\sim 70\%$ to the energy budget of our Universe. In this presentation, we focus on a specific probe of the Dark Energy, namely the integrated Sachs-Wolfe (iSW) effect : This effect of gravitational origin induces secondary anisotropies in the CMB and is due to large-scale structures. The gravitational potentials of the latter are slowly decaying in a Λ-dominated Universe, and therefore give a net difference in energy to the CMB photons that travel across them. This effect shows in the power spectrum of the Cosmic Microwave Background (CMB) temperature anisotropies at large angular scales but its small amplitude and the cosmic variance at those ℓ make its direct detection very challenging, if not impossible, when using only the CMB itself. To circumvent this limitation, cosmologists have devised a way to exploit the link between this imprint on the CMB and the large-scale structures causing it, first by simply cross-correlating the CMB with matter density maps (galaxy maps in practice) and then comparing the results to a null hypothesis and to what is expected from theory. During the last decade or so, a growing interest has risen in this field thanks to the development of large galaxy surveys in many wavelengths. However, this method has yet to produce a definitive and conclusive detection of the ISW effect from current surveys, with significances ranging so far from negligible up to more than 4σ, and with sometimes conflicting results throughout the literature.

We make here a short report of our work presented in Ilić et al. (2013) and Planck Collaboration (2013), where we consider an alternative method of measuring the iSW effect, namely through the impact of individual superstructures in the CMB temperature. Unfortunately, the amplitude of such effect with respect to the primary CMB anisotropies does not allow us to detect it structure by structure. However, stacking techniques can be profitably adopted to enhance the signal-to-noise ratio (S/N). With the help of the Wilkinson Microwave

[1] Institut d'Astrophysique Spatiale, Université Paris Sud, 91405 Orsay, France

Anisotropy Probe (WMAP) five year maps, such a technique has been applied by Granett et al. (2008) (Gr08 thereafter) to the supervoids and superclusters they identified in the catalogue of luminous red galaxies (LRGs) in the Data Release 6 (DR6) of the Sloan Digital Sky Survey (SDSS). Focusing on the most significant (in terms of the density contrast) 50 supervoids and 50 superclusters, Gr08 report a combined mean temperature deviation of 9.6 μK, at a significance just above $4\,\sigma$, which they interpret as a signature of the iSW effect. Using the Millennium simulation and measuring the iSW effect that is expected in a standard ΛCDM universe, Gr08 find that it is $\sim 2\,\sigma$ lower (at 4.2 μK) than what they obtained from the WMAP data. Other studies have also measured a somewhat higher iSW effect than expected, although with small statistical significance. The high significance and the stronger-than-expected amplitude of the iSW effect detected through stacking have also stimulated a number of investigations, which yielded mixed conclusions (cf. Ilić et al. 2013, and references therein).

Should we conclude that the large CMB temperature deviations measured in association with superstructures signal a tension with the ΛCDM model? Here, we would like to take a further step towards answering that question. Since the study of Gr08, new CMB maps have been released and other superstructure catalogues have been published. We do the stacking analysis with the new data and look for the iSW signal that could be associated with the large scale structure. We pay particular attention to the bias introduced into the results by selection effects and illustrate it with an explicit example.

2 The data used

The first and foremost way to improve stacking studies was to use the latest CMB data to improve and validate our stacking studies. We conducted two separate works on the topic: one that used WMAP 7-year data (the latest at the time of the study) which led to the publication of a paper (Ilić et al. 2013), and another inside the Planck collaboration itself by leading the stacking section in the iSW-dedicated cosmological paper (Planck Collaboration 2013). Although the CMB data is different, the protocol that we devised is largely the same for both new studies and the catalogues of structures used are identical. The impact of foregrounds and the associated possibility of false signals is often a source of uncertainty in iSW studies. We therefore consider and assess their possible influence by redoing our analyses on the foreground reduced maps released by both teams in the same frequency channels.

The first catalogue of superstructures (clusters and voids) that we considered was created and studied by Gr08. Since it was already explored with WMAP 5-year data, it will serve us as a "fiducial" set when testing all the steps of our own stacking procedure. This will also be the opportunity to revisit the work of Gr08 with the newer seven-year data from WMAP. Pan et al. (2012) (Pan12) published a catalogue of cosmic voids and void galaxies identified in the seventh data release (DR7) of the SDSS. Using the VoidFinder algorithm as described by Hoyle & Vogeley (2002), they identified and catalogued 1055 voids with redshifts lower than $z = 0.1$. Finally, the most recent catalogue considered in the present study was released by Sutter et al. (2012) (Sut12). Using their own modified version of the void finding algorithm ZOBOV, Sut12 also built a void catalogue from the SDSS DR7, taking particular care to account for the effects of the survey boundary and masks. In the latest version of their catalogue, they found a total of 1495 voids, which they divided into six distinct subsamples of increasing redshift, spanning $z \sim [0, 0.4]$. This catalogue stands out by the large amount of information provided about its voids.

3 Stacking protocol

The analysis of these three different catalogues requires us to have a robust and well defined procedure for a systematic analysis of all the structures considered. First, the standard stacking procedure that we apply in this study consists in the following steps, for each superstructure sample or subsample: we retrieve the galactic longitudes and latitudes of the structures considered, and use a custom code based on the HEALPix package to cut a patch in the considered CMB map centred on each structure. The final stacked image is then constructed as the average image of all CMB patches weighted by their corresponding weight patches. Two main products are then extracted from the stacked image. Firstly, the radial temperature profile starting from the centre of the image, by computing the mean temperature of the pixels in rings of fixed width and increasing angular radius. Then, the aperture photometry profile, using a compensated filter approach. At each angle θ, we compute the photometry as the difference between the mean temperature of the pixels inside the disk of angular radius θ and the temperature of the pixels in the surrounding ring of same area, i.e. the ring enclosed between circles of

radii θ and $\theta\sqrt{2}$. We mainly focus on the analysis of these two profiles (the image itself is useful for illustration purposes only), where we look for any remarkable signal whose significance we need to assess (as described later section).

Each of the different CMB maps that we use inherently has a different resolution and contains different types and levels of foregrounds that may contaminate them. Before progressing any further, we assessed the impact of the properties of each map, using our fiducial stacking (i.e. using the Gr08 void positions) as a basis. First, to have a consistent stacking analysis through all the considered frequencies, we need to "standardise" those maps by first smoothing them at the lowest resolution in order to lose as little information as possible. The stacks at each frequency, both raw and smoothed, give roughly the same results with only percent-level differences especially for the photometry profiles – the most useful products here. One other source of concern comes from the influence of foregrounds present in the CMB maps, because they might mimic the expected iSW signal in the stacked images. To assess their possible impact, we performed the stacking of the Gr08 voids first on raw and then on foreground cleaned CMB maps at all frequencies. We obtained systematic offsets of a few micro-kelvins in the radial temperature profiles and less in the photometry profiles. This indicates that we mainly remove an almost uniform background, which does not influence the aperture photometry of the stacked image much.

When taken alone, the stacked images and their associated profiles are not enough to conclude anything about a possible detection of the iSW effect. Any peculiar feature that seems to stand out could very well be a random event well within statistical fluctuations. As a consequence, we have to take great care in assessing the significance of our results. We have devised a systematic way to compute the significance adopting a Monte Carlo approach. We consider the stack of N_v voids, identified in the data, whose significance we try to estimate. We pick many sets (at least 10000) of N_v random positions on the sky confined within the area covered by the SDSS. For each random set, we perform the same analyses as for the data voids; i.e., we produce a stacked image of the N_v patches extracted from the same CMB maps, and compute its radial temperature and photometry profiles. We store all these profiles in memory and end up with thousands of temperature profiles and photometry profiles. After this, for each angular size of the profiles, we compare the results from the stack of data voids to the statistical distribution of results from the random stacks. In practical terms, we calculate the S/N of the data temperature or photometry profiles, at each angle θ considered. Applying this procedure to the fiducial stacking of the Gr08 voids, we found that this estimation of the significance was robust and used it in the remainder of our study for all our results.

4 Results

The work of Gr08 reported a $3.7\,\sigma$ signal ($-11.3\,\mu$K) in the stacking of their voids on a scale of 4°. With the same dataset we find a reasonable agreement with a preferred scale of $\sim 3.7^\circ$ with an S/N ~ 3.3 ($-10.8\,\mu$K). These differences can be imputed to our use of WMAP 7 maps instead of the WMAP 5 ILC map for Gr08 and, to a lesser extent, to light differences in the stacking procedure, profile calculations, or significance estimation. While we can argue about its cosmological origin, the signal seems to be persisting and is essentially identical across frequencies as expected for the iSW effect. However, we found an important feature in the temperature profile of the stacked image and its significance. Indeed, the central cold spot of the signal (below 3.5°) does not particularly stand out compared to random stacks ($1\,\sigma$ significance only). On the other hand, we measure a wide hot ring with around the spot a higher significance (up to $2\,\sigma$) on scales between 3.5° and 10°. Interpreting it in the light of the iSW effect, this would imply the presence of much higher overdensities surrounding the already large supervoids. Considering the filamentary structure of our Universe, this situation is unlikely, and the source of this hot ring remains unknown. This peculiarity leads us to question whether the measured central cold spot – physically interpreted as an iSW signal – is really remarkable. It might as well be due to random fluctuations of the CMB, of which the significance in the photometry profile is coincidentally strengthened by a surrounding hot region in the stacked image.

The two other catalogues used in our analysis, when taken as such, yield mixed results, with no significance on the same level as the Gr08 catalogue. While discouraging, one has to remember that according to current theoretical predictions, we expect this iSW signal to be difficult to detect. Preliminary analysis strongly suggested that we needed to take the size of each individual void into account in the stacking procedure to improve the significance of the results. We therefore kept each subsample in its entirety and did the stacking analysis again, but this time rescaling the voids according to their effective radii. Beginning with the fiducial stacking of the voids of Gr08, the signal identified before still appears after rescaling, with the best significance around

scales between 0.7 and 0.9 times the void effective radii. The significance of the signal is also found to be lower (S/N$\sim$ 2.8 versus $\sim$ 3.3). This is partly due to the increased variance of the signal induced by the rescaling. But it is also a consequence of the lower amplitude measured for the signal, at odds with our expectations of the rescaling procedure and a possible further hint of a contribution from random CMB fluctuations. On the other hand, the temperature profile of the rescaled stack is closer to expectations, with a higher significance cold spot in the centre. Again, no signal of particular importance arises from this new analysis of Pan12 voids (except at very small angular sizes, most likely due to random fluctuations and not in relation to any underlying structure). Concerning the Sut12 catalogue, signals seem to arise in several of the rescaled profiles, especially on a scale equal to 0.5-0.55 times the voids effective radii, with a clear departure from the previous (without rescaling) results for some of the subsamples. However, some other subsamples do not benefit from the rescaling procedure. A possible explanation may come from the presence in these particular subsample of some of the largest voids in the whole Sut12 catalogue, which are supposed to yield the strongest iSW effect.

This indicates that instead of considering each subsample separately, a better approach may be to combine them all and stack the voids starting from the largest ones. Indeed, in theory the noise should scale as usual roughly as the inverse square root of the number of stacked voids, but the stacked iSW signal is also expected to drop at some point due to the addition of smaller and less contributing voids. By starting from the largest voids, we intend to select the supposedly largest iSW contributions in order to keep the stacked signal from dropping too fast and effectively to boost the S/N of the detection. We carried out this analysis on the 1495 voids of Sut12, first focusing on the whole photometry profiles and increasing progressively the number of stacked voids. As expected, a negative signal consistently appears around an aperture of 0.54 times the voids effective radii. As intuited before, its amplitude gradually decreases as we include smaller and smaller voids in the stacking. To estimate the significance of this signal, we focus on the value of the photometry at this particular aperture scale. Similarly to the previous section, we estimate the significance of these values by repeating the analysis many times after randomly shifting the stacked positions. We note once again that the photometry is stable across frequencies and consistently negative for practically any number of stacked voids, but the shape of this curve and its significance are hard to interpret. The significance first rises up to $\sim 2.3\,\sigma$ for the first 200 stacked voids, a behaviour that would be expected from an ISW signal that progressively takes over the CMB noise. After this, the S/N quickly decreases and then oscillates between about $1\,\sigma$ and $2\,\sigma$ before dropping, after stacking more than 1300 voids. Although this significance appears to vary quite significantly, the stability of the signal itself (always negative and on the same scale) may indicate that this variability is due to random CMB fluctuations. In summary, the rescaling process had positive results on the much larger catalogue of Sut12, highlighting a particular scale around half the void sizes in all the tests performed, in apparent agreement with both intuitive arguments and theoretical works in the literature. Although the maximum observed significance only reaches around $2.3\,\sigma$ and the signal depends quite significantly on the number of stacked voids and their size, the persistent nature of the signal seems to bolster the case for iSW detection.

5 Conclusions

In this work, we revisited the stacking of voids in CMB maps as a potential probe of dark energy through the expected iSW effect from these structures. We devised a complete protocol for a stacking procedure from a careful choice of maps to a rigorous estimation of the significance. We first applied it to the catalogue of voids of Gr08 and did not find any significant difference, if not a little weaker signal and associated S/N (by $0.4\,\sigma$). We then extended the analysis to two new void catalogues by Pan et al. (2012) and Sutter et al. (2012). The first did not yield any significant result, most likely owing to the limited range of redshift and radii of the sample. The second new catalogue, however, hinted at more significant signals (although not nearly as strong as the Gr08 results) with a trend for the preferred scale in the signal, which seemed to point to half the mean size of the voids used in the stacking. This was not found with the Gr08 voids, for which the highest significance scale was close to the mean void size, but it is more coherent with our expectations because of the irregular geometry of the stacked voids. In any case, the rescaling of the CMB patches (according to the void sizes) prior to stacking proved to be a mandatory step toward obtaining a significant signal in the photometry profiles, especially in light of our results with the incremental stacking of the largest voids of the Sut12 catalogue.

Along with these results, we also addressed the risks of possible selection effects that could easily lead to an overestimation of the significance. We also stressed that the surface density of the voids within the SDSS area make them overlap significantly, making it even more difficult to formulate clear expectations about, and interpretations of, the measured signals. Finally, it is known that voids are actually difficult to identify with

certainty and that one must proceed with caution when analysing such void samples. Another instance of this is that while being identified in the same SDSS DR7 set, two void subsamples of Sut12 lie within the same redshift range as the voids identified by Pan12, but they cover quite a different range in size and are distributed differently in redshift. We argue, therefore, that, combined with the unavoidable overlap of voids along a line of sight mentioned above, any claim of a detection of an iSW-like signal by the stacking of voids and/or claim of an oddity with respect to ΛCDM would be premature.

References

Granett, B. R., Neyrinck, M. C., & Szapudi, I. 2008, ApJ, 683, L99

Hoyle, F. & Vogeley, M. S. 2002, ApJ, 566, 641

Ilić, S., Langer, M., & Douspis, M. 2013, A&A, 556, A51

Pan, D. C., Vogeley, M. S., Hoyle, F., Choi, Y.-Y., & Park, C. 2012, MNRAS, 421, 926

Planck Collaboration. 2013, ArXiv:1303.5079

Sutter, P. M., Lavaux, G., Wandelt, B. D., & Weinberg, D. H. 2012, ApJ, 761, 44

SF2A 2013
L. Cambrésy, F. Martins, E. Nuss and A. Palacios (eds)

THE SEARCH FOR NEW MILKY WAY DWARF GALAXIES IN THE PAN-STARRS 1 PANOPTIC SURVEY

B. P. M. Laevens[1,2], N. F. Martin[1,2], H.-W. Rix[2] and Pan-STARRS 1 collaboration

Abstract. We present the latest results of the on-going search for faint dwarf galaxies in the surroundings of the Milky Way within Pan-STARRS 1 data. Covering three quarters of the sky the on-going Pan-STARRS 1 survey is a photometric survey in optical and near-infrared bands. Applying a convolution method to identify overdensities, followed by a preliminary analysis of the object detection significance led to no obvious dwarf galaxy candidates in regions of the sky not previously surveyed by the Sloan Digital Sky Survey. This result questions the isotropy of the Milky Way dwarf galaxy satellite system.

Keywords: Dwarf Galaxies, Pan-STARRS

1 Introduction

Over the course of the last forty years, Local Group dwarf galaxies (DGs) have been a source of increasing interest for a variety of reasons. Such galaxies are the faintest and smallest galaxies known, with large mass to light ratios. They are probes of both the dark matter (DM) on the galactic scale, and of the faint end of galaxy formation. The first eight Milky Way (MW) DGs were found through visual inspection of photographic plates, making up the MW 'Classical' DGs. Aside from the serendipitous discovery of Sagittarius through spectroscopy (Ibata et al. 1994), a veritable explosion of DG discoveries was made with the advent of deep photometry from the Sloan Digital Sky Survey (SDSS) bringing the total census of MW DGs to 25 (see Walker 2013 for a review).

Milky Way dwarf galaxies, as well as those orbiting M31 have been of increasing interest given their apparent tension with two tenets of galaxy formation in a ΛCDM universe. The number of DGs that we observe is at least an order of magnitude lower than the number of DM haloes predicted from simulations. Why is only a fraction of the DM haloes populated? The so-called Missing Satellite Problem (Klypin et al. 1999; Moore et al. 1999) can be solved by several mechanisms linked to galaxy formation physics (re-ionisation, supernova feedback,... e.g. Macciò et al. 2010). Secondly, observations as early as Lynden-Bell (1976) suggest the anisotropic orientation of DGs around the MW, another aspect not generally accepted by simulations. Indeed recently it was shown by Ibata et al. (2013) that ~ 50 % of M31's DGs lie in 'a vast thin plane'. Similar recent results re-emphasise this observation around the MW, in the form of the Vast Polar Structure of Satellite Galaxies (VPOS) (Pawlowski et al. 2012).

The Panoramic Survey Telescope And Rapid Response System 1 (Pan-STARRS 1 or PS1) has the major advantage of providing a homogeneous coverage of three quarters of the night sky. Even though its depth is similar to that of the SDSS, its spatial extent is at least double that of the SDSS data release used for DG searches, thereby opening up a sizeable new area to the search for faint MW companions. In particular, and contrary to the SDSS, PS1 covers a sizeable region outwith the plane of satellites, thereby allowing for a clear test of the validity of the VPOS. Here, we report on our on-going search for unknown DGs around the MW within the single-epoch data of the survey.

[1] Observatoire astronomique de Strasbourg, Université de Strasbourg, CNRS, UMR 7550, 11 Rue de l'université, F-67000 Strasbourg, France
[2] Max-Planck Institut für Astronomie, Königstuhl 17, D-69117 Heidelberg, Germany

2 The Pan-STARRS 1 Survey

Pan-STARRS 1 is a 3.5 year survey targeting three quarters of the total sky, northwards of $\delta = -30^{o}$, hence it is also known as the PS1 3π Survey. Using a 1.8 metre telescope in Haleakala, Hawaii, in combination with a 1.4 GPixel camera and field of view of 3.3 degrees, data is collected in five optical and near-infrared bands: g_{P1}, r_{P1}, i_{P1}, z_{P1} and y_{P1}. The sky is observed four times per year per filter over the course of the survey's duration. In these proceedings, only data produced from the individual images are used, yielding photometric depths that are ~ 1 magnitude shallower than the SDSS.

3 Dwarf Galaxy Detection Algorithm

To find DGs over large areas of sky, an automated detection algorithm is necessary, allowing for spatial overdensities of rightfully coloured stars, potentially corresponding to new DGs, to be extracted from the 2 billion stars of the survey. Such methods have successfully been applied in the past and identified new DGs in the SDSS (Koposov et al. 2008; Walsh et al. 2009). Therefore, a similar technique as described in the aforementioned Koposov et al. (2008) paper is applied in these proceedings, but modified and adapted to the intricacies of the PS1 data.

The spatial location of stars with appropriate colours and magnitudes is convolved with a composite kernel that include a peaked positive Gaussian of the expected size of a DG, and a negative contribution of a much wider Gaussian that subtracts the contribution of the contaminating sources in the surrounding field to the signal measure. Varying the size of the positive part of the kernel allows us to search for stellar overdensities of varying sizes.

Before conducting the convolution, the data are prepared in the following way: all magnitudes are de-redenned using the Schlegel et al. (1998) maps, in combination with the extinction coefficients for PS1 (Schlafly & Finkbeiner 2011), accounting for the presence of dust; likely extended objects are weeded out by requiring similar aperture and psf magnitudes for an object; and colour and magnitude cuts are applied. In detail, only stars bluer than $r - i = 0.8$ are considered as observable stars from a MW satellite at tens to a few hundred kiloparsecs and are unlikely to be redder than this limit. Furthermore, to avoid the presence of faint artifacts in the data, we cull the catalogue to only keep stars with r_0<21.5 and i_0<21.5.

Due to the nature of the single epoch PS1 data, this work also accounts for the lack of data in the form of holes present in the survey. These holes are mainly due to chip gaps and bad weather. To this end, for a given band, the sky is binned into 0.5x0.5 arcmin^2 pixels. For each pixel, the closest star that appears in two other bands is determined. If this star is also present in the band of interest, then that pixel is deemed to be complete, else not. The completeness mask thereby inferred is folded in the convolution calculation.

4 Detection Significance

The convolution algorithm is applied to the whole PS1 sky for a grid of centres separated by only 2 arcminutes. It yields a fine-scale image of the local stellar under- or overdensities in the shape of the chosen Gaussian. In order to determine the significance of a given pixel, we compare its value to the rms value of all neighbouring pixels within a box of four square degrees. We consider only detections of overdensities that are at least 4-sigma above the background and produce a list of candidates to investigate further. A Colour-Magnitude Diagram (CMD) of the identified candidate is compared to a neighbouring field region to check for the presence of CMD features expected for a DG (main sequence turn-off, red giant branch, horizontal branch,) Artifacts in the data catalogue available at the time of this search generate artificial detections that can easily be sieved out of the candidate list. Nevertheless, known faint dwarf galaxies discovered in the SDSS are recovered, as examplified in Figure 1 for Canes Venatici I (CVnI). The left panel shows the convolution map for the patch of the sky that includes CVnI, while the right panel shows the significance map of the same region. Figure 2 shows two CMDs containing the CMD for CVnI and a field region. All CMD objects are ones that satisfy the colour-box criterion discussed in section 3.

Applying the detection algorithm along with the significance analysis allows for the most booming and obvious SDSS satellites to rediscovered. Amongst those detected are Böotes I, CVnI and Ursa Major II. No new DG is

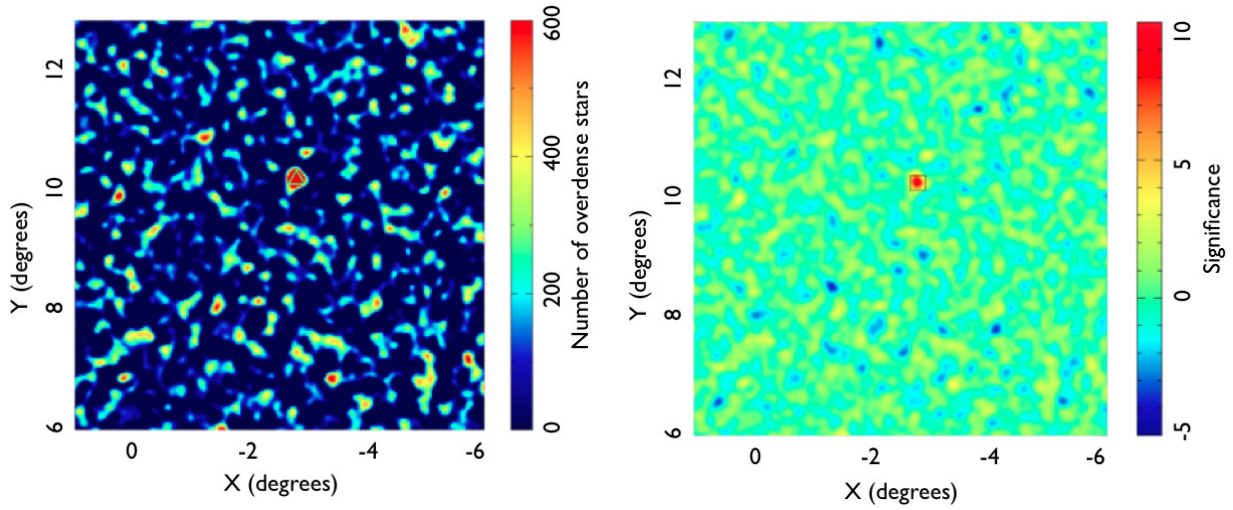

Fig. 1. Left: Differential Image Map representing the integrated counts under the kernel after convolving data with a kernel of positive/signal Gaussian width 4' and negative/background Gaussian width 20'. The green triangle shows the location of CVnI at $X = -2.8^{o}$ and $Y = 10.2^{o}$ **Right:** The corresponding significance map, highlighting CVnI as a detection with a signal-to-noise ratio above 10.

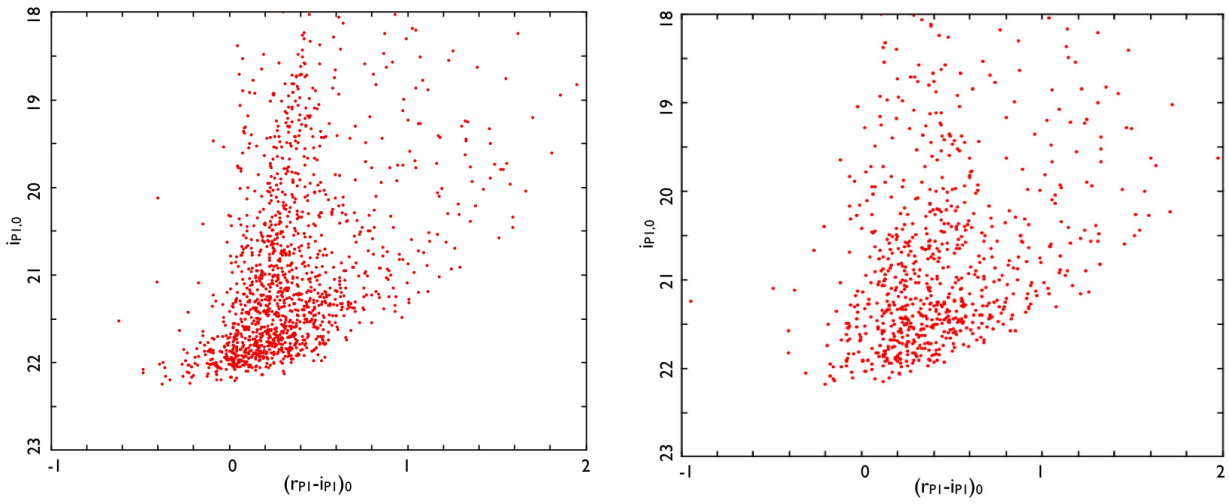

Fig. 2. Left: PS1 CMD of CVnI. The red giant branch stars of CVnI are clearly visible and produce the high-significance detection visible in Figure 1 **Right:** PS1 CMD of field region in the vicinity of CVnI.

confidently identified, even in the large regions that were not covered by the latest SDSS-based DG searches.

5 Results and Conclusion

We report on our on-going search for the presence of new MW DGs in the panoptic PS1 survey. Candidate detections are identified by convolving the stellar catalogue generated from the single epoch PS1 data, accounting for the spatial inhomogeneity of the survey's footprint. However, despite the detection of some of the faint DGs found in the SDSS, no obvious new DG candidate can be identified.

This preliminary result could partly stem from the use of the shallow single epoch PS1 data and we are currently conducting a more in-depth analysis based on the full depth catalogues, However, if it holds true , this result

would certainly question the isotropy of MW satellites around their host.

References

Ibata, R. A., Gilmore, G., & Irwin, M. J. 1994, Nature, 370, 194
Ibata, R. A., Lewis, G. F., Conn, A. R., et al. 2013, Nature, 493, 62
Klypin, A., Kravtsov, A. V., Valenzuela, O., & Prada, F. 1999, ApJ, 522, 82
Koposov, S., Belokurov, V., Evans, N. W., et al. 2008, ApJ, 686, 279
Lynden-Bell, D. 1976, MNRAS, 174, 695
Macciò, A. V., Kang, X., Fontanot, F., et al. 2010, MNRAS, 402, 1995
Moore, B., Ghigna, S., Governato, F., et al. 1999, ApJ, 524, L19
Pawlowski, M. S., Pflamm-Altenburg, J., & Kroupa, P. 2012, MNRAS, 423, 1109
Schlafly, E. F. & Finkbeiner, D. P. 2011, ApJ, 737, 103
Schlegel, D. J., Finkbeiner, D. P., & Davis, M. 1998, ApJ, 500, 525
Walker, M. 2013, Dark Matter in the Galactic Dwarf Spheroidal Satellites, ed. T. D. Oswalt & G. Gilmore, 1039
Walsh, S. M., Willman, B., & Jerjen, H. 2009, AJ, 137, 450

SF2A 2013
L. Cambrésy, F. Martins, E. Nuss and A. Palacios (eds)

OPTICAL STUDY OF THE DAFT/FADA GALAXY CLUSTER SURVEY

N. Martinet[1], F. Durret[1], D. Clowe[2], C. Adami[3] and the DAFT/FADA team

Abstract. DAFT/FADA (Dark energy American French Team) is a large survey of ∼90 high redshift ($0.4 < z < 0.9$) massive (M$> 2 \times 10^{14}$ M$_\odot$) clusters with HST weak lensing oriented data, plus BVRIZJ 4m ground based follow up to compute photometric redshifts. The main goals of this survey are to constrain dark energy parameters using weak lensing tomography and to study a large homogeneous sample of high redshift massive clusters. We will briefly review the latest results of this optical survey, focusing on two ongoing works: the calculation of galaxy luminosity functions from photometric redshift catalogs and the weak lensing analysis of ground based data.

Keywords: Galaxies: clusters, luminosity function - Lensing: weak lensing

1 Introduction

The DAFT/FADA (Dark energy American French Team) project (`http://cencos.oamp.fr/DAFT/`) has been undertaken to tackle some questions of modern cosmology, such as the acceleration of the expansion of the Universe, the large scale structure formation and the Universe content. Galaxy clusters are particularly important in this context (e.g. Nichol (2007)). The two main goals of this large cluster survey are to build a large cluster database to mine for years, and to apply weak lensing tomography on a test sample to constrain dark energy and prepare future very large tomography surveys.

DAFT/FADA is a large survey of ∼90 high redshift ($0.4 < z < 0.9$) massive ($M > 2 \times 10^{14} M_\odot$) clusters. All of them have HST data (ACS or WPC2) allowing a weak lensing analysis. Thanks to archive data and about 70 nights granted to the survey on 4m class telescopes, we built a ground based follow up in the BVRIZ optical bands and in the J near infrared band (see `http://cencos.oamp.fr/cgi-bin/DAFT/daft_status.pl` for the detailed status of the survey). This multi-band database enables us to measure reliable photometric redshifts (see Guennou et al. (2010)). This exceptional data set will be used to perform weak lensing tomography with clusters (WLTC). This technique is based on the idea that every background galaxy around the cluster is weakly lensed, so the signal from the combination of all the background galaxies around the cluster can be measured at high signal-to-noise levels, over a large range of radii (see e.g. Jain & Taylor (2003)). This shear signal combined with the photometric redshifts of the background galaxies provide a purely geometrical method for determining w (the parameter in the dark energy equation of state). We already performed the weak lensing analysis of a subsample of about 10 ACS clusters (Murphy et al. (2013)) but need more clusters to get an estimation of w.

The ground based data have also been used to investigate some cluster properties such as the intra cluster light in distant clusters (Guennou et al. (2012)). Combining those with X-ray archive data (when available) and spectroscopic data, we investigated the evolution of substructures within clusters (Guennou et al. (2013a)) and conducted a joint strong lensing and dynamic study for the very massive cluster LCDCS0504 (Guennou et al. (2013b)).

Here we present two ongoing works: the calculation of galaxy luminosity functions from photometric redshift catalogs and the weak lensing analysis of ground based data. The first one will allow us to better understand

[1] UPMC Université Paris 06, UMR 7095, Institut d'Astrophysique de Paris, 98bis Bd Arago, F-75014, Paris, France, email: martinet@iap.fr

[2] Department of Physics and Astronomy, Ohio University, 251B Clippinger Labs, Athens, OH 45701

[3] LAM, OAMP, Université Aix-Marseille & CNRS, Pôle de l'Etoile, Site de Château Gombert, 38 rue Frédéric Joliot-Curie, 13388 Marseille 13 Cedex, France

the optical behavior of clusters and their evolution with redshift. The second one will come as a complement to the substructure study already done with X-rays and spectroscopic data (Guennou et al. (2013a)) and will provide us with a shear catalog both deep and large, when combined with the HST imaging shear catalog.

2 Galaxy Luminosity Function

The current model of the Universe starts with the Big Bang and predicts the evolution of the density and density perturbation growth leading to the formation of large scale structures. In this framework, building a detailed picture of galaxy and large-scale structure growth is necessary to understand the Universe evolution. To achieve these goals we propose to analyse the evolution of the galaxy luminosity function (GLF) of clusters with both redshift and mass. There are contradictory results concerning the evolution of the faint end of the GLF which is said to decrease (Rudnick et al. (2009)) or to be constant (De Propris et al. (2013)) with redshift. Our sample presents a good redshift coverage and we should be able to discriminate between the two observed behaviours when the analysis is complete (Martinet et al. 2014, in preparation).

Magnitudes are extracted via the MAG_AUTO keyword of SExtractor (Bertin & Arnouts (1996)) on BVRIZ and J band images. We then cross-correlate our catalogs with a 2 arcsec matching radius. We compute our final photometric redshift (photo-z) catalog by applying the LePhare software (Arnouts et al. (1999), Ilbert et al. (2006)). LePhare compares the sampling of the spectrum with several theoretical spectral energy distributions and comes up with the best theoretical set of properties corresponding to the galaxy under study (photo-z, type, k-correction, color...). As we are using data from various telescopes we ask LePhare to model all the magnitudes as if the images had been taken at the VLT. Finally we correct for galactic extinction using the cirrus maps of Schlegel et al. (1998).

Cluster members are determined in a semi-statistical way, selecting galaxies with photometric redshifts in a $\pm$ 0.2 range from the cluster redshift. We then calculate a luminosity function in bins of 0.5 magnitude and retrieve field galaxy counts calculated in the same redshift and magnitude intervals by Ilbert et al. (2005). To be able to fit a Schechter function (Schechter (1976)) we then need to estimate the completeness of our sample. To do this we model a gaussian point spread function (PSF), include it in the image with a given magnitude and redetect it. The PSF is first estimated from the image stars using PSFEx (Bertin (2011)). We model a hundred stars for each bin of 0.5 magnitudes and try to redetect them. When the redetection rate is inferior to 90% we consider that we have reached the acceptable star completeness. The 90% completeness on galaxies is estimated to be lower than that of stars by $\sim$0.5 magnitude (e.g. Adami et al. (2006)), depending also on the galaxy type. As an example, the GLF of MS 1054-03 (hereafter MS 1054) in the R band is shown in Fig. 1 along with its best fit Schechter parameters. The fit is shown in red and only galaxies brighter than the 90% completeness limit (red vertical line) are taken into account.

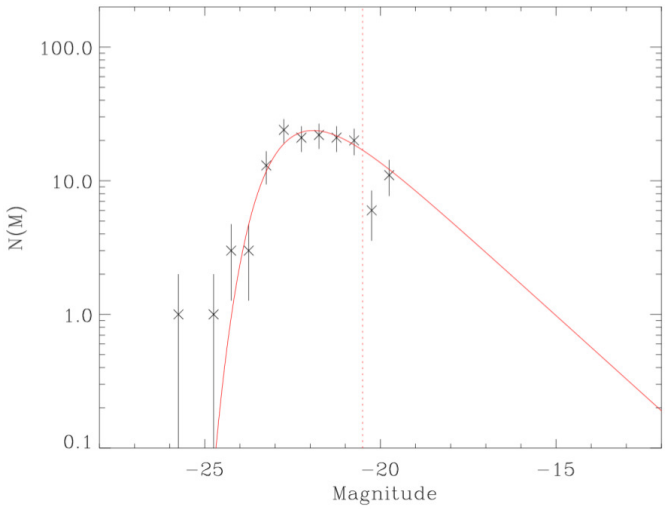

	Schechter parameters
α	-0.41 $\pm$ 0.32
M*	-22.48 $\pm$ 0.34
ϕ*	63.7 $\pm$ 15.8

Fig. 1. MS 1054-03 (z=0.8231) R band galaxy luminosity function and parameters corresponding to the best fit by a Schechter function (red curve). The vertical red line shows the 90% completeness. Only galaxies brighter than this limit are taken into account when performing the fit.

The faint end slope of the Schechter fit to the GLF of MS 1054 is $\alpha = -0.41$. This is far from the usual slope of about -1 found for low redshift clusters (e.g. De Propris et al. (2013)). However, MS 1054 is at a redshift $z = 0.8231$ and this decrease of the faint end of the GLF could be in agreement with the behaviour of high redshift clusters observed by Rudnick et al. (2009). Of course, these are only preliminary results and we still have to check all the possible systematics in our analysis. For example, when combining our photometric catalogs we lose all the objects that are not detected in all 6 bands. This will be addressed soon by applying a completeness correction using single band catalogs.

3 Ground Based Weak Lensing

Since HST data are available for all the DAFT/FADA clusters, one could ask why bother making a weak lensing (WL) analysis on ground based data. Indeed, data from space are not contaminated by our atmosphere and therefore reach a much better seeing and completeness. However, even if ground based data are of lower quality, they are very useful because they cover a field of view much larger than that of the HST (3.4'×3.4' for ACS). With wider ground based images we will better sample the cluster to its outskirts, while the HST data only give access to the cluster core. In particular, WL on large fields will allow to study the substructures of clusters and to compare them with those detected from optical spectroscopy and from X-rays by Guennou et al. (2013a) and will help to break the mass sheet degeneracy to increase the accuracy of the WLTC. The final objective is to combine shear catalogs from HST and ground based images to obtain a shear catalog which is both large and deep in the cluster center.

The principle of lensing studies is to connect the distortion of light on background galaxies due to a foreground object called the lens. This distortion results in a size and shape modification (respectively the convergence and shear) of the lensed background galaxy images which are proportional to a linear combination of the second derivatives of the lens potential and to the ratio of the source and lens distances to the observer. In our case the measurement of the ellipticity of background galaxies lensed by a cluster gives access to the mass distribution of the cluster, knowing all distances through the calculated photometric redshifts. Our WL reduction follows the usual KSB method (Kaiser et al. (1995)). The main point is to measure the anisotropy of the instrument PSF on the stars found in the image and then to correct the galaxy shapes from this instrumental bias using some mathematical recipes. This method relies on the gaussianity of the PSF which can be a strong approximation for some instruments. Once we obtain corrected galaxy shapes, we reduce the noise by fitting the shear sample with polynoms and regenerating less noisy shear values. We also applied our programs to the simulated fields of STEP2 (Massey et al. (2007)) with constant shear in order to measure the bias of our technique. We found a 13% bias that we corrected for in our analysis. Object positions and magnitudes are extracted with SExtractor (Bertin & Arnouts (1996)) while ellipticities are measured with the IMCAT software (`http://www.ifa.hawaii.edu/~kaiser/imcat`).

The final step is to separate the background galaxies from the cluster members and the foreground galaxies. This is necessary to avoid diluting the shear signal when taking into account the ellipticities of galaxies which are not lensed by the cluster, and is usually done through a color color cut. As colors of galaxies reflect their components, they are linked to the galaxy formation history. Hence, using Bruzual & Charlot (2003) we can compute the theoretical color a galaxy should have according to its type and redshift. Fig. 2 shows a (B-V) versus (V-I) color–color cut diagram for LCDCS0541. The dashed region is the region removed from our catalog as corresponding to cluster members and foreground galaxies. Note that after we have all the photo-zs in hand we will perform a more acccurate cut, identifying the galaxies for which we are able to calculate the redshift.

A detection significance is obtained by fitting a singular isothermal sphere (SIS) profile centered on the optical center of the cluster (i.e. the BCG). The shear is then averaged in boxes and smoothed with FFT to draw contours of iso-mass on the original image. A comparison between the results obtained from the space analysis (Murphy et al. (2013)) and from the ground is given in Fig. 3 in the case of LCDCS0541. Both contour maps encircle the optical center and the detection significance is very similar: 7.9σ with VLT/FORS2 and 7.8σ with HST/ACS.

4 Conclusions

DAFT/FADA is a promising survey especially in terms of both cluster properties and lensing studies. As explained in the introduction we have already obtained some nice results using the optical data we have in hand: a large photometric redshift sample (Guennou et al. (2010)), an analysis of the intra cluster light of

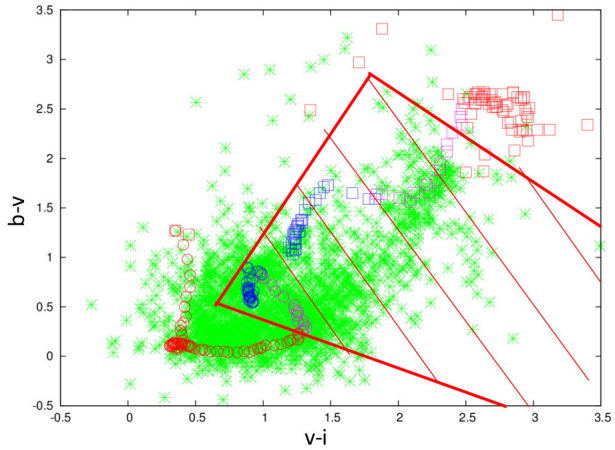

Fig. 2. B-V versus V-I color color diagram for LCDCS0541. Green crosses correspond to all observed galaxies. Blue, purple and red circles respectively correspond to theoretical spiral galaxies lower, in and higher than the interval of ± 0.2 around the redshift of the cluster. Blue, purple and red squares respectively correspond to theoretical elliptical galaxies lower, in and higher than the interval of ± 0.2 around the redshift of the cluster. The dashed region is the region removed from our catalog as corresponding to cluster members and foreground galaxies.

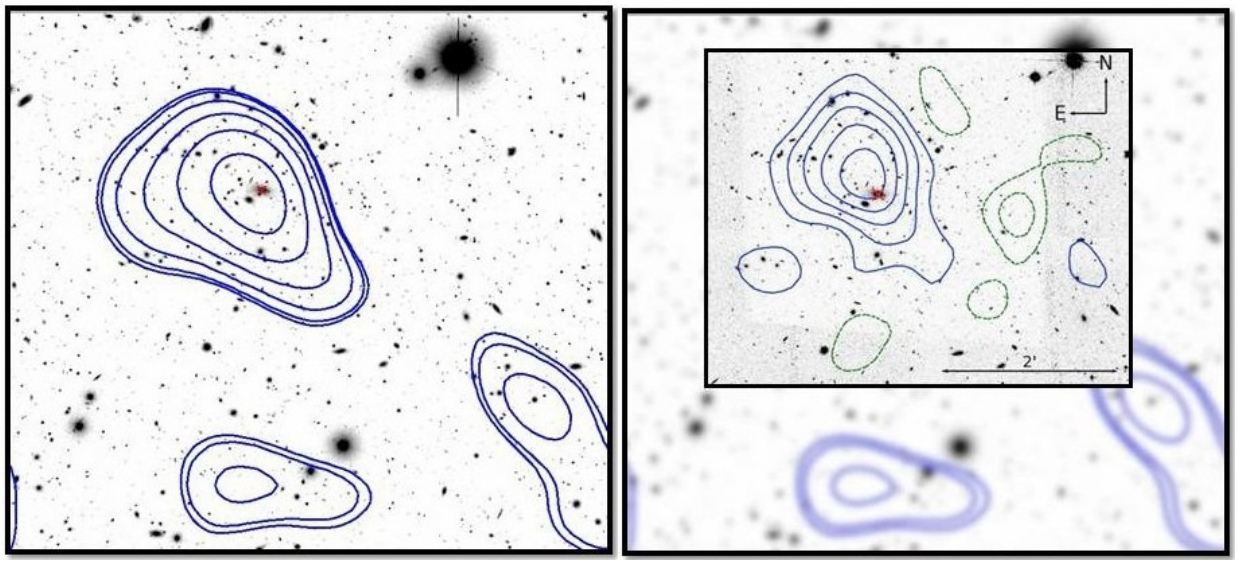

Fig. 3. Left: mass contour map of LCDCS0541 based on VLT/FORS2 data. The level of the weak lensing detection is 7.9σ. **Right:** mass contour maps of LCDCS0541 computed from 5 HST/ACS fields superposed to the ground based map. The level of the weak lensing detection is 7.8σ. Red crosses correspond to the optical cluster center.

distant clusters (Guennou et al. (2012)), an HST/ACS weak lensing reduction pipeline (Murphy et al. (2013)), a detailed picture of cluster substructures based on X-rays and optical spectroscopy (Guennou et al. (2013a)), and the detailed study of one cluster core with strong lensing and dynamics (Guennou et al. (2013b)).

We presented here two ongoing works with some nice prospects. First we showed how we computed the luminosity function of clusters using photometric redshifts. Note that the redshift coverage of our sample should allow us to discriminate between the two current behaviors of the faint ends of the GLF observed in the literature. Then we depicted how we conducted the weak lensing analysis on ground based images. We showed that even if ground based data are less deep than HST data, they allow to achieve comparable results thanks to their larger field of view. Our ultimate goal is therefore to merge both space and ground based catalogs to get a shear catalog which is deep in the cluster core and reaches the cluster outskirts with a lower galaxy density.

Acknowledgements: We acknowledge long term financial support from CNES.

References

Adami et al. 2006, A&A 451, 1159
Arnouts et al. 1999 MNRAS, 310, 540
Bertin, E. & Arnouts, S. 1996, A&AS 317, 393
Bertin 2011, ASPC 442, 435
Bruzual & Charlot 2003, MNRAS 344, 1000
De Propris et al. 2013, arXiv:1307.1592
Guennou et al. 2010, A&A 523, 21
Guennou et al. 2012, A&A 537, 64
Guennou et al. 2013a, A&A submitted
Guennou et al. 2013b, A&A submitted
Ilbert et al. 2005, A&A 439, 863
Ilbert et al. 2006, A&A, 457, 841
Jain & Taylor 2003, PhRvL, 91, 1302
Kaiser et al. 1995, ApJ 449, 460
Massey et al. 2007, MNRAS 376, 13
Murphy et al. 2013, ApJ submitted
Nichol 2007, ASPC, 379, 89
Rudnick et al. 2009, ApJ 700, 1559
Schechter 1976, ApJ 203, 297S
Schlegel et al. 1998, ApJ, 500, 525

SF2A 2013
L. Cambrésy, F. Martins, E. Nuss and A. Palacios (eds)

THE EXTENDED HI DISK OF THE NEARBY SPIRAL GALAXY NGC 2683

F. Nehlig[1], B. Vollmer[1] and R. Ibata[1]

Abstract. New deep VLA HI observations of the nearby spiral galaxy NGC 2683 are presented. A kinematic model was made in order to reproduce both, high resolution (VLA C+D array with a resolution of 20") and low resolution (VLA D array with a resolution of 1') data cubes. Using two different resolutions to match the model gives precious additional constraints to deal with a degenerated parameter space. Different flares, heights, warps and velocity lags as a function of galactic radius were tested. The thin HI disk shows an exponential flare beyond the optical radius which saturates at large radii. A warp component is seen but only within the optical radius. Multiple complex substructures were detected within the HI flare. The presence of an HI halo around the optical disk was also tested and excluded. This work gives insight into the recent gas accretion history of this nearby spiral galaxy.

Keywords: Galaxies: individual: NGC 2683 - Galaxies: ISM - Galaxies: Kinematics and dynamics

1 Introduction

The HI disk of galaxies can be perturbed by outflows from the star forming disk or from external gas infall. Internal perturbation, as galactic fountains (see Shapiro & Field 1976; Fraternali & Binney 2006, and references therein) can significantly affect the HI disk via stellar winds and supernova explosions. Fraternali et al. (2005) argued that a galactic fountain could be responsible of the velocity lag observed in the high-latitude gas of NGC 891. Accretion of intergalactic gas via merging of small gas-rich satellites (van der Hulst & Sancisi 2005) is another way to perturb the HI disk. Evidence of such merging can be found by studying the morphologies of HI disks, which often present warps or disk lopsidedness (Sancisi et al. 2008). Moreover, it is still not clear which role the atomic gas disk plays in the galaxy ecosystem (Schiminovich et al. 2010). To further investigate the role of the HI disk for the evolution of a spiral galaxy, NGC 2683 is a good candidate. NGC 2683 is an Sb spiral galaxy located at a distance of 7.7 Mpc (Tonry et al. 2001). The vertical profile of the gas is directly accessible since the galaxy is viewed edge-on. Casertano & van Gorkom (1991) observed NGC 2683 during 1h with the VLA in D array configuration. They found that the gas distribution is fairly symmetric and close to the plane of the optical disk. The derived rotation curve peaks at about 215 km s^{-1} at $\sim$ 3 kpc from the galaxy center and then decreases monotonically.

In the present work we aim to characterize the presence of a flare, a warp, a halo component and a kinematic lag in NGC 2683. We compared our kinematic models of the HI disk to both, high (C+D array) and low (D array) resolution new VLA observations.

2 Observation and data reduction

NGC 2683 was observed in December 2009 during 9h with the VLA in D array configuration. The total bandwidth of 3.125 MHz was divided into 128 channels with a channel separation of 5.13 km s^{-1}. Calibration was achieved using VLA standard calibration procedure. We obtained an rms noise level of 1. mJy/Beam in a 5 km s^{-1} channel. In addition, we also reduced 8.5 h of archival C array data. C and D array observations were combined into a single data set leading to a resolution of $21'' \times 20''$, with an rms noise level of 0.3 mJy/beam. The resulting HI gas distributions maps are presented in Fig. 1 at low (right panel) and high resolution (left panel). As observed by Casertano & van Gorkom (1991), the atomic hydrogen is distributed over a diameter of $26.5'$, i.e. almost 3 times the optical radius. A ring-like structure can also be seen at the extremity of the HI disk, offset by about 1 kpc from the optical disk. The high resolution data (C+D array) shows multiple and complex substructures.

[1] Observatoire astronomique de Strasbourg, 11,rue de l'université,67000 Strasbourg, France

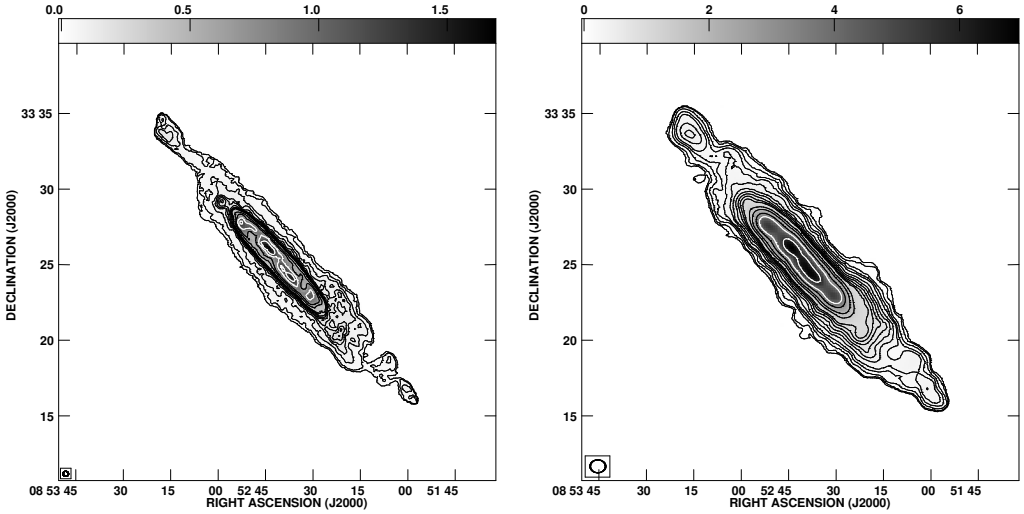

Fig. 1. Left panel: HI gas distribution of NGC 2683 C+D array observations. The beam size is $21'' \times 20''$. The contours levels are $(2, 4, 6, 8, 12, 16, 20, 24, 28, 32, 48, 64, 96, 128, 192, 264, 392) \times 10$ mJy/beam km s^{-1} or 2.6×10^{19} cm^{-2}. Horizontal wedge is in units of Jy/beam km s^{-1}. Right panel: HI gas distribution of NGC 2683 D array observations. The beam size is $61'' \times 51''$. The contours levels are $(1, 2, 4, 6, 8, 12, 16, 20, 24, 28, 32, 48, 64, 96, 128, 192, 264, 392) \times 30$ mJy/beam km s^{-1} or 10^{19} cm^{-2}. Horizontal wedge is in units of Jy/beam km s^{-1}.

3 The kinematic model

3D modeling was made using a symmetric mean rotation velocity. The HI surface density was de-projected following Warmels (1988). Using the rotation curve and the de-projected HI surface density profile, we can create a model data cube. The presence of a thin disk, a gas halo around the thin disk, a velocity lag, a warp contribution, and different flares were all tested with different inclination angles of the disk. Simulations can been seen in Fig. 2 in four characteristic velocity channels for the low resolution and the high resolution. The resulting total emission map are presented in Fig. 3. High resolution data give constraints on the inner thin disk, whereas low resolution allowed us to study the HI flare.

4 Results

4.1 The inner disk

The presence of a gas halo around the thin HI disk was tested in our kinematic model. The comparison between the gas halo model and the high resolution (VLA C+D array) data excludes the presence of an HI gas halo around the thin inner HI disk. The halo could not be studied with the D array data since high resolutions data are required to study this faint component of the galactic disk.

4.2 The flare of NGC 2683

The FWHM$_z$ thickness of the HI gas from NGC 2683 was derived and compared with the Milky Way FWHM$_z$ thickness (Kalberla & Kerp 2009), and a sample of 8 HI rich, late-type, edge-on galaxies from O'Brien et al. (2010). For NGC 2683, the HI characteristic exponential length scale of the flare is within the range of other spiral galaxies (see Fig. 4). The flare profile of NGC 2683 saturates at $R \sim 16$ kpc and decreases after $R \sim 25$ kpc. The HI ring structure begins at this latter radius. A warp component within the flare is added to better reproduce the data. The warp extends between $r \sim 7$ kpc and $r \sim 14$ kpc, the warp lines of nodes are located in the plane of the sky.

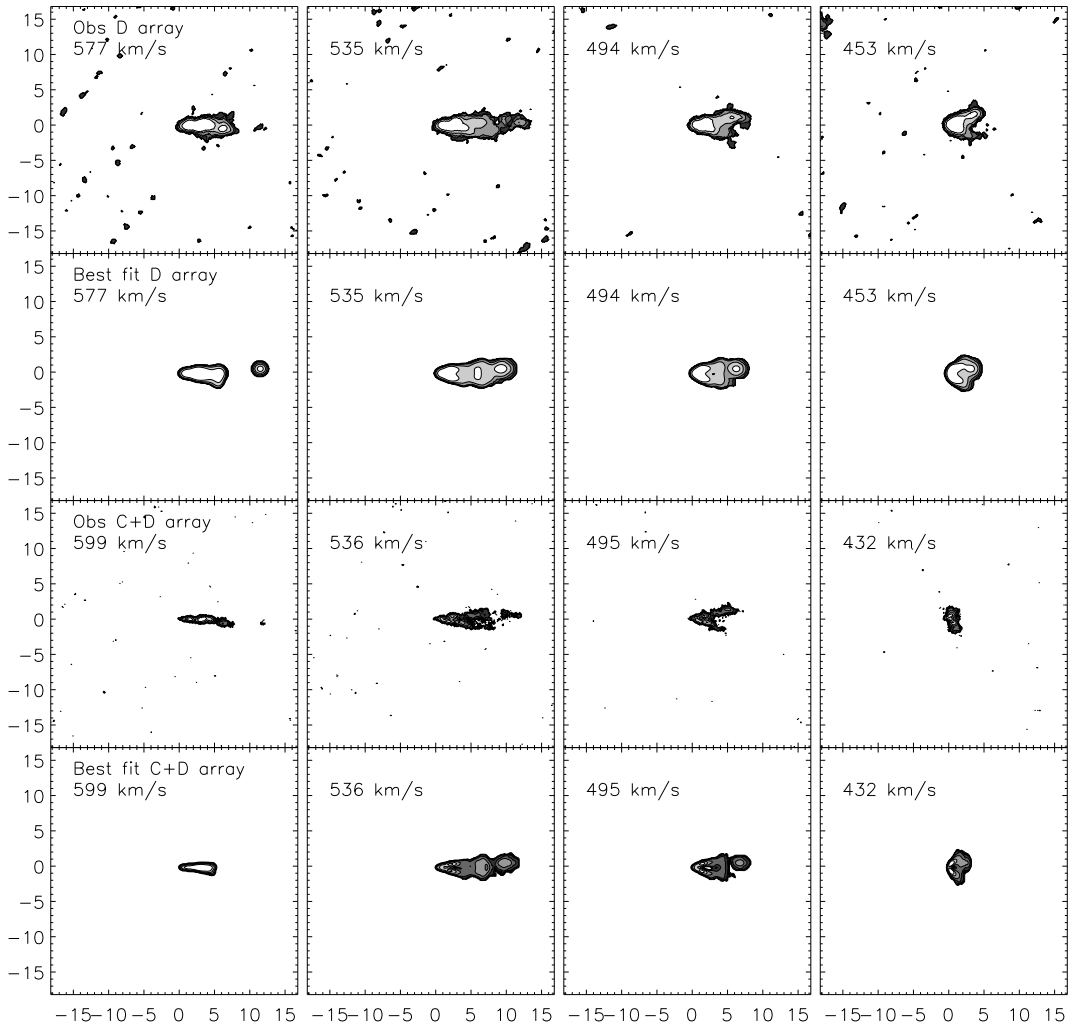

Fig. 2. High (1' resolution) and low (20" resolution) resolution observations and simulations. From top to bottom: D array observations in four characteristic velocity channels, Best fit model as it would be seen in the D array configuration, C+D array observations, Best fit model for the C+D array configuration. Contours levels are the same as for the observations.

5 Conclusion

New deep VLA HI observations of the nearby spiral galaxy NGC 2683 are presented. These new observations show multiple complex substructures in the HI flare, and the presence of an HI ring vertically offset from the disk plane at large radii. In addition to these observations, archival data were used to obtain two different resolution data sets. A 3D kinematic model was constructed to test the presence of a warp, a gas halo around the thin disk, a velocity lag, and a flare with various profiles. Whereas the low resolution data constrain the flare, the high resolution allowed us to study the inner HI disk. We excluded the presence of a gas halo around the inner thin HI disk. The best fit model contains a classical flare which saturates at a galactic radius of R $\sim$ 16 kpc. Significant and complex substructures were found within the flare. This study gives insight into the recent gas accretion history of this nearby spiral galaxy.

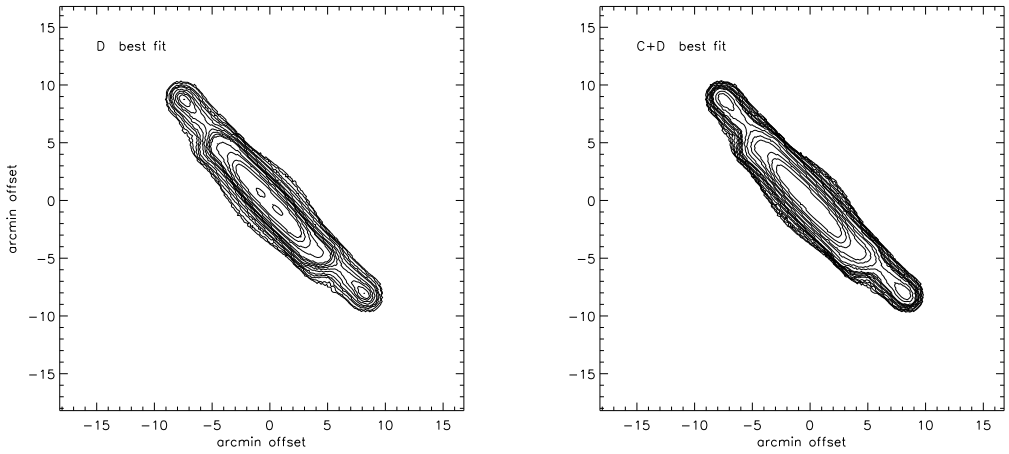

Fig. 3. High (right panel) and low (left panel) resolution simulations of the total emission map of NGC 2683, contours levels are the sames as for the observations (Fig. 1)

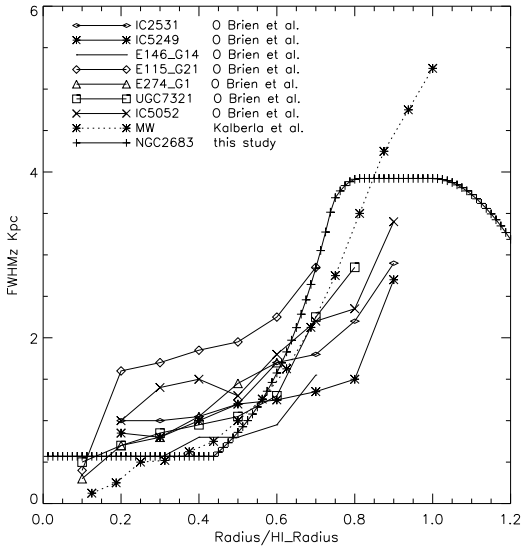

Fig. 4. Comparison between the best fit flare model, and flares of other spiral galaxies from the literature.

References

Casertano, S. & van Gorkom, J. H. 1991, AJ, 101, 1231

Fraternali, F. & Binney, J. J. 2006, MNRAS, 366, 449

Fraternali, F., Oosterloo, T. A., Sancisi, R., & Swaters, R. 2005, in Astronomical Society of the Pacific Conference Series, Vol. 331, Extra-Planar Gas, ed. R. Braun, 239

Kalberla, P. M. W. & Kerp, J. 2009, ARA&A, 47, 27

O'Brien, J. C., Freeman, K. C., & van der Kruit, P. C. 2010, A&A, 515, A62

Sancisi, R., Fraternali, F., Oosterloo, T., & van der Hulst, T. 2008, A&A Rev., 15, 189

Schiminovich, D., Catinella, B., Kauffmann, G., et al. 2010, MNRAS, 408, 919

Shapiro, P. R. & Field, G. B. 1976, ApJ, 205, 762

Tonry, J. L., Dressler, A., Blakeslee, J. P., et al. 2001, ApJ, 546, 681

van der Hulst, J. M. & Sancisi, R. 2005, in Astronomical Society of the Pacific Conference Series, Vol. 331, Extra-Planar Gas, ed. R. Braun, 139

Warmels, R. H. 1988, A&AS, 72, 427

SF2A 2013
L. Cambrésy, F. Martins, E. Nuss and A. Palacios (eds)

GAMMA-RAY BURSTS AS COSMOLOGICAL PROBES

S.D. Vergani[1]

Abstract.

Gamma-ray bursts (GRBs) are short, intense bursts of gamma-rays which during seconds to minutes outshine all other sources of gamma-ray emission in the sky. Following the prompt gamma-ray emission, an 'afterglow' of emission from the X-ray range to radio wavelengths persists up to months after the initial burst. The association of the class of long GRBs with the explosion of broad-line type Ic SNe hence with the death of massive stars, makes this class of GRBs a tracer of star formation across the observable Universe up to the highest redshifts. They can be used to probe the reionization and the first stars.

GRBs allow galaxies to be selected independently of their emission properties (independently of dust obscuration and, uniquely, independently of their brightnesses at any wavelength) and they also permit the study of the gas in the interstellar medium (ISM) systematically and at any redshift by the absorption lines present in the afterglow spectra. Moreover, the fading nature of GRBs and the precise localization of the afterglow allow a detailed investigation of the emission properties of the GRB host galaxy once the afterglow has vanished. GRBs therefore constitute a unique tool to understand the link between the properties of the ISM in the galaxy and the star formation activity, and this at any redshift. This is a unique way to reveal the physical processes that trigger galaxy formation.

The *SVOM* space mission project is designed to improve the use GRBs as cosmological probes.

Keywords: Gamma-ray burst: general, Cosmology: observations, early Universe, dark ages, reionization, first stars, Galaxies: evolution, Galaxies: ISM

1 Introduction

Gamma-ray bursts (GRBs) are the most extreme cosmic explosions. They are detected from space thanks to the flash of high-energy photons released within a transient relativistic jet, which signals the explosion. This short lasting *prompt emission* is followed by an *afterglow*, detectable from the X-ray to the radio wavelengths for hours to months, depending on the frequency domain and on its intrinsic brightness. The production of the ultra-relativistic jet is associated with the formation of a black hole by the explosion of a massive star or by the merger of two compact objects.

The study of GRBs impacts several branches of physics and astrophysics. In fact, GRBs can be used to study the physics of jets, of relativistic shocks and radiative processes. Moreover they constitute excellent candidate sources for multi-messenger astrophysics (high-energy neutrinos and gravitational waves). Being connected with the last phases of stars, they are of great interest also for the stellar physics and evolution domain. Thanks to their exceptional brightness GRB afterglows can be used as powerful extragalactic background sources. They behave like distant lighthouses capable of unveiling the properties of the universe at different redshifts. Furthermore the class of long GRBs (LGRBs; see Kouveliotou et al. 1993 for a definition) is associated with the deaths of the most massive stars, making LGRBs especially suitable as tools to investigate star formation in the early Universe.

The following sections are focused on the use of LGRBs as cosmological probes (see also Petitjean & Vergani 2011) and on the future perspective that the *SVOM* satellite could fulfill.

[1] GEPI, Observatoire de Paris, CNRS, Univ. Paris Diderot, 5 place Jules Janssen, 92190 Meudon, France

2 Advantages and disadvantages of using LGRBs as cosmological probes

There are at least four factors that make LGRBs potentially very powerful for the study of galaxy evolution and of the very high redshift universe up to the reionization epoch. First of all GRBs are extremely bright at all redshift and even their afterglow brightness is only marginally decreasing with redshift (Lamb & Reichart 2000). This, combined with the association of LGRBs with the death of massive stars, makes LGRBs observable in principle up to $z > 15$ with present day instruments, and therefore tools to probe the early universe, the epoch of reionization, the first stars and the chemical enrichment of the universe. A further help in this direction comes from the power-law shape of the afterglow continuum, that makes the study of the absorbing gas easier compared to quasars (QSOs). Another advantage is that the afterglow emission is fading quite rapidly with time, allowing the study of the GRB host galaxies. These last form a sample of star forming galaxies selected independently of their emission properties (independently of dust obscuration and, uniquely, independently of their brightnesses at any wavelength), therefore complementary to the galaxy survey samples. Furthermore GRBs offer the unique opportunity to investigate systematically both the neutral gas using the afterglow spectra absorption lines AND the ionized gas by the emission lines of the host galaxy spectra. GRBs therefore constitute a unique tool to understand the link between the properties of the interstellar medium of galaxies and their star formation activity, and this at any redshift. This is a unique way to reveal the physical processes that trigger galaxy formation.

The transient nature of GRBs is, on the other hand, also the main disadvantage of the use of these sources as cosmological probes. The optical/near-infrared afterglow observations, necessary for a precise localization allowing the observation of the afterglow spectrum and the association with the host galaxy, have to take place as early as possible after the GRB prompt emission detection. Moreover it is not possible to carry out observation over long integration time so as to obtain high signal-to-noise spectra for all GRBs. To date, less than 30% of GRBs have a measured redshift*. More than 1100 GRBs have been detected, but the afterglow spectra are about 300 and the sample of host galaxies detected at least in one optical band is formed by less than 200 galaxies.

3 Afterglow spectroscopy

Thanks to their exceptional brightness, GRB afterglows can be used as powerful extragalactic background sources. The gas in front of the GRB selectively absorb part of the light and consequently is revealed by spectroscopic observations. The afterglow spectrum shows the signatures of the gas associated with the GRB host, with the IGM and with other galaxies present along the GRB line of sight.

Many are the gas properties that can be measured through the absorption lines present in the afterglow spectra, mainly for GRBs at $z > 2$. In fact, at those redshift the damped Lyman-α absorption (DLA) of the neutral hydrogen associated with the GRB host galaxy is in the frequency range covered by the optical-NIR spectrographs, together with the metal lines. It is possible to determine directly the neutral hydrogen and metals column densities and hence the metallicity of the gas. The H_2 and CO absorption features can also be present (Prochaska et al. 2009; Krühler et al. 2013).

3.1 Chemical Enrichment

The metallicity and abundance measurements can be use to add information on the chemical enrichment of the Universe. Differently from QSOs that probes random lines of sight of the foreground galaxies, GRBs mostly probes the gas associated with the star forming regions of their host. As shown in Figure 1 (left panel; see Sparre et al. 2013 and references therein), LGRBs are playing a fundamental role to add information at $z > 4.5$, and testify of an interstellar gas already quite enriched even at high redshift.

3.2 Reionization and PopIII stars

It is possible to probe the reionization epoch using the absorption signatures imprinted by neutral hydrogen in the intergalactic medium in the spectrum of GRB afterglows at high redshift (see Fig. 1, right panel). When the Universe is neutral, a broad and extended absorption trough with a red damping wing will be seen in the

*http://www.mpe.mpg.de/~jcg/grbgen.html

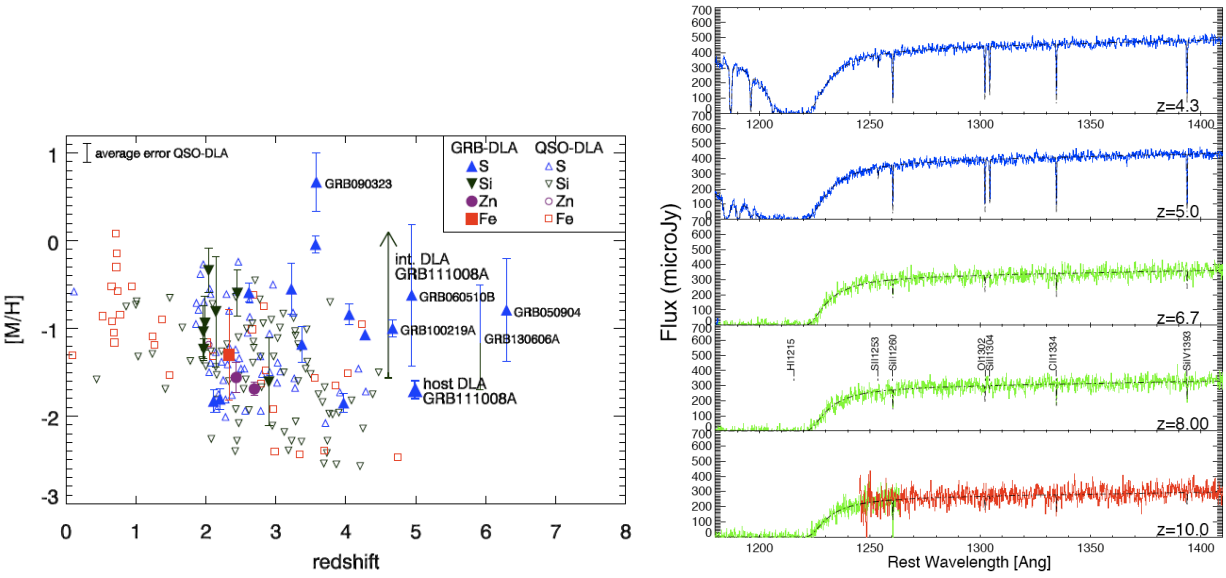

Fig. 1. Left: From Sparre et al. (2013). Metallicities as a function of redshift for GRB-DLAs (filled symbols) and QSO-DLAs (open symbols). **Right:** From McQuinn et al. (2009). Simulation of high-z GRB afterglow optical and near infrared spectra at $R \sim 3000$. The impact of the IGM on the spectrum is apparent in the left-side of the spectra.

spectrum. GRBs have the advantage compared to QSOs to be able to probe higher redshifts ($z > 8$). They also do not produce the large-scale proximity effect of QSOs that ionize the IGM to a distance of several Mpc. The neutral gas from the host galaxy located in front of the GRB already produces a damping wing (upper panel of the figure) but the additional signature of the IGM is much stronger (other panels) and can be detected even at intermediate spectral resolution.

The formation of the first objects in the Universe is a vividly debated issue and numerous models have been proposed (see Bromm 2013 for a review). These objects have an important impact on the first stages of structure formation and on the reionization history of the IGM, as they provide the first sources of light, heat and metals in the Universe (Ciardi & Ferrara 2005). LGRBs represent the most promising way to directly experience the explosion of the first stars. Indeed, the high mass expected for these stars (between 100 and 200 solar masses) strongly suggests that they will end their life producing a GRB. The spectroscopic observation of only one of the afterglow of such an explosion would correspond to a tremendous breakthrough by revealing the physical state of the gas in the surrounding of such remote objects. Recently, simulations of the expected afterglow spectral features of a GRB in a PopIII environment have been performed (Wang et al. 2012) showing that they can be detectable with future spectrographs, and confirming that GRBs may open one of the few direct windows into the crucial epoch of the first stars.

4 Observations of the GRB host galaxies

Once the afterglow vanished, it is possible to carry out photometrical and spectroscopical campaigns to study the properties of the GRB host. Using the emission lines present in the spectra it is possible to determine the dust extiction (by the Balmer decrement), the star formation rate (SFR, by the H-α or [OII] lines) and the metallicity mainly through indirect indicators (R_{23}, N2, etc...). Thanks to the spectral energy distribution (SED) built using multi-band photometry of the host it is possible to estimate also the stellar mass of the galaxy and the age of the stellar population (e.g.: Savaglio et al. 2009).

Most exciting is the combination of the gas properties obtained by the afterglow spectroscopy and those retrieved by the host observations. A systematical study in this sense can bring important informations on the physical processes that trigger galaxy formation. The kinematics and geometry of the gas can be assessed as well. First attempts in this way have been performed by Vergani et al. (2011b) and Chen (2012).

5 X-shooter

One of the best instrument available to carry out both afterglow spectroscopy and host galaxy studies is the ESO (European Southern Observatory) X-shooter spectrograph (Vernet et al. 2011) installed at the VLT (Very Large Telescope) in Paranal (Chile). This first ESO new generation instrument has the unique capability to produce intermediate resolution spectra from the UV to the near-infrared (NIR), covering simultaneously a spectral range from 300 to 2400nm. Two modes of observations are possible: the classical slit mode and the integral field unit (IFU) mode (see Vergani et al. 2011a for an example of the use of both modes applied to GRBs). The X-shooter large spectral range and sensitivity allow for the first time detailed studies of faint objects even at high redshift.

The French GEPI and APC laboratories were part of the consortium that built the instrument and participated to two X-shooter Guarantee Time Observation (GTO) programs dedicated to GRBs, ended in 2013: 1. The French-Italian GTO to observe LGRB host galaxy (40 host galaxies up to $z = 3$); 2. The GTO to observe the spectra of GRB afterglows (~ 40 afterglow spectra). Thanks to the large wavelength coverage it has been possible to use the X-shooter afterglow spectra to determine abundances and metallicities of the gas associated with the GRB hosts up to $z \sim 6$, bringing new information for chemical enrichment studies at $z > 4$ (see Fig. 1). Furthermore, the first detections of the emission lines of the host galaxies at $z > 1.5$ have been obtained, adding important information on the properties of the LGRB host galaxy population and its evolution with redshift (e.g.: Krühler et al. 2012; see Sect. 6).

6 The population of LGRB hosts

The study of the population of LGRB hosts is of particular interest in the perspective of using LGRBs as star formation tracers up to the highest redshifts. In the last few years an increasing number of works have tackled this issue (e.g.: Kistler et al. 2013, see Fig. 2). The main problem here is to know if LGRB hosts can be used as proxy of star forming galaxies at any redshift.

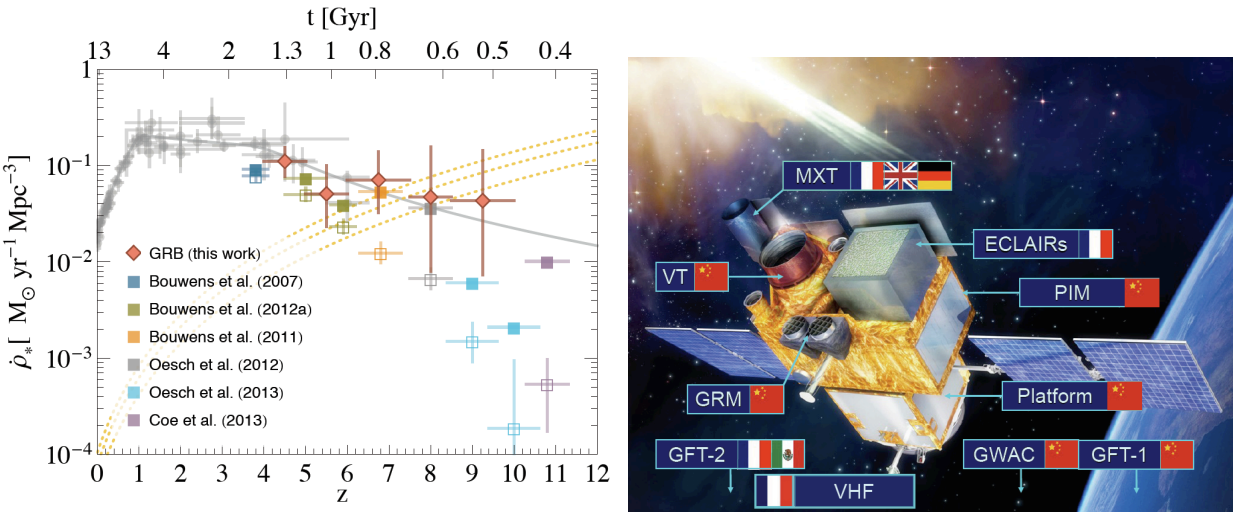

Fig. 2. Left: From Kistler et al. (2013). The cosmic rate of star formation in the first Gyr of galaxy formation is still highly debated, and the few GRBs so far detected at $z > 5$ may suggest a much higher activity of massive star formation than was derived from deep surveys. **Right:** The *SVOM* mission satellite and instruments.

Studies of LGRB host galaxies carried out mainly at $z < 1$ have shown that they have a lower metallicity compared to other galaxies at similar masses (e.g.: Levesque et al. 2010), tracing an environment younger and richer in gas than the galaxies selected by other techniques. On the other hand Mannucci et al. (2011) demonstrate that at $z < 1$ LGRB hosts are found to be consistent with the Fundamental Metallicity Relation, and there are more and more evidences that at higher redshift several LGRB hosts are not metal poor (e.g.: Krühler et al. 2012). Very recently, Boissier et al. (2013) highlighted the presence of a bias in the distribution of GRB host properties with respect to the star-forming galaxy population. It is important to note that the observations of GRB hosts are very sparse and inhomogeneous, so that they can not be used for statistical

analysis. All the results listed above are based on GRB host samples that are far from being complete and that are likely biased. For example, since the hosts are generally identified only for those bursts for which an accurate (optical) position is available, bursts exploding in dusty environments (i.e. part of the so-called *dark burst* population) have been likely under-represented. Current researches are now able to cover the hosts of these event as well, mainly thanks to the X-shooter, GROND[†] and Herschel[‡] facilities or to dedicated campaigns (Hjorth et al. 2012; Perley et al. 2013).

To overcome these problems and have an unbiased picture of the properties of GRB hosts, complete samples of GRBs are necessary. Two complete samples have become available in 2012: the BAT6 sample presented in Salvaterra et al. (2012), and the TOUGH sample (Hjorth et al. 2012), larger in number, but less complete in redshift. These samples offer the opportunity to study the population of LGRB hosts in a statistical unbiased way. The availability of large LGRB samples complete in redshift is of capital importance to study the LGRB redshift distribution and luminosity function (see Salvaterra et al. 2012).

Since LGRBs can happen at very high redshift, it is of great interest to use them to study the properties of high redshift galaxies. To date six LGRBs have a spectroscopically confirmed redshift at $z > 5$, including the record older GRB 080423 at $z = 8.2$ (Salvaterra et al. 2009; Tanvir et al. 2009). For five of them deep observations with the Hubble Space Telescope have been carried out and result in very deep limits on their magnitudes, even down to 30.3(AB) in H-band (Tanvir et al. 2012). Hence LGRBs pinpoint the extremely faint star forming galaxies belonging to the faint end of the luminosity function, that forms the bulk of the first galaxies population and that should significantly contribute to reionization (Salvaterra et al. 2011). High redshift LGRB host galaxies are the perfect target for the future JWST[§] and E-ELT[¶].

7 SVOM[‖]

In the next couple of decades the use of LGRBs as cosmological probes could experience a significant step forward thanks to the new facilities that will be available at different wavelength domains, such as JWST, SKA[**] and E-ELT (together with the new generation instruments on the VLT). Nonetheless, the success will depend on the availability of satellites triggering the GRB explosions and sending precise localizations to the Earth.

To date, most of the detections come from the *Swift* satellite (Gehrels et al. 2004) that is capable to observe both the prompt and afterglow emissions. The *FERMI* mission[††] is the second source of triggers of bursts, but its position errors are too big to allow an efficient follow up from ground-based instruments. *Swift* has been flying since 2005. On the chance that it will not be available anymore during next decade, the possibility of using LGRBs as cosmological probes will be lost. New GRB space missions are necessary.

The *SVOM* satellite is a Chinese mission with French participation whose launch should take please before 2020. On board of *SVOM* there will be a combination of multi-wavelength space payload (see Fig. 2). GRBs will be detected by the ECLAIRs wide-field camera working from 4 to 150 keV, whereas the Gamma-Ray Monitor (GRM) will enable to measure the spectral parameters of the prompt emission. The 0.3-10 keV Micro channel X-ray Telescope (MXT) and the Visible Telescope (VT) covering simultaneously the 400-900 nm range will detect the afterglow and refine the position of the GRBs from a few dozens of arcsecs to sub-arsec accuracy, respectively. The VT will also give information on the redshift of the GRBs, capital for the ground-based follow up strategy.

Another innovation of the *SVOM* mission will be the implementation of a dedicated ground segment in order to optimise the reactivity of the GRB follow-up, and hence to maximize the mission science return. The ground segment will consist of the Ground Wide Angle Camera (GWAC, in China) working in the V band and covering the ECLAIRs field of view, and of two robotic Ground Follow-up Telescopes (GFT) located in China and in Mexico. This French-Mexican one will extend its spectral coverage to the near IR (J & H) and be equipped with a spectrograph. Together, these two GFTs will be able to observe 40% of the ECLAIRs GRBs.

[†] http://www.mpe.mpg.de/~jcg/GROND/
[‡] http://www.esa.int/Our_Activities/Space_Science/Herschel
[§] http://www.esa.int/Our_Activities/Space_Science/JWST
[¶] http://www.eso.org/sci/facilities/eelt/
[‖] This Section is partly based on Godet et al. (2012) and on *SVOM science case*, SVOM collaboration internal report, 2013
[**] http://www.skatelescope.org/
[††] http://fermi.gsfc.nasa.gov/

SVOM will locate 70-80 GRBs/yr. Thanks to its unique features (the low-energy threshold of ECLAIRs, the sensitivity of the VT, a set of dedicated ground follow-up instruments, and a pointing strategy optimized for ground follow-up) it will possible to measure the redshift of more than 50% of the detected GRBs (compared to about 30% nowadays), to dramatically enhance the possibility to study the GRB line of sight, to identify quickly high-z GRBs candidates with their lack of visible emission in the VT, and to collect 15 GRBs at $z > 5$ during the nominal duration of the mission.

8 Conclusion

LGRBs can be unique tools to probe galaxy formation and evolution, and star formation at the highest redshift up to the first stars. Great progress can be achieved thanks to the facilities available for the GRB follow-up observations in the next decades (JWST, E-ELT, SKA,...). Nonetheless this will be possible only if *Swift*-like mission, as *SVOM*, will be operating.

References

Boissier, S., Salvaterra, R., Le Floc'h, E., et al. 2013, A&A, 557, A34

Bromm, V. 2013, ArXiv:1305.5178

Chen, H.-W. 2012, MNRAS, 419, 3039

Ciardi, B. & Ferrara, A. 2005, Space Sci. Rev., 116, 625

Gehrels, N., Chincarini, G., Giommi, P., et al. 2004, ApJ, 611, 1005

Godet, O., Paul, J., Wei, J. Y., et al. 2012, in Society of Photo-Optical Instrumentation Engineers (SPIE) Conference Series, Vol. 8443

Hjorth, J., Malesani, D., Jakobsson, P., et al. 2012, ApJ, 756, 187

Kistler, M. D., Yuksel, H., & Hopkins, A. M. 2013, ArXiv:1305.1630

Kouveliotou, C., Meegan, C. A., Fishman, G. J., et al. 1993, ApJ, 413, L101

Krühler, T., Fynbo, J. P. U., Geier, S., et al. 2012, A&A, 546, A8

Krühler, T., Ledoux, C., Fynbo, J. P. U., et al. 2013, A&A, 557, A18

Lamb, D. Q. & Reichart, D. E. 2000, ApJ, 536, 1

Levesque, E. M., Kewley, L. J., Berger, E., & Jabran Zahid, H. 2010, AJ, 140, 1557

Mannucci, F., Salvaterra, R., & Campisi, M. A. 2011, MNRAS, 439

McQuinn, M., Bloom, J. S., Grindlay, J., et al. 2009, in astro2010: The Astronomy and Astrophysics Decadal Survey, ArXiv:0902.3442

Perley, D. A., Levan, A. J., Tanvir, N. R., et al. 2013, ArXiv:1301.5903

Petitjean, P. & Vergani, S. D. 2011, Comptes Rendus Physique, 12, 288

Prochaska, J. X., Sheffer, Y., Perley, D. A., et al. 2009, ApJ, 691, L27

Salvaterra, R., Campana, S., Vergani, S. D., et al. 2012, ApJ, 749, 68

Salvaterra, R., Della Valle, M., Campana, S., et al. 2009, Nature, 461, 1258

Salvaterra, R., Ferrara, A., & Dayal, P. 2011, MNRAS, 414, 847

Savaglio, S., Glazebrook, K., & Le Borgne, D. 2009, ApJ, 691, 182

Sparre, M., Hartoog, O. E., Krühler, T., et al. 2013, ArXiv:1309.2940

Tanvir, N. R., Fox, D. B., Levan, A. J., et al. 2009, Nature, 461, 1254

Tanvir, N. R., Levan, A. J., Fruchter, A. S., et al. 2012, ApJ, 754, 46

Vergani, S. D., Flores, H., Covino, S., et al. 2011a, A&A, 535, A127

Vergani, S. D., Piranomonte, S., Petitjean, P., et al. 2011b, Astronomische Nachrichten, 332, 292

Vernet, J., Dekker, H., D'Odorico, S., et al. 2011, A&A, 536, A105

Wang, F. Y., Bromm, V., Greif, T. H., et al. 2012, ApJ, 760, 27

Session 12

Champ magnétique interstellaire et circumstellaire, mesures, structure et origine

SF2A 2013
L. Cambrésy, F. Martins, E. Nuss and A. Palacios (eds)

PROPERTIES OF INTERSTELLAR FILAMENTS OBSERVED WITH *HERSCHEL* : WHAT CAN WE SAY ABOUT THEIR FORMATION AND EVOLUTION?

D. Arzoumanian[1], Ph. André[2], N. Peretto[3], V. Könyves[1,2] and P. Palmeirim[2]

Abstract. We present a scenario for filament formation and evolution motivated by recent observational results of nearby molecular clouds. The analysis of more than 270 filaments observed in 8 regions by the *Herschel* Gould Belt survey show that the filaments are characterized by a narrow distribution of central width sharply peaked at ∼0.1 pc. This typical filament width corresponds, within a factor of ∼ 2 to the sonic scale below which interstellar turbulence becomes subsonic, which may suggest that the filaments form as a result of the dissipation of large-scale turbulence. The analysis of IRAM 30m molecular line observations of a sample of these filaments show evidence of an increase in non-thermal velocity dispersion with column density which suggest an evolution of the supercritical filaments in mass per unit length while accreting surrounding material. Relative orientations of magnetic field lines and filamentary structures indicate that interstellar magnetic fields may play an important role in shaping the structure of, at least, some molecular clouds and help in channeling low-density material onto star forming filaments.

Keywords: ISM, star formation, interstellar filament formation and evolution, magnetic fields

1 Omnipresence of filaments in molecular clouds

Interstellar filaments have recently received special attention, thanks to the high quality and dynamic range of *Herschel* observations. While molecular clouds (MC) were already known to exhibit filamentary structures (cf. Schneider & Elmegreen 1979), *Herschel* observations revealed the omnipresence of the filaments in the galaxy (e.g., André et al. 2010; Molinari et al. 2010; Schneider et al. 2012). Recent results from the *Herschel* Gould Belt survey (HGBS) showed that most of the prestellar cores are located within gravitationally unstable filaments for which the mass per unit length exceeds the critical value $M_{\rm line} > M_{\rm line,crit} = 2\,c_s^2/G \sim 16\,M_\odot$/pc (Ostriker 1964), where $c_{\rm s} \sim 0.2$ km/s is the isothermal sound speed for $T \sim 10$ K, while the subcritical filaments for which $M_{\rm line} < M_{\rm line,crit}$ are devoid of any bound cores (André et al. 2010; Arzoumanian et al. 2011; Palmeirim et al. 2013). This early result suggests an intimate connection between the filamentary structure and the formation process of prestellar cores and protostars. Statistical analysis of the filaments is now possible thanks to the resolution and sensitivity of *Herschel* (Pilbratt et al. 2010) SPIRE (Griffin et al. 2010) and PACS (Poglitsch et al. 2010) observations which are ideal to characterize the properties of the filamentary structure and investigate the physical processes involved in their formation and evolution.

2 A characteristic width for interstellar filaments revealed by *Herschel*

A sample of 278 filaments observed by the HGBS were extracted and analyzed. Mean radial column density profiles for each filament were derived from the column density maps constructed from *Herschel* images (as explained in Könyves et al. 2010; Palmeirim et al. 2013). The constructed column density radial profiles were modeled with a Plummer-like function (cf. Arzoumanian et al. 2011). The observed density profiles of the filaments approach a power law, at large radii with $\rho(r) \sim r^{-2}$ (Arzoumanian et al. 2011; Hill et al. 2012; Palmeirim et al. 2013), and none of them shows the steep density profile of the Ostriker (1964) model of an isothermal filament in hydrostatic equilibrium, for which $\rho(r) \sim r^{-4}$. Masses per unit length of the filaments were derived by integrating the column density profiles over radius $M_{\rm line}^{\rm obs} = \int \Sigma_{\rm obs}(r) {\rm d}r$.

[1] IAS, CNRS (UMR 8617), Universit Paris-Sud, Btiment 121, 91400 Orsay, France

[2] Laboratoire AIM, CEA/DSM–CNRS–Université Paris Diderot, IRFU/Service d'Astrophysique, C.E.A. Saclay, Orme des Merisiers, 91191 Gif-sur-Yvette, France

[3] School of Physics & Astronomy, Cardiff University, Queens Buildings, The parade, Cardiff CF24 3AA, UK

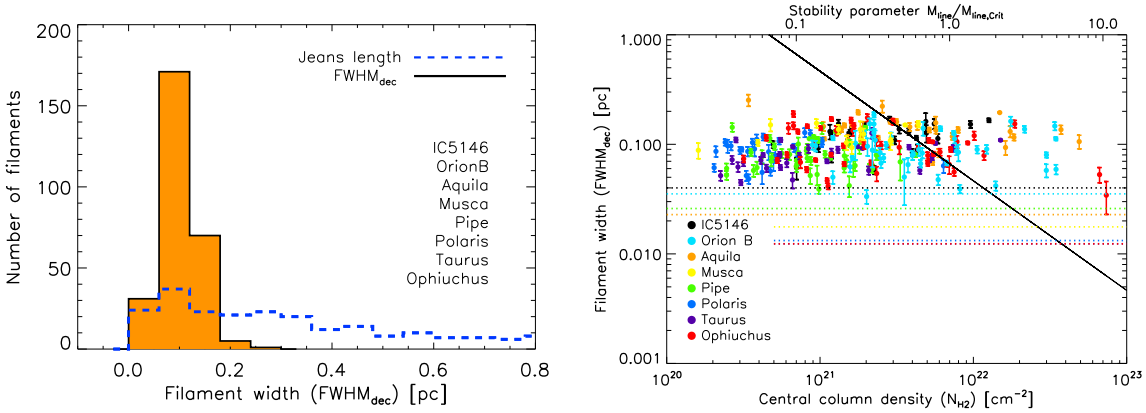

Fig. 1. Left: Distribution of deconvolved FWHM widths for the 278 filaments (black solid histogram, filled in orange), with a median value of 0.09 pc and a standard deviation of 0.04 pc. For comparison, the blue dashed histogram represents the distribution of central Jeans lengths corresponding to the central column densities of the filaments [$\lambda_J = c_s^2/(G\Sigma_0)$] for T = 10 K. **Right**: Mean deconvolved width versus background subtracted central column density for the same filament sample. The spatial resolutions of the column density maps used in the analysis for the different regions are marked by the horizontal dotted lines. The solid line running from top left to bottom right shows the central (thermal) Jeans length as a function of central column density. The upper x-axis scale corresponds to an estimation of the mass per unit length of the filaments in units of the thermal critical line mass, where $M_{\rm line} = W\Sigma_0$ with W = 0.1 pc and $M_{\rm line,crit} = 2c_s^2/G$ (improved versions of Fig. 6 and 7 from Arzoumanian et al. 2011).

The filament central widths were measured from Gaussian fits to the radial column density profiles. The analyzed filaments have a narrow distribution of FWHM widths centred around a typical value of 0.09 ± 0.04 pc (Fig. 1–left). The same filaments, observed in 8 regions (listed in Fig. 1) located at distances from 140 pc to 460 pc, span more than three orders of magnitude in central column density (Fig. 1–right) implying a distribution of central Jeans lengths from 0.02 pc up to 1.3 pc, which is much broader than the observed distribution of widths.

3 Proposed scenario for filament formation and evolution

We complemented the analysis of filament properties derived from *Herschel* imaging data with molecular line observations to gain insight into the gas kinematics of interstellar filaments. We used $C^{18}O$ and N_2H^+ line observations obtained with the IRAM 30m telescope to measure the velocity dispersions of a sample of filaments detected as part of the *Herschel* Gould Belt Survey in the IC5146, Aquila, and Polaris interstellar clouds (Arzoumanian et al. 2013).

Correlating the velocity dispersion measurements with the filament column densities derived from *Herschel* data, we see that interstellar filaments can be divided into two groups: thermally subcritical filaments, which have transonic velocity dispersions ($c_s \lesssim \sigma_{tot} < 2\,c_s$) independent of column density; and thermally supercritical filaments, which have higher velocity dispersions scaling roughly as the square root of column density ($\sigma_{tot} \propto \Sigma^{0.5}$). Assuming that the filaments have Gaussian radial column density profiles an estimated filament mass per unit length is given by $M_{\rm line} \sim \Sigma_0 \times W_{\rm fil}$ where $W_{\rm fil} \sim 0.1$ pc is the typical filament width (Arzoumanian et al. 2011). Interestingly, the observationally estimated $M_{\rm line}^{\rm threshold}$ for the column density threshold $\sim 8\times10^{21}$ cm^{-2}, which seems to divide the filament sample into two groups (cf. Fig. 2), is equal within a factor of ~2 to the theoretical $M_{\rm line,crit} \sim 16$ M$_\odot$/pc (for T=10 K). Thereby, the filament $M_{\rm line,crit}$ corresponds to a column density boundary, where subcritical filaments (left hand side of the boundary) have roughly constant velocity dispersions with a mean value of (0.26 ± 0.05) km/s, while the velocity dispersions of supercritical filaments (right hand side of the boundary) increase as a function of projected column density $\sigma_{\rm tot} \propto {N_{H_2}}^{0.5}$. Moreover, the filament virial line masses $M_{\rm line,vir} = 2\,\sigma_{\rm tot}^2/G$ (replacing $M_{\rm line,crit}$ in the presence of nonthermal motions – see Fiege & Pudritz 2000), show that thermally supercritical filaments are in approximate virial balance, while thermally subcritical filaments are unbound (Arzoumanian et al. 2013). This result shows that the gravitational stability criterion, based on the thermal critical line mass, assuming that the filaments have thermally dominated velocity dispersions (André et al. 2010), is consistent with a more complete view of the total velocity dispersion of filaments.

The observational evidence of a characteristic filament width may be consistent with a scenario for filament formation from dissipation of large-scale supersonic interstellar turbulence (Padoan et al. 2001). In such a picture, filaments coincide with stagnation gas associated with regions of locally converging turbulent motions, where compression is at a maximum

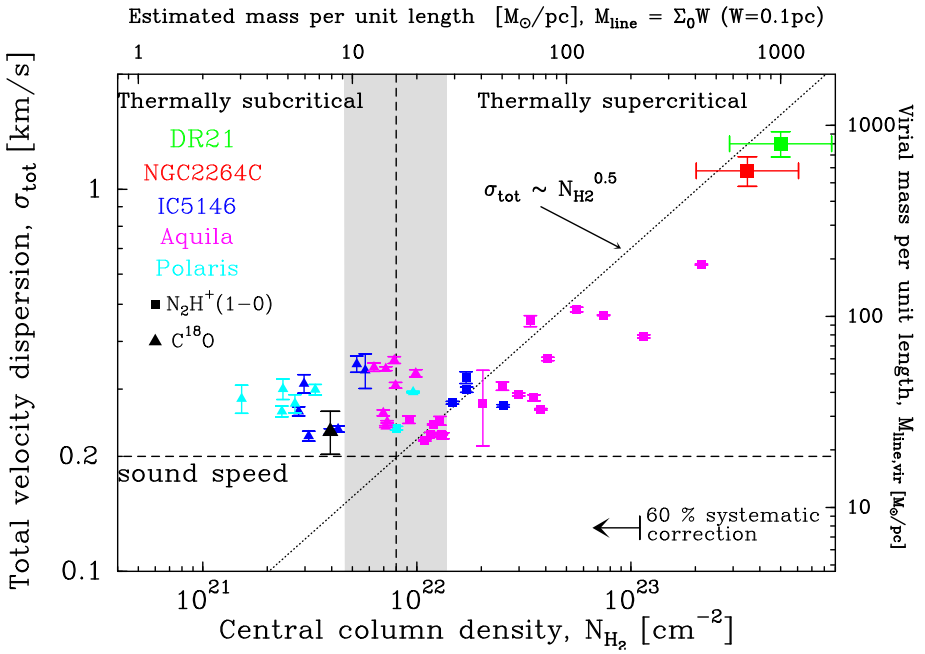

Fig. 2. Total velocity dispersion versus observed central column density: blue for IC5146, magenta for Aquila, cyan for Polaris, red for NGC2264C, and green for DR21 filaments. The horizontal dashed line shows the value of the sound speed ~ 0.2 km/s for T=10 K. The vertical dashed line marks the boundary between thermally subcritical and thermally supercritical filaments where the estimated mass per unit length $M_{\rm line}$ is approximately equal to the critical value $M_{\rm line,crit} \sim 16$ $M_\odot$/pc for T=10 K, equivalent to a column density of 8×10^{21} cm^{-2}. The grey band shows a dispersion of a factor of 3 around this nominal value. The dotted line running from the bottom left to the top right corresponds to $\sigma_{\rm tot} \propto N_{H_2}{}^{0.5}$ (cf. Arzoumanian et al. 2013).

and relative velocity differences at a minimum, and are thus expected to have relatively low (transonic) internal velocity dispersions (cf. Klessen et al. 2005). The line-of-sight velocity dispersions measured here for subcritical filaments are consistent with this picture. The typical filament width would correspond to the dissipation scale of the ion-neutral friction in the ISM as suggested by Hennebelle (2013). While the turbulent picture provides a plausible mechanism for *forming* the filaments, the fact that prestellar cores tend to form in gravitationally unstable filaments suggests that gravity is a major driver in the subsequent *evolution* of the supercritical, self gravitating filaments. The higher velocity dispersions of supercritical filaments may not directly arise from supersonic interstellar turbulence but may be driven by gravitational contraction/accretion (cf. Klessen & Hennebelle 2010). The accretion driven turbulence in supercritical filaments has been supported by numerical simulations of Heitsch (2013).

Based on our observational results, we propose an evolutionary scenario whereby supercritical filaments undergo gravitational contraction and increase in mass per unit length through accretion of background material while remaining in rough virial balance. We further suggest that this accretion process allows supercritical filaments to keep their approximately constant inner widths (0.1 pc) while contracting (Arzoumanian et al. 2013).

4 Role of interstellar magnetic field in the formation and evolution of filamentary structures

This growth in mass per unit length of supercritical filaments by accretion of surrounding material is suggested by low-density striations or subfilaments observed connected perpendicularly to the main filaments and apparently feeding them from the side. Examples include the B211/B213 filament in Taurus where the typical velocities expected for the infalling material are consistent with the existing kinematical constraints from CO observations (Palmeirim et al. 2013, and see Fig. 3), the Serpens South filament (Könyves et al. 2010; Sugitani et al. 2011), the Musca filament (Pereyra & Magalhães 2004), and the DR21 ridge in Cygnus X (Schneider et al. 2010).

The orientation of the striations aligned with optical polarization vectors in the Taurus field (see Fig. 3) suggests that the magnetic field participates in shaping the morphology of the filamentary structure in the cloud and helps channeling low density material onto the supercritical filament in form of low-density striations. This picture is also consistent with observations of near-IR polarization measurements towards the Serpens South filamentary region which reveal a relatively uniform magnetic field perpendicular to the supercritical star-forming filament (Sugitani et al. 2011).

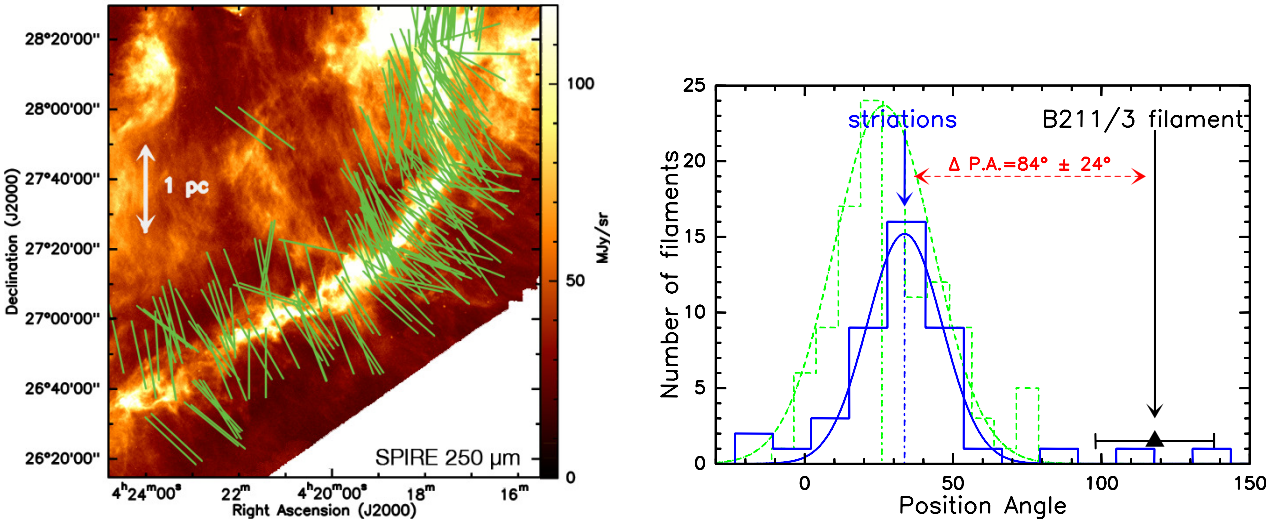

Fig. 3. Left: *Herschel* SPIRE 250 μm image of the Taurus B211/B213 filament and its local cloud. The green segments show the optical and infrared polarization vectors from Heyer et al. (2008); Heiles (2000), and Chapman et al. (2011) tracing the magnetic field orientation. The plane-of-the-sky projection of the magnetic field appears to be oriented perpendicular to the B211/B213 filament and roughly aligned with the general direction of the striations (cf. Palmeirim et al. 2013). **Right**: Orientation of the low-density striations identified in the Taurus field (blue histogram). The position-angle distribution of available optical polarization and infrared vectors are shown by the green dashed histogram. Gaussian fits to these distributions are superimposed, indicating a peak position angle of 34° ± 13° for the striations and 26° ± 18° for the B-field polarization vectors. The B211 filament has a mean position angle of 118° ± 20° (black triangle and horizontal error bar) and is thus roughly perpendicular to both the low-density striations and the local direction of the magnetic field (Fig. 4 from Palmeirim et al. 2013).

These observational results are supported by theoretical arguments which predict that, in the presence of a strong magnetic field, low-density, thermally subcritical filaments should be preferentially oriented parallel to the field lines, while high-density, self-gravitating filaments should be preferentially oriented perpendicular to the field lines (e.g., Nagai et al. 1998). This difference arises because in the presence of a magnetic field, motions of slightly ionized gas do not encounter any resistance along the field lines but encounter significant resistance perpendicular to the field lines. Consequently, an initial perturbation in a low-density part of the cloud will tend to expand along the field lines and form an elongated structure or a subcritical filament parallel to the field. Conversely, a self-gravitating structure will tend to contract along the field lines, forming a condensed, self-gravitating sheet (cf. Nakamura & Li 2008) which can itself fragment into several supercritical filaments oriented perpendicular to the field (e.g. Nagai et al. 1998).

This *bimodal orientation* of molecular structures and filaments has also been noticed in MHD simulations of cloud evolution where dense molecular structures tend to be oriented perpendicular to the magnetic field lines while fainter structures are aligned with the field lines (Soler et al. 2013).

Theoretical considerations, observational results as well as analysis on data performed by numerical simulation seem to agree on the existence of a correlation between the filamentary structure and the configuration of the magnetic field lines in molecular clouds. This suggests that magnetic field may play a role in shaping the morphology of the filamentary clouds and participate in the formation and evolution of interstellar filaments which existence, at least the supercritical ones, appear to be directly connected to the star formation process in molecular clouds.

Acknowledgements. DA acknowledges support by the European Research Council grant MISTIC (ERC-267934)

References

André, P., Men'shchikov, A., Bontemps, S., et al. 2010, A&A, 518, L102+

Arzoumanian, D., André, P., Didelon, P., et al. 2011, A&A, 529, L6

Arzoumanian, D., André, P., Peretto, N., & Könyves, V. 2013, A&A, 553, A119

Chapman, N. L., Goldsmith, P. F., Pineda, J. L., et al. 2011, ApJ, 741, 21

Fiege, J. D. & Pudritz, R. E. 2000, MNRAS, 311, 85

Griffin, M. J., Abergel, A., Abreu, A., et al. 2010, A&A, 518, L3+
Heiles, C. 2000, AJ, 119, 923
Heitsch, F. 2013, ApJ, 769, 115
Hennebelle, P. 2013, A&A, 556, A153
Heyer, M., Gong, H., Ostriker, E., & Brunt, C. 2008, ApJ, 680, 420
Hill, T., Andre, P., Arzoumanian, D., et al. 2012, A&A, 548, L6
Klessen, R. S. & Hennebelle, P. 2010, A&A, 520, A17
Könyves, V., André, P., Men'shchikov, A., et al. 2010, A&A, 518, L106+
Molinari, S., Swinyard, B., Bally, J., et al. 2010, A&A, 518, L100+
Nagai, T., Inutsuka, S.-I., & Miyama, S. M. 1998, ApJ, 506, 306
Nakamura, F. & Li, Z. 2008, ApJ, 687, 354
Ostriker, J. 1964, ApJ, 140, 1056
Padoan, P., Juvela, M., Goodman, A. A., & Nordlund, Å. 2001, ApJ, 553, 227
Palmeirim, P., André, P., Kirk, J., et al. 2013, A&A, 550, A38
Pereyra, A. & Magalhães, A. M. 2004, ApJ, 603, 584
Pilbratt, G. L., Riedinger, J. R., Passvogel, T., et al. 2010, A&A, 518, L1+
Poglitsch, A., Waelkens, C., Geis, N., et al. 2010, A&A, 518, L2+
Schneider, N., Csengeri, T., Bontemps, S., et al. 2010, A&A, 520, A49+
Schneider, N., Csengeri, T., Hennemann, M., et al. 2012, A&A, 540, L11
Schneider, S. & Elmegreen, B. G. 1979, ApJs, 41, 87
Soler, J. D., Hennebelle, P., Martin, P. G., et al. 2013, ApJ, 774, 128
Sugitani, K., Nakamura, F., Watanabe, M., et al. 2011, ApJ, 734, 63

SF2A 2013
L. Cambrésy, F. Martins, E. Nuss and A. Palacios (eds)

MAGNETIC FIELD AND ANGULAR MOMENTUM EVOLUTION MODELS

Florian Gallet[1]

Abstract. The magnetic field in young stellar object is clearly the most important component when one dealing with the angular momentum evolution of solar-like stars. It controls this latter one from the pre-main sequence, during the "disk locking" phase where the stars magnetically interact with their surrounding disk, to the main-sequence through powerful stellar winds that remove angular momentum from the stellar surface. We present new models for the rotational evolution of solar-like stars between 1 Myr and 10 Gyr with the aim to reproduce the distributions of rotational periods observed for star forming regions and young open clusters within this age range. Our simulations are produced by a recent model dedicated to the study of the angular momentum evolution of solar-type stars. This model include a new wind braking law based on recent numerical simulations of magnetized stellar winds and a specific dynamo and mass-loss prescription are used to link the angular momentum loss-rate to angular velocity evolution. The model additionally allows for a core/envelope decoupling with an angular momentum transfer between these two regions. Since this former model didn't include any physical star/disk interaction description, two star/disk interaction processes are eventually added to it in order to reproduce the apparent small angular velocities to which the stellar surface is subject during the disk accretion phase. We have developed rotational evolution models for slow, median and fast rotators including two star/disk interaction scenarios that are the magnetospheric ejection and the accretion powered stellar winds processes. The models appear to fail at reproducing the rotational behaviour of solar-type stars except when a more intense magnetic field is used during the disk accretion phase.

Keywords: Stars: solar-type, Stars: magnetic field, Stars: evolution, Stars: rotation, Stars: winds, outflows subject, verb, noun, apostrophe

1 Introduction

Classical T Tauri stars (CTTs) are very active pre-main sequence stars surrounded by an accretion disk (Edwards et al. 1994; Hartmann et al. 1998). The impact of their magnetic field on their dynamics and on the structure of their environment is very strong and lead to numerous physical phenomenon such as the truncation the disk and accretion of the material from it along funnel flows down to the stellar surface, launch of stellar winds along the opened magnetic field lines (Matt & Pudritz 2008a; Matt et al. 2012; Cranmer & Saar 2011), and ejection of material because of magnetic star/disk interaction (Shu et al. 1994; Ferreira et al. 2000; Romanova et al. 2009; Zanni & Ferreira 2009, 2013). The magnetic interaction between the star and its surrounding accretion disk remains one of the major unsolved issue concerning the angular momentum evolution of CTTs. It is now observationally clear (see Edwards et al. 1993; Bouvier et al. 1993; Rebull et al. 2004) that during the first 10 Myr of their life the stars are prone to held constant their rotation for several Myr (Irwin & Bouvier 2009; Gallet & Bouvier 2013). Since CTTs accrete mass and angular momentum from their disk and they still contract during the pre-main sequence (PMS), they should spin-up in a few million years. Hence, this suggests that during this period a large fraction of the angular momentum is removed from the stars. Many theoretical advances have been made during the last years about the impact of the accretion/ejection phenomenon on the angular momentum evolution of young suns such as the magnetospheric ejection process (hereafter MEP, Zanni & Ferreira 2013) that describes the magnetic interaction between a stellar magnetosphere and an accretion disk, and the accretion power stellar wind (hereafter APSW, Matt & Pudritz 2005, 2008a,b) that predicts powerful stellar jets powered directly by the accreted material.

[1] UJF-Grenoble 1/CNRS-INSU, Institut de Planétologie et d'Astrophysique de Grenoble (IPAG) UMR 5274, F-38041 Grenoble, France

The aim here is to examine the impact of these different star/disk interaction scenarios on the angular velocity evolution and the conditions for which the surface angular velocity of the stars is held constant during the early PMS phase when the stars are still surrounded by an accretion disk. Since some previous works by Collier Cameron et al. (1995) and Matt et al. (2010) already studied such interaction we will focus on reproducing the rotational evolution of solar-like stars by comparing the models to the observations. This is the first time that these specific scenarios are incorporated into a "global" angular momentum evolution model which gives us the chance to analyse the impact of these interactions on the MS rotational behaviour.

2 Angular velocity evolution

We use the model described in Gallet & Bouvier (2013) that is dedicated to the study of the angular momentum evolution of solar-type star. Since this model didn't include any physical description of the star/disk interaction process we want to examine the impact of star/disk interaction scenarios on the early PMS angular momentum evolution. A more detailed description of the former model can be found in Gallet & Bouvier (2013). In this "new" model we combined the magnetospheric ejection (Zanni & Ferreira 2013) and accretion powered stellar wind (Matt & Pudritz 2005) processes during the disk accretion phase. We found that a more intense magnetic field, compare to the mean magnetic field used in Gallet & Bouvier (2013), is required to reproduce the early-PMS clusters.

The free parameters of the model are the initial rotation period P_{init} at 1 Myr, the core-envelope coupling time-scale τ_{c-e}, the disk lifetime τ_{disk}, and the calibration constant of the wind braking law K_1. This study adopts the same parametrization as described in Gallet & Bouvier (2013). Additionally, two free parameters are added here: the mass loss rate efficiency constant Q_{acc}, and the strength of the magnetic field B_{mod}. We computed the angular velocity evolution of the fast, median, and slow rotator models, and examine the impact of the two star/disk interaction mechanisms on this evolution. Figure 1 shows the angular velocity evolution of the fast, median, and slow rotator models, respectively in blue, green, and red.

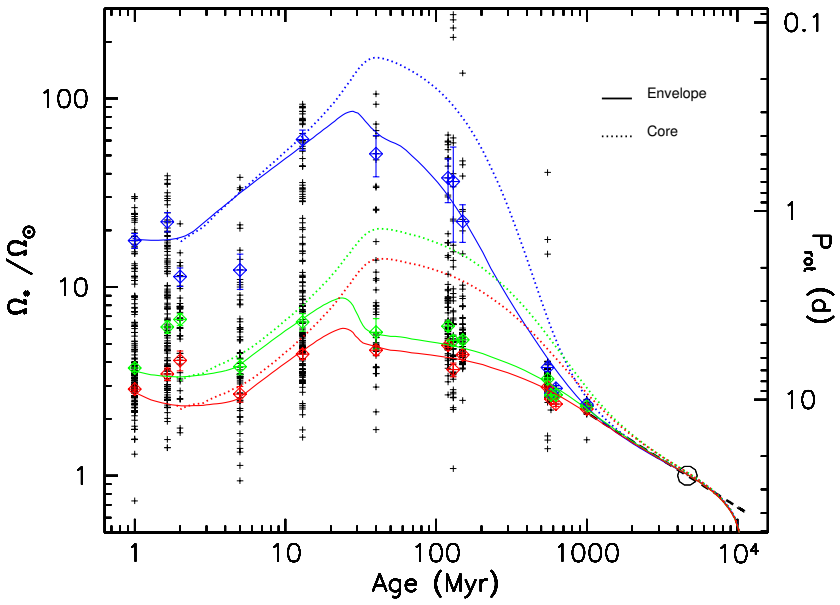

Fig. 1. Angular velocity of the radiative core (dashed lines) and of the convective envelope (solid lines) is shown as a function of time for fast (blue), median (green), and slow (red) rotator models in the case $Q_{acc} = 1\%$. The angular velocity is scaled to the angular velocity of the present Sun. The blue, red and green tilted square and associated error bars represent the 90th percentile, the 25th percentile, and the median, respectively, of the rotational distributions of solar-type stars in star forming regions and young open clusters obtained with a rejection sampling method (see Gallet & Bouvier 2013)). The open circle is the angular velocity of the present Sun and the dashed black line illustrates the Skumanich's relationship, $\Omega_* \propto t^{-1/2}$.

For the fast rotator model a disk's lifetime of 2.5 Myr is used that lead to a rapid increase of the surface angular velocity of the stars during the PMS. The quite low initial rotation period $P_{init} = 1.4$ d is dictated

by the fast rotation rate exhibited in the Orion Nebulae Cluster at 1 Myr and the NGC 6530 cluster at 1.65 Myr. To fit the observational constraints from the PMS to the ZAMS a relatively short core/envelope coupling timescale of 10-15 Myr is needed. To reproduce the early-PMS observations we numerically set $B_{mod} = 1000$ G. For the median and slow rotator models the initial rotation periods are 7 and 9 d, respectively, as fixed by the rotation period distributions of the youngest PMS clusters. For both models we chose a disk lifetime of 5 Myr to reproduce the late PMS clusters. To account for the moderate velocities on the ZAMS, we had to assume a much longer core-envelope coupling timescale than for fast rotators, namely 28 and 30 Myr for median and slow rotator models, respectively. The slow decline of surface rotation is due to angular momentum of the core resurfacing at the stellar surface on a timescale of $\simeq$100 Myr in slow and moderate rotators and it accounts for the observed evolution of the lower envelope of the rotational distributions of early MS clusters. To reproduce the observations in these cases, B_{mod} is set at 1600 and 1300 G for the slow and median rotator models, respectively.

3 Conclusions

We combined two star/disk interaction scenarios in the "global" angular momentum evolution model described in Gallet & Bouvier (2013) with the aim to study the angular velocity evolution of solar-like stars during the early-PMS phase. We found that the models fail to reproduce the observations except when a more intense magnetic field is used during the disk accretion phase. In presence of weak magnetic field the torque applied by the accretion disk on its star is not sufficient enough to efficiently extract angular momentum from the stellar surface to compensate the stellar contraction that otherwise dominate this evolution. These results are certainly not new since the star/disk interaction process is not a modern issue and that it has already been studied in the literature through different mechanisms (e.g. Collier Cameron et al. (1995); Matt et al. (2010)). The major difference of this study is that the resulting angular velocity evolution produces by the star/disk interaction is directly compare to the observations. However, this is a preliminary result and a more physical model is still to be developed especially in studying the impact of a non-axisymmetric and multipolar magnetic field on the angular velocity evolution.

I thank the SF2A organisational committee for this very nice and fruitful week in Montpelier.

References

Bouvier, J., Cabrit, S., Fernandez, M., Martin, E. L., & Matthews, J. M. 1993, A&A, 272, 176

Collier Cameron, A., Campbell, C. G., & Quaintrell, H. 1995, A&A, 298, 133

Cranmer, S. R. & Saar, S. H. 2011, ApJ, 741, 54

Edwards, S., Hartigan, P., Ghandour, L., & Andrulis, C. 1994, AJ, 108, 1056

Edwards, S., Strom, S. E., Hartigan, P., et al. 1993, AJ, 106, 372

Ferreira, J., Pelletier, G., & Appl, S. 2000, MNRAS, 312, 387

Gallet, F. & Bouvier, J. 2013, A&A, 556, A36

Hartmann, L., Calvet, N., Gullbring, E., & D'Alessio, P. 1998, ApJ, 495, 385

Irwin, J. & Bouvier, J. 2009, in IAU Symposium, Vol. 258, IAU Symposium, ed. E. E. Mamajek, D. R. Soderblom, & R. F. G. Wyse, 363–374

Matt, S. & Pudritz, R. E. 2005, ApJ, 632, L135

Matt, S. & Pudritz, R. E. 2008a, ApJ, 678, 1109

Matt, S. & Pudritz, R. E. 2008b, ApJ, 681, 391

Matt, S. P., MacGregor, K. B., Pinsonneault, M. H., & Greene, T. P. 2012, ApJ, 754, L26

Matt, S. P., Pinzón, G., de la Reza, R., & Greene, T. P. 2010, ApJ, 714, 989

Rebull, L. M., Wolff, S. C., & Strom, S. E. 2004, AJ, 127, 1029

Romanova, M. M., Ustyugova, G. V., Koldoba, A. V., & Lovelace, R. V. E. 2009, MNRAS, 399, 1802

Shu, F., Najita, J., Ostriker, E., et al. 1994, ApJ, 429, 781

Zanni, C. & Ferreira, J. 2009, A&A, 508, 1117

Zanni, C. & Ferreira, J. 2013, A&A, 550, A99

SF2A 2013
L. Cambrésy, F. Martins, E. Nuss and A. Palacios (eds)

THE LARGE-SCALE MAGNETIC FIELD IN PROTOPLANETARY DISCS

J. Guilet[1,2] and Gordon I. Ogilvie[1]

Abstract. We study the time evolution of the large scale poloidal magnetic field in a global model of thin accretion disc, with a particular attention to protoplanetary discs. With transport coefficients usually used (coming from a crude vertical averaging), the magnetic field strength does not increase radially inward, leading to weak magnetic fields in the inner part of the disc. We show that with more precise transport coefficients taking into account the vertical structure of the disc as obtained by Guilet & Ogilvie (2012, 2013), the magnetic field can significantly increase radially inwards. The magnetic field profile adjusts in such a way as to reach an equilibrium value of the plasma β parameter (the ratio of the midplane thermal pressure to the magnetic pressure) in the inner parts of the disc. This value of β depends strongly on the disc aspect ratio and the magnetic Prandtl number, and we find that it corresponds to a plasma β parameter in the range $10^4 - 10^7$ for protoplanetary discs. Such a magnetic field strength is expected to have a significant impact on the dynamics of the protoplanetary disc by increasing the strength of MHD turbulence and allowing the launch of an outflow.

Keywords: protoplanetary discs, accretion discs, magnetic fields, MHD, ISM: jets and outflows.

1 Introduction

The presence of a magnetic field in protoplanetary discs has important consequences for driving turbulence and for launching an outflow. Both processes lead to angular momentum transport and are thus crucial to explaining the accretion rate onto the central star. The presence of a strong magnetic field in the inner parts of protoplanetary discs is furthermore strongly suggested by observations of powerful collimated jets from T-Tauri star systems (Ferreira et al. 2006). Such a magnetic field can also affect the evolution of planets embedded in the disc by changing their migration rate and direction (Terquem 2003; Guilet et al. 2013). The strength of the magnetic field remains, however, very uncertain both from an observational point of view (since direct measurements of its strength are still lacking) and from a theoretical perspective.

The evolution of a large scale magnetic field in an accretion disc has been a long standing theoretical problem since Lubow et al. (1994) found that the diffusion of this field was much more efficient than its advection in a geometrically thin disc. As a consequence, they found an almost uniform magnetic field strength presumably leading to a negligibly weak magnetic field in the inner parts of the disc, which is problematic for magnetically-driven jet models. In Guilet & Ogilvie (2012, 2013) we showed that the vertical structure of the disc could lead to a faster advection and a slower diffusion of the magnetic field than previously thought. This suggests that the magnetic field could increase radially inwards and could therefore potentially solve this problem. Determining the radial structure and intensity of the magnetic field requires however the study of a global model of an accretion disc. Such a global model is the subject of this article and will be described in more detail in a forthcoming paper (Guilet & Ogilvie in preparation).

The physical and numerical setup used are described in Section 2. In Section 3, we present the magnetic field configuration obtained when using the transport coefficients of Guilet & Ogilvie (2012). We discuss the consequences for protoplanetary discs and conclude in Section 4.

[1] Department of Applied Mathematics and Theoretical Physics, University of Cambridge
Centre for Mathematical Sciences, Wilberforce Road, Cambridge CB3 0WA, UK
[2] Max-Planck-Institut fur Astrophysik, Karl-Schwarzschild-Str. 1, D-85748 Garching, Germany

2 Formalism

We study the evolution of the large-scale poloidal magnetic field around a thin accretion disc (with a small aspect ratio $h \ll 1$). We assume that no outflow is launched from the disc such that outside the disc the density vanishes and the magnetic field configuration is current free. We also neglect the currents present in the star such that the magnetic field originates from currents inside the disc and from currents at infinity that create a uniform background magnetic field. We compute the time evolution of the magnetic flux function ψ as defined by Ogilvie (1997), proportional to the magnetic flux threading the disc, and related to the magnetic field by:

$$B_r = -\frac{1}{r}\frac{\partial \psi}{\partial z}, \tag{2.1}$$

$$B_z = \frac{1}{r}\frac{\partial \psi}{\partial r}, \tag{2.2}$$

The time evolution of the magnetic flux function in the equatorial plane of the disc is determined by transport processes in the accretion disc through:

$$\frac{\partial \psi}{\partial t} + v_\psi \frac{\partial \psi}{\partial r} = 0, \tag{2.3}$$

where v_ψ is the transport velocity of the magnetic flux. This transport rate of magnetic flux has a component due to the advection by the accreting matter, and a second component due to the diffusion of the magnetic field by an effective turbulent resistivity. In the simple vertical average derived by Lubow et al. (1994) the transport rates are independent of the magnetic field strength. The advection velocity is assumed to be the same as that of mass (density averaged), which for a steady state disc far from the boundary is

$$v_{\rm adv} = -\frac{3}{2}\frac{\nu}{r}, \tag{2.4}$$

where ν is the effective turbulent viscosity. The diffusion velocity of the magnetic field is

$$v_{\rm diff} = \frac{\eta}{H}\frac{B_{rs}}{B_z}, \tag{2.5}$$

where η is the effective turbulent resistivity, H is the vertical scale height of the disc, and B_{rs} is the radial magnetic field at the surface of the disc. B_{rs} is proportional to the height integrated current inside the disc and can be computed from the magnetic flux distribution by inverting an integral equation (see Lubow et al. 1994 and Ogilvie 1997).

More precise transport rates have been computed by Guilet & Ogilvie (2012) in an analysis that takes into account the vertical structure of the accretion disc. They found that the vertical structure has a large effect on the transport rate as compared to aforementioned vertical averages used in the past by Lubow et al. (1994), Heyvaerts et al. (1996) and Reynolds et al. (2006): for magnetic fields such that the magnetic pressure is smaller than the thermal pressure at the midplane of the disc, the advection is faster and the diffusion slower than these rough estimates. Indeed, the diffusion rate decreases with decreasing magnetic field strength because the magnetic field lines can bend over a larger height, while the advection velocity increases because of the faster radial velocity in the low density region away from the midplane. In the following, we use the transport rates obtained by Guilet & Ogilvie (2012).

In order to solve the time evolution of the magnetic flux distribution, we use a second order finite difference numerical algorithm (see Guilet & Ogilvie in preparation for more details). The radii are normalised by the radius of the inner edge of the disc, time by the Keplerian angular frequency at this inner edge and the surface density such that the mass accretion rate in the α disc model is equal to 1.

3 Equilibrium magnetic field profile

We compute the time evolution of the magnetic field profile from an initial condition where the magnetic field is uniform and equal to the background magnetic field. After a time shorter than the viscous time (and therefore shorter than the lifetime of protoplanetary discs), a stationary configuration is obtained, which is shown in

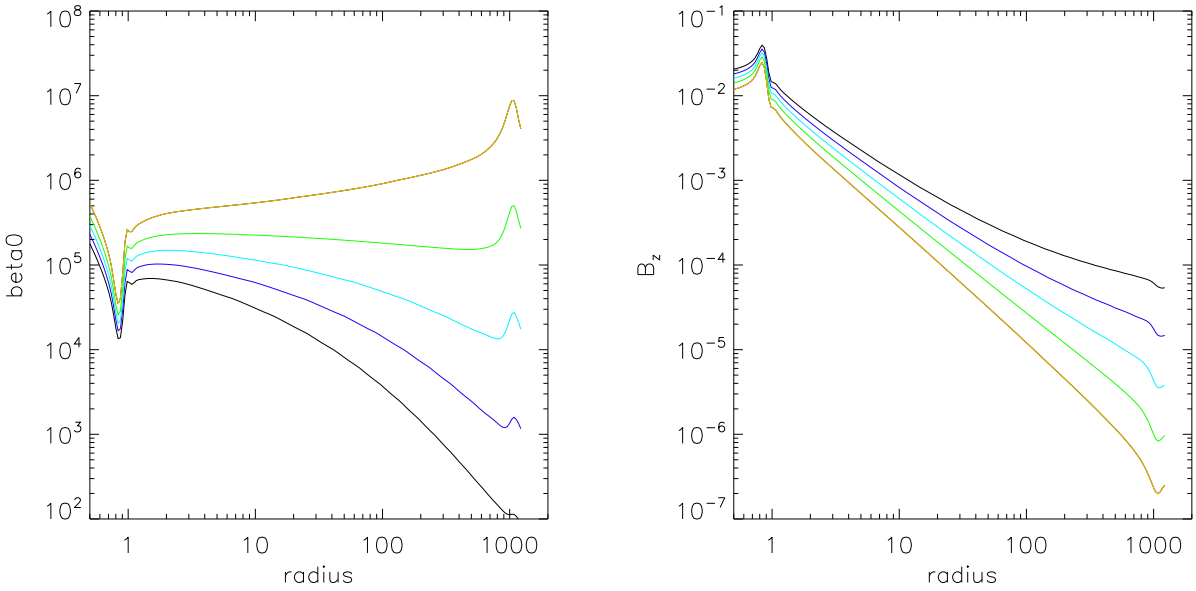

Fig. 1. Radial profiles of the plasma β parameter (ratio of midplane thermal pressure to the magnetic pressure, left panel) and the magnetic field strength (right panel) after a stationary state is reached. The disc is an α disc model with a uniform aspect ratio $h = 0.05$ and magnetic Prandtl number $\mathcal{P} \equiv \nu/\eta = 1$. The different colours show the results of simulations with different values of the background magnetic field strength, with β at the outer edge of the disc ranging from $\beta = 10^2$ (orange) to $\beta = 10^6$ (black).

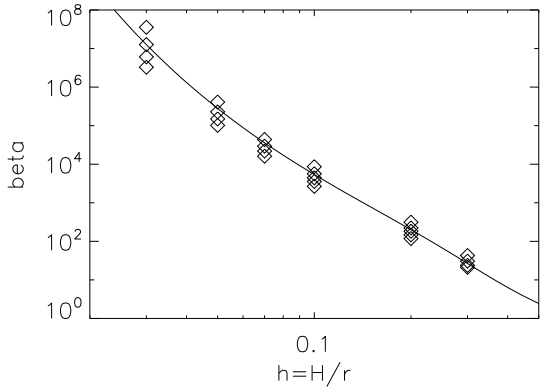

Fig. 2. Ratio of thermal pressure to magnetic pressure (β_0) near the inner edge of the disc as a function of the aspect ratio of the disc. The results of numerical simulations with several background magnetic field strengths are shown with diamond symbols. A semi-analytical prediction is shown with the full black line.

Figure 1. The different colours show results from simulations with different values of the background magnetic field strength corresponding to values of β in the range $10^2 - 10^6$ at the outer edge of the disc. The advection of magnetic flux by the accretion flow leads to a significant amplification of the magnetic field in the inner part of the disc, and the stationary magnetic field profiles increase radially inward. Interestingly, the evolution of the magnetic field favours a particular value of the ratio of thermal to magnetic pressure $\beta \sim 10^5$: if the background magnetic field is close to this strength at the outer edge of the disc, then the stationary magnetic field profile corresponds to a uniform thermal to magnetic pressure ratio (green line). If the background magnetic field is weaker (respectively stronger) than this at the outer edge, then the magnetic field increases more (respectively less) steeply inwards in order to reach this equilibrium value of β in the inner parts of the disc. This comes

from the fact that weak magnetic fields are advected faster and diffused at a slower rate than strong magnetic fields, and can therefore sustain a steeper radial profile of magnetic field strength.

This magnetic field strength is expected to depend mainly on the aspect ratio of the disc h and the magnetic Prandtl number $\mathcal{P} \equiv \nu/\eta$ through the parameter $\mathcal{P}h$ (Lubow et al. 1994; Guilet & Ogilvie 2012). In Figure 2, we show the dependence of the equilibrium value of β as a function of the aspect ratio of the disc with the expected value of the magnetic Prandtl for MHD turbulence of $\mathcal{P} = 1$. The equilibrium β is estimated by measuring β near the inner edge of the disc for different values of the background magnetic field (diamond symbols) and compared successfully to an analytical estimate using a self similar solution of the exterior magnetic field (see Guilet & Ogilvie in preparation for more details). Note that the equilibrium value of β depends steeply on the aspect ratio of the disc, and for parameters relevant to protoplanetary discs it lies in the range $10^4 - 10^7$.

4 Conclusion

We studied the global structure of the poloidal magnetic field in an accretion disc, with a particular attention to protoplanetary discs. In contrast to previous studies, we find that the transport coefficients taking into account the vertical structure obtained by Guilet & Ogilvie (2012) allow the magnetic field to significantly increase radially inwards. The magnetic field profile tends towards a stationary solution which favours a uniform equilibrium thermal to magnetic pressure ratio. This ratio depends on the aspect ratio of the disc and the magnetic Prandtl number of MHD turbulence and is typically in the range $\beta = 10^4 - 10^7$ for a protoplanetary disc, the large range coming from the steep dependence on the aspect ratio and the (somewhat uncertain) turbulent magnetic Prandtl number. Such a magnetic field strength is rather weak in the sense that the magnetic pressure remains significantly smaller than the thermal pressure at the disc midplane. It can however have profound consequences on the dynamics of protoplanetary discs. It could for example quench MRI turbulence and enable the launch of an outflow powerful enough to drive accretion at a rate compatible with observation (Bai & Stone 2013; Bai 2013). At larger radii where ambipolar diffusion is significant, it could by contrast foster the development of MRI turbulence (Simon et al. 2013). It is remarkable that the range of magnetic field strength found in our analysis coincides with the values needed in these studies in order to explain the observed mass accretion rates.

Note that we have not taken into account ambipolar diffusion and the Hall effect, which are expected to have an important effect in the outer parts of protoplanetary discs. In this calculation, we also did not describe the effect of an outflow, which could play an important role in driving accretion once such magnetic fields are present (Bai & Stone 2013; Bai 2013). Future work should take these processes into account in order to have a more precise description of the magnetic field evolution.

JG acknowledges support from the STFC and from the Max-Planck-Princeton Center for Plasma Physics.

References

Bai, X.-N. 2013, ApJ, 772, 96
Bai, X.-N. & Stone, J. M. 2013, ApJ, 769, 76
Ferreira, J., Dougados, C., & Cabrit, S. 2006, A&A, 453, 785
Guilet, J., Baruteau, C., & Papaloizou, J. C. B. 2013, MNRAS, 430, 1764
Guilet, J. & Ogilvie, G. I. 2012, MNRAS, 424, 2097
Guilet, J. & Ogilvie, G. I. 2013, MNRAS, 430, 822
Heyvaerts, J., Priest, E. R., & Bardou, A. 1996, ApJ, 473, 403
Lubow, S. H., Papaloizou, J. C. B., & Pringle, J. E. 1994, MNRAS, 267, 235
Ogilvie, G. I. 1997, MNRAS, 288, 63
Reynolds, C. S., Garofalo, D., & Begelman, M. C. 2006, ApJ, 651, 1023
Simon, J. B., Bai, X.-N., Armitage, P. J., Stone, J. M., & Beckwith, K. 2013, ApJ, 775, 73
Terquem, C. E. J. M. L. J. 2003, MNRAS, 341, 1157

SF2A 2013
L. Cambrésy, F. Martins, E. Nuss and A. Palacios (eds)

MAGNETIC FIELDS IN OLD SUPERNOVA REMNANTS

A. Gusdorf[1], T. Hezareh[2], S. Anderl[3] and H. Wiesemeyer[2]

Abstract. We review the motivations and methods for studying magnetic fields in relatively old supernova remnants (SNRs), such as W28, W44, 3C 391, and IC 443. We first explain the common methods of determination of interstellar magnetic fields through measurements of polarization levels in cosmic dust and spectral line emission. We then present the methods used in our study, i.e., shock modelling of molecular line emission, and application of non-Zeeman circular polarization of spectral lines. We finalize with the new perspectives of this study.

Keywords: ISM: supernova remnants – Physical data and processes: magnetic fields – Shock waves – Submillimeter: ISM – ISM: individual objects: W28, W44, IC443, & 3C391 – cosmic rays.

1 Supernova remnants and magnetic fields

Supernovae play a key role in the energy input in the interstellar medium (ISM). At their latest stage of evolution, i.e., at the so-called 'supernova remnant' (SNR) stage, these objects drive shocks that compress, accelerate and heat the ambient gas. Strong infrared and sub-millimeter spectral line emission is observed from such sources, as presented in this review: W28, W44, IC 443, 3C 391. This emission can be used to study the physical and chemical processes in shock environments and to constrain shock model parameters for such regions. Subsequently, general conclusions can be drawn on the effects of SNRs on the ambient ISM (Gusdorf et al. 2013). These effects include the contribution of SNRs to the energetic balance of galaxies, their input of turbulence, and triggered second generation star formation. Moreover, a detailed analysis of the molecular emission in SNRs can also contribute to the interpretation for the observed γ-ray emission, and hence a better understanding of the acceleration mechanisms and population of cosmic rays.

Among the shock parameters that can be constrained through the modelling of molecular line emission in SNRs, the magnetic field strength is of particular importance: it strongly influences the type of shock (C- or J-type) propagating in the ISM, hence the associated cooling processes and ultimately the amount of energy that is radiated away. Furthermore, the magnetic field strength is required to determine the proportion of electrons and hadrons in the cosmic ray population detectable around SNRs. Indeed, both electrons and hadrons generate γ-ray emission through interactions with the dense ISM. The analysis of high-energy spectra is consequently not sufficient to disentangle their contributions. However, relativistic electrons also interact with the magnetic field, giving rise to synchrotron emission, observable from radio to X-ray wavelengths. The proportion of electrons in the cosmic rays population can hence be determined if the magnetic field strength is known, and then be confirmed by the interpretation of γ-rays spectra.

In this brief contribution, we will review the 'classical' determinations of the magnetic field strength in the ISM, and then present the methods our team uses, based on shock modelling of molecular emission and the interpretation of the polarization of spectral lines of the CO molecule.

[1] LERMA, UMR 8112 du CNRS, Observatoire de Paris, École Normale Supérieure, 24 rue Lhomond, F75231 Paris Cedex 05, France
[2] Max Planck Institut für Radioastronomie, Auf dem Hügel 69, 53121 Bonn, Germany
[3] Argelander Institut für Astronomie, Universität Bonn, Auf dem Hügel 71, 53121 Bonn, Germany

2 Observational methods for measuring magnetic fields

Interstellar magnetic fields cause the emission of dust particles and atomic and molecular gas species to be polarized. Measurement of this (usually weak) polarized emission is the key to determine the orientation and strength of the ambient magnetic field. For example, in the submillimeter regime, the thermal radiation from non-spherical dust particles becomes linearly polarized perpendicular to the magnetic field lines. A dust polarization map therefore reveals the projection of the magnetic field orientation in the plane of the sky (e.g., Hildebrand et al. 1999). Recent developments in intricate calculations of the dispersion of polarization vectors have led to determination of physical parameters such as the turbulent correlation length in a cloud, the turbulent-to-large-scale magnetic field strength ratio, and the plane-of-the-sky component of the magnetic field strength (Hildebrand et al. 2009, Houde et al. 2009, 2011, 2013).

Magnetic fields can also cause molecular spectral lines to be linearly polarized (Goldreich & Kylafis 1981). Molecules align with the ambient magnetic field and the presence of a source of anisotropy in the medium, such as velocity gradients parallel or perpendicular to the magnetic field, or an external anisotropic radiation, causes a population imbalance in the magnetic sublevels. This causes the emission from these molecules to be linearly polarized. Depending on which sublevel population dominates, the detected linear polarization can be parallel or perpendicular to the magnetic field (Cortes et al. 2005).

Finally, the only direct way of obtaining the strength of magnetic fields is through the Zeeman effect. More precisely, the line-of-sight component of the field can be obtained by measuring the net circular polarization of a molecular spectral line with a significant Zeeman splitting coefficient (e.g., Crutcher et al. 1999, or Claussen et al. 1997, 1999 for applications to SNRs environments). In rare cases where the Zeeman splitting is directly resolved between right- and left- circularly polarized spectra, the total field strength can be constrained (see Hoffman et al. 2005 for measurements in the W28 SNR).

3 Our Work

3.1 Shock modelling

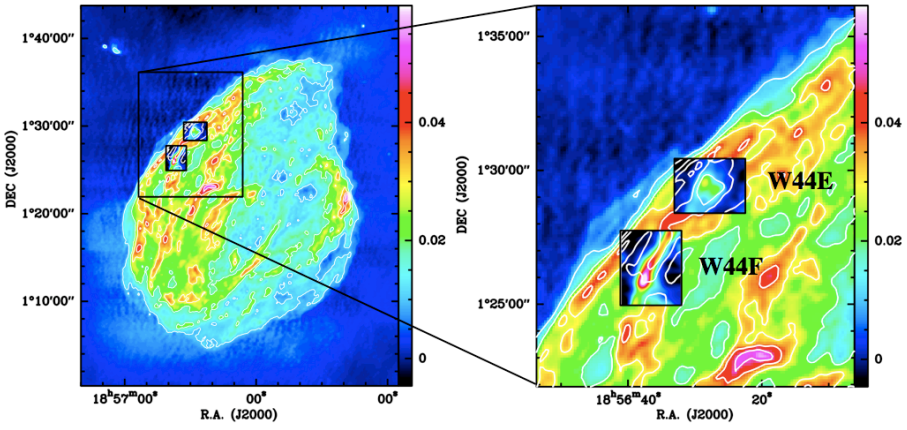

Fig. 1. An example of the regions investigated in our shock modelling studies: W44, Anderl et al., in prep. **Left:** wide-field radio continuum image at 1442.5 MHz, with wedge in units of Jy/beam, from Giacani et al. (1997). **Right:** zoom in the regions W44E and W44F. The insets consist of our CO (6-5) maps, where the intensity is integrated across the velocity range of the shocked gas. The white contours on both panels are radio continuum in steps of 10 mJy.

Our first method of determination of magnetic fields is based on the comparison of molecular line observations with shock models. Dense clumps associated with SNR shells are selected for observations of molecular lines that best trace the shocked gas: CO, a very good density and temperature probe for its abundance and dipole moment and H_2, for its quadrupole transitions at very high temperatures. Several spectral lines of these molecules are targeted, and the corresponding integrated intensities (for CO) or column densities (for H_2, whose lines are naturally optically thin) are used in a so-called 'spectral line energy distribution' (or SLED, for CO) or excitation diagram (for H_2). These observed quantities are then systematically compared to a grid of modelled ones, generated by a state-of-the-art, one-dimensional shock code, designed to simulate the propagation of

stationary C- or J-type shocks, or of non-stationary CJ ones in a dense molecular medium. Such a comparison was first performed in the G knot of SNR IC 443 Cesarsky et al. (1999), using the rotational lines of H_2 observed by ISO. Since then, it has been applied to shocks associated with star formation (e.g. Gusdorf et al. 2011), and again to SNRs such as W28 and 3C 391 (Gusdorf et al. 2012, Gusdorf et al., in prep), and W44 (Anderl et al., in prep). Figure 1 shows an example of the regions where our analysis has been conducted in the SNR W44.

Our goal is to constrain input parameters of our shock models, including pre-shock density $n_{\rm H}$, shock velocity $v_{\rm s}$, age, and type, and the magnetic field strength in the direction perpendicular to the propagation of the considered shock wave. The magnetic field strength determines the type of shock driven in the ISM. In a poorly magnetized medium, the shock corresponds to the propagation of a strong discontinuity in the medium (in temperature, for instance), hence the name 'J-type' (J for Jump) shock. On the contrary, in a strongly magnetized medium, the magnetic field component perpendicular to the shock smoothens this discontinuity, and the maximum temperature and gas compression are attenuated, hence the name 'C-type' (C for Continuous) shock. Both the H_2 excitation diagram and CO SLED reflect this temperature and density differences, hence the suitability of our method to constrain shock parameters. As our shock models self-consistently computes the abundance of over 125 molecules, we can use additional molecules in a similar way to lift a possible degeneracy. So far, the magnetic field values perpendicular to the shock direction yielded by this method have always been found compatible with those inferred from Zeeman measurements from (post-shock) OH masers.

3.2 Application for Non-Zeeman circular polarization observations

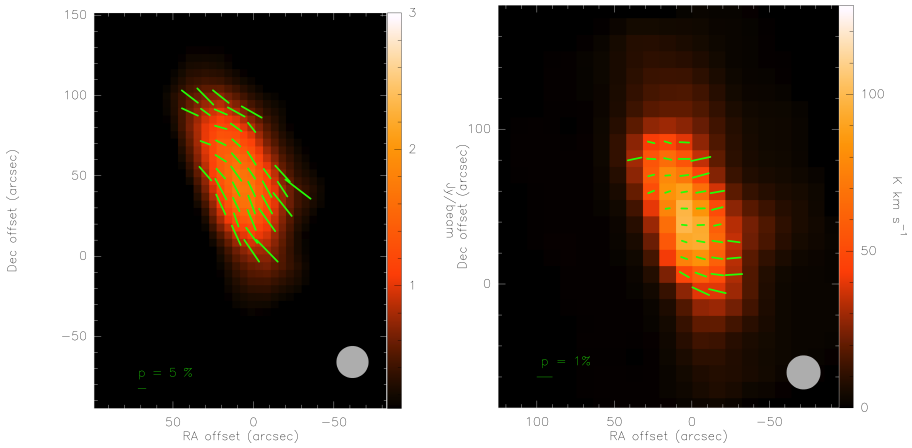

Fig. 2. Left: Dust polarization map of clump G in SNR IC 443 obtained at the APEX telescope. The polarization vectors are perpendicular to the magnetic field lines. **Right:** Polarization map of CO (1–0) in clump G in SNR IC 443 obtained at the IRAM 30-m telescope. The combination of the dust and CO linear polarization maps resulted in the realization of linear-to-circular polarization conversion in CO emission. The cause of this polarization conversion is suggested to be a change of magnetic field orientation in this clump, along the line of sight. From Hezareh et al. (2013).

In a recent study, Hezareh et al. (2013) compared linear polarization maps of dust continuum (observed with the APEX telescope) with polarization maps of CO (2–1) and (1–0) transitions in clump G in SNR IC 443. The dust polarization map shows levels of polarization of up to 10%, and shows a magnetic field orientation perpendicular to the long axis of the source (Figure 1a). The linear polarization maps of CO also reveal polarization levels consistent with what is expected from the Goldreich-Kylafis effect. However, no 0° or 90° difference was seen between the polarization angles of the two sets of maps.

In addition to linear polarization in CO, circular polarization was also detected for the same molecular transitions, with intrinsic levels of up to 0.5–1%. The detected circular polarization is not caused by the Zeeman effect, as the splitting factor for the CO molecule is 4 orders of magnitude smaller than that of the routinely observed molecules like CN and OH. Hezareh et al. (2013) showed that these observations are a result of linear-to-circular polarization conversion in CO emission. The cause of this conversion is explained in a physical model based on anisotropic resonant scattering (Houde et al. 2013). In this model, linearly polarized CO emission (through the Goldreich-Kylafis effect for instance), propagates through the depth of the clump along the line-of-sight, and strikes similar species of molecules in the foreground layer (somewhere in the outer

envelope). If the magnetic field orientation has changed with respect to the deeper regions of the source, then the CO molecules will absorb this linearly polarized emission at the transition frequency to a virtual state and re-emit it via anisotropic resonant scattering with a phase shift between its scattered amplitudes. This phase shift between the orthogonally polarized components of the scattered emission can cause a transformation of linear to circular polarization.

Hezareh et al. (2013) measured this phase shift in their observations and used its value at every pixel of the CO maps to convert the observed circularly polarized flux into linear and recalculate the CO polarization vectors to obtain the anticipated consistency with the dust polarization vectors. Houde et al. (2013) showed that according to this physical model, the amount of the observed phase shift between the components of the incoming signal in each pixel of the maps is a function of the excitation temperature and column density of the observed species, and also the square of the strength of the plane-of-the-sky component of the magnetic field. If the anisotropic resonant scattering model is proven to be the indeed the cause of the confirmed polarization transformation, then a beam-per-beam method for the determination of the magnetic field strength in the plane of the sky will be made possible. This application will be investigated in Hezareh et al., in prep.

4 Conclusion

One of the most significant shortcomings of our shock model is its simple, one-dimensional shock geometry. This means we always assume that the molecular emission comes from a shock layer parallel to the line of sight and seen face-on. Although this method takes a step further compared to more simple approaches (such as 'slab' LVG techniques), the complexity of the observed regions ideally requires multi-dimensional computations, that are very time demanding for current processors. To overcome this difficulty, Kristensen et al. (2008) and Gustafsson et al. (2010) have developed a pseudo-multidimensional model, where one-dimensional shock layers are stitched on curves or surfaces of shocks. The major drawback of this technique is the lack of knowledge on the orientation of the magnetic field with respect to the adopted curves or surfaces. If the anisotropic resonant scattering model discussed in Section 3.2 is indeed causing the linear-to-circular conversion of the observed line polarization, then the combination of dust and CO polarization maps will open a new way to not only trace the changes in magnetic field orientation in extended sources along the line of sight, but also estimate the field strength at several positions in the source and considerably restrict the number of free parameters associated with the current pseudo-multidimensional shock models.

A. Gusdorf acknowledges support by the grant ANR-09-BLAN-0231-01 from the French *Agence Nationale de la Recherche* as part of the SCHISM project. S. Anderl acknowledges support by the DFG SFB 956, the International Max Planck Research School (IMPRS) for Astronomy and Astrophysics, and the Bonn-Cologne Graduate School of Physics and Astronomy.

References

Cesarsky, D., Cox, P., Pineau des Forêts, G., et al. 1999, A&A, 348, 945
Claussen, M. J., Frail, D. A., Goss, W. M., & Gaume, R. A. 1997, ApJ, 489, 143
Claussen, M. J., Goss, W. M., Frail, D. A., & Desai, K. 1999, ApJ, 522, 349
Cortes, P. C., Crutcher, R. M., & Watson, W. D. 2005, ApJ, 628, 780
Crutcher, R. M., Troland, T. H., Lazareff, B., Paubert, G., & Kazès, I. 1999, ApJ, 514, L121
Giacani, E. B., Dubner, G. M., Kassim, N. E., et al. 1997, AJ, 113, 1379
Goldreich, P. & Kylafis, N. D. 1981, ApJ, 243, L75
Gusdorf, A., Anderl, S., Güsten, R., et al. 2012, A&A, 542, L19
Gusdorf, A., Giannini, T., Flower, D. R., et al. 2011, A&A, 532, A53
Gustafsson, M., Ravkilde, T., Kristensen, L. E., et al. 2010, A&A, 513, A5
Hezareh, T., Wiesemeyer, H., Houde, M., Gusdorf, A., & Siringo, G. 2013, A&A, 558, A45
Hildebrand, R. H., Dotson, J. L., Dowell, C. D., Schleuning, D. A., & Vaillancourt, J. E. 1999, ApJ, 516, 834
Hildebrand, R. H., Kirby, L., Dotson, J. L., Houde, M., & Vaillancourt, J. E. 2009, ApJ, 696, 567
Hoffman, I. M., Goss, W. M., Brogan, C. L., & Claussen, M. J. 2005, ApJ, 627, 803
Houde, M., Hezareh, T., Jones, S., & Rajabi, F. 2013, ApJ, 764, 24
Houde, M., Rao, R., Vaillancourt, J. E., & Hildebrand, R. H. 2011, ApJ, 733, 109
Houde, M., Vaillancourt, J. E., Hildebrand, R. H., Chitsazzadeh, S., & Kirby, L. 2009, ApJ, 706, 1504
Kristensen, L. E., Ravkilde, T. L., Pineau Des Forêts, G., et al. 2008, A&A, 477, 203

SF2A 2013
L. Cambrésy, F. Martins, E. Nuss and A. Palacios (eds)

COSMIC RAY TRANSPORT IN THE TURBULENT INTERSTELLAR MEDIUM

A. Marcowith[1], R. Cohet[1] and C.D. Vigh[1]

Abstract. Cosmic Rays are an important component of the interstellar medium and likely play a dynamical role in its evolution from large galactic scales to molecular clouds scales. In this short review, we will discuss the interplay between interstellar medium and magnetic fields and cosmic rays in order to identify this role more properly.

Keywords: Cosmic-Rays: Transport, Interstellar medium: interstellar phases-magnetic field-turbulence.

1 Introduction: Cosmic Ray spectra and Cosmic-Rays

Cosmic Rays (CRs) are charged particles composed of 86% of protons, 11% of Helium nuclei and 1% of leptons plus some heavier nuclei as traces. Since a century after their discovery by V.Hess their origin is still highly debated and remains an unsolved issue of modern astrophysics. In this short review we will be interested in galactic CRs, i.e. particles with energies under 10^{17-18} eV, and especially with particles with energies in the range between MeV and TeV. To be more explicit we consider different types of sub-population. Let us first consider low energy CRs (MeV-GeV) protons (for heavier nuclei one has to consider the energy per nucleon) and low energy CR leptons (keV-MeV), we will call them low energy CRs (LECRs) hereafter. These particles are sub-relativistic with an unknown spectrum because of the solar modulation. It is only since the recent results of the two Voyager missions informations about their spectrum start to be collected (Potgieter 2013). LECRs are of prime importance in the interstellar medium (ISM) studies since they contribute to the ionization process readily at the start of several chemical reactions at the base of molecules synthesis. GeV hadrons and MeV leptons may be distinguished as mildly energy CRs (MECRs). These particles are important for the synthesis of light elements that occur in spallation reactions. Their spectrum also badly known because of the solar modulation. Finally, at higher energies particles are in the relativistic regime (we will call them high energy CRs or HECRs). Their spectrum is not sensitive to the solar wind anymore and has been measured since the beginning of cosmic ray studies *. HECRs are important because they probe the high-energy galactic sky and the CR sources which are likely connected with the lifecycle of massive stars. HECRs are important also because they loose their energy by collision with the interstellar matter in pion production and hence can trace the dense zones of the ISM: the HII regions and the molecular clouds (MCs). One, may be overlooked, question is the role of these different CR populations in the global and local ISM dynamics. To evaluate this effect, we need first to expose the mathematical formalism of CR transport in turbulent magnetic fluctuations (section 2). Hence, we can discuss ISM-CR connection by considering first the impact of the ISM over CRs by the means of the different transport properties of CR in each ISM phase (section 3) and then the impact of CRs over the ISM by the means of different effects (wave production, galactic magnetic dynamo and spallation in section 4). Note that a special section will discuss the case of CR in interaction with MCs (section 4.4), before concluding. A large part of the materials discussed in this review can be found in a special volume of the memorie della Societa Astronomica Italiana (Marcowith et al 2011).

[1] Laboratoire Univers et Particules de Montpellier, Université de Montpellier II/CNRS, place E.Bataillon, cc072, 34095 Montpellier France.
*http://pdg.web.cern.ch/pdg/2013/reviews/rpp2012-rev-cosmic-rays.pdf

2 A brief introduction to CR transport theories

The CR transport in turbulent fluctuations that pervade the ISM is needless to say a very complex problem in modern astrophysics. This, for several reasons: the basic properties of the turbulence is badly known and quite complex. It involves intermittency and anisotropy with respect to the mean (large scales) magnetic field (noted hereafter B_0). The level of fluctuations δB is not small with respect to B_0 (Ferrière 2001). The properties of the ISM itself are also badly known, the medium is heterogeneous with different temperature, pervaded by multiple shocks and stellar winds and with various degree of ionization. The so-called ISM phases have in details complex geometries. All these effects do have a direct impact over CR transport. Finally, there are several ways CRs can interact with the turbulent ISM through: advection in winds, stochastic acceleration on waves and by multiple shock encountering, resonant and non-resonant interaction (see next). All in all, there are still a large steps to purchase between the description of the microphysics CR interaction with magnetic fields and the macroscopic description of their transport from sources to the Earth.

The principles of CR transport are based over the solution of the Lorentz equation that controls the CR trajectory (all equations displayed here are in C.G.S units). Considering an electromagnetic turbulent field $\delta\vec{E}, \delta\vec{B}$ embedded in a mean magnetic field $\vec{B}_0$, we have for a particle of charge q, mass m and Lorentz factor γ.

$$\frac{d\vec{p}}{dt} = q\left(\delta\vec{E} + \frac{\vec{p}}{\gamma mc} \wedge (\vec{B}_0 + \delta\vec{B})\right) \ . \tag{2.1}$$

As the fields are random variables so are the particle momentum p and pitch-angle cosine $\mu = \vec{p}.\vec{B}_0/pB_0$. The first, second and third terms on the RHS of Eq. 2.1 are responsible respectively for CR stochastic acceleration, gyro-motion, and both pitch-angle diffusion and perpendicular transports. Hence, the transport process is controlled by the time correlation of the different fluctuating components. As an illustrative example let us consider the time variation of μ, $\dot{\mu}$. The latter can be expressed in terms of the components of $\delta\vec{B}$. The time correlation integrated over the time defines the pitch-angle cosine diffusion coefficient $D_{\mu\mu}$. To derive it, we calculate the correlation of the magnetic forces between time $t = 0$ and time t expressed with the help of their Fourier components defining the turbulence magnetic correlation tensor. In the case of an homogeneous turbulence we have: $\langle \delta B_i(\vec{k}, t)\delta B_j(\vec{k}', 0)\rangle = P_{ij}(\vec{k}, t)\delta(\vec{k} - \vec{k}'), (i, j) = (x, y, z)$, where $\langle . \rangle$ is an ensemble average over, e.g., several magnetic realizations. The correlation function of the magnetic forces is at position $\vec{x}$ and at time t defined as:

$$R_{ij}(\vec{x}, t) = \int d^3\vec{k} P_{ij}(\vec{k}, t) \exp(i\vec{k}.\vec{x}) \ .$$

Actually the exact solution of the above equation is not accessible as 1) P_{ij} is complex and not known in the ISM 2) the tensor R_{ij} depends on the solution $\vec{x}(t)$, it is an integro-differential equation which itself depends on the effect of P_{ij} on the particle trajectory. The most obvious way to short cut the problem is to assume that $\vec{x}$ is given by the unperturbed gyro-motion of the particle around B_0, this is the so-called quasi-linear theory (QLT). It does work only if $\delta B \ll B_0$ and for short timescales (Shalchi 2009). If an approximated form of P_{ij} can be derived and the QLT is assumed it is relatively easy to derive $D_{\mu\mu}$ (Schlickeiser 2002):

$$D_{\mu\mu} = \int dt \langle \dot{\mu}(t)\dot{\mu}(0)\rangle = \int d^3\vec{k} \Sigma_n \alpha_n(\vec{k}) R_n(\vec{k}, t) \ .$$

Here α_n depends on the tensor components P_{ij} and R_n is the resonance function which in the QLT limit and static turbulence reduced to the Landau-Synchrotron resonance $\delta(\omega - k_\parallel v_\parallel - n\Omega)$ between waves of pulsation ω and wavenumber k and particles with velocity v and synchrotron pulsation $\Omega = qB_0/\gamma mc$. In case of HECRs, the important waves are in the magneto-hydrodynamical (MHD) regime and the dominant resonance are obtained for $n = 1$ and gives $kr_L \sim 1$. The coefficient $D_{\mu\mu}$ controls the random walk of μ along the mean magnetic field and hence the spatial parallel diffusion coefficient. This coefficient is hence strongly dependent on the type of waves that travel along the field lines that can resonate with the particles. In fact, another type of resonance with $n = 0$ (the Tcherenkov resonance) appeared to be important as well, as it couples waves and particles as $kr_L < 1$ (Yan & Lazarian (2004), and next section). Finally, the fact that the magnetic field lines are turbulent induces a perpendicular transport due to their wandering. This effect depends on the correlation tensor choice and may induce some non diffusive transport (Shalchi 2009; Kota & Jokipii 2000) like sub-diffusion.

3 Impact of magnetic fields and interstellar medium over the transport of cosmic rays

3.1 CR transport in different ISM phases

Considering the different ISM phases is important as the MHD waves that pervade the ISM may be strongly absorbed at some specific scales because of their interaction with the background plasma. Two types of damping can be considered: either collisional and collisionless (Yan & Lazarian 2004). The ratio of the turbulence wavelength λ_T over the thermal proton mean free path ℓ_{mfp} due to collisions determines the dominant damping in the different phases. If the ratio $\rho_1 = \lambda_T/\ell_{mfp} > 1$ (< 1) then the damping is in the collisionless (collisional) regime. ISM phases are decomposed into ionized phases themselves decomposed into hot and warm ISM (HISM, WISM, in fact partially ionized) and neutral phases themselves decomposed into warm ISM (WNM, in fact only partially neutral), cold (CNM) ISM and molecular clouds (MCs) (Jean et al 2009). One can also include the galactic halo (low density, high temperatures) as a particular phase (Yan & Lazarian 2004). The latter authors did addressed in some details the propagation of CR in the ionized phases considering the turbulence to be injected at large scales $\lambda_T \sim 100$ parsecs (pc), likely by the supernova remnants (SNR). They considered the anisotropic phenomenological model of Goldreich & Sridhar (Goldreich & Sridhar 1995) to derive a form of the correlation tensor and hence calculate the diffusion coefficients including the possibility for the turbulent spectrum to be cut off by a phase dependent damping process. (The anisotropy here has to be understood with respect to the mean, large scale magnetic field $\vec{B}_0$, that is the magnetic field presents at scales $\sim \lambda_T$.) Note that due to the anisotropic cascade and the anisotropic damping this cut off scale depends on the angle $(\vec{k}, \vec{B}_0)$. The choice of the GS phenomenology to describe the MHD turbulence in the ISM may be subject of questioning but as the basic properties of this model are recovered in numerical experiments of turbulence (see Cho & Lazarian (2003) and references therein) we will consider it as a fiducial model in this review. Yan & Lazarian (2008) concluded that the CR parallel mean free path $\lambda_{CR,\parallel} \propto 1/D_{\mu\mu}$ is largely controlled by the action of fast-magnetosonic waves (compressible MHD modes) rather than the gyro resonance produced by shearing Alfvén waves, strongly inefficient in CR particle diffusion process in the GS spectrum (Chandran 2000). The CR mean free path in the energy range between 10 GeV and 100 TeV in the ionized phases is limited to be in the range 1-10 pc. Under 10-100 GeV starts the process of self-generated waves to become important (see section 4.1).

The CR perpendicular transport is mostly produced by the magnetic field line wandering due to the interaction of shear Alfvén waves that travel along the field lines. The regime of the perpendicular transport depends on the ratio of the $\rho_2 = \lambda_{CR,\parallel}/\lambda_T$. If $\rho_2 > 1$, the diffusion of CRs depends also on the Alfvénic Mach number $M_A = \delta V/V_A$, the ratio of the turbulent velocity fluctuations at λ_T and the local Alfvén velocity. This ratio controls the stiffness of the magnetic field lines. In particular, Yan & Lazarian (2008) found a suppression of the perpendicular diffusion compared to the parallel one scales as M_A^4 in the sub-Alfvénic ($M_A < 1$) case. They further found that sub-diffusion is negligible for CRs in the Alfvénic turbulence (see the review by Lazarian et al (2012)).

Recent test particle numerical simulations solving the Eq.2.1 under the effect of magnetic fluctuations produced in MHD simulations have started to test the above analytical solutions. The caveats in these simulations is that the turbulence has a limited dynamical extension in the Fourier space and that the different damping processes can not be accounted in a one-fluid MHD description. However the first results tend to confirm the previous findings (Beresnyak et al 2011; Xu & Yan 2013).

3.2 The special case of LE-CRs

As already pointed out in the introduction LECR are of particular importance in the ISM due to their ionization performances. But it appears that the way they are transported is only badly known. It would also be important to understand their propagation in some special environments such as the region where SNR shocks do interact with MC where recent ion radicals measurements concluded to enhancements of the ionization rate (Ceccarelli et al 2011). LECR are characterized by small Larmor radii at scales much lower than the large scale cut off scales discussed above. Hence, LECR are at least transported by perpendicular diffusion produced by the magnetic field line wandering process. One possibility, which needs to be investigated further, is the scattering efficiency in the regime of damped turbulence (at small scales) (Shalchi & Busching 2010). This regime can be of particular importance in partially neutral media (Cho & Lazarian 2003).

4 Impact of cosmic rays over magnetic fields and interstellar medium

4.1 Wave production

CR sources are known to be strong sites of magnetic field fluctuations production. In particular there are now strong observational, theoretical and numerical arguments in favor of strong magnetic field amplification in young supernova remnants (e.g. see the review by Schure et al (2012)). It appears that the MHD turbulence is generated by the streaming motions of CR accelerated at the SNR shocks in the ISM background plasma. The latter reacts by producing fluctuations that carry a part of momentum of the CRs to limit the effect of streaming. But the process does not stop as the kinetic energy of the matter dominate both CR and magnetic field energy densities. A recent analysis also shows that a return current is settled to counterbalance the CR streaming (Bell 2004; Pelletier et al 2006). In both cases, strong magnetic field fluctuations that can overtake the mean magnetic field are generated, scatter CR, produce faster acceleration and particular transport diffusion coefficients (Marcowith et al 2006; Marcowith & Casse 2010). An important question still under the debate is the way CRs do escape from their sources and pass from zones where the turbulence is self-generated to zones where the CR transport is controlled by MHD turbulence injected at large scales (see the previous section). The transition likely involves further generation of waves by the streaming instability (Malkov et al 2013) that limit the CR diffusion away from the source.
However, self-generated wave are not limited to the sources or to the region close to the sources. Some streaming modes can be produced at the edge of molecular clouds (see section 4.4). The possibility of galactic wind triggered by the streaming motion of escaping CR has been discussed for a long (see Uhlig et al (2012) and the references therein). There, CRs can indirectly induce a heating of the WIM as the waves are subject to non-linear Landau and ion-neutral damping (Weiner et al 2013). In fine, due to the anisotropy of CR in the ISM, a minimum amount of streaming modes are generated. The streaming modes are strongly damped by the background turbulence (the one injected at large scales) and as the CR energy distribution is soft (the flux is $J(E) \propto E^{-2.75}$ above a few GeV) above energies of the order of 10-100 GeV only(Farmer & Goldreich 2004; Yan & Lazarian 2004). This means that the CR parallel mean free path in this tiny energy range (a few hundred MeV-10 GeV) is likely controlled by the self-generated streaming modes. This regime is important as it probes gamma-rays produced by pion decay in the sensitive band of Fermi.

4.2 Large scale magnetic field dynamo

CRs due to their pressure gradient can produce a force that induces fluid motions. This effect can especially be important above the galactic disk where CR escape from the sources into the halo. Due to the CR streaming (see above) the gas and the frozen-in magnetic field lines are pushed away. The latter are distorted due to the differential rotation of the gas in the Galaxy and can reconnect (Parker 1992). The process has been estimated in two-fluid MHD simulations to efficiently convert small-scale magnetic fields of SNR into galactic-scale magnetic fields (Hanasz et al 2004). The resulting magnetic field structure resembles the X-shaped magnetic fields observed in edge-on galaxies. However the galactic dynamo process can also have different origins (discussed in the review by C. Gissinger in these proceedings).

4.3 Spallation

Interaction of GeV CR with the interstellar matter does produce secondary lighter nuclei. These reactions can be diagnosed using line emission in the hard X-ray and soft gamma-ray domains (Tatischeff 2001). Such lines have only been observed up to now in solar flares episodes but not in galactic sources due to the lack of sensitivities of MeV gamma-ray telescopes. This detection would required a huge improvement in instrumental performances. However, it seems not unrealistic to detect diffuse gamma-ray line emission but a Compton telescope with a sensitivity 30 times larger than COMPTEL. At soft X-ray frequencies the fluorescence iron line at 6.4 keV can probe the interaction of a population of LE and MECR with interstellar matter. This seems in particular the case in the Arch clusters in the galactic center (Dogiel et al 2013)

4.4 CR and molecular clouds: ionization, heating and propagation

There are growing evidences that LECR can enhance the ionization rate in diffuse clouds (Indriolo & McCall 2012) whereas the trend is that the ionization rate in dense cores is to be reduced by an order of magnitude (Ceccarelli 2011). However, the proximity of a strong CR source may change this picture (Indriolo et al 2010).

Recent models involving the combination of ionization losses and the effects of magnetic mirroring and focusing in the MC environment. They evaluate the variation of the ionization rate with the hydrogen column density (Padovani & Galli (2011) see also the contribution by M.Padovani to these proceedings). If this approach gives satisfactory qualitative results, it does not include any turbulence. In MCs, the magnetic field is likely turbulent, hence CR can be scattered by several mechanisms involving magnetic fluctuations (Cesarsky & Völk 1978): resonant scattering (see section 3.1), CR trapping and non-resonant CR interaction with long wavelength waves. It is also well-kown since the late 70's (Skilling & Strong 1976; Cesarsky & Völk 1978) that ionization losses trigger the streaming of CRs outside the MC and produce the exclusion of the particles out of the cloud up to an energy of $\sim$ 100 MeV in standard ISM conditions. Considering all these processes one can indeed expect an enhance ionization at the edge of the cloud and a depletion in the cloud cores. But the solution of the CR density in the cloud depends on the solution of CR density in the inter-cloud medium. Recently, Everett & Zweibel (2011) have reconsidered these solutions including the background galactic CR gradient produced by the CR minimum anisotropy. The authors found the above exclusion mechanism to be weaker and predicted a constant CR density in the cloud that can be tested with the help of observations.
As CRs do produce waves and these waves are damped by ion-neutral friction, the medium is locally heated. It appears, in the analysis of Everett & Zweibel (2011), that the heating due to the presence of a galactic CR gradient is in most of the parameter space (see their table 1) sub-dominant over the conduction. Exception may be found in cases of high magnetic fields (> 30 μG) and high internal CR pressure ($> 10^{-11}$ erg/cc).
Concerning the penetration of ME and HECRs, the mechanisms considered in the analysis of Cesarsky & Völk (1978) do not in general permit a confinement of CR with energy above a few hundred MeV in the MC over timescales longer than the dominant loss timescales. At high energy, this means that CR cross the cloud before having substantially lost their energy by pp interaction. But the detailed propagation of CRs inside MCs is strongly connected to the properties of the turbulence (geometry, intermittency, coherence length, spectra) that are not well known. Further numerical calculations (see the contribution by P.Hennebelle in these proceedings) may help to specify such quantities and constrain the CR transport coefficients around and in dense cores.
Finally, one should mention recent promising efforts in the modeling of the effect of CR transport on thermal stability of MCs (see the discussion in Shadmehri (2009)). It is found a stabilizing effect that depends on the diffusion coefficient and the ratio of CR pressure to gas pressure. But this linear analysis needs some non-linear extension using numerical simulations.

5 Conclusions

CRs are closely coupled to the magnetic field and gas in the ISM. The magnetic field is essential to confine CRs and to scatter them. If the ISM turbulence follows the Goldreich-Sridhar phenomenology, recent analysis showed the importance of considering the supply of fast magneto-sonic waves in the calculation of the CR parallel mean free path. A good assessment of the properties of each phase is important as clear predictions about the perpendicular transport are now available, but the latter depends strongly on the local Alfvénic Mach number which is not known with good accuracies. Also, these analytical calculations have to be confronted to direct numerical simulations of test CR particles propagating in MHD turbulence even if the latter have some intrinsic dynamical limitations. The CR-magnetic field connection have been considered in various places in the ISM: at large scales in CR wind driven scenario as well as CR induced dynamo and at small scales in CR and MC interaction showing a growing evidence of the strong impact of CRs over their environment. If several pieces of the puzzle have now emerged a global view of the role of CRs in the ISM is still missing. First, CR acceleration at fast SNR shocks involves non-linear complex calculations due to the CR back-reaction over the gas and the magnetic field as a good part of the CR power lies in the HE component (even if the production of magnetic fluctuations induce a softening of the CR distribution). The way CR escape from the sources in also a non-linear problem that only received some recent solutions but limited to 1D, hence 3D simulations seem mandatory to understand these processes. It comes out that the presence of a strong CR source may strongly influences its environment certainly over scales of a few hundred parsecs (see the discussion in Nava & Gabici (2013)). This impact has been somehow overlooked in most of the modeling effort up to now and needs to be accounted to understand the dynamical effects of CR over the ISM and magnetic field structures in our Galaxy as well as the reconstruction of the transport of CR in our Galaxy.

The authors thank S. Cabrit, K. Ferrière and P. Hennebelle for their invitation to this special workshop organized during the SF2A 2013 general meeting. This work has been supported by the COSMIS ANR project and by the national program PCMI.

References

Bell A.R. 2004, MNRAS, 353, 550.
Beresnyak A., Yan H., Lazarian A. 2011, ApJ, 728, 60.
Ceccarelli C., Hily-Blant P., Montmerle T., Dubus G. et al 2011, ApJ, 740, L4.
Ceccarelli C. 2011, Mem. S.A.It, 82, 919.
Cesarsky C.J. & Völk H.J. 1978, A&A., 70, 367.
Chandran B. 2000, Phys. Rev. Lett., 85, 4656.
Cho J. & Lazarian A. 2003, MNRAS, 345, 325.
Dogiel, V. A.; Chernyshov, D. O.; Tatischeff, V.; Cheng, K.-S. et al 2013, ApJ, 771, L43.
Everett J. & Zweibel E. 2011, ApJ, 739, 60.
Farmer A. & Goldreich P. 2004, ApJ, 604, 671.
Ferrière K. 2001, RvMP, 73, 1031.
Goldreich P. & Sridhar H. 1995, ApJ, 438, 763.
Hanasz M., Kowal G., Otmianowska-Mazur K., Lesch, H. 2004, ApJ, 605, L33.
Indriolo N. & McCall B. J. 2012, ApJ, 745, 91.
Indriolo N., Blake G. A., Goto M., Usuda T. et al 2010, ApJ, 724, 1357.
Jean P., Gillard W., Marcowith A. & Ferrière K. 2009, A&A, 508, 1099.
Kota J. & Jokipii R.L. 2000, ApJ, 531, 1067.
Lazarian A., Vlahos L., Kowal G., Yan, H. 2012, SSR, 173, 557.
Malkov M. A., Diamond P. H., Sagdeev R. Z., Aharonian F. A. et al 2013, ApJ, 768, 73.
Marcowith A., Bykov A., Ferrière K. & Montmerle T. (edt) 2011, Cosmic Rays and their InterStellar Medium environment: CRISM, Mem. S.A.It, volume 82.
Marcowith A. & Casse F. 2010, A&A, 515, 90.
Marcowith A., Lemoine M. & Pelletier G. 2006, A&A, 453, 193.
Nava L. & Gabici S. 2013, MNRAS, 429, 1643.
Padovani M. & Galli D. 2011, A&A, 530, 109.
Parker E.N. 1992, ApJ, 401, 137.
Pelletier G., Lemoine M. & Marcowith A. 2006, A&A, 453, 181.
Potgieter, M.S. 2013, SSR, 176, 165.
Schure K. M., Bell A. R., O'C Drury L., Bykov A. M. 2012, SSR, 173, 491.
Schlickeiser R. 2002, Cosmic Ray astrophysics, Springer Verlag editor.
Shadmehri M. 2009, MNRAS, 397, 1521.
Shalchi A. & Büsching I. 2010, ApJ, 725, 2110.
Shalchi A. 2009, Non-linear Cosmic Ray transport theories, Springer Verlag editor.
Skilling J. & Strong A.W. 1976, A&A 53, 253.
Tatischeff V. 2003, EAS Publications Series, Volume 7, Final Stages of Stellar Evolution, Proceedings of the conference held 16-21 September, 2001 in Aussois, France. Edited by C. Motch and J.-M. Hameury, p.79.
Uhlig M., Pfrommer C., Sharma M., Nath B.B. et al 2012, MNRAS, 423, 2374.
Wiener J., Zweibel E. G., Oh, S. P. 2013, ApJ, 767, 87.
Xu S.& Yan H. 2013, arXiv1307.1346.
Yan H. & Lazarian A. 2004, ApJ, 614, 757.
Yan H. & Lazarian A. 2008, ApJ, 673, 942.

SF2A 2013
L. Cambrésy, F. Martins, E. Nuss and A. Palacios (eds)

THE ROLE OF COSMIC RAYS IN THE PROTOSTELLAR DISC FORMATION

M. Padovani[1], P. Hennebelle[2] and D. Galli[3]

Abstract. Cosmic rays represent the main actors in regulating the chemical evolution and in setting the ambipolar diffusion time of a molecular cloud. We summarise the processes causing the energy degradation of cosmic rays due to their interaction with molecular hydrogen, also focusing on the magnetic effects that influence their propagation. Making use of magnetic field configurations generated by numerical simulations, we show that the concentration and the wrapping of the field lines in the collapse region lead up to a drop of the cosmic-ray ionisation rate, and consequently of the ionisation fraction, helping to decouple the gas from the magnetic field.

Keywords: ISM: cosmic rays – ISM: clouds, magnetic fields

1 Introduction

Cosmic rays (CRs) play a fundamental role in the interaction with the interstellar matter. They affect numerous physical and chemical processes, being responsible for the evolution of molecular clouds and the formation of the first prestellar structures. In fact, when the visual extinction is higher than about 3–4 magnitudes, the UV radiation field becomes too weak to ionise a cloud and CRs become the foremost ionising agents of the densest regions. As a consequence, CRs are accountable for the ignition of the chemistry in the interstellar medium that arises from the atomic and molecular hydrogen ionisation. Being charged particles, CRs are also partially coupled with interstellar magnetic fields so that they act as regulators on the formation of a protostellar disc.

We are witnessing an era of strong development of new telescopes with higher and higher resolution allowing new observing techniques so as to constrain the CR flux at energies lower than about 1 GeV. Observations of H_3^+ in diffuse clouds (e.g. Indriolo et al. 2012), detections of OH^+ and H_2O^+ in low H_2 fraction regions (Neufeld et al. 2010, Gerin et al. 2010), enhanced CR ionisation rate (ζ^{H_2}) in molecular clouds close to supernova remnants (Ceccarelli et al. 2011) as well as γ luminosity of molecular clouds (e.g. Montmerle 2010) pose the question about how to reconcile the high values of ζ^{H_2} estimated in diffuse regions with those ones measured in denser clouds that are more than one order of magnitude lower. This problem has been addressed using different strategies, analysing the effects of Alfvén waves on CR streaming (Skilling & Strong 1976, Hartquist et al. 1978, Padoan & Scalo 2005, Rimmer et al. 2012), magnetic mirroring and focusing (Cesarsky & Völk 1978, Chandran 2000, Padovani & Galli 2011, hereafter PG11), or the possible existence of a low-energy flux of CR particles able to ionise diffuse but not dense clouds (Takayanagi 1973, Umebayashi & Nakano 1981, McCall et al. 2003, Padovani et al. 2009, hereafter PGG09).

In the following, we resume our previous studies about the dependence of ζ^{H_2} on the column density passed through (Sect. 2) and on the magnetic field configuration (Sect. 3). In Sect. 4 we examine the evolution of ζ^{H_2} for a number of numerical simulations, discussing the variations of ζ^{H_2} in protostellar discs. In Sect. 5 we summarise our conclusions with an outlook on future prospects.

[1] Laboratoire de Radioastronomie Millimétrique, UMR 8112 du CNRS, École Normale Supérieure et Observatoire de Paris, 24 rue Lhomond, 75231 Paris cedex 05, France

[2] CEA, IRFU, SAp, Centre de Saclay, 91191 Gif-Sur-Yvette, France

[3] INAF–Osservatorio Astrofisico di Arcetri, Largo E. Fermi 5, I–50125 Firenze, Italy

2 Column-density effects on the CR ionisation rate

While entering an interstellar cloud, CRs mainly interact with molecular hydrogen and are subject to different energy loss processes depending on their energy and their composition (namely protons, electrons, and heavy nuclei). Table 1 lists the processes degrading the CR spectrum.

The quantity that describes the CR braking for the component k, called *energy loss function*, is defined by

$$L_k(E_k) = -\frac{1}{n(\mathrm{H_2})}\left(\frac{\mathrm{d}E_k}{\mathrm{d}\ell}\right), \tag{2.1}$$

where $n(\mathrm{H_2})$ is the density of the medium in which the particle of energy E_k propagates and ℓ is the path length. The spectrum of CR particles of species k at depth $N(\mathrm{H_2})$, $j_k(E_k, N)$, namely the number of particles

Table 1: List of the energy loss processes during the collision between CRs and $\mathrm{H_2}$.

Energy loss process	CR component affected
Coulomb interactions	p, e
Elastic interactions	p
Inelastic interactions	p, e
Ionisation	p, e
Bremßtrahlung	e
Synchrotron emission	e
Inverse Compton scattering	e
Pion production	p
Spallation	p

per unit area, time, solid angle, and per energy interval, can be related with the local interstellar spectrum incident on the surface of the cloud, $j_k(E_k, 0)$, using the definition of $L_k(E_k)$. Assuming that (*i*) the direction of propagation of a CR does not change critically inside the cloud (Takayanagi 1973) and that (*ii*) the number of particles is conserved (ignoring electron capture reactions of CR protons with $\mathrm{H_2}$ and He as well as the $\alpha+\alpha$ fusion reactions that form ^{6}Li and ^{7}Li because of the small cross sections, Meneguzzi et al. 1971), $j_k(E_k, N)$ is related to $j_k(E_k, 0)$ by

$$j_k(E_k, N) = j_k(E_{k,0}, 0)\frac{L_k(E_{k,0})}{L_k(E_k)} \tag{2.2}$$

where $E_{k,0}$ is the initial energy of the CR and E_k is the energy of the CR at depth $N(\mathrm{H_2})$.

In PGG09 we show that even if a local interstellar spectrum is devoid of low-energy particles, a low-energy tail is produced by the slowing-down of CR protons and electrons during their propagation. Our modelling is able to explain the decrease of $\zeta^{\mathrm{H_2}}$ with increasing hydrogen column density computed from observations. In particular, a proton component at low energies, and most likely also an electron component, could be necessary to reproduce the data. Figure 1 is the updated version of Fig. 15 in PGG09 including most recent estimates.

3 Magnetic-field effects on the CR ionisation rate

CRs are charged particles and interact with the magnetic field threading a molecular cloud. In PG11 we investigate the propagation of CRs along field lines accounting for magnetic mirroring and focusing that act reducing and amplifying the CR flux, respectively. In fact, assuming the conservation of the kinetic energy of a particle, $E_{\mathrm{kin}} = (\gamma-1)mv^2$, and of its magnetic momentum, $\mu = \gamma m v^2 \sin^2\alpha/2B$, it is possible to prove that, depending on the initial angle, α_{ICM}, between the particle's velocity and the magnetic field, a CR can cross the entire core or can be bounced out (*mirroring*), leading to a decrease of $\zeta^{\mathrm{H_2}}$. Conversely, supposing the same number of CRs per length of field line and being the CR flux proportional to the density of magnetic field lines per unit area, the CR flux in the cloud must be a factor $\chi = B/B_{\mathrm{ICM}}$ larger than the flux in the intercloud medium (ICM), where B is the magnetic field module (*focusing*). As a consequence, $\zeta^{\mathrm{H_2}}$ will be boosted in regions with higher magnetic field.

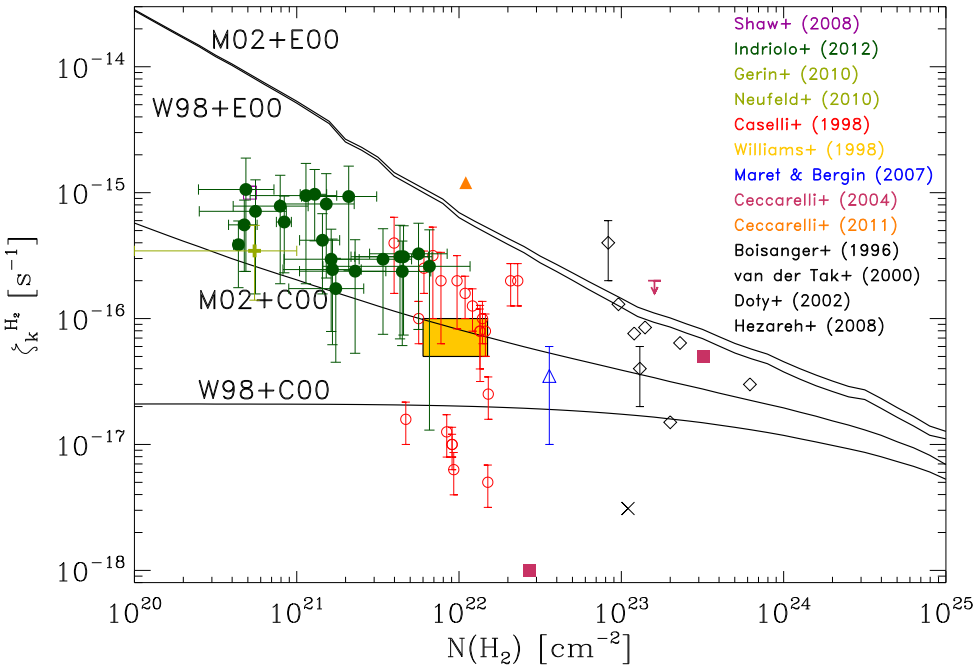

Fig. 1: Total CR ionisation rate, ζ^{H_2}, as function of $N(H_2)$ according to our models (*solid* curves) in comparison with available observational data. Model labels are given in PGG09.

The evolution of the pitch angle along its trajectory is then given by

$$\alpha = \arccos\sqrt{1-\chi+\chi\cos^2\alpha_{\rm ICM}}\,, \tag{3.1}$$

and the column density "seen" by a CR reads

$$N(\alpha) = \int_0^{\ell_{\rm max}(\alpha)} n(\ell)\,{\rm d}\ell\,, \tag{3.2}$$

where $\ell_{\rm max}$ is the maximum depth reached inside the core and $n(\ell)$ is the H_2 volume density. If α reaches $\pi/2$, then the particle is bounced back, otherwise, having enough energy, it crosses the core as sketched in Fig. 2.

4 CR ionisation in protostellar discs

In Padovani, Hennebelle & Galli (2013b), hereafter PHG13, we check the possibility that a reduction of the CR flux due to the field line twisting in a collapsing cloud can decrease ζ^{H_2}, and then the ionisation fraction. For this purpose, we follow the path of CRs using magnetic field configurations generated by numerical simulations related to a rotating collapsing core (described in PHG13 and detailed in Joos et al. 2012), performed with the AMR code RAMSES (Teyssier 2002, Fromang et al. 2006). We assume the model M02+C00 (see Fig. 1 and PHG13) as "fiducial" spectrum in order to describe ζ^{H_2} as function of the column density. For each field line and each initial pitch angle $\alpha_{\rm ICM} \in [0, \pi/2)$, we compute $\zeta^{H_2}(\alpha)$ following Padovani, Galli & Glassgold (2013a), hereafter PGG13,

$$\zeta^{H_2}(\alpha) = \frac{\zeta_0^{(\rm low\ N)}\zeta_0^{(\rm high\ N)}}{\zeta_0^{(\rm high\ N)}\left[\dfrac{N(\alpha)}{10^{20}\ {\rm cm}^{-2}}\right]^a + \zeta_0^{(\rm low\ N)}\left[\exp\left(\dfrac{\Sigma(\alpha)}{\Sigma_0}\right)-1\right]}\,, \tag{4.1}$$

where $\Sigma(\alpha) = \mu m_{\rm p} N(\alpha)/\cos\alpha$ is the effective surface density seen by a CR propagating with pitch angle α, $m_{\rm p}$ the proton mass, and $\mu = 2.36$ the molecular weight for the assumed fractional abundances of H_2 and He.

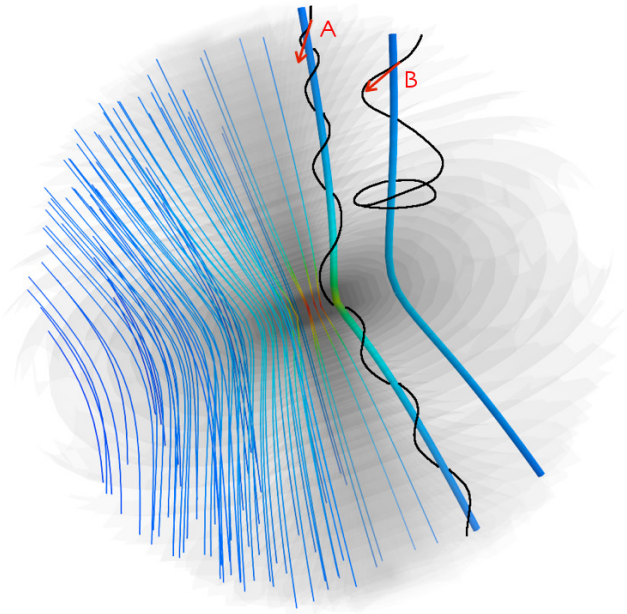

Fig. 2: Sketch of magnetic field lines for a purely poloidal field superposed to density isocontours in grey scale. The two helicoidal *solid black* lines show potential opposite scenarios for the CR path: depending on the CR initial pitch angle, determined by the velocity vector (*red arrows*) and the magnetic field, the particle passes through the core (path A) or goes backwards (path B).

The fitting coefficients of Eq. (4.1) are given in PGG09 and PGG13. In order to evaluate ζ^{H_2} along a field line, we average the contribution of all the particles with different $\alpha_{\rm ICM}$ over the solid angle. Then we multiply the result by χ to account for focusing

$$\zeta^{H_2} = \chi \frac{\int \zeta^{H_2}(\alpha)\, \mathrm{d}\Omega_\alpha}{\int \mathrm{d}\Omega_\alpha} = \chi \int_0^{\pi/2} \zeta^{H_2}(\alpha) \sin\alpha \, \mathrm{d}\alpha \,. \tag{4.2}$$

In PHG13 we test a large number of magnetic configurations, varying the initial orientation between the magnetic field direction and the rotation axis, $\alpha_{\rm B,J}$, as well as the mass-to-flux ratio, λ. Here we focus on two cases leading to the formation of a keplerian disc whose parameters are: ($\mathcal{A}$) $\lambda = 5$ (intermediate magnetisation), $\alpha_{\rm B,J} = \pi/2$ (perpendicular rotator), and $t = 10.756$ kyr; ($\mathcal{B}$) $\lambda = 17$ (weak magnetisation), $\alpha_{\rm B,J} = 0$ (parallel rotator), and $t = 6.620$ kyr, where t is the time after the formation of the first Larson's core*.

Results for the case ($\mathcal{A}$) are presented in the left column of Fig. 3. It is worth noting in the face-on view (upper left panel) a large region of $r \sim 200$ AU and $n \gtrsim 10^9$ cm^{-3} with $\zeta^{H_2} \lesssim 10^{-18}$ s^{-1}. Here the ratio between the toroidal component and the magnetic field module, B_φ/B, is larger than about 0.4. Even lower values, with a minimum of 2×10^{-21} s^{-1}, are reached in the inner area with an extent of a few tens of AU. This can be also appreciated in the edge-on view (upper right panel) where ζ^{H_2} is so low that we can assume the gas to be effectively decoupled with the magnetic field. The lower panel shows how the rotation perpendicular to the y axis forces the field lines (initially with a poloidal configuration along the x axis) to wrap around the rotation axis.

A similar set of plots for the case ($\mathcal{B}$) is displayed in the right column of Fig. 3. The high mass-to-flux ratio leads to a weakening of the magnetic field braking, so that the rotation is able to strongly twist the field lines (lower panel). This explains why the decrease of ζ^{H_2} broadens perpendicularly to the disc plane (upper left panel) and it is not circumscribed to the high-density domain ($n > 10^9$ cm^{-3}). In fact, being the field lines very tangled, the magnetic mirror is even more marked, creating a large region along the x axis where $\zeta^{H_2} \sim 10^{-18}$ s^{-1}. As for the case ($\mathcal{A}$), the region with $n \gtrsim 10^9$ cm^{-3} and $\zeta^{H_2} \lesssim 10^{-18}$ s^{-1} shows $B_\varphi/B \gtrsim 0.4$.

*It is the core formed in the centre of the pseudo-disc with $n \gtrsim 10^{10}$ cm^{-3} and $r \sim 10 - 20$ AU.

In the (y, z) plane (upper right panel) one can see the presence of the face-on disc and the rapid decrease of ζ^{H_2} that reaches about 10^{-20} s^{-1} in the inner 10^{10} cm^{-3} iso-density contour.

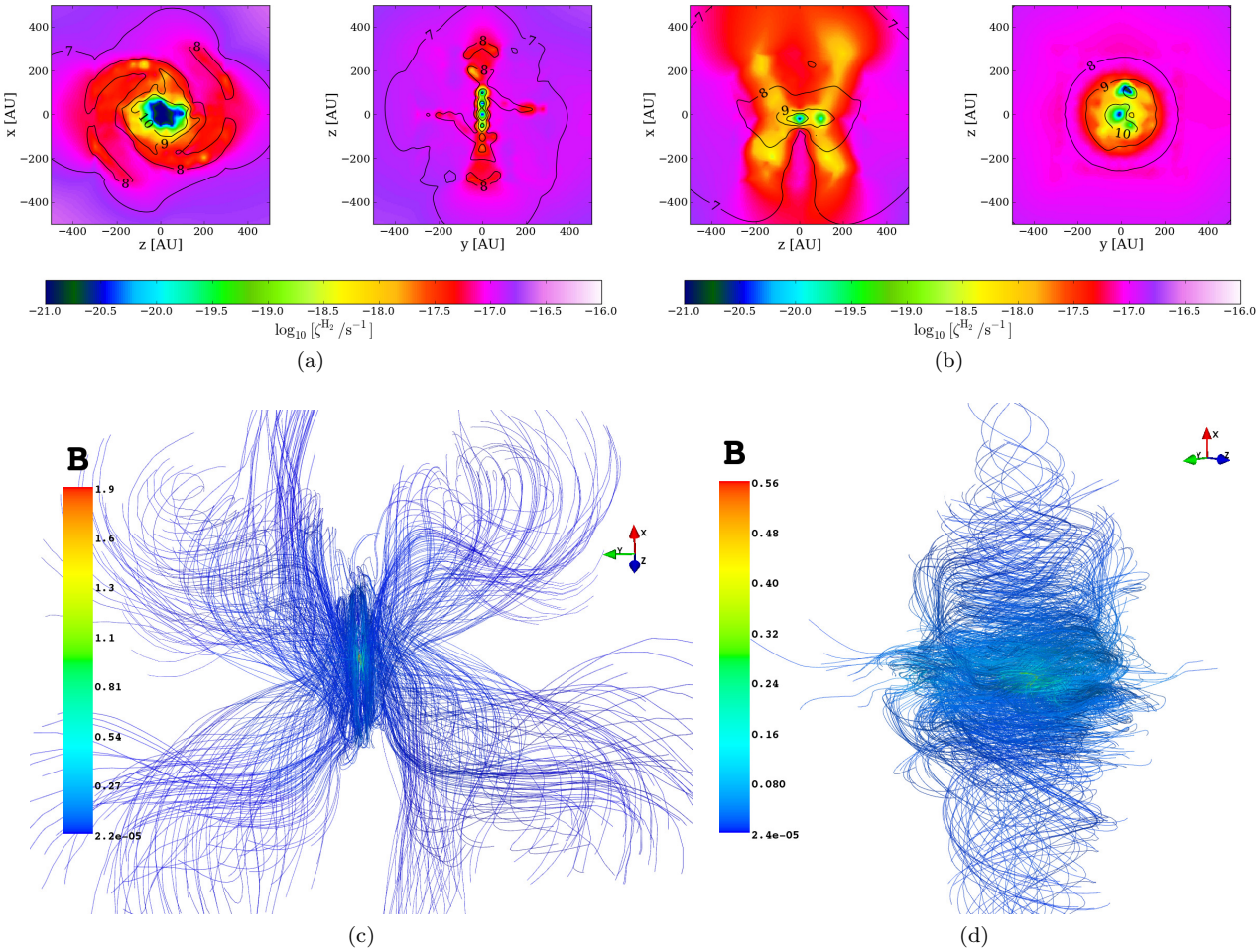

Fig. 3: **Left column:** CR ionisation maps and iso-density contours (*black solid lines*) for the case ($\mathcal{A}$). Upper panels show a slice of a plane parallel to the magnetic field direction (on the left) and of a perpendicular plane (on the right). Both planes contain the density peak and labels show $\log_{10}$ $[n/\mathrm{cm}^{-3}]$. The lower panel shows the magnetic field line morphology in the central 600 AU of the RAMSES data cube. **Right column:** Same as left column plots, but for the case ($\mathcal{B}$).

5 Conclusions and future prospects

Magnetic mirroring and focusing set the extent to which CRs can determine the coupling between magnetic fields and the gas. In Sect. 4 we show the importance of accounting for the true path of CRs along magnetic field lines with the inclusion of magnetic effects (see also Sect. 5 in PHG13 for a comprehensive discussion). Being aware of the fact that the correct manner of dealing with CR propagation should be computing their distribution simultaneously with the MHD simulation, we believe that our conclusions represent an important proof of concept. In particular, in the central 100 AU region, the number density is higher than 10^{10} cm^{-3} and a H_2 column density larger than 10^{25} cm^{-2} is promptly reached. This actually means entering the exponential attenuation regime where the CR ionisation rate is independent of the CR spectrum assumed and drops below 10^{-18} s^{-1}. However, we prove that even in the high-density region, the presence of a magnetic field can reduce ζ^{H_2} up to a factor larger than 10, well below the ordinarily used value of 10^{-17} s^{-1}. We conclude that the morphology of the ζ^{H_2} maps depends both on the density profile and on the magnetic field line configuration.

Non-ideal MHD models predict that magnetic braking becomes inefficient at densities $n > 10^{12}$ cm^{-3}, when

magnetic field diffusion becomes faster than the dynamical evolution (Dapp et al. 2012). In our models we observe that the drop in $\zeta^{\mathrm{H_2}}$ takes place in some cases even at lower densities ($n > 10^9$ cm^{-3}), resulting in very low ionisation fractions. It will be important to study the consequences of the reduced CR ionisation rate on the magnetic diffusion coefficients (ambipolar, Hall, and Ohm). In order to test this hypothesis, a self-consistent MHD collapse calculation including CR propagation is needed.

References

Caselli, P., Walmsley, C. M., Terzieva, R., et al. 1998, ApJ, 499, 234

Ceccarelli, C., Dominik, C., Lefloch, B., et al. 2004, ApJ, 607, L51

Ceccarelli, C., Hily-Blant, P., Montmerle, T., et al. 2011, ApJ, 740, L4

Cesarsky, C. J. & Völk, H. J. 1978, A&A, 70, 367

Chandran, B. D. G. 2000, ApJ, 529, 513

Dapp, W. B., Basu, S. & Kunz, M. W. 2012, A&A, 541, A35

de Boisanger, C., Helmich, F. P. & van Dishoeck, E. F. 1996, ApJ, 463, 181

Doty, S. D., van Dishoeck, E. F., van der Tak, F. F. S., et al. 2002, A&A, 389, 446

Fromang, S., Hennebelle, P. & Teyssier, R. 2006, A&A, 457, 371

Gerin, M., De Luca, M., Black, J. et al. 2010, A&A, 518, L110

Hartquist, T. W., Doyle, H. T. & Dalgarno, A. 1978, A&A, 68, 65

Hezareh, T., Houde, M., McCoey, C., et al. 2008, ApJ, 684, 1221

Indriolo, N. & McCall, B. J. 2012, ApJ, 745, 91

Joos, M., Hennebelle, P. & Ciardi, A. 2012 A&A, 543, 128

Maret, S. & Bergin, E. A. 2007, ApJ, 664, 956

McCall, B. J., Huneycutt, A. J., Saykally, et al. 2003, Nature, 422, 500

Meneguzzi, M., Adouze, J. & Reeves, H. 1971, A&A, 15, 377

Montmerle, T. 2010, in ASP Conf. Ser. 422, High Energy Phenomena in Massive Stars, ed. J. Martí, P. L. Luque-Escamilla, & J. A. Combi (San Francisco, CA: ASP), 85

Neufeld, D. A., Goicoechea, J. R., Sonnentrucker, P., et al. 2010, A&A, 521, 10

Padoan, P. & Scalo, 2005, ApJ, 624, L97

Padovani, M., Galli, D. & Glassgold, A. E. 2009, A&A, 501, 619 (PGG09)

Padovani, M. & Galli, D. 2011, A&A, 530, A109 (PG11)

Padovani, M., Galli, D. & Glassgold, A. E. 2013, A&A, 549, C3 (PGG13)

Padovani, M., Hennebelle, P. & Galli, D. 2013, A&A, *in press* (`http://arxiv.org/abs/1310.2158`)

Rimmer, P. B., Herbst, E., Morata, O. et al. 2012, A&A, 537, 7

Skilling, J. & Strong, A. W. 1976, A&A, 53, 253

Takayanagi, M. 1973, PASJ, 25, 327

Teyssier, R. 2002, A&A, 385, 337

Umebayashi, T. & Nakano, T. 1981, PASJ, 33, 617

van der Tak, F. F. S. & van Dishoeck, E. F. 2000, A&A, 358, L79

van der Tak, F. F. S. & van Dishoeck, E. F. & Evans, N. J., II et al. 2000, ApJ, 537, 283

Williams, J. P., Bergin, E. A., Caselli, P. et al. 1998, ApJ, 503, 689

SF2A 2013
L. Cambrésy, F. Martins, E. Nuss and A. Palacios (eds)

THE STRUCTURE OF THE THERMALLY BISTABLE, TURBULENT AND MAGNETIZED ATOMIC GAS

E. Saury[1], A. Bracco[1], F. Boulanger[1], M.-A. Miville-Deschênes[1] and P. Hennebelle[2]

Abstract. The work presented here is focused on the evolution of the atomic and diffuse interstellar medium that provides the initial conditions to the formation of molecular clouds. We quantify the roles of thermal instability, turbulence and magnetic field in the formation of CNM gas out of the WNM with numerical simulations performed with the code HERACLES.
First, we present the results of a study of the WNM-CNM transition in the non-magnetized case. With WNM initial conditions and stirring in of turbulent motions at large scales, the hydrodynamical simulations reproduce basic observational statistics of the diffuse ISM as the mass in the cold phase. A process of compression is needed to create CNM through the thermal instability, either with a majority of compressible modes of the injected turbulent velocity field or with an initial density of the WNM higher than the fiducial value for the thermal equilibrium.
Lastly, we present a set of MHD simulations based on the parameter study performed in the hydrodynamical case and compare their ability to create CNM and their properties regarding the dust polarization, as the maps of the stokes parameters and the dispersion of the polarization angle. We obtain a good agreement with the recent results of the Planck satellite.

Keywords: turbulence, magnetic field, instabilities, ISM:clouds, ISM:structure

1 Introduction

One of the main current questions in Astrophysics is the understanding of the star formation process, directly related to the processes involved in the cooling and the condensation of the gas yielding to intricate filamentary structures of molecular clouds. Magnetic field, thermal instability and turbulence are playing dominant roles in this complex dynamics.
Observations of the atomic interstellar medium (HI, dust) show that discrete structures of cold and optically thick gas (CNM, T∼100K, n∼ 100 cm^{-3}) are surrounded by a much more diffuse, warm and optically thin medium (WNM, T∼ 8000K, n∼ 0.5cm^{-3}), detected on each line of sight (Dickey et al. 2003). Heiles & Troland (2003) studied the fraction of cold atomic gas and found that around 40% of the HI is in the CNM phase, and that its volume filling factor is equal to 1%. Moreover, the width and the relative smoothness of the 21 cm emission spectra (Miville-Deschênes & Martin 2007; Dickey et al. 2003) indicate that their turbulent broadening is less or equal to the thermal broadening, leading to a subsonic or sonic Mach number.
We want to adress here two questions : Can the WNM gas at the thermal equilibrium values of temperature and density transit to CNM with turbulent motions alone or is some extra form of compression needed ? What is the impact of the magnetic field on the formation of the cold structures in the ISM ?

2 Numerical methods

All the following simulations are performed with the code HERACLES (González et al. 2007) on a fixed grid. The gas cooling drives the thermal instability. It comprises the main heating and cooling processes of the atomic medium for our range of temperature [10 K, 10^4 K] and is based on the results of Wolfire et al. (2003) : the

[1] Institut d'Astrophysique spatiale, bâtiment 121, Université Paris-XI, 91405 ORSAY CEDEX, France
[2] Laboratoire AIM, CEA/DSM-CNRS, Université Paris Diderot, IRFU/SAp, 91191 Gif-sur-Yvette, France

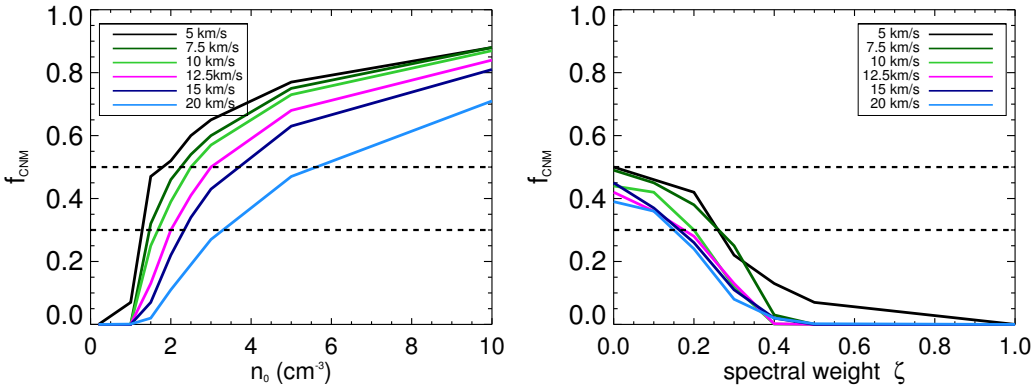

Fig. 1. Behavior of $f_{\rm CNM}$ depending, **on the left**, on the initial density with ζ fixed to 0.5 and depending, **on the right**, on the projection weight ζ with the initial density n_0 fixed to $1\,{\rm cm}^{-3}$. The different colors of the plain lines represent the different values of the turbulent velocity field amplitude, the two dashed lines frame the range of $f_{\rm CNM}$ we want to reproduce.

heating is induced by the photoelectric effect on the grains, and the cooling by CII and OI lines, hydrogen Lyman-α line and electrons recombination on the grains.
A force field **f** generates the large scales motions and is applied in Fourier space. We define the amplitude given to the field as $v_{\rm S}$. The modes of the turbulent forcing are computed with the stochastic process of Ornstein-Uhlenbeck (Eswaran & Pope 1988; Schmidt et al. 2006). The method is similar to Schmidt et al. (2009) and Federrath et al. (2010). A Helmholtz decomposition is applied to the random field and projects it on its compressive and solenoidal components. The projection weight ζ represents the ratio of solenoidal (divergence-free) to compressive (rotation-free) modes of the turbulent velocity field. Choosing a spectral weight $\zeta = 1$ creates a physical force divergence free, i.e. purely solenoidal. Taking $\zeta < 1$ generates dilatational components which compress or rarify the gas. Finally, $\zeta = 0$ creates a rotation-free field, i.e. purely compressive. In a natural state, meaning that the energy is naturally distributed between the compressive and solenoidal modes as the 2:1 mixing, ζ takes the value of 0.5. In this case, the Helmholtz operator is proportional to the identity operator and the projection does not alter the energy repartition between the different modes.

3 Parameter constraints on hydrodynamical simulations

We computed a set of 90 hydrodynamical simulations at small resolution (128^3 cells, $B_0 = 0\,\mu$G) in order to determine which initial conditions reproduce the observed properties of the cold H I out of WNM: a biphasic medium with a CNM mass fraction of 40%, a volume filling factor for the CNM around 1% and a sub or transonic turbulence ($\mathcal{M} \sim 1$). To do so, we use a box size of 40 pc and an initial temperature of 8000 K for all simulations. We vary the initial density n_0 from 0.2 to $10\,{\rm cm}^{-3}$, the large scale amplitude $v_{\rm S}$ at 20 pc from 5 to $20\,{\rm km\,s}^{-1}$(leading to Mach numbers from 0.2 to 2.5) and the projection weight from purely solenoidal modes ($\zeta = 1$) to purely compressive modes ($\zeta = 0$) (see Saury et al. 2013, for a detailed study of these simulations).
The main constraint we are considering here is the mass fraction of CNM created in the simulation, $f_{\rm CNM}$, computed as the ratio of the mass in the pixels where $T < 200\,{\rm K}$ and the total mass in the simulation. The obtained values are presented on Figure 1. For the case on the left, the projection weight ζ is fixed to 0.5 and we vary the initial density and the large scale velocity $v_{\rm S}$. The transition from WNM to CNM never occurs when the initial density is smaller than $1.5\,{\rm cm}^{-3}$. On the other hand, all the simulations with $n_0 > 3\,{\rm cm}^{-3}$ create more than 30% of cold gas in mass. On the right part of Fig. 1, we represent the evolution of $f_{\rm CNM}$ with the projection weight while n_0 is fixed to $1\,{\rm cm}^{-3}$. We observe that the solenoidal modes (ζ close to 1) are not efficient to create the cold gas and that a majority of compressive modes is necessary ($\zeta < 0.3$). We also emphasize that the highest amplitudes of the turbulence are not efficient to trigger the transition, on the contrary. This is due to the fact that, for the highest values of $v_{\rm S}$, the cooling time of the WNM becomes larger than the turbulent time: the compressed WNM gas does not have time to cool down before being re-expanded by the turbulent motions.
For the second part of the work presented here, we will consider simulations with the following initial conditions: $n_0 = 2\,{\rm cm}^{-3}$, $\zeta = 0.5$ and $v_{\rm S}$ =$7\,{\rm km\,s}^{-1}$. To validate this choice, we computed the volume filling factor of the

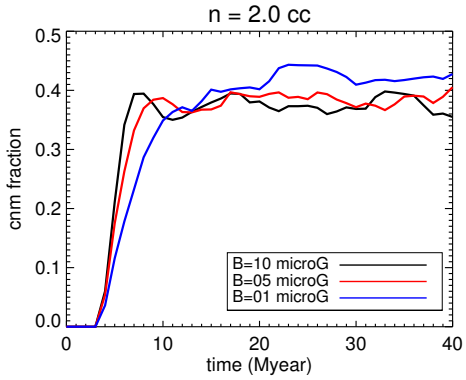

Fig. 2. Time evolution of the cold gas mass fraction $f_{\rm CNM}$ for three MHD simulations (128^3 cells) with different initial values of the magnetic field: 1, 5 and 10 μG.

CNM, close to 4%, and the mean Mach number, equal to 1.2. The fundamental statistical properties of the CNM are all well reproduced in this simulation.

4 MHD simulations and dust polarization

In order to study the magnetized turbulence properties of the diffuse interstellar medium, we computed MHD simulations at small (128^3 cells) and high (512^3 cells) resolution with the initial conditions obtained previously and the three following values of the magnetic field B_0: 1, 5 and 10 μG. B_0 is initially uniform and parallel to the $x-$axis. We investigated the effect of the magnetic field on the formation of cold gas by computing $f_{\rm CNM}$. Its evolution with time is shown on Figure 2 for the three simulations at small resolution. We averaged $f_{\rm CNM}$ on the time range [10 My,20 My] and obtained 41 ± 3, 38 ± 2 and 37 ± 2 for B_0 equal to 1, 5 and 10 μG respectively. This suggests that the magnetic field has no real impact on the mass fraction of CNM formed in the simulations and validates the parametric study on hydrodynamical simulations.

As $f_{\rm CNM}$ cannot be used as a constraint on the magnetic field amplitude, we created synthetic polarization maps using the high resolution simulations (512^3). Observationally, the study of the polarization of dust thermal emission at infrared and submillimeter wavelengths is a method to measure the component of the magnetic field perpendicular to the line of sight (Hildebrand et al. 2000). The Stokes parameters I, Q and U are built by an integration along the line of sight through the simulations (following the method used in Fiege & Pudritz (2000) and Falceta-Gonçalves et al. (2008)) and can be compared statistically to the Planck results. Figure 3 presents these maps for the simulation with $B_0 = 5\,\mu$G (because of their similarities with the 5 μG case, we don't present here the maps for the two other simulations). We note that most of the structures in the intensity map (I) have a counterpart in Q and U, which may be used to determine the structure of the magnetic field in the filaments. A comparison with observations is therefore promising, the satellite Planck having the sensitivity to detect the brightest filaments, even in the diffuse H I.

The analysis of the Planck data showed a correlation between the polarization fraction $p = P/I$ and the dispersion function of the polarization angle $\Delta\psi$ (Bernard 2013). The polarization fraction $p = P/I = \alpha_{\rm dust}\cos^2\gamma$ combines the intrinsic polarization fraction of the dust $\alpha_{\rm dust}$ and the structure of the magnetic field, γ being the angle between $\mathbf{B}$ and the plane of the sky. On the other hand, the dispersion function of the polarization angle provides only information on the magnetic field. Their comparison is a mean to distinguish the properties of the matter and the structure of the magnetic field. In order to compare the simulations to observations, we computed the P/I map (left part of Fig. 4) and $\Delta\psi(0)$ (right part of Fig. 4) for the simulation with an initial B_0 equal to 5 μG. As explained in Hildebrand et al. (2009), $\Delta\psi^2(l) = 1/N\ \sum_{i=1}^{N}[\psi(\mathbf{r}) - \psi(\mathbf{r}+\mathbf{l_i})]^2$ is a measure of the difference in angle for each pair of points separated by the distance $|\mathbf{l}|$. As observed on the data and on simulations of molecular clouds (Levrier 2013), we note an anti-correlation between the polarization fraction P/I and $\Delta\psi(0)$.

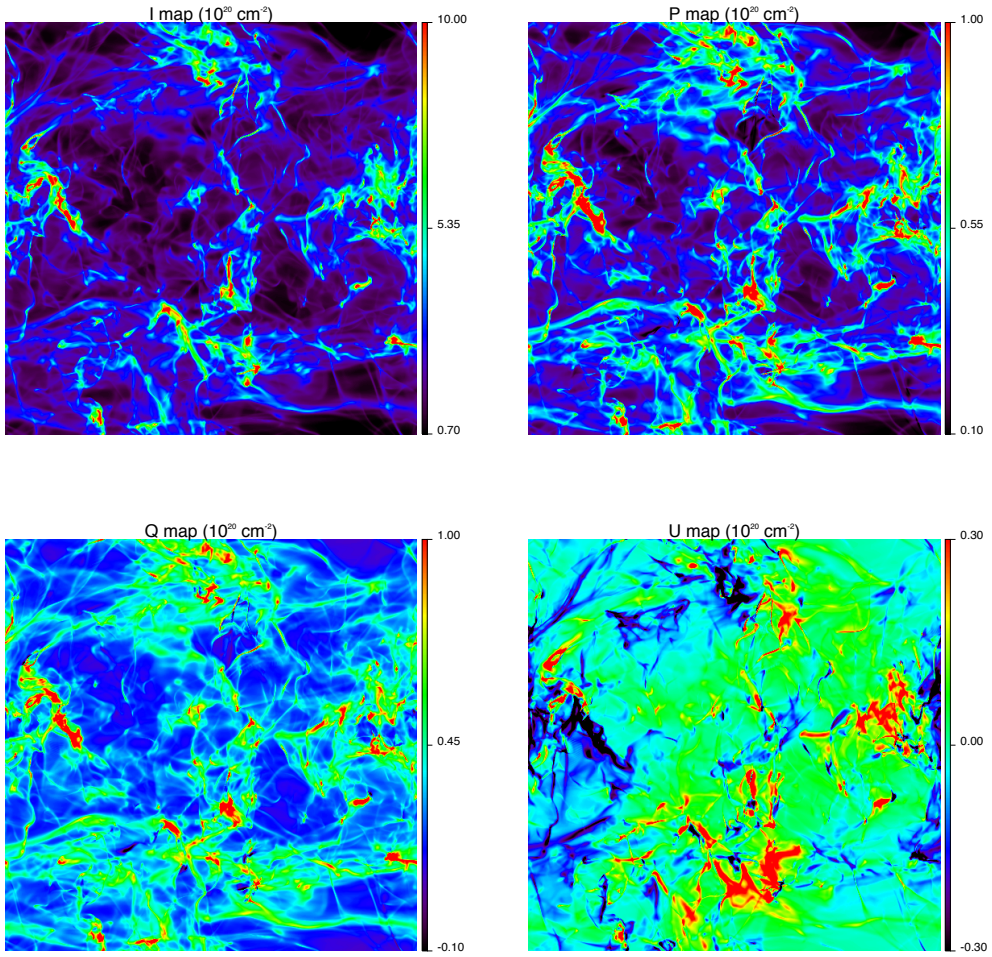

Fig. 3. Stokes parameters: I map (**top left**), P map (**top right**), Q map (**bottom left**) and U map (**bottom right**).

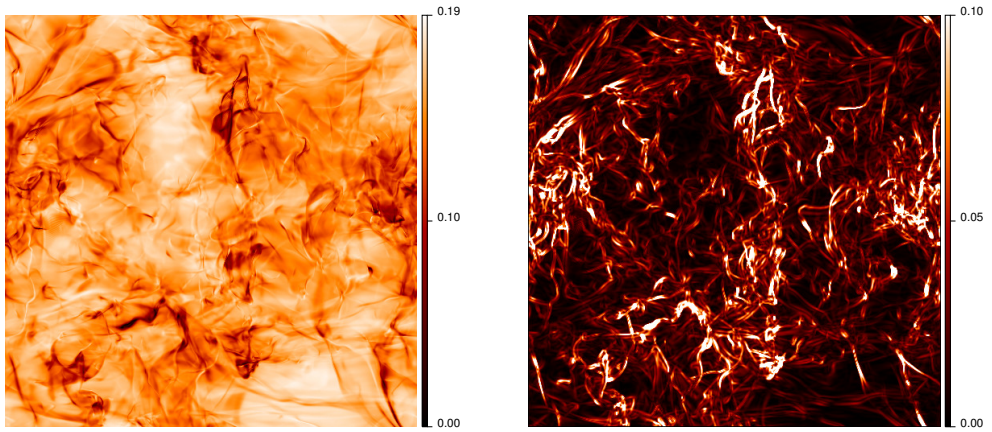

Fig. 4. **Left**: map of the polarization fraction P/I, **right**: dispersion of the polarization angle $\Delta\psi(0)$

5 Conclusions

We performed a parametric study on hydrodynamical simulations to determine the initial conditions that lead to the formation of 40% of CNM with a Mach number close to 1. We conclude that the ISM turbulence cascade on its own cannot induce a transition from WNM into CNM at the fiducial density of the WNM set by thermal equilibrium (Fig. 1). The production of CNM is likely to be due to turbulent motions of moderate amplitude associated with compression by e.g. the expansion of H II regions, a supernova explosion or spiral density waves.

We computed MHD simulations of the diffuse H I and studied the properties of the polarization fraction and the dispersion of the polarization angle. These results are being compared with Planck observations and with simulations of molecular clouds. Our goal is to qualify statistical methods relating maps of Stokes parameters to physical parameters characterizing interstellar turbulence, as e.g. the ratio between kinetic and magnetic energy.

Eléonore Saury acknowledges support from the MISTIC ERC grant #267934

References

Bernard, J.-P. 2013, 47th ESLAB Symposium : The universe as seen by Planck, Oral presentation : http://www.rssd.esa.int/SA/PLANCK/docs/eslab47/Session07_Galactic_Science/47ESLAB_April_04_11_25_Bernard.pdf

Dickey, J. M., McClure-Griffiths, N. M., Gaensler, B. M., & Green, A. J. 2003, ApJ, 585, 801

Eswaran, V. & Pope, S. B. 1988, Computers and Fluids, 16, 257

Falceta-Gonçalves, D., Lazarian, A., & Kowal, G. 2008, ApJ, 679, 537

Federrath, C., Roman-Duval, J., Klessen, R. S., Schmidt, W., & Mac Low, M. 2010, A&A, 512, A81+

Fiege, J. D. & Pudritz, R. E. 2000, ApJ, 544, 830

González, M., Audit, E., & Huynh, P. 2007, A&A, 464, 429

Heiles, C. & Troland, T. H. 2003, ApJ, 586, 1067

Hildebrand, R. H., Davidson, J. A., Dotson, J. L., et al. 2000, PASP, 112, 1215

Hildebrand, R. H., Kirby, L., Dotson, J. L., Houde, M., & Vaillancourt, J. E. 2009, ApJ, 696, 567

Levrier, F. 2013, 47th ESLAB Symposium : The universe as seen by Planck, Poster presentation

Miville-Deschênes, M.-A. & Martin, P. G. 2007, A&A, 469, 189

Saury, E., Miville-Deschênes, M.-A., Hennebelle, P., Audit, E., & Schmidt, W. 2013, arXiv:1301.3446

Schmidt, W., Federrath, C., Hupp, M., Kern, S., & Niemeyer, J. C. 2009, A&A, 494, 127

Schmidt, W., Hillebrandt, W., & Niemeyer, J. C. 2006, Computers and Fluids, 35, 353

Wolfire, M. G., McKee, C. F., Hollenbach, D., & Tielens, A. G. G. M. 2003, ApJ, 587, 278

Session 13

Enseignement

SF2A 2013
L. Cambrésy, F. Martins, E. Nuss and A. Palacios (eds)

MASTER TRAINING COURSE FOR DETECTION TECHNIQUES

P. Kern[1]

Abstract. The LabEx FOCUS proposes a training course to the detection techniques. It will be proposed yearly to the students of master or of engineering school . This theoretical and practical training will be given during a full week at the Observatoire de Haute Provence. The teachers are members from the laboratories of the FOCUS consortium.

Keywords: Detection, education, instrumentation, Infrared, visible

1 Introduction

The LabEx FOCUS (FOCal plane arrays for Universe Sensing) is dedicated to the development of novel high technology matrix arrays detectors aimed to equip the next generation facilities for Universe Sciences. The LabEx is hosted by the Grenoble University PRES, and is supported by the local network of world-class industrial and academic partners that are specialists of the detection. A LabEx is a funding tools of the french government under the PIA program (Programme dInvestissement dAvenir), which gives support to local federation of researchers or that addresses a specific thematic through a suitable consortium.

FOCUS addresses three complementary research programs:

- Detectors for the far IR and (sub) millimeter direct imaging. It includes bolometers and KID developments.
- Detectors for the near and mid IR.
- Advanced detection systems, such as new photo-counting devices or curve detectors which can lead to a drastic simplification of the design of an instrument.This third theme is also aimed at leaving room for future researches not yet considered.

The partners' expertise ranges from technology to astrophysics, including instrumentation, signal processing and sensor science. The partners are:

- In Grenoble: IPAG, Institut Néel, LPSC, IRAM and IMEP
- in Paris area: SAp / CEA and ONERA
- in Marseille: LAM

in Grenoble, , and LAM in Marseille.

Funding is provided for a period of eight years and should support research, teaching and valorization activities. Throughout his teaching activity, FOCUS is organizing a week of training course dedicated to detection in astrophysics. Funding is also dedicated to supporting the educational experience, training, but also for existing training programs of the partner from the different universities. In this paper we describe the content of the training week to be held at the Observatoire de Haute Provence next November.

[1] IPAG, Observatoire de Grenoble, 38041 Grenoble, France

2 Contents of the course

This week of training is shared between theoretical lectures et practical works related to the detection in astrophysics. It is aimed at the training of students that consider for their PhD an observational or instrumental work, in order to provides them with the basics of the detection in astrophysics.

Theoretical lectures are given in the mornings or afternoons and experimental work will be held in the afternoon or during the nights. The experimental work used teaching or professional equipments, some of them funded by FOCUS.

For later versions of this training, lectures are scheduled in English to be able to accept students from foreign universities.

2.1 Theoretical program

The lectures address the following topics:

- Astrophysical introduction and general notions. What are the needs and the typical measurements in astrophysics (photometry, imagery, spectroscopy, and so on): what can be measured by a detector?
- Reminder of the required notions: photometry, image formation, sampling, image and pupil of an optical instrument ...)
- Physics of the detector, different types of detectors, detector characterization.
- Noise and signal processing: various contributions *which noise is dominating ?*).
- Instrumentation regarding to astrophysical applications (how is designed an instrument, specification of the detector, integration of the detector in the instrument) handling of the detector (electronics, optics, cryogeny).
- Current developments in detection and the next generation.

2.2 Experimental work

The experimental work will be done during the afternoons and evenings either in laboratories or on telescopes of the observatory.

- Practical activities by group of 3 students:
  - Detector characterization in laboratory (OHP and LAM support).
  - Transit observation on telescope (OHP support)
  - FTM Characterization in laboratory (ONERA support).
- Demonstration using research equipments
  - Operation of several IR camera, cooled or not, at various bandwidths. Application to nocturne imagery (ONERA support).
  - Radial Velocity observation using OHP facilities (OHP astronomer support)
  - Night glow observation (OH lines emission) in visible and NIR (ONERA support).

3 Participants

The course will receive up to fifteen french and foreign students from various Master (astrophysics, physics) and engineering schools.

The students will be proposed by their Masters. Some PhD students can be also proposed by their supervisors.

the selection of the students will take into account the following requests, mandatory to be able to follow the lectures of the week and to have the elements for the proposed experiments.

- Basic physics

- Geometrical Optics
- Physical optics (diffraction, spectroscopy, polarization)
- Signal processing (especially Fourier formalism, sampling principles

4 Organization

For the first year the training course will be from the 18th to the 22th of November 2013. The students arrive in OHP on the Sunday evening and leave on the Friday evening.

The LabEx insures the funding for the accommodation of the students and for the equipment for some of the experimental setup.

The team includes teachers, engineers and researchers from ONERA, CEA/LETI, CEA/SAp, IPAG and OHP. Isabelle Ribet from ONERA ensures the coordination of the program. Pascal Gallais from SAp and Gilles Duvert from IPAG coordinate all experimental work at OHP.

Session 14

Atelier de l'AS SKA-Lofar

SF2A 2013
L. Cambrésy, F. Martins, E. Nuss and A. Palacios (eds)

SIMULATIONS OF THE BARYONIC ACOUSTIC OSCILLATIONS 21 CM SIGNAL DURING THE REIONIZATION

Dominique Aubert [1]

Abstract. The imprint of baryonic acoustic oscillations in the structure of the intergalactic gas is in principle detectable during the epoch of reionization, at $z > 6$. Using large scale cosmological simulations post-processed to take in account the impact of radiative transfer, we assess the redshift evolution of the 21 cm signal at the BAO scale, evolution that is driven by the birth of the first UV sources that convert the neutral emitting hydrogen into an ionized and non radio-emitting gas. We find that the modelisation and the properties of the sources and their radiation is crucial to this evolution and show for instance that the inclusion of preheating due to X-Rays has a strong impact on the 3D power spectrum of the 21 cm brightness temperature. Conversely, the detection (or the lack of) of BAOs could therefore provide a constrain on the nature of the sources during the EoR in addition to providing a new range of redshifts to use the oscillations as cosmological standard rulers.

Keywords: Reionization, Numerical Simulation, Cosmology

1 Introduction

The epoch of reionization saw the hydrogen content of the Universe returning to an ionized state after a brief period when it was predominantly neutral after the Recombination. The process is thought to have ended at $z \sim 6$ as probed by quasar spectra, culminating with a quick transition where a network of HII regions overlapped rapidly, driven by a growing number of UV sources. This epoch can be probed via the redshifted 21 cm signal by the current and next generation of large radio observatories, where facilities such as SKA promise to be able to track the evolving topology of the neutral hydrogen as it disappears during the reionization.

As explained in the next section, the 21 cm signal is modulated by the neutral state of the hydrogen, its temperature and of course the underlying density distribution. On scales larger than, say, 100 comoving Mpc, and at this epoch ($z > 6$), this distribution still evolves linearly and therefore still contains the signature of the baryonic acoustic oscillations (BAOs hereafter) that were frozen in the cosmic gas distribution at the recombination. This signal is detected in the CMB ($z \sim 1100$, e.g. Planck Collaboration et al. (2013)), in the structure of the Lyman-alpha forest ($z \sim 2$, Busca et al. (2013)) and in the distribution of galaxies ($z \sim 0$, see e.g. Eisenstein et al. (2005)). Probing this signal during the reionization epoch ($20 < z < 6$) would therefore open a new window for the study of the BAOs, and strengthen their position as a multi-epoch cosmological probe.

However, the emissivity of the gas evolves as HII regions appear, grow and overlap. One can therefore ask, how effectively large is the redshift window of observation ? Previous studies on the subject are not fully conclusive (see e.g. Mao & Wu 2008; Rhook et al. 2009). It is found that BAOs can be detected until z=6-8 when ionized fraction can be as high as 10%. However, such studies often rely on simple analytic or semi-analytic reionization models and neglect for instance the fluctuations induced by the non-uniform X-ray background that could be important to forecast the 21 cm signal of neutral hydrogen (see e.g. Baek et al. (2010)).

In the current work, we aim at investigating this subject using numerical simulations of the reionization at high resolution. The gas and source evolution are provided by hydrodynamical simulations whereas the multi-frequency radiative transfer is performed as a post-processing step. Simulation outputs provide the ingredients for a simple modeling of the 21 cm signal that we analyze by estimating its power spectrum. Even though this work has been triggered with SKA in mind, we focused on the intrinsic detectability of the BAO features, without considering instrumental effects at the current stage even though they will *in fine* put additional limitations on their observation.

[1] Observatoire Astronomique de Strasbourg, UMR 7550, CNRS, Universite de Strasbourg

2 Methodology

The gas distribution is provided by a cosmological simulation performed by the adaptive mesh refinement (AMR) code RAMSES (Teyssier 2002). The box size is $1h^{-1}$ Gpc and sampled by 2048^3 coarse cells. Initial conditions were generated with Mpgrafic (Prunet et al. 2008), using WMAP-9 cosmological parameters (Hinshaw et al. 2013) and the transfer function of Eisenstein & Hu (1998). 3 additional levels were triggered by the AMR ensuring a 16384^3 formal resolution. Even though BAOs are large scale features, the high number of coarse resolution elements and the finer levels allow to reduce the impact of resolution on the simulated SFR. Star formation is performed on the fly using the implementation of Rasera & Teyssier (2006), with $\delta = 10$, an admittedly small value but necessary in such large scale simulated volume that is unable to capture small scale high density peaks. The simulation has been run down to $z = 5.3$ on 2048 cores of the Equipex Meso-center of the University of Strasbourg, providing 50 snapshots to cover the reionization epoch.

The hydrodynamical simulation being done, its outputs (star and density fields) were post-processed by the radiative transfer code ATON (Aubert & Teyssier 2008, 2010). This code uses a moment description of the radiative transfer equation, assuming an M1 closure relation between the radiative energy density and pressure. The transfer is performed for 3 groups of photons with typical energies equal to 18 eV, 200eV and 1 keV. The inclusion of large mean free path X-rays is important for the subsequent analysis: these high-energy photons are crucial to model the large scale reheating that occurs during the reionization and are therefore prone to affect the large scale 21cm signature of BAOs. The code also tracks the out-of-equilibrium ionization state and the cooling processes of hydrogen (only). ATON is fully ported on multi-GPU architecture, enabling x80 acceleration factors compared to CPUs : not only it allows us to use a simple (but conditionally stable) explicit scheme for the transport but also removes the necessity to use a reduced speed of light. In the current work, the 2048^3 density fields were averaged down to 512^3 cubes that were post-processed on 8 K20 Nvidia GPUs, also located at the Strasbourg University computing facility.

The source distribution is obtained from the distribution of stellar particles computed by the hydrodynamical simulation and their emissivity is set to achieve a reionization at $z \sim 6$: it should be noted that the star formation is far from being converged and the stellar particles therefore act merely as tracer of the geometrical distribution of stars. In the most simple fashion, each source is considered as an X-ray emitter, with 0%, 1% (being the most realistic see e.g. Glover & Brand (2003))or 10% of its luminosity emitted as X-rays and respectively labeled as UV, X and SX models. The stellar contribution to the source spectrum is assumed to be a 50000 K black body whereas the X-ray part is assumed ot be attached to a QSOs with a $\nu^{-1.6}$ spectral dependence. The resulting ionization histories for the 3 models are shown in Fig. 1 and can barely be distinguished. It illustrates the dominant role of UV photons over the X photons on the reionization process.

3 Results

The post-processing being completed, we have access to the evolution of ionization, temperature and density during the reionization. The 21 cm brightness temperature δT_b is provided by (Mellema et al. 2013) :

$$\delta T_b \sim 27 x_{\rm HI}(1+\delta)\sqrt{\frac{1+z}{10}\frac{\Omega_m}{0.27}}\left(1-\frac{T_{\rm CMB}(z)}{T_S}\right)\left(\frac{\Omega_b}{0.044}\frac{h}{0.7}\right)\left(\frac{1-Y_p}{1-0.248}\right)\left(1+\frac{1}{H(z)}\frac{dv}{dr}\right)^{-1} \text{mK} \qquad (3.1)$$

In the current work, we approximate the spin temperature T_S by the kinetic one. The 21 cm maps are analyzed in Fourier space using the 3D power spectrum $P_{\delta T \delta T}(k)$ defined as

$$\langle \delta T_b(\mathbf{k}, z)\delta T_b(\mathbf{k}', z)\rangle = (2\pi)^3 P_{\delta T \delta T}(k, z)\delta_D(\mathbf{k}-\mathbf{k}'). \qquad (3.2)$$

We show in Figure 1, the redshift evolution of $\Delta^2(k) = k^3 P_{\delta T \delta T}(k)/(2\pi)^3$ for the UV model, i.e. without any contribution from the X-rays. Clearly, BAOs can be detected until $z \sim 10$, corresponding to an ionized fraction of 1% in our simulations. The signal disappears as a high frequency feature kicks in at $k \sim 0.2$ Mpc^{-1}, driven by the rise of a network of small HII regions.

In Figure 2, we present $\Delta^2(k)$ for the 3 models at 4 different redshifts. At early times, all model present clear BAOs signatures. However, the approximation $T_S \sim T_K$ is likely to be crude at the initial stages of reionization when the Ly-α coupling is weak and so would our 21cm forecast. Later on, significant differences can be spotted between our different source models. Again, the UV model exhibit baryon wiggles at any time within this redshift range, whereas X-ray models present strong features at low spatial frequencies. They are induced by large scale temperature fluctuations, on larger distances than the ionization fronts. In the case of

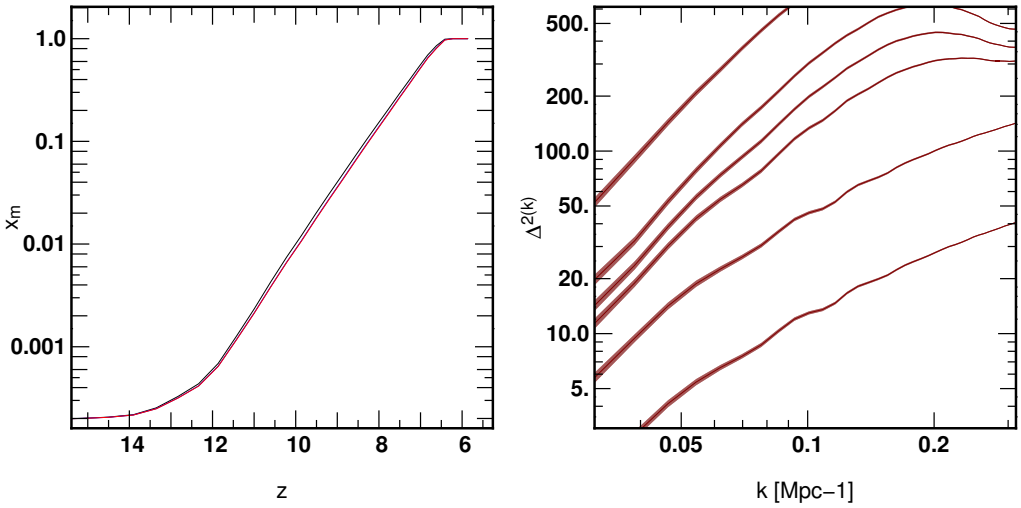

Fig. 1. Left: redshift evolution of the neutral fraction for the UV, X and SX models. Full reionization is achieved by $z \sim 6.5$ and the three models provide indistinguishable average reionization histories.**Right** measurement of the δT_b power spectrum $\Delta^2(k)$ in the UV model at z=15.8, 12.33, 10.6,10.2,9.85 and 9.18 (from bottom to top), corresponding to mass weighted neutral fractions of 0.0002, 0.0004, 0.0047, 0.006, 0.01 and 0.03. BAOs features can be distinguished on large scales until $x_m \sim 1\%$.

the SX model (corresponding to a 10 % luminosity in X-rays), the BAOs are drowned in this feature as soon as $z \sim 14$ ($x \sim 0.02\%$), while the X model is less dramatic even though the BAOs are washed out by $z \sim 12$ ($x \sim 0.06\%$). In general the X model present its large scale feature at higher frequency than for the SX model: soft-X rays seem to be the dominant source of large scale heating for the X model whereas harder photons contribute more efficiently in the SX one, with larger mean free path.

Qualitatively, these results are not surprising : X-rays have large mean free paths and their impact on large scale reheating can be important for the modeling of 21 cm signal. As a consequence, a large scale modification of the signal compared to a simulation devoid of X-rays is normal. Quantitatively, a mean free path of 300 h^-1 Mpc is expected for the hardest photons of our model, i.e. a length scale commensurable with the BAO scale. Still, one could have naively expected that a uniform temperature background would have been set rapidly thus reducing the impact of temperature fluctuations: this would have been an appropriate approximation for smaller scales, but generally not for the ones considered here. Still, one can note that a high frequency wiggle can still be distinguished in the SX model when z=11.5 : this scale would be small enough compared to the temperature fluctuation ones but its significance remain to be thoroughly investigated. Overall these simulations emphasize the relevance of a proper modeling of high-energy photons: a crude modeling (as the one described here) can erase this signature, hence the need for an accurate description of the amplitude of this contribution and the way it rises.

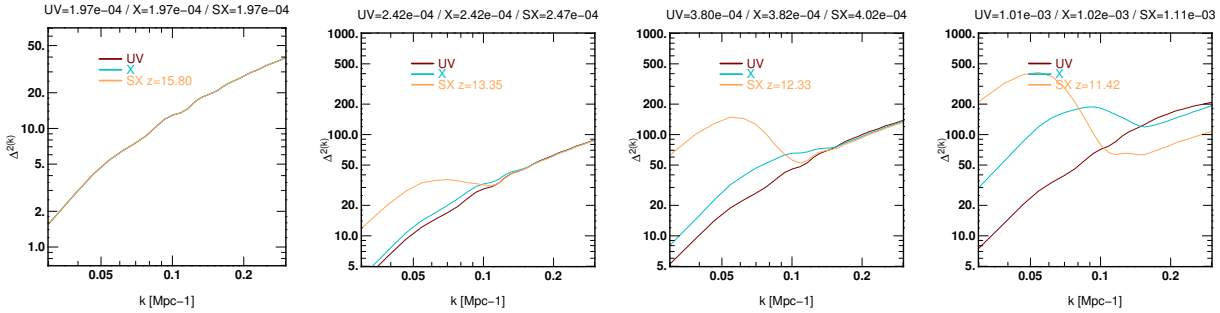

Fig. 2. Evolution of the temperature brightness power spectrum $\Delta^2(k)$ for the UV, X and SX models at 4 different redshifts. Neutral fractions are also provided for reference above the frames.

4 Discussion & Prospects

At this stage, our protocol must be considered as exploratory: X-ray source models, resolution issues, 21 cm modeling or the statistical treatment of the signal to name a few can all be debated. Rather than aiming at a definitive and quantitative answer, this work points toward issues that should be systematically treated in future, more complete investigations. Still, these preliminary investigations seem to imply that there is a possibility that BAOs should be detected behind a fluctuating 'foreground' generated by the heating sources of reionization. On the one hand, we have a weak signal, the BAOs, where their exact location in frequency space is known and on the other hand complex temperature fluctuations that are triggered by the source distribution and properties.

Let us finally note that spotting the oscillations could be an ideal application of the power spectrum decomposition suggested by e.g. Barkana & Loeb (2005):

$$P(k,\mu,z) = P_{\mu^0}(k,z) + \mu^2 P_{\mu^2}(k,z) + \mu^4 P_{\delta\delta}(k,z) \tag{4.1}$$

where μ is the cosine of the angle between the light of sight and $\mathbf{k}$ and appears because of the last velocity term in equation 1. It should be noted, that on scales considered here, the dynamics is close to linear and the velocity field can easily be computed from the density field, even though we have access to the self-consistent velocity provided by the simulations. By fitting $P(k,\mu,z)$ with a fourth order polynomial, the 'pure' density power spectrum $P_{\delta\delta}(k,z)$ that contains the BAOs can be recovered from the highest order term. Our preliminary investigations show that this decomposition can indeed provide the density structure below the features induced by the X-ray fluctuations but on scales, typically 50 Mpc, smaller than the one of interest. At the current stage we may be limited by the cosmic variance effect at the BAO scale, which is increased when one consider the line-of-sight dependence of the power spectrum instead as the usual averaged one. As a consequence, our simple polynomial fits on these scales are poorly constrained. Larger simulations are underway to see if this effect is dominant or if more subtle inversion procedure should be envisioned.

D.A. thanks B. Semelin for his insightful comments and direction. This work is supported by the ANR JCJC Grant EMMA. Simulations have been performed at the Mesocentre of the Universite de Strasbourg as part of the 2012 Meso Challenge.

References

Aubert, D. & Teyssier, R. 2008, MNRAS, 387, 295
Aubert, D. & Teyssier, R. 2010, ApJ, 724, 244
Baek, S., Semelin, B., Di Matteo, P., Revaz, Y., & Combes, F. 2010, A&A, 523, A4
Barkana, R. & Loeb, A. 2005, ApJ, 624, L65
Busca, N. G., Delubac, T., Rich, J., et al. 2013, A&A, 552, A96
Eisenstein, D. J. & Hu, W. 1998, ApJ, 496, 605
Eisenstein, D. J., Zehavi, I., Hogg, D. W., et al. 2005, ApJ, 633, 560
Glover, S. C. O. & Brand, P. W. J. L. 2003, MNRAS, 340, 210
Hinshaw, G., Larson, D., Komatsu, E., et al. 2013, ApJS, 208, 19
Mao, X.-C. & Wu, X.-P. 2008, ApJ, 673, L107
Mellema, G., Koopmans, L. V. E., Abdalla, F. A., et al. 2013, Experimental Astronomy, 36, 235
Planck Collaboration, Ade, P. A. R., Aghanim, N., et al. 2013, ArXiv e-prints
Prunet, S., Pichon, C., Aubert, D., et al. 2008, ApJS, 178, 179
Rasera, Y. & Teyssier, R. 2006, A&A, 445, 1
Rhook, K. J., Geil, P. M., & Wyithe, J. S. B. 2009, MNRAS, 392, 1388
Teyssier, R. 2002, A&A, 385, 337

SF2A 2013
L. Cambrésy, F. Martins, E. Nuss and A. Palacios (eds)

LOW FREQUENCY EMISSION IN GALAXY CLUSTERS- $MACSJ0717.5+3745$

M.Pandey − Pommier[1], J. Richard[1], F. Combes[2], K. Dwarakanath[3], B. Guiderdoni[1], C. Ferrari[4] and D. Narasimha[5]

Abstract. Cluster of galaxies being the largest gravitationally bound systems, are the ideal laboratories to study the formation and evolution of large scale structures within the Universe. High sensitivity radio observations of galaxy clusters have helped to investigate the non−thermal emission mechanism (in the form of *relics*, *halos*, *mini − halos*) within the Intra Cluster Medium (ICM) and their interaction during cluster mergers. These non-thermal emissions play an important role in the overall understanding of the physical evolution of the ICM and are closely related to their X-ray properties. We present here the observational properties of diffuse non-thermal sources detected in the galaxy cluster: $MACSJ0717.5+3745$. We discuss their classification, equi-partition magnetic field, radio power and spectral properties based on the new observations acquired with the GMRT down to 235 MHz, as well as the published results in the archive. We discuss in general the statistical properties of non-thermal components within galaxy clusters over a redshift range, $0 < z < 1$ (the epoch of their formation), and outline the important contribution that are expected in this area from sophisticated radio facilities (like LOFAR, SKA, etc.).

Keywords: Cosmology, large−scale structures of Universe, galaxy clusters- $MACSJ0717.5+3745$, radiation mechanisms, non−thermal, radio telescope

1 Introduction

Cluster of galaxies are the largest gravitationally bound systems in the Universe, that are formed by mergers of smaller clusters and galaxy groups, as well as through continuous accretion of gas. They serve as a tool to study the formation and evolution of large scale structures in the Universe and can be used to probe the properties of magnetic fields present within them and in even larger structures: filaments connecting galaxy clusters (Feretti et al. 2012). Important progress in the study of Inter Cluster Medium (ICM) and their interactions in galaxy clusters have been made with multi−wavelength observations (Boselli & Gavazzi 2006; Markevitch & Vikhlinin 2007); however, scarce information is available about the physical properties and the origin of nonthermal diffuse ICM, that also play a vital role in the evolutionary stage of galaxy clusters (Dursi & Pfrommer 2008; Parrish et al. 2009). In fact, deep radio observations have shown that significant diffuse synchrotron emission is present in some clusters at Mpc−scale, and which indicate there are magnetic fields and cosmic rays within the cluster volume (Feretti et al. 2005, Kale & Dwarakanath 2009). This Mpc−scale cluster radio structures are generally divided into *relics* and *halos* depending on their position in the cluster, polarization and spectral properties (Ferrari et al. 2008). Further in the case of few clusters double *relics* structures are also detected (Kale et al. 2012). Furthermore, a magnetic field of μG level has been detected in these Mpc−scale structures with relativistic particles in cluster outskirts. The origin of these relativistic particles is explained by the so−called electron primary model acceleration (Enβlin et al. 1998).

[1] Université de Lyon, Lyon, F-69003, France ; Université Lyon 1, Observatoire de Lyon, 9 avenue Charles André, Saint-Genis Laval, F-69230, France ; CNRS, UMR 5574, Centre de Recherche Astrophysique de Lyon ; Ecole Normale Supérieure de Lyon, Lyon, F-69007, France

[2] LERMA, Observatoire de Paris, 61 avenue de l'Observatoire, 75014 Paris, France

[3] Raman Research Institute, Bangalore 560 080, India

[4] Laboratoire Lagrange, UMR7293, Universite de Nice Sophia-Antipolis, CNRS, Observatoire de la Cote d'Azur, 06300 Nice, France

[5] Theoretical Astrophysics Group, Tata Institute of Fundamental Research, Homi Bhabha Road, Bombay 400 005, India

2 Non−thermal emission and their spectral properties in galaxy cluster: $MACSJ0717.5+3745$

In this paper we present results on the study of non−thermal emission in one of the most studied galaxy cluster-$MACSJ0717.5+3745$ at redshift $z = 0.5548$. Fig. 1 (Top Panel) shows the deep radio observations on the source down to 0.235 GHz with the Giant Metrewave Radio Telescope (GMRT). This system hosts an elongated centrally placed chair−shaped filament of 853 kpc at 0.235 GHz, and a very low−surface brightness powerful radio *halos* of 1.6 kpc at 0.235 GHz (Pandey−Pommier et al. 2013). The morphology of this source is very similar to the X−ray emission of the cluster, which is related to the thermal intra-cluster component (Fig. 1 Bottom Panel). It is evident from figure 1 that, the non−thermal diffuse emission is brighter at lower frequencies. The halo structure was not detect at 1.4 GHz *FIRST* survey data, due to high noise level. The bottom right panel of Fig. 1 shows the radio contours at 0.61 GHz overlaid on the Chandra X−ray map of$MACSJ0717.5+3745$. The Chair−shaped filament is centrally placed between the 4 different clusters involved in collision (marked with C1, C2, C3 and C4) within the ICM. The bottom left panel shows spectral index map between 0.61 and 0.235 GHz with overlaid Chandra X−ray contours.

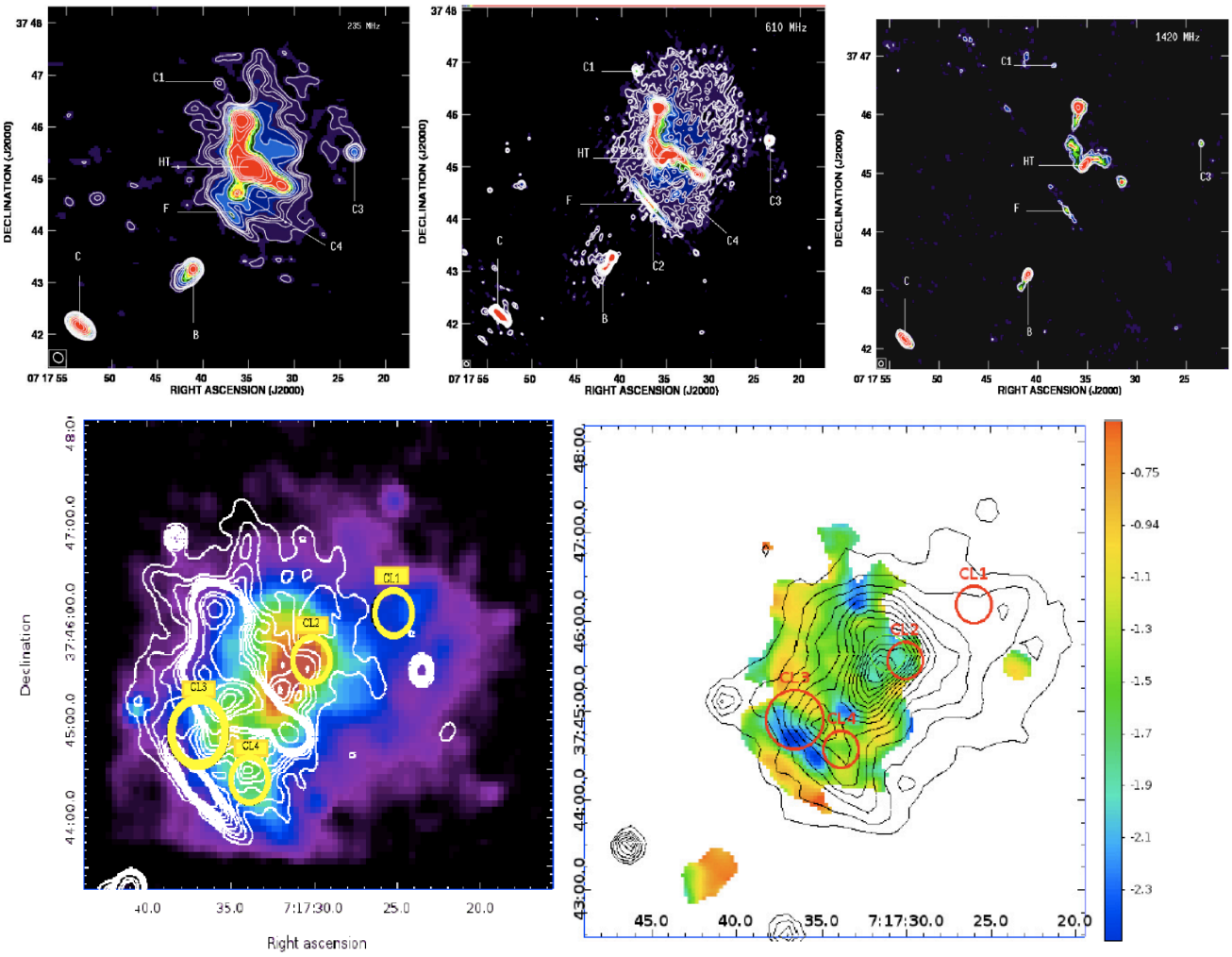

Fig. 1. *from top left to top right - 3 panels* High resolution radio images of massive galaxy cluster $MASCJ0717.5+3745$ ($z = 0.5548$) at 0.235 GHz from GMRT (*Top left*) at FWHM beam of $13.46'' \times 10.76''$ resolution, 0.61 GHz from GMRT (*Top middle*) at FWHM of $5.70'' \times 4.82''$ resolution and 1.42 GHz from FIRST survey (*Top right*) at FWHM of $5'' \times 5''$ resolution. Contours start at (3σ) and scale by a factor of $\sqrt{2}$. (*Bottom right*) radio contours at 0.61 GHz overlaid on Chandra image. (*Bottom left*) Spectral index error map between 0.235 and 0.61 GHz image with overlaid Chandra X-ray contours. The red and yellow circles (C1, C2, C3, C4) shows galaxies in 4 different clusters involved in collision-extracted from Pandey−Pommier et al. 2013.

A detailed understanding of the origin of the centrally placed '*Chair-shaped*′ filament is still debated (e.g. Pandey−Pommier et al. 2013, Bonafede et al. 2009, van Weeren et al. 2009). The location of the filament being coincident with regions in the cluster having higher temperatures, suggests that the '*Chairshaped*′ filament is probably the result of a largescale shock wave within the cluster where particles are accelerated during merger events. The less−steep spectral index of the bright '$Chair-shaped$′ filament, $\alpha^{0.61}_{0.235}$= -0.92 to −1.5 further supports this scenario (ref. Fig. 2 Top Panel). The overall radio spectrum of the halo is very steep with typical spectral index ranging from $\alpha^{0.61}_{0.235}$ = -0.85, close to the cluster center, up to about α = -2.3 towards the outer edge, that traces the outer cooler region of the cluster and a mean spectral index of $\alpha^{0.61}_{0.235}$ = -1.17±0.37. Based on the size of the halo and mean spectral index, a standard equipartition magnetic field of 3.43 μG was derived from our observations.

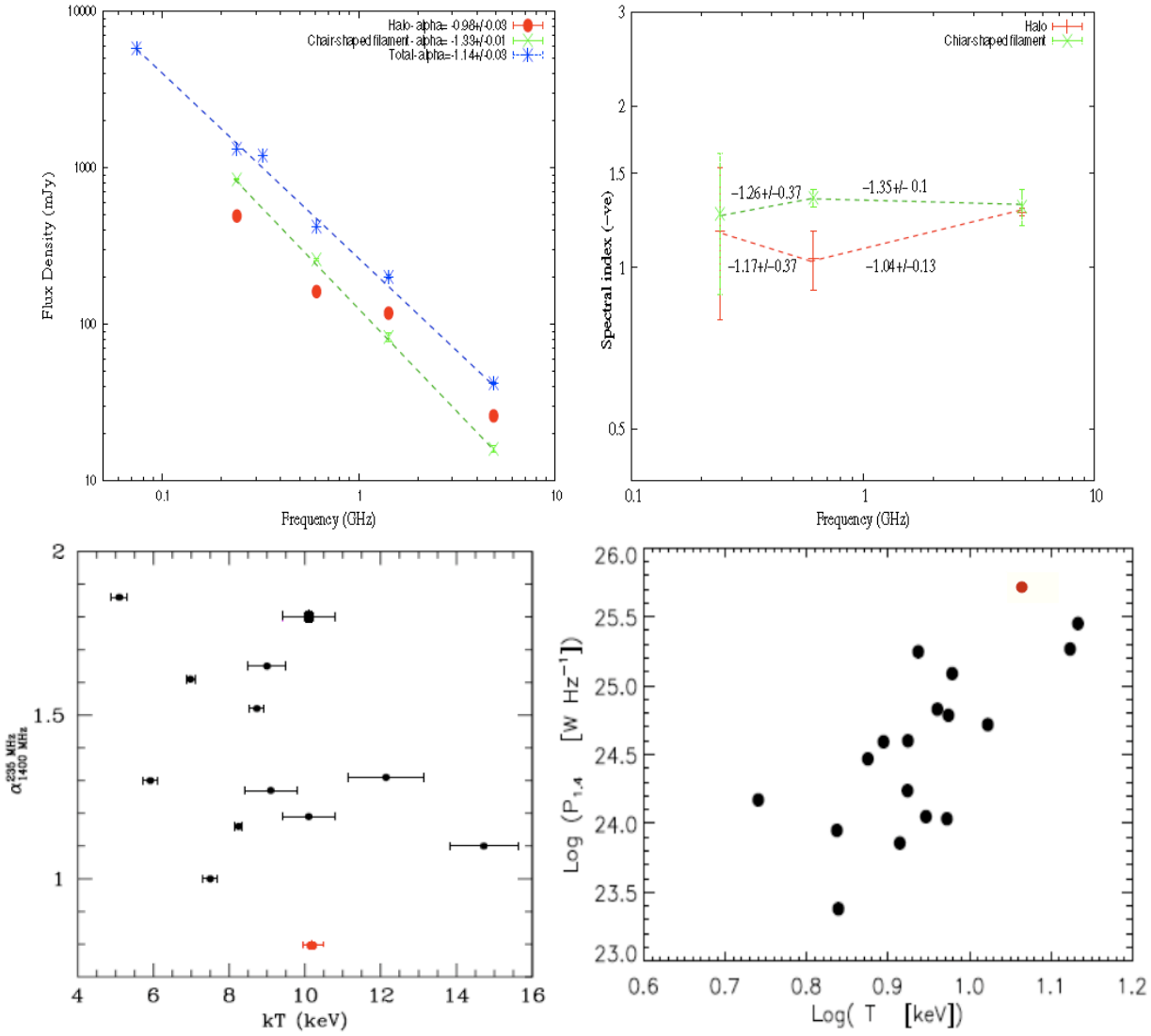

Fig. 2. *Top left panel:* Integrated radio spectra of the halo, '$Chair-shaped$′ filament source and total(halo+'$Chair-shaped$′ filament source). *Top right panel:* spectral index variation with respect to frequency for the halo and '$Chair-shaped$′ filament source (Pandey−Pommier et al. 2013). *Bottom left panel:*Spectral index of radio *halo* in the 235 MHz-1.4 GHz interval as function of the cluster X-ray temperature (adapted from Venturi et al. 2013 and Giacintucci et al. 2013).The red points mark the position of $MACSJ0717.5+3745$. *Bottom right panel:* Radio power in the halo of galaxy clusters with respect to X-ray temperature (extracted from van Weeren et al. 2009). The red point marks the radio power measured in $MACSJ0717.5+3745$ with our observations

Giovannini et al. (2009) recently derived a correlation between the radio−halo, integrated spectral index and the average X−ray gas temperature for a large sample of nearby radio *halos* . As per the correlation, hot clusters ($T > 10keV$) show an average spectral index = −1.1 to −1.2, and cold clusters ($T \leq 8$ keV) show steep spectra (average spectral index = −1.7). The radio spectrum derived from our new observations on the present radio halo with $\alpha \sim -1.17$ further confirms the result that $MACSJ0717.5+3745$ is a high−temperature merging cluster, $T = 10.2 \pm 2.4keV$ (Ma et al. 2009) that shows agreement with the correlation between the radio−halo, integrated spectral index and the average X−ray gas temperature. Venturi et al. (2013) further found that, based on the mass, the radio *halos* show different spectral index depending on the energy release into particle re−acceleration during mergers. The most massive hot clusters ($T > 8$ keV) with *halos* show flatter spectra, while moderately massive clusters ($T \sim 5-8$keV) shows *halos* with both steep and flat spectra (Cassano et al. 2006, Cassano et al. 2010). In Figure 2, we report the distribution of spectral index ($\alpha^{235MHz}_{1400MHz}$) in radio−halo clusters versus the X−ray temperature,kT (keV) adapted from Venturi et al. (2013), with the position of $MACSJ0717.5+3745$ shown by a red point (with kT=10.2 ± 2.4 keV). Thus, it is the distant massive cluster with most powerful radio halo showing spectral index, $\alpha^{0.235}_{1.42} = -0.8$, less steep than other hotter clusters, further suggesting its complex nature. $MACSJ0717.5+3745$ cluster hence, is an interesting candidate that provides an upper limit for our understanding of mass−spectral index correlation of giant radio *halos* in distant massive hotter clusters showing multiple mergers. Fig. 2, Bottom Panel also shows the correlation plot of radio power within the halo with respect to X−ray temperature, where $MACSJ0717.5+3745$ is shown to have most powerful radio halo at redshift, $z = 0.5548$, thanks to our new sensitive GMRT observations.

3 Statistical properties of non-thermal emission in galaxy clusters

The statistical studies based on observational data from the archive shows that non−thermal emission in the form of radio *relics* and *halos* are known up to now only in a few galaxy clusters (ref. Fig. 3, Feretti et al. 2012), in fact the non−thermal emission being rare is not present in most of the clusters. Theoretical models presented by Cassano et al. 2010, as well as observational data, confirms that diffuse intra-cluster radio sources are generally characterized by steep synchrotron spectra ($\alpha = -1.2$) and low-surface brightness and hence, best detected at long wavelengths (MHz- regime). Further, at GHz regime, the possible spectral steepening due to electron aging, make them difficult to be imaged at higher frequencies and more easily detectable at the long wavelengths observational facilities like GMRT, LOFAR, SKA etc, and as confirmed by our observations. These instruments are therefore best suited for the discovery of diffuse radio emission in hundreds of massive galaxy clusters up to z = 1 (epoch of formation)(ref. Fig. 3, Cassano et al. 2012). Thanks to its wide frequency coverage, high sensitivity and large field of view (FoV), LOFAR will further open up new radio windows down to 10 MHz, to further study the non-thermal component in large-scale structures within the Universe (Rottgering et al. 2011).

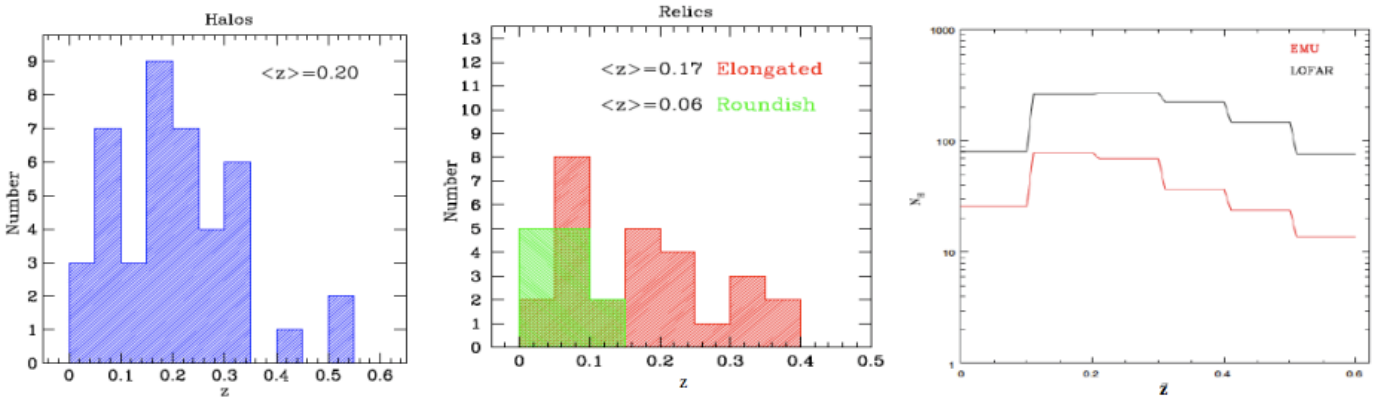

Fig. 3. *Top left panel:* Number count of radio *halos*, *Top middle panel:* Number count of radio *relics* extracted from Feretti et al. 2012 and *Top right panel:* RH distribution in redshift intervals in the Australian SKA Path-finder (ASKAP) Evolutionary Map of the Universe (EMU) survey (red line) and LOFAR (black line) surveys extracted from Cassano et al. 2012

We thank the staff of the GMRT, who made these observations possible. The GMRT is run by the National Centre for Radio Astrophysics of the Tata Institute of Fundamental Research. This research had made extensive use of the NASA/IPAC extragalactic sources data base NED, Data from the NASA/NVSS survey, and the public archives from the *HST* and *Chandra*.

References

Bonafede, A., Feretti, L., Giovannini, G., et al. 2009, A&A, 503, 707, 720

Boselli, A., & Gavazzi, G., 2006, PASP, 118, 517B

Cassano, R., Brunetti, G., & Setti, G. 2006, MNRAS, 369, 1577

Cassano, R., Ettori, S., Giacintucci, S., et al. 2010, ApJ, 721, L82

Cassano, R., Brunetti, G., Norris, R. et al. 2012, A&A, 2012, 548, 100

Dursi, L. J., & Pfrommer, C. 2008, ApJ, 677, 993

Enβlin, T.A., Biermann, P.L., Klein, U., & Kohle, S., 1998, A&A, 332, 395

Feretti, L. 2005, Advances in Space Research, 36, 729

Feretti, L. & Giovannini, G., 2008, Plionis M., L'opez-Cruz O, Hughes D (eds) Lect notes phys, vol 740, Springer, Dordrecht, p 143

Feretti, L., Giovannini, G., Govoni, F., Murgia, M., 2012, A&A, 20:54

Giovannini, G., Bonafede, A., Feretti, L., et al. 2009, A&A, 507, 1257

Kale, Ruta; Dwarakanath, K. S.; Bagchi, Joydeep; et al. 2012; MNRAS; 425; 250

Kale, R. & Dwarakanath, K. S. 2009, ApJ, 699, 1883

Ma, C.-J., Ebeling, H., & Barrett, E. 2009, ApJ, 693, L56

Markevitch, M., & Vikhlinin, A. 2007, Phys. Rep., 443, 1

Pandey−Pommier, M.; Richard, J.; Combes, F.; et al. 2013; A&A, 557, A117

Parrish, I. J., Quataert, E., & Sharma, P. 2009, ApJ, 703, 96

Rottgering, H., Afonso, J., Barthel, P., et al. 2011, Journal of Astrophysics and Astronomy, 32, 557

van Weeren, R., Rottgering, H. J. A., Bruggen, M. and Cohen, A., 2009, A&A, 505, 991, 997

Venturi, T.,Giacintucci, S., Dallacasa, D., et al., 2013, A&A

SF2A 2013
L. Cambrésy, F. Martins, E. Nuss and A. Palacios (eds)

CHARACTERIZATION AND INITIAL RESULTS WITH EMBRACE

S.A. Torchinsky[1], A.O.H. Olofsson[2], A. Karastergiou[3], B. Censier[1], M. Serylak[1,3], P. Renaud[1] and C. Taffoureau[1]

Abstract. EMBRACE is a prototype instrument using an array of nearly 5000 densely-packed antenna elements creating a fully sampled, unblocked aperture. This technology is proposed for the Square Kilometre Array and has the potential to provide an extremely large field of view making it the ideal survey instrument. We describe the system, its flexibility, and early results from the prototype.

Keywords: Square Kilometre Array, SKA, aperture array, EMBRACE

1 Introduction

The Square Kilometre Array (SKA) Dewdney *et al.* (2009) will be the largest radio astronomy facility ever built with more than 10 times the equivalent collecting area of currently available facilities. The SKA will primarily be a survey instrument with exquisite sensitivity and an extensive field of view providing an unprecedented mapping speed. This capability will enormously advance our understanding in fundamental physics including gravitation, the formation of the first stars, the origin of magnetic fields, and it will give us a new look at the Universe in the time domain with a survey of transient phenomena.

A revolution in radio receiving technology is underway with the development of densely packed phased arrays. This technology can provide an exceptionally large field of view, while at the same time sampling the sky with high angular resolution. The Nançay radio observatory is a major partner in the development of dense phased arrays for radio astronomy, working closely with The Netherlands Foundation for Radio Astronomy (ASTRON). The joint project is called EMBRACE (Electronic MultiBeam Radio Astronomy ConcEpt). Two EMBRACE prototypes have been built. One at Westerbork in The Netherlands, and one at Nançay. These prototypes are currently being characterized and tested at the two sites. Conclusions from the EMBRACE testing will directly feed into the SKA and will have a decisive impact on whether or not dense array technology is used for the SKA.

The date for selection of technology for the SKA is 2016. If dense arrays are not selected for the SKA, then the SKA will have a much reduced mapping speed compared to what has come to be expected by the astronomical community. It is therefore of crucial strategic importance that work on EMBRACE succeeds in showing the viability of dense arrays for radio astronomy.

EMBRACE has been operational since 2011, and a number of tests have been carried out over the past two years. Much of the work for the first year has been focused on low-level testing and debugging of the system, especially related to the control software, data acquisition, and phase calibration algorithms. Other tests of basic functionality include pointing at sources and tracking the movement of sources in the sky, compensating for the Earth's rotation. Higher level engineering measurements are also being carried out. These aim to quantify the performance of the system by calculating parameters such as the system temperature, and the beam profile.

[1] Station de radioastronomie de Nançay, Observatoire de Paris, France
[2] Onsala Space Observatory, Chalmers University of Technology, Gothenburg, Sweden
[3] Department of Physics, Oxford University, UK

2 EMBRACE System Description

EMBRACE is a SKA Pathfinder for the mid frequencies. Two EMBRACE stations were built, largely financed by the European Commision Framework Program 6 project SKADS. EMBRACE is the first large-scale demonstrator of the dense aperture array technology for radio astronomy.

EMBRACE@Nançay is a phased-array of 4608 densely packed antenna elements (64 tiles of 72 elements each). For mechanical, and electromagnetic performance reasons, EMBRACE@Nançay has, in fact, 9216 antenna elements, but only one polarization (4608 elements) have fully populated signal chains. For more details on EMBRACE architecture see Kant *et al.* (2010, 2011)

2.1 Hierarchical Analogue Beam Forming

EMBRACE@Nançay uses a hierarchy of four levels of analog beamforming leading to 16 inputs to the LOFAR backend system for digital beamforming. The first beamforming is of 4 Vivaldi elements done on the integrated circuit "beamformer chip" developed at Nançay (Bosse *et al.* 2010). The output of 3 beamformer chips is summed together on a "hexboard" and 6 hexboards make a tile. At Nançay, we have one further analog summing stage with 4 tiles making a tileset. This final stage is done on the Control and Down Conversion (CDC) card in the shielded container. The cables running from individual tiles to the CDC cards are 15 m in length, and there are phase perturbations between the various connectors and length of cable leading from each tile. This is calibrated out using an algorithm implemented in the Local Control Unit. The output of the tilesets is fed into a LOFAR-type RCU and RSP system for digital beamforming (Picard *et al.* 2010).

2.2 Beamformer Chip

At the heart of EMBRACE is the integrated analog circuit called the Beamformer Chip which was developed at Nançay. This chip applies the phase shifts necessary to four antenna elements to achieve pointing in the desired direction. The beamformer chip forms two independent beams for each set of four antenna elements. Over 4000 chips were produced for the EMBRACE stations at Westerbork and Nançay (Bosse *et al.* 2010).

3 EMBRACE Monitoring and Control Software

The Monitoring and Control software for EMBRACE was developed at Nançay, and continues to be improved. An extensive Python package library on the SCU (Station Control Unit) computer gives scripting functionality for users to easily setup observation scripts for various targets and types of observation. Integrated statistics data are acquired from the LCU (Local Control Unit) and saved into FITS files. Raw data (beamlets) are captured from LCU Ethernet 1Gbps outputs and saved into binary files (Renaud *et al.* 2011).

4 Results

4.1 Beam parameters

Figure 1 shows a drift scan of Cas-A. This is effectively a measurement of the EMBRACE@Nançay main lobe since Cas-A is small enough to be considered a point source for EMBRACE@Nançay. The main lobe is Gaussian, and the FWHM of 1.47 deg at 1176 MHZ is the expected value.

We typically cannot determine noise temperatures and instrument efficiencies as separate quantities. For example, to determine the $T_{\rm sys}$, we'd need to fill the entire beam pattern with a uniformly radiating blackbody with a well known physical temperature such as an absorber. Conversely, the main beam efficiency cannot be determined without calibrating the intensity scale with a $T_{\rm sys}$ value. The same goes for the area efficiency which is the ratio of measured power over the incident field power entering the geometrical cross section of the instrument. What we can do is either assume a reasonable value for an efficiency and then use sources with either well-known brighnesses and geometries or with well known source fluxes.

The Sun is used as a reference source using simple frequency interpolation based on "quiet Sun" measurements. At this time, approaching a solar 11-year maximum, the values we get for $T_{\rm sys}$ should be considered lower limits. At meter frequencies – where the solar flux originates mostly in the corona – the flux may vary by factors of 10 or more. The variation is much less severe around 1200 MHz but there is no way to know

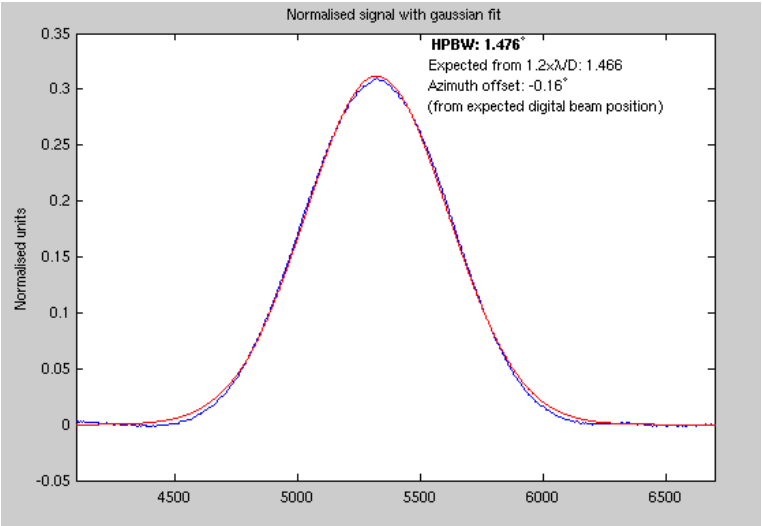

Fig. 1. Drift scan of Cas-A showing the expected shape of the beam main lobe.

by exactly how much since the Sun is poorly monitored in the lower L-band. Even at frequencies as high as 2.8 GHz, the day-to-day variation can be as high as 25%.

The Sun with its ∼0.5° extension is nearly a point source and we can ignore the main beam gain variation over the source. For a measurement with raw uncalibrated measurements x (on-source) and y (off-source), we may assume that these values are proportional to detected noise and source powers.

$$\frac{T_{\rm sys}}{\eta_{\rm A}} = \frac{S \times A}{k} \frac{y}{x-y} \tag{4.1}$$

where A is the geometrical area and $\eta_{\rm A}$ is an efficiency of how much of the availble power the instrument surface is able to pick up. The Sun temperature was taken to be ∼ 90000 K at 1176 MHz. For a tileset, $A = 4.5$ m^2, and assuming that $\eta_{\rm A}$ is equal to 70% gives a $T_{\rm sys}$ of ∼ 120 K.

4.2 Intrinsic Power Variation

Long duration observations performing tracking across the sky show an apparent power variation as a function of pointing direction. Numerous repeated observations have shown that this power variation is intrinsic to the instrument, and is completely independent of source strength in the beam. A 10 hour tracking observation of Cas-A showing a power variation was repeated many times, including following the same azimuth-elevation track but shifted in time such that Cas-A was not in the beam (i.e. tracking empty sky at the same declination but different right-ascension of Cas-A). The power variation is not a function of the source strength in the beam, as demonstrated by GPS satellite tracking which does not show the power variation increasing with the much stronger GPS carrier strength compared to Cas-A.

Two remedies have been implemented, the first of which uses a classic ON-OFF type observing, but with the multi-beam capability of EMBRACE, the ON and OFF beams can be measured simultaneously. The pointing configuration is shown in Figure 2. The power variation is thus reduced by several orders of magnitude.

The second remedy takes advantage of the imaging capability of EMBRACE and also further demonstrates that the power variation is entirely an intrinsic system artefact. The power variation can be eliminated by subtracting an array correlation matrix (ACM) measured at an empty sky position. This corrector ACM is subtracted from the subsequent ACM produced at each integration. The corrector ACM is a constant and need only be measured once, and then applied to all subsequent observations.

4.3 Astronomical Observations

A number of astronomical observations have been done successfully, in addition to the drift scan of Cas-A shown in Fig. 1.

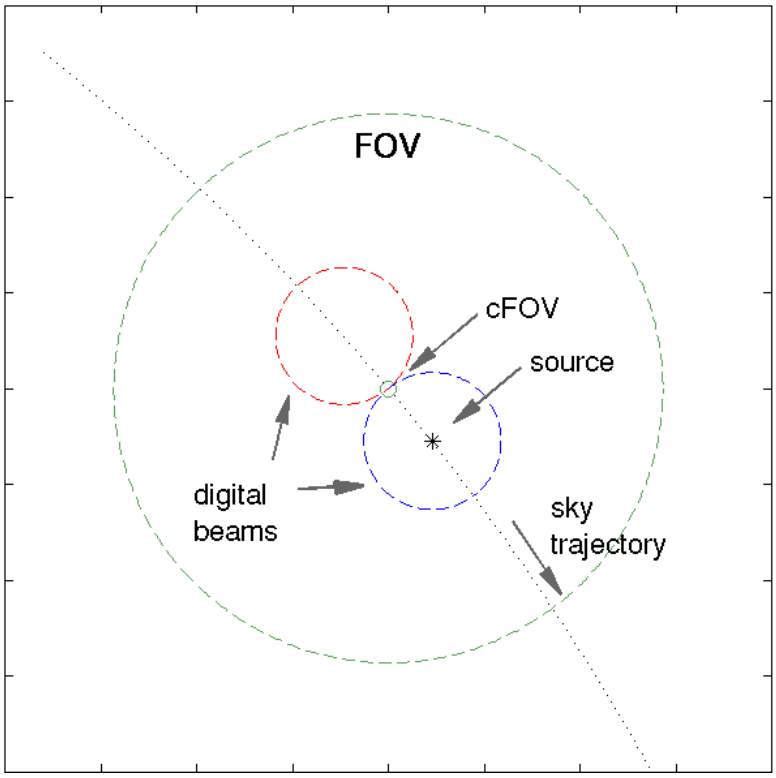

Fig. 2. The pointing strategy for tracking a source points at ON and OFF source positions simultaneously. The OFF position is along the trajectory of the source across the sky.

Figure 3 demonstrates over 9 hours of tracking the pulsar B0329+54. The pulse is clearly detected after several minutes, and the array continues tracking measuring continuously the pulsar, except where RFI has been filtered at 21500 seconds. The array was configured with a bandwidth of 12 MHz (62 beamlets) centred at 1176.45MHz. The array was phased-up using the GPS BIIF-2 satellite, and the phase parameters were applied for the observation of B0329+54. The high data rate output from the RSP boards is read by a data acquisition system running the Oxford ARTEMIS pulsar processing software (Serylak et al. 2013; Armour et al. 2012).

Figure 4 shows a drift scan of the Sun using the multibeam capability of EMBRACE@Nançay. Six beams were pointed on the sky along the trajectory of the Sun, including three partially overlapping beams. The result shows the Sun entering and exiting each beam as expected, and the off-pointed beams are 3 dB down from the peak, as expected.

Figure 5 shows the spectroscopic capability of EMBRACE@Nançay. This is a spectrum of the galaxy M33 after a one hour integration using the ON-OFF pointing strategy as shown in Fig. 2.

5 Future Developments

EMBRACE@Nançay continues to be tested with the goal of verifying its long term stability, and improving the calibration. EMBRACE@Nançay is also being used as a testbed for developments of RFI mitigation algorithms, and a new Data Model.

Future hardware developments include the further integration of functionality on-chip with the goal of reducing power consumption and improving performance. A dual polarization tile is also under development for a future, large scale, demonstrator.

6 Conclusions

EMBRACE@Nançay is a demonstrator of a new technology for radio astronomy. We have demonstrated its capability as a radio astronomy instrument, including astronomical observations of pulsars and spectroscopic

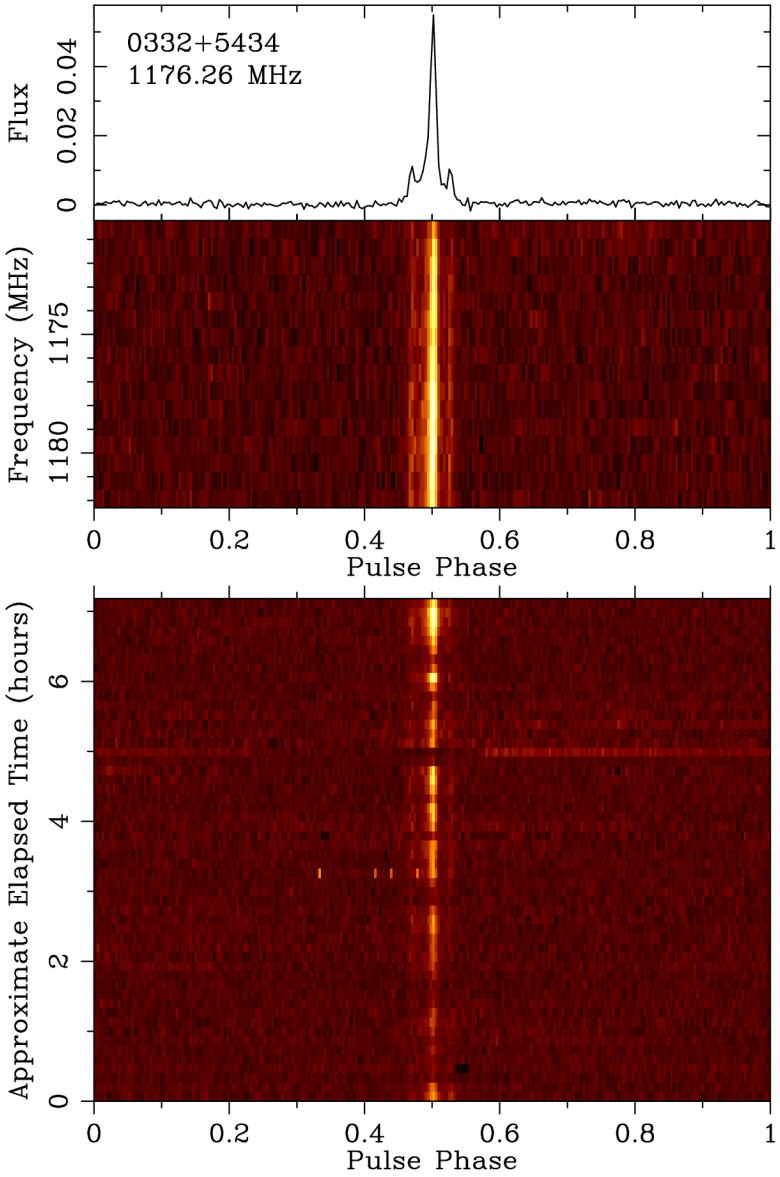

Fig. 3. Pulsar B0329+54 was detected after several minutes as shown in this dynamic plot folded at the pulsar period of 715 msec.

observations of galaxies. We have also demonstrated its multibeam capability. Dense aperture array technology is a viable solution for the SKA, offering the benefit of an enormous field of view and flexibility making it the most rapid astronomical survey machine.

EMBRACE was supported by the European Community Framework Programme 6, Square Kilometre Array Design Studies (SKADS), contract no 011938. We are grateful to ASTRON for initiating and developing the EMBRACE architecture. EMBRACE at Nançay would not have been possible without the efforts of Philippe Picard who led the project from 2005-11.

References

Armour, W., Karastergiou, A., Giles, M., et al. 2012, Astronomical Data Analysis Software and Systems XXI, 461, 33

Bosse, S., Barth, S., Torchinsky, S.A., Da Silva, B. *Proc. European Microwave Integrated Circuits Conference,* (EuMIC 2010), 27-28 September 2010, Paris, France, pp. 106 - 109

Dewdney, P.E., Hall, P.J., Schilizzi, R.T., Lazio, T.J.W., *Proceedings of the IEEE*, Vol. 97, No. 8, pp. 1482-1496, ISSN: 0018-9219

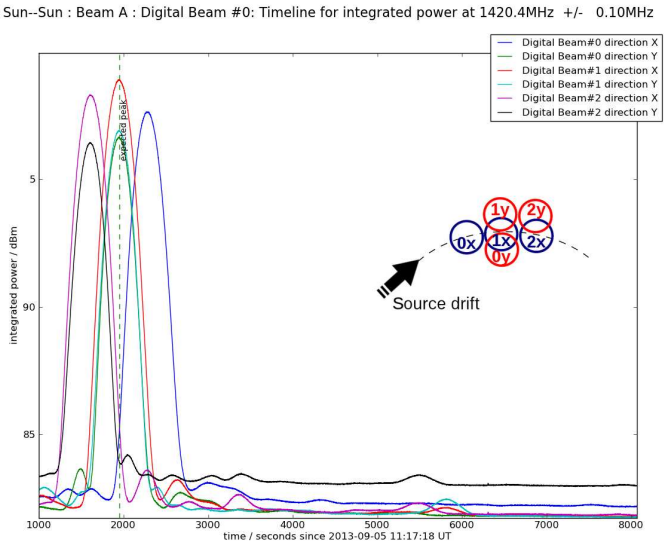

Fig. 4. This drift scan of the Sun used 6 beams of EMBRACE@Nançay pointing along the trajectory of the Sun across the sky (inset top right).

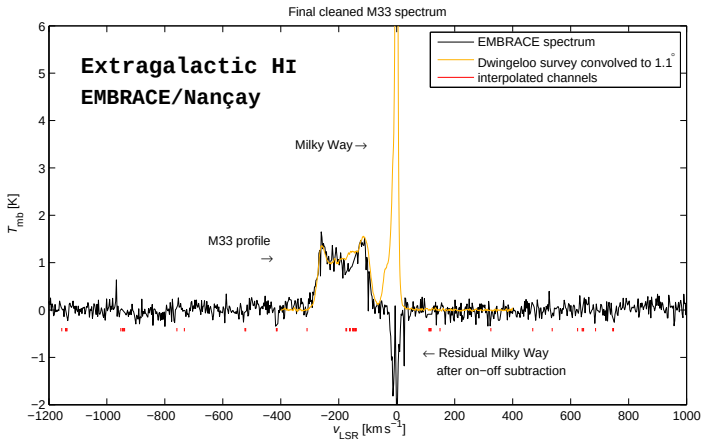

Fig. 5. EMBRACE@Nançay detected the galaxy M33 after a one hour integration using the ON-OFF pointing strategy described in the text.

Kant, G.W., van der Wal, E., Ruiter, M., Benthem, P. 2010 in *Proc. Wide Field Science and Technology for the SKA*, Limelette, Belgium, S.A. Torchinsky *et al.* (eds), ISBN 978-90-805434-5-4 , pg. 227

Kant, G.W., Patel, P.D., Wijnholds, S.J., Ruiter, M., van der Wal, E. *IEEE Trans. A&P* **59**, 1990.

A.O.H. Olofsson, S.A. Torchinsky, L. Chemin, S. Barth, S. Bosse, J.-M. Martin, W. Paule, P. Picard, S. Pomarède, P. Renaud, C. Taffoureau, G.W. Kant, J.E. Noordam, S.J. Wijnholds, R. Keller, S. Montebugnoli 2010 in *Proc. Wide Field Science and Technology for the SKA*, Limelette, Belgium, S.A. Torchinsky *et al.* (eds), ISBN 978-90-805434-5-4 , pg. 253

Picard, P., Renaud, P., Taffoureau, C., Macaire, V., Mercier, L., Paule, W. 2010 in *Proc. Wide Field Science and Technology for the SKA*, Limelette, Belgium, S.A. Torchinsky *et al.* (eds), ISBN 978-90-805434-5-4 , pg. 235

P. Renaud, C. Taffoureau, P. Picard, J. Borsenberger, S.A. Torchinsky, A.O.H. Olofsson, F. Viallefond, "Monitoring and Control of EMBRACE, a 4608 Elements Phased Array for Radio Astronomy," 2011, Proceedings Astronomical Data Analysis Software Systems, Paris, 6-10 November, 2011

Schieder, R., & Kramer, C. 2001, A&A, 373, 746

Serylak, M., Karastergiou, A., Williams, C., et al. 2013, IAU Symposium, 291, 492

Session 15

Atelier du PNHE

SF2A 2013
L. Cambrésy, F. Martins, E. Nuss and A. Palacios (eds)

ATHENA+: THE FIRST DEEP UNIVERSE X-RAY OBSERVATORY

D. Barret[1], K. Nandra[2], X. Barcons[3], A. Fabian[4], J.W. den Herder[5], L. Piro[6], M. Watson[7], J. Aird[8], G. Branduardi-Raymont [9], M. Cappi[10], F. Carrera[11], A. Comastri[12], E. Costantini[13], J. Croston[14], A. Decourchelle[15], C. Done[16], M. Dovciak[17], S. Ettori[18], A. Finoguenov[19], A. Georgakakis[20], P. Jonker[21], J. Kaastra[22], G. Matt[23], C. Motch[24], P. O'Brien[25], G. Pareschi[26], E. Pointecouteau[27], G. Pratt[28], G. Rauw[29], T. Reiprich[30], J. Sanders[31], S. Sciortino[32], R. Willingale[33], J. Wilms[34] and on behalf of the The Hot and Energetic Universe white paper contributors and the Athena+ supporters[35]

[1] [a]Université de Toulouse; UPS-OMP; IRAP; Toulouse, France & [b]CNRS; Institut de Recherche en Astrophysique et Planétologie; 9 Av. colonel Roche, BP 44346, F-31028 Toulouse cedex 4, France
[2] Max-Planck-Institut fur extraterrestrische Physik, P.O. Box 1312, Giessenbachstrasse, 85741 Garching, Germany
[3] Instituto de Fsica de Cantabria, Edificio Juan Jordá, Avenida de los Castros, s/n, E-39005 Santander, Cantabria, Spain
[4] Institute of Astronomy, University of Cambridge, Madingley Road, Cambridge, CB3 0HA, United Kingdom
[5] SRON Netherlands Institute for Space Research, Sorbonnelaan 2, 3584 CA Utrecht, Netherlands
[6] INAF, IASF Sezione di Roma, Via Fosso del Cavaliere 100, Tor Vergata, 00133 Roma, Italy
[7] University of Leicester, Department of Physics & Astronomy, University Rd, Leicester LE1 7RH, United Kingdom
[8] Department of Physics, Durham University, South Road, Durham, DH1 3LE, UK
[9] University College London, Mullard Space Science Laboratory, Holmbury St Mary, Dorking RH5 6NT, United Kingdom
[10] INAF, IASF Bologna, Via P Gobetti 101, 40129 Bologna, Italy
[11] Instituto de Fisica de Cantabria (CSIC-UC), Avda. de los Castros, 39005 Santander, Spain
[12] INAF Osservatorio Astronomico di Bologna, Via Ranzani 1, 40127 Bologna, Italy
[13] SRON, Netherlands Institute for Space Research, Sorbonnelaan 2, 3584 CA Utrecht, Netherlands
[14] University of Southampton, School of Physics and Astronomy, Highfield Campus, Southampton SO17 1BJ, United Kingdom
[15] CEA Saclay, Service d'Astrophysique, L'Orme des Merisiers Bat 709, BP 2, 91191 Gif-sur-Yvette Cedex, France
[16] Department of Physics, Durham University, South Road, Durham, DH1 3LE, UK
[17] Astronomical Institute AS CR, Fricova 298, CZ-25165 Ondrejov, Czech Republic
[18] INAF, Osservatorio Astronomico di Bologna, Via Ranzani 1, 40127 Bologna, Italy
[19] Department of Physics, University of Helsinki, Gustaf Hallstromin katu 2a, 00014 Helsinki, Finland
[20] Max-Planck-Institut fur extraterrestrische Physik, P.O. Box 1312, Giessenbachstrasse, 85741 Garching, Germany
[21] SRON Netherlands Institute for Space Research, Sorbonnelaan 2, 3584 CA Utrecht, Netherlands
[22] SRON Netherlands Institute for Space Research, Sorbonnelaan 2, 3584 CA Utrecht, Netherlands
[23] Università degli Studi Roma Tre, Dip.to di Matematica e Fisica, Via della Vasca Navale 84, 00146 Roma, Italy
[24] Observatoire Astronomique Strasbourg, 11 rue de l'Universit, 67000 Strasbourg, France
[25] University of Leicester, Department of Physics & Astronomy, University Rd, Leicester LE1 7RH, United Kingdom
[26] INAF-Osservatorio Astronomico di Brera, Osservatorio astronomico di Brera, Via Bianchi 46, 23807 Merate, Italy
[27] [a]Université de Toulouse; UPS-OMP; IRAP; Toulouse, France & [b]CNRS; Institut de Recherche en Astrophysique et Planétologie; 9 Av. colonel Roche, BP 44346, F-31028 Toulouse cedex 4, France
[28] CEA Saclay, Service d'Astrophysique, L'Orme des Merisiers Bat 709, BP 2, 91191 Gif-sur-Yvette Cedex, France
[29] Institut d'Astrophysique-Géophysique, Université de Liège, IAGL, 17 allée du 6 Août (Bât B5c), Sart Tilman, 4000 Liège, Belgium
[30] Argelander Institute for Astronomy, Bonn University, Auf dem Hügel 71, 53121 Bonn, Germany
[31] Max-Planck-Institut fur extraterrestrische Physik, P.O. Box 1312, Giessenbachstrasse, 85741 Garching, Germany
[32] INAF, Osservatorio Astronomico di Palermo G.S. Vaiana, Piazza del Parlamento 1, 90134 Palermo, Italy
[33] University of Leicester, Department of Physics & Astronomy, University Rd, Leicester LE1 7RH, United Kingdom
[34] University of Erlangen-Nuremberg, Dr. Karl Remeis-Sternwarte and ECAP, Sternwartstr. 7, 96049 Bamberg, Germany
[35] Full lists can be accessed at `http://www.the-athena-x-ray-observatory.eu`

Abstract. The Advanced Telescope for High-energy Astrophysics (*Athena+*) is being proposed to ESA as the L2 mission (for a launch in 2028) and is specifically designed to answer two of the most pressing questions for astrophysics in the forthcoming decade: How did ordinary matter assemble into the large scale structures we see today? and how do black holes grow and shape the Universe? For addressing these two issues, *Athena+* will provide transformational capabilities in terms of angular resolution, effective area, spectral resolution, grasp, that will make it the most powerful X-ray observatory ever flown. Such an observatory, when opened to the astronomical community, will be used for virtually all classes of astrophysical objects, from high-z gamma-ray bursts to the closest planets in our solar neighborhood. In this paper, we briefly review the core science objectives of *Athena+*, present the science requirements and the foreseen implementation of the mission, and illustrate its transformational capabilities compared to existing facilities.

Keywords: Accretion, accretion disks – Equation of state – Black hole physics – Techniques: high angular resolution – Techniques: imaging spectroscopy – Techniques: spectroscopic – Telescopes Surveys – Stars: winds, outflows – ISM: supernova remnants – Galaxy: center – Galaxies: high-redshift – (Galaxies:) intergalactic medium – (Galaxies:) quasars: general – (Galaxies:) quasars: supermassive black holes – (Cosmology:) large-scale structure of Universe – (Cosmology:) dark ages, reionization, first stars – X-rays: binaries – X-rays: galaxies – X-rays: galaxies: clusters – X-rays: general – X-rays: ISM – X-rays: stars

1 *Athena+* science objectives: The Hot and Energetic Universe

How did ordinary matter assemble into the large scale structures we see today? To answer this question we must trace the physical evolution of galaxy clusters and groups, as the most massive structures in the Universe, from their formation epoch to the present day. These structures grow over cosmic time by accretion of gas from the intergalactic medium, with the endpoint of their evolution being todays massive clusters of galaxies, the largest bound structures in the Universe. Hot gas in clusters, groups and the intergalactic medium dominates the baryonic content of the local Universe, so understanding how this component forms and evolves is a crucial goal (Nandra et al. 2013).

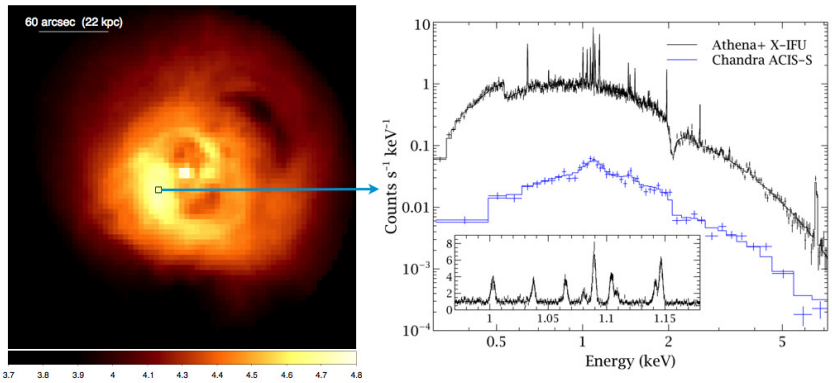

Fig. 1. Simulated *Athena+* observations of the Perseus cluster, highlighting the advanced capabilities for revealing the intricacies of the physical mechanisms at play. The left panel shows a simulated 50 ks X-IFU observation (0.5-7 keV), displayed on a log scale. The spectrum on the right is from the single $5'' \times 5''$ region marked by the box, with the existing *Chandra* ACIS spectrum for comparison. The inset shows the region around the iron L complex. With such observations velocity broadening is measured to 10–20 km s^{-1}, the temperature to 1.5% and the metallicity to 3% on scales < 10 kpc in 20–30 nearby systems, and on < 50 kpc scales in hundreds of clusters and groups. Such measurements will allow us to pinpoint the locations of jet energy dissipation, determine the total energy stored in bulk motions and weak shocks, and test models of AGN fueling so as to determine how feedback regulates hot gas cooling (from Croston et al. 2013).

While the framework for the growth of structures is set by the large scale dark matter distribution, processes of an astrophysical origin also have a major effect (Pointecouteau et al. 2013; Ettori et al. 2013; Croston et al. 2013, and references therein). To understand them, it is necessary to measure the velocities, thermodynamics and chemical composition of the gas to quantify the importance of non-gravitational heating and turbulence in the structure assembly process (Pointecouteau et al. 2013; Ettori et al. 2013). The temperature of the hot gas is such that it emits primarily in the X-ray band, but current and planned facilities do not provide sufficient

collecting area and spectral resolution to settle the key issue of how ordinary matter forms the large scale structures that we see today. The key breakthrough is to enable spectroscopic observations of clusters beyond the local Universe, out to z=1 and beyond, and spatially resolved spectroscopy to map the physical parameters of bound baryonic structures (Pointecouteau et al. 2013; Ettori et al. 2013). Technological advances in X-ray optics and instrumentation can deliver simultaneously a factor 10 increase in both telescope throughput and spatial resolving power for high resolution spectroscopy (Willingale et al. 2013; Barret et al. 2013), allowing the necessary physical diagnostics to be determined at cosmologically relevant distances for the first time. At even larger scales, the locations and kinematics of the missing baryons predicted to reside in the warm hot phase of the intergalactic medium and providing a tracer of the large scale dark matter structures of the local Universe, can only be fully revealed via high resolution X-ray spectroscopy (Kaastra et al. 2013).

One of the critical processes shaping hot baryon evolution is energy input commonly known as feedback from supermassive black holes (Croston et al. 2013; Cappi et al. 2013) (see Fig. 1). Remarkably, processes originating at the scale of the black hole event horizon seem able to influence structures on scales 10 orders of magnitude larger (Cappi et al. 2013; Dovciak et al. 2013). This feedback is an essential ingredient of galaxy evolution models, but it is not well understood. X-ray observations are again the key to further progresses, revealing the mechanisms which generate and launch winds close to black holes and determining the coupling of the energy and matter flows on larger galactic and cluster scales (Georgakakis et al. 2013; Cappi et al. 2013; Dovciak et al. 2013).

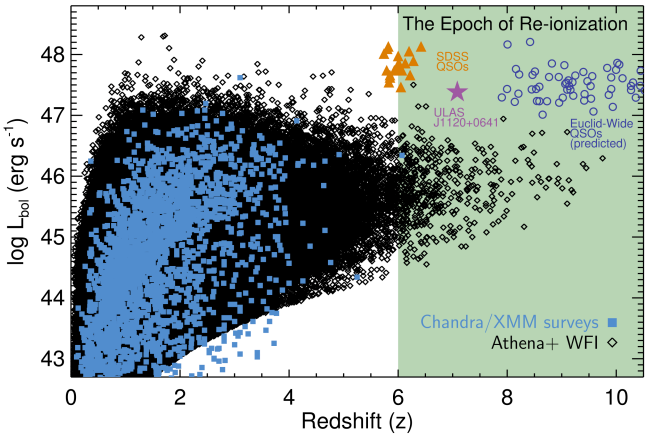

Fig. 2. Predictions for the redshifts and luminosities of 600,000 AGN that will be identified with a multilayered 1-year *Athena+* WFI survey, compared to current *Chandra* and *XMM-Newton* surveys. *Athena+* will discover hundreds of X-ray selected AGN in the epoch of reionization at $z > 6$, sources which are around 2 orders of magnitude fainter than current optical and near-IR surveys (e.g. SDSS, UKIDSS), thus providing an essential complement to the luminous QSOs that Euclid will identify in the next decade (Roche et al. 2012), including in particular the most obscured ones missed by those surveys (for a discussion see, Aird et al. 2013).

The second key question to be addressed by *Athena+* is that of how black holes grow and shape the Universe (Nandra et al. 2013). The widespread importance of black hole feedback means that we cannot have a complete understanding of galaxies without tracking the growth of their central supermassive black holes through cosmic time. A key goal is to push the frontiers of black hole evolution to the redshifts where the first galaxies are forming, at $z = 6 - 10$ (Aird et al. 2013; Georgakakis et al. 2013, and references therein). X-ray emission is the most reliable and complete way of revealing accreting black holes in galaxies, but survey capabilities need to be improved by a factor ~ 100 over current facilities to reach these early epochs and perform a census of black hole growth (Aird et al. 2013) (see Fig. 2). This requires a combination of high sensitivity, which in turn depends on large throughput and good angular resolution, and wide field of view. Again, the required technologies to provide this leap in wide field X-ray spectral imaging are now within our grasp (Rau et al. 2013). The same high throughput needed to detect these early black holes will also yield the first detailed X-ray spectra of accreting black holes at the peak of galaxy growth at $z = 1 - 4$, measurements which are impossible with current instrumentation. These spectra will show, for example, if the heavily obscured phase of black hole evolution is associated with the termination of star formation in galaxies via feedback (Georgakakis et al. 2013).

The Hot and Energetic Universe includes almost all known astrophysical objects, from the closest planets

to the most distant quasars and gamma-ray bursts. The instrument suite required to achieve the science goals described above provides *Athena+* with unprecedented observatory capabilities, enabling breakthrough observations to be performed for a wide range of objects, of interest to the whole astronomical community. This covers Solar system bodies and exoplanets, stars, compact objects , supernova remnants, the interstellar medium, and luminous extragalactic transients, such as gamma-ray bursts. Key topics to be addressed include: i) Establish how planetary magnetospheres and exospheres, and comets, respond to the interaction with the solar wind, in a global way that in situ observations cannot offer (Branduardi-Raymont et al. 2013), ii) assess the mass loss rates of high velocity chemically-enriched material from massive stars to understand the role they play in the feedback processes on Galactic scales (Sciortino et al. 2013), iii) discover how mass loss from disk winds influences the binary evolution and impact the interstellar medium (Motch et al. 2013), iv) understand the physics of core collapse and type Ia supernova remnants and determine the chemical composition of the hot and cold gas of the interstellar medium, as a tracer of stellar activity in our and other galaxies (Decourchelle et al. 2013), v) distinguish Population III from Population II star forming regions as gamma-ray burst progenitors (Jonker et al. 2013).

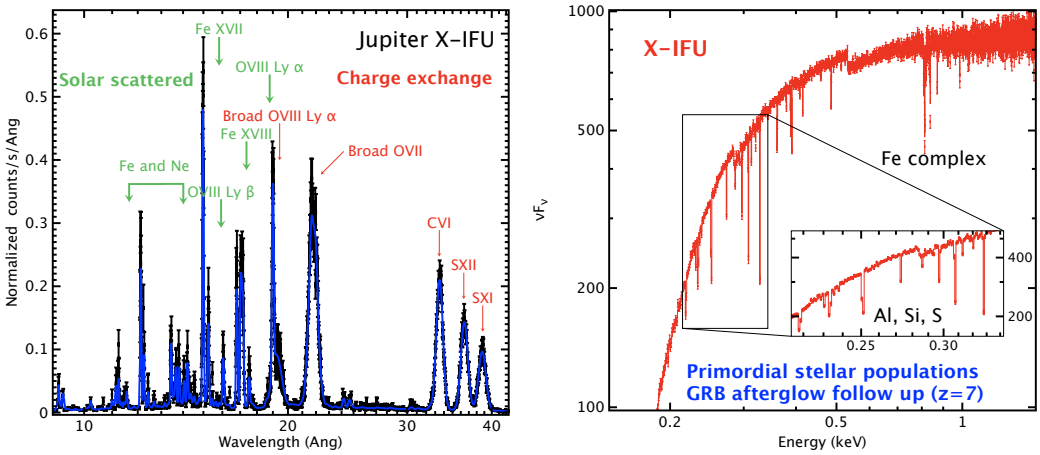

Fig. 3. Left: Simulated *Athena+* X-IFU spectrum of Jupiter for an exposure time of 20 ks: the wavelength coverage extends to the 30 – 40 Å band allowing to resolve the C/S ambiguity (from Branduardi-Raymont et al. 2013). **Right:** A simulated X-IFU X-ray spectrum of a GRB afterglow at $z = 7$, showing the capability of *Athena+* in tracing the primordial stellar populations. This medium bright afterglow (fluence=0.4×10^{-6} erg cm^{-2}) is characterized by deep narrow resonant lines of Fe, Si, S, Ar, Mg, from the ionized gas in the environment of the GRB. An effective column density of 2×10^{22} cm^{-2} has been adopted. The abundance pattern measured by *Athena+* can distinguish Population III from Population II star forming regions (from Jonker et al. 2013).

2 The *Athena+* mission concept

Athena+ in an X-ray observatory-class mission delivering a transformational leap in high-energy observational capabilities. A lightweight X-ray telescope based on ESA's Silicon Pore Optics (SPO) technology provides large effective area with excellent angular resolution, to be combined with state-of-the-art instrumentation for spatially resolved high resolution X-ray spectroscopy (provided by the X-ray Integral Field Unit, X-IFU, Barret et al. 2013) and wide field X-ray imaging (provided by the Wide Field Imager, WFI, Rau et al. 2013). *Athena+* will thus deliver superior wide field X-ray imaging spectroscopy and timing capabilities, far beyond those of any existing or approved future facilities. Mapping the dynamics and chemical composition of hot gas in diffuse sources requires high spectral resolution imaging (2.5 eV resolution) with low background; this also optimizes the sensitivity for weak absorption and emission features needed for WHIM studies or for faint point source characterisation. An angular resolution of 5 arcsec is required to disentangle small structures of clusters and groups and, in combination with a large area, provides high resolution spectra, even for faint sources. This angular resolution, combined with the mirror effective area and large field of view (40 arcmin) of the WFI provides the deep survey area and detection sensitivity (limiting flux of 10^{-17} erg cm^{-2} s^{-1} 0.5 – 2 keV band) required to detect AGN at $z > 6$ within a reasonable survey time. The science requirements and enabling

technologies for *Athena+* are summarized in Table 1.

Parameter	Requirements	Enabling technology/comments
Effective Area	2 m^2 @ 1 keV (goal 2.5 m^2) 0.25 m^2 @ 6 keV (goal 0.3 m^2)	Silicon Pore Optics developed by ESA. Single telescope: 3 m outer diameter, 12 m fixed focal length.
Angular Resolution	5″ (goal 3") on-axis 10" at 25' radius	Detailed analysis of error budget confirms that a performance of 5" HEW is feasible.
Energy Range	0.3-12 keV	Grazing incidence optics.
Instrument Field of View	Wide-Field Imager: (WFI): 40' (goal 50') X-ray Integral Field Unit: (X-IFU): 5' (goal 7')	Large area DEPFET Active Pixel Sensors. Large array of multiplexed Transition Edge Sensors (TES) with 250 μm pixels.
Spectral Resolution	WFI: < 150 eV @ 6 keV X-IFU: 2.5 eV @ 6 keV (goal 1.5 eV @ 1 keV)	Large area DEPFET Active Pixel Sensors. Inner array (10"x10") optimized for goal resolution at low energy (50 μm pixels).
Count Rate Capability	> 1 Crab (WFI) 10 mCrab, point source (X-IFU) 1 Crab (30% throughput)	Central chip for high count rates without pile-up and with micro-second time resolution. Filters and beam diffuser enable higher count rate capability with reduced spectral resolution.
TOO Response	4 hours (goal 2 hours) for 50% of time	Slew times < 2 hours feasible; total response time dependent on ground system issues.

Table 1. Key parameters and requirements of the *Athena+* mission. The enabling technology is indicated.

The strawman *Athena+* payload comprises three key elements:

- A single X-ray telescope with a focal length of 12 meters and an unprecedented effective area (2 m^2 at 1 keV). The X-ray telescope employs Silicon Pore Optics (SPO), an innovative technology that has been pioneered in Europe over the last decade mostly with ESA support. SPO is a highly modular concept, based on a set of compact individual mirror modules, which has an excellent effective area-to-mass ratio and can achieve high angular resolution ($< 5''$) and a flat response across the field of view (Willingale et al. 2013) (see Fig. 4).
- The X-ray Integral Field Unit (X-IFU), an advanced actively shielded X-ray microcalorimeter spectrometer for high-resolution imaging, utilizing Transition Edge Sensors cooled to 50 mK (Barret et al. 2013).
- The Wide Field Imager (WFI), a Silicon Active Pixel Sensor camera with a large field of view, high count-rate capability and moderate resolution spectroscopic capability (Rau et al. 2013).

Athena+ is based on a conventional design retaining much heritage from *XMM-Newton*. Considerations of observing efficiency and thermal stability favour an L2 orbit reached by Ariane V. *Athena+* will be an observatory whose program will be largely driven by calls for proposals from the scientific community, but may be complemented by key programs for science goals requiring large time investments. A nominal mission lifetime of 5 years would allow the core science goals set out in the White Paper to be achieved, while preserving a large fraction of the available time for broad based science programs (Nandra et al. 2013).

With such a mission configuration *Athena+* will truly provide transformational capabilities, as illustrated in Fig. 4. It will provide an improvement factor > 100 in high spectral resolution throughput (e.g. compared to *ASTRO-H* microcalorimeter and *XMM-Newton* gratings). It will open high-resolution X-ray spectroscopy to the high redshift Universe (up to $z \sim 3$ without mentioning gamma-ray bursts), while it is currently limited to redshifts less than ~ 0.3. It will provide a factor of more than 10 in bare throughput (i.e. area on axis) for spectral-timing-imaging observations compared to the *XMM-Newton* PN camera. Thanks to the combination

of effective area, field of view, angular resolution (and its flatness across the field of view), *Athena+* will deliver an improvement factor larger than 100 in survey speed compared to *Chandra* (see Fig. 4, lower panels).

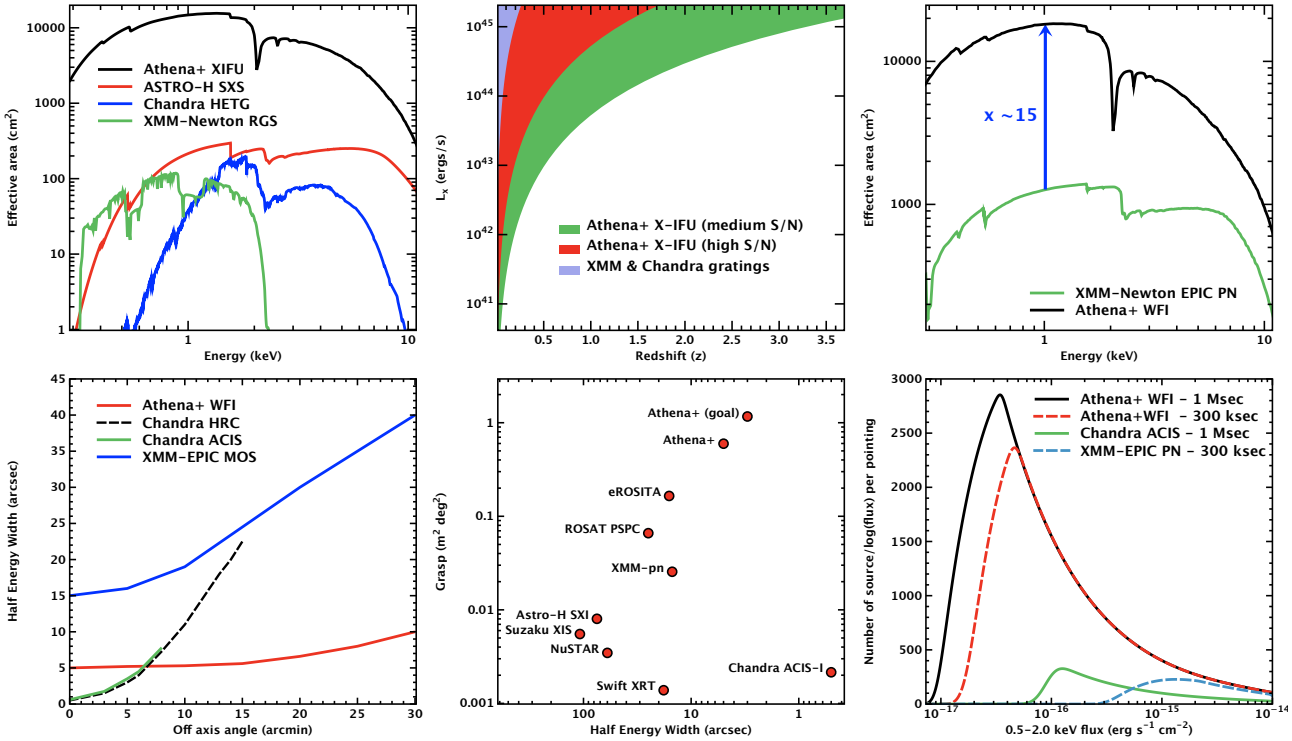

Fig. 4. Top left: Effective area curves for high resolution X-ray spectrometers, operational and planned. **Top center:** $L_x - z$ curve for high resolution X-ray spectroscopy, compared to current X-ray gratings. **Top right:** Effective area curves for spectral-timing-imaging observations with the *XMM-Newton* PN camera and the *Athena+* wide field imager. **Bottom left:** Half Energy Width (arcsec) (PSF variation across the field of view) comparison between existing X-ray imagers and the *Athena+* wide-field imager. **Bottom center:** Grasp of previous, operational and planned missions as a function of angular resolution. Grasp is defined as the product of effective area at 1 keV (10 keV for *NuSTAR*) and the instrument field of view. **Bottom right:** Number of sources per logarithmic flux interval expected in single *Athena+* WFI pointings at high Galactic latitudes compared to *Chandra* and *XMM-Newton*.

3 Conclusions

Athena+ is designed to tackle two of the most pressing questions of modern astrophysics: How did ordinary matter assemble into the large scale structures we see today? and how do black holes grow and shape the Universe? *Athena+* provides the necessary angular resolution, spectral resolution, throughput, detection sensitivity, and survey grasp to answer these two questions. The technologies for *Athena+* are mature, being based on much previous heritage and major technology developments in Europe. *Athena+* as an X-ray observatory, will open up a vast discovery space leading to completely new areas of scientific investigation, continuing the legacy of discovery that has characterized X-ray astronomy since its inception. The implementation of *Athena+* for launch in 2028 will guarantee a transformation in our understanding of The Hot and Energetic Universe, and establish European leadership in high-energy astrophysics for the foreseeable future.

We gratefully acknowledge the comments and inputs of the White Paper Review Team: M. Arnaud, J. Bregman, F. Combes, R. Kennicutt, R. Maiolino, R. Mushotzky, T. Ohashi, K. Pounds, C. Reynolds, H. Röttgering, M. Rowan-Robinson, C. Turon and G. Zamorani. It is also a pleasure to thank the 1178 *Athena+* supporters, recorded as of November 8, 2013.*

*All information related to *Athena+*, including the list of supporters can be found on the *Athena+* web site: `http://www.the-athena-x-ray-observatory.eu`.

References

Aird, J., Comastri, A., Brusa, M., et al. 2013, An *Athena+* supporting paper: The formation and growth of the earliest supermassive black holes, 2013arXiv1306.2325

Barret, D., den Herder, J. W., Piro, L., et al. 2013, An *Athena+* supporting paper: The X-ray Integral Field Unit (X-IFU) for Athena+, 2013arXiv1308.6784

Branduardi-Raymont, G., Sciortino, S., Dennerl, K., et al. 2013, An *Athena+* supporting paper: Solar system and exoplanets, 2013arXiv1306.2332

Cappi, M., Done, C., Behar, E., et al. 2013, An *Athena+* supporting paper: Astrophysics of feedback in local AGN, 2013arXiv1306.2330

Croston, J. H., Sanders, J. S., Heinz, S., et al. 2013, An *Athena+* supporting paper: AGN feedback in galaxy clusters and groups, 2013arXiv1306.2323

Decourchelle, A., Costantini, E., Badenes, C., et al. 2013, An *Athena+* supporting paper: The astrophysics of supernova remnants and the interstellar medium, 2013arXiv1306.2335

Dovciak, M., Matt, G., Bianchi, S., et al. 2013, An *Athena+* supporting paper: The close environments of supermassive black holes, 2013arXiv1306.2331

Ettori, S., Pratt, G. W., de Plaa, J., et al. 2013, An *Athena+* supporting paper: The astrophysics of galaxy groups and clusters, 2013arXiv1306.2322

Georgakakis, A., Carrera, F., Lanzuisi, G., et al. 2013, An *Athena+* supporting paper: Understanding the build-up of supermassive black holes and galaxies at the heyday of the Universe, 2013arXiv1306.2328

Jonker, P., O'Brien, P., Amati, L., et al. 2013, An *Athena+* supporting paper: Luminous extragalactic transients, 2013arXiv1306.2336

Kaastra, J., Finoguenov, A., Nicastro, F., et al. 2013, An *Athena+* supporting paper: The missing baryons and the warm-hot intergalactic medium, 2013arXiv1306.2324

Motch, C., Wilms, J., Barret, D., et al. 2013, An *Athena+* supporting paper: End points of stellar evolution, 2013arXiv1306.2334

Nandra, K., Barret, D., Barcons, X., et al. 2013, *The Hot and Energetic Universe*: A White Paper presenting the science theme motivating the *Athena+* mission, 2013arXiv1306.2307

Pointecouteau, E., Reiprich, T. H., Adami, C., et al. 2013, An *Athena+* supporting paper: The evolution of galaxy groups and clusters, 2013arXiv1306.2319

Rau, A., Meidinger, N., Nandra, K., et al. 2013, An *Athena+* supporting paper: The Wide Field Imager (WFI) for Athena+, 2013arXiv1308.6785

Roche, N., Franzetti, P., Garilli, B., et al. 2012, MNRAS, 420, 1764

Sciortino, S., Rauw, G., Audard, M., et al. 2013, An *Athena+* supporting paper: Star formation and evolution, 2013arXiv1306.2333

Willingale, R., Pareschi, G., Christensen, F., & den Herder, J.-W. 2013, An *Athena+* supporting paper: The Optical Design of the Athena+ Mirror, 2013arXiv1307.1709

SF2A 2013
L. Cambrésy, F. Martins, E. Nuss and A. Palacios (eds)

THE SPECTRAL CATALOGUE OF *INTEGRAL* GAMMA-RAY BURSTS

Ž. Bošnjak[1,2,3], D. Götz[1], L. Bouchet[3,4], S. Schanne[1] and B. Cordier[1]

Abstract. We present a spectral catalogue of gamma-ray bursts detected by the *INTEGRAL* satellite. In the period between December 2002 and February 2012 *INTEGRAL* observed 83 GRBs. The spectral parameters were derived by combining the data from the two main instruments on board *INTEGRAL*, the spectrometer SPI (Spectrometer on *INTEGRAL*) nominally covering the energy range 18 keV - 8 MeV, and the imager IBIS (the Imager on Board the *INTEGRAL* Satellite) with spectral sensitivity in the range 15 keV - 10 MeV. In addition to the spectral analysis performed over a broad energy range for the complete sample of *INTEGRAL* GRBs, we have derived the IBIS light curves and durations for the previously unpublished 28 events observed between September 2008 and February 2012. We compare the prompt emission properties of the *INTEGRAL* GRB sample with the BATSE and *Fermi* samples.

Keywords: gamma-rays burst: general - catalogs - methods: data analysis

1 Introduction

To date the most complete catalogues of spectral GRB properties comprise the events observed by BATSE (Burst And Transient Source Experiment) on board the *Compton Gamma Ray Observatory* in operation from 1991 to 2000 (Gehrels et al. 1994), by the *Swift* satellite launched in 2004 (Gehrels et al. 2004), and by the *Fermi* satellite launched in 2008 (Gehrels & Razzaque 2013). The spectral parameters - peak energy, low- and high-energy power law indices - are associated with the parameters of the energy dissipation and the emission mechanisms of the prompt emission and provide the constraints for the gamma-ray burst models.

INTEGRAL (Winkler et al. 2003) is an ESA mission launched on October 17, 2002 dedicated to high resolution imaging and spectroscopy in the hard X-/soft γ-ray domain. It carries two main coded-mask instruments, SPI (Vedrenne et al. 2003), and IBIS (Ubertini et al. 2003). SPI is made of 19 Ge detectors, working in the 20 keV–8 MeV energy range, and is optimized for high resolution spectroscopy. IBIS is made of two pixellated detection planes: the upper plane, ISGRI – *INTEGRAL* Soft Gamma-Ray Imager (Lebrun et al. 2003), is made of 128×128 CdTe detectors and operates in the 15 keV–1 MeV energy range. The lower detection plane, PICsIT – PIxellated CsI Telescope (Di Cocco et al. 2003), is made of 64×64 pixels of CsI, and is sensitive between 150 keV and 10 MeV. In order to provide a broad energy coverage and a good sensitivity for the *INTEGRAL* GRB spectra, we combined the data from the IBIS/ISGRI and the SPI instruments for the spectral analysis. The SPI data can provide better spectral information at energies where IBIS/ISGRI effective area becomes low, and therefore are suitable to determine the GRB spectral peak energy (typically at $\sim$ a few 100 keV).

2 Spectral and temporal analysis

The spectra were analysed using the C-statistic (Cash 1979); for the C-statistic to be applied, we needed to provide on-burst spectra and background spectra separately for every GRB. This cannot be obtained by the *INTEGRAL* standard Off-line Scientifc Analysis software (OSA), and therefore we developed additional tools

[1] AIM (UMR 7158 CEA/DSM-CNRS-Université Paris Diderot) Irfu/Service d'Astrophysique, Saclay, F-91191 Gif-sur-Yvette Cedex, France
[2] Department of Physics, University of Rijeka, 51000 Rijeka, Croatia
[3] Université de Toulouse, UPS-OMP, IRAP, Toulouse, France
[4] CNRS, IRAP, 9 Av. Colonel Roche, BP 44346, F-31028 Toulouse Cedex 4, France

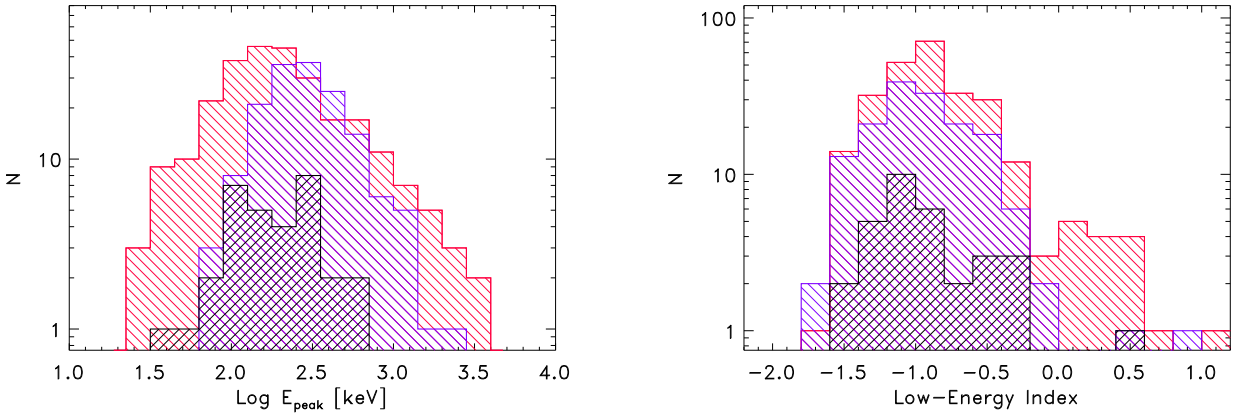

Fig. 1. Left: distribution of the spectral peak energies. **Right:** distribution of the low energy spectral power law indices. The sample of *INTEGRAL* GRBs is shown in black; BATSE results (violet) and *Fermi*/GBM results (red) of the time-integrated spectral analysis were used for the comparison. Only long events were selected, fitted with the Band or cut-off power law model, and having the fluence in the same range as *INTEGRAL* GRBs.

to extract the spectra in the required format. For the SPI instrument, a spectrum for each of the 19 (where applicable) Ge detectors was computed. The net individual GRB spectra (i.e. on-burst – off-burst spectra) have the advantage (with respect to the global spectra produced by OSA software) of being more accurate since the background spectra were computed for each GRB and each detector, taking into account the local spectral and temporal background evolution. The response function takes into account the exposed fraction of each detector given the GRB direction. For the IBIS/ISGRI spectra, we selected only the pixels that were fully illuminated by the GRB in order to compute the off-burst and on-burst spectra. A corresponding ARF was computed, taking into account the reduced ($\sim 30\%$) area of the detector plane we used. For each GRB we computed and fitted the time-integrated spectrum, using all the available SPI spectra and one ISGRI spectrum.

We report the results of the spectral anlysis for 59 out of 83 GRBs, and make a comparison of our results with the BATSE and *Fermi*/GBM samples (see Fig. 1) of gamma-ray bursts of equivalent brightness and duration. We found that *INTEGRAL* sample of GRBs has spectral peak energies consistent with the distribution obtained by *Fermi*/GBM (KS probability = 0.55), and not consistent with the distribution of BATSE GRBs (KS probability = 6×10^{-3}) in a given fluence range. The distribution of the low energy power law slopes obtained for ISGRI/SPI GRBs is consistent with both, *Fermi*/GBM (KS probability = 0.23) and BATSE (KS probability = 0.92) GRB samples.

We determined the T_{90} duration for sample of GRBs observed after September 2008 (for the GRBs observed before September 2008, see Vianello et al. 2009). The GRB durations were determined using only the IBIS/ISGRI light curves obtained for 20–200 keV energy band (see Fig. 2). The maximum of the T_{90} distribution for *INTEGRAL* GRB sample is at ~ 30 s, which is comparable to the samples obtained by BATSE and *Fermi*/GBM. The distribution of long GRB durations from *Swift*/BAT sample is shifted towards longer times, coherently with the longer BAT triggering time scales (see Sakamoto et al. 2011). The paucity of the short events in *INTEGRAL* sample (6%) is expected for the imaging instruments, as e.g. the *Swift*/BAT, where a minimum number of counts is required to localize an excess in the derived image, making confirmation of real bursts with fewer counts difficult.

3 Conclusions

The GRB catalog we presented contains a limited number of events with respect to other missions' databases. Our results offer however an important insight in the possible instrumental biases in spectral and temporal parameters distributions, and also provide the spectral parameters for a sample of faint GRBs with good statistics.

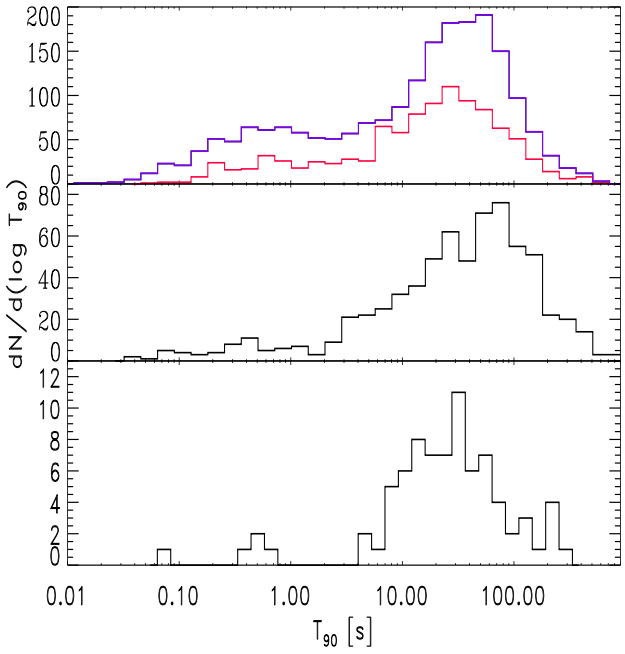

Fig. 2. Distribution of the duration T_{90}. **Top:** Distribution of durations derived from BATSE (violet) and *Fermi*/GBM (red) light curves in the 50-300 keV band (c.f. Kouveliotou et al. 1993). **Middle:** The T_{90} durations derived using *Swift*/BAT instrument on 15-150 keV (c.f. Sakamoto et al. 2011). **Bottom:** Distribution of durations for 20-200 keV light curves obtained from IBIS/ISGRI.

The authors thank Thomas Maccarone, Patrick Sizun and Fabio Mattana for discussions on data analysis. ZB acknowledges the French Space Agency (CNES) for financial support. ISGRI has been realized and maintained in flight by CEA-Saclay/Irfu with the support of CNES. Based on observations with INTEGRAL, an ESA project with instruments and science data centre funded by ESA member states (especially the PI countries: Denmark, France, Germany, Italy, Switzerland, Spain), Czech Republic and Poland, and with the participation of Russia and the USA.

References

Cash, W. 1979, ApJ, 228, 939
Di Cocco, G., Caroli, E., Celesti, E., et al. 2003, A&A, 411, L189
Gehrels, N., Chincarini, G., Giommi, P., et al. 2004, ApJ, 611, 1005
Gehrels, N., Chipman, E., & Kniffen, D. 1994, ApJS, 92, 351
Gehrels, N. & Razzaque, S. 2013, Frontiers of Physics
Kouveliotou, C., Meegan, C. A., Fishman, G. J., et al. 1993, ApJ, 413, L101
Lebrun, F., Leray, J. P., Lavocat, P., et al. 2003, A&A, 411, L141
Sakamoto, T., Barthelmy, S. D., Baumgartner, W. H., et al. 2011, ApJS, 195, 2
Ubertini, P., Lebrun, F., Di Cocco, G., et al. 2003, A&A, 411, L131
Vedrenne, G., Roques, J.-P., Schönfelder, V., et al. 2003, A&A, 411, L63
Vianello, G., Götz, D., & Mereghetti, S. 2009, A&A, 495, 1005
Winkler, C., Courvoisier, T. J.-L., Di Cocco, G., et al. 2003, A&A, 411, L1

SF2A 2013
L. Cambrésy, F. Martins, E. Nuss and A. Palacios (eds)

THE SPIRAL MODES OF THE SASI: ANGULAR MOMENTUM REDISTRIBUTION AND ORIGIN OF PULSAR SPINS

J. Guilet[1,2] and Rodrigo Fernández[3,4]

Abstract. The accretion shock formed during the collapse of massive stars is subject to the Standing Accretion Shock Instability (SASI). In three-dimensions, spiral modes of this instability can efficiently redistribute angular momentum and thereby impart a spin to the forming neutron star, even when the progenitor star is non-rotating. Here we present an analytical description of the angular momentum redistribution caused by these spiral modes. Our analysis, valid in the limit of small mode amplitude, shows that the angular momentum separation is driven by the Reynolds stress generated by the spiral mode. Analytic solutions compare favorably with previous three-dimensional hydrodynamic simulations of the SASI in the linear and weakly non-linear phases. Reasonable agreement is also found when extrapolating the solutions into the fully non-linear phase. From this analysis, we derive an approximate expression for the minimum period imparted to the neutron star as a function of the relevant accretion flow parameters at the time of explosion. Implications for the birth spin periods of pulsars are discussed.

Keywords: hydrodynamics, instabilities, shock waves, stars: neutron, stars: rotation, supernovae: general

1 Introduction

Neutron stars are formed during the gravitational collapse of massive stars. This core collapse also powers a supernova explosion that ejects the outer layers of the progenitor. The dynamics of the explosion has important consequences for the properties of the resulting neutron star, such as its final mass, space velocity, spin, and magnetic field (see, e.g., Janka 2012 for a review). In particular, the standing accretion shock instability (SASI; Blondin et al. 2003; Ohnishi et al. 2006; Foglizzo et al. 2007; Scheck et al. 2008) causes shock oscillations that create a global asymmetry of the explosion. The SASI is driven by an unstable cycle between the shock and the proto-neutron star surface involving advected and acoustic perturbation (Foglizzo et al. 2007; Foglizzo 2009; Guilet & Foglizzo 2012). Blondin & Mezzacappa (2007) showed that SASI spiral modes have the ability to redistribute angular momentum in the postshock region, and suggested that this process could impart enough angular momentum to the neutron star to significantly change its spin. This angular momentum redistribution was later confirmed by numerical simulations (Blondin & Shaw 2007; Fernández 2010) and in an experimental analog of SASI (Foglizzo et al. 2012). In this proceeding, we present an analytical description of this angular momentum redistribution, which is described in more detail in Guilet & Fernández (2013). The formalism is presented in Section 2, and compared with 3D numerical simulations in Section 3. Finally, in Section 4 we give an approximate expression for the spin that can be imparted to the neutron star by this process and discuss the consequences for neutron star rotation periods at birth.

2 Formalism

We consider a standing spherical accretion shock around a central protoneutron star of mass M and radius r_* that is subject to a spiral SASI mode around some axis. The upstream accretion flow is non-rotating. We assume

[1] Department of Applied Mathematics and Theoretical Physics, University of Cambridge
Centre for Mathematical Sciences, Wilberforce Road, Cambridge CB3 0WA, UK
[2] Max-Planck-Institut fur Astrophysik, Karl-Schwarzschild-Str. 1, D-85748 Garching, Germany
[3] Department of Physics, University of California, Berkeley, CA 94720, USA
[4] Department of Astronomy & Theoretical Astrophysics Center, University of California, Berkeley, CA 94720, USA

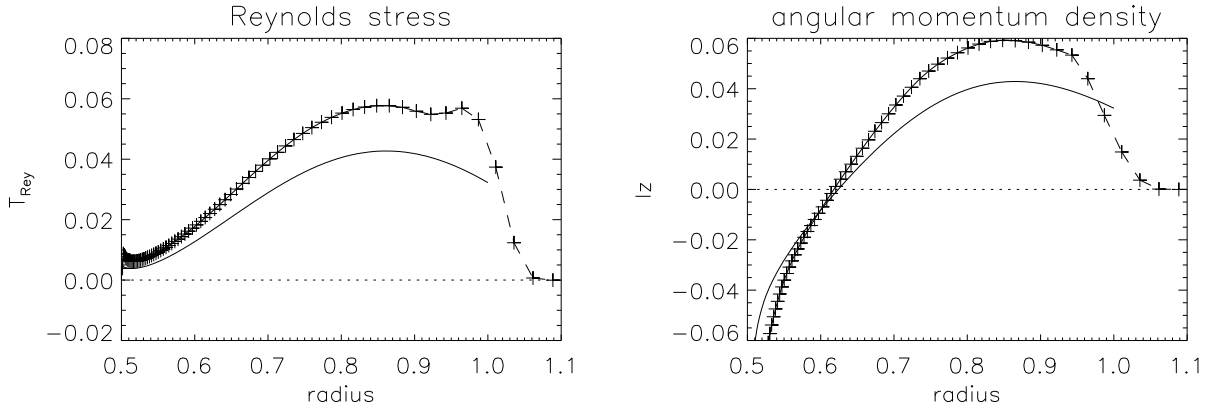

Fig. 1. Radial profiles of the surface-integrated Reynolds stress (left) and angular momentum density (right) resulting from an $l = 1$ spiral mode. The radius is normalized by the shock radius, the Reynolds stress by $\dot{M}r_{\rm sh0}|v_{\rm sh0}|$, and the angular momentum density by $\dot{M}r_{\rm sh0}$. The dashed lines with + signs show values from model R5_L11_HR of Fernández (2010) at $t = 30$, while the full lines show the semi-analytical predictions. See Guilet & Fernández (2013) for details.

that the flow can be described as a stationary background with superimposed small amplitude perturbations:

$$\rho(r,\theta,\phi,t) = \rho_0(r) + \delta\rho(r,\theta,\phi,t) + \delta^2\rho(r,\theta,\phi,t) + ... \quad (2.1)$$

$$v_r = v_0 + \delta v_r + \delta^2 v_r + ... \quad (2.2)$$

$$v_\phi = \delta v_\phi + \delta^2 v_\phi + ... \quad (2.3)$$

where δ and δ^2 denote first- and second order Eulerian perturbations, respectively, with $\delta \gg \delta^2$. We retain perturbations up to second order because this is the first non-zero contribution to the surface integrated angular momentum l_z. The evolution of the first order perturbations can be computed with a linear analysis as in Foglizzo et al. (2007).

Using this expansion, the angular momentum conservation can be written as:

$$\partial_t l_z + \partial_r(l_z v_0) = -\partial_r T_{Rey}, \quad (2.4)$$

where $l_z \equiv \iint r\sin\theta\rho v_\phi \,\mathrm{d}^2 s$ is the angular momentum density integrated over a spherical shell, and $T_{Rey} \equiv \iint \rho_0 \delta v_r \delta v_\phi r \sin\theta \,\mathrm{d}^2 s$ is the surface integrated Reynolds stress, describing the angular momentum flux driven by the non-axisymmetric perturbations of the spiral mode. The Reynolds stress can be computed using the linear eigenmodes and Equation (2.4) can then be solved to obtain the angular momentum density driven by a SASI spiral mode:

$$l_z = -\frac{T_{Rey}}{v_0} + \frac{e^{-2\omega_i \tau_{\rm adv}}}{v_0}\int_{r_{\rm sh}}^{r} \frac{2\omega_i e^{2\omega_i \tau_{\rm adv}}}{v_0} T_{Rey}\,\mathrm{d}r, \quad (2.5)$$

where ω_i is the growth rate of the spiral mode, and $\tau_{\rm adv}$ is the advection time from the shock to the radius r considered.

3 Comparison with numerical simulations

We now compare these analytical predictions with the 3D numerical simulations of Fernández (2010). Figure 1 shows the radial profile of the surface integrated Reynolds stress and angular momentum density in the linear phase of their model R5_L11_HR dominated by a spiral mode with spherical harmonics $\{l, m\} = \{1, 1\}$. The analytically predicted shapes of the Reynolds stress and angular momentum profiles agree very well with the numerical simulations, while the magnitude match within 30% which is the expected accuracy given the numerical resolution. The Reynolds stress has the same sign as m, thus transporting angular momentum outward. On the other hand, the angular momentum density changes sign at an intermediate radius: angular momentum redistribution caused by the Reynolds stress creates a region of positive angular momentum below the shock, and a region of negative angular momentum above the PNS surface.

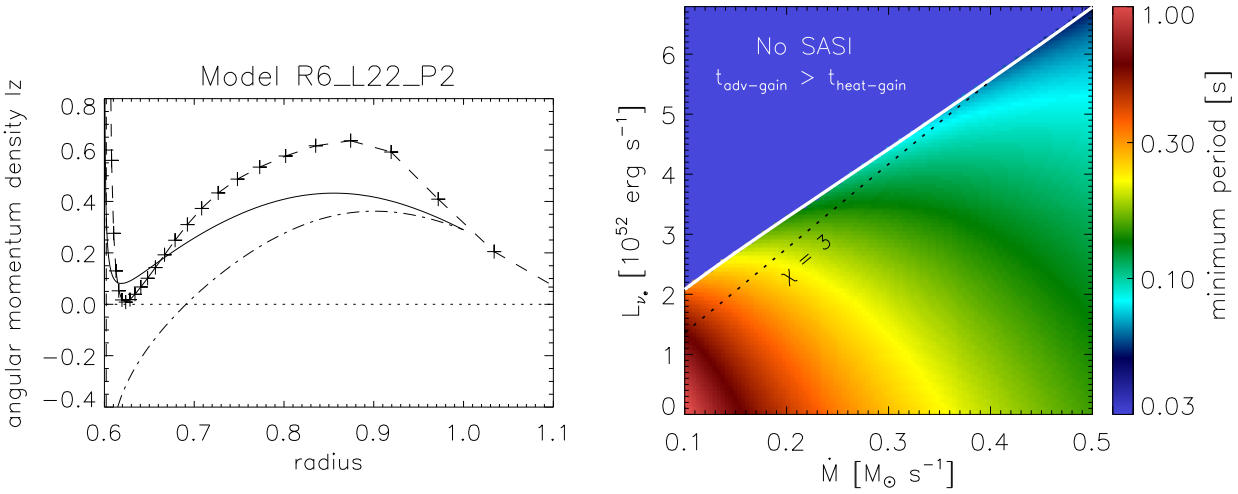

Fig. 2. Left: Time-averaged profile of surface integrated angular momentum density in the non-linear phase of model R6_L22_P2 dominated by an $\{l, m\} = \{2, 2\}$ spiral mode. Simulation results are shown with + signs and a dashed line, while the analytical prediction extrapolated to the saturated phase is shown with a full black line. For comparison, we also show the predicted angular momentum density in the case of a growing mode (from eq. 2.5, dot-dashed black line). **Right:** Minimum neutron star rotation period that can be generated via a spiral SASI mode, as inferred from equation (4.1). The input parameters (shock radius, shock compression ratio, SASI period, and postshock velocity) are computed from the steady-state solutions of Fernández (2012), which employ a realistic equation of state. The region marked 'No SASI' is such that the runaway condition in spherical symmetry (Janka & Keil 1998) is met, thus the SASI does not have time to develop before explosion. The dashed line shows the threshold $\chi = 3$, below which the SASI is expected to dominate the dynamics (Foglizzo et al. 2006). See Guilet & Fernández (2013) for details.

In the non-linear phase of SASI activity, our approximations are not valid anymore, in particular because the spiral mode stops growing. This can be approximately taken into account to extrapolate our results to the non-linear phase by setting the growth rate to zero, in which case Equation (2.5) becomes: $l_z = -\frac{T_{Rey}}{v_0}$. The left panel of Figure 2 shows that this prediction is in acceptable agreement with the time-averaged angular momentum profile of model R6_L22_P2 of Fernández (2010). In contrast to the linear phase, the angular momentum density is positive over most of the domain because matter with the opposite sign of angular momentum has had time to accrete onto the protoneutron star.

4 Approximate expression for the neutron star spin

When the explosion occurs, a net spin can be imparted to the forming neutron star if the matter below the shock with an angular momentum of a given sign is ejected while the matter with the opposite sign of angular momentum is accreted onto the protoneutron star (Blondin & Mezzacappa 2007). A simple approximate expression for the total angular momentum redistributed by a SASI spiral mode can be obtained by approximating the radial profile of angular momentum density by a flat profile. This analytical estimate is found to agree with the numerical simulations of Fernández (2010) within a few tens of percents. Assuming a moment of inertia of the neutron star of $I = I_{45} \times 10^{45}\,\mathrm{g.cm^2}$, we can then estimate the minimum period of uniform rotation of the neutron star in the optimistic scenario where all this angular momentum is ejected:

$$P \simeq 290\, I_{45} \left(\frac{10}{\kappa}\right) \left(\frac{P_{sasi}}{50\,\mathrm{ms}}\right) \left(\frac{120\,\mathrm{km}}{r_{\mathrm{sh}} - r_*}\right) \left(\frac{v_{\mathrm{sh}}}{3000\,\mathrm{km.s^{-1}}}\right) \left(\frac{0.3\,\mathrm{M_\odot.s^{-1}}}{\dot{M}}\right) \left(\frac{150\,\mathrm{km}}{r_{\mathrm{sh}}}\right)^2 \left(\frac{r_{\mathrm{sh}}}{3\Delta r}\right)^2 \mathrm{ms}. \quad (4.1)$$

where κ is the compression ratio of the shock, P_{sasi} the oscillation period of the SASI spiral mode, r_{sh} and r_* the radii of the shock and protoneutron star respectively, $\dot{M}$ the mass accretion rate, and Δr the amplitude of the shock deformation caused by the spiral mode. Note the dependence on the square of the amplitude and the shock radius.

The right panel of Figure 2 shows the result of evaluating equation (4.1) with parameters from the steady-state accretion shock models of Fernández (2012). The minimum period is computed as a function of the mass

accretion rate and electron neutrino luminosity, assuming a spiral mode amplitude $\Delta r = 0.3 r_{\rm sh}$. This figure shows that shorter periods are obtained with larger neutrino luminosities – which yield larger shock radii – and larger accretion rates. The normalization indicates that massive progenitors with large accretion rates, where strong SASI activity is expected (Müller et al. 2012; Hanke et al. 2013; Ott et al. 2013), can lead to periods $\sim$ 100 ms or less. In contrast, progenitors that have a lower accretion rate and which may be expected to suppress SASI activity (e.g., Müller et al. 2012; Takiwaki et al. 2012; Murphy et al. 2013; Dolence et al. 2013; Couch 2013), would otherwise acquire very moderate amounts of angular momentum if the SASI were present, with minimum periods in the range $0.3 - 1$ s. Note that the latter value is comparable to the spin periods obtained by Wongwathanarat et al. (2010, 2013).

From an observational point of view, the spin of neutron stars at birth is still poorly constrained. The difficulty comes from the fact that the observed period of pulsars is very different from their initial period because of spin down, and that the true age of most pulsars is unknown. Population synthesis studies nevertheless suggest that a distribution of initial spin peaking around 300 ms is consistent with observations (e.g., Faucher-Giguère & Kaspi 2006). The age of some pulsars can be estimated when they are associated with a supernova remnant, which then allows to constrain their initial spin period. Despite poor statistics and sometimes large uncertainties, these observations suggest that a significant fraction of neutron stars have initial periods longer than 100 ms (e.g. Popov & Turolla 2012 and references therein). The range of pulsar spin periods we obtain is therefore of the same order of magnitude as that inferred from the observations, and we conclude that angular momentum redistribution by a SASI spiral mode can be relevant to explain these observations.

5 Conclusions

We have developed an analytical description of the angular momentum redistribution driven by SASI spiral modes, which compares favorably with the results of the 3D numerical simulations of Fernández (2010). Angular momentum redistribution is due to the Reynolds stress of the SASI mode, which causes angular momentum with the same rotation direction as the spiral mode to accumulate below the shock, while angular momentum with the opposite sign is accreted onto the proto-neutron star.

We derived an approximate analytical expression for the maximum angular momentum that can be imparted to the neutron star if all the SASI active region is ejected during the explosion. The expected minimum neutron star spin periods in uniform rotation are comparable with values estimated by observations of pulsars associated with supernova remnants and by population synthesis studies for the bulk of the pulsar population. Our analysis further suggests that the angular momentum of the nascent neutron star should be positively correlated with the mass accretion rate at the time of explosion if progenitors are slowly rotating. As a consequence, neutron stars born from progenitors with a shallow density profile – for which the SASI should dominate the explosion dynamics (e.g., Müller et al. 2012; Hanke et al. 2013; Iwakami et al. 2013) – should rotate faster on average than those arising from stars with steeper profiles, which are generally less massive.

We emphasize that the analytical formula for the angular momentum redistributed by a spiral mode depends strongly on the amplitude of the spiral mode, which was taken as an input from the simulations. A semi-analytical description of the saturation of SASI as obtained by Guilet et al. (2010) could then be combined with our treatment to obtain a fully predictive analytical description of the angular momentum redistribution.

Note that the above prediction is contingent on a very optimistic scenario in which the mass cut at explosion coincides with the surface where the angular momentum changes sign. Prolonged SASI activity up to the point of explosion, as seen in the 2D models of Müller et al. (2012), is essential for this spin-up mechanism to work. Furthermore, our analysis applies if the initial rotation of the progenitor is negligibly slow. More generally, the initial spin of neutron stars is likely to result from a combination of angular momentum initially present in the progenitor and that redistributed by the SASI. Further studies using a rotating progenitor will be needed to clarify the consequences on the dynamics and on the spin of neutron stars.

Finally, we note that the present study neglects the effects of magnetic fields, which can transport angular momentum via the Maxwell stress. The influence of a magnetic field on the linear growth of SASI has been studied in a planar toy model by Guilet & Foglizzo (2010). One possible extension of the present study is including magnetic effects in the angular momentum redistribution in spherical or even cylindrical coordinates. Guilet et al. (2011) have shown that Alfvén waves can be amplified in the vicinity of an Alfvén surface, where the advection velocity equals the Alfvén speed. This phenomenon may also have interesting consequences on the angular momentum redistribution.

We thank Henrik Latter, Thierry Foglizzo and Benjamin Favier for helpful discussions. JG acknowledges support from the STFC and from the Max-Planck-Princeton Center for Plasma Physics. RF acknowledges support from the University of California Office of the President, and from NSF grants AST-0807444 and AST-1206097.

References

Blondin, J. M. & Mezzacappa, A. 2007, Nature, 445, 58
Blondin, J. M., Mezzacappa, A., & DeMarino, C. 2003, ApJ, 584, 971
Blondin, J. M. & Shaw, S. 2007, ApJ, 656, 366
Couch, S. M. 2013, ApJ, 775, 35
Dolence, J. C., Burrows, A., Murphy, J. W., & Nordhaus, J. 2013, ApJ, 765, 110
Faucher-Giguère, C.-A. & Kaspi, V. M. 2006, ApJ, 643, 332
Fernández, R. 2010, ApJ, 725, 1563
Fernández, R. 2012, ApJ, 749, 142
Foglizzo, T. 2009, ApJ, 694, 820
Foglizzo, T., Galletti, P., Scheck, L., & Janka, H.-T. 2007, ApJ, 654, 1006
Foglizzo, T., Masset, F., Guilet, J., & Durand, G. 2012, PRL, 108, 051103
Foglizzo, T., Scheck, L., & Janka, H.-T. 2006, ApJ, 652, 1436
Guilet, J. & Fernández, R. 2013, ArXiv e-prints
Guilet, J. & Foglizzo, T. 2010, ApJ, 711, 99
Guilet, J. & Foglizzo, T. 2012, MNRAS, 421, 546
Guilet, J., Foglizzo, T., & Fromang, S. 2011, ApJ, 729, 71
Guilet, J., Sato, J., & Foglizzo, T. 2010, ApJ, 713, 1350
Hanke, F., Müller, B., Wongwathanarat, A., Marek, A., & Janka, H.-T. 2013, ApJ, 770, 66
Iwakami, W., Nagakura, H., & Yamada, S. 2013, ApJ, submitted, arXiv:1308.0829
Janka, H.-T. 2012, Ann. Rev. Nuc. Part. Sci., 62, 407
Janka, H.-T. & Keil, W. 1998, in Supernovae and cosmology, ed. L. Labhardt, B. Binggeli, & R. Buser, 7
Müller, B., Janka, H.-T., & Heger, A. 2012, ArXiv e-prints
Murphy, J. W., Dolence, J. C., & Burrows, A. 2013, ApJ, 771, 52
Ohnishi, N., Kotake, K., & Yamada, S. 2006, ApJ, 641, 1018
Ott, C. D., Abdikamalov, E., Mösta, P., et al. 2013, ApJ, 768, 115
Popov, S. B. & Turolla, R. 2012, Ap&SS, 341, 457
Scheck, L., Janka, H.-T., Foglizzo, T., & Kifonidis, K. 2008, A&A, 477, 931
Takiwaki, T., Kotake, K., & Suwa, Y. 2012, ApJ, 749, 98
Wongwathanarat, A., Janka, H.-T., & Müller, E. 2010, ApJ, 725, L106
Wongwathanarat, A., Janka, H.-T., & Müller, E. 2013, A&A, 552, A126

SF2A 2013
L. Cambrésy, F. Martins, E. Nuss and A. Palacios (eds)

STUDY OF ULTRA-HIGH ENERGY COSMIC RAYS FROM THE RADIO SIGNAL AT THE PIERRE AUGER OBSERVATORY

Jennifer Maller[1] and for the Pierre Auger Collaboration[2]

Abstract. Deployed at the end of 2010 at the Pierre Auger Observatory, the first stage of the Auger Engineering Radio Array, AERA24, consists of 24 radio stations covering an area of 0.5 km^2. AERA measures the radio emission from cosmic-ray induced air showers. The amplitude of this radio emission is used to constrain the characteristics of the primary particle: arrival direction, energy and nature. These studies are possible thanks to an instrumentation development allowing self-triggered and externally-triggered measurements in the MHz domain and an improved understanding of radio emission processes. In May 2013, 100 new stations were installed to cover an area of $\simeq$ 6 km^2, for a total of 124 stations. This stage 2 will provide higher statistics and will enhance both the estimate of the nature of the primary cosmic ray and the energy resolution above 10^{17} eV as an addition to detectors such as the Auger fluorescence telescopes and particle detectors. We will present the main results obtained with the stage 1 of AERA and the current status of the experiment. We will end with a brief overview of the GHz-experiments installed at the Pierre Auger Observatory.

Keywords: AERA, radio detection, high energy cosmic rays, Pierre Auger Observatory

1 Introduction

One of the challenging questions related to cosmic rays concerns their nature. Improving our knowledge about the composition of cosmic rays allows us to constrain the models concerning their origins and their production mechanisms in the astrophysical sources. The electric field of radio emission induced by the shower is sensitive to the whole shower development and can be measured with a high duty cycle, and thus is a promising technique to identify observables sensitive to the nature of the primary cosmic ray.
In Europe two experiments have given the first modern results concerning the study of extensive air showers at low energy (because of their small area: less than 1 km^2): CODALEMA (D. Ardouin et al. 2005) in France and LOPES (H. Falcke et al. 2005) in Germany.
The **A**uger **E**ngineering **R**adio **A**rray installed at the Pierre Auger Observatory has recently been extended and covers, with its stage 2 installed since the beginning of May 2013, approximately 6 km^2 with 124 radio stations. AERA allows the study of the radio emission during the development of the shower in the MHz domain. In this frequency range, two mechanisms lead to a polarized coherent radio signal.
The first one, **the geomagnetic effect** is due to the action of the geomagnetic field on the charged particles of the shower and leads to the creation of a linearly polarized electric field along the vector $-\mathbf{v} \times \mathbf{B}$. This phenomenon was described by Kahn and Lerche in 1966 (F. D. Kahn & I. Lerche 1966) and has been confirmed by several experiments.
The second one, **the charge excess effect**, was predicted by Askaryan in 1962 (G. A. Askaryan 1962) and is due to the annihilation of positrons in the shower and to the Compton effect leading to a negative charge excess in the shower front. It leads to the creation of a signal which is radially polarized with respect to the shower axis.
The main objective of AERA is to characterize the primary cosmic ray: nature, energy and arrival direction. For this it is necessary to disentangle the mechanisms responsible for the radio emission occurring during the

[1] Subatech, Université de Nantes, École des Mines de Nantes, CNRS/IN2P3, Nantes, France
[2] Pierre Auger Observatory, Av. San Martín Norte 304, 5613 Malargüe, Argentina
(Full author list : http://www.auger.org/archive/authors_2013_06.html)

development of the shower. This can be done by analyzing the polarization of the measured electric field as presented in section 2.2. AERA will also permit one to test the performances of a large radio array compared to the other techniques.

2 AERA - 1^{st} stage

AERA is deployed in the low energy extension of the Pierre Auger Observatory in order to have a large statistics and high-quality super-hybrid measurements. It enables the comparison of radio observables with those obtained with the SD (regular and infill array) and the nine fluorescence telescopes close to AERA installed on both the HEAT and Coihueco sites. .
The stage 1 of AERA has operated at the observatory since 2010 and has taken taking data since 2011 with 24 stations spaced by 144 m and covering 0.5 km^2. Each station is equipped with:

- a **L**og **P**eriodic **D**ipole **A**ntenna measuring both EW and NS polarizations between 30 and 80 MHz,
- an electromagnetic compatibility box containing the electronics to prevent for the triggering of the station by itself,
- solar panels, batteries and GPS.

Thanks to this equipment AERA is completely autonomous in power supply and can also be used in a self-trigger mode for which the measured signal triggers the station if its level exceeds a predefined threshold. This defines the first level trigger T1. After a pulse-shape analysis performed directly at the station level, each station sends on average 500 level 2 triggers per second (T2). The corresponding timestamps are sent to the central data acquisition system. All T2s coming from all AERA stations are treated in real time to search for cosmic ray candidates studying the time difference between several pair of AERA stations event by event to check the compatibility of this event with the arrival of an air shower on the array. This is the level 3 trigger (T3).
AERA can also be externally triggered by the SD stations close to the array, and very soon by the fluorescence telescopes HEAT and Coihueco.

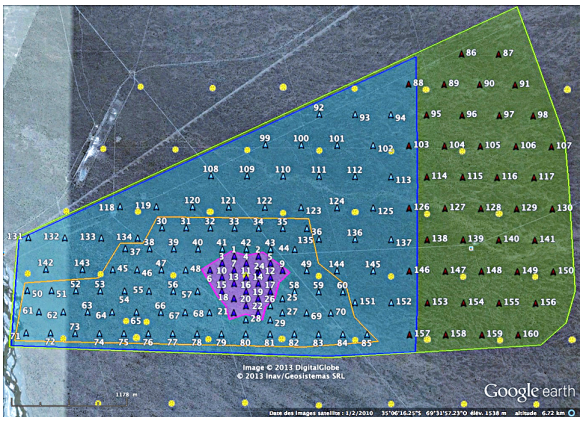

Fig. 1. AERA - In purple is shown the 1^{st} stage with 24 stations, in blue are shown the 100 new stations of the 2^{nd} stage installed since May 2013 and in green the last stations scheduled for 2014.

2.1 Proposed rejection algorithm

In the self-trigger mode the stations are mostly triggered by anthropic background and thunderstorms sending a huge number of T2s, occupying a large fraction of the bandwidth and saturating the disks. The background transients lower the detection efficiency of cosmic rays. To use this technique we must develop efficient rejection algorithms at level 1 or 2 of the trigger to increase the purity of the recorded signals.
We present here an example of such an algorithm which was developed for RAuger (B. Revenu for the Pierre Auger and CODALEMA Collaborations 2012), a prototype radio-detection experiment which was one of the pathfinders for AERA. The results of this prototype are described in (The Pierre Auger Collaboration,

S. Acounis, D. Charrier, T Garçon, C. Rivière, & P. Stassi 2012b). The study presented here was performed using the data of the upgraded version of RAuger which was composed of three autonomous radio stations located near the **C**entral **L**aser **F**acility at the center of the SD. These stations were equipped with Butterfly (D. Charrier for the CODALEMA Collaboration 2012) antennas developed for CODALEMA and are now equipping the stage 2 of AERA. The proposed selection algorithm has been established using two different data sets:

- air-shower events detected in coincidences between the RAuger stations and the SD stations close to the array,
- background events.

We study the time evolution of the filtered signal in a short time window containing the main pulse as illustrated in figure 2. In this time window and for each trace we sum up bin after bin the square of the amplitude of the signal to compute a normalized cumulative function. This cumulative function is defined as follows:

$$C(i) = \frac{\sum_{k=b_{start}}^{b_{start}+i} s_{EW}(k)^2}{\sum_{k=b_{start}}^{b_{end}} s_{EW}(k)^2}, \ with\ 0 \leqslant i \leqslant b_{end} - b_{start}. \tag{2.1}$$

We have observed that, in most cases, a background trace has a longer duration than a cosmic ray trace. We define the rise time of the signal as the time needed for the cumulative function to rise from 10% to 70%. We observe (figure 3), that the rise time for cosmic rays (red triangles) is significantly smaller than the rise time of the background transients (black diamonds). The values 10% and 70% and the frequency range for the filtering (30-60 MHz) have been optimized for this experiment.

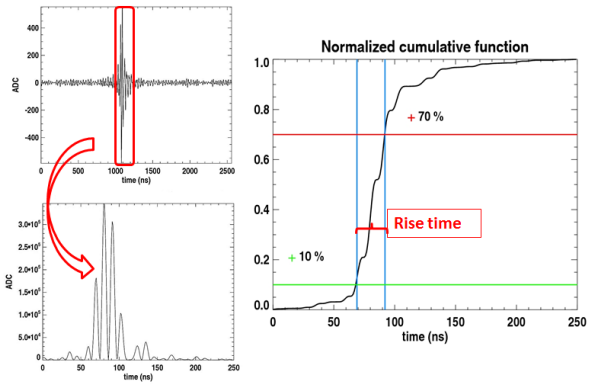

Fig. 2. Top-left: signal filtered in 30-60 MHz with the illustration of the used time window (in red) containing the main pulse; bottom-left: square of the filtered signal which is summed up bin after bin; right: cumulative function in black, the rise time (in red) is the time needed for the cumulative function to go from 10% (green line) to 70% (red line).

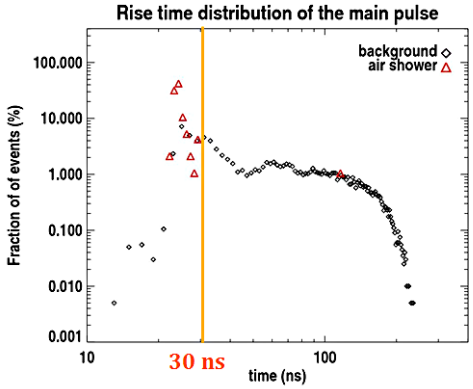

Fig. 3. Rise time distribution for two data sets: air shower events (red triangles) and background events (black diamonds). The upper limit cut on the rise time is set at 30 ns.

This rejection method has an efficiency of approximately 90% on the RAuger2 data (cut at 30 ns, orange line in figure 3). One cosmic ray trace is rejected by this method (isolated red triangle above 100 ns in figure 3). This signal is of very bad quality and is thus probably a random coincidence. The algorithm has been installed on CODALEMA since the beginning of 2013 with an efficiency of approximately 94% (D. Torres Machado for the CODALEMA Collaboration 2013) and is currently being tested on the AERA data.

2.2 Polarization studies

As discussed previously, the study of the polarization of the measured electric field allows a better understanding of the emission processes: several studies have confirmed the dominance of the geomagnetic effect (The Pierre Auger Collaboration et al. 2012b; D. Ardouin et al. 2012; M. Melissas for the Pierre Auger Collaboration

2012). These experiments have shown an excess of events coming from directions far from the direction of the geomagnetic field, which is a signature of the geomagnetic effect. When comparing the direction of the measured electric field with the expected direction due to this dominant mechanism ($-\mathbf{v} \times \mathbf{B}$) (K. Weidenhaupt for the Pierre Auger Collaboration 2012) as shown in figure 4, we observe some discrepancies which can indicate the presence of at least one other mechanism.

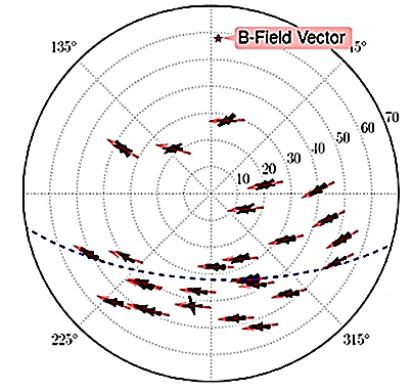

Fig. 4. Skymap showing the comparison between the direction of the measured electric field (in black) and the direction of $\mathbf{v} \times \mathbf{B}$ (in red). The geomagnetic filed is shown with the red star.

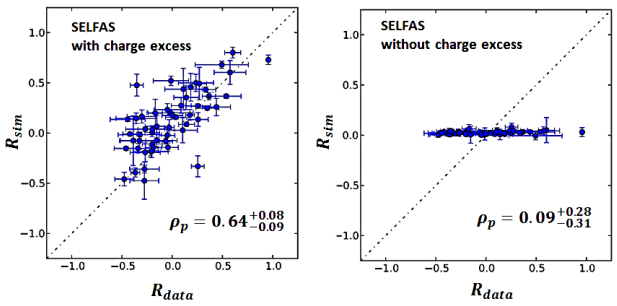

Fig. 5. Comparison between the R-parameter for data in abscissa with the R-parameter for two simulations: one performed with geomagnetic and charge excess effect (left) and another with only geomagnetic effect (right).

The charge excess effect contributes to the secondary mechanism with a radial polarization contrary to that of the geomagnetic effect. To study the charge excess contribution, we define an R-parameter:

$$R = \frac{\sum_{i=1}^{N} E_x(t_i) E_y(t_i)}{\sum_{i=1}^{N} (E_x(t_i)^2 + E_y(t_i)^2)} \tag{2.2}$$

where the x axis (EW polarization) is aligned with the direction of $\mathbf{v} \times \mathbf{B}$ projected in the horizontal plane and the y axis (NS polarization) is perpendicular to x. By construction, $R = 0$ in the case of a pure geomagnetic emission. Thus, R measures the deviation from this effect.
We compare the R-parameter values obtained from the data to the values obtained using simulated data. For each event two simulations are performed: one includes only geomagnetic mechanism and the other one includes both mechanisms. The results presented in figure 5 have been obtained using the simulation code SELFAS2 (V. Marin & B Revenu 2012) but the same results hold with other simulation codes (T. Huege for the Pierre Auger Collaboration 2013) such as CoREAS (T. Huege et al. 2013) , REAS3.1 (M. Ludwig & T. Huege 2011) , EVA1.01 (K. Werner et al. 2012) , ZHAires (J. Alvarez Muñiz et al. 2012) and MGMR (K. D. de Vries et al. 2012). The correlation is studied with the Pearson coefficient. We observe a much higher correlation level when both mechanisms are used in the simulation as shown in the left-figure. The phenomenon is thus much better described when we add a radial component in the polarization of the electric field, which is the main characteristic of the charge excess effect.

2.3 Energy estimation

The radio signal strength is strongly correlated to the primary cosmic ray characteristics, among them its energy. The results reported by RAuger (The Pierre Auger Collaboration et al. 2012b), CODALEMA (O. Ravel for the CODALEMA Collaboration 2012), LOPES (A. Horneffer for the LOPES Collaboration 2007) assume a radially symmetric lateral distribution function (LDF) as proposed in the past (H. R. Allan 1971), and show a linear dependence between the electric field strength and the primary energy. Preliminary results obtained by AERA (C. Glaser for Pierre Auger Collaboration 2013) are in good agreement with these observations. We now need more statistics which will be provided very soon by the stage 2 of the experiment. However, it has become clear (B Revenu 2013; A. Corstanje et al. 2011) that a 1D exponential LDF is not suited to the radio signal. More complicated 2D LDFs should be used for these analyses.

3 AERA - stage 2

The stage 2 of the experiment has been deployed at the observatory since May 2013 with 100 new stations covering 6 km^2 (blue part in figure 1), with two different grid sizes: 250 m for the stations included in the inner contour line and 375 m for the others. These new stations are equipped with Butterfly antennas (The Pierre Auger Collaboration et al. 2012a) which will provide a better sensitivity. Stage 2 will increase both the estimate of the nature and the energy resolution of the primary cosmic ray by the use of additional detectors. The final stage of AERA, scheduled for 2014, will be composed of 160 stations covering 12 km^2 (green part of the map shown in figure 1).

4 Conclusion

The study of high energy cosmic rays through the radio emission induced by air showers is a promising technique to identify observables sensitive to their characteristics and in particular to their nature, thanks to a high duty cycle and a sensitivity to the whole shower development.
The geomagnetic effect has been confirmed as the dominant mechanism and polarization studies together with simulations have highlighted the contribution of a radially polarized signal with respect to the transverse plane of the shower. This contribution could be interpreted as the charge excess effect.
The stage 1 of AERA has been taking data since 2011 with 24 radio stations running in self-trigger and external-trigger modes. The measurement of high energy cosmic rays by AERA and the additional detectors of the low energy extension could help study in detail the transition from a galactic to an extragalactic origin of cosmic rays thanks to the analysis of super-hybrid coincidences.
AERA has been extended in May 2013 with 100 new stations. With this stage 2, AERA now covers 6 km^2, which will significantly increase the statistics of UHECR recorded radio signals.

References

A. Corstanje, M. d. Akker, L. Bähren, H. Falcke, & W. Frieswijk et al. 2011, (2011) arXiv:1109.5805.
A. Horneffer for the LOPES Collaboration. 2007, Proc. of 30th ICRC (2007) Merida, Mexico
B Revenu. 2013, AIP Conf. Proc., 1535, 56
B. Revenu for the Pierre Auger and CODALEMA Collaborations. 2012, Nucl. Instrum. Meth. A 662 (2012) S130
C. Glaser for Pierre Auger Collaboration. 2013, AIP Conf. Proc., 1535, 68
D. Ardouin et al. 2005, Nucl. Instrum. Meth. A 555 (2005) 148
D. Ardouin et al. 2012
D. Charrier for the CODALEMA Collaboration. 2012, Nucl. Instrum. Meth. A, 662, S142
D. Torres Machado for the CODALEMA Collaboration. 2013, Proc 33rd ICRC (2013) Rio de Janeiro, Brasil
F. D. Kahn & I. Lerche. 1966, Proc. Roy. Soc. A 289 (1966) 206.
G. A. Askaryan. 1962, Soviet Phys. JETP 14 (1962) 441
H. Falcke et al. 2005, Nature 435 (2005) 313
H. R. Allan. 1971, Progress in Elementary Particle and Cosmic-Ray Physics 10 (1971) 169, North Holland
J. Alvarez Muñiz, W. R Carvalho Jr., & E. Zas. 2012, Astropart. Phys. 35 (2012) 325.
K. D. de Vries, van den Berg, A., O. Scholten, & K. Werner. 2012, Astropart. Phys. 34 (2010) 267.
K. Weidenhaupt for the Pierre Auger Collaboration. 2012, Proc. Vulcano Workshop (2012) Vulcano, Italy
K. Werner, de Vries, K., & O. Scholten. 2012, Astropart. Phys. 37 (2012) 5.
M. Ludwig & T. Huege. 2011, Astropart. Phys. 34 (2011) 438
M. Melissas for the Pierre Auger Collaboration. 2012, AIP Conf. Proc. 1535 (2013) 63
O. Ravel for the CODALEMA Collaboration. 2012, Nucl. Instrum. Meth. A 662 (2012) S89
T. Huege, M. Ludwig, & C. W. James. 2013, AIP Conf. Proc. 1535 (2013) 128.
T. Huege for the Pierre Auger Collaboration. 2013, Proc 33rd ICRC (2013) Rio de Janeiro, Brasil,
The Pierre Auger Collaboration, D. Charrier, L. Denis, et al. 2012a, JINST, 7, P10011
The Pierre Auger Collaboration, S. Acounis, D. Charrier, et al. 2012b, JINST, 7, P11023
V. Marin & B Revenu. 2012, Astropart. Phys., 35, 733

SF2A 2013
L. Cambrésy, F. Martins, E. Nuss and A. Palacios (eds)

CIRCUMSTELLAR BUBBLE CREATED BY TWO MASSIVE STARS

Z. Meliani[1], A. J. van Marle[2] and A. Marcowith[3]

Abstract. The massive stars are formed in clusters then numerical models of wind-blown bubble should evolve bubble created by several stars. Aims. We develop a two-dimensional (2D) model of the circumstellar bubble created by two massive stars, a 40 M_{odot} star and a 25 M_{odot} star, and follow its evolution with MPI-AMRVAC hydrodynamics code until the end of the stellar evolution and he supernova explosion of each star. The stars are separated by approximately 16 pc and surrounded by a cold medium with a density of 20 particles per cm3. The simulations showed that the evolution of a wind-blown bubble created by two stars deviates from that of the bubbles around single stars. In particular, once one of the stars has exploded, the bubble is too large for the wind of the remaining star to maintain and the outer shell starts to disintegrate. The lack of thermal pressure inside the bubble also changes the behavior of circumstellar features close to the remaining star. The supernovae are contained inside the bubble, which reflects part of the energy back into the circumstellar medium.

Keywords: hydrodynamics, circumstellar matter, stars, winds, outflows, supernovae remnants, bubbles

1 Introduction

The winds of massive stars create large-scale (10 pc) bubbles around their progenitors. Weaver et al. (1977) did the analytical study of these bubbles. The time-dependent nature of stellar winds were incorporate in numerical model by (Garca-Segura et al. 1996b), (van Marle et al. 2005), (Dwarkadas 2007) and (Toalá & Arthur 2011). However, these models only considered the evolution of a bubble blown by a single star. However, since massive stars are typically formed in star clusters, it is unlikely that any single star could form a bubble on a scale of tens of parsecs, without encountering other massive stars. The expanding bubble should instead collide with other, similar bubbles and merge as in the case of WN8-WN9h (Mauerhan et al. 2010). A good example of the resulting bubble can be found in the Rosetta nebula around cluster NGC 2244 (Li & Smith 2005).

Because of the numerical problems associated with modeling the bubbles of multiple stars, attempts to account for the influence of multiple stars on the evolution of the bubble have been limited to the details of the colliding winds of binary stars (e.g. Folini & Walder (2000); Pittard & Parkin (2010); van Marle et al. (2011)), or dealt with only part of the stellar evolution.

In this proceeding, we present the result of a two-dimensional (2D) numerical simulation that models the evolution of a bubble, blown by the winds of two massive stars by following all evolution phases of the stars.

2 Setup

We use the MPI-AMRVAC hydrodynamics code (Meliani et al. 2012; Keppens et al. 2012), which solves the conservation equations for mass, momentum, and energy on an adaptive mesh grid. The effect of radiative cooling is included (van Marle & Keppens 2011), using a cooling curve for solar-metallicity gas generated with the CLOUDY code. We set a minimum temperature of 100 K throughout the simulation, which limits the amount of compression due to radiative cooling, preventing numerical problems. Here we neglect the effect of photoionization, which would increase the gas temperature within the Strmgren radius to about 10000 K.

[1] LUTh, Observatoire de Paris, 5 place Jules Janssen, 92195 Meudon, France
[2] Institute of Astronomy, KU Leuven, Celestijnenlaan 200D, 3001 Heverlee, Belgium
[3] Laboratoire Univers et Particules (LUPM) Universit Montpellier, CNRS/IN2P3, CC72, place Eugne Bataillon, 34095 Montpellier Cedex 5, France

We set up our simulation as a 2D cylindrically symmetric grid in the r,z-plane. The grid has a basic resolution of 120 240 gridpoints over 100 200 pc. The adaptive mesh has four layers, allowing for an effective resolution of 960 1920 gridpoints. At the start of the simulation, this grid is filled with gas with a constant density of $10^{-22.5}$ g cm^{-3} and solar metallicity. The stars are defined as small spheres (R = 1.5 pc), placed 16.2 pc apart that are filled, at the beginning of each timestep, with material according to the wind parameters given in Table 1. The duration of the evolutionary phases and the mass-loss rates are based on the parameters for a 25 M_{odot} star and a 40 M_{odot} star used by (van Marle et al. 2005), respectively. Wind velocities reflect those typically found in observations ((Lamers & Cassinelli 1999), and references therein). For the 40 M_{odot} star, the mass-loss rate in the final phase (the Wolf-Rayet phase) has been reduced to reflect the values obtained by (Vink & de Koter 2005).

When a star reaches the end of its evolution, we fill a sphere (R = 0.75 pc) with a constant density and thermal energy according to the supernova values given in Table 1. The masses reflect the final masses of the stars as well the as values calculated by, e.g., Eldridge & Tout (2004). For simplicity, we use a supernova energy of 10^{51} erg, which is typical of core-collapse supernovae (e.g. (van Marle et al. 2010), and references therein).

Table 1. Wind and supernova parameters.

Phase	t_{end} [Myr]	$\dot{m}$ [$M_\odot$ yr^{-1}]	v_w[km s^{-1}]	M [$M_\odot$]	E (10^{47} [erg])
40 $M_\odot$					
MS	4.3	1.0×10^{-6}	2000	4.3	1710
RSG	4.5	5.0×10^{-5}	15	10	0.224
WR	4.77	1.0×10^{-5}	2000	3.0	1190
SN					10 000
hline 25 $M_\odot$					
MS	6.5	2.0×10^{-7}	1500	1.3	170
RSG	7	1.0×10^{-5}	15	5.0	0.112
SN					10 000

3 Result

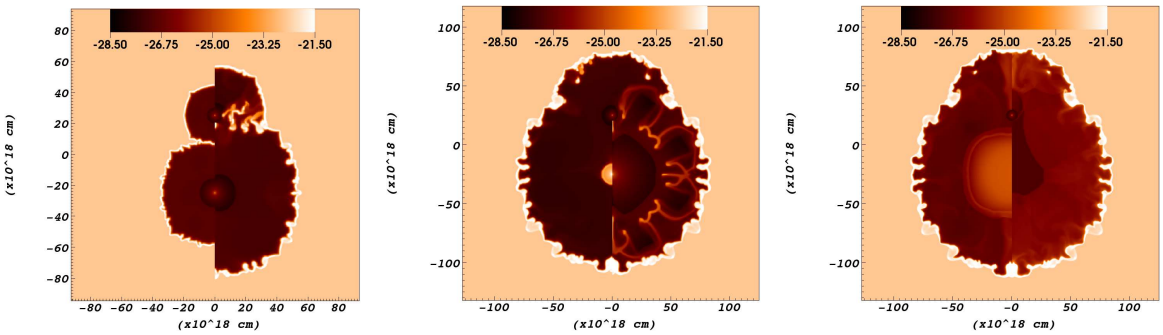

Fig. 1. Logarithm of the density of the circumstellar medium in g/cm3 after 1.17 and 2.35 Myr (left panel), after 4.42 and 4.58 Myr (center panel), and after 4.774 and 4.783 Myr (right panel). On the left, the shells of the two bubbles encounter each other (left panel, left side) and are destroyed in the process. The remnants are pushed toward the lightest of the stars (left panel, right side). On the right, the 40 M star (at Y = 2.5 2019 cm) goes through the RSG phase, which forms a thin shell at the wind termination shock (center panel, left side) and then the WR phase. The WR wind sweeps up the RSG wind and the RSG shell is destroyed in the collision. The debris of the collision moves outward into the hot shocked gas (central panel, right side). Finally, the 40 M star explodes as a supernova, which expands into the circumstellar bubble (right panel, left). Once it has hit the outer shell, the supernova bounces back and starts flowing inward (right panel, right).

Each star initially creates its own circumstellar bubble. These bubbles follow the pattern predicted by Weaver et al. (1977): the wind expands freely until it hits the termination shock. The kinetic energy of the wind is then turned into thermal energy creating a volume filled with very hot (T 107 108 K) shocked wind material. The high thermal pressure of the shocked wind material causes it to expand, sweeping up a shell of shocked ISM, which moves outward. Eventually, the swept-up shells of the two bubbles encounter each other

and both are fractured during the collision (left panel of Fig. 2). The remnants are pushed into the bubble with the lowest thermal pressure (resulting from the weakest wind, and therefore, typically, the lightest star). Once the shells have been fractured, the two bubbles merge, creating a single, aspherical bubble in which the thermal pressure is equalized as the shocked gas of the two stellar winds mixes. The thin outer shell is unstable and shows both linear thin-shell (Vishniac 1983) and Rayleigh-Taylor instabilities.

The 40 M star, which has the shortest lifespan, leaves the main sequence and goes through the RSG and WR phases (central panel of Fig. 2). The RSG wind forms a thin shell at the termination shock, which is destroyed by the WR wind. Finally, the star explodes as a supernova. At this time, the bubble is still quite aspherical, despite the outer shell being driven by the thermal pressure in the shocked wind. It has a maximum length (along the axis connecting the stars) of 57 pc. At the position of the 40 M star, it is 52 pc wide, whereas at the position of the 25 M star the width is only 39 pc. The shape of the outer shell still indicates that it is the merger of two spherical bubbles.

The supernova quickly expands into the low density bubble that has been created by the stellar winds, but stops when it reaches the contact discontinuity separating the shocked wind from the shocked ISM (right panel of Fig. 2). The injection of energy from the supernova (approximately three times the total energy injected so far by the stellar winds) causes the bubble to expand more rapidly (left panel of Fig. 3). Because the supernova has injected a lot of energy, but (relatively) little mass, the density inside the bubble decreases quickly during the expansion and the Rayleigh-Taylor instabilities in the outer shell grow quickly. The bubble is left with only one source of energy, the wind from the 25 M star, which is insufficient to maintain the expansion of the bubble. As a result, the thermal pressure inside the wind bubble decreases leading to a loss of compression at the outer shell, which starts to expand because of its own internal pressure (left panel of Fig. 3). During this phase, the asymmetrical shape of the bubble starts to disappear as the isotropic pressure in the shocked wind bubble pushes the shell outward equally in all directions.

Eventually, the 25 M star reaches the RSG phase, which further reduces the energy being added to the bubble. A thin shell forms at the wind termination shock (central panel of Fig. 3). This initially happens close to the star because of the low ram pressure of the slow RSG wind. However, owing to the relatively low pressure in the bubble, this shell can move farther away from the star than would have been possible if the 25 M star had been alone (R 6.5 pc, rather than R 4.8 pc when comparing the right side of the center panel of Fig. 3 with Fig. 1).

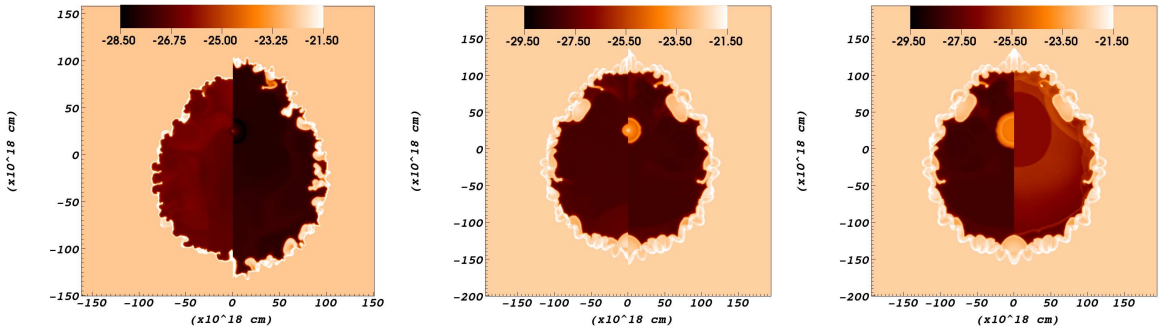

Fig. 2. Logarithm of the density of the circumstellar medium in g/cm3 after 4.86 and 5.60 Myr (left panel), after 6.58 and 7.0 Myr (center panel), and after 7.01 and 7.07 Myr (right panel). On the left, the mass, ejected by the first supernova has spread throughout the bubble, which, due to the injection of energy, expands rapidly. The density inside the bubble decreases and the Rayleigh-Taylor instabilities in the outer shell become more pronounced. In the central panel, the 25 M star has reached the RSG phase and forms a shell at the wind termination shock that moves away from the star as the thermal pressure in the bubble decreases over time. Finally, on the right, the 25 M star explodes as a supernova, which sweeps up the RSG shell and fills the bubble.

Finally, the 25 M star reaches the end of its evolution and explodes (right panel of Fig. 3), sweeping up the surrounding RSG wind as well as the RSG shell. The bubble has lost most of its asymmetry; it has a length of 105 pc and a maximum width of 104 pc. The outer edge of the shell has an almost spherical shape. As in the case of the first star, the supernova quickly expands into the low density shocked wind bubble until it reaches the outer shell, then falls back inward. From this moment on, the bubble has no energy source. While energy continues to be lost from the bubble by thermal conduction, turbulent mixing, and radiative cooling, the outer shell starts to push inward owing to is own internal pressure, which is considerable because of its relatively high

density. Assuming a typical speed for gas in the shell of 1...2 km s-1 (the sound speed for gas at a 102103 K), the gas in the outer shell would take a minimum of 2.5 × 107 years to reach the center, though in practice it would take longer owing to the continuing resistance of the hot bubble.

4 Conclusions

The presence of multiple stars inside the circumstellar bubble influences the evolution of the bubble in several ways.

The most obvious is in terms of the outer shape of the bubble, which is strongly aspherical during the early phase of its evolution. This effect is clearly visible until after the supernova explosion of the first star. In addition, remnants of the collision between the two outer shells of the individual bubbles remain visible within the shocked wind bubble until after the supernova explosion of the 40 M star.

The collapse of the outer shell, which is caused by a decrease in the internal pressure of the bubble, is unique to the multi-star scenario. It can only occur when the bubble persists for an extended period of time (105 106 yr) with a significantly diminished energy source (the wind of the remaining star). The effective result is that the outer shell resembles the single-star shell of the star with a stronger wind. As long as the 40 M star exists, the shell looks like a shell created by a single 40 M star. Afterwards, it starts to resemble the circumstellar shell of a 25 M star as it becomes relatively thick. However, it is far more instable as a result of the instabilities created in the initial evolution. This lack of internal pressure also affects the medium close to the 25 M star: the RSG shell can move further away from its progenitor than would have been the case for a single-star bubble.

The supernovae are contained by the outer shell and do not break out of the bubble. This is surprising, considering the amount of energy in the supernova. However, the mass of the outer shell is very high. A bubble with R = 30 pc and an ambient medium density of $10^{-22.5}$ g cm-3 has a 5.3 104 M outer shell that forms a very effective barrier against a supernova, which is high in energy, but low in mass.

We neglected the effect of photoionization, which would give the gas a minimum temperature of about 10000 K during the main sequence and WR phases. During these phases, the shells would become thicker owing to their higher thermal pressure. This increase in pressure within the outer shell would also hasten its expansion after the first supernova.

We conclude that simulating the bubbles around more than one star improves our understanding of the evolution of the circumstellar bubbles of massive stars. Self-evident truisms, self-fulfilling prophecies and the like.

Z.M. acknowledges support from PNHE and ELGA. A.J.v.M. acknowledges support from FWO, grant G.0277.08, K.U. Leuven GOA/2008/04 and GOA/2009/09. We thank Dr. Wang Ye at the Department of Physics & Astronomy, University of Kentucky, for providing us with the radiative cooling curve.

References

Dwarkadas, V. V. 2007, ApJ, 667, 226

Folini, D., & Walder, R. 2000, Ap&SS, 274, 189

Garca-Segura, G., Mac Low, M.-M., & Langer, N. 1996b, A&A, 305, 229

Li, J. Z., & Smith, M. D. 2005, ApJ, 620, 816

Lamers, H. J. G. L. M., & Cassinelli, J. P. 1999, Introduction to Stellar Winds (Cambridge, UK: Cambridge University Press)

Keppens, R., Meliani, Z., van Marle, A. J., et al. 2012, J. Comput. Phys., 231, 718

Mauerhan, J. C., Wachter, S., Morris, P. W., Van Dyk, S. D., & Hoard, D. W. 2010, ApJ, 724, L78

Meliani, Z., Keppens, R., Casse, F.,& Giannios, D.;, 2007, MNRAS, 376, 1189

Toal, J. A., & Arthur, S. J. 2011, ApJ, 737, 100

Pittard, J. M., & Parkin, E. R. 2010, MNRAS, 403, 1657

van Marle, A. J., Langer, N., & Garca-Segura, G. 2005, A&A, 444, 837

van Marle, A. J., Smith, N., Owocki, S. P., & van Veelen, B. 2010, MNRAS, 407, 2305

van Marle, A. J., & Keppens, R. 2011, Computers & Fluids, 42, 44

van Marle, A. J., Keppens, R., & Meliani, Z. 2011, A&A, 527, A3

Vink, J. S., & de Koter, A. 2005, A&A, 442, 587

Vishniac, E. T. 1983, ApJ, 274, 152

Weaver, R., McCray, R., Castor, J., Shapiro, P., & Moore, R. 1977, ApJ, 218, 377

SF2A 2013
L. Cambrésy, F. Martins, E. Nuss and A. Palacios (eds)

DUST IN THE WIND I: SPECTROPOLARIMETRIC SIGNATURES FROM DISK-BORN OUTFLOWS

F. Marin*[1] and R. W. Goosmann[1]

Abstract. In this first research note of a series of two, we conduct optical/UV investigations of the spectropolarimetric signatures emerging from the structure of quasars (Elvis 2000) applied to a purely theoretical, dusty model. We aim to explore the similarities/differences between an absorbing, disk-born outflow and the usual dusty torus that is supposed to hide the internal regions of active galactic nuclei (AGN). Using radiative transfer Monte Carlo simulations, we compute the continuum polarization signatures emerging from the model setup of Elvis (2000). We find that a dust-filled outflow produces very low amount of wavelength-depend polarization degrees, associated with a photon polarization angle perpendicular to the projected symmetry axis of the model. The polarization percentages are ten times lower than what can be produced by a toroidal model, with a maximal polarization degree found for intermediate viewing angle (i.e. when the observer's line-of-sight crosses the outflowing material). The structure for quasars unsuccessfully blocks the radiation from the central irradiating source and shows a spectropolarimetric behavior that cannot be conciliated with observations. Either a new set of morphological parameters or different optical thickness must be considered.

Keywords: Galaxies: active - Galaxies: Seyfert - Polarization - Radiative transfer - Scattering

1 Introduction

According to the unified model of radio-quiet AGN (Antonucci 1993), most of the observational differences between Seyfert-like galaxies can be attributed to an orientation effect. The broad line features, spectroscopically detected in type-1 (pole-on) AGN, disappear in type-2 (edge-on) spectra as the emission region (the Broad Line Region, BLR) is hidden behind an optically thick, circumnuclear medium (Antonucci & Miller 1985; Pier & Krolik 1992). This hypothetical region, responsible for the anisotropic radiation pattern of quasi-stellar objects (QSO), was recently confirmed by Jaffe et al. (2004) and Wittkowski et al. (2004). Using mid-infrared interferometric measurements, they spatially resolved the direct emission coming from a torus-like structure in the hearth of NGC 1068. A simple toroidal configuration was first postulated to achieve obscuration of the central AGN region (Krolik & Begelman 1986, 1988), but such a model suffers from several hydrodynamic issues that cannot sustain parsec-scale cohesion. More complex models using clumps or filamentary structures are actually considered to replace this basic torus model (Nenkova et al. 2008b,a, 2010; Schartmann et al. 2008; Hönig & Kishimoto 2010; Heymann & Siebenmorgen 2012).

In its structure for quasars, Elvis (2000) tried, among many other goals, to overcome the need for an obscuring torus around the equatorial plane of the central engine. To do so, he supposed that the obscuring medium is not static but results in an outflow, originating close to the supermassive black hole (SMBH) and its accretion disk that powers the AGN. Such a wind is expected to arise from a narrow range of radii on the accretion disk and is driven by internal radiation pressure. In Elvis (2000), the outflow is essentially composed of ionized gas, but the presence of dust originating close to the accretion disk remains theoretically possible. According to Czerny & Hryniewicz (2012), dust can be formed in accretion disk atmospheres, rises similarly to the electronic disk-born wind, but is soon evaporated by the central irradiation source (Elvis 2012).

* frederic.marin@astro.unistra.fr

[1] Observatoire Astronomique de Strasbourg, Université de Strasbourg, CNRS, UMR 7550, 11 rue de l'Université, 67000 Strasbourg, France

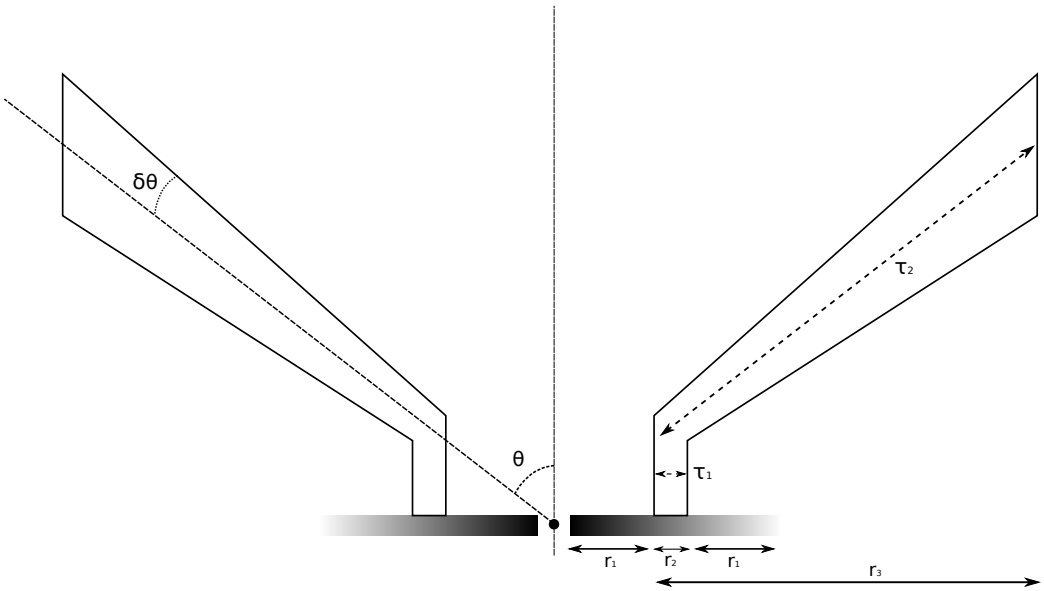

Fig. 1. Schematic view of the structure proposed by Elvis (2000) and implemented in STOKES. The outflow arises vertically from the accreting disk and is bent outward by radiation pressure along an inclination of 60° relative to the symmetry axis of the model. The half-opening angle of the wind is equal to 3°. The radial optical depths of the wind base and of the outflowing material are set to τ_1 and τ_2 respectively.

In this research note, the first of a series of two, we aim to investigate such a purely theoretical hypothesis. We replaced the ionized matter that is supposed to arise from the accretion disk by a dust mixture, and ran STOKES simulations (Goosmann & Gaskell 2007; Marin et al. 2012b). We produce polarization spectra that we compare to the usual torus configuration used for circumnuclear obscuration.

2 Model setup

To explore the polarization signatures of dust in the structure for quasars proposed by Elvis (2000), we use the radiative transfer Monte Carlo code STOKES to compute the polarization emerging from a continuous medium, whose geometry is summarized in Fig. 1. The continuum source is defined as an isotropic, disk-like region emitting a unpolarized spectrum with a power-law spectral energy distribution $F_* \propto \nu^{-\alpha}$ and $\alpha = 1$. From the disk, the wind arises vertically at a distance r_1 from the model origin. The outflowing column has a width set to r_2. Due to radiation pressure, the wind is bent by an angle θ relative to the symmetry axis of the model, with a half-opening angle $\delta\theta$, and extends up to r_3. According to Elvis (2000), we parametrize our model using $r_1 = 0.0032$ pc (10^{16} cm), $r_2 = 0.00032$ pc, $r_3 = 0.032$ pc, $\theta = 60°$ and $\delta\theta = 3°$.

The outflow is filled with a typical "Milky Way" dust mixture (Wolf & Henning 1999), already used in previous AGN simulations (Goosmann & Gaskell 2007; Marin et al. 2012b,a; Marin & Goosmann 2012). We opted for an optically thick model, with $\tau_1 \sim 36$ and $\tau_2 \sim 3600$, in order to approximate the obscurring impact of a regular dusty torus. This purely theoretical model is not necessarily physical as such a dense absorbing medium may not form or survive so close to the accretion disk.

3 Spectropolarimetric results

The spectropolarimetric signatures of the dusty outflows are presented in Fig. 2. The fraction F/F_* of the central flux is wavelength-independent for all viewing angles, but the normalization of F/F_* in polar and equatorial inclinations is different. At $i = 9°$, most of the flux comes from the unobscured central source. However, photons reprocessing on the dust funnel are mostly absorbed due to 1) the Mie scattering phase function, promoting forward and backward scattering, and 2) the albedo of the absorbing dust. Across the outflowing gas ($i = 61°$)

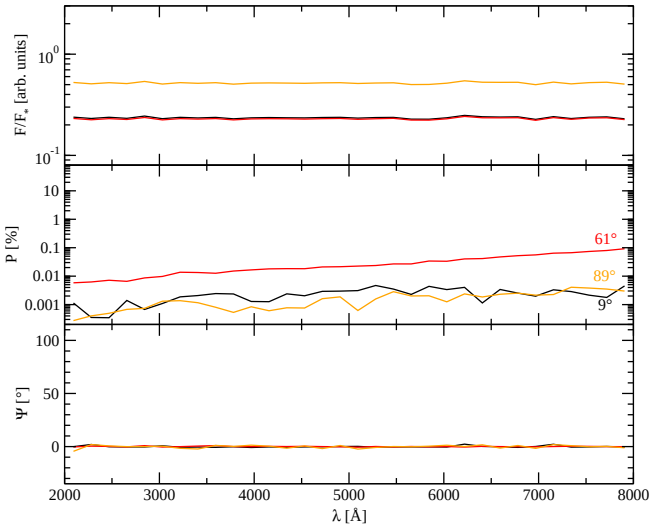

Fig. 2. Modeling a dust-filled structure for quasars outflow using a uniform model such as in Fig. 1, seen at different viewing inclinations, i (black : 9° – red : 61° – orange : 89°). *Top*: the fraction, F/F_* of the central flux; *middle*: polarization, P; *bottom*: polarization angle, ψ.

absorption is most efficient and F/F_* small. Along the equatorial plane ($i = 89°$), F/F_* is found to be higher than expected from toroidal circumnuclear, dusty regions (Goosmann & Gaskell 2007; Marin & Goosmann 2011; Marin et al. 2012b). The low optical depth of the wind column, associated with forward scattering dominated reprocessing, tend to increase the escape probability, resulting in a larger flux detected at edge-on inclinations.

The combination of an extended, disk-like radiating source and a small optical depth in the poloidal direction of the outflow increases the escape probability and is responsible for relatively high polarization degree at lines-of-sight passing through the dust medium ($P < 0.1$ % for $i = 61°$). Due to dilution by the extended emitting source and absorption by the dusty wind, the degree of polarization at polar ($i \sim 9°$) and equatorial ($i \sim 89°$) angles is lower ($P < 0.01$ %). We also observe that the percentage of polarization is no longer wavelength-independent and rises towards the red part of the spectrum. It is a consequence of the Mie scattering phase function that becomes less anisotropic at longer wavelengths, allowing a larger fraction of photons to escape, contributing to the increase of P.

As expected from previous studies (Goosmann & Gaskell 2007; Marin et al. 2012b), the dust-induced polarization position angle is equal to 0° at all inclinations, indicating an orientation of the electric field vector perpendicular to the wind axis..

4 Discussion

One of the goals of Elvis (2000) was to get rid of the usual, dusty torus model by introducing disk-born outflows. It is then interesting to compare the theoretical model presented in this research note to a uniform, dusty torus scenario (Kartje 1995; Wolf & Henning 1999; Young 2000; Watanabe et al. 2003; Goosmann & Gaskell 2007; Marin et al. 2012b). Spectropolarimetric modeling of circumnuclear obscuration by optically thick material showed that P is expected to rise with inclination, until the observer's line-of-sight crosses the torus horizon ($P < 20$ %), and then decreases down to zero at type-2 viewing angles. Moreover, the fraction F/F_* of the central flux should decrease with increasing inclination. The situation is quite different with a dusty outflow. Even if the polarization degree behavior is approximatively reproduced with the expected perpendicular polarization angle, P never exceeds 0.1 %. F/F_* does not behave as for a dusty torus and strong fluxes are detected along the equator, which is in contradiction with observations (Antonucci & Miller 1985).

It is also instructive to examine the difference between the structure for quasars with a flow of warm, highly ionized matter (WHIM) to its dusty counterpart (Elvis 2000 and Marin & Goosmann, 2013, in press). The WHIM spectra show wavelength-independent behaviors, either in F/F_*, P or ψ. In this case, the equatorial viewing angle is found to produce a maximal polarization degree ($P \sim 0.3$ %) associated with a parallel photon

position angle (i.e equals to 90°). The intermediate WHIM inclination has a similar P degree to our modeling, but both the wavelength dependence of P and the ψ angle can distinguish one model from the other.

5 Summary and conclusions

Using Elvis (2000)'s prescriptions to characterize a disk-born outflow, we modeled the optical/UV, continuum polarization emerging from an academic realization of the model where the WHIM was replaced by dust. The resulting photon flux is wavelength-independent and stronger for equatorial viewing angles. The polarization degree spectra show wavelength-dependent signatures, increasing in the red tail, with a minimum P for polar inclinations and a maximum P along the outflowing direction. The overall polarization angle ψ is perpendicular (i.e equal to 0°) with respected to the projected symmetry axis of the model.

We thus find that a dusty, disk-born outflow shows strong differences in terms of spectropolarimetric signatures, with respect to either a regular, dusty torus or a WHIM scenario. Such a conclusion strengthens our previous spectropolarimetric exploration of the structure for quasars (Marin & Goosmann, 2013, in press). A possible way to by-pass this problem is to consider another set of morphological parameters, where the wind has a different bending angle and/or a different collimation angle.

A second research note, focusing on the imaging capabilities of STOKES applied to this model will be presented. In the future, we also aim to push further our investigations by looking at different wavebands and computing the emission and absorption lines in different velocity fields.

References

Antonucci, R. 1993, ARA&A, 31, 473

Antonucci, R. R. J. & Miller, J. S. 1985, ApJ, 297, 621

Czerny, B. & Hryniewicz, K. 2012, Journal of Physics Conference Series, 372, 012013

Elvis, M. 2000, ApJ, 545, 63

Elvis, M. 2012, in Astronomical Society of the Pacific Conference Series, Vol. 460, AGN Winds in Charleston, ed. G. Chartas, F. Hamann, & K. M. Leighly, 186

Goosmann, R. W. & Gaskell, C. M. 2007, A&A, 465, 129

Heymann, F. & Siebenmorgen, R. 2012, ApJ, 751, 27

Hönig, S. F. & Kishimoto, M. 2010, A&A, 523, A27

Jaffe, W., Meisenheimer, K., Röttgering, H. J. A., et al. 2004, Nature, 429, 47

Kartje, J. F. 1995, ApJ, 452, 565

Krolik, J. H. & Begelman, M. C. 1986, ApJ, 308, L55

Krolik, J. H. & Begelman, M. C. 1988, ApJ, 329, 702

Marin, F., Goosmann, R., & Dovčiak, M. 2012a, Journal of Physics Conference Series, 372, 012065

Marin, F. & Goosmann, R. W. 2011, in SF2A-2011: Proceedings of the Annual meeting of the French Society of Astronomy and Astrophysics, ed. G. Alecian, K. Belkacem, R. Samadi, & D. Valls-Gabaud, 597–600

Marin, F. & Goosmann, R. W. 2012, in SF2A-2012: Proceedings of the Annual meeting of the French Society of Astronomy and Astrophysics, ed. S. Boissier, P. de Laverny, N. Nardetto, R. Samadi, D. Valls-Gabaud, & H. Wozniak, 587–590

Marin, F., Goosmann, R. W., Gaskell, C. M., Porquet, D., & Dovčiak, M. 2012b, A&A, 548, A121

Nenkova, M., Sirocky, M. M., Nikutta, R., Ž. Ivezić, & Elitzur, M. 2008a, ApJ, 685, 160

Nenkova, M., Sirocky, M. M., Nikutta, R., Ž. Ivezić, & Elitzur, M. 2010, ApJ, 723, 1827

Nenkova, M., Sirocky, M. M., Ž. Ivezić, & Elitzur, M. 2008b, ApJ, 685, 147

Pier, E. A. & Krolik, J. H. 1992, ApJ, 399, L23

Schartmann, M., Meisenheimer, K., Camenzind, M., et al. 2008, A&A, 482, 67

Watanabe, M., Nagata, T., Sato, S., Nakaya, H., & Hough, J. H. 2003, ApJ, 591, 714

Wittkowski, M., Kervella, P., Arsenault, R., et al. 2004, A&A, 418, L39

Wolf, S. & Henning, T. 1999, A&A, 341, 675

Young, S. 2000, MNRAS, 312, 567

SF2A 2013
L. Cambrésy, F. Martins, E. Nuss and A. Palacios (eds)

DUST IN THE WIND II: POLARIZATION IMAGING FROM DISK-BORN OUTFLOWS

F. Marin*[1] and R. W. Goosmann[1]

Abstract. In this second research note of a series of two, we aim to map the polarized flux emerging from a disk-born, dusty outflow as it was prescribed by Elvis (2000). His structure for quasars was achieved to unify the emission and absorption features observed in active galactic nuclei (AGN) and can be used as an alternative scenario to the typical dusty torus that is extensively used to account for AGN circumnuclear obscuration. Using Monte Carlo radiative transfer simulations, we model an obscuring outflow arising from an emitting accretion disk and examine the resulting polarization degree, polarization angle and polarized flux. Polarization cartography reveals that a disk-born outflow has a similar torus morphology in polar viewing angles, with bright polarized fluxes reprocessed onto the wind funnel. At intermediate and edge-on inclinations, the model is rather close to a double-conical wind, with higher fluxes in the cone bases. It indicates that the optically thick outflow is not efficient enough to avoid radiation escaping from the central region, particularly due to the geometrically thin divergence angle of the outflow. As parametrized in this research note, a dusty outflow does not seem to be able to correctly reproduce the polarimetric behavior of an usual dusty torus. Further refinement of the model is necessary.

Keywords: Galaxies: active - Galaxies: Seyfert - Polarization - Radiative transfer - Scattering

1 Introduction

The anisotropic obscuration of the central region of AGN and quasars is well explained by the unified scheme (Antonucci 1993; Urry & Padovani 1995). In this scenario, the fueling engine of AGN (a supermassive black hole SMBH and its surrounding, reprocessing accretion disk) is hidden along the equatorial plane by a circumnuclear medium situated at a few parsecs from the SMBH (Krolik & Begelman 1986, 1988). Illuminated by the continuum source, the obscuring material is expected to re-emit in the infrared domain, as the UV-heated dust particles re-emit at lower wavelengths. Such hypotheses were strongly supported by early photometric infrared observations of Seyfert-like galaxies (Low & Kleinmann 1968; Kleinmann & Low 1970b,a), and an indubitable confirmation was found by Jaffe et al. (2004) and Wittkowski et al. (2004). They observed the dusty heart of NGC 1068 using mid-infrared interferometry and resolved the outer morphology of the obscuring region. The resulting morphology is close to a toroidal configuration; a geometry usually adopted in many AGN simulations (Kartje 1995; Wolf & Henning 1999; Young 2000; Watanabe et al. 2003; Goosmann & Gaskell 2007; Marin et al. 2012b). However, the actual morphology of the circumnuclear gas surrounding the AGN equator is highly debated. While simple, torus-like models give a sufficient approximation for radiative transfer simulations, more complex structures are actually investigated (see Elitzur & Shlosman 2006 for a review).

This research note focuses on the peculiar model given by Elvis (2000, 2012), where the dusty torus is pictured as an optically thick, equatorial outflow originating close to the supermassive black hole. While the presence of dust grains at a hundred of gravitational radii seems uncommon, Czerny & Hryniewicz (2012) proved that dust can be formed in accretion disk atmospheres. The dust mixture is protected by an internal, shielding outflow composed of a flow of warm, highly ionized matter (WHIM) and can rise from the disk atmosphere, before being evaporated at high altitudes. It results in a dust outflow that propagates mainly along the equatorial plane, an

* frederic.marin@astro.unistra.fr

[1] Observatoire Astronomique de Strasbourg, Université de Strasbourg, CNRS, UMR 7550, 11 rue de l'Université, 67000 Strasbourg, France

interesting configuration to explain the edge-on obscuration of AGN (Antonucci & Miller 1985; Pier & Krolik 1992).

Using an academic model inspired by our previous analyses (Marin & Goosmann, accepted) of the model proposed by Elvis (2000), we aim to produce polarization maps of a dusty outflow in order to compare it with observations. This research note is the second in a series of two, both included in this volume. Polarization spectra were investigated in the first issue (Marin & Goosmann, submitted).

2 Model setup

The empirically-derived structure for quasars presented by Elvis (2000) stipulates that a flow of matter arises from a narrow range of radii on the accretion disk. The material is bent and accelerated outward by internal radiation pressure, with an angle $\theta = 60°$ and a divergence angle $\delta\theta = 3°$. This angular parametrization is given by the ratio of narrow absorption line (NAL) to absorption-free AGN (Reynolds 1997; Crenshaw et al. 1999), while the morphological parameters (distance to the ionizing source r_1, width of the column flow r_2) are derived from constraints of the broad emission line (BEL) region (Peterson 1997). To follow the prescription of Elvis (2000) and our previous investigation (Marin & Goosmann, submitted), we set r_1 to 0.0032 pc (10^{16} cm) and r_2 to 0.00032 pc (10^{15} cm). The wind extends up to $r_3 = 0.032$ pc (10^{17} cm). The dust mixture, filling our model, is taken from Wolf & Henning (1999). We opted for an optically thick outflow, with optical depths $\tau_2 \sim 3600$ along the wind and $\tau_1 \sim 36$ along the equator. The model is summarized in Marin & Goosmann (submitted, Fig. 1).

We use the radiative transfer Monte Carlo code STOKES (Goosmann & Gaskell 2007), upgraded with a polarization imaging technic (Marin et al. 2012b,a) to compute the net polarization emerging from the model. The unpolarized, input spectrum comes from an isotropic, disk-like emitting region and has a power-law spectral energy distribution $F_* \propto \nu^{-\alpha}$ and $\alpha = 1$.

3 Wavelength-integrated polarization m

In Fig. 1, we present the simulated polarization cartography of the dusty model by Elvis (2000). The maps simultaneously show the polarized flux, PF_ν, the polarization percentage P, and the polarization position angle, ψ. The angle ψ is represented by black bars drawn in the center of each spatial bin and the length of the vector is proportional to P. A vertical bar indicates a polarization of $\psi = 90°$, a bar leaning to the right denotes $90° > \psi > 0°$ and a horizontal bar stands for $\psi = 0°$. For each pixel, the Stokes parameters are integrated over the full 2000 – 8000 Å range.

At a polar viewing angle (Fig. 1, top-left), the funnel of the outflow is illuminated by the central source, and multiple forward and backward scattering events are responsible for the high polarized flux detected in the vicinity of the emitting region. The illumination decreases with distance from the source and nearly no polarized flux is detected at the most extended parts of the outflows. The spectropolarimetric pattern is similar to the polarization maps produced for an isolated dusty torus (Marin et al. 2012b) and appears not to be distinguishable by polarization imaging.

In the intermediate inclination case (Fig. 1, top-right), the flux mainly comes from backscattering events on the lower part of the model, where photons escaping from the geometrically thin outflow ($\delta\theta = 3°$) are reprocessed. Due to the important optical depth along the wind flow, all of the polarized flux is absorbed at the wind base. The overall shape of the model is that of a double-cone, with a maximum polarized flux detected in the wind bases. However, the flux gradient, as seen from previous modeling of hourglass-shaped outflows (Marin et al. 2012b), is absent due to the hollow geometry of the model.

Finally, along the equatorial viewing angle (Fig. 1, bottom), the outflow is nearly invisible as it absorbs most of the incident photon flux. However, a large fraction of radiation can escape by transmission through the equatorial medium and collaborate to rise the polarization degree detected in type-2 viewing angles. A few photons are detected on the northern part of the map, due to rare backscattering events on the top-end of the upper wind, since the inclination of the model is not exactly 90°.

4 Discussion

Polarization mapping is a unique tool to visualize the morphological differences between different reprocessing media. In the context of the model for quasars presented by Elvis (2000), it appears that the polarization

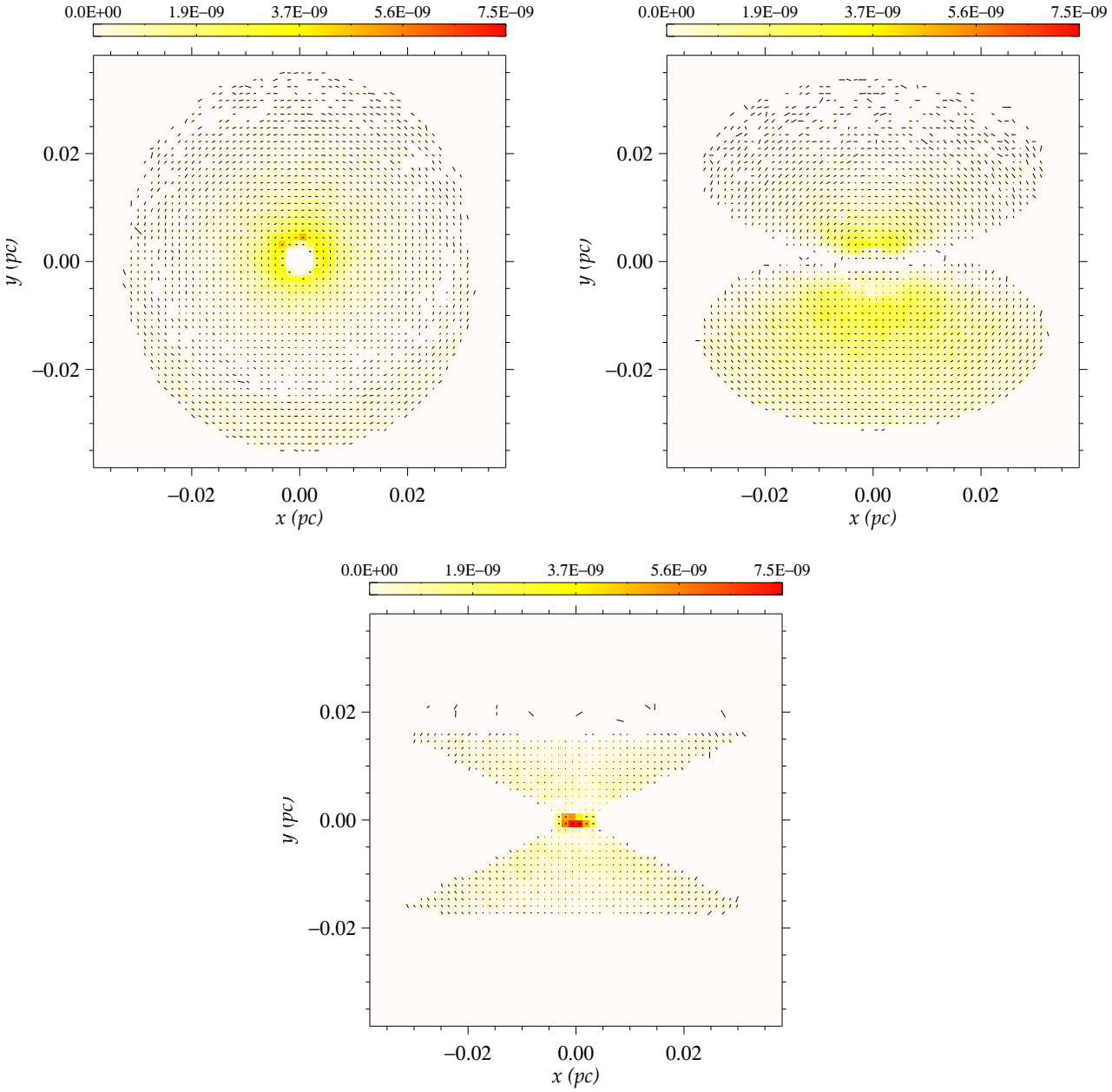

Fig. 1. Modeling the polarized flux, PF_ν, induced by complex reprocessing in the structure for quasar (Elvis 2000). PF_ν is color-coded and integrated over the 2000 – 8000 Å band. *Top-left*: face-on image; *Top-right*: image at $i \sim 60°$; *Bottom*: edge-on image.

signatures show a wide panel of geometries, revealing the outermost part of the structures. In comparison with a usual, dusty torus (Marin et al. 2012b), type-1 views are rather similar between a torus and a disk-born wind. The funnel of the model is highly irradiated, while the extended parts of the regions are less impacted by the input radiation. Looking at an intermediate viewing angle, a dusty wind becomes more similar to a double-cone geometry in terms of flux repartition. The small width of the outflow allows radiation to escape from the inner regions and the polarized flux is stronger than in type-1 inclinations. The main difference between a torus and a disk-born wind is seen at equatorial, type-2 viewing angles. The central part of the map shows the brightest flux, associated with intermediate degrees of polarization. The rest of the model is nearly invisible due to absorption.

If we think that a dusty outflow fits in with the observed presence of dusty NLR clouds at larger distances

from the irradiation source, then it is hard to reconcile the resulting polarization maps with the observations of IC 5063 (Morganti et al. 2007). This southern Seyfert-2 galaxy shows an ionized structure extending out to 15 kpc in a remarkable, X-shaped morphology (Morganti et al. 2003). In Marin & Goosmann (2013, in press), we found that a bi-phased outflow well reproduce both the polarization degrees and the geometrical X shape. Here, we complementary demonstrate that a wind uniquely filled with dust grains cannot reproduce the flux morphology of IC 5063 as the hollow outflows mostly absorb the inner radiation.

5 Summary and conclusions

As a complementary work to the spectrophotometric modeling of a dusty outflow (Marin & Goosmann, submitted), based on morphological constraints presented in Elvis (2000), we modeled the optical/UV polarization maps of a theoretical, dusty model. We found that the resulting maps present various geometries, depending on the observer's viewing angle. While for a polar inclination, a dusty disk-born outflow can be mistaken for a regular, obscuring torus, intermediate and edge-on views show rather different results. New observational campaigns, using polarimetric imagers would greatly help to disentangle between a hydrostatic torus and a dynamic outflow, but our present conclusions show that a pure dusty outflow hardly reproduces the observational data. As suggested in Marin & Goosmann (2013, in press), refining the bending and divergence angles of the flow could lead to better simulations. The academic model presented here should not be taken as an actual model to replace a toroidal region, but as a step toward an upgrade of the model by Elvis (2000).

Future work, focusing on broadband polarimetric signature, velocity fields and absorption/emission features will be conducted to push forward the conclusions drawn in Marin & Goosmann (2013, in press).

References

Antonucci, R. 1993, ARA&A, 31, 473

Antonucci, R. R. J. & Miller, J. S. 1985, ApJ, 297, 621

Crenshaw, D. M., Kraemer, S. B., Boggess, A., et al. 1999, ApJ, 516, 750

Czerny, B. & Hryniewicz, K. 2012, Journal of Physics Conference Series, 372, 012013

Elitzur, M. & Shlosman, I. 2006, ApJ, 648, L101

Elvis, M. 2000, ApJ, 545, 63

Elvis, M. 2012, in Astronomical Society of the Pacific Conference Series, Vol. 460, AGN Winds in Charleston, ed. G. Chartas, F. Hamann, & K. M. Leighly, 186

Goosmann, R. W. & Gaskell, C. M. 2007, A&A, 465, 129

Jaffe, W., Meisenheimer, K., Röttgering, H. J. A., et al. 2004, Nature, 429, 47

Kartje, J. F. 1995, ApJ, 452, 565

Kleinmann, D. E. & Low, F. J. 1970a, ApJ, 161, L203

Kleinmann, D. E. & Low, F. J. 1970b, ApJ, 159, L165

Krolik, J. H. & Begelman, M. C. 1986, ApJ, 308, L55

Krolik, J. H. & Begelman, M. C. 1988, ApJ, 329, 702

Low, J. & Kleinmann, D. E. 1968, AJ, 73, 868

Marin, F., Goosmann, R., & Dovčiak, M. 2012a, Journal of Physics Conference Series, 372, 012065

Marin, F., Goosmann, R. W., Gaskell, C. M., Porquet, D., & Dovčiak, M. 2012b, A&A, 548, A121

Morganti, R., Holt, J., Saripalli, L., Oosterloo, T. A., & Tadhunter, C. N. 2007, A&A, 476, 735

Morganti, R., Oosterloo, T., Holt, J., Tadhunter, C., & van der Hulst, J. M. 2003, The Messenger, 113, 67

Peterson, B. M. 1997, An Introduction to Active Galactic Nuclei

Pier, E. A. & Krolik, J. H. 1992, ApJ, 399, L23

Reynolds, C. S. 1997, MNRAS, 286, 513

Urry, C. M. & Padovani, P. 1995, PASP, 107, 803

Watanabe, M., Nagata, T., Sato, S., Nakaya, H., & Hough, J. H. 2003, ApJ, 591, 714

Wittkowski, M., Kervella, P., Arsenault, R., et al. 2004, A&A, 418, L39

Wolf, S. & Henning, T. 1999, A&A, 341, 675

Young, S. 2000, MNRAS, 312, 567

SF2A 2013
L. Cambrésy, F. Martins, E. Nuss and A. Palacios (eds)

e-mail: manuela.vecchi@cern.ch

RECENT RESULTS FROM THE AMS-02 EXPERIMENT IN SPACE

M. Vecchi[1] and the AMS-02 Collaboration

Abstract. The AMS-02 detector is a large acceptance magnetic spectrometer operating onboard the International Space Station since May 2011. The main goals of the detector are the search for antimatter and dark matter in space, and the measurement of cosmic rays composition and flux. The first publication of the AMS-02 Collaboration is a precision measurement of the positron fraction in primary cosmic rays in the energy range from 0.5 to 350 GeV, based on more than 6 million positron and electron detected events. AMS data confirm that the positron fraction is steadily raising from 10 to 250 GeV but, from 20 to 250 GeV, the slope decreases by an order of magnitude. Moreover, no anisotropy is observed on the positron fraction. In the present document, an overview of the AMS-02 detector will be given, the detection techniques of electrons and positrons in cosmic rays will be discussed, and the measurement of the positron fraction will be described.

Keywords: astroparticle, cosmic rays, positron fraction, AMS-02

1 Introduction

The Alpha Magnetic Spectrometer is a general purpose particle physics detector, operating in space since May 2011. It will achieve a unique long duration mission of about 20 years, aiming at performing antimatter and dark matter searches, as well as cosmic ray composition and fluxes measurements. The AMS detector is composed of several sub-detectors, as it can be seen in figure 1-left. The experiment is installed onboard the International Space Station (ISS), that follows a Low Earth Orbit at about 400 km altitude with respect to the Earth surface, well located to detect cosmic particles before they interact with the outer layers of the atmosphere. This makes the ISS one the most interesting environment to perform cosmic rays studies. AMS being a space-born detector, the data acquisition parameters change as a function of the detector position with respect to Earth, as it is shown in figure 1-right: the average trigger rate is 700 Hz, however several kHz are detected at the Poles and in the South Atlantic Anomaly, due to different geomagnetic cutoff values.

2 Measurement of the positron fraction with AMS-02

Electrons and positrons represent only a tiny fraction of the cosmic radiation reaching the Earth's atmosphere, however the understanding of their origin and production mechanisms is one of the hottest topics in astroparticle physics, especially because these particles are sensitive observables in the context of the indirect search for dark matter annihilation in our Galaxy. Due to their low mass, electrons and positrons experience severe energy losses during their propagation, so that their observation horizon is limited to few hundreds of pc: for this reason the study of these particles can let us explore the sources of cosmic rays in our Galaxy.
The first publication of the AMS-02 Collaboration is a precision measurement of the positron fraction, i.e. the ratio between the positron flux and the all-electron flux (electrons and positrons). The positron fraction is expected to be a decreasing function of energy, if positrons are only secondary particles, produced in the primary cosmic rays interactions with the interstellar medium. However, previous measurements [Adriani (2009)] [Ackermann (2009)] showed that above 10 GeV the positron fraction is not consistent with expectations from pure secondary origin, implying that a nearby source of positrons could be *hidden* in our Galaxy. The results reported in this proceedings are based on the data collected during the first 18 months of operation,

[1] National Central University, No.300, Jhongda Rd., Jhongli City, Taoyuan County 32001, Taiwan (R.O.C.)

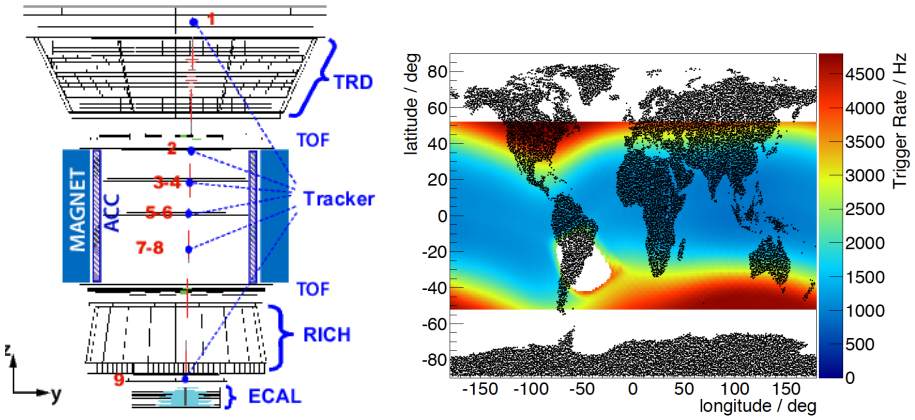

Fig. 1. Left: A 369 GeV positron event as measured by the AMS detector on the ISS, in the (y-z) plane. Tracker planes 1-9 measure the particle charge and momentum [Delgado (2013)]. The Transition Radiation Detector (TRD) [Gast (2013)] identifies the particle as an electron/positron. The Time of Flight (TOF) [Quadrani (2013)] measures the charge and ensures that the particle is downward-going. The Ring Imaging CHerenkov detector (RICH) [Giovacchini (2013)] measures the charge and velocity. The Electromagnetic Calorimeter (ECAL) [Adloff (2013)] independently identifies the particle as an electron/positron and measures its energy. A permanent magnet provides a magnetic field of about 0.15 T. **Right**: Trigger rate as a function of orbital position. Variations are correlated with the geomagnetic cutoff rigidity.

corresponding to about 8% of the total expected AMS data sample, presented in [Aguilar (2013)].

The key of success for the detection of electrons and positrons relies on three factors: the detector high acceptance and the long duration of the AMS mission, the excellent energy resolution of the calorimeter [Adloff (2013)], parametrized as $\sigma(E)/E = \frac{10.4\pm0.2\%}{\sqrt{E[GeV]}} \oplus (1.4\pm0.1)\%$, and a very good background rejection. The main sources of background for this search come from lepton-hadron misidentification (protons identified as positrons) and from the charge confusion (electrons identified as positrons). This latter has two different sources. The first come from the finite resolution of the tracker and multiple scattering, and it is reduced by applying the requirement on the energy-momentum match as well as on the tracker track quality parameter. The second source of charge confusion is related to the production of secondary particles along the track of the primary electron (positron) in the tracker and it is reduced by requiring, for a given particle, a geometric match between the tracker track and the electromagnetic shower in the calorimeter. Both sources of charge confusion are found to be well reproduced in the Monte Carlo simulation. As an example, in the 82-100 GeV bin, the uncertainty on the number of positrons due to charge confusion is 1 %.

The main challenge for this kind of measurement comes from the fact that the data sample is dominated by the background, protons, that is $10^{3\div4}$ more abundant than signal (positrons). Three sub-detectors are used for signal identification and background rejection, namely the tracker, the transition radiation detector (TRD) and the electromagnetic calorimeter (ECAL). For the positron fraction measurement, the tracker is used to identify the sign of the charge, together with the absolute charge.

The TRD can distinguish between electrons (positrons) and protons by detecting the transition radiation, and independently identify nuclei by measuring dE/dx. Signals from 20 layers are combined in a TRD estimator formed from the log-likelihood probability of the electron (positron) hypothesis to the proton hypothesis. Using the TRD a rejection factor of $10^{3\div4}$ at 90% signal efficiency is achieved, as shown in figure 2a.

The electromagnetic calorimeter is an imaging detector, made of 98 lead foils and 50000 scintillating fibers, corresponding to 17 radiation lengths. The 3-dimensional capabilities of the detector are obtained by stacking alternate superlayers with fibers parallel to the x and y axis. An ECAL estimator, based on the a Bosted Decision Tree algorithm, has been developed to identify electrons (positrons) and to reject protons. The background rejection power of the ECAL estimator, when combined to the energy/momentum matching requirement, reaches about 10^4, as shown in figure 2b. A proton rejection of 10^6 can be reached by combining the three independent detectors.

Signal events are identified by requiring a track in the TRD and in the tracker, a shower in the ECAL and a measured velocity in the TOF $\beta \simeq 1$, consistent with a down-going particle of charge one. In order to reject secondary electrons and positrons produced in the interaction of primary cosmic rays with the Earth atmosphere,

the energy measured with the ECAL is required to exceed by a factor of 1.2 the maximal Stoermer cutoff for either a positive or a negative particle at the geomagnetic location where the particle was detected.
The selection efficiency for electrons and positrons is about 90% in the acceptance of the ECAL: after the selection is applied, the remaining sample is composed of about 7 million primary electrons and positrons, and 700000 protons. The positron fraction is measured as a function of the ECAL energy, the binning being chosen according to the ECAL energy resolution. The number of signal events versus energy is determined using the TRD estimator as well as the energy-momentum matching. For every energy bin, the 2-dimensional reference spectrum for signal and background are fitted to data. The fit is performed separately to positive and negative momenta, providing the number of positrons and electrons respectively.

2.1 Results

The measured positron fraction is shown in figure 2-right, as a function of the energy measured by the ECAL. AMS data confirm the results from previous experiments [Adriani (2009)] [Ackermann (2009)], with high precision: below 10 GeV the positron fraction decreases with increasing energy, as expected if electrons and positrons are produced in the interaction of primary cosmic rays with the interstellar medium. From 10 to 250 GeV the

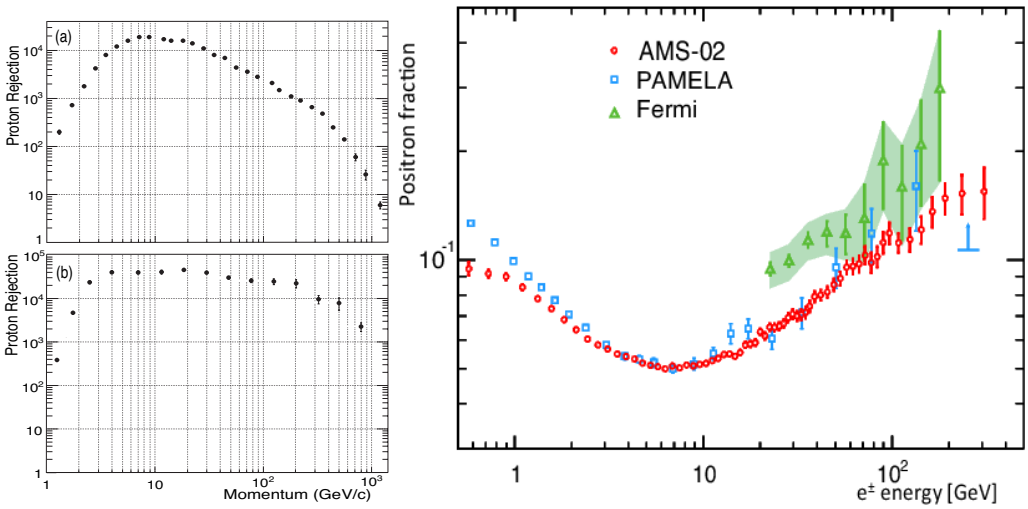

Fig. 2. Left: (a) the proton rejection measured by the TRD as a function of the tracker momentum, at 90% selection efficiency for e±. (b) the proton rejection measured by ECAL and the tracker, for 90% efficiency on the signal. **Right**: The positron fraction from AMS-02 [Aguilar (2013)], compared to the results of PAMELA[Adriani (2009)] and Fermi[Ackermann (2009)].

positron fraction is steadily increasing, in contrast with the pure secondary origin of positrons. AMS data are in good agreement with PAMELA data above 10 GeV, where the effects of the Solar Modulation start to be negligible. The slope of the positron fraction versus energy decreases by an order of magnitude from 20 to 250 GeV and no fine structure is observed.

2.2 Model for the interpretation of AMS data

To fit AMS data, the e^+ and e^- fluxes, Φ_{e^+} and Φ_{e^-}, have been parametrized as the sum of individual diffuse power law spectra and the contribution of a single common source of $e^{\pm}$:

$$\Phi_{e^+} = C_{e^+} E^{-\gamma_{e^+}} + C_s E^{-\gamma_s} e^{-E/E_s}; \tag{2.1}$$

$$\Phi_{e^-} = C_{e^-} E^{-\gamma_{e^-}} + C_s E^{-\gamma_s} e^{-E/E_s}, \tag{2.2}$$

(with E in GeV) where the coefficients C_{e^+} and C_{e^-} correspond to relative weights of diffuse spectra for positrons and electrons, and C_s to the weight of the source spectrum; γ_{e^+}, γ_{e^-} and γ_s are the corresponding spectral indexes; and E_s is a characteristic cutoff energy for the source spectrum. With this parametrization the positron fraction depends on 5 parameters. A fit to the data in the energy range 1 to 350 GeV based

on the number of events in each bin yields a $\chi^2/d.f. = 28.5/57$ and $\gamma_{e^-} - \gamma_{e^+} = -0.63 \pm 0.03$, *i.e.*, the diffuse positron spectrum is softer, that is, less energetic with increasing energy, than the diffuse electron spectrum; $\gamma_{e^-} - \gamma_s = 0.66 \pm 0.05$, *i.e.*, the source spectrum is harder than the diffuse electron spectrum; $C_{e^+}/C_{e^-} = 0.091 \pm 0.001$, *i.e.*, the weight of the diffuse positron flux amounts to ∼10 % of that of the diffuse electron flux; $C_s/C_{e^-} = 0.0078 \pm 0.0012$, *i.e.*, the weight of the common source constitutes only ∼1 % of that of the diffuse electron flux; $1/E_s = 0.0013 \pm 0.0007\,\mathrm{GeV}^{-1}$, corresponding to a source cutoff energy of $760^{+1,000}_{-280}$ GeV. The fit is shown in Figure 3 as a solid curve. The agreement between the data and the model

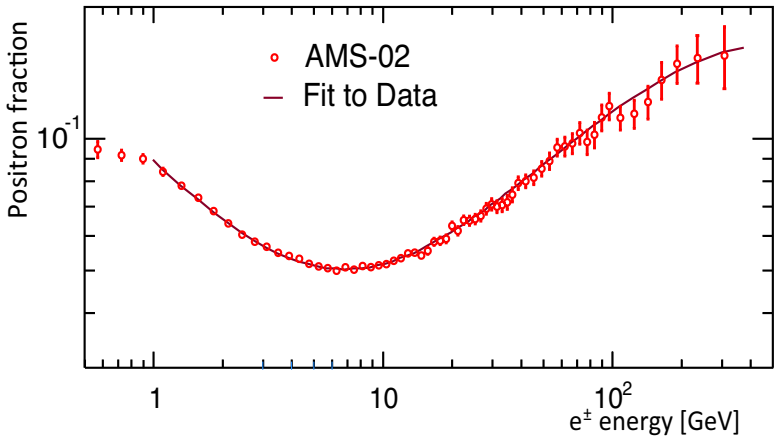

Fig. 3. The positron fraction measured by AMS, fit with the minimal model. For the fit, both the data and the model are integrated over the bin width [Aguilar (2013)].

reveals that the positron fraction is consistent with $e^{\pm}$ fluxes each of which is the sum of its diffuse spectrum and a single common power law source. The model has been shown to be insensitive to solar modulation effects during this period. Indeed, fitting over the energy ranges from 0.8–350 GeV to 6.0–350 GeV does not change the results nor the fit quality. Furthermore, fitting the data with the same model extended to include different solar modulation effects on positrons and electrons yields similar results.

3 Conclusions

AMS-02 is a particle physics experiment onboard the ISS since 2011, whose main physics goals are the search for antimatter and dark matter in space, as well as the precise measurement of cosmic rays composition and flux. The recently published positron fraction measurement was described. Above 10 GeV the positron fraction raises with increasing energy, being incompatible with the pure secondary production of positrons, and it shows no significant anisotropy. The data have been compared to a simple model, where both the electron and positron flux are described as the sum of individual diffuse power law spectra and a single common source. This model shows and excellent fit to the data, and it has been shown to be insensitive to the solar modulation. AMS-02 data confirm the results from previous experiments with unprecedented precision, giving evidence for the existence of new physical phenomena. AMS data will provide fundamental clues to understand the origin of those phenomena, as soon as more statistics is be available.

References

Ackermann, M., e. a. 2009, Phys. Rev. Lett., 458, 607
Adloff, C. e. a. 2013, NIM A, 714, 147
Adriani, O. e. a. 2009, Nature, 458, 607
Aguilar, M. e. a. 2013, Phys. Rev. Lett., A 110, 141102
Delgado, C. e. a. 2013, Proc of ICRC
Gast, H. e. a. 2013, Proc of ICRC
Giovacchini, F. e. a. 2013, Proc of ICRC
Quadrani, L. e. a. 2013, Proc of ICRC

SF2A 2013
L. Cambrésy, F. Martins, E. Nuss and A. Palacios (eds)

QUASI-PERIODIC OSCILLATIONS FROM ROSSBY WAVE INSTABILITY

F. H. Vincent[1], P. Varniere[2], H. Méheut[3], T. Paumard[4], G. Török[5] and M. Wildner[5]

Abstract. We study the Rossby wave instability model of high-frequency quasi-periodic oscillations (QPO) of microquasars. We show ray-traced light curves of QPO within this model and discuss perspectives of distinguishing alternative QPO models with the future Large Observatory For X-ray Timing (LOFT) observations.

Keywords: Accretion, accretion disks Hydrodynamics Instabilities Radiative transfer Methods: numerical

1 Introduction

High-frequency quasi-periodic oscillations (QPOs) of microquasars have attracted a lot of attention in the recent years (for a review see Remillard & McClintock 2006). Up to now, no consensus has emerged regarding the nature of these events. Many different models have been proposed, that are still today candidates to account for QPOs. Stella & Vietri (1999) and Stella et al. (1999) suggest that QPOs could arise from the modulation of the X-ray flux by the periastron precession and the Keplerian frequency of blobs of matter orbiting in an accretion disk around the central compact object. Also QPOs could be due to modulation of the X-ray flux by oscillations of a thin accretion disk surrounding the central compact object (see Wagoner 1999; Kato 2001). Fragile et al. (2001) propose that QPOs are due to the modulation of the X-ray flux caused by a warped accretion disk surrounding the central compact object. Pointing out the 3:2 ratio of some QPOs in different sources, Abramowicz & Kluźniak (2001) have proposed a resonance model in which these pairs of QPOs are due to the beat between the Keplerian and epicyclic frequencies of a particle orbiting around the central compact object. Schnittman & Bertschinger (2004) investigated in great detail predictions of a model of hot spot radiating isotropically on nearly circular equatorial orbits. In their study, the hypothetic resonance between the Keplerian and radial epicyclic frequencies gives rise to peaks in the modeled power spectrum.

Tagger & Varnière (2006) advocate the fact that QPOs in microquasars could be triggered by a Rossby wave instability (RWI) in the accretion disk surrounding the central compact object. Ray-traced light curves have been recently developed for this model by Vincent et al. (2013). This article aims at exploring the case for the RWI model of QPOs, as well as discussing perspectives of distinguishing alternative models with future observations.

2 Scenario of a quasi-periodic oscillation within the Rossby model

The Rossby wave instability (Lovelace et al. 1999) will be triggered in an accretion disk provided the following quantity

$$\mathcal{L} = \frac{\Sigma\Omega}{2\kappa^2}\frac{p}{\Sigma^\gamma}, \tag{2.1}$$

[1] N. Copernicus Astronomical Centre, ul. Bartycka 18, 00-716, Warszawa, Poland
[2] AstroParticule et Cosmologie (APC), Université Paris Diderot, 10 rue A. Domon et L. Duquet, 75205 Paris Cedex 13, France
[3] CEA, Irfu, SAp, Centre de Saclay, F-91191 Gif-sur-Yvette, France
[4] LESIA, Observatoire de Paris, CNRS, Université Pierre et Marie Curie, Université Paris Diderot, 5 place Jules Janssen, 92190 Meudon, France
[5] Institute of Physics, Faculty of Philosophy and Science, Silesian University in Opava, Bezrucovo nm. 13, CZ-74601 Opava, Czech Republic

where Σ is the surface density, Ω the rotation velocity, κ the radial epicyclic frequency, p the pressure and γ the adiabatic index, reaches an extremum. For an accretion disk surrounding a Schwarzschild black hole, this quantity will naturally reach an extremum as the epicyclic frequency reaches a maximum close to the innermost stable circular orbit (ISCO) as illustrated in Fig. 1, in the upper left panel.

Once the instability is triggered, it will develop spiral density waves that will spread on both sides of the extremum (or corotation) radius (see Fig. 1, upper right and lower panel). Rossby vortices develop at the corotation radius and aggregate most of the density. The mode number of the instability, or number of spiral arms ($m = 4$ for instance in the lower panel of Fig. 1) is evolving with time, always from higher values of m to smaller values of m. When the instability is fully developed, modes $m = 1$ or 2 or 3 can dominate, or a combination thereof. At a given time, different modes can coexist. This is clearly visible in Fig. 2 showing the ray-traced light curve of an accretion disk surrounding a Schwarzschild black hole subject to the RWI: the red curve clearly shows the evolution, and superimposition, of different modes.

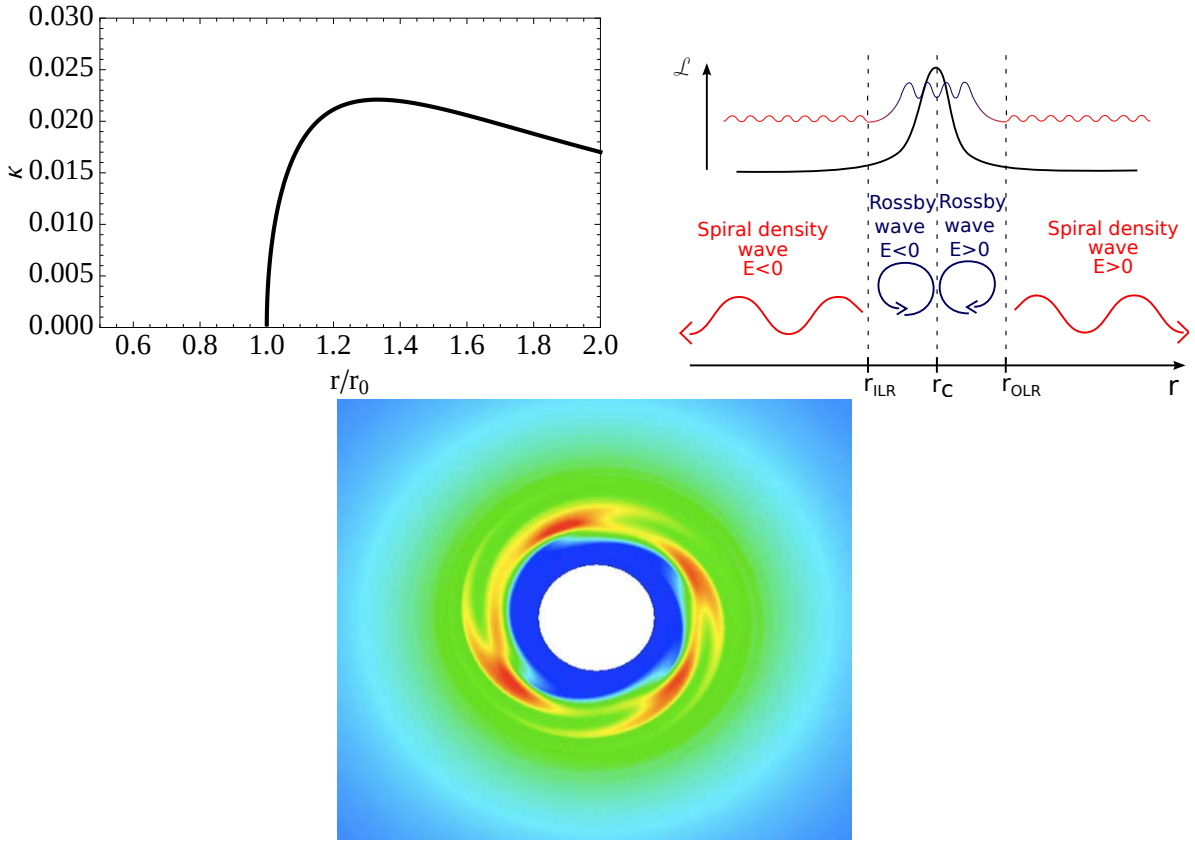

Fig. 1. Upper left: radial epicyclic frequency distribution κ as a function of r in an accretion disk surrounding a Schwarzschild black hole. An extremum occurs at a radius somewhat bigger than the ISCO radius r_0. **Upper right:** development of the Rossby wave instability. Density waves propagate on both sides of the extremum (or corotation) radius r_C, and Rossby vortices appear at the corotation (figure from Meheut et al. 2013). However, in our case where the instability is triggered near ISCO by the extremum of epicyclic frequency, hardly any waves are emitted at radii smaller than the corotation radius. **Lower:** density map of the disk when the Rossby instability is fully developed. Four spiral arms are clearly visible while most of the density is concentrated in the four Rossby vortices.

To summarize, here is one possible scenario that would lead to QPOs due to the RWI in microquasars:

- initial state: an accretion disk around a Schwarzschild black hole with inner radius $r_{\rm in}$ above the radius of the maximum of epicyclic frequency κ; no instability;
- when $r_{\rm in}$ becomes smaller than the maximum of κ, the RWI is triggered and develops, with different modes being present; this is the QPO;
- as $r_{\rm in}$ increases, it gets bigger than the maximum of κ and the instability is quenched.

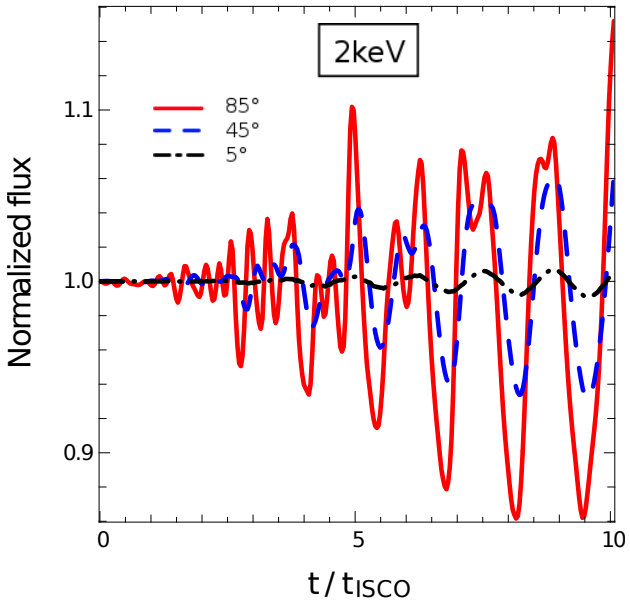

Fig. 2. Ray-traced light curve of an accretion disk surrounding a Schwarzschild black hole subject to the Rossby wave instability, seen under an inclination of 5° (black - face-on), 45° (blue) or 85° (red - edge-on). The energy of the observed radiation is 2 keV. The time is given in units of the ISCO Keplerian orbital time. The modulation of the intensity due to relativistic beaming leads to a modulation of the light curve at a few percent level, highly depending on the inclination. At high inclination, the modal signature of the instability appears clearly with higher mode number at early times, decreasing to mode $m = 1$ dominating at the end of the simulation.

As a consequence, the evolution of the inner radius of the accretion disk dictates the triggering of the instability and the appearance of QPOs.

3 Towards distinguishing alternative models?

One very interesting feature of the RWI model is the modal signature that is clearly illustrated in Fig. 2.

Our future aim is to develop observational strategies to distinguish alternative models of QPOs. In this perspective the future X-ray timing instrument LOFT (Feroci et al. 2012) is very interesting, as its spectral ability allows it to generate much more precise spectra than the current RXTE data. Future work will thus be devoted to simulating LOFT power spectra of QPOs described by various models, in order to determine whether the spectral signature of the various models may be used to distinguish them.

Fig. 3 gives a very first, illustrative, LOFT simulation. It shows a light curve and power spectrum, as observed by LOFT, corresponding to the theoretical light curve depicted in Fig. 2. However, this simulation assumes a black hole of the order of $1000\,M_\odot$, which changes the time scale and allowed us to get this illustrative result without having to resort to intensive computations which will be needed to reach the time resolution required for a $10\,M_\odot$ black hole, typical of a microquasar. Fig. 3 must then be seen as an illustration of the simulations we are aiming at. It shows very clearly the spectral signature of the RWI with three distinct peaks at one, two and three times a fundamental frequency a bit lower than the ISCO frequency. This is logical as the RWI develops at a radius somewhat bigger than the ISCO radius.

4 Conclusions

We have advocated here one model of high-frequency QPOs of microquasars: the Rossby wave instability model.

This model allows to modulate the light curve of microquasars at a few percent level, with the modulation depending strongly on inclination. It allows to explain naturally the coexistence of different modes in the observed QPO signal.

Future work will be dedicated to developing LOFT simulations of this RWI model, and compare its observed spectral signature to alternative models.

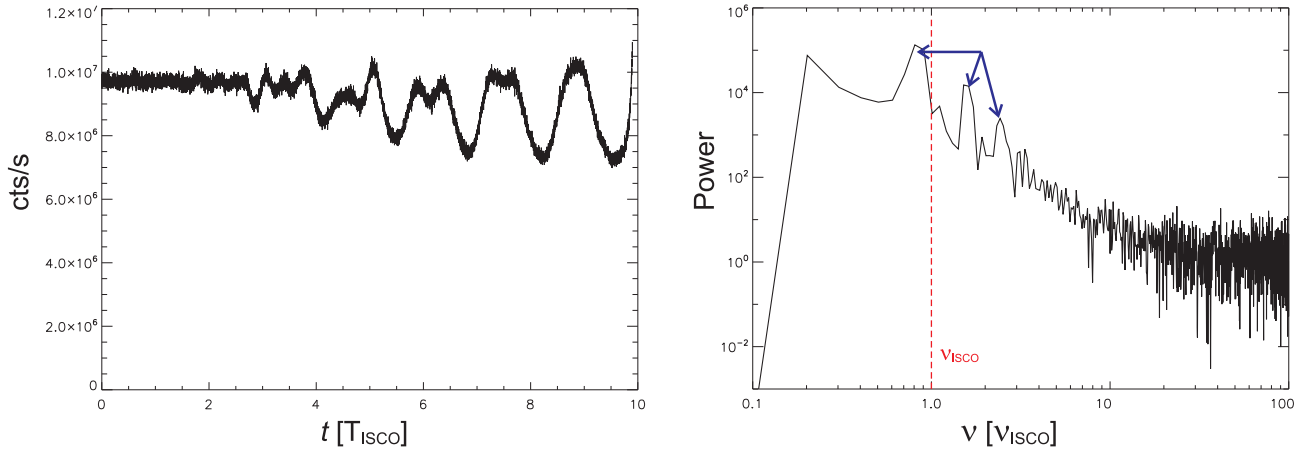

Fig. 3. Left: simulated light curve of a LOFT observation of RWI in an accretion disk surrounding a 1000 $M_\odot$ black hole (see text for details). **Right:** corresponding power spectrum. The spectral signature of the RWI, with three peaks at one, two and three times a fundamental frequency, is clearly visible.

This work has been financially supported by the French Programme National des Hautes Energies (PNHE). Some of the simulations were performed using HPC resources from GENCI-CINES (Grant 2012046810).

References

Abramowicz, M. A. & Kluźniak, W. 2001, A&A, 374, L19
Feroci, M., Stella, L., van der Klis, M., et al. 2012, Experimental Astronomy, 34, 415
Fragile, P. C., Mathews, G. J., & Wilson, J. R. 2001, ApJ, 553, 955
Kato, S. 2001, PASJ, 53, 1
Lovelace, R. V. E., Li, H., Colgate, S. A., & Nelson, A. F. 1999, ApJ, 513, 805
Meheut, H., Lovelace, R. V. E., & Lai, D. 2013, MNRAS, 430, 1988
Remillard, R. A. & McClintock, J. E. 2006, ARA&A, 44, 49
Schnittman, J. D. & Bertschinger, E. 2004, ApJ, 606, 1098
Stella, L. & Vietri, M. 1999, Physical Review Letters, 82, 17
Stella, L., Vietri, M., & Morsink, S. M. 1999, ApJ, 524, L63
Tagger, M. & Varnière, P. 2006, ApJ, 652, 1457
Vincent, F. H., Meheut, H., Varniere, P., & Paumard, T. 2013, A&A, 551, A54
Wagoner, R. V. 1999, Phys. Rep., 311, 259

Session 17

SPIRou : un SpectroPolarimètre InfraRouge pour le CFHT

SF2A 2013
L. Cambrésy, F. Martins, E. Nuss and A. Palacios (eds)

PERSPECTIVES FOR THE STUDY OF GAS IN PROTOPLANETARY DISKS AND ACCRETION/EJECTION PHENOMENA IN YOUNG STARS WITH THE NEAR-IR SPECTROGRAPH SPIROU AT THE CFHT

A. Carmona[1], J. Bouvier[1] and X. Delfosse[1]

Abstract. Near-IR atomic and molecular transitions are powerful tools to trace the warm and hot gas in the circumstellar environment of young stars. Ro-vibrational transitions of H_2 and H_2O, and overtone transitions of CO at 2 μm centered at the stellar velocity trace hot (T$\sim$ 1500 K) gas in the inner few AU of protoplanetary disks. H_2 near-IR lines displaying a blueshift of a few km/s probe molecular disk winds. H_2 lines presenting blueshifts of hundreds of km/s reveal hot shocked gas in jets. Atomic lines such as the HeI line at 10830 Å and the Hydrogen Paschen β and Brakett γ lines trace emission from accretion funnel flows and atomic disk winds. Bright forbidden atomic lines in the near-IR of species such as [Fe II], [N I], [S I], [S II], and [C I] trace atomic and ionized material in jets. The new near-IR high resolution spectrograph SPIROU planned for the Canada France Hawaii Telescope will offer the unique capability of combining high-spectral resolution (R$\sim$75000) with a large wavelength coverage (0.98 to 2.35 μm) in one single exposure. This will provide us with the means of probing accretion funnel flows, winds, jets, and hot gas in the inner disk simultaneously. This opens the exiting possibility of investigating their combined behavior in time by the means of monitoring observations and systematic surveys. SPIROU will be a powerful tool to progress our understanding of the connexion between the accretion/ejection process, disk evolution, and planet formation.

Keywords: star formation, young stars, protoplanetary disks, accretion, ejection, high-resolution infrared spectroscopy

1 Introduction

The extraordinary diversity of the extrasolar planetary systems discovered has renewed our interest in understanding the planet formation process. Planets form in the circumstellar disks that surround stars in their pre-main sequence. Such "protoplanetary disks" are composed of gas (99%) and dust, they extend typically hundreds of AU, have masses of a few percent of the central star, and have a lifetime on average of a few million years. What is their geometry? What are their density, temperature, and chemical structure? What are the principal physical and chemical mechanisms setting that structure? What are their dynamics? How do they dissipate? To determine how disks are is crucial to understand planet formation.

Young stars are complex dynamical entities. In addition to disks, they display jets, winds, and magnetospheric accretion funnel flows. In fact the presence of collimated outflows and the presence of accretion disks appear to be inseparable phenomena. How are these different components interrelated? How is the disk structure linked to accretion/ejection processes? How do jets and accretion columns affect the radiation field interacting with the disk? How do accretion/ejection phenomena affect the planet formation process? How does this complex system involve in time? What is their impact in the stellar evolution? To understand the circumstellar environment of young stars as a whole, it is a crucial aspect to understand early stellar evolution and the origin of planetary systems.

[1] UJF-Grenoble 1 / CNRS-INSU, Institut de Planétologie et d'Astrophysique de Grenoble (IPAG) UMR 5274, Grenoble, F-38041, France

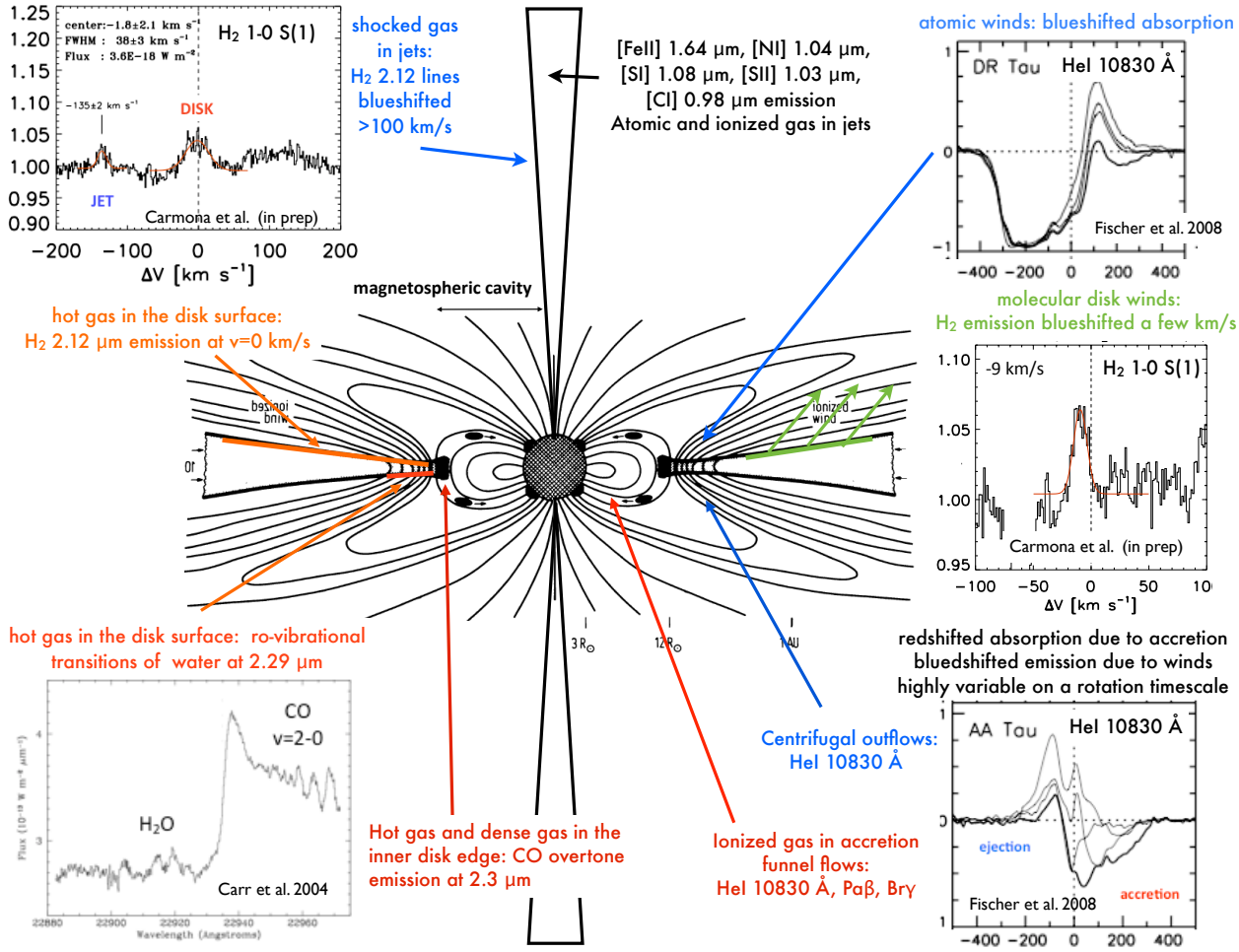

Fig. 1. Summary of diagnostics of gas in the circumstellar environment of young stars that will be covered by SPIROU. T Tauri star cartoon adapted from Camenzind (1990).

2 Probing the gas in the circumstellar environment of young stars with SPIROU

The dust content of circumstellar disks is traced by its thermal and scattered light emission. The gas content of circumstellar disks, winds, outflows, collimated jets, and accretion flows is investigated employing spectral lines. Atomic and molecular transitions trace regions at different temperatures and densities. Their integrated fluxes, line shapes, velocity shifts, and line-ratios have the imprint the excitation mechanisms and the dynamics of the medium where the lines originate. Different regions are traced at different wavelengths as a function of the temperature of the medium producing the lines. Cold gas (T <100 K) situated in the outer region of a protoplanetary disk (R> 10 AU), or cold gas excited by shocks by outflows or jets are traced with molecular transitions in the sub-mm and mm wavelengths ($\lambda > 400$ μm). Warm gas ($100 < T < 1000$ K) located in the surface layer of a disk between a few AU and 10 AU (i.e. the giant planet forming region) will be probed by mid-IR ($8 - 100$ μm) and far-IR ($100 - 400$ μm) transitions. Hot gas (T> 1000 K) in the inner few AU of disks (i.e. the terrestrial planet forming region), accretion funnel flows, disk winds, and jets are traced by near-IR ($1 - 8$ μm) emission.

The keys to discern between the different origins of a line are its shape and velocity shift with respect to the central star (see Fig. 1). Emission produced by a circumstellar disk will *centered at the velocity of the star* and will produce the characteristic double peak profiles due to Keplerian rotation. The double peaked profile provide us information of the region in the disk emitting the line. The lines are broader if the line is emitted closer to the star. The line high velocity wings indicate the inner-most radius emitting the line. The double peak separation provides us information about the outer radius. The double peak separation and the line width tell us about the disk inclination. Emission produced by a collimated jet, or a fast moving outflow, will be

blue-shifted hundreds of km/s. Emission produced by a disk wind will be *asymmetric and/or blue-shifted a few km/s.* The presence of outflows and winds can also be seen as blueshifted absorption lines on the top emission component (i.e. P Cygni profile). Accretion flows are traced by inverse P Cygni profiles (red-shifted absorption on the top of an emission component). Emission from fast moving jets, winds, or outflows from the inner most disk can be traced already at low spectral resolution (R∼2000 or 150 km/s), however, to exploit the dynamical information encoded in the lines from of disks or disk winds, high-spectral resolution (R>10000) is a must. Furthermore, in the case of disk emission, high-spectral resolution is required to separate the gas lines from telluric absorption and detect weak emission lines on the top of the strong dust continuum.

SPIROU will trace in one exposure the $0.98-2.35$ μm region at a spectral resolution 75000. In this region, we can study H_2 near-IR emission, for example the 1-0 S (1), 1-0 S(0), and 2-1 S(1) ro-vibrational lines at 2.12, 2.22, and 2.24 μm (e.g. Bary et al. 2003; Ramsay Howat & Greaves 2007; Carmona et al. 2011), ro-vibrational water emission at 2.29 μm (e.g. Carr et al. 2004; Thi & Bik 2005); and CO overtone $\Delta v = 2$ bandhead emission at 2.3 μm (e.g. Chandler et al. 1995; Najita et al. 1996; Thi et al. 2005). These molecular near-IR transitions trace hot gas (T>1000 K) in the inner few AU of disks. They probe different excitation mechanisms, temperatures, and densities. For example, near-IR H_2 lines are excited in the upper layers of the disk either by UV-radiation or X-rays and are sensitive to earth-masses of gas at ∼1000 K. CO overtone emission, in contrast, requires very dense ($n_{\rm H} > 10^{10}$ cm^{-3}) and hot ($T = 2000 - 4000$ K) gas to be produced. Furthermore, H_2 near-IR lines are good tracers of hot shocked gas in outflows and collimated jets extending at hundreds of AU. They have also the potential of tracing molecular disk winds excited by energetic radiation from the central source. The near-IR window covered by SPIROU permits us to measure atomic lines such as the HeI line at 10830 Å and the Hydrogen Paschen β (1.28 μm) and Brakett γ (2.17 μm) lines. These lines are primordial for the study of the magnetospheric cavity, the accretion/ejection process, and the interface between the disk and the star. These lines are powerful tools to study accretion funnel flows and atomic disk winds (e.g. Fischer et al. 2008). Bright forbidden atomic lines in the near-IR such as the [Fe II] lines at 1.64, 1.59, 1.53, 1.32, and 1.25 μm, the [N I] lines at 1.04 μm, the [S I] lines at 1.08 and 1.13 μm, the [S II] lines at 1.03 μm, and the [C I] lines at 0.98 μm trace neutral and ionized material in jets (e.g. Giannini et al. 2006). In Figure 1, we present a cartoon summarizing the different diagnostics of the circumstellar environment of young stars covered by SPIROU.

Current high-resolution (R> 10000) near-IR spectrographs have limited wavelength coverage. For example, the near-IR spectrograph CRIRES at ESO/VLT (R∼90000) covers in one exposure 0.02 μm. NIRSPEC at Keck (R∼25000) covers 0.18 μm in one setting. The unique capability of SPIROU would be to offer a coverage of 1.37 μm (0.98 to 2.35 μm) in one single setting with a resolution of 4 km/s. This will provide us with the means of measuring diagnostics of accretion, winds, jets, and disks, all simultaneously in one shot. SPIROU is expected to reach a S/N >100 in a 2 km/s pixel in 1h of exposure for objects with magnitudes up to J=12 and K=11, thus a 5 σ flux sensitivity of $\sim 10^{-19}$ W m^{-2} in a line of width 8 km/s . The sensitivity and large spectral coverage provided by SPIROU will permit us to investigate in detail a large number of sources employing short exposure times. This opens the exiting possibility of investigating the evolution in time of disks, winds, and jets simultaneously by the means of monitoring observations. SPIROU will be a powerful tool to progress our understanding of the connexion between the accretion/ejection process, disk evolution, and planet formation.

Acknowledgements: A. Carmona acknowledges funding from the Agence Nationale pour la Recherche (ANR) of France under contract ANR-2010-JCJC-0504-01.

References

Bary, J. S., Weintraub, D. A., & Kastner, J. H. 2003, ApJ, 586, 1136
Camenzind, M. 1990, in Reviews in Modern Astronomy, Vol. 3, Reviews in Modern Astronomy, ed. G. Klare, 234–265
Carmona, A., van der Plas, G., van den Ancker, M. E., et al. 2011, A&A, 533, A39
Carr, J. S., Tokunaga, A. T., & Najita, J. 2004, ApJ, 603, 213
Chandler, C. J., Carlstrom, J. E., & Scoville, N. Z. 1995, ApJ, 446, 793
Fischer, W., Kwan, J., Edwards, S., & Hillenbrand, L. 2008, ApJ, 687, 1117
Giannini, T., McCoey, C., Nisini, B., et al. 2006, A&A, 459, 821
Najita, J., Carr, J. S., Glassgold, A. E., Shu, F. H., & Tokunaga, A. T. 1996, ApJ, 462, 919
Ramsay Howat, S. K. & Greaves, J. S. 2007, MNRAS, 379, 1658
Thi, W.-F. & Bik, A. 2005, A&A, 438, 557
Thi, W.-F., van Dalen, B., Bik, A., & Waters, L. B. F. M. 2005, A&A, 430, L61

SF2A 2013
L. Cambrésy, F. Martins, E. Nuss and A. Palacios (eds)

WORLD-LEADING SCIENCE WITH SPIROU - THE NIR SPECTROPOLARIMETER / HIGH-PRECISION VELOCIMETER FOR CFHT

X. Delfosse[1], J.-F. Donati[2], D. Kouach[2], G. Hébrard[3], R. Doyon[4], E. Artigau[4], F. Bouchy[5], I. Boisse[5], A.S. Brun[6], P. Hennebelle[6,7], T. Widemann[8], J. Bouvier[1], X. Bonfils[1], J. Morin[9], C. Moutou[10], F. Pepe[11], S. Udry[11], J.-D. do Nascimento[12], S.H.P. Alencar[13], B.V. Castilho[14], E. Martioli[14], S.Y. Wang[15], P. Figueira[16], N.C. Santos[16] and the SPIRou Science Team

Abstract.

SPIRou is a near-infrared (nIR) spectropolarimeter / velocimeter proposed as a new-generation instrument for CFHT. SPIRou aims in particular at becoming world-leader on two forefront science topics, (i) the quest for habitable Earth-like planets around very- low-mass stars, and (ii) the study of low-mass star and planet formation in the presence of magnetic fields. In addition to these two main goals, SPIRou will be able to tackle many key programs, from weather patterns on brown dwarf to solar-system planet atmospheres, to dynamo processes in fully-convective bodies and planet habitability. The science programs that SPIRou proposes to tackle are forefront (identified as first priorities by most research agencies worldwide), ambitious (competitive and complementary with science programs carried out on much larger facilities, such as ALMA and JWST) and timely (ideally phased with complementary space missions like TESS and CHEOPS).

SPIRou is designed to carry out its science mission with maximum efficiency and optimum precision. More specifically, SPIRou will be able to cover a very wide single-shot nIR spectral domain (0.98-2.35 μm) at a resolving power of 73.5K, providing unpolarized and polarized spectra of low-mass stars with a $\sim$15% average throughput and a radial velocity (RV) precision of 1 m/s.

Keywords: Extrasolar planets, Super-Earths in the habitable zone, Star / planet formation, Stellar magnetic fields, Velocimetry, Spectropolarimetry.

[1] UJF-Grenoble 1/CNRS-INSU, Institut de Planétologie et d'Astrophysique de Grenoble (IPAG) UMR 5274, 38041 Grenoble, France

[2] UPS-Toulouse / CNRS-INSU, Institut de Recherche en Astrophysique et Planétologie (IRAP) UMR 5277, Toulouse, F31400 France

[3] Institut dAstrophysique de Paris, CNRS, Université Pierre et Marie Curie, 98bis Bd. Arago, 75014 Paris, France

[4] Département de physique and Observatoire du Mont-Mégantic, Université de Montréal, C.P. 6128, Succursale Centre-Ville, Montréal, QC H3C 3J7, Canada

[5] Aix Marseille Université, CNRS, LAM (Laboratoire dAstrophysique de Marseille) UMR 7326, 13388, Marseille, France

[6] Laboratoire AIM Paris-Saclay, CEA/Irfu Université Paris-Diderot CNRS/INSU, 91191 Gif-sur-Yvette, France

[7] LERMA (UMR CNRS 8112), Ecole Normale Supérieure, 75231, Paris Cedex, France

[8] Paris Observatory, LESIA UMR 8109, Meudon, France

[9] LUPM, Université Montpellier II, CNRS, UMR 5299, Place E. Bataillon, 34095, Montpellier, France

[10] Canada-France-Hawaii Telescope Corporation, 65-1238 Mamalahoa Hwy., Kamuela, HI 96743, USA

[11] Observatoire Astronomique de l'Université de Genève, 51 Ch. des Maillettes, 1290 Sauverny, Versoix, Suisse

[12] Departamento de Física Teórica e Experimental (DFTE), Universidade Federal do Rio Grande do Norte (UFRN), CP 1641, 59072-970 Natal, RN, Brazil

[13] Departamento de Física - ICEx - UFMG, Av. Antnio Carlos, 6627, 30270-901 Belo Horizonte, MG, Brazil

[14] Laboratório Nacional de Astrofísica/MCT, Rua Estados Unidos 154, 37504-364 Itajubá, MG, Brazil

[15] Institute of Astronomy and Astrophysics, National Taiwan Univ., Taiwan

[16] Centro de Astrofísica, Universidade do Porto, Rua das Estrelas, 4150-762, Porto, Portugal

Requirement	Value
Simultaneous Spectral Range	full coverage from 0.98-2.35 m (YJHK bands)
Resolving Power	>70K (goal 75K)
RV Precision	<1 m/s (rms)
Polarimetric Performance	relative precision: better than 2% (goal 1%); sensitivity: 10 ppm
Instrument Sensitivity	S/N>100 per 2 km/s pixel in 1 hr at J=12 & K=11; bright limit: H<3.5 (goal H<1) - faint limit: H∼14
Observational Efficiency	>70% & >90% for 15 min & 1 hr visit respectively
Sky Coverage	up to airmass 2.5 (zenithal distance 70°)

Table 1. Summary of SPIRou scientific requirements

1 Introduction

The science programs SPIRou proposes to tackle are forefront (first priorities for most research agencies worldwide), ambitious (competitive and complementary with science programs carried out on much larger facilities, e.g., ALMA/ESO and JWST/NASA) and timely (ideally phased with complementary instruments, e.g., TESS/NASA, CHEOPS/ESA and JWST/NASA). SPIRou plans to concentrate on two main scientific goals. The first one is to search for and characterize habitable exo-Earths orbiting very-low mass stars (vLMSs) using high-precision radial velocity (RV) measurements. This search will expand the initial, exploratory studies carried out with visible instruments (e.g., HARPS/ESO) and will survey in particular large samples of stars mostly out of reach of existing instruments. In particular, carrying out a new large- scale survey at nIR wavelengths will boost the sensitivity to habitable exo-Earths by typically an order of magnitude on planetary mass (with respect to existing instruments). SPIRou will also work in close collaboration with space- and ground- based photometric transit surveys like TESS/NASA, CHEOPS/ESA and ExTrA* to identify the true planets among the candidates they will discover.

The second main goal is to explore the impact of magnetic fields on star and planet formation, by detecting fields of various types of young stellar objects (e.g. class-I, -II and -III protostars, young FUor-like protostellar accretion discs) and by characterizing their large-scale topologies. SPIRou will also investigate the potential presence of giant planets around protostars and in the inner regions of accretion discs. In particular, this study will vastly amplify the initial exploration surveys carried out at optical wavelengths within the MaPP (Magnetic Protostars and Planets) and MaTYSSE (Magnetic Topologies of Young Stars and the Survival of close-in massive Exoplanets) CFHT Large Programs (LPs). It will also ideally complement the data that ALMA/ESO has just started collecting on outer accretion discs and dense prestellar cores. SPIRou will also be able to tackle many additional exciting research topics in stellar physics (e.g., dynamos of fully convective stars, weather patterns of brown dwarfs), in planetary physics (e.g., winds and chemistry of solar-system planets), galactic physics (e.g. stellar archeology) as well as in extragalactic astronomy. We detail these goals below, giving in the main cases the typical samples that need to be explored and their observational properties.

2 SPIRou

2.1 Science requirements and instrument concept

SPIRou is designed to carry out its science mission with maximum efficiency and optimum precision. More specifically, SPIRou will be able to cover a very wide single-shot nIR spectral domain (0.98-2.35μm) at a resolving power of 73.5K, providing unpolarized and polarized spectra of low-mass stars with a ∼15% average throughput and a RV precision of 1 m/s. Table 1 list the main scientific requirements of SPIRou, needed to carry out most science goals detailled in Sec 3 and 4.

The very-wide simultaneous spectral range, including in particular the K band, is crucial to SPIRou. It maximizes the instrument efficiency, both for the exoplanet programs - the K band totaling ∼40% of the RV content in a full YJHK spectrum for an average M dwarf (see Fig 1) - and for the magnetic fields and star/planet formation themes - the relative spectropolarimetric weight of the K band reaching 60-70% given the increase of

*ExTrA is a recently funded ERC project whose aim is to detect transiting Earth-like planets around M-dwarfs from the ground. As a low resolution multiple-object spectrograph, ExTrA will allow extremely accurate photometry in narrow wavelength bands

the Zeeman effect with wavelength as λ^2. Moreover, the K band is the only window to access class I embedded protostars, a key stellar sample to be explored for the first time with SPIRou. The wide spectral coverage and spectropolarimetric capabilities are also unique to SPIRou; other nIR RV instruments currently under planning (Carmenes on Calar Alto, IRD on Subaru, HZPF on the HET) do not cover beyond the H band nor include a polarimeter. The spectral resolution is also very important, not only to maximize the velocimetric efficiency, but also to ensure high enough spectropolarimetric sensitivity to Zeeman signatures; with a spectral resolution of at least 73.5K, SPIRou is nearing optimal performances.

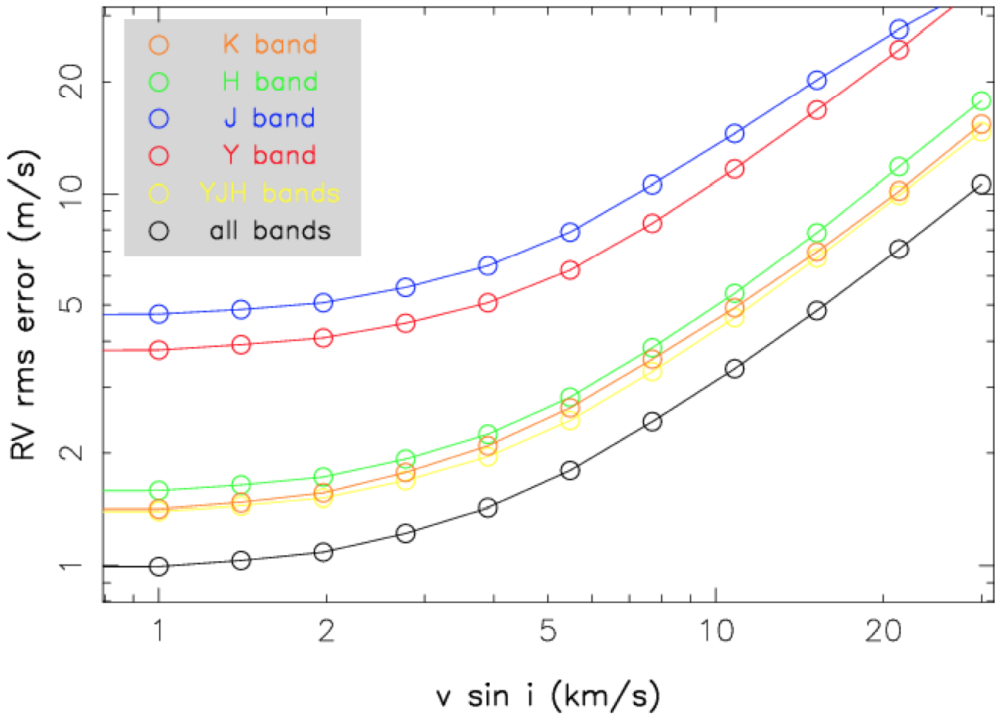

Fig. 1. RV rms photon-noise error (in m/s) vs rotational broadening ($v \sin i$) for a M7 dwarf (2,700 K) and for the different nIR bands (color curves), assuming a spectral resolution of 75K and a peak S/N of 160 per 2 km/s pixel. A RV precision of 1 m/s can be reached at low $v \sin i$'s. The K band (orange) is the main contributor to the RV precision and contributes almost as much as all other bands (yellow). Without the K band, a twice longer exposure time would be required to reach the same RV precision. Note that this estimate is likely pessimistic by potentially as much as a factor of 2, nIR synthetic spectra systematically under-estimating the strength of many molecular and even atomic features.

The resulting instrument concept proposed for SPIRou is a direct heritage from previous successful instruments built by various members of the SPIRou project team: HARPS at the 3.6-m ESO telescope (Mayor et al. 2003), ESPaDOnS at CFHT (Donati 2003) and SOPHIE at 1.93-m OHP telescope (Bouchy & Sophie Team 2006; Bouchy et al. 2013). More specifically, SPIRou includes a cryogenic high-resolution spectrograph inspired from the evacuated spectrograph of the HARPS velocimeter, a Cassegrain unit derived from the ESPaDOnS spectropolarimeter, a fiber-feed evolved from those of ESPaDOnS and the HARPS/SOPHIE velocimeters, and a Calibration/RV reference unit largely copied from those of SOPHIE and HARPS.

2.1.1 The Cassegrain unit

The Cassegrain unit consists of 2 modules mounted (on top of each other) at the Cassegrain focus of the telescope. The upper Cassegrain module includes an ADC correcting the entrance beam for the atmospheric refraction and a tip-tilt module stabilizing the entrance image to better than 0.05" rms; this module also includes a calibration wheel allowing to inject light from the calibration unit into the instrument. Beginning with a circular instrument aperture of diameter 1.3", the lower Cassegrain module mainly includes an achromatic polarimeter made of two 3/4-wave dual ZnSe Fresnel rhombs coupled to a Wollaston prism, splitting the beam into 2 orthogonal linear-polarization states. The 2 beams emerging from the beamsplitter are injected into 2

separate fibers at polarimeter output

2.1.2 The fiber link and pupil slicer

The fiber link conveys the light from the twin orthogonally polarized beams coming out of the Cassegrain polarimeter into the cryogenic spectrograph. This link consists of a dual 35-m circular fluoride fiber custom-made with purified material to ensure a throughput of >90% over the entire spectral range of SPIRou; this fiber link also includes a pupil-slicer at spectrograph entrance to minimize injection losses without affecting the spectrograph resolution. The last section of the fiber link includes a triple 90μm octogonal fiber (2 for the science fibers and 1 for a simultaneous RV reference) ensuring a high scrambling of the near-field image is at least 1000.

2.1.3 The cryogenic spectrograph

The high-resolution échelle spectrograph is bench-mounted, protected by one active and 3 passive thermal shields, and enclosed within a cryogenic dewar. Thanks to a dual-pupil design and an off-the-shelf commercial R2 échelle grating (w/ 23.2 gr/mm), the spectrograph can record the entire spectral range on a Hawaii 4RG detector (15μm square pixels). The pixel size translates into an average spectral bin of 2.28 km/s and the spectrograph features a non-Gaussian instrumental profile yielding a spectral resolving power of 73.5K. The optical design of the spectrograph ensure a high total average throughput of 45% (detector included). The spectrograph is cooled down to 80 K and thermally stabilized at a rms level of $\sim$2 mK; this thermal stability ensures in particular that the corresponding spectral drift at detector level is <0.70 m/s on timescales of 1 night. This drift can be monitored, and thus mostly corrected for, by recording the RV reference spectrum; in this case, the residual spectral drift at detector level reduces to <0.25 m/s.

2.1.4 The calibration and RV reference module

The calibration module and RV reference unit is used to provide the instrument with all the required laboratory lamps, and in particular halogen lamps (for flat fields, used to correct for the detector pixel-to-pixel sensitivity differences), hollow-cathode lamps (e.g., Th/U spectra, used to derive the pixel-to-wavelength calibration relation) and include an additional RV reference, in the form of a flat field lamp coupled to a Fabry-Perot (FP) etalon, thermally stabilized at a level of $\sim$10 mK rms to ensure that spectral lines do not drift by more than 0.25 m/s rms throughout one night. This thermalized FP unit (and possibly even the Th/U lamps) could be replaced in the future with a nIR tunable laser comb (stable to <0.10 m/s) to further improve the overall RV precision of the instrument.

2.2 The international project team

The SPIRou project team gathers a number of partners from different institutes and countries. More specifically, the team includes several institutes from France (IRAP and OMP in Toulouse, IPAG in Grenoble, OHP and LAM in Marseille, plus an extended science team from IAP / LESIA / CEA / LERMA / IAS / LUTH / LATMOS based in Paris and surroundings), from Canada (UdeM / UL in Montréal and Québec City, NRC in Victoria), from Switzerland (Geneva Observatory), from Taiwan (ASIAA in Taipei), from Brazil (LNA in Itajuba, plus additional science contribution from UFRN / UFMG in Natal and Belo Horizonte), from Portugal (CAUP in Porto) and from CFHT.

3 Main science goal #1 : exoplanets around very-low-mass stars

3.1 Scientific context

One of the 2 main goals of SPIRou is to search for, and to characterize, exo-Earths orbiting low-mass stars - with a particular interest for planets located in the habitable zone (HZ) of their host stars. The study of exoplanetary systems is one of the most exciting areas of astronomy today. Identifying habitable Earth-like planets and searching for biomarkers in their atmospheres is among the main objectives of this new century's astronomy, motivating ambitious space missions (e.g., JWST, TESS, CHEOPS, EChO, PLATO). Among the various techniques developed to detect exoplanets, two are very efficient and complementary. Whereas RV studies look for Doppler shifts induced by orbiting planets in the spectrum of their host stars, giving access to

the planet mass, long-term photometric monitoring searches for regular occultations caused by planets transiting the visible stellar disc, yielding the planet radius. For exoplanets detected with both techniques, one can estimate their densities and thus constrain their bulk compositions. Provided host stars are bright enough, one can even probe the outer atmosphere of transiting planets using transit spectroscopy, opening the new research field of exoplanetology (Charbonneau et al. 2007).

In this context, much interest has recently been focused on low-mass M dwarfs, around which habitable super-Earths are much easier to detect. To be considered potentially habitable, planets must be within the proper range of orbital distances where liquid water can be stable on their surface. This constraint also imposes limits on the atmospheric pressure at the planet surface, and thus indirectly on the planet mass. The range of orbital distances for HZs also strongly depends on the mass (and thus on the temperature) of the host star, with lower temperatures moving HZs closer in. Habitable exo-Earths around M dwarfs are thus expected to produce much larger RV wobbles (4× to 8× for M4 and M6 dwarfs, respectively) compared to the same planet orbiting a Sun-like star. A 1 m/s RV precision is sufficient to detect habitable telluric planets around M dwarfs - the much shorter orbital periods (of order of weeks) vastly decreasing the timescale over which observations must be collected; this is how the first likely- habitables super-Earths were discovered (Udry et al. 2007; Mayor et al. 2009; Delfosse et al. 2013; Bonfils et al. 2013b).

Photometric transits are also much deeper for M dwarfs as a result of their smaller radii - by 11× and 45× for M4 and M6 dwarfs, respectively. A prime goal of the coming years is to discover Earths or super-Earths whose atmosphere can be scrutinized and characterized with space missions (such as JWST and/or EChO) in the next decade. Since atmospheric characterization primarily requires as deep an atmospheric transit as possible on the one hand, and as bright a star as possible on the other hand (in the nIR, where absorption from atmospheric molecules mostly concentrates), M dwarfs are optimal targets for this quest (Rauer et al. 2011). Today, only a handful of very-bright transiting systems have been discovered up to now - most being giant gaseous planets - but many more are expected with forthcoming space missions like TESS or PLATO.

Last but not least, statistical properties of planets around M dwarfs (compared to those around Sun-like stars) can provide key information on planetary formation, and in particular on the sensitivity of planet formation to initial conditions in the protoplanetary disc (e.g., Ida & Lin 2005). That M dwarfs vastly dominate the stellar population in the solar neighborhood and are likely hosting most planets in our Galaxy only makes this study even more crucial.

3.2 The SPIRou planet search

Based on high-precision RV measurements, the SPIRou planet search we propose will greatly expand the current exploratory studies carried out with existing visible velocimeters (e.g., HARPS@ESO, SOPHIE@OHP) by giving access to a large sample of stars inaccessible with existing instrumentation. The SPIRou planet search will in particular build upon the success of the pioneering HARPS RV survey of M dwarfs (Bonfils et al. 2013a), which demonstrated that super-Earths with orbital periods <100 d are more numerous around M dwarfs than around Sun-like stars, with an occurrence frequency close to 90%; moreover, preliminary results suggest that about half of these super-Earths are located in the HZs of their host stars. With existing velocimeters such as HARPS, RV measurements with a precision of 1 m/s are possible for only the ∼100 brightest M dwarfs. This is clearly insufficient, either to have a realistic chance of detecting several transiting habitable super-Earths or to achieve a proper statistical survey of rocky exoplanets around M dwarfs. Given their low temperatures, red and brown dwarfs are much more accessible at nIR wavelengths (see Fig 2). In addition to a 1 m/s RV precision and a high throughput, SPIRou offers the widest simultaneous nIR spectral coverage (0.98-2.35 μm) yet available on any telescope, making it optimally suited for carrying out efficient, systematic RV exoplanet surveys of M dwarfs.

SPIRou will also crucially contribute to the forthcoming extensive photometric surveys of transiting planets around M dwarfs, either from space (e.g., TESS, CHEOPS, PLATO) or from the ground (e.g., ExTrA). Spectroscopy is indeed mandatory to discard false detections (e.g., background eclipsing binaries), to establish the planetary nature of all transiting objects detected around low-mass dwarfs through photometric monitoring and to measure their mass from RV measurements. A high-precision velocimeter working in the nIR will thus be essential to monitor all candidates detected with ground and space photometers around bright M dwarfs, and in particular around late-M ones, hardly accessible to velocimeters working in the visible. A nIR spectrograph will also usefully contribute to the quest for close-in transiting exo-Earths around bright M dwarfs through a systematic survey prior to any photometric observations.

More specifically, SPIRou will contribute to exoplanet science along 3 main avenues, that we foresee as the prime exoplanet themes of the SPIRou planet search.

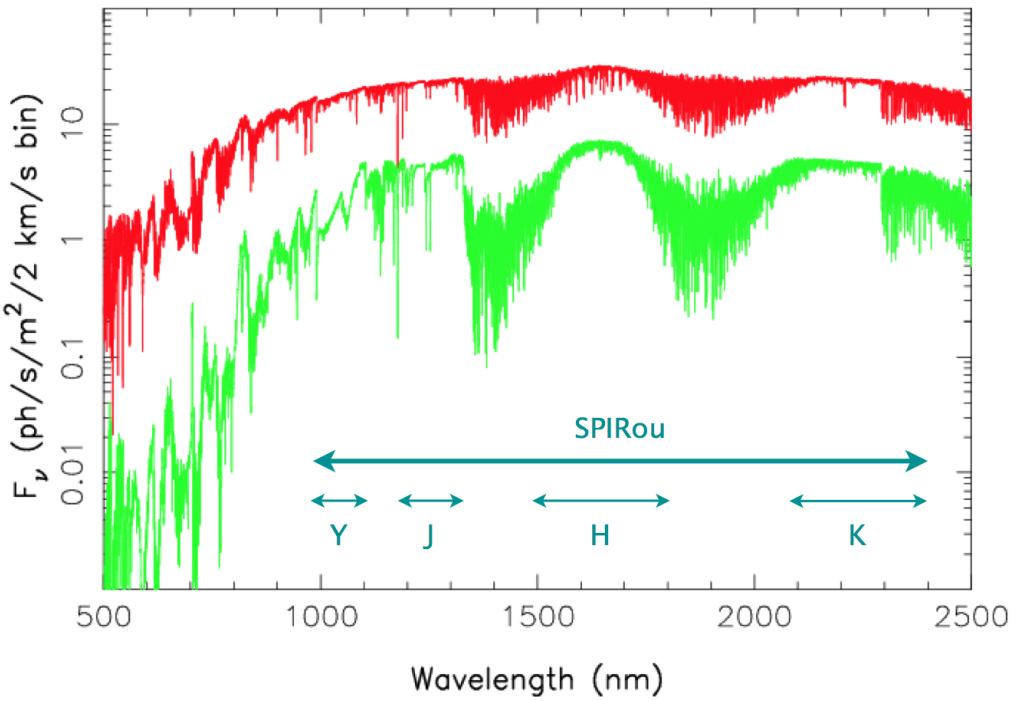

Fig. 2. Photon distribution (per 2 km/s velocity bin size) for a M6 (3,100 K, red) and M8 (2,300 K, green) dwarfs at 10 pc (derived from NextGen models (Allard et al. 1997). M6 and M8 dwarfs respectively produce ∼30 and ∼1000 times more photons (per velocity bin) in HK than in V.

3.2.1 Follow-up of transiting planet candidates uncovered by future photometric surveys

Among the 3,500+ planet candidates yet found by Kepler, only a few tens have been validated and characterized through RV measurements, the vast majority of candidates orbiting stars that are too faint for current RV surveys (see Santerne et al. 2013, for more details). The goal of future photometric surveys is to detect planet candidates around brighter stars, with a specific emphasis on nearby M dwarfs. Among them, the TESS space mission, to be launched in 2017 and predicted to detect ∼300 super-Earths, is certainly very promising. Since (i) most Earths and super-Earths detected with TESS will orbit around M dwarfs, and (ii) less than ∼30% of them will be accessible to optical RV follow-ups (Deming et al. 2009), SPIRou will be the best RV instrument to monitor in the nIR the ∼150 best candidates visible from CFHT, to confirm or reject their planetary nature and to determine their masses.

Monte Carlo simulation show that with ∼60 visits per star and with S/N∼160 spectra per visit SPIRou has the capacity to validate and characterize planets of Earth Mass, orbiting mid-M dwarfs with a period of ∼30 d. This observational effort requires a total of 150 CFHT nights.

3.2.2 RV survey of a large sample of M-dwarfs

As TESS will majoritarly operate on 27-d windows of continuous monitoring for most stars, the majority of planet candidates showing at least 2 transits will have periods <20 d and will not be located in the HZ of their host stars. For planets with longer periods, and in particular for those located in the HZ, RV-driven planet searches will be more efficient. Our Monte Carlo simulations demonstrate that (see Fig 3), with a survey focussing on ∼600 M dwarfs (requiring 600 CFHT nights for >60 visits per stars), SPIRou could potentially detect ∼450 new exoplanets, ∼300 being less massive than 5 $M_\oplus$; among the latter sample, ∼50 would be orbiting in the HZ and ∼15 would be transiting, while ∼2 would have both characteristics. This survey should allow to determine $\eta_\oplus$, the faction of habitable planets in the Solar neighborhood, with an accuracy of <10%. Photometric follow-ups of all planets detected with SPIRou will be achieved, e.g., with CHEOPS and ExTrA, to determine which ones are transiting, once their ephemeris and transit windows are well known. Identifying transiting habitable super Earths is crucial for all future attempts at detecting biomarkers in their atmospheres

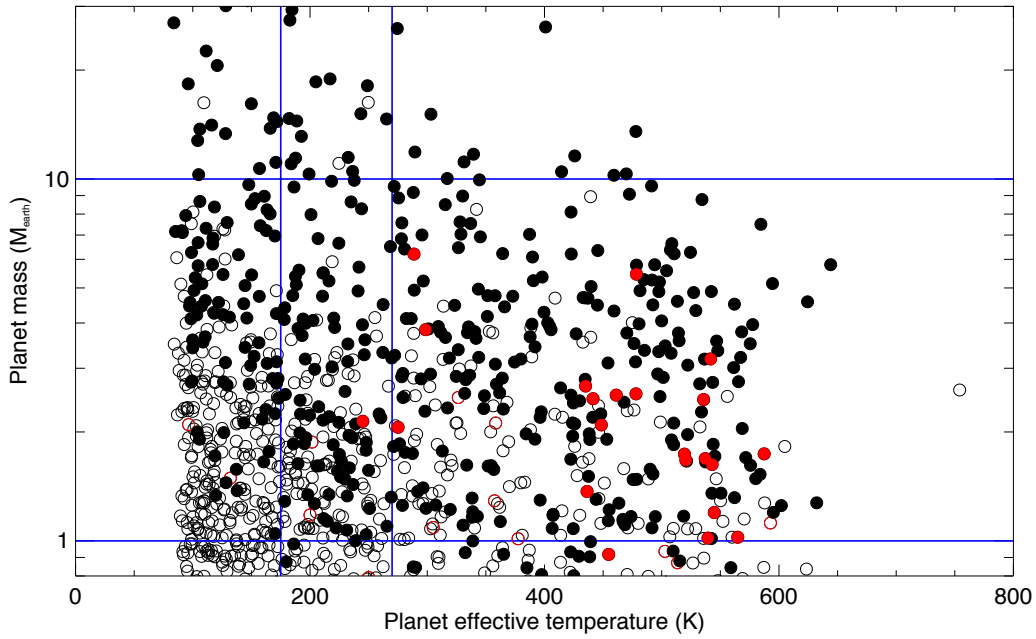

Fig. 3. Planets found with a 600-target survey according to our Monte Carlo simulation. Filled circled indicate detected planets, open circles undetected ones and red circles (both filled and open) represent transiting planets. Blue lines show notional limits for the habitable zone, both in mass and temperature. Most planets with >2 $M_\oplus$ in the habitable zone are detected, including one transiting. Interestingly, a sample of sub-$M_\oplus$ planets with T_{eq} >350 K is also detected.

with JWST or EChO.

3.2.3 Occurrence frequency of planets around M dwarfs

By expanding the sample by 10× (with respect to the existing optical surveys of M dwarfs) and thus by bringing a 3 fold improvement in the statistics of planet properties, the SPIRou observations outlined in the 2 first items of our planet search will provide much more reliable constraints on planet formation models. Moreover, by extending the RV monitoring on a selected sample of M dwarfs and on a larger time span, SPIRou will likely reveal additional bodies in most systems at larger period. This extended monitoring, not included in the first part of RV of our planet search, will be carried out on the ∼350 most interesting M dwarfs with detected planets / systems and will require an additional amount of 250 CFHT nights to achieve 40 more visits per star.

4 Main science goal #2 : magnetic fields and star / planet Formation

4.1 Scientific context

The other main goal of SPIRou is to explore the impact of magnetic fields on star and planet formation, by detecting and characterizing magnetic fields of various types of young stellar objects (e.g., classical T Tauri stars, embedded class-I protostars, young protostellar accretion discs). This quest will expand the pioneering surveys carried out in the framework of the study with optical spectropolarimeter, mainly ESPaDOnS@CFHT.

Studying how Sun-like stars and their planetary systems form comes as a logical addition to the direct observation of exoplanets. Within the last decades, this research field underwent major observational and theoretical advances, for instance by clarifying the crucial role of magnetic fields, not only on the gravitational collapse of giant molecular clouds (e.g., Hennebelle & Fromang 2008), but also on the formation of accretion discs and pre-stellar cores (e.g., Hennebelle & Teyssier 2008) from which stars and their planetary systems are born.

At an age of ∼1 Myr, low-mass protostars emerge from their dust cocoons, most often surrounded by a massive accretion disc in which planet form and migrate. This is the so-called “classical T Tauri” (cTTS or class-II protostar) stage - one of the best studied phase of stellar formation thanks to its relative accessibility to

existing instruments. Observations suggest in particular that magnetic fields of cTTSs are strong enough (i) to disrupt the central regions of the surrounding accretion discs, thereby generating magnetospheric gaps at the heart of the discs, (ii) to guide the plasma from the discs to the stars along discrete magnetospheric accretion funnels, and (iii) to drastically slow-down their rotation rates by magnetically coupling stellar surfaces with the inner edges of the accretion discs (e.g., Bouvier et al. 2007).

Spectropolarimetric observations secured with ESPaDOnS@CFHT enabled to disclose, for a small sample of ∼15 cTTSs, the large-scale magnetic topologies that link low-mass protostars to their accretion discs, and to demonstrate that this topology strongly relates to the internal structure of the protostar, and thus to both its age and mass (e.g., Donati et al. 2010). When the protostar is young enough and has a low-enough mass to be fully-convective, its large-scale magnetic topology is dominated by a strong dipolar-like field roughly aligned with the stellar rotation axis - thereby providing a quantitative explanation of the physical star/disc coupling mechanism through which the protostar is strongly spun down (e.g., Zanni & Ferreira 2013). These observations are however still rather sparse as a result of the relative faintness of cTTSs (at optical wavelengths); moreover, younger class-I protostars (with ages <1 Myr), for which magnetic fields are expected to have an even bigger evolutionary impact, are still out of reach of existing instruments, their dust cocoon hiding them completely from view at optical wavelengths.

4.2 The SPIRou survey of magnetic protostars

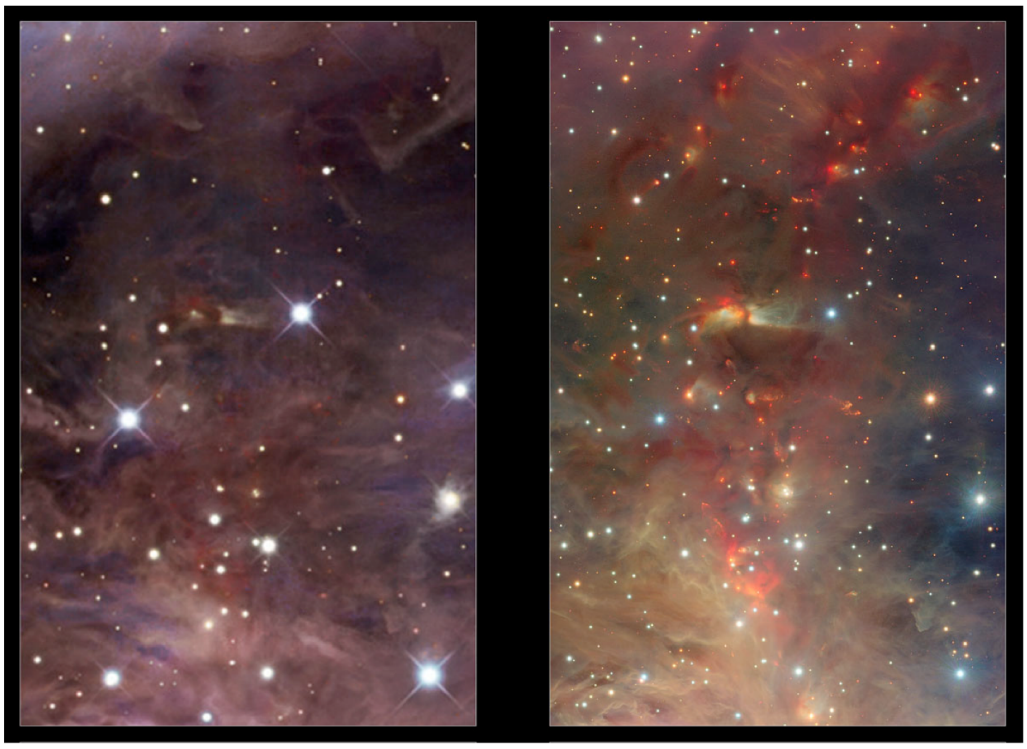

Fig. 4. The Orion nebula as seen in visible (left) and IR (right) light (ESO/VISTA). In the IR, dust cocoons around young stars are much more transparent.

With a much higher magnetic sensitivity than ESPaDOnS, thanks to both the increased nIR brightness of protostars (especially in K, see Fig 4) and the enhanced Zeeman effect at larger wavelengths, SPIRou will provide a much deeper and more systematic access to large-scale fields of class-I and -II protostars. More specifically, it will allow (i) to survey a 5-10× larger sample of cTTSs than the very limited one currently accessible with ESPaDOnS, and (ii) to extend for the first time this study to the brightest class-I protostars thanks to the K band coverage. The suggested SPIRou survey will ideally complement ALMA observations of pre-stellar (class-0) cores and of their magnetic fields, and will thus bring one of the key missing pieces in our understanding of star / planet formation.

SPIRou will also have the power to detect hot Jupiters orbiting around more-evolved class-III protostars (the so-called "weak-line T Tauri" stars or wTTSs) and thus to verify whether close-in giant planets are either much more or much less frequent around low-mass protostars than around mature, Gyr-old Sun-like stars. These observations will thus yield a direct observational test of the formation and migration of hot Jupiters, allowing to estimate the relative fraction produced through disc migration (acting during the formation stage) and that attributable to interactions / scattering (occurring much later). Finally, SPIRou will also be able to observe the innermost regions of protostellar accretion discs, out of reach of ALMA, to detect and characterize their magnetic fields and to identify the potential presence of migrating hot Jupiters (e.g., Donati et al. 2005; Powell et al. 2012).

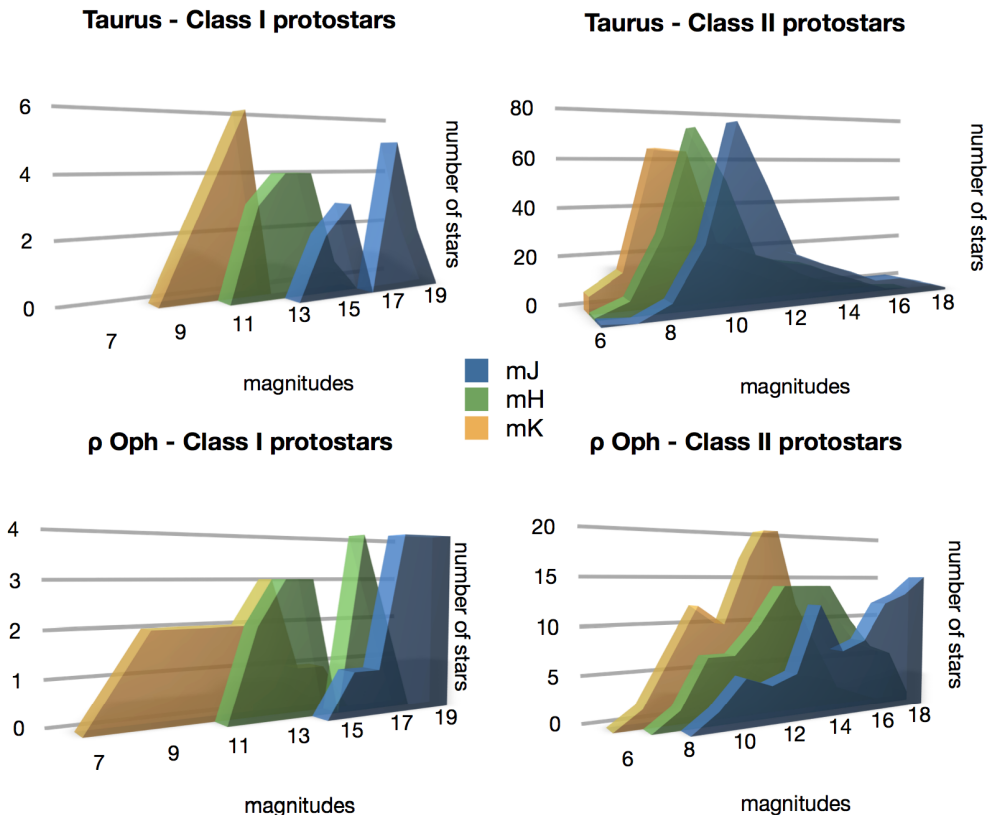

Fig. 5. JHK magnitude histograms of class-I (left) & -II (right) protostars in Taurus (up) and ρ Oph (bottom). Class-I protostars are mostly brighter than 12 in K only (as a result of obscuration, especially in ρ Oph), whereas a significant fraction of class-II protostars are accessible in all 3 bands.

With a survey carried out on 5 of the most accessible star forming regions (e.g., Taurus/Auriga, TW Hya Association, ρ Ophiuchius, Lupus, Orion Nebula Cluster; see Fig 5), SPIRou can detect for the first time the large-scale fields of ∼50 embedded class-I protostars, bringing yet unknown information on how magnetospheric accretion operates at so early a step in the formation process. In addition to this, SPIRou will be able to monitor ∼200 class-II and -III protostars (cTTSs and wTTSs), expanding the pioneering ESPaDOnS survey by 5-10× into full-scale surveys of magnetic protostars and their close-in giant planets. This survey will require a total of 250 CFHT nights; on top of this, monitoring a small sample of ∼10 protostellar accretion discs will require an additional 50 nights.

5 Additional science goals

In addition to the two main goals, SPIRou will be a very innovative and efficient instrument for tackling many more science themes. A few of them are briefly outlined below.

5.1 Large-scale dynamos of M-dwarfs

Using the spectropolarimetric data collected for the exoplanet survey of M dwarfs, SPIRou can also study the large-scale dynamo fields of fully convective dwarfs. These magnetic fields are indeed the main source of their activity and therefore a potential drawback for the habitability of their planets (Lecavelier des Etangs et al. 2012; Vidotto et al. 2013); studying dynamos of fully convective bodies can also be very informative on magnetic fields of Earth-like exoplanets (e.g., Christensen et al. 2009; Reiners & Christensen 2010) and usefully complement direct sensitive radio observations (e.g., LOFAR, Zarka 2010), with the ultimate aim of working out whether magnetic fields of exoplanets can improve their habitability.

Published studies of large-scale fields of fully-convective dwarfs have already demonstrated that these magnetic topologies are very sensitive to the aspect ratio of the convective zone and even suggest, for very-low mass dwarfs, a bistable behavior of the underlying dynamo processes potentially similar to that invoked for planetary dynamos (Morin et al. 2008, 2010, 2011). By comparing magnetic topologies of M dwarfs with theoretical predictions and results of numerical simulations, and by trying to generalize these results to planetary dynamos, one should ultimately be able to better understand the physical processes capable of amplifying and sustaining large-scale magnetic fields in both fully-convective dwarfs and planets (e.g., Schrinner et al. 2012). Using data from the exoplanet survey, SPIRou will provide a thorough census of magnetic topologies of M dwarfs (and in particular of fully-convective ones) that will usefully guide theorists towards more realistic, generalized dynamo models in better agreement with observations of both stellar and planetary large-scale fields.

5.2 Studies of planetary atmospheres

SPIRou can also very efficiently contribute to atmospheric studies of telluric or giant planets, whether or not they belong to the solar system.

In the case of the solar system, SPIRou will be able to carry out spatially-resolved, detailed spectroscopic studies of the chemical composition (at both low and high altitudes), of the wind dynamics and of the auroral emission of planetary atmospheres. These studies will allow in particular to better understand the complex interactions between atmospheric volatiles, planetary interiors, surfaces and climates (e.g., Bézard et al. 2009); they can also accurately estimate wind velocities at different atmospheric locations and altitudes, as well as their temporal variability (e.g., Widemann et al. 2008). Finally, auroral emission (and polarization) can inform on potential links between planetary atmospheres and magnetospheres. Thanks to its wide spectral domain (including the K band), to its high RV precision and to its spectropolarimetric capabilities, SPIRou will be able to very significantly contribute to chemical and dynamical studies of solar-system planet atmospheres.

Exoplanet atmospheres are obviously much more elusive and tricky to detect and to characterize. In the particular case of transiting exoplanets, atmospheres can be scrutinized either by transmission during a planetary transit, or by occultation during a planetary eclipse. For close-in planets (and in particular hot Jupiters), it could be possible to detect from the ground the spectral contribution of the star-lit side of the planet, by monitoring the Doppler shift (induced by the planet orbital motion) of specific atmospheric species (e.g., CO, Snellen et al. 2010). SPIRou will thus be able to contribute to this quest in a original way, thanks to its wide spectral domain and to the K band in particular (that includes a number of key atmospheric markers).

5.3 Weather patterns of brown dwarfs

Studying the atmospheres of ultra-cool L and T brown dwarfs (BDs) is yet another obvious research field for SPIRou. Despite huge modeling efforts invested since the discovery of BDs, many questions remain open - likely related to the complex physics of BDs atmospheres and in particular to mechanisms of dust clearing through specific weather patterns occurring in their atmospheres (e.g., Radigan et al. 2012). The disc-averaged spectral energy distribution (SED) of ultra-cool BDs may indeed not be representative of any single region, and thus cannot be modeled using a unique set of physical parameters (e.g., temperature, dust-settling, grain properties). Evidence that this is likely the case comes from the fact that ultra-cool BDs often exhibit photometric variability at a level of a few % up to a remarkable 25% (Artigau et al. 2009). This variability is apparently due to a combination of rotational modulation and intrinsic evolution on short timescales, likely caused by weather-like clearings in the dust- cloud deck (e.g., Littlefair et al. 2006). Unravelling the physics of these weather patterns and distinguishing between the several theoretical scenarios requires observations capable of localizing the dust clouds in BD atmospheres and following their rapid evolution with time.

Doppler imaging through high-resolution nIR spectroscopy is a very attractive and viable approach to map weather patterns of BDs; most BDs are indeed rapid rotators and often exhibit rotational modulation, both photometrically and spectroscopically, providing ideal conditions for Doppler imaging. Though not yet applied to stars cooler than mid-M due to their intrinsic faintness at optical wavelengths, Doppler imaging of BDs in the nIR is perfectly feasible with SPIRou, opening a new window for studying chemical inhomogeneities in their atmospheres. SPIRou will be able to monitor ∼10 L and T BDs among the best suited for this experiment, for a total amount of 30 nights.

6 The SPIRou Legacy Survey

The amount of observing time required to complete the two main science goal is large (1300 nights). In this context, SPIRou only makes sense if coupled to a SPIRou Legacy Survey of 500 CFHT nights on a timescale of ∼5 yr focussed mostly on both main science goals. The current plan is to divide the SPIRou Legacy Survey into three main components, two of them being dedicated to exoplanets around M dwarfs, while one will be concentrating on large-scale magnetic fields and young hot Jupiters of class-I-III protostars.

7 Calendar

SPIRou has successfully passed the preliminary design phase (PDR) in October 2012 and is now in the final design phase. Provided SPIRou is selected by CFHT and succeeds the upcoming final design review (FDR), it should be installed on the 3.6-m CFH telescope in early 2017 after the following phases :

- early 2014: design validation (FDR)
- 2014-2015: construction and acceptance tests of all individual SPIRou subsystems
- 2016: instrument integration and acceptance tests at IRAP
- 2017: installation at CFHT, first light, technical commissioning and science verification

We further stress that, with this schedule, SPIRou is ideally phased with the predicted launch times of both TESS and CHEOPS (2017) as well as that of JWST (2018).

References

Allard, F., Hauschildt, P. H., Alexander, D. R., & Starrfield, S. 1997, ARA&A, 35, 137

Artigau, É., Bouchard, S., Doyon, R., & Lafrenière, D. 2009, ApJ, 701, 1534

Bézard, B., Tsang, C. C. C., Carlson, R. W., et al. 2009, Journal of Geophysical Research (Planets), 114, 0

Bonfils, X., Delfosse, X., Udry, S., et al. 2013a, A&A, 549, A109

Bonfils, X., Lo Curto, G., Correia, A. C. M., et al. 2013b, A&A, 556, A110

Bouchy, F., Díaz, R. F., Hébrard, G., et al. 2013, A&A, 549, A49

Bouchy, F. & Sophie Team. 2006, in Tenth Anniversary of 51 Peg-b: Status of and prospects for hot Jupiter studies, ed. L. Arnold, F. Bouchy, & C. Moutou, 319–325

Bouvier, J., Alencar, S. H. P., Harries, T. J., Johns-Krull, C. M., & Romanova, M. M. 2007, Protostars and Planets V, 479

Charbonneau, D., Brown, T. M., Burrows, A., & Laughlin, G. 2007, Protostars and Planets V, 701

Christensen, U. R., Holzwarth, V., & Reiners, A. 2009, Nature, 457, 167

Delfosse, X., Bonfils, X., Forveille, T., et al. 2013, A&A, 553, A8

Deming, D., Seager, S., Winn, J., et al. 2009, PASP, 121, 952

Donati, J.-F. 2003, in Astronomical Society of the Pacific Conference Series, Vol. 307, Solar Polarization, ed. J. Trujillo-Bueno & J. Sanchez Almeida, 41

Donati, J.-F., Paletou, F., Bouvier, J., & Ferreira, J. 2005, Nature, 438, 466

Donati, J.-F., Skelly, M. B., Bouvier, J., et al. 2010, MNRAS, 409, 1347

Hennebelle, P. & Fromang, S. 2008, A&A, 477, 9

Hennebelle, P. & Teyssier, R. 2008, A&A, 477, 25

Ida, S. & Lin, D. N. C. 2005, ApJ, 626, 1045

Lecavelier des Etangs, A., Bourrier, V., Wheatley, P. J., et al. 2012, A&A, 543, L4
Littlefair, S. P., Dhillon, V. S., Marsh, T. R., Shahbaz, T., & Martín, E. L. 2006, MNRAS, 370, 1208
Mayor, M., Bonfils, X., Forveille, T., et al. 2009, A&A, 507, 487
Mayor, M., Pepe, F., Queloz, D., et al. 2003, The Messenger, 114, 20
Morin, J., Donati, J.-F., Petit, P., et al. 2008, MNRAS, 390, 567
Morin, J., Donati, J.-F., Petit, P., et al. 2010, MNRAS, 407, 2269
Morin, J., Dormy, E., Schrinner, M., & Donati, J.-F. 2011, MNRAS, 418, L133
Powell, S. L., Irwin, M., Bouvier, J., & Clarke, C. J. 2012, MNRAS, 426, 3315
Radigan, J., Jayawardhana, R., Lafrenière, D., et al. 2012, ApJ, 750, 105
Rauer, H., Gebauer, S., Paris, P. V., et al. 2011, A&A, 529, A8
Reiners, A. & Christensen, U. R. 2010, A&A, 522, A13
Santerne, A., Donati, J. F., Doyon, R., et al. 2013, These Proceedings
Schrinner, M., Petitdemange, L., & Dormy, E. 2012, ApJ, 752, 121
Snellen, I. A. G., de Kok, R. J., de Mooij, E. J. W., & Albrecht, S. 2010, Nature, 465, 1049
Udry, S., Bonfils, X., Delfosse, X., et al. 2007, A&A, 469, L43
Vidotto, A. A., Jardine, M., Morin, J., et al. 2013, A&A, 557, A67
Widemann, T., Lellouch, E., & Donati, J.-F. 2008, Planet. Space Sci., 56, 1320
Zanni, C. & Ferreira, J. 2013, A&A, 550, A99
Zarka, P. 2010, in Astronomical Society of the Pacific Conference Series, Vol. 430, Pathways Towards Habitable Planets, ed. V. Coudé du Foresto, D. M. Gelino, & I. Ribas, 175

SF2A 2013
L. Cambrésy, F. Martins, E. Nuss and A. Palacios (eds)

CHARACTERIZING SMALL PLANETS TRANSITING SMALL STARS WITH SPIROU

A. Santerne[1], J.-F. Donati[2], R. Doyon[3], X. Delfosse[4], E. Artigau[3], I. Boisse[1], X. Bonfils[4], F. Bouchy[5], G. Hébrard[6,7], C. Moutou[5,8], S. Udry[9] and the SPIRou science team

Abstract. SPIRou, a near infrared spectropolarimeter, is a project of new instrument to be mounted at the Canada France Hawaii Telescope in 2017. One of the main objectives of SPIRou is to reach a radial velocity accuracy better than 1 $m.s^{-1}$ in the YJHK bands. SPIRou will make a cornerstone into the characterization of Earth-like planets, where the exoplanet statistics is very low. This is even more true for planets transiting M dwarfs, since only 3 low-mass planets have been secured so far to transit such stars. We present here all the synergies that SPIRou will provide to and benefit from photometric transit-search programs from the ground or from space (*Kepler*, *CHEOPS*, *TESS*, *PLATO 2.0*). We also discuss the impact of SPIRou for the characterization of planets orbiting actives stars.

Keywords: transit; exoplanet; photometry; radial velocity, infrared spectroscopy

1 Introduction

As they pass in front of their host star, transiting exoplanets are providing us numerous key information to understand the diversity of planets in the galaxy. For these planets, it is possible to determine their mass and radius and thus their bulk density, needed to determine their nature (rocky, gazeus, water-world, etc...) and model their internal structure as well as their orbital configuration (orbital period, eccentricity, obliquity). This provides strong constraints to planet's formation, migration and evolution theories. Last but not least, transiting exoplanets are today the only targets to explore atmospheric composition from transmission spectroscopy during the transit.

Nearly 300 transiting planets have been confirmed so far with only a handful of terrestrial or very-low mass planets having an accurate determination of mass and radius (see Figure 1). To explore this regime of low-mass planets, small stars like M dwarfs are the most favorable for detection since they allow larger signals in both photometry (the depth of the transit scales as $1/R_\star^2$) and radial velocity (hereafter RV; the amplitude of the RV variation scales as $1/M_\star^{2/3}$). For example, for a planet in the habitable zone, the RV signal is seven times larger around a M dwarf than around a solar-type star (two effects combined: the habitable zone is closer to the stars and the mass of the star is lighter).

Since atmospheric characterization primarily requires deep transits on the one hand, and bright stars on the other hand (in the nIR, where absorption from atmospheric molecules mostly concentrates), M dwarfs are

[1] Centro de Astrofísica, Universidade do Porto, Rua das Estrelas, 4150-762 Porto, Portugal
[2] UPS-Toulouse / CNRS-INSU, Institut de Recherche en Astrophysique et Planétologie (IRAP) UMR 5277, Toulouse, F31400 France
[3] Département de physique and Observatoire du Mont Mégantic, Université de Montréal, C.P. 6128, Succursale Centre-Ville, Montréal, QC H3C 3J7, Canada
[4] UJF-Grenoble 1/CNRS-INSU, Institut de Planétologie et d'Astrophysique de Grenoble (IPAG) UMR 5274, 38041 Grenoble, France
[5] Aix Marseille Université, CNRS, LAM (Laboratoire d'Astrophysique de Marseille) UMR 7326, 13388 Marseille, France
[6] Institut dAstrophysique de Paris, CNRS, Université Pierre et Marie Curie, 98bis Bd. Arago, 75014 Paris, France
[7] Observatoire de Haute-Provence, CNRS/OAMP, 04870 Saint-Michel-l'Observatoire, France
[8] CNRS, Canada-France-Hawaii Telescope Corporation, 65-1238 Mamalahoa Hwy., Kamuela, HI 96743, USA
[9] Observatoire de Genève, Université de Genève, 51 chemin des Maillettes, Sauverny 1290, Switzerland

therefore optimal targets for this quest. Detailed simulations show that atmospheric components of Earth-like extrasolar planets will produce a detectable signal for planets around M dwarfs planets using JWST/NASA and/or ELTs, but not for similar planets around Sun-like stars (e.g. Rauer et al. 2011; Tinetti et al. 2012). Today, only a handful of very-bright transiting systems have been discovered. A prime goal of astronomy is to discover other Earths and super-Earths whose atmosphere can be scrutinized and characterized with space missions (such as JWST) in the next decade, including the search for biomarkers.

Dedicated searches for planets around M dwarfs in radial velocity have been performed for years (e.g. Delfosse et al. 1998; Marcy et al. 1998, 2001, with the HiReS and HARPS spectrographs) unveiling ~ 10 very low-mass planets (e.g. Rivera et al. 2005), including super-earths in the habitable zone of Gl 581(Mayor et al. 2009), Gl 667C (Delfosse et al. 2013; Feroz & Hobson 2013) and Gl 163 (Bonfils et al. 2013b). Very importantly, these surveys also revealed that small planets are very common around small stars, and that, $41\%^{+54\%}_{-13\%}$ of the M dwarfs harbor a super-earth planet in the habitable zone (Bonfils et al. 2013a). Among the planets found around M dwarfs in RV surveys, only two have been found to transit their host star: GJ 436 b (Butler et al. 2004; Gillon et al. 2007) and GJ 3470 b (Bonfils et al. 2012). The Mearth ground-based photometric survey dedicated to M dwarfs reported a third super-Earth with measured mass and radius: GJ 1214 b (Charbonneau et al. 2009). All of them present a bulk density close to Neptune's density (see Fig. 1). A giant planet transiting a M dwarf has been characterized among the *Kepler* candidates by Johnson et al. (2012), totalizing only four fully-characterized planets known to transit M dwarfs.

To improve the statistics on this population of planets and to discover the prime targets for mission dedicated to extra-solar planet's atmospheric characterization, it is very important to characterize many more planets transiting nearby M dwarfs. Since M dwarfs are quite faint in the optical but luminous in the infrared, such studies are much more efficient with infrared facilities.

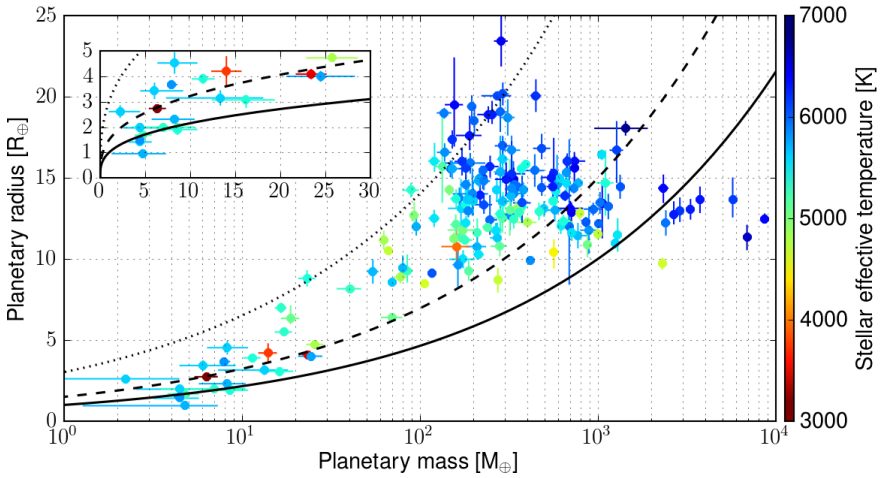

Fig. 1. Mass-radius diagram of transiting exoplanets discovered so far. The colors display the effective temperature of the host stars. The inset is a zoom to the transiting super-Earths. Only a few small planets have been characterized around small stars (here displayed in red). The solid, dashed and dotted lines display the density of the Earth, Neptune and of 0.2 g.cm^{-3} (respectively).

2 The SPIRou spectrograph

The SPIRou spectrograph (SpectroPolarimètre Infra-Rouge) is a project for a near infrared spectropolarimeter that will be mounted at the 3.6-m Canada France Hawaii Telescope (CFHT) in 2017. The main goals of this unique spectropolarimeter will be both to search for habitable exo-Earths orbiting low-mass & very-low mass stars using high-accuracy RV (better than 1 m.s^{-1}) and to explore the impact of magnetic fields on star & planet formation, by detecting magnetic fields of various types of young stellar objects and by characterizing their large-scale topologies (Artigau et al. 2011). This spectropolarimeter will be a high-resolution (R $\sim$ 75

000) stabilized spectrograph covering a spectral range between 0.98 μm and 2.35 μm (i.e. YJHK photometric bands) with a large throughput (up to 15%). Thanks to its large throughput, SPIRou will be able to provide spectrum with a signal-to-noise ratio (SNR) of $\sim$ 110 per pixel in one hour on a star of magnitude J = 12 or K = 11. SPIRou is expected to reach a photon noise of 1m.s^{-1} with a SNR of 160. Therefore SPIRou will be the best instrument for RV studies of M dwarfs, especially in the context of transiting planet surveys.

3 Current and future transiting planet surveys

Current and future (optical or infrared) photometric surveys are targeting M dwarfs to find new transiting planets. Ground-based nIR spectroscopy is essential in this context: spectroscopy is indeed mandatory to establish the planetary nature of all transiting objects detected around low-mass dwarfs through photometric monitoring (and discard false detections, e.g., caused by background eclipsing binaries ; Santerne et al. 2012) and to measure their mass from the RV amplitude of their host dwarfs orbital motion. SPIRou will also detect planets in a dedicated M-dwarf RV survey, that will be after search for transits by ground- or space-based observatories.

3.1 Kepler

The *Kepler* space telescope (Borucki et al. 2009) detected 95 planet candidates (the so-called Kepler Objects of Interest, i.e. KOIs) transiting M dwarfs (Dressing & Charbonneau 2013) with more than 2000 planet candidates (Batalha et al. 2013) transiting FGK stars. These KOIs present radii in the range 0.5 R$_\oplus$ – 17 R$_\oplus$ and orbital periods in the range 0.5 – 82 days. Most of them have a radius similar to the one of the Earth. Assuming bulk densities from the solar system planets (Neptune's density for planet candidates larger than 2.5 R$_\oplus$ and the Earth density for those smaller than 2.5 R$_\oplus$), it is possible to estimate their RV semi-amplitude. Figure 2 displays this expected RV amplitude, as function of the J magnitude of the host star. The majority of these KOIs are expected to present a RV semi-amplitude larger than 1 m.s^{-1}. Radial velocity follow-up have been initiated with optical facilities (e.g. with SOPHIE, HiReS, HARPS-N) but no low-mass planet has been characterized yet. Observations with an infrared spectrograph, like SPIRou, would be much more efficient. If SPIRou was already built, it would already be able to characterize new small planets transiting the smallest *Kepler* stars. However, since the *Kepler* targets are faint, this would required a lot of telescope time.

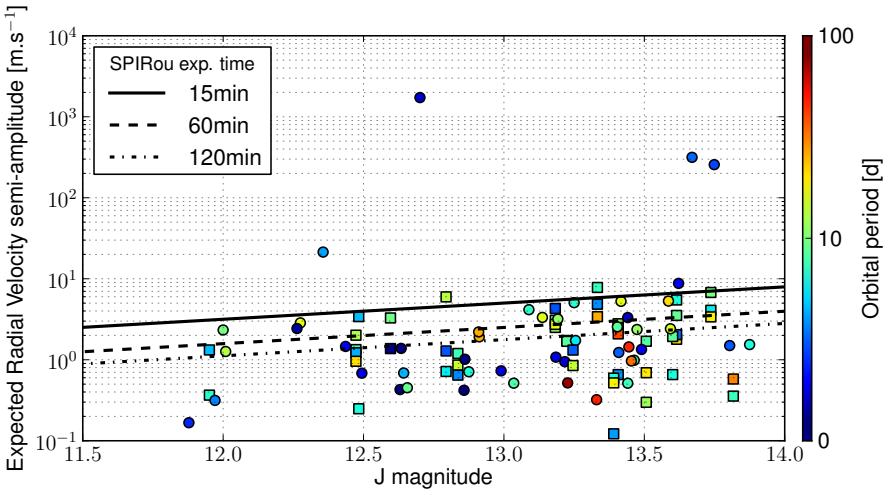

Fig. 2. Expected radial velocity semi-amplitude of the 95 KOIs from Dressing & Charbonneau (2013) as function of the J magnitude of their host star. The color of the mark indicates the orbital period of the candidate, while their shape indicates the multiplicity of the system: circles for single-planet candidates and squares for multiple-planetary systems. The black solid, dashed and dot-dashed lines indicate the RV accuracy that SPIRou will reach in 15 minutes, 1 hour and 2 hours (respectively) of exposure time.

3.2 Ground-based dedicated M dwarf surveys

Several ground-based photometric surveys are only targeting M dwarfs to detect small transiting planets. For example, the Mearth observatory was used to discover the transiting mini-Neptune GJ 1214 b (Charbonneau et al. 2009). Other similar facilities are in preparation, such as ExTrA, Apache and Speculoos. For example, the ExTrA (Exoplanets in Transit and their Atmospheres) infrared observatory that will start observations in 2015 and is expected to discover nearly 50 new small planets (down to 0.5 $R_\oplus$) transiting bright M dwarfs (Bonfils, private communication). The infrared spectrograph SPIRou will be able to characterize these new transiting planets with a better efficiency than other optical facilities. Moreover, those ground-based observatory will be able to perform a photometric follow-up of the new planets that SPIRou will detect as part of the RV survey.

3.3 TESS

TESS (Transiting Exoplanet Survey Satellite) is a all-sky space-based photometric survey of all stars brighter than V magnitude of 12 (Ricker et al. 2010) and M-dwarfs until V=13 (Charbonneau, private communication) that will be launched in 2017. This survey will therefore include numerous M dwarfs. *TESS* is expected to detect more than 300 earth and super-earth transiting bright stars*. The vast majority of them will orbit around M dwarfs due to the deeper signal for smaller stars. Since (i) most Earths and super-Earths detected with TESS will orbit around M dwarfs, and (ii) less than $\sim 30\%$ of them will be accessible to optical RV follow-up (Deming et al. 2009), SPIRou will be the best RV instrument to monitor in the near infrared the ~ 150 best candidates visible from CFHT (assuming ~ 60 visits per star and spectra SNR of ~ 160 per visit, this observational effort will represent a total of 150 CFHT nights).

3.4 PLATO 2.0

PLATO 2.0 (PLAnetary Transit and Oscillations of stars; Rauer et al., 2013) is a M3 mission candidate to the ESA Cosmic Vision program. If selected, *PLATO 2.0* will operate from 2024 to 2031+. Its main objective is to detect transiting planets out to the habitable zone of bright Sun-like stars and to characterize the host star simultaneously through asteroseismology. Since they orbit bright stars, those planets will be more easily characterizable with ground-based spectrographs than the much fainter *Kepler* targets. With *PLATO 2.0*, it will be possible de measure the density of planets with an unprecedented accuracy. Like *TESS*, *PLATO 2.0* will observe thousands of bright M dwarfs but will deeper probe their planet population, towards smaller planets and longer orbital periods (even longer than the habitable zone of early-M dwarfs). To characterize these unique planets that only *PLATO 2.0* will be able to find, infrared spectrographs like SPIRou are needed.

3.5 Synergies with CHEOPS

CHEOPS (CHaracterising ExOPlanets Satellite Broeg et al. 2013) is the first S-class mission selected by ESA in its Cosmic Vision Program. The objective of this space mission is to detect new transiting planets around bright stars by performing a photometric follow-up of known planets detected by RV surveys. In operation between 2017 and 2021, *CHEOPS* will be able to observe photometrically the first planets detected by SPIRou as part of its RV survey.

4 SPIRou and stellar activity

Stellar activity is one of the main limitation to the characterization of transiting planets (e.g. Hartman et al. 2011). The case of CoRoT-7 (Léger et al. 2009) is a good illustration of this limitation in the context of the characterization of small planets around active stars (for a complete view of the saga about the mass of CoRoT-7 b, see: Queloz et al. 2009; Lanza et al. 2010; Hatzes et al. 2010; Pont et al. 2011; Boisse et al. 2011; Ferraz-Mello et al. 2011; Hatzes et al. 2011). To better disentangle stellar activity from the planetary signal in CoRoT-7 b, new data from *CoRoT* and HARPS have been obtained simultaneously and will be discussed in Haywood et al. (submitted), Barros et al. (in prep.), Hatzes et al. (in prep.) and Lanza et al. (in prep.). A similar configuration have been discussed in the case of Alpha Cen Bb where the stellar activity signal is larger

*http://science.nasa.gov/media/medialibrary/2013/04/22/secure-RICKER-TESS_NASA_APS_17Apr2013_NoVideo_v4-1.pdf

than the planetary one (Dumusque et al. 2012; Hatzes 2013).

By observing in the infrared, SPIRou is expected to be less sensitive to stellar activity since the contrast between the photosphere and the spots is smaller in the infrared than in the optical (Martín et al. 2006; Prato et al. 2008). A few observations with SPIRou will therefore help to better model stellar activity and better constrain planetary masses detected with current spectrographs (e.g. HiReS, HARPS, HARPS-N, SOPHIE) or future ones (e.g. ESPRESSO, APF). Furthermore, since SPIRou is designed as a spectropolarimeter to study the magnetic fields of stars, it will be a powerful facility to understand stellar activity of stars (e.g. Morin et al. 2008, 2010, 2011) and to constrain exoplanetary masses orbiting actives FGKM type stars.

5 Conclusions and discussion

SPIRou will be a pioneer high-resolution spectropolarimeter to reach a radial velocity accuracy better than 1 m.s^{-1} in the infrared (YJHK bands). This will be a cornerstone for the studies of extrasolar planets around M dwarfs (especially for those in transit) in a domain where the statistics is very low: only $\sim$ 10 low-mass planets known to orbit M dwarfs, including 3 in transit. The new SPIRou instrument will have strong synergies with current and future photometric ground-based observatories (e.g. Mearth, ExTrA) and space missions (*Kepler*, *CHEOPS*, *TESS*, *PLATO 2.0*), being the most efficient spectrograph to characterize the mass of planets orbiting M dwarfs. The observations that SPIRou will perform will be extremely useful for planet formation, migration and evolution theories, as well as to provide fully-characterized planets as key targets for future atmospheric characterization with, e.g. *JWST*, *ECHO* from space and the E-ELT from the ground.

In a more general context (i.e. not limited to M dwarfs studies), SPIRou will also support the characterization of new planets orbiting actives stars that will be in the scope of spectrographs like SOPHIE, HARPS, HARPS-N, ESPRESSO, APF, etc...

AS acknowledges the support by the European Research Council/European Community under the FP7 through Starting Grant agreement number 239953. AS is also grateful to the administrative council of SF2A for providing him a grant to attend the 2013's annual meeting.

References

Artigau, É., Donati, J.-F., & Delfosse, X. 2011, 16th Cambridge Workshop on Cool Stars, Stellar Systems, and the Sun, 448, 771

Batalha, N. M., Rowe, J. F., Bryson, S. T., et al. 2013, ApJS, 204, 24

Boisse, I., Bouchy, F., Hébrard, G., et al. 2011, A&A, 528, A4

Bonfils, X., Gillon, M., Udry, S., et al. 2012, A&A, 546, A27

Bonfils, X., Delfosse, X., Udry, S., et al. 2013a, A&A, 549, A109

Bonfils, X., Lo Curto, G., Correia, A. C. M., et al. 2013b, A&A, 556, A110

Borucki, W. J., Koch, D., Jenkins, J., et al. 2009, Science, 325, 709

Broeg, C., Fortier, A., Ehrenreich, D., et al. 2013, European Physical Journal Web of Conferences, 47, 3005

Butler, R. P., Vogt, S. S., Marcy, G. W., et al. 2004, ApJ, 617, 580

Charbonneau, D., Berta, Z. K., Irwin, J., et al. 2009, Nature, 462, 891

Delfosse, X., Forveille, T., Mayor, M., et al. 1998, A&A, 338, L67

Delfosse, X., Bonfils, X., Forveille, T., et al. 2013, A&A, 553, A8

Deming, D., Seager, S., Winn, J., et al. 2009, PASP, 121, 952

Dressing, C. D., & Charbonneau, D. 2013, ApJ, 767, 95

Dumusque, X., Pepe, F., Lovis, C., et al. 2012, Nature, 491, 207

Feroz, F., & Hobson, M. 2013, arXiv:1307.6984

Ferraz-Mello, S., Tadeu Dos Santos, M., Beaugé, C., Michtchenko, T. A., & Rodríguez, A. 2011, A&A, 531, A161

Gillon, M., Pont, F., Demory, B.-O., et al. 2007, A&A, 472, L13

Hartman, J. D., Bakos, G. Á., Torres, G., et al. 2011, ApJ, 742, 59

Hatzes, A. P., Dvorak, R., Wuchterl, G., et al. 2010, A&A, 520, A93

Hatzes, A. P., Fridlund, M., Nachmani, G., et al. 2011, ApJ, 743, 75

Hatzes, A. P. 2013, ApJ, 770, 133
Johnson, J. A., Gazak, J. Z., Apps, K., et al. 2012, AJ, 143, 111
Lanza, A. F., Bonomo, A. S., Moutou, C., et al. 2010, A&A, 520, A53
Léger, A., Rouan, D., Schneider, J., et al. 2009, A&A, 506, 287
Marcy, G. W., Butler, R. P., Vogt, S. S., Fischer, D., & Lissauer, J. J. 1998, ApJ, 505, L147
Marcy, G. W., Butler, R. P., Fischer, D., et al. 2001, ApJ, 556, 296
Mayor, M., Bonfils, X., Forveille, T., et al. 2009, A&A, 507, 487
Martín, E. L., Guenther, E., Zapatero Osorio, M. R., Bouy, H., & Wainscoat, R. 2006, ApJ, 644, L75
Morin, J., Donati, J.-F., Petit, P., et al. 2008, MNRAS, 390, 567
Morin, J., Donati, J.-F., Petit, P., et al. 2010, MNRAS, 407, 2269
Morin, J., Dormy, E., Schrinner, M., & Donati, J.-F. 2011, MNRAS, 418, L133
Pont, F., Aigrain, S., & Zucker, S. 2011, MNRAS, 411, 1953
Prato, L., Huerta, M., Johns-Krull, C. M., et al. 2008, ApJ, 687, L103
Queloz, D., Bouchy, F., Moutou, C., et al. 2009, A&A, 506, 303
Rauer, H., Gebauer, S., Paris, P. V., et al. 2011, A&A, 529, A8
Ricker, G. R., Latham, D. W., Vanderspek, R. K., et al. 2010, Bulletin of the American Astronomical Society, 42, #450.06
Rivera, E. J., Lissauer, J. J., Butler, R. P., et al. 2005, ApJ, 634, 625
Santerne, A., Díaz, R. F., Moutou, C., et al. 2012, A&A, 545, A76
Tinetti, G., Beaulieu, J. P., Henning, T., et al. 2012, Experimental Astronomy, 34, 311

Session 18

Atelier PNCG : IR galaxies

SF2A 2013
L. Cambrésy, F. Martins, E. Nuss and A. Palacios (eds)

NEW RESULTS FROM THE HERSCHEL REFERENCE SURVEY

A. Boselli[1]

Abstract. The *Herschel* Reference Survey is a SPIRE guaranteed time key project aimed at studying the properties of the interstellar medium of a K-band selected, volume-limited ($15 \leq D \leq 25$ Mpc) complete sample of 322 galaxies spanning a large range in morphological type and stellar mass. We study the far infrared colours of the late-type galaxies of the cluster with the purpose of tracing with an empirical approach the relationships between the shape of the observed spectral energy distribution (SED) and different physical parameters such as the star formation rate, the birthrate parameter (or specific star formation rate), here taken as a tracer of the hardness of the inciding radiation, the intensity of the ionising and non ionising radiation, the metallicity and the Hα and FUV attenuation. We also show that the far infrared shape of the SED cannot be fitted with a modified black body with a fixed grain emissivity parameter β. All this analysis is a brief summary of a work presented in Boselli et al. (2012).

Keywords: Galaxies: ISM; dust; spiral; Infrared: galaxies

1 Introduction

Dust plays a major role in the matter cycle within galaxies. Formed by the aggregation of metals produced and injected into the interstellar medium (ISM) by stars during their evolution, dust is heated by the stellar radiation and re-emits in the infrared spectral domain. Dust is important in the process of star formation because acts as catalyst in the formation of molecular hydrogen inside giant molecular clouds, where star formation takes place. At the same time, absorbing the stellar radiation, and in particular the one emitted by the youngest, massive stars, its infrared radiation can be used as a direct tracer of star formation. The far infrared emission is also of paramount importance for quantyfing the amount of dust attenuation, and is thus necessary in the study of the different stellar populations in galaxies (e.g. Boselli (2011)).
With the purpose of studying the physical properties of the ISM of galaxies of different type and luminosity, the SPIRE extragalactic consortium has defined a guaranteed time key project, the *Herschel* Reference Survey (HRS), to observe 322 nearby galaxies in the bands at 250, 350 and 500 μm (Boselli et al. (2010)). The HRS is a complete, K-band selected, volume-limited ($15 \leq D \leq 25$ Mpc) sample suitable for any kind of statistical study. The SPIRE data of the HRS sample have been presented in Ciesla et al. (2012). We present here the most recent scientific results based on the analysis of the SPIRE data, in particular those relative to the far infrared colours of late-type galaxies. To avoid any possible effect related to the interaction of galaxies with the surrounding environment, we limit our analysis to unperturbed galaxies selected according to their HI-deficiency parameter $HI-def \leq 0.4$ (see Boselli & Gavazzi (2006) for the definition and the scientific interpretation of this parameter). These results have been recently published in Boselli et al. (2012) and Boselli et al. (2010). This work takes benefit from the large amount of multifrequency data that the team has acquired in these last years which are critical for defining the physical properties of the observed galaxies. These include gas metallicities obtained from integrated spectroscopy (Hughes et al. 2013; Boselli et al. 2013), atomic and molecular gas data (Boselli et al. 2013b), GALEX UV and optical photometry (Boselli et al. 2011; Cortese et al. 2012a), Halpha imaging (Boselli et al., in prep.). Most of these data have been made available to the community through our dedicated database at http://hedam.lam.fr/. Other interesting results on the analysis of the HRS far infrared data can be found in Cortese et al. (2010), Sauvage et al. (2010), Pohlen et al. (2010), Gomez et al. (2010), Eales et al. (2010), Boquien et al. (2012), Cortese et al. (2012b), Smith et al. (2012), Eales et al. (2012), and Boquien et al. (2013).

[1] Aix Marseille Université, CNRS, LAM (Laboratoire d'Astrophysique de Marseille) UMR 7326, 13388, Marseille, France

2 The far infrared colours of normal galaxies

The multifrequency data in our hands allow us to define several physical variables to characterise the properties of the HRS galaxies. These variables are the star formation rate SFR, determined as in Boselli et al. (2009), the birthrate parameter b (Boselli et al. 2001) here taken as a tracer of the hardness of the inciding radiation, the Hα surface brightness, tracer of the density of the ionising radiation, the H-band effective surface brightness $\mu_e(H)$, tracer of the density of the general interstellar radiation field, the metallicity 12 + log(O/H) and the Hα $A(H\alpha)$ and FUV $A(FUV)$ attenuation, this last determined as in Cortese et al. (2008). Figure 1 shows the relationship between different far infrared colours, defined as the ratio of the far infrared flux densities measured in different bands, and these different physical parameters.
The widely used $S60/S100$ IRAS colour is often adopted as a direct tracer of the starburst activity of the target galaxies. This index is sensitive to the emission of the warm dust component principally heated by young stars and is thus a *warm dust sensitive index*. The colour indices $S60/S250$, $S100/S250$ and $S100/S500$ are sensitive to the relative weight of the warm and cold dust component since the peak of the emission of normal, star forming galaxies such as those analysed in this work lies in between 100 and 200 μm, thus in between the two photometric bands used to define these indices. They are related to the wavelength position of the peak of the dust emission, and are thus *dust peak sensitive indices*. The SPIRE colour indices $S250/S350$, $S250/S500$ and $S350/S500$ are indices tracing the emitting properties of the coldest dust component (*cold dust sensitive indices*). Indeed they sample the Rayleigh-Jeans tail of the dust emission dominating in mass in normal galaxies.

Figure 1 shows that the warm dust sensitive index $S60/S100$ is not related to the direct tracers of the star formation activity (SFR, $\Sigma(H\alpha)$), while it is only correlated to the birthrate parameter b. Galaxies still active in forming stars at the present epoch ($b \geq 1$) have, on average, $S60/S100$ flux density ratios ($S60/S100 \simeq 0.6$) slightly larger than quiescent objects ($b \leq 1$; $S60/S100 \simeq 0.4$). This indicates that, whenever integrated values are used, the contribution of the warm dust component to the total emission of late-type galaxies is principally controlled by the history of star formation (or the hardness of the radiation field) rather than by the present day activity. Figure 1 also shows poorly defined and dispersed relations between the peak sensitive $S100/S500$, $S100/S250$ and $S60/S250$ colour indices and the surface brightness of the ionising ($\Sigma(H\alpha)$) and non-ionising ($\mu_e(H)$) interstellar radiation field and the FUV attenuation ($A(FUV)$). Among these colour indices, only $S60/S250$ and $S100/S250$ correlate very mildly with the birthrate parameter. This evidence suggests that the position of the peak of the dust emission, or in other words the mean temperature of the dust, is governed, as expected, by the general interstellar radiation field. We also see strong correlations between the cold dust sensitive $S250/S350$ and $S250/S500$ colour indices and $\Sigma(H\alpha)$, $\mu_e(H)$ and $A(FUV)$. Warmer colours are observed in those galaxies with higher radiation fields and higher extinction. The same colour indices are only barely related to the present day star formation activity and the metallicity. Again, these plots indicate that the emission of the cold dust component is also controlled by the general interstellar radiation field and partly by the metallicity. What is surprising, however, is that the correlations with these cold dust sensitive indices are significantly stronger than with the peak sensitive indices which are sampling a warmer dust component. The first presentation of these results and their interpretation are extensively given in Boselli et al. (2012).

The relationships observed between the different far infrared colour indices can be due either to variations of the mean temperature of the emitting dust or to variations in the dust grain emissivity properties that might change in different types of galaxies. Assuming that dust grains are in thermal equilibrium with the radiation, which is probably the case for $\lambda \geq 250$ μm, the far infrared emission of galaxies is generally approximated by one (or more) modified black body $B(\nu, T)$, with a resulting emitted flux density:

$$S_{dust}(\nu, T) \propto \nu^{\beta} B(\nu, T) \tag{2.1}$$

where β is the grain emissivity index whose value ranges between ~ 1.5 and ~ 2 (Hildebrand 1983). Although not physical, this simple analytical prescription is often used both in extragalactic and cosmological studies since it reproduces fairly well the observed far infrared spectral energy distributions of galaxies. Our new homogeneous and complete set of data, in particular those obtained by SPIRE in the spectral domain 250-500 μm, can be used to see whether this simple modified black body assumption is realistic. At the same time this dataset can help us to understand which of the two main parameters regulating the dust emissivity, the grain emissivity index β or the dust temperature T, is the main driver of the observed colour-colour far infrared relations and for their scatter. To this aim we plot in Fig. 2 the SPIRE colour-colour indices $S250/S350$ vs. $S350/S500$ for galaxies coded according to the different physical parameters already used in the previous figure

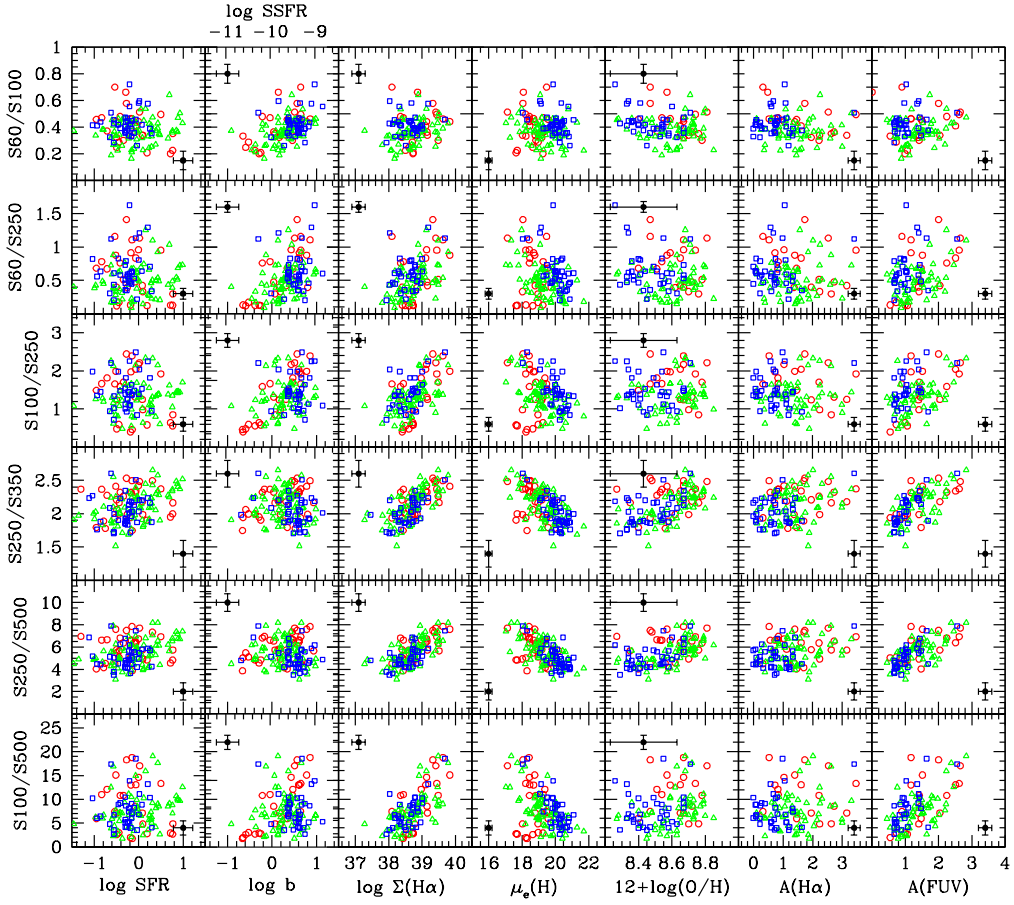

Fig. 1. The relationship between the far infrared colour indices and different tracers of the physical properties of the interstellar medium, from left to right: first column: the logarithm of the star formation rate (in $M_{\odot}yr^{-1}$) measured as described in Boselli et al. (2009); second column: the logarithm of the birthrate parameter b (or the specific star formation rate $SSFR$); third column: the logarithm of the Hα effective surface brightness (in erg s^{-1} kpc^{-2}); fourth column: the H-band effective surface brightness (in AB mag $arcsec^{-2}$); fifth column: the metallicity index 12+log(O/H); sixth column: the Balmer extinction $A(H\alpha)$ (in magnitudes); seventh column: the FUV attenuation $A(FUV)$ (in magnitudes). Red open circles for Sa-Sb, green empty triangles for Sbc-Scd and blue open squares for Sd-Im-BCD. The typical error bar is indicated with a black symbol (from Boselli et al. (2012)).

and compare them to the expected values obtained for a modified black body with a grain emissivity index β = 2 (solid line) and β = 1.5 (dotted line). Clearly, the observed relations can not be represented by a modified black body with a dust grain emissivity index of β = 2, but are better reproduced when β = 1.5.

The observed relationship between the two colour indices has a slope slightly flatter than the one predicted by a single modified black body of fixed grain emissivity index. We can thus not exclude values of $\beta > 1.5$ in galaxies with the highest flux density ratios. Similarly, in the objects with the lowest flux density ratios, β might be < 1.5. This evidence might indicate that both β and T vary along the sequence. Indeed, there is a quite strong degeneracy between β and T given that at these low temperatures a variation of T of $\sim$ 5 K is almost equivalent to a variation of β of $\sim$ 0.5. Furthermore, we have to remember that β and T might also be inversely correlated (Désert et al. 2008; Shetty et al. 2009; Veneziani et al. 2010; Anderson et al. 2010; Bracco et al. 2011).

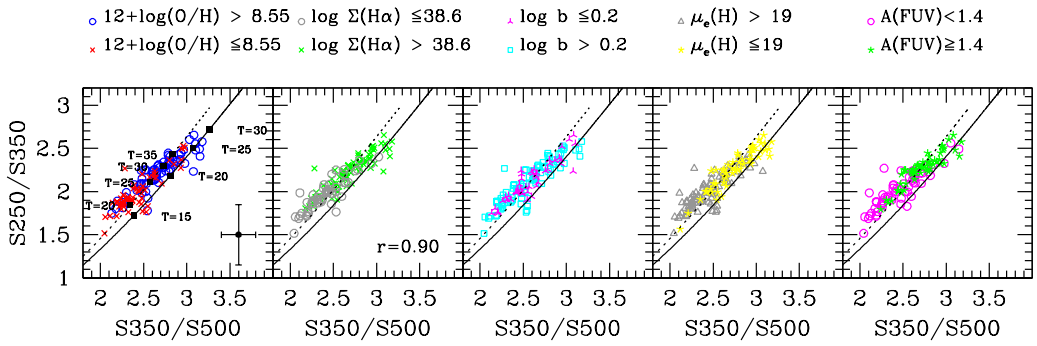

Fig. 2. The relationship between the SPIRE colour-colour indices $S250/S350$ vs. $S350/S500$ for galaxies coded according to their different physical parameters (from Boselli et al. (2012)). The colour-colour relation is compared to the expected relations obtained for a modified black body with a grain emissivity index $\beta = 2$ (solid line) and $\beta = 1.5$ (dotted line). Black squares indicate different temperatures for the two modified black bodies (left panel). The Spearman correlation coefficient of this relation is r=0.90.

This work is done on behalf of the SPIRE extragalactic working group, which includes more than 50 astronomers from different world institutes. *Herschel* is an ESA space observatory with science instruments provided by European-led Principal Investigator consortia and with important participation from NASA.

References

Anderson, L. D., Zavagno, A., Rodón, J. A., et al. 2010, A&A, 518, L99
Boquien, M., Boselli, A., Buat, V., et al. 2013, A&A, 554, A14
Boquien, M., Buat, V., Boselli, A., et al. 2012, A&A, 539, A145
Boselli, A. 2011, A Panchromatic View of Galaxies
Boselli, A., Boissier, S., Cortese, L., et al. 2009, ApJ, 706, 1527
Boselli, A., Boissier, S., Heinis, S., et al. 2011, A&A, 528, A107
Boselli, A., Ciesla, L., Cortese, L., et al. 2012, A&A, 540, A54
Boselli, A., Eales, S., Cortese, L., et al. 2010, PASP, 122, 261
Boselli, A. & Gavazzi, G. 2006, PASP, 118, 517
Boselli, A., Gavazzi, G., Donas, J., & Scodeggio, M. 2001, AJ, 121, 753
Boselli, A., Hughes, T. M., Cortese, L., Gavazzi, G., & Buat, V. 2013, A&A, 550, A114
Bracco, A., Cooray, A., Veneziani, M., et al. 2011, MNRAS, 412, 1151
Ciesla, L., Boselli, A., Smith, M. W. L., et al. 2012, A&A, 543, A161
Cortese, L., Bendo, G. J., Boselli, A., et al. 2010, A&A, 518, L63
Cortese, L., Boissier, S., Boselli, A., et al. 2012a, A&A, 544, A101
Cortese, L., Boselli, A., Franzetti, P., et al. 2008, MNRAS, 386, 1157
Cortese, L., Ciesla, L., Boselli, A., et al. 2012b, A&A, 540, A52
Désert, F.-X., Macías-Pérez, J. F., Mayet, F., et al. 2008, A&A, 481, 411
Eales, S., Smith, M. W. L., Auld, R., et al. 2012, ApJ, 761, 168
Eales, S. A., Smith, M. W. L., Wilson, C. D., et al. 2010, A&A, 518, L62
Gomez, H. L., Baes, M., Cortese, L., et al. 2010, A&A, 518, L45
Hildebrand, R. H. 1983, QJRAS, 24, 267
Hughes, T. M., Cortese, L., Boselli, A., Gavazzi, G., & Davies, J. I. 2013, A&A, 550, A115
Pohlen, M., Cortese, L., Smith, M. W. L., et al. 2010, A&A, 518, L72
Sauvage, M., Sacchi, N., Bendo, G. J., et al. 2010, A&A, 518, L64
Shetty, R., Kauffmann, J., Schnee, S., & Goodman, A. A. 2009, ApJ, 696, 676
Smith, M. W. L., Gomez, H. L., Eales, S. A., et al. 2012, ApJ, 748, 123
Veneziani, M., Ade, P. A. R., Bock, J. J., et al. 2010, ApJ, 713, 959

SF2A 2013
L. Cambrésy, F. Martins, E. Nuss and A. Palacios (eds)

UV-TO-IR SPECTRAL ENERGY DISTRIBUTIONS OF GALAXIES AT $Z > 1$: THE IMPACT OF *HERSCHEL* DATA ON DUST ATTENUATION AND STAR FORMATION DETERMINATIONS

V. Buat[1], S. Heinis[2] and M. Boquien[1]

Abstract. We report on our recent works on the UV-to-IR SED fitting of a sample of distant ($z > 1$) galaxies observed by *Herschel* in the CDFS as part of the GOODS-*Herschel* project.

Combining stellar and dust emission in galaxies is found powerful to constrain their dust attenuation as well as their star formation activity.

We focus on the caracterisation of dust attenuation and on the uncertainties on the derivation of the star formation rates and stellar masses, as a function of the range of wavelengths sampled by the data data and of the assumptions made on the star formation histories

Keywords: High-redshift galaxies, galaxy evolution, photometry

1 Introduction

Star formation rates (SFR) and stellar masses ($M_{\rm star}$) are the main parameters estimated from large samples of galaxies and they are commonly used to constrain their star formation history and the evolution of their baryonic content. The slope and dispersion of the relation found between SFR and $M_{\rm star}$ both at low and high redshift (e.g. Brinchmann et al. 2004; Noeske et al. 2007; Rodighiero et al. 2011) directly depends on the measurement accuracy of these parameters.
Two major methods are commonly used to measure SFRs. The first approach consists of using empirical recipes. The SFR is deduced by applying conversion factors between an observed emission coming mostly from young stars and the SFR (e.g. Kennicutt 1998). Another widespread method is to exploit the full panchromatic information available for a given sample by fitting the spectral energy distributions (SEDs). The coupling stellar (UV-optical) and dust (mid and far-IR) has proven to be particularly powerful to measure SFRs and overcome the issue of dust attenuation, either with empirical recipes (e.g. Kennicutt & Evans 2012, for a review) or with physically motivated fitting codes (da Cunha et al. 2008; Noll et al. 2009). However the impact of the star formation history remains an open issue, especially at high redshift or in extreme objects (Kobayashi et al. 2013; Schaerer et al. 2013).
$M_{\rm star}$ derivations are almost insensitive to dust attenuation but strongly depend on the assumed stellar population synthesis model and star formation history (e.g. Papovich et al. 2001; Pforr et al. 2012; Maraston et al. 2010). For a given set of assumptions about the stellar population synthesis model, including metallicity and star formation history, and adopting an initial mass function, the stellar masses are robustly estimated. However systematic differences appear when different assumptions are made and these input parameters are either non or very poorly constrained (e.g. Marchesini et al. 2009). The uncertainty about the star formation history itself induces large variations in stellar mass derivation (Bell et al. 2003; Pforr et al. 2012).

2 Datasets and tools

2.1 Observations and sample used

We select galaxies in the GOODS-S field with accurate measurements of the UV, visible, NIR and IR rest frame emissions. We start with the multi-wavelength catalogue of Cardamone et al. (2010), which includes the GOODS

[1] Aix-Marseille Université, CNRS, LAM (Laboratoire d'Astrophysique de Marseille) UMR7326, 13388, Marseille, France
[2] Department of Astronomy CSS Bldg., Rm. 1204, Stadium Dr. University of Maryland College Park, MD 20742-2421

Spitzer IRAC and MIPS data. In addition to broad band optical data, deep intermediate-band imaging from the Subaru telescope provide photometry with fine wavelength sampling and estimate more accurate photometric redshifts. We restrict the field to the $10' \times 10'$ observed by the PACS instrument (Poglitsch et al. 2010) on board of the *Herschel* Space Observatory (Pilbratt et al. 2010) at 100 and 160 μm, as part of the GOODS-*Herschel* key programme (Elbaz et al. 2011). We refer to Buat et al. (2012) and Buat et al. (2013, A&A submitted) for a detailed description of the collected data. The final sample contains 236 sources with $1 < z < 3$. 32 objects are detected with PACS at 100 and 160 μm, 40 only at 100 μm and 8 only at 160 μm. 28 photometric bands are compiled from U to 24 μm (all the galaxies are detected at 24 μm). The rest-frame luminosity at 1530 $\mathring{A}$ of each galaxy is obtained by modelling a power-law between 1300 and 2500 $\mathring{A}$ in the rest frame of the sources.

2.2 SED fitting tool: CIGALE

SED fitting is performed with the CIGALE code (Code Investigating GALaxy Emission)* developed by Noll et al. (2009). CIGALE combines a UV-optical stellar SED with a dust component emitting in the IR and fully conserves the energy balance between the dust absorbed stellar emission and its re-emission in the IR. The output parameters are all estimated from their probability distribution function (PDF) with the expectation value and its standard deviation. The input parameters are similar to those used in Buat et al. (2012) except for the star formation histories. For the purpose of the present analysis, we explore several models: single stellar populations exponentially decreasing or increasing and two stellar populations with a recent one on top of an older population created with an exponentially decreasing SFR. All models are built with an age of the creation of the first stars taken either free or fixed ($z_f \simeq 8$). A first, global, comparison of the models is performed by comparing the reduced best-fit χ^2 distribution given by the code as shown in Fig.1. The best-fit χ^2 distributions appear similar for all models but the fixed-age decl.-τ model which is unable to reproduce the data. We also exclude free-age rising-τ models from the following discussions since these models are introduced to increase the age of the stellar populations (Maraston et al. 2010).

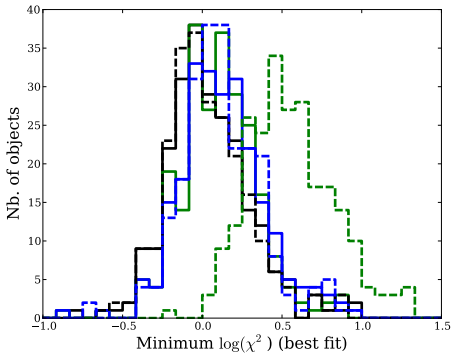

Fig. 1. Distributions of reduced χ^2 values obtained for the best fits and plotted in a logarithmic scale. Black: 2-populations model, green: decl.-τ model, blue: rising-τ model. The solid lines are obtained for models with the age of the stellar population taken free, the dashed lines correspond to a fixed age for the stellar population.

3 SFR and $M_{\rm star}$ determinations

3.1 Full UV-to-IR SEDs

Adopting different star formation histories do not modify SFR measurements (Fig.2, left) with systematic shifts lower than 0.05 dex whereas it has has a clear impact on $M_{\rm star}$ determinations (Fig.2, right) with systematic differences reaching 0.3 dex between the most extreme cases. Because of the outshining by young stars, older stellar populations are hidden and τ- models are likely to give only lower limits to the total stellar mass. Models considering an old and young population give higher masses. The very good agreement found between SFR determinations with either a single stellar population or with an over-imposed burst of constant star formation

*http://cigale.oamp.fr

should be found surprising. Actually Reddy et al. (2012) have shown that for ages larger than $\sim$ 100 Myr rising-τ models lead to a constant production of the UV light, in the present study stellar populations are older than 2 Gyr for the rising-τ model so we expect a robust determination of the SFR. The effective star formation history we obtain for the decl.-τ model is close to a constant SFR: the $t_{\rm f}/\tau$ ratio is found most of the time lower than 1 and the age of the stellar population is found larger than 100 Myr for 94% of our galaxies, also ensuring a stationarity in the production of the UV light. Therefore the agreement between our SFR estimations is expected. It is worth noticing that the presence of IR data give us a robust measurement of the dust attenuation, allowing us to fit the true intrinsic UV continuum of our galaxies

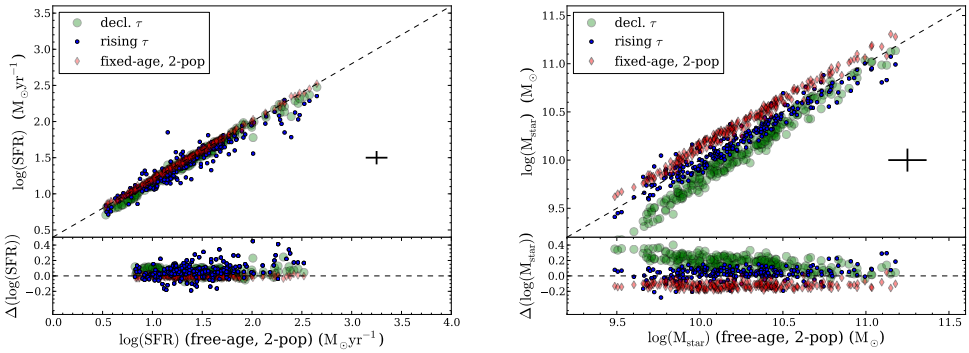

Fig. 2. Comparison of SFR (**left panel**) and $M_{\rm star}$ (**right panel**) determinations from different models. The x-axis is from the baseline model (free-age 2-populations), the y-axis corresponds to free-age decl.-τ (green circles), fixed-age rising-τ (blue dots) and 2-populations (red diamonds) models. Typical uncertainties on parameter estimations are indicated by a black cross. $\Delta(SFR) = \Delta(\log(SFR_{\rm 2pop}) - \log(SFR_{\tau-{\rm model}})$ and $\Delta(M_{\rm star} = \Delta(\log(M_{\rm star-2pop}) - \log(M_{\rm star-rising-\tau})$

3.2 The impact of IR data on SFR determinations

We now perform the SED fitting excluding IRAC4, MIPS and PACS data and considering only the free-age 2 populations model. Without IR data, results substantially change for the parameters linked to the recent star formation. A large dispersion is found between values of SFR estimated with and without IR data (corresponding to 0.65 mag). Omitting IR data strongly affects the accuracy of dust attenuation and SFR with an average uncertainty multiplied by a factor $\sim$ 2 and the distribution of these parameters is found flatter. It it illustrated in Fig. 3 with a strong dependence of the SFR estimates when IR data are not present on the SFR of the galaxies estimated with the whole dataset: assuming that SFRs estimated with the whole dataset are reliable, low SFRs are overestimated and large SFRs underestimated when IR data are missing. Excluding NIR or intermediate band data do not affect significantly the SFR measurements.

Star forming galaxies are often classified as Main Sequence and Starburst galaxies according to the value of their specific SFR (SSFR= SFR/ $M_{\rm star}$). The evolution of SSFR with redshift also place constraints on galaxy formation scenarios (e.g. Fontanot et al. 2009). In Fig.3 we show the influence of introducing or not IR data to estimate SSFRs. 30% of the sample exhibit a difference in SSFR which exceeds a factor 2. Such a factor 2 (0.3 dex) is in the order of the dispersion of the Main Sequence measured with IR data (e.g Noeske et al. 2007; Rodighiero et al. 2011). Starburst galaxies are defined to have a SSFR exceeding by a factor 2 that of a Main Sequence galaxy with the same mass by Elbaz et al. (2011) (note however that Rodighiero et al. (2011) and Sargent et al. (2012) adopt a more conservative ratio of 4 between the SSFR of starburst and Main Sequence galaxies). Indeed, a large uncertainty is expected in the determination of SSFR without IR data for very dusty systems. However in galaxies with a moderate to low dust attenuation ($A_{\rm FUV}$ $<\sim$ 3 mag) SSFR is found overestimated by a factor larger than 2 in 30% of the cases due to an overestimation of $A_{\rm FUV}$. The percentage reaches 40% for galaxies with $A_{\rm FUV}$ $<\sim$ 2 mag with larger SSFRs found without IR data in 80% of the cases. The variation of the SSFR with z is a matter of debate, especially at high redshift with the presence or not of a plateau in SSFR at $z >\sim 4$ (e.g. Bouwens et al. 2012; Heinis et al. 2013), the analysis being complicated by the presence of intense emission lines in the photometric bands (de Barros et al. 2012). If a substantial dust attenuation occurs at high redshift (Finkelstein et al. 2012) it may well also affect the analysis and ALMA

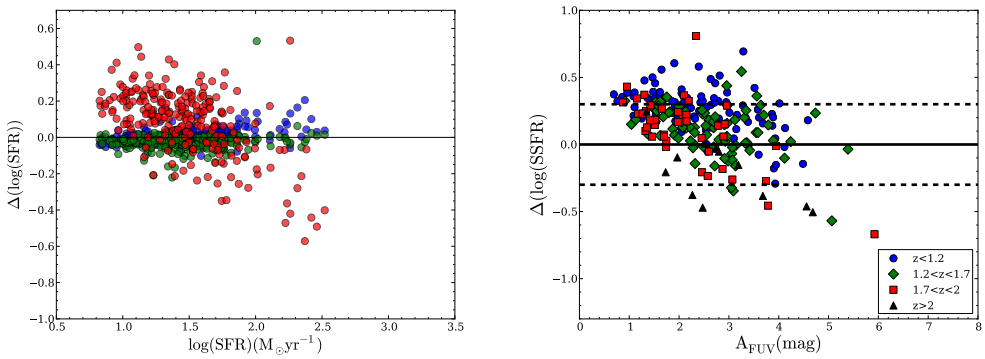

Fig. 3. Left: Comparison between SFR estimations for the free-age 2-populations model with and without optical intermediate bands, NIR and IR data. Xaxis: all the dataset is used. Yaxis: parameters estimated without intermediate band data (blue circles), without NIR data (green circles) and without IR data (red circles). **Right:** Difference between SSFR measured with and without IR data as a function of dust attenuation in FUV for different redshift bins. The solid line correspond to a perfect agreement in both measurements and dotted lines to a factor 2 of difference. $\Delta\log(\mathrm{SFRS}) = \log(\mathrm{SSFR}_{\mathrm{noIR}}) - \log(\mathrm{SSFR}_{\mathrm{alldata}})$.

observations will be mandatory to reliably measure SFRs in these objects as emphasized by Schaerer et al. (2013).

References

Bell E. F., McIntosh D. H., Katz N., Weinberg M. D., 2003, ApJS, 149, 289
Borch A., Meisenheimer, K., Bell, E., et al., 2006, A&A, 453, 869
Bouwens, R. J., Illingworth, G. D., Oesch, P. A., et al. 2012, ApJ, 754, 83
Brinchmann J., Charlot S., White S. D. M., et al. 2004, MNRAS, 351, 1151
Buat, V., Noll, S.., Heinis, S., et al. 2012, A&A, 545, 141
Cardamone, C.N., van Dokkum, P.G., Urry, C.M., et al. 2010, ApJSS, 189, 270
da Cunha, E., Charlot, S., & Elbaz, D. 2008, MNRAS, 388, 1595
Daddi E., Dickinson, M., Morrison, G., et al. 2007, ApJ, 670, 156
de Barros, S., Schaerer, D., Stark, D.P. 2012, arXiv:1207.3663
Elbaz, D., Dickinson, M., Hwang, H.S., et al. 2011, A&A, 533, 119
Fontanot, F., De Lucia, G., Monaco, P., Somerville, R. S., & Santini, P. 2009, MNRAS, 397, 1776
Finkelstein, F.S., Papovich, C., Salmon, B., et al. 2011, ApJ, 756, 164
Heinis, S., Buat, V., Bethermin, M., et al. 2013, in preparation
Kennicutt, R.C. 1998, ARA&A 36, 189
Kennicutt, R.C. & Evans, N.J. 2012, ARA&A 50, 531
Kobayashi, M. A. R., Inoue, Y., & Inoue, A. K. 2013, ApJ, 763, 3
Maraston, C., Pforr, J., Renzini, A., et al. 2010, MNRAS, 407, 830
Marchesini, D., van Dokkum, P. G., Förster Schreiber, N. M., et al. 2009, ApJ, 701, 1765
Noeske, K. G., Weiner, B. J., Faber, S. M., et al. 2007, ApJ, 660, L43
Noll, S., Burgarella, D., Giovannoli, E., et al. 2009, A&A, 507, 1793
Papovich, C., Dickinson, M., & Ferguson, H. C. 2001, ApJ, 559, 620
Pforr, J., Maraston, C., & Tonini, C. 2012, MNRAS, 422, 3285
Pilbratt, G., Riedinger, J.R., Passvogel, T., et al. 2010, A&A 518, L1
Poglitsch, A., Waelkens, C., Geis, N., et al. 2010, A&A, 518, L2
Reddy, N., Pettini, M., Steidel,C. et al. 2012, ApJ, 754, 25
Rodighiero, G., Daddi, E., Baronchelli, I., et al. 2011, ApJ, 739, L40
Sargent, M. T., Béthermin, M., Daddi, E., & Elbaz, D. 2012, ApJ, 747, L31
Schaerer, D., de Barros, S., Sklias, P. 2013, A&A 549, 4

SF2A 2013
L. Cambrésy, F. Martins, E. Nuss and A. Palacios (eds)

DUST ATTENUATION AND FUV+FIR STAR FORMATION RATE DENSITY: WHAT DID WE LEARN FROM *HERSCHEL* AND WHAT WOULD *WISH* BRING?

D. Burgarella[1], V. Buat[1], C. Gruppioni[2], O. Cucciati[2], S. Heinis[1], T. Yamada[3], I. Iwata[4] and the PEP/HerMES team

Abstract. In this paper, we present a work on the evolution in redshift of the dust attenuation (A_{FUV})and the total (FUV + FIR) star formation rate density ($SFRD_{TOT}$). Our main conclusions are that: 1) the dust attenuation A_{FUV} is found to increase from $z = 0$ to $z \sim 1.2$ and decreases until our last data point at $z = 3.6$; 2) At $z > 2$, we observe either a plateau or a small increase to $z \sim 3$ and then a decrease to $z = 3.6$; 3) the peak of A_{FUV} is delayed with respect to the maximum of $SFRD_{TOT}$ but the origin of this delay is not understood. This work is further detailed in (Burgarella et al. 2013). To better understand this and try to move further in redshift, we present a space mission project called *WISH*. The primary goal of WISH is to push back the high-redshift frontier well into the epoch of reionization by utilizing its unique imaging and spectroscopic capabilities in the 1 - 5 μm range and a dedicated survey strategy.

Keywords: galaxies, cosmology, star formation rate density, dust attenuation, re-ionization, early Universe

1 Introduction

Even though astronomers have tried to measure the evolution of the cosmic star formation rate density (SFRD) by moving higher and higher in redshift. It quickly became clear that at low-z (i.e. at least $z \sim 2$), one of the main issues was to account for the total SFRD and not only for the far-ultraviolet (FUV) because of dust. This translates into either a dust correction of the FUV SFRD or, better, a measure of the total i.e., FUV plus far-infrared (FIR = bolometric IR) SFRD. Takeuchi et al. (2005) estimated the cosmic evolution of the SFRD from the FUV and FIR. An increase of the fraction of hidden SFR is found to $z = 1$ where it reaches 84%. The dust attenuation increases from $A_{FUV} \sim 1.3$ mag locally to $A_{FUV} \sim 2.3$ mag at $z = 1$. From the FUV only Cucciati et al. (2012) show that the mean dust attenuation A_{FUV} agrees with Takeuchi et al. (2005) over the range $0 < z < 1$, remains at the same level to $z \sim 2$, and declines to ~ 1 mag at $z \sim 4$.

Using FUV luminosity functions (LFs) published in Cucciati et al. (2012) and FIR LFs from *Herschel** (Gruppioni et al. 2013), we are able to constrain the redshift evolution of $\log_{10}(L_{FIR}/L_{FUV})$ (IRX) to $z \sim 4$ for the first time directly from FIR data. With this information, we estimate the redshift evolution of ρ_{FIR}/ρ_{FUV} as well as $\rho_{TOT} = \rho_{FIR} + \rho_{FUV}$.

Through the last decades, the deep surveys unveiled the history of formation and evolution of galaxies. Yet, the high redshift frontier in the study of the early universe still remains almost closed or at most ajar. This is the epoch of the formation of the first-generation of stars and galaxies. The objects formed in the first couples of 100 Myrs are considered to have reionized the baryonic matter and made a dramatic change in the thermal history of the universe. We present a space mission project called Wide-field Infrared Surveyor for the High-redshift (*WISH*) dedicated to discover and study primordial galaxies at $3 < z < 15$.

Throughout this paper we adopt a ΛCDM cosmology with $(H_0, \Omega_m, \Omega_\Lambda) = (70, 0.3, 0.7)$, where H_0 is in $\mathrm{kms}^{-1}\mathrm{Mpc}^{-1}$. All SFR and stellar masses presented assume, or have been converted to, a Salpeter IMF.

[1] Aix-Marseille Université, CNRS, LAM (Laboratoire d'Astrophysique de Marseille) UMR 7326, 13388, Marseille, France

[2] INAF-Osservatorio Astronomico di Bologna, via Ranzani 1, 40127, Bologna, Italy

[3] Astronomical Institute, Tohoku Univ. (Japan)

[4] Subaru Telescope, National Astronomical Observatory of Japan (United States)

*From two *Herschel* Large Programmes: PACS Evolutionary Probe (PEP, Lutz et al. 2011) and the *Herschel* Multi-tiered Extragalactic Survey (HerMES, Oliver et al. 2012)

2 Cosmic Dustiness

Fig. 1 (left) presents the dust attenuation in the FUV vs. z and the ratio of the FIR-to-FUV luminosity densities (LDs). The FUV dust attenuation is estimated from the IRX and converted to A_{FUV} using Burgarella et al. (2005)†. The redshift evolution of A_{FUV} agrees with Cucciati et al. (2012) (no FIR data). Fig. 1 (left) suggests a maximum at $z \sim 1.2$ followed by a decrease to $z \sim 4$ of A_{FUV}. From the UV slope, β, a continuous decline at least to $z = 6$ is found (Bouwens et al. 2009). At $z = 3.6$, A_{FUV} is about at the same level as measured at $z = 0$. Beyond $z = 4$, we do not expect any increase.

3 Cosmic Star Formation Rate Density

Fig. 1 (right) suggests a flattening of the total SFRD up to $z \sim 3$ where the UV data favor a peak followed by a decrease. All in all, our total SFRD agrees fairly well with that of Hopkins & Beacom (2006) in the same redshift range. Barger et al. (2012) published a FIR SFRD based on SCUBA-2 data that also agrees with ours at $2 < z < 4$. Preliminary results from *Herschel*/SPIRE estimated by Vaccari et al. (2013, in prep.) agree with these trends. We fit $SFRD_{TOT}$ by combining two Gaussians (see Burgarella et al. 2013). The cosmic SFRD presents a (weak) maximum at $z \sim 2.5 - 3.0$ (i.e., between 2.6 - 2.1 Gyr) while the dust attenuation presents a maximum at $z \sim 1.2$ (i.e. 5 Gyr). We have no definite explanation for this delay of ~ 3 Gyr so far.

The bottomline from this analysis is that it appears to be better to study the early universe at $z > 5$ in the rest-frame FUV than in the rest-frame FIR because of the low dust attenuation (lower than locally). The rest-frame FUV is redshifted in the near-infrared (NIR) at $z > 5$. This is the main reasons why the WISH mission will observe in the wavelength range 1 - 5 μm.

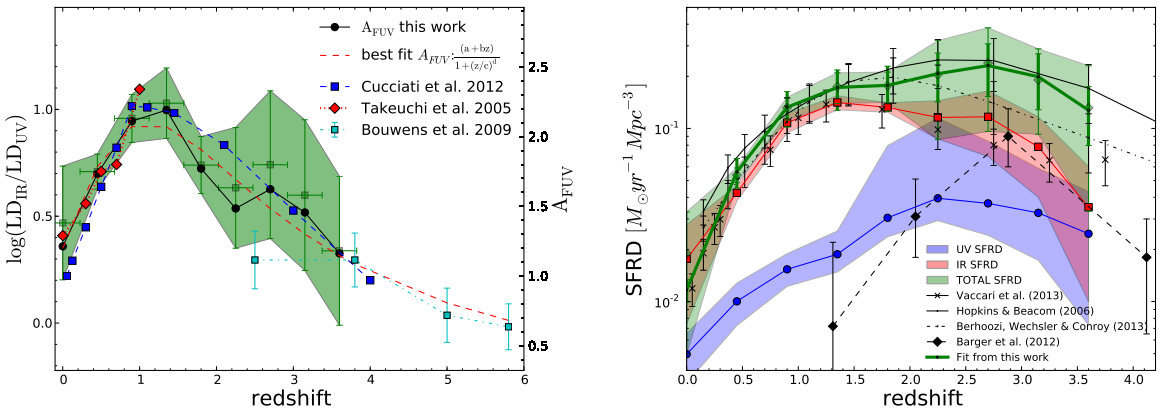

Fig. 1. Left: ratio of the FIR-to-FUV LDs (IRX) on the left-hand axis and FUV dust attenuation (A_{FUV}) on the right-hand axis. The red dotted line with red diamonds is taken from Takeuchi et al. (2005). The green filled area and green dots are the associated uncertainties. Black dots denote the values directly computed from the LFs. At $z = 3.6$, A_{FUV} reaches about the same value as at $z = 0$. Takeuchi et al. (2005) (red diamonds) used an approach identical to ours while a SED analysis (no FIR data) is performed in Cucciati et al. (2012) (blue boxes). Bouwens et al. (2009) are estimates based on the UV slope β. Right: SFRD in the FUV (blue), in the FIR (red), and in total (i.e., FUV + FIR) in green (other colors are due to overlaps of the previous colors). The lines are the mean values, while the lighter colors show the uncertainties.

4 The WISH space mission

The Wide-field Imaging Surveyor for High-redshift (WISH) is a proposed mission concept being developed by the WISH Working Group in Japan under the Science Committee of ISAS and JAXA (Yamada et al.

†The conversion from IRX to A_{FUV} from Burgarella et al. (2005) is valid at $\log_{10}(L_{FIR}/L_{FUV})$>-1.2: A_{FUV} = -0.028 $[\log_{10} L_{FIR}/L_{FUV}]^3$ + 0.392 $[\log_{10} L_{FIR}/L_{FUV}]^2$ + 1.094 $[\log_{10} L_{FIR}/L_{FUV}]$ + 0.546

(2010), Yamada et al. (2012)). French institutes propose to the French space agency (CNES) to contribute to WISH both scientifically and instrumentally (spectrograph and tests) under the coordination of the Laboratoire d'Astrophysique de Marseille. Tab1 gives the mains characteristics of WISH.

Table 1. WISH in a nutshell

Launch	$\sim$ 2020	
Optics	1.5m M1	cooled to 100K
Optics	Diffraction limited at 1 - 5 μm	0.2 - 0.4" FWHM
Wavelength range	1 - 5 μm	
FOV	900 arcmin^2 (photometry)	0.5 - 1 arcmin^2 (spectroscopy)
Main surveys		
Ultra Deep Survey (UDS)	100 deg^2	Photometry to ABmag 28
Multiband survey (+ UDS)	100 deg^2	Photometry to ABmag 28
Ultra Wide Survey (UWS)	1000 deg^2	Photometry to ABmag 24-25
Extreme Survey (XS)	0.25 deg^2	Photometry to ABmag 29-30
Deep Spectroscopic Survey (DSS)	1 deg^2	Spectroscopy to 8 $\times$ 10^{-17} erg cm^{-2} s^{-1}
Wide Spectroscopic Survey (WSS)	10 deg^2	Spectroscopy to 8 $\times$ 10^{-16} erg cm^{-2} s^{-1}

Name	λ center µm	FWHM µm
Filter 0	1.040	0.280
Filter 1	1.360	0.360
Filter 2	1.775	0.470
Filter 3	2.320	0.620
Filter 4	3.030	0.800
Filter 5	3.965	1.070
Filter 5e	4.215	1.570
Filter 6	4.500	1.000

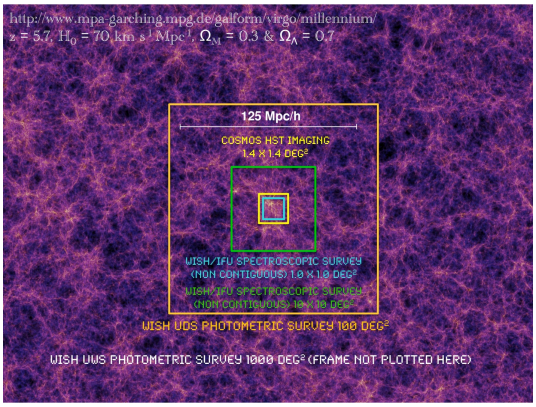

Fig. 2. Definition of the filters and sensitivity in imaging.

The definition of the filters and sensitivities in imaging are given in Fig. 2. The conceptual design and the optimum survey strategy of WISH has been developed to detect photometrically a large number of the rest-frame UV-luminous galaxies: $\sim$ 10^4 galaxies at z=8 - 9, $\sim$ 10^{3-4} galaxies at z=11 - 12, and $\sim$ 10^2 galaxies at z=14 - 17. As a reference, estimations for Euclid comes to about a few hundreds LBGs and a few tens QSOs at $z > 8$. More details about WISH can be found on the following websites: `http://people.lam.fr/burgarella.denis/denis/WISH.html` and `http://www.wishmission.org/en/index.html`.

5 Conclusions

On the one hand, the variation of the cosmic dust attenuation with redshift suggests a peak in the dust attenuation at $z \sim 1.2$ followed by a decline to $z = 3.6$. On the other hand, the total (FUV+FIR) cosmic SFRD increases from $z = 0$ to $z \sim 1.2$, remains flat to $z \sim 2.5 - 3.0$ followed by a decrease at higher redshifts and reaches the same level at $z \sim 5 - 6$ as is measured locally if we assume no variations in this trend. The peak of the dust attenuation is delayed with respect to the maximum of the total SFRD by about 3 Gyrs.

Fig. 1 taken at face value would suggest that the universe's dusty era (meaning dust attenuation higher than in the local universe) started at z = 3 - 4 simultaneously with the rise of a universe-wide star-formation event.

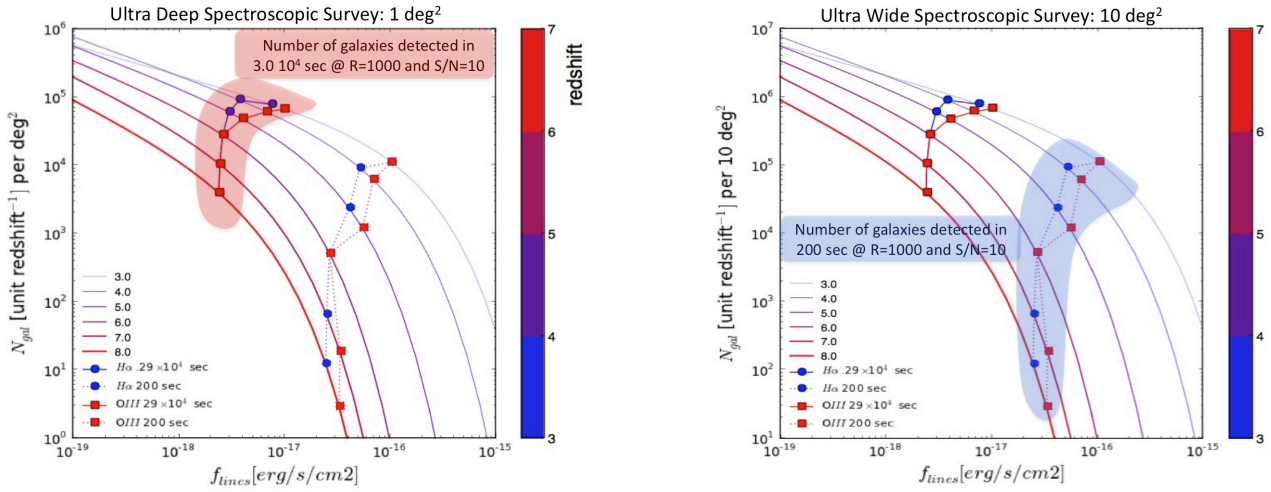

Fig. 3. Both the Ultra Deep (left) and Ultra Wide Spectroscopic(right) Surveys will provide large galaxy samples at $3 < z < 8$. For the first time, we will have data in hand to seriously constrain the formation and early evolution of galaxies in this redshift range from line spectroscopy for several to millions of galaxies. Even JWST would have a hard time performing this science unless a large part of the observing time would be dedicated to this theme (about 80 % of WISH time will). Vertical lines (with boxes and dots) refer to the observational limits with WISHSpec for the two surveys, as scaled down from the performances of JWST accounting for the size and the resolutions. An instantaneous field of view of 1 arcmin is assumed.

Figs. 1 also allows us to follow the SFRD over most of the Hubble time in a consistent way. However, large uncertainties prevented us from closing the case. This work is further detailed in (Burgarella et al. 2013).

To go further in redshift, we need to detect and characterize galaxies at higher redshifts. WISH will dedicate 80% of its observing time to studying the first galaxies and the very early formation of stars and elements. More specifically, WISH will:

- Find the very first gravitationally-bound structures that were assembled in the Universe – precursors to today's galaxies, groups and clusters of galaxies – and trace the subsequent co-evolution of galaxies and super-massive black holes.
- Trace the formation and evolution of the super-massive black holes at galactic centres – in relation to galaxy and star formation – and trace the life cycles of chemical elements through cosmic history.

Finally, it is important to underline that WISH will be very a valuable facility to provide exotic and $z > 10$ galaxies for the ELTs, JWST and ALMA thanks to its wide field of view.

References

Barger, A. J., Wang, W.-H., Cowie, L. L., et al. 2012, ApJ, 761, 89
Bouwens, R. J., Illingworth, G. D., Franx, M., et al. 2009, ApJ, 705, 936
Burgarella, D., Buat, V., Gruppioni, C., et al. 2013, A&A, 554, A70
Burgarella, D., Buat, V., & Iglesias-Páramo, J. 2005, MNRAS, 360, 1413
Cucciati, O., Tresse, L., Ilbert, O., et al. 2012, A&A, 539, A31
Gruppioni, C., Pozzi, F., Rodighiero, G., et al. 2013, MNRAS, 432, 23
Hopkins, A. M. & Beacom, J. F. 2006, ApJ, 651, 142
Lutz, D., Poglitsch, A., Altieri, B., et al. 2011, A&A, 532, A90
Oliver, S. J., Bock, J., Altieri, B., et al. 2012, MNRAS, 424, 1614
Takeuchi, T. T., Buat, V., & Burgarella, D. 2005, A&A, 440, L17
Yamada, T., Doi, M., Goto, T., et al. 2010, in Society of Photo-Optical Instrumentation Engineers (SPIE) Conference Series, Vol. 7731, Society of Photo-Optical Instrumentation Engineers (SPIE) Conference Series

Yamada, T., Iwata, I., Ando, M., et al. 2012, in Society of Photo-Optical Instrumentation Engineers (SPIE) Conference Series, Vol. 8442, Society of Photo-Optical Instrumentation Engineers (SPIE) Conference Series

SF2A 2013
L. Cambrésy, F. Martins, E. Nuss and A. Palacios (eds)

EMISSION LINE PROPERTIES FROM BROAD-BAND PHOTOMETRY: IMPACT ON SELECTION AND PHYSICAL PARAMETER ESTIMATION

S. de Barros[1], H. Nayyeri[1], N. Reddy[1] and B. Mobasher[1]

Abstract. Several works have now shown that nebular emission can have a significant impact on broad-band photometry of high-redshift galaxies ($z > 3$), and how this can affect parameter estimation from SED fitting. While relatively small spectroscopic samples have been used to estimate this impact, we here focus on a large spectroscopic sample (N$\sim$ 2300) at $z \sim 2$, with measured Hα fluxes for $\sim$ 100 galaxies. Under appropriate assumptions, our SED fitting code is able to reproduce observed Hα fluxes, and we infer that $\sim$ 20% of our sample have parameters significantly affected when nebular emission is taken into account.

We also determine how nebular emission can affect selection and parameter estimation of evolved galaxies (Balmer Break galaxies) at high-redshift ($z \sim 4$).

Keywords: galaxies: starburst galaxies: high redshift galaxies: evolution galaxies: star formation

1 Introduction

Although nebular emission (i.e. emission lines and nebular continuous emission from HII regions) is ubiquitous in regions of massive star formation, strong or dominant in optical spectra of nearby star forming galaxies, and present in numerous types of galaxies, its impact on the determination of physical parameters of galaxies, in particular at high redshift, has been neglected until recently (cf. overview in Schaerer & de Barros 2011).

The analysis of samples of $z \sim 6$–8 and $z \sim 3$–6 LBGs observed with *HST* and *Spitzer* further demonstrates the potential impact of nebular emission on the physical parameters derived from SED fits of high-z galaxies (Schaerer & de Barros 2010; de Barros et al. 2012; Schaerer et al. 2013). It has now become clear (Schaerer & de Barros 2009, 2010; Ono et al. 2010; Lidman et al. 2012) that nebular emission (both lines and continuum emission) must be taken into account for the interpretation of photometric measurements of the SEDs of star-forming galaxies at high-z. In parallel, diverse evidence of strong emission lines galaxies with strong emission lines and/or strong contributions of nebular emission to broad-band fluxes has been found at different redshifts, e.g. by Shim et al. (2011); McLinden et al. (2011); Atek et al. (2011); Trump et al. (2011); van der Wel et al. (2011); Labbe et al. (2012); Stark et al. (2013); Smit et al. (2013). Unfortunately, at redshift as high as $z \sim 3$, direct measurement of emission lines remains a difficult task with current facilities, while some results at $3.0 < z < 3.8$ are encouraging (e.g. Schenker et al. 2013).

The main idea of this work is to use a spectroscopic sample at $z \sim 2$ (Erb et al. 2006), where measurements of emission lines (Hα) are already available for a significant subsample. This subsample is used to test the ability of our SED fitting code (but the results can be generalized to any SED fitting code accounting for nebular emission) to reproduce properly observed emission lines, under different assumptions. Once our code calibrated, we infer the impact of nebular emission on parameter estimation. In parallel, we also determine how nebular emission can affect selection and physical parameter estimation of evolved galaxies at $z \sim 4$ (Nayyeri et al. 2013). We adopt a Λ-CDM cosmological model with H_0=70 km s^{-1} Mpc^{-1}, Ω_m=0.3 and Ω_Λ=0.7. All magnitudes are expressed in the AB system (Oke & Gunn 1983).

[1] Department of Physics and Astronomy, University of California, Riverside, 900 University Avenue, Riverside, CA 92521, USA

2 SED fitting code

We use a recent, modified version of the Hyperz photometric redshift code of Bolzonella et al. (2000), taking into account nebular emission (lines and continua). We consider a large set of spectral templates (Bruzual & Charlot 2003), covering different metallicities and a wide range of star formation (SF) histories (exponentially decreasing, constant and exponentially rising SF), and we add the effects of nebular emission following the method presented in Schaerer & de Barros (2009, 2010). We account for attenuation from the intergalactic and the interstellar medium . With these assumptions we fit the observed SEDs by straightforward least-square minimization.

In practice we adopt a spectral templates computed for a Salpeter IMF (Salpeter 1955) from 0.1 to 100 $M_{\odot}$, and we properly treat the returned ISM mass from stars. Nebular emission from continuum processes and lines is added to the spectra predicted from the GALAXEV models as described in Schaerer & de Barros (2009), proportionally to the Lyman continuum photon production. The relative line intensities of He and metals are taken from Anders & Fritze-v. Alvensleben (2003), including galaxies grouped in three metallicity intervals covering $\sim 1/50$–1 $Z_{\odot}$. Hydrogen lines from the Lyman to the Brackett series are included with relative intensities given by case B. For galactic attenuation we use the Calzetti law (Calzetti et al. 2000). The IGM is treated following Madau (1995).

We test two attenuations, one applying the same attenuation to the stellar and nebular emission, and the other following Calzetti (1997), who find a more important attenuation for nebular emission in comparison with stellar emission, with $E(B-V)_{\star} = 0.44 \times E(B-V)_{neb}$.

3 Data

Galaxies at redshifts $1.4 \leq z \leq 3.7$ were selected using the BM, BX, and Lyman-break galaxy (LBG) rest-UV color criteria (Steidel et al. 2003, 2004; Adelberger et al. 2004). The imaging data were obtained mostly with the Palomar Large Format Camera or the Keck Low Resolution Imaging Spectrograph (Oke et al. 1995; Steidel et al. 2004). The photometry and spectroscopic follow-up for this survey are described in Steidel et al. (2003, 2004); Adelberger et al. (2004). To probe the strength of the Balmer break in $z \sim 2$ galaxies, we used J and/or Ks imaging (Palomar/WIRC and Magellan/PANIC). We also used Spitzer/IRAC data. The IRAC coverage of our galaxies typically included either channels 1 (3.6μm) and 3 (5.8μm) or channels 2 (4.5μm) and 4 (8.0μm), with a small fraction of galaxies having coverage in all four channels. Additionally, for a small fraction of this $z \sim 2$ sample, we obtained (HST)/WFC3-F160W (H band) data.

The search and characterization of evolved galaxies at $z \sim 4$ has been done with Wide Field Camera 3 (WFC3) near Infra Red observations in the GOODS-S field performed as a part of the CANDELS project. The U-band data in the GOODS-S area were taken using the VIMOS instrument on Very Large Telescope. Optical data comes from HST/ACS, with F435W, F606W, F775W and F850LP filters. Near-infrared observations are in the F098M and F105W filters with the former one being used for the GOODS-S ERS, F125W and F160W. GOODS-S has also observations by the VLT HAWK-I Ks filter at effective wavelength of 2.2 μm. Finally, we also use Spitzer/IRAC data in all four channels (for a detailed description of the data, see Nayyeri et al. 2013, and references therein).

4 Physical parameters of $z \sim 2$ star-forming galaxies

First, we test the ability of the three star formation histories (exponentially declining/rising, and constant) used here, to reproduce observed Hα fluxes, since these different histories lead to different prediction of line strength (de Barros et al. 2012; Schaerer et al. 2013). Only declining SFH is unable to reproduce observed fluxes, leading to lower $f(H\alpha)_{SED}$ in comparison with $f(H\alpha)_{obs}$. In Figure 1, we show the result with a rising SFH (similar results with a constant SFH). While different attenuation between nebular and stellar emission seems physically motivated, our results clearly show that applying the same differential attenuation than Calzetti (1997) leads overall to underpredict Hα fluxes (Figure 1, right), while for some individual objects, this leads to improve the correlation between observed and predicted Hα fluxes. Similarly, Kashino et al. (2013) find that the Calzetti (1997) relation evolves at higher redshift, which may indicate a more uniform dust distribution in high-z galaxies as compared to local galaxies.

We also test SED fitting with a lower age limit (> 50 Myr), to avoid conflict between dynamical timescale and age. Using this limit improve marginally the agreement between predicted and observed fluxes.

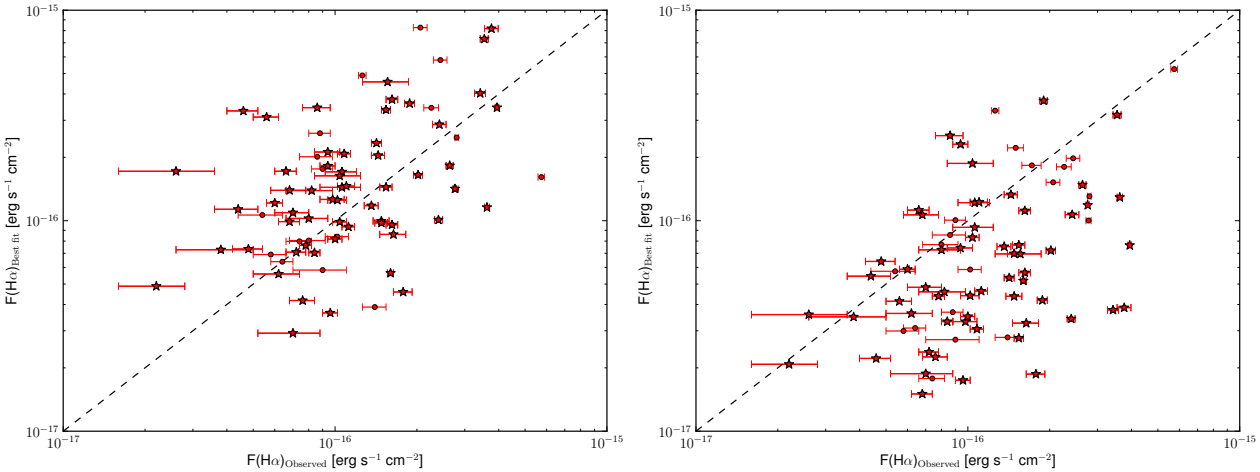

Fig. 1. Left: Hα fluxes inferred from best-fit SED fitting vs observed Hα fluxes, with a rising SFH, applying the same attenuation to the stellar and nebular emission. **Right:** same but with a differential attenuation (Calzetti 1997). Red stars: galaxies with Hα falling in one filter (F160 or K band), red dots: galaxies with Hα line falling in no filter.

Relying on our consistency test between predicted and observed Hα flux, we use only rising (since constant leads to similar results) SFH, with similar attenuation between stellar and nebular emission, to infer physical properties of our $z \sim 2$ sample, and determine how nebular emission affects parameter estimation. The main parameter expected to be affected by nebular emission is age (Schaerer & de Barros 2009), since some lines (Hβ, [OIII] doublet, [OII]) can mimic a Balmer break. We compare results of our fit without and with nebular emission, and we find that 468 galaxies (20% of our sample) have $\log(\mathrm{Age}) - \log(\mathrm{Age_{NEB}}) \geq 0.3$.

At $z \sim 2$, stellar masses are strongly constrained by IRAC data, since no strong emission lines fall in these filters. However, the stellar mass estimation can be affected by nebular emission if age is significantly affected too, since the mass to light ratio evolves with age. Indeed, in Figure 2, we show the comparison between stellar mass estimated without nebular emission ($\mathrm{M_\star}$) and stellar mass estimated with nebular emission ($\mathrm{M_{\star NEB}}$), for galaxies for which age estimation changes when accounting for nebular emission ($\log(\mathrm{Age}) - \log(\mathrm{Age_{NEB}}) \geq 0.3$). The impact of nebular emission is however not very strong since we find only 293 galaxies (12% of the sample) with $\log(\mathrm{M_\star}) - \log(\mathrm{M_{\star NEB}}) \geq 0.3$

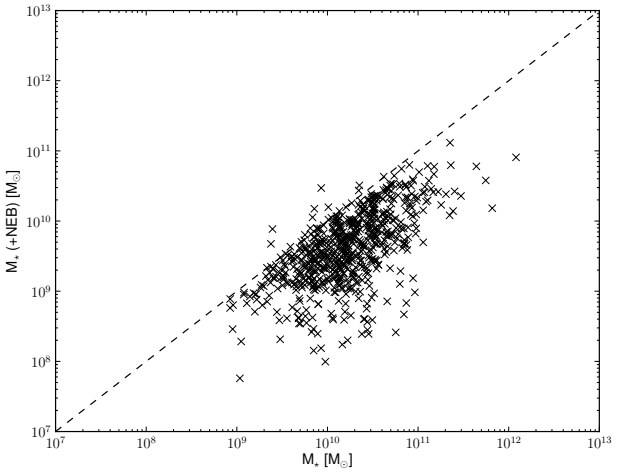

Fig. 2. Stellar mass estimated without nebular emission vs stellar mass estimated with nebular emission for galaxies with $\log(\mathrm{Age}) - \log(\mathrm{Age_{NEB}}) \geq 0.3$. The dashed is the one to one relation.

In another paper, we will present detailed results and implications for star formation history.

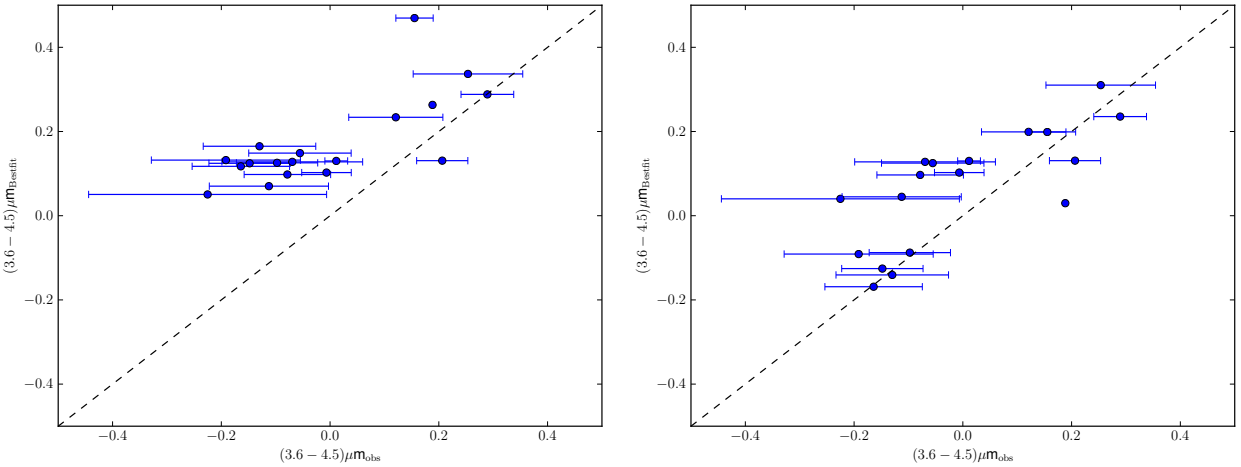

Fig. 3. Left: (3.6-4.5)μm observed color vs (3.6-4.5)μm best-fit SED color for objects with $3.8 < z_{\rm phot} < 5.0$, without taking into account nebular emission. **Right:** same but accounting for nebular emission.

5 Selection and physical properties of evolved galaxies at $z \sim 4$

Using evolutionary tracks, we define a color-color selection to identify evolved galaxies at $z \sim 4$, i.e with a strong Balmer break (see Nayyeri et al. 2013, for selection criteria). Contamination is mainly due to dusty starburst galaxies, while nebular emission can allow low-redshift starburst to pass the selection in narrow ranges of redshift, when flux in selection filters is enhanced by some emission lines.

The physical properties of $z \sim 4$ galaxies are more strongly affected by nebular emission in comparison with $z \sim 2$ galaxies, since strong emission lines (e.g. Hα) affect IRAC fluxes at $z > 3.8$. While no current facilities allow direct measurements of emission lines (except Lyα) at those redshift, Hα line is found in the 3.6μm filter at $3.8 < z < 5.0$, whereas very few lines are expected in the 4.5μm filter. Excess in the 3.6μm filter is interpreted as an additional flux due to the Hα line, and the (3.6-4.5)μm color is basically a model independent measurement of the Hα strength (Shim et al. 2011; de Barros et al. 2012; Stark et al. 2013). In Figure 3, we show the ability of our SED fitting code to reproduce observed (3.6-4.5)μm color of objects identified as evolved galaxies. As at $z \sim 2$, we show that our SED fitting code provide fits consistent with the observed strength of Hα.

SED fitting of our complete sample of evolved galaxies shows that an upper limit of $\sim 20\%$ of the sample show contamination by emission lines, which affects age, stellar mass, dust and star formation rate estimation. Typically, ages are reduced, stellar masses decreased, and dust attenuation and SFR increased. The complete analysis of these evolved galaxies can be found in (Nayyeri et al. 2013).

6 Conclusions

We present an homogeneous study of a sample of 2389 star-forming galaxies at $z \sim 2$, all spectroscopically confirmed, with deep photometry from up to 8 μm. We also use available measurement of Hα line for ~ 100 galaxies. Using a modified version of the *HyperZ* photometric redshift code which takes into account nebular emission (Schaerer & de Barros 2009), we explore a range of star formation history (constant, exponentially decreasing and rising). We test different star formation histories and differential attenuation between stellar and nebular emission (Calzetti 1997) to reproduce observed Hα fluxes. Declining SFH is unable to provide consistent f(Hα)$_{\rm SED}$, while differential attenuation leads also to underestimated f(Hα)$_{\rm SED}$ in comparison with observed fluxes. The main parameter affected by nebular emission is age, since some lines can mimic a Balmer break (Schaerer & de Barros 2009, 2010). While stellar mass is strongly constrained by IRAC data, changes in age estimation also affects significantly stellar mass estimation for a fraction of our sample (12%).

At $z \sim 4$, the characterization of evolved galaxies is more affected when nebular emission is accounted for in SED fitting, since strong emission lines can affect IRAC fluxes. Selection of such galaxies is mostly contaminated by dusty starburst galaxies, with only little effect of nebular emission. While we do not have access to observational evidence of strong emission lines at this redshift, the (3.6-4.5)μmcolor provide empirical evidence of strong Hα emission, color reproduced consistently by our SED fitting tool. $\sim 20\%$ of our sample

identified as evolved galaxies at $z \sim 4$ is significantly affected by nebular emission, leading to younger ages, lower stellar masses, higher dust attenuation and higher SFRs. Complete results of this study are presented in Nayyeri et al. (2013).

We thank the SF2A organisers. SdB also thanks the SF2A for its financial support. SdB is supported by a Swiss National Science Foundation Early.Postdoc fellowship.

References

Adelberger, K. L., Steidel, C. C., Shapley, A. E., et al. 2004, ApJ, 607, 226
Anders, P. & Fritze-v. Alvensleben, U. 2003, A&A, 401, 1063
Atek, H., Siana, B., Scarlata, C., et al. 2011, ApJ, 743, 121
Bolzonella, M., Miralles, J., & Pelló, R. 2000, A&A, 363, 476
Bruzual, G. & Charlot, S. 2003, MNRAS, 344, 1000
Calzetti, D. 1997, AJ, 113, 162
Calzetti, D., Armus, L., Bohlin, R. C., et al. 2000, ApJ, 533, 682
de Barros, S., Schaerer, D., & Stark, D. P. 2012, ArXiv e-prints
Erb, D. K., Shapley, A. E., Pettini, M., et al. 2006, ApJ, 644, 813
Kashino, D., Silverman, J. D., Rodighiero, G., et al. 2013, ArXiv e-prints
Labbe, I., Oesch, P. A., Bouwens, R. J., et al. 2012, ArXiv e-prints
Lidman, C., Hayes, M., Jones, D. H., et al. 2012, MNRAS, 420, 1946
Madau, P. 1995, ApJ, 441, 18
McLinden, E. M., Finkelstein, S. L., Rhoads, J. E., et al. 2011, ApJ, 730, 136
Nayyeri, H., Mobasher, B., Ferguson, H., et al. 2013, ApJ, submitted
Oke, J. B., Cohen, J. G., Carr, M., et al. 1995, PASP, 107, 375
Oke, J. B. & Gunn, J. E. 1983, ApJ, 266, 713
Ono, Y., Ouchi, M., Shimasaku, K., et al. 2010, ApJ, 724, 1524
Salpeter, E. E. 1955, ApJ, 121, 161
Schaerer, D. & de Barros, S. 2009, A&A, 502, 423
Schaerer, D. & de Barros, S. 2010, A&A, 515, A73+
Schaerer, D. & de Barros, S. 2011, ArXiv e-prints
Schaerer, D., de Barros, S., & Sklias, P. 2013, A&A, 549, A4
Schenker, M. A., Ellis, R. S., Konidaris, N. P., & Stark, D. P. 2013, ArXiv e-prints
Shim, H., Chary, R.-R., Dickinson, M., et al. 2011, ApJ, 738, 69
Smit, R., Bouwens, R. J., Labbe, I., et al. 2013, ArXiv e-prints
Stark, D. P., Schenker, M. A., Ellis, R., et al. 2013, ApJ, 763, 129
Steidel, C. C., Adelberger, K. L., Shapley, A. E., et al. 2003, ApJ, 592, 728
Steidel, C. C., Shapley, A. E., Pettini, M., et al. 2004, ApJ, 604, 534
Trump, J. R., Impey, C. D., Kelly, B. C., et al. 2011, ApJ, 733, 60
van der Wel, A., Straughn, A. N., Rix, H.-W., et al. 2011, ApJ, 742, 111

SF2A 2013
L. Cambrésy, F. Martins, E. Nuss and A. Palacios (eds)

THE M33 CO(2-1) SURVEY - STAR FORMATION AND MOLECULAR CLOUDS FORMATION

C. Druard[1,2], J. Braine[1,2] and K. F. Schuster[3]

Abstract. The IRAM Large Program consisting of observing the CO(2-1) transition in the Triangulum galaxy M33 is now over. This very sensitive survey covered the disk of the galaxy up to 8 kpc. Here we present the results and the techniques used in the data reduction process as well as the integrated intensity map. We determined that the velocity dispersion between molecular and atomic gas is very low. Whith this dataset, molecular cloud detection algorithm were also able to found more than 500 giant molecular clouds.

Keywords: galaxies, Local Group, ISM, molecular clouds, star formation

1 The observation of M33

The Triangulum galaxy, M33, is one of the closest spiral galaxies (840 kpc). With a mass of ∼10% of the Milky Way, M33 provides a stepping-stone between large spirals and smaller irregular galaxies like the Magellanic clouds. With its half-solar metallicity, gas-rich medium, and young stellar population, M33 is an ideal step towards younger and lower metallicity objects. Its proximity and optimal inclination allow us to study its molecular gas content, in terms of global/local dynamics and of giant molecular clouds and star formation. M33 has been observed at many FIR wavelengths in the framework of the Herschel HerM33es key project. We also dispose of a large amount of data at many different wavelength (UV, X, HI ...).

We have now completed the IRAM M33 large program of very sensitive 230GHz CO(J=2-1) observations covering the optical disk (figure 1) with a 12" spatial resolution (∼50pc) allowing us to detect ∼500 clouds. The observations were done using the 30-meter telescope of the Institut de RadioAstronomie Millimtrique (IRAM) on Pico Veleta in Spain. This work is a follow-up to Gardan et al. (2007) and Gratier et al. (2010) with a partial coverage of the disk. M33 was observed with the multi-pixel receiver HERA Schuster et al. (2004) using On-The-Fly mapping technique which enhance the mapping speed. The main goals of this Large Program are to identify the Giant Molecular Clouds (GMCs) and study their evolution.

2 Data processing

After 5 years of observations we obtained up to 2.10^8 spectra in about 400 hours in a field of view of 55'x400' which accounts for about 400Go of raw data. Data reduction was done using the IRAM GILDAS reduction packages CLASS and GREG. The difficulty was to optimize the reduction process while staying consistent whith the previous works of Gardan et al. (2007) and Gratier et al. (2010). This process can be summarized into these following steps:

1. at first we eliminate poor data
2. we cut every spectra from -500 km/s to 0 km/s velocity shift, corresponding to M33 velocity range
3. we fit a 0 order baseline to get rid of the continuum in each spectrum

[1] Univ. Bordeaux, LAB, UMR 5804, F-33270, Floirac, France
[2] CNRS, LAB, UMR 5804, F-33270, Floirac, France
[3] IRAM, 300 rue de la Piscine, 38406 St. Martin dHères, France

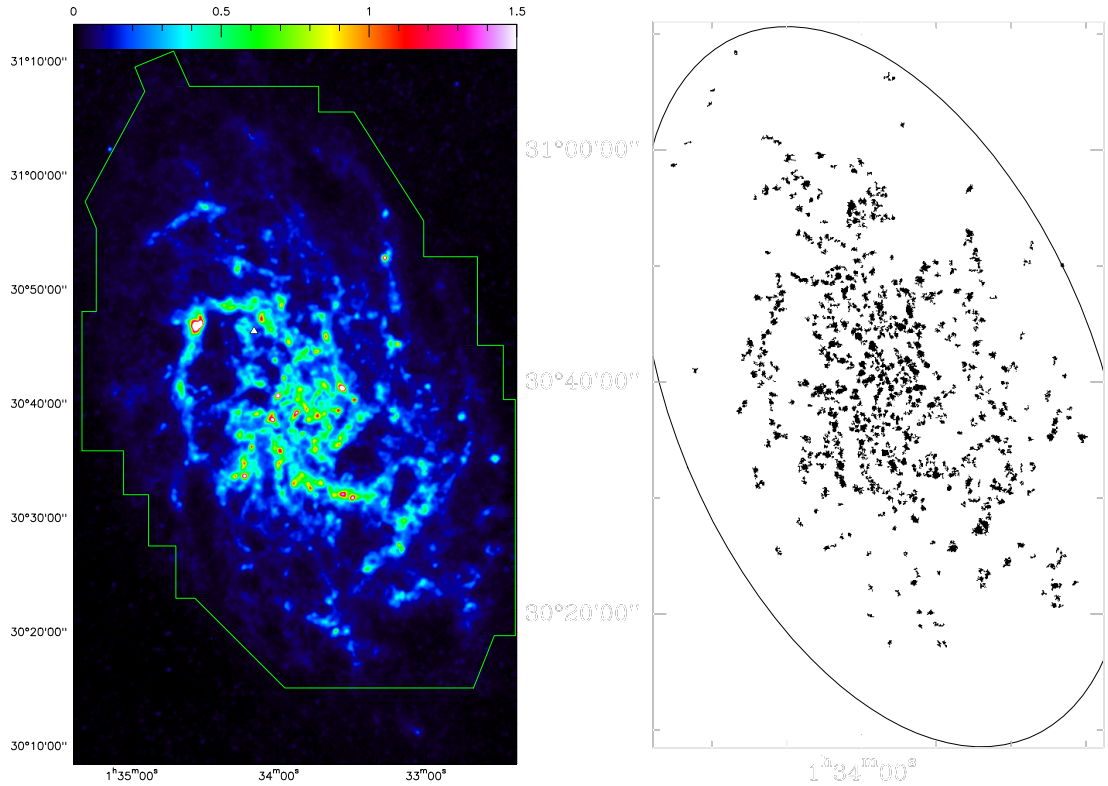

Fig. 1. Left: The Triangulum galaxy M33. This image shows the full coverage of the CO(2-1) mapped field with the edges in yellow on top of a Herschel 250m UV data that traces hot dust. **Right:** Molecular clouds detected in M33 with the CPROPS algorithm.

4. we compare the RMS noise of each spectrum with the theoretical noise given by the radiometer equation $\sigma_{theo} = 2\frac{T_{sys}}{\sqrt{\Delta_\nu t}}$ (where T_{sys} is the system temperature, Δ_ν the channel width and t the integration time of the spectrum). The spectra presenting a RMS noise higher tha $1.1\sigma_{theo}$ are filtered out ($\sim$ 11% of the dataset)

5. since each position in M33 is associated with more than one spectra, we build a datacube (3D position-position-velocity map)and then convert it back to regularly gridded spectra with higher signal to noise ratio than the previous ones.

6. we fit a third order polynomial baseline on each spectra. This time we use velocity-windows inside which the signal is excluded from the fit. For this we use HI 25"x25"x1.27km/s VLA maps from Gratier et al. (2010), making the assumption that the molecular gas cannot be present at positions and velocities where there is no atomic gas. The limits of these windows are computed with the following technique: we detect HI higher than 4σ (10K) in the HI datacube and then we go down on each side of the HI peak to the first channel at or below 0K that gives us the corresponding velocity associated with the upper or lower limit. For areas where there is no HI detected, window limits are given by the rotation curve given in Corbelli & Schneider (1997) $\pm$30km/s.

7. we build a last cube with a spectral resolution of 2.6km/s and a spatial resolution of 12"

We obtain a data-cube with a relatively homogeneous RMS noise of 20mK as seen in figure 2.

3 First results

3.1 Integrated intensity m

Integrated intensity maps were also produced using the same masking techniques than during the reduction process. Only the channels corresponding to velocities associated with HI emission were used to compute these

maps. This adaptive fit technique ensures the map not to contain too much noise and, at the same time, increase the sensitivity to diffuse CO emission. The obtained map is shown in figure 2. We can see that, apart from diffuse emission, the CO is located in the first kiloparsecs of the disk and regroup into clouds.

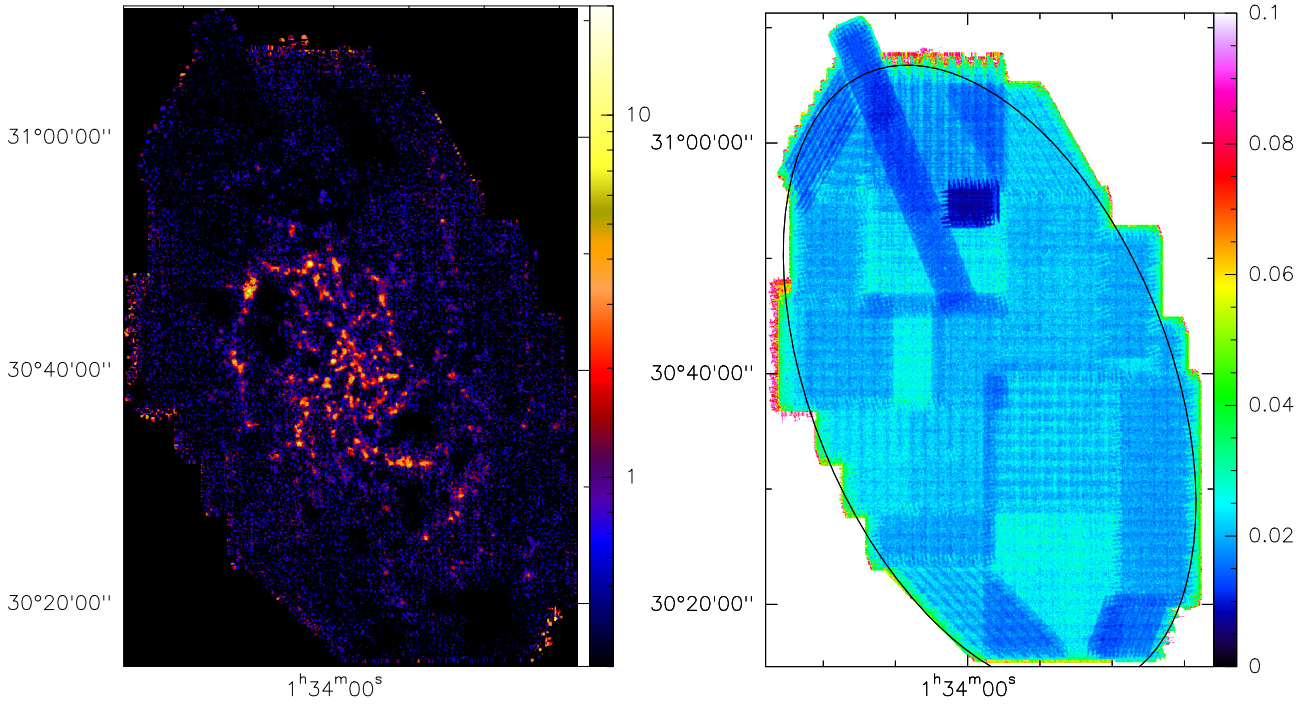

Fig. 2. Left: Integrated intensity map of the CO(2-1) line in K.km/s. Combination of HI-0K mask and rotation curve mask (where there is no HI detected) was used to compute this map.. **Right:** RMS noise map of M33 in Kelvin. The black ellipse corresponds to a distance of 7kpc from the center.

3.2 Centered cube

Comparisons with the HI emission shows that the CO-HI velocity dispersion is extremely low. A useful technique to "better see" the CO emission is to stack every spectra around the velocity of the HI peak since weak CO emission cannot be seen in singular spectra. To do this we produced recentered data-cubes : each CO spectrum is centered at a reference velocity corresponding to the HI peak velocity at this position in the sky. With this new data-cube we were able to stack the signal in larger areas where the CO peak velocity were not previously homogeneous. We produced stacked spectra corresponding to HI-free areas to verify our first hypothesis of no CO at positions and velocities different from HI. The produced stacked spectra were indeed consistent with the signal that we would obtain from error beam pickups of the 30m telescope. The stacked spectra corresponding to the whole disk show a very narrow velocity dispersion on the global scale of ∼11km/s, which means that CO follows well the HI in terms of position and velocities.

3.3 Molecular clouds detection

The CO emission has been decomposed into clouds using the CPROPS detection algorithm (Rosolowsky et al. 2007) which also computes properties associated to each detected GMC. At this distance, we are able to resolve GMCs down to the size of 50pc. More than 500 GMCs were detected whithin this new dataset compared to the 337 clouds detected by Gratier et al. (2012) with half the disk coverage and we found that the linewidth of these clouds is smaller for a given size than in the Milky Way. This cloud sample is the largest up to date in an external galaxy. Figure 1 shows the repartition of these clouds which total mass is about 1.8 $10^8 M_\odot$ which is coherent with previous studies and can be compared with 3.3 $10^8 M_\odot$, which is the total mass of M33 computed from the whole CO(2-1) emission. We intend to use this sample to characterize each clouds in terms of star forming activity using tracers like Hα, FUV, 24μm. This sample will also be useful to understand the

formation conditions of these clouds, study their distribution on the disk, the evolution of some parameters with the position or the radial distance and understand better the conditions of formation of these GMC in subsolar metallicity environment.

References

Corbelli, E. & Schneider, S. E. 1997, ApJ, 479, 244
Gardan, E., Braine, J., Schuster, K. F., Brouillet, N., & Sievers, A. 2007, A&A, 473, 91
Gratier, P., Braine, J., Rodriguez-Fernandez, N. J., et al. 2012, A&A, 542, A108
Gratier, P., Braine, J., Rodriguez-Fernandez, N. J., et al. 2010, A&A, 522
Rosolowsky, E., Keto, E., Matsushita, S., & Willner, S. P. 2007, ApJ, 661, 830
Schuster, K.-F., Boucher, C., Brunswig, W., et al. 2004, A&A, 423, 1171

SF2A 2013
L. Cambrésy, F. Martins, E. Nuss and A. Palacios (eds)

EXTREME [CII] LINE COOLING IN RADIO-GALAXIES: A SIGNATURE OF TURBULENT DISSIPATION IN ACTIVE GALACTIC NUCLEI?

P. Guillard[1], N. Nesvadba[1], P. Ogle[2], M. Lehnert[3], F. Boulanger[1], P. Appleton[4] and G. Pineau des Forêts[1 5]

Abstract. Observations by the *Spitzer Space Telescope* have revealed a population of radio galaxies with enhanced infrared molecular hydrogen (H_2) line cooling, above that expected by star formation heating alone. We present *Herschel* observations of these galaxies, which show unusually powerful [CII]λ158μm line emission of very broad line-width. The C^+/PAH and C^+/FIR flux ratios are found to be extremely large, in most cases greatly in excess of that expected by photoelectric heating of the gas, and comparable in power to the mid-infrared H_2 lines. In contrast, [OI] emission is found to be quite weak. We show that the [CII] line emission mostly traces the molecular gas, and that a very large fraction of this gas is diffuse and warm. We also briefly discuss the possible heating sources of the gas (turbulent heating and/or cosmic rays). These results have profound consequences on our interpretation of FIR cooling lines at high-redshifts and on our understanding of dissipation of energy, feedback and energetics of galaxy formation in general. The fact that C^+ and H_2 can be strongly enhanced in shocks and turbulent systems in general will be of great importance for ALMA (and perhaps SPICA) observations which will extend *Herschel* observations to much higher redshifts, where the proportion of turbulently-heated molecular gas may be more important.

Keywords: AGN feedback, radio-galaxies, 3C 326, turbulence, interstellar medium, molecular gas

1 Introduction: what is the efficiency of AGN feedback at low redshifts?

AGN feedback is now widely postulated to regulate galaxy growth over cosmic time (e.g. Springel et al. 2005), in particular to reconcile the predicted mass functions with observations (Benson et al. 2003) showing that most massive local galaxies have old stellar populations (e.g. Thomas et al. 2005; Croton et al. 2006). At high redshifts, AGN-driven winds are invoked to clear out the reservoir of cold molecular gas, which quenches the starburst associated with the early phase of massive galaxy formation (e.g. Silk & Rees 1998; Nesvadba et al. 2006). At lower redshifts, AGN feedback is also needed to complement starburst-driven feedback in order to heat the gas over long timescales, thus regulating star formation and limit gas accretion (e.g. Begelman & Cioffi 1989).

The energy released by the central supermassive black hole is in principle enough to balance the gas cooling and remove the gas from the dark matter halo of a galaxy. However, it is not clear what is the efficiency of this process. What fraction of the AGN energy goes into: (1) the heating of the X-ray emitting cocoon of tenuous gas? (2) the heating of the cold molecular gas? (3) the driving of mass-loaded outflows? What is the dynamical coupling efficiency of the AGN mechanical energy to the different phases of the host interstellar medium (ISM)? These are the questions we are trying to address with detailed observations of low-redshift radio-galaxies.

2 Herschel observations of powerful, turbulent radio-galaxies

Local radio-loud galaxies are ideal candidates to study how the AGN energy is dissipated and distributed amongst the gas phases since we can estimate the mechanical energy of their jets with a relatively good accuracy, and the spatial scale over which this energy is deposited (which can reach Mpc scales, e.g. Machalski et al. 2008).

[1] Institut d'Astrophysique Spatiale, Université Paris Sud, UMR 8617 du CNRS, 91405 Orsay
[2] Spitzer Science Center, Caltech, Pasadena, CA 91125, USA
[3] Institut d'Astrophysique de Paris, UMR 7095 du CNRS, Université Pierre et Marie Curie, 98bis Bd Arago, 75014, Paris
[4] Nasa Herschel Science Center, Caltech, Pasadena, CA 91125, USA
[5] LERMA (UMR 8112 du CNRS), Observatoire de Paris, 61 Avenue de l'Observatoire, F-75014 Paris, France

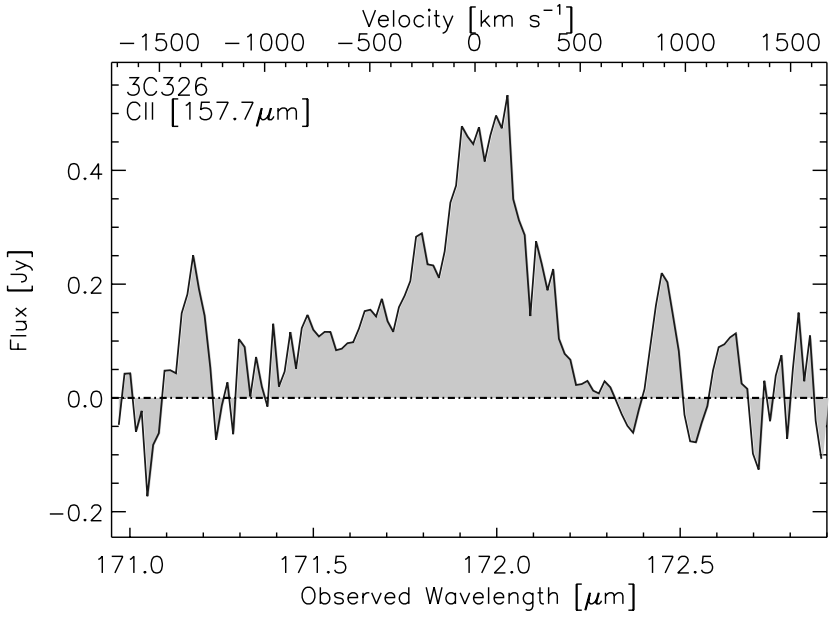

Fig. 1. [CII]λ158 spectrum in 3C326 N observed with *Herschel/PACS* (from Guillard et al. 2013a). The total line flux is 1.2×10^{-17} W m^{-2}, corresponding to a line luminosity of 6.2×10^7 L$_\odot$ for a redshift of $z = 0.0895$. A clear blue-shifted broad wing is detected, with a velocity shift of -445 km s^{-1} with respect to the narrower component (after Gaussian decomposition).

We observed the [CII]λ158μm and [OI]λ63μm lines with the PACS far-infrared spectrometer (Poglitsch et al. 2010) onboard the *Herschel* Space Observatory (Pilbratt et al. 2010) in a sample of nine powerful radio-galaxies known to have outflows of HI gas (Morganti et al. 2005) and bright, shock-excited rotational H_2 line emission (Guillard et al. 2012). The PACS observing mode and data reduction are discussed in Guillard et al. (2013b). In the following we briefly summarize the observational results.

In all radio-galaxies* we detect bright [CII] lines, with fluxes ranging from 10^{-17} to 3×10^{-16} W m^{-2}, corresponding to line luminosities of $10^7 - 5 \times 10^9$ L$_\odot$. The [CII] lines are all very broad, with intrinsic FWHM ranging from 400 to 1200 km s^{-1}. 3/7 galaxies show significant blue-shifted wings or very broad symmetric components underlying a narrower line. The example of the 3C 326 galaxy, one of the most extreme object in terms of H_2 turbulent heating (Ogle et al. 2010; Nesvadba et al. 2010), is shown in Figure 1, and discussed in details in Guillard et al. (2013a).

3 [CII] line cooling and turbulent heating

The [CII]λ158μm line is the main coolant of the cold neutral medium ($T \approx 100-300$K, $n_{\rm H} \approx 10^2-3\times10^3$ cm^{-3}) heated by UV radiation, and therefore controls the balance between the $\approx$ 5000 K gas and the cold neutral medium. This makes [CII] a key line diagnostic to probe the formation of cold gas.

The masses of [CII]-emitting gas, derived from the observed [CII] luminosity and the theoretical C^+ cooling rate, range from 2.5×10^7 to 1.2×10^{10} M$_\odot$ (Guillard et al. 2013b) for a gas temperature of 100 K and a hydrogen density of $n_{\rm H} = 6000$ cm^{-3} (equal to the [CII] critical density with H_2 as collision partner). A gas temperature is 100 K is optimal for [CII] line emission. At higher temperatures Oxygen cooling starts to take over, and lower temperatures are below the excitation temperature of the transition†. So any deviation from this temperature would require more gas mass to account for the [CII] line emission. The comparison of these masses to the observed gas masses in the different ISM phases shows that the molecular gas is the only reservoir of gas containing enough mass to produce the [CII] emission, the masses of ionized and atomic gas being too low. Therefore, a large fraction of the molecular gas in those radio-galaxies is warm ($T > 100$ K), which is in

*Except two galaxies 3C 293 and 4C 12.50 which do not have [CII] measurements.
†$^2P_{3/2} \rightarrow ^2 P_{1/2}$, $E_{ul}/k = 92$ K.

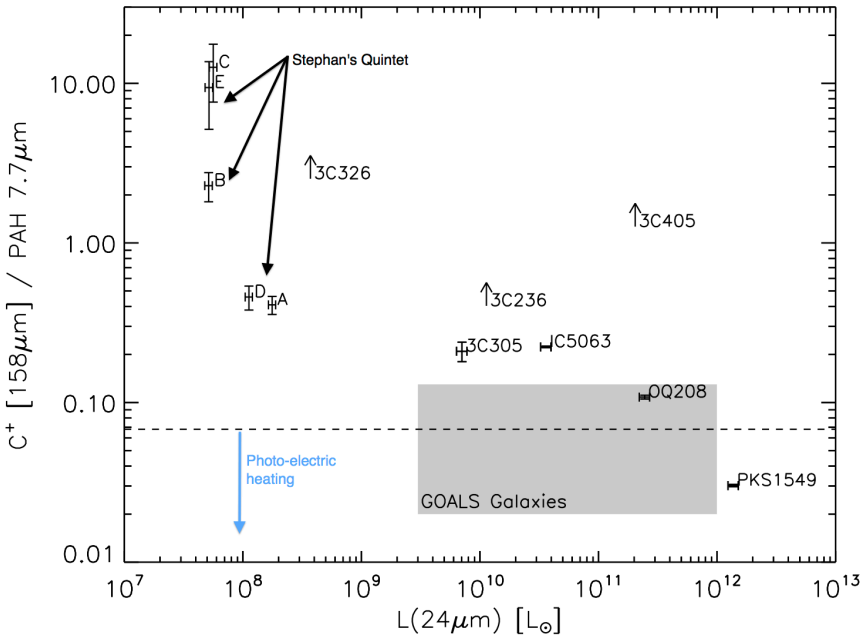

Fig. 2. [CII]λ158μm to PAH 7.7μm flux ratio as a function of the monochromatic 24μm luminosity (observed by *Spitzer/IRS*, from Guillard et al. 2012). The dashed line is the upper limit on the C^+-to-PAH ratio compatible with photoelectric heating of the gas. 5/7 galaxies are clearly above that limit. The grey area shows the rage of ratios observed in the GOALS sample (Díaz-Santos et al. 2013). The letters denote different regions of the Stephan's Quintet shock region, (Appleton et al. 2013). This diagnostic appears to be highlight the enhancement of the C^+ emission due to the dissipation of turbulent energy.

agreement with the large amounts of warm H_2 gas detected (Ogle et al. 2010), sometimes comparable to the H_2 masses derived from CO observations (Nesvadba et al. 2010).

The weakness of the [OI] and CO lines in those radio-galaxies, except for 3C 405, suggest that the average molecular gas density is moderate, with $10^2 < n_{\rm H} < 10^4$ cm^{-3} (Guillard et al. 2013a,b). Together with the constraint on the gas temperature discussed above, this suggests that the average pressure of the warm H_2 is relatively low ($5 \times 10^4 < P/k < 5 \times 10^5$ K cm^{-3}).

What is the main heating source of the [CII]-emitting gas? In star-forming galaxies, the excitation of the [CII] line mostly arises from the collisions between C^+ and the warm gas (mostly H and H_2 partners) heated by the photo-electric effect from PAH molecules (dominant) and small grains (e.g. Bakes & Tielens 1994). Therefore, the [CII]-to-PAH luminosity ratio is a direct measure of the efficiency of photoelectric heating, which is a few percent. Figure 2 shows that 6/7 radio-galaxies studied here have unusually large [CII]/PAH ratios, showing that UV photons cannot be the main source of heating of the [CII]-emitting gas. Extreme [CII]/PAH ratios have also been detected in other systems like galaxy interactions (Stephan's Quintet, Appleton et al. 2013, and the Taffy galaxies, Peterson et al. in prep.).

Nesvadba et al. (2010) and Ogle et al. (2010) argued that the dissipation of turbulent energy is the primary heating source of the warm H_2 gas in those radio-galaxies. Since the [CII] line emission is mostly coming from the molecular gas, we assume that the [CII] line is tracing the kinematics of the H_2 gas. Indeed, the [CII] line and the ro-vibrational H_2 1-0S(3) line observed by Nesvadba et al. (2011) have remarkably similar profiles (see the discussion about the 3C 326 line kinematics in Guillard et al. 2013a). The turbulent kinetic luminosity associated with the H_2 gas velocity dispersion alone is a factor of > 2 higher than the total [CII]+H_2 cooling rate for all galaxies, so turbulent heating is energetically plausible (Guillard et al. 2013a), and we interpret the [CII] line emission within this framework of turbulent dissipation. In general, since the jet is perpendicular to the disk plane, this turbulent energy is likely to be injected over a spatial scale comparable to the vertical scale height of the disk, and can maintain high values of the disk thickness (Guillard et al. 2013a). This vertical turbulent support can stabilize the molecular disk against fragmentation into bound, star-forming clumps, and

is a possibility to explain why some of these sources have heavily suppressed star formation activity (Nesvadba et al. 2010).

We note that cosmic ray heating, although energetically possible at high ionization rates ($10^{-14} < \zeta < 5\times10^{-12}$ s^{-1}), would require high gas densities ($n_{\rm H}$ larger than a few 10^3 cm^{-3}) for the gas to remain molecular (see discussion in Ogle et al. 2010), which is not suggested by the weakness of the [OI] and CO lines (see above). Therefore, cosmic rays may not be the main heating source in the diffuse molecular gas. However, cosmic rays must play an important chemical role in maintaining a high fractional abundance of C^+, the CO molecules being dissociated by secondary electrons (Mashian et al. 2013; Guillard et al. 2013a).

4 Conclusions and implications on the interpretation of high redshift observations

We detect strong [CII] line emission in a small sample of radio-galaxies chosen to show signs of jet-driven outflows, at levels brighter than what is expected from star formation. We show that the molecular gas is the only mass reservoir capable of explaining the observed [CII] luminosity, and that the bulk of this gas is warm ($T \approx 100$ K) and diffuse ($10^2 < n_{\rm H} < 10^4\,{\rm cm}^{-3}$). We interpret the [CII] observations in the framework of turbulent dissipation, believed to be the heating source of the warm H_2 gas, and offering a natural link between the [CII] and rotational H_2 line observations by *Spitzer*. The dissipation of a small fraction of the jet mechanical energy ($\approx 10\%$) can maintain large amounts of H_2 gas (10^8 – 5×10^{10} M$_\odot$) at low pressure, thus in a physical state not favourable for star formation. This suggests that AGN-driven turbulence in the H_2 gas plays a key role in the way the AGN mechanical energy is dissipated and star formation regulated.

Bright [CII] line emission in turbulence-dominated systems – boosted by shocks (Lesaffre et al. 2013) or vortices (Godard et al. in prep.), and above levels expected from star formation alone – may have important impact on our interpretation of far-infrared line cooling in gas at high-redshifts. Dissipation of turbulence is likely to be a generic feature of early stages of galaxy build-up, and we may have already some first observational signatures of that dissipation at $z \approx 2$ through enhanced H_2 line emission (Ogle et al. 2012) and perhaps also [CII] (Seymour et al. 2012).

References

Appleton, P. N., Guillard, P., Boulanger, F., et al. 2013, ArXiv e-prints
Bakes, E. L. O. & Tielens, A. G. G. M. 1994, ApJ, 427, 822
Begelman, M. C. & Cioffi, D. F. 1989, ApJ, 345, L21
Benson, A. J., Bower, R. G., Frenk, C. S., et al. 2003, ApJ, 599, 38
Croton, D. J., Springel, V., White, S. D. M., et al. 2006, MNRAS, 365, 11
Díaz-Santos, T., Armus, L., Charmandaris, V., et al. 2013, ApJ, 774, 68
Guillard, P., Nesvadba, N., Lehnert, M., & Boulanger, F. 2013a, A&A, to be submitted
Guillard, P., Ogle, P., Appleton, P., et al. 2013b, ApJ, to be submitted
Guillard, P., Ogle, P. M., Emonts, B. H. C., et al. 2012, ApJ, 747, 95
Lesaffre, P., Pineau des Forêts, G., Godard, B., et al. 2013, A&A, 550, A106
Machalski, J., Kozieł-Wierzbowska, D., Jamrozy, M., & Saikia, D. J. 2008, ApJ, 679, 149
Mashian, N., Sternberg, A., & Loeb, A. 2013, MNRAS
Morganti, R., Tadhunter, C. N., & Oosterloo, T. A. 2005, A&A, 444, L9
Nesvadba, N. P. H., Boulanger, F., Lehnert, M. D., Guillard, P., & Salome, P. 2011, A&A, 536, L5
Nesvadba, N. P. H., Boulanger, F., Salomé, P., et al. 2010, A&A, 521, A65+
Nesvadba, N. P. H., Lehnert, M. D., Eisenhauer, F., et al. 2006, ApJ, 650, 693
Ogle, P., Boulanger, F., Guillard, P., et al. 2010, ApJ, 724, 1193
Ogle, P., Davies, J. E., Appleton, P. N., et al. 2012, ApJ, 751, 13
Pilbratt, G. L., Riedinger, J. R., Passvogel, T., et al. 2010, A&A, 518, L1
Poglitsch, A., Waelkens, C., Geis, N., et al. 2010, A&A, 518, L2
Seymour, N., Altieri, B., De Breuck, C., et al. 2012, ApJ, 755, 146
Silk, J. & Rees, M. J. 1998, A&A, 331, L1
Springel, V., Di Matteo, T., & Hernquist, L. 2005, MNRAS, 361, 776
Thomas, D., Maraston, C., Bender, R., & Mendes de Oliveira, C. 2005, ApJ, 621, 673

SF2A 2013
L. Cambrésy, F. Martins, E. Nuss and A. Palacios (eds)

MASS ASSEMBLY IN QUIESCENT AND STAR-FORMING GALAXIES SINCE $Z \simeq 4$ FROM ULTRAVISTA DR1 IN THE COSMOS FIELD

O. Ilbert[1], H. J. McCracken[2], O. Le Fèvre[1], P. Capak [3], J. Dunlop [4], A. Karim [5], M. A. Renzini [6], K. Caputi[7], S. Boissier[1] and the COSMOS team

Abstract. We estimate the galaxy stellar mass function and stellar mass density for star-forming and quiescent galaxies out to $z = 4$. We construct a sample of 220000 galaxies selected at $K_s < 24$. Our analysis is based on photometric redshifts with a precision of $\sigma_{\Delta z/(1+z)} = 0.008$ at $i^+ < 22.5$ and $\sigma_{\Delta z/(1+z)} = 0.03$ at $1.5 < z < 4$. We find a mass-dependent evolution of the global and star-forming populations, with the low-mass end of the mass functions evolving more rapidly than the high-mass end. For the mass function of the quiescent galaxies, we do not find any significant evolution of the high-mass end at $z < 1$ while we observe a clear flattening of the faint-end slope. From $z \sim 3$ to $z \sim 1$, the mass density of quiescent galaxies increases by 1.6 dex. We investigate the link between direct SFRD measurements and the evolution of the mass density. The star formation history that we infer from our mass density evolution is in excellent agreement with direct SFRD measurements at $z < 1.5$, while we find differences of 0.2 dex at $z > 1.5$ consistent with the expected uncertainties. Finally, we present a new method to infer the specific star formation rate from the mass function of star-forming galaxies and we find a continous increase of the sSFR with redshift out to $z \sim 4$. The photometric catalogues and associated photometric redshifts are available at http : //terapix.iap.fr/article.php?id_article = 844.

Keywords: Galaxies: distances and redshifts – Galaxies: evolution – Galaxies: formation – Galaxies: star formation – Galaxies: stellar content

1 Introduction

The galaxy stellar mass function (hereafter MF) is a fundamental indicator of the physical processes that regulate mass assembly in galaxies across cosmic time. Stellar mass assembly in galaxies is the result of star formation and mergers. Star formation is regulated by numerous physical processes: the amount of accreted gas available by radiative cooling or cold accretion ; AGN feedback which could shut down the star formation ; or by other processes such as supernovae-driven winds in less massive haloes. The relative contribution and operating timescales of these different processes regulate the stellar mass growth and the migration from star-forming galaxies to quiescent galaxies. The evolutionary tracks of the quiescent and star-forming MF as a function of look-back time reveal the major paths taken by different galaxy populations across cosmic time. This measurement quantifies the efficiency in forming new stellar populations and the quenching efficiency depending on the epoch and galaxy mass.

Measuring the stellar masses is challenging beyond $z \sim 1$: the availability of deep wide field near-IR multi-band photometry is essential. Spectral features like the D4000 or Balmer break move into the near-IR at $z > 1.5$, and several near-IR bands are required to properly sample the spectral energy distribution (SED) and enable stable photometric redshifts and stellar masses from SED-fitting techniques. The COSMOS field is one of the best available fields to derive the MF thanks to the large area (2 deg^2) and the large amount of deep ($I_{AB} \sim 26.5$) multi-wavelength data available (more than 35 bands). The UltraVISTA survey covered 1.5 deg^2 of the COSMOS field with deep NIR data ($K_s < 24$). Thanks to these data, we were able to derive accurate photometric redshifts at $z > 1.5$, well tested with more than 35000 spectroscopic redshifts. We estimated the galaxy stellar mass function and stellar mass density for star-forming and quiescent galaxies out to $z = 4$. This study is published in Ilbert et al. (2013).

[1] Aix Marseille Université, CNRS, LAM (Laboratoire d'Astrophysique de Marseille) UMR 7326, 13388, Marseille, France
[2] Institut d'Astrophysique de Paris, UMR7095 CNRS, Université Pierre et Marie Curie, 98 bis Boulevard Arago, 75014 Paris, France
[3] Spitzer Science Center, California Institute of Technology, Pasadena, CA 91125, USA
[4] Institute for Astronomy, University of Edinburgh, Royal Observatory, Edinburgh, EH9 3HJ, UK
[5] Argelander-Institute of Astronomy, Bonn University, Auf dem Hügel 71, D-53121 Bonn, Germany
[6] Dipartimento di Astronomia, Universita di Padova, vicolo dell'Osservatorio 2, I-35122 Padua, Italy
[7] Kapteyn Astronomical Institute, University of Groningen, P.O. Box 800, 9700 AV Groningen, the Netherlands

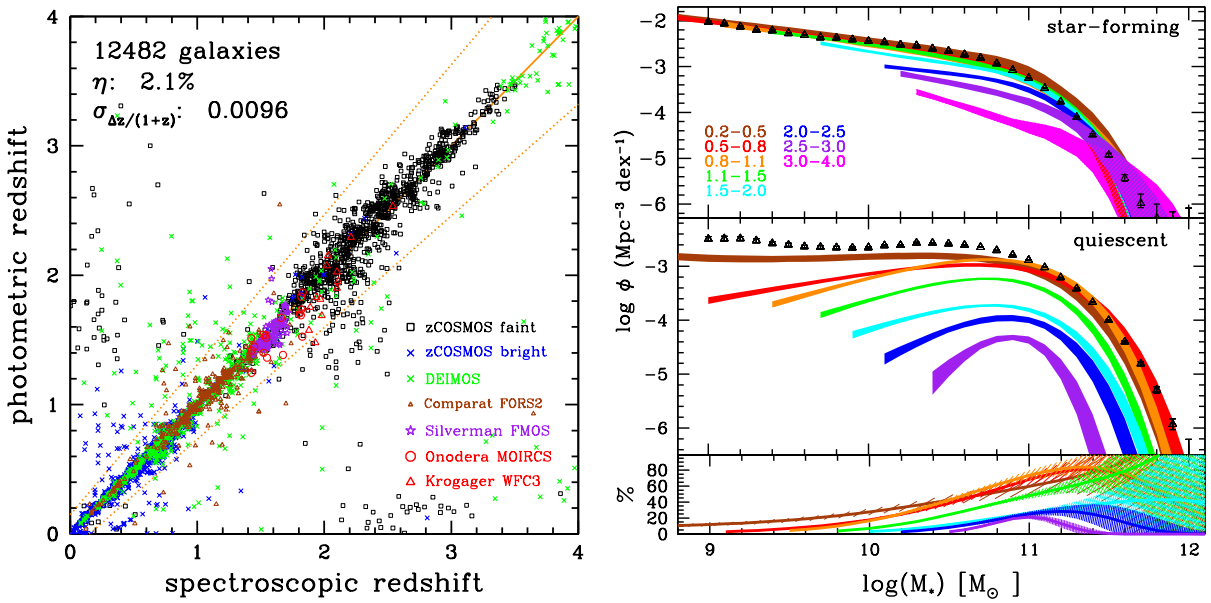

Fig. 1. Left: Photometric redshifts versus spectroscopic redshifts. Only secure spectroscopic redshifts at $K_s < 24$ are considered. Different colors color to the different spectroscopic samples listed in section 2. **Right:** Galaxy stellar mass functions up to $z = 4$ for the star-forming population (top panel) and for the quiescent population (middle panel). The fraction of quiescent is given in the bottom panel. Each color corresponds to a redshift bin.

2 Data

Our photometric catalogue comprises near-infrared data taken on the VISTA telescope as part of the UltraVISTA project and optical broad and intermediate-band data taken with the SUPRIME camera on Subaru in support of the COSMOS project (Capak et al. 2007). The near-infrared data we use here corresponds to the UltraVISTA DR1 data release fully described in McCracken et al. (2012). The first UltraVISTA DR1 data release covers 1.5 deg^2 in four near-infrared filters Y, J, H and K_s. Fluxes are measured on PSF-homogenised images in 25 bands including optical broad and intermediate-band Subaru data taken for the COSMOS project. We also add four bands at $3.6-8\mu m$ from S-COSMOS and the GALEX NUV band. We keep only the sources at $K_s < 24$ located in areas with a good image quality.

The photometric redshifts are derived using `Le_Phare` (Arnouts et al. 2002, Ilbert et al. 2006) following a procedure similar to Ilbert et al. (2009). We use elliptical and spiral galaxy templates from the Polletta et al. (2006) library, complemented with blue star-forming templates generated with Bruzual & Charlot (2003) SPS models. Extinction is added as a free parameter and several extinction laws are considered (Calzetti et al. 2000, Prevot 1984 and a modified version of the Calzetti laws including a bump at 2175Å). Emission lines are added to the templates using an empirical relation between the UV light and the emission line fluxes.

It is essential to check that our photo-z are robust at $z > 1.5$ before extending our analysis at higher redshift. We combine several spectroscopic samples to test the accuracy of the photometric redshifts, including zCOSMOS-bright with 20700 bright VIMOS/VLT spectra selected at $i^+ < 22.5$ (Lilly et al. 2007), zCOSMOS faint with 9500 faint VIMOS/VLT spectra selected at $1.5 < z < 3$ (Lilly et al., in preparation), 2300 DEIMOS/Keck redshifts which combined several selected sub-populations of blue star-forming and infrared galaxies at $0.5 < z < 6$ (Capak et al., in preparation), 835 FORS2/VLT redshifts at $0.6 < z < 1.8$ (Comparat et al., in preparation), 138 FMOS/Subaru redshifts at $1.4 < z < 1.8$ (Silverman et al., in preparation), 18 faint quiescent galaxies at $z < 1.9$ obtained with MOIRCS/Subaru (Onodera et al. 2012) and 16 faint quiescent galaxies at $1.85 < z < 2.6$ obtained with the WFC3 grism observations from the 3D-HST survey (Krogager et al., 2013).

The comparison between photometric and spectroscopic redshifts is shown in Figure.1. Our photometric redshifts have two regimes: at $i^+_{AB} < 22.5$ ($z_{med} \sim 0.5$), precision 1% with less than 1% of catastrophic failures. In the high redshift range $1.5 < z < 4$, the precision of the photo-z is tested against the zCOSMOS faint sample, and is 3% for $i^+_{med} \sim 24$ galaxies. Therefore, we can ensure that our photo-z are robust at $z > 1$ and we are now able to extend MF measurements to $z = 4$.

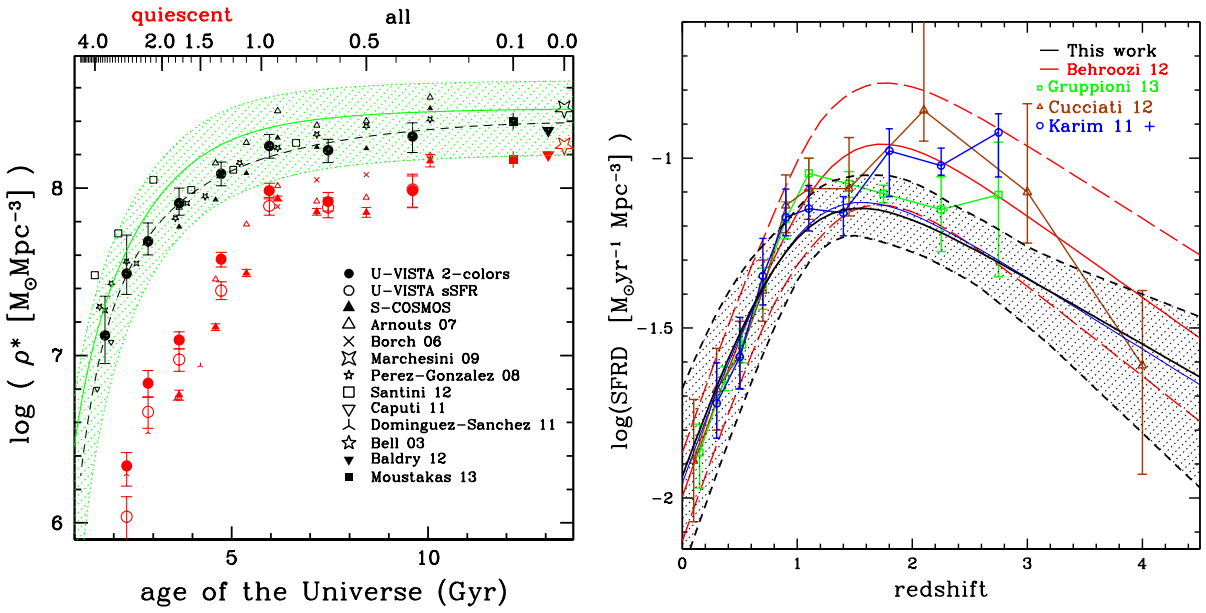

Fig. 2. Left: Stellar mass density as a function of cosmic time. Black and red points correspond to the full and quiescent populations, respectively. The solid circles correspond to our new results using UltraVISTA. The green shaded area corresponds to the cosmic SFR compiled by Behroozi et al. (2013) and integrated over cosmic time. **Right:** A comparison between the star formation history inferred from the UltraVISTA mass density (black solid line and dashed area) and direct SFRD measurements listed in Section 3.

3 Evolution of the Stellar Mass Function and Mass Density

We used stellar population synthesis (SPS) models to convert luminosity into stellar mass. The templates are generated using the SPS models from Bruzual & Charlot (2003), assuming exponentially declining star formation histories. We measured the stellar mass functions using the tool ALF (Ilbert et al. 2005). This tool includes several non-parametric estimators and we verified that the three non-parametric estimators are in good agreement over the considered mass ranges (Ilbert et al. 2004). Our error budget includes the Poissonian errors, the photo-z and stellar mass uncertainties and the cosmic variance. We also correct for the Eddington bias when we fit the non-parametric data.

Right panel of Figure 1 shows the MFs of quiescent and star-forming galaxies. We isolate the quiescent population using a classification based on the rest-frame colours $NUV - r^+$ and $r^+ - J$. This classification separates cleanly dusty star-forming galaxies and quiescent galaxies. We do not find any significant evolution of the high-mass end at $z < 1$ for the quiescent population (any evolution being limited to $\Delta M < 0.2 dex$), while we observe a clear flattening of the slope in the same redshift range. We interpret this evolution of the low-mass end of the MF as arising from continuous quenching of galaxies between $z \sim 1$ and $z \sim 0.1$, probably by physical processes related to environment (see Peng et al. 2010).

The UltraVISTA data allow us to trace the growth in stellar mass density in quiescent galaxies from $z \sim 3$ to the present day. From $z \sim 3$ to $z \sim 1$ we find a rapid increase in the stellar mass density of all quiescent galaxies, independent of stellar mass. We confirm that the steep rise of more than one order of magnitude of this population between $1 < z < 2$ observed in previous works (Arnouts et al., 2007; Ilbert et al., 2010). This must indicate that a fraction of star-forming galaxies is continuously quenched at $z > 1$. Because of the different faint-end slopes of the MF between the quiescent and global populations at $z < 3$, we infer that the physical processes which quench the star formation are more efficient above $\mathcal{M} \gtrsim 10^{10.7-10.9} \mathcal{M}_{\odot}$. This scenario is consistent with the model proposed by Peng et al. (2010) who introduce a "mass quenching" process. Since the high-mass end of the quiescent MF stops evolving at $z < 1$, we conclude that: 1) star formation is not efficient enough at $z < 1$ to produce new massive star-forming galaxies, which could be quenched later; 2) major mergers between massive galaxies are not sufficiently frequent at $z < 1$ to increase significantly the density of massive quiescent galaxies.

We find that the evolution of the star-forming MF is strongly mass-dependent. The low-mass end evolves more rapidly than the high-mass end. If we consider an evolution purely driven by star formation, the low-mass galaxies evolve by almost 1 dex between $1.5 < z < 2$ and $0.2 < z < 0.5$, while the stellar mass of the most massive galaxies increases by less than 0.2 dex in the same time interval. The lack of evolution of the massive end can be interpreted as a direct consequence of star formation being drastically reduced or quenched when a galaxy becomes more massive than $\mathcal{M} > 10^{10.7-10.9} \mathcal{M}_{\odot}$.

4 Link the star formation history and mass density

In Figure 2 (left), we compare the mass density obtained with our data (solid black circles) and the mass density evolution expected by integrating the SFRD compilation of Behroozi et al. (2013, green line and shaded area). We find that the expected mass density is systematically higher by 0.05-0.2 dex than our data, while still consistent with the uncertainties.

We also infer the star formation history from the mass density evolution following Wilkins et al. (2008). We parametrize the star formation history with three free parameters. We fit these three free parameters to reproduce the observed mass density. Our inferred star formation history and the associated uncertainties are shown with the black solid line and the shaded area in Figure 2 (right). The inferred star formation history is compared with the data compiled by Behroozi et al. (2013) and the most recent measurements of the SFRD at $0 < z < 4$ based on UV (Cucciati et al. 2012), IR (Gruppioni et al. 2013) and radio data (Karim et al. 2011). This inferred star formation history is in excellent agreement with SFRD measurements at $z < 1.5$, while we find differences of 0.2 dex at $z > 1.5$. However, considering the size of the uncertainties at $z > 1.5$, the SFRD and mass density data still provide a consistent picture of the star formation history.

We also develop a new method to estimate the specific SFR (SFR/M) from the mass function evolution. By comparing the star-forming MFs at two different epochs (after having removed the contribution of galaxies quenched during the considered time interval), we derive the sSFR from $z \sim 0.5$ up to $z < 4$. We find that the sSFR increases continuously at $1 < z < 4$ for our considered mass range $10^{10}\mathcal{M}_{\odot} \leq \mathcal{M} \leq 10^{10.5}\mathcal{M}_{\odot}$. This new method is complementary to direct sSFR measurements at $z > 2$, which are very sensitive to dust extinction (e.g. Bouwens et al. 2009) or SED modeling (e.g. Stark et al. 2013).

We gratefully acknowledge the contributions of the entire COSMOS collaboration consisting of more than 100 scientists. More information on the COSMOS survey is available at http://www.astro.caltech.edu/cosmos. Based on data products from observations made with ESO Telescopes at the La Silla Paranal Observatory under ESO programme ID 179.A-2005 and on data products produced by TERAPIX and the Cambridge Astronomy Survey Unit on behalf of the UltraVISTA consortium.

References

Arnouts S., Moscardini L., Vanzella E. et al., 2002, MNRAS, 329, 355
Arnouts S., Walcher C.J., Le Fèvre O. et al., 2007, A&A, 476, 137
Behroozi P.S., Wechsler R.H. & Conroy C., 2013, 770, 57
Bruzual G. & Charlot S., 2003, MNRAS, 344, 1000
Calzetti D., Armus L., Bohlin R.C. et al., 2000, ApJ, 533, 682
Capak P., Abraham R.G., Ellis R.S. et al., 2007, ApJS, 172, 284
Cucciati O., De Lucia G., Zucca E. et al., 2012, A&A, 548, 108
Eddington A. S., 1913, MNRAS, 73, 359
Gruppioni C., Pozzi F., Rodighiero G. et al., 2013, MNRAS, 432, 23
Ilbert O., Tresse L., Arnouts S. et al., 2004, MNRAS, 351, 541
Ilbert O., Tresse L., Zucca E. et al., 2005, A&A, 439, 863
Ilbert O., Arnouts S., McCracken H.J. et al., 2006, A&A, 457, 841
Ilbert O., Capak P., Salvato M. et al., 2009, ApJ, 690, 1236
Ilbert O., Salvato M., Le Floc'h E. et al., 2010, ApJ, 709, 644
Ilbert O., McCracken H.J., Le Fèvre O. et al., 2013, A&A, 556, A55
Karim A., Schinnerer E., Martínez-Sansigre A. et al., 2011, ApJ, 730, 61
Krogager J.K et al., 2013, submitted to ApJ, astro-ph/1309.6316
Lilly S.J., Le Fèvre O., Renzini A. et al., 2007, ApJS, 172, 70
McCracken H.J., Milvang-Jensen B., Dunlop J. et al., 2012, A&A, 544, 156
Onodera M., Renzini A., Carollo M. et al., 2012, ApJ, 755, 26
Peng Y.J., Lilly S.J., Kovač K. et al., 2010, ApJ, 721, 193
Polletta M., Tajer M., Maraschi L. et al., 2007, ApJ, 663, 81
Scoville N., Aussel H., Brusa M. et al. 2007, ApJS, 172, 1
Stark D., Schenker M.A., Ellis R. et al., 2013, ApJ, 763, 129
Wilkins S.M., Trentham N. & Hopkins A.M., 2008, MNRAS, 385, 687

SF2A 2013
L. Cambrésy, F. Martins, E. Nuss and A. Palacios (eds)

SEARCHING FOR PROTOCLUSTERS IN THE FAR–INFRARED WITH HERSCHEL/SPIRE

E. E. Rigby[1], H. J. A. Röttgering[1], N. A. Hatch[2], B. Sibthorpe[3], Y. K. Chiang[4] and R. Overzier[4 5]

Abstract. Protoclusters, the high-redshift ancestors of local galaxy clusters, are powerful laboratories for tracing the emergence of large-scale structure, and studying the evolution of galaxies in dense environments. This article presents the results of the first far-infrared, wide-field survey of protoclusters, the ancestors of local galaxy clusters, carried out using the SPIRE instrument on-board the *Herschel* Space Observatory, over the key redshift range $2 < z < 4$.

Examination of the environment within 6 comoving Mpc of the central radio galaxy in each field, reveals that ∼11% of fields contain a $> 3\sigma$ far-infrared excess in source numbers, and there is a tentative trend for the most powerful radio galaxies to host the largest galaxy overdensities. These protocluster candidates are generally contained within 6 comoving Mpc, which is in agreement with simulations and previous work.

Keywords: galaxies, clusters, high–redshift, far–infrared

1 Introduction

Studies of protoclusters, the high–redshift seeds of local rich clusters, are an important tool for understanding galaxy and cluster formation during a crucial epoch of their evolution. Historically these overdense structures have been located by targeting luminous high–redshift radio galaxies (HzRGs) as these massive objects are the likely progenitors of Brightest Cluster Galaxies; see Miley & De Breuck (2008) for a review.

Far–infrared observations are a key tool in finding and characterising star–forming protocluster members. They allow the amount of dust–obscured star formation at $2 < z < 4$, when these galaxies build up most of their stellar mass, to be measured by breaking the degeneracy between age and dust content in spectral energy distribution modelling.

The normal field of view of most infra–red or optical instruments is comparable, or even smaller than the angular size of protoclusters ($\sim 10'$), which severely hampers their study. The *Herschel* Space Observatory (Pilbratt et al. 2010)*, with its combination of sensitivity and fast mapping speed, has improved this situation and far–infrared protocluster candidates are beginning to be discovered within the surveys carried out with *Herschel* (e.g. Ivison et al. 2013; Valtchanov et al. 2013, Clements et al. in prep). However, since protoclusters are rare structures the numbers discovered in this way are likely to be low.

This article presents the results of a targeted, survey of 26 HzRG fields that uses the Spectral and Photometric Imaging REciever (SPIRE; Griffin et al. 2010) on–board *Herschel* to map an area sufficient to encompass the full protocluster extent, together with its surrounding environment. For further details see Rigby et al. (2013). Throughout this article a concordance cosmology is assumed, with values for the cosmological parameters of $H_0 = 71$ km s^{-1}Mpc^{-1}, $\Omega_m = 0.27$ and $\Omega_\Lambda = 0.73$. This gives a physical scale at $z = 2$ of 8.475 kpc/$''$ and 7.083 kpc/$''$ at $z = 4$. These correspond to ∼1.5 comoving Mpc/$'$ and ∼2.1 comoving Mpc/$'$ respectively.

[1] Leiden Observatory, P.O. Box 9513, 2300 RA, Leiden, The Netherlands
[2] School of Physics and Astronomy, University of Nottingham, University Park, Nottingham NG7 2RD, UK
[3] SRON Netherlands Institute for Space Research, Landleven 12, 9747 AD, Groningen, The Netherland
[4] Department of Astronomy, The University of Texas at Austin, Austin, TX 78712
[5] Observatório Nacional, Rua José Cristino, 77. CEP 20921-400, São Cristóvão, Rio de Janeiro-RJ, Brazil

*Herschel is an ESA space observatory with science instruments provided by European-led Principal Investigator consortia and with important participation from NASA.

2 The *Herschel* protocluster survey

The 26 HzRGs selected for this work have $L_{500\mathrm{MHz}} > 10^{28.5}$ W Hz^{-1} and are evenly spread across $2 < z < 4$. Eight are known protoclusters, identified via previous Lyα or Hα observations. They were observed at 250, 350 and 500 μm with SPIRE, and the resulting maps cover areas of 400 – 900 arcmin^2.

The SPIRE data were reduced using the standard *Herschel* pipeline and individual catalogues for each of the 3 bands were created using the STARFINDER algorithm (Diolaiti et al. 2000). These were then combined, using the 500 μm catalogue as a prior, to create a matched catalogue for each field. Of the 26 original fields, 7 were excluded from the subsequent analysis as they were contaminated by galactic cirrus. Full details of the data reduction and source extraction can be found in Rigby et al. (2013).

2.1 High–redshift selection

Before searching for potential protocluster–related overdensities in the far–infrared data it is useful to impose a cut to select sources which lie near the redshift of the HzRG in each field. A simple colour cut ($f_{350\mu m}/f_{250\mu m} \geq 0.85$ for instance) will select sources with $z \gtrsim 2$ (e.g. Amblard et al. 2010), but, since the HzRGs cover $2 < z \lesssim 4$, contaminating foreground galaxies will still remain in a large proportion of the fields. A more sophisticated approach is to use a custom–colour selection, tailored to the redshift of each HzRG; this technique is illustrated in Figure 1. This allows the search to be restricted to sources with estimated redshifts within $\pm 0.2(1+z)$ of the HzRG only.

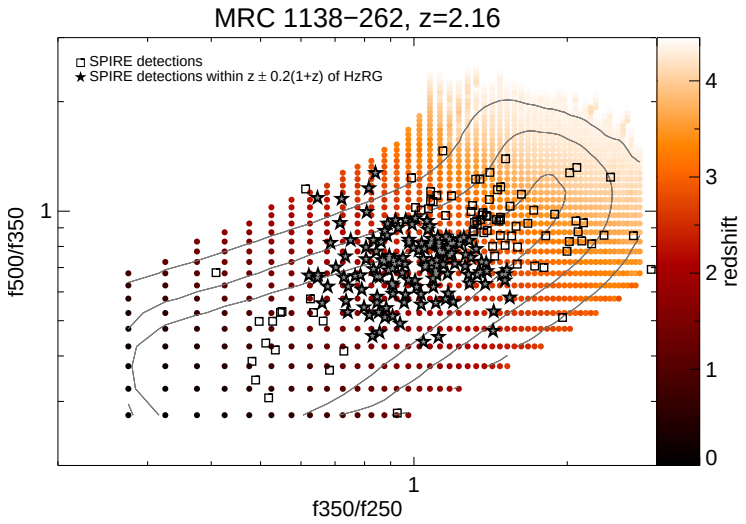

Fig. 1. SPIRE colour–colour diagram for one of the HzRG fields, illustrating the custom–colour redshift selection. Catalogue sources are selected to lie within $\pm 0.2(1+z)$ of the redshift of the HzRG by comparing their SPIRE colours with those of an artificially redshifted galaxy template (constructed following Roseboom et al. 2012). Stars and squares indicate sources selected and rejected as potential protocluster members respectively; solid points show the colour track of the template galaxy, broadened by a Gaussian uncertainty of 10%, as it evolves in redshift. Lines show the 1, 2 and 3σ contours in the template distribution.

3 Surface density analysis

After applying the custom colour redshift selection to each field the galaxy surface density is calculated by counting the number of sources within 6 comoving Mpc of the HzRG position. A reference field, drawn from the SPIRE archive, is used to determine the surface density of background galaxies for comparison, after applying the same colour selections. Figure 2 shows the results, plotted against the redshift and radio luminosity of the central HzRGs. Of the 19 fields, 2 are $> 3\sigma$ overdense and both are not previously known protoclusters (only 1 of the known protoclusters shows signs of an overdensity, but only at the 2σ level). Larger overdensities tend to

lie at $L_{500\mathrm{MHz}} \gtrsim 10^{29}$ and $z < 3$, but there are no definite trends with either parameter. However, this apparent preference for brighter HzRGs is consistent with previous work Galametz et al. (2012, and references therein).

The 2 fields with the strongest overdensities are detected at the 3.9 and 4.3σ level respectively. The probability of finding 2 $\geq 3\sigma$ overdensities such as these by chance, given that 19 fields were observed is 5×10^{-4}. These results, therefore, are inconsistent with being due to random background fluctuations.

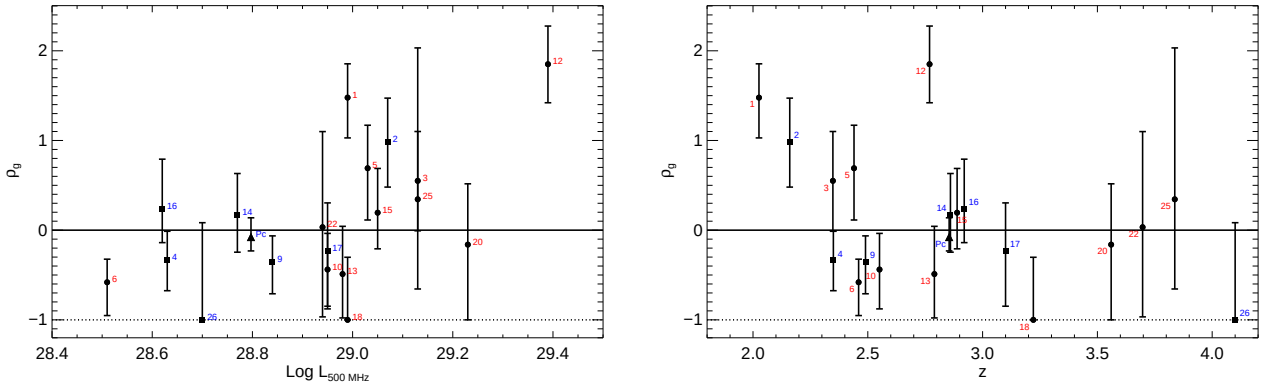

Fig. 2. Left: The overdensity of galaxies in each field as a function of radio power of the central HzRG. This is defined as $\rho_{\mathrm{g}} = (\rho_{\mathrm{obs}} - \rho_{\mathrm{bkg}})/\rho_{\mathrm{bkg}}$ where ρ_{obs} and ρ_{bkg} are the observed surface density and mean background surface density respectively. **Right:** The overdensity of galaxies in each field as a function of redshift of the central HzRG. In both cases galaxies are colour–selected from the matched catalogue and counted within a radius of 6 comoving Mpc and $\pm 0.2(1+z)$ of the position and redshift of the HzRG; only the 19 low–cirrus fields are considered. Numbers correspond to the field labels. Blue colours and square symbols highlight the 7 known protoclusters, and the average overdensity of these fields is labelled 'Pc'. A value of $\rho_{\mathrm{g}} = -1$ (indicated by the horizontal dotted line) corresponds to a field containing no galaxies which satisfied the position and redshift criteria.

4 Are the overdensities consistent with HzRG-centred protoclusters?

A simple characterisation of the galaxy overdensities seen here can be found by comparing them to protocluster predictions from cosmological simulations. Chiang et al. (in prep) follow the evolution with redshift of ~ 3000 clusters in the Millennium Simulation (Springel et al. 2005; Guo et al. 2011), and can therefore match the properties of a local massive cluster to the high–redshift protocluster it grew from. This is compared to the *Herschel* results by applying a redshift–dependent cut in star–formation rate ($SFR \geq c10^{0.2z}$ $\mathrm{M}_{\odot}$/yr), assuming that the detected galaxies mirror the highest rank of SFR in the simulated galaxy population at a given redshift.

Figure 3 shows the variation in the number of member galaxies with radial extent for three separate bins in simulated cluster mass (defined at $z = 0$). Also shown is the position of the average $\geq 3\sigma$ galaxy overdensities seen in the *Herschel* data; this implies an enclosed mass for these structures of $> 10^{14}$ $\mathrm{M}_{\odot}$, which is consistent with that determined previously for HzRG–selected protoclusters (e.g. Venemans et al. 2007; Hatch et al. 2011). However, it should be noted that the large redshift range searched means that contamination of the overdensity from foreground and background galaxies is likely. Firm confirmation of the galaxy excesses seen here can only be done by reducing the redshift uncertainty.

5 Summary and Conclusions

Investigating the far–infrared environments surrounding 19 HzRGs has revealed significant galaxy overdensities in 2 fields. These are unlikely to be due to random background fluctuations and are consistent with simulated protoclusters of mass $> 10^{14}$ $\mathrm{M}_{\odot}$.

The surface density of these fields at these wavelengths is generally low, which must in part be due to the large SPIRE beam making overdensities hard to identify here. Overall these results demonstrate that *Herschel* has the potential to identify protocluster candidates, but that this is a less successful technique here than at other wavelengths. It is likely that SPIRE is probing different structures than those identified using classical

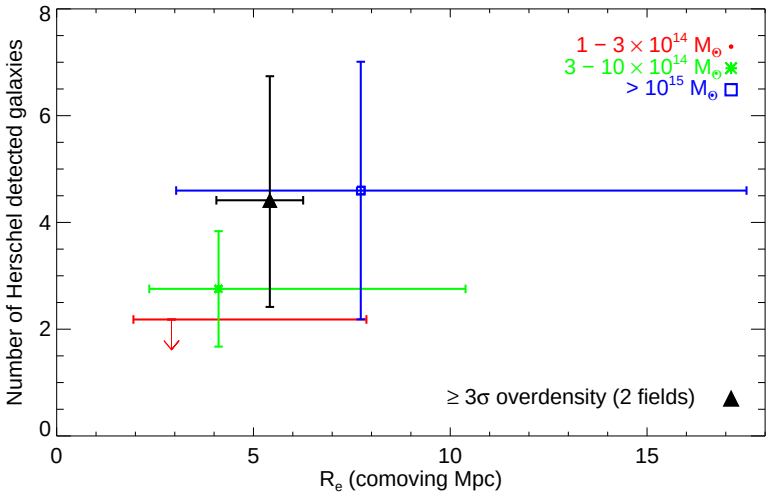

Fig. 3. The number of galaxies contained within simulated protoclusters as a function of their radial extent, for 3 different bins in descendent (i.e. $z = 0$) mass (coloured points). The black triangle shows the average size and number of galaxies of the $\geq 3\sigma$ overdensities in the *Herschel* sample. The uncertainties on the simulated points represent the spread in the simulated distribution; the uncertainties on the real data point come from the spread in the radial extent calculation.

narrow–band or mid–infrared imaging. Future work will combine these SPIRE data with forthcoming radio imaging to improve the selection of protocluster member galaxies, and understand the different far–infrared populations.

References

Amblard, A., et al. 2010, A&A, 518, L9
Diolaiti, E., Bendinelli, O., Bonaccini, D., et al. 2000, Proc. SPIE, 4007, 879
Galametz, A., Stern, D., De Breuck, C., et al. 2012, ApJ, 749, 169
Griffin, M. J., et al. 2010, A&A, 518, L3
Guo, Q., White, S., Boylan-Kolchin, M., et al. 2011, MNRAS, 413, 101
Hatch, N. A., De Breuck, C., Galametz, A., et al. 2011a, MNRAS, 410, 1537
Ivison, R. J., Swinbank, A. M., Smail, I., et al. 2013, arXiv:1302.4436
Miley, G., & De Breuck, C. 2008, A&A Rev., 15, 67
Pilbratt, G. L., et al. 2010, A&A, 518, L1
Roseboom, I. G., Ivison, R. J., Greve, T. R., et al. 2012, MNRAS, 419, 2758
Rigby, E. E., Hatch, N. A., Röttgering, H. J. A. et al. 2013, MNRASsubmitted
Springel, V., White, S. D. M., Jenkins, A., et al. 2005, Nature, 435, 629
Valtchanov, I., Altieri, B., Berta, S., et al. 2013, arXiv:1309.4223
Venemans, B. P., Röttgering, H. J. A., Miley, G. K., et al. 2007, A&A, 461, 823

Session 19

L'exploration des systèmes planétaires avec PLATO

SF2A 2013
L. Cambrésy, F. Martins, E. Nuss and A. Palacios (eds)

ASTROPHYSICAL FALSE POSITIVES IN EXOPLANET TRANSIT SURVEYS: WHY DO WE NEED BRIGHT STARS ?

A. Santerne[1], R. F. Díaz[2], J.-M. Almenara[2], A. Lethuillier[2], M. Deleuil[2] and C. Moutou[2,3]

Abstract. Astrophysical false positives that mimic planetary transit are one of the main limitation to exoplanet transit surveys. In this proceeding, we review the issue of the false positive in transit survey and the possible complementary observations to constrain their presence. We also review the false-positive rate of both *Kepler* and *CoRoT* missions and present the basics of the planet-validation technique. Finally, we discuss the interest of observing bright stars, as *PLATO 2.0* and *TESS* will do, in the context of the false positives. According to simulations with the Besançon galactic model, we find that *PLATO 2.0* is expected to have less background false positives than *Kepler*, and thus an even lower false-positive rate.

Keywords: transit; exoplanet; false positive; galactic model; photometry; radial velocity

1 Astrophysical false positives in transit surveys

Transiting exoplanets are the only planet for which it is possible to measure independently their mass and their radius. From these measurements, it is then possible to determine their bulk density and to model their internal structure. Since they pass in front or behind their host star, it is also possible to probe their atmosphere composition through transmission or emission spectroscopy. Therefore, transiting exoplanets strongly constrain theories of planet formation, migration and evolution (e.g. Mordasini et al. 2009, 2012).

Many photometric-transit surveys are searching for new transiting exoplanets, from the ground with e.g. SuperWASP, HATNet, etc... (Collier Cameron et al. 2007; Bakos et al. 2007) and from space with *CoRoT* (Baglin et al. 2006) and *Kepler* (Borucki et al. 2009). However, searching for new transiting exoplanets is not an easy task. Many configurations of diluted eclipsing binaries or diluted transiting planet might mimic the photometric transit of an exoplanet (Cameron 2012; Santerne et al. 2013, and Fig. 1). If they are not rigorously identified, those fake exoplanets (so-called "false positives") might bias the distributions of planets used to constrain theories of planet formation, migration and evolution. More importantly, those false positives might lead planet theorists to wrong conclusions (C. Mordasini, Planet Validation Workshop).

To establish a new transiting exoplanet, one should first check that the observed photometric signal is due to a planet or to a false-positive scenario. For that, different kind of complementary observations can be used:

- Ground-based high-resolution photometry (Deeg et al. 2009) or centroid measurement (Bryson et al. 2013) to reject background eclipsing binary contaminating the target's PSF (Almenara et al. 2009). Adaptive optics images (Adams et al. 2012) or speckle observations (Howell et al. 2011) can also be used to constrain, closer to the star, the presence of a contaminant.
- Infrared photometry to constrain the presence of a contaminating star with a different color than the target (Fressin et al. 2012).
- High-resolution spectroscopy to identify multiple stellar systems (e.g. Santerne et al. 2012).

[1] Centro de Astrofísica, Universidade do Porto, Rua das Estrelas, 4150-762 Porto, Portugal
[2] Aix Marseille Université, CNRS, LAM (Laboratoire d'Astrophysique de Marseille) UMR 7326, 13388, Marseille, France
[3] CNRS, Canada-France-Hawaii Telescope Corporation, 65-1238 Mamalahoa Hwy., Kamuela, HI 96743, USA

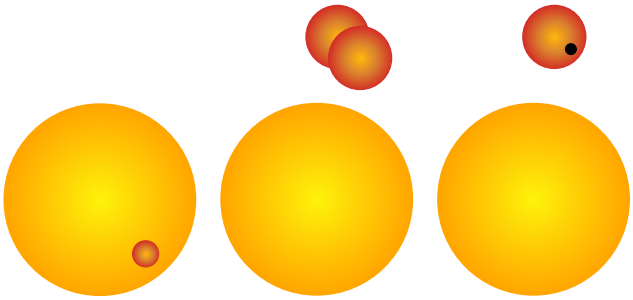

Fig. 1. Sketches of the main false-positive scenarios occurring in transit surveys. From left to right: undiluted eclipsing binary (e.g. eclipsing low-mass star); background eclipsing binary or eclipsing binary in triple system; background transiting planet or companion transiting planet

Precise radial-velocity (RV) observations can be used to measure the mass of the transiting object. If this transiting object has a mass compatible with the planet's mass range, the planet is therefore established (e.g. Santerne et al. 2011b,c).

2 The false-positive probability

The *CoRoT* and *Kepler* space missions have discovered respectively $\sim$ 600 (Deleuil et al., in prep.) and $\sim$ 3000 exoplanet-candidates (Batalha et al. 2013) around host stars of magnitude ranging between $\sim$ 10 and 16. Radial velocity follow-up observations of such faint stars are limited by the photon noise (Santerne et al. 2011a). Figure 2 displays the expected radial velocity semi-amplitude of the *Kepler* candidates (assuming an Earth density for KOIs smaller than 2.5 $R_\oplus$, and the density of Neptune for those larger than 2.5 $R_\oplus$) as function of the magnitude of the host star. The majority of the *Kepler* candidates are expected to present a RV signal at the level of a few $m.s^{-1}$ on stars fainter than the 14^{th} magnitude. Such precision is below the photon noise of current spectrographs, like SOPHIE and HARPS, in one hour of exposure time (Santerne et al. 2011a, and Fig. 2). We therefore anticipated that only a small fraction (5% to 10%) of all the *Kepler* candidates can be established as bona-fide planet by measuring the Doppler reflex motion of the host star. For the *CoRoT* candidates, only 5% of the candidates have been established as planet and another $\sim$ 5% of the candidates are not resolved pending future observations with improved capabilities (e.g. with ESPRESSO on the ESO–VLT).

Identifying the false positive detections is a crucial task. Since only a small fraction of the *Kepler* and *CoRoT* candidates can be established as bona-wide planets, one alternative solution is to estimate the false positive probability (FPP) of the candidates. If the FPP is very low, planets statistics used to constrain theories might be done based on the candidates. Unfortunately, even if the FPP is low in average, there might exists some regions of the candidates parameters space which are more affected by the false positives (the FPP is not expected to be a constant value over all the candidates' parameter space; Santerne et al. 2012; Fressin et al. 2013). If the theories try to reproduce high-FPP regions of the parameters space, it might incorrectly constrains the theories.

The FPP of the *CoRoT* mission has been estimated to be around 80% (Deleuil et al., in prep.). The FPP of the *Kepler* mission has been much more discussed. First, Morton & Johnson (2011) found a low-value of the FPP, in average lower than 5% and lower than 10% for 90% of the *Kepler* candidates. By observing with the SOPHIE spectrograph at Observatoire de Haute-Provence, Santerne et al. (2012) found a much higher FPP ($34.8\% \pm 6.5\%$) for the giant close-in *Kepler* candidates. This observational value is not compatible with the Morton & Johnson (2011) estimation. Later, Fressin et al. (2013) re-estimate the overall *Kepler* FPP to be $9.4\% \pm 0.9\%$ by modeling the efficiency of the *Kepler* pipeline to detect planets. This last value, is compatible with the measurement from Santerne et al. (2012), in the giant close-in regime. Finally, Santerne et al. (2013) studied the occurrence of eclipsing binaries for which only the secondary eclipse is seen from the Earth (because of some fine tuning of the orbital eccentricity, argument of periastron and orbital inclination) and re-evaluate the global *Kepler* FPP to $11.3\% \pm 1.1\%$.

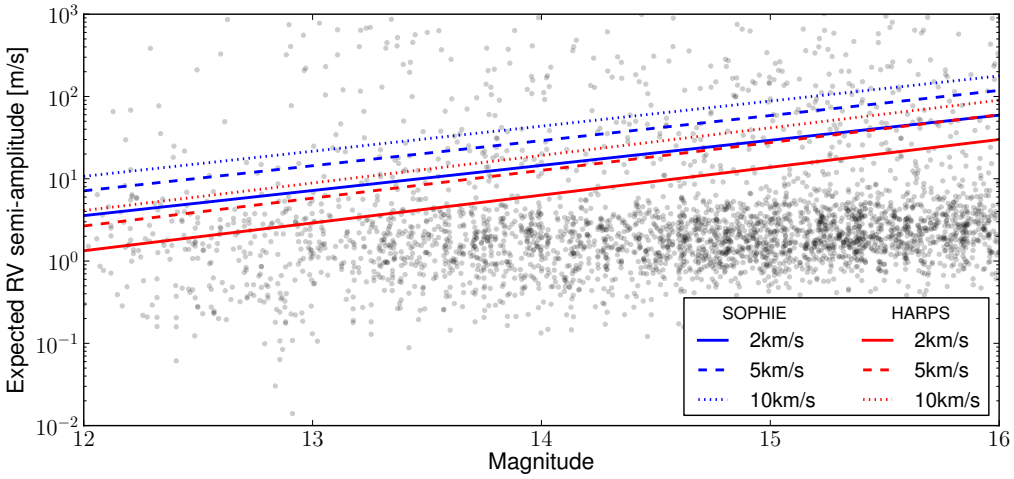

Fig. 2. Expected radial velocity amplitude of the *Kepler* candidates as function of the magnitude of their host star. The mass of the candidates, needed to estimate the amplitude, has been estimated using the estimated radius and densities of solar system objects. The red and blue solid, dashed and dotted lines represent the photon noise limitation in an one-hour exposure time observation with HARPS and SOPHIE (respectively) for a star with a vsini of 2km s^{-1}, 5km s^{-1} and 10km s^{-1} (respectively).

The difference between *Kepler* and *CoRoT* FPP can be explained by the fact that *Kepler* is much more efficient to reject background eclipsing binary and background transiting planet than *CoRoT*, thanks to the measurement of the centroid during the transit. This can also be explained by the fact that the *Kepler* telescope observed at higher latitude in the galactic plane than *CoRoT*, where the stellar background is slightly less dense.

The *Kepler* FPP of $11.3\% \pm 1.1\%$ is still too high to allow statistical analysis of the transiting planets based on the *Kepler* candidates neglecting the false positives. About 300 of these candidates are thus expected to be impostors (This number corresponds to $\sim 1/3$ of all the planets discovered since 18 years). Moreover, these impostors can be more common in some regions of the parameter space, as for example, in the giant candidate regime (Santerne et al. 2012). According to the recent study of Fressin et al. (2013), most of the *Kepler* false positives are produced by background eclipsing binaries and planet transiting a star physically bound with the target.

3 The planet-validation technique

To establish the planetary nature of a candidate, another alternative solution is the so-called planet-validation technique (Torres et al. 2011). It consists in computing the probability of the planet scenario against an exhaustive set of false-positive scenarios. If the planet scenario is significantly the highest-probable scenario, thus the planet is considered as validated. Such model comparison can only be done in the Bayesian framework in which hypothesis have a probability (this is not the case in the frequentist approach). Basically, the odds ratio between each pair of scenarios is computed as following:

$$\mathcal{O}_{ij} = \frac{p\left(H_i|D,I\right)}{p\left(H_j|D,I\right)} = \frac{p\left(H_i|I\right)}{p\left(H_j|I\right)} \cdot \frac{p\left(D|H_i,I\right)}{p\left(D|H_j,I\right)} = \frac{p\left(H_i|I\right)}{p\left(H_j|I\right)} \cdot \frac{\int_{\vec{\theta_i}} p\left(\vec{\theta_i}\middle|H_i,I\right) \cdot p\left(D\middle|\vec{\theta_i},H_i,I\right) d\vec{\theta_i}}{\int_{\vec{\theta_j}} p\left(\vec{\theta_j}\middle|H_j,I\right) \cdot p\left(D\middle|\vec{\theta_j},H_j,I\right) d\vec{\theta_j}}, \tag{3.1}$$

where H_i is the hypothesis i (e.g. transiting planet or background eclipsing binary, etc...), D is the available data, I the *a priori* information and $\vec{\theta_i}$ is the parameter space of the model relative to the hypothesis i. To compute this equation, it is needed to compute, first, the hypothesis prior factor (first part of the equation), and then, the Bayes' factor (second part of the equation) which is the ratio between the two hypothesis *posterior* distributions marginalized over the whole parameter space. While the Bayes' factor is estimated from the data

using tools such as PASTIS (Díaz et al. 2013), the first term of this equation required to know the probability of the two considered hypothesis. When validating a planet, this hypothesis prior factor is the ratio between, e.g., the probability that a given star host a planet, over the probability that a given star is aligned by chance with an eclipsing binary.

To compute these *a priori* hypothesis probability, the occurrence of planets and binaries as well as the background stellar density are needed. The occurrence rate of planets and binaries have been estimated based on results from dedicated surveys (Howard et al. 2010; Mayor et al. 2011; Fressin et al. 2013; Halbwachs et al. 2003; Raghavan et al. 2010). The background density can be estimated using galactic star-count models like TRILEGAL (Girardi et al. 2005) or the Besançon Galactic Model (Robin et al. 2003). Roughly, a target of magnitude m_{v_t} which present a transit of depth δ_t might be mimicked by a background eclipsing stellar contaminant of magnitude m_{v_c} and depth δ_c following the equation:

$$m_{v_c} - m_{v_t} = 2.5 \log \left(\frac{\delta_c}{\delta_t} \right) \tag{3.2}$$

Therefore, an equal mass eclipsing binary with depth $\delta_c = 50\%$ might mimic a 50ppm-depth transit on a star 10 magnitude* brighter. Since *CoRoT* and *Kepler* targeted stars with magnitude up to 16, the population of potential false positives are stars up to magnitude 26.

4 Towards brighter stars with TESS and PLATO 2.0 space missions

Observing stars much brighter than *CoRoT* and *Kepler* targets, such as those in the scope of *TESS* and *PLATO 2.0* have a main interest for transiting exoplanet characterization: radial velocity follow-up will be much more efficient, being limited only by the instrumental precision of spectrographs. With the next-generation spectrographs like ESPRESSO (ESO – VLT), it will be possible to characterize the mass of planets down to Earth-like planets in the habitable zone. Therefore, it will be possible to constrain the bulk density of *TESS* and *PLATO 2.0* planets with an unprecedented accuracy. In the case of *PLATO 2.0*, stellar mass, radius and age of planet hosts will be determined precisely thanks to simultaneous asteroseismology, improving even more the accuracy of planet's physical parameters. Many other scientific interests (in planetology as well as stellar physics) will be conducted by targeting bright stars and are discussed in Rauer et al. (2013) in the context of the *PLATO 2.0* mission.

Targeting bright stars also have a great interest in terms of astrophysical false positives. Indeed, we might expect that by targeting stars brighter than those observed by *Kepler*, the background stellar density will be much lower, and thus, there will be much lower background false positives (background eclipsing binaries and background transiting planets). This is true only if the instrument's PSF size and the stellar density of the various fields are similar. To qualitatively compare the two effects, we generated field population using the Besançon galactic model within 1 deg^2 up to magnitude R=27 for extreme coordinates in the *Kepler* fields (from b = 5.6° – l = 75.7° to b = 20.9° – l = 76.5°) and in the preliminary-defined northern long run of the *PLATO 2.0* mission (from b = 0° – l = 68.5° to b = 65° – l = 40°). We then extrapolated the star count provided by the Besançon galactic model to the exclusion radius of *Kepler* and *PLATO 2.0* (See Fig. 3). For *Kepler*, we considered that *Kepler* is able to discard background eclipsing binaries located in a different pixel than the target, hence with an exclusion radius of 2 arcsec† (See Fig. 3). Typically, considering a *Kepler* target of magnitude 16, there is between 0.04 and 0.5 background star within a radius of 2 arcsec that might mimic a planetary transit down to an Earth-size planet. If we assume than *PLATO 2.0* will have the same efficiency than *Kepler* to discard background eclipsing binaries, but with pixels of 15 arcsec (Rauer et al. 2013), there will be between 0.04 and 3.6 stars in the background of a 12$^{\text{th}}$ magnitude target that might mimic an Earth-size planet. These numbers are much larger than for the *Kepler* mission. Fortunately, *PLATO 2.0* will observe stars with 8 up to 32 telescopes (Rauer et al. 2013). Assuming that the centroid precision follows the square root of the number of telescope, we find that the maximum number of background stars aligned by chance with *PLATO 2.0* targets of magnitude 12 mimicking down to an Earth-size planet are 0.45 and 0.11 star for 8 and 32 telescopes (respectively). This means that we might expect less background false positives in the *PLATO 2.0*

*in the same bandpass

†the pixels of the *Kepler* telescope are 3.96 arcsec large

mission compared with *Kepler*, and thus, a lower false-positive rate for *PLATO 2.0* (assuming that the rate of bounded false positives is similar for *Kepler* than *PLATO 2.0*). Since *TESS* will observe stars with only one telescope with large pixels, we expect a large number of background false positives, at least for targets close to the galactic plane.

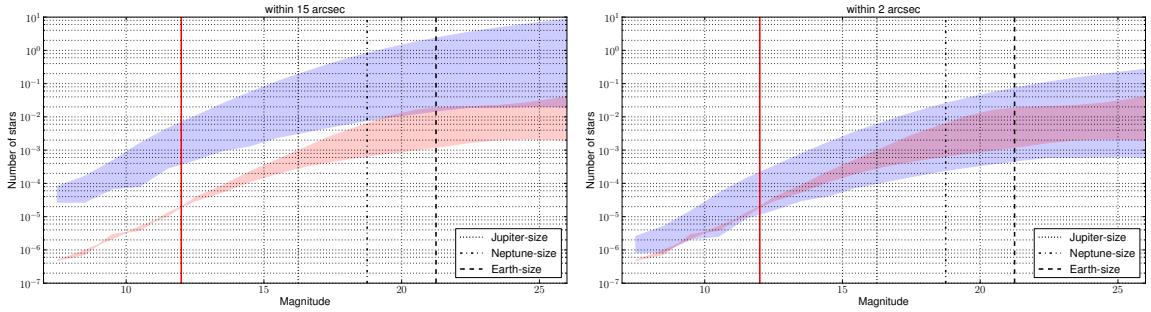

Fig. 3. Background stellar density for *Kepler* field (red area) and *PLATO 2.0* northern field (blue area). The vertical red line indicates a magnitude 12 star and the dotted, dot-dashed and dashed lines indicate the maximum magnitude of a equal-mass eclipsing binary to mimic a Jupiter-size planet, a Neptune-size planet and an Earth-size planet (respectively). **Left** Background stellar density within a radius of 15 arcsec for *PLATO 2.0* and 2 arcsec for *Kepler*. **Right:** Background stellar density within a radius of $\sim$ 2 arcsec for both mission.

We stress that these results are a rough estimation of the false-positive probability of the *PLATO 2.0* mission, in comparison with *Kepler*. A more rigorous analysis of the expected false-positive probability of this mission will be performed as soon as the *PLATO 2.0* fields and list of targets are defined.

5 Conclusions and discussion

Astrophysical false positives are a classical nuisance of exoplanet transit surveys. Neglecting them might lead exoplanet theorists to wrong conclusion. It is therefore crucial to account for them in statistical analysis of transit candidates. For that, the best option is to establish all the candidates by measuring their mass using dedicated Doppler observations. Unfortunately, the *CoRoT* and *Kepler* targets are too faint to allow the characterization of the smallest candidates. The false-positive rate is the key value to perform statistical analysis of the candidates to derive planet properties. For the *CoRoT* mission, the false-positive rate is about 80% while the *Kepler* false-positive rate has been quite discussed. The latest estimation find a value of $11.3\% \pm 1.1\%$ (Santerne et al. 2013). Another possibility is to validate statistically all candidates using tools such as `PASTIS` (Díaz et al. 2013).

Next-generation transit space missions (namely *TESS* and *PLATO 2.0*) will target much brighter stars than *CoRoT* and *Kepler*. First, the Doppler observations will be much more efficient to characterize small planets (especially with new spectrographs like ESPRESSO) and then, we might expected to have less false positives in the scope of *PLATO 2.0* than *Kepler* since the background of bright targets is less dense in potential false positives than for faint targets. We therefore anticipate a lower false-positive rate for *PLATO 2.0* than for *Kepler*. On the other hand, *TESS* will observe bright targets with large pixels within which a significant amount of potential false positives might reside. However, this will strongly depends on the galactic latitude of the target. A more detailed study of the expected false-positive probability of both missions can be performed as soon as the target list is defined.

AS acknowledges the support by the European Research Council/European Community under the FP7 through Starting Grant agreement number 239953. RFD is supported by CNES. AS also acknowledges the administrative council of SF2A for providing him a grant to attend this meeting.

References

Adams, E. R., Ciardi, D. R., Dupree, A. K., et al. 2012, AJ, 144, 42

Almenara, J. M., Deeg, H. J., Aigrain, S., et al. 2009, A&A, 506, 337
Baglin, A., Auvergne, M., Boisnard, L., et al. 2006, 36th COSPAR Scientific Assembly, 36, 3749
Bakos, G. Á., Noyes, R. W., Kovács, G., et al. 2007, ApJ, 656, 552
Batalha, N. M., Rowe, J. F., Bryson, S. T., et al. 2013, ApJS, 204, 24
Borucki, W. J., Koch, D., Jenkins, J., et al. 2009, Science, 325, 709
Bryson, S. T., Jenkins, J. M., Gilliland, R. L., et al. 2013, arXiv:1303.0052
Collier Cameron, A., Bouchy, F., Hébrard, G., et al. 2007, MNRAS, 375, 951
Cameron, A. C. 2012, Nature, 492, 48
Deeg, H. J., Gillon, M., Shporer, A., et al. 2009, A&A, 506, 343
Díaz, R. F., Almenara, J.-M., Santerne, A., et al. 2013, submitted to MNRAS
Faigler, S., Tal-Or, L., Mazeh, T., Latham, D. W., & Buchhave, L. A. 2013, ApJ, 771, 26
Fressin, F., Torres, G., Pont, F., et al. 2012, ApJ, 745, 81
Fressin, F., Torres, G., Charbonneau, D., et al. 2013, ApJ, 766, 81
Girardi, L., Groenewegen, M. A. T., Hatziminaoglou, E., & da Costa, L. 2005, A&A, 436, 895
Halbwachs, J. L., Mayor, M., Udry, S., & Arenou, F. 2003, A&A, 397, 159
Holman, M. J., Fabrycky, D. C., Ragozzine, D., et al. 2010, Science, 330, 51
Howard, A. W., Marcy, G. W., Johnson, J. A., et al. 2010, Science, 330, 653
Howell, S. B., Everett, M. E., Sherry, W., Horch, E., & Ciardi, D. R. 2011, AJ, 142, 19
Mayor, M., Marmier, M., Lovis, C., et al. 2011, arXiv:1109.2497
Mordasini, C., Alibert, Y., Benz, W., & Naef, D. 2009, A&A, 501, 1161
Mordasini, C., Alibert, Y., Georgy, C., et al. 2012, A&A, 547, A112
Morton, T. D., & Johnson, J. A. 2011, ApJ, 738, 170
Rauer, H., Catala, C., Aerts, C. et al. 2013, submitted to EA
Raghavan, D., McAlister, H. A., Henry, T. J., et al. 2010, ApJS, 190, 1
Robin, A. C., Reylé, C., Derrière, S., & Picaud, S. 2003, A&A, 409, 523
Santerne, A., Endl, M., Hatzes, A., et al. 2011a, European Physical Journal Web of Conferences, 11, 2001
Santerne, A., Díaz, R. F., Bouchy, F., et al. 2011b, A&A, 528, A63
Santerne, A., Bonomo, A. S., Hébrard, G., et al. 2011c, A&A, 536, A70
Santerne, A., Díaz, R. F., Moutou, C., et al. 2012, A&A, 545, A76
Santerne, A., Fressin, F., Díaz, R. F., et al. 2013, A&A, 557, A139
Torres, G., Fressin, F., Lissauer, J. J., et al. 2011, Bulletin of the American Astronomical Society, #112.06

Session annulée

Patrimoine des Observatoires

SF2A 2013
L. Cambrésy, F. Martins, E. Nuss and A. Palacios (eds)

DE ASTRONOMICIS INSTRUMENTIS IN UNIVERSITATE MONSPELIENSI

H. Reboul[1]

Abstract. Montpellier hosted one of the first French observatories, and has therefore a long and rich tradition in the development of astronomy as a research topic or as a teaching subject since the 17^{th}th century. This is the reason why such a large collection of astronomical instruments could be gathered and preserved. Recently, the Science university of Montpellier has worked towards the inclusion of this collection on the French National Heritage List (at least for 56 items out of the 240 listed in the inventory), and some of them have been repaired. You will find below the history of this collection which can be accessed online.

Keywords: history, instrumentation, telescopes

1 Introduction

During the 17^{th} century, many scientific societies were created in Languedoc. Both the instruments and the rare books collections preserved by the universities of Montpellier bring a testimony of a long tradition of astronomical observations and teaching. The historical content inside this short review is mainly founded on the following works: Roche (1881); Faidit (1986, 1993, 2001, 2007).

2 The Observatory of the Babote Tower in the 18th century

The Société Royale des Sciences de Montpellier which was officially founded in February 1706 **belonged** to the Parisian 'Académie des Sciences'.

On the 12^{th} May 1706, the academicians used telescopes fastened on masts to make a detailed observation of the total eclipse of the sun; the accounts of this occurrence were published in the Society's Proceedings.

The Assembly of the Languedoc contributed to this scientific progress, and gave their sponsorship by paying for the building of the observatory in the Babote Tower which began to be used in 1745. They also helped the astronomers by buying them an 8-inches Nairne Gregorian telescope in 1784. The scientific works of the astronomers during that period were manifold, focusing on all the usual astronomical topics, but also on the major map-making enterprise at the end of the 18th century in Languedoc.

3 Research and teaching in the 19th century

Created in 1808, the Science Faculty appointed an astronomy professor as soon as 1810. Edouard Roche was a professor in the Faculty during 34 years; it is in Montpellier that he published his major works (i.e. those defining "Roche's" limits and lobes) which would however be acknowledged by the scientific community only a century later. He did a lot for the preservation and the increase of the scientific heritage of the Faculty.

[1] LUPM (UMR 5299) CC 72, Université Montpellier 2, Pl. E. Bataillon, 34095, MONTPELLIER Cedex 5, France

4 From photography to digital images

Photography was the medium through which spectra and images are taken during almost a century. Both its unlinear response and one time use has led towards the invention of very complex instruments to set the standards of these pictures and to extract the astrophysical signals they register. The Montpellier Astronomy Laboratory, created in 1960 has been able to buy, use and keep these instruments and their gradual modifications until the digital photography era.

5 An experiment in astrophysics

The Montpellier Astronomy Laboratory has been able to keep the entirety of the scientific equipment used during its two spatial missions " Artificial Comet " in 1966 and 1969. Among them are spectrographs with fast film reloading and ultra-luminous optics (F/D = 0.65).

6 Preservation and cultural heritage policy

In the sixties, some of these instruments were showcased in the corridors of the Astronomy Laboratory at the Science university. In 1999, they were shown in different exhibitions and 56 of them were listed on the National Heritage List with the help of the DRAC-LR in 2005 and 2006. Dated from 1725 to 1980, 11 of them date back to the 18th century, 17 to the 19th century, and 28 to the 20th cent.

The repairing of the instruments dating from the 18th and 19th century has been paid for by the Scientific Heritage Section of the University: the inventory of the collections it preserves can be accessed online via its website at the following address: `http://www.collections.univ-montp2.fr/les-collections-de-lum2/astronomie/nosearch`. Furthermore, the Association des Amis des collections gives its advice and expertise whenever it is needed.

Some of the items are shown for 18^{th} (Fig. 1) and 19^{th} and 20^{th} (Fig. 2) centuries.

7 Conclusions

An important part of the 18th-century Montpellier Observatory heritage could be transmitted to the Science Faculty. The continuity of the astronomical work of the Faculty has made possible the preservation of most of the major instruments that were used throughout this period. The Science University's undertaking of a heritage preservation policy has made possible the collecting of almost 240 items, among which 56 are now listed on the National Heritage List. It remains now to be found a place where they could be studied and admired more widely.

Many thanks to Elizabeth Denton, curator of the rare books department in the Science university library for fruitful exchanges on the context of that work and for many improvements of this paper.

References

RocheE., 1881, 'Notice sur l'Observatoire de l'ancienne société des sciences de Montpellier', Mémoires de l'Académie des Sciences de Montpellier

Faidit, J.-M., 1986, 'L'Observatoire de la Babote', ISBN 2-9501264-0-5

Faidit, J.-M., 1993, 'Les 'amateurs de sciences' d'une province et le ciel au XVIIIe siècle : Astronomie et Astronomes en Languedoc : approche d'histoire des sciences'. Thèse de l'université Montpellier III

Faidit, J.-M., 2001, "Le pavillon d'astronomie du jardin des plantes" , ISBN 2-9516194-0-5

Faidit, J.-M., 2007, "Limites et lobes de Roche", ISBN 978-2-7117-4017-8

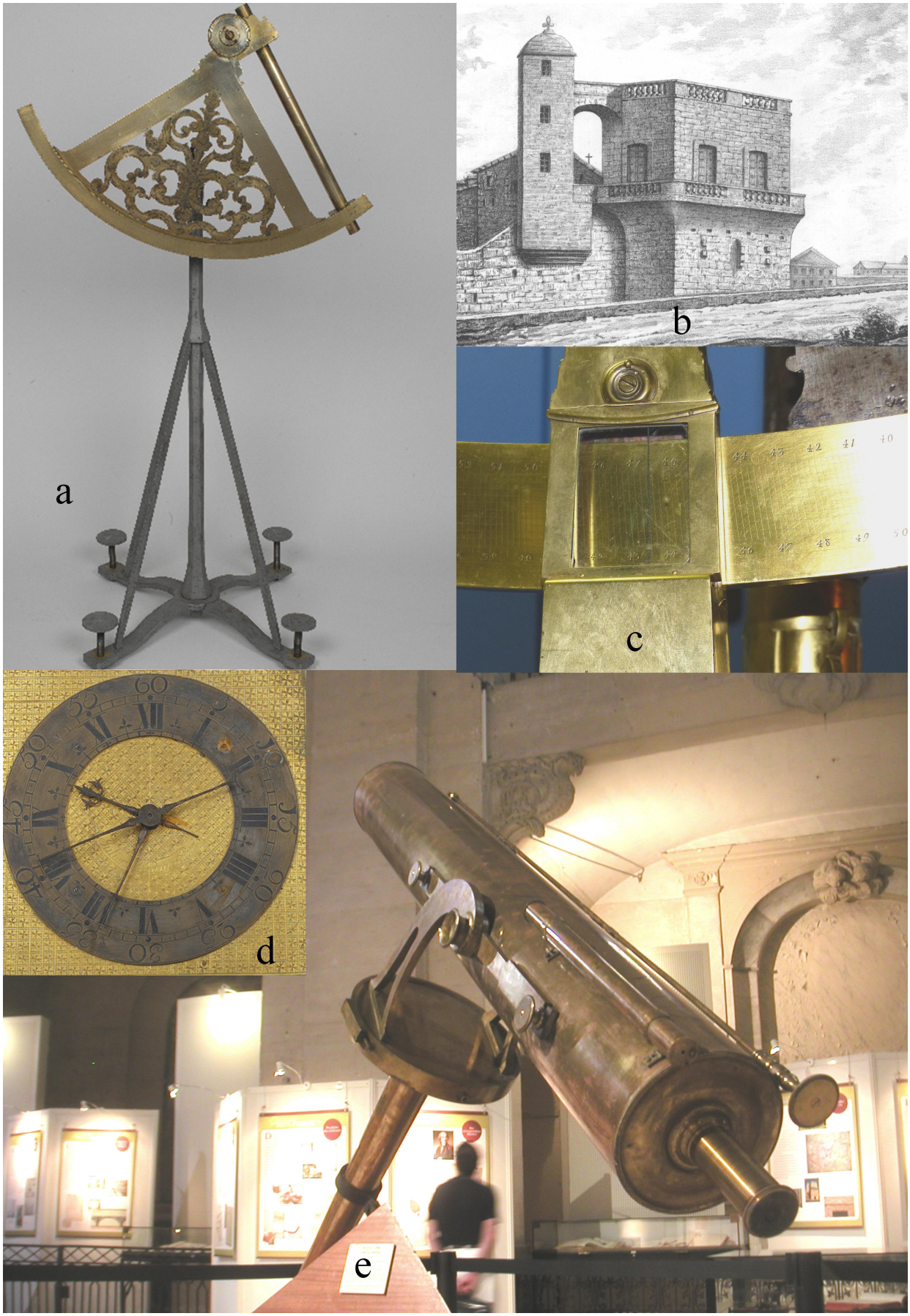

Fig. 1. 18th cent. : **a)** Quadrant by Cadot, Paris in 1730. **b)** Babote Montpellier Observatory (before the building of the second floor in 1788). **c)** detail of 2 feet quadrant by Langlois, Paris in 1736. **d)** Clock by Le Roy,Paris circa 1740.**e)** Gregorian telescope by Nairne, London in 1770 (as shown in 2007 before its repair).

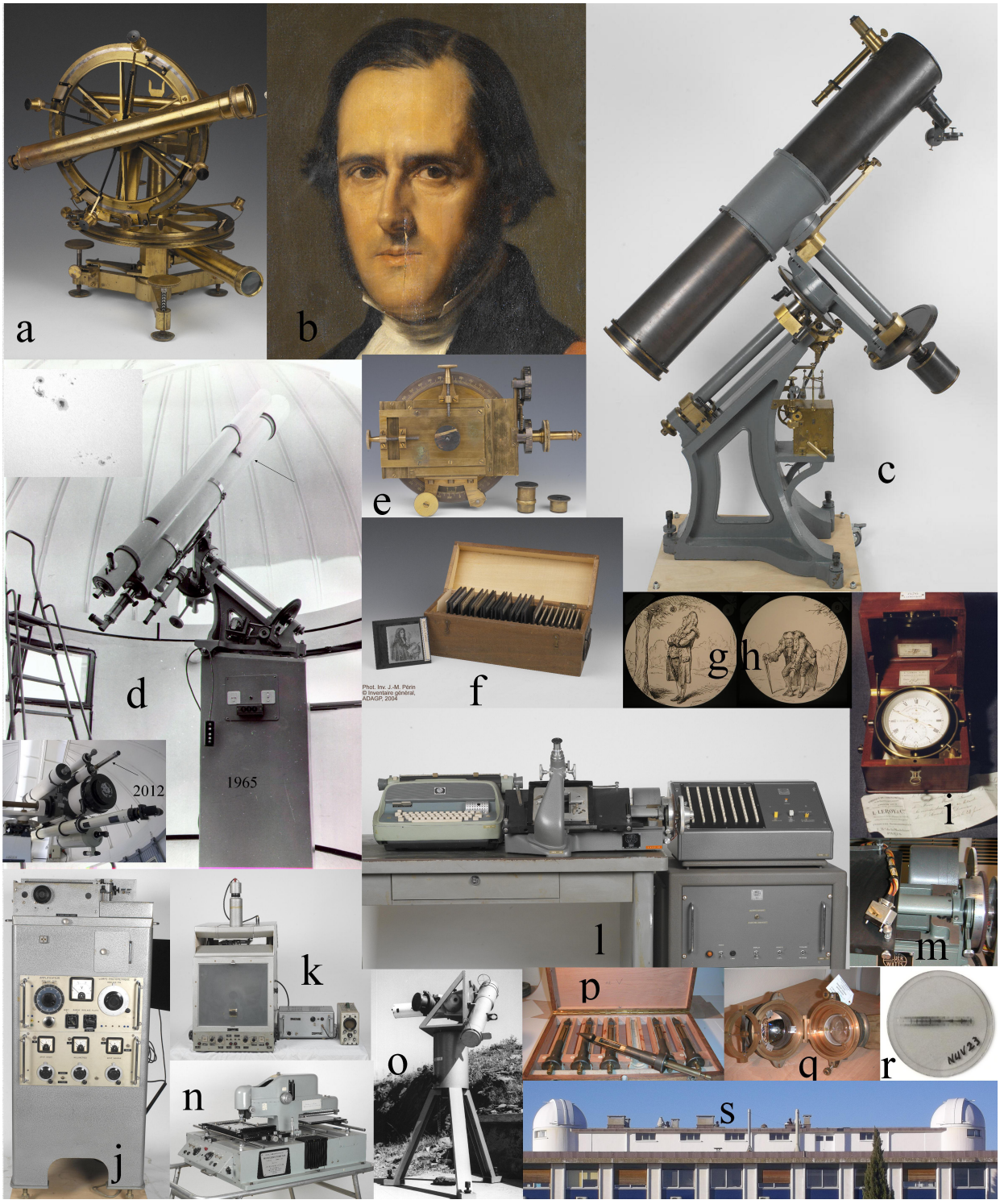

Fig. 2. 19^{th} and 20^{th} cent. : **a)** Theodolite by Gambey, Paris, 1826. **b)** Edouard-Albert Roche, painting by Matet, 1867. **c)** Foucault Telescope by Eichens, Paris, 1877. **d)** Eichens refracting telescope through the centuries : constructed by Eichens in 1873, the main picture shows its installation at OUM2 (Observatory of UM2) in 1964 and insets display, in 2012, its position and sunspots obtained through its lens. **e)** Micrometric ocular of Eichens refracting telescope (d), 1873 . **f, g, h)** Pedagogic and humoristic (g, h) slides, 1900. **i)** Marine chronometer by Louis Leroy, Paris, circa 1900. **j)** Challonge Registering microphotometer by laffineur, 1962. **k** Iris photometer by Askania, 1965. **l, m)** Digital microscope by Hilher & Watts, 1961, modified in 1965 to punch cards. **n** double-beam registering microdensitometer by Joyce, Loebl & Co., circa 1967. **o, p, q, r** 'Artificial Comet' Spatial mission, telescopes, spectrographs, fast-loading film-holders, F/0.65 catadioptric objective of the nebular spectrograph, by REOSC, Paris 1966. r is a spectrum of Kohoutek comet on 26/11/1973 obtained with the silicium F/065 objective on the nebular spectrograph mounted at the Cassegrain focus of the 500 mm telescope of OUM2 (70 min exposure on 103 aO). **s)** general view of OUM2 in 2012.

Author Index